

Green Power, Materials and Manufacturing Technology and Applications II

Edited by
Shaobo Zhong and Zhigang Liu

TTP TRANS TECH PUBLICATIONS

**Green Power, Materials
and
Manufacturing Technology
and
Applications II**

Edited by
Shaobo Zhong
Zhigang Liu

Green Power, Materials and Manufacturing Technology and Applications II

Selected, peer reviewed papers from the
2nd International Conference on
Green Power, Materials and Manufacturing Technology
and Applications
(GPMMTA2012),
July 17-19, 2012, Kunming, China

Edited by

Shaobo Zhong and Zhigang Liu



Copyright © 2012 Trans Tech Publications Ltd, Switzerland

All rights reserved. No part of the contents of this publication may be reproduced or transmitted in any form or by any means without the written permission of the publisher.

Trans Tech Publications Ltd
Kreuzstrasse 10
CH-8635 Durnten-Zurich
Switzerland
<http://www.ttp.net>

Volume 214 of
Applied Mechanics and Materials
ISSN print 1660-9336
ISSN cd 1660-9336
ISSN web 1662-7482

Full text available online at <http://www.scientific.net>

Distributed worldwide by

Trans Tech Publications Ltd
Kreuzstrasse 10
CH-8635 Durnten-Zurich
Switzerland

Fax: +41 (44) 922 10 33
e-mail: sales@ttp.net

and in the Americas by

Trans Tech Publications Inc.
PO Box 699, May Street
Enfield, NH 03748
USA

Phone: +1 (603) 632-7377
Fax: +1 (603) 632-5611
e-mail: sales-usa@ttp.net

PREFACE

Dear Distinguished Delegates and Guests,

2nd International Conference on Green Power, Materials and Manufacturing Technology and Applications (GPMMTA2012) was held in Kunming, China, from July 17-19, 2012, serving as a platform for expertise exchange. GPMMTA 2012 had drawn the attention of researchers from various disciplines: Sustainable Power, Sustainable Materials, Green Manufacturing Technology and Applications, etc.

Persons who attended the conference were engineers, scientists, managers of various companies and professors of the universities abroad and home. We have had record number of submission 632 this year. From which 181 papers have been accepted for presentation at the conference and will be published by TTP, in Advanced Materials Research (AMR) Journal (ISSN: 1022-6680), which is online available in full text via the platform www.scientific.net. AMR should be indexed by EI according the previous TTP index results.

We express our special gratitude to all the members of the General Committee Chairs, Program Committee Chairs, Technical Program Committee and Steering Committee who worked so hard to prepare the conference and who supported the conference so professionally.

International Conference on Green Power, Materials and Manufacturing Technology and Applications (GPMMTA2012) is organized by Southwest Forestry University, Electric Power Research Institute of YNPG, Guizhou University, Yunnan normal University, Jinan University, Tsinghua University, Wuhan Institute of Technology, Shanxi University of Traditional Chinese Medicine and sponsored by National Natural Science Foundation of China (NSFC). Their kind support makes GPMMTA 2012 become possible. Especially, we should thank the TTP.

Finally, we would like to thanks all the authors, speakers and participants of this conference for taking part in and contributing to the International Conference on Green Power, Materials and Manufacturing Technology and Applications.

We hope you have a unique, rewarding and enjoyable week at GPMMTA2012 in Kunming, China.

With our warmest regards,

GPMMTA2012 Organizing Committees

July 17-19, 2012

Kunming, China

GPMMTA 2012

Committees

Conference Chairs

Maode Ma Nanyang Technological University, Singapore
Ying Lu, Monash University, Australia

Program Committee Chairs

K.N.Cao, Electric Power Research Institute, YNPG, China
J.B.Guo, Tsinghua University, China
Zoe Huang, Auckland University of Technology, New Zealand
D.D.Wang, Electric Power Research Institute, YNPG, China
Y.J.Wang, Wuhan University of Technology, China
X.H. Cheng, Guilin University of Technology, China

Organizing Chair

J.S.Shi, Yunnan normal University, China
C.C.Liu, Jinan University, China
Z.G.Liu, Southwest Forestry University, China
T.Han, Electric Power Research Institute, YNPG, China
G.X.Li, Guizhou University, China
F.J. Mai, Guilin University of Technology, China

Contact Co-Chairs

Z.G.Liu, Southwest Forestry University, China
W.J.Du, Chongqing Normal University, China
Publication Chair
M.D.Ma, Nanyang Technological University, Singapore
W.J.Du, Chongqing Normal University, China

Technical Program Committee

Xizhang chen, Jiangsu University, China
Haiqing Si, Nanjing University of Aeronautics and Astronautics, China
Meiqiang Cai, Zhejiang Gongshang University, China
Zirong Zhou, Dongguan University of Technology, China
Enrico Gregori, Institute of Informatics and Telematics, Italian National Research Council (CNR), Italy
Shiwen Mao, Auburn University, USA
Hanif D. Grado Serali, Virginia Tech, USA
George Athanasiou, University of Thessaly, Greece

Ozgur Ercetin, Sabanci University, Turkey
Svilen Ivanov, University of Magdeburg, Germany
John C. S. Lui, Chinese University of Hong Kong, Shatin, Hong Kong, Hong Kong
Hwangnam Kim, Korea University, Korea,
Jun Zou, McMaster University, Canada
Shafiullah Khan, Brunel University, United Kingdom
Sung-Ta Tsai, National Chengchi University, Taiwan
Luciano Lenzini, University of Pisa, Italy
Hassanein Hossam, Queens University, Canada
Sirisha Medidi, Boise State University, USA
Yajun Li, Shanghai Jiao Tong University, China
Rongbo Zhu, South-Central University for Nationalities, China
Yuan Lin, Norwegian University of Science and Technology, Norwegian
Jianxin Chen, University of Vigo, Spain
Hui Wang, University of Evry in France, France
Xiyin Wang, Hebei Polytechnic University, China
Dianxuan Gong, Hebei Polytechnic University, China
Chunxiao Yu, Yanshan University, China
Yanbin Sun, Beijing University of Posts and Telecommunications, China
Mingyi Gao, National Institute of AIST, Japan
Guofu Gui, CMC Corporation, China
Haiyong Bao, Fuji Xerox Co., Ltd., Japan
Xiwen Hu, Wuhan University of Technology, China
Mengze Liao, Cisco China R&D Center, China
Yangwen Zou, Apple China Co., Ltd., China
Yajun Guo, Huazhong Normal University, China
Liang Zhou, ENSTA-ParisTech, France
Xi Zhang, Texas A&M University, USA
Weihua Zhuang, University of Waterloo, Canada
Jayesh Seshadri, University of Texas at Austin, USA
Pan Li, Mississippi State University, USA
Cheng Li, Memorial University, Canada
Nael Abu-Ghazaleh, State University of New York at Binghamton, USA
Yang Xiao, University of Alabama, USA
Abd-Elhamid Taha, Queen's University, Canada
Michele Rossi, University of Padova, Italy
Venkatesha Prasad, Delft University of Technology, Netherlands
Mina Guirguis, Texas State University, USA
Nils Aschenbruck, University of Bonn, Germany
Ragip Kurceren, Nokia Research, USA
Haining Wang, College of William and Marry, USA
Onur Altintas, Toyota InfoTechnology Center, Japan
Suresh Subramaniam, George Washington University, USA
Dominic Shupke, Nokia Seimens, Germany

Abdallah Shami, University of Western Ontario, Canada
Dimitri Androustos, Ryerson University, Canada
Muhammad Jamil Anwas, Lahore University of Management Science Lahore, Pakistan
Mian Muhammad Awais, Lahore University of Management Science Lahore, Pakistan
Ing. Vitoantonio Bevilacqua, Polytechnic of Bari, Italy
Tim. B. Littler, Queen's university Belfast, UK
Jinde Cao, Southeast University, China
Wenming Cao, Zhejiang University of Technology, China
Dechang Chen, Uniformed Services University of the Health Sciences, USA
Mei-Ching Chen, Tatung University, Taiwan
Rong-Chang Chen, National Taichung Institute of Technology, Taiwan
Chi-Cheng Cheng, National Sun Yat-Sen University, Taiwan
Ziping Chiang, Leader University, Taiwan
Key-Sun Choi, Korea Advanced Institute of Science and Technology, Korea
Daniel Coca, The University of Sheffield, UK
Du-Wu Cui, Xi'an University of Technology, China
Donald C. Wunsch, University of Missouri – Rolla, USA
Sylvia Encheva, Stord/Haugesund University College, Norway
Minrui Fei, Shanghai University, China
John Q Gan, University of Essex, UK
Michael Granitzer, Know-Center Graz, Austria
Saeed Hashemi, Tehran University, Canada
Jiankun Hu, RMIT University, Australia
Zhao-Hui Jiang, Hiroshima Institute of Technology, Japan
Michael J.Watts, Lincoln University, New Zealand
Tai-hoon Kim, Defense Security Command, Korea
Seong G. Kong, The University of Tennessee USA
Worapoj Kreesuradej, King Mongkut's Institute of Technology Ladkrabang, Thailand
Haibing Yin, Peking University, China
Yanliang Jin, Shanghai University, China
X.G.Yue, Southwest Forestry University, China
B.H.Gu, Wuhan University of Technology, China
J.Liu, Wuhan University of Technology, China
C.X.Lei, Guizhou University, China
L.L.We, Henan Polytechnic University, China
X.W.Chai, Wuhan Institute of Technology, China
Z.Q.Zhao, Shanxi University of Traditional Chinese Medicine
Y.Y.Li Dongguan University of Technology, China
P. Cheng, East China Normal University, China
Y. Du, Henan University, China
H.Q. Lou, Donghua University, China
N.Xu Chengdu College Sichuan Normal University, China

GPMMTA 2012

Reviewers

T.R. Melia, Cisco Systems, Switzerland
W.M. Eddy, NASA/Verizon, USA
H.R. Haddadi, University College London, UK
J.H. Ott, Helsinki University of Technology, Finland
S.-Y. Hua, National Central University, Taiwan
K.J. Li, University of Georgia, USA
G.H.Gao, Henan Institute of Science and Technology, China
M.J. Stiernerling, NEC Europe Labs, Germany
F. Kuo, University of Goettingen, Germany
J.G. Qu, Hebei United University, China
J.X. Chen, University of Vigo, Spain
R.C. Tang, Ocean University of China, China
L.X. Shi, IBM Research Lab, China
R. Zhu, South-Central University for Nationalities, China
G.X. Danilewicz, Poznan University of Technology, Poland
Y.Z. Xu, Polytechnic University, USA
K.W. Xu, Arizona State University, USA
H.J. Wang, College of William and Marry, USA
C.X. Wu, University of Toronto, Canada
S.H. Yan, Hebei United University, China
W.M. Zhang, North Dakota State University, USA
D.L. Liu, ShenYang Ligong University, China
Y.X. Tang, Illinois State University, USA
L. Zhou, ENSTA-ParisTech, France
A.M. Yang, Hebei United University, China
W.X. Wei, NEC Labs America, USA
Y.L. Zhao, Northwestern University, USA
G.F. Gui, CMC Corporation, China
A.D. Baiocchi, University of Roma, Italy
L.C. Feng, Hebei Polytechnic University, China
M.Z. Liao, Cisco China R&D Center, China
O.X. Altintas, Toyota InfoTechnology Center, Japan
S.J. Giordano, University of Pisa, Italy
Y. Lin, Norwegian University of Science and Technology, Norwegian
Y.W. Zou, Apple China Co., Ltd., China
X.G. Zhang, Nanyang Normal University, China
Z.G. Wei, Beijing Forestry University, China
Y.J. Li, Shanghai Jiao Tong University, China

H.B. Nguyen, The Aerospace Corporation, USA
D.U. Sarkar, University of Miami, USA
H.Y. Bao, NTT Co., Ltd., Japan
C.A. Wei, Hainan Medical University, China
X.W. Hu, Wuhan University of Technology, China
S.B. Zhong, Chongqing Normal University, China
Z.Q. Liu, AT&T, USA
I.R. Guardini, Telecom Italia Lab, Italy
Y.L. Jin, Shanghai University, China
E.R. Hossain, University of Manitoba, Canada
D.X. Gong, Hebei Polytechnic University, China
D.W. Niyato, Nanyang Technological University, Singapore
L.X. Le, Massachusetts Institute of Technology, USA
H.Chen, Hu'nan University, China
L.L. Wang, Beijing University of Posts and Telecommunications, China

Table of Contents

Preface, Committees and Reviewers

Chapter 1: Materials Engineering and Application

Ethanol and Diesel Fuel Mix the Preparation and Physical and Chemical Properties of Research Q. Li	3
Molecular Dynamics Simulations of the Glass Transition Temperature of Amorphous Cellulose X.M. Zhang, M.A. Tschopp, S.Q. Shi and J. Cao	7
Preparation and Properties of Shape Memory Epoxy Resin Composites X.H. Jing, Y.Y. Liu, Y.X. Liu and H.F. Tan	12
Granulation Technology Experiments of Novel Mesoporous Composite Water Purification Material T.X. Li, Y.C. Zou and S.X. Jiang	17
Controlling Factors of Hydrocarbon Accumulation and Optimization of Favorable Blocks for Both Flanks of Putaohua Reservoir in Southern Daqing Placanticline D.S. Xiao, H.L. Chen and H.F. Chen	23
SEM Image Processing of PP/Rice Husk Composite Using MATLAB H. Zhang, C.X. He, D.R. Lu and M. Yu	27
Study on Organic Montmorillonite Modified Recycled Optical-Grade Polycarbonate Nanocomposite F.Q. Guo, Y.Y. Li, B. Guo and H. Liang	31
High Performance Concrete in Highway Bridge in Cold and Arid Regions Z.Y. Wang	35
Heat Treatment Process of the Flue Gas Desulphurization Gypsum and its Influence on the Properties of Cement Y. Li, J.H. Wu, B. Hao and D.C. Liu	40

Chapter 2: Mechanical Engineering and Application

Research on Material Features in Design Technique of Tennis Materials X.F. Xu	47
Scheduling Optimization for Parking and Taking Car about the Vertical Circulation Type Stereo Garage S. Li, H.R. Li, X.B. Zhang and M.F. Ji	52
Intelligent Information Processing Based on Classical Logic and Applied Mechanics Y.X. Lu and Z.Q. Zhang	58
Casing Drilling Technology to Drilling Site W.L. Gao	63
Basic Process of the Performance Test of the Turbine Generators N. Li	67
Integrated Nine-Switch Power Converter Based on Discontinuous Pulse-Width Modulation Q. Wang	71
Research of Flow Field and Temperature Field in 2D Annular Space of Air-Gap L. Tang, Y.P. Lu, H.Y. Deng and Z.M. Wang	76
Heat Storage Performance of Heating System of Phase Change Heat Storage Y. Sun, F. Xu, Y.J. Shi, X.Y. Ji and T.L. Liu	82
Analysis of the Multi-Tooth Meshing Effect of Three-Ring Gear Reducer Y. Li and C. Zhu	87
Demodulation Method of Distributed Fiber Bragg Grating Sensor Based on Whispering Gallery Mode Optical Microcavities Z. Fang, W.C. Wu, B.J. Peng, F. Xu, J.C.W. Zhu, K. Xu, L. Wang and G.Z. Wu	92

Experimental Study on Anti-Fatigue Damage Structural Design of Diesel Engine Bearings Z.J. Guo	97
Numerical Simulation of Partial Cavitating Flow of 2-D Hydrofoil in Viscous Flow X.H. He, L. Gao, H.B. Liu and Z.G. Li	102
Cardiac Motion Estimation with Coronary Angiographic Image Sequences Z. Sun and H. Bai	108
Effects of Coefficient of Excess Air on the Combustion Performance of Marine Two-Stroke Diesel Engine H.J. Wei and H.B. Xie	114
Solutions of Optical Transmission Analysis Y.J. Li	119
Study on the Methods of Measuring Magnetic Field S.K. Zhu	124
Study on Wear Behaviors and Grain Effects of PCD Cutting Tools in Turning Granite S.Z. Liu, Z.L. Kou, R. Zhang, C.L. Liu, Y. Li, R.Q. Li and X.Z. Yan	130
Condensing Heat Recovery of Existing Large-Scale Refrigeration System D.Y. Zheng, B. Guo, W.D. Liu and X. Chen	136
Integrated Instrument Based on SOPC Z. Ma, M.L. Liu, A.H. Yang and Y.Y. Liu	141
An Improved Wavelet Threshold Denoising Method for Transformer Partial Discharge Signal F.C. You and Y. Zhang	148
A Research on the DC-Link Current and Capacitance of the Static Excitation Regulator on a 12/3-Phase Dual Stator-Winding Induction Generator B.T. Zhang and D. Wang	154
Application of Rigid-Flexible Coupling in Stiffness Calculation of Double Wishbone Suspension H.N. Wang, X.W. Hou and X.P. Su	161
Dynamics Analysis and Vibration Suppression of a Flexible Rotation Beam F.S. Ren, S.L. Chen and Z.G. Yao	165
Juice Extractor Stent Plastic Mould Structure Design X.Z. Cao	173
Research of Multi-Channel Hygrothermoscope Acquiring System X.B. Wu	177
Generation of High Intensity Sound by Random Vibrations L.M. Shi	183
Multiple Targets Passive Localization Technology Based on a Tolerant High Resolution Algorithm Q. Ling, X.L. Sheng, J. Lu, M.R. Jiang and Y. Guo	188
Research of Sound Transmission Loss of Aircraft Sidewall with the Resonators L.M. Shi	194
Research on Mechanical Wind Machine of Constant Velocity M.C. Ding, X. Ding and L. Zhang	200
Realization of the Viterbi Algorithm in MLSE with Intersymbol Interference Y. Lu, Q.Y. Xu and Z.G. Liu	208
Optimization of Control Parameters with Switching Operation Mode on Hybrid Brake System for Electric Vehicles R. He, J.B. Yu and R.C. Wang	213
Applied Mechanics-Based Devices in Mobile Human-Computer Interaction Y.S. Chang and Q.Y. Hua	219
Influence of Thermal Distortion of Mirrors in Laser Resonators on Laser Modes J.X. Yan, F. Peng and Y.F. Peng	223
Lens Design with Silicon Wafer for Terahertz Wave Transmission Y. Wan, M.H. Jia, H.W. Gong, Y. Yang and Y. Cui	227
Precise Time Measurement Using CTMU X.Q. Zuo and Y.X. Liu	232

Based on Image Procession to Measure Flame Emission Characteristic and Radioactive Properties J. Yao	237
Study on Influence Factors of NMR T2 Spectrum Inversion P.J. Li, H.A. Chen, Z.Y. Luan and Y.F. Gu	244
Analysis of High-Speed Energy-Storing Flywheel Rotor X.H. Zhang, X.F. Zhao and X.L. Zhang	249
Leakage Failure and Principle of Underground Low Voltage Grid J.M. Geng and C.G. Li	254
Research on the High Leakage Reactance of the Superconducting Controllable Reactor L. Wang, K.N. Cao, M. Song, D.D. Wang, N.N. Hu, Y. Zhang, L. Liu, W.D. Wang and S.M. Zhou	259

Chapter 3: Structural and Civil Engineering

Research of Practice-Based Design in Building Construction II D.H. Lv	267
Effect of Corrosion on Mechanical Properties of Reinforcing Bar HPB400 P. Li and Y. Wang	272
Study on Precast Slab Track for Taiwan High Speed Rail Y.C. Shiau, R. Chen, M.H. Lin and C.M. Huang	276
Block Sand Mechanism Experiment and Analysis of Vegetation Flexible Dam F. Liu, G.H. Wei, L. Ma and L.L. Chen	282
Study on the Deformation Characters of the Coal Roadways with Compound Rock Strata and Water Spraying Roof H. Yan, T.F. Xu and J. Wang	287
Calculation Method of Upgrade and Side Strengthening Old Bridge Based on Applied Mechanics X.C. Zeng and J.Y. Wang	292
Experimental Study on Double Truss Cable Supporting System of Coal Roadways in the Isolated Coal Pillar and Fold Region H. Yan, T.F. Xu and Y. Li	296
Application of Fracture Prediction and Modeling Technology in Tight Sandstone Gas Reservoir in Xinchang Gas Field of Sichuan Basin L.C. Qu and C.R. Bian	301
Prediction Scheme of Torsional Strength of Reinforced Concrete Beam H.C. Huang	306
Study on Composite Slab Structure K.W. Ding and Y. Zhang	311
Research on Stability Bearing Capacity for Pole and Tower Compression Members with Two Legs Connection X.L. Cao	315
On 3-D Modeling CAD System of Production Platforms X.J. Chu	320
Subway Station Seismic Structure Dynamic Model K. Liu	327
Study on <i>In Situ</i> Shearing Strength Test for the Retaining Wall Bottom in a Bank Revetment Project G. Zhang, J.R. Ma, J.X. Chen, H.L. Zhou and D.H. Wang	333
Study of Light Pollution about Night Landscape Lighting X.Q. Yang	338
On Visual Aesthetic Feeling of Microlite Decorating Plate Y.G. Yang	343
Green Industrial Buildings Lighting Design Based on DIALux H. Li, G.S. Li, L.P. Wang and Z.X. Liu	348
Research of Green Concrete S.Z. Yang	353

Chapter 4: Manufacturing Technologies and Application

Control Methods of the Concentrated Moisture Exhaust System for Tobacco Primary Processing Y.S. Wu	361
Effect of Microbiological Additive on the Diversity of Microbial Community and the Dynamic Distribution during High-Temperature Composting Process H.T. Li, X.H. Xu and J. Liu	366
An Experimental Study on Edge-Breakage of Explosive Parts in Machining Using Micro-Photographic Observation Method W. Tang, W. Liu, Q. Xi, T. Liu and D.G. Zhang	370
Coal Gangue Image Edge Detection Based on Wavelet Transform T.Y. Li	375
Mercury Processing in PVC Production T.Y. Li	381
Numerical Analysis of a New Type of Oil Boom with Diversion X.S. Wang, B. Ning, R.M. Yuan and X.X. Zhang	386
Research on Wood Drying Technology Based on Mechanics X. Zhang	390
Influences of Heat Treatment on Spinning Process with Large Thinning Rate and Performance of 30CrMnSiA D. Han, H. Yang, M. Zhan, M.Y. Yang, S.Z. Mou and T. Li	395
Experiment System and Test Technology of Oil Fire and Explosion X.S. Jiang, B. Wang, W.H. Liu, Y.H. Ou, D. Wang and H.B. Qian	401
Analysis on Monitor and Experiment of Blasting Vibration for Sijiaying Iron Mine J. Guo, D.Q. Gan, J. Tan and G.B. Yan	407
Mining Method of Macheng Iron Ore J. Guo, D.Q. Gan, J. Tan, J.L. Jia and G.B. Yan	412
Power System with Wind Power Connection Anti-Peak Regulation Ability Analysis D.F. Yang and S.Q. Zhou	417
Effect of Different NPK Fertilizers Cooperating Application on Yield and Quality of High Starch Maize R.X. Ma, J.S. Wang, X.Z. Li and W.C. Liu	423
Power Transmission and Transformation Project Using Analytic Network Process Y.H. Huang	430
Effect of Co Concentration on Composition and Electromagnetic Shielding Properties of Ni-Co-P M.Q. Wang, J. Yan, H.P. Cui, S.G. Du, Y. Guo and H.G. Li	436
Numerical Simulation of Eddy Air-Curtain Dust Controlled Flow Field in Hard Rock Mechanized Driving Face W.M. Cheng, W. Nie, G. Zhou, J.L. Yang, W.Z. Du and X.H. Zhang	440
Effects of Beipiao Wind Power Development Planning on Local Birds Ecosystem L. Wang, J.H. Zhu and Z.Q. Ma	445
A Parameters Optimization of the CO₂ Laser Drilling Process for HDI Microvia Fabrication Y.Z. Hu, W. He, W.D. Xue, Z.H. Tao, Y.X. Huang, H. Xu and W.Q. Lv	451
Nano-Machining Polishing Method on Metal Materials M. Yin	455
Quality Control Measures of Concrete Work Y. Chen, C.Z. Yan and C. Ouyang	460
City Power Grid Planning and Coordination Mechanism M.L. Huang and Y.X. Li	464
Multidimensional Grey Evaluation Method for Aeronautic Electronic Components & Devices Selection X.F. Wang, C. Gao and G.C. Fu	469
Risk Assessment of Error Forgetting and Omitting of Manufacturing Controller J.G. Kong, H. Liu and X.Y. Zheng	475

Green Agricultural Products Supply Chain Management Mode under Low Carbon Economy F.L. Luo	481
Research on Active Aided Knowledge System Push-Pull Technology Oriented the CAPP X.A. Zhang and R. Li	486
Tech-Application for Excess Energy Supplement to Cut Cost in Pump Station Y.S. Zhang, X.M. Li, Y. Chen, L.S. Zhang and Y.B. Jia	491
Optimizing and Simulating Production Line Balance Based on Human Factors P.H. Li, Z.J. Fan, J. Zhou and J.X. Deng	495
Facility Layout Model of Production Line Based on Operation Comfort P.H. Li, Z.J. Fan, J. Zhou and J.X. Deng	500
Research on the Green Building Revolution - Solar Energy Research and Development in Taiwan Y.C. Shiau, I.T. Lu, C.I. Tsai and C.Y. Lee	505
AP1000 Nuclear Reactor and Primary Loop Modeling Based on Relap5-3D and 3Keymaster Simulation Platform H.M. Wei, X. Zhang and T.L. Liu	510
Experimental Study on Influence Function of Particle Size at Low-Temperature Oxidation of the Coal Q.L. Zuo, G.Z. Wang and X.C. Gao	515
Improved Phosphate Ore Leaching with Physical Mutagenized Acidithiobacillus Ferrooxidans Based on Modified Logistic Model E.W. Wang, S.M. Lei and W.Q. Gong	520
 Chapter 5: Control, Monitoring and Computer Technologies	
Research on Optimization Control Strategy for Limiting Short-Circuit Current Based on Fuzzy Quantitative Control G.L. Li, S.M. Sun, Y. Cheng, H.B. Li and S. Yuan	527
Study Based on TMS320F2812 Synchronous Generator Field Regulator Z.T. Zhang, X.P. Shi and X.L. Shi	531
Intelligent Monitoring Design and Research of Modern Instrumentation Failure Alarm S.F. Yu, X.P. Shi and X.L. Huang	534
Research of Data Server Application Software for NBI Mechanical Control on EAST X.D. Zhang, Z.M. Liu, P. Sheng, C.D. Hu and Y.Z. Zhao	538
Mechanics Performance of Elevator Monitoring System Based on GPRS and ZIGBEE Network X.Q. Zhang	543
A Information Management Methods Design of Mechanical CAD Drawings X.X. Liang and C.G. Wei	548
Remodeling and Texture Mapping for Rule Polyhedron Based on Open Scene Graph K.F. Wang and J.M. Cheng	553
Mine Detection Technology in Mine Safe Production J. Guo, D.Q. Gan, J. Tan and C. Ren	558
Study of Mechanics Control Server Application Software on EAST-NBI Y.Z. Zhao, C.D. Hu, P. Sheng and X.D. Zhang	562
Optimized RBF for CBR-Recommendation System J.Y. Li, X.P. Liu and R. Li	568
Stability Property of Uncertain Networked Control System with Random and Bounded Delay J. Yao	573
Transfusion Monitoring and Controlling System Based on Wireless Communication J. Ma, Y.Q. Wen, L.Y. Du, X.X. Liang and C.G. Wei	579
Metadata Caching Subsystem for Cloud Storage D.J. Niu, T. Cai, Y.Z. Zhan and S.G. Ju	584
Research on Two-Speed CAN BUS Technique in Automobile Manufacturing System T. Gong and H. Yan	591

Research of ISIC-CDIO Question Answer System for Materials Teaching Based on Android H. Yan and H.Y. Hu	596
Research of Decision Support Technologies in Multi-Dimensional Data Environment Z.G. Qiu	601
Research of Mine Wireless Video Monitoring Sub-Station Based on WIFI W.L. Lei, X.C. Ren and Y.H. Fan	605
Preconditioned Symmetric Linear BCG Method for Solving FEM Electromagnetism Problems Y.H. Li	610
Spatial Analysis Model for Agricultural Land Grading Based on GIS W.L. Kou, S. Gan and X.P. Yuan	615
Research and Implementation of Multi-Bus Converter Based on Intelligent Sensor G.P. Lu, Z.Y. Ge, W. Zhong and C.G. Hou	620
Design of Wireless Power-Meter Reading Data Collector Based on CC2430 Z.Y. Chen, J.X. Gu and W.X. Bu	625
Application of Three Order Cumulants in Fault Diagnosis W.B. Wu, S.Q. Yang and Y.J. Huang	630
Review on Application Research of Multi-Agent Theory in Industrial Process Control J.C. Liu, Y.L. Jiang, S.B. Tan and P.S. Ming	635
A Simulation Research of Artificial Intelligence Control X. Xiong and C.D. Lu	640
Flowers Temperature and Humidity Control System Based on Applied Mechanics W.M. Shao, H.T. Li and L.H. Jin	644
Digital I/O Training Kit Development for Arduino Platforms H.H. Huang, C.Y. Liu, M.C. Huang, I.C. Ko and J.M. Lee	649
Application of Modular Design in the Intelligent Building Product Designing L. Chen, R. Jiao and J.Q. Liao	654
Research on Wireless Alarming System of Transformer Substation W.H. Li, L.S. Wang and F.Y. Wang	659
Study of Physics Experiment Teaching System Based on Virtual Reality Technology S.J. Chen	664
Correction Algorithm of USB Touch Screen Driver in vxWorks M. Li and H.P. Guo	669
Plate Production Line Automation Control System Based on Automatic Gauge Control W.W. Yu and X.T. Wang	674
Constant Low Speed PLC Control System of GKD3B Locomotive X.P. Zhang	679
A Family Remote Control System Research Based on GSM Module Y.Z. He	684
STBC Study on Reservoir Dispatching and Hydrology Satellite Monitor System X.L. Cao, X.J. Wang and Y. Zhu	690
Board Microcomputer Control System to Export Diesel Locomotive X.P. Zhang	695
Research of Automatic Welding Machine Controlling System Based Single-Chip J.H. Song	700
Machine-Printed Invoice Number Based on Fuzzy Recognition X.P. Xian	705
Expert System for Fault Intelligence Diagnosis of Gasoline Engine J.P. Wang	711
Implementation of FIR Filter Based on DSP W. Wang	717
Research on Program Calling and File Sharing between Windows and Linux L. Zhang, M. Yuan, T. Liu, L. Wang and P. Gao	721
Study of Control and Detection on Firing Circuit X.H. Li, Y.J. Wang, H.B. Jia and J. Liu	725
Detector on Dam's Piezometric Tube Level L.S. Wang, D.H. Xi and L.J. Wang	730

Research of Stand-Alone Photovoltaic Power Generator Monitoring System G.S. Chen	735
Fault Diagnosis of Power Transformers Based on Membrane Computing Optimizing Neural Network Z.J. Yuan, H. Deng and W.J. Liu	740
Remote Measurement & Control of Ship Mooring System Y.L. Liu, L.F. Tao and E.L. Lin	745
Algorithm Based on Layering Search to Routes Planning of Vehicle Navigation System X. He, Y.Y. Gao and T. Chen	749
Research on Remote Meter Reading System Based on PLC Technology Y.J. Zhang	755
Simulation Environment for Dangerous Chemicals Transportation H.Y. Hu, W.D. Li, P.F. Wang and L.N. Sun	760
Fuzzy Self-Tuning PID Controller in SEHS L. Sun	765
Research of Universities Teaching Materials and Resources Based on Semantic Grid Portal Construction C.L. Hu, W. Liu and J.D. Zhang	771
Research of Optimal Control Model with Multiple Inputs and Multiple Outputs Based on Logic Algebra Y.C. Ling	775
Eyelid Noise Detection Based on Gray-Scale Morphology and Judgement of Noise Occlusion S. Li, L. Qian and Y.Q. Wang	780
Application of Multivariable Non-Linear Decoupling Control Based on Neural Network J.B. Zhang, D.H. Fan and R.Z. Hu	786
MHD: A New Method towards Privacy Protecting Datasets Published F. Liu, Y. Jia and W.H. Han	792
Simulation of Large Amount of Data Liquid-Solid Coupling Based on the SPH H. Fang, L. Zhang, Y. Liu and S.B. Sun	799
A Study on Component Composition Technology Based on XCM Y.Y. Liu	804
Based on OLAP Realize Real-Time Integrated Analysis of the Underground Metal Mines Cost Information J. Guo, D.Q. Gan, J. Tan and X.L. Yao	809

Chapter 6: Mechatronics and Applications

Precise Mechanics Control and Simulation of Automotive ABS Y.K. Wang and P. Tan	817
Simulation of Automatic and Intelligent Mechanical Arm X. Wang	822
Explosion-Proof Soft Starter Control System Based on DSP X. Niu and Y.Q. Wang	830
Analysis of Attribute Reduction of Rough Set and CNC Machine Fault Diagnosis Based on Particle Swarm Z. Wu	835
Numerical Control Machines Performance Test Platform J. Song and M. Li	840
Simulation Method for ARM Fragment Killing Ground Targets H. Wang and Y.J. Zhao	845
Nonlinear Adaptive Observer-Based Fault Diagnosis for Satellite Actuator Z. Wang	851
An Acoustic Source Localization Method Based on Equal Distances Multi-Sensors Array X.W. Wang, B.Y. Sun, B. Li, L.L. He and C.Q. Hu	856
Research on Wideband Guiding System Receiving Technology Y.L. Chen and S.Y. Lv	862

Ultrasonic Rangefinder Based on P89LPC932 W.D. Cheng and L.S. Zhang	867
Microcontroller System Design for Robotic Vehicles C.Y. Liu, C.Y. Chen and C.F. Huang	872
Data Fusion of Ultrasonic Wave Sensor Static State Based on BP Neural Network X.S. Wang	877
A Discrete Realization of Higher Resolution Phase Detection P.S. Liao and C.H. Lee	882
Analysis of Characteristics and Safety of Numerically Controlled Lathe Y.N. Zhou	887
Three-Degree-of-Freedom Step Motor Control Strategy Based on DSP Y.B. Tang, J.C. Yang, Z.Y. Zhang, X.K. Gu and Q.L. Liu	893
Study of a Novel Demodulation Method for FBG Sensor L. Wang, B.J. Peng, F. Xu, D. Wu and H.W. Wu	898
M Optimized Multi Virtual Gravity L.P. Yuan, L.M. Yuan and H.Y. Lu	903
Research on Video Processing System Based on Artificial Fish Swarm Algorithm X.M. Fang and X.B. Gao	909
Study of Remote Sensing and Remote Sensing Robot Technology F.Q. Guo and Y.Q. Wang	914
Study on Multidisciplinary Design Optimization of 3-RRS Parallel Robot J. Zhang and B.L. Li	919
Modeling and Simulation Research of NC Machine Servo System Based on Fuzzy PID Control M.Y. Ao	924
Coupled-Field Finite Element Analysis of MEMS Compound Electrostatic Actuator by Using the ANSYS Software Y.J. Chen, Q.H. Chen, Y.M. Li and W.G. Wu	929
Modeling and Simulation of a Switchable Chaotic System with Fractional Order S.H. Huang	935
Reform of CNC Machine Tool and Programming Based on CDIO Model J.P. Liu and Y.Z. Li	939
Research of Virtual Cutting Based on Hap Tic Feedback Y. Zhou and D.M. Hu	944

CHAPTER 1:
Materials Engineering and Application

Ethanol and Diesel Fuel Mix the Preparation and Physicochemical Properties of Research

Qiang Li

School of Transportation Science and Engineering, Beihang University, Beijing, 100191, China

Shandong Transport Vocational College, Shandong Weifang, 261206, China

ljzylq@126.com

Keywords: Ethanol; Diesel; Mixed Fuel; Physical and Chemical Properties.

Abstract. To ethanol fuel engine performance and the physical and chemical properties were introduced, and the mixed fuel ethanol diesel phase soluble characteristic test, hybrid fuel mixture fuel of cold, mixed fuel filter point of viscosity and lubricity, mixed fuel distillation range and hybrid hexadecane value, hybrid density and calorific value and mixed fuel phase separation and stability analysis of numerical calculation.

The Preparation of the Ethanol and Diesel Fuel Mix

In the experiment, the preparation of the fuel the order in accordance with the diesel-ethanol-n-butanol the sequence of the, the first in a container into diesel oil, then add the ethanol, a little bit a stir, then added to the container n-butanol, will good fuel mixture mixing into sealed transparent plastic containers, oscillation, until the static stability, observe the appear stratified time. In the experiments volume method, all kinds of fuel ratio are volume ratio.

The Main Physical and Chemical Properties of Ethanol Fuel

Ethanol contains the polarity of hydroxyl OH group, formulas for C_2H_5OH , hydroxyl and hydroxyl in alkyl is the combination of alkyl alcohol, and the same atomic number than the paraffin, alkyl alcohol molecular weight, specific gravity, boiling point, atmospheric pressure under the boiling point $Q_iH_uR_e$ are high.

In order to more fully understand the nature of the fuel ethanol, first will influence the performance of the main characteristics of fuel ethanol as follows:

Chemical Components and Combustion Products

Ethanol is oxygen-bearing fuel, so the theory of ethanol fuel air fuel too low petrol and diesel. Because ethanol oxygen levels and H/C value bigger, so burning more moisture, and less CO_2 . Pure ethanol engine exhaust steam for gasoline engines of about 1.4 times and 1.5 times for diesel engine. Due to the exhaust of water content in high, so a winter in alcohol engine car will be significantly behind the white steam tail. The engine starts in alcohol, warm during the machine in cylinder and high temperature, easy in the cylinder wall form the condensation, promote the formation of acid and the increase of wear.

The Ignition of Ethanol Performance

Hexadecane value (CN) is the measure of the fuel on fire performance index. Higher hexadecane value to improve the engine cold start sex, reduce combustion noise and extend engine life plays a very important role. Figure 1 is hexadecane value with the change rule of ethanol content, ethanol volume fraction of 10% ethanol diesel hexadecane value is not add ethanol diesel reduced 5.5 units, 15% ethanol and biodiesel reduced 3.8 units. Help solvent, hexadecane value were different degrees of improvement.

Ethanol fuel the watery poor, hexadecane value is only 8, than diesel hexadecane value 40 ~ 55 much lower, thus with ethanol fuel mixing ratio increases, ethanol diesel fuel hexadecane value down gradually. This makes in the compression ignition engine fuel burning ethanol is difficult.

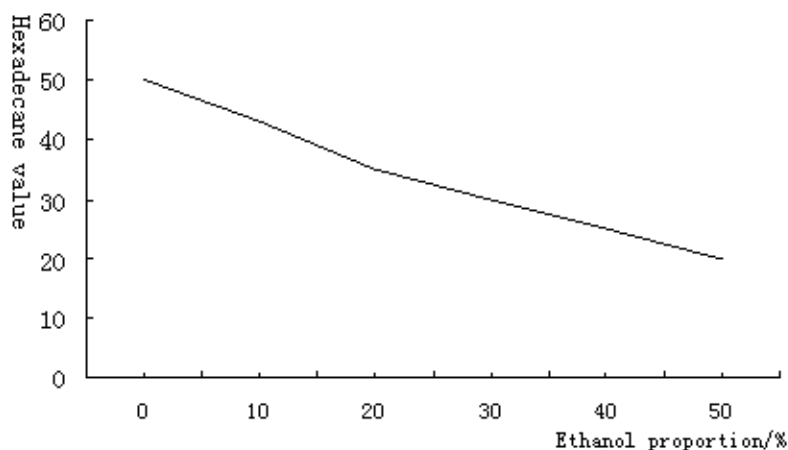


Fig. 1.1 The mixture of fuel ethanol proportion of the influence of hexadecane value

The Boiling Point of Ethanol and Condensation Point

Relative to the gasoline for, low boiling point of ethanol helps fuel-air mixture formation. But lack of high volatile components, adverse to start. In addition, because of the high ethanol latent heat of vaporization produced by cooling effect, also interfere with the operation temperature in completely vaporization, such as gasoline in the carburetor to freeze, the influence of the regular work carburetor phenomenon. As for burning ethanol content of ethanol for diesel fuel mix, not because of ethanol burn with the increase of the proportion, affect the mixed fuel low-freezing.

The Octane Value of the Ethanol

As gasoline engine fuels, fuel octane rating is the important measure of anti-explosion index. Ethanol fuel octane obviously higher than gasoline, therefore is not only good gasoline engines ethanol alternative fuel, is also raises the gasoline octane number of good additives.

Calorific Value of the Ethanol

Ethanol fuel with oxygen and heat value than oil low fuel Ethanol is about diesel low calorific value of 63%, thus with ethanol fuel mixing ratio increases, ethanol diesel fuel the low heat value fall gradually; But because of the air fuel ethanol theory is low fuel oil, theory of the mixture with oil fuel mixture calorific value theory of basic same calorific value. So the engine burn ethanol fuel burning or content, will adjust the flow of, will not affect the power of the engine.

Ethanol and Diesel Fuel Mix Physical and Chemical Properties of the Main Research

Pure ethanol at normal temperature in theory be able to 0 ~ 30% or 70% ~ 100% proportion and no water the azeotropic distillation of the diesel, but because the ethanol absorbs water easily, it and diesel mix of water and temperature after quite sensitive, so when ethanol diesel water content in more than a certain proportion the mixture will happen after the separation, and when temperature drop of ethanol and biodiesel after solubility deteriorated. Because ethanol hexadecane value is very low, so in diesel with ethanol, hybrid hexadecane value can be reduced.

Ethanol and biodiesel azeotropic distillation in certain proportion, the mixed fuel physical and chemical characteristics such as the density, viscosity and surface tension, flash point, boiling point, such as changes of low-freezing parameters, and not according to the proportion of linear weighted.

Mixed Fuel Filter Point of Cold

Cold filter point is the international public, low temperature performance evaluation index of the fuel oil. Diesel fuel mix for ethanol, because of the ethanol low-freezing for-114 °C, and the mixed fuel filter point will not because cold ethanol is mixed and down, but also can maintain the good low temperature performance. So add ethanol fuel ratio will not affect the mixed fuel filter point of cold.

The Viscosity of the Mixed Fuel and Lubricity

Viscosity fluid internal friction resistance is the measure of the scale of the size, is a fluid resistance shearing action ability. The influence of temperature on the fuel viscosity is very big, the temperature rises, the liquid fuel molecules by vibration, weakened the between the molecules

ShuFuLi, increasing liquidity, viscosity and decline. The viscosity of the liquid fuel with temperature change relations (viscosity-temperature curve) is fuel, and especially the alternative fuel important quality characteristics. Fuel oil viscosity depends mainly on its chemical composition, distillation range, temperature and pressure. Fuel oil viscosity increases with temperature drop, the decline of the steep rate characterization of the fuel oil viscosity properties, generally speaking, oil department to liquid fuel viscosity-temperature curve for good with gentle, namely viscosity with the influence of the temperature of don't want too big. Because in diesel engine, the fuel oil supply system and in plays lubrication and prevent leakage role. Modern diesel engine oil supply system three pieces of the dual gap only 1 ~ 3 μm . Fuel oil viscosity is too big, can increase its motion resistance, increase engine power loss, and the increase of the thing had little second I wear. Expand its clearance, thus increasing fuel oil in a loss of accidentally.

The diesel engine fuel system requirements of high pressure jet with good lubricity, if poor lubricity, it will aggravate the pump assembly.now pieces of wear and tear. Viscosity in a certain extent, to reflect the fuel lubricity. Because the viscosity of the ethanol is very low, only about a third of diesel oil, so the viscosity of the mixed fuel ethanol diesel also decrease, and with the increase of the proportion of ethanol, viscosity down degree increase.

Mixed Fuel the Distillation Process

The fuel is the most essential process fuel fractions of characteristics, it is deciding whether the burning in internal combustion engine and for what type of internal combustion engine. Fuel oil distillation curve is the distillate of rate of change with temperature curve. Fuel oil distillation curve represents the form in the fuel oil light, medium, heavy fractions distribution proportion. And this distribution proportion for fuel oil in the engine fire, burning and heat release time and strength has played a decisive role. So, fuel oil distillation curve of internal combustion engine combustion process quality and engine machine's power, economy, sewage, sex, noise, vibration, the cold start sex and that there is a close relationship between the acceleration, etc. The addition of ethanol in diesel fractions of cheng big effect.

Hybrid Hexadecane Value

Hexadecane value is used to characterize diesel fire performance is a measure of. Higher hexadecane value to improve the engine cold start sex, reduce combustion noise and extend engine life plays a very important role. Ethanol fuel hexadecane value for 8, is far less than that of diesel, and the poor of ethanol watery, in internal combustion engine is hard to direct pressure in the fuel, but with the exogenous ignition. With ethanol burn diesel, hybrid hexadecane value will be mixed with ethanol burn to determine the proportion. In order to diesel hybrid the ignition of fuel ethanol performance have an intuitive evaluation indexes, this paper application experience of diesel fuel ethanol fuel mix formula of hexadecane value are calculated.

The Density of the Fuel Mix and Heat Value

Fuel to the density of calorific value to the accuracy of the calculation influence thermal efficiency. So the hybrid density measurement. Due to the heat value measurement difficult, so in calculating the thermal efficiency by the density calculate calorific value.

Fuel has high calorific value of the calorific value and low calorific value of the points. High calorific value is completely out of fuel combustion heat and combustion products of one of water vapor condensation after release quantity of heat combined, and it is completely burning fuel that can be issued after the total quantity of heat. Low heat value is high calorific value minus the water vapor condensation after release in that part of the calorific value of the heat. Internal combustion engine exhaust water vapor contain of condensing heat, is actually hard to recovery. So, commonly used low heat value said. Internal combustion engine is the basis of reactive power conversion heat engine, fuel engine contains quantity of heat is the source of power output. So low calorific value of fuel is to evaluate the dynamic performance and fuel economy of internal combustion engine is one of important index.

Mixed Fuel and Stability Phase Separation

Ethanol diesel fuel mix high water content in separate happens, mixed fuel is not stable. Figure 2 shows 10% ethanol in diesel oil, add 0.1% of the water in the various temperature after to help solvent demand. It shows, in order to maintain the fuel mix of temperature in the stability and add the least help solvent, water content in the mixed fuel requirements as low as possible. In addition the temperature of the fuel, it would help to improve the stability of the mixed fuel.

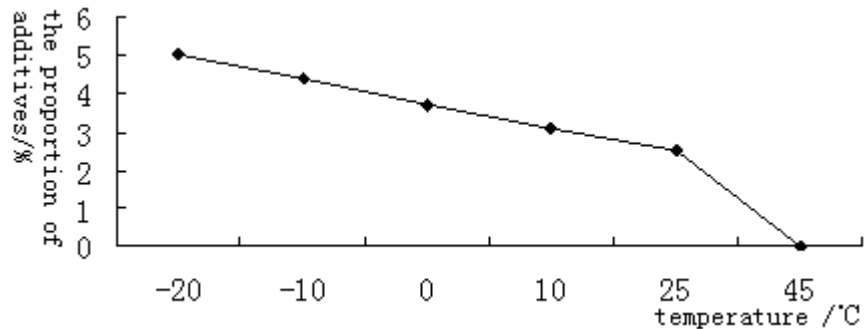


Fig. 2 10% ethanol diesel stability testing

References

- [1] LiJieDong, zhang jian. With the development of energy significance.
- [2] MaJianYing. Biological energy one of biodiesel. Economic reference. 2005-4.
- [3] YuShiTao. Ethanol diesel application research. Jilin university master's degree thesis. 2002.
- [4] CaiHan east, JiXueMei compile. Alcohol (alcohol) affects U.S. corn industry. The economic daily. 2004-12
- [5] ShiLaiFu compile. American and European countries develop biofuels. Reference message. The 2005-1-17
- [6] CuiXinCun. The problem of alternative fuels of internal combustion engine. Mechanical industry press
- [7] DuBaoGuo. Ethanol-diesel fuel in diesel engine fuel mixes the applied. Dalian university of technology master thesis. 2003.3
- [8] MaFuJun. In diesel engine, experimental study of burning ethanol diesel. Dalian university of technology master thesis. 2002.3
- [9] LiuPeng, SongChongLin etc. Ethanol-diesel fuel mix on diesel engine performance and the influence of emissions. Combustion science and technology. 2003.8. Vol. 9 th.

Molecular Dynamics Simulations of the Glass Transition Temperature of Amorphous Cellulose

Xiumei Zhang^{1,a}, M.A. Tschopp^{2,b}, Sheldon Q. Shi^{3,c} and Jun Cao^{1,d}

¹College of Electromechanical Engineering, Northeast Forestry University, Harbin 150040, China

²Center for Advanced Vehicular Systems, Mississippi State University, Starkville, MS 39762, USA

³Mechanical and Energy Engineering, University of North Texas, Denton, TX 76207, USA

^{a,d}xiumeizhang1@gmail.com, ^bmtschopp@cavs.msstate.edu, ^cSheldon.Shi@unt.edu

Keywords: Molecular Dynamics Simulation, Amorphous Cellulose, Glass Transition Temperature, Reactive Force Field

Abstract. Molecular modeling and dynamics simulations were used to generate equation of state properties of amorphous cellulose with the reactive force field ReaxFF which has been extensively parameterized and validated for hydrocarbon in a previous communication. Obtaining specific volume as a function of temperature for amorphous cellulose, the change in slope of the specific volume vs. temperature curves can be used to locate glass transition temperatures (T_g) reliably. With the results, there was reasonable agreement between experimental results and values of density and T_g obtained from the simulations. In addition, the suitable ReaxFF time step was investigated to help conserve the total energy of the system. The results show that the glass transition temperature can be used to verify the equilibration of the amorphous cellulose and to provide insight into the further deformation simulations.

Introduction

Cellulose is unquestionably the most abundant naturally reproducible organic compound [1]. It is one of the most popular and the most used polysaccharide by industry in either its native or regenerated forms as reinforcement and fillers when making environmentally friendly products. Recognition of characteristic features of cellulose strongly depends on the ratio between crystalline and amorphous domains. Many studies have enlightened in terms of several different crystalline forms since its discovery 160 years ago[2], whereas the structure and the morphology of the amorphous phase still has been less extensively investigated, especially the mechanical behavior of cellulose at the molecular level is a complex undertaking. Therefore understanding the structure of amorphous cellulose is a key step to characterize the properties of cellulose fibers.

The glass transition temperature (T_g) of amorphous cellulose is a critical parameter of fundamental importance for understanding the mechanical properties. The instruments that can detect the thermodynamic, mechanical and dielectric changes of a substance may be used to determine the glass transition temperature. T_g is usually measured by using differential scanning calorimetry (DSC) and atomic force microscope (AFM). However, experimental techniques suffer from some limitations to analyze the structure of disordered materials. For instance, it is still challenge to isolate fibrils in both micro- and nano- scales at a reasonable cost with low degradation by using chemical and mechanical methods [3]. The new tools and techniques are required to synthesize nanoscale objects and learn their many incredible properties. Molecular modeling represents a useful tool for providing atomic-scale detail to better understand structures and micro- and macro-properties of materials. It complements and informs experimental work and in certain cases, can provide information not easily obtained from experimental analysis.

In this research the molecular dynamics simulation is proposed for calculating the glass transition temperature of amorphous cellulose. Molecular dynamics is used for the numerical solution of Lagrange or Newtonian equations for classical multiparticle systems, as well as for postprocessing

and computer visualization of the time-dependent solution data. Since the early 1980s, molecular modeling has already been used to explain X-ray diffraction data for crystalline cellulose to characterize the structure of cellulose I and cellulose II [4]. There has been a recent surge of interest in using molecular dynamic simulation techniques to determine the structure and properties of amorphous polymers [5, 6]. However, some of studies made that the molecular [7, 8] dynamics simulations were too short to relax the chains completely in a glassy state at the chosen temperature. [9, 10]

The objective of this study is to use the advantages of reactive force field to study the T_g of the amorphous cellulose by isothermal-isobaric molecular dynamic simulation (NPT-MD) in the temperature range of 250-450 K. The temperature at the discontinuity is taken as the simulated T_g value for amorphous cellulose. The fully atomistic model of amorphous cellulose have been constructed and developed via nanoscale molecular simulations. Comparison between the previous theoretical and experimental data allows us to estimate the reliability of the force field to simulate the amorphous cellulose system. The long term goal of this research is to set the stage for cellulose deformation micromechanical behavior.

Models and Simulation Methods

Molecular Modeling Cellulose is a linear polysaccharide with two glucose units bridged together by 1,4- β -D-glucosidic bonds. Two glucose units form a cellobiose as depicted in Fig. 1[1]. The amorphous cellulose model consisted of multiple cellulose chains that are arranged parallel up and edge-to-edge. The simulations were performed for two different chain lengths (10 and 20 monomers) with each chain consisted of twenty glucose units or 422 atoms for a total of 4220-8440 atoms. The initial configuration of the system was generated using commercial Materials Studio software from Accelrys and the model cubic cell was built by means of the Amorphous Cell Protocol, originally proposed by Theodorou and Suter [12]. The chains were placed in a periodic computational box with the chain axis parallel to the z axis of the box.

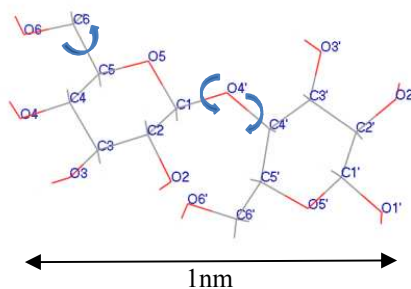


Fig. 1 The repeat unit of a single cellulose chain

All subsequent molecular dynamics simulations were performed using the LAMMPS simulation tool [13]. The unit cell models were replicated by $2 \times 2 \times 2$ to simulate more atoms. The glass transition temperature obtained equilibrated structures at each temperature. Standard minimization procedures were applied to the constructed cell in order to minimize the energy of each system. Furthermore, the system was fully equilibrated at 450 K under isobaric - isothermal conditions (NPT ensemble) with a small time step. The equilibrium density of the amorphous cell was achieved by running NPT dynamics at fixed atmospheric pressure ($P=0.0001$ GPa). Then subsequent MD simulations were carried out at 20 K intervals from 450 K to 250 K using the final equilibrium structure obtained at the higher temperature as the starting structure for the next temperature. At each target temperature, a 100 ps NPT-MD simulation was carried out with the last 25 ps used for data collection.

Reactive Force Field. There are mainly two categories in terms of computer simulation, the Monte Carlo (MC) and molecular dynamics (MD). Of the two methods, MD potentially is the more useful one since it can provide information on the time evolution of a system as well as its time-averaged properties. The interatomic force field for amorphous cellulose is based on the reactive

force field [14, 15]. ReaxFF is a general bond-order-dependent force field that provides accurate descriptions of bond breaking and bond formation during dynamic simulations. The main difference between the traditional unreactive force fields and ReaxFF is that the connectivity in ReaxFF is determined by bond orders calculated from interatomic distances that are updated every MD step. This allows for bonds to break and form during the simulation. Eq. 1 shows that ReaxFF partitions the overall system energy E_{system} into contributions from various partial energy terms, i.e.

$$E_{system} = E_{bond} + E_{under} + E_{over} + E_{val} + E_{pen} + E_{tors} + E_{conj} + E_{vdw} + E_{coulomb} \quad (1)$$

These partial energies include bond energy E_{bond} , atom under-/overcoordination E_{under} , E_{over} , valence angle E_{val} , penalty energy E_{pen} , torsion angle E_{tors} and conjugation energy E_{conj} terms to properly handle the nature of preferred configurations of atomic and resulting molecular orbitals and terms to handle van der Waals E_{vdw} and Coulomb $E_{coulomb}$ interactions. These latter non-bonded interactions are calculated between every atom pair, irrespective of connectivity, and are shielded to avoid excessive repulsion at short distances. This treatment of nonbonded interactions allows ReaxFF to describe covalent, ionic, and intermediate materials, thus, greatly enhancing its transferability.

Results and Discussion

Simulation Conditions. With ReaxFF, a suitable time step is required because the charges and bond orders are allowed to change at every time step. The ultimate aim is to simulate the longest possible time with the smallest amount of computational effort. The choice of time step is therefore a compromise between a large value which will require less molecular dynamics MD steps for a given simulated time, and a small value which allow each time step to be calculated faster. The time step must be sufficiently small that dynamics correctly conserve the total energy of the system.

Fig. 2 shows a greater temperature fluctuation from the initial value in the 1 fs time step case while the temperature is computed more stable using 0.5 fs time step. Notice the large bump in temperature for the 1 fs timestep case as the simulation cell is equilibrated. Another sign of instability with the 1 fs is the ejection of atoms from the simulation cell, which can occur if atoms get too close. Therefore, future simulations need to use a time step of lower than 0.5 fs.

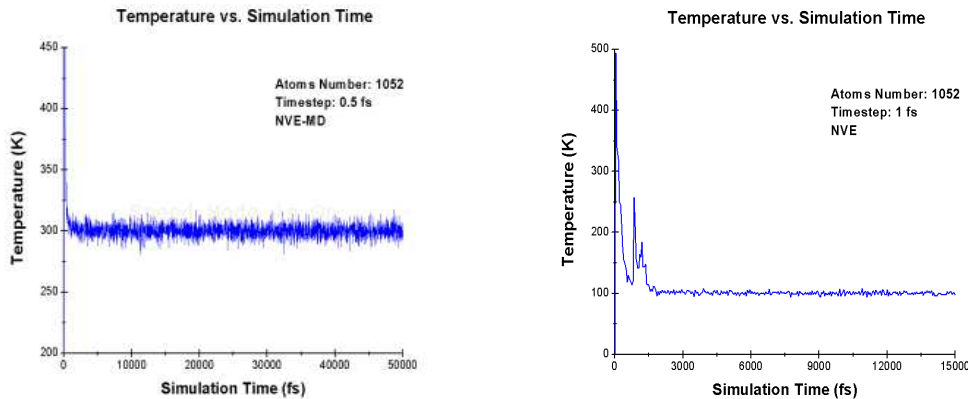


Fig. 2 Evolution of temperature as a function of simulation time for 0.5 fs (left) and 1 fs (right) using a constant volume and energy (NVE) molecular dynamics simulation

Glass Transition Temperature. The glass transition temperature was used to verify the equilibration of the amorphous cellulose system. The glass transition temperature T_g , delimiting the glassy regime to the rubbery one, is an important characteristic of polymeric material. Fig.3. shows two examples of the unit cell specific volume fluctuation during dynamics at 350 K and 250K, respectively. Table 1 lists the calculated specific volume at each temperature from 450 K to 250 K. The plot of specific volume vs. temperature was illustrated in Fig.4. The intersection of the two linear trend lines fitted to the ends of the data gives an estimate of the glass transition temperature. The

calculated values 336 K are closer to those calculated by other groups using molecular dynamics simulations with different force field [16]. Using molecular dynamics is likely to give an overestimate of the T_g value, because the cooling rate in an MD study is in the nanosecond range, in contrast, the rate in experiment such as DSC is in the range of minutes.

Conclusions

Molecular dynamics simulation proves to be a useful and successful tool in predicting glass transition temperature of amorphous cellulose. Preliminary molecular dynamic simulations have been presented for amorphous cellulose which models were successfully generated. Specific volumes of amorphous models with NPT ensembles conditions were calculated, and their dependency on temperature was obtained in cooling cycles. The calculated glass transition temperatures could be identified by the intersections of two linear trend lines. The good agreement between simulation results for glass transition temperature and experimental data indicate that ReaxFF is a good force field for molecular dynamics studies of amorphous cellulose. Also, the result presented here clearly indicate that the equilibration of amorphous cell can have a significant effect on the value of T_g obtained from simulation.

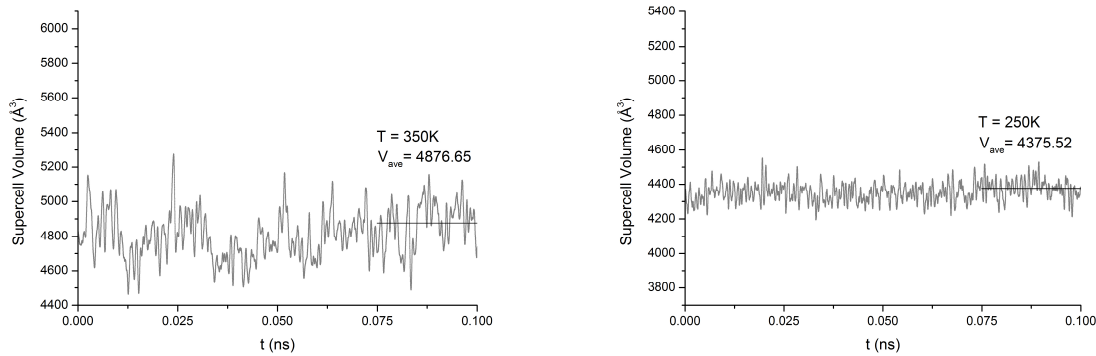


Fig. 3 Unit cell specific volume Versus Dynamics Time

Table 1. List of specific volume of equilibrated system at decreasing temperatures

Temp (K)	450	430	410	390	370	350	330	310	290	270	250
Vspec(Å ³)	5229.3	5157.87	5202.7	5011.28	4983.32	4876.65	4720.65	4517.34	4503.63	4406.06	4375.52

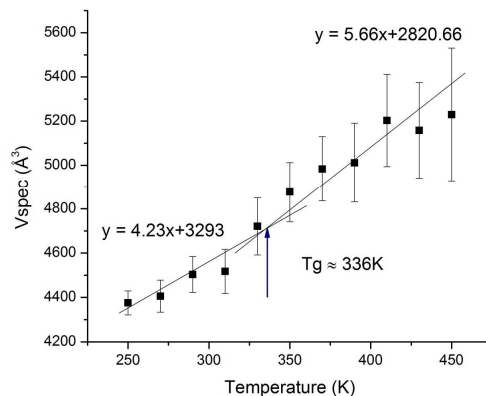


Fig. 4 Plot of specific volume evolution as a function of temperature

Acknowledgements

This work was supported by National Natural Science Foundation of China (NSFC) 30972301/C040301, the National Science Foundation (NSF) of US, CMMI0928641 09080796, the Center for Advanced Vehicular Systems/CAVS of Mississippi State University, the Foundation of Excellent Doctoral Dissertation of NEFU (Grap09). Additionally, the authors would like to acknowledge the insightful comments from the reviewers.

References

- [1] Kamide K. Cellulose and cellulose derivatives: molecular characterization and its applications [M]. Elsevier,2005.
- [2] Zugenmaier P. Conformation and packing of various crystalline cellulose fibers [J]. Progress in Polymer Science. 2001, 26(9):1341-1417.
- [3] Qingzheng Cheng, David DeVallance, Jingxin Wang and Siqun Wang. Advanced Cellulosic Nanocomposite Materials [M].
- [4] Marhöfer R J, Reiling S, Brickmann J. Computer simulations of crystal structures and elastic properties of cellulose[J]. 1996,100(8): 1350-1354.
- [5] Frankland S J V, Harik V M, Odegard G M, et al. The stress–strain behavior of polymer–nanotube composites from molecular dynamics simulation[J]. Composites Science and Technology. 2003, 63(11): 1655-1661.
- [6] Montès H, Mazeau K, Cavaillé J Y. The mechanical β relaxation in amorphous cellulose [J]. Journal of Non-Crystalline Solids. 1998, 235-237(0) :416-421.
- [7] Kelley S, Rials T, Glasser W. Relaxation behaviour of the amorphous components of wood [J]. Journal of Materials Science. 1987, 22(2): 617-624.
- [8] Chui C, Boyce M C. Monte Carlo Modeling of Amorphous Polymer Deformation: Evolution of Stress with Strain [J]. Macromolecules. 1999, 32(11): 3795-3808.
- [9] Chen W, Lickfield G C, Yang C Q. Molecular modeling of cellulose in amorphous state. Part I: model building and plastic deformation study [J]. Polymer. 2004, 45(3): 1063-1071.
- [10] Hossain D, Tschopp M A, Ward D K, et al. Molecular dynamics simulations of deformation mechanisms of amorphous polyethylene[J]. Polymer. 2010, 51(25): 6071-6083.
- [11] Yashiro K, Ito T, Tomita Y. Molecular dynamics simulation of deformation behavior in amorphous polymer: nucleation of chain entanglements and network structure under uniaxial tension [J]. International Journal of Mechanical Sciences. 2003,45(11): 1863-1876.
- [12] Theodorou D N, Suter U W. Detailed molecular structure of a vinyl polymer glass [J]. Macromolecules. 1985,18(7), 1467-1478.
- [13] Plimpton S. Fast parallel algorithms for short-range molecular dynamics [J]. Journal of Computer Physics.1995, 117(1): 1-19.
- [14] van Duin A C T, Dasgupta S, Lorant F, et al. ReaxFF: A Reactive Force Field for Hydrocarbons [J]. The Journal of Physical Chemistry A. 2001, 105(41): 9396-9409.
- [15] van Duin A C T, Strachan A, Stewman S, et al. ReaxFFSiO Reactive Force Field for Silicon and Silicon Oxide Systems [J]. The Journal of Physical Chemistry A. 2003, 107(19): 3803-3811.
- [16] Simperler A, Kornherr A, Chopra R, et al. Glass Transition Temperature of Glucose, Sucrose, and Trehalose: An Experimental and in Silico Study[J]. The Journal of Physical Chemistry B. 2006, 110(39): 19678-19684.

Preparation and Properties of Shape Memory Epoxy Resin Composites

Xianghai Jing^{1,2,a}, Yuyan Liu^{1,2,b}, Yuxi Liu^{1,2,c} and Huifeng Tan^{2,3,d}

¹Department of Polymer Materials and Engineering, Harbin Institute of Technology,
Harbin, Heilongjiang, 150001, China

²National Key Laboratory of Science and Technology on Advanced Composites in Special
Environments, Harbin Institute of Technology, Harbin, Heilongjiang, 150001, China

³Center for Composite Materials, Harbin Institute of Technology,
Harbin, Heilongjiang, 150001, China

^ajxh19820623@163.com, ^bliuyy@hit.edu.cn, ^cliuyuxiemail@126.com, ^dtanhf@hit.edu.cn

Keywords: Shape memory, Epoxy resin, Kevlar fiber, Carbon fiber, Composite

Abstract. Kevlar fiber and carbon fiber reinforced shape memory epoxy composites were prepared respectively. The fold-deploy shape memory properties of the composite system were studied at the temperature which was 30°C higher than the glass transition temperature of resin. The results shows that shape fixed rate and shape recovered rate of the composites are decreased with the increase of Kevlar and carbon fiber volume. The shape fixed rate of Kevlar fiber reinforced shape memory composite is higher than that of carbon fiber reinforced shape memory composite, but the shape recovered rate of the former is much lower than the latter.

Introduction

The shape memory polymer processes the characteristic of large recoverable strain, excellent shape retain ability and repeated memory effect, which is an ideal choice for a deployable structure [1,2]. The shape memory polymer alone cannot obtain high strength and stiffness, but when the shape memory polymers were prepared with reinforced fibers, particles and fillings, whose mechanical property and memory property can probably be improved. The shape memory polymer composites are very potential structure function materials, which have a very broad perspective in space deployable structures [3,4].

Researches of domestic scholars about shape memory polymer are more focused on thermoplastic polymer, and the research or analysis about thermosetting polymer is too few. However, most composite components used for space structures are thermosetting resins. Since the late 1990s, foreign countries have begun to study the shape memory thermosetting resin, especially the epoxy resin. The shape memory thermosetting epoxy resin displays excellent shape recovery characteristics, stiffness, and strength and environment resistance. In the present study, most of the thermosetting shape memory composites use TP type epoxy resin developed by ILC or TEMBO type epoxy resin developed by CTD. On the basis of study on thermosetting shape memory polymer, CTD developed fiber reinforced TEMBO shape memory composite, and was named Elastic Memory Composite (EMC). W.H. Francis et al. found that EMC laminates reinforced with carbon fibers are capable of nominal bending strain values of greater than 5% without damage. The primary mechanism that allows these high packaging strains is microbuckling and nonlinear, post-microbuckling response of the carbon fibers [5]. By the experiments and mathematical computations, M.S. Lake et al. discovered that in order to reduce resin strains to within allowable limits, it is necessary to have higher resin content in an EMC laminate than a traditional fiber-reinforced composite. Fiber volume fractions of between 40% and 50% are adequate to ensure reasonable resin strain levels [6].

In this paper, the self-made thermosetting shape memory epoxy resins are taken as matrix, and the Kevlar fiber and carbon fiber are taken as reinforced materials to prepare shape memory composites. The shape memory properties of the composite system were studied.

Experimental

Preparation of Samples The Kevlar fiber and carbon fiber reinforced shape memory epoxy resin composites were prepared with different fiber content (10%, 15% and 20%). The epoxy resin and fibers were placed in the metal mold for heating and high-pressure cure moulding by molding process. The specimens are rectangular and the size of which is 250mm×25mm×2mm. The shape memory epoxy matrix was made by our laboratory, the performance parameters of which are shown in Table 1. The performance parameters of fabrics are shown in Table 2. The Kevlar fiber and carbon fiber reinforced composites are named KF/EP and CF/EP, respectively.

Table 1 Performance parameters of shape memory epoxy

Shape memory temperature [°C]	Shape fixed rate [%]	Shape recovered rate [%]	Shape recovered time [s]
95	>99	100	120

Table 2 Performance parameters of Kevlar fiber and carbon fiber

	Style	Reinforcement		Weave	Fiber Count (10mm)		Weight [g/m ²]	Thickness [cm]
		Yarn			Warp	Weft		
		Warp	Weft					
Carbon fiber	XW-03-A-200	3K	3K	Plain	5	5	200	0.30
Kevlar fiber	XW-1500-A-240	1500	1500	Plain	7	7	240	0.30

Measurements of Shape Memory Characteristics The shape memory properties of composites were studied by fold-bend test method. First, the materials were heated to $T_g+30^\circ\text{C}$ and maintained for 10 min. The materials were bended to U type at this temperature, then cooled naturally to room temperature and maintained for 10 min without removing the external force. The folded specimens are shown in Fig. 1. Subsequently, the composites were heated from room temperature to $T_g+30^\circ\text{C}$ and occurred dynamic recovery. The shape memory testing tool was self-made, as shown in Fig. 2. The shape fixed rate and shape recovered rate of the materials were tested.

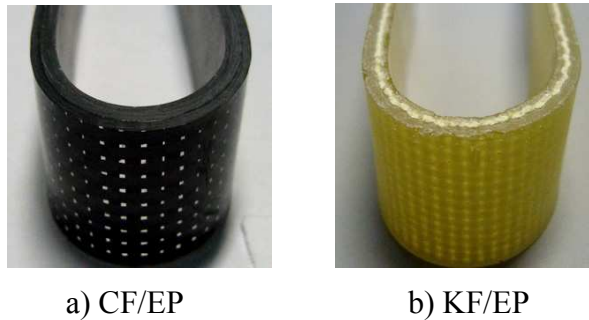


Fig. 1 Photographs of fixed shape of CF/EP and KF/EP

The shape fixed rate is used to describe the capability that deformation of shape memory materials at high temperatures is fixed at low temperatures, whose calculative method is shown in Eq. 1:

$$R_f(T) = \frac{\theta_{fixed}}{\theta_{max}} \times 100\%. \quad (1)$$

Where $R_f(T)$ is the shape fixed rate when the temperature for fold and bend is T , θ_{fixed} is the bending angle after fixing the shape, θ_{max} is the maximum fold-bend angle.

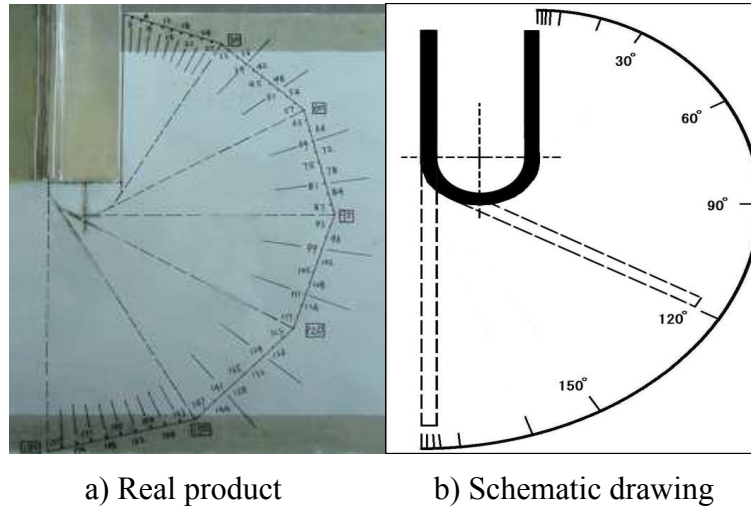


Fig. 2 Shape memory testing tool

The shape recovered rate is used to describe the capability that shape memory material recovers its original shape after a series of thermo-mechanical deformations, whose calculative method is shown in Eq. 2:

$$R_r(T) = \frac{\theta_{fixed} - \theta_{final}}{\theta_{fixed}} \times 100\% . \quad (2)$$

Where $R_r(T)$ is the shape recovered rate when the temperature for recovering is T , θ_{fixed} is the bending angle after fixing the shape, θ_{final} is the bending angle after recovering.

Result and Discussion

Shape Fixed Rate of Composites.

Effects of Fiber Content on Shape Fixed Rate. The variation laws of shape fixed rate of Kevlar fiber and carbon fiber reinforced composites with different fiber content are shown in Fig. 3.

From the graphs in Fig. 3, the fixed rate of Kevlar fiber or carbon fiber is affected by the fiber content. The shape fixed rate of Kevlar fiber reinforced composite is 99.7% when the content of fiber is 10%. The shape fixed rate is decreased to 99.3% when the content of fiber is 20%. The shape fixed rate of carbon fiber reinforced CF/EP composite is 99.4% when the content of fiber is 10%. The shape fixed rate is decreased to 99.0% when the content of fiber is 20%. The main reason for decrease of the shape fixed rate with the increase of fiber content is that the fiber has no shape memory effect, which produces regular elastic deformation when bending and folding at high temperatures. When the shape is fixed after cooling, the shape of resin is fixed, which force the fiber to maintain the bending shape. Yet the fiber that produces regular elastic deformation has the tendency to return to linetype, which bring a certain degree of deploying force to resin system to decrease the shape fixed rate. The less the fibers content in composite, the more the resins content. The deploying force that produced by regular elastic deformation of fiber is less, and the capability of fixing shape of resin is greater, which improve the shape fixed rate with the decreasing of fiber content.

Effects of Fiber Type on Shape Fixed Rate. As can be seen from Fig. 3, the fixed rate of KF/EP is superior to CF/EP. The main reason for the less effective fixity of carbon fiber composite is that carbon fiber is fiber material which has strong stiffness and strength. When the fiber content is less than 20%, the content of shape memory matrix resin in composites is high, and the storage energy of deformed composites by folding at high temperature is large, which exists in the materials in the form

of distortion energy. The stress in freezing phase at low temperature is greater than or equal to the bending stress of fiber, so the fixed rate of composites is greater. When the content of fiber is more than 20%, the content of resin in the composites is low. The driving force for carbon fiber with high rigidity and high modulus subjected to bending to recover to its straight status is higher than the storage stress in the freezing phase resin. The less the resin content, the less the storage stress. Thus the more the fiber content, the harder composite to fix.

For shape memory materials, the general requirement of shape fixed rate is more than 95%. It can be concluded from the test results that, when the content of fiber is less than 20%, the shape fixed rates judge the Kevlar fiber and carbon fiber reinforced composites both can serve as shape memory composites. Also, it shows the resin system has good shape fixed rate.

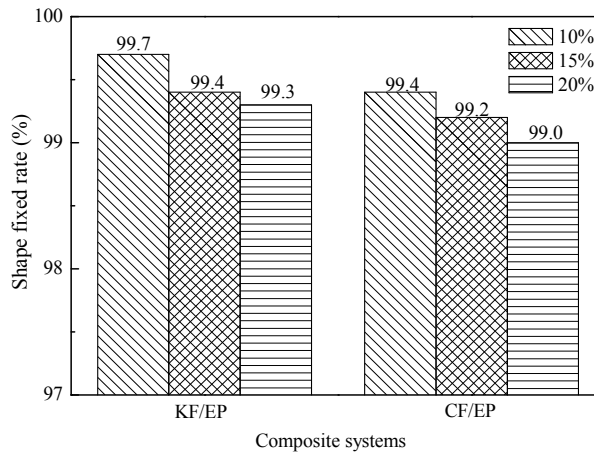


Fig. 3 Shape fixed rate of KF/EP and CF/EP with different fiber content

Shape Recovered Rate of Composites.

Effects of Fiber Type on Shape Recovered Rate. The variation laws of shape recovered rate of CF/EP and KF/EP systems with different fiber content (10%, 15% and 20%) are shown in Fig. 4. As can be seen from the shape recovered rates of two kinds of composites, the shape recovered rate of carbon fiber composite is superior to that of Kevlar fiber composite. The main reason is that the stiffness and strength of carbon fiber composite are both larger than Kevlar fiber composite. The storage energy of “freeze” by bending and folding is large, which existed in the materials in the form of distortion energy and is released at high temperature. Plus, the bending carbon fiber is bound by resin, and the shear stress between resin and fiber improve, which improve the bending recovered force, so the shape recovered rate of carbon fiber composite is higher than Kevlar fiber. When the fiber content is more than 20%, the content of resin in composites is low, the stored strain energy in the matrix is low, and shear force between fiber and matrix is small, thus the bending recovered force is small and the recovered rate will be decreased.

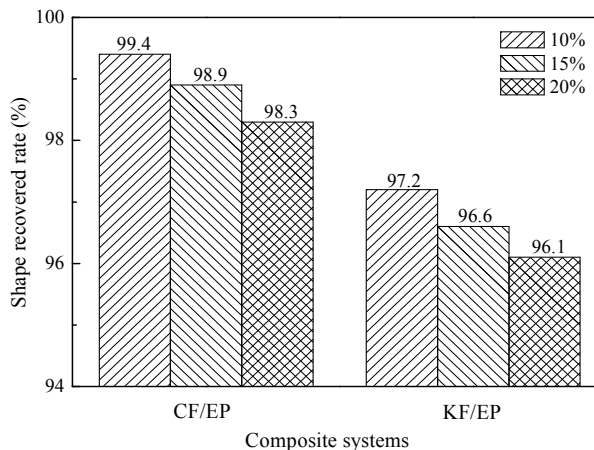


Fig. 4 Shape recovered rate of CF/EP and KF/EP with different fiber content

Effects of Fiber Content on Shape Recovered Rate. The variation laws of shape recovered rate of composites with the temperatures are shown in Fig. 5 and Fig. 6, respectively. From the graphs in Fig. 5 and Fig. 6, the shape recovered rates of two kinds of fiber reinforced composites both cannot achieve 100%, and are lower than the recovered rate of shape memory resin system without reinforced fiber. The shape recovered rates are decreased with the increasing of fiber content, the main reason of which is that the content of shape memory resin decreases with the increasing of fiber content, and the whole shape memory effect of composite decreased, bringing down shape recovered rate.

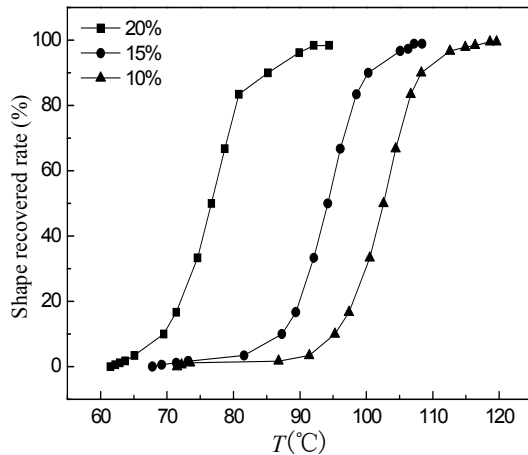


Fig. 5 Change of shape recovered rate of KF/EP with resin system

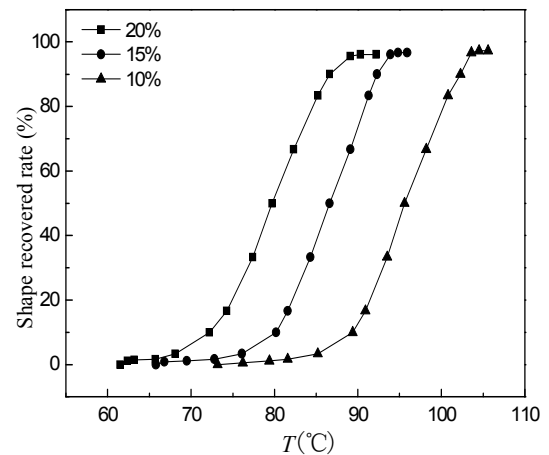


Fig. 6 Change of shape recovered rate of CF/EP with resin system

Conclusions

For Kevlar fiber and carbon fiber reinforced shape memory composites, the shape fixed rate and shape recovered rate of the composites were decreased with the increase of Kevlar and carbon fiber volume. The shape fixed rate of Kevlar fiber reinforced shape memory composite was higher than that of carbon fiber reinforced shape memory composite, but the shape recovered rate of the former were much lower than the latter. This is because the rigidity and strength of carbon fiber composite are both larger than Kevlar fiber composite. The stored energy of “freeze” by bending and folding is large, which existed in the materials in the form of distortion energy and is released at high temperature. In addition, the bending carbon fiber is bound by resin, and the shear stress between resin and fiber improve, which increase the bending recovered force.

Acknowledgements

This work was financially supported by the Program for Harbin city science and technology innovation talents of special fund project (2012RFXXG091) and Pre-research Fund Project of National Defense.

References

- [1] R. Biju, C. Gouri and C.P. Reghunadhan Nair: *Eur. Polym. J.* Vol. 48 (2012), p.499
- [2] K. Gall, M.L. Dunn, Y. Liu, D. Finch, M. Lake and N.A. Munshi: *Acta Mater.* Vol.50 (2002), p.5115
- [3] S.A. Madbouly and A. Lendlein: *Adv. Polym. Sci.* Vol. 226 (2010), p.41
- [4] J. Bu, P. Wang, L. Ai, X. Sang and Y. Li: *Adv. Mater. Res.* Vol. 287-290 (2011), p. 2756
- [5] W.H. Francis, M.S. Lake, and J.S. Mayes: 47th AIAA/ASME/ASCE/AHS/ASC Structures, Structural Dynamics, and Materials Confere, AIAA 2006-1764 (2006), p.1
- [6] M.S. Lake, N.A. Munshi, M.L. Tupper and T. Meink: AIAA Space 2001 Conference and Exposition, AIAA 2001-4602 (2001), p.1

Granulation Technology Experiments of Novel Mesoporous Composite Water Purification Material

Tianxin Li^{1, a}, Yongcun Zou^{2, a}, Shanxue Jiang^{3, b}

^{1,3}Civil and Environmental Engineering school, University of Science and Technology Beijing, Beijing 100083

²State Key Laboratory of Inorganic Synthesis and Preparative Chemistry, College of Chemistry, Jilin University, Changchun 130012, P.R. China

^aemail:terdili@tom.com, ^bemail: shanxue_jiang@163.com

Keywords: Water Purification Material; Mesoporous Material Granulation Technology

Abstract. A novel mesoporous composite water purification material was synthesized from natural zeolite to possess certain water purification properties as well as in proper particle size range for optimal fluid flow, particle retention and mass transfer in fixed bed applications. The meerschaum was used as the framework material in the experimental manufacturing procedure, polyethylene alcohol with carboxylic methylic cellulose was used as cohesive reagent, and H₂O₂ as bubble-forming agent. And the resulted granular product has good abrasion resistance ability with the measured impact breaking time reaching 12 hours. In addition, its decoloring rate is only 4.4% lower and its COD_{Cr} removing is only 13.2% lower than those of the original powder product, respectively. As a whole, the granulation potential and significantly expands the zeolite wastewater treatment application range with (only is not necessary) minor reduction of its treatment efficiency.

Experiment

When a water purification material is used there is a clear assumption, the smaller particle size is, the larger proportion of surface area is, getting more contact between the cleaning material and the pollutant, and ensuring a better purification effect. And many articles have been published on the topic of water purification material [1, 2, 3, 4, 5]. However, in practical applications, the smaller particle size is, the greater water resistance is, as well as the more loss in the treatment. Accordingly, it is better neither too large nor too small in particle size [6]. In this paper, mesoporous material granulation technology [7, 8, 9] is used in water purification.

Experiment Materials and Evaluation Indexes

The preparation process is as follows: natural clinoptilolite → acid etching → heating ablation technique with additive → organic ion exchange → rebaking ablation → granulation → application [10, 11, 12]. Granularity < 0.061 mm

Evaluation indexes include evaluation of orifices proportion, evaluation of the particle withstanding impact capacity and evaluation of treatment efficiency.

Project of Experimentation

Meerschaum was used as the base material, polyethylene alcohol and carboxylic methylic cellulose were used as cohesive reagent, H₂O₂ was used as bubble-forming reagent. Method of experimentation: firstly, add some quantities of meerschaum into the powder of water purification. Secondly, add some quantities of polyethylene alcohol into the glass after mixing up symmetrically. Thirdly, heat up and blend fully under certain temperature for some time until it turned out to be colloid. Then, add some carboxylic methylic cellulose and mix up symmetrically. After that, pour H₂O₂ solution of certain volume and concentration into the glass and mix up again. Following, make out granules with the diameter of about 2 mm manually. Finally, put the crucible with these granules in a heat system and dry them all under a certain temperature.

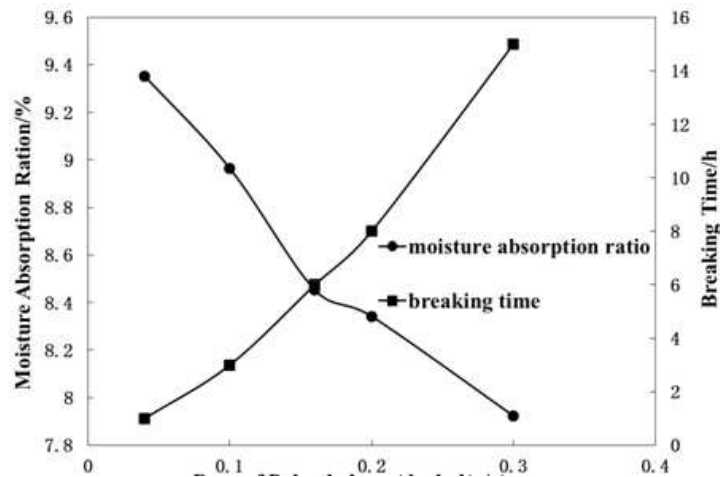


Fig. 1 The influence of dose of polyethylene alcohol on moisture absorption ratio and breaking time of resisting concussion

The Outcome and Discussion of Experiment

The Dose of Polyethylene Alcohol

The system was tested under different doses of polyethylene alcohol firstly, when the temperature of polyethylene alcohol was 60°C during heating and blending, the concentration of serosity and H₂O₂ was 2mg/g and 3% respectively, the dose of meerschaum, CMC and H₂O₂ were 0.04g/g, 0.1g/g and 0.4mL/g respectively, and the temperature of baking was 50°C. The influence on moisture absorption ratio and capability of resisting concussion was showed as Fig 1.

First, moisture absorption ratio of granule materials became smaller as the dose of polyethylene alcohol increased. The moisture absorption had the biggest values when the doses ranged from 0.04g/g to 0.2g/g. Second, breaking time of resisting concussion became longer as the dose of polyethylene alcohol increased. This showed that the capability of resisting concussion was strengthened because of adding polyethylene alcohol. However, the dose of 0.2g/g can meet the acquirement to intensity of granules. In all, the dose of 0.2g/g polyethylene alcohol was most suitable.

The Dose of Meerschaum

The details were showed in Fig 2. First, moisture absorption ratio of granule materials increased as the dose of meerschaum increased, and the suitable doses ranged from 0.04g/g to 0.08g/g. Second, breaking time of resisting concussion become longer at the first attempt, and then it decreased as the dose of polyethylene alcohol increased. And the breaking time resisting concussion, reached the lowest value when the dose was 0.1g/g, at that moment the exterior intensity became an inferior value.

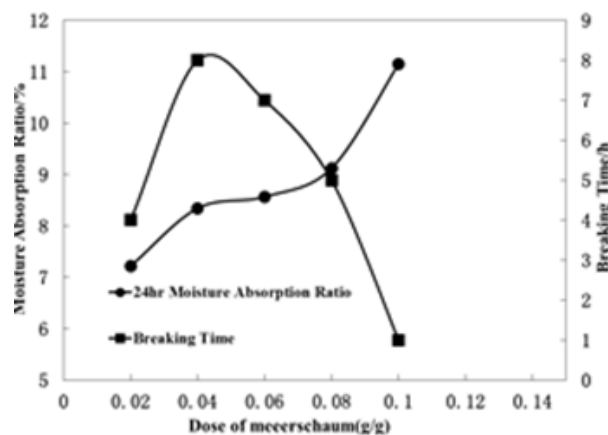


Fig. 2 The influence of dose of meerschaum on moisture absorption ratio and breaking time of resisting concussion

However, with fiber framework, meerschaum made granules' framework even more incompact, especially when a bigger amount of meerschaum was added. In all, the dose of 0.04g/g meerschaum was the most suitable.

The Dose of CMC

Another kind of cohesive reagent called CMC should be used to strengthen adherence. The result was showed in the Fig 3.

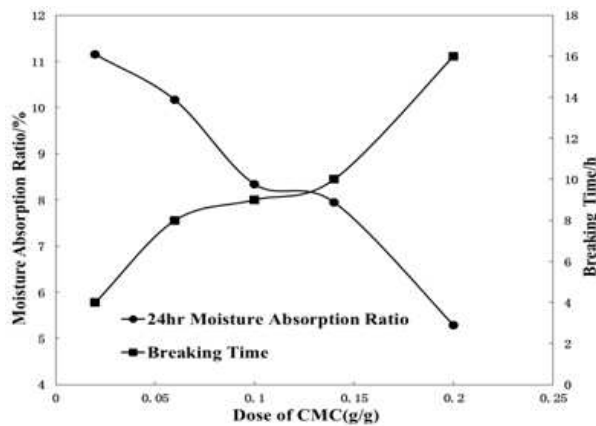


Fig. 3 The influence of dose of CMC on moisture absorption ratio and breaking time of resisting concussion

First, moisture absorption ratio of granule materials decreased as the dose of CMC increased. And the most suitable dose range of CMC was 0.02g/g~0.06g/g. Second, breaking time of resisting concussion became longer as the dose of CMC increased and became closer when the dose were 0.06g/g and 0.1g/g. So the most suitable dose of CMC was 0.06g/g.

The Heating and Blending Temperature during Adding Polyethylene Alcohol

The temperature can affect conglutination and the capacity of forming membrane of polyethylene alcohol should be optimized. The result was showed in the Fig 4.

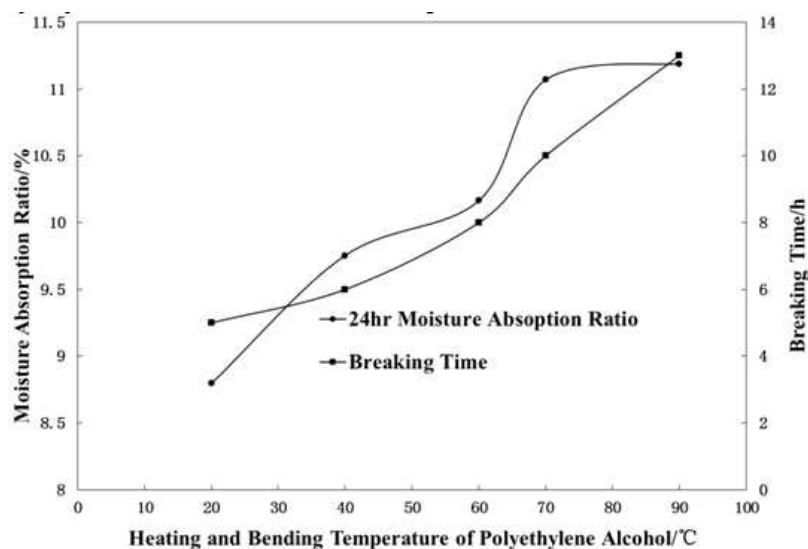


Fig. 4 The influence of heating and blending temperature during adding polyethylene alcohol on moisture absorption ratio and breaking time of resisting concussion

First, moisture absorption ratio of granule materials increased as the dose of polyethylene alcohol increased, but the scope was small. Second, the most suitable temperature of heating and blending was 70°C.

The Dose and Concentration of H₂O₂

From Fig 5, moisture absorption ratio increased as the dose of H₂O₂ increased with the promise of equal concentration. The dose of 0.2mL/5g~0.4mL/g H₂O₂ and the concentration of 3% were most suitable.

From table 1, breaking time of resisting concussion became shorter as the dose of H₂O₂ increased. The most suitable condition of H₂O₂ was the concentration value of 3% and the dose of 0.4mL/g which can made moisture absorption ratio highest and capability of resisting concussion better.

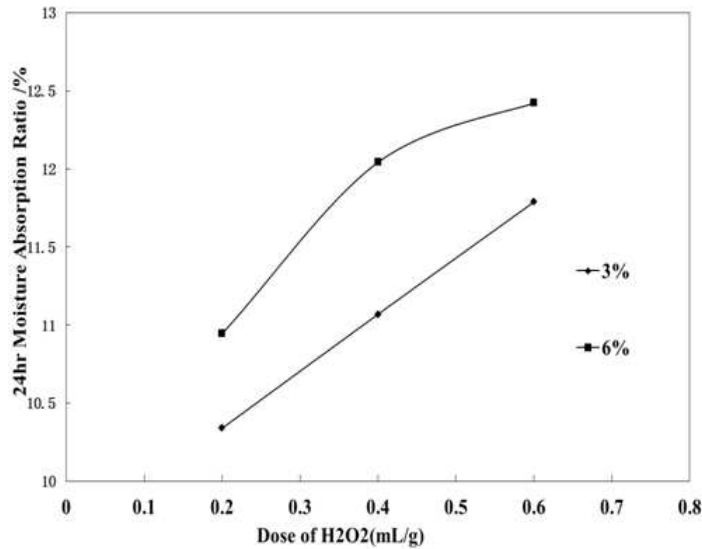


Fig. 5 The influence of H₂O₂ dose and concentration on moisture absorption ratio

Table 1 The influence of H₂O₂ concentration and dose to capability of resisting concussion

The concentration of H ₂ O ₂ (%)	3			6		
The dose of H ₂ O ₂ (mL/g)	0.2	0.4	0.6	0.2	0.4	0.6
The breaking time of resisting concussion (h)	<13	<10	<6	<8	<4	<2

The Baking Temperature

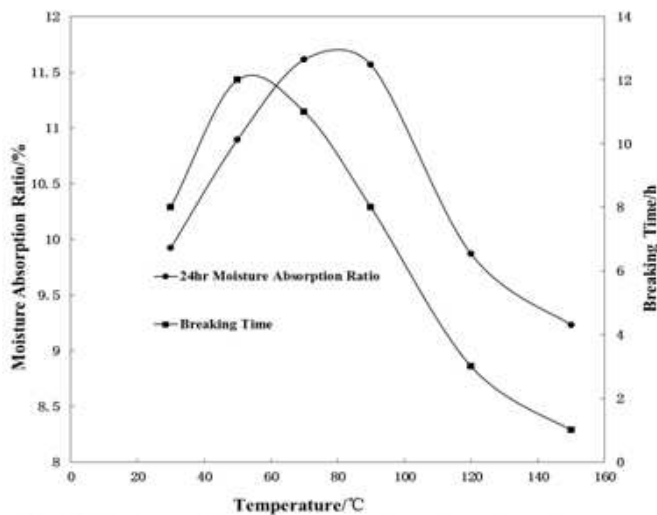


Fig. 4 The influence of breaking time on moisture absorption ratio

From Fig 6, as temperature value rose, the moisture absorption ratio of granule materials increased first and began to decrease sharply when the temperature reached 80°C. The most suitable baking temperature was 50~70°C. Besides, breaking time of resisting concussion became longer at the first place as the temperature rose, then decreased sharply to 1h in 150°C when temperature exceeded 70°C. The most suitable baking temperature was 50°C with the consideration of both moisture absorption ratio and capacity of resisting concussion.

The Treatment Efficiency of Resulted Granulars

Weigh up 5g granules and powder of water purification material respectively, pour into 100mL dyestuff waste water, and carry out static adsorption experimentation. The result was as shown in Table 2. The treatment efficiency of resulted granular of water purification material was worse than that of powder. If the condition allows, it is better to use powder material whose treatment efficiency was higher. Still, the treatment efficiency of resulted granular was good, its decoloring rate is only 4.4% lower and its COD_{cr} removing only 13.2% lower than those of the original powder product, respectively.

Table 2 Comparison of adsorption efficiency between resulted granulars and apricot hull- active carbon

Sample	dyestuff waste water	adsorption outcome of resulted granular of water purification material	adsorption outcome of powder of water purification material
Testing indexes			
chroma (times)	7400	410	80
decoloring rate (%)	\	94.5%	98.9%
COD _{cr} (mg/L)	3040	665	266
COD _{cr} removing rate (%)	\	78.1%	91.3%

Conclusion

The experimental manufacturing procedure with meerschaum as the base material, polyethylene alcohol with carboxylic methylic cellulose as cohesive reagent, and H₂O₂ as bubble-forming agent was studied. The best parameters were as follows: the dose of polyethylene alcohol, meerschaum and CMC was 0.2g/g, 0.04g/g and 0.06g/g respectively. The heating and blending temperature during adding polyethylene alcohol was 70°C. The concentration and dose of H₂O₂ was 3% and 0.4mL/g respectively. The baking temperature was 50°C. The moisture absorption ratio of resulted granule materials can reach 10.894%, and the breaking time of resisting concussion can last 12h. The outcome of static adsorption experiment indicated that its decoloring rate was only 4.4% lower and its COD_{cr} removing only 13.2% lower than the original powder product, respectively. Synthetically, the manufacturing procedure was feasible.

Acknowledgment

Supported by the opening foundation of the State Key Laboratory of Inorganic Synthesis and Preparative Chemistry (2011)

References

- [1] Liang X, Xi B, Xiong S, et al. Porous soft magnetic material: The maghemite microsphere with hierarchical nanoarchitecture and its application in water purification[J]. *Materials Research Bulletin*, 44(2009), 12,p.2233-2239.
- [2] Srivastava R. Eco-friendly and morphologically-controlled synthesis of porous CeO₂ microstructure and its application in water purification[J]. *Journal of Colloid and Interface Science*, 348(2010), 2,p.600-607.
- [3] Chen H, Ma X, Dai H. Reuse of water purification sludge as raw material in cement production[J]. *Cement and Concrete Composites*, 32(2010), 6,p.436-439.
- [4] Dehou S C, Wartel M, Recourt P, et al. Physicochemical, crystalline and morphological characteristics of bricks used for ground waters purification in Bangui region (Central African Republic)[J]. *Applied Clay Science*, 59–60(2012)69-75.

- [5] Romanos G E, Athanasekou C P, Katsaros F K, et al. Double-side active TiO₂-modified nanofiltration membranes in continuous flow photocatalytic reactors for effective water purification[J]. *Journal of Hazardous Materials*, 211–212(2012)304-316.
- [6] Wilson.J.R, et al. Structural and chemical changes of cell wall types during stem development. Consequences for fibre degradation by rumen microflora[J]. *Australian Journal of Agricultural Research*, 1997, 48(2):165
- [7] Han R, Liu J, Zhang Y, et al. Dewatering and granulation of sewage sludge by biophysical drying and thermo-degradation performance of prepared sludge particles during succedent fast pyrolysis[J]. *Bioresource Technology*, 107(2012)429-436.
- [8] Vialpando M, Backhuijs F, Martens J A, et al. Risk assessment of premature drug release during wet granulation of ordered mesoporous silica loaded with poorly soluble compounds itraconazole, fenofibrate, naproxen, and ibuprofen[J]. *European Journal of Pharmaceutics and Biopharmaceutics*, 81(2012), 1,p.190-198.
- [9] Zhao B, Zhang Y, Dou X, et al. Granulation of Fe–Al–Ce trimetal hydroxide as a fluoride adsorbent using the extrusion method[J]. *Chemical Engineering Journal*, 185–186(2012)211-218.
- [10] Li T X, Lin H, Song C Y, et al. Acid etching technique for preparation of mesoporous composite environmental materials.*J Univ Sci Technol Beijing*, 2004, 26(3): 237-239.
- [11] Li T X, Lin H, Song C Y, et al. Application of heating ablation technique with additive in the preparation of a new kind of meso-porous water purification material.*Tech Equip Environ Pollut Control*, 2005(2):36-39.
- [12] Li T X, Lin H, Song C Y, et al. Study on preparing a new kind of water purifying material by organic ion exchange-rebaking ablation process.*Environ Prot Chem Ind*, 2005, 25(1): 54-58

Controlling Factors of Hydrocarbon Accumulation and Optimization of Favorable Blocks for Both Flanks of Putaohua Reservoir in Southern Daqing Placanticline

Dianshi Xiao¹, Hongli Chen² and Haifeng Chen³

¹ Northeast Petroleum University, Daqing, Heilongjiang, China, 163318;

² Northeast Petroleum University, Daqing, Heilongjiang, China, 163318;

³ Northeast Petroleum University, Daqing, Heilongjiang, China, 163318;

Keywords: Accumulation control factors, resource evaluation, Putaohua reservoir, Southern Daqing Placanticline

Abstract. Putaohua reservoir in south of Daqing Placanticline is rich in oil and gas resources. However, the distribution of oil and gas is so complex and the hydrocarbon accumulation process is still unclear by now. Due to low proven reserves, it is not effective to explore the reserves. By use of the logging interpretation and results of production test and together with analysis of the oil and gas distribution and hydrocarbon accumulation process of Putaohua reservoir in south of Daqing Placanticline, the controlling factors of hydrocarbon accumulation in aspects of oil and gas migration pathway, developmental characteristics of sand, local structure etc are discussed in order to optimize potential blocks. The hydrocarbon of Putaohua reservoir in both flanks in south of Daqing Placanticline is from the local K_{1qn1} source rock. Hydrocarbon migration mainly depends on vertical movement and is supported by short-distance lateral migration; hydrocarbon accumulation is mainly affected by restrictions of oil source fault and high fault block, so that most of hydrocarbon accumulate in the distributary channel and distal bar of reverse faulting footwall, horst, reverse fault and other high fault blocks where are closely adjacent to the oil source faults.

Introduction

Daqing Placanticline with most concentrated hydrocarbon resources, productive layers and greatest production is the second-level tectonic unit in the north of Songliao Basin. From north to south, it is composed by seven third-level tectonic unit, i.e. Lamadian, Saertu, Xingshugang, Gaotaizi, Taipingtun, Putaohua and Aobaota [1], of which Putaohua and Aobaota, containing three oil-bearing layer, from bottom-up namely Fuyu, Putaohua and Heidimiao reservoirs, is located in the southern Placanticline. Putaohua is the most important reservoir of these three reservoirs. Currently, all principal parts of the southern Placanticline have entered into intensive development phase so that the focus is gradually moving to the slopes of both flanks [2]. However, it is difficult to evaluate the reserves and optimize favorable areas of both flanks of Putaohua reservoir mainly due to: (1) a variety of reservoir types, complex water and oil distribution and unclear understanding to the controlling factors of hydrocarbon accumulation; (2) the reservoir is dominated by interbedded thin sandstone and mudstone with rapid lateral variation so that it is hard to conduct spatial prediction and investigate the oil reservoir scale and areas. To this end, it urgently needs to study the hydrocarbon accumulation of Putaohua reservoir and reveal the geological conditions and key controlling factors of such complex reservoir on the basis of existing geological knowledge and exploration results in order to provide guidance for potential resources assessment and optimization of advantageous blocks in the blank areas of both flanks of Putaohua reservoir.

Distribution of Oil and Water and Hydrocarbon Accumulation Process

The complex fault system of Putaohua reservoir matched well with the intermittent sand body in delta front. A variety of reservoirs were developed in both flanks slopes, including lithology, fault lithology, fault block and tectonic lithology. The west flank is mainly composed by lithology and fault

lithology and the east flank is dominated by lithology and tectonic lithology. The distribution of oil and gas of Putaohua reservoir is extremely complex mainly due to the co-control of tectonic structure and lithology: besides up oil-down water, inversion combination, such as up water-down oil or up oil-middle water-down oil are also common in aspect of vertical direction; non uniform oil-water interface exists along horizontal direction. Affected by tectonic factors, the fault block often presents a normal transition relationship as ‘high yield of pure oil, middle yield of water and oil and low yield of pure water’. Controlled by lithology factors, inversed results exist within certain local fault block, i.e. ‘high yield of water and low yield of pure oil’.

Previous researches found that the accumulation pattern of Putaohua reservoir in southern Placanticline is “generate at the bottom source and preserve at up position with lateral short-distance migration” [3]. Hydrocarbon of Putaohua reservoir is mainly from local K_{1qn} source rock. The source rock mainly expelled hydrocarbon in the deposition end of K_{1m2} ; Therefore, active faults of inversed period^[4] can be used as the vertical migration pathway and deliver the oil and gas upward to Putaohua reservoir, and then oil and gas is migrated laterally driven by buoyancy at short distance along the sand body of Putaohua reservoir. Affected by lithology and fault, hydrocarbon is accumulated in the lithologic, fault lithologic, fault block and tectonic lithologic traps near the oil source faults.

Controlling factors of hydrocarbon accumulation. Hydrocarbon accumulation is an integrated geological process at space and temporal in petroliferous basin and affected by a variety of geological factors. For Putaohua reservoir in both flanks of Southern Daqing Placanticline, vertical migration pathway, development and distribution of sand body and local tectonic structures are critical controlling factors of hydrocarbon accumulation.

Effects of vertical migration pathway on hydrocarbon accumulation. Due to small scale of sand bodies and poor lateral continuity, lateral hydrocarbon migration is constrained in short distance so that hydrocarbon is mainly distributed along vertical migration pathway (hereinafter referred to oil source fault). Oil source faults are the key faults to control accumulation of Putaohua reservoir. According to the fine anatomy of high oil yielding zone and water yielding zone, 90% of high oil yielding zones have developed or are close to the oil source faults and 70% of water yielding zones are lack of or far way from the oil source faults. In addition, testing production of single well is positively correlated with the distance oil source fault, i.e. the closer the oil source fault the larger the testing oil production of single well, and vice versa the less production.

The configuration of oil source fault and sand body not only controls the horizontal distribution of hydrocarbon but also determines the hydrocarbon accumulation layer. Due to rare vertical cutting of sand body and overlap contact, the vertical continuity is poor. Each sand body developed vertically in Putaohua reservoir forms an independent oil and water system. When the sand body is communicated by fault effectively, there is the possibility that oil and gas accumulate in the sand body. When the sand body and oil source fault are lack of communication, the sand body is usually water-bearing layer.

Effects of sand body development on hydrocarbon accumulation. In aspect of micro level, oil-bearing property of reservoir sand body is closely related to type of sand body, thickness and physical properties. Sand bodies of Putaohu reservoir can be classified into four types: distributary channel sand, distal bar sand, main sheeted sand and non-main sheeted sand, among of which distributary channel sand body is the thickest with the most outstanding reservoir properties, followed by distal sand body and main sheeted sand body. Non-main sheeted sand body is the thinnest one. The relationships between thickness of single sand layer, reservoir interpretation and testing production are shown in Table 1. Table 1 show that the thicker the single sand layer, the high probability of logging interpretation of reservoir and the larger testing oil production capacity of single layer. Therefore, it is known that distributary channel sand body presents the best oil-bearing performance, followed by distal bar sand body and main sheeted sand body and then non-main sheeted sand body.

Table 1 Thickness of single sand layer, probability of reservoir development and testing production capacity

thickness of single sand layer (m)	0-0.5	0.5-1	1.0-1.5	1.5-2.0	≥ 2.0
Probability of reservoir development (%)	40.5	39.8	62.5	67.8	80.2
average testing production capacity (t/d)	0.01	0.8	1.5	3.8	6.8

In aspect of macro level, the developmental characteristics of sand bodies determine the manner of hydrocarbon migration in the region and horizontal distribution of oil and water. Sand bodies of Putaohua reservoir mainly present intermittent strip or sheet distribution with poor lateral continuity. The lateral migration distance of hydrocarbon along sand is limited. The hydrocarbon migration of both flanks of Putaohua reservoir mainly depends on vertical migration and supplemented by lateral migration; the sand bodies at high parts and low parts are usually not connected laterally. When both can effectively communicated with oil source fault, the plane will show that there is hydrocarbon in both high parts and low parts. When there is lack of communication between sand body of high parts and oil source fault, the plane will show oil-yielding at low parts and water yielding at high parts.

Effects of local tectonic structure on hydrocarbon accumulation. Vertical and lateral migration of hydrocarbon is driven by buoyancy. The high fault blocks are located in upper position with smaller fluid potential so that the buoyancy is larger during migration process. Therefore, high fault blocks are the mainstream direction of hydrocarbon migration and accumulation places. According to the statistics of oil source fault that both sides have drilled, the high-yielding industrial oil wells developed at footwall are obviously more than hanging wall. This is mainly due to the tectonic position of footwall is higher than hanging wall (all oil source faults are normal faults), which is conducive to filling of oil and gas. In addition, the lateral sealing ability of footwall is stronger than hanging wall^[5,6], resulting in greater height of sealing oil column for footwall of oil source fault; Especially when the fault orientation is opposite to strata, the inversed fault footwall will form a 'ridge type' shape. Furthermore, the Putaohua oil reservoir at footwall will directly connect with K_{1y23} mudstone at hanging wall and the lateral sealing capacity will be enhanced. Block traps formed by such type of fault footwall has the greatest testing oil production. 14.75t/d high yield industrial oil is obtained from production test of Ao 9 well.

Fault and stratigraphic combination form three types of fault blocks: fault terrace, horst and graben fault and also can be subdivided into inversed fault terrace, forward fault terrace, monoclinic horst, central concave horst and graben fault. The production test results for these five classes of fault blocks are given in Figure 1 and the results show that inversed fault terrace, forward fault terrace and monoclinic horst belong to high fault blocks and are conducive to capture and accumulate hydrocarbon. The oil layers developed better in these sites, particularly the inversed fault terrace has the highest testing oil production capacity; while the graben and central concave horst are low fault blocks with relatively lower tectonic location, which is not conducive to hydrocarbon accumulation. Such types mostly are water layers from testing results although adjacent to oil source fault.

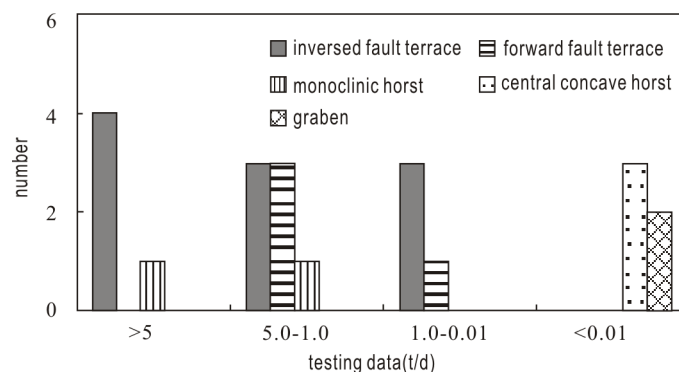


Fig. 1 Testing data for five classes of fault blocks

Optimization of Potential Areas to Increase Reserves

According to the analysis above, hydrocarbon accumulation of both flanks of Putaohua reservoir is mainly constrained by oil source fault and high fault block. In the case of absence of any of them, it is impossible to accumulate hydrocarbon. Prediction of favorable areas is conducted combining with deposition characteristics, tectonic characteristics and oil-water distribution. The prediction mainly considers the areas adjacent to the oil source fault, located in high fault blocks (footwall of inverted fault, inverted fault terrace, horst or local forward tectonic structure) as well as reservoir sand body development areas (distributary channel or distal bar); According to three principles above, prediction is conducted based on sub-layers and reservoir types. Through compositing favorable areas of each layer and combining with thickness of sand body, oil reservoir type and production capacity, favorable potential blocks are selected. Finally, 14 preferable potential blocks of both flanks in total are optimized. It is predicted that these blocks contain 44 km² oil-bearing areas and preserved 943.9×10⁴ oil reserves.

Summary

Through analysis of the control effects of oil source fault, development of sand body and local tectonic structures on hydrocarbon accumulation of both flanks of Putaohua reservoir in Daqing Placanticline, following conclusions can be made:

The oil-water distribution in both flanks of Putaohua reservoir is mainly affected by tectonic structure and lithology together. Reservoir types mainly include lithology, fault lithology and tectonic lithology.

Oil source faults are the key vertical pathway for hydrocarbon migration. Oil source faults and sand body control the horizontal and vertical distribution of oil and gas together; the high fault blocks, such as inverted positive fault footwall, horst and inverted fault terrace, are main accumulation sites; delta-front distributary channel and distal bar sand bodies are thick and have good bearing performance, which are good for hydrocarbon injection and accumulation.

References

- [1] Zhao Bin, Liu Chai, Wang Shihuang, et al. Reversal Tectonic Structure of Daqing Placanticline and Its Identification [J]. Journal of Jilin University (Earth Science), 2006, 36(S1):101-103.
- [2] Zhang Wenqi, Che Tingxin, Wang Changsheng, et al. Controlling Factors on Hydrocarbon Accumulation in the Saddle of Northern Putaohua Oilfield, Songliao Basin [J]. Geoscience, 2008, 22(4): 599-605.
- [3] Hou Qijun, Feng Zhiqing, Feng Zihui. Continental Petroleum Geology of Songliao Basin [M]. Beijing: Petroleum Industry Press, 2009, 460-484.
- [4] Fu Xiaofei, Ping Guidong, Fang Ruidong, et al. Study on the Hydrocarbon 'Intrusion' Accumulation Law of Fuyang Reservoir in Sanzhao Sag. Acta Sedimentologica Sinica, 2009, 27(3):558-565.
- [5] Li Mingcheng. Hydrocarbon Migration (Third edition) [M]. Beijing: Petroleum Industry Press, 2004: 1-320.
- [6] Luo Qun, Jiang Zhenxue, Pang Qisong. Mechanism and Model of Fault Controlling Petroleum Accumulation [M]. Beijing: Petroleum Industry Press, 2007:1-52.

SEM Image Processing of PP/Rice Husk Composite Using MATLAB

Huan Zhang^{1, 2, a}, Chunxia He^{1, b}, Derong Lu^{1, c} and Min Yu^{1, d}

¹College of Engineering, Nanjing Agriculture University/Jiangsu Key Laboratory for Intelligent Agricultural Equipment, Nanjing, Jiangsu, 210031, P. R. China

²College of Mechanical and Electronic Engineering, Qingdao Agriculture University, Qingdao, Shandong, 266109, P. R. China

^ahuan0804@163.com, ^bChunxiahe@tom.com, ^cderong2000@163.com, ^dabigwizard@163.com

Corresponding Author: Chunxia He

Keywords: PP/Rice Husk Composites, Building Material, Microstructure, SEM, Image Processing.

Abstract. As a novel environmental protection, sustainable and energy-saving building material, Wood Plastic Composites (WPC) has been acknowledged gradually and has been used extensively in the trade of building materials in Chinese mainland. By acquiring SEM images of PP/rice husk composite and using digital image processing based on MATLAB, the composite microstructure images were subsequently processed, e.g. image gray adjust, filtering, smoothing, region segmentation, morphological processing, etc. The image processing results show that the processed images are clearer and more discriminative than those unprocessed, which hereafter facilitate to analyze the relationship between microstructure and macroscopic properties of WPC in depth for the future.

Introduction

At present, Wood plastic composite materials (WPC) have developed rapidly with its advantages of resource utilization and environmental protection in the global, especially having the deep and wide applications in the line of building materials in practice, so the market prospects of PP/rice husk composite are very promising. Machine vision detection by the means of digital image processing of biomass based material preparation is a new and nondestructive method, with many benefits such as extreme speediness, strong identification, high repetition, large sample capacity, low cost, non-fatigue and so on [1]. Therefore, this novel inspection method used for examining and analyzing the microstructure, morphology and fracture based on Scanning Electron Microscope (SEM) images has been applying more and more intensively and has been developing more and more perfectly.

In this paper, a image processing software platform with multiple function based on MATLAB is introduced, which include image preprocessing, e.g. image smoothing, filtering, gray balance and gray tension, as well as some fundamental image analysis, for example region segmentation, morphological operation, image marking, and etc. With the platform above SEM images of PP/rice husk composite can be processed and analyzed conveniently and efficiently.

Materials and Method

Materials Rice husk was supplied by Nanjing Beautiful Scenery Compound Materials Company (P. R. China) with their average particle size passing through 40, 60 and 80 mesh respectively, and PP was obtained in the market from Nanjing Yangtze petrochemical Co. Ltd (P. R. China). Scanning Electron Microscope (SEM) was offered from Japan JEOL electronic company with the type of JSW-6300.

Main experimental equipments include high-speed mixer (type: SHL-500), twin screw extruder (type: SJSZ), crusher (SJ-300), oven (type: WJ-A), etc.

Method Weighing dried PP, wood fiber; compound additives and paraffin were put into a high-speed mixer to stir for 10 minutes, and then drained.

Extruded samples the uniformly mixed materials were extruded into granulation by the twin screw extruder at 170-200 °C, regulating the extruding temperature and extrusion speed, controlling the extruding speed, and setting the extruding pressure to 20-30 MPa when samples extruded. The aim of granulation is to heat melting, mixing, wood plasticization and discharging volatile, so the fully plasticization can be got in the production of WPC shapes. With the help of heating and shearing force in the process of granulation it is easy for the WPC mixture to shape particles; Injected before drying. Wood fiber is easy to absorb water, so it is necessary to dry the extruded particles in the oven in 4h at 110 °C; Injection sample. The dried pellets were put into the injection molding machine, and adjusted the suitable temperature and injection pressure to make the qualified samples according to the different ratio of raw materials.

WPC material samples were then cut into little bars with the specified dimensions, and it was a need to clean, dry and spray gold before shooting pictures. To observe and shoot the SEM images of collected specimens with JSW-6300 Scanning Electron Microscope was followed, of which accelerating voltage is 20kV, magnification is 400 X and 2,000 X respectively and image resolution is 1232×912.

Results and Discussion

Results Because the output images from SEM are true color and the image segmentation need to use gray image, so it is required to change the image format first. After that, to use gray transform, i. e. image enhancement, to transform the original gray images into the enhanced ones, such as histogram equalization, image sharpness, linear and nonlinear smoothness and filtering. The purpose of these techniques is to realize the gray scale image enhancing and sharp, which mainly based on the independent pixels for subsequently processing. To use gray scale transform and adjustment to compensate the uneven illumination of the original images to make the following ones in the same or similar gray distribution [2].

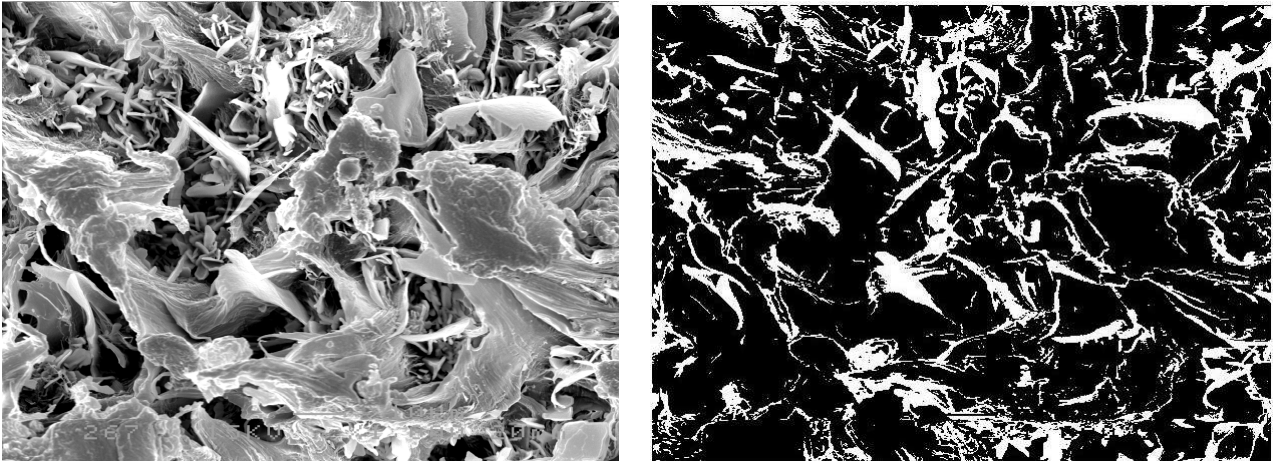
Noise Reduction Because the images are taken from SEM at the spot which may be introduced different noises from different sources, it is necessary to use some image processing of noise reduction, due to this median filtering method was adopted here.

Object edge detection. There are many kinds of image edge detection operator, and each operator has its advantages and disadvantages in application. Based on the image processing effect comparison it is advisable to select a fit operator according to the actual situations and the needs for some specific analysis. It was determined to use Otsu thresholding method and the Sobel edge detection operator to make threshold segmentation and extract the object boundary set after several practical effects comparison.

Morphological processing to get the main outline from the edge extraction of points set, it is essential to use dilation, erosion operations or opening and closing function of the above images.

After the image processing measures mentioned above the processed images are clearer and more discriminative than the unprocessed ones obviously, so it will facilitate the subsequent processing for advanced image analysis and comprehend.

The unprocessed and processed SEM image of PP/rice husk composite (Take 20% content of rice husk for example), see Fig. 1.



a) The unprocessed SEM image of composite (b) The processed SEM image of composite
 Fig. 1 The Unprocessed and Processed SEM Image of PP/Rice Husk Composite

Discussion. Preliminarily, through SEM pictures it can be seen that low content of PP/rice husk powder occurs intertwining, drawing thread with good wrapped. When rice husk powder content reaches 40% and above, from the viewpoint of fracture morphology it shows that a large number of rice husk fiber are pulled out of PP matrix, leaving many cavities which lead to the decrease of mechanical properties of composite material.

By using the digital image processing and analysis of SEM image of PP/rice husk composite a quantitative description bridge between the microstructure and macro-properties of WPC could be built afterwards [3, 4].

GUI Design

GUI Design Outline. GUI (Graphical User Interface) is composed of the window cursor, button, menu, text, and objects through which user can selectively activate the graphical objects by some methods, such as a mouse moving or a keyboard tapping, so the computer can generate some actions or changes, which include the realization of calculation and drawing [5]. GUI is a graphical user interface with a variety of graphic objects, a typical graphics interface includes graphical displaying area, function button and user customer menu. In order to make the interface to achieve various functions, the need for each graphic object layout and programming should be met. In this way, as long as the user activates the corresponding object, the corresponding code for the user to develop the graphical user interface will be fulfilled, which provides a convenient and efficient integrated development environment for GUI design.

GUI Design Processes. GUI interface design includes interface design stage and program implementation stage. The specific design processes are as follows: analyzing the main function of WPC material image processing system to understand all design tasks; drawing the sketch of image processing system interface from the viewpoint of the final user; Configuring the static interface and checking according to the sketch; Listing dynamic function code of graphical interface.

The interface convert to the executable files in the design often repeats steps among the above processes, so the development process is not one-way. The design process and its implementation often cannot be completed all at once according to the expected demands, which regularly requiring an iterative processes. Some problems will be encountered which unable to solve temporarily, so it is necessary to continuously make modification and adjustment until the troubles could be shot.

GUI sketch of SEM image processing and analysis system of PP/rice husk is shown in Figure 2.

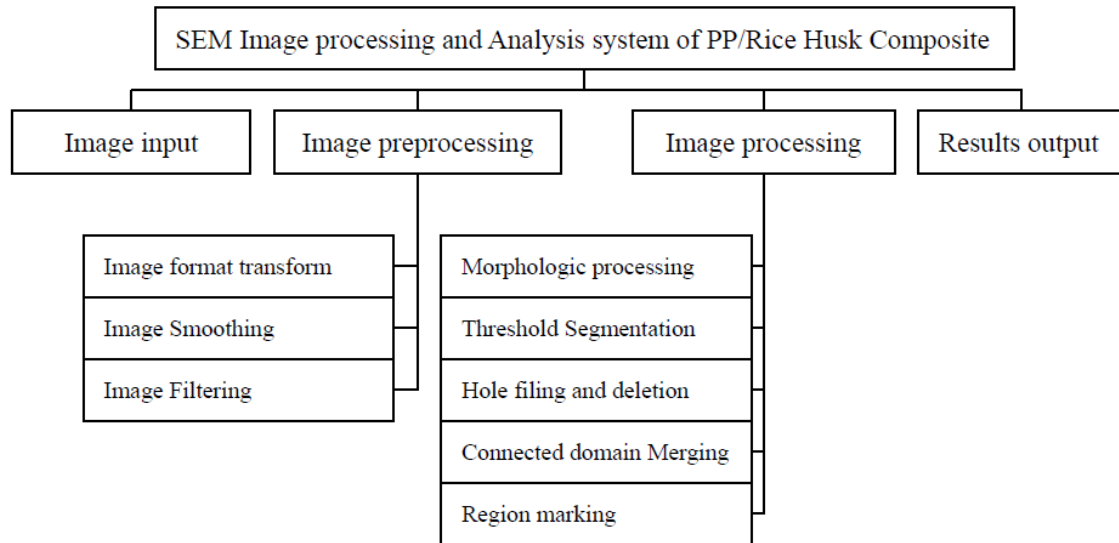


Fig. 2 GUI Sketch of SEM Image Processing and Analysis System of PP/Rice Husk Composite

Conclusions

It is proved that digital image processing of PP/rice husk WPC using MATLAB is fast and effective in practice. After SEM images preprocessing of WPC material bar histogram equalization make images contrast enhanced and gray scale widened, and gray stretch make micro fiber and texture in SEM images shown clearly; Smoothing and filtering of SEM images can effectively suppress the interference and noise in the original ones; Morphological processing of SEM images can effectively eliminate some disturb message to promote the ability to pick up the useful information. With this integrated software platform of SEM Image processing based on MATLAB the possibility of analysis and comprehension the relationship between microstructure and macroscopic properties of PP/rice husk WPC for the future is available.

References

- [1] Mark Craves, Bruce Batchelor: *Machine Vision for the Inspection of Natural Products* (Springer-Verlag, London 2004)
- [2] Chunxia He, Shengming Xiao, Derong Lu, et al. Processing and analysis of SEM images of nano-SiC-PTFE composites microstructure, *Journal of Wuhan University of Science and Technology* Vol.34 (2011), p. 23-26, in Chinese
- [3] A. Sasov, T. D. Ermakova, M. Lotmentsev. Quantitative analysis of images depicting structure of polymers and polymer composites, *Polymer Science U.S.S.R* Vol.33 (1991), p. 597-605.
- [4] N. Bird, M. C. Diaz, A. Saa, et al. Fractal and multifractal analysis of pore-scale images of soil, *Journal of hydrology*, Vol.322 (2006), p. 211-219
- [5] Rafael C. Gonzalez, Richard E. Woods, Steven L. Eddins: *Digital Image processing using MATLAB* (Gatesmark publishing, New Jersey 2003)

Study On Organic Montmorillonite Modified Recycled Optical-grade Polycarbonate Nanocomposite

Fuquan Guo^{1, a}, Yingying Li¹, Bin Guo² and Hao Liang³

¹Department of Materials Science and Engineering, Luoyang Institute of Science and Technology, Luoyang, Henan, 471023, China

²Department of Chemistry and Materials, Nanjing Forestry University, Nanjing, Jiangsu, 210037, China

³Department of Chemical Engineering, Huizhou University, Huizhou, Guangdong, 516007, China
^afqgzl@163.com

Keywords: Organic Montmorillonite, Nanocomposite, Optical-grade Polycarbonate, Modification.

Abstract. Optical-grade polycarbonate (PC) was separated from optical disks by a chemical approach and used to prepare nanocomposite to make full use of the wasted polymers. A quaternary ammonium-modified montmorillonite (organic montmorillonite, OMMT) was chosen as a modifier and an auxiliary functional resin (CBT160) was utilized to exfoliate the layers of montmorillonite. The characterization results of X-ray diffraction (XRD) and transmission electron microscopy (TEM) for PC/ OMMT (5wt %) revealed that an exfoliation structure of the nanocomposite was obtained. The mechanical measurements show a great increase in tensile strength and Izod impact strength of PC/ OMMT nanocomposite compared with the recycled optical-grade PC.

Introduction

Polycarbonate (PC) is considered as one of the most important engineering polymers with a unique combination of attractive engineering properties. These include exceptionally high-impact strength even at low temperatures, low moisture absorption, good heat resistance, good rigidity and electrical properties, and high light transmission. It possesses good dimensional stability (high creep resistance) over a broad temperature range. The transparency of polycarbonate has led to its use as an impact-resistant substitute for window glass. Optical-grade polycarbonate refers to the polycarbonate used in the optical aspects, especially used as optical disks such as CD, VCD, DVD and BD, which contain about 93% PC content by weight. Wasted optical-grade polycarbonate is a challenging problem because the long period of the decomposition in natural conditions and the subsequent pollution caused to the earth.

Polycarbonate, like other polycondensation polymers, can be easily recycled without significant loss of properties. Optical-grade polycarbonate, however, possess a weight-average molecular weight of 18000, which is much lower than that of injection-grade or extrusion-grade polycarbonate. The low weight-average molecular weight means high melt flow rate and poor mechanical properties of optical-grade polycarbonate and at the same time the recycled optical-grade polycarbonate cannot be used as optical devices again because of the degradation of optical property so that the direct applications were very limited.

Modifications can significantly improve the mechanical or thermal properties of polymeric materials and at present nano-based technology is the effective means for polymer modification. Nanocomposites are composed of a polymer matrix and layered silicate platelets having approximately 1 nm thickness and large aspect ratio. In the last two decades, nanocomposites have attracted much attention from both industry and academia, because they may offer enhanced mechanical and/or physical properties (e.g., high modulus and high heat-distortion temperature) that are not readily available from conventional particulate-filled thermoplastic polymers. One of the advantages of such nanocomposites lies in that the concentration of layered silicates required is much

lower (say, less than 7wt %) than that (e.g., 40~60wt%) required for the conventional particulate-filled thermoplastic composites to achieve a similar property enhancement. The lower specific gravity of nanocomposites as compared to conventional thermoplastic composites can offer potential cost benefits as well.

In this paper, the recycled PC from optical disks was blended with a small amount of organically modified montmorillonite (OMMT) in the mixer of RM-200 torque rheometer with the assist of a functional polymerable resin. The micromorphology of the obtained nanocomposite shows an exfoliated dispersion level of OMMT in the PC matrix, which greatly improves the mechanical properties, such as toughness and tensile strength. The nanocomposite can be used as engineering plastics and make the wasted PC become new resources.

Experimental

Optical-grade PC was collected from the wasted CD, VCD, DVD and BD. The detailed procedure is as follows. Firstly, the wasted optical disks were put into the 20wt% aqueous solution of sodium hydroxide at 40~50°C and then exposed to the ultrasonic in a ultrasonic cleaner at 120W for about one hour and finally washed by water, dried, and crushed for next step.

OMMT (DK2) is a quaternary ammonium-modified montmorillonite with the layer distance of 2.4 nm and was supplied by Zhejiang Fenghong New Material Co., Ltd and used as received. An auxiliary functional resin (CBT160) was used in melt-mixing of OMMT and PC to ensure the nanocomposite exfoliated. CBT160 is the cyclic form of polybutylene terephthalate (PBT), having ultra-low viscosity that makes them well suited for numerous low-pressure processes such as casting, rotational molding, and composite processing methods. Thermal stability and compatibility in combination with numerous polymer and filler systems make CBT resins useful in various applications. CBT160 resin easily enters the layers of the OMMT and polymerizes to PBT which help to expand and exfoliate the layers.

Optical-grade PC, OMMT (5wt %) and CBT160 (5wt%) were melt-mixed in the mixer of RM-200 torque rheometer for about 10 minutes to get the resulting nanocomposite. Before the melt mixing, all the ingredients were dried in a vacuum oven at 80 °C for 24 hours. X-ray diffraction (XRD) patterns were recorded using a Bruker D8 focus XRD diffractometer equipped with a Gobel mirror, using Cu K α radiation of 0.154 nm with a voltage of 40 kV and 40 mA of current intensity. A Jeol JEM-2100 transmission electron microscope was used to characterize the structure of the nanocomposite at an accelerating voltage of 100 kV. Mechanical properties were carried out on MTS CMT4304 electronic universal testing machine for tensile strength and MTS ZBC7000 pendulum impact testing machine for IZOD impact toughness.

Results and Discussions

Due to its ease of use and availability, XRD is most commonly used to probe the nanocomposite structure. This technique allows the determination of the spaces between structural layers of the silicate utilizing Bragg's law: $\sin\theta = n\lambda/2d$, where λ corresponds to the wave length of the X-ray radiation used in the diffraction experiment, d the spacing between diffractive lattice planes and θ is the measured diffraction angle or glancing angle. By monitoring the position, shape and intensity of the basal reflections from the distributed silicate layers, the nanocomposite structure may be identified.

The layers' spacing (d -spacing) in the organic montmorillonite can be calculated from the peak at 3.7° from Fig 1 (b). The value of d -spacing is about 2.4 nm, while the general value of the pristine montmorillonite is about 1 nm. Thus the quaternary ammonium-modification is an effective way to expand the d -spacing of the pristine montmorillonite to facilitate the polymer intercalating into the layers of OMMT and eventually exfoliating the layers.

In contrast, the extensive layer separation associated with exfoliated structures disrupts the coherent layer stacking and results in a featureless diffraction pattern as described in Fig. 1(a). Thus, for exfoliated structures no more diffraction peaks are visible in the XRD diffractograms either because of a much too large spacing between the layers or because the nanocomposite does not present ordering.

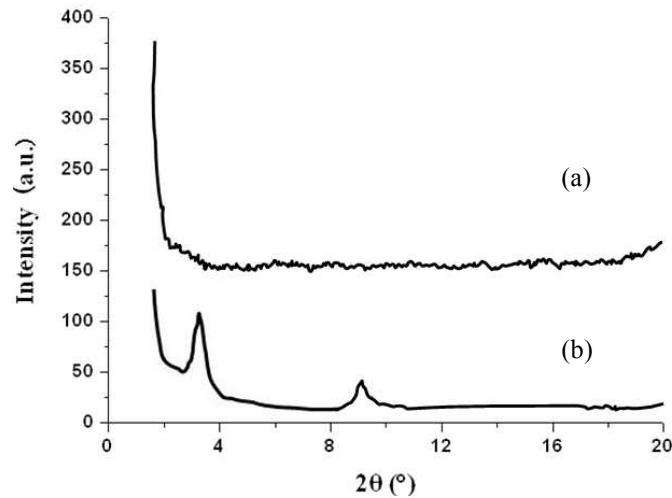


Fig. 1 XRD patterns of PC/OMMT nanocomposite (a) and organically modified montmorillonite (b).

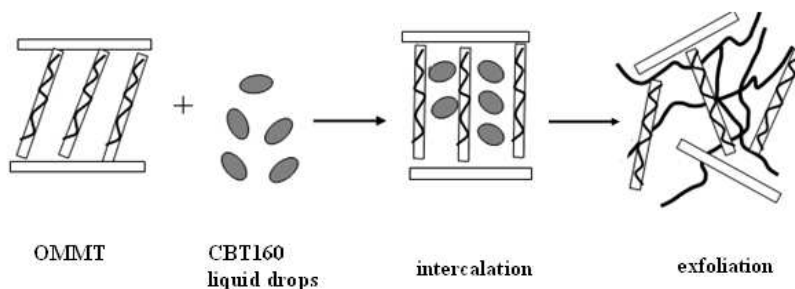


Fig. 2 Mechanism of the auxiliary functional resin CBT160 in preparing exfoliating nanocomposite

However, polymer tends to intercalate into the layers of OMMT in the general melt-mixing process preparing polymer/OMMT nanocomposite because of the lack of motive power in a nano scale of the layers. In this work, a functional resin (CBT160) was used in the intercalating and exfoliating process as described in Fig. 2. CBT160 takes on a liquid with very low viscosity and strong polarity and thus would enter into the layers of the OMMT when melt-mixed at about 230 °C. The subsequent polymerization of CBT160 by means of catalyst already existing in CBT160 would bring about the exfoliation in OMMT owing to the expansion and heating caused.

Fig. 3 shows the morphology of PC/OMMT nanocomposite at high magnification and it can be observed that the organically modified montmorillonite is totally exfoliated in the PC matrix (i.e. exceeding 8 nm in the case of ordered exfoliated structure). This is consistent with the XRD results. In this case, the disappearance of the diffraction peak is observed and one must rely on TEM observation to define the overall structure. With the help of resin, the exfoliation procedure seems easily because of the polymerization of CBT in the OMMT layers.

Table 1 summarizes the mechanical properties of PC and PC/OMMT (5wt %) nanocomposite. It is clear that the tensile strength of PC/OMMT increase about by 38% compared with virgin PC while the Izod impact strength of PC/OMMT is more than threefold that of virgin PC. The values of melt flow rate decreases from 30 g/10min to a relative low value of 13 g/10min, which mean the nanocomposite acquire a good molding capacity. So the PC/OMMT nanocomposite prepared would meet the demands of engineering polymers in the practical applications.

Summary

Optical-grade PC was collected and utilized as a polymer matrix to prepare nanocomposite to make full use of the wasted polymer and achieve the goal of protection of environment. A quaternary ammonium-modified montmorillonite (DK2) was chosen as a modifier and an auxiliary functional resin (CBT160) also was used to play an important role in exfoliating the layers of montmorillonite. Two complementary techniques were used to characterize the structures of nanocomposite: XRD and transmission electron microscopy (TEM). The results show an exfoliation structure of nanocomposite was obtained and the subsequent mechanical measurements also confirm the characterization of structure. The PC/OMMT nanocomposite thus reveals the potential applications in polymeric areas.

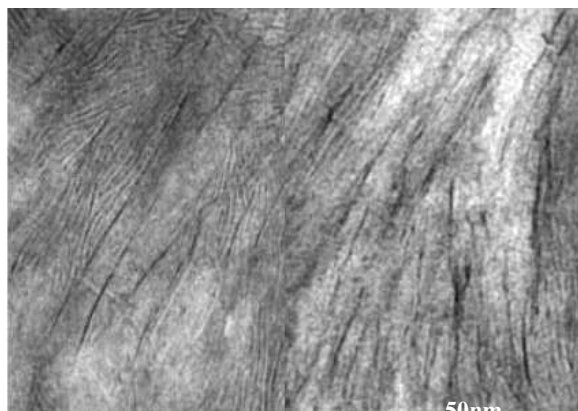


Fig. 3 TEM micrographs of PC/OMMT nanocomposite exfoliated structure.

Table 1 Mechanical properties of PC and PC/OMMT nanocomposite.

Contents of OMMT (%)	Tensile strength (MPa)	Izod impact strength (KJ/m ²)	Melt flow rate (G/10min)
0	45	12	30
5	62	39	13

Acknowledgements

This work was financially supported by the Programs for Science and Technology Development of Henan province (082102340026) and of the Education Department of Henan Province (2009B430009) and Henan province college young backbone teachers' fund (2010GGJS-173).

References

- [1] X.Q. Zhang, M.S. Yang, Y. Zhao, S.M. Zhang, X. Dong and X.X Liu: J. Appl. Polym. Sci. Vol. 92 (2004), p552.
- [2] E. Giza, H. Ito, T. Kikutani and Okui N: J. Polym. Eng. Vol. 20 (2000), p403.
- [3] L.S. Loo and K.K. Gleason: Polymer Vol. 45 (2004), p5933.
- [4] P. Russo, D. Acierno, D. Maio and G. Demma: Eur. Polym. J. Vol. 35 (1999), p1261.
- [5] J. Brus, M. Urbanová, I. Kelnar and J. Kotek: Macromolecules Vol. 39 (2006), p5400.
- [6] I. Gonzalez, J.I. Eguiazabal and J. Nazabal: Polym. Eng. Sci. Vol. 46 (2006), p864.
- [7] A.B. Morgan and J.D. Harris: Polymer, Vol. 44 (2003), p2313.
- [8] T. Fox: Polymer Vol. 45 (2004), p7639.
- [9] R.K. Shah and D.R. Paul: Polymer Vol. 47 (2006), p4075.
- [10] N. Nassar, L.A. Utracki and M.R. Kamal: Int. Polym. Proc. Vol. 20 (2009), p423.

High Performance Concrete in Highway Bridge in Cold and Arid Regions

Zhiyuan Wang

Transportation Institute of Inner Mongolia University, No.24, Zhaojun Road, Yuquan District,
Hohhot City, Inner Mongolia 010070, P.R. China
e-mail: Zhiyuanwang112@163.com

Keywords: High Performance Concrete, Highway Bridge, Construction Technology

Abstract. High performance concrete originated in the generation of high strength concrete, and it is a new high technology of concrete, is in common with high quality and in concrete. High durability on the perspective of improvement and become, use a lot of high quality raw materials and modern technology, is the main development direction of concrete. Because its comprehensive performance by the superiority of the focus of the society, the strict construction technology in the extensive application in the highway bridge, high performance can the use of concrete can improve the efficiency of its safety and avoid unnecessary accidents.

Introduction

With the requirements of the transportation is increasing day by day, the development of "the long life low maintenance Road", using the high performance concrete pavement, improve the concrete flexural strength and durability is the trend of the development of road surface coagulation.

International goals. In 1997 at the 16th international mix the meeting of road surface, and puts forward a design that not only puts forward road average strength requirement, also put forward the development direction of the requirements in the durability of tensile strength to put forward 17 MP high strength concrete, used for surfacing continuous concrete pavement. Improve the density of concrete pavement surface, penetration-proof quality is very important, but it is required Want to achieve high performance concrete through.

High performance concrete bridge road intensity. High performance pavement coagulation an important feature of the soil is high discount strength. With high performance concrete pavement can improve the bearing capacity of the pavement, prolong service life or thinning of the pavement In order to reduce the thickness of the project cost.

The durability of the high performance concrete bridge road high-performance pavement mix. The main characteristics of the soil is to have enough durability, can fight the climate and environment. Long-term damage, ensure that the design of the road in use within the time limit, concrete can enough work normally.

High performance concrete pavement deformation character. Dry shrinkage pavement plate surface product is very big, big evaporation, dry shrinkage may cause road surface produces shrinkage crack, need to strengthen maintenance; Bending the elastic modulus of high performance concrete pavement of bending elastic modulus Quantity E, the measured, grade 1 to 4.305 104 MP, 2 level 4.845 104 MP, 3 level 4.605 104 MP. Strength at 3 high performance concrete pavement of the match ad in than, the aggregate amount less, coarse aggregate limiting grain size is small.

The Application of High Performance Concrete Bridge

High performance concrete is widely used in many offshore structures and grew up across the bridge building, including across the bridge would grow up the things. They are used primarily for the Lord Beam, pier department and the pier base, silicon powder mixed cement. High performance concrete with extensive should be performance is pouring, and stamped firm and not segregation, superb, can keep for a long time. Mechanical properties, the early high strength, high toughness and

volume stability, in bad make with the conditions of long service life, high strength, high liquidity and good durability. In the application of high performance concrete bridge, and extend the use fixed number of year of the bridge and gain better economic benefits. There are concerns that high performance concrete, and not just is high strength concrete. Durability, ease of maintenance and construction of the economy perform has become a target of the engineering construction. The current domestic application good as above its action the sea with concrete bridge, the design life in 100, the use of "offshore mix of high performance Soil "of fly ash, is the waste decayed for magical, become special content And material, make the sea work both high strength and durability of concrete, corrosion properties. And easy construction, direct saving material cost 20 million Yuan. Effect not only on decide, also be able to sense the strain of concrete. The high performance concrete bridge engineering application is the advantage of (1) spans longer; (2) the main girder spacing more; (3) Component thinner; (4) durability strengthened; (5) to strengthen the mechanical properties.

The Application of Concrete in Highway

High performance concrete with high construction sex, high volume stability, high durability and enough mechanical strength, therefore it can take a relatively long time with scour, abrasion, Freezing, water permeability, erosion and other heavy environment, high performance concrete application in highway , the durability is extremely outstanding advantages, on the one hand, it can improve the sub grade construction quality, ensure embankment don't sink; On the other hand, need to be solved in strength grade of concrete highway low, cement consumption, thus formed the cement consumption and the durability between requirements Contradiction. The durability of the high performance concrete is for main index, and at the same time with high strong, the early strength, high construction high sex (high flow, high cohesiveness, high can casting sex) optimal can the opposite sex. The preparation of the basic idea is to choose the raw materials, optimization ratio of concrete, mixed with composite efficient admixtures. At the same time with some after treatment. Industrial waste like silicon ash, fly ash and slag, etc, and from the white concrete things flow over, construction technology into consideration, to obtain high flow pattern, low segregation, quality even. At the same time in its durability to well within normal concrete. The high performance concrete highway should be based on the characteristics of concrete highway, combined with high perform can the advantage of concrete, considering its all aspects of performance requirements to develop them .Research. But if can change from the construction technology of concrete highway, do not use sliding mode paving construction, and use high current state (close to self-leveling), the slump to reach 240-270 NLM concrete construction, the method to further enrich the highway. The connotation of the high performance concrete, it's with the economic benefit and social benefit will be no can be measured.

The Application of High Strength Concrete Construction Technology

With good mixing equipment mixing performance, Horizontal-axis type mixer or inverse streaming mixer can in short time will the stir well, using other equipment have a test as the uniformity of the thing.

The preparation of the high performance concrete, the measurement of the various raw materials should be allowed it. Use machine would work degrees that mouth stable, wave small, in addition to feed and says the device is higher demand, an important control factor is the sand water content, even if mixing equipment jacket has the advanced water content determination and the control equipment, the operator still should pay close attention to the positive stir in the concrete, in its viscosity change happened, try to adjust in time.

Casting is not only difficult operation, but also can't carry on after the admixture adds.

Because of the high performance concrete water cement ratio small, usually secrete water less or not secrete water. Therefore, must be done immediately after casting wet maintenance, in order to prevent the plastic shrinkage crack the generation of seam, due to the large amount of gelled material, to prevent excessive inside and outside temperature the temperature cracks appear, heat preservation measures must be taken.

In the prefabricated T beams and small box girders of Chinese highway bridges, the mainly transverse connection structures between beams were diaphragms. As for the connection constructions of diaphragm joints, there were mainly in two ways, steel plate connections and whole-situ concrete connection. The steel plate connections were often used in the past. Under the influence of the vehicle load and other factors, there were more problems raised, such as the concrete of connection steel plate surface spalled, the connection steel plate corrosion and other issues, seriously even the weld cracking of connection steel plate, and the diaphragms could not play normal work performance, Or even a single beam under load [1]. The whole-situ concrete connections were more used now, the application effect of whole-situ concrete connecting structure was obviously better than steel plate connecting structure [2]. But the whole-situ concrete connection has its own shortcomings, if the structural setting was inappropriate, there were concrete cracking also, and influenced the performance of diaphragm [3, 4]. The studies of the structure construction of diaphragms were more at home and abroad, but less of the transverse connections and the study were limited steel plate connection structures only, did not involve the whole-situ concrete connection structures [5, 6]. Therefore, combined with the concrete cracking that may raised in wet joint connection concrete, the structure size of whole-situ concrete connection and new-old concrete bonding were studied in this paper. Height and thickness of the whole-situ concrete connection were the same size of diaphragm, but for the width of the whole-situ concrete connection, there was no clear define in specification. From the view of construction, the wider the better of whole-situ concrete connection, larger width could not only increased the construction space, but benefited of connection and arrangement of reinforcements, and reduced the weight of pre-T beam at certain extents, conducive of lifting and placing of T beam. But from the point of the autogenously shrinkage of concrete in whole-situ concrete connection, Width changed, concrete shrinkage stress may changed, the possibility of concrete cracked in whole-situ concrete connection and at the bonding surface of wet joint and diaphragm would changed. In order to study the influence of shrinkage stress by width of the whole-situ concrete connection, the ANSYS model of the whole-situ concrete connection was established in this paper. Height of the whole-situ concrete connection was used 160cm, thickness was used 18cm, width was used 30cm, 50cm, 70cm and 90cm respectively, and simulated the stress state of concrete under autogenously shrinkage. Concrete grade was C40, according to the specified of autogenously shrinkage and Mix of concrete in Engineering structural Crack Control and Practical Handbook of Concrete Structure, the concrete shrinkage of 90 days was adopted as the standard value of analysis. And in accordance with the influence of the ultimate shrinkage of concrete by different reinforcement ratio in Engineering structural Crack Control, the whole-situ concrete connection maximum stress were calculated when the reinforcement ratios (including the different modulus ratio). For the concrete cracks, on the material itself, it was not exact to say that the cracking was caused by insufficient of tensile strength. For the cracking caused by deformation, it was not comprehensive to emphasize the tensile strength only, the more important was the material deformation resistance, defined as ultimate tensile of material, meant the relative tensile deformation of material at last. For the wet joints structure of diaphragm, the reinforcement analysis mainly meant structural reinforcement analysis. In the position of whole-situ concrete connection, the number of crack resistance reinforcement should increased, combined with the specific condition of the project, the appropriate reinforcement diameter was no more than 8mm, and the appropriate reinforcement spacing settings was dense as possible but not affect the concrete construction of whole situ concrete connection. There were problems of new and old concrete bonding at the concrete joint surface between whole-situ concrete connection and diaphragm. For the combination of old and new concrete, there were more results of relevant research [9-14]. Lin Yongjun indicated that, in order to improve adhesion with surface, artificial chiseling of the old concrete surface was necessary, and the other measures should be taken after chiseled, such as smear of chemical interface agent, smear of concrete paste and Configuration of shear reinforcement. The calculation formula of bond strength of new and old concrete was given after test. Based on analysis, combined with the specific condition of diaphragm construction, in the construction of whole-situ concrete connection, the diaphragm should be

chiseled at first, and the scum should be rinsed with water. For economic and other reasons, the special concrete was generally not used in the whole-situ concrete connection construction. As general interface agents could not improve the tensile bond strength of new and old concrete, so the interface agent did not required in bonding surface. As anchorage bars could improve the bonding effect of new and old concrete greatly, so the bars of whole-situ concrete connection should connected with bars of diaphragms, so as to play good effects.

Concrete is strong in compression, inexpensive, and stiff, while steel is strong in tension and compression, lightweight, easy of handing and fabrication, but more expensive. The benefits of combining the two common materials have long been recognized and a variety of composite system has been developed and widely used in both buildings and bridges. Concrete filled steel tube composite [1-5] are the most favorable composite system for columns or structures with compression carrying members. The steel shell provides confinement to the concrete; in return, concrete provides supports that prevent premature local buckling or crippling of the steel and allow effective composite action, which leads to a remarkable increase of strength and ductility of the structure. Composite girders are another commonly used composite system for bridges or structures with flexural members. An important advantage of using composite system is that construction can be accelerated through separation of operations. Initially, a bare-bone steel frame can be erected to carry the gravity load during construction thus significantly reduces the needs for shoring and formwork. As the erection progresses, concrete are placed to form the composite system with needed stiffness and strength to carry added dead load and live loads at completion. This construction advantage has been applied in a recent developed vertical erection-rotation method for arch bridge construction [6]. The developed erection method offers a practical, safe, accelerated, and self-shoring mean for median span arch bridge with better structure integrity and improved stability during construction. Using this method, prefabricated steel tubular segments can be erected in field vertically like a typical column construction on temporarily restrained hinge devices. The complete half-leaves were rotated down to meet at the closure and form a base arch frame. The completed base frame are then made to composite by infilling concrete in the negative moment region, quarter-span from skewbacks, and by placing a cast-in place reinforced concrete topping for positive bending region for the remaining quarter-spans from the crown, thus form a composite cross section with variations based on stress distribution. There are a number of codes and standards that provide bases for the design of concrete-filled steel box-sections, but there is no unique method to calculate compressive or moment resistance. Since the load carrying characteristics of a composite arch rib may fail due to global or local instability before the ultimate μ is reached, the section should also be checked for local buckling, local crippling, and global lateral-tensional buckling modes of failure [7, 8]. An in-depth understanding of the load carrying characteristics of the proposed composite section under combined compression and bending both theoretically and experimental is thus very crucial for an optimized design of composite combination.

Conclusions

High performance concrete with its superior performance makes ordinary concrete to high perform can become inevitable trend of development. High performance concrete is the concrete technology the sign of progress. The high performance concrete application for highway bridge is itself a kind of optimization, bridge for the development of the cause is a big security, but in the construction work. In the process, must pay attention to the implementation of all processes degree, must strictly according to the request and mining take effective technical measures, the comprehensive quality of standards must be properly deal with the construction of the entire process.

References

- [1] R. B. Fleischman, G. Wan, (2010) "Appropriate Over strength of Shear Reinforcement in Precast Concrete Diaphragms," *Journal of Structural Engineering* 11:1616-1626
- [2] Tanya Green¹, Nur Yazdani, and Lisa Spainhour, (2009) "Contribution of Intermediate Diaphragms in Enhancing Precast Bridge Girder Performance," *Journal of Performance of Constructed Facilities* 8:142-146
- [3] C. S. Cai¹, Marcio Araujo, Anand Chandolu, et, (2010) "Diaphragm Effects of Prestressed Concrete Girder Bridges: Review and Discussion," *Practice Periodical on Structural Design and Construction* 8:161-167
- [4] Christopher D. Eamon, Andrzej S. Nowak, (2009) "Effect of Edge Stiffening and Diaphragms on the Reliability of Bridge Girders," *Journal of Bridge Engineering* 4:206-214
- [5] J. X. Yu. (2003) Reinforcement Measures and Crack Analysis of Diaphragm of Concrete Simply Supported Beams. *Railway Construction* 8:3-4
- [6] Z. G. Liang, Y. Zhang, J. L. Liu. (2007) Disease and Reinforcement of the Diaphragm of Fabricated T- beam Bridges. *China Municipal Engineering. Young, The Technical Writer's Handbook*. Mill Valley, CA: University Science, 1989. 5:92-93M
- [7] T. M. Wang. (1997) *Engineering Structural Cracks Control*. Beijing: China Building Industry Press
- [8] Z. X. Guo, P. S. Sun, Y. J. Liu. (2005) *Practical Handbook of Concrete Structure*. Beijing: China Building Industry Press
- [9] Y. J. Lin, Y. J. Qian, Z. L. Wang. (2006) Research on calculation method of new-old concrete interface cohesion strength. *Industrial Construction (Supplement)* 36:844-846
- [10] J. P. Gao, J. L. Pan, Y. G. Wang. (2001) Effect of Different Bonding Agents on Bond Strength between Fresh Concrete and Hardened Concrete. *Journal of Harbin University of C. E. and Architecture* 34(5):25-29
- [11] J. P. Gao, J. L. Pan. (2001) Specimen for Testing Bond Strength between Fresh and Hardened Concrete. *Journal of Harbin University of C. E. and Architecture* 34(2):32-35
- [12] Z. F. Zhao, G. F. Zhao, C. K. Huang. (1999) Research on the tension shear behavior of the adhesion of young and old concrete. *Journal of Building Structures* 20(6):26-31
- [13] L. S. Zhang, J. J. Guo. (2007) Experiment on shear property of new and old concrete bonding with planting steel. *Industrial Construction* 37(11):71-73
- [14] X. M. Peng, X. H. Li, D. S. Cai. (2001) Model Test for the Shearing Stresses in the Adjoining Faces between the Old and New Concrete. *Bridge Construction* 2(3):40-44

Heat Treatment Process of the Flue Gas Desulphurization Gypsum and Its Influence on the Properties of Cement

Li Yue¹, Wu Jianhui², Hao Bin¹ and Liu DaCheng³

¹Tangshan College, Tangshan, China

²Hebei Province Key Laboratory of Occupational Health and safety for Coal Industry, Division of Epidemiology and Health Statistics, Hebei United University, Tang Shan

³Tangshan College, No.38,Huayan Road, Tangshan City, Hebei Province, China

e-mail: gemingzhuanwa@126.com,wujianhui555@163.com,tsxyhxx@163.com,tsldc@sohu.com

Keywords: Flue Gas Desulphurization Gypsum, Thermal Treatment, Phase, the Properties of Cement

Abstract The Crystal Transformation of flue gas desulphurization (FGD) gypsum was analyzed by differential thermal analysis (DTA) and X-ray Diffraction (XRD). FGD gypsum was used as cement setting retarder and the influences on the properties of cement were studied by treating FGD gypsum at different heat treatment processes. The results reveal that in the case of adding the same amount, the setting time of cement shortened with the increasing of heat treatment temperature of FGD gypsum. The influence of different heat treatment processes on the strength of cements was not obvious and the strength development was good. The water consumption of normal consistency for cements changed slightly. Stability was qualified.

Introduction

Flue gas desulfurization (FGD) gypsum is a kind of by-products in the process of wet desulfurization, its main component is calcium sulfate dehydrate and its color is yellowish-white. With the development of our country's desulfurization project, flue gas desulfurization gypsum becomes another type of solid waste in thermal power plant except the fly ash, plenty of land is used for the storage of flue gas desulfurization gypsum, and the environment is polluted [1]. So studying the properties of flue gas desulfurization gypsum and making full use of it are benefit for the development of our country's desulfurization project.

Flue gas desulfurization (FGD) gypsum's chemical composition is similar with the natural gypsum, the content of calcium sulfate dihydrate is up to 95%, the content of impurity is little, grain-size is smaller than natural gypsum [2]. It can be used as cement setting retarder instead of natural gypsum theoretically [3]. To clarify the utilization of FGD gypsum as the retarder of cement-based materials and its feasibility, this paper explored the effects on the properties of the slag cement with different temperature treatment of FGD gypsum, provided an application approach to solving the production of large numbers of FGD gypsum in domestic in recent years, achieved the purpose of recycling, created a good economic, social, and environmental benefits.

Experimental Raw Materials and Methods

Table 1 Chemical compositions of raw materials

	SiO ₂	Al ₂ O ₃	Fe ₂ O ₃	CaO	MgO	SO ₃
Cement	21.88	5.01	3.64	63.39	2.41	1.03
Scoria	34.71	13.74	1.15	36.18	11.09	0.03
Desulfurization Gypsum	2.86	1.12	0.36	32.12	1.09	39.57

In this experiment the cement was prepared at the laboratory. The contents of the cement, scoria and gypsum in the cement are 50%, 45% and 5%, respectively. The chemical compositions of raw materials were shown in Table 1 [4].

The FGD gypsum's phase transformation was tested by differential thermal analysis (DTA), and its drying temperature and heat treatment temperature were preliminarily confirmed. To study, the influence of different heat treatment temperature of FGD gypsum, on the performance of the cement. The FGD gypsum's phase composition after heat treatment was studied by XRD. The cement's water consumption of normal consistency, setting time, soundness and strength of cement mortar were tested according to GB/T1346-2011.

Experimental Results and Discussion

Physicochemical Properties of FGD Gypsum According to literature [5], dihydrate gypsum lost the crystal water in twice during heating. First, $3/2$ water molecules were lost to generate semi-hydrated gypsum. As the temperature increases, the rest of the half water molecules were lost to generate anhydrite. Fig 1.1 is the DTA of FGD gypsum drying at 40°C . From the figure we can figure out that the composition of FGD gypsum is dihydrate gypsum at the temperature below 110°C , and FGD has almost no phase transformation, its main components is dihydrate gypsum. A dehydration reaction of FGD gypsum is carried out and semi-hydrated gypsum is formed at 160°C . A dehydration reaction of FGD gypsum is carried out again at 160°C , that is dihydrate gypsum start to lost its crystal water and semi-hydrated gypsum was generated. A dehydration reaction of FGD gypsum happened at 180°C again. In another words, semi-hydrated gypsum started to lose its crystal water. The exothermic peak at 465°C reflect that FGD gypsum's crystal lattice recombination and corresponded to form the anhydrite[6]. Heat treatment temperature was respectively 40, 120, 140, 160, 180 and 240°C . Heat treatment processes were as follows: the samples were dried at 40°C to constant weight, calcined under the temperature of 120, 140, 160, 180 and 240°C , respectively, keep the system at the design temperature for 60min.

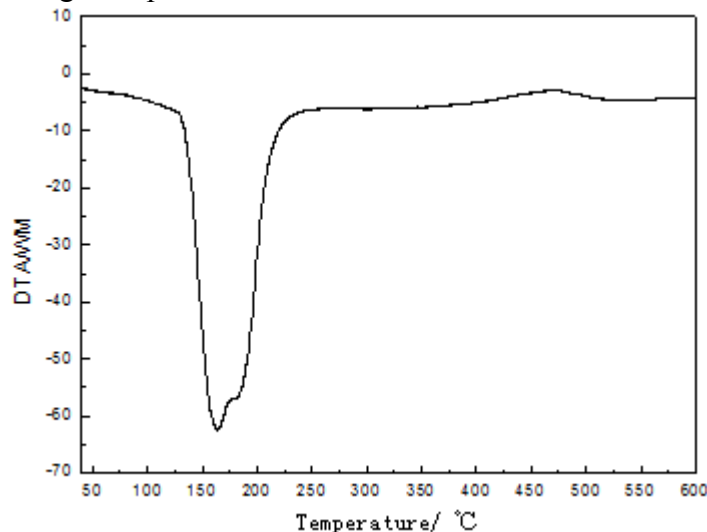


Fig. 1 The DTA of FGD gypsum drying at 40°C

FGD gypsum that calcined at 40 and 120°C were studied by XRD, the diffraction patterns were shown in Fig. 2 and Fig. 3. The composition of FGD gypsum that calcined at 40°C is dehydrate gypsum, the composition of FGD gypsum that calcined at 120°C has semi-hydrated gypsum in the pattern and the composition of the pattern is the mixture of dihydrate gypsum and semi-hydrated gypsum.

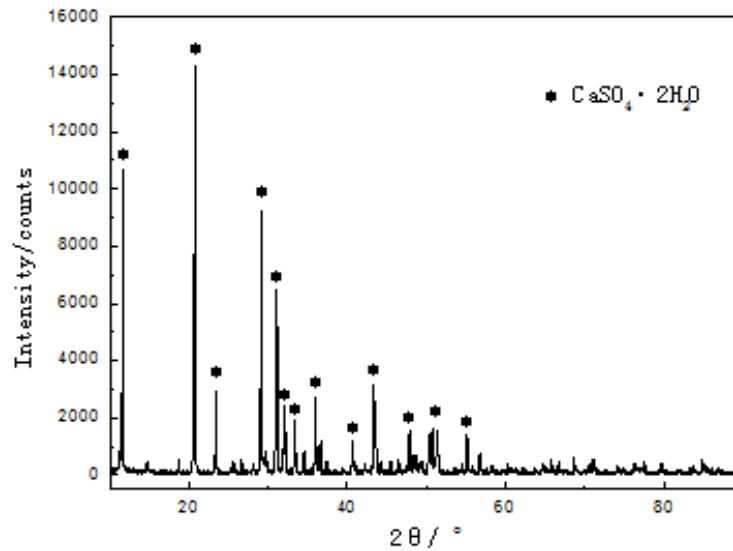


Fig. 2 The XRD of FGD gypsum drying at 40°C

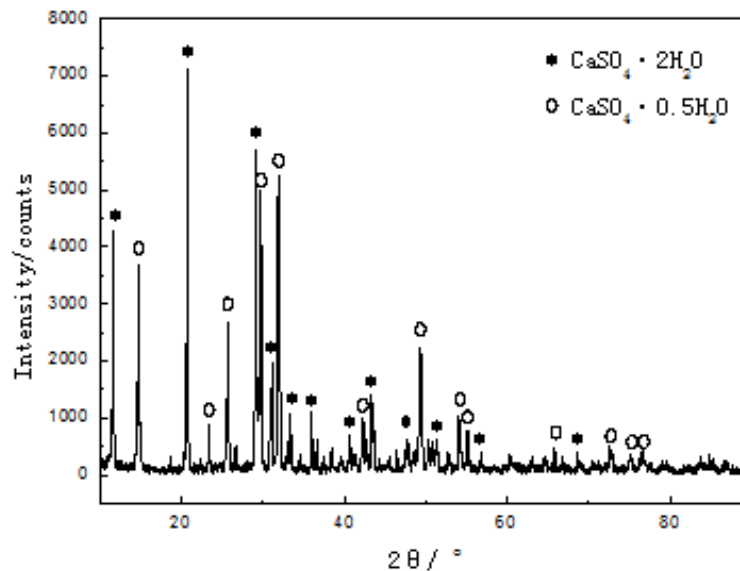


Fig. 3 The XRD of FGD gypsum drying at 120°C

The particle size distribution of FGD gypsum that calcined at 40°C is shown in Table 2. As shown in the Table 2: the particles below 63μm are 97.20%, compared with the grinding natural gypsum, FGD gypsum's grain-size is smaller [7].

Table 2 The particle size distribution of FGD gypsum

Grain diameter/μm	Differential distribution /%	Cumulative distribution /%
0.11	0.69	0.69
0.35	0.45	7.55
10	0.2	13.76
18.01	3.12	20.14
33.58	16.31	52.98
41.34	17.11	70.09
50.88	16.75	86.84
62.63	10.36	97.20
77.09	2.78	99.99
>77.09	0.01	100

Influence of the Heat Treatment Temperature of FGD Gypsum on Cement Properties The FGD gypsum that calcined at 40, 120, 140, 160, 180 and 240°C were mixed into the cements. The cement's water consumption of normal consistency, setting time, soundness and strength of cement mortar were shown in Table 3.

Table 3 The cements' normal consistency, setting time, soundness and strength of cement mortar

Sample	Heat treatment temperature /°C	Normal consistency /%	Soundness	Initial setting time /h:min	Final setting time /h:min	Flexural strength /Mpa		Compressive strength /Mpa	
						3d	28d	3d	28d
1	40	28.62	Qualify	4:25	6:25	4.5	6.8	22.3	45.6
2	120	28.70	Qualify	3:45	5:50	4.7	7.1	22.8	46.1
3	140	28.65	Qualify	2:55	5:10	4.4	6.8	21.8	44.8
4	160	28.66	Qualify	2:30	4:40	4.8	7.0	21.5	44.6
5	180	28.68	Qualify	1:50	3:55	4.5	6.9	22.5	45.8
6	240	28.66	Qualify	1:15	3:25	4.6	7.0	22.2	44.9

As shown in Table 3: when the additive amount of the FGD gypsum was 5%, the cements' setting time was in line with national standards. It is said that the FGD gypsum after being calcined can be used to adjust the setting time of the cement, and the setting time of the cements shortened with the increasing of heat treatment temperature of FGD gypsum. This is because FGD gypsum lost the crystal water with the increase of temperature, the content of dihydrate gypsum that can be used as setting retard decreased.

The influence of different FGD gypsum on strength of the cements was not obvious and the strength development is good. The water consumption of normal consistency for cements changed slightly. Stability was qualified [8].

Conclusion

The FGD gypsum was studied by DTA and XRD. The results reveal that phase transition of the FGD gypsum took place at 120°C, and semi-hydrated gypsum was formed. with the increase of temperature, the content of dihydrate gypsum that can be used as setting retard decreased.

In the case of adding the same amount, Heat treatment process of the FGD gypsum was the main influencing factor on the setting time of cement. The setting time of cements shortened with the increase of heat treatment temperature of FGD gypsum. It is said that the FGD gypsum after being calcined can be used to adjust the setting time of the cement.

In the case of adding the same amount, the influence of different FGD gypsum on strength of the cements was not obvious and the strength development is good. The water consuming of normal consistency for cements changed slightly. Stability was qualified.

Reference

- [1] GUO Da-jiang, YUAN Yun-f, HU Hao-ran, ZHANG Bin. (2010) Influence of FGD Gypsum on the Properties of Portland Cement. BULLETIN OF THE CHINESE CERAMIC SOCIETY 29(2):387-360
- [2] Song Liangshan. (2010) Using Desulfogypsum as Retarding Agent in Cement Production. CEMENT TECHNOLOGY 1(6): 92-93
- [3] Lan Qing. (2010) Experience of substituting desulfogypsum for natural gypsum. Cement engineering 4(8): 79-81
- [4] Wang Yulan, LiYang (2011) Research on Performances of Cement and Concrete with Desulfurized Gypsum as Retarder. Coalash 4(67):24-26

- [5] Pavel Tesarek, Jaroslava Drchalova, et al. (2006) flue gas desulfurization gypsum: Study of basic mechanical, hydric and thermal properties [J]. *Construction and Building Materials* 6(34):1-10
- [6] TONG Shi-tang (2001) Study on Analysis for Crystal Species of Gypsum by Applying Differential Scanning Calorie (DSC). *J. of Wuhan Uni. of Sci. & Tech.(Natural Science Edition)* 24(3): 243-246
- [7] Liu Xiaoqin, Qin Honggen, Chen Huisu. (2010) Summary of Characteristics of Desulfurized Gypsum and Its Application. *Coalash* 4(9):43-46
- [8] ZHOU Hong. (2010) Experimental Research on Desulfurized Gypsum as Cement Retarder. *Shanxi science and technology* 25(4):110-114

CHAPTER 2:
Mechanical Engineering and Application

Research on Material Features in Design Technique of Tennis Materials

Xiangfeng Xu

Tennis Teaching and Research Section, Wuhan Sports University, China

XuXiangfeng2012@yeah.net

Keywords: Tennis, Material, Feature, Design, Technique

Abstract. Tennis is being loved by more and more people now. Moreover, it is gradually becoming an important leisure and recreation activity. As for this, material features involved with tennis design is currently widely studied and noticed by scholars domestic and overseas. Based on the positive results obtained by researchers domestic and overseas, the paper further summarized and generalized the development process of tennis racket frame and the material features of tennis racket string. Besides, the technical process of tennis racket design is also analyzed. Eventually, by integrating the pressure carrying feature of tennis racket, by taking carbon fiber tennis racket as the example, the paper has calculated related mechanical indexes, so as to high-lighten its excellent performance. In addition, racket string also has significant influence on ball speed and accuracy rate. By looking up related literatures, the intrinsic relationship is also revealed.

Introduce

Tennis is a sport event with profound cultural history. It has elegant nature and meets people's demand for fashion [1]. With the time passes by, at present, tennis has already become an important leisure, recreational and fitness activity noticed and loved by more and more people. Since the very beginning, the development process of tennis has already attracted scholars' attention, never interrupted. Because of such wide attention and participation, as well as numerous scholars' continuous research, the activity is always developing rapidly [2]. At present, the professionalization degree of tennis is becoming increasing deeper than before, and people demands on tennis are also continuous improved. For this reason, tennis materials, especially materials for tennis racket and strings, are playing increasingly important role in tennis competitions. The performance and quality of tennis racket have objectively become important factors restricting tennis players' performance and competition result [3]. Thus, researches on tennis racket materials have very significant and practical meaning to theoretical research and practical competitions.

Introduction to Tennis Racket Design

In tennis racket design, components with significant influence on the overall performance include racket frame and racket string. Tennis racket has a long development history [4]. Since tennis racket was invented in the last century, it has experienced a long development process.

According to related design information and literature, material for tennis racket has basically experienced the following development process:

Table 1 Development Process of Tennis Racket Frame Material

Material	Time	Feature	Remarks
Wood	Early	Good performance in elasticity, controlling, shock absorption	Limited strength, easily affected by temperature and moisture
Metal	1960s	Excellent elasticity	Heavy weight, strong shock force
Aluminum		Light weight, low shock force	Lower elasticity and durability than steel
Glass Fiber	1969	Excellent handling, low shock force	Low strength
Carbon Fiber	1975	Light weight, high strength, good elasticity	High price

Currently, when selecting the material for tennis racket, they are often influenced and restricted by their personal living standard and purpose for the tennis racket [5]. If the tennis racket is purchased just for personal interest or fitness, they may choose aluminous racket. If the tennis racket is used for professional competition, they will prefer to choose carbon fiber racket for better performance.

Similar to tennis racket frame, strings for tennis racket also experienced a series of complicated evolution process, shown as follows:

Table 2 Development Process of Tennis Racket String Material

Type	Feature
Gut String	Good elasticity, easily abraded and broken
Chemical Synthesis Gut String	Firm and reliable, good elasticity, complicated processing technique, high price, relying much on importation
Nature's Bio Gut	Biodegradation
NANOCUBIC, VECTRAN	Polyester string, Nanotechnology

Comparatively, design techniques of tennis racket string are much more complicated than that of tennis racket frame [6]. The performance of tennis racket string is affected by the material of string, as well as the processing technology of string. In other words, even if good materials are applied, poor processing technology could still lead to unqualified racket string.

Design and processing of tennis racket frame is relative simple, mainly including the following procedures:

Table 3. Design and Processing of Tennis Racket Frame

Procedure	Processing Technology
Step 1	Design of geometric shape of frame
Step 2	mould making
Step 3	NC processing
Step 4	Post-stage processing, finishing

Most domestically-made tennis racket strings adopt the production technology of thread twisting, while is comprised by a series of very meticulous and complicated processing technologies [7]. Generally, the following procedures are included:

Table 4 Design and Processing of Tennis Racket String

	Manufacturing Process	Manufacturing Technology
Thread Twisting	Nylon	Twisting
	Nylon Twisting	Re-twisting
	Nylon Fiber	Spindle changing, starching
	Semi-finished Product	Unfolding, shaping
	White Product	Dying and drying
	Colored Product	
Coated Woven	High Strength Filament	Pre-processing
	Core of String	Weaving
	Material of Coat	Coating
	Finished Product	

Analysis on Mechanical Characters in Tennis Racket Design

Joint structure of tennis racket is quite simple. However, its force carrying process is rather complicated. For some key components with complicated force bearing nature, the mechanical character of material is consequently quite important [8]. When conducting mechanical analysis and computation according to the force bearing feature of tennis racket, the following assumption is often adopted:

The head (elliptical ring) of tennis is constant section;

When considering static force balance condition, the weight of strings will not be considered;

Wooden racket is solid rectangular section, while GRP and CFRP are rectangular tube section, with their handles being made with two rectangular tubes extended from the elliptical ring.

Basic Analysis Principles of Force Bearing under Bending, Side Pressure and Twisting Situation

The Equation of Total Energy on Tennis Racket Is:

$$U = \frac{M^2 ds}{2EJ} + \frac{M_k^2 ds}{2GJ_k} \quad (1)$$

In the equation, M and Mk are separately the bending moment and torque;
EJ and GJk are separately the anti-bending and anti-twisting strength.

Deflection at a certain point shall be: $\delta = \frac{\partial U}{\partial P_0}$

In the equation, P0 is unit pressure at the deflection point.

The intersection angle shall be: $\delta = \frac{\partial U}{\partial M_0}$

In the equation, M0 stands for the unit moment at the intersection angle to be calculated.

Tennis Racket Displacement Equation is: If bending moment M0 and torque M0k are caused by unit pressure P0 or M0, displacement of the tennis racket at certain point can hereby be figured out with the following formula:

$$y = \int \frac{MM^0 ds}{EJ} + \int \frac{M_k M_k^0 ds}{GJ_k} \quad (2)$$

According to the aforementioned calculation principles and methods, the paper has computed and analyzed the pressure bearing feature of carbon fiber tennis racket. The reason for our choosing carbon fiber racket as the example is that, carbon fiber racket is widely used in professional competitions, with better practical performance. The carbon fiber tennis racket mentioned here refers to composite fiber (including carbon fiber and glass fiber) reinforced plastic tennis racket. This type of tennis racket has higher strength, lighter weight, better elasticity and more comfortable feeling. After calculation, major results and some test values are listed in the following table:

Table 5. Computation and Analysis Result of Tennis Racket Mechanics with Carbon Fiber Tennis Racket as the Example

Performance	Three-point Bending		Cantilever Bending		Cantilever Twisting	
	Computed Value	Tested Value	Computed Value	Tested Value	Computed Value	Tested Value
Deflection f_x (mm)	1.38	1.30	19.9	18.0		
Stress σ_x (MPa)	0.8		13.8		6.3	
	6.1		11.1		7.3	
	0		19.4			
Torsion Angle					1.87	2.13

It can be seen from the above results that, the tested values are quite close to the computed values. However, worthy to be noticed that, the basic performance of materials for tennis racket could not be accurately mastered. Besides, owing to the dispersion of material performance and affected by practical processing techniques, the errors between computed values and tested values could not be completely avoided. From the above computation, we are also able to get a qualitative understanding over the basic performance of carbon fiber tennis racket. It can be seen that, under pressure bearing state, carbon fiber tennis racket has better deflection, with excellent stress carrying state, and smaller torsion angle. These facts have fully reflected the outstanding performance of carbon fibers as the basic material for tennis racket.

Special Features in Technical Design of Tennis Racket String

At the moment batting, the mechanical process is very complicated. However, by drawing support from corresponding physical model, we can construct a simplified calculation equation. On this basis, physical and mathematical deduction and experiment methods can be used to calculate the changes of tensile force and displacement of racket string.

Dynamical Equation: Dynamical equation is established for the tennis racket, shown as follows:

$$m_2 \frac{d^2 x_2}{dt^2} = k[l_0 - (x_2 - x_1)] \quad (3)$$

Here, we assume that the tennis racket is doing uniformly accelerated motion, i.e.:

$$x_1 = v_0 t + \frac{1}{2} a t^2 \quad (4)$$

By drawing support from the above two equations, we will be able to figure out the separation time between ball and racket, as well as the instantaneous ball speed on batting.

Tensile Force Performance of Tennis String: The tension force tennis racket string is pre-set. Its degree is often quantitatively reflected by pounds. Normally, the tension force of racket string is a certain value between 55 pounds and 66 pounds. In order to study the influence of racket string tension force on batting effect, the paper has looked up related literatures, and conducted corresponding researches. Domestic scholars have also conducted questionnaire survey over 18 athletes. On this basis, statistical analyses on the relation between racket string tension force and batting speed and accuracy rate. The results are shown in the following table:

Table 6 Batting Speed under Different String Tension Force

String Tension Force (Pound)	Test Sample Amount	$\mu \pm S/km \cdot h^{-1}$	Min/km·h ⁻¹	Max/km·h ⁻¹
47	18	114±9.9	95	130
53	18	119±8.3	104	132
58	18	119±8.5	102	134
64	18	117±9.2	103	133

It can be seen from the above table that, ball speed under 47 pounds' string tension force is obviously lower than tennis racket of 53 pounds, 58 pounds and 64 pounds. In other words, within a certain range, higher string tension force leads to higher ball speed.

Table 7 Accuracy Rate under Different String Tension Force

String Tension Force (Pound)	Off Line	Beyond Bottom Line	Beyond Sideline	Fair Ball
47	9	13	5	73
53	7	22	5	67
58	5	16	5	74
64	8	9	6	77

From the above table, we may find that, when the tension force of string is 53 pounds, the frequency of beyond bottom line is of the highest, leading to maximum fault rate. This has provided valuable reference for practical design.

Conclusion

The material for tennis racket string is very complicated. Currently, polyester string based on nanotechnology has best performance, with wide market prospect;

Processing techniques for tennis racket is very simple. However, processing techniques for racket strings are relatively complicated;

The paper has calculated the mechanical indexes of carbon fiber tennis racket, which in return high lightened the outstanding performance of tennis racket made with such material;

Tension force of racket string has important relation with ball speed and batting accuracy rate. Higher tension force leads to higher ball speed. When string tension force is set at 53 pounds, the frequency of beyond the bottom line is of the highest, leading to maximum fault rate.

References

- [1] Li Changhua: Properties and Usage of Carbon Fiber. Guangxi Chemical Fiber Newsletter, vol. 2(2002), p. 23-24.
- [2] Shen Jianyong and Fu Jing. Ethic Problems and Countermeasures from the Development of Nanotechnology in Competitive Sports, Sports and Science, 2001(01);
- [3] Weijie SHEN, Haixin SUN, En CHENG, Yonghuai ZHANG: Performance Analysis of DFT-Spread based OFDM Transmission System over Underwater Acoustic Channels, JCIT, Vol. 6, No. 7, pp. 79 ~ 86, 2011.
- [4] Suma S.A., Dr. K.S.Gurumurthy: New Improved echo canceller based on Normalized LMS Adaptive filter for Single talk and Double talk Detection, Subband echo cancellation, Acoustic Echo cancellation, JNIT, Vol. 1, No. 2, pp. 61 ~ 74, 2010.
- [5] Nai-zhang Feng, Mingjian Sun, Liyong Ma: Compressed Sensing Photoacoustic Imaging based on Correlation Criterion, IJACT, Vol. 3, No. 5, pp. 201 ~ 207, 2011.
- [6] Wen-Chang Tsai: Effects of Core Materials and Operating Parameters on Core Losses in a Brushless DC Motor, IJEEI, Vol. 2, No. 1, pp. 51 ~ 61, 2011.
- [7] Joanna Verran, Deborah L. Rowe, Robert D. Boyd: Visualization and measurement of nanometer dimension surface features using dental impression materials and atomic force microscopy. International Biodeterioration & Biodegradation, vol. 51, 3(2003), pp. 221-228.
- [8] Ye Zhang, Xi'e Shi, Ji Man Kim: Synthesis and catalysis of nanometer-sized bimodal mesoporous aluminosilicate materials. Catalysis Today, vol. 93-95, 1(2004), pp. 615-618.

Scheduling Optimization for Parking and Taking Car about the Vertical Circulation Type Stereo Garage

Shu Li, Hongru Li, Xiaobo Zhang and Mengfan Ji

Mailbox 48, Northeastern University, Shenyang, Liaoning Prov, China

e-mail: allivy@126.com

Keywords: Vertical and Circulation Type Stereo Garage; Parking and Taking a Car; Scheduling Optimization; Queuing Theory

Abstract. The vertical circulation type stereo garage has some advantages such as its simple construction, low cost, easy combination and less ground occupation. Regarding the problem of parking and taking car in the vertical circulation type stereo garage, the paper studies the queue system in the garage through a queue theory, the management strategy of scheduling optimization for parking and driving is obtained. The simulation experiment proved that, the whole vertical circulation garage by the optimization method stated in this paper has some advantages such as average short time for parking and taking car one time, high efficiency for average service rate.

Introduction

Recently, with the rapidly development of national economy and automobile manufacturing in China, the quantity of automobiles retained are rapidly increasing. In the large cities such as Beijing, Shanghai, the quantity of civil cars are continually increased in the decade [1]. But the street construction and parking lots are built slowly comparatively to it. With the progressively increasing of automobile amount, the difficulty for parking will become more severe, especially for residential areas, public consumption places and so on. So the development of parking lots to space is imperative under the situation [2]. Comparing to the traditional natural underground garage, the vertical garage as a new parking pattern has more outstanding advantages such as saving ground, more efficiently guarantee personal and car safety, easy management for in or out garage as well as flexible configuration[3], we can say that this kind of garage is indispensable choice for effectively improving city static traffic. At present, the main form of mechanical structure for the vertical garage are classed as several types such as vertical circulation, multiple layers, horizontal circulation, lifting and shifting, lifting guide railway, elevator lift, go and back in vehicle, type of combination, tunneling and stack, round horizontal water circulation. Vertical circulation type stereo garage is welcome due to its simple construct, low cost of manufacture, easy combination and less surface of ground occupation. Regarding to the problem of parking and access in the vertical circulation type stereo garage, the paper studies the queue system in the garage through the queue theory [4], the management strategy of scheduling optimization for parking and driving is put forward.

Description of Vertical Circulation Type Stereo Garage

The structural drawing of a single vertical type stereo garage is shown in Fig. 1. According to the needs for the parking amount, the number of layers for the parking lot in the single structure garage can be managed between three layers to seven layers. Fig. 1 is the mechanical structure of the vertical circulation type stereo garage with 10 lots at 6 layers. For different requirements, this structure can be regarded as a combination structure for an whole vertical circulation type stereo garage, more single vertical circulation type stereo garages can be used to combine a whole vertical circulation type stereo garage. In fact, a whole vertical circulation type stereo garage can be composed of several single vertical circulation type garages. To make easy to understand, here 18 single vertical circulation type garages with 4 layers where 7 cars can be parked, are selected. The diagram of a

whole vertical circulation type stereo garage is shown as in Fig. 2, where the garages are ranged in three rows, every row has 6 single vertical circulation type garages. A whole vertical circulation type stereo garage can park at most 126 cars; the largest surface occupied is $457 m^2$. Parking and taking car passage from the vertical circulation garage is to utilize carrying car plate to transport cars to correspondent passage position of the entrance at bottom layer of some vertical circulation garage from the entrance. While parking, after receiving the indication from the system, carrying plate is waiting that the car is transported to the garage designated, the vertical circulation garage will circle the idle car place to the bottom, the carrying plate rotates 90 degree, takes the car waiting to stop into a storage location. When taking a car, the vertical garage receives the indication from upper system, the operation is opposite to the parking, carrying plate transports the car taken to the entrance.

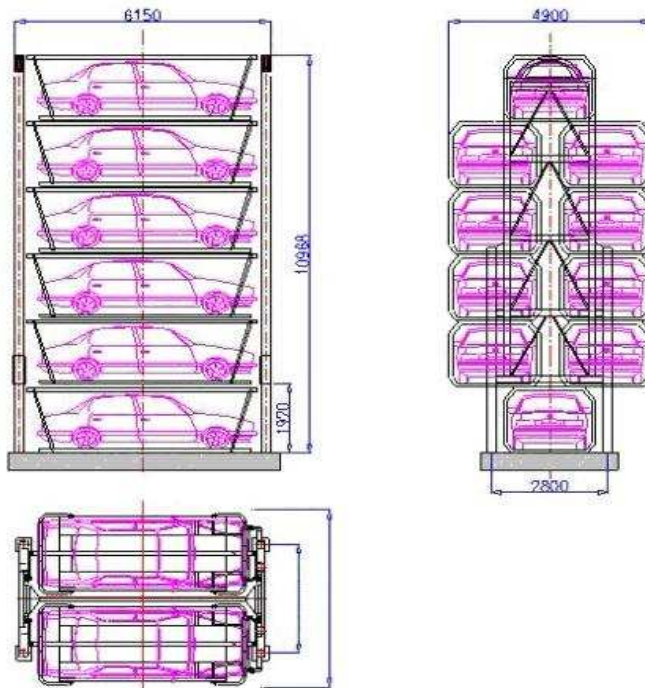


Fig. 1 Structure diagram for a single vertical circulation type garage

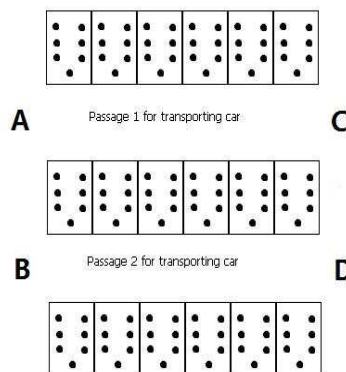


Fig. 2 Structure diagram for a whole vertical circulation type garage

Theory of Scheduling Optimization of Parking and Taking Car

Queuing Theory Queuing is phenomena met often in daily life and production. There is a queuing phenomenon with form and without form, for example, storage regulation of the reservoir, blocking and leading the vehicle and boats in the traffic centre of the train station and dock [5-6]. Which queues is somebody, but may be somewhat. The queuing theory calls the objet to be served as “consumer”, takes somebody who supply service as “service desk” or “servicer”. Any queuing process of queuing problem can express in Fig. 3.

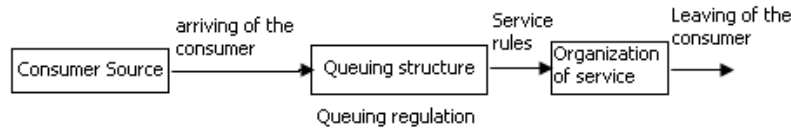


Fig. 3 Queuing theory

Random is a common feature of the queuing system, it means that the arriving case (arriving interval one after another) and the service accepted by consumer are random. Generally, in the queuing system studied with queuing theory, there is at least one of two momentums between arriving interval and service time, queuing theory is called also random service system theory.

Principle of Scheduling System Priority principle of parking car: after having made the parking and taking process, the lift mechanism returns to the entrance and exit of the garage for order, there is a carrying car plate on the lift mechanism for the next car to directly park into.

Priority principle of taking car: lift mechanism made the storage and take process, and it returns to the entrance of the garage for order, the lift mechanism does not carry the plate carried in order to make directly an operation for taking car.

Waiting for order at the original place: after having finished the taking operation, the lift mechanism stops at the original place for accepting the next task.

Cross parking and taking principle: garage system can accept more missions of parking and taking car in a time, the system takes the optimistic service order to minimize single car parking and taking time.

Time Model Optimism The parking lots in the vertical garage are controlled by compiling arithmetic in the upper computer, in order to reduce the time that the whole queue needs to waiting when parking and taking, building the mathematics model on basis of the queuing principle.

Through gathering data about the practice vertical garage, and on the basis of actual data, according to the queuing theory, an optimism model is created for the whole vertical recirculation garage.

As shown in the Fig. 2, the garage has two carry passages which are high independent, for discuss easily, both paths can be assumed as relatively independent. A carrying car passage has two entrance and exit ports, but these ports are equal relative, can be equal to one. Therefore, while a queuing theory model for vertical garage is built, it can be regarded as a single information desk model. It is got by analyzing the data that, the relation between the arriving and leaving car and time is dependent to Poisson distribution, so that the model of queuing theory of vertical garage is: model M/M/1.

Total time of construction of a single parking and taking car created by queuing theory is as below.

Total time to park and take car is as that

$$t_k = \sum_{i=1}^k \max \{ p_{1i} t_1, q_i t_2 \} + \min \{ p_{1i} t_1, p_{2i} t_1 \} + t_{i0} \quad (1)$$

Here: t_k - total time for parking and taking a car; p_{1i} - as parking i times, numbers of garages leaped cross from target port to target garage; p_{2i} - as parking i times, a number of garages leaped cross from target port to target garage; q_i - as parking i times, the number of turning of the object garage; t_1 - operation time from number 1 garage to number $i+1$; t_2 - time needed by turning of vertical regulation stereo garage; t_{i0} - as parking i times, waiting time for carrying plate.

Range of time distribution:

$$t_m = t_{k \max} - t_{k \min} \quad (2)$$

Here: t_m - scope of time distribution for taking car single time; $t_{k \max}$ - most value of parking or taking one time; $t_{k \min}$ - least value of parking or taking one time.

Average arrival rate is:

$$N_a = \frac{\sum_{i=1}^k n_i f_{in}}{100} \text{ (vehicle/hour)} \tag{3}$$

Here: N_a - average arrival rate; n_i -number of cars when parking I times; f_{in} -times of cars occurred when parking i time.

Average time for parking and taking car every time:

$$t_a = \frac{\sum_{i=1}^k t_i f_{it}}{100} \text{ (s)} \tag{4}$$

Here: t_a - average time for parking or taking a car every time; t_i - time for parking and taking a car when parking i time; f_{it} - times for car occurred when parking i time.

Average service rate:

$$f = \frac{1}{t_a} \text{ (h}^{-1}\text{)} \tag{5}$$

Here: f - Average service rate

Based on the statistical checking method, it is thought that number of cars arriving is submit to the Poisson distribution of parameters $\lambda = N_a$, parking and taking time submit to negative index distribution of $\mu = \frac{1}{t_a}$ [7].

Therefore, the rate of utilization of vertical garage $\rho = \frac{\lambda}{\mu}$, waiting time for queuing of consumer

(expected value) $W_q = \frac{\rho}{\mu - \lambda}$.

Simulation Experiment

According to the above mathematic model, C# language is used to write program in the upper computer and to make a simulation experiment of control algorithm. Through hundred times of experiment simulation, the distribution case of number n_i of cars arrived every minute in 100 minutes is shown as below:

Table 1 Number n of cars arrived every minute in 100 minutes

Number n_i of cars arrived	0	1	2	3	4	5	≥ 6
Number f_{in} of cars occurred	10	28	29	16	10	6	1

Average arrival rate can be obtained $N_a = \frac{\sum_{i=1}^k n_i f_{in}}{100} = 126$ (vehicle/hour).To make the vehicle

high efficient, more safe and stable, the mechanical structure transport speed controlling t_1, t_2 will be regulated at certain rate, combining the optimizing algorithm in the upper computer, the different

t_a will be gotten. According to the results obtained from simulation experiment made randomly on 100 cars parked, we can know that the longest time for a single parking is $t_{k_{max}} = 84$ second, the shortest time for a single parking is $t_{k_{min}} = 8$ second, range of time distribution of single parking is: $t_m = t_{k_{max}} - t_{k_{min}} = 76$ second.

Table 2 The relationship between parking and taking vers number occurred

Time for parking and taking car t_i / s	0	$0 \sim \frac{1}{6}t_m$	$\frac{1}{6} \sim \frac{2}{6}t_m$	$\frac{2}{6} \sim \frac{3}{6}t_m$	$\frac{3}{6} \sim \frac{4}{6}t_m$	$\frac{4}{6} \sim \frac{5}{6}t_m$	$\geq t_m$
Number occurring f_{it}	10	28	29	16	10	6	1

It is known from the data above that average time required by single parking or taking car

$$t_a = \frac{\sum_{i=1}^k t_i f_{it}}{100} = 26.6 \text{ second, average service rate } f = \frac{1}{t_a} = 0.0376 .$$

Average time and service rate for single parking and taking a car is the most important instruction to scale the efficiency of the vertical garage. Now the general mechanisms are mainly such as vertical lifting type, lifting and shifting type, elevator type, stack at street. To make an integrative evaluation on the performance of the vertical circulation stereo garage, comparing to 4 instructions generally acceptable to the average time of parking and taking cars[7-8], the result is shown in table 3.

Table 3 Comparing average times of parking and taking cars from different vertical garage

Type of garage	Vertical circulation	Vertical lifting	Lifting and shifting	Elevator	Tunneling Stack
Average time for single parking and taking t_a / s	26.60	67.68	40.70	57.69	60.00

Conclusion

In this paper, the vertical circulation type stereo garage, the paper studies the queue system in the garage through a queue theory, the management strategy of scheduling optimization for parking and driving is obtained. The simulation experiment show that, there is some advantages in the whole vertical circulation garage by using the optimization method, such as average short time for parking and taking car one time, high efficiency for average service rate. It's with a higher value.

References

[1] Fu LH, Song H (2002) Vertical Garage: Necessary for Development of City Static Traffic [J]. Science of Transportation and Economy 3:384-386

[2] Men HW, Pan HX (2004) Prospects for Development of Vertical Garage in China[J]. Mechanization of Construction 14:4-5

[3] Xu Ni (2009) Application and Research of Intelligent Vertical Garage [J]. Development and Creation of Mechanical Products 22:60-61

[4] Yang XF, Xiao H (2004) Comparative Analysis of Automatically Parking and Taking Car In the Vertical Garage[K]. Mechanical Manufacture and Automation 5(33):47-53

[5] Hua X (1987). Queuing Theory and Random Service System [M]. Shanghai Translation and Publishing Company, 1987

-
- [6] Koh SG, Kwon HW, Kin YJ (2005) An analysis of the end of aisle order picking system: Multi aisle served by a single order picker[J]. International Journal of Production Economics 11(98):162-171
- [7] Fintzel K, Bendahan R, Vestri C, Bougnoux S (2004) 3D Parking Assistant System[J]. IEEE Intelligent Vehicles Symposium 120:381-385
- [8] Xu G N, Cheng HN (2008) Scheduling Principle Optimization for Vertical Garage Based on Queuing Theory[J]. Mechanism of Crane Transportation 3:50-55

Intelligent Information Processing based on Classical Logic and Applied Mechanics

Yanxin Lu and Ziqun Zhang

Informatization Office, Fudan University, Shanghai 200433, China

ziquanz150@126.com

Keywords: Information, Artificial Intelligence, Classical Logic, Knowledge Reasoning, Predicate Logic

Abstract. Intelligent information processing is one of important research parts of knowledge reasoning as well as methods in artificial intelligence. In this paper, the application of classical logic in artificial intelligence for intelligent information processing is mainly studied, and also accurate definitions of mathematical statements are given with logic rules, thus laying a good foundation for the research field of computer intelligent information processing.

Introduction

Logic is the foundation of all mathematical reasoning, and can be practically applied in artificial intelligence. Studies on artificial intelligence show that knowledge representation, knowledge reasoning and knowledge application are not only the most fundamental, but also the most important. The most direct and the most complete theoretical basis for artificial intelligence to emerge and development is predicate logic. In the artificial intelligence research and application field, logic reasoning is one of the most enduring sub-fields of artificial intelligence research. Applying the formalization of the deductive process of predicate logic language can help us more clearly understand some sub-propositions of reasoning. Knowledge reasoning as well as methods is one of important research parts of artificial intelligence.

Natural Deductive Reasoning

Natural deductive reasoning refers to the process of starting from a group of known real facts and deducing result directly with reasoning rules of classical logic. In this deduction, the most basic reasoning rule is syllogism including hypothetical reasoning, disjunctive reasoning and hypothetical syllogism.

Resolution Deduction Reasoning

Resolution deduction reasoning refers to a machine reasoning technology based on Robinson's resolution principle, and also is called as resolution principle. It was proposed by J.A. Robinson based on the theory of Herbrand, and also is a reasoning method based on logic and applying proofs by contradiction. Herbrand's theory and Robinson's resolution principle are issues discussed based on set of clauses. Therefore, concepts related to set of clauses are introduced below.

Atomic predicate formula: single predicate formula or its negation

Text: atomic predicate formula and its negation

Clause: disjunction of any script

Empty clause: clauses including no scripts, marked with NIL

Set of clauses: set composed by clauses and empty clauses

After the acquisition of above concepts, Robinson's resolution principle is introduced next. Its basic thought is as follows: (1) the result of the question to prove is denied first and then added into set of clauses, and thus an expanded set of clauses is gained; (2) try to test whether the expanded set of clauses contains empty clause, suggesting it is unclassifiable if it contains, but resolution method continues to use if it does not, and then proper clauses are selected from set of clauses for resolution until empty clause is deduced or the resolution cannot continue.

The definitions of resolution and resolution formula: Set C_1 and C_2 are any two clauses in set of clauses; if text L_1 in C_1 and text L_2 in C_2 are complementary, L_1 and L_2 can be eliminated from C_1 and C_2 , and also the rests of C_1 and C_2 can compose new clause according to disjunctive relationship. This process is called as resolution, and C_{12} is the resolution formula of C_1 and C_2 .

The process of applying proposition resolution principle to prove the theorem is as follows.

Deny target formula G , gaining $\neg G$;

Place $\neg G$ into the known set of formulas F , gaining $\{F, \neg G\}$;

Convert $\{F, \neg G\}$ to the set of clauses (S);

Resolve the clauses in S with resolution principle, and also incorporate the resolution formula gained each time into S . This is repeated for many times: resolution stops if empty clause appears, and thus the target formula is proven to be true.

In the beginning of the proving, all clauses in S , namely the original formula, are assumed to be true. Then, the clauses in S , including complementary clauses, are resolved with proposition resolution principle, and all resolution formulas are incorporated into S . This operation is repeated, and finally an empty clause NIL is resolved, suggesting S is unsatisfiable and contradicted, the original hypothesis that $\neg P$ is true is false. Therefore, P is proven to be true.

Next, predicate logic resolution principle is introduced. Resolution principle is a reasoning method expressed mainly based on predicate logic knowledge. The basic method of predicate logic resolution is generally the same with the proposition logic resolution principle, but its process is much more complex.

Convert the proved question to predicate formula according to proof by contradiction, to prove it is a contradiction

Convert predicate logic formula to prenex normal form

Convert prenex normal form to conjunctive normal form

Write the set of clauses

Implement resolution with resolution method

In above, the resolution deduction reasoning is discussed, and it owns the following advantages:

It provides people with a simple method for realizing the proof and solving of questions.

It owns a simple form, and also rules are very simple. Third, it can be used for mechanization reasoning or theorem proving.

However, it has some disadvantages.

Resolution deduction reasoning is not human's natural way of thinking.

Clause is an expression with low efficiency, and converting formula standardization to highly-uniform and standard clause set will make the heuristic knowledge or ultra logical meaning implied in formula.

Deductive Reasoning based on Rules

In system based on rules, there are two reasoning methods, which are forward chaining and backward chaining. The forward chaining reasoning system based on rules is operated from known facts, situations, or rules to target, or action. It is a reasoning process from "if" to "then". Questions to be solved are divided into three parts (fact, set of rules and target) by the forward chaining reasoning based on rules, and also certain restrictions are imposed on them.

The backward chaining reasoning system based on rules is opposite to the forward chaining reasoning system in operational process. It is a reasoning process from then to if, and an operational process from target to fact. The operational process will be discussed with examples as follows.

Example: As shown in Fig 1.1, Assume there are facts and rules in the following.

Facts:

F1: TEACHER (TOM)

TOM is a teacher

F2: \neg RAGES (TOM)

TOM never gets rages

F3: PATIENT (TOM)

TOM is in patience

F4: PUPIL (MICKY)

A student is named as MICKY

Rules

- R1: $(PATIENT(x_1) \wedge TEACHER(x_1)) \rightarrow KINDLY(x_1)$ Teacher in patience is a kindly teacher
 R2: $(KINDLY(x_2) \wedge \neg RAGES(x_2)) \rightarrow \neg AFRAID(y_2, x_2)$ being friendly and getting no rages is not afraid
 R3: $TEACHER(x_3) \rightarrow HUMAN(x_3)$ teacher is human
 R4: $STUDENT(x_4) \rightarrow HUMAN(x_4)$ student is human
 R5: $PUPIL(x_5) \rightarrow STUDENT(x_5)$ Pupil is students

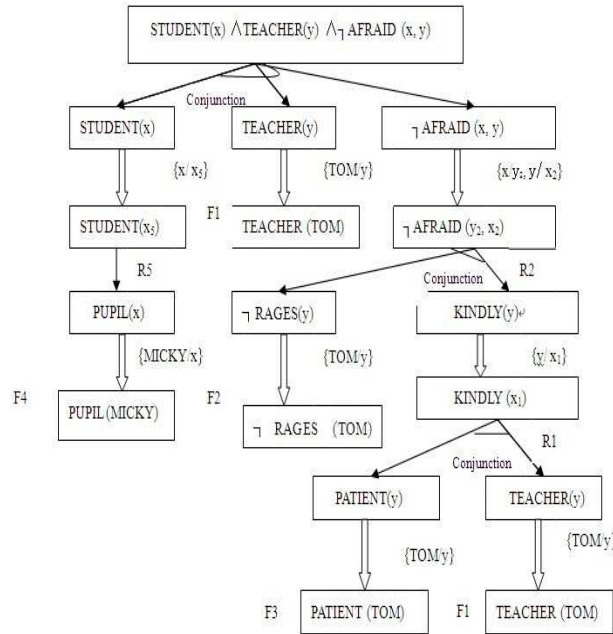


Fig. 1 Assume there are facts and rules

Therefore, there is a question: Do the student and teacher exist? Is the student is not afraid of the teacher?

The target formula of this question can be expressed as follows.

$$(\$x) (\$y) (STUDENT(x) \wedge TEACHER(x) \wedge \neg AFRAID(x, y)) \quad (1)$$

After the conversion of the above target formula:

$$ENT(x) \wedge TEACHER(x) \wedge \neg AFRAID(x, y) STUD \quad (2)$$

The deduction process of solving this question with backward chaining is shown below.

From the solution graph gained from the reasoning process, it can be seen that the displacements terminated on fact nodes are $\{MICKY/x\}$ and $\{TOM/y\}$, and the solution to the question can be gained if $\{MICKY/x\}$ and $\{TOM/y\}$ are applied in target formula.

$$STUDENT(MICKY) \wedge TEACHER(TOM) \wedge \neg AFRAID(MICKY, TOM) \quad (3)$$

This formula means that there is a student named as MICKY and a teacher named as TOM and the student is not afraid of the teacher.

In the following, a comparison is made between forward chaining deductive system and backward chaining deductive system, so as to prove their requirements on facts, set of rules, and target.

From the above comparison, it is not difficult to find that both forward chaining deductive system and backward chaining deductive system have some limitations. To bring their advantages into full play, overcome disadvantages and reduce use limitations, the two methods can be integrated together. That is the combination of forward chaining and backward chaining, or two-way deductive reasoning.

Table 1 A comparison is made between forward chaining deductive system and backward chaining deductive system

	Forward Chaining System	Backward Chaining System
Use conditions	(1) Fact expression is any form (2) F rule and form: $L \rightarrow W$ (L is single text (monomial), W is any form) (3) Target formula is disjunctive form of text	(1) Fact expression is text conjunction (2) B rule and form: $W \rightarrow L$ (L is single text, W is any form) (3) Target formula is any form
Simplification Process	(1) Eliminate existential quantifiers from fact expression; simplified formula is constrained by universal quantifier (2) Eliminate existential quantifiers from rules; simplified rule is constrained by universal quantifier (3) Eliminate universal quantifier from target formula; simplified formula is constrained by existential quantifier	(1) Eliminate universal quantifier from target formula; simplified formula is constrained by existential quantifier (2) Eliminate existential quantifiers from rules; simplified rule is constrained by universal quantifier (3) Eliminate existential quantifiers from fact expression; simplified formula is constrained by universal quantifier
Reasoning Process	Start from facts and apply rules forward until target formula is gained	Start from facts and apply rules backward until the known fact given at the beginning is gained
Clause Form	Disjunction expression of text	Conjunction expression of text
Subset Form	Conjunction expression of clauses (conjunctive normal form)	Disjunction expression of clauses (Disjunctive normal form)

Acknowledgment

National Institute of Parasitic Diseases, Chinese Center for Disease Control and Prevention; Key Laboratory of Parasite and Pathogen Biology; WHO Collaborating Center for Malaria, Schistosomiasis & Filariasis, Shanghai 200025, China.

References

- [1] Cong Jin (2007) Artificial Intelligence Tutorial. Tsinghua University Press
- [2] Cralos Bento(2006) Progress in Artificial Intelligence. Springer
- [3] Mingyuan Ma (2006) Artificial Intelligence and Introduction to Expert System. Tsinghua University Press
- [4] Suo Luo, Weige Nuo (2006) Artificial Intelligence: A Modern Method. Tsinghua University Press
- [5] Winston (2005) Artificial Intelligence. Tsinghua University Press
- [6] Wansen Wang (2007) Principle and Application of Artificial Intelligence. Electronic Industry Press
- [7] Jose, Jolio Alferes (2004) Logic in Artificial Intelligence. Springer
- [8] Nelson.Victor P (1997) Digital Logic Circuit Analysis and Design. Prentice-Hall Inc
- [9] Zhongwan Lu (2002) Mathematical Logic Oriented at Computer Science. Science press

- [10] Hongsheng Wang (2006) Principle and Application of Artificial Intelligence. Defense Industry Press
- [11] Naples (2005) Computability and Mathematical Logic. Electronic industry press.
- [12] Guojun Wang (2006) An Introduction to Digital Logic and Its Resolution Principle. Science press
- [13] Nordex (2007) Mathematical Logic. The People's Posts and Telecommunications Press

Casing Drilling Technology to Drilling Site

Gao Wenlong

Liaohé Second Project, the First Drilling Company, GWDC, CNPC, Panjin 124010

Keywords: Casing Drilling; Drilling Technology; Construction; Analysis

Abstract. Oil development is an important industry of modern construction, for the entire socio-economic development of great significance. The continuous development of all regions of the oil used for exploration and drilling technology have given the stringent requirements, construction problems if the operation would cause serious consequences. Casing Drilling technology is the focus of the entire construction; this paper analyzes the use of technology in the drilling site, and put forward some reasonable proposals to raise the level of promotion of the construction site.

Introduction

The oil exploitation is always an important part in China's modern industries. The potential economic values in the oil exploitation industry are extensive, and are indispensable in the market economy. After the oil exploitation industry was implemented comprehensively in the new period, the casing drilling technology has been a frequently-used construction method. Besides, China's national government actively put forward the scientific progress road, which actually raises much higher requirement on the construction of drillings.

Problems in the Casing Drilling

China's oil industry has undergone a highly long development period. However, it has been recognized by many people in depth that a variety of problems have existed in the oil construction although its engineering projects and technologies have achieved a continuous update. With the purpose of ensuring the smooth implementation of the engineering projects, the engineering units in China are necessary to make adjustments to their construction plans and operation standards in an all-round way. In accordance with the development of the current oil industry, the problems in China's oil construction can be concluded as followings.

Technological Problem As the number of the oil engineering projects increases continuously, the needs on the construction personnel are raised as well. However, the engineering units often employ the construction personnel without standards, with the purpose to enhance their own operation efficiency. Great numbers of construction personnel directly participate in the construction without receiving any normal and professional training. Therefore, these construction personnel whose technological knowledge does not reach the basic standards will bury hidden dangers for the oil engineering quality. Worse, the rework and repair will give rise to the material waste and other problems [1].

Material Problem The material waste is the largest problem in the oil construction at the present time. A number of engineering units do not attach importance to the resources consumption caused by the material waste. There are some construction personnel do not conduct their tasks according to the specific drilling contrition blueprint, making the constructions of all small projects give rise to the larger material consumption. For example, multiple engineering units do not control the material equipments reasonably, and result in different wastes during the construction.

Inspection Problem After the oil construction comes to an end, the owner will implement a series of decorations on the relevant parts. However, if the construction personnel do not attain a reasonable control on the technological methods, the material wastes will also be generated to different extent, which is unfavorable to the realization of the energy conservation concept of the casing drilling technology. Additionally, a good number of materials are necessarily employed in the oil exploitation, so the pollution will be more serious if an error occurs to the selection of materials.

Comparison on the Casing Drilling and the Traditional Construction

The casing drilling construction technology has changed the traditional construction technological plans. The casing is used to replace the drill pipe to add relevant torques and bit pressures into drills, which drives the completion of the operations such as the rotation of drills and the drilling of bottom-hole. Compared with the earlier drilling construction, the casing well drillings possess various advantages, boosting the technological reform innovation of the well drilling engineering, and hence creating prodigious economic values for the owners. These can be mainly reflected from the following four aspects:

Protecting Environment In contrast to the early stage, the raw materials consumed by the oil industry in the modern society are increasingly more; the utilization efficiency of the engineering materials is reduced constantly. To ensure the oil construction operation, only the engineering units make use of great numbers of raw materials, the engineering needs can be fulfilled [2]. The proposal of the casing drilling construction technology concept can lower the consumption of materials at the premise of the fulfillment of the engineering needs, allowing the construction operations not to give rise to the damages to environments.

Reducing Costs The realization of the maximum economic benefit is the focal point which is pursued by the oil units, and therefore the reduction of cost is an objective that each unit pays active pursuits to. Moreover, the casing drilling is able to uninterruptedly reduce the material consumption by the oil exploitation, and lessen the cost investment on the engineering projects, and therefore ensure the project to create highly greater economic benefit after its completion. It is a universal belief that the casing drilling technology is the requirement of the reality of the oil exploitation in this new period.

Technical Renovation In the early and traditional oil concept, the construction technology rested in a relatively backward stage, and the whole oil industry was hard to obtain ideal construction results, and also the operational properties of the petroleum distillates cannot receive a full play. After the utilization of the new technology, however, China's oil industry accomplishes a rapid development, and boosts the oil construction technical renovations at the premise of the ensured oil properties, and hence roots a solid foundation for the creation of new oil in the future.

Aspects Necessary to be stressed in the Casing Drilling Construction

Although the casing drilling technology has been widely applied in the modern well drilling construction, there are multiple problems in China's casing drilling construction owing to the shortages of operation talents and construction equipments. This situation offers resistance to the development of the modern oilfields. In the face of various forms of construction operations, it is essential for people to attach more attentions to the aspects necessary to be stressed in the casing drilling construction, trying to enhance the efficiency of the well drilling constructions. The aspects necessary to be stressed can be concluded as followings.

Control of the Well Deflection With regard to the whole casing drilling construction, the control on the well deflection is a key step. It is easy to give rise to all kinds of construction problems if the deflection within the well cannot be controlled with moderation. For this reason, the construction personnel necessarily ensure the verticality of the casing pipes into the well, and the bit pressure is better to be controlled within the standard range between 10 KN to 30KN. Therefore, the pressing of the casing pipes is essential to be controlled well in the construction, aiming to prevent the well deflection owing to the excessively high pressure. In the operation of the well drillings, it is also necessary to hold a moderate control on the torque, feeding and rotary speed, because all these factors are likely to give rise to a well deflection.

Construction Technology The effective construction technology can be formulated in accordance with the well drilling construction sites, which can drive the casing drilling technology to attain the satisfied effects. To drive the construction technology to emit its effects, it is necessary for the construction personal to make appropriate adjustments to the drilling equipments as shown in Fig 1. The specific step is installing the back pressure valve on the top of the drilling and the

bottom of the casing string respectively, by which the fastening of the well mouth can be reinforced. After the termination of the well drilling, it is essential to process the stick property of the drilling fluid, because this can avoid the sides of the well drilling being wore and tore.

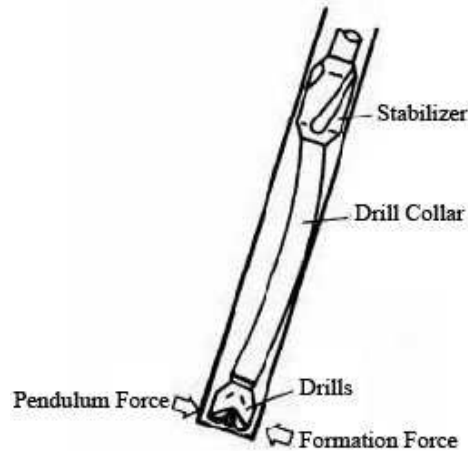


Fig 1: The Drilling Technological Process

Protection of Casing Pipes After the operation of a casing drilling is completed, it is necessary to formulate the purposeful maintenance plans according to the actual situation of the drilling sites, and this is the premise of ensuring the long-term service life of the well drilling. In general, the solution to protect the casing pipes is to apply the casing pipe exclusive glue in the casing drilling, so as to ensure the thread position with highly reliability and keep all joints stable and solid. To prevent the damages from rotation during the drilling process, it is essential to install the corresponding external preservatives, and simultaneously the construction personnel must hold a moderate control on each operation step.

Control of Parameters In the course of the casing drilling construction, all small and big parameters are essential to be applied, and this is also an aspect that must be emphasized during the drilling. As long as a parameter is controlled improperly, it will exert an unfavorable impact on the quality of the whole drilling. Generally, the parameters necessary to be controlled mainly include the bit pressure in the range of 10-30KN, the rotation speed in the range of 60-120r/min, the total pump pressure in the range of 6-7MPa, etc. Thus, the construction of the drilling without difficulties can be ensured from multiple aspects^[3]. Besides, the personnel to manage the drilling construction must strengthen the technical guidance to the constructors, making them to know well the standards of the parameters.

The Application of New Technologies to the Drilling Operation

The speedy development of the socialist market economy pushes forward society the informatization. The innovative operation technologies cored at computers are applied to the construction with a gradual step. The application of new technologies ensures the accuracy, rationality and scientificness of the drilling construction. Currently, the three computer technologies which have been applied to the casing drilling are the GPS position technology, structural simulation technology and virtual reality.

GPS Position Technology GPS position technology has multiple features: (1) identifying the sunshine and vibration deformations in the mouth of the well; (2) avoiding the errors caused by artificial factors; (3) posing few constraints on the selection of the controlling network base point at the drilling sites; (4) the difference of the observation base point exerts a small impact on the accuracy of the observation; (5) the construction measurement is with high accuracy, no errors and no transmission and accumulation [4]. Currently, the GPS position technology has been widely applied to the civil-engineering's reconnaissance, design, construction and so on. Along with the improvement of the fundamental theories of the GPS position technology, it will be more widespread in the China's oil exploitation industry.

Virtual Reality The virtual reality is a cross technology that develops based on the computer graphics and simulation technology as well as the sensor technology. It features the interactivity, independence and receptivity, etc. The application of the virtual reality can visually express the distribution of oilfields, and also provides an intuitive view for the formulation of the drilling construction plans [5].

Structural Simulation Technology The computer simulation is a process to create a model to simulate the movements happening in a particular system. The application of computer simulation can shorten the construction decision-making time and avoid the wastes of capitals, human resources and time, but also are highly safe and reliable. In the construction of the modern oilfield exploitation, the simulation system mainly includes the construction plan, construction simulation system, computer structural simulation technology, etc.

Intelligent Measurement Technology Through the engineering settings allocated by computers, the construction personnel can undertake the inspection on the properties of the drilling construction equipments, and hence ensure the engineering functions of the whole drilling construction technology can be brought into full play. For instances, in the earlier stage of the casing drilling construction, the application of computer technologies can make clear the actual conditions within the well bottom and implement the effective inspections, by which the allocated drilling equipments can reach the ideal requirements.

Conclusion

Under the impacts from various factors, there are multiple problems in China's casing drilling technology, and these will hinder the orderly operation of the on-site drillings. In the face of various problems in the modern oilfield exploitation and construction, it is necessary for people to undertake the tasks in all aspects, attach great importance to the problems in the construction of casing drillings, and completely control all the links of the construction. All these are essential to be emphasized.

References

- [1] Zhao Dongdai. Research on the Modification of Casing Drilling Construction Technology [J]. China Petroleum Technology, 2009, 35(12): 33-35.
- [2] Cao Xueyun. Problems Necessary to be noted in the Exploitation of Oil Fields [J]. Journal of Nanjing University of Science and Technology, 2009,35 (12): 33-35.
- [3] Feng Kaiping. The Application of Building Energy Conservation in the Engineering [J]. Oilfield Exploitation Technology, 2009, 41(6): 63-65.
- [4] Fang Toujun. Analysis on the development of China's Oil Exploitation Industry [J]. Journal of Zhengzhou University, 2009, 28(11):71-73.
- [5] Zhu Jianzhang. Current Situation of China's Building Energy Conservation Materials [J]. Modern Construction Research, 2009, 21(7): 51-52.

Basic Process of the Performance Test of the Turbine Generators

Nan Li

Beihang University, Beijing 100191 China

e-mail: linan20112@126.com

Keywords: Performance Test, Turbine Generators, Heat Rate

Abstract: This report elaborates the performance test of the turbine generators, it gives the standard, the working condition, the methods of the performance test and the calculation methods, and in order to reduce the heat rate, increase the efficiency of the turbine, it offers some corresponding suggests. And then, software that is used for the performance test of the turbine generators is given; it is used for calculating and proofreading the main standards rapidly.

Background

A steam turbine is a device that extracts thermal energy from pressurized steam and uses it to do mechanical work on a rotating output shaft. Because the turbine generates rotary motion, it is particularly suited to be used to drive an electrical generator [1]. The steam turbine is a form of heat engine that derives much of its improvement in thermodynamic efficiency through the use of multiple stages in the expansion of the steam, which results in a closer approach to the ideal reversible process. The general errors are around 0.625%. Reheat turbines are also used almost exclusively in electrical power plants [2].

Basic Process of Performance Detection

The Objective of the Detection It mainly tests the heat consumption rate and the power consumption rate of the steam turbine. In addition, some suggestions on lowering the heat consumption rate are given in the paper.

That's Heat consumption test of steam turbine. Measurement of the rate of oxygen consumption provides a simple, versatile and powerful tool for estimating the rate of heat release in fire experiments and fire tests. The method is based on the generalization that the heats of combustion per unit of oxygen consumed are approximately the same for most fuels commonly encountered in fires.

Output test of Steam Turbine. A measurement of the rate of oxygen consumption can then be converted to a measure of rate of heat release. Data on heats of combustion are presented to support this generalization. They are respectively: TRL working condition, TMCR working condition, VWO working condition, stopping HP heater, and side condenser working condition [3]. In this way, the output of steam turbine can be tested.

Detection Standards and Benchmark

Detection Standards

“Performance Test Code 6 on Steam Turbines” ASME PTC6-2004 accredited by American Society of Mechanical Engineers [5].

Water and Steam Attribute Table

“IAPWS-IF97” formula is accredited by the International Association for the Properties of Water and Steam [6].

Detection Benchmark

The examination on the heat consumption working condition is based on the full-opening valve standard while the other working conditions are based on the loading benchmark.

Other Standards

It is based on “Thermal power unit start acceptance test guide” by the Ministry of water resources and electric power in People’s Republic of China, and on the “Measurement of flow by means of orifice plates, nozzles and Venturi tubes inserted in circular fluid flow” by the national standard of the People’s Republic of China (GB/T 2624.1-2006, GB/T 2624.2-2006, GB/T 2624.3-2006, GB/T 2624.4-2006).

Experimental Measuring Point and Instrument

Experimental Measuring Point

The experimental measuring points are respectively the temperature measuring point, pressure measuring point, flow rate measuring point, water location measuring point and electric measuring point.

Flow Rate Measurement

Flow measurement is the quantification of bulk fluid movement. Flow can be measured in a variety of ways. Positive-displacement flow meters accumulate a fixed volume of fluid and then count the number of times the volume is filled to measure flow.

Other flow measurement methods rely on forces produced by the flowing stream as it overcomes a known constriction, to indirectly calculate flow. Flow may be measured by measuring the velocity of fluid over a known area. Two ROSEMOUNT 3051 type differential pressure transmitters grading 0.05 are used.

The turbine flow meter translates the mechanical action of the turbine rotating in the liquid flow around an axis into a user-readable rate of flow. The turbine tends to have all the flow traveling around it. Two ROSEMOUNT 3051 type differential pressure transmitters grading 0.075 are used.

Temperature Measurement

Many methods have been developed for measuring temperature. Most of these rely on measuring some physical property of a working material that varies with temperature. One of the most common devices for measuring temperature is the glass thermometer. This consists of a glass tube filled with mercury or some other liquid, which acts as the working fluid. Type ROSEMOUNT 488 temperature transmitter are adopted.

High-precise ROSEMOUNT 3051 grading 0.075 are adopted. Everyday pressure measurements, such as for tire pressure, are usually made relative to ambient air pressure. In other cases measurements are made relative to a vacuum or to some other ad hoc reference.

Electric Power Measurement

Electric power measurement adopts detection power table typing WT3000 with the grade of 0.1. Another type of thermometer that is not really used much in practice, but is important from a theoretical standpoint, is the gas thermometer.

Water Level Measurement

The water levels in surface water and groundwater systems are commonly measured at different locations. For example, river levels are taken at gauging stations and groundwater levels may be taken at nearby monitoring bores. Water level measurements taken at a site are usually relative to an arbitrary benchmark.

Other Measurements

The system has stated the other measurements.

Data Collection

Detection data collection system has adopted the latest IMP distributed data collection device. Signals such as temperature, pressure, and electric power rate can be automatically collected and handled according to the corresponding data.

Detection Method and Procedures The heat power system follows strictly the system isolation and checks carefully. It makes inspection and determination.

Supply water to the system. Adjust the water level of the box. Avoid fierce movement.

Adjust the boiler combustion. Maintain stability within sustainable time in the experiment.

Adjust the functional parameters so as to make it satisfy the experiment. Maintain the stability of the parameters in order to meet the requirements of the test.

Adjust the high pressure main stop valve and the loading valve in order to meet the requirements of the experiment.

Stop the boiler soot-blowing.

Determine the data collection system and the instrument in normal working condition. Experimental recorders enter into the appointed position.

Start data collection and records according to the unified time.

During the experimental period, measure the leakage that cannot be isolated by the heat power system.

Calculation of Detection Results

Data treatment: In a reheat turbine, steam flow exits from a high pressure section of the turbine and is returned to the boiler where additional superheat is added.

Electric power calculation

$$P_e = K_w \times K_{pt} \times K_{ct} \times (W_1 + W_2) \quad (1)$$

Main flow of condensate calculation

$$F_{cw} = 1.264466652 \times 10^{-4} \times C \times \varepsilon \times d^2 \times \sqrt{\frac{\Delta P \times \rho}{1 - \beta^4}} \quad (2)$$

System leakage calculation

$$F_{un} = F_{hl} + F_{dl} - F_{ml} \quad (3)$$

The Objective of the Detection

$$F_{fw} = F_{cw} + F_{1h} + F_{2h} + F_{3h} + F_{De} + F_{dl} - F_{rhsp} - \Delta F_p \quad (4)$$

Main stream flow rate calculation

$$F_{ms} = F_{fw} - F_{bml} - F_{un} \quad (5)$$

Detection Heat Power Rate Calculation

$$HR_t = (F_{ms} \times (H_{ms} - H_{fw}) + F_{crh} \times (H_{hrh} - H_{crh}) + F_{rhsp} \times (H_{hrh} - H_{rhsp})) / P \quad (6)$$

Proofreading of experimental results

$$\frac{BF}{\log MV} \sqrt{\frac{p_o \cdot psig}{2400}} \times (f) \quad (7)$$

Software Compile and Proofreading

The steam then goes back into an intermediate pressure section of the turbine and continues its expansion. Extracting type turbines are common in all applications. The author makes use of the Microsoft Excel to calculate the performance of steam turbine.

Software Usages

In an extracting type turbine, steam is released from various stages of the turbine, and used for industrial process needs or sent to boiler feed water heaters to improve overall cycle efficiency. Extraction flows may be controlled with a valve.

The meaning of Software

Software that is used for the performance test of the turbine generators is given, which is used for calculating and proofreading the main standards rapidly.

References

- [1] J. Tong (1996) Steam turbine performance experiments. America: Machine Engineering Association.
- [2] Tianchong JIAN (1986) Steam turbine Principles: Water conservancy and electric power press
- [3] Wenshuang Duan.(1980) Thermal power plant thermal equipment and system. North China Electric Power University: electronic publishing house
- [4] Qingmin Xu (1987).Equipment and function of Small power station steam turbine. Xi'an electricity College:Water conservancy and electric power press
- [5] WANG Nai-ning (1987).Steam turbine heat power design: Water conservancy and electric power press
- [6] W. J. Wu (1983).Steam turbine general assembly design. Harbin steam turbine Company Limited.

Integrated Nine-Switch Power Converter based on Discontinuous Pulse-width Modulation

Wang Qin,

Suzhou Institute of Industrial Technology, Suzhou, Jiangsu, 215104

Keywords: Power Conditioner, Nine-Switch Converter, Discontinuous Pulse-Width Modulation.

Abstract. This paper evaluates the shortcomings of the application experience before nine-switch the newly proposed converter. A better understanding of development, the conclusion is, nine-switch converter is not an attractive option "alternative of two consecutive converter parallel of the bridge. Instead, nine-switch converter is more suitable for replace back-to-back inverter in" series-shunt "of the system, in a good example is the unified power quality conditioner.

Introduction

Since the first introduces, static power converter is developing rapidly development and many converter topology discovery in public now easy to literature. With its development also quickly identify the scope of application, in power converters can promote to improving the system of your positive qualities. In most cases, identify the power converter used connections series or parallel. In addition, they need to be programmed and voltage or current regulation scheme (or power) so as to compensate for harmonic, reactive power flow, imbalance and the voltage of the support. The more strict laws and regulations provide high quality extrusion divergence and a series of Rectifier Bridge to join their task execution voltage adjustment, and the other the current regulation. Almost always, two converter are connected in a continuous configuration, use twelve switch, in total, sharing a common dc-link capacitor (also can be in a distributed micro grid micro-source [1]), as shown in figure, as shown in fig 1 (a).

Successive configuration so far most of the operation circumstance can communicate well, but it must improve its loss as reduce, components and complexity would prefer if not or only slight degradation performance. Improve the contribution, puts forward a single stage of the development of the comprehensive ability of air conditioning, realize the converter using nine-switch two sets of output terminals, not twelve-switch back-to-back converter. Early nine-switch puts forward converter [2], [3] at about the same time, are recommended for double motor drive, rectifier-inverter system and uninterrupted power supply system.

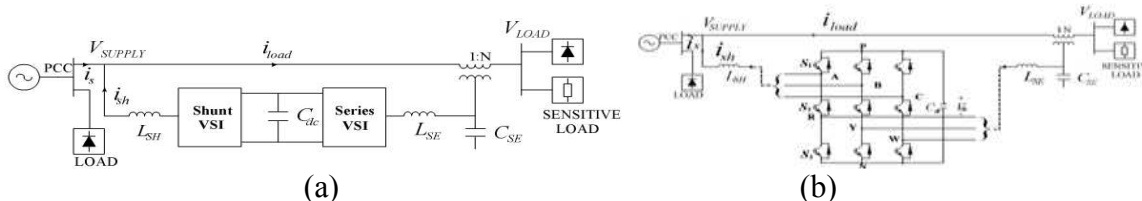


Fig. 1 System representations of (a) back-to-back and (b) nine-switch power conditioners

System Description and Operating Principles of Nine-Switch Power Conditioner

Fig. 1(a) shows the per-phase representation of the commonly investigated back-to-back unified power quality conditioner (UPQC). In parallel shunt converter point-of-common-coupling (PCC) and a series of converter is in series with the isolated transformer feed through the distribution. Parallel converter to compensate usually load control harmonics, reactive power tide and don't balance, from basic current sine utility grid, no matter the extent of the nonlinear load. Added series converter control blocks grid harmonics and doesn't balance such a three-phase voltage always appear in the basic load contacts. Inverse distribution function and parallel inverter voltage

regulation and series performs the rules of general inverter may [1], but no task of the specific provisions, UPQC can be seen as a good "lie between", blocking interference originated in the end to the other side from reproductive system.

Although many researchers have been proved effective, however continued complex and clinical UPQC, although it provides independent control of two converters, decoupling dc-link capacitors? It is no doubt due to the series converters, and its control output voltage generally small, because only a small amount of the harmonic compensation and don't balance in normal conditions to steady state, especially for strong grids ($\vec{V}_{SUPPLY} \approx \vec{V}_{LOAD}$). In particular, a discussion found in [3] states that the converter modulation ratio can be as low as 0.05 if the converter is sized to inject a series voltage of 1p.u. during sag occurrence.

Computational problems linked to such a low than have put forward in [3], but still failed to fully problem is topological unresolved, may not be easy to solve if dc-link voltage need to share and no new component is allowed. Trading must surface, this means that more realistic problem is how to reduce address them, but not eliminate them altogether. Provide possible solutions, and proposed the implementation power air conditioning nine-switch converter used first documented in [2] criticism, not a continuous configuration. Can only change did a study, confirmed that the nine-switch converter will not cover system cost and performance. It is very important, because in the previous cases, in nine-switch converter is used in motor drive and rectifier-inverter system, some of the more serious limitations surface, can make the discussion nine-switch briefly introduced the frequency converter, as follows.

Table 1 Switch states and output voltages per phase

S ₁	S ₂	S ₃	V _{AN}	V _{RN}
ON	ON	OFF	V _{dc}	V _{dc}
ON	OFF	ON	V _{dc}	0
OFF	ON	ON	0	0

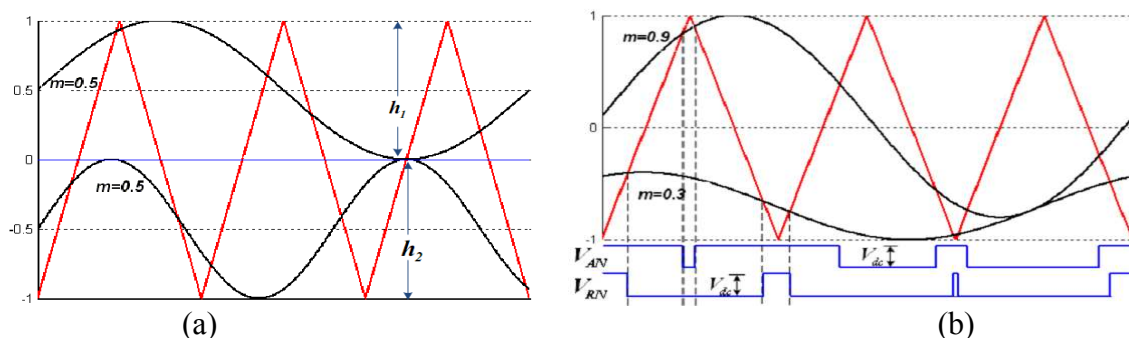


Fig. 2 Modulating arrangements for references having (a) the same frequency and amplitudes above 0.5, (b) different frequencies but the same amplitude of 0.5

As illustrated in Fig. 1(b), the nine-switch converter is formed by tying three semiconductor switches per phase, giving a total of nine. To be more specific, the allowable switching states are listed in Table I, where it is shown that the converter can connect its two output terminals per phase to either V_{dc} or 0V, or the upper terminal to the upper dc rail P and the lower terminal to the lower dc rail N. The last combination of connecting the upper terminal to N and the lower terminal to P is however not realizable, hence constituting the first limitation faced by the nine-switch converter. That limitation is nonetheless not practically detrimental, and can be resolved by coordinating the two modulating references per phase drawn in Fig. 2(a), such that the reference for the upper terminal is always placed above that of the lower terminal.

Imposing the above-identified rule of thumb governing reference placement would indeed always bypass the forbidden state of V_{AN} = 0V and V_{RN} = V_{dc}, as demonstrated by the potential transitional details drawn at the bottom of Fig. 2(a). Its effectiveness is however burdened by additional constraints limiting the reference amplitudes and phase-shift. These limitations are especially prominent for references having sizable amplitudes or different frequencies with the

former illustrated in Fig. 2(a) and the latter illustrated in Fig. 2(b). In particular, Fig. 2(a) shows two references of common frequency limited in their phase displacement, while Fig. 2(b) shows two references of different frequencies limited to a maximum modulation ratio of 0.5 each, in order to avoid crossover. Limited phase has recently been proof standard and adapt to the online uninterrupted power supply system, this also is really a neat, intelligent application of nine-switch converter. However constitute only a single application, so nine-switch converter full potential have not yet put forward?

In normal operation conditions, the output voltage amplitude of the shunt converter is relatively larger voltage inverter along the distribution of food series put forward. It only means that need to adjust the reference parallel inverter is far higher than related series converters; this may be the only inverse harmonic component of the compensation for the purpose (4, 5). The details in the chart will lead to the carrier the broader vertical distance, as shown in figure 2 (b) on tap control terminals, reduce the h2 control lower series terminal ($h1 \gg h2$).

Despite a higher voltage dc-link is still need as a balance, more reduced, and absolutely not anything close to double. Reference [3], for example, statements, in the modulation than series converters can be as low as 0.05, this means that dc-link increase of the voltage is only 5%, the same parallel voltage amplitude, such as in a series of converter, is by nine-switch converter modulation in than 0.95 haven't triplen offset increase (increased triplen also increased by a factor of 1.15 percentage). The dc-link slight increased voltage will not overstress semiconductor switching is very big, so be regarded as an acceptable balance "series-shunt" converter is replaced. Save three semiconductor switching here is also regarded as more outstanding, serious, because they represent for continuous switch series compensation purpose configuration.

Another issue to address, before the nine-switch converter can be confirmed as a favorable topology for power conditioner, is to study its compensating ability under voltage sag condition. As an illustrative example, the PCC voltage in Fig. 1(b) is assumed to dip by some amount, which would then subject the higher shunt terminal of the nine-switch converter to a reduced voltage level. In contrast, the lower series terminal must now immediately inject a sizable series voltage at the fundamental frequency ($\vec{V}_{SERIES} = \vec{V}_{LOAD}^* - \vec{V}_{SUPPLY}$, where \vec{V}_{LOAD}^* is the demanded load voltage reference), so as to keep the load voltage close to its pre-fault value.

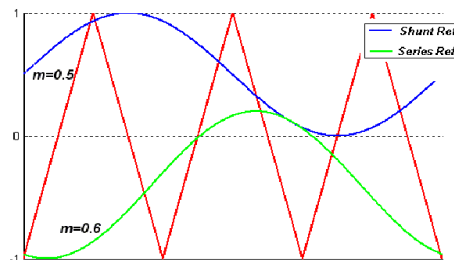


Fig. 3 Modulating arrangement for references having the same frequency, but with the higher reference reduced in amplitude during voltage sag

Updating these sag operating scenarios to the carrier domain then results in the shunt terminal using a reduced reference, and the series terminal widening its reference range to include a sizable fundamental component. Since both references are now predominantly fundamental with sizable amplitudes, their placement can be like that drawn in Fig. 3, subject to the same phase-shift limitation mentioned earlier. Fortunately, this restriction will not hinder the air conditioning operation nine-switch demand since the great, into the series voltage phase limited is usually accompanied by a severe depression in the PCC, thus greatly reducing the tap a reference. The smaller shunt reference in turn preferential open more space to series reference changes, allowing it to assume more requirements and amplitude phase system needs. This increased flexibility reference position series could detect plot comparison chart 2 (a) and figure 3, there have more space, the latter is higher than the shunt reference changes, and was in the demolition of PCC sag.

Modulations and Control

In the verification of the nine-switch power air conditioning applicability, appropriate modulation and control strategy put forward the control now. The main goal is to reduce the switch loss, remain the same performance standards for continuous counterpart.

Because in traditional back-to-back found independence converter, its modulation can through each a focused placed in three-phase reference the life of vertical carrier. The focus will make back-to-back converter performance level to close to the optimal space vector modulation (SVM) scheme. Yet this central position cannot be converted nine-switch power regulator, the reference must be placed at any of the other, in the second part of the explanation (B). Get the best performance for two terminal harmonics of the nine-switch converter is so impossible. But this is not a serious limitation since modern semiconductor equipment and power conversion technology will greatly frustrate any specific spectral got modulation scheme.

So, not for spectrum advantage, the aim was to develop a modulation scheme, can save switching losses. Direct selection will choose that traditional discrete modulation scheme, including the famous 60° and 30° -discontinuous-discontinuous scheme. However, unlike traditional voltage-source inverter in the upper and lower dc-rails large supply of lock, nine-switch converter only available for reference dc-rail upper clamping and the lower for reference dc-rail clamped low. That means that popular choice- 30° 60° -discontinuous planning is not suitable for nine-switch converter because they need to both sides of the upper and lower dc-rail clamping. More specifically, usually with the 120° -discontinuous modulation scheme may is the right choice, because it only need nine-switch converter the upper or lower d-rail clamping, not two.

To further evaluate its suitability, the relevant offset and modified reference expressions are derived, and listed in (3), before subsequently plotting them in Fig. 4, showing clearly the two references needed per phase.

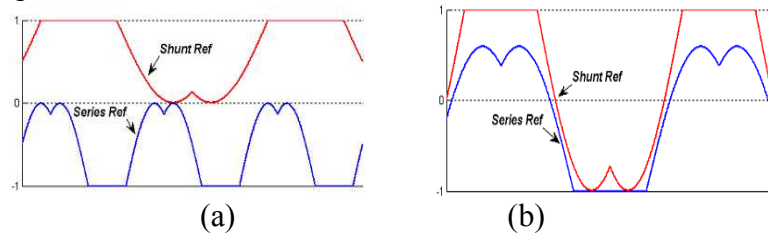


Fig. 4 120° -discontinuous references for nine-switch converter with modulation ratios and frequencies set to (a)

$$M_{SH} = M_{SE} = 0.5, \omega_{SH} \neq \omega_{SE}, \text{ and (b) } M_{SH} = 1 \times 1.5, M_{SE} = 0.8 \times 1.15, \omega_{SH} = \omega_{SE}$$

Sinusoidal References

$$\begin{cases} V_A = M_{SH} \cos(\omega_{SH}t + \theta_{SH}) \\ V_B = M_{SH} \cos(\omega_{SH}t - 120^\circ + \theta_{SH}) \\ V_C = M_{SH} \cos(\omega_{SH}t + 120^\circ + \theta_{SH}) \end{cases} \quad (1)$$

$$\begin{cases} V_R = M_{SE} \cos(\omega_{SE}t + \theta_{SE}) \\ V_Y = M_{SE} \cos(\omega_{SE}t - 120^\circ + \theta_{SE}) \\ V_W = M_{SE} \cos(\omega_{SE}t + 120^\circ + \theta_{SE}) \end{cases} \quad (2)$$

120° -Discontinuous Modified References

$$V'_\gamma = V_\gamma + V_{SH}, \quad V_{SH} = 1 - \max(V_A, V_B, V_C) \quad \gamma = A, B \text{ or } C$$

$$V'_\delta = V_\delta + V_{SH}, \quad V_{SE} = 1 - \min(V_R, V_Y, V_W) \quad \delta = R, Y \text{ or } W \quad (3)$$

Where $\{M_{SH}, \omega_{SH}, \theta_{SH}\}$ are the modulation ratio, angular frequency and initial phase of the shunt terminal, while $\{M_{SE}, \omega_{SE}, \theta_{SE}\}$ are the corresponding quantities for the series terminal.

Even more appealing is that the reduction in losses is attained without complicating the physical realization, since the needed discontinuous offsets merely replaces the original dc offsets added to separate the two references. Per. phase, like demonstrated in Fig.2. The introduced 120°-discontinuous offsets are also comparatively much simpler to compute than those associated with the 60°- and 30°-discontinuous schemes. Therefore, the presented 120°-discontinuous scheme is indeed an attractive alternative, as compared to the existing scheme where only dc offsets are added.

Where necessary, it should also help to regulate the load voltage to compensate for any slight fundamental voltage variation. This second functionality is however more relevant under voltage sag condition, where a sizable series voltage ($\vec{V}_{SERIES} = \vec{V}_{LOAD}^* - \vec{V}_{SUPPLY}$) needs to be injected to keep the load voltage nearly constant. The overall control block representation adopted is shown in Fig. 5, where the subsystem responsible for voltage harmonic compensation is distinctly identified within the rectangular enclosure.

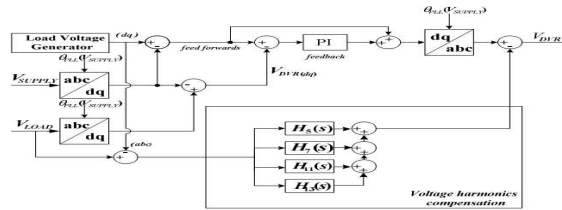


Fig. 5 Series control block representation

As drawn in the figure, the harmonic compensation subsystem is realized by including multiple resonant regulators in the stationary frame for singling out and eliminating only those prominent low-order harmonics detected in the load voltage, including the 5th, 7th, 11th and 13th components. Transfer functions of the resonant regulators $H(s)$ and their inclusion in a Bode diagram are shown in (4) and Fig. 6 respectively.

$$H_n(s) = 2K_I \omega_c \frac{s + \omega_c}{s^2 + 2\omega_c s + \omega_n^2 + \omega_c^2} \tag{4}$$

Where K_I , ω_n and ω_c represent the gain parameter, chosen harmonic resonant frequency and cut off frequency by introduced for raising stability, but at the expense of slight transient sluggishness.

Summary

To further boost performance, the article puts forward an improved-discontinuous 120° modulation scheme proposed lower overall transformation calculation of the converter 33%. Divergence and the series of control scheme, then add compensation reactive power and voltage harmonic, hang down, allowing the nine-switch converter is an attractive function of strength and reduced switch calculation air conditioning, etc. The simulation result shows the smooth performance of the proposed expected ability of air conditioning.

References

[1] Y. W. Li, Viathgamuwa D. M. and P. C. Loh, “A grid-interfacing power quality compensator for three-phase three-wire microgrid applications,” IEEE Trans. on Power Electronics, vol. 21, pp.1021-1031, 2010.

[2] C. Liu, B. Wu, N. Zargari and D. Xu, “A novel three-phase three-leg AC/AC converter using nine IGBTs”, IEEE Trans. on Power Electronics, vol. 24, pp. 1151-1160, 2009.

[3] T. Kominami and Y. Fujimoto, “A novel three-phase inverter for independent control of two three-phase loads,” in Proc. IEEE-IAS’07, pp. 2346-2350, 20010.

Research of Flow Field and Temperature Field in 2D Annular Space of Air-Gap

Lu Tang, Yiping Lu, Haiyan Deng and Zuomin Wang

School of Mechanical & Power Engineering, Harbin University of Science and Technology, Harbin, China

e-mail: luy2010@yahoo.com.cn

Keywords: Numerical Simulation, Rotating Flow, Air-Gap, Turbo-Generator, Radiation Heat Transfer

Abstract: The flow in air-gap of turbo-generator was simplified to the rotating flow model in the 2D concentric cylinder annular space. According to the CFD principle, the rotating flow model equations of the laminar flow and the turbulent flow were solved with Finite Volume Method. After being compared with the analytical solution of the 2D concentric cylinder Couette shear flow, the 2D air-gap model, the boundary conditions and the calculation results were proved to be accurate. On the basis of the study of the velocity field, the energy equation and the radiation equation were added to study the temperature field in the annular space. The convection and the radiation heat transfer were considered under the first boundary conditions. The turbulent flow and temperature distribution of the annular space under the steady-state were analyzed.

Introduction

At present, some hypothesis of reasonable simplification were made on all the researches in allusion to flow and heat transfer within stator and rotor of turbo-generator, but in view of the complexity of rotating flow in air gap between stator and rotor, there are fewer studies about flow and heat transfer of cooling medium in air gap at home and abroad. Air gap is the boundary of outlet and inlet of flow and heat transfer of rotor and stator respectively, thus, flow field and temperature field of air gap have a greater impact on aerodynamic field and temperature field of stator and rotor. In the case of high-speed rotation of rotor, heat exchange occurs in centrifugal field with secondary flow [1-2] in air gap between stator and rotor, which affects flow and heat exchange of ventilation system within rotor greatly. Therefore, it is important to study the distribution of flow field and temperature field in air gap of turbo-generator.

Domestic and foreign scholars have done some studies on characteristics of physical field in air gap of electrical machine. Ma youfu. Etc studied the characteristics of inflow slot wedge and outflow slot wedge of gap-pickup turbo-generator adopting RNG $k-\epsilon$ turbulent model by fluent software for numerical simulation [3]. M.Kuosa. etc studied the characteristics of flow and heat transfer in air gap of electrical machine with 10 000-80 000rpm by experiment and numerical simulation with $k-\epsilon$ sst, $k-\omega$ turbulent model and so on using FINFLO[4] software and the results of numerical simulation of turbulent time-averaged model did not appear Taylor vortex is discovered. Yan hongfeng studied the characteristics of flow field and temperature field of wedge-shaped air-gap of horizontal evaporation cooling motor with the method of Fluent software combined with the experiment [5], which did not deal with the analysis of heat exchange influence of convection and radiation in air gap. Xiongbing.etc proposed a generator with new cooling method, in which evaporative cooling is adopted in stator while air cooling is adopted in rotor and air flows out from air gap [6], further explanation that study of the flow field is very important. Combined with a given example of air gap of air cooling turbo-generator in this article, flow and heat transfer of air gap is simplified to the issue of rotating flow and heat transfer in annular space, in which rotates inside the cylinder and stills outside the cylinder [7]. The 2-D annular physical model of air gap (Fig. 1) is established using Gambit. Boundary conditions setting and iterative calculation have been done by fluent software. Comparing the acquired numerical solution with the analytical solution, numerical results are proved to be accurate. On this basis, the influence of convection heat transfer and radiation heat transfer to flow field and temperature field in annular space of air gap is analyzed.

Model Selection

Physical Model Air gap system of air cooling turbo-generator is shown in Fig. 1, radius of rotor and stator is r_1, r_2 respectively, air gap space is δ , rotor rotates with angular velocity Ω , stator is immovable, incompressible air is full of the space between them. Cylinder is long enough, the 2-D steady flow of annular space is studied briefly. The physical model of 2-D concentric cylinder annular air gap space is established using Gambit.

Mathematical Model Governing equation includes mass conservation equation, momentum conservation equation, energy conservation equation. Turbulent time-averaged equation is applied widely in project for turbulent state. Turbulent kinetic energy equation and turbulent energy dissipation rate equation reflecting characteristics of turbulence is replenished at the same time [8]. In addition, calculation governing equation of radiation heat transfer is involved in this article:

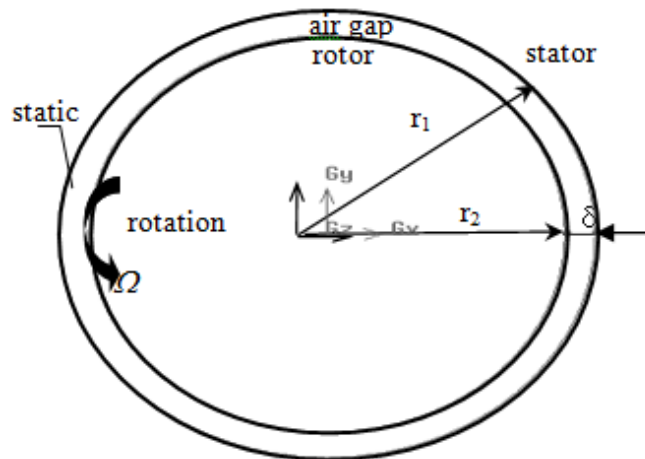


Fig. 1 Structure diagram of annular space in air gap

$$Q_i = \frac{\varepsilon_i}{1 - \varepsilon_i} (E_{b,i} - J_i) A_i \dots \dots \dots (1)$$

$$J_i = E_i + \rho_i \sum_{j=1}^N X_{ij} J_j \dots \dots \dots (2)$$

Where Q_i is radiant heat transfer rate transferred between walls, ε_i is wall emissivity, J_i is wall effective radiation, X_{ij} is angle factor, Monte Carlo method is adopted to calculate X_{ij} in Fluent software [8].

In allusion to the model of air gap in this article, relative clearance $(r_1 - r_2) / r_1$ is very small, flow instability depends on Taylor number barely [7]:

$$Ta = r_1 \delta^3 \frac{\Omega_1^2 - \Omega_2^2}{\nu^2} \dots \dots \dots (3)$$

Where Ω_1, Ω_2 is the speed of rotor and stator ($\Omega_2 = 0$) respectively according to turbo-generator, ν is kinematic viscosity. When $Ta \geq 1,708$, air flow is steady laminar flow, which is Couette flow in air gap; When $Ta \geq 160,000$, air flow is turbulence [7]. When the speed of rotor less than 0.45rpm, flow state in air gap is laminar flow by calculating in allusion to the physical model in this article. When the speed of rotor more than 4.29 rpm, flow state is turbulence. The speed of generator is 3000 rpm at steady state, which accounts for overall flow state is exuberant turbulent flow in air gap of generator.

Mesh Generation and Boundary Conditions In the calculation of Fluent software, the multiple reference system model is chosen, the wall of rotor is set as rotating wall, the wall of stator is set as stationary wall. The pressure of air gap is standard atmospheric pressure; fluid is regarded as incompressible fluid.

When the laminar flow field is calculated, since the variation gradient of various physical quantities along radial direction is small in air gap that uniform grid is adopted along radial direction. Since the variation gradient of physical quantities in nearby zone of stator and rotor walls is large when turbulent flow field is calculated that proportional grid is adopted and close grid is adopted in the zone which closes to wall, sparse grid is adopted in the middle part of air gap, which is used to adapt the variation trend of physical quantities. Turbulent model adopts RNG $k-\varepsilon$ two-equation model [8] considering rotation. Enhanced wall treatment is adopted in the zone closes to wall. The magnitude of distance y^+ which is dimensionless is 1 in the zone closes to wall which locates at the contiguous region of fluid and wall. The requirement of enhanced wall treatment is satisfied, results does not change along with grid after several trial calculation.

Segregated and implicit solver is adopted in discretization governing equations, the method of PRESTO is chosen in pressure interpolation on account of swirling flow; pressure-velocity coupling equations adopt SIMPLE algorithm. The second-order upwind scheme is applied to all the other equations. The residual of energy equation is 1×10^{-6} and residual of all the other equations is 1×10^{-3} when iterative calculation is in progress.

Results Analysis

Laminar Flow Analysis Laminar flow which exists exact solution is chosen to calculate firstly in order to ensure the correctness of calculation model and results and compare numerical results with exact solution.

Swirling flow is Couette shear flow under the state of laminar flow, the flow is steady flow in annular space of air gap as shown in Fig. 1. The radius r_1 of rotor is 0.53m, wall temperature is T_1 and rotates with angular velocity Ω_1 ; the radius r_2 of stator is 0.5975m, stationary, wall temperature is T_2 . The dimensionless analytical solution of velocity distribution obtained in cylindrical coordinate when the variable u, T and P is the function of radius barely[7]:

$$\frac{u}{r_1 \Omega_1} = \frac{\frac{r_1}{r_2}}{1 - \left(\frac{r_1}{r_2}\right)^2} \cdot \frac{1 - \left(\frac{r}{r_2}\right)^2}{\frac{r}{r_2}} \quad (4)$$

The numerical solution of u distribution along radial direction is calculated under the condition of a speed is 0.10rpm, 0.25rpm, 0.45rpm respectively by Fluent software in this article. The comparison of numerical solution and analytical solution is shown in Fig. 2. Text S stands for numerical solution, Text A stands for analytical solution in the figure. We can know from Fig. 2, the curve of numerical solution and analytical solution is anastomotic when the speed is same under the state of laminar flow. It accounts for the correctness of correlative setting and results in Fluent software.

Turbulence Analysis When the speed is more than the second critical velocity 4.29rpm, flow state is turbulence. Turbulent equations is solved under the working condition of a rotor speed is 1500rpm, 3000rpm respectively in this article ignore the wall temperature of stator and rotor. Velocity distribution obtained along radial direction in air gap is shown in Fig. 3.

It can be seen from Fig. 3, velocity distribution of air gap is "S"-type distribution, which coincides with results and analysis in literature [7]. Calculation and results is proved to be accurate; in addition, velocity gradient in boundary layer of rotor wall is huge, flow velocity decreases rapidly along with the increasing distance from the wall; velocity gradient in boundary layer of stator wall is relative smaller. Velocity variation characteristics are contrary to that in boundary

layer of rotor wall. Flow velocity decreases gradually along with the increase of radius r between the two boundary layers. Flow velocity increases along with the increase of speed at the positions with the same radius under the working condition of different speed.

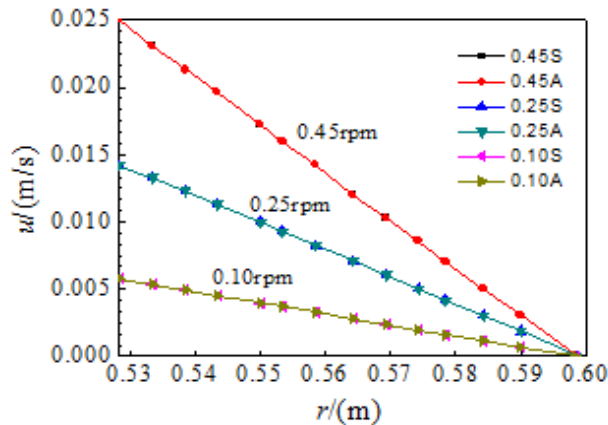


Fig. 2 Compare numerical solution with analytical solution of velocity distribution of laminar flow along radial direction

Convective Heat Transfer Influence In engineering problems, there is temperature difference between stator surface and rotor surface, radiation heat transfer exists between them while convective heat transfer exists between stator, rotor wall and air, therefore, computational complexity can be minished effectively and the accuracy of calculation results can be ensured by analyze the effect of these factors above to flow of air gap and distinguish which is the key effect, which is secondary in connection with corresponding predigestion on mathematical model and its boundary conditions.

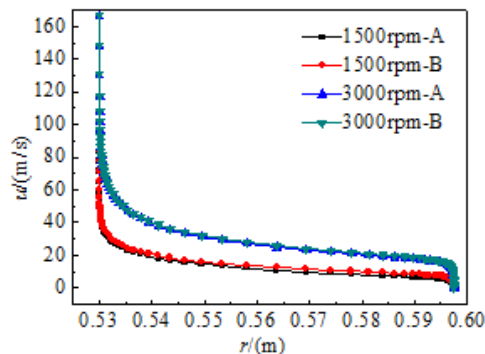


Fig. 3 The effect of convective heat transfer on velocity distribution in air gap

On the basis of turbulent equations, energy conservation equation is appended. Surface temperature of stator and rotor is set as 348K, 363K respectively. When the speed of rotor is 1500rpm, 3000rpm respectively, velocity distribution of turbulence and temperature distribution and so on is solved under the conditions above. Also, comparing the results with air velocity distribution ignore wall temperature of stator and rotor, as shown in Fig. 3 (working condition A stands for isothermal flow, working condition B stands for non isothermal flow considering convective heat transfer); in addition, temperature distribution along radial direction of air gap is shown in Fig. 4 under three working conditions.

Fig. 3 shows that velocity distribution curve is almost coincident no matter take the air convective heat transfer of the wall into account or not under the conditions of a same speed, which accounts for that convective heat transfer between stator wall and rotor wall has little effect on velocity distribution of air gap under turbulent state. The reason is that temperature difference between stator and rotor is less and gap distance is smaller, air density difference caused by temperature difference is very small in air gap, in addition, rotor speed is greater, which leads to the convective heat transfer between stator, rotor wall and air almost has no effect on velocity distribution. We can know that velocity distribution of air gap depends on rotor speed mainly.

Fig. 4 shows that rotor speed has a greater impact on velocity distribution of air gap, the overall level of turbulent extent increases in air gap (as shown in Fig. 6), convective heat transfer strengthens along with rotor speed rises, which leads to air average temperature rises of air gap. Temperature gradient of thermal boundary layer of rotor side is lower than that of stator side; air temperature gradient near the rotor decreases along with the speed rises, which in contrast to stator side.

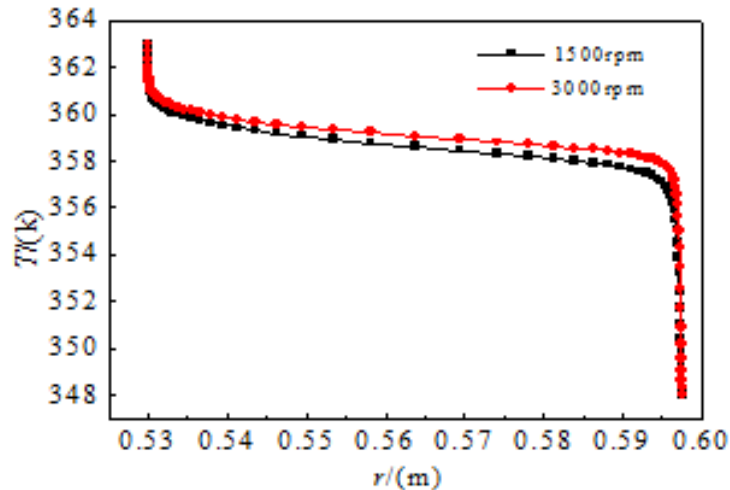


Fig. 4 The effect of rotor speed on air temperature distribution in air gap

Radiation Heat Transfer Influence All kinds of thermal calculation of generator ignored radiation heat transfer rate of wall. Radiation and convective heat transfer exist between stator wall and rotor wall objectively in annular space of air gap. Therefore, on the basis of the model above, radiation heat transfer model is appended, analyze the share that radiation heat transfer occupies is very important. Since rotor surface consists of forged steel and aluminium, which occupies 64.8% of the forged steel and aluminum occupies 35.2%, the emissivity of forged steel is 0.8 and that of aluminum is 0.2, then the emissivity of rotor surface uses weighted mean $\varepsilon_1 = 0.8 \times 64.8\% + 0.2 \times 35.2\% \approx 0.6$; stator surface consists of stalloy, $\varepsilon_2 = 0.8$. Since air is light transmission medium in air gap space. The surface of stator and rotor is diffused greybody surface; effective radiation heat transfer model among greybody surface is adopted. In order to analyze the conditions of different speed, neglect the error caused by radiation heat transfer, convective heat transfer and radiation heat transfer equations of turbulent flow is calculated respectively while rotor speed is 1500rpm, 3000rpm and stable convergent solution is obtained. The comparison of calculation results is shown in Table 1.

Table 1 The comparison of radiation heat transfer rate and convective heat transfer rate under different conditions

Speed[rpm]		1500	3000
Taking into account the radiation heat transfer and convective heat transfer	total heat transfer rate	2072.9	3177.1
	radiation heat transfer rate	269.9	269.9
	convective heat transfer rate	1803.0	2907.2
Taking into account the convective heat transfer only	convective heat transfer rate	1802.8	2907.5

Table 1 shows that total heat transfer rate and convective heat transfer rate increase while radiation heat transfer rate is constant along with rotor speed rises, which accounts for flow disturbance in air gap strengthens along with increasing speed and leads to convective heat transfer is enhanced; radiation heat transfer rate of air gap is constant under the condition of the surface temperature of stator and rotor is constant, which accounts for radiation heat transfer rate has nothing to do with rotor speed. The share of radiation heat transfer rate that occupies total heat transfer rate decreases gradually along with increasing speed, radiation heat transfer rate occupies 8.50% of total heat transfer rate when the speed is 3000rpm.

Conclusion

2D annular space model of air gap is established and the correctness of model setting and boundary conditions is validated by the basic theory of rotating flow, characteristics of each physical quantity in space is analyzed. The following conclusion is obtained on common condition:

Convective heat transfer among stator wall, rotor wall and air has little effect on air velocity distribution under turbulence state; air average temperature goes up in air gap along with increasing rotor speed; radiation heat transfer rate has nothing to do with speed, radiation heat transfer rate occupies 8.50% of total heat transfer rate approximately when the speed is 3000rpm.

Acknowledgment

Project Supported by National Natural Science Foundation of China (50976027); Natural Science Foundation of Heilongjiang Province (E200807)

References

- [1] K.S. Ball, B.Frouk and V.C. Dixit. (1989) Experimental Study of Heat Transfer in a Vertical Annulus with a Rotating inner Cylinder, *International Journal of Heat Mass Transfer* 32(8):1517-1527
- [2] N. Bolicinc. (1985) in: *The Aerodynamics and Heat Transferring in Electrical Machine*, Mechanical Industry Publications, Beijing, China 22:20-27
- [3] Youfu Ma, Yichao Yuan and Yuzheng Liu. (2008) Numerical Studies on the Ventilation Characteristics of Concave Outflow Slot Wedge Applied to Gap-pickup Rotor in Turbo-generator, *Proceedings of the CSEE* 28(20):131-136
- [4] M. Kuosa, P. Sallinen. (2004) Numerical and Experimental Modelling of Gas Flow and Heat Transfer in the Air Gap of an Electric Machine, *Journal of Thermal Science* 13(3):264-278
- [5] Hongfeng Yan. Study on the Gas-flow and Heat-transfer in the Wedge-shaped Air-gap of Horizontal Evaporation Cooling Motor, Chinese Academy of Sciences Graduate School (Institute of Electrical Engineering) (2003) ,p. 19-37
- [6] Bin Xiong, Guobiao Gu. (2008) Turbo-generator with Evaporative Cooling of Stator and Air Cooling of Rotor, *Large Electric Machine and Hydraulic Turbine* 4:14-17
- [7] F. M. White (1991)*Viscous Fluid Flow*, New York: McGraw-Hill
- [8] Fluent Inc. (2003) *FLUENT User's Guide*. Fluent Inc

Heat Storage Performance of Heating System of Phase Change Heat Storage

Sun Yong, Xu Feng, Shi Yongjiang, Ji Xiaoyang and Liu Tianliang

Hebei institute of Architectural Engineering, No. 33 Jianguo Road Zhangjiakou 075024, China
e-mail: xsunyang@126.com

Keywords: Phase Change Heat Storage, Heating System, Heat Storage Performance

Abstract: An experimental table of the heating system of phase change heat storage is built with thermal-storage tank packaging phase change material, which transferred heat with internal fluid. The flow rate, inlet temperature, outlet temperature of internal fluid and the temperature of heat storage material are measured. The influences on the properties of heat storage system are analyzed.

Introduction

From the aspect of energy conversion, the uses of solar energy have two kinds of methods including photo-thermal and photo-electric. The use of photo-thermal transportation has fully developed, especially in solving the needs in life, such as domestic hot water, heating and solar house. But there are some contradictions between the application and the law of solar radiation: when the temperature is low, the supply of solar energy is usually insufficient. So heat storage technology is a good solution to this problem.

According to the references [1-2], the phase-change thermal storage equipment is put up. Analyzing the factors, such as the temperature of internal fluid and flow rate influence on heat storage performance based on the experiment, we can get more useful information to apply to engineering.

Experimental Systems

Experimental Equipment

The experimental table is made up of phase-change thermal storage equipment, water system, data acquisition system and temperature control system. Phase-change thermal storage equipment is the key of the experimental table. Thermal storage tank is cylindrical design. The height of ladle body is 700mm. The inner radius is 560mm. There are seven isometric helix layers inside the thermal storage tank. Phase change material fills each layer, which exchanges energy with heat transfer fluid. In this structure, heat exchange area is equal and parallel coils are used to reduce flow resistance. Parallel coils also ensure temperature distribution is even and increase stability and timeliness of the absorbing and releasing of phase change material. Entrance and exit of each coil are welded in one standpipe. Inlet standpipe is located in the center of thermal storage tank. Outlet standpipe is piped in inner wall of thermal storage tank. The length of pipe of each layer, the inner radius and the outer radius are 4.5m, 11mm and 13mm. To reduce heat loss, the insulating layer is encapsulated in outer wall of tank and all out pipe. Heat transfer fluid enters each coil through standpipe and exchange energy with phase change material by coils, which finishes thermal storage process.

In the experiment, the temperature is measured by copper-constantan thermocouples. Data acquisition system is building thermal temperature and heat flux automatic test. Temperature control system is made up of transmit digital display adjuster Contactor and thermal resistance, flow rate is measured by rot meter. The arrangement of diagram of temperature measuring point is shown as Fig. 1.

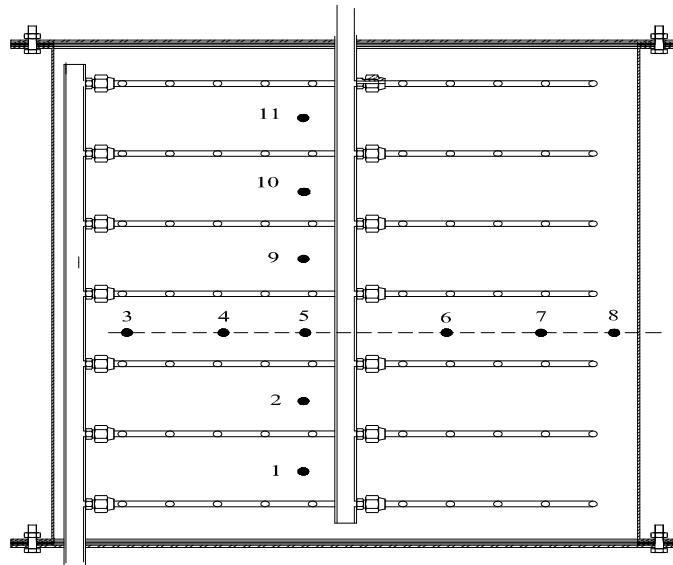


Fig. 1 The arrangement diagram for temperature measuring point

Experimental Process After the initial temperature field is built, shut the valve C, and open the valve D in the bypass of the heat accumulator. Start the temperature control system. The inlet temperature of the heat accumulator is set at 70°C on the digital display adjuster. Heat water to the experimental condition inlet temperature is 70°C.

After the inlet temperature reaches 70°C, shut the valve D in the bypass of the heat accumulator, and open the inlet valve C of the heat accumulator. Adjust valve a, make the rot meter read for 140L/h. Then the experiment began.

In experimental process, the temperature of the phase change materials and the inlet and outlet temperatures are measured by data acquisition system. When the inlet and outlet temperatures close to each other and thermocouple temperature changes on every measuring point is less than 0.2°C in the phase-change thermal storage materials, stop heating and heat storage is end. Then stop data acquisition and derive the dates by computers.

Experimental Results and Analysis

Outer temperature of internal fluid are 70°C,75°C,80°C, flow rate of internal fluid are 140L/h,200L/h 300 L/h, one new phase change material that transformation temperature is 58°C-60°C; completely experiment method is used in the experiment.

With the Change of Time, the Temperature of the Phase Change Material is Changing During the Phase Change Process When heat transfer fluid temperature is 75°C, and its flow rate is 200L/h, Fig. 2 is the temperature-time curves of measuring point 4. From the Fig. 2, the heat storage process is made up of three stages: stag of solid sensible heat storage; stage of phase change latent heat storage; stage of liquid sensible heat storage. Fig. 3 and Fig. 4 show the information that the temperature of internal radial measuring points change as time changes when heat transfer fluid temperature is 75 °C ,and its Flow Rate is 200L/h .

The temperature rise rate of different measuring points along the radius is different at the beginning of thermal storage stage. The temperature rise rates of measuring point 5 and point 13, which are near the intake standpipe, are higher than others. The temperature rise rate decreases from the central zone outwards along the radius, such as measuring point 8 and point 16.

The reason of the phenomena is that the temperature of fluid decreases along the water flow direction after the heat transfer fluid exchange energy with phase change material when heat transfer fluid enter the coil through the water standpipe. So the temperature difference of fluid and phase change material decrease along the radius, which results in different temperature rise rates along the radius at the beginning of thermal storage stage.

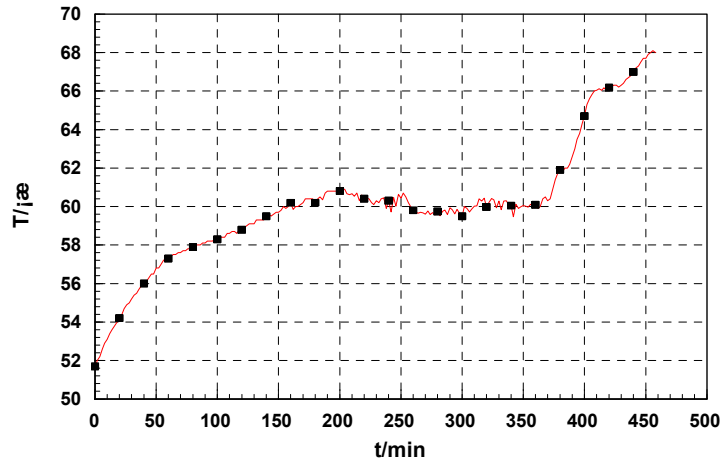


Fig. 2 The temperature-time curves of measuring point 4(75°C, 200L/h)

It can be seen from Fig.3 and Fig.4 that radial measuring points temperature of first layer are higher than the fourth layers'. The possible reason is that the install of the coil is installed parallel, Which makes the waterpower uneven and results in the flow rate of upper layer coil higher .It also could be found that the measuring points' property curves of first layer have little difference. The main reason, on one hand, is that the initial temperature filed is uneven. On the other hand, the flow rate near the entrance of upper coil is higher, which strengthens the heat transform and makes the temperature rise rate higher, so the latent heat storage stage is short.

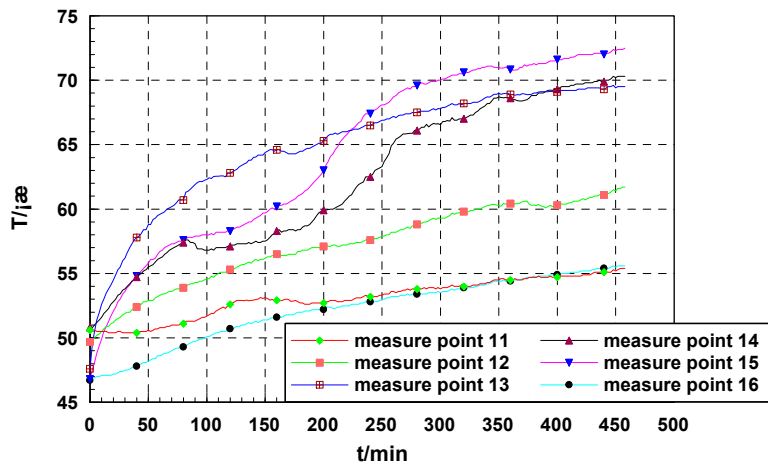


Fig. 3 First layer measuring points temperature profile (75°C,200L/h)

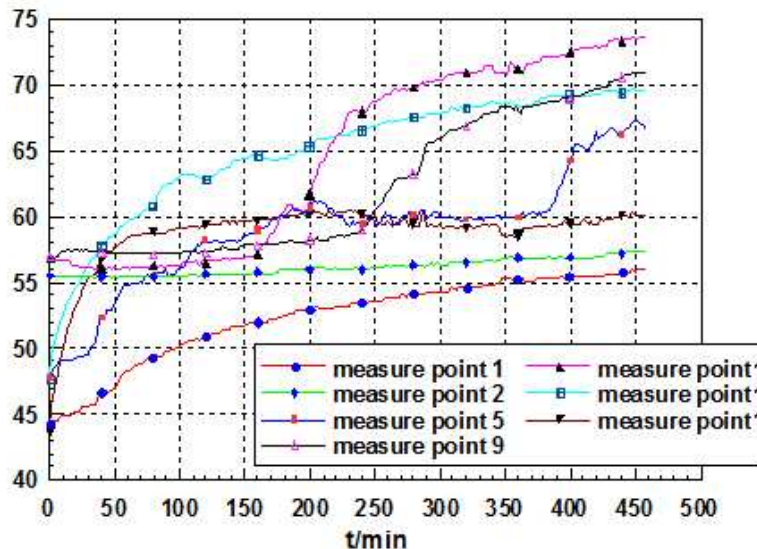


Fig. 4 Longitudinal measuring points temperature profile (75°C, 200L/h)

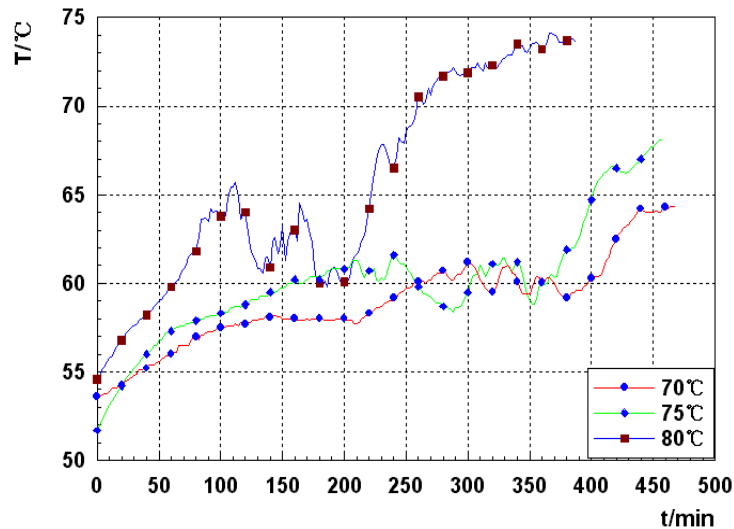


Fig. 5 Temperature-time curve of measuring point 4

Fig. 5 shows the changing conditions that the temperature of longitudinal measuring points in phase change thermal storage equipment changes with time, when the inlet temperature is 75°C and the flow is 200L/h.

That can be seen from longitudinal measuring points temperature profile that: Different longitudinal points have different law of temperature change. In thermal storage process, longitudinal temperature changing along the direction of water flow appears decreasing trend. The temperature of phase transition material corresponding to measuring points near the entrance of the flow is relatively high. These points firstly perform phase change process, while the temperature of measuring point 1 and point 2 in bottom layer changes slowly. This is because ‘thermal media’ enters from upper layer and exits from bottom, the upper material’s temperature increases fast. The time of phase change thermal storage corresponding to each measuring points is close. But the finishing time of thermal storage process of upper material is shorter.

Due to measuring point 1 and 17 are located in avise of thermal storage tank, the effect of thermal exchange is inferior to central field, the phase transition material’ temperatures are relatively low .So the time of thermal storage is relatively long.

The Influence of Heat Transfer Fluid Inlet Temperature Has on Heat Storage Process Fig. 5 is based on that when the flow of heat transfer fluid is 200L/h, inlet temperature are 70°C,75°C,80°C, the temperature of typical measuring points of phase transition material in phase change thermal storage equipment ,its temperature changes with time. This image shows that when the flow of heat transfer fluid doesn't change ,the influence of changing heat transfer fluid inlet temperature has on each measuring point's temperature in heat accumulator .When the flow is 200L/h, the changing law of each measuring point's temperature is similar .We can see from the graph that:

Take measuring point 7 as an example, as the inlet temperature rises, the changing speed of measuring point's temperature with time is increasing. The speed of temperature rising is faster. The process of sensible thermal storage was finished in short time 50 minutes after thermal storage began, heat transfer fluid, which inlet temperature is 80°C, phase change material has basically entered phase transition latent heat stage .While heat transfer fluid is 70°C, phase change material is still in the stage of solid sensible heat thermal storage. This is because that the higher the inlet temperature of heat transfer fluid is, the effect of enhancement of each heat transfer unit is more apparent. Especially in later melting stage, as inlet temperature increases higher and higher, the temperature difference is bigger and bigger, the easier and easier melting process is promoted. All those contribute to difference among thermal storage process.

Because Coils are isometric helix type, the distance between the outermost layer and Thermal Storage tank cylinder shell is uneven ,besides measuring point 16 was arranged in where outer coils is far from cylinder shell .In this point, phase transition material and heat transfer fluid couldn't

perform sufficient heat exchange. So the deviation between temperature distribution curve of this measuring point and phase change thermal storage characteristic curve is large. The temperature of measuring point is low.

Conclusions

The heat storage performance of heating system of phase change heat storage is researched by building the experimental table of phase change thermal storage equipment. The rule of heat storage is mastered. The research provided reference basis for engineering application of phase change thermal storage equipment.

Acknowledgments

This work is partially supported by Science and technology plan projects of education department of hebei province of China (2009430)

References

- [1] S. Ahmet, K. Kamil. (2002) Thermal performance of a eutectic of lauric and stearic acids as PCM encapsulated in the annulus of two concentric pipes [J] .Solar Energy, 32:493-504
- [2] N. Nallusamy, S. Sampath, R. Velraj. (2007) Experimental investigation on a combined sensible and heat latent storage system integrated with constant/varying heat sources [J] .Renewable Energy 32:1206-1227
- [3] N. R. Vyshak, G.Jilani. (2007) Numerical analysis of latent heat thermal energy storage system [J] .Energy Conversion and Management 48(7):2161-2168

Analysis of the Multi - tooth Meshing Effect of Three- ring Gear Reducer

Yuan Li¹ and Chen Zhu²

¹School of Mechanical Engineering and Automation, University of Science and Technology, Liaoning, Anshan, Liaoning 114051, China

²The Ministry of Science and Technology, Liaoning, Anshan Liaoning 114051, China

E-mail: 33003761@qq.com, herr_morgen@163.com

Keywords: Three- Ring Gear Reducer, Multi- Tooth Meshing Effect, Finite Element Method

Abstract. Three-ring reducer is a type of epicyclic gear drive with small tooth number difference and internal gear. It is different from other gear transmission, that the load shearing factor of multi tooth contact is much smaller. On the basis of analyses of geometry, tooth deformation and manufacturing errors, a mathematical model which describes the state of multi tooth contact and the load distribution characteristics of tooth was developed. The multi- tooth meshing effect of the three- ring gear reducer is studied used the finite element method and ANSYS finite element software. While three- ring gear reducer is running, the number of teeth contacted simultaneously, their load distribution characteristics and the von Mises stress change are gained.

Introduction

Based on the synthetic analyses of technical development trend of Planet gear transmission reducers with parallel axis, three-ring type gear reducer is developed to adapt the development needs of mechanical engineering. It works in principle of the involutes planetary gear drive with small teeth difference, belongs to K-H type planetary gear drive with small teeth difference. The input power through the power split "approach, with three-phase parallel double crank mechanism as input mechanism, comprises three identical drive ring plate output. The main form of transmission has a series of advantages comparing with the various existing forms, such as large transmission ratio, high loading capacity, compact volume etc. As three-ring type gear reducer belongs to planetary gear drive with small tooth number difference, elastic deformation of teeth will fill the original room gap in the load, cause the phenomenon of multi-tooth engaging in the same time, that is the multi-tooth meshing effect. This makes the bearing capacity of three-ring gear reducer gear is greatly improved. However, at present, various reducer manufacturers in the design stage have not been considered in this effect so that the bearing capacity of the gear reducer which they published in its product design table is far below the actual carrying capacity, resulting in waste. Therefore, grasp the actual bearing capacity of three-ring gear reducer, obtain bearing gear load distribution relation becomes very important. In this paper, analysis of is carried out through the finite element method by ANSYS software. Explore the reason of high loading capacity of three-ring gear reducer in theory.

Establishing the Finite Element Model of Gear Pair Establishing a precise finite element model is the foundation to carry out the analysis of the multi-tooth meshing effect of three-ring gear reducer, it plays a very important role to improve the computational efficiency and ensure the accuracy of analysis. It is so difficult establish precise gear tooth profile that using CAXA electronic board to achieve it, saved as IGES format, then imported into ANSYS, as is shown in Fig. 1. Next, selecting the unit and meshing. In this paper using uses Solid45, 3D contact elements CONTACT174 and TARGET170. In order to ensure the partition unit can not only satisfy the calculation accuracy, and does not affect the computation time, meshing fine and dense in the local stress concentration areas, and meshing rough in other areas. Therefore, the contacting surface and the gear tooth root fillet where the transition to the precise grid of points are meshed accurately, as is shown in Fig. 2.

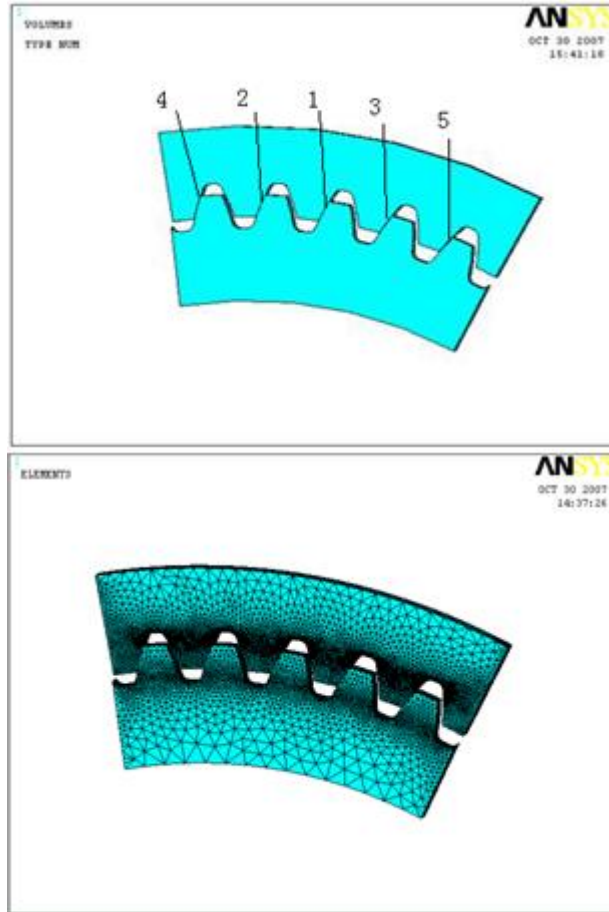


Fig. 1 Finite element model of gear pair

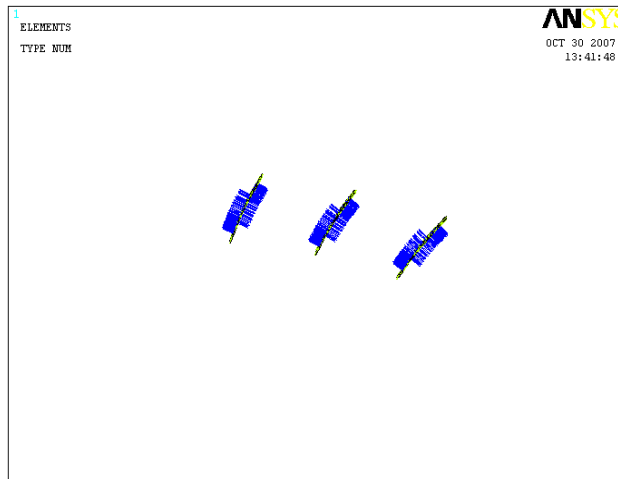


Fig. 2 Grid division of gear pair

Creating the Contacting Pairs of Gear Pair For most contacting problems, contacting wizard provides a simple method of tectonic contacting that will guide to establish contacts Define the target surface and the contact surface, set the real constant, and then the contacting pairs of gear pair are established, as is shown in Fig. 3.

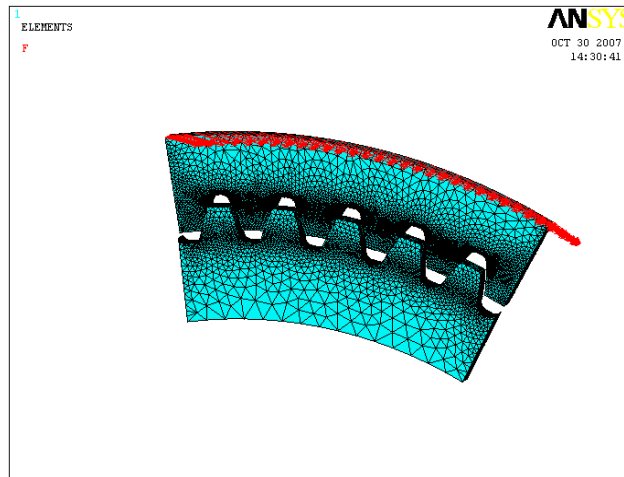


Fig. 3 The contacting pairs of gear pair

Impose Constraints and Loading. When three- ring gear reducer is operating, the internal gear as the driving wheel, and the external gear to the driven wheel. As the equivalence of relative motion, plus fixed constraints on the external gear and constraints which can rotate around axis on the internal gear. Apply force on the body edge of the inner gear, simulating the gear transmission torque, as the entity unit Solid45 is moved along the three axes of freedom, without rotational degrees of freedom, and the default node coordinates and Cartesian coordinates parallel. In order to apply tangential force, all nodes coordinate system of the inner gear are converted to overall cylindrical coordinate system, it makes the node coordinates X axis is parallel with polar coordinates X axis (radial) and the node coordinates Y axis is parallel with polar coordinates Y axis, and then load in the ANSYS loader. The force exerted is decided by $F_y = \frac{M}{r.num}$, in formula, M is torque of the internal gear, r is the maximum outer circle of internal gear plate, and num is the total number of nodes of the outer ring, as is shown in Fig. 4.

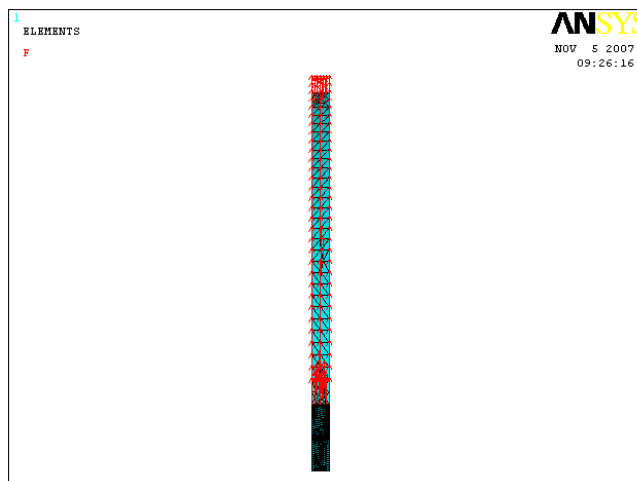


Fig. 4 Loading of gear pair

Examples of Calculation Reference of the gear used in this paper : external gear teeth $z_1=51$, internal gear teeth $z_2=52$; $m=6$; $\alpha = 20^\circ$; $h_a^* = 0.7$; $c=0.3$; $x_1=-0.121$; $x_2=0.3399$, both of the gears use 45 steel quenched and tempered. Input torque and the theoretical engagement position are two main factors on the multi- tooth meshing effect for the analysis. While three- ring gear reducer is running, the number of teeth contacted simultaneously, their load distribution characteristics and the von Mises stress change are gained

Analysis of Results Graphic display of results is an intuitive and effective way for results show, to inspect all kinds of data strictly, or interested in the results of some local in the graphical display, viewing the solving numerical results through data list. The gear stress cloud chart is as shown in Fig. 5. Through it we can see that the maximum contact stress appeared on the tooth surface of the external gear, is 242.365MPa which is far less than the allowable contact stress. We can obtain the actual contacting tooth and load distribution of three- ring gear reducer, as is shown in Fig. 6. We can see that there are three teeth bearing the load. The first teeth bears load maximum, and the second and the third teeth bears decreasing.

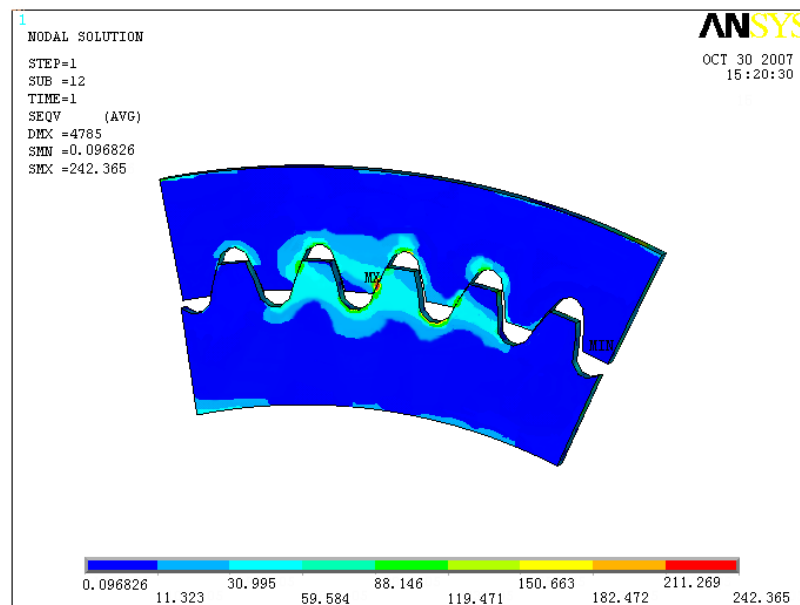


Fig. 5 Stress cloud chart of gear pair

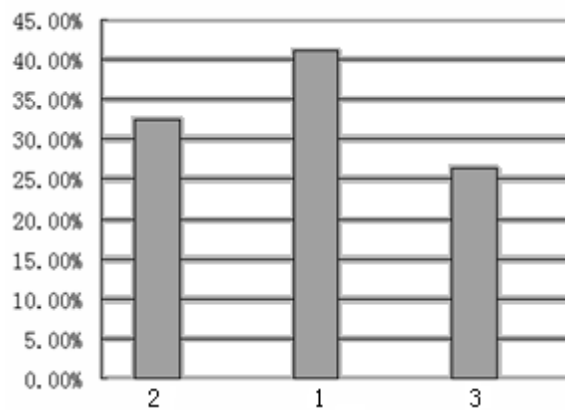


Fig. 6 Load distribution

Conclusions

On the basis of multi- tooth meshing effect of three-ring gear reducer in actual situation, established the finite element model of gear pair, and then the constraint conditions, the applied load and the calculation methods are analyzed. Through the analysis obtained the largest Von Mises stress of three-ring gear reducer. Meanwhile, obtained the actual load tooth number and load distribution of three-ring gear reducer through the analysis, and elaborated the high bearing capacity of three-ring gear reducer.

References

- [1] Chen Jianchao, Chen Shuxun, Huang Yongqiang (2003). Kinematics and dynamics analysis of the three-ring reducer. *Mechanical transmission*, 231:123-128.
- [2] Liu Weiqiang, Zhang Qixian (1995). Load balanced research of SH three-ring reducer. *Chinese Journal of Mechanical Engineering*. 31:229-236.
- [3] Liang Yongsheng, Li Huamin, Xin Shaojie (2000). Load balanced mechanism and its dynamics analysis of three- ring gear reducer. *Mechanical design*. 298:172-179.
- [4] Wu Nanxing, Sun Qinghong (2002). Research on dynamic simulation technology of mechanical system. *Manufacturing automation*.102:245-251.
- [5] Zhu Caizhao, Qin Datong, Li Runfang, Song Shengde (2000). Contacting teeth and load distribution of three-ring reducer. *Journal of agricultural machinery*.231:423-439.
- [6] Ying Guangchi (2004). Research on elastic meshing effect of three-ring reducer. [Master degree thesis], Tianjin: Tianjin University.422:235-242.
- [7] Shu X L (1995). Determination of Load Sharing Factor for Planetary Gearing with Small Tooth Number Difference. *Mechanism and Machine Theory*. 301:21-28.

Demodulation Method of Distributed Fiber Bragg Grating Sensor Based on Whispering Gallery Mode Optical Microcavities

Zheng Fang^{1,a}, Weicen Wu^{2,b}, Baojin Peng^{3,c}, Fei Xu, Jianchengwu Zhu, Ke Xu, Lu Wang, Gengzhu Wu^{4,d}

Zhejiang Normal University, Institute of Information Optics Jinhua 321004

Keywords: Demodulation; Optical Microcavities; Whispering Gallery Modes; Plastic Optical Fiber; FBG

Abstract. A new system on demodulation of distributed fiber Bragg grating (FBG) sensor is built which is based on Whispering Gallery Modes Optical Microcavities. In order to eliminate the temperature effect on strain measurement two adjacent FBGs (one for sensing, the other for reference) with similar central wavelength and different lengths as a probe by parallel connection are utilized. Studies have shown that the Whispering Gallery Mode Optical Microcavities with special properties of selecting specific light, when the light couple into the cavity and shocking back and forth, only the specific light can couple out, it can be expressed as: $2\pi rn = k\lambda$, where r is the cavity radius, n is the refractive index of the cavity, λ is the wavelength of the light coupled out, k is taken a positive integer. Using the feature of Whispering Gallery Modes Optical Microcavities to demodulate the spectral signal of the sensing probe, Combined with the light detector, signal amplifiers, computers and other devices to display the detected strain in real time. Experiment result shows that it is feasible to demodulate action spectrum and the cross of FBG for temperature and the strain is solved. It is testified that the initial establishment of the laboratory system is stable, reliable, and less expensive.

Introduction

Currently, Optical fiber sensing technology is a hotspot for the research home and abroad. There are many critical related researches and prospects for application in many fields, especially in large-scale construction, the design process of aerospace vehicle and a safe state health monitoring. Especially the distributed fiber optic sensors are paid close attention in the field of large-scale structural monitoring [1, 2]. With the continuous improvement of the fiber Bragg grating (FiberBraggGrating FBG)'s manufacturing skills, especially in the establishment of the FBG automated production platform, to produce high-performance, low-cost FBG has become possible. However, there are still many deficiencies in distributed fiber Bragg grating (FBG) sensor signal technologies and devices, such as Complex operations, the not-superior performance, high cost. That mentioned above seriously affected the in-depth study of the optical fiber sensing technology and extensive use.

Whispering Gallery Mode Optical Microcavities [4, 5] is a new type of cavity structure. Its special nature in the different conditions makes it under the spotlight in the recent years, thus leading to the heated study. It is mainly obtained by the laser hitting fiber. When an optical fiber gets close to the cavity of a specific radius and combine with it, the light waves will shock propagation back and forth in the body cavity. Studies show that only the light of specific wavelengths and the cavity function after a finite number, the relationship between the two is expressed as: $2\pi rn = k\lambda$, r is the radius of the Whispering Gallery Microcavity, n the refractive index of the cavity, λ the wavelength of light coupled out and k a positive integer. So we can change the radius of the micro-cavity to filter out specific wavelengths, following which we can achieve a distributed FBG demodulation.

This article takes full advantage of the light waves of the Whispering Gallery Mode Optical Microcavities to select features. Combined with the hydraulic equipment, the light detector, signal amplifier, computer, we design a novel demodulation device for distributed fiber Bragg grating. The device has advantages of high stability, simple operation, relatively low cost.

Analysis of Experimental Setup and Principle

The experiment setup is shown in Fig. 1. The light emitted by the wide spectrum of light after passing a 3dB coupler receive the distributed fiber Bragg grating. The measured temperature or pressure is applied on a fiber Bragg grating. Then a specific wavelength of light waves reflected by each grating goes into the Whispering Gallery Mode Optical Microcavities by the coupler. Based on the optical properties of whispering gallery mode optical microcavities which is combined with the controller, the computer implements distributed FBG demodulation. And it is photoelectric converted by the light detector. After amplification by the amplifier circuit the voltage signal, we sent it to a computer for analysis, storage, and it will show the size of the measurement on the computer according to the user's requirement. Immediately it will issue a warning signal when the measured variables pass the warning line. And make timely adjustments by analyzing.

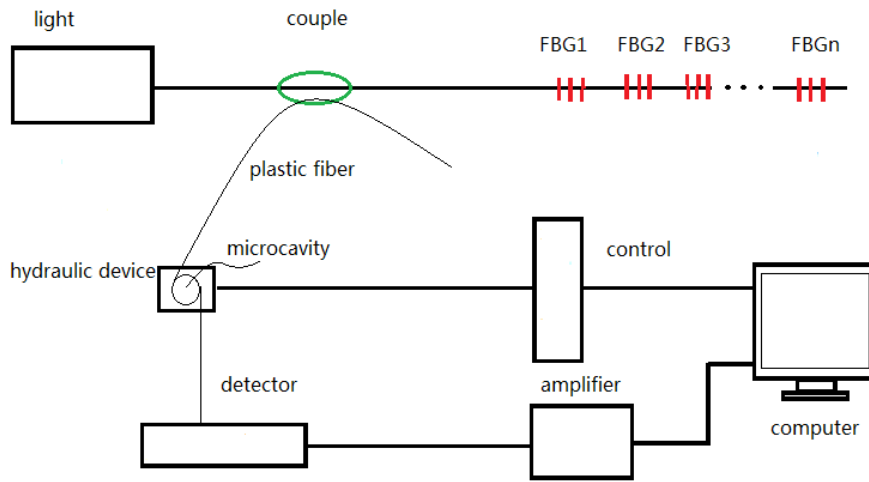


Fig. 1 Schematic of experimental setup

Using Double FBG Sensing Probe to Eliminate the Temperature Effect In order to eliminate the temperature effect on strain measurement two adjacent FBGs with similar central wavelength and different lengths as a probe by parallel connection are utilized. FBG2 which is pasted in the object to be measured (such as bridge) is used for sensing, and it is insensitive to temperature and strain. FBG1 whose both ends are fixed on glass tube is used for reference, and it is only insensitive to temperature. Optical fiber and glass tubes have the same thermal expansion coefficient, so FBG1 and FBG2 temperature sensitive coefficient are same. The central wavelength drift caused by temperature changes cancel each other out, thus it can eliminate the influence of temperature on the strain measurement effectively. Therefore, when sensing probe are unaffected by strain, the side-play mount of two FBG center wavelengths are same, producing only one reflection signal. When sensing probe is affected by strain, the side-play mount of two FBG center wavelengths are different, producing two reflection signals. Because of the difference of two FBGs' lengths, reflectivity is different. Namely the peak intensity of two signals are different, and the peak of FBG1 reflected signal is greater than the peak of FBG2 reflected signal. The side-play mount of two FBG center wavelengths are shown that

$$\Delta\lambda_1 = K_2\Delta T,$$

$$\Delta\lambda_2 = K_2\Delta T + K_1\varepsilon, \quad (1)$$

There, K_1 is the strain sensitivity of FBG2, K_2 is the temperature sensitivity of double FBG, ΔT is the change of temperature, ε is axial strain. Obviously, the difference of two grating reflection wavelength is the linear function of FBG2 strain,

$$\Delta\lambda = \Delta\lambda_2 - \Delta\lambda_1 = B\varepsilon, \quad (2)$$

There, B is the linear factor. [6]

Center wavelength of distributed sensing probe drift will not appear cross phenomenon when external strain occurs, that is, each sensor spectrum is independent. Computer controls the size of cavity radius periodically by connecting hydraulic devices, while computer could real-time detect and display each sensor's center wavelength so that its drift under external strain could be real-time computed. The external strain should be determined according to eq.2, and then realizing the real-time control.

Demodulator In order to determine the wavelength shift amount $\Delta\lambda$ and then measured strain, where using the whispering gallery mode optical microcavities, the controller and computer to demodulate the Distributed FBG.

Whispering Gallery Mode Optical Microcavities

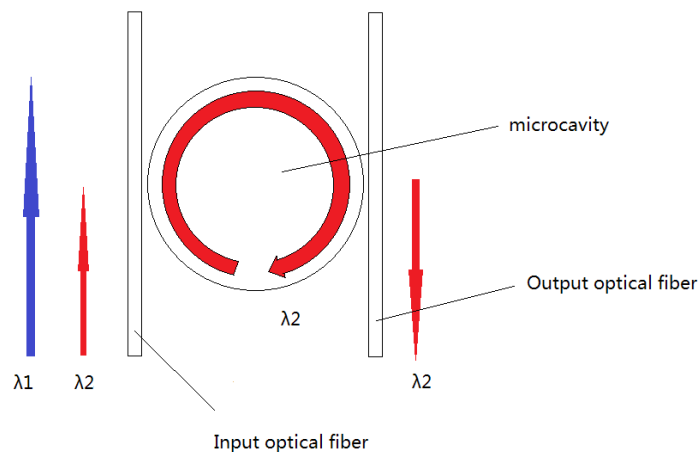


Fig. 2 Schematic of WGMs Optical microcavity

Whispering Gallery Mode Optical Microcavities is a new type of cavity structure. Its special nature in the different conditions makes it under the spotlight in the recent years, thus leading to the heated study. It is mainly obtained by the laser hitting fiber. When an optical fiber gets close to the cavity of a specific radius and combines with it, the light will shock propagation back and forth in the body cavity. Studies show that only the light of specific wavelengths and the cavity function after a finite number, the relationship between the two is expressed as: $2\pi rn = k\lambda$, r is the radius of the whispering gallery microcavity, n the refractive index of the cavity, λ the wavelength of light coupled out and k a positive integer. Show in Fig. 2. So we can change the radius of the micro-cavity to filter out specific wavelengths, in order to achieve the demodulation of the distributed FBG. We use plastic optical access to the micro-cavity consider that we need to change the radius of the microcavity in the experiment, the good toughness of the plastic optical fiber to meet the experimental requirements.

Before coupling experiments we have through the method of melting to go in addition to the cladding part of the plastic optical fiber, as shown in the Fig. is the heart of the fiber. To Using the Stepper motor to change the distance between the heart of the fibers and microcavity to couple slowly.

Controller and computer system Controller is mainly used to control the size of microcavity radius. Due to the WGMs microcavity's radius which meets specifications is very small, and it has a high accuracy standard and high-tech requirement to achieve retractility control, using high accuracy hydraulic system can meet the experimental needs. The function of accuracy hydraulic is to change the applied force by controlling the system's pressure. In the experiment, in order to control the size of microcavity that is placed in accuracy hydraulic system, it should periodically change the pressure of accuracy hydraulic system which is connected with computer that causes cyclical change of microcavity radius.

Data acquisition Distributed FBG reflector in Fig. 1 by the optical signal back out through the whispering gallery modes optical microcavities demodulation by the photocell changes in light intensity changes in current or voltage, then the amplifier circuit to 0-5V changes voltage sent to the PC A / D card for data acquisition, real-time analysis of process data and display the test of the dependent variable. This A / D card 10 cards with 16 channels. Write the corresponding channel in the channel optional; to 210H to 212H to write an 8-bit digital to start A / D converter; When 210H lowest bit D0 is 0:00, the conversion is complete; acquisition results from the 212H (put 8) and 213H (lower 2) read out. The device shown in Fig. 1, collected by computer automatic control signal generator, optical switching and amplification circuit output signal simultaneously and with accurate report of the brightest probe strain. VB and VC are to write the entire software.

Experiment Result

Considering that it is essential to change the size of microcavities, we use a variety of plastic optical fiber in the experiment, (diameter is 0.25mm, 0.5mm, 0.75mm, 1.0mm, etc.). Plastic optical fiber has lower melting point and plasticity strong, which is in line with the experimental requirements. In order to acquire regular microcavities sphere, we try a variety of ways, such as direct combustion of the plastic optical fiber, lens aggregation melt optical fiber. The microcavities structure we acquired are not the same and the dimensions are large. It does not accord with the experimental requirement. Our project team use high power, high precision carbon dioxide lasers, the microcavities played by carbon dioxide laser platform are smaller in terms of dimension. It is about 100 microns. By repeated use of laser hitting all kinds of optical fibers, we can sift out regular microcavities. We can observe and analyze the microcavities through laser platform's CCD port connecting with computer and with software. Carbon dioxide laser platform is shown in Fig. 3.

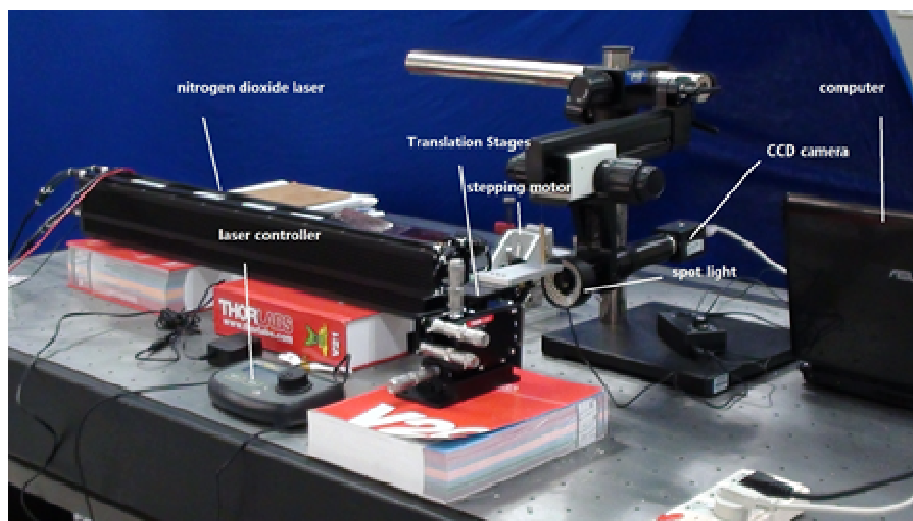


Fig. 3 Laser platform

The characteristic of current got microcavities is not ideal due to the technical restrictions and hardware device in the laboratory. The demodulation device that we attempted to build has a obvious test result. But according to the research on the whispering gallery mode optical microcavities from abroad, it is possible to obtain microcavities with theoretical characteristics. We had simulation about the characteristics of microcavities and demodulation experiment using some software, the simulation results show that when the radius of microcavities is between 40-60 microns, the characteristics can fully shown and close to the theoretical Fig. and it is possible to use the computer-controlled distributed FBG demodulation method.

Conclusion

The preliminary experimental results and computer simulation show that it is possible to use the method of whispering gallery mode optical microcavities for distributed fiber Bragg grating demodulation. We are able to solve the problem of temperature and strain cross-sensitivity. However, due to the hardware and technical restrictions, we don't fully establish the set of demodulation system based on whispering gallery mode optical microcavities. We have some technical problems in some critical step. For example, what ways can we adopt to obtain smaller and regular microcavities, how to precisely control the radius of microcavities. We are working hard to find the solution. But simulation using some software shows that it is possible to use the whispering gallery mode optical microcavities demodulation method. Although we have hardware and technical problems, but it provides a new thinking mode for realizing distributed FBG demodulation. We are fully convinced that it is not difficult for us to develop a complete demodulation system if we continue to try and experiment using this method.

References

- [1] SUN Ru-jiao, SUN Li-ming, SUN Zhi. Application of FBG sensing technologies to large bridge structural health monitoring[J]. Journal of Tongji University(Natural Science), 2008, 36(2): 149–154. (in Chinese)
- [2] WANG Yan-ling, YUE Qian-jin, ZHU Xiao-huan, et al. Subsidence monitoring of jacket oil platforms[J]. The Ocean Engineering, 2010, 28(4): 122–126. (in Chinese)
- [3] FENG Chun, LI Shi-hai, LIU Tian-ping. Experimental study on burying technology of fiber grating sensor system in driven pile[J]. Transducer and Microsystem Technologies, 2009, 28(9): 12–15. (in Chinese)
- [4] DONG Yu-feng, WANG Yu-ling, WU Chun-mei. Experimental study of FBG sensors to reinforced concrete structural health monitoring[J]. Journal of Daqing Normal University, 2010, 30(6): 75–77. (in Chinese)
- [5] B. Min, E. Ostby, V. Sorger, E. Ulin-Avila, L. Yang, X. Zhang, and K. Vahala, "High-Q surface-plasmon-polariton whispering-gallery microcavity," *Nature* 457, 455-459 (2009).
- [6] Zhu G P, Xu C X, et al. [J]. *Appl. Phys. Lett.* 2009.94.051106

Experimental Study on Anti-fatigue Damage Structural Design of Diesel Engine Bearings

Zhenjie Guo

Zibo Vocational Institute, Zibo, Shandong 255013 China

Keywords: Diesel Engine Bearings; Fatigue Damage; Improvement Measures; Experimental Study

Abstract. With higher requirements on energy-saving and environmental protection of diesel engine in the modern times, the loads on main bearing and connecting rod bearing of diesel engine are continuously increased, and also working conditions are even more critical. Bearings are the key moving parts of diesel engine, and play an important influence on reliability, service life and other performances of diesel engine. Therefore, the reasons for fatigue damages to its bearings greatly affect fatigue life. In traditional designs, effects of the problem are studied few. In this paper, therefore, this problem is studied for discussing the formation reasons and solutions for it theoretically.

Introduction

In recent years, with higher requirements on specific power and economical efficiency designs of modern diesel engines, the loads on main bearing and connecting rod bearing of diesel engine are continuously increased, and also working conditions are even more critical. Bearings are the key moving parts of diesel engine, and play an important influence on reliability, service life and other performances of diesel engine. Therefore, requirements on diesel engine bearing lubrication design are more and more important.

Diesel engine bearings are structured with three layers usually^[1], including a layer of steel back, a layer of copper alloy sintered or casted on steel back, and a layer of lead-based surface coating (15 to 25 μm thick). Because specific powers of modern diesel engines are high, fatigue damage frequently appeared in bearing surface coating layer. Therefore, to enable bearings to work under high specific power, people are studying that bearings are composed by copper alloy layer sintered or casted on steel back and several surface coating layers as follows: (1) thinner lead-based coating; (2) coating (3-7 μm thick) containing solid lubricant; (3) aluminum-tin alloy coating formed with PVD (Physical vapor deposition) process.

Experiment showed that multi-coating had a tie with bearing capacity; if load was increased to a certain degree, fatigue damage of surface multi-coating appeared generally; thinner multi-coating possesses higher anti-fatigue capability: when the thickness of these parts has decreased, but embedded performance and wear-life are sacrificed, and also bearings became more sensitive to cylinder degree, shaft finish, and form and position deviation between shaft and hole.

In this paper, the reasons for the fatigue damage of diesel engine bearings of a local factory are studied, the factors affecting fatigue damage of diesel engine bearings are analyzed, the formation reasons and solutions for the fatigue damage are discussed, and finally measures improving fatigue damage of bearings are proposed.

Theoretical Analysis

Contact between bearing and shaft can be regarded as the line contact of two cylinders as shown in fig 1 below, and is actually long and narrow rectangle contact, and lubricating fluid can be approximately one dimensional flow. According to theoretical analysis and experimental results, its lubricating state should comply with the Dawson-and Hutchinson (D-H) elastic hydrodynamic lubrication theory, and its computation formula is [2]

$$h_{\min} = 2.65\alpha^{0.54}(\eta_0 u)^{0.7} E^{-0.03} R^{0.43} W^{-0.13} \quad (2)$$

Meanings of all parameters in above equation are as follows.

α — Pressure viscosity

η_0 — Dynamic viscosity, Pa •S

u — Mean velocity of contact point (entrainment velocity), m/s

E — Comprehensive elastic modulus of two surfaces, N/m²

R — Synthetic curvature radius, mm

W — Loading of unit length, N/mm

Lubrication conditions of contact surface can be judged with following equation.

$$\lambda = \frac{h_{\min}}{\sqrt{\sigma_1^2 + \sigma_2^2}} \geq [\lambda] \quad (3)$$

In above, h_{\min} is the oil-film thickness; $[\lambda]$ is allowable film thickness ratio; σ_1 and σ_2 are root mean square deviations of two surfaces' roughness, respectively.

It is in boundary lubrication state if $\lambda < 1$. Boundary oil film is a very thin layer of adsorbed oil film or chemical reaction film, and cannot partition the asperities of two friction surfaces. The strength of boundary oil film can be improved and bearing life can be longer if oiliness additives or extreme pressure additives are added into lubricants.

It is in a partially elastohydro dynamic lubrication state if $\lambda = 1 \sim 3$. If $\lambda = 1 \sim 1.2$, the oil film continuous rate is under 50% and can still produce surface scratches and wear, and the bearing fatigue life will be lower than the calculated basic rated life generally. If $\lambda = 1.2 \sim 3$, the oil film continuous rate will increase and transition to complete oil film. Only slight wear is generated on contact surface, and the bearing fatigue life will reach or exceed the calculated basic rated life generally.

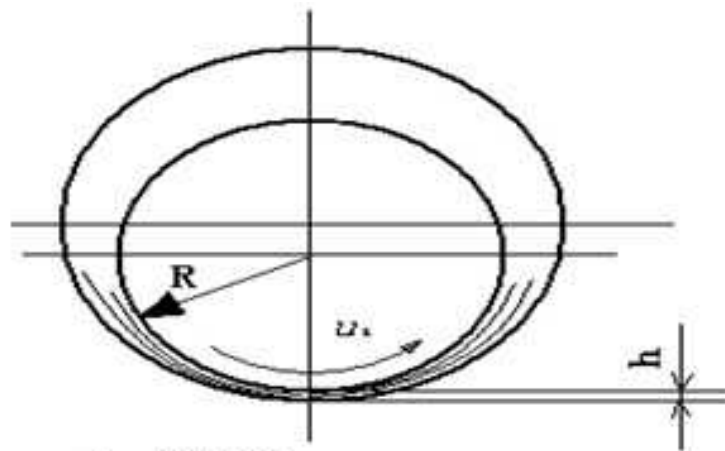


Fig. 1 Lubricating Model

It is in a complete elastohydro dynamic lubrication state if $\lambda \geq 3$. In most cases, wear is negligible, and the bearing fatigue life is at least as three times as the calculated basic rated life^[3].

Analysis of Main Reason for Bearing Fatigue Damage and Experimental Research

In addition to external factors such as poor lubrication conditions of bearing, main reason for the fatigue damage at the alloy layer of bearing is load exceeds the fatigue limit of material, and this is called as overload^[3]. The method used for evaluating if bearing is overload is its specific pressure, namely using the value of bearing maximum load/projected bearing area as basis. Assume that all given bearing variables are the same, and then the load of each bearing decides its fatigue life^[4]. However, researches show that main factor affecting the fatigue life of diesel engine bearings is peak pressure of oil films of the lubricant oil between bearings and shafts.

Peak pressure of oil films is that a layer of lubricant oil film is formed in the lubricant oil between bearings and shafts and can reach the highest pressure value under the action of load.

There are many factors affecting the peak pressure of oil films of lubricant oil. For example, oil viscosity, bearing length and diameter, gap, shaft rotate speed, load and direction, and ratio between rotate speed and load change can affect the peak pressure of carrying oil film. The relationship between peak pressure of oil film and bearing fatigue damage is very conspicuous.

In general, diesel engine is certain in power, and so is its bearing load, but load parameters are unchanged. The size of diameter is determined by the strength and life of crankshaft journal.

In the early design, designers are free to select the lengths of diesel engine bearings, but the selection of the best bearing lengths will often be affected if space is considered. Fig 2 shows that the peak oil film of the connecting rod bearing of a diesel engine working in full load conditions is affected by the length of bearing. Curve is nonlinear, and there is an inverse relationship between peak oil film pressure and bearing length.

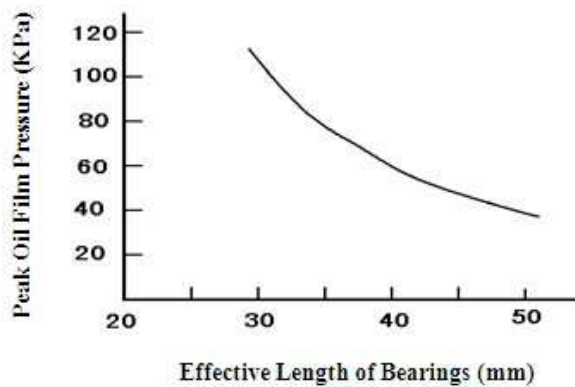


Fig. 2 Relationship between bearings and peak oil film pressure

Peak oil film pressure can also be affected by oil viscosity and temperature of bearings. Through experiment, it can be known peak pressure of oil film changes with the change of the parameters: peak pressure of oil film rises by 7.4% if commonly-used SAE30 is replaced with SAE20, but drops by 5.2% if SAE40 is used. Therefore, it can be seen there is a proportional relationship between the change of peak oil film pressure and the engine oil temperature. Thus, in general conditions, the life of bearings reaching critical fatigue is affected by multiple factors such as oil viscosity, grades and temperature, fuel oil dilution effect, and cooling fluid pollution. No matter high oil viscosity is obtained with thickened or low temperature, the fatigue life of bearings can be promoted to be longer because peak oil film pressure is lower.

Table 1 shows the relationship connecting rod bearing clearance and oil-film peak pressure mentioned above. From table 1, it can be seen that peak oil film pressure changes by 10 ~ 15% if the clearance has a change of 0.01mm. Because peak oil film pressure is affected greatly by the clearance, clearance control is an important index when methods of improving fatigue life of bearings are being considered.

Table 1 The relationship connecting rod bearing clearance and oil-film peak pressure

Oil-film peak Pressure (KPa)	Bearing Clearance (mm)
53	0.048
54.6	0.05
58.5	0.056
62.7	0.06
67	0.066
68.3	0.07

From the above experiment, it can be known that the peak oil film pressure always increases along with the enlargement of the clearance. Therefore, the peak oil film pressure can be decreased with the method of lowering the clearance. However, bearing temperature will increase if the clearance is too small, but may be adversely affected if the clearance exceeds secured value. For this reason, appropriate clearance control has changed into a key indicator.

The method of lowering the clearance refers to reducing the manufacturing tolerances of hole, bearing wall and shaft. Thus, the clearance range is narrower, but the smaller tolerances, the higher the manufacturing costs. Considering cost, the tolerances of shaft or hole are not allowable to be too small according to mechanical processing capacity and large production requirement.

Internal combustion engine bearings can be divided into “load bearing” and “non-load bearing”. “Load bearing” refers to the bearings carrying the maximum force usually caused by gas pressure; “non-load bearing” only carries small inertial force. The biggest oil film pressure and the smallest oil film thickness appear in “load bearing”. For connecting rod bearing, upper bearing is carried; for main bearing, lower bearing is carried.

Therefore, for a pair of bearings installed on shaft, only one of them carries peak oil film pressure. If the radius of such a bearing is reduced to a proper δ value, a same value (i.e. δ) will be added in the inner-hole radius of another bearing, so as to keep the total diameter clearance consistent with the original. In this way, lubrication can be ensured, and also the role of peak pressure of oil film can be reduced, unnecessary to excessively improve machining accuracy.

To prove the correctness of oil films with unequal wall thickness to carry oil film pressure, the bearings were tested at bearing fatigue test bench.

Alloy bearing (Cu-Sn-Ni-Pb) were selected, δ was 0.01 mm. A 6-cylinder turbocharged diesel engine was used as test bench.

Experimental result shows the peak oil film pressure of bearing was greatly reduced to the theoretical value 9.49 Mpa in different operating conditions; fatigue cracks throughout the entire width appeared in 3 bearings with the same wall thickness, but not in bearings with unequal wall thickness.

Table 2 Experimental result of bearings

Item	Material	Wear Pattern
Bearing 1 with the same wall thickness	Cu-Sn-Ni-Pb/steel	Fatigue Cracks
Bearing 2 with the same wall thickness	Cu-Sn-Ni-Pb/steel	Fatigue Cracks
Bearing 3 with the same wall thickness	Cu-Sn-Ni-Pb/steel	No Cracks
Bearing 4 with the same wall thickness	Cu-Sn-Ni-Pb/steel	Fatigue Cracks
Bearing 1 with unequal wall thickness	Cu-Sn-Ni-Pb/steel	No Cracks
Bearing 2 with unequal wall thickness	Cu-Sn-Ni-Pb/steel	No Cracks
Bearing 3 with unequal wall thickness	Cu-Sn-Ni-Pb/steel	No Cracks
Bearing 3 with unequal wall thickness	Cu-Sn-Ni-Pb/steel	No Cracks

In contrast test, bearings with the same wall thickness ran for 150 hours under the peak oil film pressure, and bearings with unequal wall thickness carrying the same load continuously ran for 280 hours.

The designs of bearings with unequal wall thickness were different, and the peak oil film pressure they carried was only 4.4MPa, and also the time for them to carry the same load is almost as twice as the duration of conventional bearings.

In another series of tests, disproof was made to the concept of unequal wall thickness. A group of variant bearings was tested for an average of 68 hours at test bench, however, a thin bearing (with a large radius clearance) among the bearings with unequal wall thickness was installed at the position bearing high load. According to theory, such a way can make peak oil film pressure increase by 23%, so fatigue life is shorter.

All these tests were made for an average of 35 hours, proving this concept once again.

Conclusion

First, the most important factor which plays a great influence on the fatigue life of the bearings of diesel engine lies in the peak oil film pressure. For this reason, the mission of making an improvement to the service life of bearings is to reduce the peak oil film pressure.

Second, the peak oil film pressure of diesel engines in overload can be reduced by the bearings with unequal wall thickness, making diesel engines carry higher loads. For this reason, the service life of diesel engine can be promoted to be longer.

References

- [1] Zhenjie Guo, Zuojun Song, Lirong Zhang, et al. Influence of Friction Loss on the Life of Connecting Rod Bearing Shell of Engine [J]. *Lubrication Engineering*, 2006 (9):152-154.
- [2] Xuanhuai Qiu. *Machine Design (Edition 4)* [M]. Beijing: Higher Education Press, 1997.
- [3] Zhenjie Guo. The Elastic Fluid Lubrication Design Cam of the Diesel Engine's High Pressure Injection Pump [J]. 2007 (5): 146-148.
- [4] Zhenjie Guo. The Abrasion Test Studies of Connecting Rod Bearing for Diesel Engine Based on Elastic Fluid Lubrication Theory [J]. *Automobile Technology*, 2008 (5): 48-50.

Numerical Simulation of Partial Cavitating Flow of 2-D Hydrofoil in Viscous Flow

Xiaohui He, Lei Gao, Hongbing Liu, Zhigang Li

Engineering Institute of Engineer Corps , PLA University of Science and Technology

Nanjing 210007 China

Keywords: Turbulence Model; Hydrofoil; Cavitating Flow

Abstract. This paper has studied the partial cavitation of 2-D hydrofoil based on the theory of viscous flow. The numerical calculation sets forth from the complete N-S equation and adopts the two-equation turbulence model closed Reynolds equation. As the basic control equation, the cavitating flow adopts the Rayleigh plesset model and calculates the zero angle of attack. At the same time, it calculates the influences of different ship speeds on the hydrofoil partial cavitating flow and analyzes the flow field of the hydrofoil. In addition, it makes comparisons on the calculation results and the published test conclusions. The results have shown that the calculation method in this paper has relatively good calculation precise degree.

Introduction

Marine aircraft wing hydrofoil and one of the main differences is that the former has the cavitation phenomenon. When the hydrofoil surface pressure decreased to or below the vaporization of the water pressure, water will be vaporized to form partial cavity, resulting in hydrofoil hydrodynamic performance and the change of hydrofoil surface erosion and vibration. Therefore in the hydrofoil study on hydrodynamic performance of the partial cavitating flow, prediction is a very important job.

Scholar Uhlma J S. ^[1] and Rowe A, Blottianx O. ^[2] adopts the the speed of the boundary integral method to calculate the hydrofoil of the cavitating flow. They are all from the iterative solution of air bubble, the dynamic boundary conditions in the approximate free instant noodles to meet, and the kinematic boundary condition of modified cavity shape, which often results in will big estimated cavitation area.

Therefore, scholar Lee C S, Kim Y G, Lee J T. ^[3] and Fine E, Kinnas S A. ^[4] adopts the velocity potential of the boundary integral method for the calculation of hydrofoil cavitating flow, the solving process and the former is similar, but the calculation method converges faster, and improves the calculation accuracy. The method is essentially based on the potential flow theory. Calculations do not consider the fluid viscous effects, which cannot describe near hydrofoil because of the viscous effect as a result of a variety of complex flow phenomena. Therefore, this article sets forth from the viscous flow theory, by solving the complete N-S equation on hydrofoil partial cavitation and investigating by numerical simulation.

Control Equation and Numerical Methods

The basic control equations of the viscous and incompressible fluid are the continuity equation, Reynolds and the $k - \varepsilon$ two equation model.

The continuity equation

$$\frac{\partial u}{\partial x} + \frac{\partial v}{\partial y} = 0 \quad (1)$$

Reynolds

$$\frac{\partial u}{\partial t} + u \frac{\partial u}{\partial x} + v \frac{\partial u}{\partial y} = -\frac{1}{\rho} \frac{\partial p}{\partial x} + \mu_{eff} \left(\frac{\partial^2 u}{\partial x^2} + \frac{\partial^2 u}{\partial y^2} \right) + \frac{\partial}{\partial x} \left(\mu_{eff} \frac{\partial u}{\partial x} \right) + \frac{\partial}{\partial y} \left(\mu_{eff} \frac{\partial v}{\partial x} \right) + F_x \quad (2)$$

$$\frac{\partial u}{\partial t} + u \frac{\partial v}{\partial x} + v \frac{\partial v}{\partial y} = -\frac{1}{\rho} \frac{\partial p}{\partial y} + \mu_{eff} \left(\frac{\partial^2 v}{\partial x^2} + \frac{\partial^2 v}{\partial y^2} \right) + \frac{\partial}{\partial x} \left(\mu_{eff} \frac{\partial u}{\partial y} \right) + \frac{\partial}{\partial y} \left(\mu_{eff} \frac{\partial v}{\partial y} \right) + F_y \quad (3)$$

In the equation $\mu_{eff} = \mu + \mu_t$, $\mu_t = \rho C_\mu \frac{k^2}{\varepsilon}$

C. The $k - \varepsilon$ two equation model

$$\frac{\partial k}{\partial t} + u \frac{\partial k}{\partial x} + v \frac{\partial k}{\partial y} = \left(\mu + \frac{\mu_t}{\sigma_k} \right) \left(\frac{\partial^2 k}{\partial x^2} + \frac{\partial^2 k}{\partial y^2} \right) + G_k + \rho \varepsilon \quad (4)$$

$$\frac{\partial \varepsilon}{\partial t} + u \frac{\partial \varepsilon}{\partial x} + v \frac{\partial \varepsilon}{\partial y} = \left(\mu + \frac{\mu_t}{\sigma_\varepsilon} \right) \left(\frac{\partial^2 \varepsilon}{\partial x^2} + \frac{\partial^2 \varepsilon}{\partial y^2} \right) + \frac{\varepsilon}{k} (C_{1\varepsilon} C_k + C_{2\varepsilon} \rho \varepsilon) \quad (5)$$

In the equation, ρ is liquid density; u , v are the velocity vectors in the direction of components x , y ; p is in fluid infinitesimal body pressure; F_x , F_y is the element of the physical. The parameter values are respectively: $C_{1\varepsilon} = 1.44$, $C_{2\varepsilon} = 1.92$, $C_\mu = 0.09$, $\sigma_k = 1.0$, $\sigma_\varepsilon = 1.3$.

In order to facilitate the analysis on the control equations, and the numerical method of unified, as well as the unified program of equations, the combination with the actual form of the control equation has made so as to firstly establish the general form of the control equation.

Comparison of control equations (1), (2), (3), (4) and (5) has been made and it can be seen that although the dependent variables in these equations are different, they are all the reflections of unit time per unit volume in the physical conservation properties. If ϕ is used to the general variables, then the control equation can be expressed as the following general form:

$$\frac{\partial(\rho\phi)}{\partial t} + \frac{\partial(\rho u\phi)}{\partial x} + \frac{\partial(\rho v\phi)}{\partial y} = \frac{\partial}{\partial x} \left(\Gamma \frac{\partial \phi}{\partial x} \right) + \frac{\partial}{\partial y} \left(\Gamma \frac{\partial \phi}{\partial y} \right) + S \quad (6)$$

In the equation, ϕ represents the general variables; u , v , p represent the solving variables; and Γ expresses the generalized diffusion coefficient. It represents μ_{eff} , $\mu + \frac{\mu_t}{\sigma_k}$, $\mu + \frac{\mu_t}{\sigma_\varepsilon}$. S

represents the generalized source, which represents the $G_k + \rho \varepsilon \frac{\varepsilon}{k} (C_{1\varepsilon} G_k - C_{2\varepsilon} \rho \varepsilon)$ and so on.

At this time, what only needs to do is consider the general equations of the numerical solution of (6), and write the equation (6) of the source, for different ϕ, Γ, S . As long as the repeat call the procedure, can be solved. This article based on staggered grid based on SIMPLE equation (6) for numerical discrete. A staggered grid unit structure as shown in figure 1.

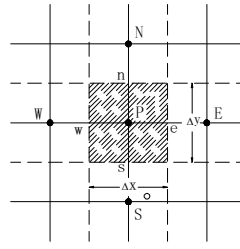


Fig. 1 Interconnected mesh

In Figure 1, the solid line shows the original grid lines, solid small dots that computing node (i.e., the main control volume center); the dotted line shows the master volume control interface. For convenient description, the said grid line with capital letter identification and dotted line represents the volume control interface with lower case letter identification (such as the pressure p and identity ρ and so on.) Calculation of the scalar in the grid node storage and computation, and the speed of each component separately in Tim grid storage and computation, Tim grid center are located at the interface of the control volume General equations of the discrete format:

$$a_p \phi_p = \sum a_{nb} \phi_{nb} + b \quad (7)$$

The following types of subscript said neighboring nodes nb include W/E/S/N.

$$a_p = (a_W + a_E + a_S + a_N) + \Delta F + a_p^0 - S_p \Delta V; \Delta F = F_e - F_w + F_n - F_s$$

$$a_W = D_W + \frac{F_W}{2}; a_E = D_e - \frac{F_e}{2}; a_S = D_s + \frac{F_s}{2}; a_N = D_n - \frac{F_n}{2}; F_w = \frac{F_{i,j} + F_{i-1,j}}{2}$$

$$F_e = \frac{F_{i+1,j} + F_{i,j}}{2}; F_s = \frac{F_{l,j} + F_{l-1,j}}{2}$$

Cavitating Flow Model

The research on cavitating flow belongs to high turbulent two-phase flow. In numerical commonly, the cavitating flow model is commonly used. In practice, a wide range of applications have been applied: open viscous wake model; spiral vortex model; Rayleigh Plesset model etc. In this paper, the calculation method is Rayleigh Plesset model. The control equation is shown as the followings:

$$R \frac{d^2 R}{dt^2} + \frac{3}{2} \left(\frac{dR}{dt} \right)^2 + \frac{2\sigma}{R} = \frac{p_B - p}{\rho} \quad (8)$$

In the equation, R —bubble diameter; p_B —pressure in the bubble; σ — surface tension coefficient; p —pressure acting on the fluid and ρ —flow density.

In order to simplify the calculation, the bubble diameter can be given by:

$$\frac{dR}{dt} = \sqrt{\frac{2}{3} \frac{p_B - p}{\rho}}$$

Algorithm Analysis

In order to testify the calculation methods in this paper, the NACA16-309 type hydrofoil model is taken as an example and numerical calculation of the partial cavitation flow on hydrofoil is made. In addition, the results are made into comparisons with the testifying results.

Calculation model

The calculation model is shown as the followings:

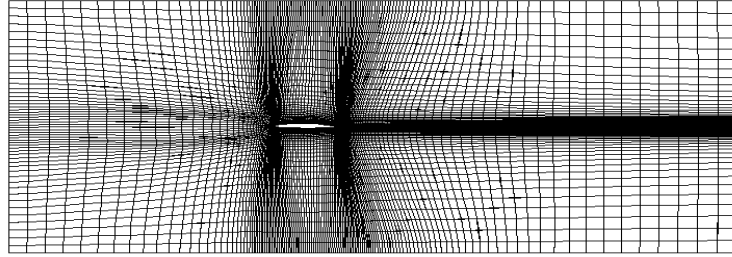


Fig. 2 Computational domain outline

Suppose that hydrofoil feature length L and left end of the model is the entrance boundary, the distance hydrofoil is $4L$ and the right end is outlet boundary. The distance hydrofoil is $6L$; and the upper and lower boundary distance hydrofoil is $2L$. Calculate the aqueous media at 15 degrees C freshwater.

Network division

Calculation of regional grid is shown in Figure 2. In order to improve the calculation precision and efficiency, focus on regional grid and make refine, the model hydrofoil is mainly around the area and the mesh are as shown.

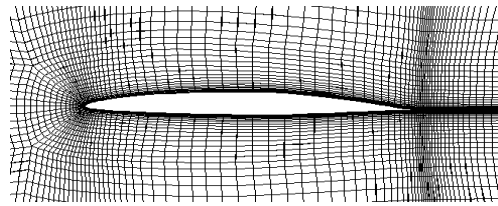


Fig. 3 The boundary mesh of the hydrofoil

The boundary condition

In this paper, the boundary conditions include the following:

Entrance conditions: set the speed entrance boundary; at given water medium velocity in K is introduced and the dielectric entrance condition, the determination method in literature ^[4] is proposed, according to the following formula calculation:

$$k = \frac{3}{2}(U \cdot T_i)^2 \quad \varepsilon = C_\eta^{3/4} \cdot \frac{k^{3/2}}{0.07L}$$

In the equation, U is uniform velocity and T_i is flow turbulence intensity.

Export conditions: the set pressure outlet, given to the static pressure distribution.

Surface condition: hydrofoil outer surface is taken as the no-slip condition, defining the particle velocity components are zero, which is:

$$u = v = w = 0$$

Its pressure satisfies:

$$\frac{\partial p}{\partial n} = \frac{\partial p}{\partial x} \cos(\alpha) + \frac{\partial p}{\partial y} \cos(\beta) + \frac{\partial p}{\partial z} \cos(\gamma)$$

The rest of the boundary of the velocity and pressure, and Xing wave height can be performed by internal corresponding calculation results obtained interpolation.

Cavity surface: supposing that the cavity surface equation is $F(x, y) = 0$, then the dynamic condition for the cavity surface is shown here:

$$\frac{DF}{Dt} = 0$$

The dynamic condition: $P = P_v$

Calculation result and analysis

Profile of the cavitation flow NACA16-309

$$\sigma = \frac{P_\infty - P_V}{\frac{1}{2} \rho V_\infty^2} \tag{9}$$

$$C_p = \frac{P_V - P_\infty}{\frac{1}{2} \rho V_\infty^2} \quad \sigma = -C_p \tag{10}$$

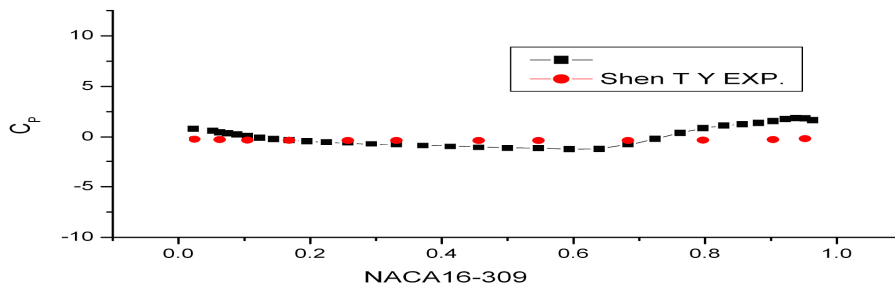


Fig. 4 The comparison about the calculation and experimentation

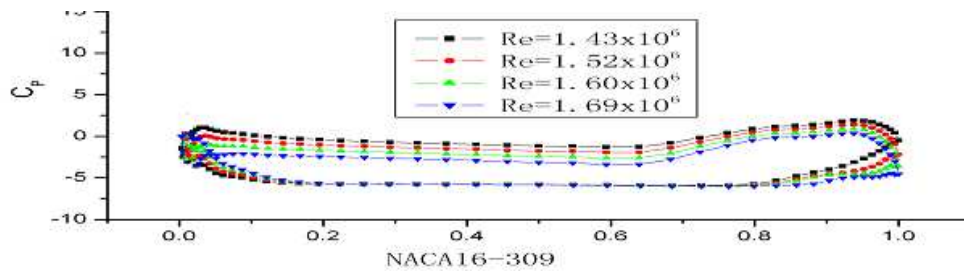


Fig. 5 The pressure coefficient under different Renault number

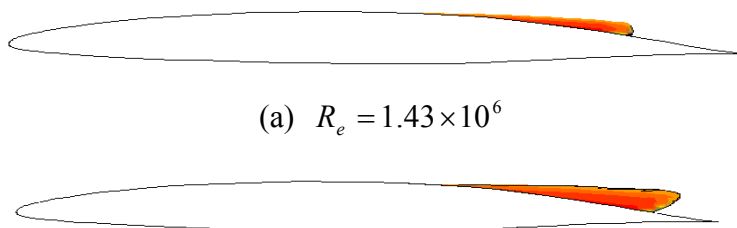
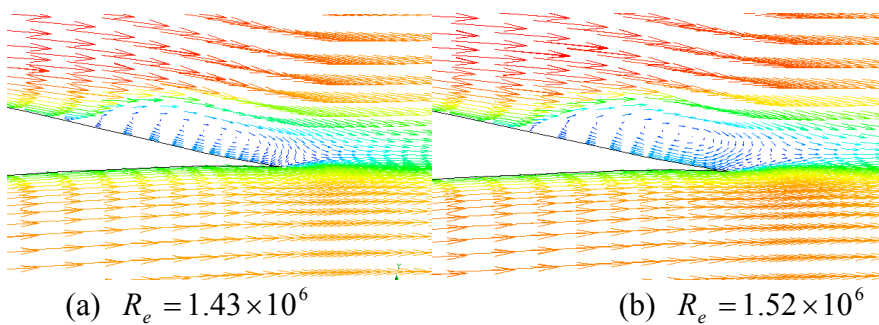
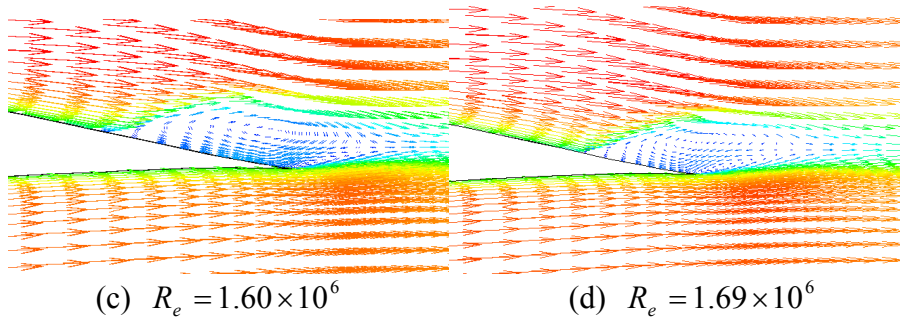


Fig. 6 The cavity shape under different Renault number

The correct BibTeX entries for the Lecture Notes in Computer Science volumes can
NACA16-309





(c) $R_e = 1.60 \times 10^6$ (d) $R_e = 1.69 \times 10^6$
 Fig. 7 The flow field under different Renault number

Conclusions

Through numerical calculation and analysis, the following conclusions can be obtained:

Based on the viscous flow theory and combine with the Rayleigh Plesset model, calculation of the two-dimensional hydrofoil partially cavitating flow problem is feasible; in terms of a two-dimensional hydrofoil partially cavitating flow, cavity shape increases with the increase of Re , and there is the development trend of hydrofoil; this article only calculates the zero angle of attack under the situation of different angle of attack. The calculation can use the method.

References

- [1] Uhlman J S. The surface singularity method applied to partially cavitating hydrofoils [J] Journal of ship research, 1987, 31(2):107-124
- [2] Rowe A, Blottianx O. Aspects of modeling partially cavitating flow [J]. Journal of ship research, 1993, 37(1):34-38
- [3] Lee C S, Kim Y G, Lee J T. A potential based panel method for the analysis of two-dimensional super—or partially activating hydrofoil, Journal of ship research, 1992, 36(2):168-181
- [4] Fine E, Kinnas. SA. A boundary element method for analysis of the flow around 3-D cavitating hydrofoils [J], Journal of ship research, 1993, 37(2):214-226
- [5] Eppler R and Shen Y T. Wing sections for hydrofoils _part 1: Nonsymmetrical profiles, Journal of ship research, 1979, 23(3):209-217
- [6] Shen Y T and Eppler R. Wing sections for hydrofoils_ part 2: Nonsymmetrical profiles, Journal of ship research, 1981, 25(3):191-200
- [7] Shen Y T and Eppler R. Wing sections for hydrofoils _part 3: Experimental Verifications, Journal of ship research, 1985, 29(1):39-50.

Cardiac Motion Estimation with Coronary Angiographic Image Sequences

Zheng Sun^a and Hua Bai^b

Department of electronic and communication engineering, North China Electric Power University,
Baoding, P.R.China

^asunzheng_tju@163.com, ^bbaihua809022895@163.com

Keywords: Coronary Artery Angiography, Cardiac Motion, Motion Estimation, Superquadrics

Abstract. An approach for estimating cardiac dynamics with X-ray coronary artery angiographic image sequences covering one or several cardiac cycles is proposed. According to *a priori* knowledge about cardiac anatomy and dynamics, complex cardiac dynamic performances are decomposed into global rigid motion, global deformation and local motion and deformation. Parameters of all components are quantitatively estimated in a manner of global-to-local and coarse-to-fine to obtain quantitative description of cardiac motion. Experimental results with clinical data demonstrated the validity.

Introduction

X-ray coronary angiography, one of catheter based imaging modalities, has been widely used in clinical diagnosis and interventional treatment of coronary artery diseases. Since coronary arterial vessels covering epicardial surface follow myocardial dynamics during cardiac cycles, cardiac dynamic information can be obtained through analyzing morphological variations of coronary vessels at different cardiac phases from dynamic X-ray coronary angiographic image sequences covering one or several cardiac cycles.

At the early stage, cardiac motion analysis was implemented through tracking bifurcation points of coronary vessels detected from bi-plane coronary angiograms [1]. Later, Coppini *et al.* [2,3] described cardiac deformation through comparing cardiac surfaces at end-diastole and end-systole which were fitted from 3D coronary vessel skeletons reconstructed from angiograms with spheric harmonics. Mishra [4] estimated stretching factor from angiographic image data to analyze cardiac surface with 3D Gauss curvature. However, all of them did not take variations of cardiac global location and orientation during cardiac cycles into consideration.

In this paper, we present a method to estimate cardiac motion and deformation in 3D using X-ray coronary angiographic image sequences as source data. Complex cardiac dynamics are decomposed in a manner of global to local and parameters of each component are quantitatively estimated to implement comprehensive quantification of cardiac motion.

Method

Complex cardiac dynamic performances during cardiac cycles include translation, rotation, expansion, contraction and twisting, etc. We decompose cardiac dynamics into global and local components which are separately analyzed using 3D coronary vessel skeletons reconstructed from a pair of nearly orthogonal coronary angiographic image sequences covering one or several cardiac cycles [5].

Estimating Global Motion

Global rigid motion According to medical observations, cardiac global motion includes global rigid motion, i.e., translation and rotation, and global deformation, i.e., expansion, contraction and twisting [6].

Since location and orientation of the heart may change during cardiac cycles, we build a local reference system (LRS) centered on the heart in order to quantitatively estimate parameters of global rigid motion. As shown in Fig.1, $O_w x_w y_w z_w$ is the imaging system coordinate system where the origin O_w is the X-ray spot, z_w -axis is perpendicular to the imaging plane $O_w x_w y_w$, and $O_o x_o y_o z_o$ is the local reference system where the origin O_o and z_o -axis are, respectively, the centroid and principle axis of the heart.

Given 3D coronary vessel skeleton points, $(x_i, y_i, z_i), i=1,2,\dots,N$, we adopt the geometrical center of these points as the approximation of the cardiac centroid. The principal axis is an axis that passes the centroid and the sum of squared distances between the axis and vessel skeleton points is minimal.

Parameters of global rigid motion are determined through analyzing variations of the location and orientation of the local reference systems at different time-points of cardiac cycles. Global displacement is the displacement between cardiac centroids at two different time-points and rotation matrix is the transformation matrix of the LRS from one time-point to another.

Before analyzing global deformation, we compensate the global rigid motion according to estimated parameters so that the LRS at the first time-point coincides with the one at the second time-point. Then, the coordinate transformation is performed to obtain coordinates of 3D vessel skeletons at both time-points based on the LRS at the first time-point.

Global deformation To estimate parameters of global deformation, 3D vessel skeleton points at both time-points whose coordinates are based on the LRS at the first time-point are separately fitted with an extended superquadrics (ESQ) surface. The parametric definition of ESQ surface is [7]

$$X(\theta, \varphi) = \begin{bmatrix} x \\ y \\ z \end{bmatrix} = \begin{bmatrix} a_x \text{sign}(\cos \theta \cos \varphi) |\cos \theta|^{f_1(\theta)} |\cos \varphi|^{f_2(\varphi)} \\ a_y \text{sign}(\cos \theta \sin \varphi) |\cos \theta|^{f_1(\theta)} |\sin \varphi|^{f_2(\varphi)} \\ a_z \text{sign}(\sin \theta) |\sin \theta|^{f_1(\theta)} \end{bmatrix} \quad (1)$$

Where $f_1(\theta)$ and $f_2(\varphi)$ are, respectively, function of longitude angle θ and latitude angle φ ($-\pi/2 \leq \theta \leq \pi/2$ and $-\pi \leq \varphi \leq \pi$). We adopt Levenberg-Marquardt algorithm [8] to solve the non-linear least square problem of fitting ESQ surface with discrete data points.

According to *a priori* knowledge about cardiac dynamics, global deformation includes expansion and contraction towards three orthogonal directions as well as twisting along the long axis of the heart. We quantitatively estimate parameters depicting global deformation including scale factors in three orthogonal directions and twisting parameter through comparing coefficients of ESQ models at different time-points.

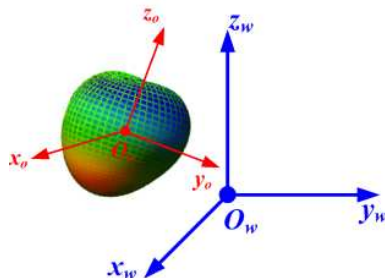


Fig.1 Local reference system

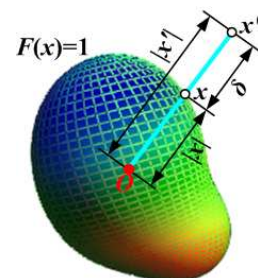


Fig. 2 Schematic diagram of residue distance

Estimating Local Motion

Compensating global deformation Before analyzing local motion and deformation, we restore vessel skeleton points at the second time-points to its original state before global rigid motion and deformation through compensating global deformation according to estimated parameters. Consequently, at this stage the differences between vessel skeleton point sets at two time-points is mainly due to cardiac local motion and deformation without consideration of computation errors.

Fitting residue distance The global shape model represented with an ESQ surface can describe the approximation of cardiac global shape. However, local details of the myocardial surface can not be reflected. In order to analyze local motion and deformation, it should be modified. As shown in Fig.2, given vessel skeleton points may not be on the fitted ESQ surface, where the radial distance between a skeleton point, x' , and the surface, i.e., δ , can be depicted as the fitting error at this point.

We fit the functional expression of the residue distance of each point on the ESQ surface according to radial distances between given 3D vessel skeleton points and the ESQ surface, which are represented with spherical coordinate (ϑ, ϕ) ($0 \leq \vartheta \leq \pi$ and $0 \leq \phi \leq 2\pi$). Spherical harmonics [9] are adopted as the basic function and the result is a series,

$$r_e(\vartheta, \phi) = \sum_{i=0}^N a_i B_i(\vartheta, \phi) \quad (2)$$

Where a_i is the i th coefficient and $B_i(\vartheta, \phi)$ is the basic function

Consequently, a more accurate shape model describing local details of the cardiac surface is obtained through adding these residue distances to the global shape model represented with an ESQ surface. According to Eq.(1), the spherical radius of a point on the ESQ surface represented with spherical coordinate (ϑ, ϕ) is

$$r_s(\vartheta, \phi) = \left[\left(a_x (\sin \vartheta)^{f_1(\vartheta)} (\cos \phi)^{f_2(\phi)} \right)^2 + \left(a_y (\sin \vartheta)^{f_1(\vartheta)} (\sin \phi)^{f_2(\phi)} \right)^2 + \left(a_z (\cos \vartheta)^{f_1(\vartheta)} \right)^2 \right]^{\frac{1}{2}} \quad (3)$$

Adding Eq.(2) to (3), a global shape model considering fitting errors is obtained,

$$r_t(\vartheta, \phi) = r_s(\vartheta, \phi) + r_e(\vartheta, \phi) \quad (4)$$

Whose vector expression is

$$X(\vartheta, \phi) = \begin{bmatrix} x \\ y \\ z \end{bmatrix} = \begin{bmatrix} a_x \text{sign}(\sin \vartheta \cos \phi) |\sin \vartheta|^{f_1(\vartheta)} |\cos \phi|^{f_2(\phi)} + r_e(\vartheta, \phi) \sin \vartheta \cos \phi \\ a_y \text{sign}(\sin \vartheta \sin \phi) |\sin \vartheta|^{f_1(\vartheta)} |\sin \phi|^{f_2(\phi)} + r_e(\vartheta, \phi) \sin \vartheta \sin \phi \\ a_z \text{sign}(\cos \vartheta) |\cos \vartheta|^{f_1(\vartheta)} + r_e(\vartheta, \phi) \cos \vartheta \end{bmatrix}. \quad (5)$$

Determining local displacement field Since bifurcations of coronary vessel tree at different time-points are correspondent, we adopt local displacements of bifurcations as sample data to fit local displacement fields to obtain the correspondence of each point on global shape models at different time-points.

As mentioned above, the global shape model is depicted as the spherical radius, $r_t(\vartheta, \phi)$, the function of spherical coordinate (ϑ, ϕ) . Consequently, the local displacement of a point on the ESQ surface is $\Delta\vartheta$ and $\Delta\phi$, which are also functions of (ϑ, ϕ) . Suppose that in the LRS at time-point t , the coordinate of i th bifurcation point is (x_{1i}, y_{1i}, z_{1i}) and its correspondence at $t + \Delta t$ is (x_{2i}, y_{2i}, z_{2i}) , ($i = 1, 2, \dots, n$ and n is the total number of given bifurcation points), where the global motion and deformation have been compensated. Their spherical coordinates are

$$\begin{bmatrix} \vartheta_i^1 \\ \phi_i^1 \end{bmatrix} = \begin{bmatrix} \text{arctg} \left(\sqrt{x_{1i}^2 + y_{1i}^2} / z_{1i} \right) \\ \text{arctg} (y_{1i} / x_{1i}) \end{bmatrix} \quad (6)$$

And

$$\begin{bmatrix} \vartheta_i^2 \\ \phi_i^2 \end{bmatrix} = \begin{bmatrix} \text{arctg} \left(\sqrt{x_{2i}^2 + y_{2i}^2} / z_{2i} \right) \\ \text{arctg} \left(y_{2i}^2 / x_{2i}^2 \right) \end{bmatrix} \quad (7)$$

And the local displacement between them is

$$\begin{cases} \Delta \vartheta_i = \vartheta_i^2 - \vartheta_i^1 \\ \Delta \phi_i = \phi_i^2 - \phi_i^1 \end{cases} \quad (8)$$

The approximate expression of $\Delta \vartheta(\vartheta, \phi)$ and $\Delta \phi(\vartheta, \phi)$ are obtained,

$$\begin{cases} \Delta \vartheta(\vartheta, \phi) = \sum_{i=0}^N b_{1i} B_i(\vartheta, \phi) \\ \Delta \phi(\vartheta, \phi) = \sum_{i=0}^N b_{2i} B_i(\vartheta, \phi) \end{cases}, \quad (9)$$

Where $B_i(\vartheta, \phi)$ is the spherical harmonics and b_{1i} and b_{2i} are the i th coefficients.

Estimating local motion According to the Helmholtz Theorem, the motion field of a small enough volume on the non-rigid body can be decomposed into translation, rotation and deformation (expansion/contraction) in three orthogonal directions. We use 2-order tensor to represent contraction/expansion and rotation component reflecting the property of non-rigid motion. Therefore, the motion field of a volume element on the non-rigid body is described as

$$\begin{bmatrix} x_{i+1} \\ y_{i+1} \\ z_{i+1} \end{bmatrix} = T_i + R_i \begin{bmatrix} x_i \\ y_i \\ z_i \end{bmatrix} + E_i \begin{bmatrix} x_i \\ y_i \\ z_i \end{bmatrix} \quad (10)$$

Where $T_i = [a_i \ b_i \ c_i]^T$ is the translation vector, R_i is the rotation tensor and E_i is the deformation tensor (strain tensor) R_i is the product of rotation matrices around x -, y - and z -axis. To simplify we suppose rotation angles are very small. Then, according to the linear approximation

$\sin \alpha \approx \alpha$ and $\cos \alpha \approx 1$, $R_i \approx \begin{bmatrix} 1 & -\gamma & \beta \\ \gamma & 1 & -\alpha \\ -\beta & \alpha & 1 \end{bmatrix}$ is obtained where two or higher order terms are

ignored. The strain tensor, $E_{3 \times 3} = [e_{ij}]$, is a two order symmetry tensor, where $e_{12} = e_{21}$, $e_{13} = e_{31}$ and $e_{32} = e_{23}$.

Overall, there are totally twelve unknown coefficients in Eq. (10), ($a, b, c, \alpha, \beta, \gamma, e_{11}, e_{12}, e_{13}, e_{22}, e_{23}, e_{33}$). For each point on the global shape model, three equations can be obtained and at least four points in a volume are needed to determine these coefficients.

Experimental Results and Discussion

In this section, some experimental results with clinically acquired image data are given to demonstrate our model. The clinical image data were acquired with PHILIPS Integris CV single-plane cardiovascular angiography system during routine cardiac catheter examinations. Roughly synchronous image pairs are selected with the aid of superimposed ECG signals. The frame rate is 30

fps. The image size is 512×512 pixels, pixel size is about 0.3 mm, and gray-levels range in [0-256]. In Fig.3 and Fig.4, two pairs of left coronary angiograms acquired at different time-points of the cardiac cycle from nearly orthogonal view angles are shown. The reconstructed 3D vessel skeletons from the two angiographic image pairs are shown in Fig.5. In Fig.6, the global shape models at the two time-points built with our method according to 3D vessel skeletons in Fig.5 are shown.

Summary

A method for estimating complex cardiac motion during cardiac cycles from dynamic X-ray coronary angiographic image sequences is presented in this paper. A cardiac dynamic model is built using 3D vessel skeletons reconstructed from coronary angiographic image sequences as input data. Complex dynamic performances of the heart are decomposed in the manner of global-to-local and coarse-to-fine and all of main components of cardiac dynamics that have been demonstrated with clinical observations are included. Consequently, the model can comprehensively reflect actual performances of the heart during cardiac cycles.

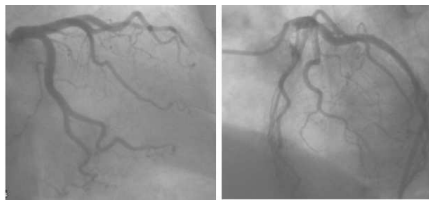


Fig.3 An angiogram pair at 1st time-point

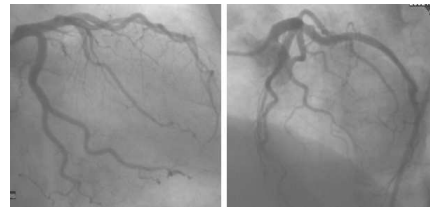


Fig.4 An angiogram pair at 2nd time-point

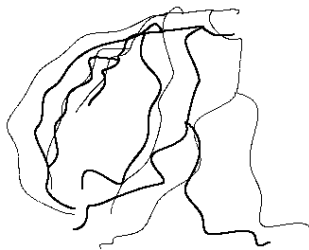


Fig. 5 3D vessel skeletons at two time-points

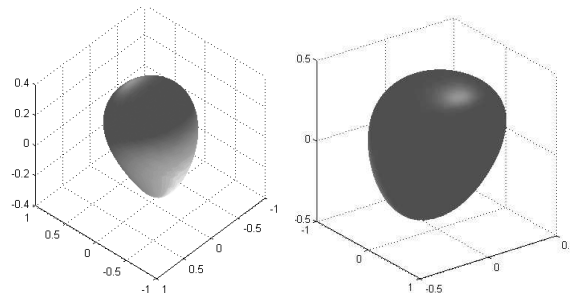


Fig. 6 Global shape model at two time- points

Acknowledgment

This work was supported by National Nature Science Foundation of China (Grant Nos.30500129 and 60973087) and the Fundamental Research Funds for the Central Universities (No.10ZG05).

References

- [1] H.C. Kim, B.G. Min, M.M. Lee, J.D. Seo, Y.W. Lee and M.C. Han: IEEE Transactions on Biomedical Engineering Vol.32 (1985), p. 503.
- [2] G. Coppini, M. Demi, A. L'Abbate and G. Valli, in: *Proceedings of IEEE International Conference on Computers in Cardiology*, IEEE Press, Washington DC, USA, Vol.9 (1988), p. 293.
- [3] G. Coppini, M. Demi, P. Marraccini and A. L'Abbate, in: *Proceedings of IEEE International Conference on Computers in Cardiology*, IEEE Press, Vienna, Austria, Vol.9 (1995), p.71.
- [4] S.K. Mishra, D.B. Goldgof and T.S. Huang, in: *Proceedings of 1991 IEEE International Conference on Computer Vision and Pattern Recognition (CVPR '91)*, IEEE Computer Society, Maui, HI, USA, (1991) p.331.
- [5] Z. Sun, M.Y. Tian and J. Sun: *Computerized Medical Imaging and Graphics* Vol.34 (2010) p. 333.

-
- [6] Hernández-Sabaté, D. Gil, E. Fernandez-Nofrerías, P. Radeva and E. Martí: IEEE Transactions on Medical Imaging Vol.28 (2009), p.1670.
 - [7] L. Zhou and C. Kambhamettu, in *Proceedings of 16th International Conference on Pattern Recognition (ICPR '02)*, IEEE Computer Society, Washington, DC, USA, Vol. 3 (2002) p. 713.
 - [8] Editorial board of modern applied mathematics handbook: *Modern applied mathematics handbook—volume of operational research and optimization theory* (Tsinghua University Press, China 1998).
 - [9] W. Zaiyu: *Equation of mathematical physics and special function* (Tsinghua University Press, China 1991).

Effects of Coefficient of Excess air on the Combustion Performance of Marine Two-stroke Diesel Engine

WEI haijun^{1,2}, XIE Haibo^{3*}

¹Marine engineering college, Dalian Maritime Univ., Dalian, China, 116026

²Merchant Marine College, Shanghai Maritime Univ, Shanghai, China, 200135

³The State Key Laboratory of Fluid Power Transmission and Control, Zhejiang Univ., Hangzhou, China, 310027

^ahxl@dlnu.edu.cn, ^bhbxie@zju.edu.cn

Keywords: Excess Air, A, Marine Diesel Engine, Fuel Oil, Combustion

Abstract. The purpose of this study is to investigate the effect of the coefficient of excess air to the performance of engine. Through a series of the sea trials for newly built ships, the factors that have a great influence of engine's performance are determined. In addition, methods of raising the coefficient of excess air are proposed to reduce the thermal load and accordingly enhance the performance of diesel engine. Finally, to achieve an efficient operation of the main engine, an example of trouble shooting and maintenance of the engine is given for practical applications. The scavenging pressure increased from 0.162 MPa to 0.207 MPa and the average exhaust temperature dropped from 423 °C to 336 °C under 90% load condition.

Introduction

Nowadays, turbocharging has been very common on diesel engines for marine and heavy machinery applications (Pulkrabek 2003)¹. A turbocharger combined with a smart turbocharging system is able to guarantee an optimum air-fuel ratio under all conditions, contributing even more to the control of soot emissions (Woodyard 2004)².

Stable combustion requires fuel, oxygen, and a source of ignition. There is roughly 21% oxygen by volume in the air. A 50% excess air condition implies approximately 10.5% oxygen remains in the boiler or engine exhaust stack. Choosing an excess air level is based on the type of fuel and the degree of combustion control that can be achieved for a specific system. Excess air levels range from about 5 to 10 percents for gas or oil fired furnaces to about 15 to 50 percents for coal and wood fired units (Richard 2003)³. For a traditional marine diesel engine, the excess air coefficient is in the range of 180% to 220% (Hsueh 1997, Technical Report 1996)⁴. It is reported that the newly designed MAN B&W SMC-C series engines which burn IFO 380 oil have excess air coefficients over 320% (MAN B&W 1996)⁵. According to the work of Robert and Philip (2002)⁶, the beneficial effect on emissions of high excess air is clear for all regulated emissions. A 40% increase in excess air at high load reduces fuel consumption by 16%, and a 100% increase in excess air by 19%. The exhaust gas recirculation (EGR) system is a very effective technique for reducing NO_x emission from a diesel engine, particularly at the high load of engine operation condition. In a turbocharged engine, however it is difficult to introduce EGR at the high load because of the high boost pressure in the air intake. Introducing and evaluating the exhaust gas recirculation system to the turbocharged engines, Yokomura et al. (2003) showed that the system with venturi is rather effective for expanding the EGR range up to high engine load conditions. Conducting an experiment, Ogawa et al. (2003) pointed out that a combination of the divided cavity, EGR and intake air throttling was effective in simultaneously eliminating knocking and reducing total hydrocarbon and NO_x. At lower overall excess air ratio conditions, NO_x reduction was shown with a biform mixture composition without slightly lean or extremely rich regions⁷.

Data of Sea Trial and Analysis

Usually, after the offer has been accepted or a buying agreement in written form of a ship has been signed, a sea trial is necessary. The sea trial data is valuable particularly when these data are analyzed. Sea trial analysis can help fix problems when they appear, and better yet, it can be used in the design process of future vessels to help avoid these problems from the outset. Abnormal exhaust is an indicator that an engine is running abnormally. Items checked underway will give a more accurate assessment. Sea trial data is collected to determine if the engines are running within the specified parameters. Engine information such as engine rpm, engine power, gear box ratio, and fuel consumption are obtained.

The conditions for the tests were calm wind and flat seas in brackish water of 20 meters depth. Speed was calculated with measured time across a run of a known distance. Vessel trim was estimated with a bubble inclinometer, and fuel rate was available through the engine's digital readout. There are estimates and predictions used in the analysis, as well as potential sources of measurement error. Given good measurement data and an accurate definition of the propeller (particularly pitch and cup), the accuracy should be well within 10%, in most cases within 5%. Fortunately, the purpose of these analyses is to find indicators and trends, so this small inaccuracy is acceptable.

Table 1 presents the comparison of predicted and measured pressures in cylinders of engine after compression. It shows that the measured pressures are a little less than the predicted ones. In addition, the largest relative error between the two data is less than 5%.

Table 1 Comparison of predicted and measured pressures in cylinders of engine after compression

p_{scav} (MPa)	atmos. press.(MPa)	$P_{scav}^{(gauge)}$. (MPa)	p_{abs} (MPa)	$p_{measure}$.(MPa)	Relative err. (%)
0.035	0.101	0.136	4.93	4.94	0
0.116	0.101	0.217	7.87	7.73	-2
0.201	0.101	0.302	10.95	10.61	-3
0.246	0.101	0.347	12.58	12.16	-3
0.25	0.101	0.351	12.73	12.28	-4
0.272	0.101	0.373	13.53	13.19	-2

A group of newly built MAN B&W vessels, burning heavy diesel oil IFO 180, were arranged to be tested. Various load conditions such as 50%, 75%, 90% and 100% were put into operations and the corresponding engine speeds, brake powers, and specific fuel consumptions were listed in Tables 2-3. Normally, the exhaust temperature increases with engine's load. However, from Tables 2 and 3, it was shown that the exhaust temperature did not necessarily increase with engine's load due to the variation of excess air supply. However, due to the lag and slow response of the turbocharger, the thermal load is higher and the excess coefficient is lower under this circumstance. In addition, the excess air coefficients are all well above three for these types of engines irrespective of load conditions.

Table 2 Data from official sea trial (Group A)

MAN B&W 6L42MC 4265kWX162r/min (Using IF180)				
load	50%	75%	90%	100%
r/min	133	154.5	163	166
output, kW	2006	3202	3842	4074
SFC, g/kW-h	177.7	168.8	168.2	168.5
p_{scav} . MPa	0.065	0.125	0.158	0.165
T_{scav} , °C	33	39.5	45	48
T_{exh} , °C	297	299	301	303

Example Analysis

A container vessel was built in 2000. The main engine of MAN B&W 7S60MCC (15820kW, 105r/min) was used. Due to long-term negligence in maintenance, the engine's performance decreased sharply in 2009. It was reported that the engine exhaust temperature increased to 420°C, which caused some cylinder exhaust valve and liner damaged. The major parameter records were shown in Table 4. The ship was then sent to dock for major repairs. Several steps, listed below, are taken with respect to the above mentioned problem.

Table 3 Data from official sea trial (Group B)

MAN B&W 7S70MCC 21770kWX91 r/min (Using IF180)				
load	50%	75%	90%	100%
r/min	78.5	89.5	95.1	98.6
output, kW	11077	16487	19651	21270
SFC, g/kW-h	177.6	172.4	172.2	172.9
$p_{scav.}$, MPa	0.116	0.206	0.26	0.27
$T_{scav.}$, °C	38	42	46	46
$T_{exh.}$, °C	266	275	291	298

Table 4 The measured data of the container given in example

Engine Specification						
Type	MAN B&W 7S60MC-C			Nominal power	15820 kW	
Nominal speed	105 rpm			No. of cylinder	7	
Cylinder bore	600 mm			Piston stroke	2400 mm	
Parameter	Before overhaul			After overhaul		
load	50%	75%	90%	50%	75%	90%
r/min	84	93.2	97.1	84	96.2	102.1
output, kW	7912	11857	14220	7912	11857	14220
SFC, g/kW-h	189.7	180	178.3	188.5	178.9	178.8
$p_{scav.}$, MPa	0.086	0.13	0.162	0.098	0.159	0.207
$T_{scav.}$, °C	39	42	46	40	44	47
$T_{exh.}$, °C	410	425	423	355	343	336

An improvement in the performance of the turbocharger Remove the cover on the manifold and clean the sediments on the grid which is installed in the expansion joint of compressor inlet. Disassemble the turbocharger and clean the both sides of turbine and compressor. Check and measure the corrosion of the moving blade. Replace the excessively deformed nozzle ring to increase the efficiencies of turbine and compressor. Clean the waste heat boiler and the stack to decrease the back pressure of turbine exit.

Reduction of the airflow resistance Circulate the chemicals to clean the airside of the air cooler. Clean the scavenging manifold, scavenging chamber and port of each cylinder.

A decrease of the scavenging temperature Unobstruct and clean water side's tube nest of the air cooler to decrease the scavenging temperature and increase the amount of intake air.

A Check of the wear conditions of the cylinder and piston. Remove the pistons and replace the unduly worn cylinders and piston rings.

An immediate improvement in engine's performance was observed after the above-stated steps were carried out. The scavenging pressure increased from 0.162 MPa to 0.207 MPa and the average exhaust temperature dropped from 423 °C to 336 °C under 90% load condition. In addition, the

pressures of compression and explosion rose accordingly. Other output conditions of the main engine are shown in Table 4. Fig.1 plots the effects of engine's load of excess air coefficient before/after overhaul. It is shown that α is always less than 2.5 and decreases with increasing load before the engine of the vessel is overhauled. However, after the engine was overhauled and maintained, an apparent raise in excess air coefficient is obtained. Note that α increases with engine's load due to sufficient air supply from the scavenging manifold and ports of cylinders. Fig.2 depicts the comparison of the data measured aboard and empirical formula of previous study. In this figure, α is given as a function of T_{exh} on the conditions that $\eta_i=45\%$, $q_w=20\%$ and $H_u=41000$ kJ/kg. Most of the measured data compare favorably with the empirical relationship. In addition, it is worthwhile to note that the excess air coefficients of the new vessels are all above 3, however, α becomes lower than 2.5 after a certain period of operation. A good maintenance of the main engine may raise the excess air coefficient but the effect is still limited.

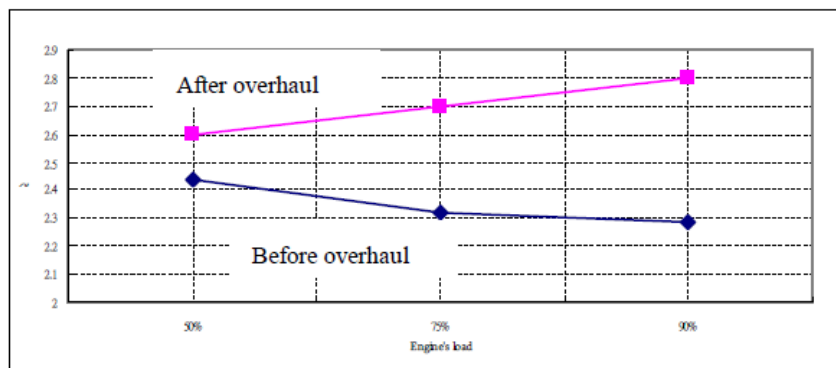


Fig. 2 The effects of engine's load of excess air coefficient before/after overhaul

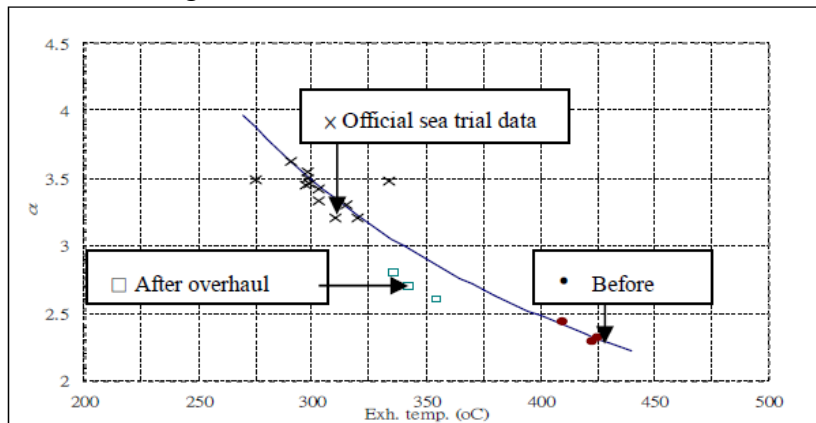


Fig. 3 Comparison of the data measured aboard and empirical formula

Conclusion

In this study, the effects of excess air coefficients for diesel engines are investigated. It is shown that α plays an important role in diesel engine during combustion. Furthermore, a larger α may change the condition of engine's combustion for diesel engines, which will burn fuel oil more efficiently and emit the complete heating value, and decreases fuel consumption as well as the thermal load of engine parts. Consequently, it will keep the best engine performance.

To increase α during operation, it will apparently improve the performance of the main diesel engine. Although the coefficients of excess air can't be measured on-site while the engine is running, an immediate assessment can be made from the scavenging air pressure, compression pressure, average exhaust temperature and thermal load through this work. In this regard, it is possible to achieve good performance of the engine at all times.

This work is supported by National Nature Science Foundation No.05975035E050202

References

- [1] MAN B&W Diesel A/S, Emission Control Two-stroke Low-Speed Diesel Engines[R]. MAN B&W Diesel A/S. 1996, p-2,12.
- [2] Ogawa, H., N. Miyamoto, S. Nakazawa, and K. Akao. Smokeless and low NO_x combustion in a dual-fuel diesel engine with induced natural gas as the main fuel[J]. *International Journal of Engine Research*, 2003(1), p1-9.
- [3] Pulkrabek, W.W. *Engineering Fundamentals of the Internal Combustion Engine*[J]. Pearson Prentice Hall, New Jersey 2003.
- [4] Yokomura, H., S. Kohketsu, and K. Mori. EGR System in a Turbocharged and Intercooled Heavy-Duty Diesel Engine[J]. *Expansion of EGR Area with Venturi EGR System*, Mitsubishi Motors, *Technical Review*, 2003(15), 14-20.
- [5] Andreadis, P.; Zompanakis, A.; Chryssakis, C.; Kaiktsis, L. Effects of the fuel injection parameters on the performance and emissions formation in a large-bore marine diesel engine[J] *International Journal of Engine Research*, 2011(1), p 14-29.
- [6] Ozsoysal, Osman Azmi. Effects of varying air-fuel ratio on the performance of a theoretical Diesel cycle[J]. *International Journal of Exergy*, 2010(6), p 654-666
- [7] Lin, C.-Y.; Huang, J.-C. An oxygenating additive for improving the performance and emission characteristics of marine diesel engines[J]. *Ocean Engineering*, 2003(13), p 1699-1715.

Solutions of Optical Transmission Analysis

Li Yongjie

North China Electric Power University

Keywords: Optical Fiber Transmission; Limiting Factor; Technical Measures.

Abstract. This article described the basic technology of optical fiber, dense wavelength division multiplexing, and focus on the loss, dispersion optical transmission constraints to analyze, and to overcome the constraints corresponding to the system power is limited, dispersion limited technical measures.

Introduction

With the development of communication, long-distance transmission system experienced a few decades from PDH (plesiochronous digital sequence) to the SDH (Synchronous Digital Hierarchy) and DWDM (Dense Wavelength Division Multiplexing) technology. So optical fiber communication systems have a development to large-capacity, high speed, long-distance direction. With the emergence and application of DWDM technology, the limiting factor for long-distance optical transmission is no longer confined to the original SDH loss and dispersion; while there have been other factors such as PMD, OSNR.

Fiber and Its Characteristics

Light is an electromagnetic wave, while optical fiber is a return optical waveguide, but optical fiber communication is a means of communication using optical fiber transmission lightwave signal. Fiber is the main media role in the optical communication system of fiber-optic communication systems to transmit information under conditions free from outside interference, low loss, small distortion of the optical signal transmitted from one end to the other end.

The fiber is composed of core, cladding, and coating of three parts [1]. Up the bare fiber core and cladding, the use of high - purity silica made. The core is located in the center of the fiber for the transmission of light waves. Cladding at the outer layer of the core, the light waves used to be confined in the fiber core. Coating used to protect the bare fiber; a coating using a silicone resin or poly amino acid ethyl ester, and secondary coating is a coating on the basis of then put nylon, polyethylene or polypropylene plastics. Fiber loss in the process of transmission of light. The so-called loss refers to the attenuation of the fiber per unit length in units of dB / km. Fiber loss directly affects the transmission distance or relay station distances, therefore, to understand and reduce the loss of the fiber optical fiber communication has a significant practical significance.

Fiber absorption loss is caused by the fiber material and impurity absorption of light energy. Light energy to heat energy in the form of consumption in the fiber, is an important loss of the fiber loss. Scattering within the fiber, will reduce the transmission of power, resulting in the loss. The most important scattering is Rayleigh scattering, which is caused by the density and composition changes of the material within. Light in the face of uneven material transmission; change the direction of transmission, resulting in scattering caused by the loss. In the uneven fiber containing oxides and doped uneven can also cause scattering, resulting in loss [2].

Have different propagation velocity due to different wavelengths of light pulses in optical fibers, optical pulse propagation along the fiber stretcher, which produce the dispersion. Fiber dispersion of optical fiber communication is extremely unfavorable. Fiber-optic transmission of digital communications is a series of pulses, the broadening of the pulse of the optical fiber transmission, resulting in pulse and pulse overlap, which produce the inter-symbol interference, thus forming a transmission code error, resulting in errors. To avoid the error appears, it is necessary to lengthen the pulse spacing, resulting in lower transmission rate, thereby reducing the communication

capacity. On the other hand, the degree of optical pulse broadening with the growth of the transmission distance is more serious. Therefore, in order to avoid errors, the optical fiber transmission distance also shortened

The Basic Techniques and Composition of the Optical Fiber Transmission System

The optical transmission technology using single-mode fiber broadband and low loss characteristics, the use of multiple wavelengths as a carrier to allow each carrier channel simultaneous transmission in the fiber. Compared with the common single-channel system, not only greatly improve the communication capacity of the network system, full use of the bandwidth of the fiber [3], and it has expanded a simple and reliable performance, and many other advantages, is that it can directly access kinds of businesses, which makes it very bright prospect.

Analog carrier communication system, in order to take full advantage of the cable bandwidth resources and improve the transmission capacity of the system using frequency division multiplexing method, a number of different frequency signal transmission in the same cable at the same time, the receiving end of each carrier different frequencies using band-pass filter to filter out the signal of each channel. Light frequency division multiplexing method in optical fiber communication systems can be used to increase the transmission capacity of the system. In fact, this multiplexing method in optical fiber communication system is very effective. Frequency division multiplexing and carrier communication system simulation with a different carrier of the light wave as a signal in optical fiber communication systems, depending on the frequency of the light waves of each channel (or wavelength), the low loss window of optical fiber is divided into several channels, resulting in an optical fiber multi-channel optical signal multiplexing transmission.

Very narrow filter of some optical devices (such as bandwidth, coherent light source, etc.) is not very mature; therefore, to achieve very dense optical channel optical frequency division multiplexing (coherent optical communication technology) is very difficult. But, based on the current level of the device can be separated by optical channel frequency division multiplexing [4]. Usually optical channel spacing (or even reuse the fiber in different windows) called optical wavelength division multiplexing (WDM), and then called in the same window channel interval smaller DWDM Dense Wavelength Division Multiplexing (DWDM). With advances in technology, modern technology has been able to achieve wavelength interval for nanoscale complex, or even wavelength spacing tenths of a nanometer complex with, but more stringent technical requirements of the device only, so the wavelength interval smaller 8 waves, 16 waves, 32 or even more wavelength multiplexing called coarse Wavelength Division Multiplexing (CWDM).

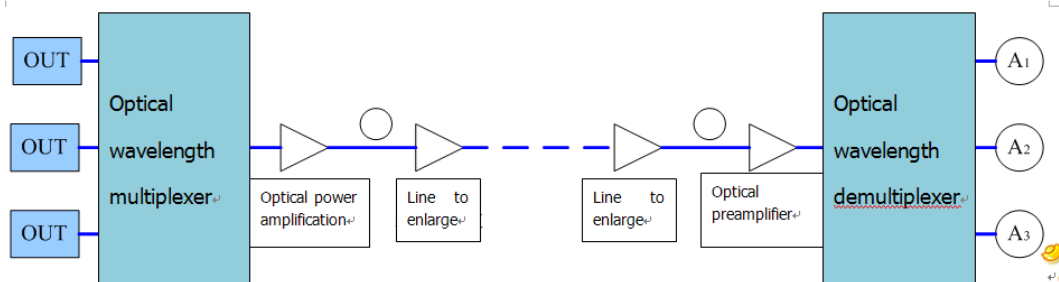


Fig. 1 Internal structure of the optical transmission system

DWDM system composition and the spectrum have been shown in Fig 1. The sender of the optical transmitter to send a different wavelength precision and stability to meet certain requirements of the optical signal with optical wavelength multiplexer multiplexed together into the erbium-doped fiber power amplifier (Erbium-doped fiber amplifier to compensate for power loss caused by the combiner, and improve optical signal transmission power). Then amplified multi-channel optical signal into the optical fiber transmission, in the middle can be decided according to the situation with or without optical line amplifier (Mainly used to improve receiver sensitivity, in order to extend the transmission distance) to reach the receiver side by light pre-amplifier into the optical wavelength filter to decompose the original separate ways optical signal.

Common Problems Affecting the Optical Transmission

System Power Limit

Optical signal transmission along the fiber, optical power will gradually become smaller. Fiber optical signal attenuation, the transmission distance is longer the greater the attenuation. Also, consider other relevant factors, including fiber optic connectors, connection, optical attenuation and other passive optical components and any additional margin of fiber attenuation introduced. Provisions allowing the attention range, the introduction of the attenuation of these factors take the value in the worst case, to do so in order to allow sufficient redundancy of the following three conditions [5] first, to adapt to future changes in the fiber optic cable configuration, such as attaching the connector to increase the cable length. The second is to adapt the optical performance changes produced by the environment. The third is to adapt to any light between the optical path, MPI -S and MPI -R device performance degradation.

And the power budget of the fiber optic system mainly depends on the difference between the light output power and receiver sensitivity. Typically, the optical receiver noise increases with the increase of the receiver bandwidth. System transmission bit rate increased from 2.5 Gbit / s to 10 Gbit / s optical receiver noise has increased four times, the theoretical receiver sensitivity reduced by about 6dB, the total power budget is reduced by at least 6dB.

System optical power budget values take the set to be combined with the technical and economic performance of the system considered. If the value is too large, will the optical transmitter and receiver unrealistically high requirements, the system costs rise. If the value is too small, the regeneration distance is too short, the increase in the number of regenerators, the same rise in the total system cost, and therefore requires a comprehensive consideration. At the same time, but also in the horizontal compatibility of the implementation system more flexibility the lower limit of the system optical power budget is actually the main power changes by the transmitter and receiver dynamic range allowed by the overload point, the upper limit is mainly determined by the minimum transmission power and the minimum receiver sensitivity.

System Dispersion Limit

Dispersion mode dispersion and chromatic dispersion Modern optical fiber communication system using only a single-mode fiber, mode dispersion only with multimode fiber, and therefore only consider the composition of the material dispersion and waveguide dispersion chromatic dispersion.

Chromatic dispersion is the phenomenon of different wavelengths in the light spectrum in the fiber group delay difference caused by the broadening of the light pulse. Optical pulse stretcher to produce inter-symbol interference (ISI), has also led to the optical receiver, the receiver sensitivity is reduced, so the need to increase the received optical power in order to maintain the level of bit error rate. Proportional to the total fiber chromatic dispersion and fiber length, fiber length is longer, the more serious the impact of fiber chromatic dispersion. Typically, the length of the fiber of the optical receiver, the receiver sensitivity degradation 1dB called dispersion-limited distance. Dispersion compensation measures can reduce or avoid the fiber chromatic dispersion limited.

The optical path penalty refers to the apparent decline of the light pulses in fiber transmission waveform distortion caused by the receiver sensitivity, bit error rate of under the conditions of measurement result, usually from the MPI -S to MPI -R between the main optical channel prices. The optical path penalty caused by the reflected light reflected power costs, the dispersion power penalty caused by chromatic dispersion and nonlinear power penalty caused by nonlinear effects. AES of the optical amplifier noise is caused by the OSNR drop caused by the reduction of receiver sensitivity. In general, the 2dB maximum is allowed by the system.

Technical Measures to Overcome the Limit in Optical Fiber Transmission System

Technical Measures to Overcome the Limitations of the System Optical Power

Reduce the loss of the optical path can only reduce the optical power limit, while the use of optical amplifiers can reduce or overcome the limit of the system optical power, and thus a fundamental solution to the problem of the transmission distance is limited due to the loss of the

optical path. Optical amplifiers (OA) a variety of forms [6] At present, the practical optical amplifiers have semiconductor optical amplifier (SOA) and erbium-doped fiber amplifier (EDFA). Among them, the EDFA has a lot of commercialization and engineering.

Doped fiber amplifier to use the rare earth ion incorporation into the core of the quartz fiber as the gain medium to achieve the amplification of optical signals in the excitation of the pump light Characteristics of the amplifier by doping elements in the decision, rather than from the media the role of quartz fiber There are many different rare earth elements, such as erbium (Er), holmium (Ho), neodymium (Nd) and praseodymium (Pr) and other rare earth metal ions, can be used to implement the different wavelengths of light amplifier. These wavelengths ranging from visible light to a wide range of infrared light, up to 2.8 among them, the erbium-doped fiber amplifiers and praseodymium-doped fiber amplifier work at 1.55 and 1.31 of the wavelength range, with excellent characteristics of high gain, high power and wide bandwidth. In particular, Erbium-doped fiber amplifier (EDFA) has led to great changes of the optical fiber communication technology

Technical Measures to Overcome the Chromatic Dispersion Limit of the System

Polarization mode dispersion refers to the differential group delay between the two orthogonal polarization modes in the single-mode fiber, digital manipulation pulse broadening error.

For application in a given time and optical frequency of the single-mode fiber, there is always the two is called the principal states of polarization (PSP) of the orthogonal polarization state. Sure sign of monochromatic light only inspire principal states of polarization does not occur due to polarization mode dispersion -induced pulse broadening. Sure sign of monochromatic uniform incentives of these two polarization states will occur due to polarization mode dispersion -induced pulse broadening

Single-mode fiber structure is completely axisymmetric (round and uniform), the two principal states of polarization in optical fibers with the same group velocity spread. Axis asymmetry (oval) or by external factors, the two principal states of polarization with a different group velocity propagation form the fast axis and slow axis on the transmission speed. The result is that the two mutually orthogonal polarization modes reach the fiber side, resulting in different group delay. Mode field polarization direction changes randomly along the fiber direction of propagation, and thus the output of the fiber polarization dispersion, two mutually perpendicular polarization mode per unit length of the transmission delay difference between the phenomenon usually called polarization mode dispersion (PMD), differential group delay (DGD), the unit is ps/km².

To overcome the system dispersion limit is to remove or reduce the factors that produce dispersion, or the optical transmission system for dispersion compensation. We can use the low-dispersion optical cable. Suppression measures can be taken to the spectral width to expand the spectral range of the laser modulation bandwidth, chirp, self-phase modulation. The new tune N / demodulation. Wavelength division multiplexing and other technology can also be used to reduce the transmission rate of a single wavelength.

At present, the practical engineering methods into three categories, there are nine measures, please see Table 1.

Conclusion

This paper developed a deep research in the optical transmission constraints and technical measures to overcome the constraints which limit the depth of Optical transmission Limited transmission distance of optical transmission network factor is always following the continuous development of telecommunications transmission technology, innovation and change. The past ten years, telecommunications technology with each passing day, the rapid development of optical transmission network experienced a shift from PDH, SDH, DWDM and other qualitative and leap. In the foreseeable future, optical transmission technology breakthrough from the increase in single-wave transmission rate and improve of the system transmission capacity.

Table 1 The main measures to overcome the system dispersion budget

Methods		Technical measures
External modulator		EA external modulator
		Mach-Zehnder (MZ) modulator
Linear dispersion adjustment technology	Passive dispersion compensation	Dispersion compensation fiber
		Chirped fiber grating
	Active dispersion compensation	Linear pre- chirp method
		Dispersion supported transmission method
		The mixed modulation of amplitude modulation and phase modulation
Non-linear dispersion accommodation		Self- phase modulation technology
		Middle spectrum inversion technique

References

- [1] Deng Zhongli Synchronous optical transmission network and wavelength division multiplexing systems, Beijing: North Jiaotong University Press, 2003.
- [2] Wang Shao Li, Wei's visit. Fiber principles and technology. Beijing: Science Press, 2005
- [3] Zhao Zisen Optical fiber communication engineering Beijing: People's Posts and Telecommunications Press, 1995.
- [4] Fu Songnian, Li Zhenjun. The latest developments of DWDM optical communication systems. Communication World, 2003 (03) :19 -21
- [5] Mao Qian. Several issues related to optical fiber communication system design. Design techniques of Posts and Telecommunications, 2002 (08) :5 -1
- [6] Feng Jianhe, Ji Yuefeng, Guan Kejian. To forward error correction to improve the performance of high-speed optical transport network analysis. Optical Communication Technology, 2001 (01, 35 -38)

Study on the Methods of Measuring Magnetic Field

Shikun ZHU

Three Gorges University, Yichang, Hubei 443002, China

Keywords: Magnetic-flux; E.H. Hall Effect; Nuclear Magnetic Resonance; Methods of Measuring the Magnetic-field

Abstract. To improve the capability of magnetic and to develop new magnetic all needs according to the parameter of various magnetic; the important way to get the parameter of magnetic is measuring magnetic. The mean content of measuring magnetic is measuring magnetic-field. This essay sets forth some essential laws of physical and relative to effect, treats many methods of measuring the magnetic-field and some problems which must be pay attention. Be willing to perform some function of deeply research about magnetic-field.

Introduction

Magnetic-field measurement is the most widely applied technology of magnetic measurement. It is not only of significance to studies in all areas of solid physics, but also makes an important contribution to studies in related subject fields. There are many methods of measuring magnetic field. In this paper, several important methods, which are commonly used in practices, are introduced.

Magnetic-flux Measurement Method

In magnetic-flux measurement based on Faraday's electromagnetic induction law, a detecting coil with N number of turns and an area of S is placed in a measured magnetic field B ; included angle between axes and magnetic-field direction of coil is φ ; if size of magnetic field B or included angle φ changes, induced electromotive force e is generated between leads of coil because of change in magnetic-flux ϕ of coil. According to Faraday's electromagnetic induction law, $e = \frac{d\phi}{dt}$ can be solved, and the integral is as follows.

$$\Delta\phi = \int edt \quad (1)$$

And also,

$$\Delta\phi = \Delta(N\vec{B} \cdot \vec{S}) = NS\cos\varphi\Delta B + NSB\Delta\cos\varphi \quad (2)$$

Therefore, change $\Delta\phi$ of flux can be realized through changes of magnetic field in coil, or changes of the included angle between axes and magnetic-field direction of coil. Two simple cases are considered.

If $\varphi=0$ (magnetic field direction and coil axes are parallel), magnetic field is turned off, or coil is parabolically moved to magnetic field $B=0$, and then $\Delta\phi = NSB$ is substituted into equation (1) to gain the following.

$$B = \frac{1}{NS} \int edt \quad (3)$$

If magnetic field B does not change, coil direction is relative to magnetic-field reverse direction, namely ϕ changes from 0° to 180° , and the $\Delta\phi = 2NSB$ is substituted into equation (1-1) to gain the following.

$$B = \frac{1}{2NS} \int edt \quad (4)$$

In equations (3) and (4), NS is known, and thus magnetic field B can be measured if $\int edt$ is measured. Time integral $\int edt$ of induced electromotive force can be measured with integrator. There are many types of integrators, and ballistic galvanometer can be used first for the measurement. For example, detecting coil is placed in magnetic field and connected with impact galvanometer in series; if magnetic flux in detecting coil instantaneously changes, the generated induced electromotive force e makes ballistic galvanometer impacted and deflected, and the maximum deflection angle is as follow.

$$\alpha_m = s_\phi \int edt = s_\phi \Delta\phi \quad (5)$$

$$\Delta\phi = \frac{\alpha_m}{s_\phi} \quad (6)$$

In equations (5) and (6), s_ϕ is magnetic-flux sensitivity, which can be calibrated with changes of known magnetic-flux generated by mutual inductor [1]. Constant magnetic field higher than 10^{-6} T can be measured with ballistic galvanometer; the measurement accuracy is between 1% ~ 2%; errors mainly source from affects of instantaneous changes of magnetic flux as well as stray flux. Electronic magnetic-flux meter was researched and development latter, which integrates induced electromotive force e of detecting coil with electronics methods. Therefore, magnetic field changing with time can be measured with it, and also it is easy to realize measurement automation and digitization; resolution can reach 10^{-9} T.

It is worth noting that detecting coil is a sensitive component of magnetic flux measurement, and its measured magnetic field is the mean of detecting coil volume [2-3].

Hall Effect Measurement Method

A piece of rectangular semiconductor material with a thickness of d is placed in a magnetic field; if a rectangular coordinate is established, its magnetic field B keeps consistent with thickness d along the z -axis direction, its length and width are along the x -axis and y -axis directions respectively; if current i is turned on along the length direction of semiconductor, Hall electromotive force U_H is generated along the direction vertical to B and i as follows.

$$U_H = R_H \frac{iB}{d} \quad (7)$$

In equation (7), R_H is Hall's coefficient; if current i is constant, Hall electromotive force U_H and measured magnetic field B are directly proportional, and U_H can be used as a measure of magnetic field. In addition to meter errors, the accuracy of Hall Effect measurement can be affected by the factors below.

Hall's Coefficient Varies along with Temperature

Methods of reducing this error are shown in the following. First, Hall components with a small Hall temperature coefficient can be selected. Second, supply current below 100 mA can be selected, so as to prevent the heating of Hall components. Third, devices with constant temperature or temperature compensation can be applied.

Magneto-Resistance Effect Makes Hall Components Change

Magneto-resistance effect makes Hall components change, thus making working current change. The solution to this problem is applying constant power supply.

Error of Inequipotential Electromotive Force

Error of inequipotential electromotive force is caused by inappropriate positions of electrodes of Hall components. If measured magnetic field is 0 and only if working current (i) is turned on, U_H has certain value, which is called as inequipotential electromotive force. To eliminate its impact, a compensation circuit can be constituted with resistance and potentiometer as long as proper adjustment can be achieved.

According to the Hall Effect field measurement meter made based on the principle of Hall Effect, the widths of measurement scopes of direct current, alternative current, pulse magnetic field, and magnetic field can be measured, reaching a magnitude order of 10^{-4} -10T and having a high sensitivity. It has been widely applied at present^[4].

Nuclear Magnetic Resonance Measurement Method

According to the principle of quantum mechanics, in the system composed by any particles, all particles have intrinsic magnetic moment μ and related intrinsic momentum moment p and the relationship between the two sides can be expressed as follows.

$$\mu = \gamma p \quad (8)$$

In equation (8), γ is called as gyromagnetic ratio, and has different values for different particles. For example, gyromagnetic ratios of Hydrogen nucleus (proton) and lithium nucleus that are commonly used in magnetic-field measurement of nuclear magnetic resonance are shown below.

$$\gamma(^1H) = 3.3618 \times 10^2 \text{ m} \cdot \text{A}^{-1} \cdot \text{s}^{-1}$$

$$\gamma(^7Li) = 1.3064 \times 10^2 \text{ m} \cdot \text{A}^{-1} \cdot \text{s}^{-1}$$

Intrinsic momentum moment of particles can be expressed as follows.

$$|p| = \sqrt{J(J+1)}\hbar \quad (9)$$

In equation (9), \hbar is simplified reduced Planck constant ($\hbar = \frac{h}{2\pi} = 1.05457266 \times 10^{-34} \text{ J} \cdot \text{S}$); h is reduced Planck constant; J is quantum number of system. If external magnetic field does not exist, particle is in an energy state marked with quantum number J , called as energy level. If the particle system is in the constant magnetic field B_z along z -direction, the energy level with J number of quantum is divided into $2J+1$ number of hyperfine energy levels. Such a phenomenon is called as Zeeman Effect. Each hyperfine energy level is marked with magnetic quantum number m_J ($m_J = J, J-1, \dots, -J$), and $2J+1$ number of values can be applied. Thus, the energy of each hyperfine energy level can be expressed as follows.

$$E = -\vec{\mu} \cdot \vec{B} = -\gamma p_z B_z = -\gamma \hbar m_J B_z \quad (10)$$

In equation (10), p_z is the projection of angular momentum in magnetic field direction ($p_z = m_j \hbar$). The energy difference between two adjacent hyperfine energy levels is as follows.

$$\Delta E = |\gamma| \hbar B_z \quad (11)$$

From equation (11), it can be seen this difference has a tie with value of external magnetic field B_z , and is corresponding to the energy $\hbar \omega_0$ of a photon. That is, if the system's particles transition among these hyperfine energy levels, electromagnetic wave with frequency ω_0 needs to be absorbed or radiated. According to the principle of quantum mechanics, in addition to the transition of $\Delta m_j = 0$, absorbed and radiated electromagnetic waves are circularly polarized waves and polarization planes are vertical to B_z if particles transition between adjacent energy levels ($\Delta m_j = \pm 1$).

Therefore, if a RF magnetic field $B_1 \cos \omega t$ is added in the system along the direction vertical to B_z and also $\omega = \omega_0$ can be established, particles of the system in a low energy level will absorb energy from RF magnetic field and then transition to a adjacent and higher level, and this is magnetic resonance [5-8], which is nuclear magnetic resonance for a nuclear system. The relationship between resonant frequency and magnetic field can be expressed as follows.

$$\omega_0 = |\gamma| B_z \quad (12)$$

For a given nucleus, $|\gamma|$ has been accurately determined. Therefore, as long as the frequency ω_0 of radiofrequency field in nuclear magnetic resonance is measured, measured magnetic field can be solved. Generally, the measuring accuracies of frequency and gyro-magnetic ratio are very high. Therefore, the accuracy of nuclear magnetic resonance measurement can reach $10^{-5} \sim 10^{-6}$, and hence it can be used for calibrating other magnetic field measurement methods [3].

Optical Pumping Magnetic Resonance Measurement Method

Optical pumping magnetic resonance is an experiment technology that dynamically combines light pumping, magnetic resonance and optical detection so as to research fine and hyperfine structures of steam atoms [9-10].

Hyperfine Structure and Zeeman Splitting of Rubidium Energy Level

Hyperfine structure of atomic energy level is generated from the interaction of nuclear magnetic moment and electron magnetic moment of atoms; if atoms are in weak magnetic field B , energy level can be further split by the interaction of total magnetic moment and electron magnetic moment into equidistant Zeeman sub-energy levels, which are shown below.

$$E = -\mu_F \cdot B = g_F m_F \mu_B B, \quad m_F = F, F-1, \dots, (-F)$$

$$g_F = g_J \frac{F(F+1) + J(J+1) - I(I+1)}{2F(F+1)}, \quad F = I + J, \dots, |I - J|$$

$$g_J = 1 + \frac{J(J+1) - L(L+1) + S(S+1)}{2J(J+1)}, \quad J = L + S, \dots, |L - S|$$

In above equation, F is the total quantum number of atoms; S and L are electron spin and orbital quantum number respectively; i is spin quantum number of atoms; J is the total quantum number of LS coupling electrons. The difference among all energy levels is as follows.

$$\Delta E = g_F \mu_B B \quad (13)$$

Ground base of rubidium is $5^2S_{\frac{1}{2}}$ ($L=0, S=\frac{1}{2}$); minimum excited state is a doublet state of $5^2S_{\frac{1}{2}}$ and $5^2S_{\frac{3}{2}}$ ($L=0, S=\frac{1}{2}$); J is $\frac{1}{2}$ and $\frac{3}{2}$ respectively. The transition from $5^2S_{\frac{1}{2}}$ and $5^2S_{\frac{3}{2}}$ can generate a line D_1 with a wavelength of 7948 \AA ; the transition from $5^2S_{\frac{3}{2}}$ and $5^2S_{\frac{1}{2}}$ can generate a line D_2 with a wavelength of 7800 \AA . I of two isotopes ^{87}Rb and ^{85}Rb of rubidium is $\frac{3}{2}$ and $\frac{5}{2}$ respectively.

Maintenances of Light Pumping Effect and Polarization

In magnetic field, the number of atoms is distributed at each energy level based on Boltzmann Effect; if steam atoms are illuminated with left circularly polarized light $D_1\sigma^+$, the following equation can be established according to light transition selection rule.

$$\Delta F = 0, \pm 1, \quad \Delta m_F = +1 \quad (14)$$

Maximum value of m_F at Zeeman sub-energy level of $5^2S_{\frac{1}{2}}$ state of ^{87}Rb is $+2$, and thus the upper transition of atoms at energy levels of $5^2S_{\frac{1}{2}}$, $F=2$ and $m_F=+2$ can't be excited, and atoms at other energy levels of $5^2S_{\frac{1}{2}}$ can absorb light $D_1\sigma^+$ and transition to all energy levels of $5^2S_{\frac{1}{2}}$. If $5^2S_{\frac{1}{2}}$ spontaneously radiates to $5^2S_{\frac{1}{2}}$ state, atoms almost can return to all sub-energy levels of $5^2S_{\frac{1}{2}}$, including energy levels of $F=2$ and $m_F=+2$. After excitement and spontaneous radiation for many times, a large number of atoms are pumped to ground states $F=2$ and $m_F=+2$ sub-energy levels, and thus an unbalanced distribution (i.e. polarization) of atoms at all energy levels is produced. Similar cases can be illuminated with left circularly polarized light $D_1\sigma^-$, and finally atoms are gathered in the $F=2$ sub-energy level. Thus, strong magnetic resonance signals can be gained with polarization. ^{85}Rb is pumped to the $m_F=+3$ sub-energy level.

The process of unbalanced distribution state returning to the balanced distribution state is called as relaxation process; polarization caused by light pumping can get back to Boltzmann distribution through relaxation process.

Magnetic Resonance Magnetic Field Measurement between Zeeman Sub-Energy Levels

In weak magnetic field, energy difference between adjacent Zeeman Sub-energy Levels is $\Delta E = g_F \mu_B B$; if a RF magnetic field B_1 with frequency ν is added in the plane vertical to B and the magnetic resonance condition below is satisfied,

$$h\nu = \Delta E = g_F \mu_B B \quad (15)$$

⁸⁷Rb is pumped to ground states $F=2$, and a large number of atoms at the $m_F = +2$ energy level can absorb energy of B_1 and transition to state $m_F = +1$, and also can transition from state $m_F = +1$ to state $m_F = +0$, etc. Because of continuous illumination from light $D_1\sigma^+$, light pumping exists and thus atoms are pumped to the $m_F = +2$ sub-energy level. Thus, pumping and transition make atoms achieved a balance. In magnetic resonance, the number of atoms at the $m_F \neq +2$ sub-energy level is larger than that of non-resonance. Therefore, the absorption of $D_1\sigma^+$ increases; magnetic resonance signals can be gained after changes of $D_1\sigma^+$ are measured. Thus, resonant frequency ν is measured; if g_F of sample atom is known, magnetic field B can be solved based on equation (4-2). Because a low-frequency RF photon is cleverly converted to a light-frequency photon (10^8 MHz), 7~8 magnitude orders can be increased for signal power.

In the actual work, the application of methods should be based on actual conditions. In general, the magnetic field measurement scopes and types, which are necessary to be measured in different fields and different circumstances, are significantly different.

References

- [1] Shuwu Yang. Ordinary Physical Experiment (Vol.2, Electromagnetism) [M]. Beijing: Higher Education Press, 2000, 153-154.
- [2] SiHua Lv, Yinkang Zhu. Modern Physics Experiment Technology [M]. Beijing: Higher Education Press, 1993, 325~326.
- [3] YaRu Zhang, MuJie Lan, DongGong Wang. Current Situation and Future Development of Studies on Micro-magnetic Fluxgate Sensor [J]. Journal of Telemetry, 2002, (4): 1-7, 16.
- [4] Yourui Tu. History and Future of Semiconductor Magnetic Field Sensors [J]. Sensor World, 2003, (11): 1-9.
- [5] Leshan Dai, Daoxuan Dai. Modern Physics Experiment [M]. Shanghai: Fudan University Press, 1995, 165-167.
- [6] Sicheng Wu, Zuquan Wang. Modern Physics Experiment [M]. Beijing: Peking University Press, 1995.330~342.
- [7] Xiaoran Zhou, Xiankai Zhao, Xi'An Tan, et al. Textbook of Modern Physics Experiment [M]. Wuhan: Wuhan University Press, 1996, 325~336.
- [8] Zhenshun Sha, Runsheng Huang. New Modern Physics Experiment [M] Nanjing: Nanjing University Press, 2001.274~286.
- [9] MuXin Lin. Textbook of Modern Physics Experiment [M]. Beijing: Science Press, 1999, 277-284.
- [10] TianZhe Zhang, You'er Dong. Modern Physics Experiment [M]. Beijing: Science Press, 268~275.
- [11] QiJun Pan, WeiMing Ma, Zhihua Zhao, et al. Development and Application of Measurement Method for Magnetic Field [J]. Transactions of China Electrotechnical Society, 2005, (3): 7-13.
- [12] Zhipeng Jiang, Zhao Wei, Kaifeng Qu. Development and Application of Magnetic Field Measurement Technology [J]. Electrical Measurement & Instrumentation, 2008, (04): 1-5.
- [13] Daming Li. Magnetic Measurement Lecture [J]. Electrical Measurement & Instrumentation, 1989 (10): 41~47, 21.
- [14] Haiying Chen. The Developments and Applications of High Specification Magnetometers [J]. Modern Instruments, 2000 (6): 5-7.

Study on Wear Behaviors and Grain Effects of PCD Cutting Tools in Turning Granite

Shenzhuo Liu^{1, a}, Zili Kou^{1, a, *}, Rui Zhang^{1, b}, Chengliang Liu^{1, c}, Yu Li^{1, d},
Rongqi Li^{1, e}, Xiaozhi Yan^{1, f}

¹Institute of Atomic and Molecular Physics, Sichuan University, Chengdu 610065, China

^aliushenzhuo@126.com, ^bruizhang1985@126.com, ^chliuchengliang8888@yahoo.cn,

^dliyu2692@163.com, ^elirongqi1985@163.com, ^f894587313@qq.com

*Author to whom correspondence should be addressed. Electronic mail: kouzili@scu.edu.cn

Keywords: Polycrystalline Diamond (PCD); Wear; Grain Effects;

Abstract. In this paper, three types of polycrystalline diamond (PCD) tools marked as PCD 030, PCD 010 and PCD 005 (equivalent to 30, 10, and 5 μ m average grain size of original diamond) were tested, and their wear behaviors was studied. The wear of PCD cutting tools in machining granite bars was investigated by a turning process. The experiments were carried out under wet condition. Wear volume was measured by optical microscopy and wear morphology was examined by scanning electron microscopy (SEM) and optical microscopy. By comparing the flank face, the experiments results show that the PCD tools with coarse original diamond grain size have long life at three cutting speeds, and the tool life of the three PCD tools decreases with the increase of cutting speed. SEM morphology by secondary electron image analysis indicates that the dominant wear mechanism for PCD 010 and PCD 005 is abrasive wear. While for PCD 030, the abrasive wear mechanism is predominant wear in the machining, occasionally some cleavage wear are also observed.

Introduction

Due to the high hardness, good wear resistance, especially the isotropy and electrical conductivity compared with single crystalline diamond, PCD has gained wide acceptance in the machining of non-traditional materials such as metal–matrix composites (MMCs), reinforced epoxies, ceramics, plastics, wood products, and non-ferrous metals [1-3]. The wear mechanisms of PCD for machining these materials have been discussed widely. Abrasive, micro-cracking, fatigue and adhesive wear mechanisms were found in the machining of some MMCs [4-10]. But the wear mechanisms of PCD tools are various in machining different materials. There has been little literature on the wear mechanisms of using PCD tools to machine granite. This paper attempts to show the wear mechanisms and influences of original diamond grain size on the wear process of PCD tools in turning granite bars. This will increase our understanding of the wear behaviors of PCD tools in turn granite.

Experimental Details

Material Detail and Machining Conditions

The machined material is granite bars named Sesame White with modest hardness. The granite bars were cut into about 80 mm in diameter cylinders beforehand. Table 1 shows the chemical composition of the material.

Table 1 Chemical Composition of Granite

SiO ₂	Al ₂ O ₃	K ₂ O	Na ₂ O	CaO	FeO	Fe ₂ O ₃	MgO	TiO ₂	P ₂ O ₅	MnO
72.04%	14.42%	4.12%	3.69%	1.82%	1.68%	1.22%	0.71%	0.30%	0.12%	0.05%

The experiments were carried out with conventional water-oil emulsion as a flood coolant. The cutting speeds selected in the experiments were 120, 150, and 180 m/min. The depth of cut was kept constant at 0.15mm. The feed rate used in the experiment was 0.1 mm/rev. Arrangements of cutting parameters are listed in Table 2. Three types of PCD tools were used in the experiments. Tool wear was measured under optical microscope and tool life for machining granite bars has been recorded. SEM analysis has been carried out on the worn tools to determine the tool wear mechanisms.

Table 2 Process parameters in different machining sets

Cutting test	Cutting speed (m/min)	Feed rate (mm/rev)	Depth of cut (mm)
	120, 150, 180	0.1	0.15

CNC turn machine. A Computerized Numerical Control (CNC) lathe SK50P/750 made in China was used for the machining test, employing constant linear velocity to turn the rotating granite bars with constant cutting depth and feed speed. This machine has both functions of constant cutting speed and constant feed rate per revolution. Even with a facing operation where the tool moves across the radial direction, constant cutting speed and feed rate can be maintained and used to evaluate the machining performance.

Cutting tools and machining parameters. The PCD tools used in the tests were produced in our laboratory (Large Volume Pressure laboratory of Sichuan University). To examine the effects of different grain sizes, three kinds of PCD inserts were used in the cutting tests. The three PCD inserts were marked as PCD 030, PCD 010 and PCD 005 (equivalent to 30, 10, and 5 μ m average grain size of original diamond). Fig.1 shows the surface morphologies by backsattered electrons image of the three polished PCD inserts. Dark particles are diamond grains, light areas are Co compounds. The difference of diamond grain size can be clearly observed from Fig.1. Generally, the amount of binder phase in PCD layer decrease of original diamond grain size. The approximate weight content of cobalt binder is 6% in PCD 030, 7% in PCD 010, 10% in PCD 005. The assembled tool geometry is given in table 3.

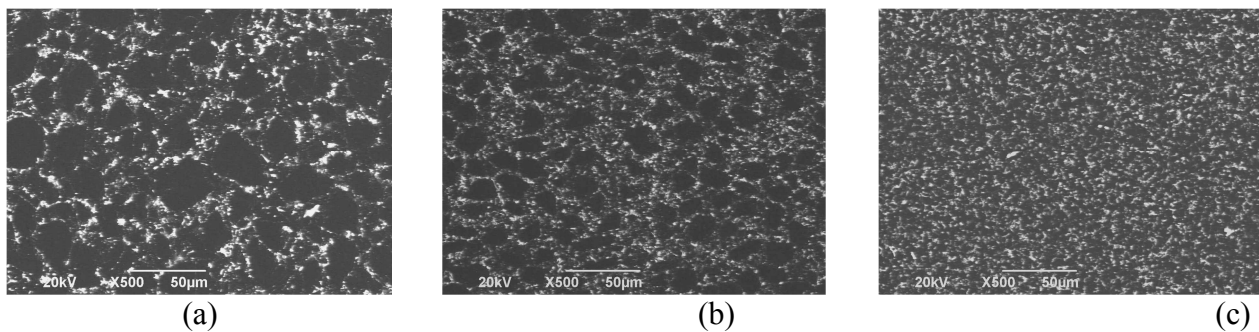


Fig. 1 The surface morphologies of three polycrystalline diamonds: (a) PCD 030; (b) PCD 010; (c) PCD 005.

Table 3 Tool geometry

Rake angle($^{\circ}$)	Relief angle($^{\circ}$)	Chamfer angle($^{\circ}$)	Chamfer length(mm)	Approach angle ($^{\circ}$)
-5	5	20	0.2	95

Wear Measurement

Generally, the end of tool life is determined by excessive wear on the flank face at conventional cutting speed. For each cutting speed selected, the time and the flank wear produced on various PCD tools was recorded. Topography of worn tool surfaces can infer which mechanisms have been dominant during the tool wear process [11]. In the machining tests, the flank wear land (V_b) was analyzed with an optical microscope for dimensional measurements. The SEM was used for wear characterization. During the machining tests, the maximum flank wear land width of the PCD tools were measured and recorded after each pass (330 mm cutting length per pass) until the tools failed. The failure criterion due to wear on the flank face was set for a maximum when $V_b=0.4$ mm.

Morphology of the Tool Surface

The flank face and cutting edge of a fresh PCD tool are shown in Fig. 2 (a) and (b), respectively. It is observed in Fig.3 that the tool wear mainly takes place on the flank face and the tool wear volume becomes larger with time (Fig.3(c) and (f)). The time required to reach the tool wear limit decreases with speeds increased. The wear on the rake face is not so significant in the tests. (Fig.3 (g) and (j))

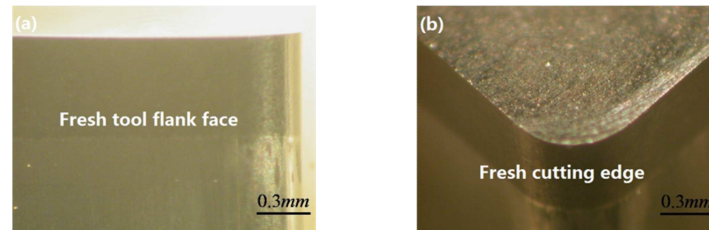


Fig. 2 Optical microscope images of a fresh tool :(a) flank face;(b) rake face.

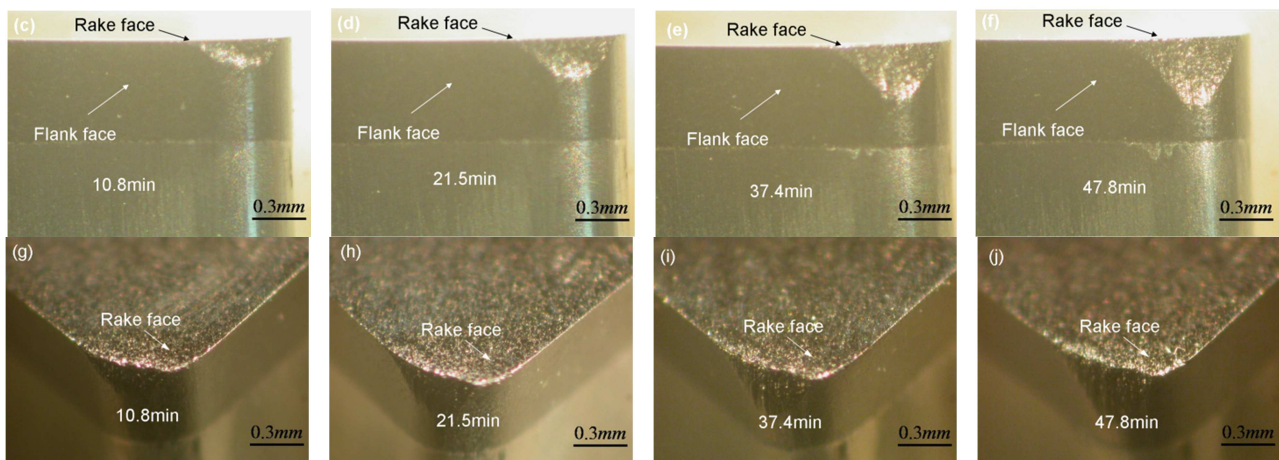


Fig. 3 Optical microscope images of a tool flank face (c-f) and rake face (g-j) at different cutting time (PCD 030, in wet condition, cutting speed: 120 m/min, feed rate: 0.1 mm/rev, and depth of cut: 0.15 mm).

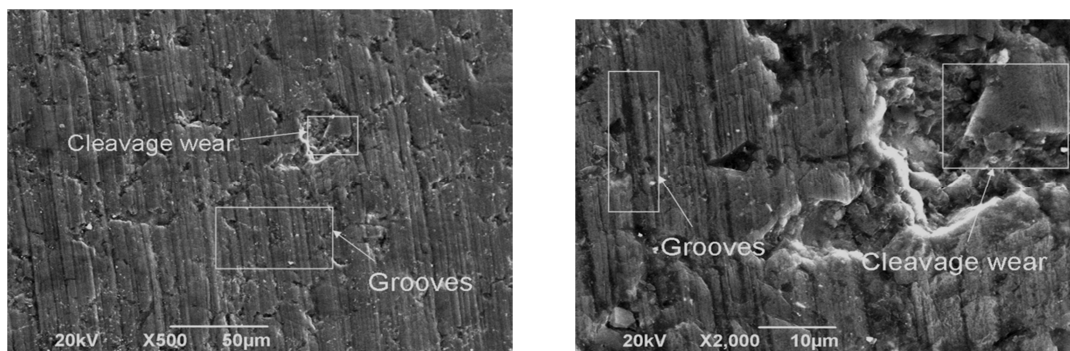


Fig. 4 SEM images of PCD 030 used in the test to machine granite bar at 120m/min for a maximum flank wear of 0.4 mm.

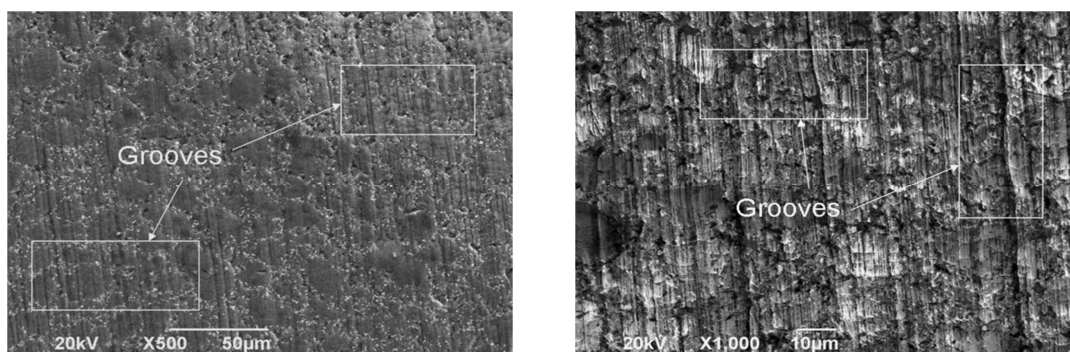


Fig. 5 SEM images of PCD 010 used to machine granite bar at 120 m/min for a maximum flank wear of 0.4mm.

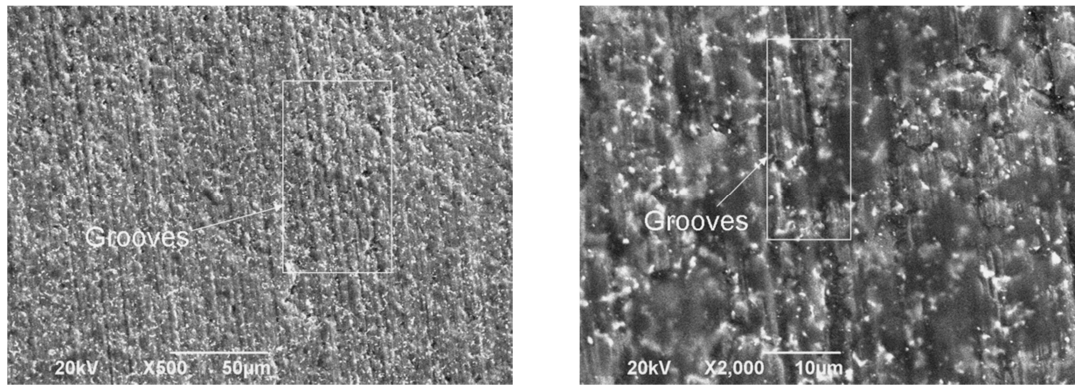


Fig. 6 SEM images of PCD 005 used to machine granite bar at 120 m/min for a maximum flank wear of 0.4 mm.

Fig.4-6. show the typical micro SEM morphology by secondary electron image of PCD used to cut the work piece at the speed of 120 m/min for a cutting time to the maximum wear on the flank face 0.4 mm. From Fig 4-6 grooves morphology can be observed clearly. The observed grooves on the flank wear scars indicate that abrasion was the dominant wear mechanism [12]. The grooves were assumed to be formed due to abrasion by the particles of SiO_2 and/or Al_2O_3 . Meanwhile, cleavage morphology can be observed on the typical micro SEM morphology by the secondary electron image of PCD 030, this kind of morphology usually occurs in the partial region of tool wear. Due to the binder phase in PCD, the toughness of PCD is much higher than single crystalline diamond. This decreases the rate of brittle rupture in PCD. This is one reason why the cleavage morphology is only produced in partial regions. The inherent cleavage cracks generate in high temperature and high pressure synthesis also contribute to the formation of cleavage wear [13].

Effects of Cutting Speed and Original Diamond Grain Size in PCD

The machining experiments show the effects of original diamond grain size on flank wear in PCD tools. Fig.7 shows the wear resistance of the three PCD tools expressed as cutting life, plotted against original diamond grain size at different cutting speeds (120, 150, and 180 m/min). Tool life was significantly influenced by temperature generated and the forces exerted at, or near the cutting edge of the tools. Therefore, changes in cutting speeds will directly influence the cutting forces and temperature generated, and hence the PCD tool lives were reduced significantly as the cutting speed increased. The longest tool life occurs in the tool of PCD 030 at the three cutting speeds, which means it has the best cutting performance. This tendency of wear with diamond grain size had been mentioned in the report of Q.S. Bai, who thought that PCD with coarse grain size ($25\mu\text{m}$) had longer tool life than that with fine grains in machining laminated flooring [14]. The size of original grain plays an important role in the wear of PCD. Usually, the wear resistance and hardness of PCD with coarse grains is higher, as proved in the experiments. However, the impact toughness becomes much lower than that with coarse grain size, which can induce poor cutting performance under sever intermittent machining conditions. So it is advisable to use PCD with much coarser diamonds .g.PCD 030) in the machining of granite when not under sever machining conditions.

Conclusions

In this study, the cutting performance, wear mechanisms and grain effects of three types of PCD cutting tools were studied in turning granite bars with flood coolant at three different speeds. Based on the results obtained, the following conclusions can be drawn:

The predominant wear was the one which developed in the flank face of the tools in turning granite.

SEM morphology by secondary electron image analysis indicates that the dominant wear mechanism for PCD 010 and PCD 005 is abrasive wear. While for PCD 030, the abrasive wear mechanism is predominant wear in the machining, occasionally some cleavage wear are also observed.

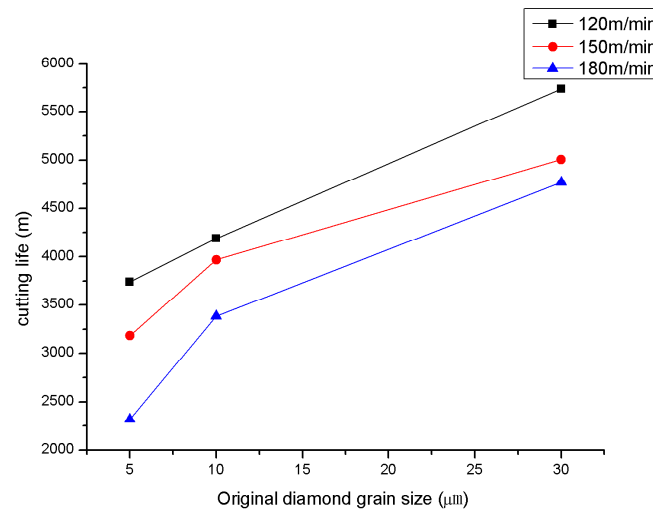


Fig. 7 Cutting life curves of PCD tools with various original diamond grain sizes.

The performance of three types of PCD cutting tools have been investigated in terms of tool life and wear mechanisms under different cutting speeds. By comparing the flank face, the experiments show that the PCD tools with coarse original diamond grain size have longer life at three cutting speeds, and the tool life of the three PCD tools decreases with the increase of cutting speed. Also results from this study show that the size of original diamond grains in PCD tools influences wear properties of tool greatly. PCD with coarse grains shows an excellent cutting performance during turning granite. Among the three PCD tools used in the cutting tests, PCD 030 has the longest tool life in turning granite.

Acknowledgements

This work was supported by the National Natural Science Foundation of China-NSAF (Grant No. 51072123).

References

- [1] J.Paulo Davim, A. Monteiro Baptista, Relationship between cutting force and PCD cutting tool wear in machining silicon carbide reinforced aluminium, *Journal of Materials Processing Technology* 103 (2000) 417-423.
- [2] K. Palanikumar, Application of Taguchi and response surface methodologies for surface roughness in machining glass fiber reinforced plastics by PCD tooling, *Int J Manuf Technol* (2008) 36:19-27.
- [3] P.Philbin, S. Gordon, Characterisation of the wear behaviour of polycrystalline diamond (PCD) tools when machining wood-based composites, *Journal of Materials Processing Technology* 162-163 (2005) 665-672.
- [4] R.M. Hooper, J.L. Hen shall, A. Klopfer, The wear of polycrystalline diamond tools used in the cutting of metal matrix composites, *International Journal of Refractory Metals & Hard Materials* 17 (1999) 103-109.
- [5] K.Weinert, A consideration of tool wear mechanism when machining metal matrix composite (MMC), *Ann. CIRP* 42 (1993) 95-98.
- [6] J.E. Caroline, Andrewes, H.Y. Feng, W.M. Lau, Machining of an aluminum/SiC composite using diamond inserts. *Journal of Materials Processing Technology* 102 (2000) 25-29.

-
- [7] J. Paulo Davim, Diamond tool performance in machining metal–matrix composites. *Journal of Materials Processing Technology* 128 (2002) 100–105.
- [8] Y. Kevin Chou, Jie Liu, CVD diamond tool performance in metal matrix composite machining, *Surface & Coatings Technology* 200 (2005) 1872 – 1878.
- [9] J.A. Arsecularatne, L.C. Zhang, C. Montross, Wear and tool life of tungsten carbide, PCBN and PCD cutting tools, *International Journal of Machine Tools & Manufacture* 46 (2006) 482–491
- [10] I. Ciftci, M. Turker, U. Seker, CBN cutting tool wear during machining of particulate reinforced MMCs, *Wear* 257 (2004) 1041-1046.
- [11] Y. Kevin Chou, Chris J. Evans, Moshe M. Barash, Experimental investigation on CBN turning of hardened AISI 52100 steel, *Journal of Materials Processing Technology* 124 (2002) 274-283
- [12] R. Zhang, Z.L. Kou, Y.E. Dou, S.Z. Liu, Wear behaviors of PCD tools in turning granite. *Advanced materials Reserch Vol 337* (2011) pp 728-734.
- [13] Y. Li, X.L. Han, X.Q. Wang. Reserch on mechanical properties and test methods of polycrystalline diamond. *Diamond Abras Eng* 2001; 5:27-30 [in Chinese].
- [14] Q.S. Bai, Y.X. Yao , Phillip Bex , G. Zhang , Study on wear mechanisms and grain effects of PCD tool in machining laminated flooring, *International Journal of Refractory Metals & Hard Materials* 22 (2004) 111-115.

Condensing Heat Recovery of Existing Large -Scale Refrigeration System

Zheng Da -yu^{1, a} Guo Bing^{1, a} Liu Wei-dang^{2, a} Chen Xin^{1, a}

¹School of Energy and Civil Engineering of Harbin Commercial University, China

²Lianyungang Foreign Trade Cold Storage, Lianyungang China

^asuperteacher73@126.com

Keywords: Large -scale refrigeration system; Modification; Condenser; Condensing heat recovery.

Abstract: Existing refrigeration systems generally put the high temperature and pressure of refrigerant vapor into the atmosphere or cooling water through the condenser to reach the purpose of condensing refrigerant. But this will lead to the environment “thermal pollution”, and a waste of energy. This paper describes a plan of modification of the existing refrigeration system, through the waste heat recovery unit can be recovered the condensing heat effectively and product hot water in 50~ 60 °C to provide bathing. This system also can improve the refrigeration system operating conditions and the efficiency of generating units to achieve the purpose of energy saving.

Introduction

Cold storage and central air conditioning system has been increasingly common in our lives along with the improving of social progress and human living standards. Usually the cooling system is concatenation of the compressor, condenser, throttling device and evaporator as well as some auxiliary equipment series, low-temperature low-pressure refrigerant vapor is inhaled to the compressor through the suction pipe, high temperature and high pressure refrigerant vapor is produced after compressed, refrigerant condensing into a low temperature and high pressure gas-liquid mixed state through the condenser, then turn to low temperature low pressure liquid refrigerant after the throttle, the evaporation of liquid refrigerant in the evaporator to absorb heat so as to achieve the purpose of cooling, the evaporation of liquid refrigerant in the evaporator to absorb heat so as to achieve the purpose of cooling. It the condenser to the environment in the condensation process to release a large number of thermal pollution of the surrounding environment [1].

Research Content and Technical Programs

For existing large and medium-sized refrigeration system condenser condensing heat discharged directly into the environment, not only making the environment begin” thermal pollution” but also a waste of energy, now the original cooling system for technological innovation, through the design of the condensing heat recovery unit will be recovery part of the condensing heat, and then collected the condensation heat is used to heat water in the tank insulation so that waste heat into useful energy to reduce emissions of waste heat, so as to achieve the environmental objectives of energy saving[2].

Original cooling system schematic is shown in fig. 1.

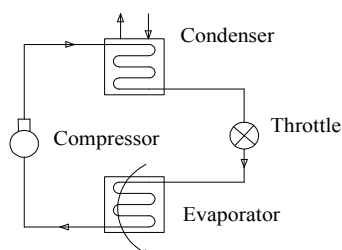


Fig.1 Basic Schematic Diagram of the Refrigeration System

Low-temperature low-pressure refrigerant vapor is inhaled to the compressor through the inspiratory tube, after compression to produce high temperature and high pressure refrigerant vapor through the condenser refrigerant condensing into a low-temperature high-pressure gas - liquid mixed state, after the throttle section the flow of liquid refrigerant into a low temperature and pressure, the evaporation of liquid refrigerant in the low pressure evaporator to absorb heat.

The refrigeration system after transformation is shown in fig. 2.

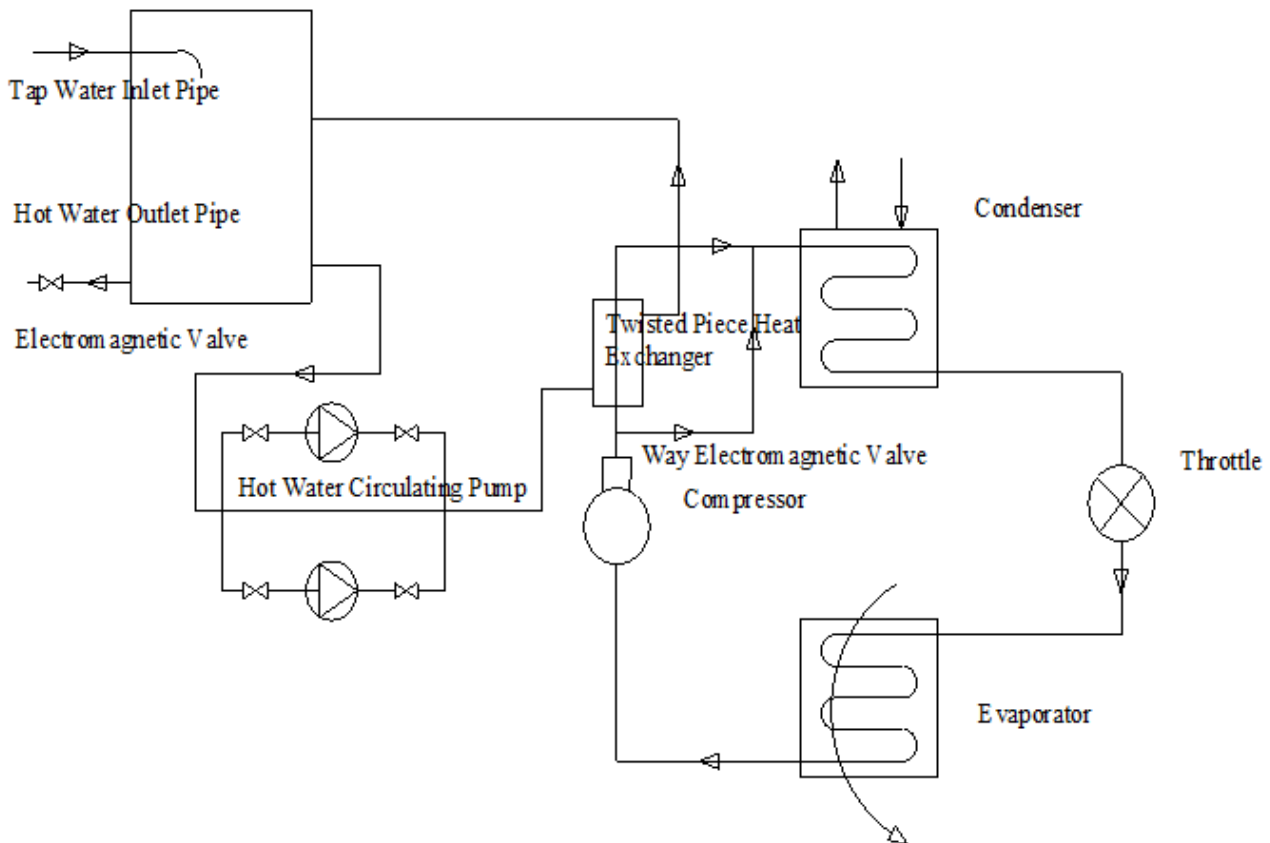


Fig. 2 The Refrigeration System after Transformation

Low temperature low pressure refrigerant vapor inhalation to the compressor through the suction pipe , after compression to produce high temperature and high pressure refrigerant vapor, turn to a lower temperature of the refrigerant vapor through the heat exchanger transfer the heat to the 20 °C water, and then through the condenser condensate into the low-temperature high-pressure gas-liquid mixed state, after the throttle the throttle into low temperature low pressure liquid refrigerant ,the liquid refrigerant in the low pressure evaporator absorbing heat through the evaporation [3] .

Heat recovery equipment including: fin heat exchanger, three-way valve, solenoid valve, tank insulation, water pumps, etc.

Work process: the tap water of 20 °C by circulating water pump pressure to reach the fin heat exchanger, after full heat exchanger into the insulation hot water tank, the circulating water pump will to stop working when the hot water temperature reaches 60 °C in insulating hot water tanks, and then 60 °C hot water by insulating pipe directly to the shower room. system begins the automatic replenishment when insulating the hot water tank water level drops below the set level, the system will to stop when it reach the level of replenishment ,then the circulating pump will to work[4].

Heat Recovery Device Energy-Saving and Refrigeration Cycle Impact

heat recovery device energy-efficient computing 20 000 t cold store cooling capacity of Lianyungang Foreign Trade Cold Storage is 1 023 5 kW , use 5 sets of piston compressors , the number of units and the model shown in Table 1 .

Unit condensing heat: $Q_k = Q_0 + N$

Where: Q_0 - Cooling capacity;
 N - Input compressor power.

Table 1 Compressor performance parameters

Model	Number of unit	Cooling capacity of standard conditions	Input power	Heat recovery
JZY8AS17	2	168	132	90
JZY812.5	2	250	95	103.5
JZY612.5	1	187.5	75	78.75

It can recovery condensation heat 544.5 kW when the 5 compressor full load operation, just open a JZY8AS17, JZY812.5and JZY612.5 in the daily operation, it can recovery waste heat 272.25kW. The temperature of the water tank insulation calculates the differential equations:

$$T \frac{d\theta}{d\tau} + \theta_0 = \theta_m$$

Where: T - the time constant; τ -the time (s);
 θ_m - the final temperature of the water in the water tank insulation can reach ($^{\circ}C$);
 θ - The water in the tank insulation instantaneous temperature ($^{\circ}C$);
 θ_0 -The recovery of waste heat (W)

$$T = \frac{G_i C_i}{KF}$$

Where: G_i - the quality of water in the tank insulation (kg);
 C_i - hot melt coefficient of water kJ/ (kg · $^{\circ}C$);
 K - Heat transfer coefficient W / (m² · K);
 F - Heat transfer area (m²).

General solution of differential equations:

$$\theta = C e^{-\frac{\tau}{T}} + \theta_m$$

Instantaneous temperature of the water in the tank insulation for the simulation and actual measurements obtained curve shows in Fig. 3and Fig. 4.

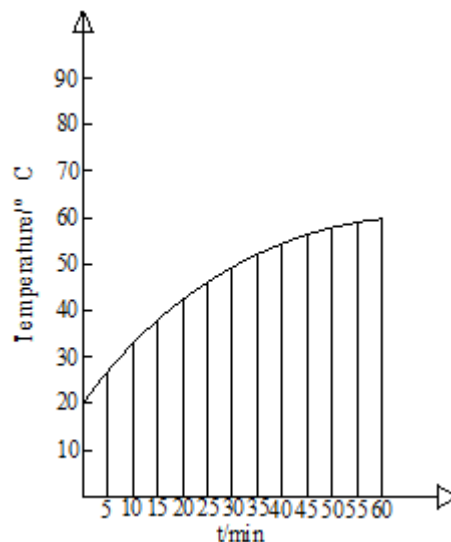


Fig. 3 The Instantaneous Temperature Curve of Water in the Water Tank Insulation Derived from Simulation and Calculation

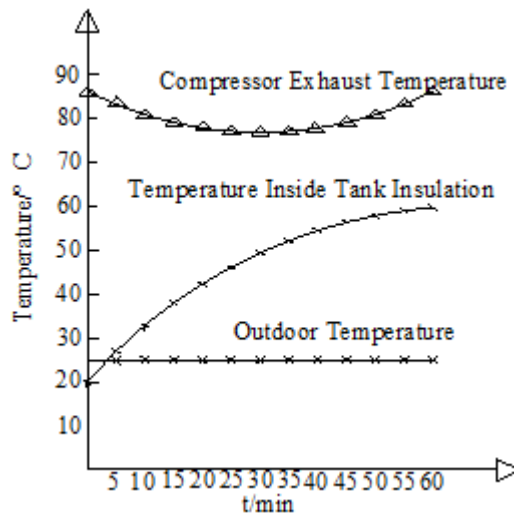


Fig. 4 Temperature Curve of Water Tank Insulation Derived from the Actual Measurements

The economic comparison (Table 2) Recovery of heat about the condensing heat

Use coal-fired boilers to prepare, assuming that the efficiency of coal-fired boiler is 30%, coal units theoretical thermal value is 29306kJ/kg, then need

$$\frac{272.25}{0.3 \times 29306} \times 3600 = 111.45 \text{ kg / h}$$

It can save 56 yuan per hour if the price of coal is 560 yuan per ton.

Use the oil-fired boiler to prepare, assuming that the efficiency of oil-fired boiler is 65%, diesel units theoretical thermal value is 42000kJ/kg, then need

$$\frac{272.25}{0.65 \times 42000} \times 3600 = 35.9 \text{ kg / h}$$

It can save 215 yuan per hour if the diesel is 6,000 yuan per ton.

Use the electric boiler to prepare, assuming that the efficiency of electric boiler is 85%, then per hour need $(272.25/0.85 \times 3600) \times 3600 = 320.3 \text{ kWh}$.

It can save 192 yuan per hour if the electricity price is 0.6 yuan / kWh.

Table 2 Each program's energy consumption table

Using the heat source	The required energy consumption	Unit price	Cost
Condensing heat recovery	1.4 kW.h	0.6yuan/kW.h	0.84
Coal	111.45 kg/h	560yuan/t	56
Diesel oil	35.9 kg/h	6000 yuan/t	215
Electricity	320.3 kW.h	0.6yuan/kW.h	192

The cost of using condensing heat recovery to prepare these heat = initial investment + operating costs.

Initial investment = solenoid valve price + fin heat exchanger price + pipeline price + two circulating pump price + a fill pump price + water tank insulation price + valve price + construction cost = 1000 + 3500 + 2000 + 530×2 + 530 + 5400 + 2000 + 4000 = 19,590 yuan

Running costs = circulating pump energy charge + supply pump energy charge = 700W×2 = 1.4 kw.

Heat recovery device on the impact refrigeration cycle Generally condensation heat of the refrigeration cycle system is taken away by the condenser, so the condenser condensate load is too large; in the design tend to increase of the condenser heat transfer area, an increase of input costs, also a waste of resources. The heat recovery unit assembly into the system can effectively reduce the load of the condenser condensate, lower compressor discharge pressure to improve the refrigeration cycle system operating conditions to improve the energy efficiency of refrigeration systems cop value [5-6].

Conclusion

Draw the following conclusions by simulation of the theoretical methods and practice

Use of such transformation method, the heat of condensation lateral environmental emissions substantially reduced, to reduce the thermal pollution of the surrounding environment of large refrigeration systems;

To improve the working conditions of the refrigeration system, improve the system's energy efficiency COP value

Bath with hot water no longer has a separate preparation, thereby reducing the running costs of heating and cooling systems;

Condensing heat recovery system to reduce the load of the condenser, which can reduce the size of the condenser, to reduce fan or pump run time, reduce the operating costs of the refrigeration system;

The transformation plan is very well economic and practical for large refrigeration units, but for small refrigeration unit to further consider its economy.

References

- [1] Jiang Huimin , Wang Yang , Ma Zuilang , Home Air Conditioning Condensing Heat Recovery Hot Water Supply Systems in Experimental Analysis [J]. Fluid Mechanics, 2006, 34 (2): 64-67
- [2] Zhang Yimin .Air Conditioning Waste Heat Recovery [J].Applied Energy Technology, 2000 (4): 19-20
- [3] Lin Fengbo,Supermarket Refrigeration System Condensing Heat Recovery Applications [J] .Qingdao University , 2006, 21 (4): 83-86
- [4] Meng Fuchun , Dong Ming , The Use of Central Air Conditioning System Condensing Heat System Control of Domestic Hot Water System [J]. Refrigeration and Air Conditioning, 2004, 4 (2): 37-4
- [5] ARIASJ, LUNDQVISTP .Heat Recovery and Floating Condensing in Supermarkets [J] .Energy and Buildings, 2006, 38 (2): 73-81
- [6] JOHN RW, WILLKB Evaporative Air Conditioning Hand Book[M] · 3 rded Fairmont Press, INC, 1997

Integrated Instrument Based on SOPC

Zheng MA, Mingliu LIU, A'Hui YANG, Youyang LIU

School of Electronic Information, Wuhan University, Wuhan 430079, China

Keywords: NIOS Soft-core; Digital Oscilloscope; DDS Signal Generator; Digital Multi-meter

Abstract. This instrument based on SOPC technology is embedded with a NIOS soft-core in Cyclone III as a control center that integrates digital oscilloscope, DDS signal generator and a simple digital multi-meter. It can measure AC signal of 200 Hz-5MHz and 10mVpp-10Vpp, display and store the wave, and can also manually and automatically adjust the amplitude and frequency. This instrument can generate sine wave of 10Hz to 1.5MHz, square wave of 10Hz to 200 KHz, triangle wave, and saw-tooth wave vary from 150mVpp to 10Vpp. Also, it can measure AC and DC voltage of 20mV to 200V, the AC and DC current of 2mA to 1A, resistance of 20Ω to 2MΩ, maintaining 5% accuracy. It is simple, easy to use, can fulfill the general experiment requirements with good performance and strong practicability.

Plans Selection and Demonstration

Selection and Demonstration of Oscilloscope Plan

Selection of Sampling Ways

Plan 1 is real-time sampling. Real-time sampling refers to sampling waveform in equal intervals of time, and usually needs above eight points in a cycle to restore originally-measured signals with no distortion.

Plan 2 is equivalent sampling. To reconstruct original signal, a small number of samples are equivalently extracted in equal intervals in each cycle, and finally samples extracted from multiple cycles are gathered in one cycle. Then, the sampling effect in measured cycles can be equivalently achieved.

Selection of Signal Conditioning Plan

One-way conditioning is applied. Namely, the same signal conditioning circuit is passed by all signals. Plan 1 provides a simple circuit, but signal frequency and amplitude are large; variable gain amplifiers THS7001 and of AD603 are used, and also an emitter follower is added in front, so as to improve system input impedance.

Selection of Peak Detection Plan

Waveform signals have been collected in system. Therefore, there have reasons to think the maximum of collected points is the peak of signal if a complete, undistorted sine wave can be output from oscilloscope.

Selection of Frequency Measurement Plan

Equal-precision frequency measurement is applied. Its precise threshold is jointly controlled by measured signal and precast door; measuring accuracy only has a tie with the frequency and stability of reference signal, but not with the frequency of measured signals.

Selection and Demonstration of Triggering Method

Digital triggering is applied. In this plan, hardware can be implemented easily, but points collected from waveform are limited in a cycle and it is possible that collected points in each time are unequal to points of triggering level, making triggering position unstable and output waveform tremble in continuous triggering.

Selection and Demonstration of DDS Signal Generator Plans

Selection and Demonstration of Frequency Synthesis

DDFS (direct digital frequency synthesis) technology based on FPGA is applied. Inspired by system clock, phase increments are accumulated according to frequency requirements; accumulated phase values are used as address code for reading the waveform data stored in memory, and then demanded waveform is gained through D/A conversion and filtering.

Amplitude Control

D/A is applied in analog-to-digital conversion and amplitude control. Under the control of FPGA, the output waveform of the first-level 1 D/A is used as the reference voltage source of the second-level D/A; the amplitude of output signal is controlled by controlling the reference source of the second-level D/A conversion. This plan provides a simple circuit, and its amplitude is controlled through FPGA. Thus, it is strongly controllable.

Selection and Demonstration of Multi-meter Plan

Selection and Demonstration of Multi-meter Range Switching Plan

Decoder and transistor drive relay are applied. In fact, relay is an "automatic switch" using small current to control large current.

Selection and Demonstration of AC and DC Conversion Plan

True-RMS conversion chip AD637 is applied. AD637 features high conversion precision, adaption to a wide range of waveform, simple establishment of its peripheral circuit, low hardware requirement, and good stability, precision ensured to meet works' requirement within error range, and high small-signal conversion precision. Thus, it is easy to achieve works' conversion requirements.

Functions and Indexes Implemented in Works

Main functions and indexes implemented in works are shown below.

Measuring AC signal of 200 Hz-5MHz and 10mVpp-10Vpp, displaying and storing simple data in SDCard with no obvious distortion

Manually and automatically adjusting oscilloscope amplitude and frequencies

Having a triggering function

Generating sine wave of 150mV-10V and 10Hz-1.5MHz

Measuring AC and DC voltages of 20mV-200V, AC and DC of 2mA-1A, resistance of 20Ω-2MΩ, and also ensuring an accuracy of 5%

Hardware Design and Main Functions Circuit

Oval Hardware Flow

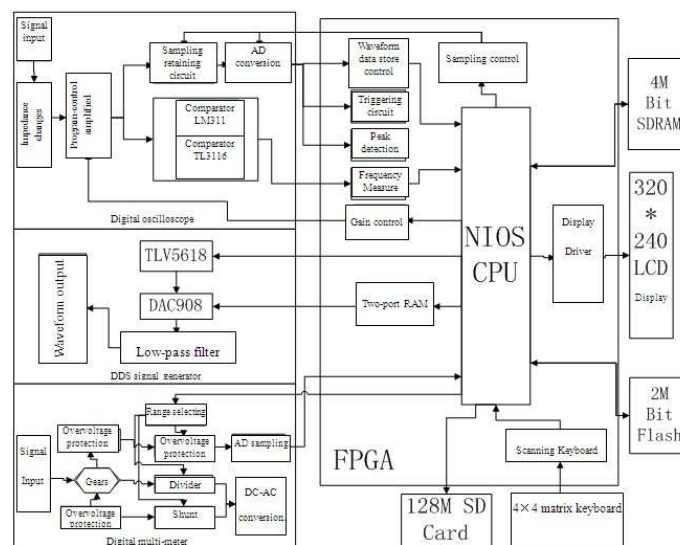


Fig. 1 Oval Hardware Flow

Design of FPGA Main Functions Circuit

Oscilloscope Frequency Measurement Module

In preset gate time T_0 , measured signal f_x and reference signal f_0 are counted simultaneously with counter 1 and counter 2, respectively. The gained values are set to be N_x and N_0 . Thus, the frequency of measured signal is $f_x = (N_x/N_0) * f_0$. Referring to the limit of highest counting frequency of counter, appropriate reference signal frequency and gate time can be chosen, and then frequency measurement accuracy (equivalent-accuracy measurement) can be kept unchanged within a certain range, as shown in figure 2.

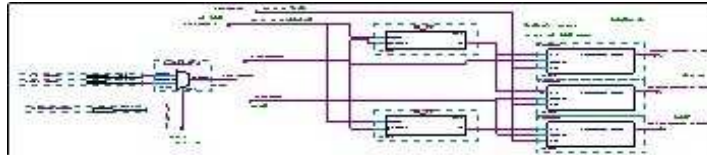


Fig. 2 Oscilloscope Frequency Measurement Module

Oscilloscope Sampling Module

By combining equivalent sampling and real-time sampling, consideration is simultaneously given to low and high frequency sampling. Real-time sampling is use for the sampling of below 100 KHz; equivalent sampling is for the sampling of 100 KHz-5MHz. FPGA circuit design is as shown in figure 3 below.

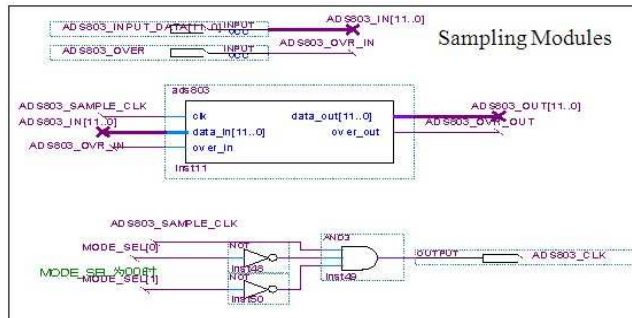


Fig. 3 Oscilloscope Sampling Module

Digital Oscilloscopes RAM Module

To ensure real-time sampling and displaying of this works, ping-pong RAM technology is applied, as shown in figure 4.

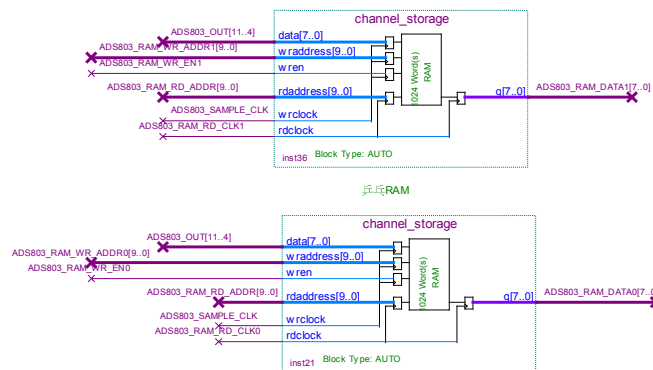


Fig. 4 Digital Oscilloscopes RAM Module

DDS Signal Generator RAM Module

Two-port RAM module (8Kbit) generated in FPGA is used as waveform memory of signal source. An entire RAM is divided into four parts, which are used for storing waveform tables of sine wave, square wave, triangle wave and saw-tooth wave. Thus, waveforms to be displayed can

be written once with huge memory cells in FPGA, preventing repeatedly writing waveforms when waveforms are switched. Besides, when addresses are written, two high bits can be just used as bit zone of waveform. Two-port RAM has two input/output control ports and two data ports; the two sets of ports are equivalent in functions, and respectively have enabling and reading effective control ports, as shown in figure 5.

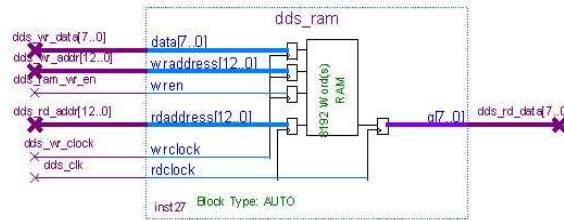


Fig. 5 DDS Signal Generator RAM Module

Digital Multi-meter AD Sampling Module

ADS7818 is used as multi-meter ad sampling module. It is serial AD (12 bit); its control module as shown in figure 6.

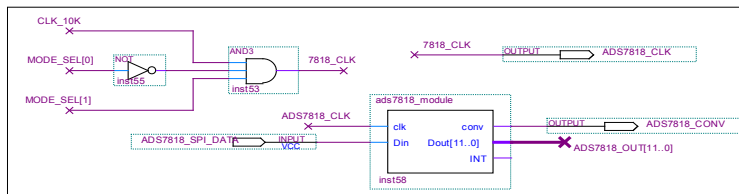


Fig. 6 Multi-meter AD Sampling Module

Oscilloscope Main Circuit and Design

Programmable Amplifier Circuit

The works is stored in higher input impedance; THS3001 is used as emitter follower at the first level. THS7001 gain adjustment range is 22dB-20dB; adjustment step is 6dB; slew rate is 175V/μs. AD603 gain adjustment range is 10 dB-30 dB; gain is controlled by voltage difference. THS7001 is used for cascading AD603, making gain adjustment range 32dB-50dB realized and gain continuously adjusted. The circuit is shown in figure 7.

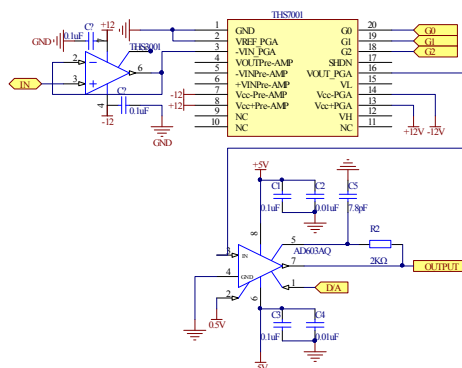


Fig. 7 Programmable Amplifier Circuit

Shaping and Frequency Measurement Circuit

LM311 is widely applied in low-frequency shaping, costs low, and has a good effect in low-frequency shaping. Therefore, shaping is implemented with LM311 in low-frequency wave of this works. The shaping circuit is as shown in figure 8.

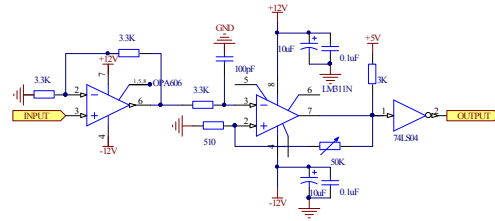


Fig. 8 Low-frequency Shaping Circuit

Because shaping can be only implemented with LM311 in low-frequency, TL3116 is used as shaping frequency measurement circuit in mid and high frequency waves. High frequency comparator TL3116 has a good effect on shaping of signals of above 200 kHz, as shown in figure 9.

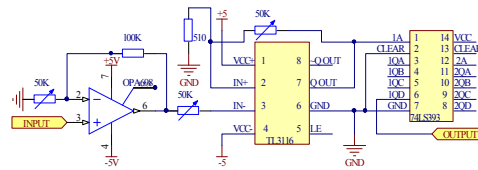


Fig. 9 High-frequency Shaping Circuit

AD Sampling Circuit

A/D converter sampling is an important part of digital signal quantification, as shown in figure 10.

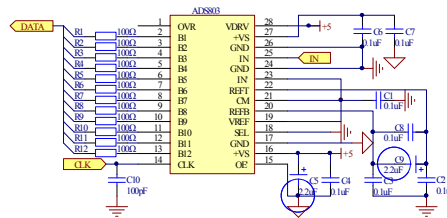


Fig. 10 AD Sampling Circuit

DDS Signal Generator Main Circuit and Design

Implementation of Post-processing Filtering

Limited by chip, active low-pass filter is difficult to work in high frequency, and also its falling edge is flat. However, these shortcomings can be overcome by elliptic filter. Therefore, seven-order elliptic filter is applied in the post-processing of DDS signal generator of this works, and its principle is as shown in figure 11.

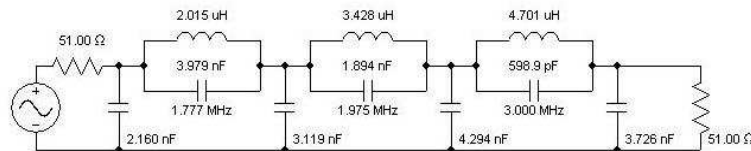


Fig. 11 DDS Filtering Circuit

Amplitude Control

D/A technique are applied. The output waveform of the first-level D/A is used as reference voltage source of the second-level D/A, so as to control the output voltage amplitude of signal generator.

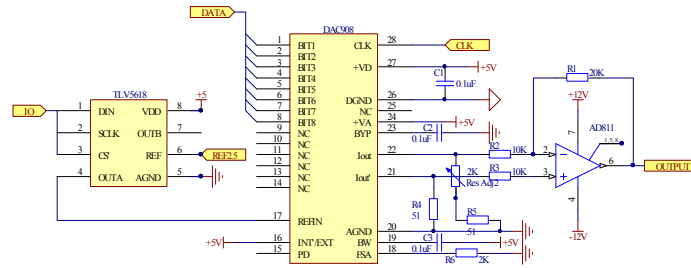


Fig. 12 Amplitude Control Circuit

Simple Digital Multi-meter Main Circuit and Design Range Switching Circuit Design

Figure 13 shows gear selecting circuit for passing of three relays. This circuit controls decoder through IO, making transistor reference level changed and gear selected.

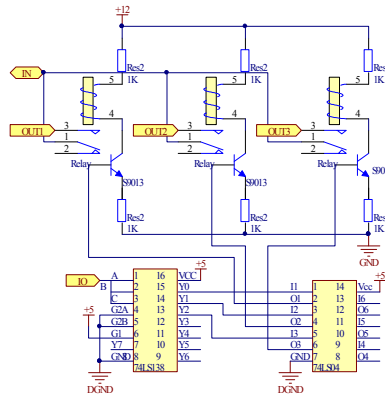


Fig. 13 Automatic Range Switching Circuit

AC-DC True-RMS Conversion Circuit

The way of establishing this circuit is shown in figure 14.

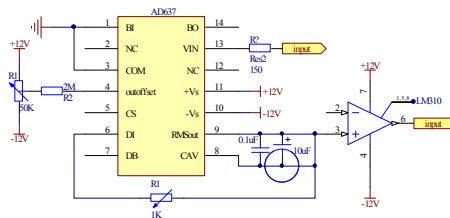


Fig. 14 True-RMS Conversion Circuit

Software Design Flow

The main flow of system is shown below.

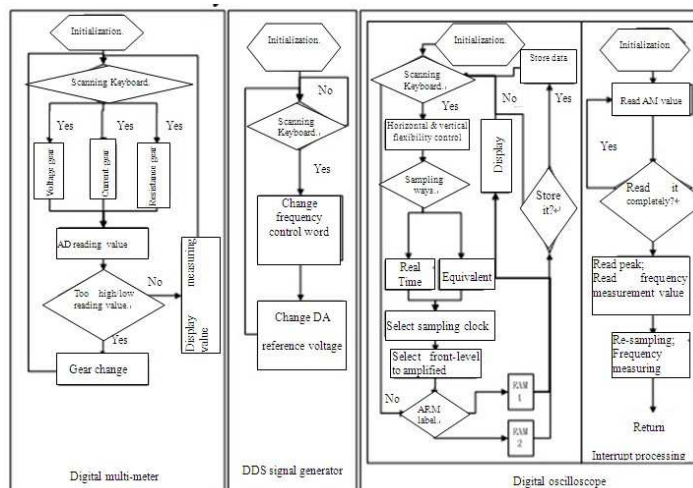


Fig. 15 System Software Design Flow

Overall System Testing

Test Instruments

Instruments includes PC (Lenovo Think Center 7339AL2, AMD Phenom 8400 x3 and Windows XP), power source (DC voltage-stabilization and current-stabilization power source SG17133SB3A), signal source (signal generator Agilent 33120A, 15MHz), and oscilloscope (digital oscilloscope Tektronix TDS1002, 60MHz (1Gs/s)).

Test Result and Implemented Functions

Measuring signal range:1Hz-5MHz; instrument input impedance: $1M\Omega$; horizontal resolution:20points/div;(2)Vertical and flexible gear: 2v/div, 1v/div, 0.5v/div, 0.1v/div, 0.05v/div,0.02v/div,/0.01v/div are implemented; (3) Real-time sampling rate is lower than 100 KHz; maximum equivalent sampling rate is 250MHz; scanning speed: six gears totally, including the eights gears (2.5ms/div, 500us/div, 50us/div, 25us/div, 5us/div, 400ns/div, 200ns/div, and 100ns/div 8); cycle measurement error is lower than 0.2%;(4) Internal triggering is implemented in FPGA; triggering level is adjustable; (5) Waveforms are with no distortion; (6) Storing simple experiential process data in SDCard; (7) Generating sine wave of 150mV-10V and 10Hz-1.5MHz; (8) Generating square wave, triangle wave and saw-tooth wave of 150mV-10V and 10Hz-200 KHz; (9) Measuring ac/dc voltage of 20 mV-200 V, ac/dc current of 2mA-1A, and resistance of 20Ω - $2M\Omega$, and also ensuring an accuracy of 7%

Conclusion

The emergence of SOPC technology makes powerful computation ability of computers and measurement control ability of hardware integrated together, reducing the cost and volume of instrument hardware. Also, through software, displaying, storing, analyzing and processing of data are implemented, abiding by the development tendency of internationally popular "soft hardware". Integrated instrument based on SOPC feature short development cycle, short development cycle, low cost, and easy-to-maintain and easy-to-extend. The instrument has a powerful extensibility.

References

- [1] Yuwen Xia. Digital System Design-Verilog Implementation (2nd edition). Beijing: Higher Education Press, 2006.
- [2] [U.S.] Beth. Translated by Leng Liu, Yongsheng Hu. FPGA Implementation of Digital Signals Processing. Beijing: Tsinghua University Press, 2002.
- [3] Genchun Huang, Xiaoqiao Chen, Wangxian Zhang. Electronic Design Guide. Beijing: Electronics Industry Press, 2007.8.
- [4] Zimei Xie. Electronic Circuit Design • Experiment • Test (2nd Edition). Wuhan: Huazhong University of Science and Technology Press, 2007.7.
- [5] Lanying Li. Nios II Embedded Soft-core SOPC Design Principles and Applications, Beijing: Beijing University of Aeronautics and Astronautics Press, 2006.11.
- [6] Chenglian Peng. SOPC Design in Practices based on NIOS. Beijing: Tsinghua University Press, 2006.11.
- [7] Hui Qin, Jing Li, Beibei Dong, Yanxia Liu, Xiaoguang Zhang. Design of Full Automatic Digital Multi-meter. Automation & Instrumentation, 2010.1.

An Improved Wavelet Threshold Denoising Method for Transformer Partial Discharge Signal

F.C.You^{1, a}, Y.Zhang^{2, b}

^{1, 2}#25 Xinghua North Road, Daxing District, Beijing 102600 China

^ayoufucheng@yahoo.com.cn, ^bliaoningzy@126.com

Keywords: Transformer, Partial Discharge, Wavelet Threshold Denoising, Threshold.

Abstract. In order to overcome the discontinuance of the hard thresholding function and the defect of slashing singularity more seriously in the soft thresholding function, and improve the denoising effect and detect the transformer partial discharge signal more accurately, this paper puts forward an improved wavelet threshold denoising method through analyzing the interference noise of transformer partial discharge signals and studying various wavelet threshold denoising method, especially the wavelet threshold denoising method that overcomes the shortcomings of the hard and soft threshold. Simulation results show that the denoising effect of the method has been greatly improved than the traditional hard and soft threshold method. This method can be widely used in practical transformer partial discharge signal denoising.

Introduction

The monitoring of transformer partial discharge signal is an important technical measure to ensure the reliability of power supply, but the signal extracted in equipment operation site contains a lot of interference noise, which seriously affects the detection sensitivity and reliability and even leads to judgment mistakes of the inspectors. Therefore how to effectively eliminate the interference noise interference has become the key issue of partial discharge signal detection.

There are a lot of transformer partial discharge signal denoising methods, such as FFT threshold filter method, finite impulse ring (FIR) filter method, infinite impulse response (IIR) filter method, Kalman filter, and adaptive filtering method [1]. In theory, these methods mostly belong to the time domain or frequency domain analysis, which is not a good combination of signal time-frequency characteristics to be analyzed. With the rapid development of wavelet theory, the wavelet analysis has the advantage of time-frequency analysis, and it has been more and more widely applied in denoising of partial discharge signals. There have been many new methods used in partial discharge signal denoising processing, and a good effect has been showed, but the existing wavelet threshold denoising method has some drawbacks. After we have analyzed the large number of domestic and foreign-related information, and have analyzed the partial discharge signals and various interference signals, and have studied various partial discharge wavelet denoising method in detail, this paper puts forward an improved wavelet threshold denoising method based on existing methods.

The Partial Discharge Signal Interference Noise Analysis

In partial discharge signal monitoring process, there are three kinds of main interference noise.

Continuously periodic interference Continuous periodic interference includes the interference caused by electric power systems carrier communication and the protection of high frequency signal, and radio interference and electric power system harmonic interference and power electronic conversion devices generated interference, under the general situation continuous periodic interference is the result of the comprehensive effect of the above interferences. Each continuously periodic interference of the time domain waveform has the fixed harmonic frequency and the bandwidth, some of them have high frequency, and the others have lower frequency. The signal of periodic interference in on-line PD monitoring system is one of the important interference sources, which exist in the course of monitoring, and the energy of which is very powerful. In frequency domain waveform we can see that the interference includes some isolated spectral lines, and each line corresponds to a frequency component, which is called the narrow band interference.

White noise interference White noise includes all kinds of random noises, such as transformer winding thermal noise, the grounding grid noise, and the various noises caused by the coupling of the power distribution lines, transformers relay protection signal lines, and the electronic components scattered grain of noise from partial discharge measurement system. In practical applications if the spectrum of noises has the continuously flat characteristics in wide band of frequency, then it can be considered a white noise.

Pulse interference. Pulse interference signal includes power lines or high voltage corona discharge, the interference caused by the division of the power switch and the thyristor rectifier equipment, and the interference caused by other testing equipment discharge in power system, and the interference caused by the test lines or adjacent lines badly connect to the ground, and the interference caused by the discharge of floating objects in other device, and the other random interference [2,7].

The signal after mix the interference and partial discharge signals is relatively complex, so how to eliminate noise interference is very difficult. With modern digital processing technology and the development of the theory of wavelet, partial discharge signals denoising method is more and more incline to software direction, the acquisition of digital signal processing. At the same time, people try to combine the hardware and software processing, to maximize the suppression and eliminate noise interference, and get partial discharge information, which forms a set of complete denoising system.

An Improved Method for Wavelet Thresholding Signal Denoising

Existing Wavelet Denoising Methods

Due to the rapid development of wavelet theory, the wavelet analysis in denoising of partial discharge signals is increasingly used, at the same time appeared a variety of wavelet denoising method.

Wavelet decomposition and reconstruction denoising method

In 1988, Mallet puts forward the concept of multi resolution analysis and gives the wavelet decomposition and reconstruction algorithm (Mallet algorithm). The method is mainly applied in the deterministic noise situation under which the useful signal and noise frequency bands are separated from each other, and it can remove noise basically and denoising effect is very good. But for the useful signal and noise band overlapping condition, the effect is not very ideal. The advantages of this method are simple algorithm and fast calculated speed, the disadvantage is the scope of application is not very extensive, especially white noise denoising and the denoising effect is poor.

Wavelet threshold denoising method

In Stanford University an academic group led by Donoho proposed wavelet threshold denoising method and it is most widely used in current engineering method. In 3.2, the method would be introduced in detail.

The translation invariant wavelet denoising method

Translation invariant wavelet denoising method is an improved method made on the basis of the threshold method and improvements. In the threshold denoising, when the signal has a mutation in the discontinuous point or when the signal has the low SNR, wavelet transform denoising is likely Pseudo Gibbs Phenomenon, namely the signals near discontinuous point will jump up and down at a specific target level. Therefore, the method does not adopt a single translation, but usually adopts N cycles of translation to denoise the translated signals by thresholding method, and then take the average values of the denoised results, which is known as "the translation-denoising-average" of the translation invariant wavelet denoising method and it is used in the case that signal contains several discontinuous points. Translation invariant method has the advantage of being able to remove the Pseudo Gibbs Phenomenon of thresholding denoising, and the denoising effect is good, the shortcoming is the calculation at a slower speed.

Denoising method based on modulus maxima

In 1992, Mallat and others proposed the representation of signal and image multi-scale edges based on signal singularity by using Lipschitz index in multiple scales to describe the signal and image noise mathematical feature, and then proposed the filtering method of modulus maxima

reconstruction [3]. Partial discharge signal is the singular signal and the modulus maxima increase with scale, and it has a positive Lipschitz exponent. The modulus maxima of the noise decreases with increasing scale, and it has negative Lipschitz exponent, the modulus maxima in the wavelet transform has the different change trend [4, 9].

An Improved Method for Wavelet Thresholding Signal Denoising

After the study of various wavelet denoising methods, this paper proposes an improved wavelet threshold denoising method that is based on the original wavelet threshold denoising methods, and uses the application of the comprehensive theory to improve the original wavelet threshold denoising methods.

In wavelet threshold denoising method, suppose that a noisy signal can be expressed as $f(t) = s(t) + n(t)$.

Where $s(t)$ is the original signal, $n(t)$ is the Gaussian white noise with variance σ^2 and obeys $N(0, \sigma^2)$.

Wavelet threshold denoising process can be divided into the following three steps [5]:

By making discrete wavelet transform of the noisy signal $f(t)$, the wavelet coefficients $w_{j,k}$ can be got, where k is the wavelet coefficients of the j -th layer wavelet space order;

After the scales corresponding to the wavelet coefficients have been treated by the threshold function, we get the estimated wavelet coefficients $\hat{w}_{j,k}$;

Using the wavelet coefficients processed by the threshold to make inverse discrete wavelet transform to reconstruct signals, we can get the denoised signal $\hat{f}(t)$

The key of the method is mainly depends on the threshold and the selection of threshold function which is related to the denoising effect [6, 8, 10]. The main threshold functions include the following three kinds:

$$\hat{w}_{j,k} = \begin{cases} w_{j,k}, & |w_{j,k}| \geq \lambda \\ 0, & |w_{j,k}| < \lambda \end{cases} \quad (1)$$

Eq. 1. The hard threshold function

$$\hat{w}_{j,k} = \begin{cases} \text{sign}(w_{j,k})(|w_{j,k}| - \lambda), & |w_{j,k}| \geq \lambda \\ 0, & |w_{j,k}| < \lambda \end{cases} \quad (2)$$

Eq. 2. The soft threshold function

$$\hat{w}_{j,k} = \begin{cases} 0, & |w_{j,k}| \leq \lambda_1 \\ \text{sign}(w_{j,k}) \frac{\lambda_2(|w_{j,k}| - \lambda_1)}{\lambda_2 - \lambda_1}, & \lambda_1 < |w_{j,k}| \leq \lambda_2 \\ w_{j,k}, & |w_{j,k}| > \lambda_2 \end{cases} \quad (3)$$

Eq. 3. The semi-soft threshold function

In the function λ_2 is the upper threshold, λ_1 is the under threshold.

The focus of wavelet threshold denoising method is the threshold function and threshold selection methods which directly determine the advantages and disadvantages of this method. However, there are still some deficiencies for this method, for example, hard threshold function discontinuity makes the denoised signal have larger deviation and still contains a significant noise compare with the original signal; Using soft threshold method, the continuity is good, but there is constant deviation

between the estimated wavelet coefficients and the wavelet coefficients of noisy signal, which makes the denoised signal's variance is too large and when noise signal is too irregular it appears too smooth; The semi-soft threshold function is the eclectic form of hard threshold function and the soft threshold function, which retains a larger coefficient and continuity, but semi-soft threshold function needs to determine two thresholds, which increases the complexity of the algorithm, and the selection of upper threshold or under threshold would affect the accuracy of the reconstructed signal.

Because the wavelet threshold denoising method has the mentioned above disadvantages, it is difficult to reach the expected effect of denoising. This paper puts forward the improved wavelet threshold denoising method, which integrates soft threshold with hard threshold denoising method and low pass filter method, and improved the method with the comprehensive theory. The denoising effect of the improved wavelet threshold denoising method is improved obviously.

The Simulation Results and Evaluation

In order to test the denoising effect of improved wavelet threshold denoising method, this paper uses Matlab software to carry out the simulation experiment.

Figure 1 is a simulation of the original transformer partial discharge signal, figure 2 is the simulation of the signal that 10dB Gauss white noise is added in the original signal, figure 3 is the signal that is denoised by the traditional soft threshold denoising method, figure 4 is the simulation of using the improved wavelet threshold denoising method in denoising the signal.

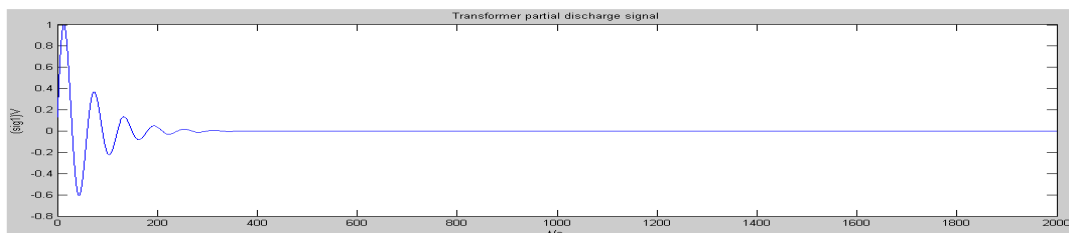


Fig. 1 The transformer partial discharge signal

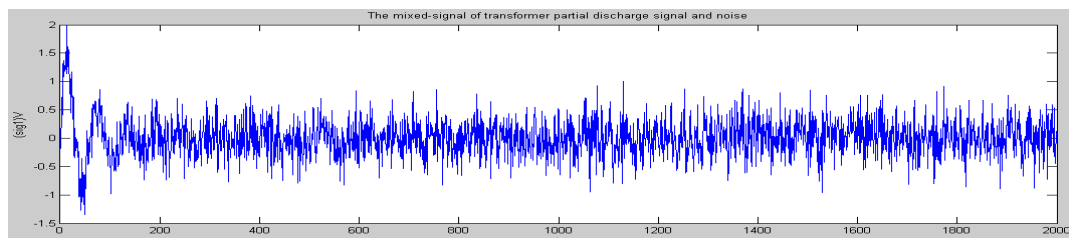


Fig. 2 The transformer partial discharge signal and noise of mixed signal

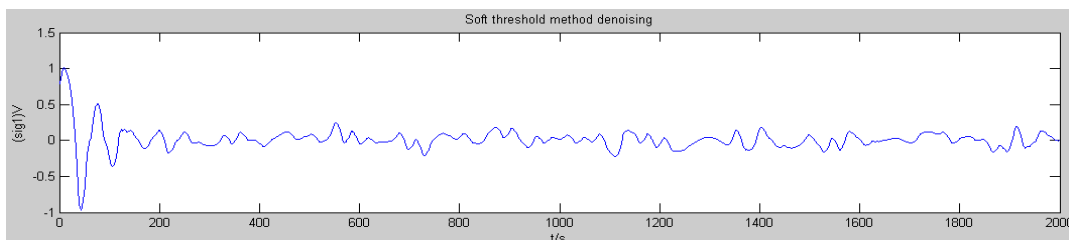


Fig. 3 The signal after denoised by the soft threshold denoising method

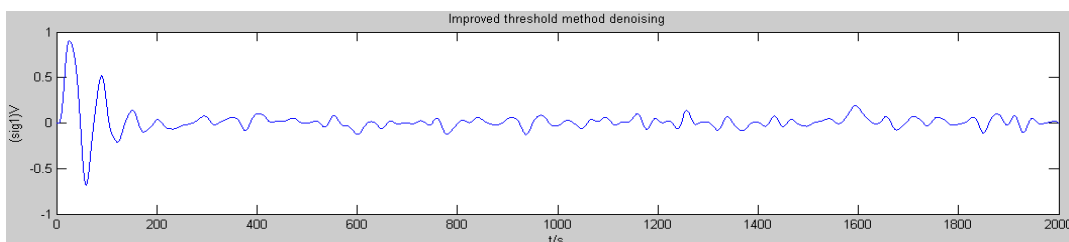


Fig. 4 The signal after denoised by the improved threshold denoising method

From the results of simulation we can see, soft threshold denoising method and the improved wavelet threshold denoising method can basically restored the original partial discharge signals. Soft thresholding denoising has good continuity, but not good to retain the original signal singular point, and the original signal cannot be recovered well, and some signals are weakened. Improved wavelet threshold denoising method ensure that under the premise of signal continuity the weakness is much smaller, and denoising speed will not change too much. Therefore, the original signal can be restored, and the denoised signal distortion degree can be reduced. The improved method has greatly increased the denoising integral effect.

Summary

This paper introduces the transformer partial discharge signals of denoising methods, which focuses on the wavelet threshold denoising method studying. Then based on analyzing the disadvantages of the wavelet threshold denoising method an improved wavelet threshold denoising method is proposed. Finally, compared with the denoising results of the improved denoising method and traditional threshold denoising method, the result shows that the denoising result of the improved wavelet threshold denoising method has the better denoising effect. Compared with traditional wavelet threshold denoising method, the method doesn't reduce the speed, and the denoising effect is improved greatly, and it also has better stability. But from the overall effect of the method it still can not achieve the desired effect in signal denoising, and some distortions will still appear at singular point. To explore the best transformer partial discharge signal denoising method, to realize the signals low distortion recovery, and to improve the accuracy of determine partial discharge are the next targets.

Acknowledgements

This paper is supported by Scientific Research Key Project of Beijing Municipal Commission of Education (No.KZ201210015015) and Institute Level Key Project Funded by Beijing Institute of Graphic Communication (No.E-a-2012-23).

References

- [1] Tan Ping, Cai Zixing: Real time Kalman filter based on non-decimated Haar algorithm, Journal of Central South University (Science and Technology), Vol .4 2, No.12, pp.3760-3764, Dec. 2011.
- [2] Mao Yizhi, Li Song, and Li Zhangqiang: Research on Denoising Method of Partial Discharge Signal of Transformer, TRANSFORMER. Vol.48, No.3 (2011), pp. 47–50.
- [3] S.Mallat, W.L. Hwang: Singularity Detection and Processing with Wavelets, IEEE Transactions on IT, Vol.38, No.2 (1992), pp. 617-643.
- [4] Qi Zefeng, Li Weiguo and Tan shuntao: Algoithm of Partial Discharge Signal Reconstruction Based on Modulus Maximum Wavelet Domain, Proceedings of the CSEE. Vol.22, No.11 (2002), pp. 28-30.
- [5] Zhang Weiqiang, Xu Chen: A Denoising Algorithm of Wavelet Threshold Based on Translation invariance, Modern Electronics Technique, Vol.6 (2003), pp. 29-31.
- [6] Garcia D Z G, Toledo M B F: A Fault Tolerant Web Service Architecture, 5th Latin American Web Congress, pp.42-49, (2007).
- [7] Bi Weimin: Study on Denoising Methods with Wavelet Packet and Pattern Recognition by Statistical Features for On-line Transformer Partial Discharge Monitoring, Chongqing University, (2003).

- [8] Ye Chongyuan, Huang Yongdong: New improvement of wavelet threshold denoising algorithm. Computer Engineering and Applications, Computer Engineering and Applications, Vol 47, No. 12 (2011), pp 141-145.
- [9] Peng Yuhua: Wavelet transform and engineering application, Science Press, (2005).
- [10] Wei Liqiang: Research on signal denoising based on wavelet transform, Hunan University, Jun 2007.

A Research on the DC-Link Current and Capacitance of the Static Excitation Regulator on a 12/3-Phase Dual Stator-Winding Induction Generator

Botao Zhang¹, Dong Wang²

¹Wuhan University of Science and Technology, College of Computer Science, 430065, Wuhan, Hubei, China

²Navel University of Engineering, Institute of Power Electronics, 430033, Wuhan, Hubei, China
Zhangbt2000@163.com, wangdong@vip.163.com

Keywords: Dual Stator-Winding Generator, Static Excitation Regulator, Switch Function, PWM, Harmonic

Abstract: By proper simplifications, the static excitation regulator on the 12/3 phase dual stator winding induction generator is described by the switch-function model. On this basis, the switch-function expression of the DC-link capacitor current is obtained and the physical meanings are discussed, and the detailed exchange procedures between the generator and capacitor are analyzed. Considering the voltage endurance capability of the capacitor and IGBT, and the current endurance capability of the capacitor, the limitation capacitance equation of the DC-link capacitor is proposed.

Introduction

A novel 12/3 phase dual stator winding induction generator with the static excitation regulator (SER) is proposed to satisfy the high speed prime mover (such as turbine up to 6000rpm speed), and a solid iron squirrel cage rotor satisfies both the mechanical requirements of high speed generation and the electrical requirements of high efficiency and then improve the power density. Its simplified circuit schematic is shown in Fig.1, and it consists of three parts: induction generator with dual stator windings, 12-phase rectifiers and self-excitation capacitor, static excitation regulator.

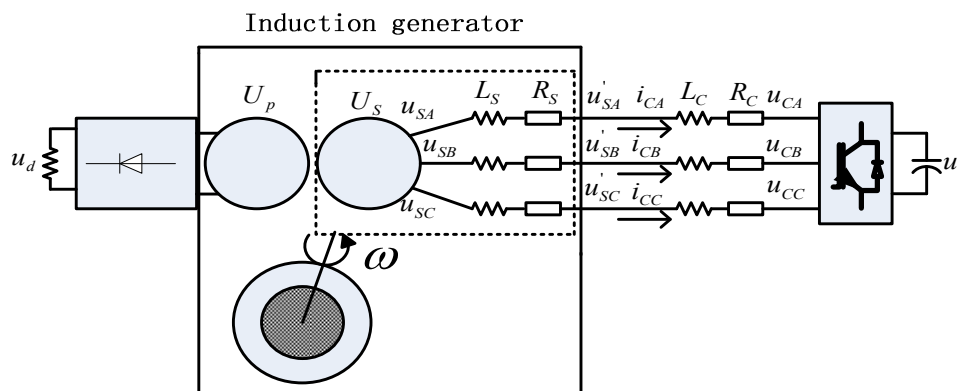


Fig. 1 Simplified schematic circuit model of the 12/3 phase induction generator system

Base on the previous researches [3]-[7], the theoretical and experimental researches on the current and capacitance of the DC-link capacitor in this paper. Some capacitance limitation equation of the DC-link capacitance are proposed in previous reports [1] [2] [3] [4] [9], but those results are deduced in the sin-period stable state. The researcher states in [9][10] that a small even no capacitor is proper when the current is pure reactive power and not considering of losses. DC current and voltage harmonics in the capacitor should be considered under the PWM control mode, and considering the current endurance of IGBT and capacitor, voltage endurance of IGBT, the capacitance should not be less and must more than the limitation minimize value.

In this work, we are going to describe the system with switch function, and deduced the s-function formula of the DC current. Following that the physical meanings of the formula are analyzed in PWM control mode, the theoretical formula of the voltage and capacitance is proposed.

Theoretical Calculation of the DC Current

The simplified system circuit schematic of the SER with s-function is shown in Fig.1 and not considering losses [8].

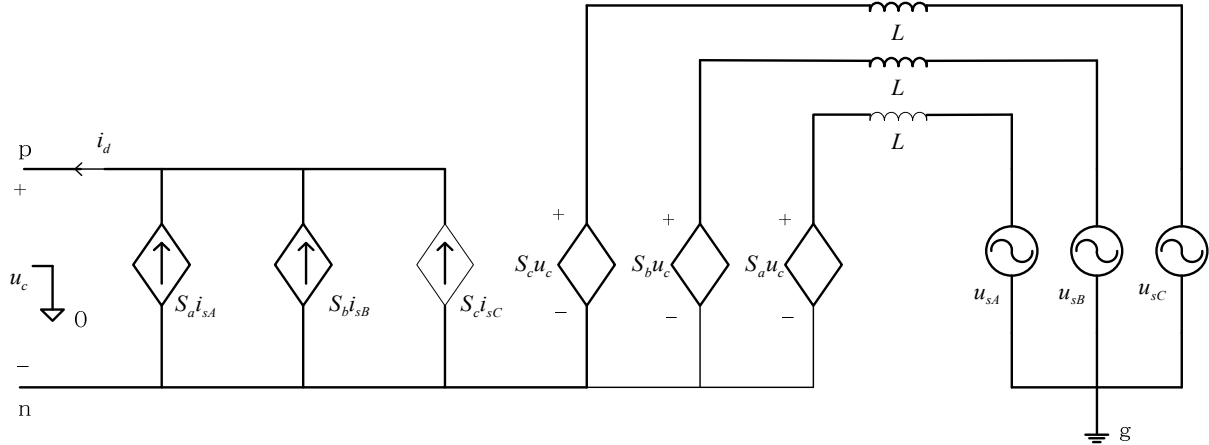


Fig. 2 The equivalent circuit of the SER system

Supposed current flowing from generator to SER DC-link, then equation of DC current is:

$$i_{dc} = S_a i_{sA} + S_b i_{sB} + S_c i_{sC} \quad (1)$$

And voltage equations are:

$$S_a u_c = L \frac{di_{sA}}{dt} + u_{sA} + u_{gn} \quad S_b u_c = L \frac{di_{sB}}{dt} + u_{sB} + u_{gn} \quad S_c u_c = L \frac{di_{sC}}{dt} + u_{sC} + u_{gn} \quad (2)$$

Supposed the system is symmetry, thus:

$$u_{gn} = u_{go} + u_{on} \quad u_{go} = 0 \quad u_{gn} = \frac{u_c}{2} \quad (3)$$

$$S_a u_c = L \frac{di_{sA}}{dt} + u_{sA} + \frac{u_c}{2} \quad S_b u_c = L \frac{di_{sB}}{dt} + u_{sB} + \frac{u_c}{2} \quad S_c u_c = L \frac{di_{sC}}{dt} + u_{sC} + \frac{u_c}{2} \quad (4)$$

And (1) also can be:

$$i_{dc} = \frac{1}{u_c} [(u_{sA} i_{sA} + u_{sB} i_{sB} + u_{sC} i_{sC}) + \frac{L}{2} \frac{d(i_{sA}^2 + i_{sB}^2 + i_{sC}^2)}{dt} + \frac{u_c}{2} (i_{sA} + i_{sB} + i_{sC})] \quad (5)$$

If the AC 3-phase current are symmetry and only considering of the fundamental factors, and: $i_{sA} + i_{sB} + i_{sC} = 0, i_{sA}^2 + i_{sB}^2 + i_{sC}^2 = \frac{3}{2} i_{sm}^2$, i_{sm} is the phase current magnitude.

Then equation (5) can be simplified:

$$i_{dc} = \frac{1}{u_c} [(u_{sA} i_{sA} + u_{sB} i_{sB} + u_{sC} i_{sC}) + \frac{3}{4} L \frac{di_{sm}^2}{dt}] \quad (6)$$

And in the sin-period stable state, the DC current is:

$$i_{dc} = \frac{1}{u_c} (u_{sA} i_{sA} + u_{sB} i_{sB} + u_{sC} i_{sC}) \quad (7)$$

Considering two extreme conditions:

The power factor is 1, and the difference between current and voltage is zero, thus $i_{dc} = 3ism * u_{sm} / 2u_c$, u_{sm} is the line voltage magnitude, and if the real current is positive, then the voltage should be rise, and vice versa.

The power factor is 0, and the difference between current and voltage is 90, thus $i_{dc} = 0$. It means that the average value of the DC current is zero when only compensating the reactive power. So the capacitance can be much less or none [7][8].

Theoretical Calculation of the DC Current in PWM Control Mode

The above analyses are based on the sin-period stable state. But in the real PWM system, the switch frequency is not so high and the harmonic current should be considered. Then we analyze the switch function equation (4).

Supposed the current keeps constant in one PWM period (i.e. $T_{PWM} = 0.5ms, f_{PWM} = 2kHz$), and then differential coefficient of current is zero, so:

$$(S_a - 0.5)u_c = u_{sA} \quad (S_b - 0.5)u_c = u_{sB} \quad (S_c - 0.5)u_c = u_{sC} \quad (8)$$

For the output of the s-function is 0 or 1, and the capacitor voltage is always above zero, then:

$$S_a = \text{sgn}(u_{sA}) \quad S_b = \text{sgn}(u_{sB}) \quad S_c = \text{sgn}(u_{sC}) \quad (9)$$

$$\text{sgn}(x) = \begin{cases} 1 & x \geq 0 \\ 0 & x < 0 \end{cases} \quad (10)$$

From equation (1) and (9) gets:

$$i_{dc} = \frac{1}{u_c} (u_{sA} i_{sA} + u_{sB} i_{sB} + u_{sC} i_{sC}) = \text{sgn}(u_{sA}) i_{sA} + \text{sgn}(u_{sB}) i_{sB} + \text{sgn}(u_{sC}) i_{sC} \quad (11)$$

As for the static VAR compensator, the current are sampled instantly, and the voltage are deduced by the w using the SPLL, so DC current can be calculated by formula (11).

If analyze the DC current in one PWM period: the control mode is SPWM, and the pulse width is generated by the symmetry regulation sample rule. And the one type pulse is shown in Fig.3. For the SVPWM control is equivalent to SPWM, so the analysis result is same.

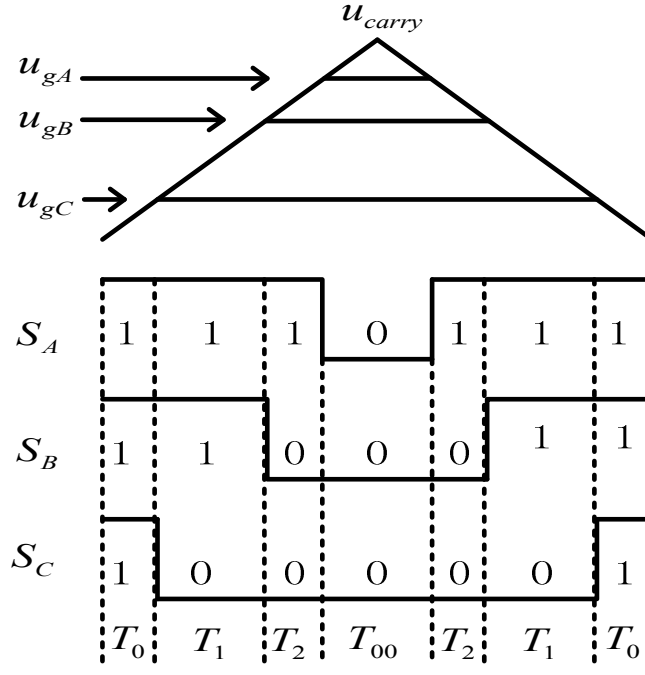


Fig. 3 The diagram of the SPWM pluses

There are seven states in one period:

- (1) $S_A S_B S_C = 111$, $i_{dc} = 0$, time is T_0 ;
- (2) $S_A S_B S_C = 110$, $i_{dc} = i_{sA} + i_{sB} = -i_{sC}$, time is T_1 ;
- (3) $S_A S_B S_C = 100$, $i_{dc} = i_{sA}$, time is T_2 ;
- (4) $S_A S_B S_C = 000$, $i_{dc} = 0$, time is T_{00} ;
- (5) $S_A S_B S_C = 100$, $i_{dc} = i_{sA}$, time is T_2 ;
- (6) $S_A S_B S_C = 110$, $i_{dc} = -i_{sC}$, time is T_1 ;
- (7) $S_A S_B S_C = 111$, $i_{dc} = 0$, time is T_0 ;

The average current in one PWM period is:

$$\overline{i_{dc}} = \frac{2(i_{sA}T_2 - i_{sC}T_1)}{T_{PWM}} \quad (12)$$

The first difficulty is the current endurance capability of the capacitor. It is known from the states (2) (3) (5) and (6), the maximum instantaneous value of the current flowing to or from the capacitor is the peak magnitude of phase current. But the current endurance capability of the capacitor is not infinite, such as an EPCOS electrolyte capacitor 3300uF/450V (Part No. B43330A5338M0000), the maximum AC current is 24.2A (120Hz), and the instantaneous value is larger. Those values are also depending on the capacitance, and decrease with the capacitance.

Theoretical calculation of the ripple voltage in the DC link capacitor

There are four cases of formula (12) in one PWM control period based on Fig.3:

- (1) $i_{sA} > 0$ and $i_{sC} < 0$: on the whole PWM, the current flows from AC link to the DC capacitor, so the DC voltage increases continuous.
- (2) $i_{sA} < 0$ and $i_{sC} > 0$: on the whole period, the current flows from the DC capacitor to AC link, so the DC voltage decreases continuous.
- (3) $i_{sA} > 0$ and $i_{sC} > 0$: on the switch state (2) and (6), the current flows from the DC capacitor to AC link, so the DC voltage decreases. On the switch state (3) and (5), the current flows from the DC capacitor to AC link, so the DC voltage increases.

(4) $i_{sa} < 0$ and $i_{sc} < 0$: on the switch state (3) and (5), the current flows from the DC capacitor to AC link, so the DC voltage decreases. On the switch state (2) and (6), the current flows from the DC capacitor to AC link, so the DC voltage increases.

When it is used for compensating reactive power and $\overline{i_{dc}} = 0$, we analyze the cases (3) and (4) in details and calculate the ripple voltage in the DC capacitor. Taking the switch states (2) in case (4) for examples and the capacitor voltage is differential coefficient of the current, we can get:

$$\Delta u_c = -\frac{1}{C} i_{sC} T_1 \quad (13)$$

And time limitation equation is:

$$T_1 + T_2 \leq \frac{T_{PWM}}{2} \quad (14)$$

We want to get the maximum value of the ripple voltage and the result is:

$$(-i_{sC} T_1)_{\max} = \frac{i_{sm} T_{PWM}}{8} \quad (15)$$

$$\Delta u_{c\max} = \frac{i_{sm} T_{PWM}}{8C} \quad (16)$$

The maximum instant voltage of the DC capacitor is:

$$u_{c_max} = \overline{u_c} + \Delta u_{c\max} \quad (17)$$

The theoretical result of the capacitance

The second difficulty is the voltage duration of the IGBT and capacitor. We must ensure the maximum peak voltage is less than the SOA (Safe Operation Area) of those devices. In fact the PWM switching frequency is not so fast (i.e. $T_{PWM} = 0.5\text{ms}$, $f_{PWM} = 2\text{kHz}$), so the way to decrease the voltage peak value is to increase the capacitance.

Define the ripple ratio ε is: $\Delta u_c = \varepsilon \overline{u_c}$ then:

$$C = \frac{i_{sm} T_{PWM}}{8\varepsilon \overline{u_c}} \quad (18)$$

To satisfy the voltage SOA of IGBT and capacitor, then the capacitance must be more than one limitation value and it is decided by the equation (18).

Experimental results

The requirements of SER are: the maximum peak value of phase current is 70A and the switch frequency is 2kHz. The reference voltage of capacitor is 600v and the ripple ratio is 1%. According to equation (18), the minimum capacitance is 1.04mF and 1.67mF is adopted in the SER.

Fig.4 is one of the experimental results.

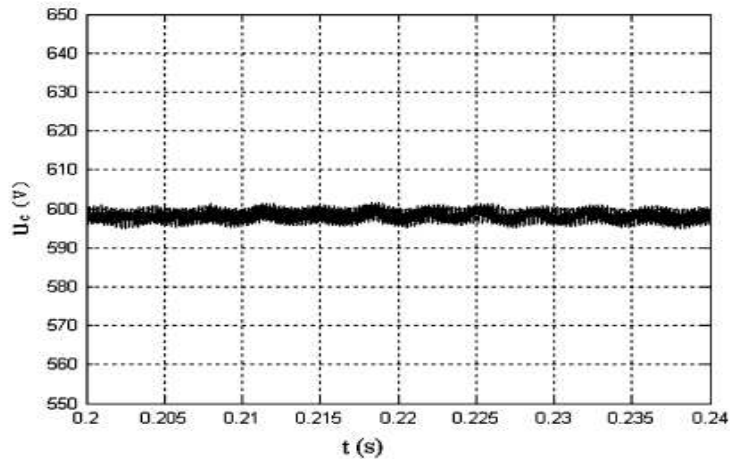


Fig. 4 Experimental waveform of the DC-capacitor voltage

The analysis results are: the phase current magnitude is 12A; the average capacitor voltage is 599V; the maximum ripple voltage is 3V. The experimental ripple voltage is more than theoretical result, and we refer it to the detection noise.

Other experiments are done and we find the maximum ripple value is inverse ratio to the capacitance, less capacitance then more ripple.

Results

The DC capacitor current can be deduced by the equation (11).

The maximum current flows from or to the capacitor is the peak phase current, then we must consider the current durance capability of the capacitor.

The ripple voltage is inverse ratio to the capacitance, then we must consider the voltage durance capability of the IGBT and capacitor.

So the minimum capacitance of the DC link capacitor is limited by the current and voltage durance capability. And this value cannot be less or none.

Appendix

the parameters of the two-level SER. Filter reactor: 3mH; DC link capacitor: 1650uF/900V; IGBT: PM75CSA120.

References

- [1] Nie Zining, Zhang Botao. The 2nd Harmonic Calculation of the Capacitor Voltage in the DC Link of the Cascade H-Bridge SVG [J]. Trans. Of China Electrotechnical Society, Vol.21, No.4, PP.112-116.
- [2] Zhang Botao, Nie Zining, Libei, Zhang Liping. Analysis of the DC-Link Capacitor Voltage Spectrum in the Cascaded Multilevel STATCOM[J]. ICIT 2008, PP.1-5.
- [3] Zhang Botao, Ma Weiming. Research on the control algorithm and dynamic characteristic of a 12/3-phase dual stator winding induction generator. Proceedings of CSEE, Vol.25, No.12, PP.143-148.
- [4] Wang Dong, Ma Weiming. Study On the Currents of Sudden DC-side Shout Circuit of a 12/3 Phase Dual stator-winding Induction Generator[J]. Proceedings of CSEE, Vol.25, No.15, PP.133-139.
- [5] Xiao Fei, Zhang Botao. A Double-winding Induction Generator and Its Excitation Strategy. Power System and Automatic, Vol.27, No.18, PP.26-29.

- [6] Wang Dong, Ma Weiming. Analysis On The Harmonic Asymmetry of 12/3-Phase Dual Winding Induction Generator[J]. Proceedings of CSEE, Vol.24, No.5, PP.148-152.
- [7] Gu WeiFeng Ma Weiming. Research On the Harmonic Resonance of the 12/3 Phase Double-winding Asynchronous Generator during its Self-Excitation[J]. Proceedings of CSEE Vol.24, No.6, PP.167-171.
- [8] Prasad N. Enjeti, Phoivos D. Ziogas, Mehrdad Ehsani. Unbalanced PWM converter analysis and corrective mearures[J]. IAS Annual Meeting, 1989, Vol.1, PP.861-870.
- [9] Wang Zaoan, Yang Jun, Liu Jinjun. Harmonic eliminate and reactive power compensation[M]. Mechanism Industry Press.
- [10] Fang Zheng Peng, John W. McKeever. A power line conditioner using cascade multilevel inverters[J]. IEEE Trans on Industrial Application, 1998, 34(6), PP. 1293-1298.

Application of Rigid-Flexible Coupling in Stiffness Calculation of Double Wishbone Suspension

H.N. Wang^a, X.W.Hou^b, X.P.Su^c

School of Mechanical and Power Engineering, Nanjing University of Technology, Nanjing 211816, China

^aemail: njut_wnh@126.com, ^bemail: hxwnjut@126.com,

^cemail: suxiaoping@vip.163.com

Keywords: Double-wishbone Independent Suspension; Torsion Spring; Suspension Stiffness; Rigid-flexible Coupling; Multi-body Dynamics

Abstract: Based on multi-body Dynamics theory, the 1/4 multi-rigid model of double wishbone suspension of automobile in ADAMS/View is created, and use ANSYS software to analyze torsion beam flexibility. Furthermore, the rigid-flexibility model has been created and the rigid change of suspension line along with the tire dynamics change is simulated. The result shows that the rigid-flexible coupling model is more accuracy than the multi-rigid one and fits the practical situation even better. This paper proposes an efficient method for analyzing the rigid of double-wishbone suspension vertical line.

Introduction

Suspension is one of the most important parts of an Automobile, which connect the body frame with axle assembly. Its works to transfer the impact caused by the road roughness to the frame and relieves the vibration to ensure the comfort as the automobile running. Because of its advantages, torsion spring and torsion suspension has been used on the suspension since early 1930s. With the further study of torsion spring and the torsion suspension, torsion spring has been broadly applied on various forms of automobiles [1, 2].

Linear stiffness of suspension affects the parameters of control stability and comfort. Because the equations are complex and many parameters have been involved, it is hard to analyses the characteristics of suspension only directly depend on the formulation in theoretical analysis [3, 4]. As the study of the rigidity of suspension line, Chen Xiaozhang et al. have created multi-rigidity dynamics model in ADAMS, they replaced the torsion beam with the torsion-spring in standard database [8]. Wang Qidong et al. deduced the complex kinetic functions and the calculation functions of rigidity through creating double-wishbone model [9].

This paper is based on the multi-body dynamics, first the torsion beam will be transformed into flexible model and double-wishbone rigid-flexible coupling system model will be created, and the force between tire and ground as well as the vertical displacement will be analyzed afterwards, then the relationship of the stiffness of the two suspension models that vary because of the tire's displacement is going to be compared, and the static force of the key torsion beam could be calculated at last.

The structure of double-wishbone torsion independent suspension

In this paper, vertical linear stiffness of double-wishbone torsion independent suspension system of a certain car was analyzed. First, the system models were necessarily simplified, and the schematic diagram of suspension with double-wishbone (As shown in Fig. 1) was presented, including the upper wishbone AB, king pin BC, lower wishbone CD and torsion bar AG, where point A and D are the centers of the upper and lower wishbone connection hinge pins respectively. Meanwhile, point B and C are centers of the ball joints where the king pin BC connects with the upper and lower wishbones. In the lateral vertical plane of a car, φ and ψ represent the oscillation angles of the upper and lower wishbones relative to the horizontal plane respectively, steering king pin angle is represented by β_0 .

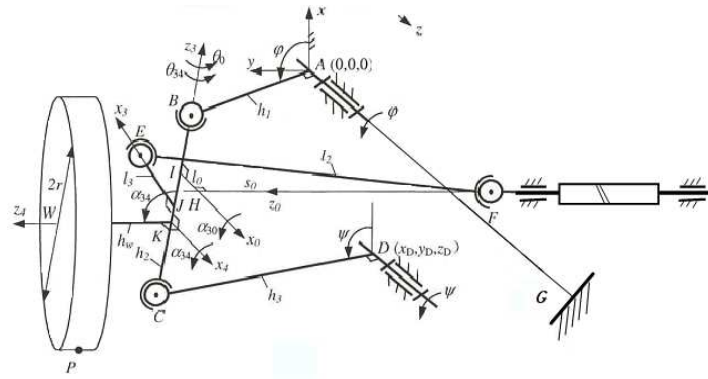


Fig. 1

The vertical linear stiffness of suspension is a very important physical parameter which affects both car handling and ride comfort. The excessively large vertical linear stiffness and high frequency vibration of front axle critically could reduce ride comfort. However, when a car is rounding a corner, excessively small vertical linear stiffness could result in serious body lateral tilt which could further give rise to poor handling and passenger's insecurity.

The linear stiffness of suspension is defined as the ratio of the variation of the interaction forces between tires and ground to the variation of the wheel displacement in the vertical direction, and expressed as

$$K = \left| \frac{\Delta F_N}{\Delta L} \right| \quad (1)$$

Where, K—The linear stiffness of suspension;

ΔF_N —Variation of interaction force between tires and ground;

ΔL —Variation of the wheel displacement in vertical direction.

Multi-body dynamics analysis of suspension system

The establishment of torsion spring system model. Assuming the suspension has a vertical center face of symmetry, a half front suspension model could be made for simplification. When making the model of Suspension with Double Wishbone, all the parts could be defined, expecting torsion as rigid bodies and ignoring the flexibility and transformation of the guide bar. To simplify the complexity of models, it is reasonable to consider the wheels as rigid bodies and disregard the friction of kinematics pairs, and let the mass of the spring is distributed to front suspension and rear suspension on a proportional basis.

In fact, the load conditions of the torsion spring are complex, so a torsion-spring in the standard library of ADAMS has been added between the torsion springs [10]. The added part can be used as torsion spring through inputting the rigidity and preload of the torsion spring, but a certain amount of error of the simulation results and experimental results will exist. In order to meet the physical truth better, torsion spring is defined as Flexible Body in this paper, which establishes a rigid body mode of double-wishbone independent suspension in the MSC. ADAMS software. Its specific operations are as follows:

Define the material properties and choose the steel in the standard library of adams.

Add constraints. Realize the relative motion through adding constraints and compose a suspension through connecting different parts.

Add drive. Add linear displacement drive to the test-bed.

Import the modal neutral document of torsion spring through the Build--Flex module of adams. Than generate the Flexible Body of torsion spring and replace the flexible body with the rigid body. Finally, establish the rigid-flexible coupling modle as Fig. 2.

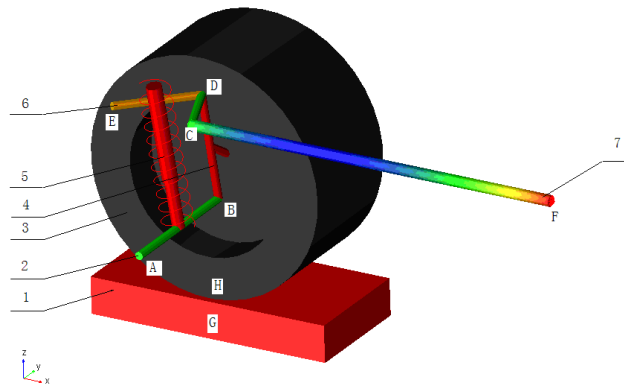


Fig.2 The torsion spring model of double wishbone independent suspension system
 1-Test-bed 2-Lower arm 3-Wheel 4-Kingpins 5-Shock absorber
 6-Upper arm 7- Flexible body of torsion bar spring

Through the Build-Flex module of ADAMS, the modal the document of torsion spring could be imported. Then the Flexible Body of torsion spring will be generated, replacing the flexible body with the rigid body. Finally, the rigid-flexible coupling model is established.

Simulation and analysis. This paper aims to calculate the suspension vertical stiffness; therefore a curve of displacement load is added to the test bed at Z direction, the center of mass of the tire, luntai.cm, will move regularly in Z direction, reacting force can be simulated in the end. Fig. 3 shows the deformation of the torsion bar and stress cloud chart in the ADAMS software, when the torsion bar tested under the maximum torsion moment, and the maximum stress is 542.32MPa, it meets the allowable stress. The suspension vertical stiffness can be calculated according to the formula (1), and the suspension stiffness curve are displayed in the Fig.3.

According to the study method on linear stiffness of double wishbone typed independent suspension, theoretical calculation of the model can be achieved. At balance position, suspension stiffness is 65.55N/mm. From Fig.4, we can measure the suspension stiffness of multi-rigid-body model and rigid-flexible model that are in balance are 71N/mm, 6.8N/mm respectively that is a little greater than the calculated value. Research shows that angle stiffness of a rubber bushing has an effect on suspension stiffness to some extent.

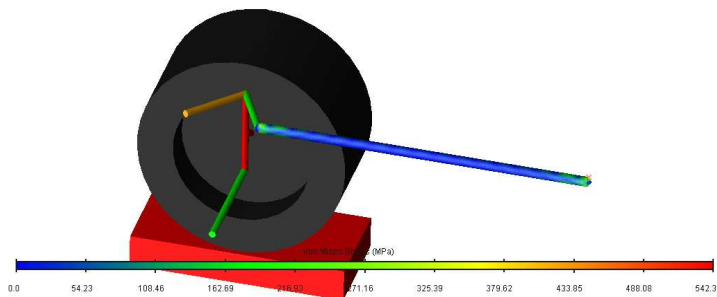


Fig.3 The torsion bar deformation and stress cloud chart

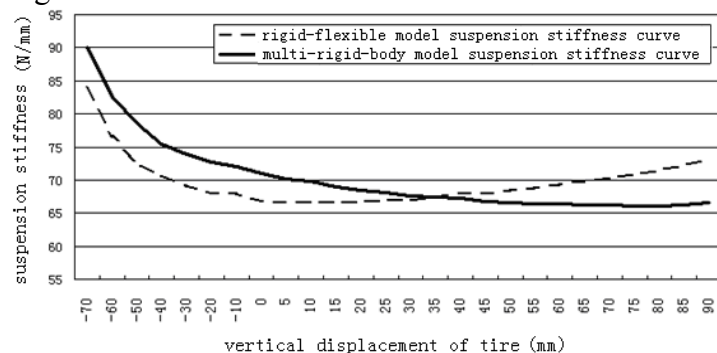


Fig.4 Suspension stiffness curve changing with the tire displacement

From the two curves in the Fig.4, we can discover that the suspension stiffness curve using rigid-flexible model test method and multi-rigid model test method decrease when the tire moves down, and near the balance position, the curve actually slopes upwards as the tire moves up, stiffness nonlinear characteristics of suspension becomes more apparent, which improves vehicle riding comfort obviously.

Conclusions

Through applying FEM method on the Static's Analysis of torsion spring, the result shows that when the torsion beam withstands the maximum torsion, the material strength can meet the practical requirement.

A multi-rigidity and rigid-flexible coupling model of double-wishbone independent suspension was built through ADAMS/VIEW and the multi-body dynamics simulation has been carried out. The result of simulation shows that rigid-flexible coupling model is more accuracy than multi-rigid one and fits with the practical test result better. Besides, the difference is smaller when compared with the test data. The result demonstrates that it is an efficient method to analyses the rigid of double-wishbone.

References

- [1] J.Li,H.J.Zou,H.Guo.Design and Experiment of Torsion Bar Spring for HJL1020. Machine Design and Research, 2002, (4): p57
- [2] Y.H.Deng,Y.J.Hu,Y.C.Yang. Matching of rigidity and equip-intensity design of twin torsion bar in double wishbone suspension with twin torsion bar. Engineering Design, 2002, (9): p44
- [3] S.T.Zhou,H.W.HUANG,W.Y.Zhu.Optimization design of torsion bar of double wishbone suspension based on random vibration analysis method. Journal of Central South University, 2011, (12): p3736
- [4] M.J.Luo,W.L.Wang.Finite element analysis and structural optimization on double-wishbone independent suspension with torsion. Machinery Design & Manufacture, 2009, (7): p19
- [5] SH.CH.Li,D.K.Chen,F.Ge, Stiffness Calculation and Force Analysis of Double Wishbone Independent Suspension with Torsion Bar. Journal of Academy of Military Transportation, 2010, (1): p51
- [6] GU Xinzhong, ZHANG Tieshan. The Match of Stiffness between Front and Rear Suspension.MECHANICAL ENGINEER. 2011, (1): p3
- [7] X.Z.Cheng,L.Q.Chen.Stiffness Calculation of Suspension with Torsion-bar Double Wishbone Based on ADAMS. Tractor& Farm Transporter, 2008, (2): p17
- [8] SH.Y.DUAN, A passenger car suspension K&C characteristics analysis and its matching research[D]. Guangxi University of Technology , 2010, (1): p3
- [9] Q.D.Wang,W.W.Chen,W.H.He.Stiffness Calculation of an Independent Suspension with Double Wishbone Based on Multi-body Dynamics.Transactions of the Chinese Society of Agricultural Machinery, 2004, (35): p132
- [10] WANG Nan,WANG Jing,PING Enshun. Kinematics modeling and simulation of double wishbone suspension basedon ADAMS/Car.MECHANICAL ENGINEER. Journal of Hebei University of Engineering.2010, (12): p55

Dynamics analysis and Vibration Suppression of a Flexible Rotation Beam

Fushen Ren^{1, a}, Suli Chen^{1, b}, Zhigang Yao^{2, c}

¹School of Mechanical Science and Engineering, Northeast Petroleum University, Daqing, 163318

²Beijing Industrial Technician College, Beijing 100123

^arenfushen@126.com, ^bslchen@163.com, ^cyzgmm@yahoo.com.cn

Keywords: Flexible Rotation Beam; Nonlinear Vibration; Transverse; Vibration Suppression

Abstract: This paper studies the complex transverse vibration behavior of drill string. The drill string was simplified as flexible rotation beam, and drill string of complex load was simplified for flexible rotation beam system. The nonlinear dynamic equations of flexible rotation beam is established and the complex dynamic response of flexible rotation beam in resonance case is analyzed by using method of nonlinear dynamics method. Research result show that the chaotic responses are sensitive to the revolving speed, the nonlinear oscillation of drilling string can be controlled by changing the rotating speed. This study has guiding significance to keep sidewall stability in the process of horizontal wells of sidetrack, improve the drilling rate and reduce the cost of the drilling.

Introduction

Scholars have done a lot of work and achieved many results in the drill string research [1, 2]. However, previous drill string of transverse vibration are based on the existing research theory of linear analysis, concentrated more on the bottom downhole assembly BHA section, and ignored the influence of nonlinear factors and flexible characteristics drill string of [4, 5]. This paper simplified the drill string as flexible rotation beam, set up the nonlinear differential equation for the flexible rotation beams. Through the dynamic response analysis of flexible rotation beam, this paper discusses transverse vibration behaviour, analyzes complex dynamic response. Research results providing theoretical guidance for well drilling process of transverse vibration problem.

The Establishment of the Kinetic Equation

For ease of analysis, the drill string is simplified to a rotating flexible beam; we define the beam axis before deformation as the X-axis, shown in Fig. 1:

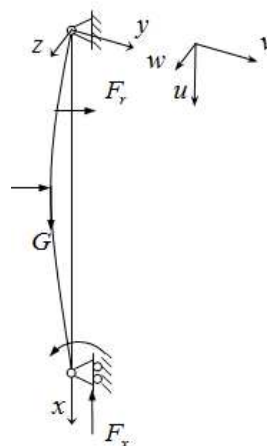


Fig. 1 The mechanical model of flexible rotating beam

Selecting the displacement field as the following equation

$$u = -y \frac{\partial v_0}{\partial x} - z \frac{\partial w_0}{\partial x}, \quad v = v_0(x, t), \quad w = w_0(x, t) \quad (1)$$

Considering the huge geometric deformation

$$\varepsilon_x = -z \frac{\partial^2 w_0}{\partial x^2} - y \frac{\partial^2 v_0}{\partial x^2} + \frac{1}{2} \left(\frac{\partial w_0}{\partial x} \right)^2 + \frac{1}{2} \left(\frac{\partial v_0}{\partial x} \right)^2, \quad \varepsilon_{xz} = \frac{1}{2} \frac{\partial w_0}{\partial x}, \quad \varepsilon_{xy} = \frac{1}{2} \frac{\partial v_0}{\partial x} \quad (2)$$

Consider that the drill string is made up of single material, so the simplified flexible beam the have two independent stiffness E_{11} and E_{12} . Simplify the force of the drill string at the drill as flexible beam axial force F_x , the power's variation at corresponding displacement Δ of F_x . When rotate with angular velocity ω , flexible beam have to withstand the centrifugal force, the variation of centrifugal force's power is $\omega^2 \sqrt{v^2 + w^2} \delta(\sqrt{v^2 + w^2})$, take advantage of Hamilton's principle to get the kinetic equation

$$\begin{aligned} & \frac{1}{2} A_{11} \left(\frac{\partial w_0}{\partial x} \right)^2 \frac{\partial^2 v_0}{\partial x^2} + A_{11} \frac{\partial w_0}{\partial x} \frac{\partial v_0}{\partial x} \frac{\partial^2 w_0}{\partial x^2} + \frac{3}{2} A_{11} \left(\frac{\partial v_0}{\partial x} \right)^2 \frac{\partial^2 v_0}{\partial x^2} + \left(\frac{1}{2} A_{12} - P \right) \frac{\partial^2 v_0}{\partial x^2} + H_1 \omega_4^2 v_0 \\ & = I_0 \frac{\partial \ddot{v}_0}{\partial t^2} - I_2 \frac{\partial^2 \ddot{v}_0}{\partial x^2} \end{aligned} \quad (3a)$$

$$\begin{aligned} & \frac{1}{2} A_{11} \left(\frac{\partial v_0}{\partial x} \right)^2 \frac{\partial^2 w_0}{\partial x^2} + A_{11} \frac{\partial w_0}{\partial x} \frac{\partial v_0}{\partial x} \frac{\partial^2 v_0}{\partial x^2} + \frac{3}{2} A_{11} \left(\frac{\partial w_0}{\partial x} \right)^2 \frac{\partial^2 w_0}{\partial x^2} + \left(\frac{1}{2} A_{12} - P \right) \frac{\partial^2 w_0}{\partial x^2} \\ & + H_1 \omega_4^2 w_0 - D_{11} \frac{\partial^4 w_0}{\partial x^4} = I_0 \frac{\partial \ddot{w}_0}{\partial t^2} - I_2 \frac{\partial^2 \ddot{w}_0}{\partial x^2} \end{aligned} \quad (3b)$$

Where

$$\begin{aligned} A_{11} &= \iint_{\Omega} E_{11} dy dz, \quad A_{12} = \iint_{\Omega} E_{12} dy dz, \quad D_{11} = \iint_{\Omega} y^2 E_{11} dy dz, \quad P = \iint_{\Omega} F_x dy dz, \\ H_1 &= \iint_{\Omega} dy dz, \quad I_0 = \iint_{\Omega} \rho dy dz, \quad I_2 = \iint_{\Omega} \rho y^2 dy dz \end{aligned}$$

For ease of analysis, introduce $\bar{w}_0 = \frac{w_0}{l}$, $\bar{v}_0 = \frac{v_0}{l}$, $\bar{x} = \frac{x}{l}$ etc dimensionless transform, for the convenience of expression, the overline of dimensionless equations is removed, the following equation's parameters are all dimensionless parameters, and take the transverse vibration displacement's two-order mode as : $w_0 = w_1(t) \sin 2\pi x$, $v_0 = v_1(t) \sin 2\pi x$. Using the method of Galerkin to discretize, obtained the motion equations of transverse vibration as show Eq. (4)

$$\begin{aligned} & \ddot{v}_1 + c_3 \dot{v}_1 + \frac{1}{2I_2 a^2 \pi^2 + 2I_0 a^4} \left(-\pi^2 A_{12} a^2 - 8D_{11} \pi^4 + \frac{1}{2} I_0 \omega^2 a^4 + 2\pi^2 P a^2 \right) v_1 \\ & - \frac{3\pi^4 A_{11} R_1^2}{8I_2 a^2 \pi^2 + 8I_0 a^4} v_1 w_1^2 - \frac{3\pi^4 A_{11} R_1^2}{8I_2 a^2 \pi^2 + 8I_0 a^4} v_1^3 = 0 \end{aligned} \quad (4a)$$

$$\begin{aligned} \ddot{w}_1 + c_3 \dot{w}_1 + \frac{1}{2I_2 a^2 \pi^2 + 2I_0 a^4} \left(-\pi^2 A_{12} a^2 - 8D_{11} \pi^4 + \frac{1}{2} I_0 \omega^2 a^4 + 2\pi^2 P a^2 \right) w_1 \\ - \frac{3\pi^4 A_{11} R_1^2}{8I_2 a^2 \pi^2 + 8I_0 a^4} w_1 v_1^2 - \frac{3\pi^4 A_{11} R_1^2}{8I_2 a^2 \pi^2 + 8I_0 a^4} w_1^3 = 0 \end{aligned} \quad (4b)$$

Perturbation Analysis

Selecting an appropriate parameter for the perturbation analysis and using the method of multiple scales to obtain the average equation of equation (4). Considering the main parametric resonance and 1:1 resonance, through the consolidation of the formula, we can get average equation in Cartesian coordinate, as show Eq. (5)

$$\begin{aligned} \dot{x}_1 = -\frac{1}{8a^2 I_2 \pi^2 + 2I_0 a^4} \left(\frac{2}{R_1} a^4 C_3 x_1 - a^2 \pi^2 P x_2 - a^4 I_0 \omega_4^2 x_2 \right. \\ \left. + \frac{9}{32} R_1^2 \pi^4 A_{11} x_2^3 + \frac{9}{32} R_1^2 \pi^4 A_{11} x_2 x_4^2 + \frac{3}{16} R_1^2 \pi^4 A_{11} x_1 x_3 x_4 \right. \\ \left. + \frac{3}{32} R_1^2 \pi^4 A_{11} x_2 x_3^2 + \frac{9}{32} R_1^2 \pi^4 A_{11} x_2 x_1^2 \right) \end{aligned} \quad (5a)$$

$$\begin{aligned} \dot{x}_2 = \frac{1}{8a^2 I_2 \pi^2 + 2I_0 a^4} \left(\frac{2}{R_1} a^4 C_3 x_2 - a^2 \pi^2 P x_1 - a^4 I_0 \omega_4^2 x_1 \right. \\ \left. + \frac{9}{32} R_1^2 \pi^4 A_{11} x_1^3 + \frac{9}{32} R_1^2 \pi^4 A_{11} x_1 x_3^2 + \frac{3}{16} R_1^2 \pi^4 A_{11} x_2 x_3 x_4 \right. \\ \left. + \frac{3}{32} R_1^2 \pi^4 A_{11} x_1 x_4^2 + \frac{9}{32} R_1^2 \pi^4 A_{11} x_1 x_2^2 \right) \end{aligned} \quad (5b)$$

$$\begin{aligned} \dot{x}_3 = -\frac{1}{8a^2 I_2 \pi^2 + 2I_0 a^4} \left(\frac{2}{R_1} a^4 C_3 x_3 - a^2 \pi^2 P x_4 - a^4 I_0 \omega_4^2 x_4 \right. \\ \left. + \frac{9}{32} R_1^2 \pi^4 A_{11} x_4^3 + \frac{9}{32} R_1^2 \pi^4 A_{11} x_4 x_3^2 + \frac{3}{16} R_1^2 \pi^4 A_{11} x_1 x_2 x_3 \right. \\ \left. + \frac{3}{32} R_1^2 \pi^4 A_{11} x_4 x_1^2 + \frac{9}{32} R_1^2 \pi^4 A_{11} x_4 x_2^2 \right) \end{aligned} \quad (5c)$$

$$\begin{aligned} \dot{x}_4 = \frac{1}{8a^2 I_2 \pi^2 + 2I_0 a^4} \left(\frac{2}{R_1} a^4 C_3 x_4 - a^2 \pi^2 P x_3 - a^4 I_0 \omega_4^2 x_3 \right. \\ \left. + \frac{9}{32} R_1^2 \pi^4 A_{11} x_3^3 + \frac{9}{32} R_1^2 \pi^4 A_{11} x_3 x_4^2 + \frac{3}{16} R_1^2 \pi^4 A_{11} x_1 x_2 x_4 \right. \\ \left. + \frac{3}{32} R_1^2 \pi^4 A_{11} x_3 x_2^2 + \frac{9}{32} R_1^2 \pi^4 A_{11} x_3 x_1^2 \right) \end{aligned} \quad (5d)$$

According to the average equation, the drill string vibration related the two variable parameters: rotation speed and axial force. The drill string axial force is difficult to forecast caused by external load, but the drill string speed can be changed. We also observed that the two parameters in the same equations, so a parameters on the effect of vibration by adjusting the other parameters to weaken.

Nonlinear Dynamics and Bifurcation Analysis

In this section, the average Eq. (5) is simulated and analyzed by using numerical methods, and get the nonlinear dynamic system response. Example 1: Fig. 2 (a) and Fig. 2 (b) are bifurcation diagrams of the system's two modal response with the angular velocity changes, the system initial conditions and parameter values of the figures are $x_{10} = -7.9$, $x_{20} = -13$, $x_{30} = -20$, $x_{40} = 15.5$, $c_3 = 0.033$, $\rho = 1.36$, $A_{11} = 0.365$.

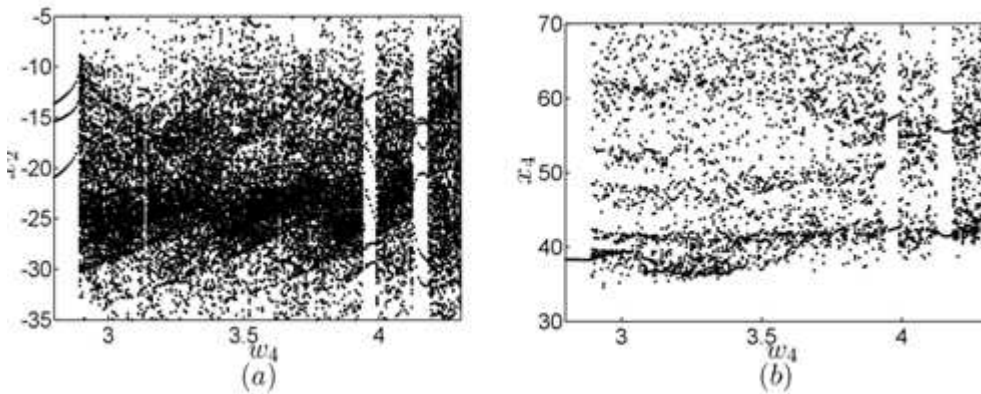


Fig. 2 Speed bifurcation diagram

From Fig. 2 we can see, the response of system has gone through the process of cycle--chaos--twice the cycle, response amplitude appear jumping phenomenon, the mechanism of the phenomenon is the energy conversion between the two modal. Only change the angular velocity ω_4 of Fig.2, the system's initial conditions and other parameters are unchanged, when $\omega_4 = 2.8$, the system will appear almost periodic motion, as shown in Fig. 3.

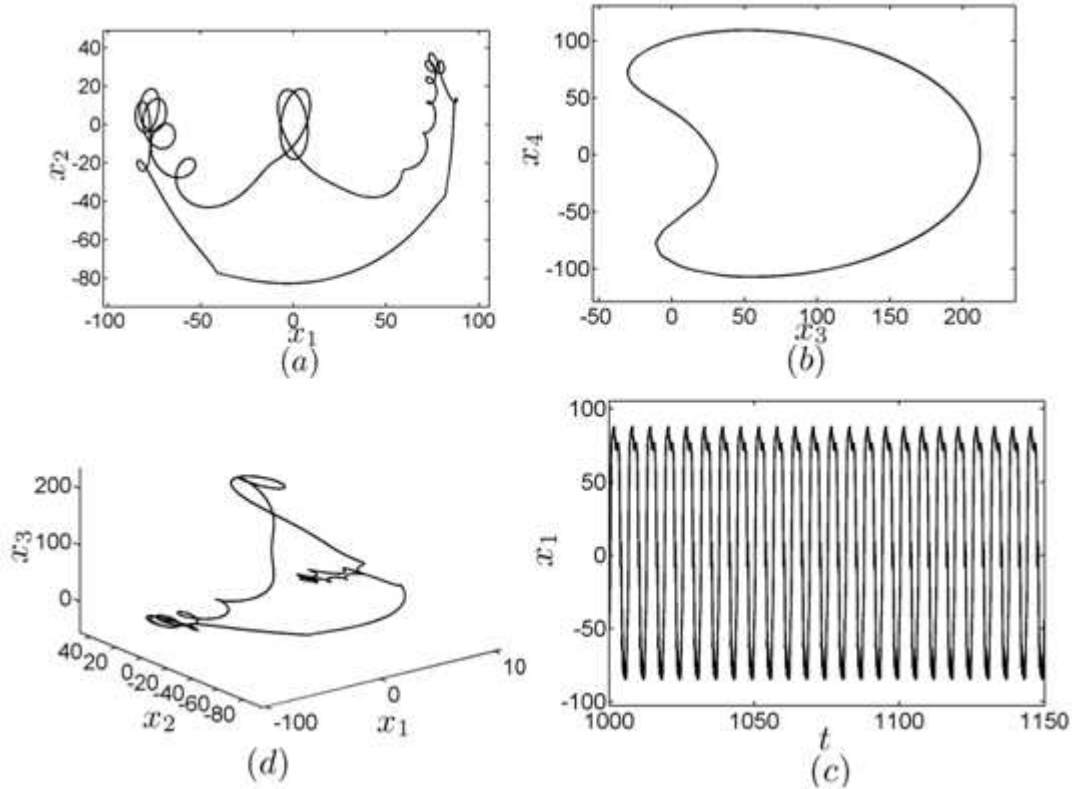


Fig. 3 When $\omega_4 = 2.8$ the cycle response of system

When increase the angular velocity $\omega_4 = 2.896$, the almost periodic motion of the system will change into six-fold periodic motion, as shown in Fig. 4.

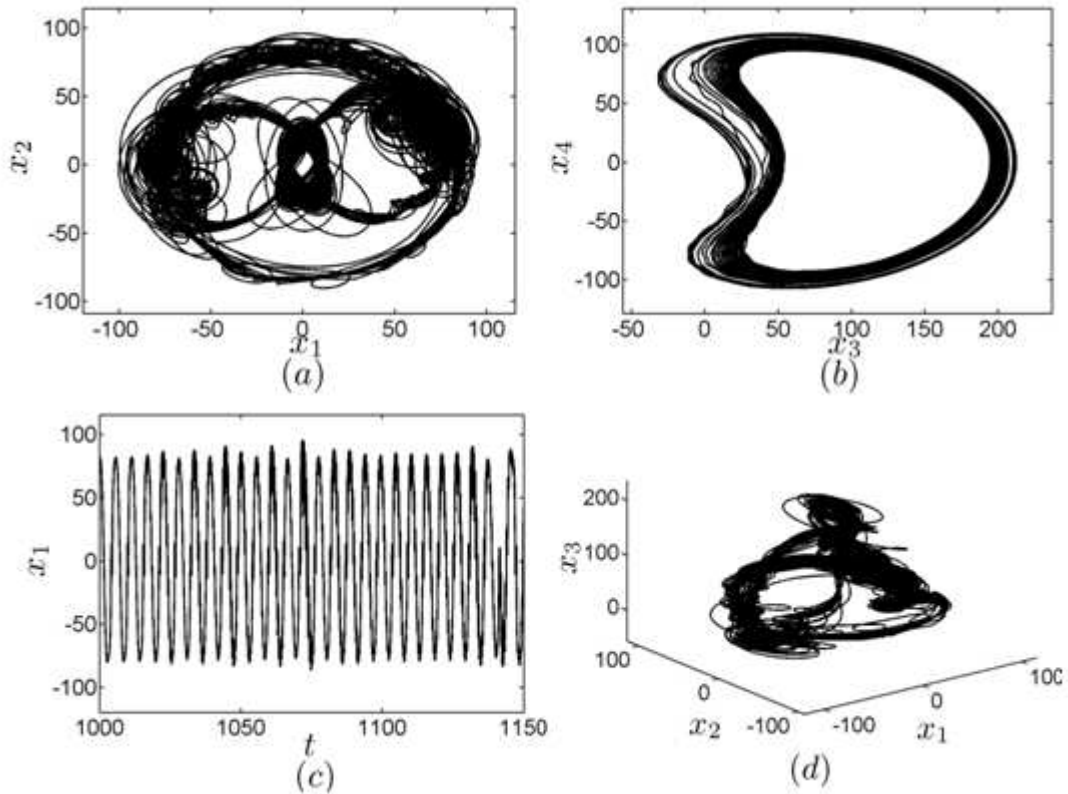


Fig. 4 When $\omega_4 = 2.896$ the chaotic response of system

Continue to increase the angular velocity $\omega_4 = 3.944$, the system becomes twice the periodic motion, as shown in Fig. 5.

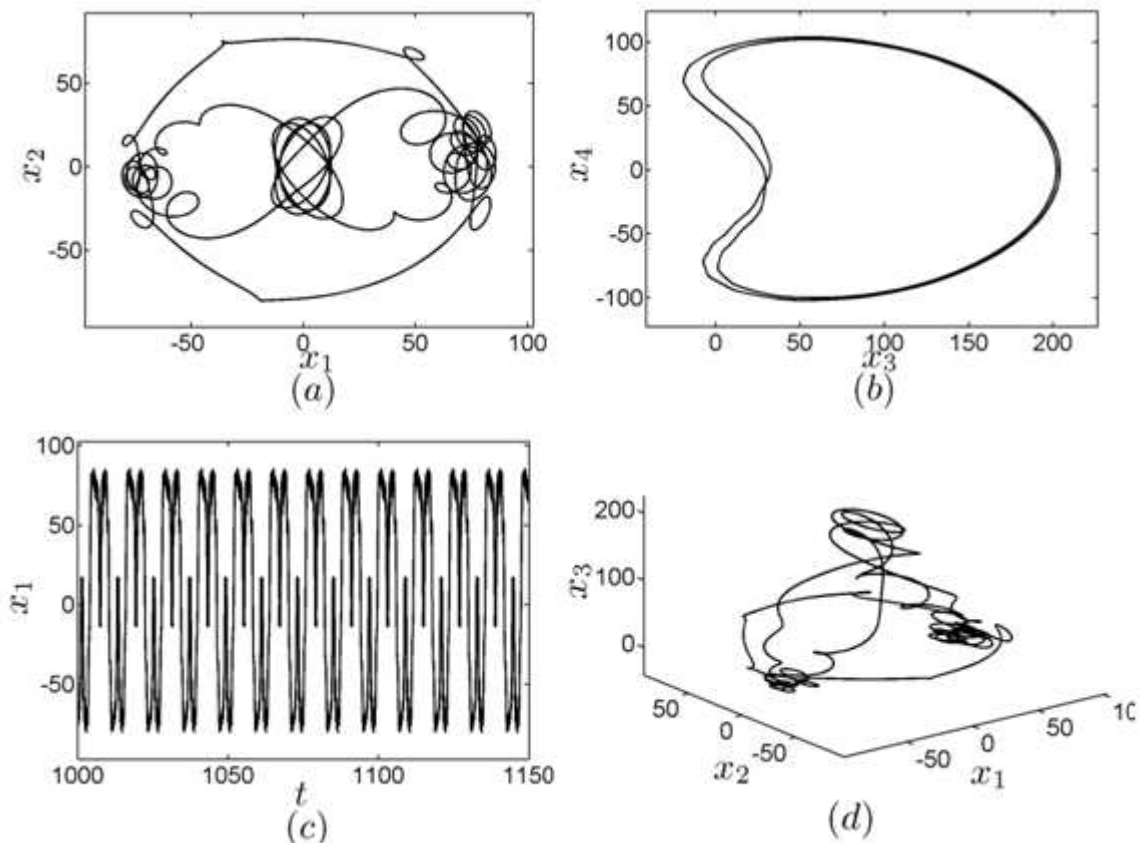


Fig. 5 When $\omega_4 = 3.944$ the cycle response of system

Example 2: The bifurcation diagrams of the system's two modal response with the angular velocity changes, as shown in Fig. 6. The system initial conditions and parameter values of the figures are $x_{10} = 8.0, x_{20} = 8.8, x_{30} = -14.3, x_{40} = 0.3, c_3 = 0.089, \rho = 1.43, A_{11} = 0.015$

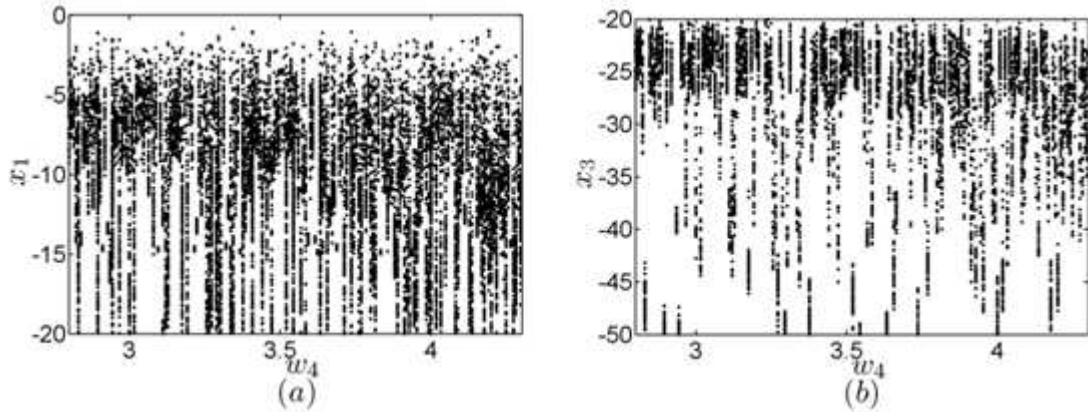


Fig. 6 Speed bifurcation diagram

From Fig. 6 we can see, most of the response of the system is chaotic, but there are cycle's responses between chaotic responses. Only change the angular velocity ω_4 of Fig. 6, the system's initial conditions and other parameters are unchanged, when $\omega_4 = 2.872$, the system will appear chaotic motion, as shown in Fig. 7.

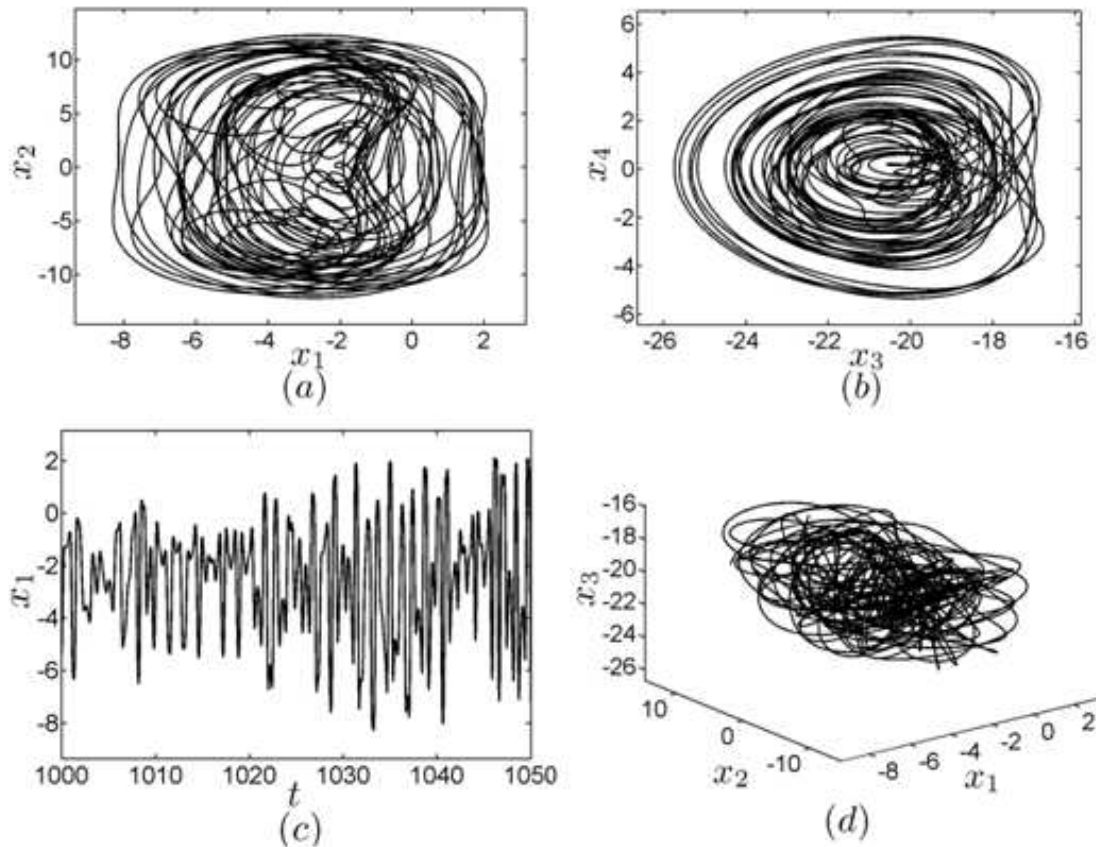


Fig. 7 When $\omega_4 = 2.872$ the chaotic response of system

When increase the angular velocity $\omega_4 = 2.912$, the system will change chaos into six-fold periodic motion, as shown in Fig. 8.

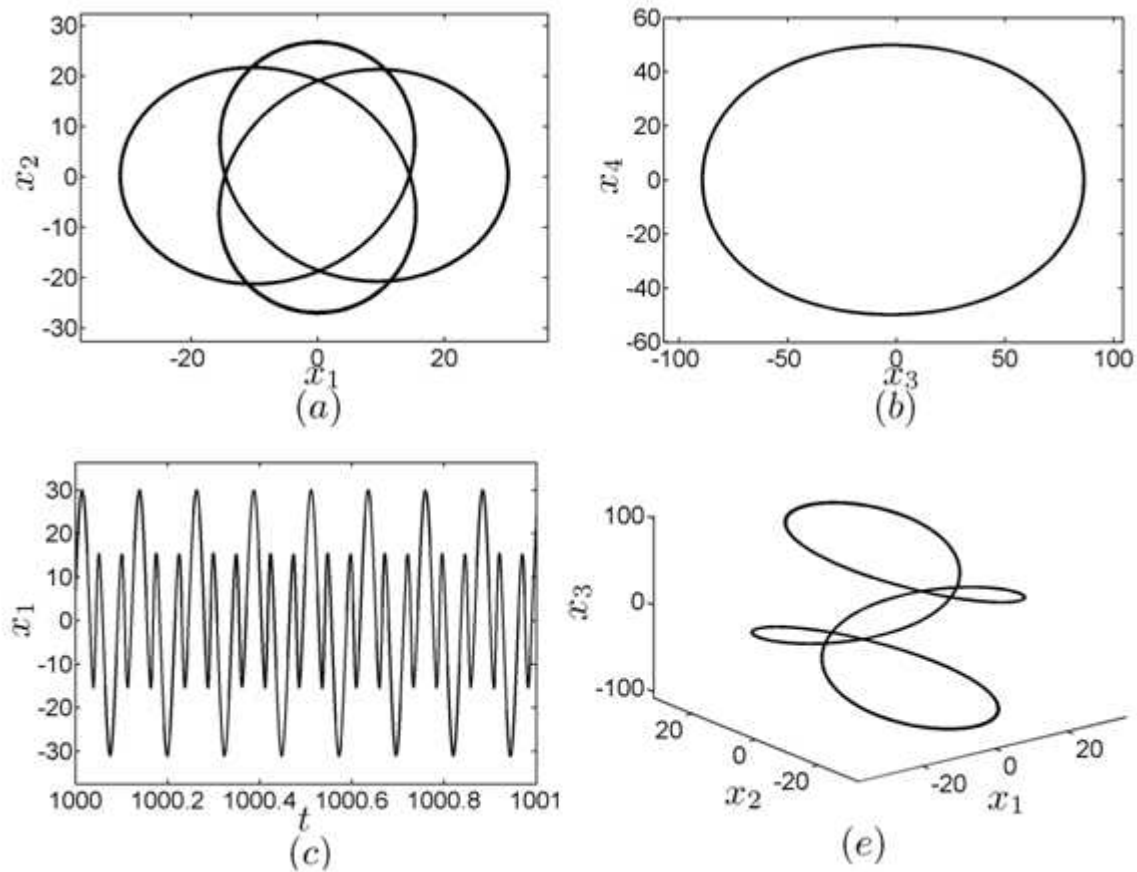


Fig. 8 When $\omega_4 = 2.912$ the cycle response of system

Through the phase diagram and the bifurcate diagram analysis, the response of the system has experienced the process of cycle-chaos-two times the cycle, response amplitude appear jumping phenomenon. The analysis results show that the flexible rotating beam's amplitude is not infinite, but limited, at the condition of v resonance. At the same time, the additional and axial force which due to the speed change work in the same item in the equation, can offset each other, when the axial force changes, for the sake of qualitatively and quantitatively controlling the flexible rotating beam vibration, can through controlling the speed's change, significantly reduce the amplitude of the vibration, control system vary from almost periodic to single cycle times, maintain the stability of the system, control system produce period-doubling bifurcation solution, thus prevent the system via the period-doubling bifurcation into chaos movement, and give the control bifurcate figure.

Conclusion

The average equation of flexible rotating beam is set up considering the nonlinear dynamics;

The complex dynamic response of flexible drill string is analysed in the case of resonance and control bifurcation diagrams is given.

In the drilling process, we can adjust the rotation rate to control the transverse vibration of drill string under constant pressure drilling condition

Acknowledgment

The authors gratefully acknowledge financial support by the scientific and technological project in Heilongjiang Province of China under Grant N.O. 2010D-5006-0307 and the Fund for Creative Technology of China Petroleum under Grant N.O. GZ11A405 and The National Natural Science Funds under Grant N.O. 11002005.

References

- [1] A. D. Batako, V. I. Babitsky, N. A. Halliwell, A self-excited system for percussive- rotary drilling[C]. Journal of Sound and Vibration, 2003, 259(1): 97-118, .
- [2] Eva M. Navarro-López, Domingo Cortés, Avoiding harmful oscillations in a drillstring through dynamical analysis[C]. Journal of Sound and Vibration, 2007: 307(23): 152-171, .
- [3] Eva.M.Navarro-López,EduardoLicéaga-Castro, Non-desired transitions and sliding-mode control of a multi-DOF mechanical system with stick-slip oscillations, Chaos[C].Solitons and Fractals,2009, 41(4):2035-2044, .
- [4] Li Guoqing,Wang Hongjun,Liu Xiushan,et al.Analysis and application of drill string vibration[J].Petroleum Drilling Techniques,2007, 35(6):54~56.
- [5] Zhu Xiaohua,Tong hua,Liu Qingyou,et al.Research on the dynamic boundary condition between revolving drill string and borehole wall[J].China Mechanical Engineering,2007,
- [6] Han Chunjie,Yantie.. Transverse drill string vibration in horizontal holes [J]. China petroleum machinery, 2005, 33(1):8~10.
- [7] QU Zhan. Influen ce of in and out drillin g f luid on t ransverse vib rat ion of th e drilling string[J].China Petroleum Machinery, 1995, 23(4):40- 43.

Juice Extractor Stent Plastic Mould Structure Design

Xiuzhong Cao

Wuxi Institute of Technology, Jiangsu Wuxi, 214121, China

caoxiuzhong@163.com

Keywords: Juice Extractor Stent; Injection Mould; the Two Cavity; Side Core-Pulling Mechanism

Abstract. The design of plastic parts structure analysis, confirmed the mould adopts the exactly two cavities, with two points type surface, three board type injection molds. Exhaust systems use the parting surface and lateral slide block clearance, plunger, cooperate with clearance to exhaust, and using a runner filling mold overall layout form. In the mold design process, the design of classification, gating system, exhaust system, cooling system, demoulding mechanism, are introduced in this paper.

The Plastic Parts Analysis

Fig. 1 is the juice extractor stent 3 d drawing, this product is used for extracting machine, the support role to spin juicer, the product shape is more complex, high accuracy, the surface does not allow to have the obvious welding scar, flash and the process technology trace, need certain cooperate with accuracy. Products have the full whole draft, everywhere stripping force are reasonable. From the whole structure analysis: products surface area is lesser, height is not big but thin, parts of the wall surface complex, cavity, cores processing difficulties. From the whole technology analysis: according to appearance and structure required products demand option runner, products must be even and cooling fully, stripping force reasonable distribution, request ejector institutions ejector even.

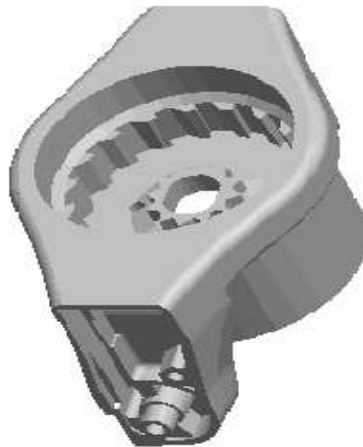


Fig. 1 Plastic parts 3 d drawing

The product structure is complex, there are three place side concave phenomenon, need to set up a heart institutions, and considering the product's size and shape, should use a module and two cavity, three plate structure, plastic from four points gate into the cavity while curing.

Sure Cavity Number of Its Arrangement

According to the plastic parts of three dimensional structure form, consider a mold a cavity and a mold cavity two two sets of plan. Introduce the following:

if the exactly a cavity, can through the point gate top feeding, easy to guarantee the quality of the part; At the same time, the mould of small size, reduce the cost of mould, but plastic parts wall thickness thicker, cause the filling plastic parts uneven, product quality can't guarantee; The filling time often, can not adapt to the mass production requirements, and greatly reduce the production efficiency.

If the two cavity exactly the decorate, although mold size increases, manufacturing costs have increased, but ensure the precision of the product, and high production efficiency, to adapt to the requirement of mass production.

After more than two sets of project of comparison, because plastic parts of itself shape and size is lesser, and itself of its special structure, considering its molding part and smoke core structure and way of the mold design, so the two forms of the cavity. The mold cavity arrangement as shown in fig. 2 shows:

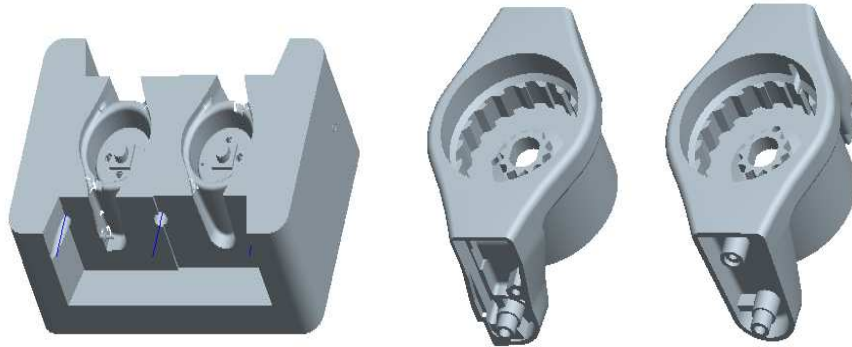


Fig. 2 Mould cavity arrangement

The Design Classification

For the plastic parts and gating system coagulates material of patterns and put the need of embedded thing, will the mold cavity properly is divided into two or more parts, these can separate the part of the contact surface, namely for the parting surface.

Parting surface form from the plastic parts of the concrete circumstances, common have level of parting surface, oblique parting surface, stepped-weir parting surface and surface parting surface and the vertical parting surface.

Points of products of the surface quality face type, size accuracy, stripping, cavity cores structure and exhaust and feeding gate and mould manufacturing will have direct influence. Therefore, in choice and determine the type points should be comprehensive analysis, comparison and consideration, choose relatively advantageous scheme.

The main points of parting surface determined as follows:

The biggest rappel/abseil stations should be products shape dimension of place, otherwise, products is not releasable. Rappel/abseil stations should be also the products of dynamic model in place be helpful for stripping.

It cannot affect the appearance products, especially to the surface quality of the request products.

Facilitate gate feeding, beneficial to the forming, easy to exhaust.

To mold processing, and the precision of the products to be guaranteed

To the installation of the activities and embedded a set piece and elastic activities thread cores of installation.

In the design of the mould, and analyzes the structure characteristics of plastic parts, and according to the gate form, with two points type surface, three board type injection mold. The first parting surface points out type gating system coagulates material, as auxiliary parting surface; The second type surface give priority to the parting surface, the parting take out after plastic parts. In the two cavity mould layout form, with the first plastic parts bedding face, namely the center for the second type surface face, so that separate fluctuation cavity; In the mould parts increase a middle board for the first parting surface, take out of the material; Plastic parts appearance had convex platform and lateral holes, adding two side smoke institutions, because plastic parts have rib and grooves, make two set piece as shown in fig. 3.

Exhaust System Design

When a plastic melt filling mold cavity, must will gating system and air in the cavity and plastic in shaping process produce low molecular volatile gases from outside mould smoothly. If the gas within the cavity is expelled not clean, plastic parts can produce gas hole, welding rickety, surface profile is not clear and filling defects such as discontent molding, in addition, the existence of gas still can produce the pressure and reduce the speed of filling mold, affect the quality of products, so the design must be considered when the mould cavity while curing exhaust problem.

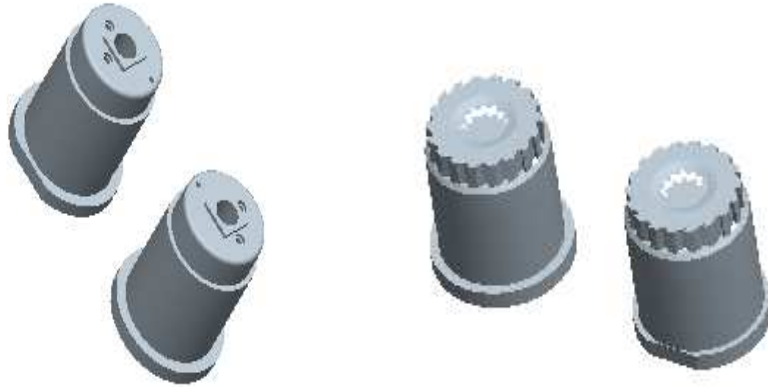


Fig. 3 Set the shape of the block diagram

Injection mould usually has three exhaust methods, namely in the points on exhaust slot open type, use fitting clearance and exhaust plug of exhaust vent.

In this mould design, does not need to open another exhaust slot, but use the parting surface and lateral slide block clearance, plunger, cooperate with clearance to exhaust. Because these clearance is objective existence, does not need to deliberately processing, so that natural exhaust. Because this kind of means other exhaust system should be set up, so the structure is simple, is usually used in injection mold a vent form.

Molding Parts Structure Form and Design

Molding parts molding plastics is directly parts, in this design mainly includes the concave die, the punch, cores, set pieces, etc. Molding parts complex shape, high precision, low surface roughness.

The Concave Die Structure Design

In this mould design for is a module and two cavity, and have set piece, so use the whole is combined-type embedded concave die, concave die of three dimensional figure as shown in fig. 4 shows:

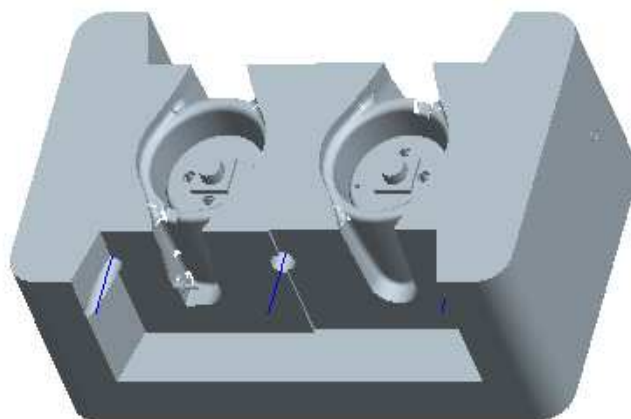


Fig. 4 Concave die design schemes

The Structure Design of the Punch

This design USES the same is combined-type the whole embedded concave die, the punch 3 d design as shown in fig. 5 shows:

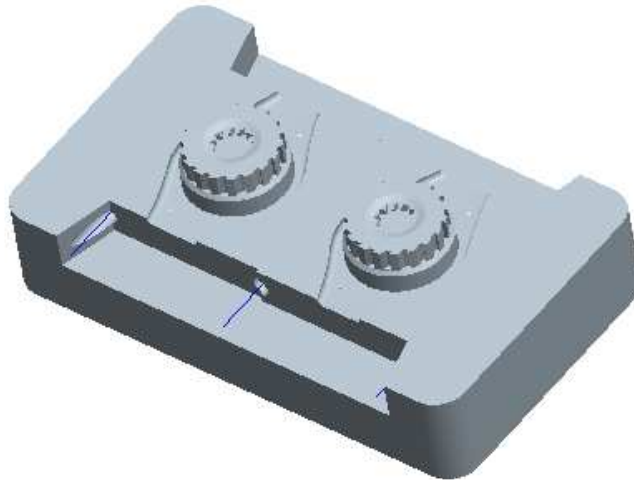


Fig. 5 Convex mold design schemes

1.6 References

- [1] liu to the English. Injection molding process. Beijing: mechanical industry press, 2004.10190
- [2] ChenXiaoKang ChenYanSi ZhouXingLong c3053. Practical mould technology handbook. Beijing: China light industry press, 2001.1
- [3] XuHeFeng, ChenYanQiu c3053. Injection mold design points and illustrations. Second edition. Chemical industry press, 1998.
- [4] the plastic mould technology manual "editorial committee made up. Plastic mould technology handbook. Beijing: mechanical industry press, 1997.6.
- [5] ZouJiJiang plastic products and its forming die design Beijing: tsinghua university press, 2005.2
- [6] GaoHongTing editor. Mould manufacturing work (intermediate). Beijing: China labor social security press, 2004.
- [7] WangWeiWei. Material molding equipment. Beijing: mechanical industry press, 2004.8
- [8] PengJianSheng. Mould design and processing SuZha manual. Beijing: mechanical industry press, 2005.6
- [9] mold design and manufacturing technology education board series. The mould structure design. Beijing: mechanical industry press, 2003.10
- [10] ChenJianHe. Mould design basis. Beijing: mechanical industry press, 2003.2
- [11] JiangJiHong, WangXiaoYue. Injection mould typical structure 100 cases. Beijing: China light industry press, 2000.5
- [12] ZhangQingHui. Die material and surface treatment. Beijing: electronic industry press, 2002
- [13] LiJiHong, LiXuan. Injection molding technology questions and answers. Beijing, mechanical industry press, 2004
- [14] LiuChangQi. Plastic mold design. Beijing: mechanical industry press, 1998.10
- [15] flexor huachang. Injection molding technology questions and answers. Beijing, mechanical industry press, 2004.3
- [16] ZouJiJiang. Plastic mould design reference material assembly. Beijing: tsinghua university press, 2005.9

Research of Multi- Channel Hygrothermoscope Acquiring System

Xiaobing Wu

Chongqing Vocational Institute of Engineering Chongqing, China

Keywords: STC89C54; DHT11; Max485; Hygrothermoscope Monitoring;

Abstract. The paper introduces a multipoint remote Hygrothermoscope monitoring system based on the MAX485 bus. The system of remote multipoint temperature control is composed of the host machine and slave machine; the host system for display and control, the slave system is responsible for collecting temperature data. Between master machine and slave machine communicate through the RS-485 bus, can realize the distant control room of the scene monitoring. The STC89C54 MCU is used as the controller and DHT11 is used as the temperate and humidity transducer. The hardware and software of the system are outlined. The system has realized multiple measuring points, easy expansion, and high reliability, anti-interference. The whole system has the advantages of simple circuit, reliable, and can be used for measuring temperature, humidity, temperature of building air conditioning control temperature and humidity monitoring and other fields.

Introduction

Remote temperature control is often encountered in the process of industrial production process control, especially some large special industrial occasions, precise control over the temperature requirements of very high. For this, the author developed a STC based remote multi-point temperature intelligent control system, the system terminal MCU multipoint temperature and humidity detection process, using CAN bus for remote data transmission system, real-time, stable and reliable, precise control, convenient operation.

The system is composed of and from the host machine is composed of two parts, from the machine implementation of multiple point temperature data acquisition and control, data through the data bus to the host, is implemented by the host display and control data input, so that users do not at the scene also can undertake to equipment operation, to achieve temperature remote monitoring.

System Hardware Circuit Design

Block Diagram of System

The system is composed of monitoring system and data acquisition system. The data acquisition system through the CAN bus to transmit data to the monitoring system, are shown in fig 1.

Principle of Work

Figure1 shows, the system is composed of two parts, respectively, and from the host machine, the two parts of the CPU is a powerful STC mcu. From machine CPU is connected with three temperature and humidity sensors (DHT11), CPU through a single bus protocol for three at a temperature of the collection, and through the RS-485 bus to transmit data to the host temperature, host receives the temperature data in the LCD displays the current temperature value, and with the user set the upper and lower limits of temperature value, CPU generated on the basis of the comparison of executive control signal.

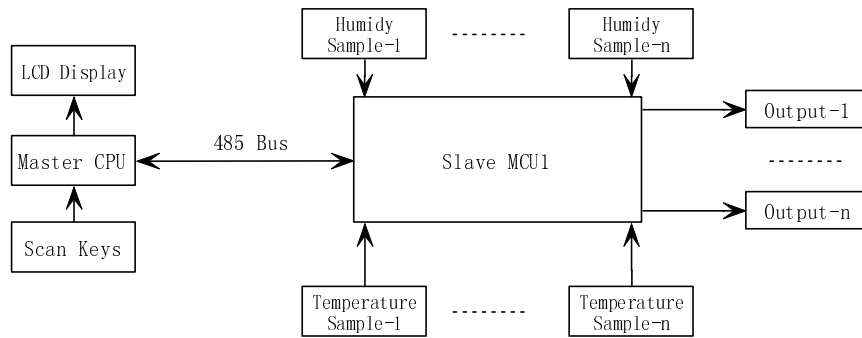


Fig. 1 The realization block diagram of system

The control signal through a bus back to the machine, from machine received after the implementation of control output, executive component is mainly photoelectric isolation and relay. If the temperature is lower than the lower limit is activated by heating, such as higher than the upper limit temperature, the heating is stopped, as in set between the upper and lower limits are not action. Thus the measuring point temperature control in the user set between the upper and lower limits, and because the user is a host of operation, from the machine in distant places, thus achieving a temperature of the remote control.

Main Control CPU

The system uses the STC chip STC89C54 as the main control CPU. STC is homebred chip, with low prices, wide application, convenient program download. As is shown in Fig 2 of chip STC89C54 pin diagram

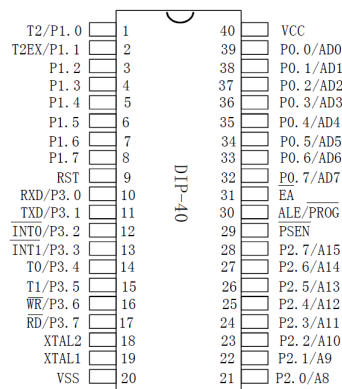


Fig. 2 Stc89c54 pin

Communication Interface Circuit

Communication interface chip using MAX485 chip, a photoelectric isolation by P521 photoelectric coupler [2]. The specific circuit is shown in fig 3.

Output Drive Circuit

The output control circuit composed of a relay and optical isolation drive, relay drive current of 5A, using 4N30, it will photoelectric isolation and composite transistor drive package in one, played a strong role in isolation, the specific circuit as shown in fig 4.

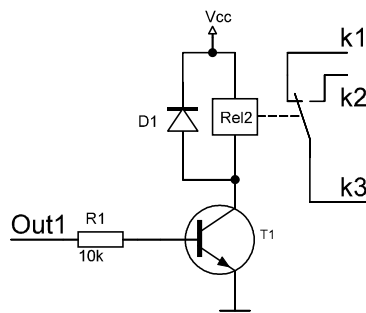


Fig. 4 Output drive circuit

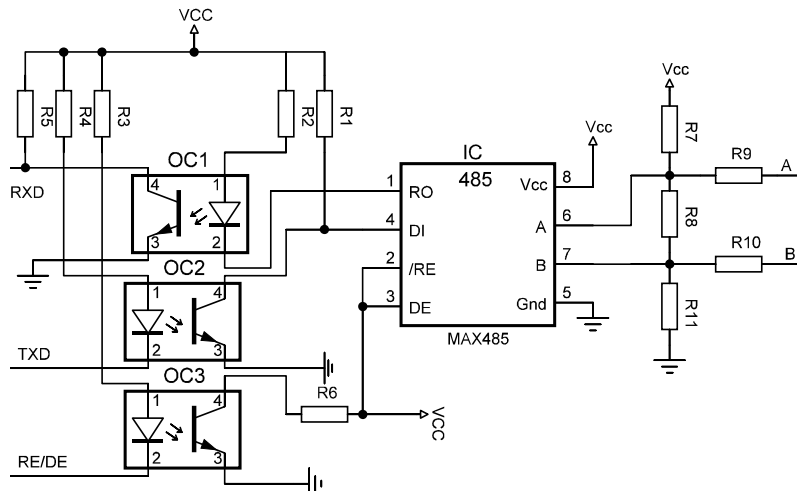


Fig. 3 Communication interface circuit

Temperature and Humidity Measuring Device (DHT11)

DHT11 is a 1-wire digital temperature and humidity sensor, CPU only one root port line can be with much DHT11 communication, occupied the port microprocessor less, can save a large amount of lead and logic circuit. It is the biggest characteristic of single bus data transmission mode, DHT11data I / O by the same line to complete. The hardware connection circuit is shown in fig 5.

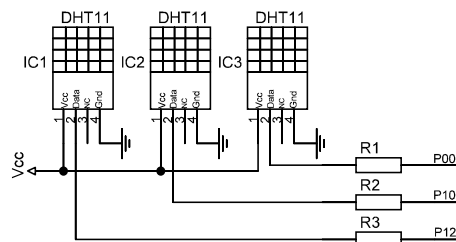


Fig. 5 The circuit of temperature and humidity measuring

The Circuit of Keyboard

Using a 4 x4 matrix key, can be obtained in 16key functions, just to meet the needs of the system. Keyboard function allocation : 0 ~9 digital input keys, check key, set / determine the key, enter key, a positive input keys, regulation of the left shift key, the right key regulation. Fig 6function keys distribution diagram, Fig 6 is the circuit diagram of the hardware.

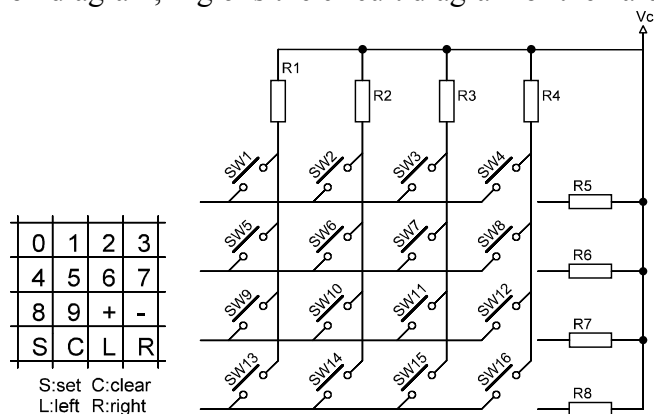


Fig. 6 The Circuit of keyboard

LCD Display

The system used a 128 x64 LCD, can display3216x 16 dot matrix Chinese characters or 648x 16characters. In the system menu function, can display a very friendly interface, convenient operation.

System Software Design

The system software using C language, C language has a module is good, strong readability, portability and many other advantages, can be widely used in the software industry.

Main Program Structure

The main program is divided into the main program from the host machine and the main program, the main program to complete the main keyboard identification, parameter display and temperature data processing. Communication in the process of data exchanged in the serial interruption service routine treatment. From the main program is mainly temperature data acquisition, and sending them to the host, the host sends the control command and execution. Communication data exchange is also in the serial interrupt service routine treatment, specific flow diagram as shown in Fig 7 the graph A is the main program flow chart, graph B is from the main program flow chart.

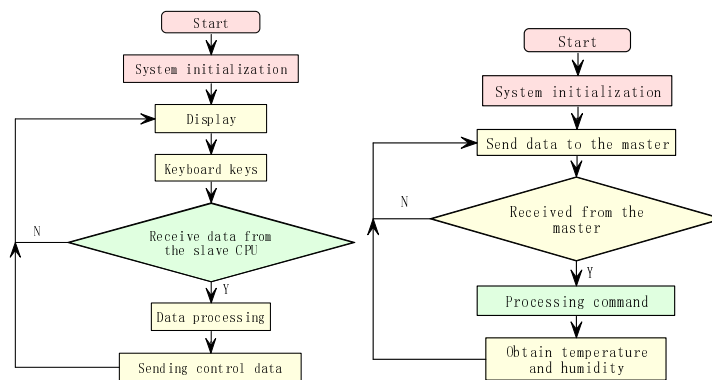


Fig. 7 Flow charts (host) left and (slave) right

Communication Protocol

Between host and slave communication must be according to certain communication protocol, specific communication is as follows:

After power on, and from the host machine serial port baud rate is 19200bit / s, from the machine every second to host transmits the monitoring data, the communication data format(table 1):

Table 1: Communication protocol

prefix code	serial number (8bit)	Humidy (16bit)		Temperature (16bit)	Control data(8bit)		End code
a	N	integer	decimal	integer	decimal	C	z

There into

"C" is the host sends the control signal; the signal is set by the user from the machine temperature data and transmitted the actual temperature data comparing the generated, used to control the output from the machine actuator.

"A" is the preamble

" N" is the three way temperature humidity sensor ID," H1"" H2" for humidity data integer and decimal part of the Department of "T1"" T2" as the temperature data of integer and decimal part of the department.

"Z" is sent over the beam code.

If in the process of communication, the host in the power after2 seconds have not received from the machine sends a test code, the host will be displayed on the LCD screen" communication is not successful," until receipt of correct test code. From the machine if not received the host response, will continue to send test data, but does not send the temperature and humidity data, until they get the host response. The host can automatically detect whether the fault lines of communication. And respond to, and in communication failure, such as a circuit switch, the system can restore to the normal communication state.

The Function of Slave Hygrothermoscope

```

Void read TRH ()
{
  TRH=0;//host set zero 18ms
  Delay ms (18);
  TRH=1;
  Delay us ();//host delay 20us
  Delay us ();
  Delay us ();
  Delay us ();
  TRH=1;//host 'interface set high
  if(!TRH) // To determine whether DHT11has a low voltage of response signals, if no then
response is out of operation
{
  Respond=2;
  While ((! TRH) && respond++);// Judge DHT11issued 80us low level signals in response to
whether or not the end
  Respond=2;
  While (TRH && respond++);//Judging from the slave is a high 80us voltage, if it is then entered
into the data receiving state
  RH temp = receive (); //receive status
  RL temp = receive ();
  TH temp = receive ();
  TL temp = receive ();
  CK temp = receive ();
  TRH=1;
  Untemp = (RH temp+ RL temp+ TH temp+ TL temp); //data verify
  If (untemp==CK temp)
  {
    RH data = RH temp;
    RL data = RL temp;
    TH data = TH temp;
    TL data = TL temp;
    CK data = CK temp;
  }
}
}
}
The read function of 8 bit:
Char receive ()
{
  Unint8 I;
  Com data=0;
  For (i=0;i<=7;i++)
{
  Respond=2;
  While ((! TRH) &&respond++);
  Delay us ();
  Delay us ();
  Delay us ();
  If (TRH)

```

```

{
  Temp=1;
  Respond=2;
  While ((TRH) &&respond++);
  }
  Else
  Temp=0;
  Com data<<=1;
  Com data|=temp;
  }
  Return (com data);
}

```

Conclusion

The system is in our country's greenhouse control present situation and existing problems of control system of greenhouse based on sufficient investigation, research and development for our country ordinary household greenhouse control intelligent greenhouse control system. To sum up, get the following conclusions: (1) based on the host computer and slave computer, greenhouse control structure model. Between the various modules function both independent and coordinated, while also providing a variety of modes of control programmer, such as small greenhouse using only the next-bit machine to work alone; (2) according to the greenhouse sensor system requirements, based on analog electronic technology and sensor system design theory, design of temperature sensor, humidity sensor system and the light sensor system, so the system has high accuracy, low cost features. (3) Based on single-chip microcomputer greenhouse comprehensive control system using single chip microcomputer, data acquisition and processing functions. Therefore, can better reduce costs, save space, with a very high price.

Reference

- [1] LI Bin, LI Qing-kun. A Supervision System of Temperature and Humidity Based on the Embedded Web Server with 1-Wire Bus. *Techniques of Automation and Application*, 2007, 26 (8) : 93-96.
- [2] Wang Zhizhen. Alarm bell in food problems[J]. *GD-HK-MO Market and Price*, 2008, 6: 11-12. (in Chinese with English abstract)
- [3] Li Zhongfeng, Cai Yunlong. Analysis of China's food grain problem[J]. *Journal of Anhui Agricultural Sciences*, 2007, 35(31):10123-10125. (in Chinese with English abstract)
- [4] Texas Instruments Incorporated. MSP430 Internet Connectivity, <http://www.ti.com>.
- [5] LAI Yushu, LI Xunbo, DU Ping an. Design of Multi channel Hygrothermoscope Based on Embedded Web Server. *Instrument Technique and Sensor*. 2006.5:10-18
- [6] Roh J S, Chang T H. Performance analysis of multi-hop sensor system for smart home network applications[J]. *Wireless and Optical Communications Networks*, 2009, 28: 1-5.
- [7] Ren F Y, Huang H N, LIN C. Wireless sensor networks[J]. *Journal of Software*, 2003, 14(7): 1282-1291
- [8] Long Yuxiang, Zhang Jing, Dai Yuxin. Design of concentrator based on ZigBee in wireless meter reading system[J]. *Lower electrical apparatus*, 2007, 20:14-17

Generation of High Intensity Sound by Random Vibrations

Shi Li-ming

College of Highway, Chang'an University, Xi'an 710064, Shannxi, China

Keywords: Random Waves; Supersonic Vibration Wave; Sound Level Limits; Sound Radiation

Abstract. Random wave difference is, there is no continuity and no column coupled harmonic wavelet. Singapore non-coherent wave stack can be the result of linear increase. We studied a cross wall at supersonic vibration wave phase speed driving most of the radiation. While recognizing that the ultimate strength of the sound waves from the total input power source was implemented in the beginning, we point out that the first phase increase in random vibration energy stored in the random structure of sound radiation is of great significance.

Introduction

We are interested in finding a mechanism by which a very strong wave field can be established within the framework of linear theory. Linear theory deals with infinitesimal perturbations to the fluid by the source which we assume to be structural surface vibrations. The path leading to the high intensity of waves is through the accumulation of wavelets. On the first order level, the accumulation means a sum of variables of zero mean in both time and space. Instincts backed up by the Fourier theorems tell us that the result of such accumulations is basically similar with the following trigonometric sum,

$$\sum_{j=0}^n \sin(\omega t + j\theta) = \frac{\sin[(n+1)\theta/2] \sin(\omega t + n\theta/2)}{\sin \theta/2} \quad (1)$$

Which remains finite as n goes to infinity except $\sin \theta/2 = 0$. The exception corresponds to resonance where the phases of wavelets are precisely locked into each other, resulting in a linear divergence of the perturbation. On the second order level, we interpret the above accumulation process as interactions among wavelets. While in normal cases, waves from different but coherent sources have a degree of destructive interference that keeps the total strength of infinite wavelets low. In resonance the coupling becomes purely constructive. An idea thus emerges pointing to the removal of any coupling and coherence among wavelets from the source. Therefore the superposition of wavelets with random phase relations gives total wave energy equal to the linear addition of individual wavelet energy as the coupling terms vanish. The wave energy diverges algebraically as random wavelets accumulated.

To explore these features of random sources, we study a model problem of sound radiation by a supersonically traveling structural vibration wave in a 2-D duct. We first study the unsteady, random Mach waves generated by a vibration wall separating an otherwise homogeneous 2-D space. Then a rigid wall is introduced to form a duct so that the unsteady Mach waves are trapped in the duct, resulting in a linear increase of sound intensity with the duct length.

Random Mach Waves

Consider a transverse wall vibration wave (henceforth the source wave) traveling at supersonic phase speed, $V > c$ from the far left to the far right. Let $(y_1, y_2, t), (x_1, x_2, t)$, denote the source and observer space-time co-ordinates respectively and $M = V/c$, $\beta = \sqrt{M^2 - 1}$, $\gamma = \sin^{-1}(1/M)$.

Obviously the wall vibration radiates Mach waves. The radiation of the sound waves would inevitably affect the wall vibration; sound is said 'coupled' with the source, a subject known as fluid-loading. But at the moment we stay with the 'de-coupled' model and insist that the amplitude

and phase speed of the source wave are constant regardless of sound radiation. Given the normal velocity $R(t - y_1/V)$ on the surface, we can get the perturbation velocity potential in the sound field via the 2-D Green function,

$$\phi(x_1, x_2, t) = \int_{-\infty}^{+\infty} dy_1 \int_{-\infty}^{t-r/c} \frac{R(\tau - y_1/V)}{\pi \sqrt{(t-\tau)^2 - (r/c)^2}} d\tau \tag{2}$$

The r is the sound travel distance. After transforming the integral plane from (τ, y_1) into $(\tau_0 = \tau - y_1/V, y_1)$, we can get the unspecified function R out of the y_1 -integral which turns out to be a constant. The remaining τ -integral becomes straightforward.

$$\phi = V \beta^{-1} \int_{-\infty}^{tm} R(\tau_0) d\tau_0 = V \beta^{-1} \eta(tm) \tag{3}$$

η is the wall displacement and $t, t_m = t - (x_1 + \beta|x_2 - y_2|)/V$ is the retarded time. Consequently we have

$$\left. \begin{aligned} p' &= -\rho_0 \frac{\partial \phi}{\partial t} = -\rho_0 V \beta^{-1} R(tm) \\ u &= \frac{\partial \phi}{\partial x_1} = -\beta^{-1} R(tm) \\ u &= \frac{\partial \phi}{\partial x_1} = R(tm) \end{aligned} \right\} \tag{4}$$

This result confirms that the sound waves are Mach waves. The radiation of Mach waves from the source wave is depicted in Figure 1. The sound wave front is advancing at speed of

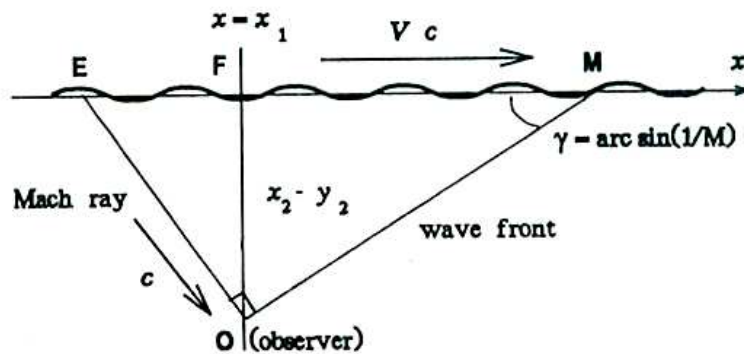


Fig. 1 Mach Waves Radiated by a Fast Traveling Vibrational Wave

That's Sound c in its normal direction \overline{EO} , which we call the Mach ray. The time interval $t - t_m = (x_1 + \beta \overline{FO})/V$ can be interpreted as that needed for signals to travel by the source wave at speed V to the point E , then from E to the observer O by sound wave at speed c , $(x_1 + \beta \overline{FO})/V = (x_1 - \overline{EF})/V + \overline{EO}/c$. The power flux across the fluid-solid interface is $p'(-v)$ (minus for downward into the fluid) per unit length in x_1 . With (2) and the geometry of Figure 1 we can see that the sound energy radiated from the length \overline{EF} all goes out across \overline{FO} , $\overline{EF}(-p'v)|_{y_2=0} = \overline{FO} p'u$

With the source wave travels from $y_1=0$ rather than from the far left. The y_1 -integral involves the observer position (x_1, x_2) relative to the starting point $y_1=0$ after considerable manipulation we are able to decompose ϕ as

$$\phi = H(x_1 - \beta^{-1}|x_2 - y_2|)\phi_m + \phi_c \tag{5}$$

Where H is the Heaviside function, ϕ_m is identical with the Math wave potential given by (1) and

$$\phi_c = \frac{V}{\pi\beta} \int_{-\infty}^{t-\tau_0/c} \eta(\tau_0) \frac{\partial}{\partial \tau_0} \sin^{-1} \frac{c(t-\tau_0) - Mx_1}{\sqrt{[V(t-\tau_0) - x_1]^2 - \beta^2|x_2 - y_2|^2}} d\tau_0 \tag{6}$$

r_o Is the distance between the observer and the starting point ϕ_c is characterized by its integral upper limit parameter, $t - r_o/c$ implying the centred waves (denoted by subscripts e). Mach waves exist only in $x_1 > \beta^{-1}|x_2 - y_2|$ while the modifying centred waves are everywhere and can be regarded as being caused by the scattering of Mach waves at the starting point. It can be shown that the random centred waves have the same $r_o^{-1/2}$ distance dependence as the harmonic ones radiated by a point source in 2-D space and that in the far field the random Mach waves dominate over the centred waves.

Sound Power inside a Duct

Now we add a lower rigid wall to the semi-infinite vibrating wall to form a 2-D duct of height h, sound waves are trapped in the duct. The effect of the lower wall can be represented by an infinite series of image sources. An observer inside the duct does not receive many waves from image sources too far away in y_2 direction due to the existence of silent zones ($x_1 < \beta^{-1}|x_2 - y_2|$). We now calculate the far field sound power inside the duct from the random Mach waves only. Much waves radiated from the upper wall are reflected back by the lower wall and trapped inside the duct. If we take the length of \overline{FO} in Figure 1 as h , we can work out that $\Delta x = (\overline{2EF}) = 2h/\beta$ is the axial distance which signals travel between two reflections, which is $\overline{2EF}/c = M\beta^{-1}h/c$ in time. After one cycle of reflections, the zigzag Mach rays, with axial-component of phase velocity $c \sin r = c/M$, lag by a distance $2\beta h = \beta^2 \Delta x$ behind, or lead by $by_{\Delta\tau} = 2\beta h/V = \beta^2 \Delta x/V$ in its phase time. That the source wave travelling at much number M on the upper wall. We may cut x_1 into segments each covering a length of Δx and define the nth segment on the upper wall to be $x_1 = (n-1)\Delta x + x_o$. Where $x_o \in [0, \Delta x]$ denotes the local axial coordinate. An observer in this segment receives reflected Much rays initially issued from segments $j = 1 \rightarrow n-1$ and that from the nth segment itself.

With acoustic pressure of many waves given in (7), we have

$$p' |_{nthseg} = -\rho_o V \beta^{-1} \left[R(t - x_1/V) + 2 \sum_{j=1}^n R(t - x_1/V - j\Delta\tau) \right] \tag{7}$$

where the constant 2 counts for the pressure doubling effect of wave reflections by the lower rigid boundary. The sound energy flux coming from the upper wall from $x_1 = 0 \rightarrow L = N\Delta x$ is thus

$$P_L = \sum_{n=1}^N \int_0^{\Delta x} \rho_o V \beta^{-1} \Delta x \left. \frac{p'(-v)}{nthdeg} dx \right| = \rho_o V \beta^{-1} \Delta x \sum_{n=1}^N \left[\Re(0) + 2 \sum_{j=1}^{n-1} \Re(j \Delta \tau) \right] \quad (8)$$

or

$$P_L = \rho_o V \beta^{-1} \Delta x \left[N \Re(0) + 2 \sum_{j=1}^{n-1} (N-n) \Re(n \Delta \tau) \right] \quad (9)$$

Is the auto-correlation of the random vibration velocity R ? Now if the auto-correlation \Re is almost zero (incoherent) beyond $\Delta \tau = 2\beta h/V$, the sum in (9) can be ignored; so that

$$\Re(\tau) = \overline{R(\tau') R(\tau + \tau')} \quad (10)$$

This means that every inch of the vibrating wall is putting energy into the duct as if there were no lower wall, while the actual confinement of the random sound inside the duct results in an algebraic accumulation of acoustic power.

So far the sound wave and the source wave are de-coupled in our model. As a result, the sound energy is increasing along x_1 without bound. In practice the source wave is produced at the starting point with a limited power input. As it leaks energy to sound (Mach) waves, its amplitude diminishes gradually. The power leaking into the sound waves per unit distance in x_1 is $p'(-v)$ which is proportional to R^2 (see (2)), i.e., to the local value of wave energy flux progressing in the wall vibration, therefore the decrease, or the radiation damping, of source wave amplitude along x_1 is exponential. The phase speed of the source wave would also change as a result of tile coupling and the whole issue is treated as a fluid-loading problem. But we avoid stepping into this subject by assuming that the rate of energy leakage into sound is so small that the source wave amplitude remains almost unchanged in many many wavelengths, therefore the linear increase of random sound wave energy inside the duct is roughly correct, at least in the early stages. Nevertheless, we understand that the ultimate limit of sound energy is imposed by the total power input from the starting point. But this fact does not deprive the phase randomness of its great significance. With a random source one can easily deliver a large amount of power into the fluid by first storing it in structural vibrations, whose acoustic impedance, or the acoustic power absorbing capacity, is much greater than that of fluid.

Conclusion

Random waves differ from harmonic waves in that there is no coherence nor coupling among wavelets. Superposition of incoherent waves results in linear addition of wave energy. We studied the Mach waves radiated by a transverse wall vibrational wave travelling at supersonic phase speed. Different Mach rays have different phases but same amplitudes. Superposition of such Mach waves inside a duct is diverging. If the source wave travel has a starting point, the Mach wave field is scattered and modified by a centered wave field which has an inverse square root amplitude dependence on the distance from the starting point. The effect of centered waves decay rapidly as the distance from the starting point increases and, in the far field (within the duct), the superposition of the trapped Mach waves dominates and gives a linear increase of sound energy flux with distance. While recognizing that the ultimate limit of sound intensity is imposed by the total source wave power input at the starting point, we point out that the phase randomness has the great significance of increasing the capacity of sound radiation by first storing the energy in random structural vibration.

References

- [1] NORIHIKO N Structural instability and tunable vibration frequency of an electromechanical resonator 2004(11)
- [2] NAYFEH A H.OUAKAD H M.NAJAR F Nonlinear dynamics of a resonant gas sensor 2009
- [3] YAO L Q.ZHANG J G.LU L Nonlinear dynamic characteristics of piezoelectric bending actuators under strong applied electric field 2004(4)
- [4] YOUNIS M I.NAYFEH A H A study of the nonlinear response of a resonant microbeam to an electric actuation 2003(1)
- [5] AGARWAL M.MEHTA H.CANDLER R N Impact of miniaturization on the current handling of electrostatic MEMS resonators 2007

Multiple Targets Passive Localization Technology based on a tolerant high resolution algorithm

Qing Ling¹, Xueli Sheng^{2, a}, Jia Lu², Meiren Jiang², Yong Guo²

¹Science and Technology on Complex Ship Systems Simulation Laboratory, Beijing, China

²Science and Technology on Underwater Acoustic Laboratory, Harbin Engineering University, Harbin, China

^ashengxueli@yahoo.com.cn

Keywords: passive location, MVDR; time reversal mirror; robust high-resolution algorithm

Abstract: The underwater target's bearing resolution capability of conventional beam forming method is strictly limited by Rayleigh limit and influenced by media's inhomogeneity heavily. Minimum variance distortionless response (MVDR) algorithms have broken through the Rayleigh limit restrictions and make higher resolutions possible. For the complexity of the marine environment and multi-path affection, time reversal mirror (TRM) is a new technology which can self-adaptively correct distortion caused by variety of multi-path effects. The concept of TR-MVDR based on vertical array is introduced and the high resolutions of TR-MVDR are studied theoretically, which can realize the focus on original position of multiple objectives with higher spatial resolution and focus gain than conventional methods. Due to the poor robustness of TR-MVDR, robustness algorithm based on fixed diagonal loading and RCB have been studied, which can improve the robustness of high-resolution location. Simulations and experiments in freshwater and the sea proved it is feasible and practical.

Introduction

Time reversal mirror (TRM) is an adaptive focus method [1] which is referred to as the process of phase conjugation that has been first demonstrated in nonlinear optics. TRM takes advantage of reciprocity, a property that integrates multi-path information, overcomes the location error caused by media's inhomogeneity and realizes self-focusing on target [2], realizes the underwater acoustic equalization adaptively [3] without prior underwater acoustic channel detailed knowledge.

The traditional direction-of-arrival (DOA) algorithm is strictly limited by Rayleigh limit. Minimum variance distortionless response (MVDR) algorithms [4] put forward by Capon in 1969 have broken through the Rayleigh limit restrictions and make higher resolutions possible.

The higher resolution and interference suppression performance of MVDR algorithm is conditioned by higher SNR and highly sensitive to the amplitude and phase of array elements. To improve MDVR's performance and meet the demand of multiple targets passive localization, TRM has been introduced into MVDR and TR-MVDR tolerant high resolution algorithm is studied in this paper. Multi-path information of underwater acoustic channel is fully used by TRM and the impact of complex environment on the high resolution algorithm is reduced sufficiently.

The principle of time reversal high resolution algorithm

The mathematical model of the acoustic pressure array outputs. The vertical receive array (VRA) consisted of N hydrophones with M coherent passive sources. The received signals were digitized and the output of t moment can be expressed as

$$\mathbf{X}(t) = \mathbf{A}(\theta)\mathbf{S}(t) + \mathbf{N}(t) \quad (1)$$

$\mathbf{A} = [\mathbf{a}(\theta_1), \mathbf{a}(\theta_2), \dots, \mathbf{a}(\theta_M)]$ in formula (1) is the Guide Matrix of array signal and Guide Vector $\mathbf{a}(\theta_m)$ can be written as $\mathbf{a}(\theta_m) = [a_1(\theta_m), a_2(\theta_m), \dots, a_N(\theta_m)]^T$. $\mathbf{X}(t) = [x_1(t), x_2(t), \dots, x_N(t)]^T$ is array output vector at time t and $\mathbf{S}(t) = [s_1(t), s_2(t), \dots, s_M(t)]^T$ is wave front vector of incident signal, $\mathbf{N}(t) = [n_1(t), n_2(t), \dots, n_N(t)]^T$ is noise vector of array output.

The weighted output of array $y(t, \theta)$ is

$$y(t, \theta) = \mathbf{W}^H \mathbf{X} \quad (2)$$

where $\mathbf{W} = [w_1, w_2, \dots, w_N]^T$ is weight vector.

The principle of MVDR algorithm. Conventional beam former is influenced heavily when strong acoustic interference exists and MVDR beam former can make the adaptive processing in different environment. In order to reduce the response of the array to the interference in unexpected position, a constraint optimization problem is constructed. The criterion of this optimization problem is that the total energy output is minimize on condition of the energy output of the signal in search position is fixed.

$$\|\mathbf{W}^H \mathbf{a}(\theta)\| = 1 \quad (3)$$

$$P(\theta) = \overline{y^2(t, \theta)} = \mathbf{W}^H \mathbf{R} \mathbf{W} \quad (4)$$

where $\mathbf{R} = E\{\mathbf{X}\mathbf{X}^H\}$ is time-space correlation matrix.

When condition present in (3) is satisfied, the energy output shown in (4) will reaches minimum. Solve this optimum problem by Lagrange method, the optimum Weight Vector can be got

$$\mathbf{W}_{\text{MVDR}} = \frac{\mathbf{R}^{-1} \mathbf{a}}{\mathbf{a}^H \mathbf{R}^{-1} \mathbf{a}} \quad (5)$$

The energy spectrum output is

$$P(\theta) = \frac{1}{\mathbf{a}(\theta)^H \mathbf{R}^{-1} \mathbf{a}(\theta)} \quad (6)$$

The research of robust MVDR algorithm. In practical applications, the real Guide Vector can't be precisely known because of all kinds of interference exist and it leads to the result that the signal energy output is reduced and the dynamic range of signal's energy spectrum is narrowed.

The fixed diagonal loading method is used to improve the TR-MVDR's tolerance and the weight vector of MVDR can be evolved from formula (6)

$$\mathbf{W}_{L-MVDR} = \frac{(\mathbf{R} + \alpha\mathbf{I})^{-1}a}{a^H(\mathbf{R} + \alpha\mathbf{I})^{-1}a} \quad (7)$$

where α is loading factor which is usually 1-10 times to the energy of noise.

The shortage of the fixed diagonal loading method lies in no accurate reference to the environmental mismatch. RCB algorithm [5] proposed by Li is used to estimate the Guide Vector directly.

Passive time reversal mirror (PTRM) location principle. Take a cell array's TRM for example to illustrate PTRM locating principle.

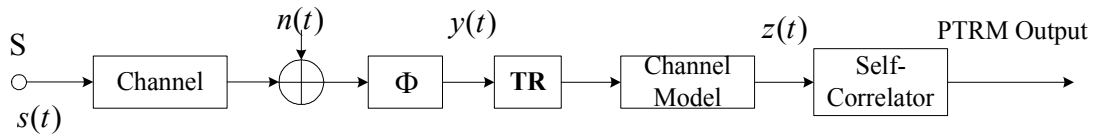


Fig. 1 Principle block diagram of PTRM

Fig.1 shows the functional block diagram of PTRM. Signal $s(t)$ transmitted by an acoustic source S through the acoustic channel I to the receiver, the received signal and the local sound pressure interference $n(t)$ superimposed on the receiver, and the filter outputs sound pressure signal $y(t)$. Next is time reversal, it is modeling in the computer by the measured parameters of the marine environment to get the sound channel, so we can get each observation point's sound pressure $z(t)$ of reversal retransmission ocean in the computer simulation. Take autocorrelation peak from each observation point's sound pressure, by the time reversal focus principle, it is known that the maximum energy output point corresponding to the related position is the position of sound source.

Time reversal high resolution algorithms. Transfer function between M 's spatial signals to the receive array with N 's elements is written as

$$\mathbf{H}(\omega) = [H_1(\omega), H_2(\omega), \dots, H_M(\omega)] \quad (8)$$

where $\mathbf{H}_m(\omega) = [H_{m1}(\omega), H_{m2}(\omega), \dots, H_{mN}(\omega)]^T$ represents the transfer function between m th signal to vertical receive array

The spectrum of VRA received signal becomes

$$\mathbf{X}(\omega) = [x_1(\omega), x_2(\omega), \dots, x_N(\omega)]^T = \mathbf{S}(\omega)\mathbf{H}(\omega) + \mathbf{N}(\omega) \quad (9)$$

where $\mathbf{S}(\omega)$ is spectrum of signal vector and $\mathbf{N}(\omega)$ is spectrum of noise vector of array which are uniform to formula (1). Transfer function matrix should be equivalent to Guide Matrix of array signal $\mathbf{A}(\theta)$. MVDR algorithm is also applicable when the Guide Vector mentioned above is

alternated to channel's Transfer function. As the result, TR-MVDR algorithm not only has the advantage caused by MVDR, but also makes full use of the multi-path information of the channel and the output can be focused in target position, then the multiple targets passive localization technology base on a tolerant high resolution algorithm

The high resolution algorithm simulation

Consider the situation that channel model is matched with the real acoustic propagation channel. For the purpose of simulation, the first receiver of VRA position $(0m, 15m)$ is used and array length is $20m$. Two passive point source located at $(3300m, 6m)$ and $(3310m, 6m)$. Location results are shown in following figures while bandwidth from $1kHz$ to $3kHz$, $SNR = 1dB$.

In Fig.2, simulation result proves the multiple targets passive location ability of TR-MVDR with VRA with error-free channel model. The peak value of TR-MVDR energy output are present at range $3300m$ and $3310m$, which means that the source can be located passively and high preciously by TR-MVDR.

Consider the situation that channel model is mismatched with the real acoustic propagation channel while other simulation conditions are the same with Fig.2.

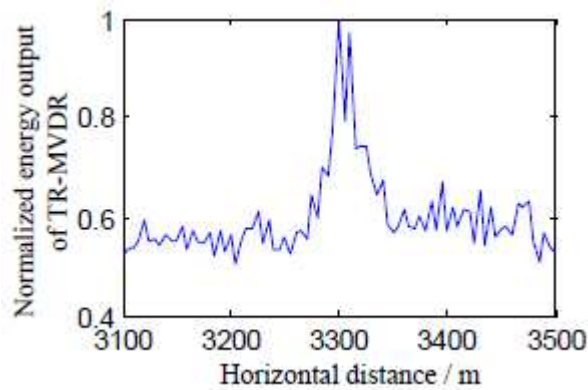


Fig. 2 Location result of TR-MVDR

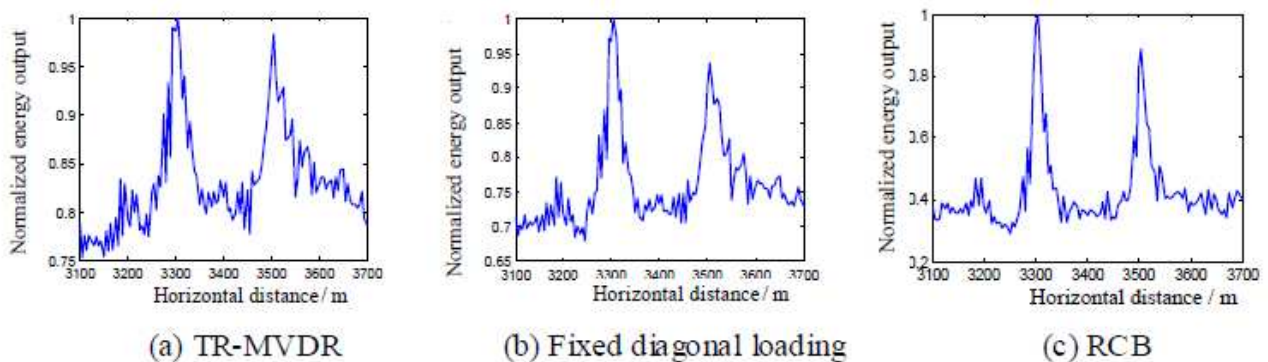


Fig. 3 Location results of TR- MVDR when the channel is mismatched

The output of TR-MVDR has too much burr when channel model is mismatched. The location performance can be improved a little by the fixed diagonal loading method. The results also provide that the pseudo focus in Fig.3(a) can be cut down obviously by RCB algorithm.

The sea experiment results of TR-MVDR algorithm

The experiment was performed in the ocean as indicated in Fig.4. A vertical array with 3 sensors was used to operate source's passive high resolution location in 160-m-deep water. An underwater explosive sound source was used as a passive source which distance from receive sensor was 11.17 km measured by GPS and depth of the explosion is 7m.

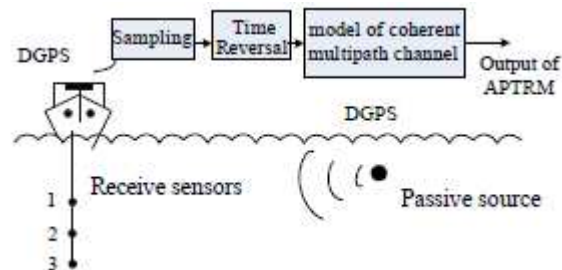


Fig. 4 TR-MVDR experimental setup in the ocean

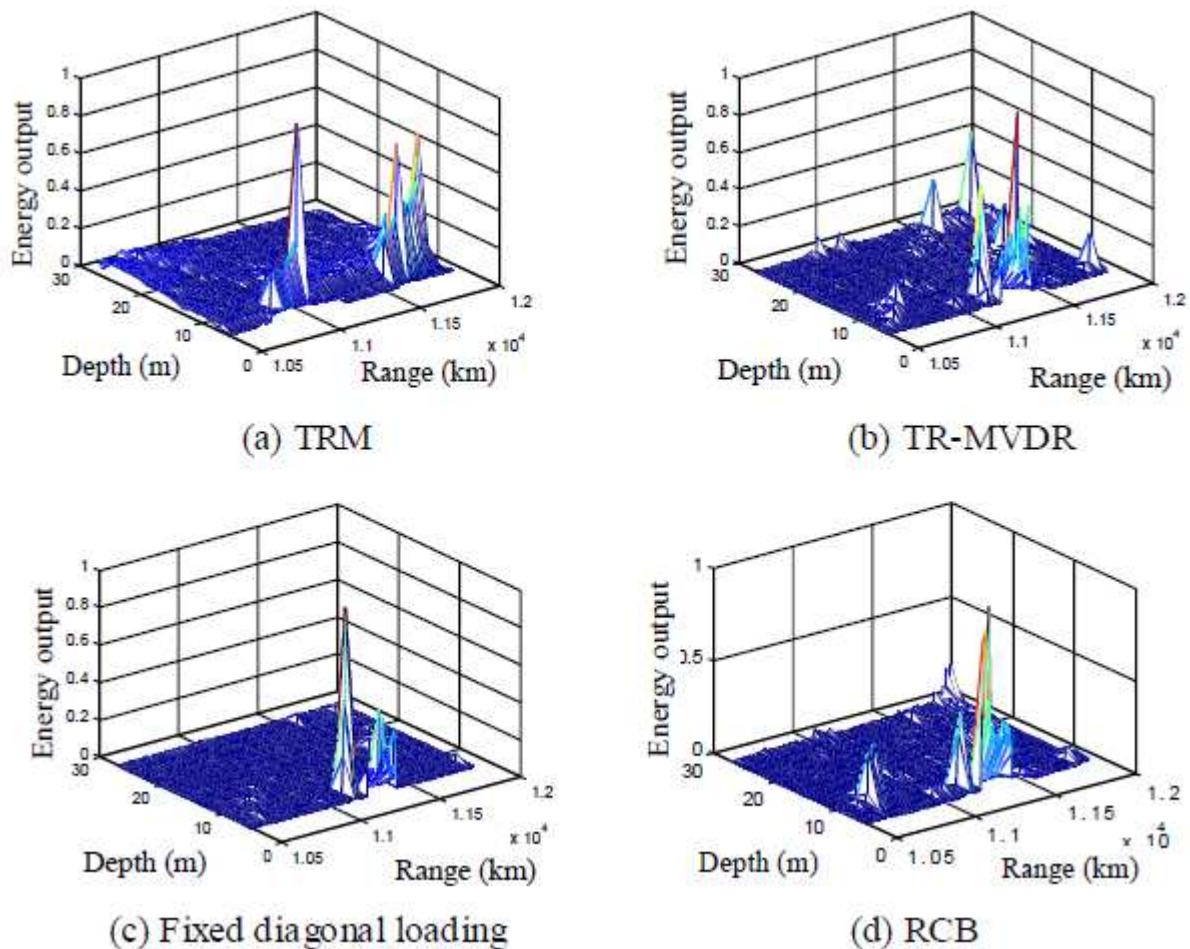


Fig. 5 The results of the sea experiment

The results of the sea experiment are shown in Fig., in which range and depth changes and the environment mismatch and environmental noise are considered. The waterfall plots show the energy outputs of TRM, TR-MVDR and TR-MVDR with fixed diagonal loading method (Fig.5(a), (b), (c)) are failed to locate the passive target. The peak value of TR-MVDR with RCB method output in Fig.5 (d) is presented at range 11.17km and depth 7m, which means that a successful

refocus may be formed by TR-MVDR with RCB method studied in this paper and the source can be located passively and feasibly without any prior knowledge. The result also provides that the improved method has good robustness and better anti-isotropic interfere ability.

Summary

MVDR are easily affected by complex underwater acoustic environments and are not sufficiently robust so it is difficult to use them in real underwater systems. TRM technology is a new method of localization, which may be effectively applied to target detection and localization. To improve its robustness, the MVDR algorithm is combined with TRM for passive detection and location. TR-MVDR makes full use of underwater multi-path channel information and reduces the effects of complex underwater environments. The performance of TR-MVDR that is based on fixed diagonal loading and robust capon beam forming (RCB) was also studied. We have implemented acoustic TR-MVDR in the ocean and hence demonstrated the feasibility of high-resolution passive location algorithm and the robustness of improved TR-MVDR

References

- [1] JACKSON D R, DOW LING D R. Phase conjugation in underwater acoustics [J]. *Acoust Soc Am*, 1991, 89: 171-181.
- [2] HUI Jun-ying, SHENG Xue-li. Underwater acoustic [M]. Beijing: National defense industry Press, 2007: 37-40.
- [3] LI Feng. The study of spatial match filter of time reversal mirror [D]. Harbin: Harbin Engineering University, 2006:1-4.
- [4] CAPON J. High-resolution frequency-wave number spectrum analysis [J]. *Proc IEEE*, 1969, 57(8): 1408-1418.
- [5] LI J, STOICA P, WANG Z S. On robust Capon beam forming and diagonal loading [J]. *IEEE Trans Signal Processing*, 2003, 51(7): 1702-1715.

Research of Sound Transmission Loss of Aircraft Sidewall with the Resonators

Shi Li-ming

College of Highway, Chang'an University, Xi'an 710064, Shannxi, China

Keywords: T.L.; Resonators; Sound Transmission

Abstract. This paper suggesting a method that improving T.L. at low frequencies of general aviation aircraft side wall configuration by installing resonators between double panel. In this paper, through the theory and experiment results, explains the proposed view is correct.

Introduction

List of Nomenclature

- C_o Speed of sound in air (m/s)
 ρ_o Mean density of air (kg/m³)
N the number quantity of the resonators
 S_r The area across neck of resonator (m²)
D separation between double-panel (m)
a resonator orifice radius (m)
V volume enclosed by partition (m³)
I The length of slug of air in resonator neck (m)
 I' The length of slug of air in resonator including (m)
V the volume of the single resonator (m³)
 M_i Mass per unit area of the ith panel (kg/m²)
 m_r Mass relating to a slug of air in the resonator (kg)
 B_t Flexural stiffness of the ith panel
 K_r Stiffness relating to a slug of air in resonator
 R_{pi} The ith panel damping
 R_r Damping related to a slug of air in resonator
 ω_r Angular resonant frequency (rad/s)
 ω Angular frequency (rad/s)
 Q_r Quality factor of resonator
k wave number
 ξ_r Displacement of sound mass of resonator
 ξ_i Displacement of sound mass of resonator
 Φ incidence acoustical pressure (rad)
 P_i Incidence acoustical pressure
 P_t Transmission acoustical pressure
T.L. noise transmission Loss (B)
 $\tau(\Phi)$ Incidence transmission coefficient
S unit area (m²)
 τ_d Field-incidence acoustic transmission coefficient
j $(-1)^{1/2}$

Theoretical Analysis

Theoretical Model The fuselage sidewall of almost all general aviation aircraft are designed as double or multiple wall configurations consisting of curved alloy aluminum plate reinforced with some structure is not generally greater than 1 mm. High levels of exterior noise are random field-incidence, and it makes the fuselage sidewall vib-rating, therefore, emitting sound wave into the cabin. From the above, theoretical model of transmission through double-panel with the resonators are developed (in Fig. (1)). In Fig. 1, the symbols are shown in list of nomenclature. It is noticed that the function of curved and reinforced skin has been considered in the equivalent thickness [2].

Formulation of T. L. of Double-Panel with Resonators From Fig. 1, the equation of motion for acoustical mass of the resonator under harmonic excitation is.

$$-\omega^2 m_r \xi_r + jR_r \omega \xi_r + K_r \xi_r = p_c S_r \tag{1}$$

$$\text{Where } m_r = \rho_0 S_r l' \quad \omega_r^2 = S_r c_o^2 (V_r I')$$

$$K_r = \rho_0 C_o^2 S_r / V_r \quad R_r = \omega_r m_r / Q_r$$

$$I' = 1.7 a l$$

Putting this parameters into equation (1), we have

$$\xi_r [\rho_0 S_r l' (\omega_r^2 - \omega^2) + j\omega_r \omega / Q_r] = p_c S_r \tag{2}$$

When the frequency of acoustic wave is content with the following conditions:

$$a. kD \ll 1 (k = \omega / C_o)$$

Then the acoustical pressure p_c in the cavity between double panels is assumed uniform.

Assuming that there are N resonators in to variance of air density, p_c is given by

$$p_c = C_o^2 d\rho \tag{3}$$

Where $d\rho$ is air density variance considering concrete conditions between double panels, we have

$$d\rho = \left\{ \left[S(\xi_2 - \xi_1) \xi_r N S_r \right] / (V - V_r N) \right\} \cdot \rho_0 C_o^2$$

Combining the above $d\rho$ with equation (2) and (3), we get by manipulating these expressions,

$$p_c \left[1 + \frac{V / (V - V_r)}{1 - (\omega / \omega_r)^2 + j\omega / \omega_r Q_r} \right] = \frac{\rho_0 C_o^2 (\xi_2 - \xi_1) \cdot S}{V - V_r} \tag{4}$$

Where $V = V_r \cdot N$. Finally we let

$$X = \left[1 + \frac{V(V-V)}{1 - (\omega/\omega_r)^2 + j\omega/\omega_r Q_r} \right]$$

$$M = \rho_0 C_0^2 S / (V - V)$$

Then, using the equation (4), we have

$$X \cdot p_c = (\xi_2 - \xi_1) \quad (5)$$

From the expressions X and M, it is clear that if there exist on the resonators in cavity between double panel, we obtain

$$X = 1 \quad \text{and} \quad M = \rho_0 C_0^2 / D$$

For N different kinds of resonators, then X is given by [2]

$$X = \left[1 + \sum_{i=1}^N \frac{V/(V-V)}{1 - (\omega/\omega_{ri})^2 + j\omega/\omega_{ri} Q_{ri}} \right] \quad (6)$$

On the basis of the theory of thin plate vibration^[4], the equation of vibration of the panels under harmonic excitation is^[5]

$$\left[-\omega^2 M_1 + B_1 (\sin\Phi)^4 + j\omega R P \right] \cdot \xi_i = f_0 \quad (7)$$

where f_0 is the amplitude of force. Equations of motion of the two infinite panels are respectively

$$Z_1 j\omega \xi_1 = P_1 - P_c \quad (8)$$

$$Z_2 j\omega \xi_2 = P_c - P_t \quad (9)$$

Where $Z_1 = j \left[\omega M_1 - B_1 (k \cdot \sin\Phi)^4 / \omega \right] + R_{pi}$, R_i is sound pressure on the location $x = 0$. Together with acoustic wave boundary conditions, we have

$$P_1 = 2 P_i - j\omega \xi_1 \rho_0 C_0 / \cos\Phi \quad (10)$$

$$P_2 = j\omega \xi_2 \rho_0 C_0 / \cos\Phi \quad (11)$$

Using the expression (5), (8), (9), (10) and (11), we get

$$\frac{P_t}{P_i} = \frac{-j2M/X}{(Z_1 + \rho_0 C_0 / \cos\Phi + M/X) \times (Z_2 + \rho_0 C_0 / \cos\Phi + M/X)^2} \quad (12)$$

Since transmission coefficient is defined by

$$\tau(\Phi) = |P_t P_i|^{-2} \quad (13)$$

Then, the field-incidence transmission coefficient is found by averaging over all of the components.

$$\begin{aligned}\tau_d &= \int_0^{\frac{\pi}{2}} \tau(\Phi) \sin\Phi \cos\Phi d\Phi / \int_0^{\frac{\pi}{2}} \sin\Phi \cos\Phi d\Phi \\ &= d\Phi / \int_0^{\frac{\pi}{2}} \sin\Phi(2\Phi) d\Phi\end{aligned}\quad (14)$$

Using the defamations of noise transmission loss, T.L. of the double panel is given by

$$\text{T.L.} = 10 \cdot 1g(1/\tau_d) \quad (15)$$

$$b: KD \gg 1$$

On this condition, the sound pressure in cavity between double sidewall is not uniform. From the above expression X, it is obvious that X is equal approximately to 1 in high frequencies region, and the functions of the resonators can be ignored completely. The noise transmission coefficient through double panel without the resonators under oblique angle of incidence is given by^[4]

$$\tau(\Phi) = \left| \frac{P_t}{P_i} \right|^2 = \left| \frac{2\rho_0 C_0^2 \sec^2\Phi \sin(KD \cos\Phi)}{Z_1^1 Z_2^1 \sin^2(KD \cos\Phi) + (\rho_0 C_0^2 \sec)^2} \right|^2 \quad (16)$$

Where is $Z_1^1 = Z_1 + \rho_0 C_0 \sec\Phi [1 - \int \cot(KD \cos\Phi)]$.

Fiddle incidence noise transmission loss of double panel without resonators can be got by using equations (14), (15) and (16).

Finally the field incidence transmission on loss for the double panel with resonators and without resonators was computed, the results are shown in the Fig. 2. Fig. 2 illustrates that transmission loss of double panel with and without resonators at 80 H_z and 160 H_z in one third octave band centre of frequency has improved by 4 dB respectively. Here it should be noted that resonant frequencies of two kinds of array of resonators are designed at 85 H_z and 160 H_z . The number of two kinds of the resonators are 40 and 32.

Physical Principle of Improving Transmission Loss by Using the Resonators From the expressions X, M and equation (5), We know that $|X|$ is absolutely larger than 1, and $|X|$ is equal to 1 when existing no resonators. Thus, the functions of resonators between double panel are to reduce the sound pressure in the cavity so that T.L. is improved. When sound wave frequency is near resonant frequency of resonators, we get:

$$|X| \approx \left[1 + \left(\frac{V}{V} Q_r \right)^2 \right]^{1/2} \quad (17)$$

It is up to maximum. From this, it is shown that the transmission loss of double panel can be increased by adding the number quantity of resonators and parameters are related to structure parameters of resonators. Moreover, from relations of Q_r value width of frequency band, Q_r value increased with frequency band decreasing. Therefore it is importance of optimum design for structure parameters of the resonators in order to make transmit sson loss be maximum.

Experiment and Analysis of Measured Results

The partition construction for testing is a piece of actual fuse lage sidewall of aircraft in area of 1.38m and it was mounted in an aperture between scource room and receiving room. The mixed resonator array whose resonant frequencies are $85 H_z$ to $8 KH_2$ regions has been experimentally measured and their results are shown in Fig. 3. Fig. 3 shows that T.L. with resonators at $80 H_z$ and $160 H_z$ in one third octave band center frequencies band improves by 4 dB and 6.5 dB, compared without resonators respectively. In other one third octave band center frequency the increase of transmission loss can be explained as results of sidewall of resonator chamber which produce the adding transmission loss.

Conclusion

Theory and experiments shows that it is a good method improving T.L. at low frequencies of general avintion aircraft side wall configuration by installing resonators between double panels.

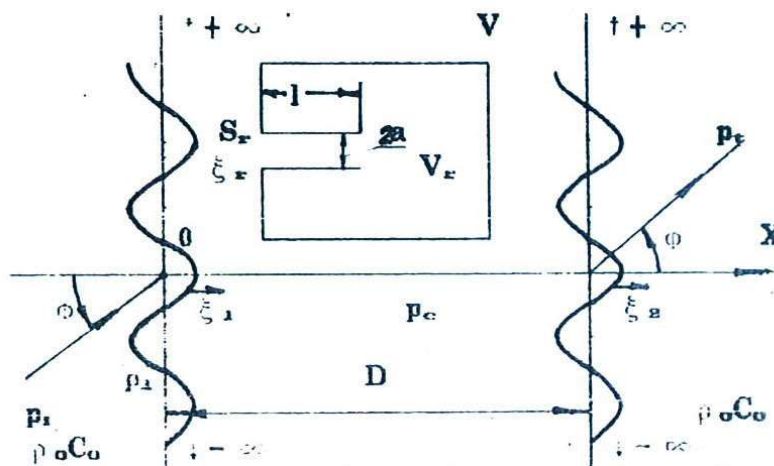


Fig. 1 Theoretical model of transmission through dluble-panel with resonator

The agreement between measured experimentally and calculated results is good, which illustrates that the theoretical models and theoretical analysis put forward in this paper are correct completely. Moreover, the physical principle of improving T.L. by using the resonators is concise

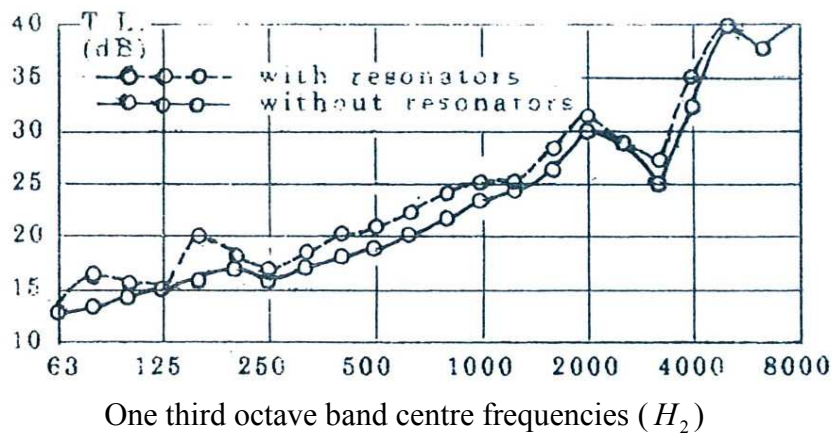


Fig. 2 Experimental results of T.L> of double panel

As the resonators designed in this paper have the characteristics of little volume and shaped conveniently. Therefore it can be used widely in the field of reducing the noise of the cabin of the general aviation aircraft.

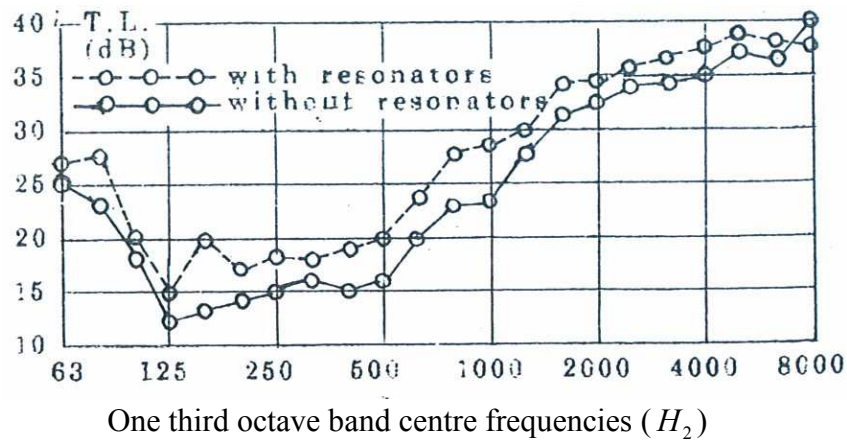


Fig. 3 Experimental results of T.L. of double panel

References:

- [1] V.R.MILLER and L.L.FAULKIER Prediction of aircraft interior noise using the statistical.
- [2] J.M.MASSON and F.J. FAHY: The use of acoustically tuned resonators to improve the sound transmission loss of double panel partition, ISVR. Technical report, NO.140.OCT.1986.
- [3] HE ZHA YONG: Acoustical theoretical fundamental published by National Defense Industrial Publishing House,1985.
- [4] SUN JIN CAI: Principle of mechanical noise of control published by Northwest Polytechnic University Publishing House.1987.

Research on Mechanical Wind Machine of Constant Velocity

Ding Ming-Cheng¹, Ding Xue², Zhang Li¹

¹ Liaocheng Vocational and Technical College, Liaocheng, Shandong 252000

² China University of Petroleum, Changjiang West Road 66#, Qingdao, Shandong 266555

chinalcdmc@sina.com, 163trickle@163.com

Keywords: Centrifugal Style Speed Controller, Variator, Section Gear Plate, Precision

Abstract. Primary technical parameters of centrifugal style speed controller were determined by Routh-Hurwitz criterion; the section gear variator could reach the standard of common gear driving of 9 grade precision indicators through design and calibration, especially suitable for low-rotate speed condition. The mechanical wind machine of constant velocity is novel in mode, briefness in structure, low in making cost and good for spreading and using.

Introduction

Complex structure and high manufacturing cost of the traditional wind turbines become bottlenecks for common use, especially for family. Mechanical wind machine of constant velocity, with no Generators, electronic controllers, inverters, batteries and other electronic devices, is a simple purely mechanical wind turbine, briefness in structure, low in making cost and good as the energy of family and other small power machines(Fig 1). The working principle is: When the instantaneous change in wind drives a transient change in the rotation of wind turbine blade 1, the ball 8 of the centrifugal governor instantaneously changes the size of radial turning radius, thus the outer gear plate 7 slides up and down. With the increasing of wind speed and ball's turning radius, the outer gear plate 7 shifts up, and the outer gear plate 7 meshes with ring gear that has larger diameter of section gear plate 4, which makes output speed of section gear plate 4 invariable. A relatively uniform speed at the output section gear plate 4 is obtained from this instantaneous change of wind. When the wind becomes extreme large, the outer gear plate 7 meshes with the fixed breaking ring gear 9, so that the wind turbine stops and be protected. As lift-type vertical axis wind turbines stand-alone (airfoil section blade) and other parts are stereotypes, this paper mainly introduced the design of two parts: centrifugal governor and section gear variator.

Design of centrifugal governor

Parameter design for main components of centrifugal governor A number of technical parameters should be designed to stabilize the output speed of section gear plate; centrifugal governor is a multi-DOF mechanism motor system. Routh-Hurwitz criteria method was often used in stability analysis of linear constant system of multi-DOF mechanical movement ([1]38-42). Determine the stability of the zero solution according to the situation of constant coefficient linear differential characteristic equation: If the roots of the characteristic equation have negative real parts all the time, the zero solution is stable. In fact, we only need to know coefficients' sign of characteristic equation.

General form of characteristic roots systems of constant coefficient linear differential equation:

$$a_0 s^n + a_1 s^{n-1} + \dots + a_{n-1} s + a_n = 0 \quad (a_0 > 0) \quad (1)$$

If all roots of eq.(1) have negative real parts, there needs n Hurwitz sub matrix $\Delta_i > 0, (i=1, 2, \dots, n)$

$$\text{In which: } \Delta_1 = a_1, \quad \Delta_2 = \begin{vmatrix} a_1 & a_0 \\ a_3 & a_2 \end{vmatrix}, \quad \Delta_3 = \begin{vmatrix} a_1 & a_0 & 0 \\ a_3 & a_2 & a_1 \\ a_5 & a_4 & a_3 \end{vmatrix}, \dots$$

For centrifugal governor motion system of mechanical wind machine of constant speed, we need to determine the condition of steady speed operation of system and main kinematical parameters, including: quality of steel ball m , length of bracket arm l , damping coefficient of friction f , intermediate velocity of section gear plate ω_0 , driving moment M_1' and moment of resistance M_2 and so on. The following is the motion stability analysis of centrifugal governor.

Suppose J as moment of inertia of section gear plate (working parts), ω as instantaneous angular velocity, M_1 as driving moment, M_2 as moment of resistance, ω_v as vertical axis instantaneous angular velocity of wind machine, φ as instantaneous angle between the arm and the vertical axis. Forces on the ball include gravity mg , centrifugal force $ml\omega_v^2 \sin \varphi$, Coriolis inertia force $2ml\omega_v\varphi' \sin \varphi$ and frictional damping force $f\varphi'$. The motion system of centrifugal governor and force diagram of the ball is shown in Fig.2.

Kinematical equation of section gear plate:

$$J\omega' = M_1 - M_2 \quad (2)$$

$$M_1 - M_1' = k(\cos \varphi_0 - \cos \varphi) \quad (3)$$

Where M_1' is the driving torsion when the outer gear plate meshes with mid-gear of section gear plate, k the scale factor related to bracket arm l , and φ_0 the value when φ equals to 60 degree.

Projection of differential equation in tangential direction of the ball's relative movement:

$$ml\varphi'' = ml\omega_v^2 \sin \varphi \cos \varphi - mg \sin \varphi - f\varphi' \quad (4)$$

Put $\omega_v = i\omega$, $B = k \cos \varphi_0 - M_1' + M_2$ into eq. (4)

Assuming: $\varphi = \varphi_0 + \Delta\varphi$, $\eta = \eta_0 + \Delta\eta = \Delta\eta$, $\omega = \omega_0 + \Delta\omega$

Keep the first order only, and then we get:

$$\left\{ \begin{array}{l} \Delta\varphi' = \Delta\eta \\ \Delta\eta' = i^2\omega^2 \cos(2\varphi_0)\Delta\varphi + i^2\omega_0 \sin(2\varphi_0)\Delta\omega - \frac{g}{l} \cos \varphi_0 \Delta\varphi - \frac{f}{m} \Delta\eta \\ \Delta\omega' = \frac{k}{J} \sin \varphi_0 \Delta\varphi \end{array} \right.$$

That is: $\Delta\eta' = -\frac{g \sin^2 \varphi_0}{l \cos \varphi_0} \Delta\varphi - \frac{f}{m} \Delta\eta + \frac{2g \sin \varphi_0}{l\omega_0} \Delta\omega$

Bring in the variable λ and characteristic roots equation was obtained:

$$\lambda^3 + \frac{f}{m} \lambda^2 + \frac{g \sin^2 \varphi_0}{l \cos \varphi_0} \lambda + \frac{2kg \sin^2 \varphi_0}{lJ\omega_0} = 0$$

From table 1 of Routh-Hurwitz criteria, necessary and sufficient condition of interference-free stable movement was gained:

$$a_1 = \frac{f}{m} > 0(\text{affirmative}); \quad a_3 = \frac{2kg \sin^2 \varphi_0}{lJ\omega_0} > 0(\text{affirmative}) ;$$

$$\text{if } a_1 a_2 - a_0 a_3 = \frac{f}{m} \frac{g \sin^2 \varphi_0}{l \cos \varphi_0} - 1 \times \frac{2kg \sin^2 \varphi_0}{lJ\omega_0} > 0, \text{ then: } \frac{fJ}{m} > \frac{2k \cos \varphi_0}{\omega_0} = \frac{2B}{\omega_0}$$

And this is the requirement of stable rotation and speed governing for the system.

Diameter of ball is 30mm; quality m is 0.1116kg in the designing.

Moment of inertia of section gear plate (Polyamide) J :

$$J = \frac{1}{2} mR^2 = \frac{1}{2} \times 5 \times 0.13^2 = 0.043(\text{kg}\cdot\text{m}^2)$$

Assume damping coefficient for friction f as 0.1.

$$\frac{fJ}{m} = \frac{0.1 \times 0.043}{0.1116} = 0.0385$$

Section gear plate intermediate angular velocity

$$\omega_0 = 2\omega_v = 40(S^{-1})$$

Scale factor k was given by experiment, and take l as 0.3m. Take 6 tests and average. The progress and data of test are shown in table 1. And k was obtained as 1.408.

Table 1 Testing and dereferencing of coefficient k

Time	Rotate speed (rpm)	Driving moment M_1 (NM)	Intermediate moment M'_1 (NM)	φ (°)	$k = \frac{M_1 - M'_1}{\cos \varphi_0 - \cos \varphi}$ ($\varphi_0 = 60^\circ$)	Shifting of outer gear plate(mm)
1	131	13.424	13.6	51.3	1.410	-41
2	152	13.493	13.6	54.8	1.409	-31
3	176	13.568	13.6	58.5	1.408	-20
4	210	13.688	13.6	64.1	1.407	22
5	223	13.735	13.6	66.2	1.406	29
6	264	13.883	13.6	72.6	1.408	43
					Average 1.408	

From this, it can be calculated:

$$\frac{2k \cos \varphi_0}{\omega_0} = \frac{2 \times 1.408 \times \cos 60^\circ}{40} = 0.0352$$

Since

$$\frac{fJ}{m} = 0.0385 > \frac{2k \cos \varphi_0}{\omega_0} = 0.0352$$

The conclusion is that speed governing system is stable.

Design of section gear variator

Structure and theory of section gear plate This variator seems to have only two gears meshing. Actually, it can achieve some level transmission. Calculation and experiments showed that this variator was compact and flexible set, satisfied the precision requirements for low-speed transmission, and is high coincidence between tooth surfaces. So far, there is no such record about the study and application of this variator at home and abroad. Here is a four-level section gear plate transmission.

Fig.3 is the structure and schematic diagram of four grade section gear plate. Variator consists of outer and section gear plate. The outer (driving gear) is a short tooth width cylindrical standard gear that tooth width ($B_1=10\text{mm}$) is slightly less than the space width ($\delta=11\text{mm}$) between teeth of the section. The section gear plate is a specific gear that four gear rings are distributed from inside to outside at the section (circular cross-section).

Basic requirements for section gear plate:

Same number of gear modulus and different number of teeth per revolution. Spacing width δ is slightly larger than outer tooth width, so as to stop two gear teeth of outer and section gear plate from meshing simultaneously.

All teeth of each gear must be extremely identical. To prevent impact by increasing tooth width, all teeth are bevel gear teeth (enough meshing strength after checking) with very small tooth width ($B=4\text{mm}$).

Each tiny bevel gear gets standard modulus at outer (larger) end, radial distribution.

Tooth thickness of each tiny bevel gear is getting smaller to the inside along the radial. However, groove width is constant (external gear teeth insert in the groove of section gear plate), and only the tooth thickness of outer (larger) end equals to it.

The diameter of the circle where the outer (larger) innermost gear lies should be as much more. So as to the upper end of outer gear could mesh with innermost end of small bevel gear, and the clearance will be the smallest when bevel gear goes to the highest point.

According to table 2, the experiment data of shifting distance of outer gear plate, the large diameter of section gear plate is $\phi 260$. The number of gear teeth z_n was calculated by $z_n = z_w r_p / r_w$. Outer gear teeth z_w and the pitch circle radius are known quantity. That r_p denotes the average radius of tooth width of a certain gear. Structure of section gear plate was shown in fig.4.

Designing and checking of primary precision index of section gear plate As rated peripheral velocity of wind machine blades v is 10m/s , a low speed, light load operation condition, section gear plate uses engineering Plastics of polyamide (PA-66). By designing and calculation (omit), take modulus m as 4, number of innermost gear teeth Z_2 as 37, pitch circle diameter of small bevel gear d_2 as 148. According to the special circumstances of its meshing, we select radial composite deviations, deviation of gear backlash, speed fluctuation deviation, contact ratio of tooth as the four main restricted indicators. The following is the main steps for designing and checking of four grade variator.

Precision design of radial composite clearance deviation of section gear plate

Its main feature is that each tooth width of the four ring gears is bevel tooth with very small tooth width. Outer gear plate shifts to upper end of gear and the innermost bevel tooth goes to the highest point, at the time they mesh, the instantaneous clearance Δ_{\max} exists (Maximum meshing clearance). This constitutes the largest meshing radial clearance deviation. Since the curvature of the innermost gear is the largest, as well as clearance, we take the innermost for research. Vertical radius the innermost bevel tooth at the smaller end is 70. The projection of radius in vertical direction at the beginning of meshing:

$$R_v = 70 * \cos 0.0849 = 69.737(\text{mm})$$

$$\text{Radial clearance } \Delta_{\max} = 70 - 69.737 = 0.263(\text{mm}).$$

Average radial clearance along the entire meshing progress:

$$\bar{\Delta} = \frac{\Delta_{\max}}{2} = 0.263/2 = 0.132 \text{ (mm)}$$

What was needed to stress, firstly, clearance Δ not always exists. On the contrary, tooth width B_1 equals 10mm along the entire outer gear plate, for which the odds is $0.263/10=0.0263$. In the inertial rotation, the chance of drive slippage and tooth removal tends to zero. Secondly, the experiments have showed that section gear plate used in wind machine is operating at low speed, and far from the resulting beat teeth, noise and so on.

From "Design handbook of machine part" ([2]699) by Wu Zongze, 9 grade precision radial composite deviations of gear F_i'' was found as 0.140.

Since,

$$\bar{\Delta} = 0.132 \leq F_i'' = 0.140$$

Therefore, the theoretical radial composite deviation was in 9 grade precision, and it can be ensured that the precision grade of section gear plate was 9.

Deviation precision checking of backlash of the gear pair

As the gear of section gear plate is small bevel gear, the type of backlash was identified as b by straight bevel gear. 9 grade precision deviation of tooth thickness was found as $E_{\bar{s}}$ as the diameter ϕ for small bevel gear is 144 and middle normal module m_n is 3.956 from "Design handbook of machine part" ([3]709-714) by Wu Zongze.

$$E_{\bar{s}} = \text{basic value} * \text{coefficient} = | -0.022 | * 4.6 = 0.1$$

Tooth thickness tolerance $T_{\bar{s}}$ was found as 0.25 as 9 grade gear run-out tolerance was 0.14. Maximum normal backlash of section gear plate was $J_{n\max 1}$.

$$J_{n\max 1} = E_{\bar{s}} + T_{\bar{s}} + E_{s\bar{\Delta}} = 0.1 + 0.25 + 0.038 = 0.388$$

Similarly, maximum normal backlash of outer gear plate $J_{n\max 2}$ was found as 0.12. Thus, the maximum total normal backlash $J_{n\max}$ is the sum of $J_{n\max 1}$ and $J_{n\max 2}$, is 0.508. Minimal total normal backlash for small bevel gear of section gear plate and straight tooth of outer gear plate is $J_{n\min}$.

$$J_{n\min} = J_{n\min 1} + J_{n\min 2} = 0.1 + 0.05 = 0.15$$

In Fig.2, average theory backlash actually produced lay at the midpoint of bevel gear tooth width when the straight gear meshed with bevel gear teeth.

$$\Delta_c = B * \frac{1}{2} * \frac{\alpha}{2} = 4 * 0.5 * 0.1697/2 = 0.1697$$

For $J_{n\min} = 0.15 < \Delta_c = 0.1697 < J_{n\max} = 0.508$, backlash of the gear pair meet the requirements of nine grade meshing transmission.

What was needed to emphasize, the backlash of 9 grade standard gear normally processed needed no measurement, which is naturally formed from the deviation of small bevel tooth width. It was supported as "positive deviation". Since it was necessary for section gear variator, and met the necessary backlash, it can be said to be "just right".

Variation deviation checking of the velocity vector of section gear plate

Because the rotor angle was the maximum when the innermost single tooth of section gear plate meshed, the innermost was taken for study. For single tooth, it was small bevel gear that the tooth width B was 4. When meshing with straight single tooth of outer gear plate, there existed extreme small deviation of the velocity vector between the larger (outside) and smaller (inside) end of small bevel gear, in the process between entering and demeshing. From theorem for the composition of motion, the left of single tooth ab rotate 0.1698 radians on base point o , at the same time, rotated relatively 0.1698 radians on b to the position $a'b'$. As rated linear velocity of wind machine v was 10m/s and diameter of blade D was 1m, the angular velocity of vertical axis, outer gear plate was ω_1 . For Z_1 equaled 25, Z_2 equaled 37, the angular velocity of section gear plate ω was 13.51 S^{-1} .

$$\omega_1 = \frac{2v}{D} = 2 * 10 / 1 = 20 (S^{-1}) \quad \omega = \frac{\omega_1 Z_1}{Z_2} = 25 * 20 / 37 = 13.51 (S^{-1})$$

Linear velocity of larger end of small bevel gear:

$$v_1 = 74\omega = 74 * 13.51 = 999.7 (\text{mm/s}) = 0.9997 \text{m/s}$$

Linear velocity of smaller end of small bevel gear:

$$v_2 = 70\omega = 70 * 13.51 = 946 (\text{mm/s}) = 0.946 \text{m/s}$$

Linear velocity difference: $\Delta v = v_1 - v_2 = 0.9997 - 0.946 = 0.0537$ (m/s)

Fluctuation ratio of linear velocity: $\eta = \frac{\Delta v}{v_1} = 0.0537 / 0.9997 \approx 0.05$.

Found from "Design handbook of machine—14th part: gear drive" ([4]213-214), the fluctuation of transmission ratio was within the required range, and transmission accuracy was 9 grade, stable.

The stability of transmission for the 2nd, 3rd and 4th circle from inside to outside increased successively. No need to check.

Also needed to note was that, on a pitch circle speaking of section gear plate, the transmission ratio which was still consistent with the nature of involute gear when they meshed was constant. Small fluctuations of velocity referred to tooth width along the bevel gear in terms of meshing. While ensuring the modulus, tooth width (not weaken the strength of tooth), increased the radius of the innermost circle of teeth or increased the number of teeth appropriately, in order to reduce the single tooth meshing angle α , fluctuation of linear velocity and sliding velocity. Without doubt, the outer diameter of section gear plate increased at this time. It was a compact section gear variator that had necessary limitations, and no effect to its operation and practicality.

Precision checking of contact ratio deviation of section gear plate

As shown in Fig.3, the schematic diagram, was that the meshing process of section gear plate and outer gear plate served as straight tooth gear meshed with gear rack and straight bevel gear (meshing from top to bottom and demeshing from bottom to top along the tooth width, similar to meshing process of bevel gears) simultaneously. We knew that transverse ratio of meshing for a pair of straight toothed spur gears was larger than gear rack. And smaller than a pair of straight bevel gears. So qualitatively speaking, the contact ratio between section and outer must be larger than a pair of straight toothed spur gears and a pair of gear racks, as well as a pair of straight bevel gears. This was the reason why the section gear variator was better than others in terms of uniform loading and reduction of tooth surface contact stress. Verification was calculated as follows:

According to the principle of contact ratio calculation of helical gear, the meshing contact ratio of section gear plate ε equaled transverse ratio of straight gear rack ε_a plus axial contact ratio of straight bevel gear ε_β . Because the inclination β of the outmost circle tooth was the minimal, as

well as the contact ration between it and outer gear plate. So it was reasonable to take the outmost of section gear plate for study. The number of teeth of outer gear Z_1 was 25, and the pressure angle of tip circle:

$$\alpha_{a1} = \arccos \frac{mZ_1 \cos \alpha}{mZ_1 + 2} = \arccos \frac{4 \times 25 \times 0.9397}{4 \times 25 + 2} = 22.8870$$

Contact ratio of gear rack:

$$\begin{aligned} \varepsilon_{\alpha} &= \frac{1}{2\pi} \left[Z_1 (\tan \alpha_{a1} - \tan \alpha) + \frac{4h_a^*}{\sin 2\alpha} \right] = \frac{1}{2 \times 3.14} \left[25 \times (\tan 22.8870^\circ - \tan 20^\circ) + \frac{4 \times 1}{\sin 40^\circ} \right] \\ &= 1.222 \end{aligned}$$

Since the number of the outmost teeth of section gear plate Z_4 was 64, tooth width of outer gear B_1 was 10, circular pitch $P_t: P_t = \pi m = 4 \times 3.14 = 12.56$, and inclination β :

$$\beta = \frac{360^\circ}{2 \times 61} = 2.95^\circ$$

Axial contact ratio of helical gear:

$$\varepsilon_{\beta} = B_1 \tan \beta / P_t = 10 \times \tan \frac{2.950}{12.56} = 0.041$$

Thus, contact ratio of section gear plate is

$$\varepsilon = \varepsilon_{\alpha} + \varepsilon_{\beta} = 1.222 + 0.041 = 1.263$$

Found from “Design handbook of machine—14th part: gear drive” ([5]15-61), 8 grade precision axial contact ratio of helical gearing ε_{β} was greater than 1.25.

Since

$$\varepsilon = 1.263 > 1.25$$

There was sufficient contact ratio.

Conclusions

Centrifugal governor on the basis of optimization design by Routh-Hurwitz criteria can ensure the output of rotate speed for section gear plate.

Section gear variator is innovative, and its greatest advantages are briefness in structure, easy for manufacture and low in making cost. Meanwhile, it meets the basic requirement of gear drive, and is suitable for low-rotate speed condition particularly.

The mechanical wind machine of constant velocity is novel in mode, briefness in structure, reliable in function and low in making cost and good for spreading and using.

Biographical notes

Ding Mingcheng, male, born in 1957, major in machinery design and manufacture, is currently a professor in Engineering department in Liaocheng vocational and technical college, Liaocheng city, Shandong province, China.

Ding Xue, female, born in 1984, major in chemical engineering and technology is currently a lecturer ship in China University of Petroleum in Qingdao, Shandong province, China.

Zhangli, female, born in 1982, major in electrical and mechanical control technology, is currently a lecturership.

References

- [1] Wang Yiqun. Engineering foundation of mechanical control(M).The press of Wuhan University of Technology, Wuhan, 2002:38-42.
- [2] Wu Zongze.Design handbook of machine part(M). China Machine Press,Bejing, 2003:699.
- [3] Wu Zongze.Design handbook of machine part(M). China Machine Press,Bejing, 2003:709-714.
- [4] Cheng Daxian.Design handbook of machine—Fourteenth part: gear drive. (M). China Machine Press,Bejing, 2003:213-214.
- [5] Cheng Daxian.Design handbook of machine—Fourteenth part: gear drive. (M). China Machine Press,Bejing, 2003:15-61.

Realization of the Viterbi Algorithm in MLSE with Intersymbol Interference

LU Ying^{1, a}, XU Quan-yuan^{1, b}, Liu Zhi-gang^{1, 2, c}

¹School of Computer and Information, Southwest Forestry University, Kunming650024, P. R. China

²Wuhan University of Technology, Wuhan 430070, P. R. China

^ayinglu513@sina.com, ^bxqy322@sina.com, ^cLiuzhigang@swfu.edu.cn

Keywords: Maximum-Likelihood Sequence Estimation (MLSE); Viterbi Algorithm

Abstract. Optimum receiver model for channels with Intersymbol Interference (ISI) and Additive White Gaussian Noise (AWGN) are introduced to deduce the Viterbi algorithm in the Maximum-Likelihood Sequence Estimation (MLSE). Finally, we use Matlab to simulate the algorithm in three different channels and analyze the experiment results. Analyses show that the Viterbi algorithm is applicable for any channel which is optimum from a probability of error viewpoint; the MLSE for channels with ISI has a computational complexity that grows exponentially with the length of channels time dispersion L ; the loss of performance is negligible when the decoding delay achieves $5L$.

Introduction

Channel distortion, which is not known a priori, lies in the most of the practical digital communication systems. Channel distortion results in ISI, which, if left uncompensated, causes high error rates. So, we research the realization of the Viterbi Algorithm in MLSE that is optimum from a probability of error viewpoint. Viterbi algorithm as a Maximum-Likelihood decoding one involves a search through the trellis for the most probable sequence. It may be regarded as an efficient, recursive algorithm that performs an optimal exhaustive search and is guaranteed to find the optimal decoding path.

Mathematical Background and Relevant Model

Optimum Receiver for Channels with ISI and AWGN

We begin with the transmitted (equivalent low-pass) signal given by Equation (1):

$$v(t) = \sum_{n=0}^{\infty} I_n g(t - nT) \quad (1)$$

Where $\{I_n\}$ represents the discrete information symbols bearing sequence and $g(t)$ is a pulse that is assumed to have a band-limited frequency-response characteristic.

And, hence, the received (equivalent low-pass) signal is expressed as

$$r_i(t) = \sum_{n=0}^{\infty} I_n h(t - nT) + z(t) \quad (2)$$

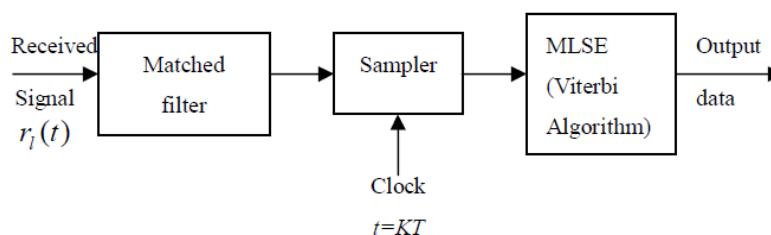


Fig. 1 Optimum receiver for an AWGN channel with ISI

Where $h(t)$ denotes the response of the channel to the input signal pulse $g(t)$ and $z(t)$ denotes AWGN.

The optimum demodulator can be realized as a filter matched to $h(t)$, followed by a sampler operating at the symbol rate $1/T$. Fig.1 Optimum receiver for an AWGN channel with ISI

The output of the matched filter can be expressed as

$$y_k = \sum_n I_n x_{k-n} + v_k \tag{3}$$

Where v_k represents the additive noise sequence of the output of the matched filter.

Fig.1 illustrates the block diagram of the optimum receiver for an AWGN channel with ISI.

As shown in Fig.2, the cascade of the transmitting filter $g(t)$, the channel $c(t)$, the matched filter $h^*(-t)$, the sampler and the discrete time noise-whitening filter $1/F^*(z^{-1})$ can be represented as an equivalent discrete-time transversal filter in the band-limited channels, having a set of tap coefficients $\{f_k\}$. The channel model can be denoted as

$$v_k = \sum_{n=0}^L f_n I_{k-n} + \eta_k \tag{4}$$

Where $\{\eta_k\}$ corrupting the output of the discrete-time transversal filter is a white Gaussian noise sequence.

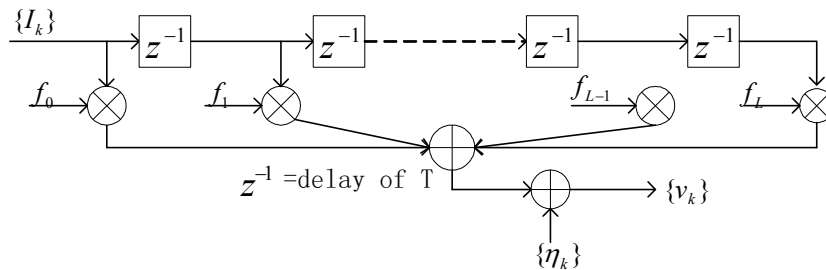


Fig. 2 Equivalent discrete-time model for an AWGN channel with ISI

The Viterbi Algorithm for the Discrete-Time White Noise Filter Model

We consider the condition of ISI that spans $L + 1$ symbols (L interfering components), and the information symbols are M -ary. According to the MLSE criterion, a finite-state machine of the equivalent discrete-time channel has M^L states and at any time k , its state is

$$S_k = (I_{k-1}, I_{k-1}, \dots, I_{k-L}), \tag{5}$$

where $I_k = 0$ for $k \leq 0$. Consequently, Viterbi algorithm can be used to determine the most probable path through the trellis.

It is convenient to define the reception output samples when communication begins is

$$\{v_k\} = v_1, v_2, \dots, v_{L+1}, \tag{6}$$

From which we compute the M^{L+1} metrics

$$\sum_{k=1}^{L+1} \ln p(v_k | I_k, I_{k-1}, \dots, I_{k-L}) = p(v_{L+1}, v_L, \dots, v_1 | I_{L+1}, I_L, \dots, I_1). \tag{7}$$

The M^{L+1} possible sequences of $(I_{L+1}, I_L, \dots, I_2, I_1)$ are subdivided into M^L groups corresponding to the M^L states. Firstly, we compute the initial metrics

$$PM_1(I_{L+1}) \equiv PM_1(I_{L+1}, I_L, \dots, I_2) = \max_{I_1} \sum_{k=1}^{L+1} \ln p(v_k | I_k, I_{k-1}, \dots, I_{k-L}) \quad (8)$$

$$= - \max_{I_1} \sum_{k=1}^{L+1} (v_k - \sum_{j=0}^L f_j I_{k-j})^2 \quad (9)$$

Then we select the surviving sequence largest probability with respect to I_1 from the M sequences in each of the M^L states, i.e., and reserve M^L surviving sequences and their metrics.

When reception of v_{L+2} , the M^L surviving sequences are extended by one stage, and the corresponding M^{L+1} probabilities for the extended sequences are computed using the previous metrics and the new increment, which is $\ln p(v_{L+2} | I_{L+2}, I_{L+1}, \dots, I_2)$. The M^{L+1} sequences are subdivided into M^L groups corresponding to the M^L possible state (I_{L+2}, \dots, I_3) and the most probable sequence is selected.

Continue the reception procedure in subsequent signal samples. When reception of v_{L+k} the metrics is

$$PM_k(I_{L+k}) = \max_{I_k} [\ln p(v_{L+k} | I_{L+k}, I_{L+k-1}, \dots, I_k) + PM_{k-1}(I_{L+k-1})] \quad (10)$$

Again, the most probable sequence from the M^L groups of the M^L possible states $(I_{L+k}, \dots, I_{k+1})$.

When the decoding delay achieves $5L$, (I_1, I_2, \dots, I_n) can be orderly decoded. And at this time, the loss of performance in channels is negligible which will be approved in this paper.

Simulating Result

We use MATLAB tool to simulate the Viterbi algorithm in four different discrete-time channels characteristics for binary antipodal signal.

Fig.3 (a) is typical of the response of a good –quality telephone channel. In contrast, the equivalent discrete-time channel characteristics shown in Fig.3 (b) and Fig.3 (c) result in severe ISI.

The special characteristics for the three channels, illustrated in Fig.4, clearly show that the channel in Fig.3 (c) has the worst spectral characteristic. Next in performance is obtained with the channel shown in Fig.3 (b), and finally, the best performance is obtained with the channel shown in Fig.3 (a). In fact, the error rate of the latter is within 3 dB of the error rate achieved with no interference.

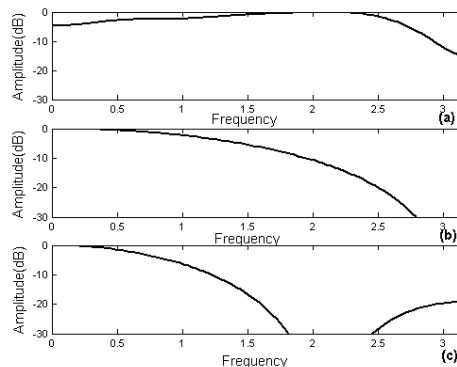


Fig. 3 Three discrete-time channels characteristics

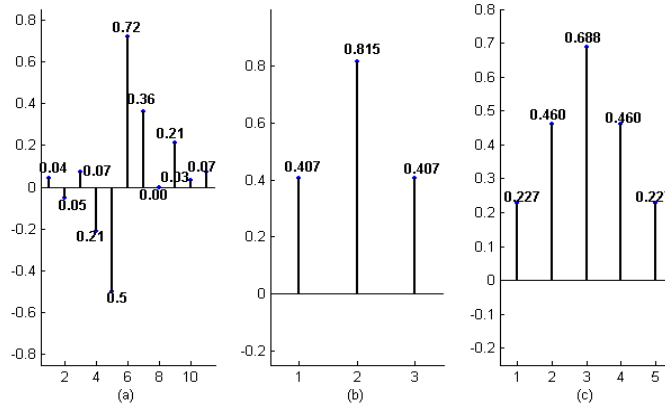


Fig. 4 Amplitude spectra for the three channels shown in Fig.3

Fig.5, 6, and 7 is channel characteristics of Fig.3 (a), (b), and (c) respectively, and all feedback delays of three channels arrive $5L$.

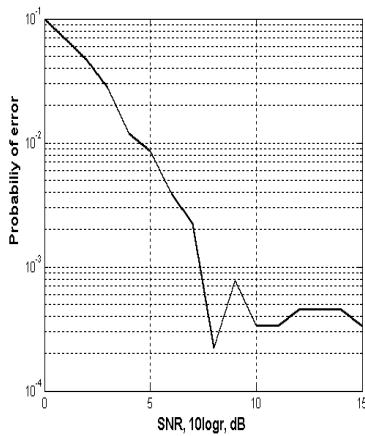


Fig.5 Error rate performance for the channel shown in Fig.3 (a)

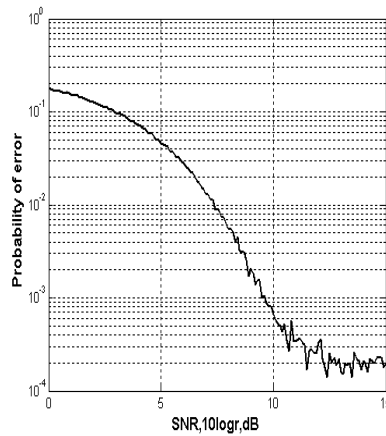


Fig.6 Error rate performance for the channel shown in Fig.3 (b)

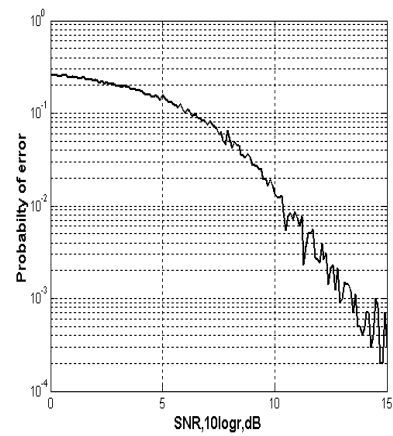


Fig.7 Error rate performance for the channel shown in Fig.3 (c)

According to the different feedback delay, Fig.8 shows error rate performances of Fig.3(b). From $2L$ to $6L$, the performances of channel characteristics improve gradually. Furthermore, the loss of performance is negligible if feedback delay exceeds $5L$.

Summary

As indicated previously, the delay in detecting each information symbol is variable. In practice, the variable delay is avoided by truncating the surviving sequence to the N most recent symbols, where $N \geq L$, thus achieving a fixed delay. In the case that M^L surviving sequences at time k disagree on the symbol I_{k-q} , the symbol in the most probable sequence may be chosen. The loss of performance resulting from this suboptimum decision procedure is negligible if $N \geq 5L$. Furthermore, we find that the MLSE for channels with ISI has a computational complexity that grows exponentially with the length of channels time dispersion according to the experiment previously.

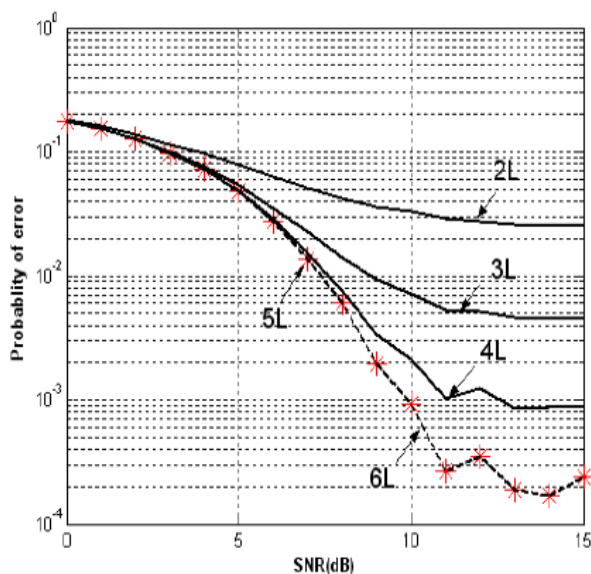


Fig.8 Error rate performances of fig.3 (b) with different feedback

References

- [1] John G. Proakis, Masoud Salehi. Digital Communications (Fifth Edition)[M]. Publishing House of Electronics Industry(2012)
- [2] John G. Proakis. Contemporary Communication Systems: Using MATLAB and Simulink (Second Edition) [M] . Xi'an Jiaotong University Press,(2003),p.209-p.259,p.317-p.359
- [3] John G.Proakis, Dimitris G.Manolakis.Digital Signal Processing[M]. Publishing House of Electronics Industry(2007)
- [4] LU Ying, SHAO Yu-bin, XU Quan-yuan. Viterbi algorithm in maximum-likelihood sequence estimation detection for channels with intersymbol interference[J]. Journal of Chongqing University (English Edition)(2004)
- [5] Xiang-Gen Xia.Modulated Coding for Intersymbol Interference Channels[M]. CRC Press(2000)
- [6] Fang Changxin. Lectures on Communication Principles[M]. Publishing House of Electronics Industry(2011)
- [7] Information on [http:// www.matlabsky.com](http://www.matlabsky.com)
- [8] Information on <http://www.ilovematlab.cn>

Optimization of Control Parameters with Switching Operation Mode on Hybrid Brake System for Electric Vehicles

Ren He^{1, 2, a}, Jianbo Yu^{1, b}, Runcai Wang^{1, c}

¹School of Automobile and Traffic Engineering, Jiangsu University, Zhenjiang, china

² State Key Laboratory of Vehicle NVH and Safety Technology, Chongqing, china

^a heren1962@163.com, ^b yujianbo1118@163.com, ^c fyruncai@163.com

Keywords: Hybrid Brake; Control Strategy; Optimization; Rate of Energy Recovery

Abstract. The safe area of braking force distribution was established theoretically by analyzing braking dynamics and the ECE R13 rules for hybrid braking system on electric vehicles. In the safe area, aiming for maximum of braking energy recovery, based on the precondition of ECE R13 and braking stability, an optimized method of motor regenerative braking force and friction braking force distribution was put forward for hybrid braking system, in which the distribution of friction braking force applied to the front and rear axle are fixed. Taking the coordinate of point with switching operation mode and rake ratio of braking force distribution as optimization target, new model of braking control strategy was set up in ADVISOR2002 and simulation was carried out, at last the optimization method was verified.

Introduction

As we know, the kinetic energy of traditional vehicles is converted to heat and dissipated when brake, which cause a waste of energy. Electric vehicles which are equipped with control system of motor can recover part of energy into energy storage system with controlling operation mode of motor when brake or in the downhill. Hybrid braking system is made up of mechanical friction braking system and regenerative braking system, which have an important effect on fuel economy, emissions and braking safety performance. Thus, it's meaningful to research the maximum of braking energy recovery on the precondition of braking performance.

The key of hybrid braking technology is control strategy, which include the braking force distribution of friction braking force applied to front and rear axle, distribution of friction braking force and motor regenerative braking force on the tractive axle. There are much achievement at home and abroad including several typical control strategy such as parallel distribution, ideal distribution and maximum energy recovery distribution of braking force [1]. The control strategy of parallel braking force distribution refer to: if braking intensity $z < z_1$, only motor regenerative braking force works; if $z_1 \leq z \leq z_2$, friction braking force and motor regenerative braking force consist of total braking force; if $z > z_2$, only friction braking force works. The control strategy of parallel braking force distribution just control motor regenerative braking force, friction braking force of front and rear axle were distributed as former rule, so control parameters is few and reliability is satisfied. The research of control parameters z_1 and z_2 for parallel braking control strategy is few, Qiaohua Liu et al put forward a method of braking distribution in different braking intensity on the precondition of ECE rule, z_1 , z_2 were valued by empirical value 0.1, 0.7, and not valued by calculation [2]. Jingang Guo et al put forward a control strategy aiming for maximum of braking energy recovery, and made the curve of braking force distribution close to the curve of ideal braking force distribution. However, the reason of control parameters with switching operation mode was not present [3]. Because of the difference of vehicle parameters and drive cycle, taking empirical value as control parameters was unscientific, which may have bad effect on braking stability performance and maximum of braking energy recovery. It's necessary to research calculation and optimized method for z_1 and z_2 . According to the standard of energy consumption and range test procedures for electric vehicles GB18386-2005 [4] in china, the test cycle was made up of four urban cycles and one suburban cycle. After calculation, the braking intensity of the test

cycle is low, the maximum of which was far below 0.7, so z_2 was not considered. In this paper, aiming for maximum of braking energy recovery, constraint about maximum motor regenerative braking force, charge and discharge power of energy storage system were analysed, an optimized method of motor regenerative braking force and friction braking force distribution was put forward on the precondition of ECE R13 regulations and braking stability. Taking the coordinate of point with switching operation mode and rake ratio of braking force distribution as optimization target, the optimal result was obtained through MATLAB toolbox [5], then new model of braking control strategy was set up in ADVISOR2002 [6] and simulation was carried out.

Analysis of Braking Safety Performance Based on ECE R13 Regulations

There are definite requirement for braking force applied to front and rear axle based on ECE R13 regulations. The front axle utilization adhesion coefficient curve should be above the rear axle utilization adhesion coefficient curve for vehicles in various loading conditions. When the adhesion coefficient φ is valued from 0.2 to 0.8, the braking intensity z should meet the demand of $z \geq 0.1 + 0.85(\varphi - 0.2)$, which make the utilization adhesion coefficient curve close to the curve of $\varphi = z$, ensuring high utilization adhesion coefficient. When front axle is locked, rear axle should be applied to certain braking force in order to make sure the vehicle stability and braking efficiency [7]. There are motor regenerative braking force and friction braking force in the front axle for hybrid braking system. So the boundary equation based on ECE R13 regulations is:

$$F_{xb1} = \frac{z+0.07}{0.85} \times \frac{G(b+zh_g)}{L} \quad (1)$$

$$F_{xb2} = Gz - F_{xb1} \quad (2)$$

In Equation(2): F_{xb1}, F_{xb2} are front and rear braking force applied to ground, N; If front and rear wheels are not locked, $F_{xb1} = F_{\mu1} + F_{re}, F_{xb2} = F_{\mu2}$, $F_{\mu1}$ and $F_{\mu2}$ are front and rear braking force applied to friction braking on vehicle, F_{re} is motor regenerative braking force, N; G is vehicle gravity, N; z is braking intensity; h_g is height of the vehicle center of gravity, m; b is the distance from rear axle to the vehicle center.

The ideal distribution of front and rear braking force applied to friction braking on vehicle (I curve), is changed to:

$$F_{\mu2} = \frac{1}{2} \left[\frac{G}{h_g} \sqrt{b^2 + \frac{4h_g L}{G} (F_{\mu1} + F_{re})} - \frac{Gb}{h_g} - 2(F_{\mu1} + F_{re}) \right] \quad (3)$$

In Equation (3): L is the distance between front and rear axle, m. The front and rear axle are locked at the same time for the ideal distribution of braking force, in which the adhesion coefficient is made full use of. However, it is difficult to realize in actual braking process.

Equation of equal braking intensity(z curve) is changed to:

$$F_{re} + F_{\mu1} + F_{\mu2} = zG \quad (4)$$

The f curves are the distribution of front and rear braking force supplied to ground when the front wheel is locked and the rear wheel is not locked, which is included in the stable condition, however, there is no steering ability in the condition. On the contrary, The r curves stand for the distribution when the rear wheel is locked and the front wheel is not locked, in which it is likely to slip on the rear axle, then the vehicle may lose its stability.

The parameters of vehicle: $m=1845\text{kg}$, $g=9.8\text{m/s}^2$, $h_g=0.595\text{m}$, $L=2.695\text{m}$, $b=1.235\text{m}$, $a=1.46\text{m}$, coefficient of aerodynamic drag $C_D=0.36$, vehicle frontal area $A=2.53\text{m}^2$, radius of the wheel $r=0.299\text{m}$, according the parameters above, we could achieve the curve of braking force distribution and ECE R13 regulations as Figure1. OA and AB stand for the distribution of the friction braking force applied to front and rear axle when the vehicles are in full load, it is better to adjust the distribution with proportional valve, which could make the distribution curve close to I curve. The equation of distribution curve is as below:

$$F_{re} = 0, OA : F_{\mu 2} = \frac{1-\beta}{\beta} F_{\mu 1} = 0.692 F_{\mu 1} (0 < z \leq 0.6); AB : F_{\mu 2} = 0.341 F_{\mu 1} + 2254.5 (z > 0.6) \quad (5)$$

According to the analysis above, the safe area is the OCEBO, the critical condition is that the low boundary CE of the safe area tangent to the boundary of ECE R13 regulations, which meet the low limit of ECE R13 regulations

Optimization of Motor Regenerative Braking Force for Hybrid Braking System

The control strategy of hybrid braking system has a direct effect on vehicle braking stability and recovery of braking energy. Aiming for maximum of braking energy recovery, the control strategy should be optimized on the precondition of braking stability. For figure 1, OC was the stage of motor regenerative braking force working alone, CE was the stage of motor regenerative braking force and friction braking force working together, so optimization targets are the coordinate of point C and rake ratio of CE, suppose the coordinate of point C is $(Gz_1, 0)$, the point D of tangency between CE and the boundary of ECE R13 is (x_1, y_1) , because the formula of ECE R13 regulations is given, K_{CE} (rake ratio of CE) could be calculated in different values of z_1 through MATLAB optimtoolbox. After calculation, the range of K_{CE} was $[0.442, 0.452]$ when the value z_1 changed from 0.04 to 0.1, so the difference of K_{CE} was less than 3%. In order to simplify the optimization, keeping $K_{CE}=0.452$ fixed when z_1 was valued from 0.04 to 0.1. The equation of CE is as below: $F_{xb2} = 0.452(F_{xb1} - Gz_1)$.

According to the analysis above, the distribution of braking force for hybrid braking system was as below:

$$0 < z < z_1, F_{re1} = Gz_1, F_{\mu 11} = 0, F_{\mu 12} = 0 \quad (6)$$

$$z \geq z_1, F_{re2} = 4321.36z + 13764.19z_1, F_{\mu 12} = 8137.12z - 8134.58z_1, F_{\mu 22} = 5622.52z - 5629.61z_1 \quad (7)$$

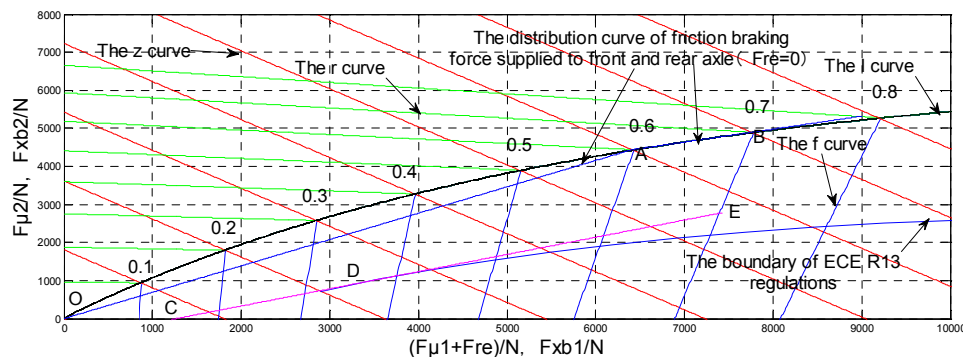


Fig. 1 Sketch of hybrid braking control strategy based on ECE R13 regulations

The sum of motor regenerative braking force in two operation mode should reach the maximum value in order to make the braking energy recovery as much as possible.

Objective function: $F_{re} = F_{re1} + F_{re2}$, range of variable $z_1: [0.04, 0.1]$;

Constraints: (1) when the braking intensity z is valued from 0.2 to 0.8, the braking force applied to rear axle should not less than the minimum value required by ECE R13 regulations, as below:

$$F_{\mu 22} = 5622.52z - 5629.61z_1 \geq Gz - \frac{z+0.07}{0.85} \times \frac{G(b+zh_g)}{L}. \quad (8)$$

In the process of hybrid braking, the motor worked as generator mode with the control signal. The characteristic curve is symmetrical in the mode of motor and generator.

The motor regenerative braking force should not exceed the maximum force applied to motor [8]:

$$F_{re} \leq F'_{re} = \frac{T i_g i_o \eta_T}{r} \quad (9)$$

In Equation (5), T is the torque of motor, Nm; i_g is gear ratios of gearbox; i_o is the gear ratio of final drive; η_T is transmission efficiency from motor to wheel. r is radius of the wheel.

Motor torque is the function of rotate speed n .

$$T = \begin{cases} \frac{9549P_n}{n_b} & n \leq n_b \\ \frac{9549P_n}{n} & n > n_b \end{cases} \quad (10)$$

In Equation (6), P_n is normal rated power of motor, kW; n_b is base speed of motor, r/min; n is the rotate speed of motor, r/min; in this paper, a series hybrid electric vehicle is researched, then

$$u_a = 0.377 \frac{n}{i_g i_o} \quad (11)$$

In Equation (7), u_a is vehicle speed, km/h, which is based on drive cycle, in this paper; u_a is determined by the cycle of electric vehicle standard GB18386-2005 in china.

The regenerative braking power of motor shouldn't exceed the charge power of energy storage system, which protects the energy storage system from over charge. Internal resistance of energy storage is related to SOC(state of charge) and temperature; For the NI-MH battery in this paper, keeping the value of SOC unchanged, the tendency of internal resistance is first increased and then decreased when temperature is changed from 0 to 40°C, and there is a minimum value near 25°C; on the contrary, keeping the value of temperature unchanged, the tendency of internal resistance is first increased and then decreased when SOC is changed from 0 to 1, and there is also a minimum value near 0.6^[9]; Keeping temperature unchanged, the charge power of energy storage would be decreased if SOC is increased, so the increase of SOC should be limited. However, the value of SOC couldn't too low to avoid decrease of discharge power [10]. In this paper, the Optimal distribution of braking force was mainly researched, so capacity of energy storage system was not considered, the charge and discharge power were supposed to meet the requirement of vehicle in various process.

Except the vehicle parameters, transmission parameters are: $i_o=1$, $i_g=6.67$ (only 1 gear ratio), $\eta_T=0.9$. Motor parameters: $P_n=75$ kw, $T_n=271$ Nm, $n_b=2641$ r/min. According to the parameters above, the math models of constraints were obtained, the best value $z_1=0.07$ was solved with MATLAB optimtoolbox, the motor regenerative braking force reached the maximum value.

Simulation Analysis

In this paper, the rate of braking energy recovery and the rate of effective vehicle energy recovery were used to evaluate the ability of energy recovery. The rate of braking energy recovery is the ratio of energy recovered into the energy storage system and the total braking energy consumption. The

rate of effective vehicle energy recovery is the ratio of energy recovered into the energy storage system and the total vehicle energy consumption, which is the sum of driving energy consumption and braking energy consumption [1].

According to the distribution of braking force in ADVISOR 2002, the fraction of motor regenerative braking force (F_{re}) and friction braking force applied to front axle (F_{ff}) are determined by detected vehicle speed through looking-up table, then the value of friction braking force applied to rear axle (F_{fr}) could be calculated on the basis of F_{ff} and F_{re} . Taking r_e as the fraction of motor regenerative braking force and f_f as the fraction of friction braking force applied to front axle, the higher of the vehicle speed, the greater of r_e and the smaller of f_f . Through calculation and analysis, the motor regenerative braking force don't be made full use of in the distribution, what's more, whether it could be accorded with constraint is unknown, so the distribution of braking force in ADVISOR 2002 have much limitation.

Based on the optimal result, a new model of braking control strategy was set up in ADVISOR2002 and simulation was carried out. Considering the selection of drive cycle, the ECE+EUDC test cycle in ADVISOR2002 was compared with the test cycle based on GB/T18386-2005, the result of which showed that the driving distance in ECE+EUDC test cycle was reduced by 0.9%, while the travel time was increased by 3.8%, the basic composition of braking, acceleration, constant speed and idling were almost consistent. It was reasonable to select ECE+EUDC test cycle in the simulation. The simulation results showed that using the optimized control strategy, the energy recovered into energy storage system was 976.1kJ, while the value was 591.2kJ before the optimization.

The vehicle driving energy consumption and braking energy consumption were associated with selected drive cycle and vehicle parameters. In this paper, The vehicle driving energy consumption and braking energy consumption were respectively 7065.2kJ and 1783.5kJ. According to the result of simulation, it could be seen that the rate of braking energy recovery and the rate of effective vehicle energy recovery were 54.73% and 11.03%, while the value before the optimization were 33.15% and 6.68%. In contrast, the rate of braking energy recovery and effective vehicle energy recovery were respectively improved by 21.58% and 4.35%.

Summary

In this paper, the safe area of braking force distribution was established theoretically by analyzing braking dynamics and the ECE R13 rules for hybrid braking system of electric vehicles. In the safe area, aiming for maximum of regenerative braking energy, an optimized method of motor regenerative braking force and friction braking force distribution was put forward. A new math model of braking control strategy was set up in ADVISOR2002 and simulation was carried out, the result of which showed that the rate of braking energy recovery and effective vehicle energy recovery were respectively improved by 21.58% and 4.35%, so the optimized method was effective.

Acknowledgments

This research was supported by the State Key Laboratory of Vehicle NVH and Safety Technology, under contract NVH SKL-201106.

References

- [1] Lv Fengyang. Study on Coordinating Control Strategy of Regenerative Braking and Pneumatic Braking for Electric Bus (Master's Dissertation), Changchun: Jilin University (2009)
- [2] Liu Qiaohua, Li Yuelin, Zuo Cui et al. Hybrids Regenerative Braking Simulation. *Chinese Journal of Automotive* 1(5), 464-468 (2011)
- [3] Guo Jingang, Wang Junping, Cao Binggang. Brake-Force Distribution Strategy for Electric Vehicle Based on Maximum Energy Recovery. *Journal of Xi'an Jiaotong University* 42(5), 607-611 (2008)
- [4] GB/T 18386-2005. Energy consumption and range test procedures in electric vehicles (2005)
- [5] Xue Dingyu, Chen Yangquan. Simulation Technique and Application of System Based on MATLAB/Simulink, second ed. TSINGHUA UNIVERSITY PRESS, Beijing (2011)
- [6] Zhao Guozhu. Research on Braking Stability of Regenerative Braking System in EV and HEV. (Master's Dissertation), Nanjing: Nanjing University of Aeronautics & Astronautics (2006)
- [7] Yu Zhisheng. Automobile Theory, fourth ed. CHINA MACHINE PRESS, Beijing (2006)
- [8] Zhao Zhiguo, Peng Yugang. Simulation on Series Electro-hydraulic Combined Braking for 4WD Hybrid Electric Car [J]. *Journal of System Simulation* 24(2), 1-8 (2012)
- [9] Hu Minghui, Qin Datong. The efficiency of a Ni-MH battery used in hybrid vehicles. *Journal of Chongqing University* 32(3), 279-282 (2009)
- [10] Qiang Jiayi, Ao Guoqiang, He Jianhui. Research on the Battery Simulation System of Electric Vehicles. *Journal of Shanghai Jiaotong University* 43(8), 1196-1200 (2009)

Applied Mechanics-based Devices in Mobile Human-computer Interaction

CHANG Yan-shuo^{1, a}, HUA Qing-yi^{1, b}

¹ Dept. of Information Science and Technology, Northwest University, XI'AN, CHINA

^achangyanshuo@foxmail.com, ^bhuaqy@nwu.edu.cn

Keywords: Smart Phone, Mobile HCI, Performance.

Abstract. To provide some suggestions of hardware specifications to relevant people, such as developers and researchers, this paper proposes a “standard” smart phone by using the revised value of parameters, like mean and mode, which are based on the analysis of smart phone hardware parameter information database. It provides a good reference for the human-computer interaction designers at both the qualitative and quantitative level.

Introduction

Mobile HCI (human-computer interaction) as a sub area focusing on one species of interactive computing systems—the portable and handheld computer [1]. Worldwide smart phones grew by 27 percent in the second quarter of 2009 according to a research firm — Gartner [2]. With the prevalence of mobile devices, the research of mobile HCI becomes increasingly meaningful.

In order to meet the mobility which is the most important feature of mobile HCI, these situations should be taken into account: mobile devices cannot be too large, which limits the size of screen, keyboard, etc; they also cannot be too heavy, which limits the capacity of battery (the more capacity, the more weight and volume); the frequency of CPU cannot be too high, or the energy will be exhausted soon and so on. So the relevant study work should be based on these constraints. The CPU frequency of smart phone is usually around 200-250MHz; Total RAM is between 64 and 128 MB; Charge ranges from 780 to 1200 millampere-hour (mAH) [3]; Phone’s screen is small [4]; The smart phone is energy hungry[5], according to the fact of eleven specific mobile phones’ battery capacity, which is not representative. The references above are only qualitative analysis based on experience, which is lack of real statistics to support. The range of mobile device parameters value is not clearly defined.

We need some accurate data and information as the basis of design in high-usability interactive system. So we – The Software Engineering Institute of Northwest University collected the information of smart phones and built a database. Among all of the parameters, few effects mobile HCI study, so we divide the parameters into two groups: relevant parameter (RP), which effects mobile HCI effectively, and non-relevant parameter (NRP), which effects mobile HCI little. In this paper, we focus on the RPs, including CPU frequency, memory capacity, screen size, battery capacity, the method of I/O, etc. Then, we propose a “standard” smart phone, which is only a conceptual phone. The parameters of “standard” smart phone constitute a set of RP, and the values (revised mean, mode and median) represent the reasonable value of the current smart phone.

The Effects of Device Hardware Features

Difficulties in Study of Mobile HCI

The Core Feature--Mobility

The core of mobile HCI that intertwines these spheres is how the users’ actions change their relation to their context. In other words, the unique aspect of mobile HCI is the strong influence of the environment—almost to the extent we could talk about Human–Computer–Environment Interaction. Mobility is essentially about change, something transforming to something else as a consequence of a

user's agency—a cycle of actions that provide new resources and place constraints for the ensuing actions. Mobility is therefore both a limiting as an enabling factor and a couple of the papers in this special issue reveal [1].

The Restrictions Caused by Mobility

The parameters of smart phone hardware are restricted by mobility. People neither take smart phone with large weight or large-size screen nor use standard keyboard or mouse. We cannot directly transplant the successful experience of PC to mobile devices.

Therefore, it is difficult to study smart phone successfully unless to be familiar with its hardware features. So the editor of *Int. J. Human-Computer Studies* commented the previous research of mobile HCI like this: “The lack of valid and actionable results, methods, and theories may be part of the reason why substantial investments in mobile technologies can fail” [6].

This paper argues that the correct theory and method is: on the one hand, from smart phone hardware and user's perspective, finding out its configuration, capacity, and features, on the other hand, analyzing the needs of users.

Three Related Claims

Claim 1: Mobile HCI research is not a simple take-ism.

The hardware differences between PC and smart phone make the experience on PC not be directly transplanted to smart phone.

Claim 2: The processing and interaction power of smart phones is weak.

The traditional view believes that the processing power of smart phone is weak, and is not suitable to complete the task of large-scale computing.

Claim 3: smart phone software architecture should adapt to its hardware features.

As described in Section 2.1.2, smart phone software architecture should adapt to its hardware features. The last decade of practice that transplants the design method of PC to smart phone has been proved to be a failure.

Research Questions

For the claims above, we need to ask the following two questions.

Question 1: What is the basic feature of RP?

RP is concerned by us, so we first want to figure out the basic characteristics of these parameters.

Question 2: How the RP changes over time?

Advances in technology led to the rapid development of hardware, so we need to study the RP change extent and trends over time.

Data Collection

To address the three research questions proposed above, we collect more than eight hundreds hardware records of smart phone with different styles from 2003 to 2010. The data covers the mainstream manufactures in the world, such as Nokia, Sony Ericsson, Motorola, HTC, BlackBerry and so on. Also it covers the most styles of the smart phone now available, so the data we collected could reflect the current state of smart phone. After data cleaning (removing lapped and erroneous data), finally we have got 815 valid records of smart phones. Handled and filtered by the program we had built, the data has been imported into the MySQL database.

Analysis and Results

A brief overview To address the three questions in Section 2.3, we do data mining by Univariate and Multivariate analysis on the SPSS software platform. The data SPSS used is exported from MySQL. The analysis below is carried out from the frequency, value, relevance and other dimensions. The following table 1 shows some statistics on the overall data, which reflects the current smart phone hardware state.

Addressing research question (1) In this section, we use descriptive statistics to address our first research question: (1). What is the basic feature of RP?

In our paper, we specify CPU frequency, Memory (ram) size, main screen size, screen resolution, external storage space, battery capacity and weight as the RPs.

CPU frequency: There are 568 records with CPU frequency in our database. The mode is 624MHz, which shows that the processor is comparable with PC's in 2000.

Memory size: According to our statistics, the RAM size of mainstream smart phones is greater than 128MB, the maximum is 1GB and the mean is 188MB.

Screen size and resolution: There are 767 records with screen size in our database. The mode is 2.8 inch and the percent of those with screen size between 2.8 inch and 3.2 inch is 42.4% in all the screen size, while the percent of those with screen size less than 2 inch is 0.7%; all of them were on sale before 2008.

Besides the screen size, the screen resolution is another important factor which effects the "Output". Screen resolution means the amount of the pixels that the monitor can display, which effects the clarity of the image. Among the screens with the same size but different resolution, the higher resolution, the more information can be displayed. So we also do statistics in this parameter in our paper.

Table 1. The data statistics

—		main screen	cpu frequency	pixel count	user space	battery capacity	phone weight
N	Valid	766	567	792	227	636	644
	Missing	49	248	23	588	179	171
Mean		2.9891	533.87	169979.46	5542.38	1155.58	135.9468
Std. Error of Mean		.02268	8.211	4512.071	603.739	17.538	2.18890
Median*		2.8880	527.66	95092.20	362.50	1192.24	127.8529
Mode		2.80	624	76800	8192	1500	120.00
Std. Deviation		.62805	195.694	127061.061	9116.263	442.635	55.59126
Variance		.394	38296.149	1.614E10	8.311E7	195926.135	3090.389

* Calculated from grouped data.

Screen size and resolution of smart phone shows that the desktop metaphor is not appropriate now. For Windows Mobile, the directly transplantation of desktop metaphor to smart phone was the main reason to its failure (without considering the context). Thus, new interaction metaphor is needed.

Capacity of battery: pointed out that although we needn't pay much attention to the energy on PC, it is critical on smart phone. Our statistics shows the maximum is 5600(mAh) and the mode is 1500(mAh). The increase of battery capacity reflects the latest and greatest technology, which gives exceptional capacity for its size and weight, and does not suffer from the memory effect. However, they are limitations on how much energy can be packed into a battery [5]. Without new technology, the energy remains to be a limitation on smart phone.

Addressing research question (2) As the value of RP changes over time, we pose our third research question: (3). How the value of RP changes over time?

The major changes are reflected in the following aspects:

Screen is increasingly larger and resolution is increasingly higher. The mean of smart phone main screen's size has increased from 2.6 inches in 2004 to slightly larger than 3.2 inches in 2010, but the rate of increase slowed after 2009. This reflects that when the manufacturing technology and cost of large screen are not a major problem, trade-off between interaction and portability is: On the one hand small screen is easy to move, but not easy to interaction; on the other hand, large screen is prone to interaction, but not conducive to move. Therefore, it can be inferred from the statistical data that the ideal screen size is between 3 inches and 4 inches.

It is obvious that CPU becomes increasingly faster (about 300Mhz in 2004 up to near 700Mhz in 2009) and memory becomes more and more larger, which shows that smart phones can process more and more tasks.

Extended storage space increases rapidly. The mean has increased 20 times, which ranges from 1G in 2003 to more than 20G in 2010. Now users can store a lot of videos and pictures.

The weight of smart phones changes little. Statistics figures from 2003 to 2010 shows that the weight of smart phones waves around 130g.

Battery capacity increases rapidly, but the rate of increase has been lowered in recent years.

More and more sensors are used in smart phones over time, such as photodiode, accelerometer, tilt, and temperature. So it is beneficial to be aware of environmental context to achieve Weiser's ubiquitous computing [7], and Norman's vanished interface.

Summary

Context is the basis of mobile HCI [8], It can be described from three dimensions: Environment, Device, and Activity. Device is an important part of context. With the advances of technology and the update of device, the work to understand the state of smart phone hardware is more critical than ever before. According to the statistics and analysis above, the major findings of our study are showed as following, (1) Divide the hardware parameters into two groups: RP and NRP. (2) Characterize the RP based on the statistics work. (3) Analyze the effect of RP on mobile HCI. (4) Build a "standard" smart phone, which allows researchers, designers and developers to understand the platform of smart phone hardware accurately. Something is imperfect in our research work, such as lack the sale information of different kinds of smart phones. Then we can't do the weighted analysis work, and this leads to that the result is not absolutely accurate. Nevertheless, the result can be a reference when we do HCI design and research work on smart phone.

Acknowledgement

This work was supported by NWU Graduate Cross-discipline Funds (10YJC06), the Shaanxi Provincial Department of Education research project (2010JK850).

References

- [1] A. Oulasvirta, S. Brewster, *Mobile human-computer interaction*. International Journal of Human-Computer Studies, v.66 n.12, pp. 833-837, December, 2008.
- [2] Information on <http://www.gartner.com/it/page.jsp?id=1126812>
- [3] O. Riva, J. Kangasharju, *Challenges and lessons in developing middleware on smart phones*. IEEE Computer, v.41, n.10, pp. 77-85, September 2008.
- [4] E. Andersson, I.-M. Isaksson, *Exploring Alternatives to the Hierarchical Menu Structure used in Mobile Phones*. Master's Thesis in Comp. Science, Umea University, Dept. of Comp. Science, 2007.
- [5] Chang, Y.F., Chen, C.S., and Zhou, H. *Smart phone for mobile commerce*, Computer Standards & Interfaces, Volume 31, Issue 4, June 2009, Pages 740-747.
- [6] John M. Carroll, Mary Beth Rosson, *Theorizing mobility in community networks*, International Journal of Human-Computer Studies, v.66 n.12, pp. 944-962, December, 2008, doi:10.1016/j.ijhcs.2008.07.003.
- [7] David Ley, Becta, *Ubiquitous Computing*, emerging technologie, Volume 2 (2007), pp. 64-79.
- [8] Ingrid Rügge , Carmen Ruthenbeck , Jakub Piotrowski , Christian Meinecke , Felix Böse, Supporting mobile work processes in logistics with wearable computing, Proceedings of the 11th International Conference on Human-Computer Interaction with Mobile Devices and Services, September 15-18, 2009, Bonn, Germany. doi>10.1145/1613858.1613949.

Influence of Thermal Distortion of Mirrors in Laser Resonators on Laser Modes

Junxi Yan^{1, a}, Fang Peng^{2, b} and Yufeng Peng^{3, c}

¹ Shangqiu Technician College of Henan Province, Shangqiu, Henan, 476000, China

^{2, 3} Department of Physics and Information Engineering, Henan Normal University, Xinxiang, Henan, 453007, China

^a476934398@qq.com, ^bzpfzyyx@163.com, ^cyufengp@hotmail.com

Keywords: Beam characteristics, Mirrors, Resonators, Thermal distortion

Abstract. Taking into account the thermal absorption of laser light on laser mirror surface, the thermal deformation of the mirror substrate was analyzed. Influence of the thermal distortions of the mirror substrate on the laser resonant modes was calculated. The expressions for the field distributions of transverse laser modes with perturbation methods were derived. By comparing them with the elegant Hermite-Gaussian modes where there were no thermal distortions, the intensity profiles of the transverse laser modes versus the amount of the thermal deformation were obtained. The results show that the larger the thermal distortions of mirrors are, the wider the intensity profiles of the fundamental mode become, and the smaller the peak intensity becomes. Meanwhile, the high-order modes will be induced.

Introduction

Some applications of high power lasers [1, 2], which are developing at a rapid rate, are limited due to the lack of suitable optical component materials. Since laser mirrors (or windows) are exposed to radiation of high power laser light, the thermal deformations in the mirrors will generate with the absorption of laser light, which degrade the beam optical quality of output laser and make the aberration become larger. If the amount of distortion varies from $\lambda/10$ to $\lambda/4$, the beam quality of output lasers becomes very poor, the output laser energy within small angular beam spread will reduce obviously. Sparks [3] concluded that the thermally induced optical distortion would be a major problem for long-focal-length laser systems, such as “laser-radar” systems.

Laabs *et al* [4] calculated the nonparaxial eigenmodes of stable resonators with a typical perturbation method. In 1980, Hauk *et al* [5] investigated the influence of mirror misalignment on spherical resonators and compared it with first-order perturbation theory. Remo [6] developed a second-order perturbation theory to compute diffraction losses incurred for small aberrations and misalignments in laser resonators. In some high-energy laser systems, such as chemical oxygen-iodine lasers, silicon is generally used as a substrate material for mirror or window because it combines the advantages of small thermal expansion coefficient with high thermal conductivity [7]. In this paper, considering the thermal distortions caused by the absorption of laser light and making use of perturbation methods, and then we analyse the laser field mode distributions in the resonator.

Theory

The heat conduction problem and geometry was illustrated in Fig.1. The laser beam is incident along the positive z direction for the mirror M_2 with thickness d and width 2a in the optical resonator.

Over the propagating depth of laser light it is assumed that the radius of the laser beam is constant, and giving a constant cross-sectional area with respect to z light energy is absorbed with a finite depth of the medium (i.e. mirror substrate materials) within the propagating region of laser light, which causes the thermal deformation of mirror substrate and a rise of temperature. With the medium described by thermal diffusivity k_d and thermal conductivity κ_c , the temperature $T(x,y,z,t)$ is given by the following heat conduction equation[8]

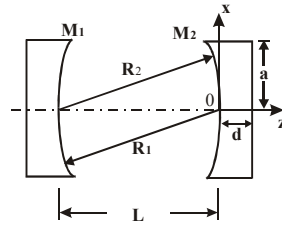


Fig. 1 Schematic diagram about the heat conduction problem and geometry

$$\frac{\partial^2 T(x, y, z, t)}{\partial x^2} + \frac{\partial^2 T(x, y, z, t)}{\partial y^2} + \frac{\partial^2 T(x, y, z, t)}{\partial z^2} + \frac{1}{\kappa_c} g(x, y, z) = \frac{1}{k_d} \frac{\partial T(x, y, z, t)}{\partial t}$$

$$\text{in } -a < x < a, -a < y < a, 0 < z < d, t > 0 \quad (1)$$

Where $g(x, y, z)$ is the power per unit volume absorbed by the medium from laser beam.

The axial thermal deformation Δd is composed of axial free thermal expansion Δd_f , longitudinal expansion Δd_a is caused by the fixture of the crosswise boundary and thermoelastic displacement Δd_t is caused by nonuniform axial temperature distributions. The equation about the axial thermal deformation is written as

$$\Delta d = \Delta d_f + \Delta d_a + \Delta d_t \quad (2)$$

Where,

$$\Delta d_f = \alpha_l \int_0^d T(r, z, t) dz,$$

α_l is the coefficient of linear thermal expansion, Δd_a can be obtained by calculating crosswise thermal strain γ_{rr} and drawing into Poisson's ratio ν , $\Delta d_a = -\nu \gamma_{rr} \cdot d$, Δd_t can be got by the theory of thermoelasticity, such as Goodier's thermoelastic potential method here Δd_t can be got by the theory of thermoelasticity, such as Goodier's thermoelastic potential method [8].

In an open resonator, the total propagation through one round trip can be described mathematically by a propagation integral [9]

$$u^{(1)}(x_1, y_1) = \exp[-ik_l L] \iint k(x_1, y_1, x_0, y_0) u^{(0)}(x_0, y_0) dx_0 dy_0 \quad (3)$$

where k_l is the propagation constant at the carrier frequency of the optical signal, L is the length of one period or round trip, the integral is over the transverse coordinates at the reference plane or input plane. The function k appearing in this integral which is called the propagation kernel, the field $u^{(1)}(x_1, y_1)$ after one propagation step which could be obtained from the initial field $u^{(0)}(x_0, y_0)$ through the operation of the linear kernel or propagator $k(x_1, y_1, x_0, y_0)$. Any arbitrary reference plane within the resonator or within one period of the equivalent lens guide, which may be chosen as the starting plane or reference plane for writing the preceding integral. The exact form of the kernel k depends on the reference plane which is chosen.

Doing analysis for resonator, we usually separate out $\exp[-ik_l L]$ about the on-axis phase shift term from the propagation kernel, as has been done in equation (3), all the necessary information for evaluating transverse field patterns is contained in the remaining kernel $k(x_1, y_1, x_0, y_0)$ with the exponential term only furnishing a constant phase shift in front. That is, for a resonator or a kernel, does there exist a set of mathematical eigenmodes $u_{nm}(x, y)$ and a corresponding set of eigenvalues γ_{nm} so that each one of these eigenmodes after one round trip satisfies the round-trip propagation expression

$$u_{nm}(x_1, y_1) = \int_{-a}^a \int_{-a}^a k(x_1, y_1, x_0, y_0) u_{nm}^{(0)}(x_0, y_0) dx_0 dy_0 = \gamma_{nm}^{(0)} u_{nm}^{(0)}(x_1, y_1) \quad (4)$$

where, $\gamma_{nm}^{(0)}$ and $u_{nm}^{(0)}(x_l, y_l)$ represent the unperturbed eigenvalue and eigenfunction respectively. With the method of separation of variables for a square mirror, we can get

$$u_{nm}^{(0)}(x, y) = F_n^{(0)}(X)G_m^{(0)}(Y) \quad (5)$$

$$\gamma_{nm}^{(0)} = \sigma_n^{(0)}\sigma_m^{(0)}. \quad (6)$$

Then we have the following two simple integral equations

$$\sigma_n^{(0)}F_n^{(0)}(X) = \sqrt{\frac{i}{2\pi}} \int_{-\sqrt{c}}^{\sqrt{c}} \exp[iXX']F_n^{(0)}(X')dX' \quad (7)$$

$$\sigma_m^{(0)}G_m^{(0)}(X) = \sqrt{\frac{i}{2\pi}} \int_{-\sqrt{c}}^{\sqrt{c}} \exp[iYY']G_m^{(0)}(Y')dY' \quad (8)$$

For convenience, we only take into consideration equation (7) in the following analysis. For an optical resonator, a distortion on the mirror surfaces will bring the additional phase shift per pass of the eigenfunction. Taking into consideration perturbation so the additional phase shift is introduced to equation (8), we get

$$\sigma_n F_n(X) = \sqrt{\frac{i}{2\pi}} \int_{-\sqrt{c}}^{\sqrt{c}} [1 + \Psi(X')] \exp[iXX'] F_n(X') dX' \quad (9)$$

where the eigenvalues σ_n and eigenfunctions $F_n(X)$ represent those in the perturbed case. $\psi(X')$ is the additional phase shift per pass of the eigenfunction and it is related to the perturbation of thermal distortions, which is given by

$$\Psi(X') = \frac{2\pi}{\lambda} \Delta d(X') \quad (10)$$

Results

For a resonator with two dimensions (x, z), the intensity profiles in the thermal distortion case could be calculated if there are only several nondegenerate transverse modes in the resonator (for example, TEM₀, TEM₁, TEM₂, and TEM₃), as shown in Figs.2a-d. δ represents the maximum deformation at the center of the mirror surface in figures. λ is the wavelength of the incident laser light.

From Fig.2a it is found that the intensity profile of the fundamental mode TEM₀ is gradually widened with the increasing of thermal deformation on the mirror surface, and the central intensity of TEM₀ is weakened. While the maximum deformation δ at the center of the mirror gets up to 0.5λ , the central intensity of TEM₀ will decrease by 50 percent, at the same time, the high-order transverse modes will generate. From figure 2b we can see that the intensity profile of TEM₁ will be widened with the increasing of the thermal deformation, the peak intensity becomes small. As shown in Figs.2c and 2d it is found that the outside peak intensity of TEM₂ and TEM₃ will increase with the increasing of the thermal deformation, but the near-central intensity will decrease.

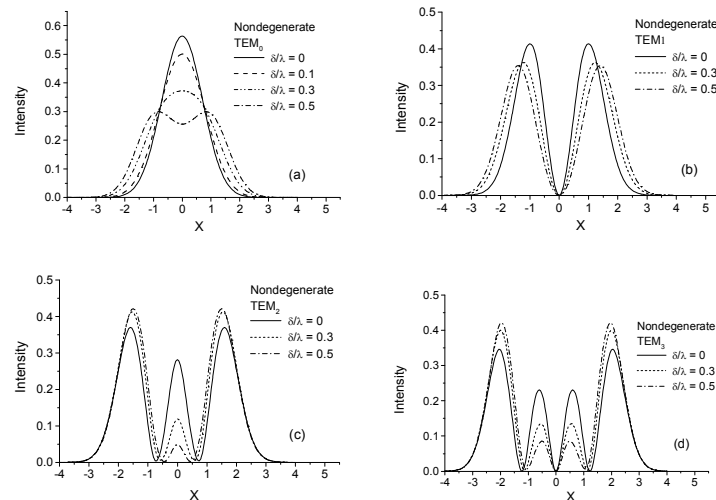


Fig. 2 Intensity profiles of transverse modes in the laser resonator under the nondegenerate perturbation with the thermal deformation of the mirror.

Conclusion

The cardinal reason for the importance of the thermally induced optical distortion is that small distortions on the mirror in a laser resonator which can cause significant reductions in the target intensity for long-focal-length systems, such as a “laser-radar” system, which must illuminate a distant object with an intensity greater than a given value, or a spot size smaller than a given value, the distortion of the laser beam with the heated mirror can degrade the performance of system. The optical distortion would be a major problem for a high power laser system.

Acknowledgments

This work was supported by National Natural Science Foundation of China under grant No.61077037, Henan Research Program of Foundation and Advanced Technology under grant No.102300413214.

References

- [1] Li G, Yu H, Duo L, et al (2009) Pulse Operation of Chemical Oxygen-Iodine Laser by Pulsed Gas Discharge with the Assistance of Spark Pre-ionization. *Chin. Phys. Lett.* 26: 114201.
- [2] Ancona A, Sibillano T, Lugara M P, et al (2006) An analysis of the shielding gas flow from a coaxial conical nozzle during high power CO₂ laser welding. *J.Phys.D: Appl.Phys.*39:563-574
- [3] Sparks M (1971) Optical distortion by heated windows in high-power laser systems. *J Appl Phys*, doi: 10.1063/1.1659888
- [4] Laabs H, Friberg AT (1999) Nonparaxial eigenmodes of stable resonators. *Berl J Quantum Electron* 35:198-207
- [5] Hauck R, Kortz HP, Weber H (1980) Misalignment sensitivity of optical resonators. *Appl Opt*, doi: 10.1364/AO.19.000598
- [6] Remo JL (1980) Diffraction losses for symmetrically tilted plane reflectors in open resonators. *Appl Opt*, doi: 10.1364/AO.19.000774
- [7] Anthony FM, Hopkies AK (1981) Actively cooled silicon mirrors. *SPIE* 0279:196-203.
- [8] Nowinski JL (1978) Theory of thermoelasticity with applications. Sijthoff & Noordhoff International Publishers, Netherland
- [9] Siegman AE (1986) Lasers. Mill Valley, California

Lens Design with Silicon Wafer for Terahertz Wave Transmission

Yong Wan^a, Minghui Jia^b, Haowen Gong^c, Yang Yang^d, Ying Cui^e

College of Physics Science, Qingdao University, Qingdao, 266071, P. R. China

^awanyong@qdu.edu.cn, ^bjjaminghui801@gmail.com, ^cbruce.kung34@gmail.com,

^d1363419773@qq.com, ^e765343525@qq.com

Keywords: Terahertz Wave; Lens; Photonic Crystal; Waveguide; Band Gap.

Abstract. Terahertz waves can pass through silicon wafer with less loss than traditional lenses. By selecting square, circular and sectors as building blocks, a serial of equivalent lenses for terahertz wave transmission were designed in the vertical plane of the silicon wafer, including hemispherical convex, concave mirror, triangular prism and spherocylinder lenses. The lens' 2-D design in this work is much simpler than its actual 3-D shape. Besides high transmit ability, silicon wafer also has high refractive index. When a lens is oriented horizontally, it can act as a graded-index photonic crystal waveguide, due to the existence of a band gap, especially for cylinder and prism lens.

Introduction

Terahertz (THz) waves can be used in a wide range of applications. Recently, there have been numerous breakthroughs on THz sources[1,2]. Transmission is becoming another major issue. The first problem is the converging or splitting of the waves. Large part of wave energy will be absorbed when THz waves pass through traditional lenses. On the other hand, THz waves can pass through a silicon wafer with less loss, especially for intrinsic (without doping) one with high resistivity. Silicon wafer also has high reflectance. These properties make silicon wafer a promising material for lenses and waveguides for THz wave transmission.

There have been several lens designs for THz wave transmission. Most of them work on traditional lenses [3-5]. There are some one-dimensional equivalent lens designs for special purposes [6-8]. In this paper, a serial of equivalent lens designs were presented, such as hemispherical convex, concave mirror, triangular prism and spherocylinder lenses. They all could be designed on planar silicon wafer. More interestingly, a lens can also act as waveguide if put horizontally, due to the existence of a band gap.

Design of Lenses

All lens designs in this paper met two criteria. Firstly, effective refractive index at each point of the lens was exactly equivalent to that at the same position of a traditional lens. Thus, accurate distribution of dielectric pillars or holes is needed. Secondly, for high-resolution imaging, both the size of the building blocks and the distance between two adjacent building blocks were less than 1/12 of the wavelength.

Since the largest size for building blocks is determined by operating frequency, it was set at 1THz (wavelength $\lambda = 300\mu\text{m}$) in this work, and the lenses were 1cm in diameter for convex and concave ones and 1cm by 1cm for triangular prism and spherocylinder lenses. For simplification, the distance between centers of building blocks in adjacent layers was set to 24 μm for all lenses in this work. The variables were size and number of building blocks in each symmetrical layer. Equation 1 was used to calculate the area fraction of dielectric pillars or holes.

$$n_{eff} = \sqrt{n_{air}^2 S_{air} + n_{di}^2 S_{di}} \quad (1)$$

Where n_{eff} , n_{air} and n_{di} are the refractive indices of local layer, air and dielectric materials, S_{air} and S_{di} are the area fractions of air and dielectric materials in local layer, respectively.

Three kinds of building blocks, namely cylinders, square blocks and circular sectors were selected. Fig 1(a), (b) and (c) showed the structures of convex lenses. For cylinder and prism lenses, they had similar structures, but the size of building blocks changed only in one dimension and number of building blocks in each layer remained constant. Fig 1 (d) and (e) showed cylinders and squares as building blocks for these lenses. For concave lenses, the structures were similar as those of convex lenses in Fig 1 (a), (b) and (c), but the dielectric building blocks were increasing in size when approaching the edge of the lens. The design procedures for all kinds of lenses were similar. The design procedure of a convex lens was shown below as an example.

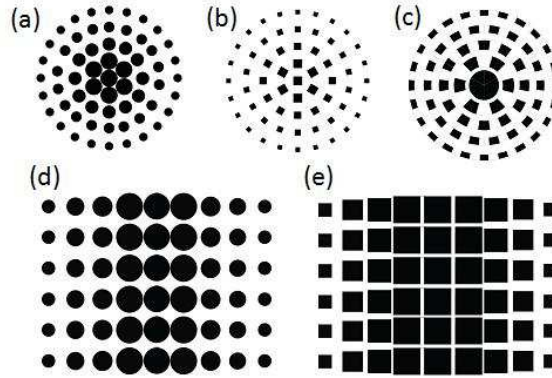


Fig. 1 Structures of lenses

Fig 1 (a), (b) and (c) are the structures of convex lenses with building blocks in the shapes of cylinders, square blocks, and circular sectors, respectively. Fig 1 (d) and (e) show cylinders and square blocks as the building blocks for cylinder and prism lenses.

Maximum refractive index: The achievable maximum value occurs when the cylinders in the innermost layer are close-packed in a tangential way, then we can choose $r = R \sin(\frac{\pi}{N})$ where r is the radius of dielectric pillar, R is the distance of centre of pillars from the centre of the lens and N is the number of pillars in the innermost layer. The maximum area fraction of dielectric pillars could be calculated by using Equation (2).

$$S_{di} = \frac{N\pi r^2}{\pi[(R+r)^2 - (R-r)^2]} = \frac{Nr^2}{4Rr} = \frac{Nr}{4R} = \frac{NR \sin(\frac{\pi}{N})}{4R} = \frac{N \sin(\frac{\pi}{N})}{4} \quad (2)$$

Distribution of refractive indices: The local refractive indices of a convex lens should satisfy Equation (3), which is a trajectory of an eclipse, where n_i , n_{min} and n_{max} are the refractive indices of i th layer, the edge and the centre, x_i is the outer radius of i th layer and R_T is the radius of the lens.

$$\left(\frac{n_i - n_{min}}{n_{max} - n_{min}}\right)^2 + \left(\frac{x_i}{R_T}\right)^2 = 1 \quad (3)$$

Radii of pillars: For each layer, the area fraction of dielectric materials could be calculated from Equation (4), where S_{di}^i is the local area fraction of dielectric materials in i th layer, N_i is number of dielectric pillars in this layer, r_i is the radius of dielectric pillars, k is the increase in number of pillars per layer when approaching the edge and a is the distance between centers of dielectric pillars in adjacent layers. Both k and a are defined prior to calculation.

$$S_{di}^i = \frac{\pi N_i r_i^2}{\pi(x_i^2 - x_{i-1}^2)} = \frac{ikr_i^2}{(ia + r_i)^2 - (ia - a + r_{i-1})^2} \quad (4)$$

For concave lens, the procedure was similar as above, but the Equation (3) should be replaced by Equation (5). For cylinder and prism lenses, the number of building blocks in each layer remained constant. Therefore, during calculation for these two lenses, Equation (3) should be replaced by Equation (6) and (7), and Equation (4) should be replaced by Equation (8), respectively.

$$\text{For concave, } \left(\frac{n_{\max} - n_i}{n_{\max} - n_{\min}} \right)^2 + \left(\frac{x_i}{R_T} \right)^2 = 1 \quad (5)$$

$$\text{For cylinder, } \left(\frac{n_i - n_{\min}}{n_{\max} - n_{\min}} \right)^2 + \left(\frac{x_i}{R_T} \right)^2 = 1 \quad (6)$$

$$\text{For prism, } \frac{n_{\max} - n_i}{n_{\max} - n_{\min}} = \frac{x_i}{R_T} \quad (7)$$

$$S_{di}^i = \frac{\pi N r_i^2}{R_T (x_i - x_{i-1})} \quad (8)$$

Results and Discussions

Fig 2, 3 and 4 showed the simulation results of four different kinds of lenses. Fig 2 showed the 1-D and 3-D plots of refractive indices versus distance from the centre for two convex lenses with different refractive index ranges (1 to 3 for Fig 2(a) and 2(b); 1.1 to 2 for Fig 2(c) and 2(d)). Similarly, the same plots for a concave lens (Fig 3), a cylinder lens (Fig 5(a) and 5(b)) and a prism lens (Fig 5(c) and 5(d)) were presented.

The lens' 2-D design in this work is much simpler than its actual 3-D shape, and this contrast is especially so in mass manufacturing. The configuration is easily adjustable based on specific needs: the building blocks can be larger when the operating frequency is lower, otherwise they can just be smaller. The maximum of the refractive index n_{\max} could also vary within a particular range for specific research requirement based on calculation results from Equation (1). The distance between centers of building blocks in adjacent layers is also adjustable, but it should not exceed 1/12 of the wavelength in case of dispersion (for the same reason, the operating frequency should be in a narrow range, i.e. from 0.5 to 2 THz in this study). In addition, other than the above-mentioned pillar-building method, holes-drilling on the silicon slab could be an alternative, if local refractive indices fulfill the first requirement in Section 2. In addition, the combination of lens with the particular THz source like GaAs semiconductor, which assumes that the source direction is perpendicular to the x - y plane, could result in a new device emitting THz wave of higher quality.

The effect of height of the pillar or the depth of the hole (represented as D) on the lenses was neglected in the above-mentioned methods. However, in reality it has to match certain requirement since the phase shift is proportional to the wave vector k times the propagation length. Generally D should be larger than 300 μm . According to Lensmaker's equation, the focal length for convex lens is related to the dimension R of the lenses and maximum value of effective refractive index n_{eff} as the following equation:

$$f = \frac{R}{n_{\max} - 1} \quad (9)$$

Besides functioning as a lens, the device could be used as a graded-index photonic crystal waveguide for the light rays on the parallel plane, which can have special function, such as slow light[9], and each particular lens has its own photonic bandgap (PBG), especially for cylinder and prism lenses with larger PBGs. Fig 4(a) is the band structure of Fig 1(a) and Fig 4(b) is the band structure of Fig 1(d), which were calculated by using the plane-wave expansion method, in which

the step length was about 0.01 length of spatial period and the eigenvalue accuracy is higher than $exp(-8)$. In addition, by removing one or some columns of pillars on the orientation of the incident light, the device will function as a better waveguide on this particular orientation. By replacing one or some columns of pillars with metal pillars, negative refraction effect will occur, and variation of the shape of these pillars may enhance negative refraction effect[10].

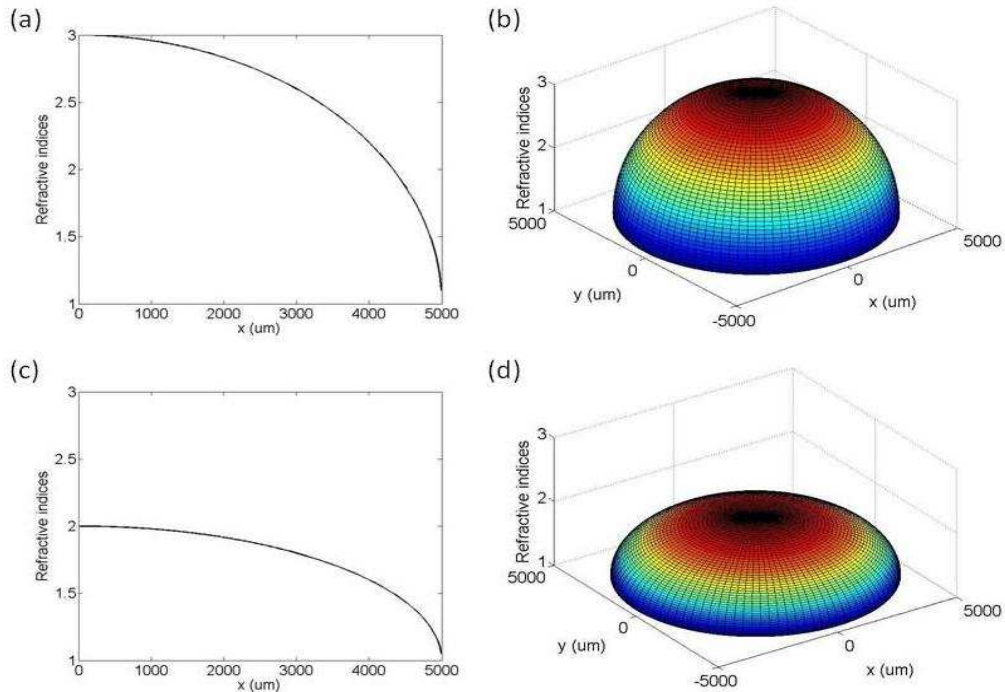


Fig. 2 1-D and 3-D simulation results for convex lenses. The refractive indices vary from 1 to 3 in Fig. 2(a) and 2(b) and 1.1 to 2 in 2(c) and 2(d).

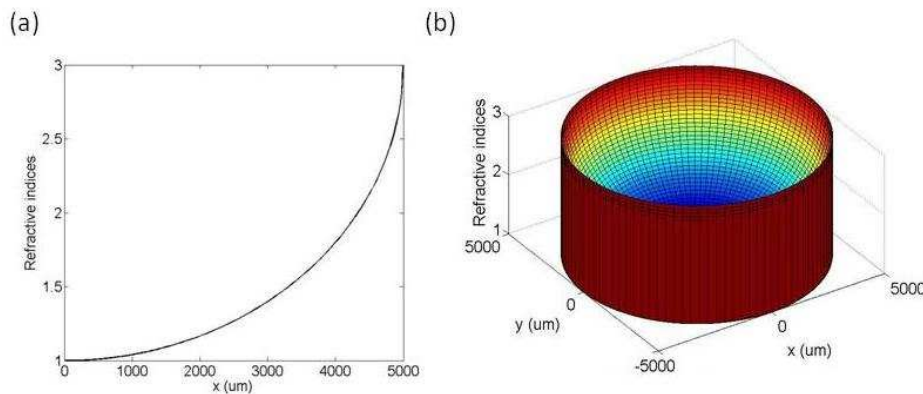


Fig. 3 1-D and 3-D simulation result for concave lenses

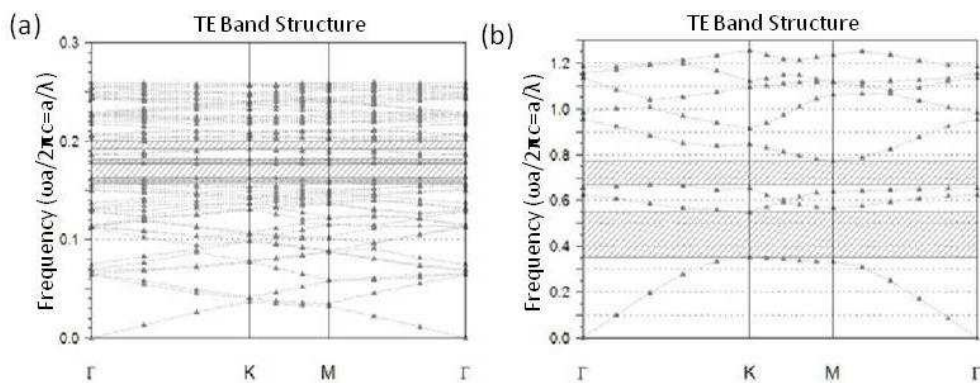


Fig. 4 (a) Band structure of the lens in Fig 1(a); (b) band structure of the lens in Fig 1(d)

Conclusions

In this study, a serial of equivalent lenses for terahertz wave transmission were designed in the vertical plane of a silicon wafer, which is much simpler to manufacture than its actual 3-D shape. The configuration is easily adjustable based on specific needs. If a lens is put horizontally, it can also act as graded-index waveguide. The new designs will promote the study and application of THz wave.

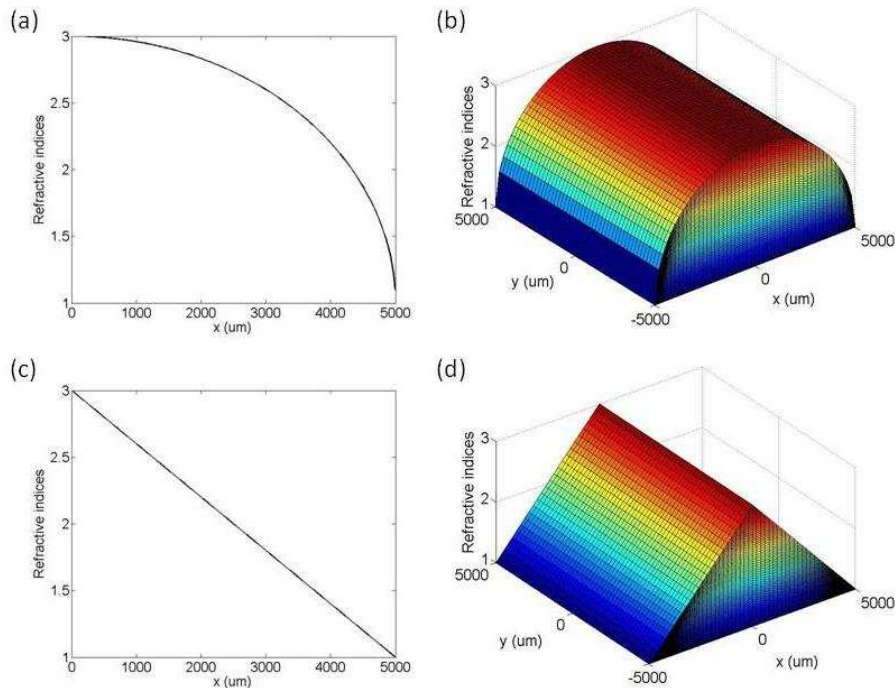


Fig. 5 1-D and 3-D simulation results for cylinder (4(a) and 4(b)) and prism (4(c) and 4(d)) lenses. The refractive indices for both cylinder and prism lenses varied from 1 to 3.

Acknowledgement

This work was supported by the National Natural Science Foundation of China (Grant No. 11144007).

References

- [1] Kumar S, Lee AWM. *IEEE J Sel Top Quantum Electron* 2008;14(2):333-44
- [2] Khosropanah P, Zhang W, Hovenier JN, Gao JR, Klapwijk TM, Amanti MI, et al. *J Appl Phys* 2008;104(113106):1-6
- [3] Lo YH, Leonhardt R. *Opt Express* 2008;16(20):15991-8
- [4] Boriskin AV, Nosich AI, Boriskina SV, Benson TM, Sewell P, Altintas A. *Microwave Opt Technol Lett* 2004;43(6):515-8
- [5] Bitzer A, Helm H, Walther M. *IEEE J Sel Top Quantum Electron* 2008;14(2):476-81
- [6] Kim S, Murakami H, Tonouchi M. *IEEE J Sel Top Quantum Electron* 2008;14(2):498-504
- [7] Kadlec C, Kadlec F, Kuzel P, Blary K, Mounaix P. *Opt Lett* 2008;33(19):2275-7
- [8] Foca E, Foll H, Cartensen J, Sergentu VV, Tiginyanu IM, Daschner F, et al. *Appl Phys Lett* 2006;88(011102):1-3
- [9] D. Luo, G. Alagappan, X.W.Sun, et al., *Opt.Comm.*, 2009, 282(2):329-332
- [10] Li J, Lu M-H, Feng L, Liu X-P, Chen Y-F. *J Appl Phys* 2007;101(013516):1-5

Precise Time Measurement Using CTMU

Zuoxiaoqiong^a, Liuyaxian^b

Wuhan Donghu University

^a32257299@qq.com, ^b286116718@qq.com

Keywords: CTMU, Precise Time Measurement, Resolution, Analog to Digital Converter

Abstract. Numerous applications require very precise time measurement. Usually, the measurement accuracy is increased by improve the MCU MIPS. It will take the high cost and current consumption, and the accuracy is limited in the MCU MIPS. Using CTMU channels work in conjunction with Analog to Digital converters, the high precise time measurement with low cost MCU can be achieved, and make the time measurement resolution to 1 nanosecond. CTMU module is available in many Microchip microcontrollers.

Introduction

CTMU stands for “Charge Time Measurement Unit”. The Charge Time Measurement Unit is a flexible analog module that has a configurable current source with a digital circuit built around it. The CTMU can be used for differential time measurement between pulse sources and can be used for generating an asynchronous pulse. By working with other on-chip analog modules, the CTMU can be used for high resolution time measurement, measure capacitance, resistance, inductance, temperature, used for humidity sensing, measure relative changes in capacitance or generate output pulses with a specific time delay [1].

The module includes the following key features:

- On-chip precision current source
- Sixteen-edge input trigger sources
- Selection of edge or level-sensitive inputs
- Polarity control for each edge source
- Control of edge sequence
- Time delay of external or internal signal asynchronous to system clock
- Integrated temperature sensing diode
- Control of current source during auto-sampling
- Four current source ranges

Block diagram of the CTMU is shown in Fig. 1.

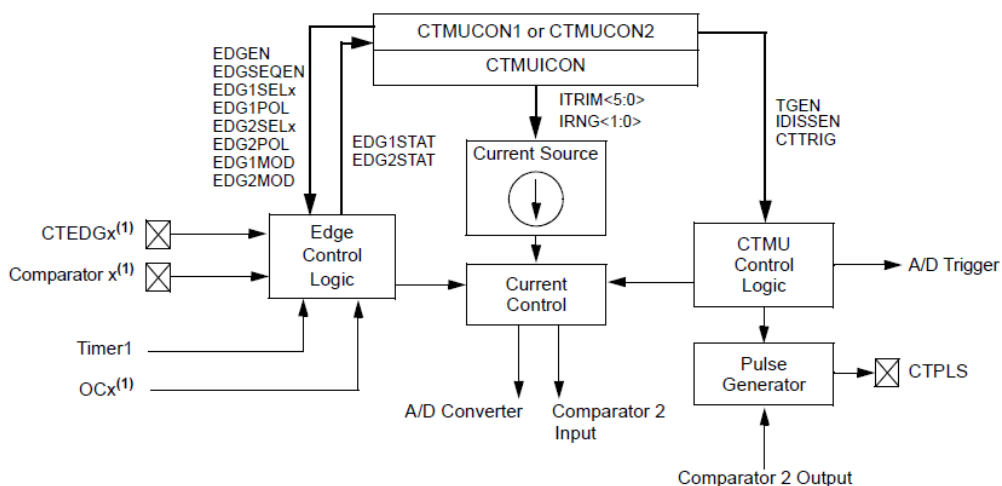


Fig. 1 CTMU block diagram

The CTMU works by using a fixed current source to charge a circuit. The type of circuit depends on the type of measurement being made. In the case of charge measurement, the current is fixed and the amount of time the current is applied to the circuit is fixed. The amount of voltage read by the A/D is then a measurement of the capacitance of the circuit. In the case of time measurement, the current, as well as the capacitance of the circuit, is fixed. In this case, the voltage read by the A/D is then representative of the amount of time elapsed from the time the current source starts and stops charging the circuit.

Theory of operation

The operation of the CTMU is based on the equation for charge, as shown in Eq.1.

$$I = C \frac{dv}{dt} \quad (1)$$

More simply, the amount of charge measured in coulombs in a circuit is defined as current in amperes (I) multiplied by the amount of time in seconds that the current flows (t). Charge is also defined as the capacitance in farads (C) multiplied by the voltage of the circuit (V), as shown in Eq. 2.

$$I \cdot t = C \cdot v \quad (2)$$

The CTMU module provides a constant, known current source. The A/D Converter is used to measure (V) in the equation, leaving two unknowns: capacitance (C) and time (t). Eq.2 can be used to calculate capacitance or time, by either the relationship shown in Eq.3 or using the known fixed capacitance of the circuit, or by Eq. 4 using a fixed time that the current source is applied to the circuit.

$$t = \frac{C \cdot v}{I} \quad (3)$$

$$C = \frac{I \cdot t}{v} \quad (4)$$

Current Source

At the heart of the CTMU is a precision current source, designed to provide a constant reference for measurements. The level of current is user-selectable across four ranges, or a total of three orders of magnitude, with the ability to trim the output in $\pm 2\%$ increments (nominal). The current range is selected by the IRNG1:0> bits (CTMUICON<9:8>) with a value of '01' representing the lowest range.

Current trim is provided by the ITRIM<5:0> bits (CTMUICON<15:10>). These six bits allow trimming of the current source in steps of approximately 2% per step. Note that half of the range adjusts the current source positively and the other half reduces the current source. A value of '000000' is the neutral position (no change). A value of '100000' is the maximum negative adjustment (approximately -62%) and '011111' is the maximum positive adjustment (approximately +62%).

Edge/Level Selection and Control

CTMU measurements are controlled by the edge or level events occurring on the module's two input channels. Each channel, referred to as Edge 1 and Edge 2, can be configured to receive input pulses from one of the sixteen edge input pins. The inputs are selected using the EDG1SEL and EDG2SEL bit pairs (CTMUCON2<5:2> and <13:10>). Further, the mode of the input sources to the Edge 1 and Edge 2 can either be level-sensitive or edge-sensitive, which is selected using the EDG1MOD bit

(CTMUCON2<15>). In addition to source, each channel can be configured for event polarity using the EDGE1POL and EDGE2POL bits (CTMUCON2<14> and CTMUCON2<6>). The input channels can also be filtered for an edge event sequence (Edge 1 occurring before Edge 2) by setting the EDGSEQEN bit (CTMUCON1<10>) [2].

Edge Status

The CTMUCON2 register also contains two status bits: EDG1STAT and EDG2STAT (CTMUCON2<9:8>) [2]. Their primary function is to show if an edge response has occurred on the corresponding channel. The CTMU automatically sets a particular bit when an edge response is detected on its channel. The level-sensitive, or edge-sensitive, nature of the input channels also means that the status bits become set immediately if the channel's configuration is changed and is the same as the channel's current state.

The module uses the edge status bits to control the current source output to external analog modules (such as the A/D Converter). Current is only supplied to external modules when EDG1STAT is not equal to EDG2STAT, and shuts current off when EDG1STAT is equal to EDG2STAT. This allows the CTMU to measure current only during the interval between edges. After both status bits are set, it is necessary to clear them before another measurement is taken. Both bits should be cleared simultaneously, if possible, to avoid re-enabling the CTMU current source.

In addition to being set by the CTMU hardware, the edge status bits can also be set by software. This allows the user's application to manually enable or disable the current source. Setting either one (but not both) of the bits enables the current source. Setting or clearing both bits at once disables the source.

Precision Time Measurement

Using the edge trigger pins (CTEDn) on the CTMU, time can be measured precisely to a resolution of under a nanosecond. This is done by charging the A/D Sample-and-Hold (S/H) capacitor between the rising edges of the two pins; the resulting voltage is directly proportional to the time. Fig. 2 shows the general scheme for time measurement. CTMU-based time measurement is synchronous to the clock running the microcontroller. The first rising edge on external pin CTED1 starts the CTMU charging and the second rising edge on external pin CTED2 stops the charging. Constant current charges capacitance linearly. Voltage on AD holding capacitor is proportional to charge time. When the CTMU charging completed, it can trig the AD converter automatically and we will get one AD converter result ADCBUF.

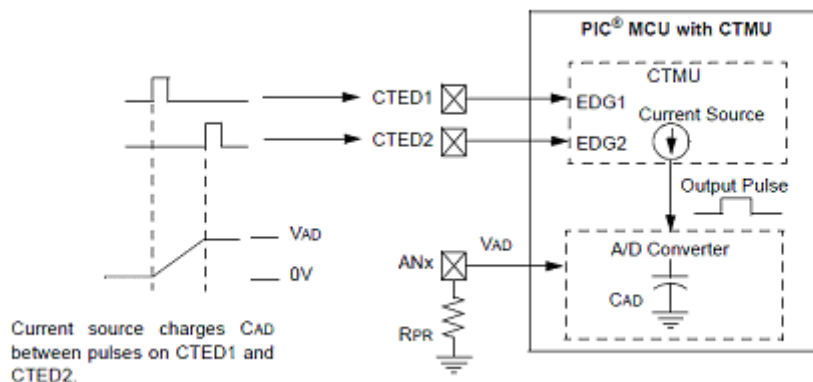


Fig. 2 Time measurement scheme

The CTMU calibration must be done before the time measurement; calibration determines the linearity slope and also can remove the offset for the CTMU and capacitor.

Step 1: Know T1 (charge for 1 TCY); Measure V1.

Step 2: Know T2 (charge for 2 TCY); Measure V2.

We can determine the charging slope $I/C=(T2-T1)/(V2-V1)=1\text{ Tcy}/(V2-V1)$. Then the time $t=ADCBUF* Tcy/(V2-V1)$.

CTMU Time measurement resolution is based on the resolution of the A/D used to convert the voltage on C. When using 10-bit A/D (1024 counts). Assume $I = 55\text{ uA}$, $C = C_{AD} + C_{PIN} = 15\text{ pF}$ and A/D $V_{REF} = V_{DD}$. If $V_{DD} = 3.0\text{V}$, then $1\text{ A/D count} = V = 3.0/1024 = 2.93\text{ mV}$. CTMU Time resolution is $T = (15\text{ pF}/55\text{ uA}) * 2.93\text{ mV} = 0.799\text{ nS}$. As can be seen in this example, a time measurement resolution less than 1 nanosecond is possible.

There are a couple of ways to increase the resolution.

Lowering the A/D V_{REF} , use external 2.5v V_{REF} . Lowering the V_{REF} voltage provides a smaller voltage (ie. time unit) per A/D count [3]. The resolution will be improved to $T = (15\text{ pF}/55\text{ uA}) * (2.5/1024) = 0.666\text{ nS}$.

Use internal CTMU channel (no external pin connection). Some Microchip microcontrollers feature CTMU modules capable of selecting an internal A/D channel which does not connect to the A/D multiplex and to an external pin. This eliminates the parasitic to improve the resolution. C is smaller, T is smaller. $T = (4\text{ pF}/55\text{ uA}) * (3.0/1024) = 0.213\text{ nS}$.

Use an external High resolution ADC. Increasing the resolution of the A/D directly affects the resolution of the CTMU. Use an external 16-bit ADC, and assume capacitance is doubled to 30 pF. Then the resolution $T = (30\text{ pF}/55\text{ uA}) * (3.0/65536) = 24.9\text{ pS}$! It's a very excellent result.

Dynamic Measurement Range

Besides for the measurement resolution, the dynamic measurement range is also a very important parameter for the time measurement, and is limited by the total capacitance ($C_{AD} + C_{PIN} + C_{STRAY}$), charge current and max A/D input voltage.

Assume 10-bit A/D (1024 counts), $I = 55\text{ uA}$ and $C = C_{AD} + C_{PIN} + C_{STRAY} = 15\text{ pF}$, the resolution is (from previous section) $T = (15\text{ pF}/55\text{ uA}) * 2.93\text{ mV} = 0.799\text{ nS}$, therefore, the Dynamic Range is $0.799\text{ nS} * 1024\text{ A/D counts} = 818\text{ nS}$ or $(15\text{ pF}/55\text{ uA}) * 3.0\text{v} = 818\text{ nS}$.

The CTMU current source requires about 0.5v of voltage overhead to maintain its programmed constant current. When V_{REF} is 3.3v, minus the current source overhead leaves a dynamic range of 2.8v or about 85% of the A/D input range. Driving the A/D input above 2.8v causes a decrease in current and therefore a non-linear output. If V_{REF} is 2.5v, which allows the current source to operate across the entire A/D input range. And the measurement dynamic range will decrease to $(15\text{ pF}/55\text{ uA}) * 2.5\text{v} = 682\text{ nS}$. For a given system, the dynamic range is negative correlation with the resolution; increase the measurement resolution will decrease the dynamic range.

For a time longer than 1nS, it needs to extend the dynamic range. And the CTMU dynamic range can be extended without the loss of resolution. Combine CTMU with Input Capture (ICAP), Output Compare (OCMP) or Timer can do longer time measurement. Timer provides "Coarse" synchronized time intervals based on instruction cycle clock, TCY (ex. 62.5 nsec @ 16 MIPS for PIC24F) and CTMU provides "Fine" asynchronous time interval measurement. Total time measured is coarse time + fine time.

Fig. 3 shows one longer time measurement example to use CTMU with ICAP. Time $t = TCY * (8002 - 2) + (T1 - T2) = 500\text{ usec} + (T1 - T2)$. Used the Input Capture, the dynamic range is extended to hundreds of micro second.

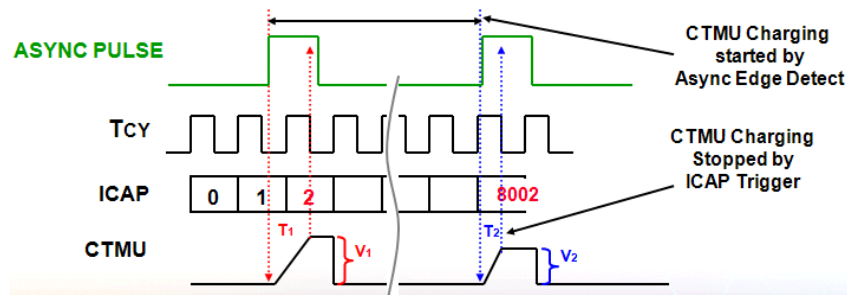


Fig. 3 Longer time measurement to use CTMU

Summary

Many Microchip microcontrollers integrate in the CTMU module. Its high performance is easy to use and configure. Work with the analog to digital converter, it can be used to do high resolution time measurement and reach less than 1 nanosecond accuracy. The CTMU module is ideal for precise time measurement.

References

- [1] Padmaraja Yedamale and Jim Bartling: See What You Can Do with the CTMU (2011).
- [2] Bruce Bohn: DS79324 Charge Time Measurement Unit Reference Manual (2011).
- [3] Lehman Lance: *Applications Using CTMU*, Microchip MASTERS Conference, Chandler, Phoenix, AZ, 2010.

Based On Image Procession to Measure Flame Emission Characteristic and Radioactive Prosperities

Jie Yao^{1,a}

¹The department of mechanic and electronic JingdeZhen Ceramic Institute ,JingdeZhen, China,333403

^a e-mail: njyaojie@yahoo.com.cn

Keywords: furnaces; Combustion diagnostics; Image processing; Radioactive property

Abstract: radioactive properties are hard to be given exactly by the existing methods. In this paper, multiple color image detectors were used to capture approximately red, green, and blue monochromatic radioactive intensity images in the visible wavelength region, and the flame emissive and the radioactive properties of the particulate media in three pulverized-coal-fired boiler furnaces were got from the flame images.

Introduction

In this paper, a convenient and practical image processing technique in the visible region is presented to measure the flame emissive and radioactive properties of particulate medium in large-scale, high-temperature pulverized-coal-fired boiler furnaces. First, the measurement principle will be outlined briefly. Then, the experimental set-ups in three large-scale boiler furnaces will be described. After that, measure mental results of flame emissive and radioactive properties of particulate medium in three boilers will be given, and the effects of furnace load, furnace size, and coal quality on the measurement results are analyzed. Finally, some concluding remarks will be discussed.

Thermal radiation is the predominant mode of heat transfer in high-temperature, large-scale, particle-laden combustion systems such as pulverized-coal-fired boiler furnaces. The medium in a pulverized-coal-fired furnace is an in homogeneous mixture of gaseous products such as CO₂, H₂O and so on, and suspended solid particles consisting of pulverized coal, char, fly ash, and soot. The radioactive heat transfer in furnaces is due to both band emission from gaseous products and continuous emission from suspended particles. The radioactive properties of gases can be evaluated, for example, through narrow-band models or wide-band models [1,2]. For the particles in combustion medium, the emissive and radioactive properties can be approximately estimated using Mie theory [3, 4]. However, as of today the knowledge about the chemical composition of these particles, their shapes and size distributions, and their optical properties are limited. Furthermore, the radioactive properties of these particles vary as their temperature, sizes and shapes change as they travel through the furnace. The accurate predictions would have to depend on in situ measurements for the flame [2]. Though the measurements of spectral emissive for pulverized coal and char particles in the infrared region have been present-ed [6,7], until now, few on-line and in situ measurements in large-scale, high-temperature boiler furnaces have been reported. In [8], the spectral emissive of a solid dispersed phase of a flame was calculated from the measurements of the spectral irradiation, and the experimental results were presented for different pulverized-coal-fired furnaces.

The flame image processing techniques in the visible region have been used as effective tools for flame study, temperature measurement, and combustion diagnose [9,10]. The authors have done simulation and experimental investigations on visualization of two-dimensional (2D) and three-dimensional (3D) temperature distributions inside pulverized-coal-fired furnaces using the image processing techniques [11, 12]. The 2D/3D temperature distributions in furnaces can be reconstructed from the boundary radioactive temperature images captured by the image detectors

after calibration. Besides that, the simulation works for simultaneously estimating the temperature profiles and the radioactive properties in a one-dimensional (1D) parallel-plane medium and a 2D rectangle furnace were reported in [14, 15], respectively.

Reconstruction of radioactive properties of particular medium

In order to simultaneously reconstruct the temperature distributions and the radioactive properties (absorption coefficient μ_j and scattering coefficient σ_s) of particulate medium in furnaces, we need an equation to relate the temperature distribution, the radioactive properties in the furnace with the boundary radioactive information received by the image detectors. In application, the furnace system studied is divided into M spatial meshes for its medium zone and M' surface meshes for its surface area, and the total number of image pixels in the image detectors is set as N . According to a new solution method proposed for the radioactive transfer equation (RTE) in an absorbing, emitting, and scattering gray enclosure [17], the radioactive intensity I received by image detectors can be calculated as:

$$I = A_r T \quad (1)$$

Where $I = (I(1) \cdots I(j) \cdots I(N))^T$ can be measured using image processing techniques described in Section 2.2, $T = (T^4(1) \cdots T^4(i) \cdots T^4(M + M'))$ represents the temperature distribution in the furnace, $A_r \in R^{N \times (M + M')}$ can be obtained from [11–13], and related with the installation and the imaging parameters of the image detectors, and the radioactive properties of particulate medium. A temperature image T_m can be calculated from two monochromatic images from a color image by Eq. (4), and it was further related to the temperature distribution T by [18]

$$T_m = A' T \quad (2)$$

Where $T = (T_m^4(1) \cdots T_m^4(j) \cdots T_m^4(N))^T$, and the relationship between matrixes A_r and A' was given in [18]. T_m holds linear relationship with T . The reconstruction of temperature and radioactive properties can be described as below. The radioactive intensity image I and the radioactive temperature image T_m can be detected by the image detectors and they serve as input data. A modified Tikhonov regularization method has been used to reconstruct the temperature distribution determined by Eq.(1) from the radioactive temperature image T_m and the detailed description can be found in [11, 12]. The inverse radioactive property problem can be formulated as an optimization problem that minimizes the errors between the calculated and the measured boundary radioactive intensity. A Newtonian-type iteration algorithm and the least-squares method are used to estimate the absorption and scattering coefficients of particulate medium [14,15].

Experiment Setup

In [11,12], a novel instrumentation system for on-line, in situ visualization of 2D/3D temperature distributions in large-scale pulverized-coal-fired boiler furnaces developed by the authors has been applied in three tangentially fired boiler furnaces. Using the instrumentation system, the experiments to measure the flame emissive and radioactive properties of particulate medium were also done in these three boilers. The schematic of furnaces and experimental set-ups are shown in Figs. 2 and 3. As shown in Fig. 2, eight image detectors were mounted in four layers along the height of boiler A (a 670t/h boiler furnace in a 200 MW power generation unit), two detectors in one layer. A color image detector consisted of a lens, an image guide and a Samsung SCC-833P color CCD camera and it has been described in [11,12]. By use of a frame-maker and a frame-grabber, the video signals captured

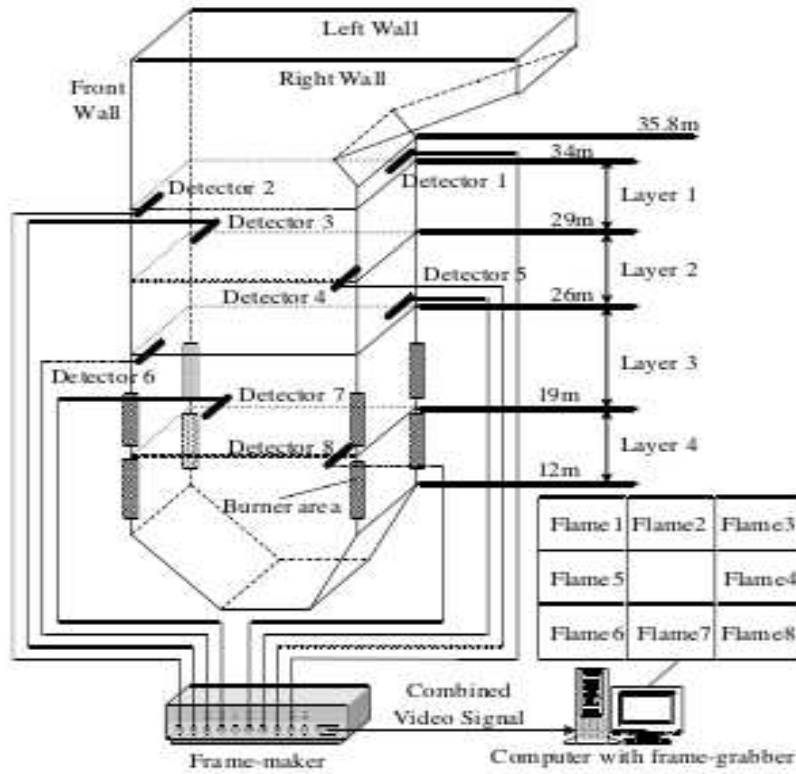


Fig.1. The furnace and experimental set-up in boiler A

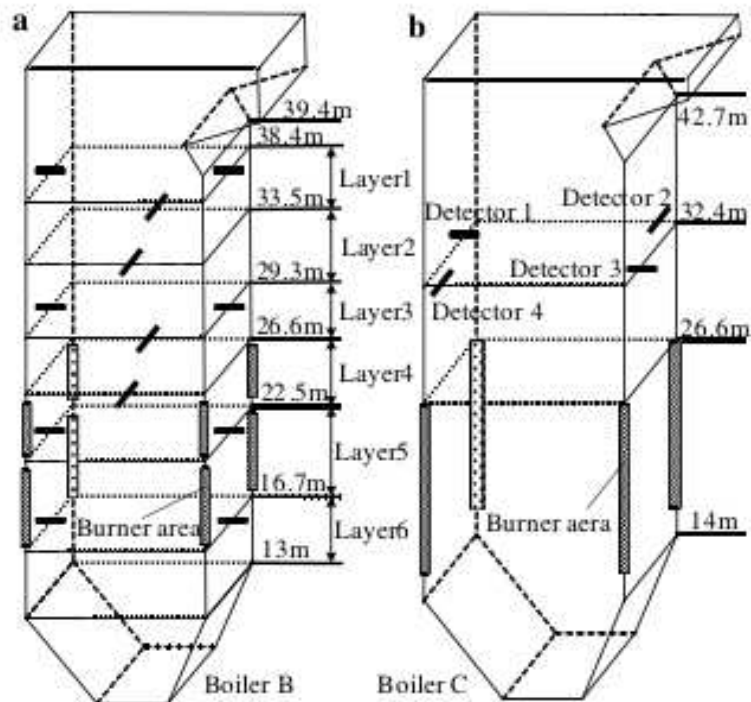


Fig.2. The furnace and the installation position of flame image detectors in boilers B

Table 1 Proximate analysis of the coals(air dried basis)

Proximate (%)	Coal A	Coal B	Coal C
Dry loss	0.40	0.60	0.80
Ash	33.70	23.69	43.45
Vol. matter	15.60	31.75	12.68
Fixed C	50.30	44.14	43.07

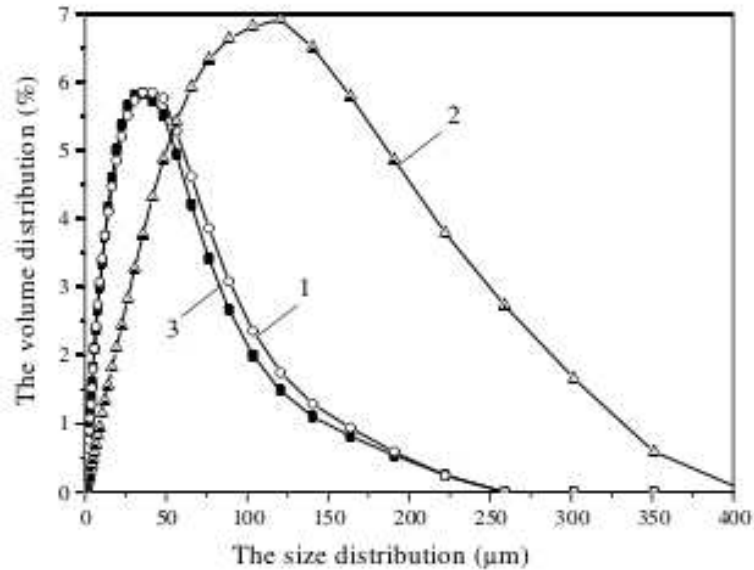


Fig.3. Size distribution of the pulverized coal particles. 1, coal A; 2, coal B; 3, coal C.

by the eight detectors were combined into one video signal which was converted into a digital, color image in a computer. A software developed by the authors was used to process flame images and to calculate the flame emissive and radioactive properties at four layers in the furnace. As shown in Fig. 3a, twelve image detectors were mounted in boiler B (a 1025 t/h boiler furnace in a 300 MW power generation unit) and the flame emissive and radioactive properties at six layers were calculated. Also as shown in Fig. 3b, four image detectors were mounted in a cross-section of furnace in boiler C (a 1025 t/h boiler in another 300 MW power generation unit) and the flame emissive and radioactive properties in the cross-section were measured. More description about the three boilers and the experimental set-ups can be found in [11,12]. Three different types of coal were fired in these three boilers, in which one was a high-volatile bituminous coal (coal B in boiler B), one a low-volatile anthracite coal (coal A in boiler A), and the third a low-volatile anthracite coal (coal C in boiler C). Table 2 shows the composition of the coals. The particle size distributions of three pulverized coals were given in Fig. 3.

Result and Analysis

the flame emissive. Many flame images were captured during the experiments. A group of representative flame images captured from boilers A, B, and C under three different loads were shown in Figs. 5–7, respectively. The emissive and temperature at different layers of the furnaces in the three boilers were shown in Tables 3–5, which are calculated from the flame images in Figs. 5–7, respectively. The measured data of each layer was the average of the data from all of image pixels in the flame images captured in the same layer. Because the flame emissive was only due to the particulate medium, it was less than the total flame emissive which includes the particulate radiation and the infrared radiation by the gaseous medium. The experimental results were analyzed as below.

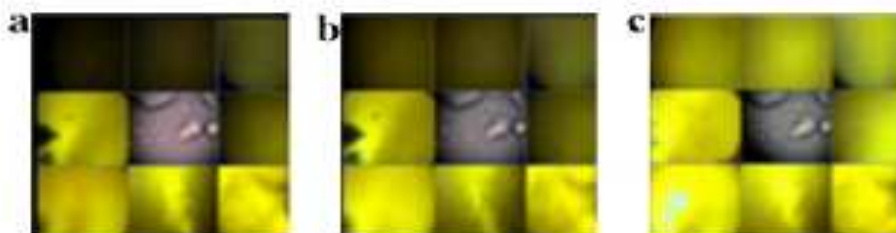


Fig.5. A group of flame images captured from boiler A under three different loads. (a)175MW. (b)190MW.(c)200MW

With the increase of load, the flame emissive of each layer also increased. As the load increased, more fuels were fed into the furnace, so the concentration of suspended particles in the furnace increased, which enhanced the radiation of the flame. Along the height of the furnace, the maximum flame emissive occurred within the upper half of the burner zone (layer 3 in boiler A, and layer 4 in boiler B) and the second was in the lower half of the burner zone (layer 4 in boiler A, and layer 5 in boiler B). In the burner zone, the concentration of particles in the flue gas was the highest.

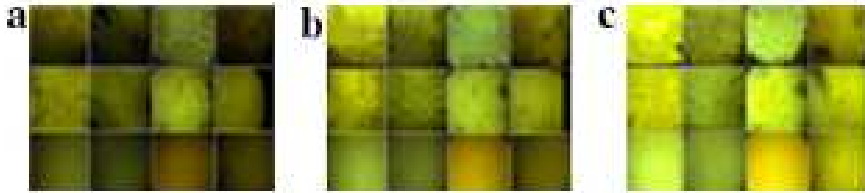


Fig.6.A group of flame images captured from boiler B under three different loads. (a)125MW. (b)250MW.(c)300MW

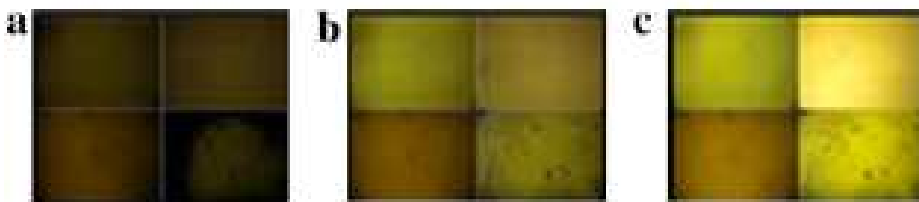


Fig.7.A group of flame images captured from boiler C under three different loads. (a)210MW. (b)245MW.(c)290MW

Table 3 The emissive and temperature in boiler A calculated from Fig.5.

	175 MW		190 MW		200 MW	
	ϵ	T (K)	ϵ	T (K)	ϵ	T (K)
Layer 1	0.251	1291	0.331	1370	0.391	1415
Layer 2	0.336	1388	0.368	1422	0.430	1474
Layer 3	0.460	1463	0.497	1483	0.529	1529
Layer 4	0.414	1425	0.451	1456	0.487	1502

Table 4 The emissive and temperature in boiler B calculated from Fig.6.

	215 MW		250 MW		300 MW	
	ϵ	T (K)	ϵ	T (K)	ϵ	T (K)
Layer 1	0.223	1322	0.268	1381	0.273	1472
Layer 2	0.254	1407	0.317	1487	0.311	1569
Layer 3	0.350	1453	0.367	1560	0.372	1671
Layer 4	0.451	1539	0.495	1682	0.550	1781
Layer 5	0.405	1518	0.479	1617	0.520	1699
Layer 6	0.377	1491	0.429	1561	0.485	1612

Table 5 The emissive and temperature in boiler C calculated from Fig.7.

	210 MW		245 MW		290 MW	
	ϵ	T (K)	ϵ	T (K)	ϵ	T (K)
Layer	0.294	1250	0.377	1318	0.459	1432

Above the burner zone, the flame emissive decreased with the increase of the height of furnace. This was because that the degree of burn-out of coal increases, while the number density of the coal and char particles decreased. The lowest flame emissive in the outlet of furnace (layer 1 in boilers A and B) was a consequence of lowest concentrations of char and the residual ash.

From comparison between the flame emissive of boiler A and B under their rated loads, an interesting phenomenon was found. At the highest layer near the outlet of the furnace, the flame emissive of boiler B was 0.273 and lower than 0.391 for boiler A, since the concentration of ash in

flue gas of boiler B was lower than that of boiler A. However, because the soot concentration in flame is directly proportional to the concentration of volatile matter, and the volatile content in coal A was less than that in coal B, the highest flame emissive in burner zone of boiler B in layer 4, 0.550, was larger than 0.529 for boiler A in layer 3. In fact, the flame in the burner zone looked more luminous because of the contribution of soot.

Because the ash content in coal C was more than that in coal B, the flame emissive in boiler C was larger than that in boiler B at the same position (layer 2 in boiler B, and layer in 32.4 min boiler C) under the rated load. The size distribution of the pulverized coal particles is the major factor which determines the size distribution of ash and char particles. From Fig. 4 and the measured emissive, the increase of the size of ash and char particles above the burner area also led to a decrease of the flame emissive, which accorded with the experimental results in [8].

An on-line continuous monitoring was conducted. The average flame emissivities of three boiler furnaces varied with the time were averaged from all the flame images captured in the same boiler, as shown in Fig. 8, being directly proportional to the load.

The radioactive properties of particular medium

In boiler C, the cross-section (layer in 32.4 m) of furnace was discrete into 100 spatial meshes for its medium zone. The temperature distribution of the cross-section was $T(i)$, $i = 1, \dots, 100$, and the absorption coefficient j and scattering coefficient r were assumed as uniform. The radioactive intensity images and temperature images as shown in Fig. 9 were calculated from the flame images in Fig. 7. The iterative processes of the radioactive properties, as shown in Fig. 10, at load of 245 MW started from different initial values e_0 ; r_0 as $(0.05, 0.05)$, $(0.5, 0.5)$ and $(0.8, 0.8)$, and they all converged to the nearly same values. The radioactive properties of the cross-section in boiler C were shown in Table 6. Using the same method, the radioactive properties at the four layers in boiler A and the six layers in boiler B were estimated and shown in Tables 7 and 8, respectively. With the increase of load, the radioactive properties of each layer increased. Along the height of the furnace, the maximum radioactive properties appeared near the burner zone (layer 3 in boiler A, and layer 4 in boiler B). Above the burner zone, the radioactive properties decreased with the increase of the height of furnace. For the absorption coefficients of combustion medium with coal A in boiler A and with coal B in boiler B, the changing trend was similar to that for the emissive caused by the influence of soot determined by the content of volatile matter. Once the absorption and scattering coefficients are known, they can be used directly in calculation of radioactive heat transfer for combustion computation and improving the technology for in situ, multi-dimensional visualization of large-scale combustion processes in coal-fired furnaces of power plants; otherwise, it will be a complicated task to get them, possibly with serious errors.

Conclusion

This article reported the experimental investigations on measurements of the flame emissive and radioactive properties of particulate medium in three pulverized-coal-fired boiler furnaces by a novel image processing technique in the visible region. As the measurements were made in the visible part of the spectrum, the results obtained were useful for radioactive heat transfer contributed by the particulate medium. From the experiments, it was seen that the flame emissive and radioactive properties decreased when the concentration of ash in flue gas increased; in the burner zone, the increase of soot concentration in flue gas significantly enhanced the flame emissive and the absorption coefficient; and the average flame emissive changed directly proportionally to the load of the furnace.

Reference

- [1] D.K. Edwards, *Advances in Heat Transfer*, Academic Press, New York, USA, 1976, p. 115.
- [2] M.F. Modest, *Radiative Heat Transfer*, McGraw-Hill, New York, USA, 1993, p. 323.
- [3] T.F. Wall, S.P. Bhattacharya, D.K. Zhang, R.P. Gupta, X. He, *Prog. Energy Combust. Sci.* 19 (1993) 487–504.
- [4] K.H. Im, R.K. Ahluwalia, *Int. J. Heat Mass Transfer* 36 (2) (1993) 293–302.
- [5] C. Kim, N. Lior, *Fuel* 74 (12) (1995) 1891–1902.
- [6] P.R. Solomon, R.M. Carangelo, P.E. Best, J.R. Markham, D.G. Hamblen, *Proc. Combust. Inst.* 21(1986) 437–446.
- [7] S.P. Bhattacharya, T.F. Wall, *Fuel* 78 (1999) 511–519.
- [8] A.G. Blokh, *Heat transfer in steam boiler furnaces*, Hemisphere, Washington, USA, 1987, p. 111.
- [9] M. Shimoda, A. Sugano, T. Kimura, Y. Watanabe, K. Ishiyama, *IEEE Trans. Energy Conversion* 5(1990) 640–645.
- [10] Y. Huang, Y. Yan, G. Riley, *Measurement* 28(2000) 175–183.
- [11] H.C. Zhou, C. Lou, Q. Cheng, *Proc. Combust. Inst.* 30 (2005) 1699–1706.
- [12] C. Lou, H.C. Zhou, *Combust. Flame* 143 (2005) 97–105.
- [13] H.C. Zhou, S.D. Han, F. Sheng, C.G. Zheng, *J. Quant. Spectrosc. Radiative Transfer* 72 (2002) 361–383.
- [14] H.C. Zhou, Y.B. Hou, D.L. Chen, C.G. Zheng, *J. Quant. Spectrosc. Radiative Transfer* 74 (2002) 605–620.
- [15] H.C. Zhou, S.D. Han, *Int. J. Heat Mass Transfer* 46 (2003) 2645–2653.
- [16] B.C. Young, D.P. McCollor, B.J. Weber, M.L. Jones, *Fuel* 67 (1988) 40–44.
- [17] H.C. Zhou, D.L. Chen, Q. Cheng, *J. Quant. Spec-trosc. Radiative Transfer* 83 (3–4) (2004) 459–481. [18] H.C. Zhou, S.D. Han, C. Lou, H. Liu, *Numerical Heat Transfer: Fundam.* 42 (3) (2002) 243–258.

Study on Influence Factors of NMR T2 Spectrum Inversion

LI Peng-ju, CHEN Hong-an, LUAN Zhao-yang and GU Yu-feng

Geoscience College, Northeast Petroleum University, Daqing 163318, China
leepjdqpi@126.com

Keywords: NMR; T2 spectrum; Inversion; Influence factors

Abstract. It is essential to investigate influence factors of inversion for improving inversion quality. Firstly to classify the influencing factors, then to make numerical experiment for each influence factor using the forward and inversion simulation technology. The results show that the collection parameters and quality of echoes have the great influence on the inversion quality, and the assigned parameters of T2 spectrum inversion have little influence. Hence, optimizing the parameter of echo collection can improve the T2 spectrum inversion quality and application effect of NMR. As for the assigned parameters, they could be selected flexibly according to the concrete conditions.

Introduction

NMR logging is very important and particular in petroleum exploration and development^[1-4]. However, the original data of the NMR logging are echo trains, the porosity, bound water, moving fluid, the type of fluid and so on, are all included in the echo trains. Hence T2 spectrum should be inverted from echo trains before extracting the above features of reservoir rock. It can be seen that the quality of T2 spectrum inversion determines the application effect of NMR. Therefore, the research of the influencing factors of T2 spectrum inversion can be considered as building a solid base for improving the geological application effect of NMR.

To classify the influencing factors

Except for the influence of the inversion method itself, the effect of NMR T2 spectrum inversion of pore media is affected and controlled by various factors. It includes as follows: Firstly, the collection parameters and quality of echoes, mainly containing echo numbers, echo spacing and SNR; secondly, the assigned parameter of T2 spectrum inversion, mainly including numbers and range of T2 value and distribution type.

Influence of the parameters and quality of echo collection

Influence of echo spacing. Echo spacing is an important controllable parameter of echo data acquisition, and it has great affect on inversion effect. Take the bimodal spectrum for example, when providing the result of the numerical experiment of inversion effect which echo spacing influences on, the simulated results of unimodal spectrum and trimodal spectrum are similar.

In the case that echo numbers is 1024, and SNR equals to 30, it can obtain a series of echo trains of which the echo spacing is during 0.2 to 1.2ms by forward technique. Then it adopts the cutoff method of M-P Generalized Inverse^[5] to invert T2 spectrum. The result contrasting with the true spectrum can be seen in fig. 1. It shows that the short components inverted of small echo spacing relatively better than the long ones, and the long components inverted of the large echo spacing relatively better than the short ones. When echo spacing is moderate, the effect of T2 spectrum inversion will be best.

So during the data collection process of the core NMR experiment and NMR logging, it should select suitable echo spacing according to the practical problems. If we want to achieve the accurate volume of bound fluid, it should choose small echo spacing so that the short relaxation components inverted correctly. If we want to obtain the right volume of moving fluid, it should select big echo spacing so that the long relaxation components inverted accurately.

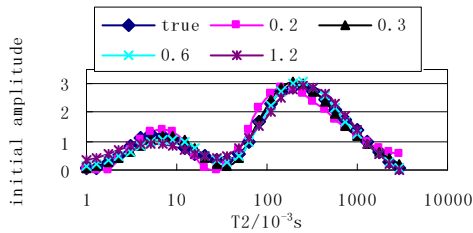


Fig.1 Comparison between the inversion results and true spectrum of different echo spacing

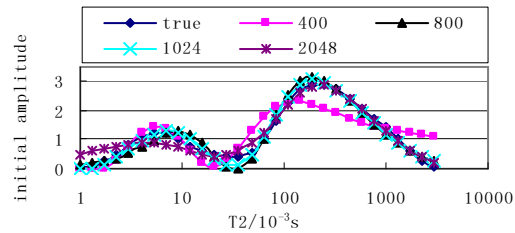


Fig.2 Comparison between the inversion results and true spectrum of different echo numbers

Influence of echo numbers. Similarly, echo numbers which influences on the inversion effect is an important parameter of echo collection. Take the bimodal spectrum for example as follows when providing the numerical experimental results of inversion effect which echo numbers influence on, the simulated results of unimodal or trimodal spectrum are similar to bimodal one.

Suppose that echo spacing is 0.3ms and SNR equals to 30, it can obtain a series of echo trains that echo numbers is 400~2048 by forward technique. Then we invert T2 spectrum, and the comparison between inversion results and true spectrum can be seen in fig.2. It shows that the long components of more echo numbers can be inverted well, and the short components of few echo numbers can be inverted well. When echo numbers is moderate, the effect of T2 spectrum inversion will be best.

Therefore, it should decrease echo numbers when measuring the volume of bound fluid, it not only saves collecting time of echoes, but also makes short relaxation components correct. When measuring volume of moving fluid, it may increase echo numbers properly to make the long relaxation components correct if not considering the cost of time.

Influence of SNR. Fig.3 shows the comparison between T2 spectrum of inversion and the true spectrum, when the number of echo is 400, echo spacing is 0.9, 1.2, 2.4 or 3.6(ms) respectively, and SNR is 100, 50, 30, 20, 10, 5 and 0. Fig.4 shows the comparison between T2 spectrum of inversion and the true spectrum, when echo spacing is 0.3ms, the number of echo is 400, 800, 1024 and 2048 respectively, and SNR is 100, 50, 30, 20, 10, 5 and 0.

It can be seen that the higher SNR is, the better the effect is. The inversion effect of low SNR is also restricted by echo spacing and echo numbers. In other words, it controlled by the nature of coefficient matrix. If echo spacing and echo numbers is moderate, the morbidity level of coefficient matrix will alleviate. In this term, the effect of inversion is still well even if SNR is very low(SNR is 5).

Fig.3 shows the simulating practical logging situation of the common echo numbers and echo spacing. Fig.4 shows the simulating situation of laboratory core measurement. Supposing echo spacing is 0.9ms and 1.2ms, We can see from Fig.3, when the collection number of echo is 400 in logging, the quality of inversion is acceptable even if SNR is 5, especially to long relaxation components. From Fig.4, using echo spacing=0.3ms in core measurement, the inversion effect is still well when SNR=5 if the number of echo reaches 4096.

Due to the consideration of the logging velocity, the number of echo usually adopts 400 or 500 when logging. Therefore, echo spacing of 0.9ms or 1.2ms has better effect on low SNR data when inverting. Because of measuring clay-bound water, the core measurement in the laboratory usually adopts echo spacing of 0.2ms or 0.3ms. Hence, in order that the inversion results are correct and reliable, it should increase echo numbers for low SNR data.

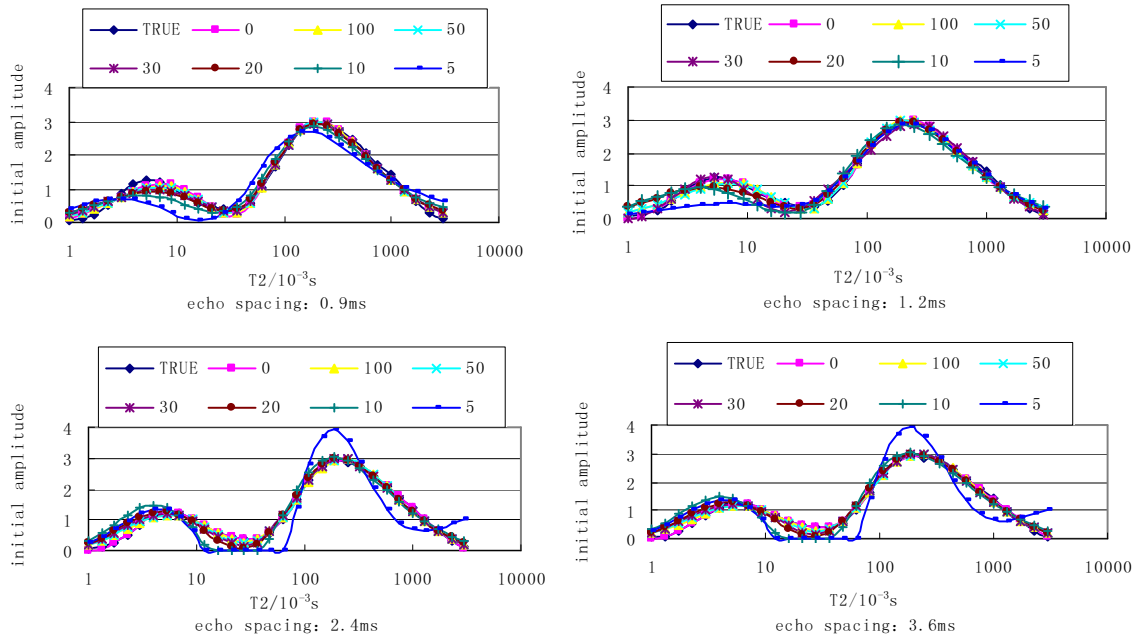


Fig.3 Influence of SNR on the inversion effect of bimodal spectrum (echo numbers=400)

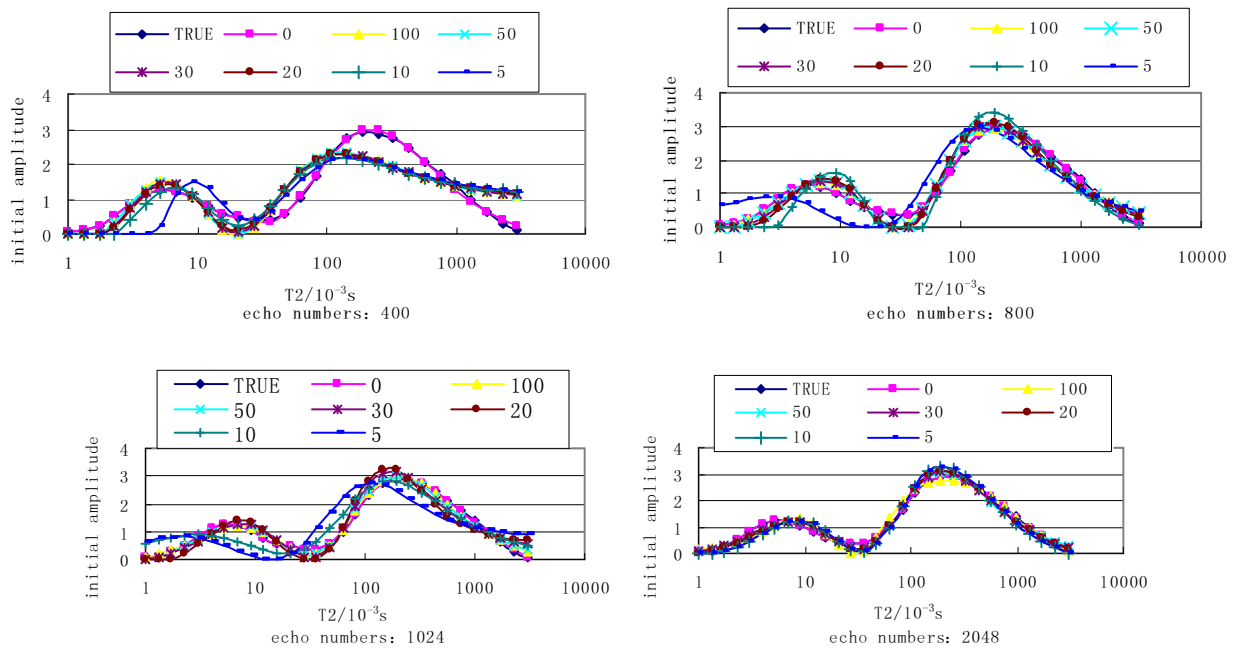


Fig.4 Influence of SNR on the inversion effect of bimodal spectrum (echo spacing=0.3ms)

Influence of the assigned parameter of T2 spectrum inversion

Influence of numbers of T2 value. Supposing the distribution range of true spectrum is 1~3000ms and the numbers of T2 value is 30. The range of T2 value does not change. If numbers of T2 value is 64 or 13 and SNR is always 30 when inverting, the comparison between inversion results and true spectrum can be seen in Fig.5 and Fig.6.

Both Fig.5 and Fig.6 adopt the contrast of integral T2 spectrum, that is to say, it regards the initial amplitude's accumulation which less than certain T2 value as the amplitude of the T2 value.

From Fig.5 and Fig.6, the inversion results of the integral T2 spectrum accord with true spectrum well. Therefore, although the numbers of T2 value are unknown in advance in T2 spectrum inversion of core measurement and of logging (in fact, T2 spectrum is continuous, and the numbers of T2 value is infinite, it just is discretized when inverting), spotting numbers can have a big room to choose as long as the inversion equations is not morbid excessively.

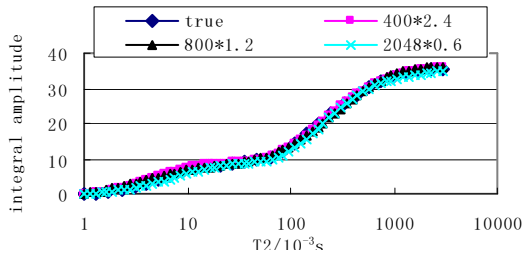


Fig.5 Comparison between true spectrum of 30 values and inversion spectrum of 64 values

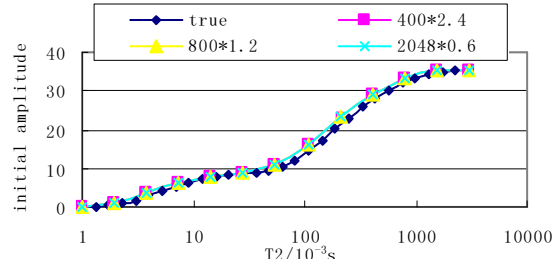


Fig.6 Comparison between true spectrum of 30 values and inversion spectrum of 13 values

Influence of range of T2 value. Supposing the range of true spectrum is 1~3000ms. Fig.7 shows the comparison between inversion spectrum and true spectrum when the range of inversion spectrum is different from true spectrum. It can be seen that when the range of T2 value is less than that of true spectrum, the redundant components of true spectrum are come down to the least or the biggest components of inversion spectrum. When the range of T2 value is larger than that of true spectrum, the inversion components excluded in true spectrum approaches to 0, and inversion spectrum corresponds to true spectrum very well.

Thus the increase of range of T2 value has little influence on the inversion effect, and the decrease of the range of T2 value just influences on the fine degree of inversion spectrum. In inversion of core measurement and logging, it cannot make sure of the range of T2 spectrum in advance (the range may be too large), this moment choosing the range of T2 value properly has less influence on inversion.

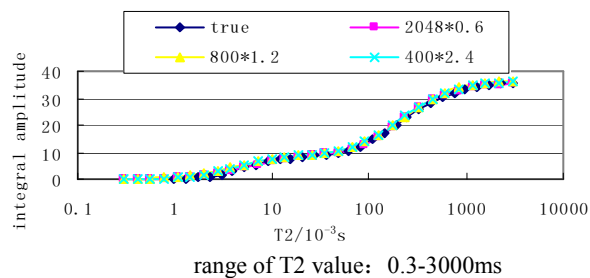
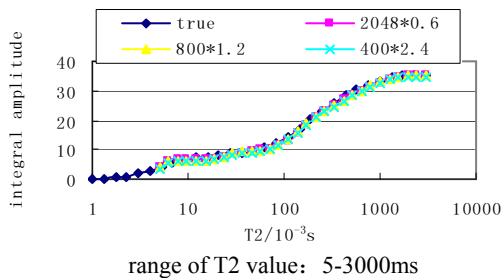


Fig.7 Comparison between inversion spectrum and true spectrum in different range of T2 value

Conclusions

- (1) The acquisition parameters and quality of echoes, have great influence on inversion quality of T2 spectrum while the assigned parameters, have little influence. Except for improving echoes SNR, it should optimize the acquisition parameters to improve application effect of NMR data. As for the assigned parameters of inversion, it can be chosen flexibly according to the specific problems.
- (2) In the process of data acquisition, if the accurate volume of bound fluid is wanted, we should choose small echo spacing and less echo numbers so that short components is correct. If we want to get precise volume of moving fluid, the big echo spacing and more echo numbers should be chosen to make long components correct.
- (3) In T2 spectrum inversion of core measurement and logging, the range of T2 value chosen properly, have little influence on inversion effect, and numbers of T2 value have more selective room.

Acknowledgements

This work is supported by scientific and technological research project “NMR reservoir fluid identification and evaluation methods” (12511019) Funded By Education Department of Heilongjiang Province, China

References

- [1] Sun B Q. NMR Inversion Methods For Fluid Typing, SPWLA 44th Annual Logging Symposium, June 22-25[C], 2003.
- [2] Freedman, R., Heaton, N., and Flaum, M.. Field Applications of a New Nuclear Magnetic Resonance Fluid Characterization Method[R]. SPE71713, 2002: 445-463.
- [3] Freedman, R. et al.. A New NMR Method of Fluid Characterization in Reservoir Rocks: Experimental Confirmation and Simulation Results, SPE75325, 2001: 452-464.
- [4] Coates G R, Xiao L Z, Prammer M G. NMR logging principles & applications[M].Huston: Sea Gulf Press,1999.
- [5] LI P J, et al. Study on the Inversion of NMR T2 Spectrum with M-P Generalized Inversion[J].Journal of Jilin University(Earth Science Edition), 2011, 41 (2) : 579-585.

Analysis of High-Speed Energy- Storing Flywheel Rotor

ZHANG Xiuhua^{1, a}, ZHAO Xuefeng^{2, b}, ZHANG Xinglei^{3, c}

^{1, 2, 3} School of Mechanical Engineering, Guizhou University, Guiyang, 550025 China

^azhangxiuhua760924@163. Com, ^bzxf801112@163.com, ^czhangxingfulove@163.com

Keywords: Flywheel, Rotor, Energy-Storing Density, Fit

Abstract. Appropriate rotor material and reasonable structure should be used for increase energy-storing density of flywheel. Theoretical analysis and design to high-speed energy-storing flywheel rotor with maximum energy-storing density is studied in the paper. The ratio of inner diameter and outer diameter and structure dimensions of a given condition flywheel rim is obtained by calculating. And the interference fit of rim/hub of the flywheel is analyzed with finite element software. One efficient and reliable calculating foundation and analysis method for the structure design of the flywheel rotor is provided.

Introduction

Flywheel Energy- Storing system has been applying to Aerospace industry, Electric power pitch peak, Uninterrupted power system, Automobile energy supply, military and so on, due to the system possess superiority of huge energy-storing density, high- efficiency, high-power, high Cost Performance ,non-pollution, continuous working, long-life and so on, since the concept of Flywheel Energy- Storing system was given in 1973 by American scientist Dr. Richard. [1] in recent years, it having good apply prospect and has been turning into a researched and developed energy-storing system by many countries in the world with developing sharply of magnetic suspension supporting technology, composite material, power electronics technology and so on.

In the paper, the structure design to energy-storing flywheel rotor with maximum energy-storing density is analyzed detailedly. A structure dimensions given condition flywheel rotor rim is obtained by calculating, And the interference fit of rim/hub of the flywheel is analyzed with finite element software. One efficient and reliable calculating foundation and analysis method for the structure design of the flywheel rotor and the interference fit of rim/hub is provided.

Energy-Storing Principle of Energy-Storing Flywheel

The flywheel rotate with high speed after the electromotor/ generator driven by the power electron convertor, electrical energy is turned into mechanical energy and stored. The Electromotor/ generator maintains a constant speed during the period, the flywheel decelerate when the electromotor/ generator receive a control required release energy, then the electromotor/ generator supply to the loads via the convertor, then the stored kinetic energy is turned into the electric energy . The flywheel system realizes the input, store and output to kinetic energy [2].

Theoretical Design of Flywheel Rotor

Now, the rim design layout involves multilayer and monolayer, using monolayer form here for analysis convenience.

Flywheel rotates with high speed around the central shaft, Its biggest storage energy E is rotating kinetic energy. The unit mass storage energy is storage density e , it is a important index of flywheel energy-storing.

$$E = \frac{1}{2} J \omega^2 \quad (1)$$

$$e = \frac{E}{m} \quad (2)$$

The hollow cylindrical flywheel axial rotational inertia and the quality:

$$J = \frac{1}{2} m(R^2 + r^2) \quad (3)$$

$$m = \pi h \rho (R^2 - r^2) \quad (4)$$

Substituting Eq.(3)(4) into Eq.(1):

$$E = \frac{1}{4} \rho V_f \cdot v_R^2 \cdot (1 - \lambda^4) \quad (5)$$

Where J is the rotational inertia of the flywheel(kg.m²), ω is the rotational angular velocity of the flywheel(rad/s), $V_f = \pi h R^2$ is the outer outline volume of the flywheel(m³), ρ is the density of the cylinder material(kg/m³), v_R is the rotational linear velocity of the flywheel rim (m/s), $\lambda = r/R$ is the ratio of inner diameter and outer diameter of the flywheel and h is the length of the flywheel(m).

According to the stress analysis of the rotational flywheel [3]:

The maximal circumferential stress is

$$\sigma_{\tau \max} = \frac{1}{4} \rho [3 + \mu + (1 - \mu)\lambda^2] \cdot v_R^2 \quad (6)$$

The maximal radial stress is

$$\sigma_{r \max} = \frac{1}{8} \rho [(3 + \mu) \cdot (1 - \lambda)^2] \cdot v_R^2 \quad (7)$$

Under the strength restraint condition

$$\sigma_{\tau \max} \leq [\sigma_{\tau}] \quad \text{And} \quad \sigma_{r \max} \leq [\sigma_r]$$

Obtain:

$$v_{R \max}^2 = \min \left[\frac{4[\sigma_r]}{\rho (3 + \mu) \cdot (1 - \lambda)^2}, \frac{[\sigma_{\tau}]}{\rho [3 + \mu + (1 - \mu)\lambda^2]} \right] \quad (8)$$

Where $[\sigma_r]$ is the radial strength limit of the flywheel material; $[\sigma_{\tau}]$ is the circumferential strength limit of the flywheel material; μ is the Poisson's ratio.

When anisotropy material is used for the flywheel material (for example carbon fiber), is making two formulas equal in Eq. (8).

$$\frac{2[\sigma_r]}{(3 + \mu) \cdot (1 - \lambda)^2} = \frac{[\sigma_{\tau}]}{3 + \mu + (1 - \mu)\lambda^2}$$

Obtain:

$$\lambda = \lambda_1 = \frac{b - \sqrt{b^2 - 4ac}}{2a} \quad (9)$$

Where $a = [\sigma_r](3 + \mu) - 2[\sigma_r](1 - \mu)$;

$b = 2(3 + \mu)[\sigma_r]$;

$c = (3 + \mu)([\sigma_r] - 2[\sigma_r])$;

λ_1 is λ value when v_{max} equal under the restraint condition of $[\sigma_r]$ and $[\sigma_r]$.

Considering these factors, when $\lambda = \lambda_1$, the character of the radial strength limit and the circumferential strength limit of the flywheel material can be utilized fully, and the energy-storing density of the flywheel can achieve maximum [4].

The Design and Analysis of the Case

Designing a flywheel in the paper, its working Rotating speed is 12000rpm, its maximum energy-storing value is 2MJ. Carbon fiber with huge energy-storing density and high σ/ρ value is used for the flywheel rim material, and the structural steel is used for the flywheel hub material, these materials parameters are showed in table 1.

Table1 The material parameters of rim/hub of the flywheel

material	$[\sigma_r]$ (MPa)	$[\sigma_r]$ (MPa)	E_θ (GPa)	E_r (GPa)	ρ (Kg/m ³)	μ
rim T 700/E-765	2550	20	129	10	1500	0.3
hub structural steel	590	590	200	200	7850	0.33

The interference fit mode of connection is used for rim/hub of the flywheel for ensuring the Stability and reliability when the flywheel rotates with high speed. Then it is very important to select reasonably the fit value to whole system. The value of 0.3mm is used for the fit value of the rim/hub of the flywheel according to the theoretical calculation in the paper.

According to Eq. (9):

$$\lambda_1 = \frac{b - \sqrt{b^2 - 4ac}}{2a} = 0.8$$

According to the actual working condition of the flywheel and the foregoing design method the value of the outer diameter of the flywheel rim is $R = 0.1 m$, the value of the inner diameter of the flywheel rim is $r = 0.08 m$, the value of the length of the flywheel $h = 0.35 m$, The value of the outer diameter of the flywheel hub is $R_1 = 0.08 m$ and the value of the inner diameter of the flywheel hub is $r_1 = 0.04 m$.

The 3D simplified model of the flywheel rotor is established in the Solidworks software, the fit mode of the rim/hub of the flywheel is interference fit. The model is imported into the Ansys software, the cloud picture by simulation calculation are showed in fig. 1 ~ fig. 4.

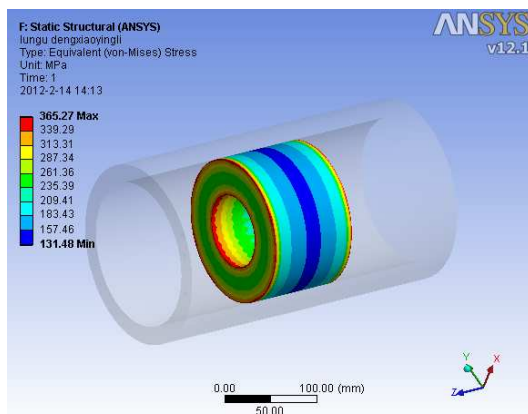


Fig. 1 Equivalent stress of the hub in 12000rpm

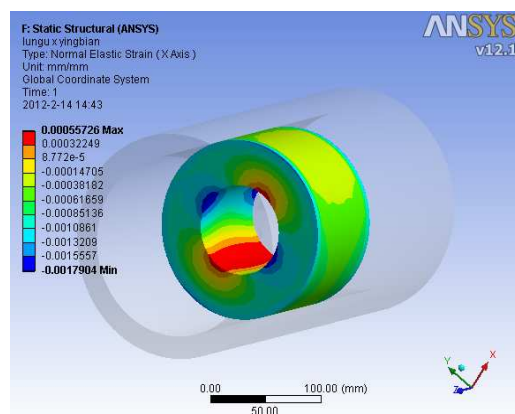


Fig. 2 Strain of the hub in 12000rpm

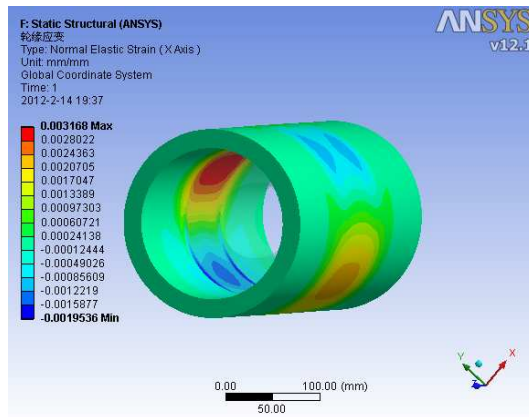


Fig .3 Strain of the rim in 12000rpm

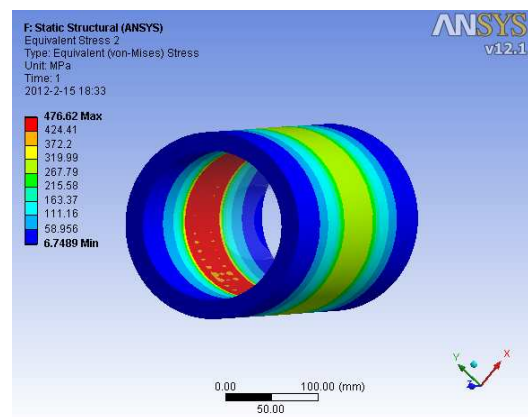


Fig .4 Equivalent stress of the rim in 12000rpm

Table2 Equivalent stress/ Strain of the rim/hub in 12000rpm

	Equivalent stress(Mpa)	Strain
rim	6.7489~476.62	-0.0019536~0.003168
hub	131.48~365.27	-0.0017904~0.00055726

The maximum equivalent stress of the hub occurs in the two ends known from fig.1, and the value is in the allowable stress range. The maximum strain of the rim/hub occur between their contact location known from fig.2 and fig.3, the rim and the hub keep interference fit mode known by theoretical calculation, the conclusions prove the design is reasonable.

Conclusion

This paper determines the structure of the high-speed energy-storing flywheel rotor through the theoretical analysis and design of energy-storing flywheel. On this basis the interference fit of rim/hub of the flywheel is analyzed with finite element ANSYS workbench software, it is concluded that the hub /rim of the flywheel is operated in a safe and stable state in set speed and amount of interference, which proves the design is reasonable. The paper provides an effective and reliable calculating basis and analytical methods for the structure design of the flywheel rotor.

Acknowledgements

The work presented in this paper was supported by International Science & Technology Corporation Subject of China (2010DFB62910).

References:

- [1] Jiang shuyun, Wei Haigang, Shen zupei, The Current Development of the Flywheel Energy Storage Reaserch [J]. Solar, 2000,21(3):424—433
- [2] Zhao Han, Yang Zhitie. The Preliminary Exploration of the Flywheel Energy-storage Device Design[J]. Solar, 2002,23(4):493—497
- [3] Zhang Tiezhu, Luo Bangjie etc. The Design and Analysis of high-speed Energy-sorage Flywheel[J] Jornal of Mechanical Engineering, 1993,29(1):24—29.
- [4] Bai Yue etc. Flywheel Rotor Design with the Composite Material [J]. Opticas, Precision Engineering, 2007,15(6):852—857.
- [5] ARNOLD S M.SALEEB A F, AL-ZOUB N R. De formation and life analysis of composite flywheel disk and multi-disk systems[R]. NANA/TM-2001-210578.

-
- [6] D.W.Swett, F.G.Blanché IV. Flywheel Charging Module for Energy Storage Used in Electromagnetic Aircraft Launch System. IEEE Transactions on Magnetics,2005,41(1): 525~528.
- [7] Li Donglin, Wang Qiang, Interference Fit Analysis Based on Exposure to Non-linear Theory of High-speed Rotor [J]. Electrical Engineering Technology.38 (08).97-99
- [8] Zhou Hequn, Wang Zhonghou, Xie Yunbo, Zhao Dongshen, Drive Shaft Based on FEA Precision Analysis of Interference Fits[J] Mechanical Transmissio[J].2010.34(1).60-62

Leakage Failure and Principle of Underground Low Voltage Grid

Junmei Geng^{1, a}, Chunguang Li^{1, b}

¹Department of Electrical Engineering, Jiyuan Vocational and Technical College, Henan Jiyuan
459000, China

^agjm72@126.com, ^blcg3396@126.com

Keywords: Leakage, Zero-Sequence Voltage, Zero Sequence Current, Additional DC Power Supply

Abstract. To describe the leakage protection of underground low voltage grid are based on zero-sequence voltage and zero sequence power direction of the current leakage protection and earth leakage protection based on the additional DC power supply two kinds. The paper gives the theoretical analysis of these two kinds of leakage, and unified the three-phase neutral point grounding system and by arc suppression coil grounding the under compensation leakage detection program, that provides a new approach for underground leakage detection.

Introduction

The leakage is underground low voltage power supply system is the most common faults in more than 80% of the total fault. Sampling is difficult to distinguish due to the leakage signal is weak, but also to the supply system neutral grounding, it is difficult to study the leakage, that is an important issue of the underground power supply protection.

At present, underground low-voltage switch used as a master switch that is often used additional DC power supply or additional high-frequency AC power leakage detection, the two principles are the same. Due to the difficulty of the two different, the more additional DC power supply, leakage detection program. That often used as a sub-switch use when leakage detection based on the zero-sequence current of the current leakage detection or power direction based on the zero-sequence voltage and zero-sequence current leakage detection, the majority of power direction leakage detection [1].

The Concept of Zero-Sequence Current and Zero Voltage

Chinese mine supply system neutral point ungrounded systems, the neutral point, a small current (or resistance) through the arc suppression coil grounding system, grounding system. Now isolated neutral system to illustrate the concept of zero-sequence current and zero voltage.

Because of white resistance and discuss the problems unrelated to the three-phase grid-to-ground model in Figure 1. Which the grid every relative impedance that can be seen to focus on the parameters of the capacitor and resistor in parallel, that is the Z represents. The three-phase voltage respectively shows \dot{V}_A , \dot{V}_B and \dot{V}_C , three relatively current with \dot{I}_{gA} , \dot{I}_{gB} and \dot{I}_{gC} , the neutral point voltage with the zero-sequence voltage \dot{V}_0 and zero-sequence current \dot{I}_g . If you do not access the dashed box part, the circuit symmetry, (\dot{V}_A , \dot{V}_B and \dot{V}_C) and (\dot{I}_{gA} , \dot{I}_{gB} and \dot{I}_{gC}) are symmetric vector. It is easy to know that the zero-sequence voltage is $\dot{V}_0 = 0$, the zero-sequence current is $\dot{I}_g = 0$.

If access dashed box part is the principle of single-phase leakage map, then (\dot{V}_A , \dot{V}_B and \dot{V}_C) and (\dot{I}_{gA} , \dot{I}_{gB} and \dot{I}_{gC}) are no longer symmetric vector. According to the method of symmetrical components, a set of asymmetric phasor can be broken down into three groups of components: zero-sequence component, the order weight and reverse component.

For example, three-phase grid-to-ground voltage can be used (1) shows.

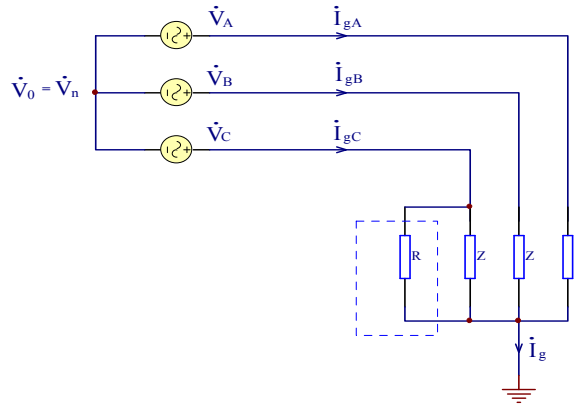


Fig.1. Neutral point ungrounded three-phase power grid to model

$$\begin{cases} \dot{V}_A = \dot{V}_{A0} + \dot{V}_{A1} + \dot{V}_{A2} \\ \dot{V}_B = \dot{V}_{B0} + \dot{V}_{B1} + \dot{V}_{B2} \\ \dot{V}_C = \dot{V}_{C0} + \dot{V}_{C1} + \dot{V}_{C2} \end{cases} \quad (1)$$

Where $\dot{V}_{A1}, \dot{V}_{B1}$ and \dot{V}_{C1} are symmetrical components, a difference of interval is 120° , Where $\dot{V}_{A2}, \dot{V}_{B2}$ and \dot{V}_{C2} are also the symmetrical components, but the difference between the interval -120° , Where $\dot{V}_{A0}, \dot{V}_{B0}$ and \dot{V}_{C0} are equal to the same phase and modulus values, $\dot{V}_{A1}, \dot{V}_{B1}$ and \dot{V}_{C1} are the order of components, $\dot{V}_{A2}, \dot{V}_{B2}$ and \dot{V}_{C2} are the reverse component, $\dot{V}_{A0}, \dot{V}_{B0}$ and \dot{V}_{C0} are the zero sequence component.

It is easy to know the synthesis of symmetrical components to 0. Figure 1 and Equation 1 can get the zero-sequence voltage $\dot{V}_O = \dot{V}_N = \dot{V}_{A0} = \dot{V}_{B0} = \dot{V}_{C0} \neq 0$; The zero sequence current $\dot{I}_g = \dot{I}_{gA} + \dot{I}_{gB} + \dot{I}_{gC} = \dot{I}_{gA0} + \dot{I}_{gB0} + \dot{I}_{gC0}$, according to KCL $\dot{I}_g = 0$, obviously can not detect zero-sequence current grid to detect leakage. This is the underground leakage detection when only a slip or as a master switch can not be used the reason of the current leakage detection or power direction leakage detection, most of the additional DC power leakage detection.

The Protection of Zero-sequence Current-leakage

The slip grid in the single-phase leakage schematic as shown in Fig. 2

By the node voltage method can be deduced

$$\dot{V}_n = -\dot{V}_C \cdot \frac{Z}{3R+Z} = -\dot{V}_C \cdot \frac{R // (Z/3)}{R} \quad (2)$$

Where (2): the occurrence of leakage constant leakage resistance the smaller the higher voltage of the grid neutral point.

For non-fault slip is $\dot{V}_0 = \dot{V}_n = \dot{V}_{A0} + \dot{V}_{B0} + \dot{V}_{C0}$, so zero-sequence current is

$$\dot{I}_{gi} = \frac{+\dot{V}_n}{Z_i} \times 3 \quad (3)$$

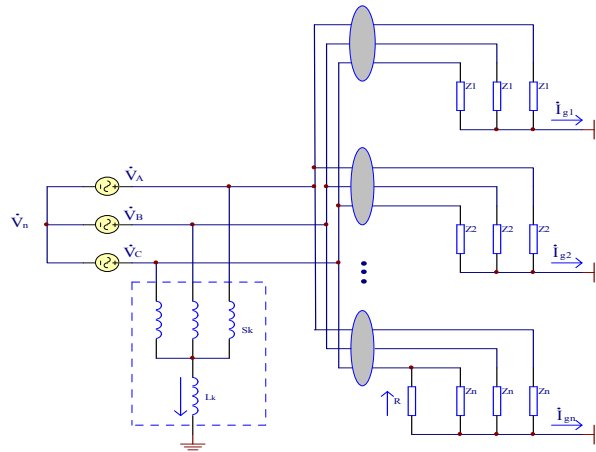


Fig. 2 Schematic of the neutral point grounding and the multi-slip grid single-phase leakage Therefore, according to KCL is easy to know that the fault slips

$$I_{gn} = -\sum_{i=1}^{n-1} I_{gi} = -(I_{g1} + I_{g2} + \dots + I_{g(n-1)}) = 3 \left(\frac{\dot{V}_n}{Z_1} + \frac{\dot{V}_n}{Z_2} + \dots + \frac{\dot{V}_n}{Z_{n-1}} \right) = -3\dot{V}_n \left(\frac{1}{Z} - \frac{1}{Z_n} \right) \tag{4}$$

Where $Z = Z_1 \parallel Z_2 \parallel \dots \parallel Z_n$.

Form formula (4) and Figure 2 is easy to know the fault slip zero-sequence current zero-sequence current in the rest of the non-fault slip. Neutral point ungrounded radial grid, if a slip occurred in the asymmetric leakage fault or personal electric shock, then all the slip road will be zero-sequence current (mainly capacitive current) flow through and flow through the zero-sequence current of fault slip is a non-fault slip zero-sequence current. Non-fault slips only flow through the slip zero-sequence current, its value is in general less than the former. The size of the zero sequence current transformers to be installed at each branch the first side reaction of each branch of zero sequence current can be done selective leakage protection. This is the advantage of zero-sequence current amplitude of the principle of selective leakage detection[2].

The Leakage Protection of Directional Power

Capacitance of the cable to the insulation resistance is very large, grid-to-ground impedance mainly in the high voltage grid. The grid on the low-voltage grid impedance performance for parallel is capacitance and resistance. So according to formula (4) analysis of known non-fault slip zero-sequence current leads the zero-sequence voltage of 0 to 90 °; from zero-sequence voltage (3) analysis of known fault slip zero-sequence current lag of 90 ~ 180°. When a slip in the grid leakage fault occurs or personal electric shock, the amplitude of zero sequence current or zero sequence voltage to determine whether leakage occurred within the power supply unit, while taking advantage of each branch of the phase relationship to determine the fault branch Road, selective removal of the power of the fault slip, which is the zero sequence power direction leakage protection.

The Leakage Protection of Neutral Point Then the Compensation Coil

Personal electric shock current and insulation resistance and distributed capacitance related to improve the cable to the insulation resistance value can reduce the electric shock current. In fact, the longer the length of the power grid, the distributed capacitance must not be ignored. When the distributed capacitance great, when the insulation resistance increases to the contrary, caused by personal electric shock current increases, the current composition of distributed capacitance has become the main factors of personal electric shock current. Therefore, in reality, simply to improve the insulation resistance to reduce the personal electric shock current is impossible.

At present compensated neutral point ungrounded power supply grid on the distributed capacitance of the most effective measures to access leakage circuit inductor, that grid to access a three-phase power reactor S_k and zero-sequence compensation reactor, L_k is a concatenation of emotional slip in Figure 2 with the dashed box shown in part.

If C relative to N branch to leakage, Z_i slip grid phase impedance, if the coil resistance is ignored, then the i th branch grid zero sequence current

$$\dot{I}_{gi} = \frac{+\dot{V}_n}{Z_i} \times 3 = +\dot{V}_n Y_i \times 3 = +\dot{V}_n (G_i + jB_{Ci}) \times 3 \approx 3\dot{V}_n \cdot (-jB_L) \tag{5}$$

According to KCL know that the fault slip has

$$\dot{I}_{gn} = -\left(\sum_{i=1}^{n-1} \dot{I}_{gi} + \dot{I}_L\right) = -\left(3\dot{V}_n \cdot \sum_{i=1}^{n-1} (G_i + jB_{Ci}) + \dot{V}_n \cdot (-jB_L)\right) = -\dot{V}_n \cdot \left(3G_{\Sigma_{N-1}} + j(3B_{C_{\Sigma_{N-1}}} - B_L)\right) \tag{6}$$

Where $\sum_{i=1}^{n-1} (G_i + jB_{Ci}) = G_{\Sigma_{N-1}} + jB_{C_{\Sigma_{N-1}}}$.

The above analysis shows that the non-fault slip of zero sequence current in the neutral point on the compensation coil is still ahead of the zero-sequence voltage $0 \sim 90^\circ$, but the zero sequence current of fault slip is no longer necessarily lag zero sequence voltage $90^\circ \sim 180^\circ$, and may even be ahead of the zero-sequence voltage of $90^\circ \sim 180^\circ$ (over the state of compensation). Neutral point on the compensation coil, followed the traditional discriminate method to determine the fault slip, apparently unable to achieve the purpose of selective leakage protection. However, if the hardware or software will be zero-sequence voltage phase shift of 90° , and then each branch of zero sequence current phases, then the zero sequence current phases of fault slip and non-fault slip relative to the phase shift zero-sequence voltage, the leading and lagging relationships can be clearly defined. Therefore, some literature in the neutral point on the compensation coil power grid, power leakage protection is no longer applicable to the argument is incomplete [3].

The Additional DC Power Supply Detection Leakage Protection

In figure 3 that shows the DC current from the protection of the positive terminal of the DC power into the ground, the grid-to-ground insulation resistance r_1, r_2, r_3 , enter the three-phase line. By the resistance of three-phase power device $1L$, artificial neutral point N_m , zero-sequence reactance $2L$, protect the sampling resistor R_Q return negative. Three-phase reactor and zero-sequence reactance of the resistor is very small when the protection of the sampling resistor R_Q certain DC current by the grid-to-ground insulation resistance is determined. Therefore only to detect the sample size of the DC voltage signal on the resistance R_Q , you can analyze the grid on the insulation.

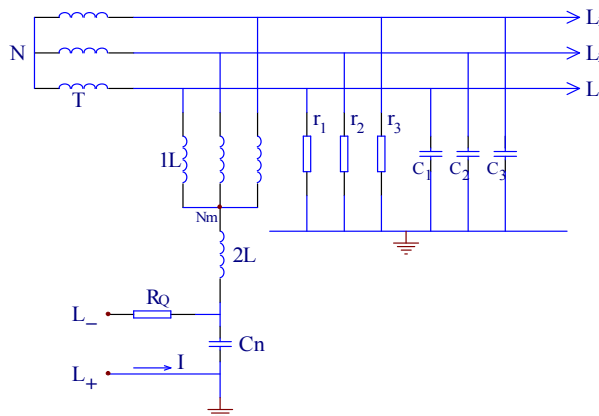


Fig. 3 Constitute a schematic diagram of additional DC power supply detection circuit

Set up the three-phase conductor to the insulation resistance and capacitance is symmetric, r and c , respectively, using the lumped parameter Z_s expressed which can be regarded as the source resistance. Touch live conductors of one phase in the human body (the men of the body resistance as R , can be regarded as an external resistor), electric shock, the current through the body, the earth, the other two relatively insulation resistance and the distributed capacitance to return to power, the other two-phase constitute a closed loop, circuit voltage for the other two-phase human touch on the phase line voltage. Ignored the influence of the capacitance, flow through the body current is

$$I = \frac{U}{R+Z_s} = \frac{U}{R+\frac{Z}{3}} \approx \frac{U}{R+\frac{r}{3}} \quad (7)$$

660V power grids, for example, the phase voltage $U = 380V$, human safe electric shock current $I \leq 30mA$, the human resistance R of about $1k$, single-phase insulation resistance $r = 35k$. This 660V power grids, each relative to the actual insulation level must be maintained at more than $35k$, and accordingly can determine the resistance of the whole single-phase leakage action is $35/3 = 11.7k\Omega$ two-phase residual operating value of $11.7 \times 2 = 23.4 k\Omega$. The rest of the voltage level and so on, as shown in Table 1.

Table 1. Leakage protection action resistance setting value $k\Omega$

Voltage (V)	Leakage types		
	Single-phase	Two-phase	Three-phase
127	1.5	3	4.5
380	3.5	7	10.5
660	11	22	33
1140	20	40	60

Conclusion

This paper to describe From a theoretical point of system analysis of asymmetric leakage of underground low voltage grid and symmetry of the electrical characteristics of the leakage fault, given the symmetry leakage insulation resistance calculation methods and results, as well as asymmetric leakage current leakage detection and power-leakage detection and correction for the calculation of the compensation coil power leakage protection, without compensation coil power leakage calculation unify, provides a theoretical basis for computer intelligent detection of leakage .

Reference

- [1] ZhangChangSen, KeXiZheng. Mine low voltage power grid leakage protection of the present situation and the development trend[J]. Coal electrical machinery, 2005 (5),p73-77
- [2] MatVeyeV M V.K ostin M K.Z hiVodernikou S, et a1. Some Results of EMC In Vestigations in Russia Substations. [J]. J CIGRE. Paris (Frace), 2002.36.103
- [3] GaoYan. WangNianBin etc. Based on the zero sequence directional power selective leakage protection system of study [J]. Science and technology of coal, 2005(11) : p43-46

Research on the High Leakage Reactance of the Superconducting Controllable Reactor

Long Wang, Kunnan Cao, Meng Song², DadaWang², Nannan Hu², Yi Zhang¹,
Li Liu³, Weidong Wang¹, Shuming Zhou³

Yunnan Power Grid Corporation of Kunming University Graduate workstation, Kun-Ming, China,
650217, kunming, China

Yunnan Electric Power Test & Research Institute (Group) Co., Ltd. Electric Power Research
Institute, 650217, Kun-Ming, China

Kunming University of Science and Technology Electric Power Engineering, 650051, Kun-Ming,
China

houdezaiwu2010@yeah.net

Keywords: Controllable Reactor; High Leakage Reactance; Power Consumption.

Abstract. High leakage reactance of superconducting controlled the working principle and structure of the reactor were introduced Description and analysis of the three modes of operation of the superconducting coil of the secondary side. Three modes of operation of the secondary winding of the two superconducting windings are open, superconducting winding short-circuit superconducting windings open circuit, two superconducting windings are short-circuit. Through the design and calculation of the characteristics of a superconducting controllable reactor three modes of operation, and prospected for high-leakage reactance of superconducting controllable reactor advantages, characteristics and development prospects.

Introduction

The reactor is an important electrical installations, widely used in power system frequency over voltage limit workers to eliminate the generator self-excitation limit operating voltage line capacitive charging power, the arc current inhibition, limiting short-circuit current peace wave. High leakage reactance of superconducting controllable reactor with the general principle of power transformers principle is similar to the two - way thyristor switch secondary superconducting control winding short circuit, the secondary superconducting winding magnetron being squeezed out, then copper coil magnetic flux loop cross-sectional area decreases, the reactor is reduced accordingly. In this paper, the working principle and the three modes of operation of high leakage reactance of the superconducting controllable reactor analysis, computational analysis of high leakage reactance of superconducting controllable reactor works.

High Leakage Reactance of the Superconducting Controllable Working Principle and Structure Diagram of the Reactor

High leakage reactance of the controllable reactor with ordinary power transformer principle is similar to the primary coil of the reactor around the system as an ordinary copper wire coil, secondary winding control windings from Superconductors wound. two - way thyristor switch secondary superconducting control winding short-circuit the secondary superconducting winding magnetron being squeezed out, the first copper coil magnetic flux loop cross-sectional area decreases, reactance corresponding decrease in the smaller. High leakage reactance of superconducting controllable reactor by the thyristor electronic switch to control the secondary superconducting control winding and the secondary superconducting control winding two short-circuit and open, fast response, to limit the switching over voltage. High leakage reactance of the superconducting controllable reactor work, the first copper coil connected in parallel lines, if all the secondary superconducting control winding open circuit, the controllable reactor is a no-load transformer. When the thyristor switch the secondary superconducting control winding short circuit,

the magnetron in the secondary superconducting control winding being squeezed out of the first copper coil of the magnetic flux loop cross-sectional area also decreases. Specific structure in Fig. 1.

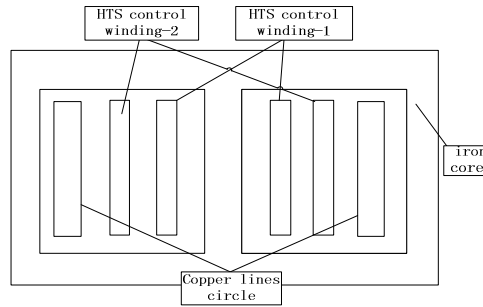


Fig. 1 High leakage reactance of the superconducting controllable reactor principle diagram

High leakage reactance of superconducting controllable reactor by superconducting control winding all open / open another superconducting coil short-circuit a superconducting coil, two superconducting coil short circuit to achieve the regulation of flux reactor in order to achieve the regulation of the reactor. Triac switch (can be used in conjunction with the ordinary circuit breaker in parallel), the superconducting winding short circuit, the magnetron is in the superconducting windings being squeezed out of the formation of the magnetic flux loop following the cut in this time the main winding area in Fig. 2, shown in part A1. The equivalent of a shell-type iron core reactor, the reactance value is determined by the height of the cross-sectional area A1 and the main winding, as determined by the number of coil turns.

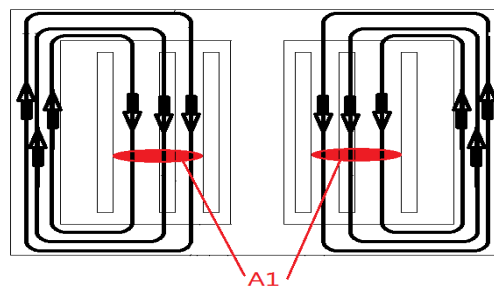


Fig. 2 Superconducting windings when a short circuit, the equivalent flux Fig

Triac switch (can be used in conjunction with the ordinary circuit breaker in parallel), the superconducting windings 2 and a short circuit, the magnetron is superconducting windings being squeezed out of a smaller cross-sectional area of the magnetic flux loop. Controllable reactor reactance value is less than to a short circuit of the superconducting windings reactance values. Can be controlled adjustment range of the capacity of the reactor required to design multiple sets of the second control winding.

Principle of the Superconducting Coil and the Uperconducting Coil 2 Open

When the superconducting coil 1 and 2 are open, the the superconductivity reactor is equivalent to a high degree of coupling of the magnetic circuit single-phase two-coil transformer, the secondary side of the no-load, equivalent circuit model shown in Fig. 3.

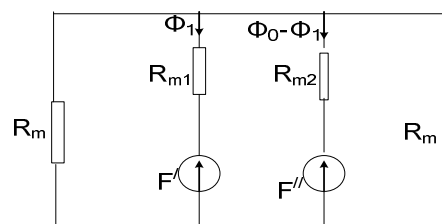


Fig. 3 Reactor magnetic circuit equivalent model of Fig.

The reactor control coil is a superconducting material, it can be ignored when carrying out the principle of analysis, resistance. Fig. 3, the reactor primary side current i is very small, and the reactor itself, the copper winding resistance R is small, so that $iR = 0$. In, $\phi_0 = BA_0, \phi_1 = BA_1, \phi_2 = BA_2,$

which A0 is the AC copper coils contained in the core cross-sectional area, A1 is the superconducting control coil contained in a cross-sectional area of the core A2 superconducting coil contained in the core cross-sectional area. No-load, the reactor core in the non-saturated linear region, and the superconducting coil 1 and coil 2 and the work of windings flow of the magnetic flux of the same size, uniform distribution of magnetic field lines. Not consider the core remanence and additional reactors initial flux, may be considered the core flux does not contain a DC component.

Superconducting Coil Short-Circuit Principle of the Superconducting Coil 2 Open

A short circuit, open the state of the superconducting coil, simply switch the superconducting coil a short circuit can be. Can be contained in the exchange of windings core flux as two-part magnetic flux and Magnetic circuit equivalent model shown in Figure 4, the exchange current can be viewed as two equivalent current i' and i'' , that is $i = i' + i''$, which i' is for the generation and superconducting windings produce alternating chain flux, i' for the exchange of windings contained in the other cross-sectional area of the core at flux, the flux at the same time the chain of the phase with superconducting windings. At this point, the reactor is equivalent to a transformer short circuit of the superconducting coil can be the equivalent circuit shown in Fig. 4

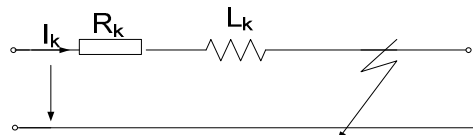


Fig. 4 HTS-1 contained an equivalent circuit of the core magnetic circuit in the short-circuit the moment

L_k Indicates the end of the copper winding inductance in the transformer, R_k is the resistance of the copper windings. The strict sense is that L_k is a changing factor, but in practice, R_k/L_k compared to the coefficients of the remaining items in the formula, it can ignore the impact of changes in L_k .

Superconducting coil, one short circuit before the reactor is equivalent to the secondary side of the no-load, and R_k is small, that a short circuit before i_k approximately 0. Obviously, from where you can see in a moment of closing short of the superconducting coil, the current work copper windings contains a transient component and the steady-state component, the above equation show that the sudden short-circuit current of the size of $t=0$ when the voltage of the initial phase angle α . The following two cases to be discussed: (1) $\alpha = \varphi_k |_{t=0}$, then $i' = I_k \sin \omega t$ that short-circuit operation of the superconducting coil 1, in the short-circuit transient current does not produce transient component, directly into the steady state. (2), is a large, $1 < K_y < 2$, in the ideal case, close to 2, then $R_k \ll L_k$ there K_y may be great short-circuit current at the moment of a short circuit of the superconducting coil. Too much short-circuit current in superconducting windings 1 will not only have a great exchange loss, and may even cause the quench of superconducting coil, the worse case may result in the whole superconducting windings a strip was burned. In addition, due to the presence of transient components, is easy to know the short-circuit current in the reactor caused by a very long time current shock; these are not conducive to the stability of the system. Dramatic changes in flux at the same time will lead to great harmonic generated in the coil current; these are not what we want to see.

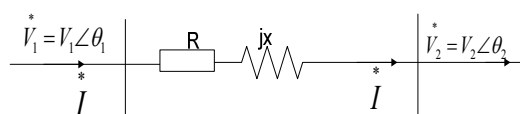


Fig. 5 35KV transmission line equivalent model of Fig

Fig. 5 shows that, $\alpha = \arctan(X_k / R_k)$ the decision by the line parameters can be obtained by actual measurement. But by the reactor design parameters determined in the actual design can be considered a controllable resistor in parallel between the superconducting controllable reactor and

system to regulate the superconducting coil in short circuit $\alpha = \varphi_k$. Short-circuit current in the superconducting coil, $i_1 = -N_0/N_1 I_k \sin \omega t$ a short circuit moment superconducting coil 1 can be obtained. Into the steady state, we can consider withdrawing from the controllable resistance.

Principle of Superconducting Coil and the Superconducting Coil Are Short Circuit

When the reactor by the state of the superconducting coil short-circuit the superconducting coil 2 open switch to the superconducting coil and the superconducting coil of the coils are shorted, simply by switching the superconducting coil shorted can. Analysis theory is still only a short-circuit analysis of the superconducting coil principle, can be contained in the exchange of winding core flux as the flux in two parts. Exchange of current i can be viewed as two equivalent current i_1, i_2 , namely, $i = i_1 + i_2$, used to generate an exchange of superconducting winding flux i_1, i_2 for other cross-sectional area of the core to produce the magnetic flux contained in the exchange of winding, the flux at the same time the chain of the phase with superconducting windings. The equivalent circuit shown in Figure 6

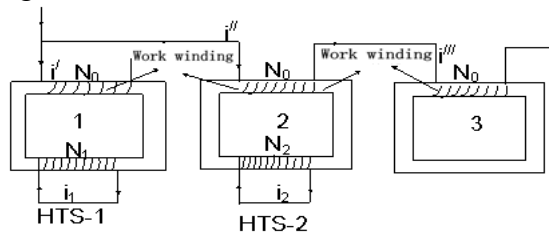


Fig. 6 HTS-1 and HTS-2 coils are short-circuit equivalent of the reactor model diagram

In this section, and they agreed to reposition itself as the HTS-coil short-circuit the moment the starting time, that is, when $t = 0$, the HTS-2 coil short-circuit. Two short-circuit before the superconducting coil, the transformer 2 is equivalent to the secondary side of the no-load and R_k is small, so that the short circuit before i_k about 0. Closing short moment in the superconducting coil, the current of the copper windings of i'' work includes the transient component and the steady-state component, a sudden short-circuit current size of $t = 0$ when the voltage of the initial phase angle α . The following two cases to be discussed: (1) $\xi = \delta|_{t=0}$, this time $i'' = I_k \sin \omega t$ Short-circuit operation of the superconducting coil 2, in the short-circuit transient current does not produce transient component, directly into the steady state. (2) $\xi = (\delta - \pi/2)|_{t=0}$, at this time $R_k \ll L'_k$, k_y will be great. In the ideal case, $1 < k_y < 2$. Ideally, at the moment of a short circuit of the superconducting coil will produce a lot of short-circuit current is too large short-circuit current in superconducting winding 1 will not only produce a lot of AC loss and even cause the loss of the superconducting coil, worse case may result in the whole superconducting winding a strip was burned. due $T_k = \omega L'_k / R_k$ to the existence of the transient component. Short-circuit current will cause a very long time in the reactor current shocks, these are not conducive to the stability of the system, dramatic changes in flux at the same time will lead to great harmonic generated in the coil current. From the above analysis to the HTS-2 at the instant of short circuit directly into the steady state, to avoid the transient component caused by the shock of the system. Is how to achieve $\xi = \delta|_{t=0}$ is critical? To real-time measurement ξ and δ signal acquisition and monitoring module. Ideally appeared $\xi = \delta$. Then immediately closing operation, the HTS-2 is about to coil short-circuit. Then immediately closing operation $\xi = \delta$, the HTS-2 is about to coil short-circuit in $|\xi - \delta| < 5^\circ$.

At this point the HTS-2 coil short-circuit current will flow through the transient component. Since c is small, although it will produce a small fundamental frequency oscillation harmonics, but the reactor and the system does not produce obvious interference can be approximated by that $c = 0$, that can be achieved in the HTS-2 coil The closing moments that enter the steady state.

When to enter the steady-state may consider withdrawal of controlled electricity group, and by the steady-state circuit, it is easy to draw the current value. In order to make in the closing moments, B1 does not contain a DC component. Ideally $t = k\pi$, when the HTS-coil short-circuit

operation. When the HTS-1 and HTS-2 coil short-circuit when compared with HTS-1 coil short-circuit when the short-circuit current of the HTS-1 coil will decrease dramatically. At this point the short-circuit current of the HTS-coil, which is A2 contains cross-sectional area of the magnetic flux is generated by the HTS-coil AC current, so the saturated case, the HTS-2 coil will produce a lot of short-circuit excitation current, the flux of the HTS-1 current in the coil cross-section of the core contained almost nothing, so the short-circuit current is very small. From the reactor capacity, compared with the HTS-coil short circuit, the HTS-2 open circuited, then the capacity of the reactor will be significantly large. This is because the exchange of winding current in the case of two superconducting coils are short-circuit, thus the capacity of the reactor. But it does not exceed its rated capacity.

Conclusion

Superconducting windings and superconducting windings 2 are open to consider the no-load voltage of two superconducting coils, the reactor capacity minimum. When a short circuit of the superconducting winding superconducting winding 2 open superconductivity reactor winding of the DC harmonic filtering. When two superconducting windings are short-circuit in the range of $|\xi - \delta| < 5^\circ$ and closing operations reactor and the system does not produce obvious interference, the capacity of the reactor. The state of these types of work, the no-load voltage of the coil will be quite large, to be a reasonable choice of the size of the reactor, including the cross-sectional area of the exchange of winding turns, the exchange of winding contained in the core of the reactor core height. Only select an appropriate size parameter in order to make the reactor has better performance.

High leakage reactance of the superconducting controllable reactor secondary superconducting control winding high-temperature superconducting materials, its induced voltage is relatively low, the power consumption in the winding is relatively small, can effectively reduce the power consumption of the reactor. Its structure and transformer can be done 500kV and 1000kV voltage level; there are no problems on the process. The controllable reactor linearity is good, with the suitable made of high resistance and reactance of the neutral point, the limit of arc current function. Can be controlled adjustment range of the capacity of the reactor required to design multiple short-circuit the secondary superconducting control winding.

References

- [1] David Seal. ARM Achitecture Reference Manual. <http://www.arm.com>,2000
- [2] Weinan Chang,Chijui Wu. Developing Static Reactive Power Compensators in a Power System Simulator for Power Education. IEEE Transactions on Power Systems,1995,10(4):1734~1741
- [3] Guihong Feng,Fengxiang Wang,Bingyi Zhang. Modeling and Characteristics of a Novel Magnet Saturation Controllable Reactor. IEEE Power Electronics and Drive Systems,2003,1:313~315.
- [4] zhongqing li,Dynamic Simulation of Stepped Controllable Shunt Reactor in Type of EHV/UHV High-Leakage Inductance Transformer Power System Technology,2010,1 :6~10..
- [5] Guihong Feng, Fengxiang Wang,Jin Wang. Design Principles of Magnetically Controlled Reactor. IEEE Electrical Machines and Systems,2001,1:212~214.
- [6] C. Y. Chung, C. T. Tse, C. K. Cheung. New Approach for Static Var Compensator Controller Design. Proceedings. DRPT 2000,2000,7(4):29~34.
- [7] Goodacre,A. N. Sloss. Parallelism and the ARM Instruction Set Architecture. IEEE Computer,2005,38(7):42~50.

CHAPTER 3:
Structural and Civil Engineering

Research of Practice-based Design in Building Construction II

Dihua LV

School of Urban Construction, Zhejiang Shuren University, Hangzhou, Zhejiang 310005

Keywords: Building Construction; Practice-based Design; Teaching Reform

Abstract. Building Construction is a course, which has a close tie with building design and also involves a considerably wide range of professional knowledge. For various reasons, it is greatly difficult for teachers to teach this course well, and also the ability of students to practically apply it is poor. After years of teaching practice, several main reasons for the problem are found. Therefore, "practice-based design" is introduced to the teaching of this course for strengthening practical teaching and improving the ability of students in practical application. Through a stage of teaching reform, a conclusion is drawn up on the results in this paper.

Introduction

Building Construction is a very important fundamental course of architecture program, but also an integrated subject featuring practices. It involves lots of knowledge such as building materials, building physics, building operations and building structure. However, because importance is attached to theories but indifference is towards practices in architecture program for a long time as well as many and diverse contents and high techniques are involved, the traditional teaching model is boring among students who lack practical experience of building construction. Therefore, many students are uninterested in this course, so that they universally feel strange about building technology after graduation [1]. From above situation, making teaching reform on Building Construction and cultivating students' comprehensive ability are of extremely vital significance.

The educational object of School of Urban Construction of Zhejiang Shuren University is to cultivate application and techniques oriented personnel. Therefore, high importance should be attached to the cultivation of the abilities of students in analyzing and solving problems. The teaching quality can be fundamentally improved only if comprehensive research and reform are implemented for the teaching of this course from multiple aspects such as teaching content organization, teaching methods and learning result evaluation and also interactions between teachers and students can be increased for stimulating the subjective initiatives of students.

Teaching Content Organizational Reform

In a long time, high importance is always attached to theories and indifference is towards practices in architecture program, making teaching and learning divorced; the course Building Construction is always fluctuating in building design and difficult to play its role [2]. Therefore, in the teaching reform discussed in this paper, the concept of practice-based design is introduced for strengthening the practice teaching of the course Building Construction and improving the ability of students in practical application of building construction techniques.

Building Construction II is divided into four chapters, namely high-rise building construction, interior building construction, long-span building construction and industrialized building construction. In each chapter, how to make students effectively master its application is the main purpose of the teaching reform.

High-rise Building Construction and Interior Building Construction

In the two specialties, high importance was attached to the understanding of construction standards, material selection, and design of nodes; all sorts of knowledge points were integrated by the author in two practice-based design assignments related to the two chapters. For example, glass curtain wall design and interior design for small restaurants can promote students to understand of emotional building design and rational node designs in combination.

In the early days of each "practice-based design" assignment, a research and investigation task was assigned to students, allowing them to directly discuss with material suppliers at construction materials market and hence knowing performances and characteristics of various materials as well as the corresponding construction forms and practices. Because the construction nodes are introduced in textbook are very limited, students were encouraged to broaden their knowledge scope in the designing process. For example, students were asked to search course information at library or in the Internet, so as to find a feasible construction way of realizing their own ideas. After design was complete, students were required to make discussions and raise questions, and thus their initiatives in learning were stimulated.

The "practice-based design" process can promote students to take the initiative to understand the characteristics and differences of different construction practices, and help teachers examine the consideration and recognition of students on interior size, materials, colors, nodes or else. Thus, the classroom teaching effect can be known well. From the gained drawing results, the interests and attentions of students in this course can be seen, and therefore good teaching feedback can be received.

Long-span Building Construction

In this chapter, high importance was attached to the learning and understanding of 10 commonly-seen long-span building construction forms, and students were required to select appropriate long-span building structure form for the design; in functions and modeling, students were guided by the teacher at the class of architecture; the understanding of the characteristics, structures and nodes of long-span building constructions was strengthened at the class of construction.

Through the above two "practice-based design" small assignments (high-rise building construction and interior building construction), students could preliminarily understand of the concept of construction nodes design and the application ability. In the long-span building construction, construction assignment and building design assignments were integrated together, making the teaching contents of the course construction further integrated with building design. This is helpful for students to understand the meaning of learning the course *Building Construction*.

Industrialized Building Construction

This chapter can't be seen commonly at domestic market, so it is not emphatically discussed in this paper. It will be explained and interpreted with a large amount of foreign examples in the process of teaching. Besides, some industrialized building construction processes will be played with multimedia tools for helping students understanding industrialized building construction, and knowledge points will be strengthened in the form of after-class assignments.

Reform of Teaching Methods

In the teaching of the course Building Construction, many practices such as construction-site practice have been applied in teaching program, but the teaching effect was very small. The fundamental measure for improving this situation is to make an enhancement to the practice teaching of the course Building Construction, but does not simply depend on "existence" or "non-existence" of a practical activity. The knowledge points that have a connection with the courses such as building materials, construction equipments and building physics can be highlighted and repeated, for the purpose of allowing the knowledge structure of students to become a complete system. In the teaching method reform of "practice-based design", a variety of ways have been taken by us.

Assignment Expression Way

The copying and drawing ways of dull and boring nodes were replaced with "practice-based design" title in which nodes design was contained; drawing book (size: A3) was replaced with two pieces of drawing paper (size: A2); some design ideas were required in drawing.

Improving Teaching Methods

In the introduction to each part of the course Building Construction, the teaching of all nodes, materials, practices and others, which are mentioned in textbook, can be vividly demonstrated by making use of the advantages of multimedia teaching and the construction process pictures as much as possible, so as to make theoretical knowledge integrated with practices better. In chapters that have a close relationship with building design course, harmonious cross-cooperation with course design can be done, so as to make an enhancement to the interaction and communication between different courses.

Carrying out Classroom Discussion

Classroom discussion is one of the most direct, the most effective, and the timeliest ways for students to get involved in teaching activities^[3]. Through raising questions and making discussion on the teaching of teachers and the "practice-based design" assignments, students were promoted to get an in-depth understanding and apply what they have learnt. As a result, the teaching effect proves to be very excellent.

Introduction to Results

Design of High-rise Building Glass Curtain Wall

Requirement on the assignment was making a design on exterior curtain wall of an updated and reused project; two or above exterior curtain walls were required to be applied. Through the design, students were expected to get an understanding of the requirements and common practices of curtain wall design of buildings, as well as the characteristics and application scope of the commonly used exterior wall materials.

Design Assignment 1 (See figure 1 and figure 2): Designer was Yangwei LV from Class 081 of architecture program

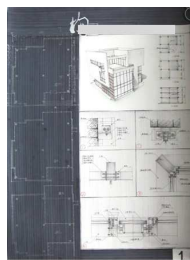


Fig.1

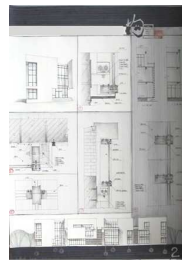


Fig.2

Comments from teacher: The plan for building design is reasonable, and construction nodes are detailed and complete; the selected form of curtain walls are matching with each other; drawing expression is self-evident and complies with the depth requirements, and also is implemented with free hand. Thus, this design is worth applying.

Design Assignment 2 (see fig 3 and fig 4): Designer was Lingxia JIANG from 091 of architecture program

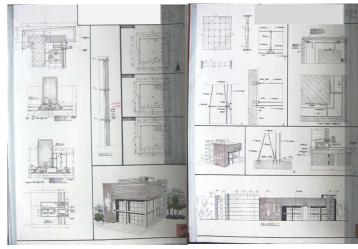


Fig.3

Fig.4

Comments from teacher: Glass curtain wall design and construction nodes are matching with each other; construction nodes for realizing the design can be acquired through outside-textbook methods, and therefore there is a spirit of innovation in this design; drawing is explicit and complete, helping achieve the purpose of the assignment.

Design of Restaurant Interior Decoration

Requirement on the assignment was to make a design on the decoration of planes, facades and ceiling under a given restaurant building condition; in the design, applied materials were required to show, and also corresponding node structure was required to be drawn. Students were expected to get an understanding of the basic interior design and construction practices and also flexibly apply them in their own designs. Design assignment made by the student designer Shanshan HUANG from class 081 of architecture program is shown in figure 5 and figure 6.



Fig.5

Fig.6

Comments from teacher: The interior space design is reasonable; wall decoration and ceiling are matching with each other, and also the construction practices of light tanks are correctly expressed, achieving the goal of expressing self-design ideas with constructed language; drawing expression is smooth, achieving the desired result.

Composition of Final Academic Results of Student

The final academic result of a student mainly comprised of "practice-based design" assignment (40%), final exam result (50%), and daily classroom attendance and after-class exercises completion (10%). Thus, the final term exam result was not used as the only judgment standard. In current final academic result, the ability of students to apply knowledge in practical cases was comprehensively taken into account, namely the completion of "practice-based design" assignment.

In such a way, the learning of a student can be truly reflected; the single model for judging the final academic result of a student is changed; students are promoted to lay a stress on daily learning, but not only on the concentrated learning at the end of a semester. According to several adjustments, the composition of the final academic result of a student in *Building Construction II* is shown below. Also, "practice-based design" assignment comprised of three parts, as shown below.

Final Academic Result	"Practice-based Design" Assignment 1	"Practice-based Design" Assignment 2	Final Exam	Daily Classroom Attendance
100%	20%	20%	50%	10%

"Practice-based Design" Assignment 20%	Market Research & Investigation Report	3%	
	Completion of Design Assignment 15%	Integrity of covered nodes	10%
		Drawing Effect	2%
		It there innovative node construction	3%
	Classroom Questions & Discussion	2%	

Through the composition of the final academic result, the ability of a student to apply what he has learnt can be truly reflected, and also the practice teaching effect can be improved.

Conclusion

Through reform and construction of teaching methods, teaching practices and academic result evaluation of *Building Construction*, certain experience has been accumulated, and it is believed that a positive help will be brought to the construction of the course *Building Construction* and the training of students in architecture program after a continuous improvement. Also, this reform is of great significance to improve the practical ability of students, promote educational innovation, and improve the quality of personnel training and the subject competitiveness of school.

Acknowledgements

This paper belongs to the Secondary Teaching Reform Subject of Zhejiang Shuren University.

References

- [1] Zhang Hong, Li Zhen. Study on the Teaching Reform of Course "Architecture Construction" [J]. *Sichuan Architecture*, 2009 (10).
- [2] Lin Zhang. Attempt on Strengthening the Practice Teaching of Course "Architecture Construction" [J]. *Journal of Northwestern Poly-technical University*, 2003 (3).
- [3] Zhenhe Fan. View of the Cultivation of Students Ability to Analyze and Solve Problems from the Practice of Teaching Reform of Building Construction [J]. *Huazhong Architecture*, 2007 (4).

Effect of Corrosion on Mechanical Properties of Reinforcing Bar HPB400

Ping Li, Ying Wang

Department of Civil Engineering, Luoyang Institute of Science and Technology, Luoyang 471023,
China

eappol@163.com

Keywords: Reinforcing Bar, Corrosion Behavior, Strength, Elongation

Abstract The corrosion behavior of reinforcing bar HRB400 in simulated concrete pore solution (3.5 wt. % NaCl solution) was studied, and the tensile mechanical properties after corrosion were tested. The results showed that, with corrosion time increasing from 240h to 720h, the corrosion rate of reinforcing bar HRB400 increases. With the increase of corrosion time (corrosion rate), the yield strength and tensile strength decrease, but the elongation decreases at first and then increases.

Introduction

As one of the most common modern building structures, reinforcing bar concrete is widely used in industrial, agriculture, military and civil construction, etc. With the existence of high alkaline concrete pore solution, the concrete usually provides a protective environment for the reinforcing bar, forms a layer of protection film, and restrains or reduces its corrosion [1-3]. Nevertheless, with the passage of time and the change of environment, the corrosion of reinforcing bar occurs at different extent because of the carbonization of concrete and the inrush of chloride, which leads to the weakening of concrete. Therefore, the corrosion of reinforcing bar has been the main factor to influence the durability and cause the failure of concrete structures [4, 5].

However, the corrosion of reinforcing bar is seldom considered in designing the concrete structure, and the excellence of concrete is not brought into action primly in service period. The damage of the reinforcing bar corrosion failure and the essentiality of taking protection measures are increasingly attaching more and more importance. The research on the corrosion and its effect on the mechanical properties of reinforcing bar are increasing [6-8]. In this paper, the corrosion behavior of reinforcing bar HRB400 in concrete structure in simulated concrete pore solution was investigated, and its tensile mechanical properties were tested before and after corrosion. It is hoped to provide help to prolong the lifespan of reinforcing bar and enhance the duration of concrete structure.

Experimental

The test material is common reinforcing bar HRB335 in concrete structure. The samples have two sizes: short samples ($\Phi 14\text{mm} \times 20\text{mm}$) used for corrosion morphology observation, and long samples ($\Phi 14\text{mm} \times 450\text{mm}$) used for corrosion rate measure and mechanical properties tests. Before corrosion, the samples are polished, cleaned, and rust-removed, and weighed by an electron balance. The tensile mechanical properties, including yield strength, tensile strength and elongation, are tested by a hydraulic pressure universal testing machine.

The corrosion media is simulated pore solution in concrete structure, and its composition is saturated $\text{Ca}(\text{OH})_2$ solution with 3.5 wt.% NaCl (written as 3.5 wt.% NaCl solution). The corrosion time is 10, 20 and 30 days, i.e. 240h, 480h and 720h. After corrosion, different treatments are carried out for different samples. For short samples, corrosion morphology observation is made by a scanning electron microscope (SEM, JSM-5610LV) after they are cleaned and dried out. For long samples, corrosion rate calculation and mechanical properties tests are made after they are immersed in thin hydrochloric acid to remove the scale on the surface.

Results

The results of corrosion rates of reinforcing bar HRB400 in 3.5 wt.% NaCl solution are given in Fig. 1. It can be seen that, with the increase of immersed time from 240h to 720h, the corrosion rate (weight loss rate) increases from 0.17% to 0.33%. Meanwhile, it also can be seen that the corrosion rate of reinforcing bar HRB400 is basically in a linear relationship with corrosion time.

The SEM morphologies of reinforcing bar HRB400 after corrosion in 3.5 wt. % NaCl solution are showed in Fig. 2. It can be seen that, with the increase of immersed time, the character of corrosion morphology is changed. At 240h, the corrosion is slight and uneven in different areas, and a small quantity of corrosion scale is on the surface (see Fig. 2a). At 480h, the corrosion is still uneven, and becomes heavier in level. Some corrosion pits are observed (see Fig. 2b). At 720h, the corrosion is uniform (see Fig. 2c). In view of the overall situation, with the corrosion time between 240h and 720h, the corrosion develops from some areas to total surface, and becomes heavier and heavier. The corrosion turns from local corrosion into overall corrosion, and the corrosion rate becomes higher and higher. The results are basically consistent with the corrosion rate results in Fig. 1.

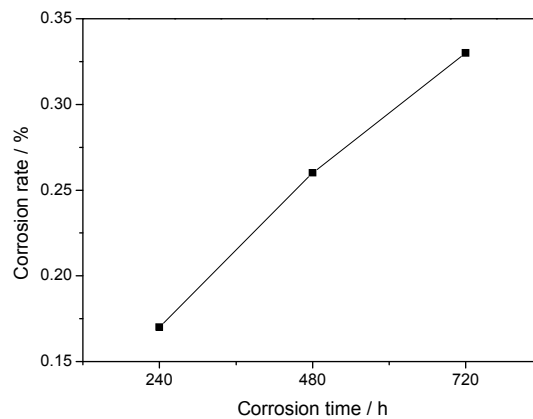


Fig. 1 Corrosion rates of reinforcing bar HRB400

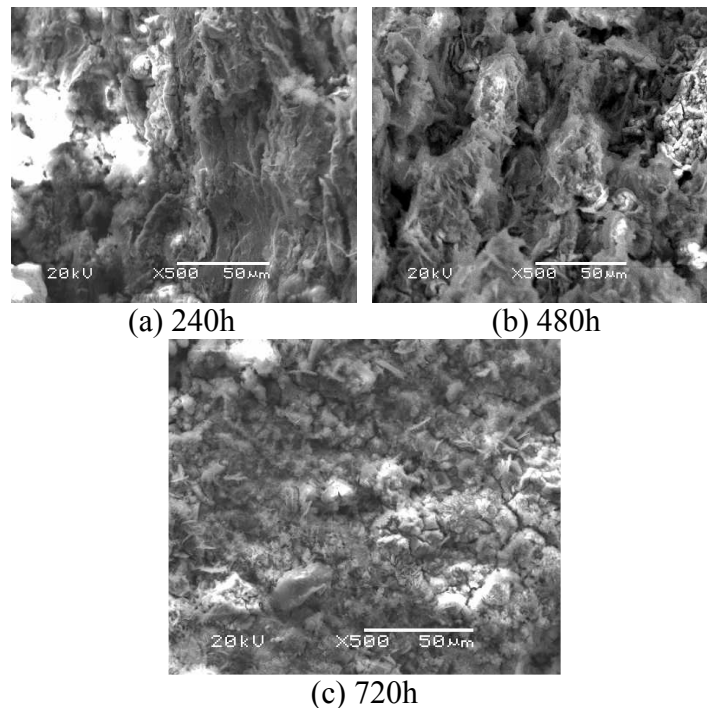


Fig. 2 Corrosion morphologies of reinforcing bar HRB400

The results of yield strength and tensile strength of reinforcing bar HRB400 before and after corrosion are shown in Fig. 3. It can be seen that, the yield strength and tensile strength of reinforcing bar after corrosion are less than those before corrosion. From the macro perspective, the

reinforcing bar produces weight loss after corrosion, and effective section area is smaller, which decrease the tensile force that it can resist. On the other hand, the surface of reinforcing bar becomes uneven after corrosion, and the stress concentration is serious, which causes further decrease of the tensile force that it can resist. From the micro perspective, corrosion is electrochemical reaction in the surface of reinforcing bar, will turn iron and steel material into rust, which change the surface morphology and the microstructure. Meanwhile, with the existence of the inner stress, the corrosion will also change the internal structure. These will affect the strength properties of reinforcing bar.

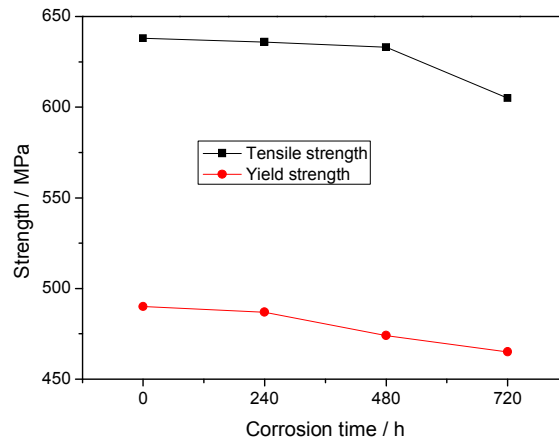


Fig. 3 Yield strength and ultimate tensile strength of reinforcing bar HRB400

According to Fig.1.3, combined with the test results of corrosion rate in Fig.1.1, it can be seen that the yield strength and tensile strength of reinforcing bar decrease with the increase of corrosion time (corrosion rate). However, the corrosion rate is not the decisive factor to decrease the yield strength and tensile strength of reinforcing bar. Because the corrosion rate reflects the weakening of the average section area due to corrosion, it is a general average index. It cannot reflect the disastrous impact of local stress concentration caused by uneven corrosion. Even if the corrosion rate is the same, the decrease in the yield strength and tensile strength of the reinforcing bar will be different. According to the above analysis, the stress concentration after corrosion should be a main reason.

The results of elongation of reinforcing bar HRB400 before and after corrosion in 3.5 wt.% NaCl solution are shown in Fig.4. It can be seen that, the variation of elongation is quite different from that of yield strength and tensile strength. With the increase of corrosion time, the elongation fluctuates, and the curve shape is similar to English letter V.

According to Fig.1.4, combined with the test results of corrosion rate in Fig.1.1, it can be seen that the elongation of reinforcing bar doesn't decrease with the increase of corrosion time (corrosion rate). However, the corrosion rate is not the decisive factor to decrease the elongation of reinforcing bar. With increasing corrosion rate, the elongation is not lower, and it can even increase after corrosion.

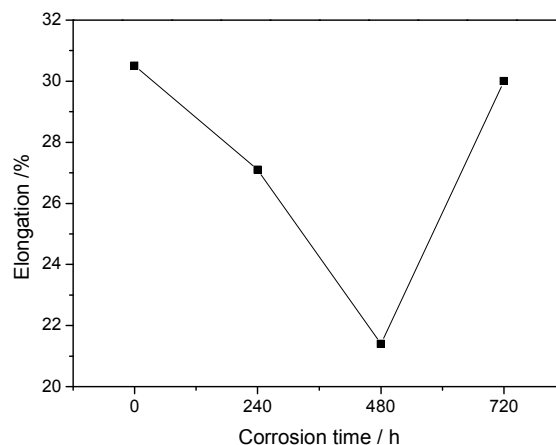


Fig. 4 Elongation of reinforcing bar HRB400

According to the above analysis, the dominant corrosion type of the reinforcing bar is different at different time. The severity of stress concentration after corrosion is also different. This should be one of the main reasons to cause the fluctuation of elongation. Under the same corrosion rate, uniform corrosion reduce less section area than local corrosion, and the stress concentration is less serious. Though it can afford less load (the yield strength and tensile strength decreases), the reinforcing bar becomes thinner in the whole, and no apparent weak positions appear. The reinforcing bar is more difficult pulled to crack than that under local corrosion (especially pit corrosion), so it can afford more plastic deformation, and the elongation is larger.

Conclusions

With corrosion time increasing from 240h to 720h, the corrosion rate of reinforcing bar HRB335 increases and the corrosion becomes heavier and heavier in 3.5 wt.% NaCl solution. With the increase of corrosion time (corrosion rate), the yield strength and tensile strength decrease, but the elongation decreases at first and then increases.

References

- [1] P. Li, D.X. Zhang. *Materials Protection*, Vol. 43 (2010), p. 44 (in Chinese)
- [2] Y. Wang, P. Li. *Advanced Materials Research*, Vol. 287-290 (2011), p. 738
- [3] Y. Wang, P. Li, H.M. Ning. *Hot Working Technology*, Vol. 39 (2010), p.133 (in Chinese)
- [4] Y.X. Guo, J.X. Gong. *Corrosion Science and Protection Technology*, Vol.19 (2007), p. 218 (in Chinese)
- [5] Z.L. Lu. *Journal of Chinese Society for Corrosion and Protection*, Vol. 27 (2007), p. 119 (in Chinese)
- [6] C. Gui. *Shanxi Architecture*, Vol. 33 (2007), p. 161 (in Chinese)
- [7] S.H. Yang, L. Zeng. *Journal of Zhengzhou University (Engineering Science)*, Vol. 26 (2005), p. 85 (in Chinese)
- [8] L. Zeng, S.H. Yang. *Henan Science*, Vol. 23 (2005), p. 877 (in Chinese)

Study on Precast Slab Track for Taiwan High Speed Rail

Yan-Chyuan Shiau^{1, a}, Ron Chen^{2, b}, Ming-Hsi Lin^{3, c} and Chih-Ming Huang^{4, d}

¹ Associate Prof., Dept. of Const. Management, Chung Hua University, Hsin-Chu, Taiwan

² Dean College of Archi. & Planning, Chung Hua University, Hsin-Chu, Taiwan

³ Graduate Students, Dept. of Const. Management, Chung Hua University, Hsin-Chu, Taiwan

⁴ Project Engineer, Taiwan High Speed Rail Corporation, Miao-Li, Taiwan

^aycshiau@ms22.hinet.net, ^barchichen@aol.com, ^ctaco.001@hotmail.com,
^dm09516042@chu.edu.tw

Keywords: Slab Track, Taiwan High Speed Rail, Precast Track System, Quality Management.

Abstract. High Speed Rail significantly saves transportation time between cities in which a stable slab track is an essential and important component. This article introduces the quality management on production of precast tracks system, which can act as a reference and application for the concrete industry in Taiwan. Case study is used to investigate the major content of this project which includes quality management, organizational structure, material management, process management and inventory management. Some other key factors are discussed which assure the success of Taiwan High Speed Rail project such as comprehensive plan in advance, strictly execution according to written document, and looking at the bigger picture & performing from the details and putting training into practice.

Preface

The Korean High Speed Train (KHST) has been tested on the Kyongbu high speed line and the Honam conventional line since 2002[1]. Chen has showed that ChinaRLS can characterize the feature of the Chinese track irregularity better than AmericaRLS [2]. From theoretical analysis and the paving test on the test line and existing line, the slab track has been proven to provide distinctive superiority far greater than conventional ballast tracks in terms of safety and comfort during high speed travel, which is also more favoured in economic aspects than the ballast track (the maintenance cost of slab tracks is approximately 1/10 of ballast tracks) [3]. Compared to conventional ballast tracks, the slab track provides the advantages such as ; better track structure and stability, better track flexibility, better durability, economic and reasonable construction price and saving of maintenance expense [4].

The J-slab track adopted by THSR (Fig. 1) [5] mainly consists of roadbed, projection, CA-mortar, J-Slab, rail and fasteners. The slab plays a significant role in the slab track system since it directly sustains and delivers external forces of the train such as loading, centrifugal force, impact and vibration, thus the requirement of quality is extremely strict.

Introduction of THSR Track Project

The length of THSR track project is approximately 345 km. Although there are some strategies to reduce vibration decrease and noise reduction [6], the full length of THSR track project is 345 km and except for the Taipei underground section, the remaining project of approximately 330 km is contracted to TST JV (Taiwan Shinkansen Track Joint Venture). The Sumitomo Mitsui is the co-vendor of TST JV, which is in charge of manufacturing of all slabs.

Quality Management for Precast Slab Track

Factory and equipment planning The factory includes main areas such as plant, mix plant and product storage. Smooth planning of moving path will provide concise and easy management of area distribution. The plant area is approximately 15,000M² (Fig. 2).

Organizational structure of quality management The production of slab tracks adopts the lump-sum manner, i.e. TST JV undertakes design, supervision and construction. The JV must submit the Inspection and Testing Plan for acquiring authorization of Statement of No Objection from THSR. The content includes construction procedures, observation point for resumption of project, sampling or testing point requiring suspension, test items, frequencies, methods and regulation of accordance, as well as development of relevant management forms. The forms shall be designed and modified by the JV. Each blank column in the forms must be filled and the columns related to the site must even be filled on site [7]. The JV is obliged to provide and keep all documents of quality records. In addition to regular audit, THSR is entitled to audit with notifying the JV and the JV cannot refuse.

Material management In order to ensure the quality of material, inspection through the correct procedures shall be made prior to entry and storage. All materials required for manufacturing slab tracks must qualify with inspection by laboratory institutes acknowledged by CNLA. The procedures and results of inspection shall comply with requirements of THSR regulation. The storage of material is managed in areas according to its characteristics (Table 1). The total storage capacity of mix plant is 600M³ and available for 3-4 days of workload. The materials are delivered to the storage bucket of mix equipment via conveyor belt and each cement storage bucket can store 150T of Type I cement [8].

Table 1.Storage area and characteristics

Material	Storing method	Storage management
Cement	Cement storage bucket	Prevent air pollution upon purchase of material. The storage bucket shall be kept clean inside while the outside is specified with type and source of cement. Upon arrival and offloading of material on site, the personnel shall supervise throughout the process.
Aggregate	Aggregate storage bucket	The storage bucket shall be kept clean inside. Entry of moisture and dust in the bucket shall be prevented.
Additive	Storage tank	Water leakage is strictly prohibited for prevention of pollution and chemical reaction. Suitable mixer shall be provided in the tank for regular mixing.
Steel bar	Inspection area	The storage area shall be kept clean and dry for prevention of surrounding chloride, grease and soil that cause rust in steel bar. Slid shall be placed during steel bar storage for prevention of direct contact with ground surface.
Square Steel bar	Material storage area	Prevent moisture that rusts material. The storage area shall be kept clean for prevention of contamination. Slid shall be placed during storage for prevention of direct contact with ground surface.
Insert A, C	Material storage area	Slid shall be placed during storage for prevention direct contact with ground surface. Storage area shall be kept clean and dry for prevention of surrounding chloride, grease and soil that cause rust in reinforcement.
Screw Set	Material storage area	Slid shall be placed during screw storage for prevention of direct contact with ground surface. The screws shall be stored in different packets.
Explosion proof steel bar	Material storage area	Slid shall be placed during storage for prevention of direct contact with ground surface.
Welding material	Material storage room	Prevent moisture that rusts material. Slid shall be placed during storage for prevention of direct contact with the ground surface.

Process Management

Mold assembly and inspection includes:

The molds (Fig. 3) shall be checked immediately upon arrival. The appearance shall be checked once per month to ensure there is no condition of damage or deformation for compliance with size requirement.

After completion of mold assembly, check the appearance, dimension, position and location of embeds.

Check precision requirement [9].

Steel bar bending and assembly includes:

The cutting and bending of steel bar shall be inspected according to the construction drawing, as well as the assembly platform of steel cage (Fig. 4).

After fabrication, check the dimension and length of steel bar (cutting and bending), which is followed by fastening fixture with wires according to the requirement of design drawing.

Record the check of steel bar fabrication and assembly on the check form.

Check embeds.

Properly fix Insert plug A, Insert Plug C and explosion proof steel bar on the steel mold for prevention of displacement due to vibration during concrete placing.

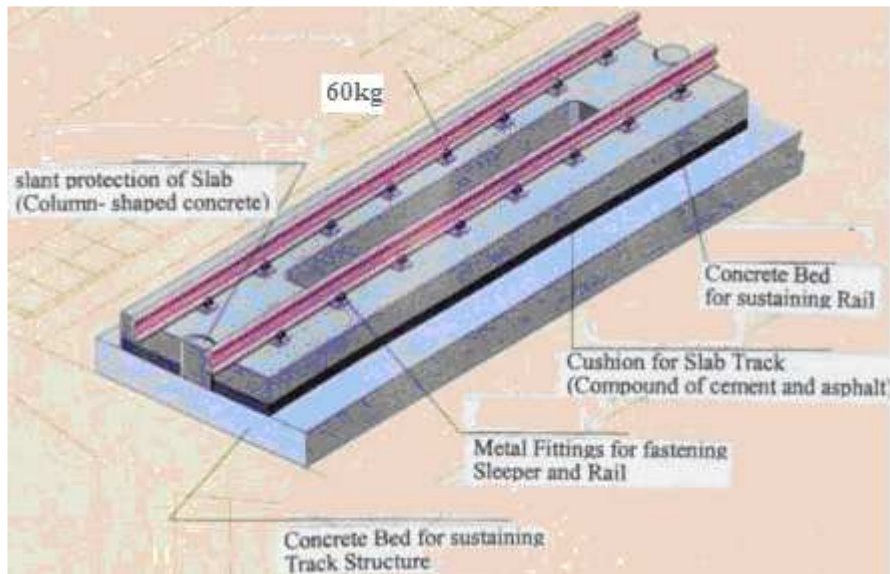


Fig. 1 J-slab track system



Fig. 2 Production line



Fig. 3 Molds for slab tracks

Inspection of steel bar and formwork assembly includes:

Check relevant positions between steel bar placement and steel mold. Please re-check in case of modification.

Fix the steel mold with clips and visually check for hammer loosening.

Concrete inspection includes:

Obtain 9 specimens for every placing, cure 6 of them together with the slab track (after steam curing, place them in the curing pool for 3 days) and the remaining 3 specimens are cured by means of the general standard.

Test the specimens cured together with the slab track for strength after formwork removal and 7-day compressive strength test. For specimens cured by means of general standard, apply the 28-day compressive strength test.

If the concrete strength does not reach 30Mpa, curing must be continued until qualified according to testing the strength.

Results of all compressive crushing are recorded and an X-R chart is produced to control the concrete quality.

Steam curing includes:

The curing starts 3 hours after concrete placing.

The rate of temperature increase and decrease shall not exceed 15 °C/hour.

The maximum temperature must be 50~60 °C and the duration shall not exceed 6 hours.

The temperature shall be controlled and recorded automatically.

Product inspection includes (Fig. 5):

Measure the length and width of the slab track with stainless ruler and every unit must be inspected.

Measure the thickness of slab track with vernier caliper and every unit must be inspected.

Measure the levelness of slab surface with special instrument and every unit must be inspected.

Use square and nylon string to check surface curvature and center line of the track and every unit must be inspected.

Use special steel gauge to measure spacing and curvature of embeds and every unit must be inspected.

Other note item includes:

The making of product marks includes manufacturing date, slab number, check number and protective coating. After completion of all checking and repairing, place the slab tracks in curing pools with water for 3 days.

Inspection and testing of ground resistance must be carried out before and after concrete placing. The ground resistance shall be less than 0.2Ω.

Perform one pulling test on insert plug A and C for production of every 500 slab tracks (Fig. 6) with test load of 49KN.



Fig. 4 Platform for steel cage



Fig. 5 Check of slab tracks



Fig.6 Pulling test of plug A & C

Inventory Management

Storage of Slab Tracks Includes:

Compact and roll the ground of piling field to the required density and pave gravel onto the ground, as well as placing the stow under the slab tracks (Fig. 7).

Fix slabs onto the steel frames with metal connector and screws to prevent toppling.

Fix 4 rubber pads on the slab surface to prevent collision between slabs.

Seal the insert holes on the slab track with tape or plastic cover to prevent stacking of dusts.

Record storage of slab tracks in detail, follow up and renew the records every day to see the date of production for slab track at each position.

Delivery checking includes:

The schedule and amount of slab track delivery will be notified by TST JV in official letter.

Before delivery, the appearance, numbering, quantity and transportation arrangement of the products will be visually checked again.

The check results before delivery will be recorded on the check form daily.

Summary

The precast concrete product is a specified good that is produced in a factory and free from natural factors such as weather and environment. As long as the planning is adequate with good operation, such product is rather easy to manage and control in the construction field. The product of HSR slab tracks demonstrate a perfect surface and extremely high precision of dimension that is almost as fine as metal products, which is not the achievement from checking at the end of the production line. The habit of the Japanese industry with thorough systemization, documentation, standardization, and hands-on principles for process of management actually cover many contents, which are worthwhile and our concrete plants have been recommended to learn from.

Comprehensive plan in advance For the mold developed for production of slab tracks, the assembly is fast, easy and safe; after testing, the stability and precision can still be maintained with excellent functions after vibration. For vibration control during concrete placing, the JV adopts fully automatic vibrating system with external mold, which automatically adjusts to different vibration frequencies according to different times, so the concrete can reach an optimal state. With development of special measurement, checking on tools and equipment, as well as continuous testing, a great amount of energy is required at the stage of initial planning, so high level quality of the product can be acquired.

Strictly execution according to written document The significance of establishing the managing structure of ISO 9001 quality documentation system is to execute according to procedures, steps and methods contained in the documents instead of demonstrating the amount of execution. The records can even trace back to the very shift, date, assembly platform of steel cage, as well as the mold set placed and batch number of steel bar used. Any cause of disqualification can be traced, reviewed and further improved. Such mindset of high self discipline in quality control that is executed in accordance with written documents sets the foundation for excellent quality.

Looking at the bigger picture and performing from the details. The work from places that are neglected needs the concept of all-position quality operation. The spacer that controls the protective layer has never received attention; yet in order to achieve consistency of product appearance and material which are made with high strength ($>40\text{Mpa}$) cement mortar (Fig. 8). In order to achieve the perfect surface of a product, steel plates are used to extract residual bubbles on the surface after completion of concrete placing and vibration of external mold (Fig. 9).



Fig. 7 Slab storage area



Fig. 9 Plates to extract bubbles

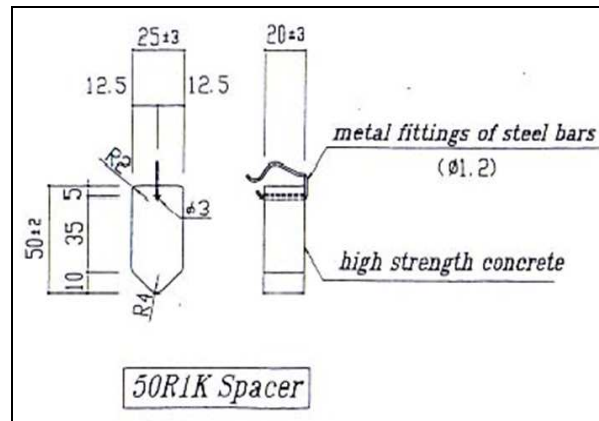


Fig. 8 Spacer

Putting training into practice: The training offered by JV to its personnel is divided into (1) Tool box talking: hazard notification and work reminder prior to daily commencement; (2) Training of new personnel: basic training of new personnel under legal regulations; (3) Professional training: training of occupational skills; (4) Regular training: training with time request or return; and (5) Special training: training for special personnel or technique.

References

- [1] C. Park, K. Kim, J. Kim, Y. Kim and S. Kim, "A study on the method of vibration analysis for Korean high speed train by the on-line test", *Key Engineering Materials*, v 321-323 II, p 1593-1596, 2006.
- [2] X. Chen, X. Tao, G. Cui and F. Wang, "Comparison on general track spectrum for Chinese main railway lines and track spectrum of American railway lines", *Advanced Materials Research*, v 250-253, p 3822-3826, 2011.
- [3] K.T. Chen, "Dynamic analysis of slab tracks", Master thesis, Civil Engineering and Disaster Prevention, National Taipei University of Technology. June 2002
- [4] C.A. Chen, "Evaluation and comparative study on performance efficiency of ballastless track for Taiwan Railways", Master thesis, Dept. of Harbor and River Engineering, National Taiwan Ocean University, 2002.
- [5] Information on <http://www.thsrc.com.tw/main/construct/track/05.asp>.
- [6] J.M. Xu, P. Wang, and D.Z. Xu, "Study on reasonable fastener stiffness of ballastless turnout's vibration decrease and noise reduction of 350 km/h passenger dedicated line", 2011 International Conference on Vibration, Structural Engineering and Measurement, Oct. 2011.
- [7] C.N. Cheng, "Light discussion on QA/AC of HSR civil works", *engineering gazette*, Mar. 24 2004.
- [8] "Compiled work information", THSR, 2004~2005.
- [9] "T220 inspection and test proposal", THSR, Oct. 2003.

Block Sand Mechanism Experiment and Analysis of Vegetation Flexible Dam

Feng Liu^{1, a}, Guang-Hui Wei^{1, b}, Liang Ma^{1, c}, Liang-Liang Chen^{1, d}

¹School of Water Resources and Civil Engineering, Xinjiang Agricultural University, Urumqi, China

^awlmqlf1999@163.com, ^bxndwgh@sina.com, ^cxjml1999@163.com, ^dxndcll@163.com

Keywords: Vegetation "Flexible Dam"; Turbid Water Experiment; Block Sand Mechanism

Abstract. By the indoor flume model experiment, this paper analyzed the block sand mechanism of turbid water appearance. The experiment was done under 1/150, 1/100 and 1/50 three base slopes with 5.09L/s, 9.08L/s and 13.08L/s three discharges. Carried on an observation to the variety that vegetation dam's in front and back single grain sediment sport speed, and silted up appearance with the sediment in the dam to carry on analysis before the dam to the plant. The experiment showed that the base slope is more big, the damping extent in sport in sediment in upper stream of vegetation dam's reduce more small, the sediment attains to lose the sand early more equilibrium, and the blocks sand result of vegetation dam is more bad.

Introduction

Plant "flexible dam" in the channel or canals, the main tank, and by certain plant spacing and line spacing, planting a certain number of sea buckthorn tree [1] Sea buckthorn is an Elaeagnaceae shrub, it has developed the spurious branches prone to deflection in the hydrodynamic effect, so called "flexible dam". It can slow down the rate of water flow, intercept flood backdrop of a large number of coarse sand, which is mainly of bed load sediment, sand fixation and restore the ecological role[2,3].

Plant "flexible dam" for the western region, in particular, provides a new idea for the Xinjiang region of sand prevention, combating desertification and soil erosion [4, 5]. College of Water Conservancy and Civil Engineering, Xinjiang Agricultural University, Hydraulic plant dam flume water model test laboratory in 2002 and 2003, respectively, to explore the plant dam in the ranks aligned and staggered under different planting densities on the canals flow[6, 7]. Derived from the experimental staggered plant "flexible dam" water blocking, sediment stronger plant "flexible dam" to reduce the flow shear stress, reducing the sediment delivery ratio, so that part of the sediment dam tour deposited, played the role of sediment trapping. Elam Sand mechanism in order to further study of plant dam, after the observation of plant dam to intercept coarse sediment deposition patterns, as well as the dam of the bedload sediment transport characteristics, we conducted a test flume muddy model[8, 9].

Test and Methodology

Test Equipment. This test is conducted in the hydraulic laboratory, Sink length 22m, width 0.4m, 0.5m high slot first with inlet valve and stilling basin, hydrostatic pool set up to eliminate the grid plate to stabilize the water. Sink the end has adjustable tailgate, fall into the tank water through the tailgate. The tank outlet is a rectangular thin-walled weir used to measure flow. With active stylus holder on the sink and read the water level, bed elevation can be measured. Sink at the top of the track with a scale, for the stylus holder moves and read the measured cross-section location. Sink orbit zero scale cross-section is denoted by the SC0+00 sections, 1m scale where the section is denoted by the SC1 +00, and the remaining section and so on according to the location of the scale. At the bottom of the sink-side consists of a fixed hinge, Activities located in the end of the bottom of the hinge of each one, used to adjust the tank bottom slope.

Selection of Model Tree Truly simulate natural sea buckthorn on water and sediment at the same time consider the similarity of the resistance and deformation of the trees, this test using the installed decorated with green plastic tree as a model tree. Plastic tree height of about 10cm long, trunk diameter of about 2mm, the upper branches and leaves, the top of the tree of the maximum transverse width of 7cm, and has a certain flexibility. Model tree roots can be used in a fixed circular hole, the test model tree is fixed in a socket on the grid. Model tree lined optimized water test water blocking the best of the $6\text{ cm} \times 9\text{ cm} \times 9$ ranks staggered arrangement shown in Figure 1, 6cm for the spacing in the rows, 9cm for spacing, 9 is the number of rows, 72cm dam planting a tree for 63 planting density of $248 / \text{m}^2$.

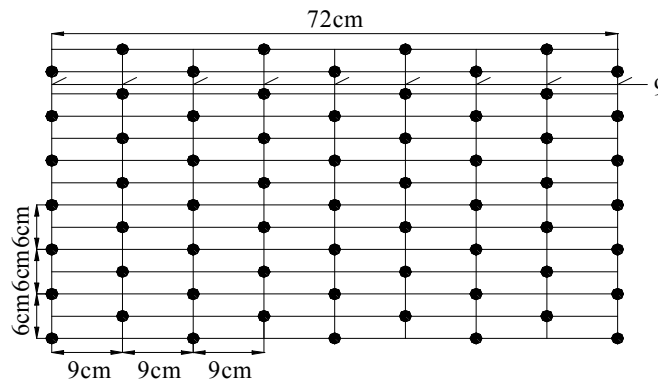


Fig. 1 Model tree layout mode schematic diagram

Model Scale In this study, the main rivers in Xinjiang coarse problem Through field investigation, the adult sea buckthorn tree height of about 10cm or so in about $1 \sim 2\text{m}$; plastic tree full test For convenience, this experiment, the main basis for the model height of the tree to determine the length scale, Normality test selection model using median diameter non-uniform natural sand bed load model sediment.

Pilot Program In order to simulate the natural groove of the side wall of bed load sediment movement, cement and coarse sand in the bottom of the tank and roughness, average roughness after roughening of 0.0165 Section at the front of the plant dam at SC8+00 The upper reaches of the inlet section in Gaza SC1+00 section. 1/150, 1/100 and 1/50 slope of the end of the three kinds of trials, each of the bottom slope of 5.09L/s, 9.08L/s, 13.08L/s, three kinds of traffic to test the three traffic in turn corresponds to not flooded, semi-submerged and submerged vegetation dam three cases.

Results and Analysis

Single Sediment Velocity Changes Before and After Planting Tree Trials observed the movement of sediment particles in the form of stop and go, but the closer the slower the movement of plant dam, we can only sample Deriving the average speed in each case were multiple sets of measurements in the upstream section of the plant before the dam, Last obtain the average. Speed measured by this method can not be a true reflection of sediment movement patterns, but there are some errors, but the qualitative description of the plant dam on sediment movement.

Table 1 is different from the bottom slope, after planting trees under different flow of different particle size range of a single sediment average velocity of the decay rate is calculated. It can be seen from Table 1, for the sediment of different particle size, the same slope the same flow, the velocity decay rate decreases with increasing particle size, and reduce minor; the same particle size and the same flow range, the speed decay rate decreases with increasing bottom slope, but the rate of decrease is relatively large. Sediment velocity of single particle analysis of test results prove that the bottom slope than the particle size should be large, the bottom slope the greater the smaller the decay rate in the sediment velocity of plant dam tour, plant dam sediment trapping effect of the worse. Meanwhile, the emergence of the plants before the dam backwater section of sediment movement speed of the front of the dam hinder math impact.

Analysis of Plants Dam Siltation Form Tank layout of the plant behind the dam, and tested in the SC1 +00 sections at a continuous sink Gaza. After the cessation of the test, you can see a certain thickness of sediment deposition in the plant before the dam and the dam. Test shows: different bottom slope, different flow and different sediment time sediment deposition in shape are more similar deposition in the surface are relatively flat, but the sediment deposition thickness, position, and vertical length.

the experiments show that the bottom slope of 1/150 and 1/50, similar to the results of the bottom slope of 1/100, which according to the following further The analysis just given plant dam caused siltation sink the bottom of the vertical and horizontal changes to the topography of a trend.

Cross-Analysis of Sediment Deposition Since the width of the test tank is only 40cm, so the transverse sediment depositions in the form of a performance for the whole section silt sediment deposition after the cross-sections are more rules, the shape is relatively flat. When the bottom slope of 1/150 and 1/100, close to the sink on both sides of the side wall at the deposition of small thickness, the midline deposition thickness, which is subject to the influence of the sink wall; the bottom slope is 1/50, due to the backwater of the instability and the impact of the waves, resulting in irregular transverse sediment deposition thickness.

The bottom slope steepening not only affects the longitudinal sediment deposition in shape, but also affected the lateral sediment deposition in shape with the bottom slope becomes larger, the plant dam tour at silting effect of variation will will affect the sand fixing effect of plant da.

Table 1 Single grain damping extent in average sport velocity after planting table

bottom slope	Particle size(mm)	flow(L/s)		
		5.09	9.08	13.08
1/150	4~5	100%	76.29%	76.76%
	3~4	100%	79.03%	74.88%
	2~3	100%	80.96%	76.30%
	1~2	100%	81.77%	74.31%
1/100	4~5	29.55%	23.21%	19.88%
	3~4	26.65%	22.86%	20.95%
	2~3	26.86%	20.58%	21.04%
	1~2	32.99%	17.29%	20.85%
1/50	4~5	8.05%	19.16%	18.75%
	3~4	7.06%	19.58%	21.70%
	2~3	7.69%	12.27%	20.87%
	1~2	0.92%	11.68%	19.40%

Longitudinal Analysis of Sediment Deposition The different flow of the bottom slope, sediment deposition thickness along the vertical increases gradually and forms a peak in front of the dam. The bottom slope of 1/150, flow and test a variety of sediment transport time, siltation strikers were not to reach the beginning of the vegetation dam cross section the SC8+00 cross section at; the bottom slope of 1/100, the flow respectively. in the longer sediment transport time, siltation forward before reaching the SC8+00 section; the bottom slope of 1/50, flow and sediment time, siltation forward reached the SC8+00 cross section. The first two of the bottom slope, the same flow, the longitudinal length of the sediment deposition as the sediment time to extend increases. And sediment deposition in the shape of the flow and sediment transport time, the smaller the flow sediment transport time is longer, the greater the thickness and length of sediment accumulation. 1/50 of the bottom slope, sediment transport time to the location of sediment deposition is not obvious. When silting striker is yet to reach the SC8+00 section, with the overall position of the bottom slope gradually become larger, sedimentation downstream movement; while When siltation striker has reached the SC8+00 section, siltation forward no longer move, only the tail continues to move downstream, the longitudinal length of the silting gradually become shorter.

The above results show that: the smaller the bottom slope, the wider the range of sediment deposition, sediment deposition in the same flow to the plant dam premises need the longer; the bottom slope, the greater, the sediment quickly reaches the plant before the dam, in plants produce a lesser extent, the dam of siltation. When sediment deposition to plant monolith length and thickness of sediment deposition with deposition in the time change and changes in upstream sediment siltation than smuggle through the plant dam to downstream sediment to be more, this time not yet achieve the sediment balance. The bottom slope of 1/150 and 1/100 of each flow and sediment transport time did not reach the sediment balance; the bottom slope of 1/50, the flow rate of 9.08L/s and 13.08L/s, respectively, sediment 6 hours and After four hours, the length and thickness of the sediment deposition and after two hours close to the sediment time to increase and there is no obvious change in sediment deposition.

Conclusion

It can be seen from the test: For the same flow of sediment of different particle size, the same slope, the velocity decay rate decreases with increasing particle size, and reduce minor; the same flow of the same size range, the velocity decay rate with increasing bottom slope decreases, but the rate of decrease is relatively large. The same flow rate, the bottom slope the greater the sediment sooner reach the sediment balance, and the deposition of the smaller the range, the sediment trapping effect of the plant dam worse.

Through the analysis of the experimental phenomena, we can draw the following conclusions:

A bottom slope of single sediment velocity than the mean diameter of the bottom slope the greater the smaller the decay rate in the plant dam tour sediment velocity, sediment retention worse the effect of plant dam.

To weaken the bottom slope greater impact could be considered more than a dozen plant layout of the dam, to extend the length of the segment of the backwater, a postponement of the sediment in the reach sediment balance of the time, while expanding the scope of sediment accumulation this can improve the fixing effect of the plant dam.

Plant Dam has good water blocking sediment retention, can significantly reduce the speed of movement of the dam of bed load sediment, a lot of sediment deposition in front of the dam down. Therefore, the plant dam is an effective method to solve the problem of the Xinjiang Rivers more than coarse.

Acknowledgement

This research work was supported by Xinjiang Agricultural University Preschool Project Funding (XJAU201008) and Xinjiang Water Resources and Hydropower Engineering Key Discipline Funding (XJZDXK2002-10-05). We give the most heartfelt thanks to the reviewers for their great contributions on the early manuscript.

References

- [1] Huai Wen-Xin, Han Jie. Experimental study on hydraulic behaviors of steady uniform flow in open channel with submerged flexible vegetation. *Journal of Hydraulic Engineering*, 2009, (7):34-40.
- [2] Huai Wen-xin, Xu Zhi-Gang, Yang Zhong-hua. Two dimensional analytical solution for partially vegetated compound channel flow. *Applied Mathematics & Mechanics*, 2008, (8):135-139.
- [3] Cheng Yan, Li Sen, Qiu Xiu-yun, etc. Study on flow characteristics of rivers and canals trees. *Journal of Xinjiang Agricultural University*, 2003, 26(2):59-64.

- [4] Yan Jie, Zhou Zhu, Qiu Xiu-yun. Plant flexible dam test and fixing water blocking mechanism analysis. *Journal of Xinjiang Agricultural University*, 2004, 27(3):40-45.
- [5] Huai Wen-xin, Han Jie, Zeng Yu-hong. Velocity distribution of flow with submerged flexible vegetations based mixing-length approach. *Applied Mathematics & Mechanics*, 2009, (3):151-158.
- [6] Dickinson, R.E., Coauthors. The Community Land Model and its climate statistics as a component of the Community Climate System Model. *J. Climate*, 2006, 19:2302-2324.
- [7] Thornton, P. E., and N. E. Zimmermann. An improved canopy integration scheme for a land surface model with prognostic canopy structure. *J. Climate*, 2007, 20:3902-3923.
- [8] Zhang Ming-liang, Chen Yong-ming, Wu Xiu-guang, etc. Compound section three-dimensional numerical simulation of floodplain flow. *Journal of Hydroelectric Engineering*, 2006, (5):16-19.
- [9] Ibrahim MB. Rainwater harvesting for urban areas: a success story from Gadarif City in Central Sudan. *Water Resour Manag*, 2009, 23:2727-2736.
- [10] Baguma D, Loiskandl W, Jung H. Water management, rainwater harvesting and predictive variables in rural households. *Water Resour Manage*, 2010, 3:427-441.

Study on the Deformation Characters of the Coal Roadways with Compound Rock Strata and Water Spraying Roof

Hong Yan^a, Tengfei Xu^b, Jun Wang^c

School of Resource & Safety Engineering, China University of Mining & Technology (Beijing),
Beijing 100083, China

^acumtbyh@foxmail.com, ^bxtfcool@126.com, ^cwangjuncumtb@163.Com

Keywords: Abscission Layer; Compound Rock Strata; Water Spraying; Bolt And Cable Support

Abstract. The coal roadways with water spraying usually have large surrounding rock deformation or roof abscission layer, especially to the roadways with compound rock strata roof, which could lead to sudden roof caving accidents, so it is imperative to research the roof characters and the corresponding controlling methods. In this paper, we firstly analyze the main reasons and characters of the roof deformation or its stability failure with bolt and cable supporting, and then the mechanical properties of the roof are tested in the lab, which could afford detailed datum to the further analysis. Based on the comprehensive researching results of this complex roof, a set of measuring device for the value of water spraying in single roof hole is developed and then applied to a typical coal roadway. Finally, some effective controlling methods are put forward to prevent from the large deformation of the roadways.

Introduction

With the continue increasing of the coal resource output in China, the bolt and cable combining support has been widely applied to the roadways in the coal mines because of these advantages such as the faster supporting speed, the weaker labor intensity, the lower supporting cost, etc than the traditional I-beam supporting. However, this type of roadways with water spraying and compound rock strata usually has large deformation or roof abscission layer, even leading to the collapse accidents when adopting the bolt and cable supporting. Many scholars have done lots of researches, [1] proposed a set of supporting design including bolt, cable, channel steel, grouting and gunite for the water spraying roadways suffering from high stress and had a field test in the Niuqiao coal mine. [2] Analyzed the loading layer and the roof pressure value combined with the deformation and pressure hypothesis of the roadway roof, and determined the proper supporting parameters of the typical roadway in Zhangji coal mine. [3] Mainly researched the influence between the draining water and the anchoring force according to the haulage gateway No.11201 in Chengjiao coal mine. [4] Further studied the mechanism of the loss pre-stressed bolting for the water spraying roadways, and proposed a new supporting technology containing high strength and high pre-stressed bolting, surface guniting and rock grouting. Although different kinds of supporting technology have been successfully tested on roadways with water spraying, the mechanical properties and deformation for the corresponding roof should be researched thoroughly, which could obtain the general controlling methods to prevent from the roof stability failure or caving accidents.

Deformation Mechanism of the Coal Roadway with Water Spraying

After excavation, the surrounding rock of the roadway usually has some roof subsidence or convergence, especially to the roadway with water spraying, as is shown in Fig.1. When adopting the traditional bolt and cable supporting technology, the roof water would flow along drilling hole, which not only seriously affects the whole strength of anchoring body formed by the bolt, cable and rock strata, but also weakens the supporting structure [5-6]. The deformation mechanism of the coal roadway with water spraying could be concluded as follows:

The early deformation stage. The surrounding rock of the coal roadway has a larger convergence, as the three-directional pressure switches to the two-directional pressure of the roadway. In this stage, the bolt and cable supporting system should afford proper pre-tightening force, and the whole roadway deformation exists and the flowing water in the roof has not effect in this stage deformation, however, the spraying water could have some bad influence on the anchor, bolt or cable.

The slow deformation stage during the roadway supporting, the spraying water in the roof could flow slowly along the drilling hole, which gradually weakens the strength of the immediate roof, such as siltstone, mudstone and fine sandstone, etc. As each stratum has different strengths and properties, the influencing results of the flowing water also have large discrepancy, and the corresponding deformation is different. The abscission layer forms at the junction of two rock strata, and the shallow rock stratum deformation is usually larger than the deep one above the excavating roadway roof.

The fast deformation stage if the roadway with water spraying supports well, this stage would not exist. However, many coal roadways suffer from the fast deformation stage. With the combined effect of flowing water and weathering factors, the immediate rock stratum would have lots of fractures and damage the whole roof and supporting strength, leading to the large roof deformation. In addition, the flowing water also seriously affects the strength of two coal sides and decreases the supporting effect. For some coal roadways, the fast deformation of the surrounding rock could turn to the final roof caving accidents with the weak supporting structure.

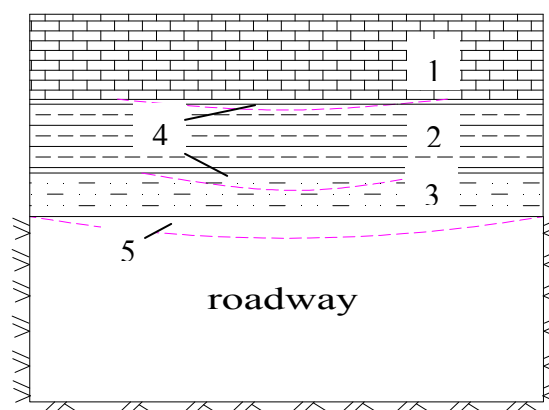
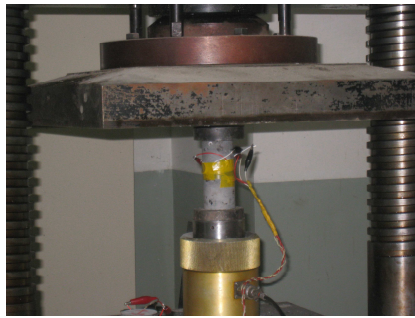


Fig.1 Roof abscission layer and deformation (1, 2, 3-rock strata, 4- abscission layer, 5-roof deformation)

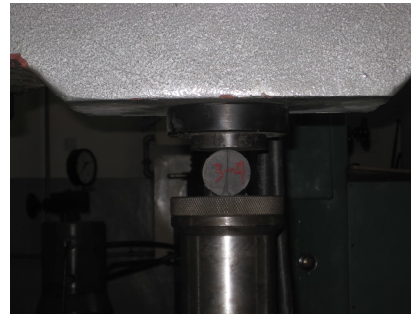
Roof Mechanical Properties Test and the Spraying Water in Drilling-Hole Measuring

For the type of coal roadways with water spraying and compound roof, it is important to analyze the roof mechanical properties before determining the supporting design and concrete parameters. According to the testing results of the roof mechanical properties, the influencing effect of the

spraying water to the roof strata could be further researched. The chosen coal roadway with spraying water and compound rock strata roof is rectangle with 3.8 m wide and 2.7m high, the immediate roof contains siltstone and coal strata, and the basic roof is limestone. The testing contents in the lab mainly include uniaxial compression, shearing and split tests, etc. As is shown in Fig.2, the testing results are as follows,



(a) uniaxial compression test



(b) split test

Fig.2 Rock mechanical properties test

Tab 1. Physio-mechanical parameters

Lithology	UCS [MPa]	EM [GPa]	PR —	TS [MPa]	IFA [°]	C [MPa]
Coal No.9	2.26	3.15	0.146	0.386	28.20	1.67
Siltstone	53.72	19.72	0.197	13.374	33.37	29.59
Limestone	74.03	65.91	0.216	9.407	36.99	30.87

According to the Tab.1, the uniaxial compression strength (UCS) of the coal No.9 is far lower than the siltstone and limestone, respectively accounting for 4.21% and 3.05%, so the abscission layer is easy to form after roadway excavation and could increase along with the supporting time. To the shear strength (SS) and tensile strength (TS), the value of the coal No.9 respectively accounts for 5.64% and 5.41% for SS and 28.86% and 41.03% for TS. From the above testing and analyzing results, the mechanical properties have great discrepancy among them, so the roof deformation might occur, especially to the limestone stratum containing water. The traditional bolt or cable support breaks the original balance tension of the flowing water and the water flows along the drilling hole, which might weaken the strength of the coal No.9 and the siltstone stratum and lead to a large deformation. However, different roof region has different water content along the trial roadway. The next step is to measure the water spraying of the roof drilling hole and then put forward the controlling methods.

As is shown in Fig.3, a device for measuring the water spraying of the roof drilling hole is designed and then applied to the trial roadway. Combined with the field testing results, the roof region could be classified to the water seepage and gushing region. The strong spraying water and weak gushing water are respectively 72-96mL/s and 126-143mL/s, which accounts for 61% of the trial region and forms the main style of the spraying and gushing water in the roof. Besides, the weak and general spraying water account for 39% of the trial region.

Controlling Strategies to Coal Roadways with Water Spraying and Compound Roof

From the above analysis results, we can obtain these conclusions: (1) The compound roof is easy to form the abscission layer at the junction between the two rock strata, so it is important to choose a proper supporting style and determine parameters. (2) The condition of water spraying in the roof could fasten the deformation development of the coal roadways, which weakens the anchoring force and corresponding strength of the supporting structure, as is shown in Fig.4, so it is important to prevent from the influence of the water in the roof, such as adopting the new style anchor agent, increasing the drainage hole in the rich water region, grouting in broken and soft strata, etc.

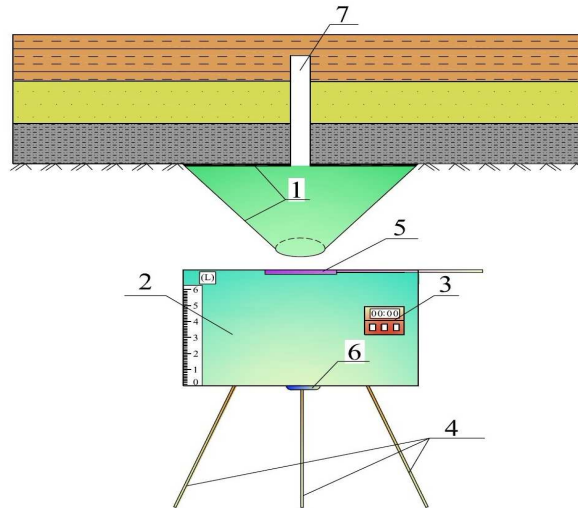
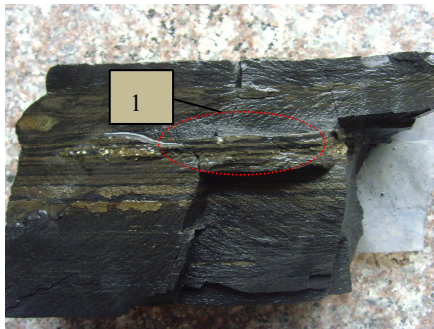


Fig.3 Device for measuring the water spraying of the drilling hole in the roof (1-funnel cloth felt, 2-cylinder measurement vessel, 3-timber, 4-foldable tripod, 5-open/closed plate, 6-water releasing button, 7-drilling hole)



(a) Water spraying action



(b) combined effect by water and weathering

Fig.4 Siltstone influenced by spraying water or weathering (1-fractures, 2, 3-the broken rocks respectively in horizontal and vertical direction)

Conclusions

The roof deformation mechanism of coal roadways with water spraying is analyzed, which could be classified to three stages, and the roof mechanical properties test and spraying water in draining-hole measuring are done respectively in the lab and typical field coal roadway.

Some controlling strategies to prevent from the large deformation of the coal roadways with water spraying and compound roof are proposed, which mainly aim at weakening the roof abscission layer induced by the factors of compound roof, water spraying and weathering action.

Acknowledgements

Work is financially supported by the Fundamental Research Funds for the Central Universities (2010YZ02).

Literature Reference

- [1] Jianwei Nie, Xinchun Zhong. Bolting beam mesh supporting design and application analysis on striking roadway with combined roof[J]. Coal Engineering, 12(10), 2009, 28-30. (In Chinese)
- [2] Qiangwei Chen. The application of comprehensive supporting technology on roadways locating in synclinal axis suffering from high stress and water spraying[J]. Coal Mining Technology, 12(2), 2007, 39-41. (In Chinese)
- [3] Panfeng Gou, Qiyong Chen, Sheng Zhang. Influence analysis of the anchor-hold of the resin bolt by the draining water in the drill hole[J]. Journal of China Coal Society, 29(6), 2004, 680-683. (In Chinese)
- [4] Mingshi Gao, Nong Zhang, Lianfu Zhang. Synthetical control technique and engineering application to roadway with false-hard roof high surrounding pressure and water disturbance[J]. Chinese Journal of Rock Mechanics and Engineering, 24(21), 2005, 3996-4002. (In Chinese)
- [5] Fulian He, Hong Yan, Lv gang Yang, etc. Anchorage experimental research on a coal roadway with water spraying and broken roof and its application[J]. Rock and Soil Mechanics, 32(9), 2005, 2591-2595. (In Chinese)
- [6] Qiangling Yao, Xuehua Li, Qundi Qu, etc. Supporting countermeasures and roof falling mechanism reacting with water in mudstone roof roadway[J]. Journal of Mining & Safety Engineering, 28(1), 2011, 28-33.

Calculation Method of Upgrade and Side Strengthening Old Bridge based on Applied Mechanics

Xiang-chao Zeng, Jing-yan Wang

Southwest forestry university civil engineering college, Kunming, yunnan, zxcgzz@sina.com

zxcgzz@sina.com

Keywords: Bridge, Reinforcement, Upgrade

Abstract. Bridge of Car 15 levels will be upgraded to Car 20 levels, in order to meet the current heavy traffic. This article introduces reinforcement scheme, and the scheme of mechanical analysis, the reinforcement design calculation, and the corresponding conclusion. Reinforcement measures for, by simply supported a bridge deck continuous (two across connect), increase the clapboard to enhance structure integrity, stick steel to the side of the beam etc. The test is satisfactory.

Introduction

Because of the economic [1] constraints, many old unsafe bridge and overload bridge in China's western region (especially Yunnan and guizhou plateau area) continues to use [2]. Consideration the economic efficiency, research of the key technology about the old bridge reinforcement and upgrade become one urgent task [3].

The domestic and foreign established principle for choose the corresponding reinforcement methods: Whatever type of strengthening plan should be considered less investment, efficiency, can not interrupt traffic, feasible in technique, good durability performance, and so on. The methods of structure reinforcement are: pressure grouting method, jet mortar method, the reinforcement layer of bridge deck reinforcing, the beam of steel plate and stickup law, increase the clapboard method, change the structure system reinforcement, and prestressed reinforcement method, seam filling Method [4]. Pressure grouting method, spraying mortar method and seam filling method are used for repatching the crack of concrete or brick, and repairing surface defect. The rest of the reinforcement, reinforcing measures will be used to improve the bearing capacity and traffic capacity of the existing bridge.

The Shear Strength Calculation Method about the Bonding Steel Beam

The Statement of Shear Strength

Quoted the expression of the shear strength, the final shear strength of the bonding steel beam composed of concrete contribution, the contribution of steel reinforcement. The shear force expression about the beams of the steel plate is as follows [5]:

$$V_n = V_c + V_s + V_p \quad (2)$$

Concrete contribution (V_c) and stirrup contribution (V_s) showed by the formula below (3) and (4) respectively

$$V_c = 0.2 f_c^{1/3} (1 + \beta_p + \beta_d + \beta_n) [0.75 + 1.4 / a / d] b_w d = 94 \text{KN} \quad (3)$$

$$\beta_p = \sqrt{p_w} - 1 \leq 0.732$$

$$\beta_d = d^{-1/4} - 1, \beta_n = 2M_d / M_u,$$

$$V_s = \left[A_v f_{yv} (\sin \alpha + \cos \alpha) / s_v \right] Z = 64 \text{ kN} \quad (4)$$

The shear strength (V_p) contribution of the bonding steel to beams considers the shear Impact [12] of the steel thickness and width:

$$V_p = \tau_{avg} h_p t_p \quad (5)$$

Here h_p is the width of the steel plate, t_p is the thickness of the steel plate beam two paste, τ_{avg} is an average of the plate shear stress. Maximum shear stress (τ_{max}) and the relationship between the average stress is as follows

$$\tau_{avg} = 2/3 * \tau_{max} \quad (6)$$

Maximum shear stress of the plate and the yield strength of the formula are as follows:

$$\tau_{max} = f_{yp} / 2 \quad (7)$$

This study focus on the application of the methods of side-reinforced concrete beam, do the experiment as follows:

Side-Reinforced Concrete Beam Test

Introducing the Experimental Beams in Detaile

The size of the beams for: 150 mm (wide) x 200 mm (high) x 2400 mm (long). Beams in compress area are conFig. d two steelbar of $D = 22$ mm, in the tension zone conFig. d three steelbar of $D = 22$ mm, stirrup for both limbs and $D = 6$ mm and spacing 170 mm. But, all of the beam are designed to shear failure, which using steel reinforcement may increase the shear strength of the beam. Beam A-1 were not strengthened for comparison, the rest of the beams reinforced. Two of the 2200 mm long steel were used to reinforcement, thickness were 2.3, 4.5 and 6.0 mm, and width of 100 mm and 150 mm respectively. The features of reinforced beam and steel plate shows in table 1. Before steel plate bonding, both sides of the beam brush cut clean with grinding wheel, steel surfaces also be cleaned up. On the surface of the steel and concrete set aside 2 mm gap, then fixated plate at the sides of the beam with $D = 10$ mm and $L = 50$ mm expansion bolt anchor. After seal the three face of the plate, encapsulate glue. There are at least 14 days of maintenance before loading. The characteristics of the encapsulating glue are in table 2; the differences of the test are in table 3.

Table 1 Properties of reinforcement and steel plates

steel plate	Yield strength(MPa)	Elastic modulus(GPa)
Steelbar diameter(6mm)	346	192
Steelbar diameter(22mm)	391	186
Steelplate`thickness(2.3mm)	378	209
Steelplate`thickness(4.5mm)	382	198
Steelplate`thickness(6mm)	398	210

Table 2 Properties of epoxy adhesive (after 7 days of curing)

tensile strength(MPa)	compressive strength(MPa)	Shear strength (MPa)	Modulus of elasticity(GPa)
49.0	72.0	15.6	2.13

Test Procedures and Equipment

The entire beam is loaded in the span of four loading in the 1940 mm length. The ratio of Shear span and effective height is for 3 in all these trials. Record the stress in reinforcing components, or the steel plate surface, or the concrete surface of the different positions. Testing instrument and the

center of the shear span correspond the bottom and middle connection of the steel plate. The displacement of the beams across the middle is measured by instruments for centigrade meter; the occurrence and extension of crack are monitored by instrument.

Table 3 Experimental variables

Beam Numbers	concrete strength(MPa)	Steel thickness (mm)	Steel plate width (mm)
C-1	38.6	-	-
C-2	42.5	2.3	100
C-3	41.5	4.5	100
C-4	37.6	6.0	100
C-5	42.0	2.3	150

Test Results and Discussion

Damage of the Strengthened Beam and the Limit Load

Table 4 Experimental results:

Beam Numbers	the strength of the visible cracks(MPa)	the strength of the final shear strength(kN)	the relative strength
C-1	36.7	98.2	1.00
C-2	63.7	116.4	1.19
C-3	63.3	106.3	1.08
C-4	63.7	126.4	1.29
C-5	80.8	132.4	1.35

Table 3 shows all the destruction of the loading beams. As expected, all of the beams happens shear failure, including of the reinforced beam. During all the non-reinforced beam, the first visible cracks occur in load shear for 36.7 kN. With the load increasing, the crack become bigger and the strain meter reading increases rapidly, and eventually the beam damage in 98.2 kN. Other beams bonding steel shows the same destroy form, but less crack numbers. Mainly the main fracture over parts of steel plate led to the destruction in the end. Soon to be limit state, steel plate strip and bend down, at the same time the concrete between the two cracks in the shear span be crushed. Due to anchor bolted beyond shear span, the role of the bolt not too big. But if bolted in shear span or close to it, the bolt will affect the steel bending strength, so as to will play a large role to the shear strength of beam eventually.

Load Displacement

Fig. 3 shows the relationship between the load and displacement that all of the experimental beams. The beams bonding the steel plate have better shearing ability than not. The beam bonding the thicker and wider have better strength than the steel beam bonding thinner and narrower steel plate. Research shows that C-4 displacement deformation reduces most, less than C-1 about 34%. On the other hand, displacement deformation of beam C-2 and C-5 fell about 25%. And the displacement deformation of the two beams decrease almost the same. The displacement deformation of beam C-4 decrease 40% in near the critical load.

Relationship between the Load and Displacement

Load (kN)

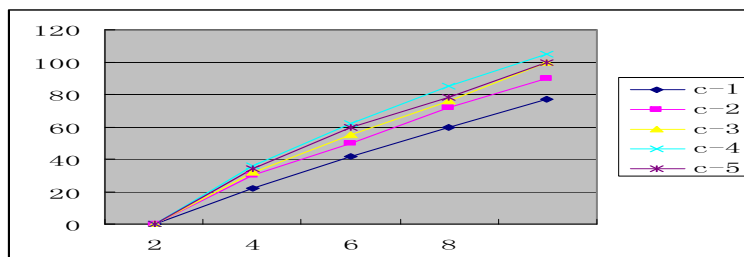


Fig. 4 Load versus mid-span displacement relationships for test beams. Load(kN)

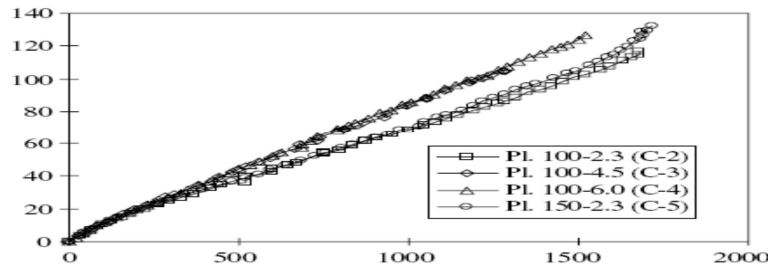


Fig. 5 Steel plate strain in mid-span of beam (horizontal) Strain

From the formula (5)-(7), we can conclude

$$V_p = f_{yp} h_p t_p / 3 = 180 \cdot 400 \cdot 5 / 3 = 120 \text{ kN} \quad (8)$$

But, unlike stirrup anchored in concrete, steel reinforcement cannot completely yield.

Eventually, $V = 158 + 120 \cdot 2 = 398 \text{ KN}$

Test results show that the method of reinforcement can improve beams in shear strength validly, and show that shear function is also increasing with the increase of the steel plate width and thickness, also show that the steel should be maximum width in order to achieve maximum contribution. Using thicker steel plate can't make shear strength in proportion to increase. Wider than thicker steel have better reinforcement effect.

Conclusion and Discussion

Put forward the calculation formula of the ultimate bearing bended capacity about the steel reinforced beam under the damage mode, through the analysis and calculation shows that: when steel reinforcement are in a certain amount, only the second beam failure mode happen within the scope of the steel reinforcement, and the yield strain of steel plate also have an influence on bearing capacity. In order to make full use of steel, reinforced beam should be controlled to happen the second failure mode, and yield large steel strain should be suggested to use in the reinforcement design.

From the bridge reinforcement examples we can see that the bearing capacity of steel-reinforced beam can be increased by more than 20%, meeting the super-heavy traffic demand. And the construction is simple, convenient. Also it can be constructed under the condition of no break traffic, which can greatly reduce the construction cost. We should say that the preferred solution is reinforced scheme. The situation discussed is the overload vehicles alone and double row vehicles across the bridge. I personally think that it is necessary to consider allowing more vehicles across in the reinforcement of the beam, to meet the developing needs of the traffic in the future. In the scheme we adopts laying steel deck on the bridge, increasing the number of wheel oneself to get scattered concentrated loading, and increasing the overall strength, to solve the problem of strength. But this is only temporary solution. And it can not solve the problem of bearing capacity. Only implement permanent reinforcement, can solve this problem. The article discusses that the method of steel-reinforced beam should be the ideal reinforcement scheme.

References

- [1] Bao An-gong, Lin Wen-xiu, Yan Xue-gang. "Engineering mechanics" of the steel plate thickness of steel reinforcement stick the influence of beam stripping finite element analysis"
- [2] Yue LiJie, Zhang JiWen. "engineering mechanics": supplement the CFRP reinforced concrete side stick flexural capacity of practical calculation method"
- [3] ShaoXuDong. "the bridge project " People's Traffic Press, 2003.10.
- [4] WangZhenQing. the highway overloading transportation introduction, People's Traffic Press, 1997
- [5] The People's Republic of China Department Standards: The Highway Engineering Technical Standard, 1981

Experimental Study on Double Truss Cable Supporting System of Coal Roadways in the Isolated Coal Pillar and Fold Region

Hong Yan^a, Tengfei Xu^b, Yang Li^c

Collage of Resources & Safety Engineering, China University of Mining & Technology (Beijing),
Beijing 100083, China

^acumtbyh@foxmail.com, ^bxtfcool@126.com, ^c405995305@qq.com

Keywords: Coal Roadway; Isolated Coal Pillar; Fold Region; DTCSS

Abstract. The gangue in parts of underground coal mines in China is not to be hoisted to ground for direct accumulation but replace the coal resource in larger residual coal pillars. In order to solve the supporting problem of roadways in the isolated coal pillar and tectonic region, we firstly research the relationship between the supporting effect and fold or isolated coal pillar factor. Based on the analyzing results, the double truss cable support system (DTCSS) is proposed, and then the corresponding support structure and superiority are studied. Finally, a typical complex coal roadway affected by factors of synclinal axes, isolated coal pillar and intersection with another roadway was experimented using DTCSS, and the monitoring results of the roadway displacement showed that both of the largest roof subsidence and the convergence of both sides were no more than 170mm, which ensured the roadway safety and proved the efficiency of the DTCSS.

Introduction

With the rapid development of the mining and supporting technologies in China, the number of ground gangue in the coal mines is also increasing. According to the statistical data in the year 2007, there is about 0.35 billion tons gangue around the coal mines, which mainly leads to the health hazard, damages the surrounding ecologic environment, occupies the massive land, etc, so it is important to reduce the gangue by adopting the filling method or other treatments. [1] Respectively analyzed the whole filling technology design with gangue, the filling technology in fully-mechanized and conventional mining face. [2] Researched the coal resource green mining and discussed the corresponding technologies system, and proposed the methods to reduce gangue such as optimizing roadways layout, increasing the number of coal roadways and decreasing the number of rock roadways, which also afford a supporting problem to difficult coal roadways. [3] Analyzed the surrounding rock stability of the high stress roadway combined with the numerical simulation and obtained the weak supporting location, which was controlled well with non-uniform support technique system. [4] Concluded the development of bolting technology for the coal roadway in China, and further introduced the bolt and cable supporting application to the complex roadways. [5] Mainly studied the relationship between the tectonic stress and the stability of roadways and got the results that the horizontal stress affected the roof abscission layer and reduced the shear strength of the roof strata which could lead to roof caving with the development of the roadway deformation. However, these complex roadways in the isolated coal pillars and tectonic region are difficult to support and desiderate to solve.

Supporting Stability Analysis of the Roadway in the Isolated Coal Pillars and Tectonic Region

Generally speaking, the layout of coal roadways in coal mines is considered to be cautious because of the effect of horizontal and vertical high stress, especially to the tectonic region or deep mines. Some isolated coal pillars are large, in other words, the isolated coal pillars contain plenty of coal resources which should be gradually mined from the perspective of energy saving. So it is a very well by excavating roadways in the isolated coal pillar and filling the gangue from the other rock roadways. Although the field supporting test has been done many times in these coal roadways with analogous geological conditions, the deformation of the surrounding rock is still very large, which not only affects the workers safety but also seriously reduces the number of the filling gangue.

With the high stress in the isolated coal pillars induced by the mining effect of near two sides working faces, the excavated roadways inside the pillar are difficult to support. For the I-beam support style, as the high stress applying to the support structure is non-uniform, the weakest rock strata region such as two abutments between the shallow roof strata and the I-beam structure, the middle shallow rock strata or coal stratum of the roof and both sides, and this type of support could not bear continuous high stress. Besides, the I-beam support belongs to the passive supporting, that is, until the roof deformation happens, this support could make action, so choosing the I-beam support has a low successful rate to control the high stress roadways. When adopting the bolt and cable support, although it is a type of positive support and could apply the pre-tightening force to the surrounding rock of roadways with high stress, the supporting force could not balance the horizontal and vertical loads, especially to the formed low supporting strength or the higher ground stress in the tectonic region, the single supporting style of bolts and cables system could not control the roadways well, as is shown in Figs.1 and 2.



(a) Damaged cable

(b) broken bolt pallet

Fig. 1 The broken cable and bolt pallet (1, 2— the concrete broken location)



Fig. 2 The surrounding rock deformation of the roadway in high stress

(1, 2-the initial and final shape of the roadway, 3-roof subsidence, 4-the convergence of both sides)

New Supporting Style to Roadways with High Stress—Double Truss Cable Support System

According to the above analyzing results, both of the conventional I-beam support or bolt and cable support could not effectively control the continuous deformation of the surrounding rock of the roadways in the isolated pillar and tectonic region, so it is very important to develop another supporting style for the complex roadways. The double truss cable support system (DTCSS) is proposed and has some advantages to control these high stress roadways than the conventional support structure. The single truss cable support system (STCSS) has been widely used in lots of complex roadways such as soft surrounding rock, large cross-section, compound mudstone roof roadways, etc [6-7]. The STCSS aims at preventing from the large roof deformation or rock strata convergence, which could ensure the roof safety during the roadway service, and has been proved to keep roof stability to the above roadways. However, as these roadways suffering from high tectonic stress, it is not enough to support roof well, and the two coal sides also have large convergence, so the DTCSS is the improvement result of the former STCSS. The characters comparison between the STCSS and DTCSS are shown in Tab.1, and the supporting structure of the DTCSS is shown in Fig.3. Combined with the DTCSS and conventional bolt, both of the roof and two sides of roadways suffering from high stress could be supported well.

Tab.1 Comparison between the STCSS and DTCSS

Support style	STCSS	DTCSS
Comparison index		
Supporting location	roof	roof and two coal sides
Adapting to roadways	large cross-section, compound mudstone roof, dynamic pressure roadways	high stress roadways, intensive dynamic pressure roadways
Pre-tightening force(Yes/No)	Yes	Yes
Length of the cable	>6m	>6m(roof), 4-6(both sides)
Matching the bolt or single cable(Yes/No)	Yes	Yes

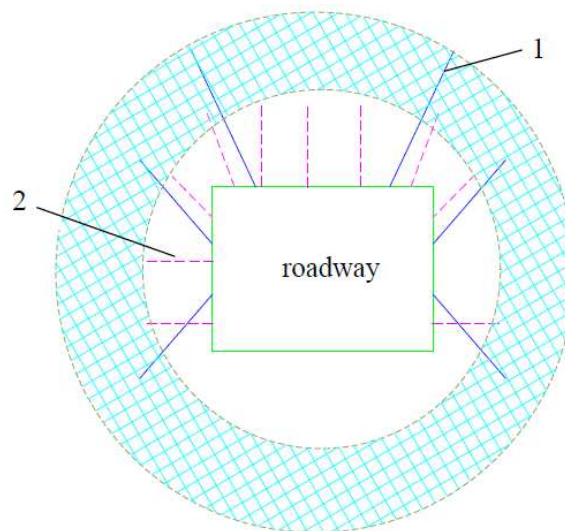


Fig. 3 Supporting structure of the DTCSS (1-cable, 2-bolt)

Field Experiment of the Typical Coal Roadway with DTCSS

The chosen coal roadway for the field experiment is affected by factors of synclinal axes, isolated coal pillar and intersection with another roadway, so the surrounding rock of the roadway bears extremely high stress. The cross section of the roadway is rectangle with 4.5m high and 4.5 m wide, the roof strata of the roadway mainly include fine sand stone, carbon mudstone and siltstone strata. Combined with the field geological conditions, numerical simulation analysis results and investigation of the analogous roadway deformation, the final concrete supporting design and parameters are determined. The field supporting experiment results show that both of the largest roof subsidence and the convergence of both sides are no more than 170 mm, which ensure the roadway safety and prove the efficiency of the DTCSS.

Conclusions

The supporting stability of the roadways in the isolated pillars and tectonic region are researched in detail and some of the roof failure reasons for conventional supporting styles controlling high stress are further analyzed, which include non-uniform load to positive I-beam support, the weak support strength to I-beam and bolt and cable combining support, etc.

A new supporting style (DTCSS) to roadways with high stress is put forward and the supporting structure is thoroughly introduced. In addition, some main characters between STCSS and DTCSS are compared, which show that the STCSS aims at the roof stability of complex roadways, and the DTCSS is superior to the STCSS for supporting the roadway with high stress.

The observation results of the trial roadway suffering from extremely high stress showed that both of the roof subsidence and convergence of two sides were little, which proved that DTCSS could effectively reduce the roadway deformation and ensure the roadway with high stress safety.

Acknowledgements

Work is financially supported by the Fundamental Research Funds for the Central Universities (2010YZ02).

Literature Reference

- [1] Xiexing Miao, Minggao Qian. Research on green mining of coal resources in china: current status and future prospects *Journal of Mining & Safety Engineering*, 26(1), 2009, 1-14. (In Chinese)
- [2] Minggao Qian, Xiexing Miao, Jialin Xu. Green mining of coal resources harmonizing with environment *Journal of China Coal Society*, 32(1), 2007, 1-7. (In Chinese)
- [3] Xuehua Li, Qiangling Yao, Nong Zhang, etc. Numerical simulation of stability of surrounding rock in high horizontal stress roadway under overhead mining *Journal of Mining & Safety Engineering*, 25(4), 2008, 420-425. (In Chinese)
- [4] Jinhua Wang. New development of rock bolting technology for coal roadway in China[J] *Journal of China Coal Society*, 32(2), 2007, 113-118. (In Chinese)

- [5] Yan Lu. Research on the stability theory and control of roadway surrounding rock in tectonic stress field [Ph.D. dissertation]. Xuzhou: China University of Mining and Technology, 2008. (In Chinese)
- [6] Fulian He, Dongpin Yin, Hong Yan. The control of thick compound roof caving on a coal roadway. *International Conference on Mine Hazards Prevention and Control*. Qingdao: Atlantis Press, 2010, 717-721. (In Chinese)
- [7] Hongliang Zhao, Jingming Yao, Fulian He, etc. Application of prestress truss cable in large cross section coal roadway. *Journal of China Coal Society*, 2007, 32(10), 1061-1065. (In Chinese)

Application of Fracture Prediction and Modeling Technology in Tight Sandstone Gas Reservoir in Xinchang Gas Field of Sichuan Basin

Qu Liangchao^{1, a}, Bian Changrong^{2, b}

¹School of Energy Resources, China University of Geosciences, Beijing 100083, China

²SINOPEC Petroleum Exploration & Production Research Institute, Beijing 100083, China

^ahnnnyqlc@126.com, ^bjsyzbcr@tom.com

Keywords: Tight Sandstone; Fractured Gas Reservoir; Curvature; Fracture Prediction

Abstract. To adopt new generation global optimization discrete scanning technology in 3D space, the seismic event occurrence can be scanned accurately. By means of analysing the relationship between fracture density of wells and seismic geometry attributes scanned precisely, it is concluded that pixel imaging attribute is effective to predict large scale fracture and curvature for small scale fracture. Based on fracture analysis, making use of lithology and curvature as constraints and starting from the well data, the density of the large scale fracture with seismic level and small scale net fracture can be predicted. According to the structure and production condition of wells, the area with fractures developed and in structural high is the advantageous area for exploration and development.

Introduction

In recent years, with the development of proven and producing reserves in low permeability reservoir, the tight sandstone fractured reservoir has played an important role in petroleum exploration and development. There are many geological factors to affect fracture development. At present [1, 2], fracture prediction technologies in domestic and abroad are generally summarized from three aspects [3, 4]: (1) tectonic stress field and curvature; (2) geostatistics method; (3) full use of seismic data. A new generation of global optimization discrete scanning technology in 3D space can accurately capture the occurrence information of seismic event, combined with the imaging logging data, seismic geometry attributes can be optimized and then to predict the fracture distribution.

The Triassic sandstone gas reservoir in Xujiache formation is a tight sandstone fractured reservoir in Xinchang gas field of Sichuan Basin. With the exploration and development, the reservoir shows a great heterogeneity-with average porosity just 3.8% and matrix permeability less than 0.3 mD. There are 2 wells with fracture developed and have a high gas production, fractures provide the permeability for gas flowing. The main factor deciding reservoir heterogeneity is the spatial distribution rule of fractured reservoir [5]. How to get information which can reflect fracture from seismic data and how to analyse and establish the relationship between fracture information and seismic attributes in well point, thus quantitative fracture prediction can be realized. So it is very urgent to solve this problem in exploration and development of the field

The Method of Fracture Prediction

The effective fracture in Xujiache formation of Xinchang gas field is structure fracture developed in late time, the area with fracture and tectonic deformation are closely related [6]. According to the geological characteristics, drilling and seismic data, using the relationships of fracture information in wells and the seismic geometry attributes which can well reflect fracture in well, quantitative fracture prediction can be realized and guide the exploration and development in this region.

Principle

The facts that strata is faulted and folded are the main reasons to produce structural fractures, and the curvature, coherence and edge detection, etc. from seismic data can well reflect the strata folding and rupture, all of these can help us to predict fractures. But fracture research can not be

done without fracture analysis, through the analysis from imaging logging, core data and fracture density, strike, opening, the relationship can be established between fracture density curves and seismic attributes. Fracture density model can be built through fracture density cube, parameters of fracture distribution can be gotten, and equivalent permeability model can be obtained by upscaling.

The New Generation Scanning Technology for Seismic Geometry Attributes

Previous fracture prediction depends more on seismic geometry attributes such as coherence, they all have shortcomings: it is easily affected by reflecting strength; the area with strong reflection strength often has high coherence. The reason is that there has a limitation to compute seismic geometry attributes, the accuracy is not enough, occurrence can not be scanned accurately, of course, and seismic geometry attributes such as coherence can not be calculated accurately.

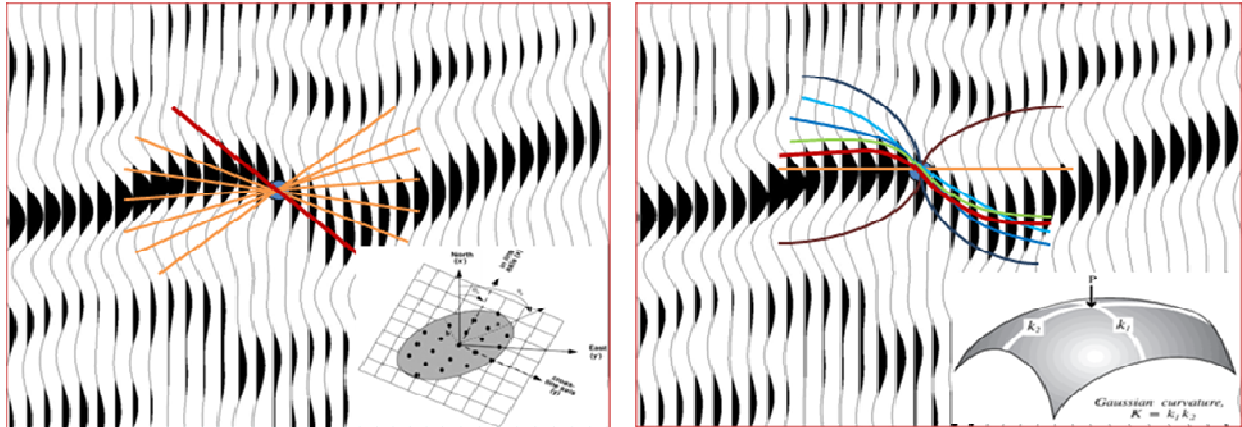


Fig. 1 The global optimization discrete scanning technology in plane and curved surface

There has a long history for seismic geometry attribute based on discrete scanning, from the first generation (based on similarity of 3 trace coherence), the second generation (based on covariance matrix of multi-trace coherence) to the third generation (based on covariance matrix of characteristic value), these algorithms are scanning occurrence of the seismic event in a plane. As Fig 1 shows, if the plane is too small, it can not be clearly scanned, if the plane is too big, it can produce many errors because the occurrence is a curved surface in 3D space [7, 8]. The new generation of global optimization discrete scanning algorithm in 3D space, it's scanning face is no longer a plane, but a curved surface, each point is scanned in 360° range [9], the occurrence will be more accurate, and more corresponding to occurrence of the actual strata. The seismic geometry attributes will be more accurate based on global optimization discrete scanning technology in 3D space.

Fracture Analysis

Fracture is the main flow passage for tight sandstone fractured reservoir in Xujiahe formation of Xinchang gas field. According to the size of the fracture [10], large scale fracture, small scale fracture and micro fracture can be divided in Xujiahe reservoir. Large scale fracture refers to the fracture with seismic level.

Small scale fracture refers to the fracture which length is in a few centimeters to several meters. Usually, small scale fractures are distributed anywhere in 3D space, and interweave to mesh, it can form the seepage channel, the bigger probability of small scale fractures interweaving into nets, the bigger contribution to the reservoir permeability. The probability of small scale fractures interweaving into nets is proportioned to fracture density, fracture trend variation and fracture length.

Micro fracture refers to the fracture which can be identified through the core slice, normally it's length is millimetre level. Micro fractures usually accompany with the matrix, is a part of matrix.

Fracture Prediction

Fracture prediction includes large scale and small scale fractures prediction. Large scale fractures can be directly detected according to the pixel imaging attribute. Based on wells, the fracture density of small scale fractures can be predicted with the seismic geometry attributes as constraints. According to the fracture density cube, fracture dip and azimuth in different group can be sorted, discrete fracture grid model can be established based on object modeling algorithm.

The Application of Fracture Prediction Technology in Xinchang Gas Field

The large scale fracture in Xujiache formation of Xinchang gas field relatively developed. Pixel imaging attribute shows that large scale fractures are mainly distributed along the fault zone, they can be divided into three groups: N60°(Northeast), N90°(Eastwest) and N120°(Northwest).

The small scale fractures in Xujiache formation of Xinchang gas field are mesh fracture. The open conductive fracture, drilling induction fracture and high resistance fracture can be identified through the imaging logging. There is a good relationship in strike between large scale fractures and small scale fractures, small scale fractures mainly developed near the main fault zone, curvature is a good instruction to tectonic deformation and available to predict small scale fractures.

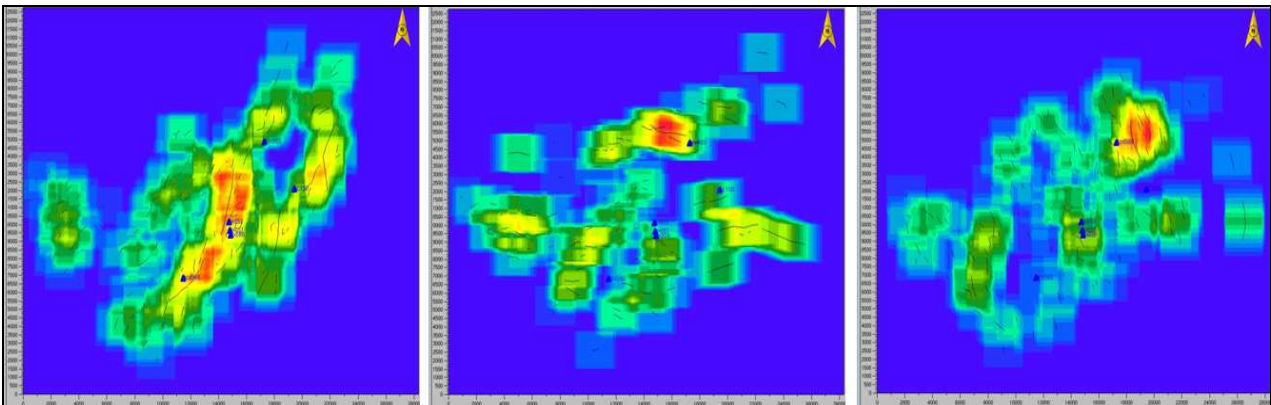


Fig. 2 The layout of large scale fracture density in N60° , N90° , N120° orientation

According to the grouping of large scale fractures, parameters such as fracture length, fracture geometry dimension, average azimuth, and Fisher coefficient can be measured. Large scale fracture density of different group can be modeled by means of the statistical results. Fig 2 shows that large scale fracture density of N60° (Northeast) is the highest in these three groups, and it is consistent with the orientation of main fault in study area.

Based on wells, the fracture density of small scale fractures can be predicted with the seismic geometry attributes as constraints. According to the facts that small scale fractures and large scale fractures generally have the same strike, the small scale fractures can be divided into four groups, they are horizontal fractures, N60°(Northeast), N90°(Eastwest) and N120°(Northwest). Table 1 is the parameters at wells, and then calculating fracture density curve for every well.

Table 1 The statistical table of small scale fracture in wells

Fracture classification	Average azimuth	Fisher coefficient	Average dip	Fisher coefficient
Horizontal fracture	21.3482	0.4923	2.3411	7.9345
N60°	330.1012	5.3401	88.6181	0.2706
N90°	85.7755	2.8611	17.9371	1.9455
N120°	22.236	3.3188	9.9586	0.8631

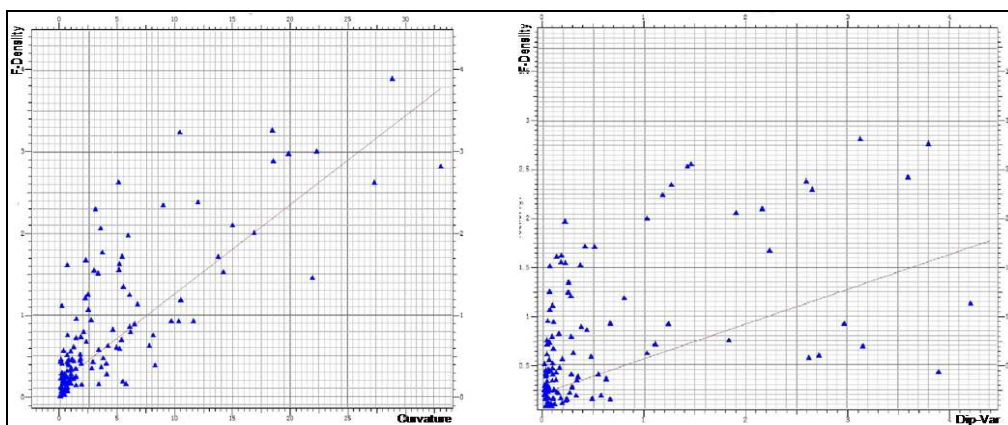


Fig. 3 The crossplot between fracture density and curvature, dip-variation

Using global optimization discrete scanning technology in 3D space to scan occurrence of the seismic event and calculate stratigraphic dip and azimuth, several kinds of seismic geometry attributes which have good instructions to tectonic deformation can be gotten. Through the intersection of fracture density curve and these seismic geometry attributes in 4 wells, Fig. 3 shows that curvature has a good relationship with fracture density, the second is the dip-variation attribute, correlation coefficients are 0.81 and 0.74 respectively. With fracture type cube as constraint, curvature and dip-variation as co-variables, small scale fracture density can be forecast through the multivariate statistics method.

Before fracture modeling, impedance cube can be obtained through the pre-stack and post-stack simultaneous inversion. Using impedance cube and facies as constraints, matrix physical properties can be modeled. Large scale fractures can be gotten from seismic data, large scale fracture modeling is to get faults and model them in software. For small scale fractures, according to the fracture density cube, the azimuth and dip of fractures in different group can be sorted, discrete fracture grid model can be established based on object modeling algorithm.

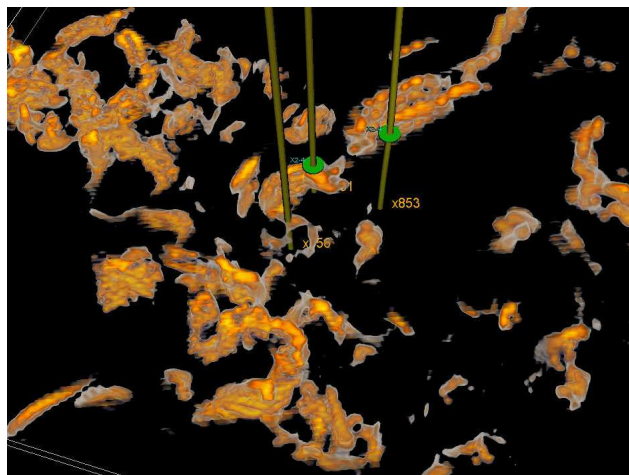


Fig. 4 Fracture distribution in 3D space

Combined with the production status of the Xinchang gas field, after overlapping fracture prediction result and structure, it is found that Xin851 well and Xin856 well have industrial gas with high production in target layer and these two wells are located in the area where fractures are relatively developed; Chuanxiao560 well has produced much water while there has developed fractures, Xin856 well begins to produce water, the reason is these two wells are not located in the structural high. Fig.4 displays the filtered fracture distribution in 3D space, the target bed of Xin851 well and Xin856 well have encountered the fracture zone, and there isn't any gas display in Xin853 well, the reason is that there isn't developing any fracture. According to this, the prospective area for exploration and development in this field is the structural high with fracture developed.

Conclusion

Fracture prediction should be carried out after fracture analysis, it needs to analyse the large scale and small scale fractures respectively. Large scale fractures can be directly identified through pixel imaging attribute; small scale fractures can be recognized through the fracture density curves in wells, adopting multivariate statistical method, fractures can be modeled by use of much information as constraints;

Pre-stack and post-stack simultaneous inversion is an effective method for reservoir prediction, and based on the new generation of global optimization discrete scanning technology in 3D space, it is effective to predict fracture by use of curvature attributes;

Fracture is an effective flow passage for tight sandstone fractured reservoir in Xujiache formation of Xinchang gas field. Prospective area for exploration and development in this field is the structural high with fracture developed.

References

- [1] Liu Hong, Cai Zhengqi, Tan Xiucheng. Forecasting of fracture reservoirs in thin carbonate rocks of precipitous structure belt, East Sichuan. *Petroleum Exploration and Development*, 2008, 35 (4): 431-436.
- [2] Liu Zhenfeng, Qu Shouli, Sun Jianguo, et. At. Progress of seismic fracture characterization technology. *Geophysical prospecting for petroleum*, 2012, 51(2): 191-198.
- [3] Fang Chen, Zeng Ligang, You Chengcai, et al. Research on methods and applications of fracture comprehensive prediction. *Natural Gas Industry*, 2007, 27(supplement A): 443-445.
- [4] Ma Ruhui. Fracture prediction of tight sandstone reservoir. *Natural Gas Industry*, 2005, 25(10): 36-37.
- [5] Kong Xuanlin, Tang Jianming, Xu Tianji. Application of seismic curvature attributes to fracture prediction in Xincang area, western Sichuan Depression. 2011, 50(5): 517-520
- [6] Zhou Xingui, Cao Chengjie, Yuan Jiayin, et al. Methods and applications of quantitative prediction and evaluation of tectonic fracture in reservoir in petroliferous basin. *Journal of Jilin University (Earth Science Edition)*, 2004, 34(1) : 80-84.
- [7] Chen Guangpo, Wang Tianqi, Liu Yingru, et al. Prediction of effective fractures in a limestone buried hill, South China Sea. *Petroleum Exploration and Development*, 2008, 35(3): 313-317.
- [8] Li Zhiyong, Zeng Zuoxun, Luo Wenqiang. A new approach for predicting fractures using principal curvature. *Petroleum Exploration and Development*, 2003, 30(6): 83-85.
- [9] Kurt J. Marfurt, R. Lynn Kirlin, Steven L. Farmer, Michael S. Bahorich. 3-D seismic attributes using a semblance-based coherency algorithm. *Geophysics*, 1998, 63(4): 1150-1165.
- [10] Chen Yefei, Cai Dongmei, Fan Zifei et al. 3D geological modeling of dual porosity carbonate reservoirs: A case from Kenkiyak pre-salt oilfield, Kazakhstan. *Petroleum Exploration and Development*, 2008, 35(4): 492-497.

Prediction scheme of Torsional Strength of Reinforced Concrete Beam

Han-Chen Huang

No. 168, Hsueh-fu Rd., Tanwen Village, Chaochiao Township, Miaoli County, 36143 Taiwan
Department of Leisure Management, Yu Da University

hchuang@ydu.edu.tw

Keywords: Artificial Neural Network, Torsional Strength, Reinforced Concrete Beam.

Abstract. This study proposes a artificial neural network with genetic algorithm (GA-ANN) for predicting the torsional strength of reinforced concrete beam. Genetic algorithm is used to the optimal network structure and parameters. A database of the torsional failure of reinforced concrete beams with a rectangular section subjected to pure torsion was obtained from existing literature for analysis. This study compare the predictions of the GA-ANN model with the ACI 318 code used for analyzing the torsional strength of reinforced concrete beam. The results show that the proposed model provides reasonable predictions of the ultimate torsional strength of reinforced concrete beams and offers superior torsion accuracy compared to that of the ACI 318-89 equation.

Introduction

Reinforced concrete structural members resist various forces, including bending, axial compression, tension, shear, and torsion; of which, torsional strength is a crucial mechanical condition [1]. The torsion failure of reinforced concrete members is generally caused by tension stress beyond the acceptable value. The nonlinear behavior of reinforced concrete under torsion is extremely complex.

Existing theories for analyzing the torsional strength of reinforced concrete beams include skew bending theory and truss analogy theory. Skew bending theory [2] assumes that when torsion exceeds the section's acceptable value, cracks occur in rectangular reinforced concrete beams and connect into a compression zone at the end of the crack, forming a skew failure surface. Hsu [3] simplified the skew failure surface of skew bending theory into a plane inclined 45° to the vertical axis and classified the torsional strength of a beams' oblique plane as the torsional strength of the reinforcement T_s and the concrete T_c . Based on this classification, ACI 318-89 calculates the ultimate torsional strength of rectangular reinforced concrete beams T_n (Eq.1)[4]:

$$T_n = T_c + T_s = 0.067x^2y\sqrt{f'_c} + \alpha_t \frac{x_1y_1A_t f_{yt}}{s} \quad (1)$$

where x = beam width, y = beam depth, f'_c = the compressive strength of the concrete, f_{yt} = yield strength of the transverse reinforcement, A_t = the area of the a closed stirrups within a space of s , s = the space between closed stirrups, x_1 = the short side length of the closed stirrup, y_1 = the long side length of the closed stirrup, and $\alpha_t = 0.66 + 0.33 (y_1/x_1)$.

In recent years, artificial neural networks have been widely employed to solve problems where the relationships between input and output variables are nonlinear, yielding satisfactory results[5]. Therefore, this study adopts a neural network to predict the ultimate torsional strength of reinforced concrete beams. After training, verifying, and testing the established model, we compare the predicted results with those of the ACI 318-89 equation.

The remainder of this paper is organized as follows: The hybrid methodology is presented in Section 2. In Section 3, we report the empirical results. Finally, our concluding remarks are provided in Section 4.

Neural Network Modeling Approach

In recent years, artificial neural networks have been employed in many fields. The main advantage of neural networks is their flexible capability for nonlinear modeling. Numerous studies have incorporated artificial neural networks with fuzzy theory or GA to improve the analysis [6]. To improve the predicative performance of artificial neural networks, this study employs a GA to determine the optimal network structure and parameters. Thus, the number of hidden nodes of a multilayer perceptrons, the slope of the activation function, and the values of the learning rates and momentum coefficients in the hidden and output layers are determined through optimization.

GA improves the performance of artificial neural networks by selecting the optimum the network parameters, modifying the node activation function and determination of weights. The optimization process is described below:

Randomize the population.

Evaluate the fitness function of each individual in the population.

Select the first two individuals with the highest fitness values and copy them directly to the next generation without genetic operations.

Select the remaining individuals in the current generation and apply crossover and mutation genetic operations to produce the next generation of individuals.

Repeat the process from the second step until all individuals in the population meet the convergence criteria.

Decode the converged individuals in the final generation to obtain the optimized parameters.

In this study, we use different operators for selection and crossover operations [7] (Table 1).

Table 1 Description of Different Operators for Selection and Crossover Operations in GA

Operation	Operator	Description
Selection	Roulette	The chance of a chromosome getting selected is proportional to its fitness.
	Top percent (x)	Randomly selects a chromosome from the top x percent of the population.
	Best	Selects the best chromosome.
	Random	Randomly selects a chromosome from the population.
	Tournament	The winner of each tournament is selected for crossover.
Crossover	One point	Randomly selects a crossover point within a chromosome, interchanges the two parent chromosomes at this point to produce two new offspring.
	Two point	Randomly selects two crossover points within a chromosome, interchanges the two parent chromosomes between these points to produce two new offspring.
	Uniform	Decides (with some probability-know as the mixing ratio) which parent will contribute each of the gene values in the offspring chromosomes.
	Arithmetic	Linearly combines two parent chromosome vectors to produce two new offspring.
	Heuristic	Use the fitness values of the two parent chromosomes to determine the direction of the search.

A multilayer perceptrons with one hidden layer and the sigmoid activation function $f(x)=1/[1+\exp(-\beta X_i)]$ (β is the function slope) was selected as the base neural structure for this study.

The Newton algorithm with a momentum term was used as the learning function $\Delta W_i(n+1)=-\eta \nabla W_i + \rho \Delta W_i(n)$, η was the learning rate, and ρ was the momentum coefficient. The conceptual model architecture is shown in Fig.1.

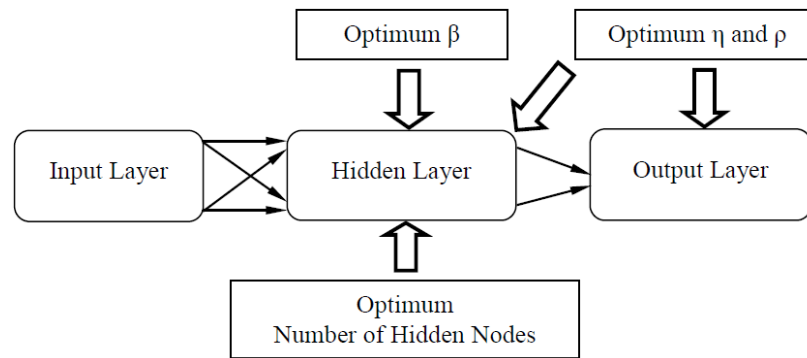


Fig. 1 Conceptual Architecture of the proposed Model

A database of the torsional failure of reinforced concrete (including normal-strength and high-strength concrete) beams with a rectangular section subjected to pure torsion was retrieved from existing literature for analysis [8-11]. Regarding the 76 samples, we randomly selected 40 for training, 15 for verifying, and 21 for testing. The input variables were beam width (x), beam depth (y), the short side length of the closed stirrup (x_l), the long side length of the closed stirrup (y_l), the Compressive strength of the concrete (f_c'), the space between closed stirrups (s), the area of closed stirrups within a space of s (A_t), the yield strength of transverse reinforcements (f_{yt}), the area of longitudinal reinforcements (A_l), the yield strength of longitudinal reinforcements (f_{yl}), $\rho_s = (A_t P_h) / (xys)$, $\rho_l = A_l / (xys)$, and the output variable was the ultimate torsional strength T_n .

Empirical Results

The empirical results based on the optimum ANN parameters, which were determined using the GA, are reported in this section. To evaluate the performance of ANN for predicting torsional strength, the absolute relative errors (ARE) after training and at various optimum conditions are provided in Table 2. The results show that different operators were used for selection and crossover operations in the GA. The optimum values for the hidden nodes and the slope of the activation function for each combination of operators are also shown in Table 2. When “Tournament” and “One point” operators were used, the ARE in the torsional strength prediction was minimized. The learning curve of GA-ANN training and validation (Figure 2) shows effective error convergence without overfitting.

To examine the accuracy and credibility of the GA-ANN model, we used correlation coefficient (r) and ARE to conduct evaluations; the results are shown in Table 3. Theoretically, higher r s values and lower ARE values indicate a superior model. Thus, the GA-ANN proposed in this study can accurately predict the ultimate torsional strength T_n , as shown in Table 3. Additionally, this model provides greater torsion accuracy compared to that of the ACI 318-89 equation considering the r and ARE.

Figure 3 shows the actual ultimate torsional strength T_{exp} and the ultimate torsional strength predicted by the models T_{pred} . Theoretically, the closer the data dot is to the diagonal (where $T_{exp} / T_{pred} = 1$), the better the predicted result. As shown in figure 3, the distribution of the result predicted by ACI 318-89 is scattered, whereas the result from the GA-ANN model are distributed closer to the diagonal.

Conclusions

This study established a artificial neural network with GA to predict the torsional strength of reinforced concrete beams. The GA enables the optimum hidden nodes of a feedforward neural network, the optimum slope of the activation function, and the optimum values of learning rates and momentum coefficients to be determined.

Predictions of the GA-ANN model were compared to those of the ACI 318-89 equation. We found that the proposed model provides reasonable predictions of the ultimate torsional strength of reinforced concrete beams and offers superior torsion accuracy compared to that of the ACI 318-89 equation considering both the correlation coefficient and absolute relative error.

Table 2 Performance of the Proposed Model for Predicting Torsional Strength

Selection operator	Crossover operator	Number of hidden nodes	β	ARE
Best	One point	17	0.720	10.40%
	Two point	26	0.494	10.07%
	Uniform	12	0.612	10.16%
	Arithmetic	16	0.090	10.02%
	Heuristic	21	0.219	8.69%
Top percent (10)	One point	7	0.297	9.46%
	Two point	17	0.091	9.70%
	Uniform	9	0.775	10.22%
	Arithmetic	19	0.751	10.49%
	Heuristic	28	0.585	9.36%
Roulette	One point	30	0.355	10.26%
	Two point	8	0.597	9.69%
	Uniform	2	0.706	9.95%
	Arithmetic	2	0.692	9.89%
	Heuristic	3	0.868	9.62%
Random	One point	20	0.664	9.81%
	Two point	21	0.668	9.19%
	Uniform	4	0.730	9.01%
	Arithmetic	2	0.764	10.16%
	Heuristic	4	0.704	10.48%
Tournament	One point	10	0.463	8.60%
	Two point	8	0.707	10.19%
	Uniform	13	0.812	9.34%
	Arithmetic	24	0.374	10.00%
	Heuristic	20	0.270	9.02%

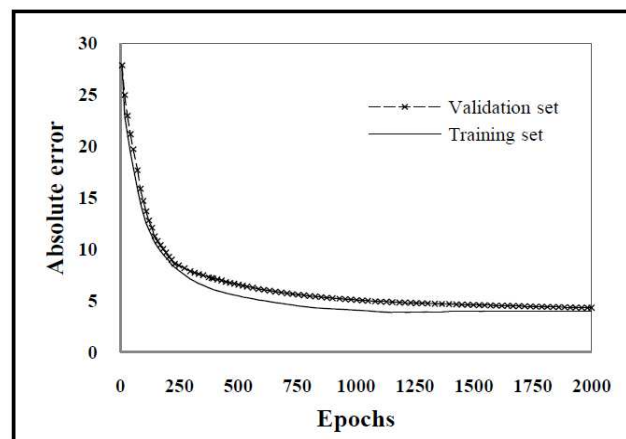


Fig. 2 The GA-ANN model Learning Curve

Table 3 The Correlation Coefficients and Absolute Relative Errors of Predictive Models

Model	Correlation coefficient			Absolute relative error		
	Training data	Verifying data	Testing data	Training data	Verifying data	Testing data
GA-ANN	0.9875	0.9865	0.9909	7.02%	8.64%	8.60%
ACI 318-89	0.9572	0.9481	0.9437	17.50%	20.13%	19.70%

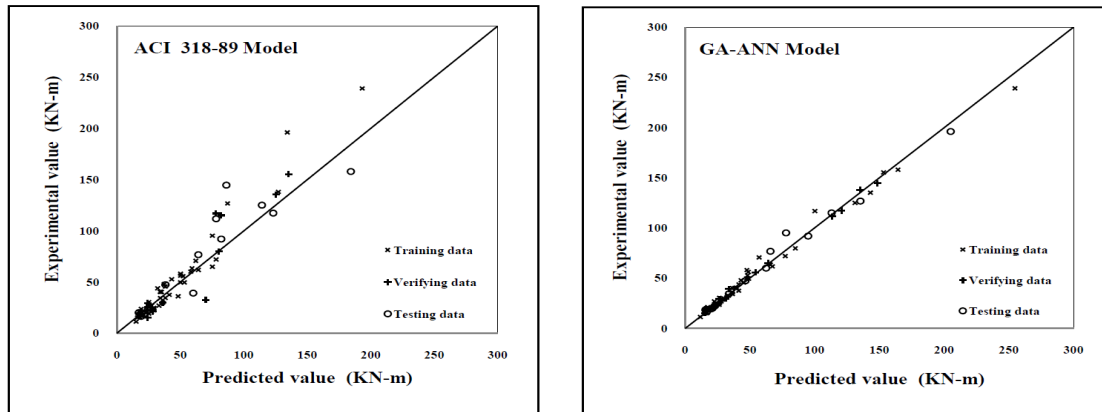


Fig.3. Scatter plot of predicted values from the Models and Actual values

References

- [1] C.W. Tang, H. J. Chen, Y. Yen. Modeling the confinement efficiency of reinforced concrete columns with rectilinear transverse steel using artificial neural networks. *Journal of Structural Engineering*, ASCE, 2003, 129(6):775-783.
- [2] N. N. Lessig. Theoretical and experimental investigation of reinforced concrete elements subjected to combined bending and torsion, *Theory of design and construction of reinforced concrete structures*, Moscow, 1958.
- [3] T. T. C. Hsu. Torsion of structural concrete-behavior of reinforced concrete rectangular members, *Torsion of Structural Concrete*, SP-18. American Concrete Institute, Detroit, 1968.
- [4] ACI Committee 318, *Building code requirements for structural concrete (ACI 318-89)*. American Concrete Institution, Detroit, MI, U.S.A. 1989.
- [5] C. Yeh. Design of high-performance concrete mixture using neural networks and nonlinear programming. *Journal of Computing in Civil Engineering*, ASCE, 1999, 13(1):36-42.
- [6] M. Sheikhan, B. Movaghar. Exchange rate prediction using an evolutionary connectionist model. *World Applied Sciences Journal*, 2009, 7:8-16.
- [7] J. Principe, C. Lefebvre, G. Lynn, C. Fancourt, D. Wooten. *Neuro Solutions Documentation*. Neuro Dimension Incorporation (<http://www.neurosolutions.com>), 2009.
- [8] N. E. Koutchoukali, A. Belarbi. Torsion of High-strength reinforced concrete beams and minimum reinforcement requirement. *ACI Structural Journal*, 2001, 98(4):462-469.
- [9] C. W. Tang. Using neural networks to predicate torsional strength of reinforced concrete beams. *The 8th national conference on structure engineering*, Taiwan, 2006.
- [10] I. K. Fang, J. K. Shiau. Torsional behavior of normal- and high-strength concrete beams. *ACI Structural Journal*, 2004, 101(3):304-313.
- [11] L. J. Rasmussen, G. Baker. Torsion in reinforced normal and high-strength concrete beams part 1: experimental test series. *ACI Structural Journal*, 1995, 92(1):56-62.

Study on Composite Slab Structure

Kewei Ding^{1, a}, Yi Zhang^{2, b}

^{1,2}School of Civil Engineering, Anhui University of Architecture, Hefei 230022, China

^adingkw@aiai.edu.cn, ^bzhy85119@163.com

Keywords: Composite Slab; Structural Form; Prestressed Laminated Concrete Slab; Large-Span.

Abstract. About the concrete laminated slab of the research and the engineering application are summarized and prospected, including the classification, advantages and disadvantages of the laminated slab, the application and development of the laminated slab of recent advances at home and abroad, Summed-up the new prestressed laminated concrete slab structure form and application of large-span, which is the important development direction of the concrete laminated slab in future.

Introduction

At present, residential construction is in stage of development, is becoming a new economic growth point in China, at the same time, housing industrialization is a reflection of a mirror of the country's social, economic, cultural and living standards. Composite structure is cast structure housing industrialization requirement is met and the collection and assembly of structural strengths in one of the structures. In particular in the application of floor structure has prominent advantages, and amount of composite slab's the largest and most widely used, on the research and development of composite slab has a great economic and social benefits.

In the area of composite structure, many European countries have begun as early as 40 in-depth studies. After the 70's concrete clamp of the overall structure of developed countries in the world have been stereotyped to component and structure of system development, and in the practice of engineering which has achieved remarkable economic and social benefits [1]. In our country, the application of a composite structure in industrial and civil engineering starting in the late 50, nearly 20 years later although the more developed countries in the world, but our research is in the area of composite slab marked results. In particular, since the beginning of the 21st century, development of study on composite slab of steady development is faster and better posture.

It is based on the above background. This article aims at reviewing the history of studies on composite slab structure, and some summary of past research, thereby contributing to the future prospects for research and development of composite slab structure.

Composite Slabs of Concepts, Classifications and Advantages and Disadvantages

Basic concepts and classification of the composite slab. Concrete composite slab refers to precast reinforced concrete or prestressed concrete panel after a precast of concrete poured to form combined with the technology of in-situ assembly of integral structure.

Behaviors of composite plate by force can be divided into "a stress concrete composite slab" and "secondary stress composite slabs". Under the bottom of precast prestressed concrete, composite slab can be divided into non-prestressed concrete composite slab and prestressed concrete composite slab.

Advantages and disadvantages of concrete composite slab. Concrete composite slab of the main benefits are: In relation to the whole Assembly floors of prefabricated, it can enhance the overall stiffness and seismic performance of structures. In relation to the whole in-situ floor slab, laminated slabs of main mechanical parts manufactured at the factory and can be made ahead, and prefabricated parts of the template can be recycled. After-pouring concrete to precast plate as a template, which can reduce formwork wet job workload and reduce the construction site.

Composite structure there are also some disadvantages, the main is superimposed on the old and new concrete can work together, is the sheer performance of old and new combined interface. This research proves the problem after a lot of testing at home and abroad by certain structural measures can guarantee their work [2].

Disadvantages in comparison, composite slabs of benefits are obvious. Shortcomings can be constantly improved to overcome. Practice and discussion of both at home and abroad to make a lot of, some of the problems have been solved, so a lot of composite slab can be applied in practical engineering.

Composite Slabs in the Application and Development of Domestic and Foreign

Composite slab in the application and development of foreign Started as early as in the 1920 of the 20th century, foreign composite structure applied to a concrete bridge, starting only 40 used in housing construction. But Application technology of composite structure in architecture in foreign countries after further development is in the 50. As the composite technology development, each country according to its own circumstances and conditions has been developed for the country's composite structure. For example Poland DMSZ-composite structure of floor, which is prestressed beam as a load-bearing components for assembly, and then put on the small beam of precast hollow clay block, then in pouring massive concrete above, so that all three works together, achieved good economic results; 70 after France and Germany also produced concrete composite slab used prestressed thin plate. In recent years, Japan developed a system of half-precast structures and also used a variety of types of PC composite Board Member, widely used in industrial plants, public buildings, and multistoried and high-rise buildings.

In terms of research, more study abroad is a combined interface shear strength and shear connection, composite shrinkage caused by the differential of the upper and lower parts of additional internal forces and deformation and ultimate deformation of precast concrete after suppression of deflection and crack resistance and calculation methods, and so on. In terms of secondary effects of stress, foreign researchers generally think of flexural bearing capacity of composite beam plate internal force and laminated with hard and have no set support before or not, do not consider the effect of secondary stress [3].

Application and development of composite slab in the domestic Composite structural system in China began in the 60's. In the 70's, prefabrication of prestressed concrete girder and cast-concrete combined clamp roof has a very good development, and in Tianjin, Zhejiang and Guangdong provinces constructed a number of this structure of the building, its economic effect is very good. In the 80's, concrete composite slab in addition to a wide range of applications in a multi-story building, are also being rapidly extended to the high-rise buildings. After the 90's, with the development of prestressed technology and development of high strength steel wire, prestressed composite slab became efficient prestressed composite slab.

In terms of research, national research priorities focused on secondary stress laminated bending "stress ahead" phenomenon and the concrete in the compression zone "strain hysteresis" phenomena and composite clamp flexural moment transfer cross section of the law. Set up by the Chinese Academy of building organizations "composite structure research thematic group" on the mechanical properties of concrete composite slab system in-depth studies, so as to establish a rational design method of composite slab provides measurement data and theory. And presented in a GBJ10-89 Code for design of concrete structures laminated plate design provisions and cross section, cross section and shear strength calculation of combined interface methods and formulas. GBJ500102-2002 Code for design of concrete structures [4] follows the achievements of the subsequently published [5].

Present Situation of Research on Prestressed Concrete Composite Slab

Since entering the new century, along with the trend of housing industry and study on prestressed composite slab of development become more quickly. Here are a few typical research fields:

Structural study on the diversification of the types. Chinese scholars in precast structures in recent years have done a great deal of innovation research. Mainly: Keyway core-concrete panels, precast rectangular fin section laminated double rectangle, prefabricated ribbed concrete floor slab of concrete, precast t-shaped prefabricated ribbed concrete floor, double t-shaped prefabricated ribbed concrete floor, sandwich concrete with precast concrete floor, fasting backplane, concrete half-through steel truss plate, prefabricated corrugated floor and so on.

Uni-directional elastic design method of prestress two-way combined slab. If still operating after the slab of prestressed concrete composite design will result in a direction of one-way reinforced too much, too little for the reinforcement of the other party. And currently using isotropic plate bending of concrete from the distribution coefficients for design is unreasonable. For this 2006 Hunan University Zhou kunpeng, Wu Fangbo characteristics of prestressed concrete composite slab with, according to the principle of elastic thin plate, derived of one-way simply supported prestressed concrete rectangular plate bending moment distribution formula [6].

Nonlinear finite element analysis of unidirectional prestressed two-way composite slab. Due to the current unidirectional prestressed two-way laminated plate theory analysis and application design, there are still some problems, so the combination of the characteristics of laminated plates and considering material nonlinear and anisotropic laminated plate and other factors, the use of nonlinear finite element program can show good coupling between precast and cast-in two parts and transmission characteristics. 2009 Guangdong architectural design Institute of Bo Wu Xuehui unidirectional prestressed two-way composite slab using ANSYS software did a nonlinear finite element stress analysis of the whole process [7].

Composite slab and slab of correlation analysis of cracking moment. At present, the quality of laminated plates and prestressed plates and structural testing are far from meeting the needs of engineering practice. 2005 Guo Legong, Yang Yanchun, Guo Lening three teachers through theoretical analysis and experimental study on prestressed concrete composite slab and made the appropriate correlation model of cracking moment between the sheets. At present, Composite slab Standard Atlas is provided only the crack resistance of prestressed sheet inspection parameters. According to the correlation, the proposed increase in crack resistance of prestressed sheet and laminated plate test coefficient value, test load of bearing capacity design allows the value criterion, so to make up for the performance test composite slab structure gaps [8].

Study on seismic behavior of prestressed composite slab. 2005 Suzhou Institute of science and technology Professor Chen Zhonghan by prestressed laminated plate under in-plane cyclic loading experimental studied on seismic behavior of prestressed composite floor. They summarized the laminated plates under in-plane shear stiffness variation, and established a board of in-plane shearing stiffness degradation expression [9].

Major existing composite slab slot form and characteristics Laminated board slot generally falls into the following two types of traditional practices, but there are drawbacks. When loading the floor in, load transfers to adjacent board of ability is bad causing the mechanical properties and structure performance greatly reduced. By optimizing precast slab slot reaches the lateral force between the plates. Optimal way is to increase the slot width, reinforce in the slot overlap lap to realize uninterrupted transmission; Reduced anchorage reinforcing steel bending angle is 30, so as to achieve the effective stress increases; Configuration structure steel bar at the bend, in order to achieve enhanced abutted interaction between concrete and steel; First of all stress in steel prefabricated floor out of the plate edge, and then use the side slot and after-pouring concrete implementation landscape force, so that the original unidirectional force becomes bi-directional force, strengthen the bond role, as well as an improved form of integral slot and structural measures [10].

Prospect of Prestressed Concrete Composite Slab

In general over the years, thanks to the efforts of researchers at home and abroad, composite structures have been included in the relevant norms of the states, and research has gradually increased to a composite widget, and also has a large number of applications for the actual project.

But superimposed components research is also relatively small, test and experiment with ways that were confined to the production of components, therefore laminated component still requires further research and development.

From the treatment of combined interface is used to configure with reinforcement to keep the combined interface has sufficient shear strength to avoid slipping, but the combination of steel exposed to the outside, make the complex manufacturing process of composite slab and the structural measures to be more reasonable.

Integral rebar lap length is too long in the slot, and further research is required to determine a reasonable lap length of reinforcement.

Laminated plates and prestressed plates and structural performance of engineering quality inspection method are far from meeting the needs of engineering practice.

The theory of long-span composite floor slabs is in the exploratory phase, theory is not yet ripe, if you want to master of laminated floors in large-span structure, still needs to be studied in more depth.

Experimental and practical application shows that laminated slab with prestressed ribbed construction speed, strong composite shear capacity, characteristic of the flexural rigidity of a larger, and that match the characteristics of the steel structure project construction speed and using prestressed laminated panels can reduce the cost of steel structural engineering, but laminated slabs of steel structural engineering and application requires further study.

Acknowledgements

This project is supported by Anhui Province National Natural Science Foundation and Anhui Provincial Laboratory Project Funding through grant No. 1106c0805024 and ZD2008001-1.

References

- [1] Zhou Wanghua. Modern concrete composite structure, M. China architecture and building press. 1998:12-180
- [2] Zhao Shunbo, Zhang Xinzhong. Principle and application of concrete composite structure design, M. Press of China Water Conservancy and hydropower. 2001:9-37
- [3] Darwin,D and Pecknold,D,A. Analysis of RC shear Panels. Under cyclic loading,J.of structural Division, Vol.102,no.ST2, February,1976.
- [4] GB50010-2002. Concrete structure design codes, S. China architecture and building press.
- [5] Zheng Luncun. PK experimental study on prestressed concrete composite slab and its application, D. Hunan University.2005, (4):1-6.
- [6] Zhou kunpeng, Wu Fangbo. Rectangular unidirectional prestressed two-way composite slab simply supported on four sides of the elastic design method, C. The journal of Shaoyang College (natural science).2006, (3):63~65.
- [7] Wu Xuehui. One-way prestressed concrete two-way superimposed slab of nonlinear finite element analysis, C. Gansu: Science and technology. 2009: 109-111
- [8] Guo Legong, Yang Yanchun, Guo Lening. Cracking moment of prestressed concrete composite slab and plate of Correlation analysis, C. Harbin industrial university press. 2005, (8):1151-1153
- [9] Chen Zhonghan, Liu Qiang, Zhu Maocun, Yin Zhiwen, Sun Rong. Experimental study on seismic behavior of prestressed composite floor, C. Journal of Suzhou Institute of science and technology.2005, (9):1~5.
- [10] Xu Youlin, Xu Tianshuang. Experimental study on transmission performance of two-way composite slab slot, C. Building science. 2003: 96-99

Research on Stability Bearing Capacity for Pole and Tower Compression Members with Two Legs Connection

Xianlei Cao^{1,2,a}

¹Anhui University of Technology, Anhui, Ma'anshan, 243002, Anhui Province, China

²State Key Laboratory of Architecture Science & Technology in West China, Xi'an University of Architecture and Technology, Xi'an 710055, China

^alei070@163.com

Keywords: High strength single angle, Numerical simulation, Analytical method

Abstract. In order to research the stability bearing capacity of high strength pole and tower compression members, analytical method and numerical simulation method were used to study stability on high strength axial compression members. Researched the impact of different slenderness ratio, different cross-section factors on the bearing capacity; energy relationship was using in analytical method, the boundary conditions issue is simplified according to different end restraint capacity; the failure modes and stability bearing capacity of members were studied by numerical simulation. Compared with the experimental results show that the numerical simulation and elastic theory analytical solution overestimate the capacity of members, but the numerical results have better agreement than the elastic theory analytical solution, which can show the numerical simulation method is right. Experiment method can obtain more secure mechanical behavior of high-strength angle steel member with axial loading.

Introduction

Although China has build a number of high-strength steel tower structural engineering, but in such structure the tower main leg using Q460 or higher strength steel, which of the stability test and theoretical analysis are still insufficient, but also there is no dedicated design of such high strength steel member design methods [1-2]. The stability performance of pole and tower compression members with two legs connection can be equivalent to the axial compression members, using the analytical method and numerical simulation method to analyze the stability of the bearing capacity of the existing data on the axial compression high strength angles, and compared with the experimental results to put forward the stability bearing capacity calculation recommended of such components[3-4].

Experiment methods

Due to the actual needs to study four kinds of angles, that is L12810, L14012, L16010 and L16012 [1], every series specimens had four slenderness ratios ($\lambda=30$, $\lambda=45$, $\lambda=60$, $\lambda=80$). The axial loading end of members use ball pin which connected to loading device. Mechanical properties are shown in Table 1; experimental results on Q460 high-strength angle steel are shown in tale 2.

The local stability is more prominent on small components of the slenderness ratio, failure models were typical of overall buckling to slenderness ratio 60 and 80 specimen. Twisting deformation is very small until the maximum load was reached. Loading device is shown in Fig 1.

Table 1 Mechanical properties

Types	f_y /MPa	f_u /MPa	δ /%	E /MPa $\times 10^5$
L125×8	530	715	22.0	1.99
L125×10	525	685	21.0	2.20
L160×10	515	680	25.0	2.02
L160×12	530	685	20.0	2.06



Fig. 1 Loading device

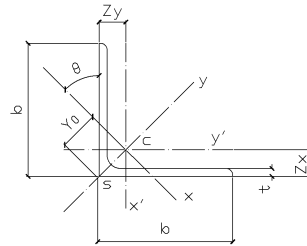


Fig. 2 Single angle section

Elastic Buckling Solution

Flexural buckling Flexural deformation function can be expressed as $v = c_1 \sin(\pi z / l)$, Buckling load can be obtained by Euler's formula:

$$P_{cr} = \frac{\pi^2 EI}{(\mu l_y)^2} = \frac{\pi^2 EA}{\lambda_y^2} \quad (1)$$

Flexural torsional buckling Bending is around the cross-section symmetry axis y , at the same time around the shear center S to reverse. The Flexural torsional buckling was shown in Fig3.

Occurrence of lateral bending and torsion, the cross-section of the balance equation is:

$$EI_y u'' + P(u + y_0 \phi) = 0 \quad (2)$$

$$EI_w \phi'' + (Pi_0^2 - GI_t + \bar{R}) \phi'' + Pu'' y_0 = 0 \quad (3)$$

Lateral bending and torsional deformation function can be expressed as: $u = C_1 \sin(\pi z / l)$, $\phi = C_2 \sin(\pi z / l)$. From both ends simply supported conditions, according to the formula (2) and formula (3):

$$P_{yw} = \frac{(P_y + P_w) - \sqrt{(P_y + P_w)^2 - 4P_y P_w [1 - (y_0 / i_0)^2]}}{2[1 - (y_0 / i_0)^2]} \quad (4)$$

When $P_{yw} < P_x = \pi^2 EI_x / l^2$, members occur flexural torsional buckling. Using

$P_y = \frac{\pi^2 EA}{\lambda_y^2}$, $P_w = \frac{\pi^2 EA}{\lambda_w^2}$ and $P_{yw} = \frac{\pi^2 EA}{\lambda_{yw}^2}$ substituted into the formula (4), we have:

$$\lambda_{yw} = \sqrt{\frac{1}{2} \left[\lambda_y^2 + \lambda_w^2 + \sqrt{(\lambda_y^2 + \lambda_w^2)^2 - 4\lambda_y^2\lambda_w^2(1 - y_0^2/i_0^2)} \right]} \quad (5)$$

Where λ_w and λ_{yw} denote the equivalent slenderness ratio of torsional buckling and flexural torsional buckling. Single angle cross-section is singly symmetry, the warping moment of inertia is $I_w = 0$ with an approximation, its favorable error normally does not exceed 3%, so that $P_w = GI_t/i_0^2$, $\lambda_w = \pi\sqrt{E/\sigma_w} = 5.07\sqrt{A/I_t} = 8.77i_0/t$. Flexural torsional buckling conditions is $\lambda_{yw} > \lambda_x$ on axial compression single angle, otherwise will cause bending buckling.

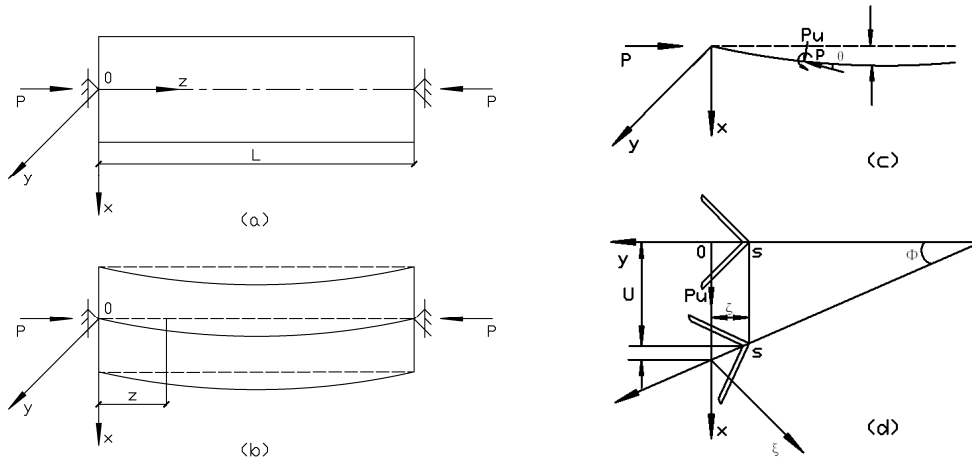


Fig.3 Flexural torsional buckling

Elastic-Plastic Analytical Method

Elastic-plastic flexural buckling when the cross-section of average stress exceeds the proportional limit of the material, part of the angle cross section will enter the plastic zone, the compression bar is into the eccentric compression state. Sometimes ignore this eccentric [6], in order to calculate simplify, can approximate the following formula in the symmetry plane bending buckling critical stress of tangent modulus, elastic-plastic bending flexion load calculation formula is as follows:

$$P_{ey} = \frac{\pi^2 E_y A}{\lambda_y^2}, P_{ex} = \frac{\pi^2 E_x A}{\lambda_x^2} \quad (6)$$

Elastic-plastic flexural torsional buckling Consider the residual stress σ_{rc} , when the cross-section average stress exceeds the effective proportional limit $(\sigma_y - \sigma_{rc})$, the members will be buckling in the elastic-plastic state. Cross-section will be divided into many units, cell area is A_i , corresponding to the stress of the cell surface is σ_i , the pressure of the cross section is $P = \int_A \sigma dA = \sum \sigma_i A_i$. First calculate the cross section stress of Wagner effect coefficient:

$$\bar{K} = \int_A \sigma [x^2 + (y - y_0)^2] dA = \sum \sigma_i [x_i^2 + (y_i + y_0)^2] A_i \quad (7)$$

The balance equation can be simplified rewritten as:

$$EI_y u'''' + Pu'' + Py_0 \phi'' = 0 \quad (8)$$

$$EI_w \phi'' + (\bar{K} - GI_{et} - G_t I_{pt}) \phi'' + Pu'' y_0 = 0 \quad (9)$$

The carrying capacity Overall, the majority of finite element analysis results are agree well with the experimental results, and the error is in the range of 10%, therefore, finite element model to analyze the axial compression specimens can achieve the expected goals.

Where, P_E means experimental result, P_A means FEM result, and P_J means analytical result.

Table 2 Comparison of results from experiment and theory

specimen	P_E / kN	P_A / kN	P_J / kN	$\alpha = P_{AN} / P_E$	$\beta = P_J / P_E$
L1258C30-1	845	952.9	1150	1.13	1.36
L12510C45-1	1145	1245.7	1469	1.09	1.28
L16010C60-1	1120	1043.0	1304	0.93	1.16
L16012C80-1	940	888.4	1213	0.95	1.29

Comparison of Bearing Capacity

Table 2 shows comparison of results from experiment and theory. The ratio α of the finite element and experimental values is in the range of 0.93 to 1.13, the ratio β of the analytical solution and experimental values is in the range of 1.16 to 1.36, analytical solutions are higher than the experimental values, and the difference is large between the actual bearing capacity, but between numerical solutions and experimental values have good agreement. Finite element analysis considering the members at both ends hinged handle is reasonable, due to the analytical method can not accurately simulate end restraint conditions, the initial defect factors, caused the analytical value is higher than the experimental values

Conclusion

By analyzed the stability bearing capacity on axial compressive high strength angles, consider the simplified test component boundary conditions, the analytical method can not accurately simulate the end constraints, the initial defects and other factors, so resulting analytical values than the experimental values highs 16 percent to 36 percent, also shows that such member end restraint can not simply look as a hinged or fixed. Provided the finite element analysis method, simulating members of actual test performance is feasible, which can achieve the project, or the test required precision. Using test method to study the stability performance of members is more reliable and safe.

Acknowledgements

The author is much appreciated the financial support for this research from Key Program of Natural Science Foundation of Educational Commission of Anhui Province (KJ2012A047) and State Key Laboratory of Architecture Science & Technology in West China.

References

- [1] CAO Xianlei: Study on Stability Capacity of Q460 High-strength Steel Single-Angle Compression Members (Xi'an University of Architecture & Technology, China 2010).
- [2] GB 50017-2003: Code for Design of Steel Structure (China Planning Press, China 2003).
- [3] L/T 5154-2002: Technical Regulation of Design for Tower and Pole Structures of Overhead Transmission Line (China Electric Power Press, China 2002).
- [4] ASCE 10-1997: Design of latticed steel transmission structures (American Society of Civil Engineers, New York 1997).
- [5] EN1993-3-1: Tower, Masts and Chimney-Towers and Masts Design (Eurocode 3-design of steel structures- part 3-1, Landon 2006).
- [6] CHEN Shaofan: Design philosophy of steel structure (Science Press, China 2005).
- [7] CAO Xianlei, HAO Jiping, ZHANG Tianguang, et al.: submitted to Journal of Civil, Architectural & Environmental Engineering (2009).

On 3-D Modeling CAD System of Production Platforms

Chu Xinjie^{1, 2}

¹. Ocean University of China, Qingdao 266003, China;

². Drilling Technology Research Institute, Shengli Petroleum Administrative Bureau, Dongying, China 257017

chuxinjie@hrst.net

Keywords: Production Platforms, 3-D Modeling CAD System, Engineering Database, Program Design, Application

Abstract. The development of 3-D modeling CAD system on production platforms is mainly discussed in this paper. A suitable petroleum platform design by using software is developed according to the design status of domestic production platforms and the principle of structural life cycle method. The research results have been successfully applied to the 3-D graphic design of production platforms. The design level of offshore platform has been remarkably raised and the design quality has been improved. The technology research on developing method, design analysis method, parameterized modeling method, information management method, version management and etc, and can also be applied to other engineering designs and have certain popularization value.

The Application of CAD Technology to Offshore Engineering and Its Problems

In recent years, along with the exploitation of China's offshore oil, the requirements on the production platform design become increasingly high. The poor-efficiency design methods are hard to meet needs on designs. Moreover, as information age and economic globalization come, China's enterprises have to possess the abilities to develop, research and innovate new products, and then they can survive in fierce market competition, otherwise they will face up to the fate of being eliminated. If large software as Auto PLANT is introduced, a mass of capital will be spent, because those software system architectures are highly huge and complex in need of specialized personnel for maintenance and also require a second development based on domestic design needs, which are hardly accepted by ordinary design units.

Therefore, the designs of domestic production platforms urgently need a kind of 3-D design software to fully consider the placeholders and crossovers of platform structural components in the designing process, and resolve the possible problems in the construction process in designing ahead of time, hence accelerating platform design speed and improving the quality of design.

The Primary Technological Problems Resolved In Research

Designing the 3-D design software of production platform and realizing the 3-D modeling design of production platform structure

Designing the engineering database of production platform (including platform structural data, platform structural steel section data and design standards, etc) for platform design and autosaving the engineering data generated in the platform 3-D designing process

Realizing dynamic controls on platform models to make the whole platform structure, modules and components capable to be displayed with the form of layers and to be animated, which is convenient for users to observe platform from all angles and hence provide suggestions for its modification

Applying the arithmetic function of 3-D entity to realize the virtual processing and manufacturing of platform components and resolve the problems possible in construction in designing ahead of time

It is introducing version management mechanism to effectively manage all design versions in the designing process.

Planning and Analysis on 3-D Modeling CAD System of Production Platforms

System Planning The overall goals and functions that the system needs to accomplish include the following:

Shorten software development cycle as much as possible and reduce development costs, and the developed products are necessary to have features of strong practical applicability, easy operation, moderate price and good technical support, hence making it easily accepted by numerous designers

The system has to provide the functions of 3-D modeling and virtual constructing

The system has to provide the function to manage the designing data

The system can realize the interactive operation of database and graphics system, so that auto-modification of components models can be realized for user modifying components data, and hence speeding up drawing modification

After identifying general the overall goals and functions of system, it is necessary to analyze and demonstrate the necessity and possibility of system development, and thus the methods to develop the system are confirmed to apply Visual Basic to the second development of AutoCAD, and then meanwhile extend SQL Sever relational database as engineering database and database system structure as clients/sever. Client PC/ server architecture are as shown in Fig. 1.

After confirming the system's general objective and function, its necessity and possibility are analyzed, and then its development method is decided to apply Visual Basic to develop AutoCAD at a second time, and meanwhile it is necessary to extend SQL Sever relational database as engineering database and database system structure as clients/sever. Client/ server architecture are as shown in Fig. 1.

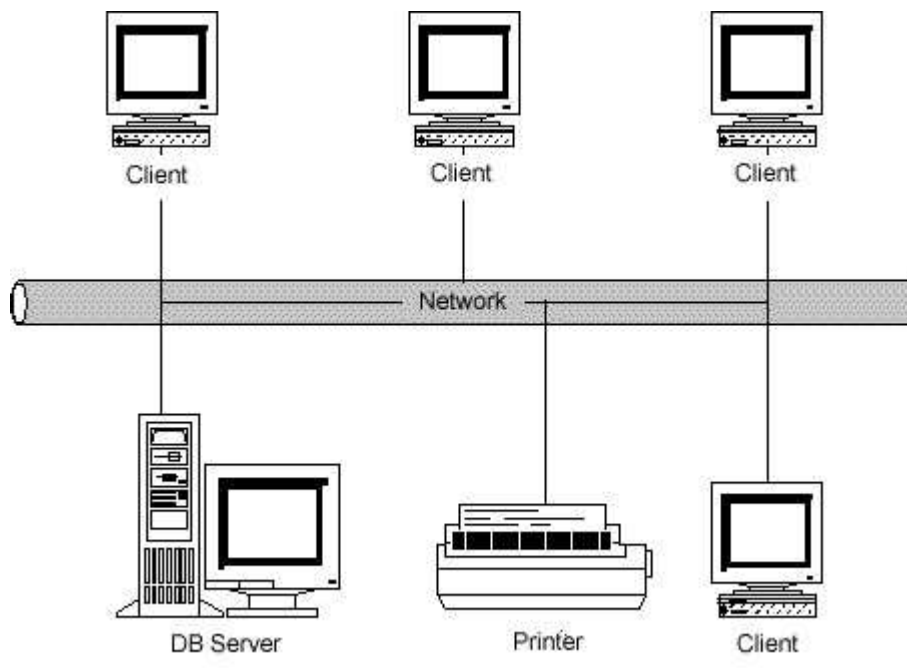


Fig. 1 Client/ Server Architecture

System Analysis

Through the analytical method (IDEF0) generally used by complex systems to analyze the system, the system functions are decomposed into layers and hence the logic model of system is obtained. The six modules of the system are identified by deeply knowing 3-D modeling CAD function needs and restrictions of production platform and combining IDEF0 structural analyzing method. The overall module structure of production platform 3-D modeling CAD system is as shown in Fig. 2.

AutoCAD File Operation Module

The module is to realize connection with AutoCAD and regard AutoCAD as a graphical window in the system, and conduct the operations such as new, open, save and close files, providing a drawing platform for 3-D graphics of the system.

Basic Data Module

The module is to provide necessary basic data for 3-D design of platform, such as platform structured data, structural steel and standard data, and hence realize data entry, maintenance and query, etc.

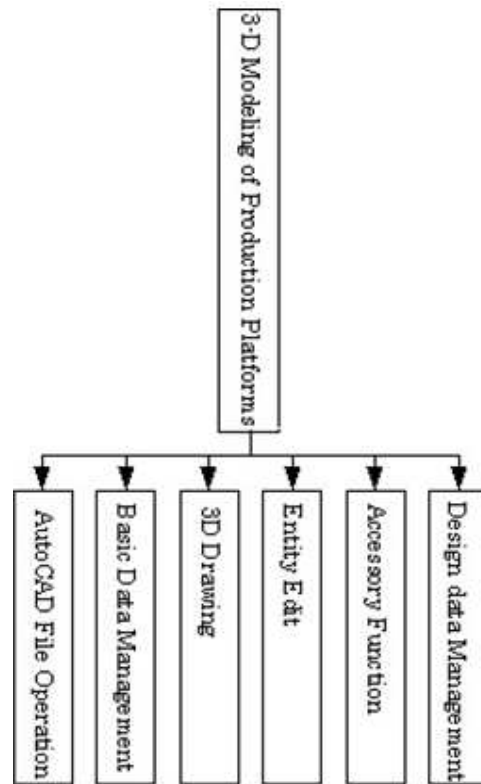


Fig. 2 The Overall Module Structure of Production Platform 3-D Modeling CAD System

Designing data module

The module is to save the engineering data in the designing process, mainly including three parts: Project data management, components data management and designing documents and components relation management. Project data management realizes the macro-control on the designed project, such as the project designing progress, all designing results and electronic document management. Components data management realizes the micro-control on the designed project and mainly manages all platform components data management in the 3-D design of platform, including the entry, maintenance, query and version management of components geometry data, structured data and computational data, and also is able to directly reflect the modification of components data in AutoCAD drawing, thus achieving auto-modification of the model. The design documents and component relation management function are to management the version incidence relation between design document and components.

Drawing Module

The module is the core module of the system, realizing the 3-D parameterized drawing for beam, pillar and plate structures of platform components. After designers select the forms, parameters and space positions of components, AutoCAD will automatically draw 3-D models and automatically store components data into database based on users' willingness.

Components Edit Module

The module is to realize the operations (e.g. connection, combination, acoustic image and delete) of the components 3-D model, and reflect the component data changes caused by all edits into database, achieving the automatic modification of components data. However, connection and combination are able to realize the component virtual processing, authentically reflecting the placeholders and crossovers of platform components, which basically achieves the virtual creation of platform.

Accessory Tool Module

The module adds some accessory functions into the 3-D design of platform, such as view control, drawing initialization, etc. View control makes the entire platform structure, modules and components to be displayed with the form of layers and to be animated, allowing users able to see the platform drawing from all directions as his willing. Original drawing can convert the well-drawn 2D structure Fig. of platform into the 3-D frame Diagram, which is convenient to identify the space positions of components in 3-D designing.

Design of Engineering Database

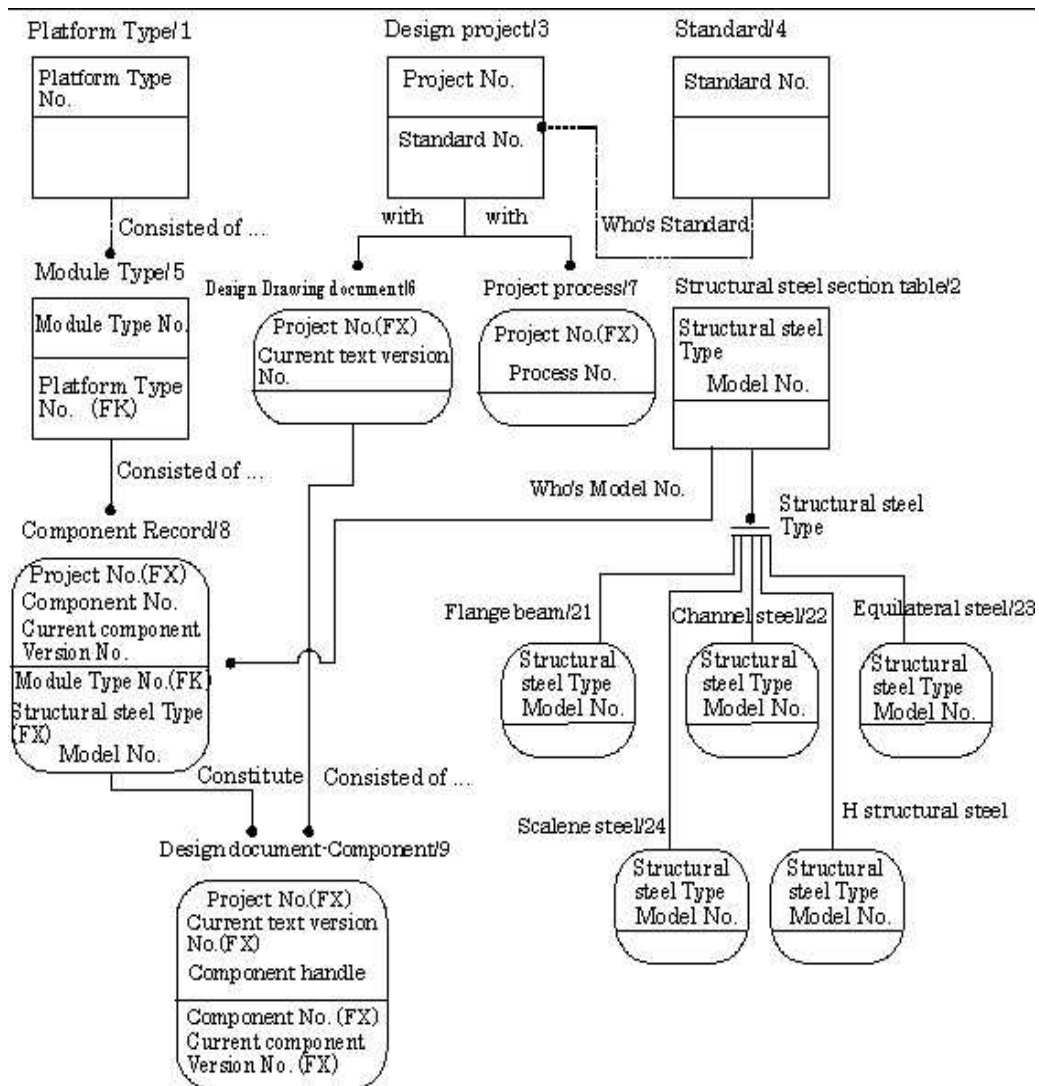


Fig. 3 The Comprehensive Diagram of the Data Model

In the 3-D modeling CAD system of production platform, the design planning of engineering database is to apply AutoCAD graphics system to manage graphics data and extend relation database SQL Server to manage non-graphics data, and also uses the unified coordinating management system developed by VB to realize the two's organic integration. In the light of the engineering database theory, it is necessary to carry on reasonable and analysis and design from the aspects such as model, structure, version management, integrality, things control and system recovering and so on, and hence the development methods of engineering database are identified, effectively storing and using a great number of data of the production platform design.

In the system, IDEF_{1X} method is applied to establish the comprehensive diagram of data model (See Fig. 3).

Program Design of Production Platform 3-D Modeling CAD

By applying structured design method and combining the function modules of system, the module structures of the system are divided and designed; and AutoCAD is re-developed by Visual Basic; the 3-D modeling of production platform is realized based on the characteristic parameterized modeling method; the engineering database operation can be achieved through ADO widgets. Furthermore, it is necessary to design a set of interval code system and conduct specific arithmetic designs for all modules, which can be implemented through VB language, and also design a simple and beautiful user operation interface.

The following are mainly conducted in the 3-D Modeling CAD program design of Production Platforms

Visual Basic applies ADO (ActiveX Data Objects) Data to access to programming model for database programming in order to control, maintain and use engineering database

Visual Basic successfully controls AutoCAD operations by ActiveX technology; through the introduction of AutoCAD object, AutoCAD is regarded as a graphical window of VB program, which can be opened, drawn, edited, closed and print operations, etc

Applying structural design method to divide and design the module structure of the 3-D modeling CAD system of production platform based on the logic model (IDEF0 system model chart) of the system

Applying characteristic parameterized modeling method to develop basic platform components modeling method, such as flange beam, angle iron, channel steel, H structural steel, circular tube and plate body, and also automatically saving components engineering information in the components modeling process and providing complete and unified component data for subsequent analysis and manufacturing process (Parameterized modeling method is convenient for components modification; it is only necessary to modify related components data to achieve automatic modification of components, and the designing process is hence speeded up.)

Applying AutoCAD entity operating function to conduct virtual processing for components, fully considering the crossover, placeholder, and connection in the designing process, and resolving the problems in construction in designing ahead of time, hence largely avoiding cost waste caused by improper design

Designing a set of interval code system and thus effectively ensuring the data rationality and effectively to be stored and applied.

Applying MDI to design program interface, so that program interface has reasonable structure, simple operation, beautiful appearance, and is convenient for users to use

Some Features of the 3D modeling program interface design of production platform:

Packaging program functions in the form of menu, and each menu option corresponding to a program function so that program structure is very clear

Using floating buttons greatly and giving each button vivid icons (floating buttons and icons make program interface vivid and lively and button function intuitive, easy to use)

Using image ActiveX greatly to support multiple images formats such as .bmp, .JPG, .jpeg, .gif, and .co (the selected images in the system all were vivid and properly describes the related program functions)

Using multi-record data operation window greatly in the form of tables (A majority of data operation interfaces adopt the form of multi-record tables so that users can simultaneously operate multiple records which are also shown in front of users, and then users can acquire an overall understanding and comparison of the data)

Using the form of father table and sub-table to display data (e.g. in version management, father table displays the current version while sub-table shows related ex-version and subsequent version so that users can get data as much as complete by simple operations)

Making simple and proper operating instructions, namely that using the tools such as image and text to simply explain some abstract operations (e.g. in flange beam drawing, images are used to display the diagram of flange beam section attached with textual description, so that users can get an intuitive and correct understanding of abstract attributes)

Designing the program interface which needs to closely connect with AutoCAD to be small and exquisite (e.g. view control and AutoCAD operation interface tightly link with each other so that user can know well what influences of his own operation on the 3-D model in AutoCAD)

The Application of the 3D Modeling CAD Program of Production Platform

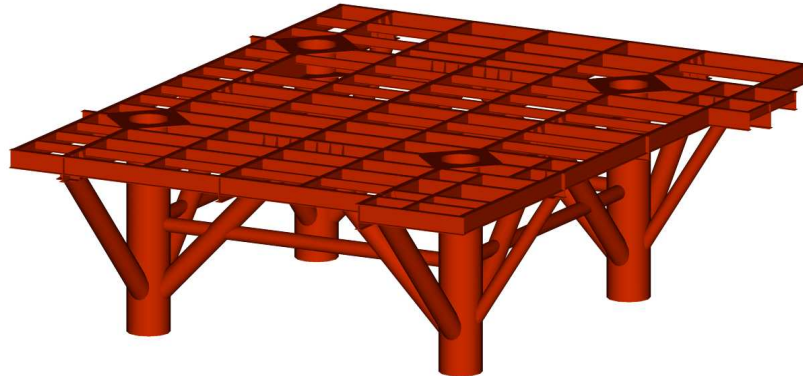


Fig. 4 The 3-D Model of Upper Shallow-Foundation Production Platform Module (Without Deck)

The 3D modeling CAD system of production platform has been put into use in multiple platforms. Practices have proved that it is convenient and fast to apply the system to design platform with beautiful design effect and complete component records.

Model can be observed from different angles through the view control of the program. The entire model structure can be displayed with the form of layers through layer control. Thus, the internal structures of all modules can be known well. The 3-D model of upper shallow-foundation production platform module (without deck) is as shown in Fig. 4 and the 3-D model of shallow-foundation production short pile is seen in Fig. 5.

From the 3-D model of diagram 5b platform short pile without pile lining, internal structure of short pile can be clearly seen

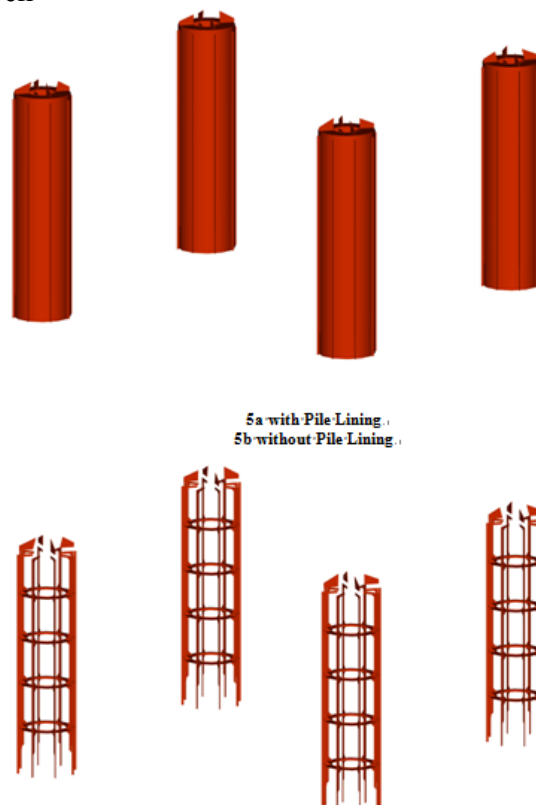


Fig. 5 The 3-D Model of Shallow-Foundation Production Short Pile

Conclusion

The 3-D modeling CAD system of Production platform adopts 3-D method to design platform. Its reasonable structure and easy operation are of great significance on the improvement of design level. System development, design analysis, parameterized modeling, information management and version management and so on can also be applied to other engineering designs and have certain popularization value.

Fund Project

National 863 “Offshore Platform with Positive Pressure Spouted & Strengthened Pile Foundation”

References

- [1] Liu Wenjian, Changwei and Jintianguo, CAD/CAM Integration Technology, Harbin: Harbin Institute Of Technology Press, 2000, 1-26
- [2] Zhao Jia, Yin Guofu, Guidelines to CAD/CAM Practical System Development, Beijing: China Machine Press, 2002, 36-85
- [3] Wan Yankai, Engineering Database System, Beijing: Tsinghua University Press, 1999
- [4] Wan Yankai, Typical Engineering Database Management System, Computer World, 12(5), 36-41
- [5] Zhou Sucheng, Xi Likang and Zhou Xiaozhe, the Construction of Ships and 3D Entity Modeling Database, Technology & Economy Information of Shipbuilding Industry, 2001, 191(3), 36-39
- [6] Wang Fu, the application of Computer aided design to offshore oil engineering, China Marine oil and gas engineering, 9(1):21-23
- [7] Yang ShuGeng, Chen Yue and Teng Mingqing, Offshore platform engineering database and 3d entity modeling technology research, Ship engineering, 25 (5) : 11-14

Subway Station Seismic Structure Dynamic Model

Ke Liu

The Civil Engineering Department in Southwest Jiaotong University-E'mei, Emei City, Sichuan Province, China

Keyword: Subway Station; Strong Seismic; Dynamic Response; Numerical Simulation

Abstract. The state with tense traffic is aggravated constantly with the swift and violent development of our country economy. Surface transport is far from enough to meet the growing demand as urban traffic pressure continued growth. Therefore, subway, as a new way of transportation is developing rapidly in many great cities. Relative displacement value at both ends of the structure component is the main factor affecting the structure of the normal use, also not to be ignored. The results can be used for reference design, construction and safety assessment for similar structure.

Introduction

Now, because there are a lot of such as subway underground structure, underground warehouse, supermarket, and underground water hose lines, they will inevitably make across each other. It is well known, it will lead to serious threat to people's life and property losses uneven ground structure surface subsidence surface subsidence process or important construction structure down-through [7, 10). It has become a very important issue; ensure the safety of the existing pipeline structure, through a new. Obviously, this problem becomes salvation keys, reasonable use of underground space full. However, general theory analysis mainly concentrated in the static analysis, the dynamic analysis is rarely, not to mention the earthquake happened in the dynamic response analysis of the existing structure, is down-through new structure. The project of south-to-north water transfer project in the tunnel down-through weeklong subway station as background, this paper expounds the dynamic performance, strong earthquake in subway station.

Engineering Background

Wukesong station is east-west direction, whose length and width are 174.98 m, 19.5 m, respectively. It belongs to the three spans frame structure. The station is down-trenched by the convey tunnel of the south-to-north water transfer project. The angle of the two centerline (the station and the two convey tunnel) is about vertical. The axis distances between the two convey tunnels are 8.2 m, adopted undermining method and two-way construction. The construction stopped at the place 22m from the station and then reinforces the soil between the station and the two tunnels by grouting, finally excavation the convey tunnels in one way. On the cross section, the diameter of the tunnel is 5.2 m, the flow cross-section is 4m, and the first lining thick is 0.3 m, the second lining thick is 0.3 m. On the vertical section, the tunnels climb as a slope of 5% respectively in the north and south at the end of the station, when down-through the station the tunnels remain flat slope. The buried depth of the roof is 15~17m, the tunnel top roof from the floor of the station structure is about 3.7 m when down-through the station. The geologic data reference the report of geotechnical investigation on west fourth ring Fuxing road. The site seismic intensity is 8 degrees and the basic types of construction sites is class II.

Model Parameters

According the report of geotechnical investigation on west fourth ring Fuxing road, two layers were assumed of the soil within the research scope. The parameters of the upper soil and lower soil of wall rock1 and wall rock2 were list in table 1. The axis distances between the two convey tunnels are 8.2 m, the axis of the two tunnels overlap the centerline of the west fourth ring road. The tunnel

top roof from the floor of the station structure is about 3.7 m when down-through the station. The width of the subway station is 19.5m, the height is 7.9m and the roof from the ground surface is 4.833m. The pillars in the station are 7.9m high, 0.9m width, 1.2m long. The pillars' horizontal spacing 5.5 m, longitudinal spacing is 6m. The parameters of selected material are listed in table I. The constitutive relationship of the soil is very complex. Elastic constitutive relation, elastic-plastic constitutive relationship are the most popular used. The dynamic mechanical model of soil mainly includes linear visco-elastic model, nonlinear elasticity and plasticity model and equivalent nonlinear visco-elastic model. The dynamic response of the structure no more than confined to elastic stage during strong seismic occurred. Partial or most of the structure is will appears the plastic deformation correspondingly [7].

Table 1 Material Parameters of the Subway Station

Model	ectional dimension m	unit weight γ (KN/m3)	Modulus of elasticity E (Pa)	Poisson's ratio μ
tunnel lining	0.55	25	3.10E+10	0.2
Roof plate	1	25	3.10E+10	0.2
Bottom plate	0.85	25	3.10E+10	0.2
Side wall	0.7	25	3.10E+10	0.2
Pillar	0.9×1.2	25	3.10E+10	0.2
Wall rock1		18	8.71E+06	0.35
Wall rock2		21	5.50E+07	0.35
			angle of friction (C)	Cohesive strength (°)
Wall rock 1			1.60E+04	22.8
Wall rock2			1.60E+04	37

Selection and Adjustment of Seismic Wave

"Code for seismic design of buildings" (GB50011-2001) specifies the choosing method of seismic wave. the correct selection of seismic wave's acceleration time histories inputting calculation model should meet the requirement of three factors that ground motion have (spectrum character, effective peak acceleration, duration) [10]. According to this actual project, a kind of seismic wave of EI CENTRO was selected to input the numerical model.

Strong earthquake is that whose magnitude above MS 6[11, 12]. The length of the motions is determined by the earthquake magnitude, the higher of the earthquake magnitude, and the longer of the duration. The relationship between earthquake magnitudes and the vibration duration was listed in table 2.

Table 2 Earthquake Magnitude and Duration

Earthquake magnitudes	5.5~6	6.5	7	7.5	8
vibration duration	8s	14s	20s	40s	60s

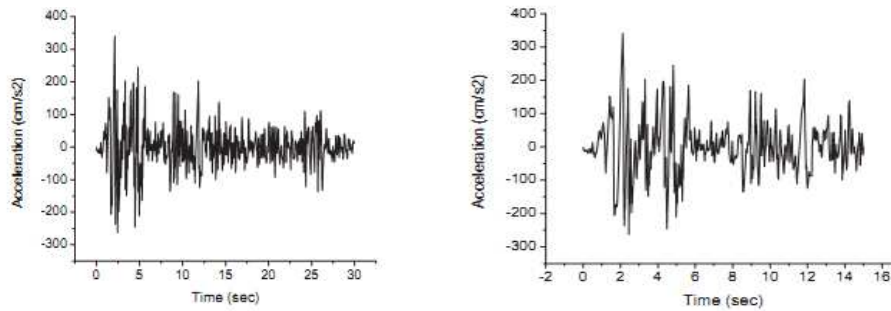


Fig. 1 Ei centro seismic wave Fig. 2 EI CENTRO seismic wave after the adjustment

After the adjustment, the EI CENTRO seismic wave was input to the model from the bottom perpendicular.

Modeling and the Observation Points

The geometrical model and its meshing are shown in figure 3, and relative position of the station and the tunnels is shown in figure 4. The scattering and reflection problems of seismic wave for Underground structure in the analog seismic response need to handle properly. Artificial boundary must be exerted for the Foundation was simulated as finite region from infinite regional. Reflex of wave was produced in artificial boundaries and affect the wave's freedom propagation. The larger Intercept range is the better of the simulation results' precision. However, the bigger engineering calculation is. Many experts and scholars studied in dealing with the calculation accuracy and save the computational time contradiction, and also got effective research achievements. Intercept 5~10 times of the size of the roof, generally. Based on the project's own characteristics: influenced by the two parallel convey tunnel under, tunnel diameter was 5.2 m, and tunnel axis spacing was 8.2 m. The maximum range of the two tunnels is 13.4 m. Considering the influence of tunnel to the metro station, the intercept range in length direction of soil is unfavorable too small, and therefore, this paper decided to intercept around 7 times size of floor of the subway station (size for model is 137m) in convey tunnel direction. Intercept about five times tunnel maximum range as the soil longitudinal calculation scope, interception width is 66 m. and height is 40 m. The positions of monitoring points are in Fig 5.

Modeling and the Observation Points

The vertical displacements of monitoring points are shown as below.

As shown in Fig 6, 7, some conclusions could be obtained. The vertical displacement's time-history of the monitoring points in subway station is similar with the time-history of input seismic wave, in the condition of EICENTRO seismic wave imputed in perpendicular. The vertical displacement doesn't appear lag phenomenon obviously. Different monitoring points have different displacement amplitude (the extent of the damage is different), but all they are less than 10 cm. the maximum vertical displacements of the monitoring points are listed in table III

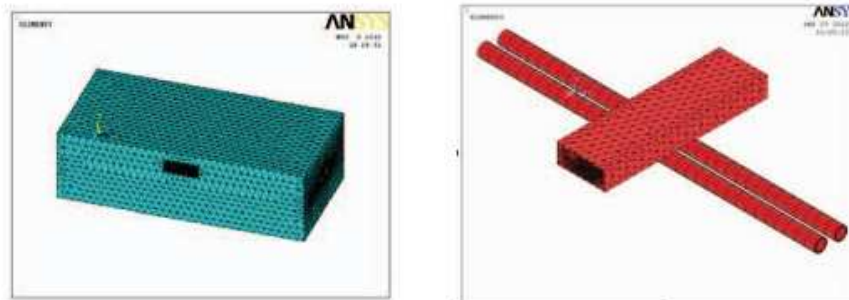


Fig. 3 Meshing of the model Fig. 4 Relative position of the station and the tunnels

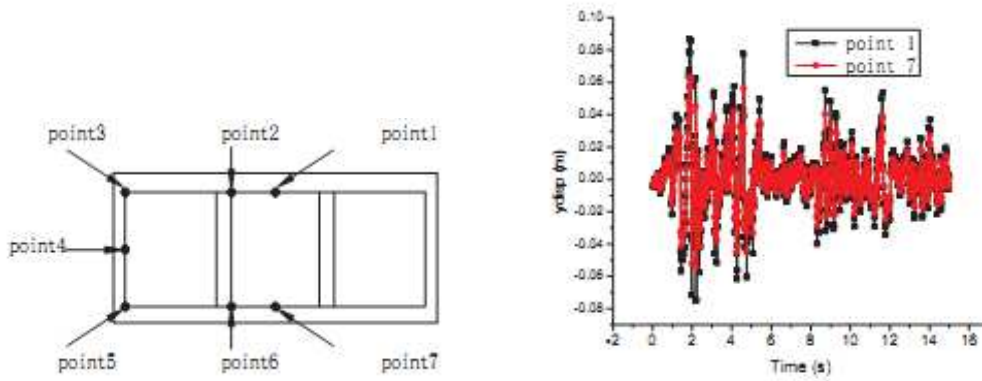


Fig. 5 The position of monitoring points Fig. 6 Historical curves between time and vertical displacement at the monitoring point N0.1 and No.7

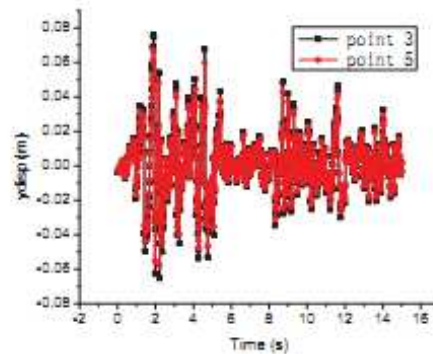


Fig. 7 Historical curves between time and vertical displacement at the monitoring point N0.3 and No.5

Maximum values of vertical displacements at the monitoring points

Point	+X(m)	-X(m)	+Y(m)	-Y(m)
1	4.10E-05	-3.55E-05	8.66E-02	-7.49E-02
2	7.41E-04	-6.40E-04	8.27E-02	-7.15E-02
3	8.08E-04	-6.98E-04	7.56E-02	-6.53E-02
4	2.76E-03	-2.39E-03	7.49E-02	-6.47E-02
5	6.90E-04	-5.96E-04	7.44E-02	-6.43E-02
6	5.91E-04	-5.11E-04	6.62E-02	-5.72E-02
7	3.34E-05	-2.88E-05	6.30E-02	-5.45E-02

As shown in table III in the function of EI CENTRO seismic wave which is input to the model in perpendicular, the peak displacement in transverse of the monitor nodes is smaller than the vertical peak displacement. The peak displacement in horizon appears at point 4 (in the middle of the side wall), the value is 2.76mm in forward direction in horizon, 2.39mm in negative in horizon direction; the peak displacement in vertical direction appear at point 1(in the middle of the roof plate), the value is 8.66cm in forward direction in vertical, 7.49cm in negative direction in vertical. The reason is that the ends of the side wall are restriction respectively by the roof plate and the bottom plate, therefore, the relative stiffness is larger than it in the middle of the side wall which induces the deformation in the ends of the side wall is smaller than it in the middle. The displacement of roof plate is similar as it in side wall. The following conclusions can also be got from table III appears an upward trend about the vertical displacement from the node in bottom plate to the roof plate. There exists an obvious amplification effect to the seismic wave by the station, an interaction was happened between the soil and the station, and a great push force to the station was generated by the soil around.

The value of maximum displacements of the points at the ends of the structural members and occur time are listed in table IV

Table 3 Maximum values of relative displacements at the monitoring points

Relative displacement (mm)	Point 1-7	Point 3-5	Point 2-6	time of occurrence (s)
away	23.62	8.63	16.53	1.88
close	-20.41	-7.46	-14.28	2.22

The relative displacement on the structure components in the vertical vibration sort by size is the roof plate, the middle of the bottom plate, the ends of the side wall, the middle of the side wall; the time of occurrence of the maximum displacement in the structure is the same and it is near the time of peak accelerator of the seismic wave. As a result of the relative stiffness at the ends of the pillar is larger than it in the roof plate and the middle of bottom plate, the side wall has deformation caused by the soil pressure around; the peak accelerator of the seismic wave is the main factor that affects the maximum relative displacement in structure components.

The maximum of tensile stress and compressive stress of the monitoring points during earthquake are listed in table V.

As shown in table č, the compressive stress of structure is smaller than 5.45MPa. As known, the allowable compression stress of concrete C30 is 14.3 MPa. The compressive stress meets design requirement. The tensile stress is also achieved to 5.45MPa. But the allowable tensile stress of concrete C30 is 1.43MPa. Obviously, the tensile stress doesn't meet design requirement. So, reinforcement assembly is necessary to the lining. In summary, the lining of the station is inclined to pull crack. The pillars and side wall are inclined to crush damage.

Table 4 Maximum values of stress including tensile and compressive at the monitoring points

Point	+X(m)	-X(m)	+Y(m)	-Y(m)
1	4.71 E+06	-5.45E+06	4.06E+03	-3.51 E+03
2	2.72E+06	-3.15E+06	2.28E+03	-1.97 E+03
3	2.42E+06	-2.09E+06	5.20E+06	-4.50 E+06
4	6.83E+03	-5.90E+03	5.35E+06	-4.62 E+06
5	3.23E+06	-2.79E+06	5.45E+06	-4.71 E+06
6	2.95E+06	-3.42E+06	5.12E+03	-4.43 E+03
7	3.84E+06	-4.44E+06	2.95 E+03	-2.55 E+03

Conclusions

Such as the description above, the first force their relative displacement, and in both ends of the earthquake in column that they tend to hurt strong too much stress condition. For the pillars of the prejudice damage horizontal vibration (press-bend hurt). The roof board and bottom bending plate incline to damage. Shear fault occurred in stress concentration section change. It should not be neglected in the influence of the peak acceleration are more the maximal displacement of structure. In particular, they also last longer have great influence on the structure of the final displacement.

The global structure of the great and the displacement is relative displacement as structure in vertical vibration. Although damage on small structure, the structure of normal use, it will affect the relative displacement of big. The structure and improve the initial force major: relative displacement. So it is relative displacement control, which should be paid attention to in the practical project.

References

- [1] Tong Jiang, Hailing Xing, Liang Su, "ELASTOPLASTIC seismic response analysis of intricate system of Shield tunnels Under the Action of Travelling Waves ," Earthquake Engineering and Engineering Vibration, vol. 24, pp. 27-32 , 2004.
- [2] Hong Zhang, Jihong Bi, Wei Zhang, "Nonlinear Seismic Response Analysis of subway tunnel," Earthquake Engineering and Engineering Vibration, vol. 24, pp. 146-153, 2004.
- [3] Haiyang Zhuang, Shaoge Cheng, Guoxing Chen, "Numerical Simulative Analysis of the mechanism of earthquake damage of Dakai subway station during KOBE earthquake ," Rock and Soil Mechanics, vol. 4, pp. 48-52, 2008.
- [4] Guobo Wang, Xianfeng Ma, Linde Yang, "Three Dimensional analysis of earthquake response on subway station and tunnel in soft soil," Rock and Soil Mechanics, vol. 30, pp. 2523-2528, 2009.
- [5] Dongliang Zhang, Guobo Wang, Linde Yang, et al, "Three Dimensional analysis of earthquake response on subway station which has series of holes in sideway," Seismic survey, vol. 32, pp. 46-50 , 2009.
- [6] Jingbo Liu, Xiangqing Liu, Bin LI, "Pushover Method for Seismic design and analysis," Journal of civil engineering, vol. 41, pp. 73-80, 2008.
- [7] Jingbo Liu, Xiangqing Liu, "Pushover analysis of Daikai subway station during the Osaka-Kobe earthquake in 1995," The 14th world Conference on earthquake engineering, Beijing, China, pp. 12-17, October, 2008.
- [8] Jingbo Liu, Yixin Du, Qiushi Yan, "The application of visco-elasticity artificial boundary and the input of seismic wave in the currency finite element analysis software," Journal of Disaster Prevention and Reduction Engineering, vol. 27(Addition), pp. 37-42 , 2010.
- [9] Jin Bian, Lianjin Tao, et al, "Response Analysis of subway station structure during strong seismic," World Earthquake Engineering, vol. 26, pp. 114 -118, 2010.
- [10] Gang Lin, Shipei Luo, Juan Ni, et al, "The earthquake damage and Elimination of subway structure," Modern Tunneling Technologies, vol. 46, pp. 36-41, 2010.

Study on In-Situ Shearing Strength Test for the Retaining Wall Bottom in a Bank Revetment Project

Guang Zhang^{1, a}, Junrong Ma^{1, b}, Jingxi Chen^{1, c}, Hualin Zhou^{1, d},
Donghua Wang^{1, e}

¹Wuhan University of technology, Wuhan, Hubei, China

^agzhang58@163.com, ^b6891533@qq.com, ^cjxchen60@163.com, ^d949100452@qq.com,
^e563812940@qq.com

Keywords: Bank Revetment, Retaining Wall, Shear Strength, In-Situ Test.

Abstract. To obtain the necessary shear strength parameters of the retaining wall bottom in a bank revetment project, in-situ shearing strength test must be conducted. There are 3 kinds of foundations. One is undisturbed soil foundation, and the other two are composite foundations. Due to the limited of the engineering conditions, each kind of foundation has prepared one specimen only. So the single shearing strength test can't separate cohesion c and friction angle φ . To solve this problem, a method which is a combination of shear strength test and sliding strength test is used. Sliding strength test is carried on specimens that have already failed after shearing strength test. This test is carried in wet conditions and cohesion values and friction angle values are obtained. In addition, the influence of the processing of composite foundation to equivalent friction coefficient is analyzed. Test result can be referenced by bank revetment projects which have similar geological conditions.

Introduction

Cohesion and friction angle values between retaining wall bottom and the foundation are necessary mechanics parameters for the design of retaining wall. In-situ shearing strength test is a popular test to obtain shear strength parameters ^[1, 2]. This test demands that there are at least 2 test specimens at each test point and generally 3 to 5 specimens are needed to get shear strength parameters. But due to the limited of founds and site conditions, sometimes each kind of foundation has prepared only one specimen in the practice. In this condition, we can't get actually cohesion and friction angle values by shearing strength test. To solve this problem, a method which is a combination of shearing strength test and sliding strength test is applied. This method did very well in our test.

Test Method

Test Conditions

This period of retaining wall has three types of foundation. First, the undisturbed soil foundation, the retaining wall will be built on the foundation directly. Second, a composite foundation, it was stabilized by small stakes when the thickness of soft soil layer is between 1 meter and 1.5 meter. The stakes are 3 meters long. Third, another type of composite foundation, it was stabilized by cement mixing piles when the thickness of soft soil layer is above 5 meters. The cement mixing pile is 9.5 meters long and its diameter is 0.5 meter. There is only one specimen at each type of foundation. The test point at the first type of foundation is named Point A, the second is named Point B and the third is called Point C.

Test Device

In the test, the concrete specimen is casted directly on the level foundation. Its concrete grade is the same with the concrete grate of the retaining wall bottom. The joint face of the specimen and foundation is used to simulate the joint face of the retaining wall bottom and foundation. Since the retaining wall is part of a bank revetment project, the groundwater level is high at test points. When casting specimens, the top surface of foundation is difficult to unwater completely. Such simulation condition can weaken the shearing strength of the joint face. But this is the same as the construction condition of the retaining wall. The loading system scheme of the test is shown in Figure 1.

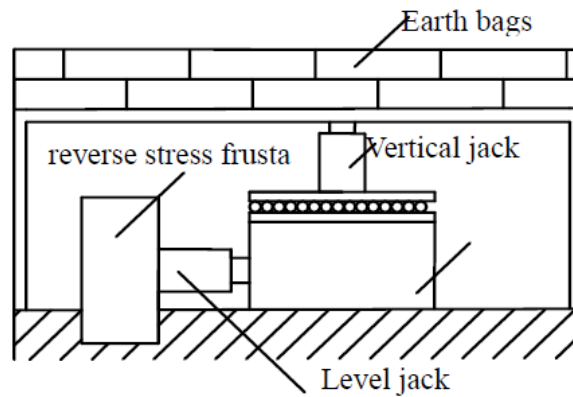


Fig. 1 The loading system scheme of the test

Load Classification and Load Application

Vertical Load

Vertical load is divided into 4 levels. The value of the maximum vertical load is 80KN. So the four levels of vertical load are 20KN, 40KN, 60KN, 80KN. Each level of vertical load is slowly increased to reservation load value at once. After this, the settlements of concrete test specimen are observed. When the settlement of specimen is less than 0.1mm per hour^[3, 4], we can think that the settlement has stabilized and then the horizontal load can be applied.

Horizontal Load

Horizontal load is applied slowly and its initial value is zero. Generally every 1 minute we increase horizontal load once, then measure and record the relevant horizontal displacement. In order to draw $S \sim u$ curve expediently, the horizontal load incremental should not be too big. In this test, the horizontal load incremental is 1.0KN and the value of maximum vertical load.

Test Sequence

For each test point, shearing strength test is conducted first, and then sliding strength test is conducted on the failed specimen. For shearing strength test, the max vertical load is 80.0KN. For sliding strength test, vertical load $P_1=20.0\text{KN}$, $P_2=40.0\text{KN}$, $P_3=60.0\text{KN}$, $P_4=80.0\text{KN}$.

Test Results and Analysis

Results of Shearing Strength Test

Shearing strength test is conducted respectively at the three test point. Based on the data which are obtained in the test, three $S \sim u$ curves are drawn. They are shown in Fig.2.

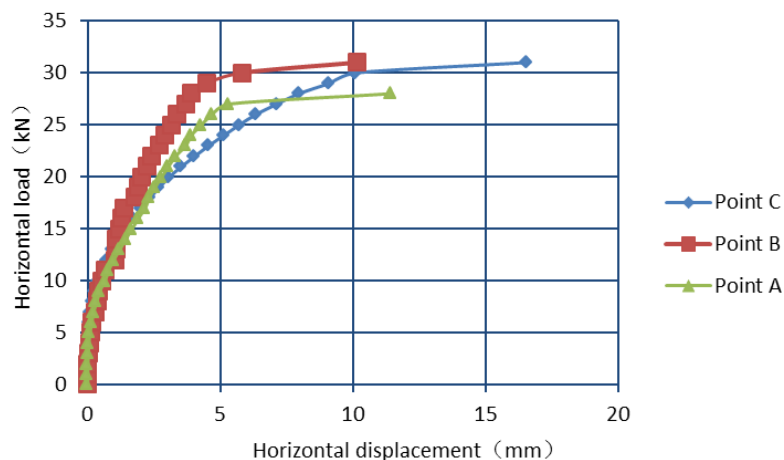


Fig. 2 $S \sim u$ curves obtained from shearing strength test

Results of Sliding Strength Test

Based on the data we obtained from the sliding strength tests at the three different test point, we can draw three sets of $S \sim u$ curves. They are shown in Fig3, Fig4 and Fig5.

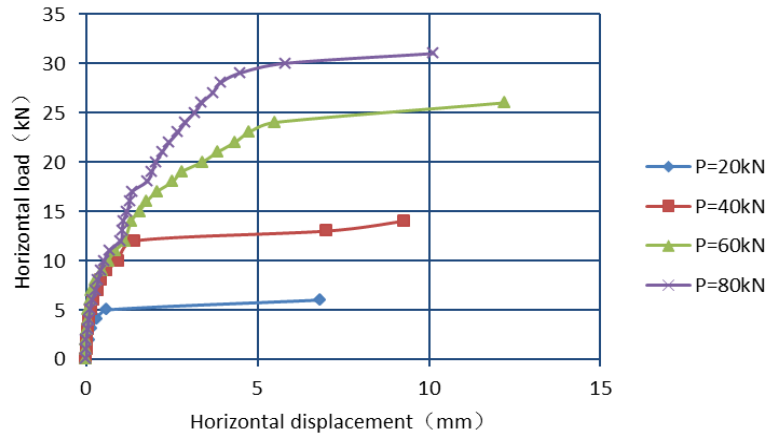


Fig. 3 S~u curves obtained from sliding strength test at Point A

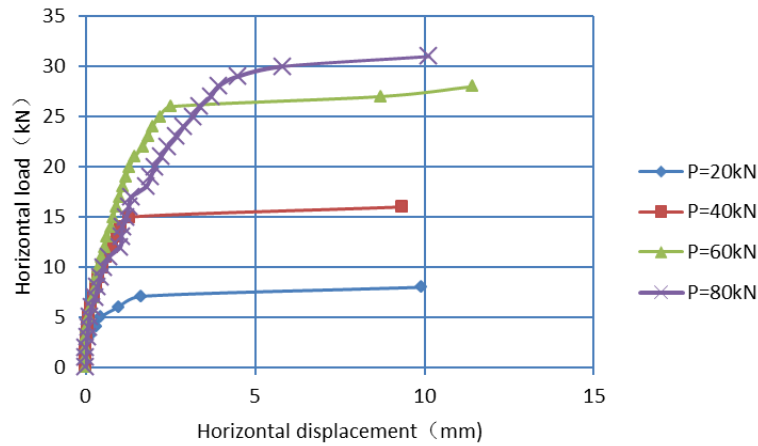


Fig. 4 S~u curves obtained from sliding strength test at Point B

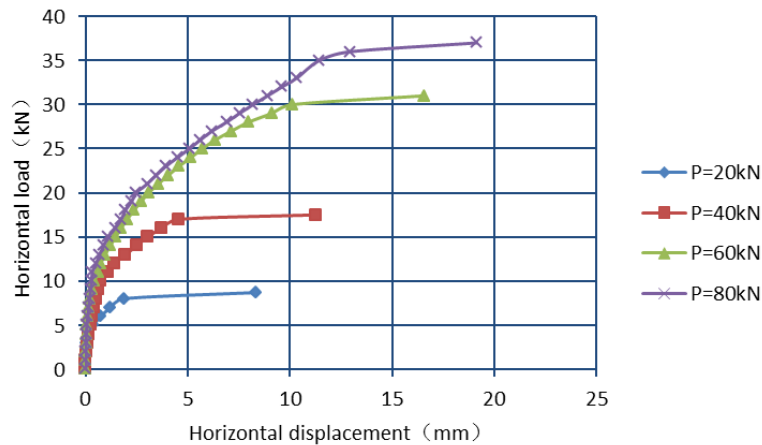


Fig. 5 S~u curves obtained from sliding strength test at Point C

Analysis of Result

When S ~ u curve appears a peak or an inflection point, we can think that the joint face has happened a shear slip failure. The horizontal load at this time is the failure load. According to Fig.2, Fig.3, Fig.4 and Fig.5, we can obtain the failure load under the relevant vertical load. We denote the failure load by S_i and the relevant vertical load by P_i .

$\sigma_i = P_i/A_i$, $\tau_i = S_i/A_i$. A_i is the bottom area of the test specimens and it is 1 m^2 in the test. The measured values of σ and τ are show in Table 1 and Table 2.

According to Coulomb failure criteria:

$$\tau_{\max} = \sigma_{\max} \cdot f + c \tag{1}$$

Table 1 Values of σ_{\max} and τ_{\max} at the three test points in shearing strength test

Measured values	Point A	Point B	Point C
σ (kPa)	80.0	80.0	80.0
τ (kPa)	31.0	36.4	36.0

Table 2 Values of σ_i and τ_i at the three test points in sliding strength test

Test point	Measured values	1	2	3	4
Point A	σ_i (kPa)	20.0	40.0	60.0	80.0
	τ_i (kPa)	5.0	12.0	24.0	27.0
Point B	σ_i (kPa)	20.0	40.0	60.0	80.0
	τ_i (kPa)	7.1	15.0	26.0	30.0
Point C	σ_i (kPa)	20.0	40.0	60.0	80.0
	τ_i (kPa)	8.0	17.0	28.0	30.0

Since the specimen has failed with shear failure, the value of c is zero in sliding strength test.

$$\tau_i = \sigma_i \cdot f \quad (2)$$

$\sigma_4 = \sigma_{\max}$, based on the above two formulas, we can figure out the following formula.

$$c = \tau_{\max} - \tau_4 \quad (3)$$

$$c_A = 31.0 - 27.0 = 4.0 \text{ kPa}, \quad c_B = 36.4 - 30.0 = 6.4 \text{ kPa}, \quad c_C = 36.0 - 30.0 = 6.0 \text{ kPa}.$$

Least square method is used to fit σ_i and τ_i which are obtained in sliding strength test.

$$f = \frac{\sum_{i=1}^n \sigma_i \tau_i}{\sum_{i=1}^n \sigma_i^2} \quad (4)$$

$$R = \frac{\sum_{i=1}^n \sigma_i \tau_i}{\sqrt{\sum_{i=1}^n \sigma_i^2 \sum_{i=1}^n \tau_i^2}} \quad (5)$$

R is correlation coefficient. The following are calculated results: $f_A=0.3483$, $f_B=0.3918$, $f_C=0.4100$; $R_A=0.994$, $R_B=0.998$, $R_C=0.995$.

The values of R are all close to 1, this indicate that the linear degree of fit beeline is high^[5]. The value of friction coefficient at point A is 0.3483, point B is 0.3918, and point C is 0.4100. The measured friction angle of point A, point B and point C is 19.20° , 21.39° and 22.29° .

Conclusions

The measured values of cohesion and friction are as following. $c_A = 4.0 \text{ kPa}$, $\varphi_A = 19.2^\circ$; $c_B = 6.4 \text{ kPa}$, $\varphi_B = 21.39^\circ$; $c_C = 6.0 \text{ kPa}$, $\varphi_C = 22.29^\circ$.

The shearing strength of point A is lower than point B and point C. But the differences are not obvious. Since point A is on the undisturbed soil foundation, point B and point C are on the composite foundations which are stabilized by small stakes and cement mixing piles respectively. We can safely draw a conclusion that the processing of composite foundations has little influence to the equivalent friction coefficient.

Test results can be referenced by bank revetment projects which have similar geological conditions.

References

- [1] Bo Xiang, Linrong Zhou and Jianlin Ma, Determination Method of Shear Strength Based on Classification of Rock Structure Surface, *Chinese Journal of Rock Mechanics and Engineering*, vol.27, pp.3547-3552, 2007.
- [2] Zhiquan Huang, Linfeng Wu, Anming Wang, e.g. Stability analysis of expansive soil slope based on in-situ shear test, *Rock and Soil Mechanics*, vol.29, pp.1764-1768, 2008.
- [3] Jian Xu, Xiulan Chen, The In-situ Shear Test Method of Retaining Wall Backing Rolled Rockfill and its Application, *Chongqing Architecture*, pp.46-49, 2006.
- [4] Yun Dong, Hejun Cai and Huili Yang, Comparison of Shear Test in Site and Lab large-scale Shear Test for Rock-soil Aggregate of Roadbed, *Chinese Journal of Rock Mechanics and Engineering*, vol.27, pp.235-238, 2005.
- [5] Wenliang Wu, Yao Zhang, Zaiqi Fu, e.g. Combined Uncertainty on the Slope of Zero-Crossing Linear Fitting, *Journal of Yunnan University Nationalities(Natural Sciences Edition)*, vol.20, pp.71-74, 2011.

Study of Light Pollution about Night Landscape Lighting

Yang XiaoQian

Zhi Xing College Of Hu Bei University, Wuhan, P.R.China, 430000

Keywords: Light Pollution, Night Landscape Lighting, Low Carbon Lighting.

Abstract. Night landscape lighting is the extension of urban space and time and it reflects the prosperous development of economic and that cultural life has become increasingly rich and colorful. However, nowadays, the phenomena of pursuing excessive brightness and decorative lighting instead of functional lighting and abusing light color and following the model blindly have become prominent problems in the construction of night landscape in our country. Light pollution problem has already become the heated focus of academic theory and lighting technology management group. This thesis is based on the light pollution of cities' night landscape lighting , analyzing the harm to biosphere, social life and urban environment caused by light pollution, expounding its sphere of influence and the main forms and summarizing the problems and reasons of light pollution about cities' night landscape lighting .The aesthetic sense about city night view needs to accord with intensity of illumination standard but also to follow the principles of humanism, environmental psychology, city aesthetics, ecology and so on.

Introduction

The light of the world, in addition to satisfying the function demand of people to "see", plays an important role in revealing atmosphere, rendering the urban environment and highlighting stereo adornment. Every city of the world is filled with bright lights, interweaving light and shade , changing light and color irregularly .The rhythm of life of "nine to five or" "work from dawn to dusk has been abandoned in cities, which put upside down the cognition about "night" in people's mind.

(Fig 1) is the synthesis distribution according to the weather satellite photographs of the earth's night sky brightness. Yellow and red display the section of the artificial lighting brightness distribution and degree. Former beautiful night sky has become just like day without beauty. This kind light pollution phenomenon is mainly caused by air molecules and aerosols reflecting the artificial lighting. Showing clearly in the graph, the United States, Britain, France and Japan are the brightest places with the greatest light pollution degree.

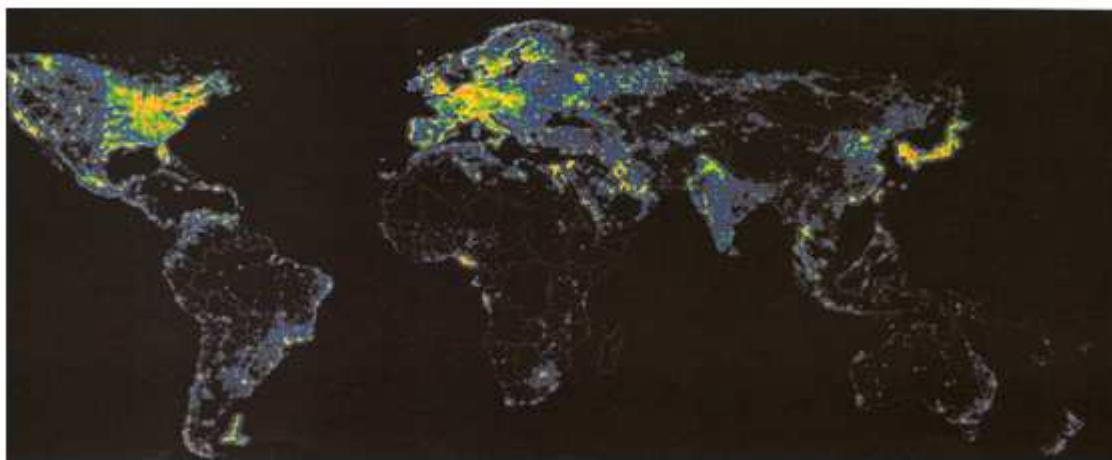


Fig. 1 The night sky brightness distribution on Earth

The degree of light pollution of China located in the eastern part of Asia is not particularly serious according to (fig 2), but we must know that the history of building lighting project of China's massive construction of city night view is less than ten years! Light pollution has been

approaching China! All major cities in China construct night view in full swing. What's more ,the planning department of many medium and small cities are preparing or implementing " bright project", "glorious engineering" or "light up engineering", and these cities compete with each other, In their opinions ,more shining the city becomes , more reputation the city will gain, this wrong idea lead serious waste of light. After the air pollution, water pollution and noise pollution, we will face a tough problem- light pollution caused by excessive artificial lighting.

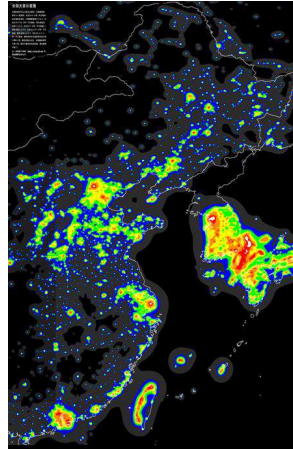


Fig. 2 The night sky brightness distribution

The Harm of Light Pollution

Although light pollution is latent, it will also be a danger. According to the survey, 96% of the citizens know little about the damage of light pollution, in fact, which worries us .Therefore, it is necessary to expose the great harm to cause the attention of people.

The Harm to the Biosphere

Physical harm

Scientific research found that the city's night lights would disrupt the normal life rule of the human body because of using artificial light source, which will make the body's organism off balance. Light pollution is also an important cause of teenagers' myopia. Today's high school students of myopia increase 60%, some experts thinks visual environment is the main cause of formation myopia instead of the habit of using eyes.

Psychological Harm

If residential environment is too bright at night, residents will be difficult to fall asleep, which will disrupt biological clock, and cause decreased appetite, depressed, lethargy and psychological pressure etc.

The Influence to Nature Living Things

Animal some insects like moths have photo taxis, Nocturnal animals are difficult to adapt the lights in the night, the lights of buildings will lure insects to tall buildings, and "desperate" tragedies often happen. According to the statistics of American bird experts, every year there are 4 million migratory birds died because of hitting high-rise building advertisement lamps.

Plant researchers found that lighting will influence physiology and ecological system of plant, such as photosynthesis, growth, sprout period, pollination, etc. For example soybean is short day crop. Although no shading problems, long time lamplight illuminate at night can cause soy crop growth period stretched, which will lead the phenomenon of no fruits. As to four flowers, weeping and host which are extraordinarily sensitive to light, long time of lighting can cause even their death.

The Dangers to Social Life

Endanger Traffic Safety

The glare caused by light pollution, light flooding and light invasions, not only interfere people's physiological rhythms, also reduce the driver's work efficiency and even cause accidents. Light pollution influences the driver's work, and endangers traffic safety. The light of the street lighting lead to disability glare, which will make drivers and pedestrians' visual ability be reduced.

The Impact of Astronomical Observations

As for astronomical observations conditions and along with the increase of the sky brightness, urban lighting of point-blank light will directly influence the astronomical observation activities, which makes the observatory has to move away from the city to a remote location. Such as China's Zi Jin Shan observatory has to choose a new location.

Lose Beautiful Night Sky

Starry night environment should be the leading role, which is the most precious natural resource, so humans should lose the beauty of the night sky as the price to developing advanced lighting technology

The Waste of Energy

Light pollution wastes a lot of electric power resources. In the United States, waste energy because of inefficient lights or lighting at the wrong time and places values nearly \$2 billion every year (2002 figures).

The Dangers to Urban Environment

The Influence of Urban Night

In the construction of urban night landscape lighting, the decoration lighting with no purpose or lack of artistic sense is easy to form handicap light, which will damage the city's night view and be boring.

The Influence to Climate

At present, coal-fired power is two-thirds in our country electric power production and three quarters of them use coal. It will produce large amounts of carbon dioxide and sulfur dioxide gas, which increases global warming trend and produce the "heat island effect". At the same time, it can form acid rain to worsen the urban environment.

The Forms of Light Pollution

Recessive Light Pollution

Recessive light pollution is potential, indirect and not easy to observe, such as the ray pollution of light, especially embodied between the 100 nm wavelength and 1 mm wavelength, namely the radiation, visible irradiation and infrared radiation, laser pollution.

Dominant Light Pollution

Dominant light pollution is relative to the recessive light pollution apparently and directly and the real-time is strong. The direction and quantity of the light interference people's normal life conditions and reduces the eyes' recognition ability on things. It mainly includes ; light, light illuminates into, excessive astigmatism and glare.

The Problems Light Pollution

Urban night landscape construction in our country is still in the primary stage .The whole plan is disordered and entire quality is not good, so light pollution problems mainly displays in the following aspects:

The Level of Plan

In early time of night lighting construction, the city 's night landscape is "thousand city one side," The plan and management of night view are insufficient, and the light pollution of engineering is happening all the time. More attention is paid to decoration lighting instead of creative lighting. The

great effect is pursuing unilaterally, ignoring lighting details. Especially to high aesthetic value of some building complexes, whatever its culture or the image characteristics, a lot of the omni lights or neon lights and LED lights decoration are used, and brightening commercial lighting sign, which will destroy the building's original culture and aesthetic orientation and is difficult to highlight "urban business card" effect.

Light pollution area intensity is great, and domestic light pollution mainly focus on the economy developed city. In the Midwest, light pollution mainly concentrate in specific areas of the city because of the economic condition is limited.

The Level of Technology

The design of urban lighting is not a simple night lighting problem, but a request of the aesthetics, psychological, art, behavior and so on to shape the image of the city, which need to urban planners, city designer, landscape designers, architects, lighting designers altogether to complete the task. However, today the urban night scene is often designed by experience the professionals of urban lighting design are relatively few.

The Level of Management

The Absence of Management

The maintenance of lighting equipment and management are deficient. If the city neon lights, advertising sign, large screen pictures, and text indicate that they are uncompleted, dirty or damaged and which are not repaired in time, the effect would be counter-productive.

The defect of light pollution prevention legislation

Light pollution management system has a serious defect, except for some local regulations and local standard outside, light pollution in the legislation is almost blank. Therefore, our country greatly needs a legislation of light pollution.

The Analysis of Light Pollution Causes

The Lack of Overall Lighting Plan

The report shows that China's most cities night lightings are lack of uniform plans or plans is out-dated and night layout is messy, which is lack of features. The urban night scene is designed by the space of urban elements which is the foundation and decide urban lighting theme, the image of the city, pursuit the image of the city space and people's visual experience intention, constructing the urban night landscape of the frame, relying on natural ecological resources, revealing culture, and selecting the most valuable landscape to light instead of imitating of plagiarism blindly. For example, the night lighting's plan of French Paris aims to protect a romantic night scene of style emotional appeal; and Venice, in Italy, is designed to protect the historic landscape.

The Lack of Culture and Environmental Protection Consciousness

Lighting the night by "bright" to assess the quality of the plan of night view is a serious wrong idea. Under this guidance, city lights flashing brightly, neon lights dazzling the fresh views, the lack of visual level, and increasing the number and power of lamps blindly cover up the scientific of the construction of the urban night scene. Personal environmental quality in protection activities is still a slice of "lowland", and become the biggest obstacle to raise environmental protection level in China.

The Lack of Ascension of Technology

The writer visited several markets of lamps and found that the artificial lighting design level in our country is low. It mainly imitates the imported products and is lack of independent innovation. The quality of lamps and lanterns of domestic product is not high and brightness is great. What's more, the scattering is overmuch, and life is short. Because the price of domestic products is cheaper to imports relatively and more attention is paid to the design of appearance and the domestic market share is high, so the light pollution is inevitable.

The Lack of Maintenance and Management of Lighting Equipment

With the construction of the urban night scene scale is more and more greater and there are more and more projects, the investments of infrastructure rise gradually. At the same time, the expense of maintenance of facilities goes up and the design of the arduous tasks can't be afforded. The responsibilities of construction of urban public space and engineering and maintenance are not implemented, which obstruct the orderly development of the night landscape projects.

The Investment Capital Is Not Stable

The investment of night lighting project is huge, besides the investments of hardware facilities such as lighting equipment, lighting pipe line, lighting control systems, the long-term investment of daily consumption, changing light sources and maintenance costs are also huge. At present, urban lighting projects resources is mainly from government investment, business investment, advertising and business capital investment and other investments. No stable source of funds, the systematic consummation of lighting project "planning-design-construction-maintaining" is pretty difficult.

Conclusion

Based on the sustainable development and low carbon lighting design requirements, the article discussed the present situations and problems which exist in urban night landscape construction in our country and focused on the cities' light pollution to reconsider the shaping of cities' landscape and light environment. The construction of night landscape is not only an art but also a beauty. In the view of author, the design concept and goal of the urban night lighting construction use lighting design as the carrier, and it is the shape to the city landscape of night instead of reproduction the day. The aesthetic sense about city night view needs to accord with intensity of illumination standard but also to follow the principles of humanism, environmental psychology, city aesthetics, ecology and so on. As to night landscape project construction, we should discuss the light environment from the angle of beauty, emphasize environmental effect, create a comfortable, beautiful human landscape, and guide people from higher level to examine and evaluate urban night landscape design.

References

- [1] Cui yuanri. Shallow said shop lighting [J]. Lighting engineering journal, 2005, 01(In Chinese)
- [2] Hao LuoXi. urban lighting design [M]. liaoning science and technology publishing house, 2005, P150 (In Chinese)
- [3] Gan ziguang. Promote the development of green lighting project [J]. Chinese street lamp, 1999(In Chinese)
- [4] Green lighting project implementation manual [M]. Beijing: China architecture & building press, 2003(In Chinese)
- [5] Luyan\Yao mengming. The store lighting [M]. First edition. Shanghai: fudan university press, 2004.22-26(In Chinese)
- [6] Mark Karlen James Benya: Architectural Lighting Design and Case Studies [J]. Mechanical Industry Press, 2005

On Visual Aesthetic Feeling of Microlite Decorating Plate

Yang Yuangao

Art Design Faculty, Hunan International Economics University

Keywords: Design; Microlite; Attribute; Visual Aesthetic Feeling

Abstract. Among all the dazzling decorating materials, microlite decorating material stands out because of its attributes and visual aesthetic feeling. It's an eco-friendly material belong to the latest designing field in the new century. And its splendid tincture, smooth surface, homogeneous reflection of light is all manifestation of its visual beauty and natural tenderness.

Introduction

The essence of design is the perfect combination of aesthetic feeling and material technology. Material is the fundamental substance of design. One of the most important principles in modern design is the abundance of traditionally superficial decoration. The modern design boasts the use of new technology and new material. It emphasizes the function of material in design where there is the interaction between material and its fantastic visual effect. Thus the material can truly realize its value of use and of aesthetic effect. The material has become a manifestation and explanation of modern design culture.

Visual aesthetic feeling is something produced during the recognizing process of mankind, it is a mark of enjoyment. The most basic and observable phenomenon of people's mental activity is one's aesthetic instinct which is a special way of recognition. To be specific, one article's beauty is mainly showed by its beauty of texture, beauty of form and beauty of decoration.

Microlite is a microcrystalline glass; a compound solid material contains a large amount of microcrystal and glass. It is made of glass processed by crystallization and heating method. Microlite decorative plate gives off a unique visual aesthetic feeling in decoration both inside and outside the buildings, it stands out in today's world where there is much competition and it strengthens the idea of low-carbon and eco-friendliness.

Predominant Material Beauty

Decoration, as we call it, is the use of beautifying methods to mask the natural disadvantages of objects in order to give prominence to their advantages and help them serve mankind's daily requirement better. That is, to create pleasing and homelike services for human. It is the process of decoration to make use of all the possible materials and technological methods to create supreme visual effect for the realization of the final purpose of satisfying people with visual beauty.

All the decorative materials have their own physical and chemical attributes that make them substantially different from others. For example, their compressive strength, corrosion resistance, thermal expansion property, water absorbency and optical property are all physical attributes that can not only determine the material's quality but also the aesthetic feeling of its texture.

The superficial characteristics of microlite material are similar to that of natural stone, and though the methods of production are to some extent similar, when compared with glass, ceramics and stone, microlite is different because of its crystal habit. What's more, it's prior to them with its various physical attributes (as in Table 1)

Table 1 Comparison of attributes of microlite material and natural stone

Attributes	Materials		
	Granite	Marble	Microlite
Density g/cm ³	2.6-2.8	2.6-2.7	2.5-2.7
Flexural Strength MPa	15.0	17.0	51.0
Shock Strength KJ/m ²	0.84	0.88	1.045

Compression Strength MPa	59-294	80-226	150-300
Mohs Hardness	5.5	3-5	≥5.5
Water Absorption%	0.35	0.3	0.00
Acid Resistance 1%H ₂ SO ₄	1.0	10.3	0.08
Alkali Resistance 1%NaOH	0.1	0.3	0.054
Thermal. Expansion. Coefficient ×10 ⁻⁷	50-150	80-260	65
Frost Resistance	0.25	0.23	0.23
Lustrousness%	80	50	≥95

The visual aesthetic feeling is presented by the combined effect of materials' physical attributes such as stability, abrasion resistance, gloss, etc. Stability is affected by thermal expansion coefficient, abrasion resistance is affected by rigidity, the maintenance of gloss is affected by acid and alkali resistance, and intensity is affected by impact strength. Through Table 1 we can see that the acid resistance and alkali resistance of microlite are prior to that of granite and marble. So the stable organic material, even if exposed long in the open air and contained environment, it can keep its superficial effect, just as semi-transparent and shiny as before, thus it will not turn to visual pollution in spite of the disturbance of weathering.

In this age when science and economy develop rapidly, people's pursuit of visual aesthetic feeling lingers no longer on superficial appearance and shortly visual enjoyment, they pursue a continuous visual joy comes from its advantageous physical and chemical attributes.

Elegant Formal Beauty

Material is the fundamental substance of design. All products are created from raw materials which are objective and sensible. The proper handling of material, combined with design concept and design method, can endow the material with validity which is one of the most important principles of design. While at the same time, formal beauty is an indispensable factor to compose a product's visual aesthetic feeling. As an abstract factor of visual aesthetic feeling, formal beauty is presented by the even, elegant, natural and smooth presentation of lines and curves of the products. To a larger extent, formal beauty brings to people imagination and aesthetic enjoyment. Form is the direct reason that calls up the feeling of aesthetics and inner sensibility.

Formal Beauty of Visibility Combined with Invisibility

It is a most common phenomenon that the sensible organs of human reflect the visibility and invisibility of an article. "Visibility" refers to an integration of objectivity and sensuality; it is external, direct, abstract and spiritual. The relationship of visibility and invisibility constitute the two systems of aesthetics. If there is no visibility, then there cannot exist invisibility, thus the design will be monotonous and rough. They two are interdependent as well as contrary; also, they are interconnected and indispensable to each other.

Microlite, a microcrystalline glass, is a new building material developed by the skills of processing glass and stone. Microlite is a concentration of the advantages of glass, ceramics and natural stone material. The professional manufacturers put the glass which contains nucleating agent or not under the crystallization progresses, turn the originally haploid glass into a compound material of microcrystal phase and glass. So, microlite obtains the optical attributes of glass. The lights searching the microlite can not only be reflected from the surface but also reflected from inside the material in a gentle, smooth and multi-dimensional way, and look like translucent and ravishing as crystal; microlite can change its image with the change of time, climate and light, as is shown in Fig.1. In building space, the microlite material's reflectivity and refrangibility can integrate and create a pleasantly invisible feeling within visible materials. The contrast of invisibility and visibility is nonmaterial and such nonmaterial can not only enrich the language of design but also state the culture of the present age.



Fig. 1 Microlite Mosaic

The Beauty of Artistic Conception --Form

“The beauty of artistic conception” is an important component of Chinese aesthetics. It is a presentation of arts. During the artistic creation, appreciation and criticizing, the beauty of artistic conception is often treated as a criterion of artistic beauty. Artistic conception is the product of objectivity (life, scenery) and subjectivity (thought, emotion). “The beauty of artistic conception is the unification of scene and sight, emotion and circumstances.”

The beauty of artistic conception, as one of the components of visual aesthetic feeling, contributes most to the conveying of spirit and implicational meaning. When an artist tries to express something with his artistic ware, he endows the ware with “emotion”, weakens its original appearance while stresses its shape and form. What’s more, by instinct, he made exaggerated the ware’s form, gives it a sense of arrangement thus ensures that the ware expresses significant formal beauty. The beauty of artistic conception is the externalization of an artist’s creative imagination, and in turn it impacts visual schemata and exists as creator of aesthetic feeling. The beauty of artistic conception is mainly reflected by its own attribute, that is, it’s transparent and translucent.

Microlite is special for its crystal habit. It can form acicular crystal tracery on the surface. And at the same time, it also has the character of glass, with which it presents a glittering and beaming surface. Its glittering and beaming feature can give a sense of aesthetics as well as a noble personality just like that of mankind. What’s more, the visual effect and emotional sense that this material can give off are incomparable. As is shown in Fig. 2, under the bright sunshine, the microlite basin is as elegant as a maid, giving off a natural tranquility and a unique peace, which offers people paramount visual enjoyment.



Fig. 2 Microlite Basin

Harmonious Decorative Beauty

All the objects need embellishment and decoration. Embellishment and decoration can beautify them, help increase their charms and makes them more attractive. The decorative beauty refers to the beauty created by artistic techniques and methods which rearrange and modify the superficial and inner structure of objects with the purpose of realizing aesthetic enjoyment. In modern design arts, decorative beauty has become a very important factor in visual arts. Visual arts are ancient arts, a developing art. In the present society where the standard of beauty is getting higher and higher, visual arts is becoming more and more fantastic with splendid charm and is beaming with bright shine. And we should know that the decorative beauty of materials is principally exhibited by materials's superficial gloss, color, level of translucent and pure, as well as interact and balance of colors.

Microlite is created from crystallization process under the high temperature similar to that when granite is formed. Microlite contains some glass phase whose vertical reflection rate is 13. When light reaches the surface of microlite plate, specular reflection will take place. The surface of polishing plate is far smoother than that of stone, it's glittering and ravishing. At the same time, the reflection rate of glass phase contained in microlite is different from original glass. Microlite's inner structure can have strong reflection of light while on the surface it can produce uniform and harmonious diffuse reflection, which can create natural and soft feeling. Such diffuse reflection not only strikingly strengthens the light reflected but also enlarges its expansion, which make the building beaming with light, looks splendid and magnificent.

Microlite is a homogeneous material produced under high-temperature sintering process. It is a method that can produce rich colors. During the process of sintering, the colors tend to distribute evenly like that of the colored glass. And with white as the basic color, luxurious color system can be created. While natural stone may crack and have chromatic difference, microlite products can come into being with various colors, pure tint, smooth texture, and elegant and gorgeous visual feeling, all this make sure that the building get to the paramount decorative effect.



Fig. 3 Diffuse reflection of high glossing

To sum up, the artistic form of decorative material is the combination of the charm of material itself and the artistic creation. It is not only a conveying of the artists' mind and idea, but also can give people visual and psychological enjoyment. Material, as media of the expression of artistic product, when combine with advanced production engineering that can endue the material with texture beauty, form beauty and decorative beauty, can greatly enrich the shaping language of design. Microlite plate material, with its unique physical and chemical attributes and visual aesthetic beauty, will build up the aesthetic standards of decorative material and turn out to be the mainstream of modern low-carbon decorative material.

References:

- [1] Wu Chungui , Producing Techniques of Glassceramic Decorative Plate and their Market Potential [J].the research of ceramics, 1999
- [2] Chen Guohuo, Kang Xiaoling, Sintering and Coloring of Glassceramic [J]. Ceramics, 2002.
- [3] He Xinwen, Presentation and Application of Internal Decorative Material [M]. Hunan Science and Technology Press, 2002.
- [4] Dong Wanli, Xu Liang, Principles for Environmental Art Design [M]. Chongqing University Press, 2003.

Green Industrial Buildings Lighting Design Based on DIALux

Heng LI^{1, a}, Guo-shun LI^{1, b}, Li-ping WANG^{2, c}, Zhu-xiong LIU^{1, d}

¹No.6 Institute of Project Planning & Research of Machinery Industry Engineering Group Co., Ltd., Zhengzhou, China

²College of Electronic Information Engineering, Henan University of Science and Technology, Luoyang, China

^ahenry929@sina.com, ^bliguoshun710@126.com, ^cwanglipinger@yahoo.com.cn, ^dzjlylx@163.com

Keywords: Green industrial buildings; Green lighting; Process feature

Abstract. To make the industry sustainable development, the Evaluation Standard for Green Industrial Building will be published in China. And the green lighting, as an important aspect of green industrial buildings has been emphasized in this standard. This paper introduces the green industrial buildings and the green lighting. The method of industrial buildings green lighting design based on DIALux has been proposed. The example of industrial building lighting based on green design is presented and simulation result shows that a large proportion of power consumption can be saved with ordinary metal halide lamps and symmetrical luminaries.

Introduction

The Chinese green lighting project has been launched by the State Economic and Trade Commission for decade's years since 1993. The green lighting carried out widely and vigorously in product development, engineering design, operation and maintenance and other aspects, and improves the energy consumption efficiency.

The statistics show that the Chinese existing industrial building area has reached more than 5 billion square meter in 2006. The industrial lighting energy consumption is proportional to the construction area and the working time of the industrial enterprise. Hypothesis to realize green lighting, the lighting power density decreases $2\text{W}/\text{m}^2$, and the working time is 1860 hours per year, the annual industrial building lighting electricity saving can be 16.6 billion kWh. While the electricity quantity of the Dayawan nuclear power plant is 15.336 billion kWh in 2011 [1]

Green Industrial Buildings and Green Lighting

As the development of the green technology, the green building has been promoted more and more widely. As different building has different function, it is difficult to assess green building using a simple standard. The industrial building is a kind of architecture to meet the requirement of industrial production. The Evaluation Standard for Green Industrial Buildings, which will be published, is the first national standard on green industrial buildings in China. In this standard, the credit of green lighting is easier to obtain than the other requirements, and the incremental cost of the green lighting is very small, even zero.

Green Industrial Buildings The green industry can be divided as the green production, the green process and the green industrial building. The green industrial building is the architecture provides suitable, health, safe and efficient use of space for the production and human, while minimizes the resources consumptions and reduces pollution to protect environment, in the whole life cycle of the building. The green industrial building is a system solutions which consists of land saving and sustainable sites, energy saving and utilization, water saving and utilization, materials saving and utilization, outdoor environment and pollution control, indoor environment and occupational health and operation and management. It is a technically challenging to complete a green industrial building design, since the design should consider both the process feature and green buildings' requirements.

Green Lighting The conception of green lighting was first proposed by the United States Environmental Protection Agency in 1991, and quickly gained the support of the United Nations and many developed and developing countries attention. The aim of green lighting is to save energy, protect environment and supply comfortable light environment to improve the work efficiency and the quality of human life. To the industry, the most important thing is reliability. So the industrial lighting should be reliable to industrial production environment. And the green light of industrial building should involve process features, architectural characteristics, investment, light sources and luminaires, therefore it is different to the other buildings lighting.

Green Industrial Buildings Lighting Design

Industrial lighting design should focus on the functional requirements that the lighting must meet technology requirements at first. Secondly, the design should consider the specific conditions of architectural. The industrial engineers need to develop a systematic, feasible scheme to meet the requirements of green lighting, reliability, operation and management.

Requirement of Process Feature In order to guarantee the process of production, such as raw materials, in-process quality inspection, sorting product acceptance etc. color rendering may be ruled. The selected light sources should consistent with current national minimum allowable values of energy efficiency and energy efficiency grades, based on the color rendering requirement.

The IP65 luminaire should be adopted where the environment may have conductive fiber, the luminaire should be adopted according to the chemical corrosive substances released under the working condition, and so on. Though the luminaries may be different according to the production condition, the luminaries' efficiency should be as high as possible.

The engineer can choose the mixed lighting where the requirements are ordinary and operation density is low, while localized lighting where the lighting requirements are different. The industrial lighting should not only consider the workshop, process section and process group, but also consider the work shifts. If only the day shift, consideration should be given to daytime equivalent transmission.

Architectural Characteristic Natural light is conducive to people's physical and mental health, and improves the production efficiency and the product quality. The indoors can be lighted by using roof skylights or Tubular Daylight devices. The Tubular Daylight devices can be conveniently controlled as lamps; though the length tubular is limited and the initial investment is expensive [2,3]. Because of cheap price and simple construction, the industrial buildings commonly use roof skylights [4]. The architect should make the best use of natural light. It can not only save the lighting electric energy cost, but also realize the harmonious coexistence of man and nature.

According to the construction can be divided into the form of multi-storey buildings, single storey building. In multilayer building, which storey height is less than 4 meter, we can the hoisting or embedded the straight tube fluorescent lamp. In machine, metallurgy and other industries, industrial buildings represented by single storey, lighting lamps can be used in roof top lifting form.

The room index is another character determines the choice of luminaries. If the lighting area length is L , the width is W and the height is h , the designer will calculate the room index through Eq. 1. According to the RI value, the designer should select a different light distribution curve of luminaries. It is very important to the green lighting design.

$$RI = \frac{L \cdot W}{h(L + W)}. \quad (1)$$

The Light Source and Luminaire. The high pressure sodium lamp has high luminous efficiency with poor color, the color rendering index is 20~30. The metal halide lamp luminous efficiency although slightly lower than high pressure sodium lamp, its color is good; the color rendering index is above 60. The color rendering properties of fluorescent lamp is good, the color rendering index is above 80, and T5 straight tube fluorescent lamp life expectancy is more than 15000 hours.

LED lamp is very hot in the lighting field because of its potentially high efficacy, long life, pure color, solid state, and eco-friendly. Compared with other light sources, it has the advantages of simple structure, compact structure, due to the use of low-voltage driving chip power supply, making it easy to implement complex dimming control [5]. But the shortcoming of it is the expensive cost.

The color rendering index of the electrodeless lamp is above 80, and the normal luminous efficiency is 65~80lm/W, some may above 80lm/W. And the vast majority of electrodeless lamp materials are recyclable, that meets the requirement of materials recycling. But the electrodeless fluorescent lamp shortcoming is also very obvious. The high-frequency electrodeless lamp is low light efficiency and short service life, while the coupler external low frequency electrodeless lamp with poor electromagnetic compatibility performance [6]. Although the luminaire may be high performance, it is difficult to match the luminaire, and keep the lighting efficient because the electrodeless lamp is big.

Generally speaking, the light source and luminaire are very important to the green lighting. We should consider the investment, reliability and the co-efficiency of the light source and luminaire in the industry.

The Lighting Power, Control and Maintenance The lighting power supply, which is directly related to the operation and maintenance of the green lighting, is very important. The lamp power factor compensation is ruled to 0.9, the voltage deviation should less than $\pm 5\%$, and the lighting load should be three-phase balance.

Although lots of lighting control systems have been carried out, there are seldom can be used in industry [7.8.9]. Since more complicated control system means more potential fault in some way, the practical control strategy is manual unless the control system has been required for some reason.

As the luminaire and room surface contamination will make the actual illumination reduction, it is necessary to establish the maintenance and management system, and assign specialized personnel responsible for lighting equipment maintenance. In the process of production, keeping the production site and surrounding environment clean and tidy, which helps to improve the reflection coefficient, will improve the use of light.

The Lighting Software. Today the current lighting software is used to study and evaluate the efficient lighting scheme for the office buildings through the use of different types of lamps. DIALux is more convenient and swifter in computing in small scale scenes than AGI32, and has very little difference with AGI32 in computing precision and speed. In large scale scenes computing, AGI32 show its sharp advantages in organization of lamps and lanterns, batch processing computing and other aspects, and the advantage in results and speed is great compared with DIALux [10]. According the industry condition, the DIALux is suit for simulating the green industrial buildings lighting design.

The famous lighting manufacturers, such as Philips and OSRAM, have provided the plug-in of their lighting product for the DIALux. And it is free to download and use or upgrade the DIALux through the internet.

A Green Industrial Buildings Lighting Design of Machinery Factory

The machinery factory process consists of painting, shot blasting, welding and cutting, shown as in Fig. 1. And the height of the factory is 10 meters. The independent type spray painting room placed in the painting zone, which provides the local lighting of the process. And the shot blasting machine also has local lighting equipment. The space of horizontal columns is about 9 meters.

The Lighting Equipment Selection. According to Chinese Standard for lighting design of buildings and the factory condition, the illuminance standard level of all the process is 200lx, the color rendering index of the shot blasting and painting is 80, and the color rendering index of welding and cutting is 60. As the factory height is bigger than 6 meter, the color rendering index of the shot blasting and painting could choose 60. So the light source and the ballast of different process can be

adapted the same type. Considering the price, color index and luminous efficiency, the metal halide lamps are good choice. From product catalog of DIALux we can find that the luminous efficiency of PHILIPS HPI-P400W-BU is above 80lm/W.

Taking the process into consideration, to make it easy to calculate room index, the factory is divided into 4 zones, shown as in Fig. 2. By Eq. 1, the room index of each zones can be calculated as $RI_{1\#} \approx 3.1$, $RI_{2\#} \approx 3.3$, $RI_{3\#} \approx 2.4$, $RI_{4\#} \approx 3.0$. So the luminaires of the zones should be the wide light distribution curve. To make the list brief, the luminaires can the same type. To match the light source, we can select PHOENIX MDK900 PR (WH) C as the high efficiency luminaires using the plug-in of DIALux.

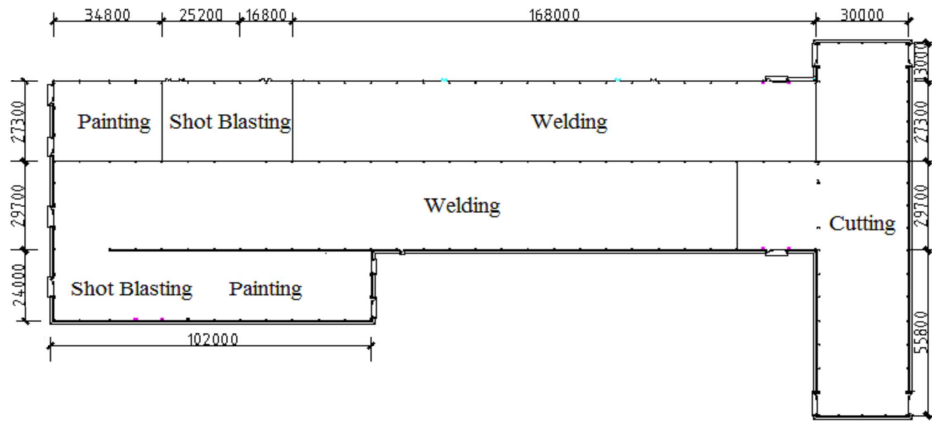


Fig. 1 Overlooking of the Factory

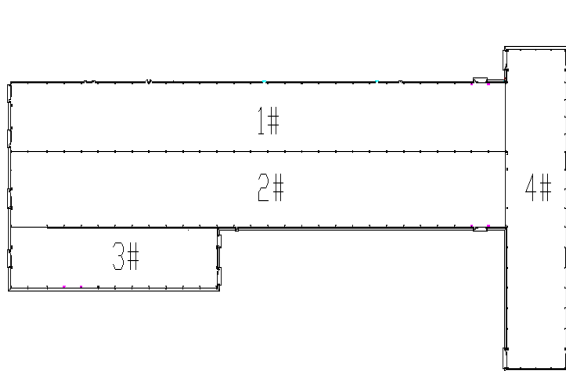


Fig. 2 Zones of the Factory

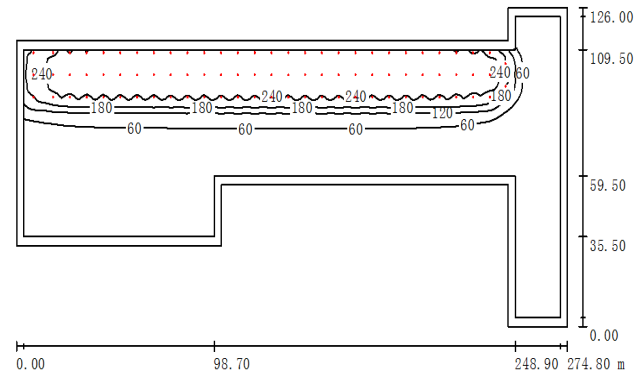


Fig. 3 Simulation of Zone 1#

The Lighting Equipment Position Calculator based on DIALux After building up the model of the factory in the computer, DIALux has been using to calculate the each position of the lighting equipment should be installed, to improve the lighting quality. Firstly, optimize each lighting zone to make the isolux contours similar to the shape of lighting area shown as Fig. 3~6. Secondly, the final simulation of the factory can be gotten as Fig. 7. By exporting the simulation result to the CAD file, each equipment position can be measured using AutoCAD.

The Energy Efficiency of the Design The lighting area of the factory is 20145m², the lighting load is 107525W, and the lighting power density is 5.34W/m². Since the power density current value is 8W/m², it decreased 33%. And the illuminance of the work area is 312lx.

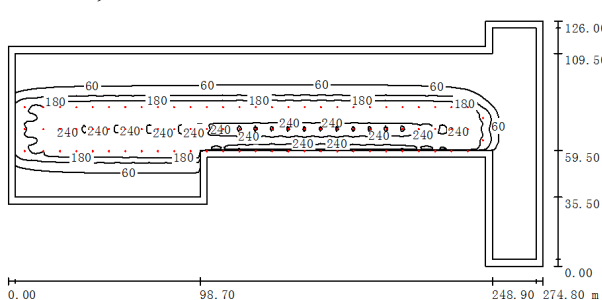


Fig. 4 Simulation of Zone 2#

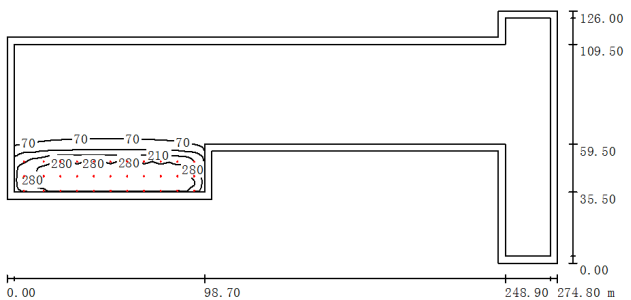


Fig. 5 Simulation of Zone 3#

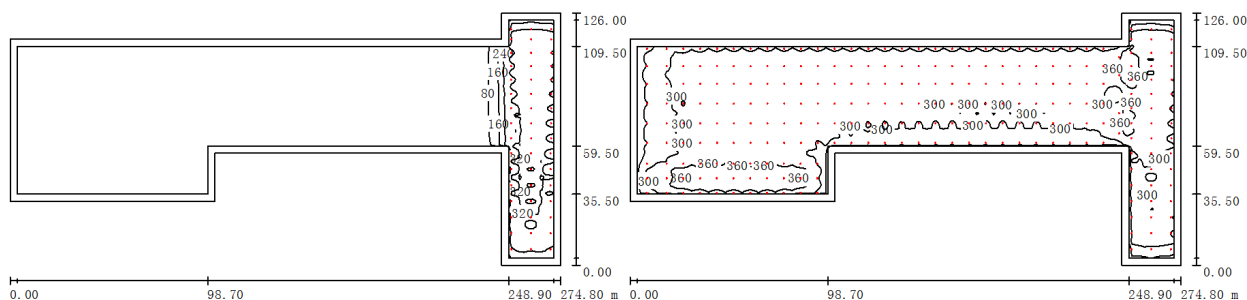


Fig. 6 Simulation of Zone 4#

Fig. 7 Simulation of the Factory

Conclusion

Green industrial buildings lighting design should meet the requirement of process and architectural by anglicizing their characters. The high performed lighting product is necessary for the project. With the help of lighting software the design may be optimized, achieve maximum energy saving.

References

- [1] <http://news.bjx.com.cn/html/20120109/335349.shtml>
- [2] ZENG Li-qiang, An illuminance ratio model based on a luminance transfer function matrix [J].Journal of Chongqing University, 2008(10):1160-1163
- [3] Chen Wang, et al., Daylighting can be fluorescent: Development of a fiber solar concentrator and test for its indoor illumination [J].Energy and Buildings, 2010, 42(5): 717-727.
- [4] Ardeshir Mahdavi, Predictive simulation-based lighting and shading systems control in buildings [J].Building Simulation, 2008, 1(1):25-35
- [5] Arpad Bergh, et al., The Promise and Challenge of Solid-State Lighting [J].Physics today, 2001, 54(12):42-47.
- [6] Wharmby, Electrodeless lamps for lighting: a review [J].Science, Measurement and Technology, IEE Proceedings A, 1993, 140(6):465-473.
- [7] Shu Xian Zhu, et al.,Control System Based on PLC and Touch Screen for Energy-Saving in Public Lighting.[J] Advanced Materials Research, 2010, 143-144:576-579
- [8] Jun Wang, et al.,Research and Design of Intelligent Lighting Control System Based on Industrial Wireless Technology. [J] Key Engineering Materials,2011, 467-469:620-624
- [9] Chao Ze Lu, et al., A ZigBee-Based Indoor Intelligent Lighting System Research and Design.[J] Applied Mechanics and Materials,2011, 71-78:2276-2279
- [10]Hu Guojian, Comparision and Analysis of Lighting Calculation Software Dialux & Agi32 [J]. China Illuminating Engineering Journal,2005, 16(3):52-55

Research of Green Concrete

Yang Shuzhen

School of Transportation Wuhan University of Technology, Wuhan, China, 430063

582786040@qq.com

Keywords: Green concrete; Sustainable development; Suggestions

Abstract. Concrete is the most widely used building material in the world, while with the large amount use of concrete, the pollution is becoming more and more serious. While green concrete can overcome ordinary concrete's shortcomings. This paper will introduce green concrete's features and analyze its prospect. What's more, according to the present situation of green concrete, points out some existing problems of green concrete, to these problems, put forward some suggestions to its development.

Introduction

With the rapid development of the social productive forces and economic, the excessive development and utilization of resources cause environmental pollution and destruction, which is a big threaten for the sustainable development and people's survival. The use of modern concrete has a history of more than 100 years. Concrete is the most widely used among the building materials. To maintain sustainable development, whether concrete can be used as the main building materials in the long term, the key lies in whether concrete can become green material. Green materials are the trend and direction of the development of civil engineering.

Ordinary Concrete's Problems

It is estimated that the production of concrete is more than 6 million cubic meters all over the world. The production of concrete in our country is about 15 cubic meters. In the process of producing concrete, the main resource--cement is not a kind of environmental friendly materials. The world's cement industry exhausts approximately 1.6 billion tonnes of carbon dioxide into the atmosphere, which accounting for about 7% of the global emissions of greenhouse gases. In addition, we need to explore many raw materials, such as limestones, clay and fuel coal, which caused extensive deforestation and soil erosion. The global consumes 100--110 billion tons of sand, gravel and gravel each year, which cause side effects to the forest area and the riverbed's ecology. Each year about 1 trillion liters of water is used to mix concrete, cleaning sand, stone and maintenance of concrete also needs lots of water. In addition, the construction and demolition of the concrete produce much solid waste, which aggravates nature's burden. What's more, construction noise, the release and diffusion of toxic substances may also cause some problems.

The durability of concrete is also an important aspects of the sustainable development. There are many circumstances that concrete constructions are damaged because of the bad durability. The American invest \$6 trillion every year to concrete projects, and the cost of maintenance and rebuilding is as high as \$300 billion dollars. The durability of concrete also has become more and more important.

Green Concrete

At present, the green concrete doesn't have a unified definition. Earlier, Wu ZhongWei academician put forward the concept of green high performance concrete and discussed it's characteristics. It is generally thought that, green concrete includes the following characteristics: meeting the sustainable development of the concrete, can reduce the pollution to the environment, and in harmony development with ecology system, and with higher strength and durability than ordinary

concrete, can choose the rich and low consumption resources, make full use of industrial waste resources and realize the recycling of regeneration resources and the low emissions of noxious substance.

Usually, the green's meaning can be summarized as:

To save resources and energy

Do not damage the environment, more benefit to the environment

The sustainable development, which can meet the needs of contemporary, and does not harm the ability of future generations to meet their needs

Features and Advantages of Green Concrete

Save More Cement Clinker, Reduce the Pollution to the Environment

As a main material of concrete, cement is a kind of unsustainable development product. Cement is the well-known pollution sources, exhausting a lot of dust and harmful gases. But the main is the emission of carbon dioxide, which has not been taken seriously by people. Cement industry's consumption is as follows:

Table 1 Cement industry's consumption

production/mt	Coal/wt	Electricity/bw	Limestone/mt	Dust/mt	CO ₂ /bt	NO _x /mt	SO ₂ /wt
100	8	83.5	0.77	8	0.5	15	7

Many countries has limited the emission of carbon dioxide, so the development of cement industry will be restricted, cement's production can't increase much. We must improve varieties and the technology to reduce the energy consumption and apply new technology. HPC uses plenty of fine admixtures instead of clinker, which can up to 60%--80%, this will be a main way out. While in GHPC, the greatest gel component is fine grinding industrial waste but cement clinker.

3.2 mix more fine admixtures whose primarily is industry solid waste

To mix fine admixtures not only can save the clinker, but also can improve the environment and reduce secondary pollution. The production of water quenching ore slag in our country is about 80 million every year, but because of the fineness is not enough, the activity is far from making use of, now it mostly only plays a role of micro aggregate. The main chemical components in slag are CaO, SiO₂, Al₂O₃ and Fe₂O₃. Usually, we use quality coefficient K to evaluate the activity of blast furnace slag:

$$K = \frac{\%CaO + \%Al_2O_3 + \%MgO}{\%SiO_2 + \%MnO + \%TiO_2}$$

The Bigger Quality Coefficient K, The Higher The Slag's Activity Is.

The production of fly ash is more than 100 million every year, but the efficiency is not high. The high quality fly ash for HPC will increase in the future. Since 1955, Canada has developed the high ratio of fly ash concrete, fly ash is about 55%--65% of the cementitious material(cement + fly ash), what's more, adding appropriate super plasticizer, can get good workability, strength and durability, this is mix slag with fly ash or silica, which achieve the goal of saving energy and improving the environment. In addition, GHPC still have some advantages such as lowing temperature rise, improving volume stability and durable grinding and so on. Here is the high ratio of fly ash concrete's hydration charts:

Play the Advantage of High Performance and Reduce the Dosage of Cement and Concrete

Reducing the dosage of cement and concrete there are many top and big span structures using high strength to reduce structure's section and weight successfully. Improving durable, guaranteeing or extending the security system, can get the biggest economic and environmental benefits.

Expand the Application Range of the GHPC

If we low the current low intensity limit of HPC from C50 ~ C60 to C30 or so, and use HPC in large volume hydraulic structure with requirements to freezing-thawing resisting, low temperature rise projects, we can receive more environment and technical and economic benefits.

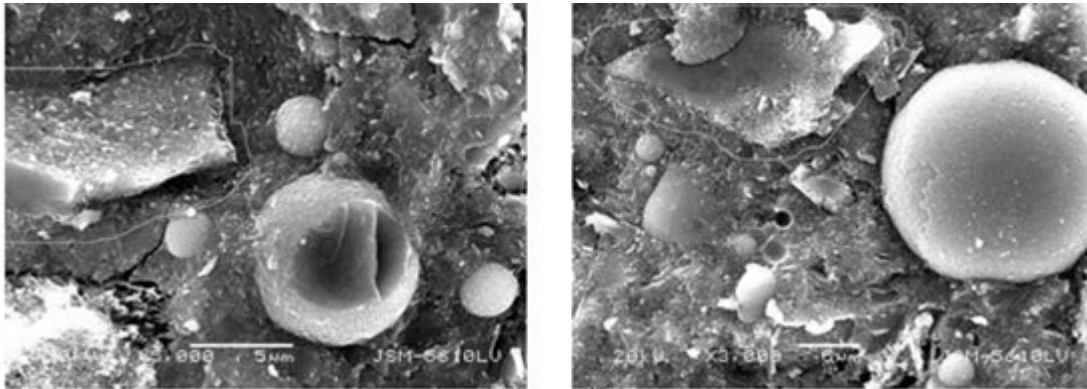


Fig. 1 The high ratio of fly ash concrete's hydration charts

The green concrete has some superiority as follows:

- Reduce the environment load when concrete is manufactured
- Reduce the environment load in the process of using concrete;
- Protect the ecological, beautify the environment;
- Make the living environment comfortable and safe.

RPC's physical and mechanical performance is as follows:

Table 2 RPC 'S physical and chemical performance

Sample	ROC-200	ROC-800	HPC
pressure	--	10-50 Mpa	--
Heating maintenance/°C	20-90	250-400	--
Compressive strength	170-230	500-800	60-100
Rupture strength	30-60	45-140	6-10
Fracture energy/J.m ⁻²	20000-40000	1200-20000	140
Elastic modulus/GPa	50-60	65-75	--
permeability	2.5	--	120
Cl ⁻ diffusion coefficient	-0.0	--	5

Existing Problems of Green Concrete

Cost Issues

The cost of concrete is increased by 50% or more because used raw materials, the production and management level and production lines are raised. For example, collecting and preparing recycling aggregate must cost a certain machinery and equipment and manpower for recycled concrete. From the point of economic indicators, the production of recycled aggregate is few profits, no profit, even deficit. If the production of recycled aggregate maintains a certain profit, its retail price will inevitably higher than the natural aggregate. Therefore, it is difficult to be accepted by users.

Early Cracking

In recent years cracking of concrete has become a hot topic at home and abroad and green concrete is no exception. That is, crack of concrete is very common. Many factors that influence early cracking of concrete are as follows: self-shrinkage, drying shrinkage, early elastic modulus, tensile strength, ultimate tensile strain, creep, water evaporation rate, structural constraint degree and so on.

Suggestions

There are some ways to promote green concrete's development: first, use less cement and sand in the process of the concrete's production. Second, improve concrete's durability as far as possible to extend the concrete structures' service life and reduce the rate of the concrete engineering reconstruction and removal. Third, control and reduce the produce of pollution sources during the production and the utilize of concrete.

Reduce the Dosage of Cement and Natural Sand

To solve the problem of the cement industry greening, the suggestions are:

To adjust to the traditional portland cement clinker mineral's composition, develop the low limestone ingredients, burn into cement clinker at low temperature, such as HBC and sulphoaluminate cement. This kind of cement hydration activity High, hydration put quantity of heat low, which is very suitable for high performance concrete prepared.

In the basis of above measures, raising the quality of sand and stone and reducing the dosage of cement concrete as much as possible.

To develop the mineral admixtures and efficient decrease water agent, making use of mineral admixture's effect of decreasing water and other effects to reduce the dosage of cement.

Degree of aggregate

About 80% of the concrete is sand and stone. To achieve this material, we need to cut down trees and expose the stone, which may cause the loss of soil and water. Here are some suggestions to save sand and stone:

our country should legislate to regulate the mining of sand and stone and let everyone knows that sand and stone are nonrenewable resources.

Strengthening the scientific research of the substitution of sand

In the process of developing new aggregate, noticing to detect the raw materials' radioactive index to avoid bring in new resources of pollution.

Enhance the Durability of Concrete

To expand the use of high performance concrete In foreign countries, high performance concrete's strength grade is required to reach 55Mpa. While in our country, ordinary concrete such as C20, C30, C40 accounts for more than 95%

Engineering designers should update the methods of designing mix proportion of concrete and achieve a turning from strength design to the durability design.

Mineral admixtures are necessary to maintain high performance concrete's durability. Engineering designers should dare to mix mineral admixtures in concrete and increase dosage and promote admixtures' development.

Our country should study and formulate regulations about green concrete. We should cooperate to study the green concrete and make it suitable for many occasions.

Control the Dust and Noise

In order to realize the green production and construction of concrete, we should promote commodities concrete and develop concrete whose liquidity is big to reduce noise.

Develop Ecological Concrete and Recycled Aggregate Concrete

Ecological concrete means that can adapt to plants' grow, adjust the balance of nature, beautify the environment and realize the coordination of human and nature. To speed up the development of ecological concrete is the requirement of sustainable development. With the development of urban, infrastructure's invest is increasing. The large amount of abandoned concrete has become a new pollution source. The solution is to develop recycled aggregate concrete.

Conclusion

Though the concept of green concrete has been put forward for a long time, the research of it in our country is still in primary stage. The green concrete used in the construction is less than 1% each year in our country. While using green concrete is the trend of sustainable development, so we should attach great importance to green issues of concrete.

Reference

- [1] Z.W. Wu: Concrete and Cement Products Vol.1(1998),p. 3
- [2] H.J. Xu: Guang Zhou Building Vol. 36(2008),p. 3
- [3] L.G. Shi, J.H. Huang, J. Wang: Guang Dong Building Vol.7(2009),p. 48
- [4] H.W. Zhao, H.P. Zhu: Concrete Vol.6(2009),p. 92
- [5] H.Q. Wu: Enterprise Technology and Development Vol.24(2009),p.83
- [6] J.H. Liu, S.M. Song.Green. High Performance Concrete Technology and Engineering Applications (China Power Press, Beijing, 2011).
- [7] Y.Y. Xia, J. Chen, X.H. Xiong: Concrete Vol.4(2011),p. 101
- [8] L. Xie: Science and Technology Information Vol.29(2010),p. 54
- [9] B.W. Yin, X.X. Yin, S.M. Liu: Theory Studies.Internet Fortune Vol.8(2010),p. 193

CHAPTER 4:
Manufacturing Technologies and Application

Control Methods of the Concentrated Moisture Exhaust System for Tobacco Primary Processing

Yusheng Wu

Xiamen Tobacco Industrial Co., LTD, Xiamen 361022 China

Keywords: Moisture Exhaust System; Control Methods; Product Quality; Peculiar Smell Processing

Abstract. In tobacco primary processing line, there are often processing emissions with as peculiar smells, condensed water and tobacco powder dusts discharged from the production of processing equipments. In this paper, through a detailed design on the concentrated moisture exhaust system of tobacco primary processing and its control methods, the moisture-exhaust air volume's instability caused by the starting and stopping of all processing equipments in production line is solved, so as to ensure the stabilities of processing equipment's parameters and cigarette's smoke flavors and simultaneously improve the effect of processing the peculiar smells of emissions.

Introduction

Along with the higher and higher requirements on environmental protection, increasingly more tobacco factories begin to collect the processing emissions with peculiar smells and tobacco powder dusts and then carry out a peculiar-smell processing, so as to make a change to the embarrassment that smell of cigarettes is sucked first before the arrival in cigarette factories.

Now, a concentrated moisture exhaust system is mainly applied in the discharge of processing emissions. In the system, moisture-exhaust air pressure and air volume fluctuate greatly, and can seriously affect the quality of cigarette products. Thus, product stability is poor, and also peculiar smell processing effect is not ideal.

Analysis on the Problems of Traditional Moisture-Exhaust System

There are some shortcomings and difficulties in the design and control methods of the traditional moisture-exhaust system, which are mainly embodied as follows.

Poor System Stability

When production line is in normal production, total air volume of system will change and subsequently affects the air volume and air pressure of other running equipments if some processing equipment in the moisture-exhaust system is started or stopped.

Uneven Moisture-Exhaust Air Pressure

The air pressures needed by all processing equipments to exhaust moisture are close in general. However, the differences between system design and control methods used currently will be great because of the different distance between processing equipment and peculiar smell processing equipment.

Unsatisfactory Peculiar Smell Processing Effect

The uneven moisture-exhaust air pressure makes a large amount of dusts, tars and other sundries in the production line directly into the peculiar smell processing system, thus giving rise to the frequent failure in control components of peculiar smell processing equipment and seriously affecting peculiar smell processing effect.

Difficult To Clean Up Sundries

After a large amount of dusts, tars and other sundries enter the peculiar smell processing system, they will solidly stick to all corners of in-walls of equipment, making it difficult to clean up them, and simultaneously increasing the system operational cost.

Unreasonable Design on System Air Speed

Suppliers and designing units of the moisture exhaust systems for tobacco primary processing of all tobacco enterprises are necessary to uniformly design the moisture-exhaust air speed at about 10-14m/s or even lower sometimes.

Design of the Concentrated Moisture Exhaust System

System Composition

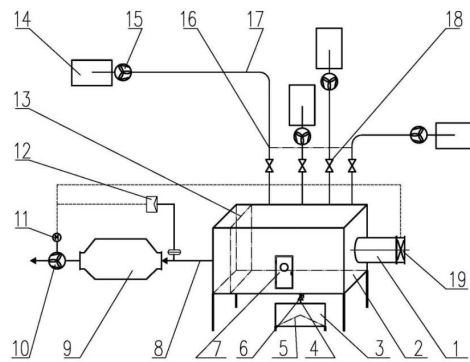


Fig. 1 Composition of the Concentrated Moisture Exhaust System for Tobacco Primary Processing

System composition is shown in figure 1. In the system, the stability of the moisture-exhaust pipe air pressure of processing equipment is balanced through controlling the real-time automatic adjustment of the frequency of moisture-exhaust fan's frequency converter, and the buffering of air pressure balance box as well as air compensation device.

System Design and Its Functions

Pipeline Design

Each moisture-exhaust pipe (17) is separately connected with corresponding processing equipment (14) and also equipped with an auxiliary moisture-exhaust fan (15), an air speed test port, a manual air-volume control valve (18), multiple inspection doors and multiple condensed-water drain outlets. The gradient of pipe is 0.3%-0.5%, and gradient direction should be down-flow to outdoor [1].

Manual air-volume control valve (18) is set adjacently to air pressure balance box, so as to easily adjust the opening of air door when system is being debugged; auxiliary moisture-exhaust fan (15) is installed at the position of moisture-exhaust outlet of processing equipment (14), and its total pressure should be ensured in model selection; emissions of corresponding processing equipment is discharged to the position 16 required by processing; air speed test port is installed between manual air-volume control valve (18) and air pressure balance box (2), so as to easily and simultaneously adjust the opening of air door and test the moisture-exhaust air speed when system is being debugged; condensed-water drain outlets are set at the low points of pipe, so as to ensure smooth discharge.

Design of Air Speed Balance Box

Air pressure balance box (2) is installed between processing equipment (14) and peculiar smell processing device (9), but is closer to peculiar smell processing device. The air pressure balance box is also connected with an air compensation device (1), a drainage device, and a primary filter (13) that is easy to install, uninstall and clean, and an inspection door (7).

In designing air pressure balance box, its volume should be ensured to be big enough, making the maximum air speed not higher than 1.2 m/s in normal operation.

Sewage discharge outlet is set at the lowest point inside air pressure balance box (2); a sewage pipe is connected with the sewage discharge outlet, and its front end is equipped with a stop valve (6) and tail end is equipped with a pool (3) containing filter (5). The condensed water, which is naturally settled in air pressure balance box, is discharged to sewage pipe via filter, so as to prevent sundries from entering sewage pipe and resulting in secondary pollution.

Design of Air Compensation Device

Air compensation device is installed under air pressure balance box (2), including an air compensation pipe (1) connecting to air pressure balance box (2). The tail end of the pipe is equipped with an automatic air volume control valve (19). This control valve is linked with the frequency signal of main moisture-exhaust fan (10), and can automatically adjust the opening of the frequency signal of main moisture-exhaust fan (10).

Design of Main Moisture-Exhaust Fan Control

PID closed-loop adjustment control is applied in main moisture-exhaust fan control (10) [2]. According to the 4-20mA signal feedback of external differential pressure transmitter (12), frequency converter (11) in this scheme compares pressure difference inside it and outputs operation frequency, and thus controls the rotate speed of main moisture-exhaust fan control.

Design of Air Speed inside Pipe

The determination of air speed inside pipe is related to duct concentration, dust properties, pipe diameter size, and pipeline layout, etc [3]. Based on use experience, air speed inside pipes connecting to processing equipments is advisable at 12-15 m/s, but not higher; air speed inside horizontal header pipe should be slightly higher and advisable at 14-18 m/s according to the actual conditions.

System Control Methods

System Debugging Method

Moisture-exhaust debugging flow is shown in fig 2, and its debugging method is introduced below. Control system is set in manual state, and automatic air volume control valve (19) under air-compensation pipe (1) is set in closing state. Peculiar smell processing system (9) is started up, and then the main moisture-exhaust fan (10) operates in the state of 20HZ frequency, and also processing equipment (14) as well as its connected auxiliary moisture-exhaust fans (15) operates normally. After operation is stable, the air speed of each moisture-exhaust pipe (17) is respectively measured, and also air volume control valve (18) is manually adjusted until the air speed of each moisture-exhaust pipe (17) is closer to each other. Then, the frequency of the main moisture-exhaust fan (10) is adjusted until the air speed of each moisture-exhaust pipe (17) meets the required (14-16m/s), and now the motor frequency is usually between 30-50HZ. At this moment, numerical reading of differential pressure transmitter (12) should be recorded as given value of pressure difference inside frequency converter (11). Then, debugging is complete, and also the system can be used in normal operation.

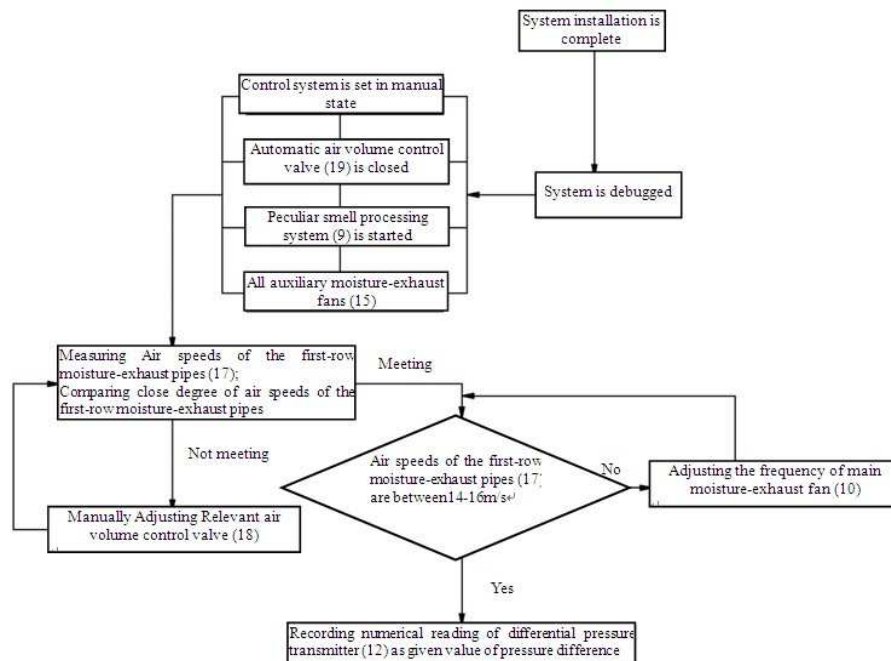


Fig. 2 Debugging Flow of Moisture-exhaust System

Control Methods of the System in Production

The automatic control flow of the system in production is shown in fig 3, and its control methods are introduced below.

Before production is ready to start in workshop, the main moisture-exhaust fan (10) begins to start after a start request signal sent by any processing equipment (14) is received by peculiar smell processing system (9), and subsequently the whole peculiar smell processing system (9) is started and so is the auxiliary moisture-exhaust fan (15) connecting to processing equipment (14). At this moment, peculiar smell processing system (9), moisture-exhaust pipe (8) between peculiar smell processing system and air pressure balance box, air pressure balance box (2), and position (16) between air pressure balance box (2) and moisture-exhaust pipe (17) are under a state of negative pressure. Then, the negative pressure value measured inside header moisture-exhaust pipe (8) is sent by differential pressure transmitter (12) located under header moisture-exhaust pipe (8) to the frequency converter (11) of the main moisture-exhaust fan (10), and the rotate speed of the main moisture-exhaust fan (10) is continuously increased until the negative pressure value tested by differential pressure transmitter (12) reaches give value of pressure difference. At this moment, if the frequency of the main moisture-exhaust fan (10) is lower than 20HZ, the automatic control valve (19) of air compensation pipe (1) located under air pressure balance box (2) is opened slowly, and also the opening of the valve continuously increases until the frequency of the main moisture-exhaust fan (10) reaches above 20HZ.

After the rotate speed of the main moisture-exhaust fan (10) is stable, the condition for starting processing equipment (14) is available and waiting for the command of production start, and then processing equipment (14) is started and enters production preheating and waiting for production in workshop.

In production, the total air volume of moisture-exhaust system will change if some processing equipment (14) shifts from production to stop. Measured negative pressure value is constantly fed back by differential pressure transmitter (12) located under header moisture-exhaust pipe (8) to the frequency converter (11) of the main moisture-exhaust fan (10), and thus the operation frequency of fan is constantly adjusted.

When more and more processing equipments (14) stop in the system, the frequency of the main moisture-exhaust fan (10) will continue to reduce; when there is only a small part of processing equipments in operation, the frequency may reduce to below 20HZ. If frequency reduces to below 20HZ, PLC of control system immediately sends frequency signals to automatic control valve (19),

and also slowly increases its opening, so as to make value fed back by differential pressure transmitter (12) gradually lower and the frequency of the main moisture-exhaust fan (10) continuously higher until its rotate speed reaches 20HZ and its optimal working state is ensured.

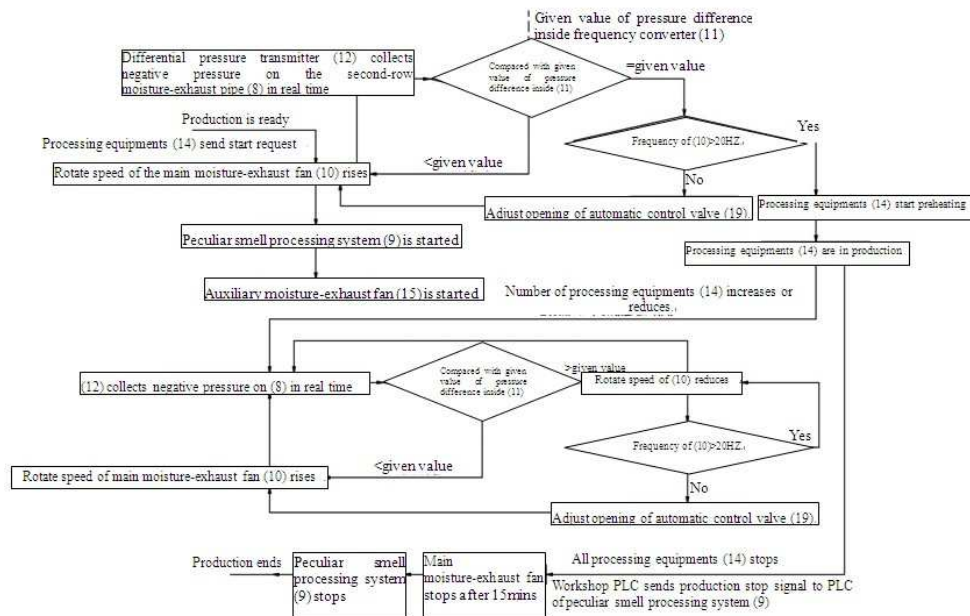


Fig. 3 Automatic Control Flow of the System in Production

After all processing equipments (14) stop, workshop central PLC sends production stop signals to the PLC control system of the concentrated moisture-exhaust system. The main moisture-exhaust fan (10) stops operating after a delay of 15 minutes so as to ensure all moisture and sundries in the whole system fully discharged and subsequently peculiar smell processing device stops. Thus, the whole production process comes to an end.

Regular Maintenance Methods of System

According to equipment operation, air pressure balance box is necessary to be maintained and cleaned regularly.

Conclusion

In this paper, an elaborate design is made on equipment system, and also the problems such as the instabilities of moisture-exhaust air volume of processing equipments, the difficulties to clean up sundries and the unsatisfactory peculiar smell processing effect are solved thoroughly by comprehensively considering energy conservation, environmental protection and system operation, ultimately ensuring the stability of various production parameters and cigarette products smoke flavors. Meanwhile, the system structure is simple, flexible, easy-to-maintain, and safe-to-operate, and therefore is a Concentrated Moisture Exhaust System solution worth applied in Tobacco Primary Processing.

References

- [1] China Tobacco. Design Specifications for Cigarette Factories [1993] No.30.
- [2] Changing Wang, Xuewu Yang. PID Control for Coal Gas Blower Frequency-change Speed Regulating System. Electric Engineering, 2003 (04).
- [3] Yusheng Wu, Hong Huang. Design on the De-dusting System of Tobacco Primary Processing. Silicon Valley, 2010 (09).

Effect of Microbiological Additive on the Diversity of Microbial Community and the Dynamic Distribution during High-Temperature Composting Process

Hong-tao Li, Xiu-hong Xu and Jia Liu

College of Resources and Environmental Sciences, Northeast Agricultural University, Harbin 150030, China

Keywords: Compost; Microbial Additives; Denaturing Gradient Gel Electrophoresis (DGGE)

Abstract. The objectives of this study were to analysis the differences of microbial community diversity between the microbial additives (MA) compost and natural compost and the distribution (spatial and temporal) of MA during high-temperature composting by PCR-DGGE technology. The results showed that the MA started temperature rapidly; prolonged the time of maintained high-temperature process and increased the diversity of microbial than natural compost. Sequence comparison revealed that the microorganisms most belonged to uncultivable, thermophilic bacteria. *Bacillus* became the dominant microorganisms after mixed with MA. MA were found in the top and middle portions of the compost throughout nearly the entire composting process, but absent in the natural compost. Our finding represents an important step towards the understanding of MA and its function in the degradation process of compost.

Introduction

In recent decades, increasing proportions of small, individual livestock farms have been replaced by large-scale, industrialized livestock operations, especially in China. A particular challenge that has arisen from this trend is the management of animal manure and waste water. Animal dung is rich in organic matter, such as nitrogen and phosphorus. If used properly, it can not only curtail the environmental issue but also aid agricultural production as a natural fertilizer (El-Din et al., 2000; Hoitink et al., 1986). Composting is a mesospheric and hemophilic process of degradation of organic material by a mixture of microorganisms, including bacteria, actinomycetes and fungi (Bernal et al., 2009). During high-temperature composting process cellulose and hemicelluloses were decomposed rapidly, the microorganisms also changed complexly. Thermophilic *Bacillus* spp. were found in high temperature of compost (Miyatake, 2005). By gaining a detailed understanding of these microorganisms we may be able to identify the composting mechanism.

Monitoring of the microbial community is important in the effective management of the composting process as microbes play key roles in the process and the appearance of some microbes reflects the quality of maturing compost (Macauley et al., 1993). Microbial additives of compost have been studied extensively (Kim et al., 2004; Nakai et al., 2004; Sasaki et al., 2006; Wakase et al., 2008), but few studies have been conducted to track the microbial additives throughout the entire process of composting. To better understand the dynamic distribution of microbial additives during high temperature composting, both spatially and temporally, the micro-ecology of the microbial additives compost technique was studied by virtue of the PCR-DGGE.

Materials and Methods

MA and compost samples. Two stacks of compost material, in which cow dung and rice straw were the major sources of organic matter, were set up. One stack was supplemented with cellulose-decomposing bacteria (0.1 %) as MA, while the second stack was used as the control (natural compost). Cellulose-decomposing bacteria was cultured at 50 °C for 3 or 7 days. Clone analysis showed that cellulose-decomposing bacterial belonged to *Bacillus*.

Composting experiments were conducted at the Horticulture Station of Northeast Agricultural University in China. The indoor composting process took about 30 days with occasional manual ventilation of the stacks. Temperature was monitored at different locations within the stacks (bottom, core and surface) throughout the process. One kilogram of fresh composting sample was collected from the three locations in the stacks at days 0, 3, 6, 9, 12, 15, 19, 22 and 25. The collected samples were placed in sterilized bags and stored at -20°C.

DNA extractions and purification DNA was extracted according to protocols described previously (Zhou, et al., 1996; Zhang, et al., 2003), with the following modifications. Three grams of the frozen compost was added to 13.5 mL DNA extraction buffer (100 mM Tris-HCl, 100 mM EDTA, 100 mM Na₃PO₄, 1.5 M NaCl, 1%CTAB, pH 8.0), incubated for 30 min at 37°C on an orbital shaker at 225 rpm/min; further, 1.5 mL 20%SDS was added and incubated for 2 h at 65°C, then centrifuged for 10 min at 6000×g, collected supernatant. Precipitation added 4.5 mL DNA extraction buffer and 0.5 mL 20%SDS, incubated for 10 min at 65°C and then re-centrifuged for 10 min at 6000×g. Merged two supernatant and mixed with an equal volume of chloroform:isoamyl alcohol (24:1), followed by another 10 min of centrifugation at 6000×g. Aqueous added 0.6×volume of isopropanol sit at room temperature for 1 h, centrifuged for 20 min at 16000×g and finally precipitation dissolved in TE.

The extracted DNA was purified using the E.Z.N.A. Gel Extraction Kit (Omega Bio-Tek, Inc., Georgia, USA). Briefly, the DNA fragments of interest were excised from the gel using a scalpel and placed in a 1.5 mL micro centrifuge tube. An equal volume of binding buffer was added and the mixture was incubated at 55°C - 60°C until the gel was completely dissolved. The DNA/a arose solution was added to a HiBind DNA column seated in a collection tube and centrifuged at 10000×g for 1 min at room temperature. The supernatant was discarded, binding buffer was added to the column and centrifuged at 10000×g for 1 min. The DNA column was washed with SPW washing buffer and centrifuged at 10000×g for 1 min. The column was dried by centrifugation for 2 min at maximal speed (13000×g), and placed in a clean 1.5 mL micro centrifuge tube. DNA was eluted by sterile water.

Denaturing gradient gel electrophoresis (DGGE) DGGE was performed with the D-gene system (Bio-Rad Laboratories, Hercules, CA, USA). PCR products (10 ml) of similar sizes were separated on an 8% (w/v) polyacrylamide gel with a urea gradient increasing from 30% at the top to 60% at the bottom. Electrophoresis was performed in 1×TAE buffer for 5 h at 60 °C. The gel was stained with silver nitrate and the DNA bands were analyzed using Quantity One software (Bio-Rad).

Microbial diversity and statistical analyses The microbial diversity index is a well-established measure of biological diversity and spatial distribution of high and low value indicators. Here, the diversity index was used to quantitatively analyze the diversity of the microbial community in the compost and was calculated using the Shannon diversity index (Shannon and Weaver, 1949):

$$Dsh = -\sum Pi \ln Pi = -\sum (Ni / N) \ln(Ni / N)$$

$$Jsh = Dsh / Lns$$

Where Dsh represented the Shannon-Weaver index; Jsh was the uniformity index; Pi was the probability of i-th DGGE band; Ni was the relative quantity of the ith RAPD band; N was the total quantity of the DGGE bands ($N = \sum Ni$); S was the community structure richness; Dsh minimum value was 0, and maximum equaled LnS.

Sequence and phylogenetic analyses The DNA bands were extracted from the cut-out gel after an overnight incubation at 4°C, and 0.5 uL of supernatant was subsequently used as the template DNA in a reapplication PCR performed with primers 338 F and 518 R. The resulting amp icons were sequenced by Boya Bio-Technology Co., Ltd., Najing, China. The closest matches of all the sequences were identified through the NCBI database (<http://www.ncbi.nlm.nih.gov/>).

Results and Discussion

DNA extractions, purification and PCR amplification DNA gel electrophoresis showed that the length of the isolated DNA was about 23.1kb, suggesting that the complete DNA fragments were obtained. Serious smearing phenomenon in the DNA gel was observed, indicating impurity of the DNA sample. After purification, the concentration of DNA samples was found to have increased significantly. Quality of the DNA was also greatly improved and no contaminating RNA or pigment was observed. PCR amplification of the purified DNA resulted in clean and high quality DNA product. The result of PCR amplification shows that the DNA length was about 240bp, similar to the predicted length based on primers GC-338 F and 518 R.

Because of the humus in compost, an accurate and straightforward method must be used to extract DNA. Otherwise the sample can be easily contaminated and negatively impact the integrity of downstream procedures and findings. In this study, after used the E.Z.N.A. Gel Extraction Kit to purify DNA, the concentration of DNA was could used for subsequent experiments.

The spatial distribution of MA during high-temperature composting PCR-DGGE experiments indicated that the spatial distribution of microbes differed among the top, core and bottom portions, which would result in an uneven degradation throughout the entire compost pile. This differential spatial distribution was likely caused by the lack of oxygen at the bottom. This hypothesis is supported by the finding that there were less aerobic cellulose-decomposing bacteria present in the bottom-most region. One possible method to increase the oxygen level is to forcefully blow air into the bottom of the compost pile, rather than performing manual ventilation techniques, which may affect the quality of composting.

Table 1. Partial sequence analysis of bacterial 16S rDNA genes

Band number	Accession No	Identified species	Similarity (%)
1	AJ582255	Uncultured Escherichia sp. partial 16S rRNA gene, clone AC24	100%
2	AJ842255	Arthrobacter sp. Nj-75 partial 16S rRNA gene, isolate Nj-75.	100%
3	EU009381	Uncultured bacterium isolate DGGE band 8 16S ribosomal RNA gene, partial sequence	99%
4	FJ609992	Uncultured Stenotrophomonas sp. clone D10 16S ribosomal RNA gene, partial sequence	95%
5	AJ582252	Uncultured Acinetobacter sp. partial 16S rRNA gene, clone AC21	92%
6	AJ966595	Uncultured bacterium partial 16S rRNA gene, clone E29	100%
7	EF489017	Uncultured Flavobacteria bacterium clone 3 16S ribosomal RNA gene, partial sequence	100%
8	EU551230	Uncultured archaeon isolate DGGE gel band 16 16S ribosomal RNA gene, partial sequence	100%
9	FM872863	Uncultured bacterium partial 16S rRNA gene, clone FB03H07	100%
10	AB244764	Sphingobacterium composti 16S rRNA gene, partial sequence	96%
11	FJ499360	Uncultured bacterium isolate DGGE gel band 19 16S ribosomal RNA gene, partial sequence	100%
12	FJ499356	Uncultured bacterium isolate DGGE gel band 15 16S ribosomal RNA	99%
13	AM710608	Pseudomonas sp. 129(43zx) partial 16S rRNA gene, strain 129(43zx)	100%

Microbial diversity analysis One interesting finding from our current study was that the MA not only facilitated the composting process, but also increased the microbial diversity of the compost (Ishii K et al., 2000). However, when the temperature was too high, the diversity index decreased. Such findings were consistency to previous reports that bacterial activity and diversity are reduced dramatically at temperatures above 60°C (Strom, 1985; Suler and Finstein, 1977).

Sequence analysis of the specific bands from the two composts The PCR-DGGE band patterns of samples obtained from different composts during high-temperature composting process differed from each other. This indicated the change in the dominant species during the high-temperature composting process. The dominant microorganisms most belonged to uncultivable, thermophilic bacteria. This strongly suggests that the PCR-DGGE analysis can be used as an alternative strategy to analyze the microbial community in the composting process, especially for uncultivable bacteria populations which have eluded traditional culture methods.

Sequence comparison results (Table 1) showed that *Bacillus* became the dominant microorganisms in MA compost, and species and quantity of *Bacillus* were increased than natural compost. *Acinetobacter* sp. and uncultured bacterium of FB03H07 were new species after mixed with MA (band 5 and 9). The dominant microorganisms in the natural compost of *Pseudomonas* sp. et al. became less or disappeared after added MA (band 10, 11, 12, 13). Some kinds of *Bacillus* appeared earlier and increased number (band 1, 2, 3, 4 and 6); while the others appeared later, but the number was not change to some extent (band 7 and 8).

Conclusions

This study focused on the differences of microbial community diversity between the microbial additives (MA) compost and natural compost and the distribution of MA during high-temperature composting by PCR-DGGE technology. The results showed that the MA started temperature rapidly; prolonged the time of maintained high-temperature process and increased the diversity of microbial. The temporal distribution of MA were present at most of the tested time points in the high-temperature compost. The spatial distribution of MS were mostly found in the middle and upper, but not the bottom. Sequence comparison revealed that *Bacillus* became the dominant microorganisms after mixed with MA.

Acknowledgement

The authors thank to the financial support of the Harbin, a special study of technological innovation fund (2008RFQXN022); Heilongjiang Postdoctoral Grant (LBH-Z07226); The Scientific Research Foundation of neau; Supported by Knowledge Innovation Project of The Chinese Academy of Sciences (KSCX1-YW-09-09-03); Ministry of Major Science and Technology of Harbin (2007AA6CN105).

References

- [1] Amann, R.I., Ludwig, W., Schleifer, K.H., 1995. Phylogenetic identification and in situ detection of individual microbial cells without cultivation. *Microbiol. Rev.* 59, 143-169.
- [2] Bernal, M.P., Albuquerque, J.A., Moral, R., 2009. Composting of animal manures and chemical criteria for compost maturity assessment. A review. *Bioresour. Technol.* 100, 5444–5453
- [3] El-Din, S.M.S.B., Attia, M., Abo-Sedera, S.A., 2000. Field assessment of composts produced by highly effective cellulolytic microorganisms. *Biol. Fertil. Soils.* 32, 35-40.

An Experimental Study on Edge-Breakage of Explosive Parts in Machining Using Micro-Photographic Observation Method

TANG Wei^{1, 2, 3} LIU Wei¹ XI Qing¹ LIU Tong² ZHANG Ding-guo³

¹ Institute of Chemical Materials, China Academy of Engineering Physics, Mianyang 621900, China;

² Graduate School of China Academy of Engineering Physics, Mianyang 621900, China;

³ School of Sciences, Nanjing University of Science and Technology, Nanjing 210094, China

tangwei@cscsci.info

Keywords: Polymer Bonded Explosive, Micro-Photographic Observation, Edge-Breakage, Cutting Lay, Crack Extension Direction, Active Rake Angle

Abstract. Crack on the sharp edge remains a major concern and a key problem cries for solution in the course of explosive cutting currently. The adoption of the idea that enlarges the cutting zone and records the cutting behaviors again has founded the micro-photographic system for the cutting process. Tests have found that this system can be applied to research the nucleation and expansion of deep rock crack and the formation and dropping of the chips. The extension direction that controls the cracks is the key to resolve the cracks on the sharp edge. As for the initial stage of cutting, the cracks usually expand from the relatively weak surface of the work piece, while the final stage of the cutting, the cracks point to the weak end face through the inner part of the work piece. The latter is easier to have the cracks on the sharp edge comparing to the former. Working orthogonal rake of tool is an important factor that affects the extension direction of the cracks. At the final stage of the cutting, if the working orthogonal rake is -6° , the angel from the crack extension direction to the main cutting direction is -35° . When the working orthogonal rake is 9° , the angel turns to be -54° . This has shown that enlarging the working orthogonal rake to a certain extend can lower the degree of crack on the sharp edge. In addition, tests have found out that the relatively small working orthogonal rake is likely to bring out potential cracks. However, enlarging the rake angle excessively will lower the rigidity of the tool and thus add risks of shocking.

Introduction

Large scale armament warhead uses explosive materials as energy source. The manufacturing process cannot be separated from mechanical processing. The mechanical processing is usually in the final stage. Once there is any problem, the loss will be great. With the improvement of design technologies and equipment level, the forms of products become complicated. The requirements of size become more specific. There are higher and higher requirements brought to the mechanical processing of explosives. Explosive material is flammable and explosive. In addition to this, it has low strength. It is easy to have brittleness extension of cracks in the cutting process. It is easy to produce sharp edge crack, affecting the product qualities or even intriguing dangers. The current studies are still in the initial stage. Document [1] acquires the cutting temperature and cutting forces' influences by the cutting parameters through test research. It has found that cutting force has large fluctuation. utting residua of chip [2] and processed surface [3, 4] have drawn the conclusion of using the transgranular fracture mainly and the intergranular fracture as assistant. The conclusion has founded solid foundation for the mechanism between tools and work pieces during the cutting process of explosives, but there are still certain limitations.

The research has established the micro-photographic system for the cutting process through designs. In addition, it carries out a series of orthogonal cutting tests of explosive materials. It has such conclusions as in the final stage of cutting; sharp edge crack is easier to occur compared to the initial stage, and enlarging the working rake angle appropriately can lower sharp edge cracks and potential crack.

The formation of micro-photographic system in the cutting process

The cutting area refers to the area that tools and working piece have interaction in the processing cycle. It has important meaning for increasing the safety of explosives processing and ensuring the processing qualities to make clear the chips formation and sharp edge cracks that are caused by crack propagation in the cutting area. The previous studies mainly rely on testing chips [2], processed surface [3, 4] and so on to reduce the cutting surface. It has certain limitations. This study establishes the micro-photographic system for the cutting process according to the following ideas: use the stereo microscope to enlarge the cutting area where tools and processed explosives interact with each other. At the same time, it uses the video camera to record the nucleation and expansion of deep rock crack and the formation of chips. Moreover, it observes the sharp edge cracks occurred in the cutting process. The micro-photographic system founded is shown as Fig 1. The efficient magnification is about 20 times to 200 times. The work distance of the objective lens is more than 20mm, which can efficiently avoid the interference of tools and the objective lens.

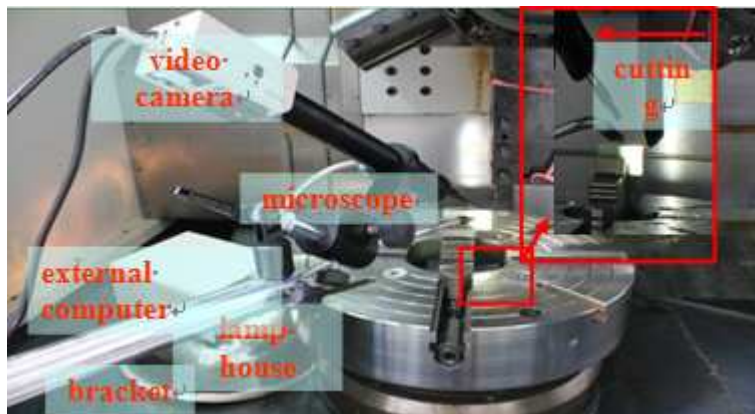


Fig 1: Micro-photographic system in the cutting process

Micro-photographic tests on sharp edge crack in explosive cutting

Analysis of the explosive cutting process Cutting refers to the dropping due to the mechanics failure for the interaction of tools and work pieces. The interaction refers to the contact and press of tools and work pieces. As for turning of the explosive materials, tools show different stress state in different places of the cutting layer. The cutting process is a dynamic process. The explosive cutting belongs to the brittle fracture under the low strain rate.

Forming and dropping of chops and sharp edge crack of explosives are caused by nucleation and expansion of deep rock crack. The difference lies in that the former is expected while the unexpected sharp edge crack is extended to the inner parts, which will have great influences to the product qualities. It can be seen that the key to relieve sharp edge crack is to control the crack extension direction.

Design of test scheme The movement relationship between cutting tool and work piece is shown as the Fig 2a. However, the cutting tool has stopped the observation of cutting area. It is not convenient for the test to use this kind of cutting method. Instead, use the orthogonal cutting method to carry out the test, and use the micro-photographic system to collect data about the chips forming and sharp edge crack in the cutting process, shown as Fig 2b.

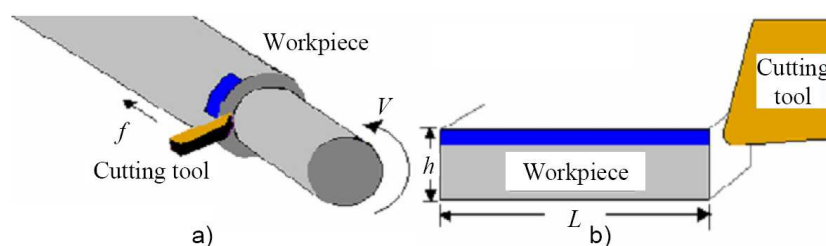


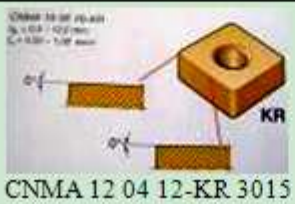



Fig 2: Turning schematic drawing

Table 1 shows the used turning tools. They are 80° diamond cutting tool produced by SANDVIK. The rake angle are a little different (1# rake angle is 15°; 2# rake angle is 0°). The other characteristics of the cutting tools are almost the same.

Table 1 Details of turning tool technology

code	Symbol of turning tool and rake angle features	Turning tool
1#	 CNMG 12 04 12-KM 3015	
2#	 CNMA 12 04 12-KR 3015	

The cutting place, parameter of cutting tool and cutting are the most important. According to the previous analysis, the key to relieve the crack sharp edge is to control the crack extension direction. The study stresses on examining the influence of cutting place and work rake angle to the crack extension direction. The test subject is polymer bonded explosive.

Testing result and discussion Cutting incipient stage. Fig 3 is the picture of the crack extension and chips forming in the cutting area in initial stage. The magnification is about 28 times (the same below). The test use 1# tool. The working rake angle is 9°.

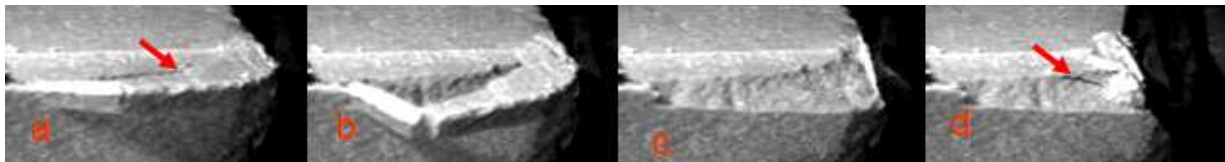


Fig 3 Chip forming/crack expansion I in initial stage of cutting

The picture shows an entire process from crack forming to chip dropping from left to right. It can be found that crack first produces in the shear band, shown as Fig 3a. It then expands fast, pointing to a weak working surface. This is consistent to the conclusion drawn by μ CT in Document [2] Fig 4. Next, Fig 3a, 3b and 4 show the tight connection between the crack and work piece. Fig 3 has shown the complete dropping of chips and forming of new crack. For example, Fig 3d and so on.

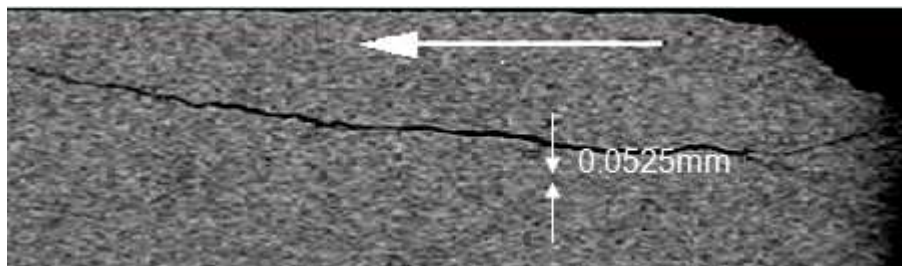


Fig 4: Crack distribution on the surface of work piece

After the first cutting, do the second cutting with the same cutting parameter. Fig 5 is the result. It can be seen that there is a relatively large triangular pyramid chip forming in the initial stage of cutting, relative to contact condition of cutting tool. This chip is completely in the inner part of the cutting layer. There is no crack extension direction pointing to the inner part of the work piece until the cutting ends.

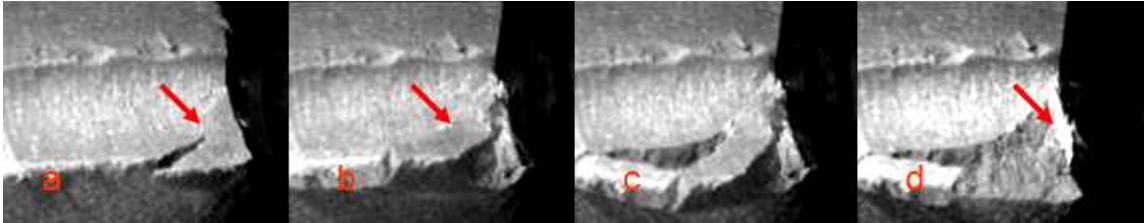


Fig 5: Chip forming/crack extension II in the initial stage of cutting

Cutting terminative stage Fig 6 and 7 are the detailed pictures of the cutting area. They have shown the nucleation and expansion of deep rock crack in the final stage as well as the cutting and the chip forming and dropping. The former adopts the 1# tools with 9° of work rake angle while the latter adopts the 2# tools with -6° of work rake angle.

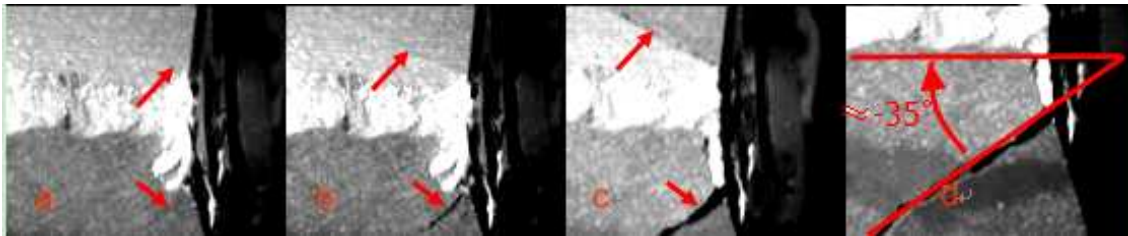


Fig 6: Chip forming/crack extension I in tooling stage

In the test, cracks extend from the inner parts of work piece. (Fig 6a, 7a) and then extends. A sharp edge crack of chips with triangular pyramid shape is produced. It can be seen that the smaller the work rake angle is, the more serious the sharp edge crack becomes.

Moreover, Fig 7a has two initial cracks. 1# crack expands rapidly while 2# crack disappears from the Fig 7c. This is not good for the delivery and storage of explosives. Fig 6 does not have the above condition. It can be seen that work rake angle can relieve the potential cracks to a certain degree.

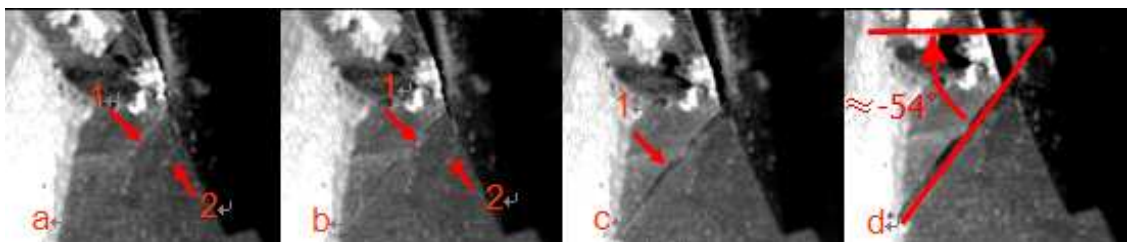


Fig 7: Chip forming/crack extension II in tooling stage

The larger the work rake angle is, the stronger the chip-breaking performance and the lower potential to have sharp edge cracks and potential cracks.

Conclusions

According to the idea that enlarges the cutting area first and records the cutting behaviors, the micro-photographic system is founded. It can be used to study the nucleation and expansion of deep rock crack and the formation and dropping of the chips.

The extension direction that controls the cracks is the key to resolve the cracks on the sharp edge. The initial and final stage of cutting will usually produce a relatively large chip of triangular pyramid shape. It can be seen that the final stage of cutting is easier to have the sharp edge crack than the initial stage.

Project supported by the National Defense Pre-Research Foundation of China (Grant No. 42601080204).

References

- [1] Zhao Xiao-dong, Bai Ping, Li Ming, et al. Experimental and Numerical Investigation into Machining Parameters for Cutting Forces and Temperatures of PBX[A]. Wang Ya-jun, Huang Ping, Li Sheng-cai. Theory and Practice of Energetic Materials[C]. Beijing, Science Press, 2005. 338-342.
- [2] Tang Wei, Li Ming, et al. Microstructure and Formation Mechanism of PBX Chips[J]. Chinese Journal of Energetic Materials (Hanneng Cailiao), 2009, 17(3):307-311. (in Chinese)
- [3] Tang Wei, Li Ming, et al. Studies on Turning Surface Micro-morphology and Roughnesses of PBX Parts[J]. Chinese Journal of Energetic Materials (Hanneng Cailiao), 2009, 17(1):59-63. (in Chinese)
- [4] Zhang Qiu, Huang Jiao-hu, et al. Micro-appearance and Formation Mechanisms of PBX Cutting Surface[J]. Acta Armamentarii (Binggong Xuebao) , 2010 , 31 (10) :1337-1340. (in Chinese)

Coal Gangue Image Edge Detection based on Wavelet Transform

Tieyun Li

Wuhai Vocational and Technical College, Wuhai, Inner Mongolia 016000 China

Keywords: Coal gangues; Edge detection; Wavelet transform; Image processing

Abstract. An edge detection algorithm is developed for coal gangue images, and the method has two advantages compared with traditional ones. Firstly, multi-resolution analysis of wavelet transform can improve the quality of edge detection. Secondly, the algorithm is faster for real time. Since the threshold directly from the coefficients of wavelet transform, the rate of recognition for coal gangue is highly raised. The experiment results show that the method is an efficient edge detection algorithm for extraction edges from the noised images of coal gangues.

Introduction

From the coal of coal gangues selection is a very important link to weed out the mass production of coal. The choice of the traditional method need lots of water, it is easy to pollute the water and surrounding environment, the urgent need to find new technology to replace old northwest area of rare in the water of our country. According to the pattern recognition theory, this paper puts forward a new method to develop the choice of coal gangue image recognition by image processing image, and then most of the coal and coal gangues can be automation technology were discussed.

Wavelet transform and multi-resolution analysis

Wavelet is a small "wave", has its own energies on time for a tool to analyze the transient, non stationary, or time-varying phenomenon. It also has oscillation wave-like features, but also has the ability to simultaneously analyzing the time-frequency and flexible mathematical basis. Wavelet transform is a widely used in math microscope and image processing. Wavelet transform of a signal means to describe the signal with a family of functions. The expression of wavelet transform for a signal $f(x)$ is [1]

$$Wf(a, x) = f^* \psi_{a,b}(x) = \frac{1}{a} \int_R f(x) \psi\left(\frac{x-b}{a}\right) dt \quad (1)$$

Where,

$$\psi_{a,b}(x) = \frac{1}{a} \psi\left(\frac{x-b}{a}\right) \quad (2)$$

That a is scale factor and b is translation factor, $\psi_{a,b}(x)$ is formed by means of translation and stretch of a basic wavelet $\psi(t)$ that must satisfy the following condition:

$$\int_R \psi(x) dx = 0 \quad (3)$$

Generally speaking, binary wavelet transform is often used in digital image processing, so $a=2^j$. If the signal is planar, such as image, the one dimension wavelet transform should be extended to two-dimensional wavelet transform. For a two-dimensional function $f(x, y)$, the wavelet transform is

$$W_s f(x, y) = f(x, y) * \psi_{a,b}(x, y) \quad (4)$$

Where, $*$ expresses the convolution along different direction, s is the scale. In two-dimensional images, the intensity of edges can be enhanced in each one-dimensional image by convolving.

If the window of the images is convolved in the x direction over an image, a peak will result at positions where an edge is aligned with the y direction. This operation is approximately like taking the first derivative of the image intensity function with respect to x or y as follows:

$$\psi_x(x, y) = \frac{x}{2\pi\delta^4} \exp\left(-\frac{x^2 + y^2}{2\delta^2}\right) \quad (5)$$

$$\psi_y(x, y) = \frac{y}{2\pi\delta^4} \exp\left(-\frac{x^2 + y^2}{2\delta^2}\right) \quad (6)$$

These are the basic wavelet transform functions, so under the condition of 2^j , the wavelet transform of $f(x, y)$ is expressed as

$$W_x^{2^j} f(x, y) = f(x, y) * \psi_x^{2^j}(x, y) \quad (7)$$

$$W_y^{2^j} f(x, y) = f(x, y) * \psi_y^{2^j}(x, y) \quad (8)$$

Where

$$\psi_x^{2^j}(x, y) = \frac{1}{2^j} \psi_x\left(\frac{x}{2^j}, \frac{y}{2^j}\right) \quad (9)$$

$$\psi_y^{2^j}(x, y) = \frac{1}{2^j} \psi_y\left(\frac{x}{2^j}, \frac{y}{2^j}\right) \quad (10)$$

After $f(x, y)$ is transformed, the modulus m_0 is given by

$$m_0 = \left\{ \left| W_x^{2^j} f(x, y) \right|^2 + \left| W_y^{2^j} f(x, y) \right|^2 \right\}^{1/2} \quad (11)$$

Both the mathematics and the practical interpretations of wavelets seem to be best served by using the concept of resolution to define the effects of changing scale. The wavelet functions are derived from the scaling function. Where an image is decomposed into finer and finer detail, the multi-resolution formulation can be used to represent the image.

The two-dimensional space $V_j^{(2)}(x_1, x_2)$ can be separated into the two one-dimensional spaces as follows:

$$V_j^{(2)}(x_1, x_2) = V_j^{(1)}(x_1) \otimes V_j^{(1)}(x_2) \quad (12)$$

So $V_j^{(2)}(x_1, x_2)$ structures a multi-resolution analysis of $L^2(R^2)$, and the sub-images can be obtained by using wavelet transform:

$$\begin{cases} A_{2^j} f_{j-1}(x_1, x_2) = \varphi(x_2) * (\varphi(x_1) \bullet f_{j-1}(x_2, x_1)) \\ D_{2^j}^1 f_{j-1}(x_1, x_2) = \psi(x_2) * (\varphi(x_1) \bullet f_{j-1}(x_2, x_1)) \\ D_{2^j}^2 f_{j-1}(x_1, x_2) = \varphi(x_2) * (\psi(x_1) \bullet f_{j-1}(x_2, x_1)) \\ D_{2^j}^3 f_{j-1}(x_1, x_2) = \psi(x_2) * (\psi(x_1) \bullet f_{j-1}(x_2, x_1)) \end{cases} \quad (13)$$

Where, ψ is the wavelet function and φ is the scale function, respectively in one-dimensional wavelet transform. Sign $*$ denotes the convolution along vertical direction, and \bullet represents the convolution along horizontal direction. In the $(j-1)$ Th level images, $A_{2^j} f_{j-1}(x_1, x_2)$ is a sub-image corresponding to low spatial frequency components, the other way round, $D_{2^j}^1 f_{j-1}(x_1, x_2)$, $D_{2^j}^2 f_{j-1}(x_1, x_2)$ and $D_{2^j}^3 f_{j-1}(x_1, x_2)$ are sub-images homologizing high frequency components in different directions.

Image smooth

The image processing is concerned with transforming the original image into one that is more amenable to the scene analysis, and involves various filtering operations that help to reduce noise, accentuate edges, and find regions.

Certain irregularities such as noises in the coal gangue images must be smoothed by an averaging operation. Averaging operation tends to suppress isolated noise speckles but also reduces the sharpness of the image and loses some small image components. An adaptive smooth filtering algorithm is used to overcome the disadvantage. The weighed function is constructed as followings:

$$W^k(x) = f(d^k(x)) \quad (14)$$

Where, $d^k(x)$ denotes the signal discontinued degree. The monotony decrease function f is defined as follows:

$$f(d^k(x)) = \exp\left(\frac{-G_x^2(x, y) + G_y^2(x, y)}{2k^2}\right) \quad (15)$$

The gradient of the image can be defined as

$$G_x(x, y) = \sqrt{f(x+1, y) - f(x-1, y)} \quad (16)$$

$$G_y(x, y) = \sqrt{f(x, y+1) - f(x, y-1)} \quad (17)$$

After k th iteration, if the gradient is larger than k , the abrupt change edges will be reserved, and the others smoothed. With wavelet function the signal is decomposed into 3 sub-layers, the noises are separated into high frequency parts. Then the coefficients are deal with by means of the threshold, and signals are reconstructed to reduce high frequency. The results with wavelet transform for reducing noises are shown in Fig. 1. The original image is shown in Fig. 1(a). Fig. 1(b) is the images of first reducing noises and Fig. 1(c) is the second reducing noises, respectively.

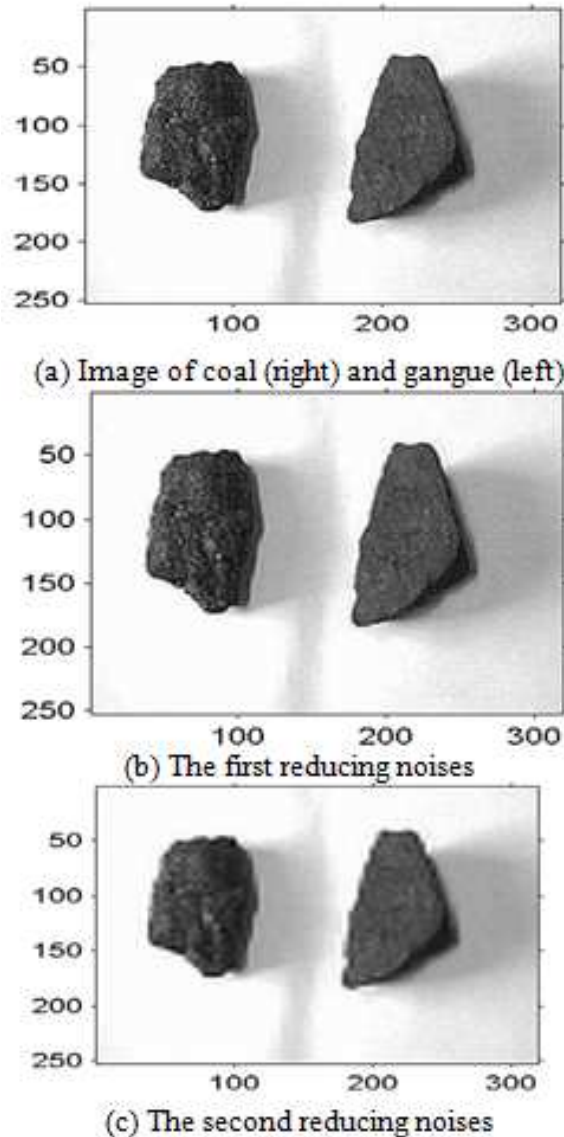


Fig. 1 Image reducing noises

It can be seen that the speckles in the original images are almost eliminated from Fig. 1.

Edge detection

Any edge of the boundaries is between image and part obviously different value of some of the properties. Edge detection is by far the most common method of meaningful interrupt detection strength value. This can be detected by the use of the first-and continuous second order derivative. There are many kinds of wavelet, such as Bubble wavelet, Hardy wavelet, Daubecies wavelet and Morlet wavelet. In this paper, the B spline wavelet is selected, because its feature varies in the similar way with edge, so the legible edges can be obtained. The m th-class B-spline function is used as scale function $\varphi(x)$, its Fourier transform is described as follows:

$$\varphi(\omega) = \left| \frac{1 - e^{j\omega}}{j\omega} \right| e^{-jk\omega} \quad (18)$$

Where, k is the sampling shift so that $\varphi(x)$ is symmetry on zero point, and m is the basic class of spline function. When m is even, $k=0.5m$, otherwise $k=0.5(m+1)$. The two-scale equation in frequency field can be expressed as

$$\varphi(2\omega) = H_0(\omega)\varphi(\omega) \quad (19)$$

Where,

$$H_0(\omega) = \frac{\varphi(2\omega)}{\varphi(\omega)} = \left| \frac{1 + e^{-j\omega}}{2} \right| e^{-jk\omega} \tag{20}$$

And the wavelet function is given as

$$\psi(2\omega) = H_1(\omega)\varphi(\omega) \tag{21}$$

H_0 and H_1 are the filters, the energy conservation equation is

$$H_0(z)H_0(z^{-1}) + H_1(z)H_1(z^{-1}) = 1 \tag{22}$$

When $m=3$, the coefficients of filters are listed in Table 1.

Table 1. Wavelet filter coefficients

	-2	-1	0	1	2	3
H_0	0	0.1250	0.3750	0.3750	0.1250	0
H_1	-0.0061	-0.0869	-0.5798	0.5798	0.0869	0.0061

From the equation (13), the wavelet function ψ is composed of some sub-images in different directions. Supposed the constructed wavelet function is [2].

$$\psi^{NB}(x, y) = \{\psi^{NB,e}(x, y) | e = 1, 2, 3\} \tag{23}$$

Wavelet function $\psi^{NB}(x, y)$ renders the wavelet in three different directions. For the given digital image $f(x, y)$, its wavelet transform can be expressed as:

$$W_{j,k_1,k_2}^e f = 2^j \iint f(x, y) \psi^{NB,e}(2^j x - k_1, 2^j y - k_2) dx dy \tag{24}$$

Where, $e = 1, 2, 3, j, k_1, k_2 \in Z$, and j is the scale.

According to Mallat theory, the modulus $\|W_{j,k_1,k_2}^e f\|$ has the local maxima values in e ($e=1,2,3$) direction. The image edges are just corresponding to these maxima values. For fast computation, the edge points can be detected by

$$B_e = \begin{cases} 1, & \|W_{j,k_1,k_2}^e f\| > \delta \\ 0, & \|W_{j,k_1,k_2}^e f\| \leq \delta \end{cases} \tag{25}$$

Result analysis

The original image of coal gangue is 256 *256 pixels, and its grayscale is 0-255. The scale of the wavelet transform is $2^1, 2^2$, respectively. The threshold is the local maxima of the wavelet coefficients. The edge detection for image of coal gangue is shown in Fig. 2.



Fig. 2 Edge detection for coal gangue

From Fig. 2, the edge is enhanced and detected. It can be seen that the speckle influence is remarkable eliminated.

In practice, many methods of edge detectors have been developed up to now, such as Sobel, Prewitt, Roberts and Laplacian of a Gaussian (LoG) edge detectors and so on. Fig. 3 show the images processed by some above edge detectors.

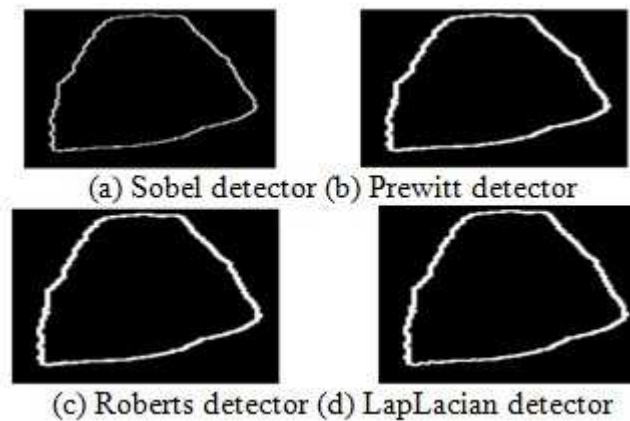


Fig. 3 Images processed with other methods

Conclusion

Based on wavelet transform, the characteristics of digital image processing technology gangues coal classification of the automation of coal gangues coal select system. Edge detection is a basic problem in coal gangue image processing and pattern recognition. Through the traditional method is image processing efficiency than the edge detector, a large number of false information from coal gangue edge will be extracted from the image, because coal gangue speckle image is always of coal dust pollution.

References

- [1] C.S Burrus, R. A. Gopinath and Haitiao Guo, "Introduction to wavelets and wavelets transforms: A primer." China Machine Press, Beijing, 2010.
- [2] Li Jianping, and Dang Yuanyan, "Application of wavelet analysis method." Chongqing University Press, Chongqing, 2009.

Mercury Processing in PVC Production

Tieyun Li

Wuhai Vocational and Technical College, Wuhai, Inner Mongolia 016000 China

Keywords: Mercury Processing, PVC Production, control technology

Abstract. Mercury is highly toxic heavy metal pollution attracted the attention of the world. This paper analyzes the situation the main industry in mercury use PVC production. Manufacture of battery, electric light, medical equipment in China. Furthermore, it discusses the details of the best technology the use of mercury emissions reduction and mercury control in that industry. The result is that certain technologies such as low mercury. In PVC industry catalyst, as mercury battery, amalgam substituted Mercury and LED light in the electric light source industry, electronics the thermometer and blood pressure in the medical device industry and so on, reduce mercury able to make full use of and emission reduction in risk mercury pollution to the environment.

Introduction

Calcium carbide method of vinyl chloride synthesis reactions to the activated carbon as the carrier chlorinated mercury accelerant, due to high temperature in chlorinated mercury sublimation, in high temperature reaction process always have a certain amount of chlorinated mercury into reaction generated into gas, refined syn gas technology different, produce the level of pollution and party type are different. Add catalyst micro activity poisoning, stopped the factors. The deactivation, chlorinated mercury catalyst must produce certain consumption. Because mercury is a scarce resource, and polluted, has caused the height of the international concern, in calcium carbide method of vinyl chloride mercury-free catalyst development. Before success reduces the consumption and production process mercury pollution, has become Calcium carbide method for polyvinyl chloride (PVC) enterprise and chlorinated mercury catalyst industry must face problems. Yunnan salinization Co., LTD is located in kunming, yunnan chlor-alkali device An NingShi, for ChongHuaGong concentration areas of yunnan province, is located in the upper reaches of Yangtze river, belong to environmental sensitive river basin. As early as in 2008, the people's government is of Kunming Ming. It required, area of drainage of waste water treatment by all water quality must reach to the urban sewage treatment plant emissions standards (GB18918- 2002) level 1 A standard. To this, the company actively response, made ensure that the "standards", and finally achieve the wastewater "zero emissions overall orders mark, around mercury pollution reduction and did a lot of work and study, obtain some progress.

The flow of mercury will check

Analysis methods of optimization, improvement and search for the implementation of the programmed Although 100000 t/a PVC device supporting a more complete test Means, basic can complete the daily production organization of raw materials, intermediate control, Ann all, environment and health requirements of analysis, but to complete the flow of mercury will check work also need to be studied further the process of different material form analysis method. Combined with calcium carbide method of vinyl chloride material characteristics, increased the cold. Atomic absorption analyzer and microwave digestion device. In order to ensure the accuracy of the data analysis, the different forms of contain Mercury samples method research and analysis, acquired the production data of the system and make check set the options laid a foundation. Considering the 100000 t/a PVC device has been put into production more than 2 years, in the short term to find PVC device mercury balance, get a complete and credible data have great difficulty. So the mercury will focus on touch check as soon as possible clear the flow of mercury and losing rule, especially to find out as early as possible sources of pollution, press according to the material flow, the mixed dehydration to dry tail exhaust for a whole party a system analysis.

A distillation tail exhaust gas samples, and the storm dry, to smoke exhaust catalyst true exhaust air pump, production device inside the atmospheric environment differences concentration, in and out activated carbon is mercury in addition to syn gas; Liquid sample have mixed dehydration condensing acid and waste. Hydrochloric acid, alkali, waste soda-wash tower before the machine, finished product, the condensed water drainage from the mother liquor, calcium carbide slag heart on clear liquid, vacuum pump cycle fluid, edible and total row wastewater, etc.; Solid sample have catalysts, and waste activated carbon, sawdust, sludge and so on. At present already complete test method of optimization and improvement, PVC production work. In the process of the flow of mercury art investigation and inspection, contain mercury wastewater treatment of device check, operation data detection, a total of 12 has more than 700 data. Prison the data show that the production environment atmosphere within the device testing results is low, far lower than the harmful factors workplace occupational exposure limits part 1 chemical harmful factors "(GBZ 2.1) limit. Solid phase samples by test results representative samples and data analysis method, means and limit, its fruit is not support the establishment of mercury device balances, as long as the strict implementation of the crisis risks waste management relevant provision, solid waste pollution can be to control.

Shall check In the preliminary check for process, according to the monitoring data of continuous adjustable the whole scheme, respectively, aiming to take common key monitoring, sustained attention and so on way. According to the testing results, conditional, and immediately the improvement is the discharge of waste water containing mercury scattered for the collection, after cyclical multiplexing, to contain Mercury wastewater treatment plant. Along with the rack cleaner tap, the rain the sewerage and other measures implementation, vinyl chloride device for trench and total drainage mercury in content gradually declined, realize the stable standards. Check the system will work contract half a year, the monitoring data can reflect the basic production load, operation now shape, corrective actions, and the difference of the device, through reading monitoring data, that, take off the mercury device activated carbon efficiency, remove the syn gas mercury; vice the mercury in content with hydrochloric acid in off the mercury in the use time of activated carbon, a very slowly rising, can be used as the basis for the judge to take off the mercury effect; Alkali washing tower waste alkali contain mercury quantity is low, the mercury in syn gas that get the effective intercept; Transformation workshop pit wastewater contain mercury quantity change is great, mercury pollution mainly comes from the change of when splashed Isaac, necessary height attention, once the plant area drainage system produce pollution, it is difficult to short-term snap after, also easy to accident emissions.

The establishment and implementation of measures

Facing local higher environmental protection requirements, the company set in cut mercury pollution scheme to satisfy (GB18918-2002) level 1 A standard at the same time, positive research and formulated a finally realize wastewater zero emission the overall scheme of the, implement the mature technology of centrifugal biochemical mother liquor (depth) processing, acetylene clean waste time sodium circulation reusing, project.

At present, most in the industry mercury wastewater treatment commonly the method of sulfide, treated can satisfy the reuse and emissions requirements. And the company always Haikou to achieve discharge standards is < 0.001 mg/L, according to this a standard must be to evaluate current of production device every step of the way. According to the characteristics of the mercury wastewater treatment, waste water to get the economy, have the efficiency of the management must be sharply reduce the discharge of sewage low contain mercury, therefore, formulated the "rack cleaner tap, rain water and the sewerage, collect high.

Set up the new wastewater collection pit. Will alkali washing tower to monomer lay aside between the gas holder slot and all drainage collect into gas holder cofferdam newly established within in the pit, used as a base, to take off the acid washing tower of the tower of process water, and turn the factory building area of the floor or equipment flush water.

The sewerage implementation of the rain. Device construction considered the south the rain; the effects of the converter are arranged in the workshop, according to the ground pollution situation, and will lead to the further roofing rain storm sewer contaminated area the nets, in the area of mercury homework early collect rainwater reuse.

Set up special assignments section in mercury. Adding new catalyst warehouse library, to meet new and old catalyst and other contain mercury solid waste management, regulating the catalyst in the factory in transportation line, eliminate spilled and. In the transformation workshop, a especially the door system flushing area concentrated wastewater treatment to avoid the overhaul of the cause time pollution.

Strengthen the water management. In converter and related production area, cancelled most production point, only a few points left to meet emergency requirements, and the valve and seal.

Strengthen site process control and no leakage management. Through the above measures to take, contain mercury wastewater quantity effectively control. Transformation workshop original wastewater pit (including discharge waste alkali washing tower base) as the only source of waste water containing mercury, contain mercury wastewater quantity reduced greatly Less, 100000 t/aPVC full load operation of the device when mercury wastewater quantity. Only 20 to 30 m³ / d, wastewater treatment and cost are the difficulty of innovation former has greatly reduced.

Facing the current environmental protection department higher request, the first priority is to contain mercury wastewater treatment technology promotion. The company has formed a characteristic calcium carbide method of vinyl chloride contain mercury wastewater treatment techniques, concrete process. Treatment of wastewater containing mercury meets the caustic soda, PVC industrial water pollution emissions standards (GB 15581) table 6 requirements, mercury content < 0.005 mg/L.

And part of the process in the industry compared, this technology has the following characteristics.

When the mercury in waste water content in a certain range change, can use fixed elixir formula, improve the treatment efficiency, vary considerably, according to treatment results adjusted formulation, rework can.

The clear separation, not adding filter aid agent and auxiliary filter Water, reduce the quantity of the sludge, and a small amount of sludge through the air basks in can bagging.

Reaction tank effective volume for 30 m³, and set before and after bigger Volume pool, is helpful for adjusting water quality and production organization.

Processing cost is low, regardless of the adjusting the pH of the acid and consumption Alkali, contain mercury wastewater treatment costs for 3 ~ 5 yuan/t

Although the syn gas activated carbon to take off the mercury, but byproduct hydrochloric acid still contain a certain amount of mercury, cannot satisfy the byproduct hydrochloric acid "(HG/T 3783) heavy Metal (to lead plan) 0.005% or requirements. Therefore, only completely disappear

In addition to produce byproduct hydrochloric acid to put an end to the transfer of mercury, and byproduct hydrochloric acid quantity and vinyl chloride device technology and operation control has close cut relationship. Vinyl chloride synthesis, chlorinated hydrogen control excessive, generally for acetylene the gas by 5% ~ 10%, if not more than control index cap, into the take off acid the tower of accurate operation of hydrogen of 2 times. In order to reduce the part of the byproduct hydrochloric acid amount, usually adopts the technology of the conventional to take off the post-mortem hydrochloric acid, this kind, too much about two-thirds of the hydrogen can be recycled.

In addition to byproduct hydrochloric acid, must use depth to take off the post-mortem process, further recovery chlorine of hydrogen, dilute acid HCl (< 1%) back to take off acid tower recycling. Efficient gas phase mercury recovery technology can remove most of the syn gas point's mercury, leaving a small bit of mercury into the byproduct hydrochloric acid, using hydrochloric acid. To take off the post-mortem process, circulation hydrochloric acid or calcium chloride mercury in will enrichment, use the following method in addition to mercury.

Using waste alkali neutralization. Because of the syn gas contains carbon dioxide carbon, alkali washing tower of the utilization rate of caustic soda is not high. Use the waste alkali not in the product of the reaction of NaOH Na₂CO₃ to counteract byproduct hydrochloric acid, take out the part of the water and acid mercury, the generation of wastewater containing mercury in wastewater send Richard device.

Cycle in acid liquid to take off the mercury. Part of the cycle hydrochloric acid bypass into the mercury device equipped with adsorbent off sorbents constantly absorbing the circulation acid mercury so as to realize the balance of mercury. The company was choose 3 kinds of different absorption agents do byproduct hydrochloric acid removal from the mercury in test, of different test conditions, no with the removal rate of mercury adsorbent differences, the first time use of adsorbent .Mercury removal rate is 79.59% ~ 97.52%, considering the subsequent recovery of mercury and contain mercury waste disposal, adsorbent choose activated carbon particles.

High mercury of catalysts, and the mercury levels low mercury catalyst respectively by 11.5%, 6.5% plan, use the deactivation catalyst mercury levels after with 3.5% plan, tons of PVC the products in both consumption, low efficiency in the use of mercury catalyst for high Mercury catalyst 2.67 times. Therefore, low development and use of mercury catalyst for calcium carbide method reducing the consumption of polyvinyl chloride (PVC) industry mercury and reduce the pollution of mercury meaning Major righteousness, and no mercury catalyst development, to become the industry mercury pollution prevention and control are the most important. Chlorinated mercury in the loss from the syn gas into, the mercury device, take off hydrochloric acid washing mercury in gas phase is effectively intercepted. Since the last century the 70 s began, calcium carbide method PVC industry by active in addition to the mercury removal from the carbon mercury in syn gas, removing the obvious effect. The company through to the byproduct hydrochloric acid mercury concentrations in the analysis and change in time to take off the mercury lives carbon, preliminary accounting also support its views, but active carbon adsorption capacity quantity, adsorption rules, use cost to be groping to continue. In fact, through the use of low mercury accelerant, mercury sharply reduce the loss, the syn gas to take off the mercury activated carbon consumption will also will be reduced correspondingly, which is beneficial to the recovery of mercury use and reduce production cost.

Vinyl chloride in syn gas off mercury, should be actively looking for adsorption efficiency and capacity are better adsorbent, through the chlorinated mercury sorbents recovery recycling, may reduce the calcium carbide method of polyvinyl chloride (PVC) industry mercury apparent disappear fee quantity. Adsorbent regeneration and recycling may reduce the take off of activated carbon mercury running cost. Therefore, a real sense of efficient mercury recovery technology is included from the production, use mercury chloride, recovery and to take off the mercury adsorbent processing the whole process of the integration of technology.

With mercury catalyst for its source in the flow of the mercury will check and process effect evaluation process, test object involves gas, liquid and solid phase. The company the current analysis methods have extraction, heat cracking method, microwave digestion cold the original. The analysis method exist to varying degrees sample processing capacity, poor little representative, dilute levels number, error control has the certain difficulty, can't solve element mercury and chlorinated mercury problems such as identification.

In order to give mercury pollution prevention and control work and providing comprehensive support, build more effective analysis system is necessary. Preliminary planning adopting micro wave digestion + icp-ms Ed, complementary with automatic measuring instrument for solid sample mercury the core of the system solutions.

Microwave digestion + icp-ms Ed method, with the icp-ms mention rose method detection limit; To microwave digestion to form detection, and exactly grasp the mercury existing form; Through the ICP, can effectively eliminate the showering cheated produce of the testing error; Testing ability to extend a space is big, the appropriate sample processing method can process of polyvinyl chloride (PVC). The gas phase, liquid and solid materials heavy metals are in the total content and form of implementation.

Automatic measurement instrument solid sample mercury is the advantage of samples and the amount quantity are bigger, sample quality for 500 mg, volume is 500 mL; 70 sample a sample of the automatic system to ensure a sample flux; Need not kind product processing, the samples have high representative; Has the ideal of the detection limit.

Through the appropriate sample is processing methods but the production process of polyvinyl chloride (PVC). The gas phase, liquid, and solid materials in the content of total hg implementation accurate inspection

To measure, is currently contain mercury materials total content detection method of the relatively optimal scheme. Defect is the only materials total mercury content detection. This method "microwave digestion + icp-ms even usage" is to contain mercury materials detection. Strong complementarily, will contain mercury is highly completion and system test materials.

Conclusions

Through the operation of the management, contain mercury wastewater treatment, hydrochloric acid to take off the post-mortem process renovation, low in mercury catalyst use and take off the mercury and other projects the step by step, this company mercury pollution prevention has obtained the certain into exhibition. The cycle of mercury recycling is the guide to industry and the policy support, calcium carbide method mercury pollution comprehensive prevention and control work polyvinyl chloride (PVC).

References

- [1] D. H. Lars et al., "Environmental costs of mercury pollution", *Science of the Total Environment*, Vol.368, pp. 352-370, 2006. J. Clerk Maxwell, *A Treatise on Electricity and Magnetism*, 3rd ed., vol. 2. Oxford: Clarendon, 1892, pp.68-73.
- [2] H. P. John et al., State review of mercury control options for coal-fired power plants. *Fuel Processing Technology*, 2003, 82: 89-165K. Elissa, "Title of paper if known," unpublished.
- [3] T.D. Brown et al., "Mercury Measurement and its Control: What We Know, Have Learned, and Need to Further Investigate", *J. Air & Waste Manage. Assoc.*, Vol. 49, pp. 628-640, 2010.
- [4] U.S. EPA, *A Study of Hazardous Air Pollution Emissions from Utility Steam Generating Units: Final Report to Congress*, EPA-453/R-98-004a; U.S. EPA Office of Air Quality Planning and Standards, U.S. Government Printing Office: Washington, DC, 2010, Feb.
- [5] M. Prestbo, S. Bloom, Mercury speciation adsorption (MESA) method for combustion flue gas: Methodology, artifacts, inter-comparison, and atmospheric implications, *Water, Air, and Solid Pollution*, 1995, 80, 145-148
- [6] Anthony Carpi, Mercury from combustion sources: A review of the chemical species emitted and their transport in the atmosphere. *Water, Air, and Soil Pollution*, 2009, 98, 241-254

Numerical Analysis of a New Type of Oil Boom With Diversion

Wang Xu-sheng Ning Bo Yuan Ren-min Zhang Xiao-xia

Maritime College of Shandong Jiaotong University, Weihai, 264200 China

Keywords: Oil Boom:Diversion Structure:Volume Of Fluid(VOF) Model:Fluent Software

Abstract. A new type of oil boom with diversion structure is put forward based on the analysis of oil blocking failure. Oil blocking effects of the new type oil boom are numerical simulated by using the CFD software Fluent. The results show that diversion structure improves the critical failure rate significantly, so do the oil blocking effects. Diversion structure play an important role in improving oil blocking effect.

Introduction

The research of prevention and control methods of oil spilling becoming particularly urgent in recent years for the accidents occurred frequently. Many scholars do research in structure optimization of oil booms, because the first step after oil spilling accidents is to lay oil booms effectively[1]. And algorithm improvements, structure optimization and three-dimensional visualization of oil blocking process have been studying. Zhang Zheng, Cheng Shiyong, Li Han etc. simulated the oil blocking process in VOF method by self-compiled program, and turbulence model would be introduced in the following study[2]. Yu Guifeng, Wu Wanqing and Feng Xing[3] studied the applicable conditions of single and twin booms by using of Fluent software, and finding that the twin-booms enhanced the relative rate of oil blocking ability($\Delta q\%$) to 2.66667 while the velocity of water is 0.2m/s. Cheng Hao found that the depth of the water should be considered while it is less than 30 times the height of booms[4]. Wei Fang studied the shape of booms's effect on oil blocking in various sea conditions to optimize the shape of the booms[5]. Liu Cheng, Shen Yongming and Liang Yan tracked oil-water interface with PLIC-VOF method, and the results showed that the pressure status in vertical direction before booms determined the stability of oil-water interface[6].

A new type of oil booms is suggested which critical failure rate is more higher than classic structure. Besides, numercal experiments are simulated by using of CFD software Fluent.

Mathematical Model

Basic equations Incompressible viscous fluid Navier-Stokes equations and continuity equation.

$$\rho \left(\frac{\partial u}{\partial x} + \frac{\partial v}{\partial y} \right) = S_m \quad (1)$$

$$\rho \left(\frac{\partial u}{\partial t} + u \frac{\partial u}{\partial x} + v \frac{\partial u}{\partial y} \right) = -\frac{\partial p}{\partial x} + \mu \left(\frac{\partial^2 u}{\partial x^2} + \frac{\partial^2 u}{\partial y^2} \right) + S_x \quad (2)$$

$$\rho \left(\frac{\partial v}{\partial t} + u \frac{\partial v}{\partial x} + v \frac{\partial v}{\partial y} \right) = -\frac{\partial p}{\partial y} - \rho g + \mu \left(\frac{\partial^2 v}{\partial x^2} + \frac{\partial^2 v}{\partial y^2} \right) + S_y \quad (3)$$

Standard k- ε model:

$$\rho \frac{dk}{dt} = \frac{\partial}{\partial x_i} \left[\left(\mu + \frac{\mu_t}{\sigma_k} \right) \frac{\partial k}{\partial x_i} \right] + G_k + G_b - \rho \varepsilon - Y_M \quad (4)$$

$$\rho \frac{d\varepsilon}{dt} = \frac{\partial}{\partial x_i} \left[\left(\mu + \frac{\mu_l}{\sigma_k} \right) \frac{\partial \varepsilon}{\partial x_i} \right] + C_{1\varepsilon} \frac{\varepsilon}{k} (G_k + C_{3\varepsilon} G_b) - C_{2\varepsilon} \rho \frac{\varepsilon^2}{k} \tag{5}$$

G_k and G_b stand for turbulent kinetic energy created by average velocity and buoyancy respectively. Y_M stands for effect of compressible turbulent kinetic energy dissipation on the overall expansion rate. Turbulent viscosity coefficient is $\mu_1 = \rho C_\mu \frac{k^2}{\varepsilon}$.

The VOF model:

$$\frac{\partial \alpha_q}{\partial t} + \frac{\partial (u \alpha_q)}{\partial x} + \frac{\partial (v \alpha_q)}{\partial y} = 0 \tag{6}$$

$$q = 1, 2 \tag{7}$$

$$\sum_{q=1}^2 \alpha_q = 1 \tag{8}$$

α_q is volume ratio of the q-phase to the unit.

Computational model The computational domain[7] is shown in Figure 1, the numerical pool are 4 meters long, and 0.3 meter in depth. The distance from the entrance of the domain to oil boom are 2.0 meters.

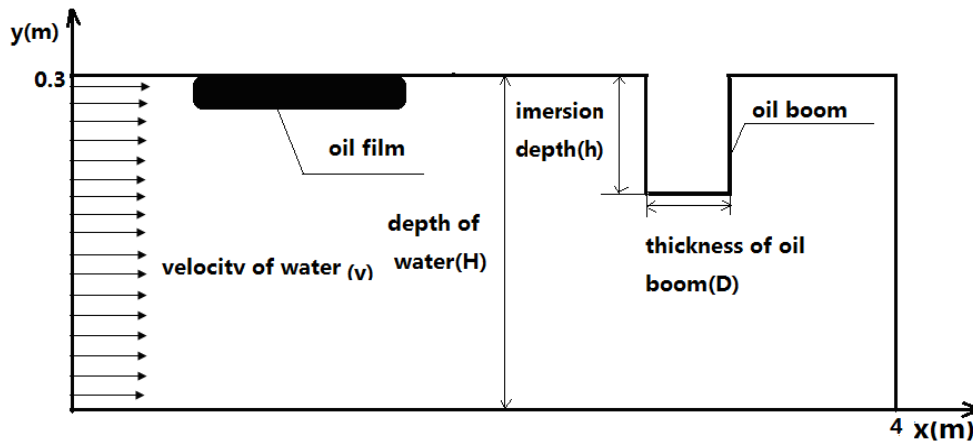


Fig.1. Computational domain

h—the immersion depth, 0.07 meter. ρ_{oil} —the density of oil, 888kg/m³, ν_{oil} —the viscosity of oil, 0.7*10⁻⁴m²/s, q—the quantity of oil, 0.01m³ / m. The initial distance from the oil film to the boom is 0.6 m, and the thickness of oil film is 0.1 meter. Numerical model calculations using k- ε model does not consider wind and wave factors. Velocity boundary condition for import. Pressure boundary for export. Friction-free for the free surface. Smooth and fixed for bottom wall. Set the acceleration of gravity as -9.81m/s² in y direction.

Table 1. Comparison of numerical results in this paper and relative literatures

Results Critical failure rate/(m•s ⁻¹)
This paper 0.23
literature[2] 0.28
literature[3] 0.24
literature[7] 0.24
literature[8] 0.24

Comparison of numerical results in this paper and others([2],[3]) are shown in Table 1. The numerical simulation method taken in this paper is reasonable, effective and reliable. For the result in this paper is in good agreement with the experimental result which shown in table 1.

The differences of flow field before and after the failure of oil blocking following. And $h=0.7\text{m}$, $D=0.1\text{m}$, $q=0.6\text{m}^3/\text{m}$. The thickness of oil film is 0.3m initially, 1.0m away from the boom.

Analysis of flow field The oil film becoming thinner in downlinking, and oil blocking failure prone to take place while the film reach the bottom of boom. That is found during the numerical experiment shown in figure 2. Oil blocking failure occurred at 4.428s .

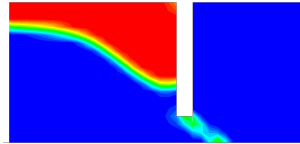


Fig. 2 Profile of oil-water interface
($v=0.3\text{m/s}$, $t=4.428\text{s}$)

The upstream along the oil boom appeared after oil blocking failure. And vertex formed during the process. So the upstream inhibited the downlinking of the oil film, and improving oil blocking effect.

New oil boom New oil boom with diversion structure is put up based on the analysis above, and it is shown in figure 3.

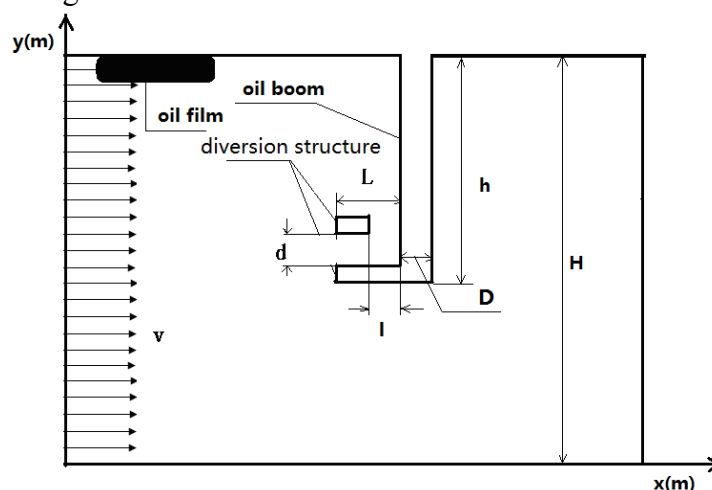


Fig. 3 Computational domain of new oil boom

Numerical experiments on new oil boom

Parameters of numerical model are follows: $h=0.7\text{m}$, $H=2\&22\text{m}$, $L=0.1\&0.2\text{m}$, $l=0.05\&0.1\text{m}$, $d=0.1\text{m}$. Quality of oil spilling $q=0.6\text{m}^3$. The oil film is 1.0m away from the boom initially, and the thickness is 0.3m .

Low viscosity oil parameters[3]: $\rho_{oil}=888\text{kg/m}^3$, $\nu_{oil}=0.7\cdot 10^{-4}\text{m}^2/\text{s}$; high-viscosity oil parameters [4]: $\rho_{oil}=915\text{kg/m}^3$, $\nu_{oil}=3.6\cdot 10^{-3}\text{m}^2/\text{s}$. In order to consider the effect of the depth of pool[4], creating two value pools now (length(m)*depth(m)): NO.1 ($8\cdot 2$) and NO.2 ($24\cdot 22$). $q=0.6\text{m}^3/\text{m}$. The film's thickness is 0.3m , 1.0m away from the boom initially.

low-viscosity oil Oil blocking failure is found at 4.72s while $L=0.1\text{m}$, $v=0.51\text{m/s}$ which shown in figure 4. To increase L to 0.2m , and experiment results show that the downlinking of the oil is inhibited while $v=0.61\text{m/s}$. That's the effect of the upstream from diversion, and improved the critical failure rate.

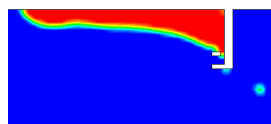


Fig. 4 Profile of oil-water interface in NO.1 pool ($v=0.51\text{m/s}$, $L=0.1\text{m}$, $d=0.05\text{m}$, $t=4.72\text{s}$)

Results of NO.2 numerical pool are the same to NO.1 except the critical rate improved a lot. So the effect of the depth of the pool on oil blocking should not be ignored.

high-viscosity oil The failure occurred at 5.6s while $v=0.6\text{m/s}$ which shown in figure 5. It can be seen that oil blocking effect is decreased due to the increasing of oil viscosity.

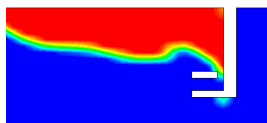


Fig. 5 Profile of oil-water interface in NO.2 pool($v=0.58\text{m/s}$, $L=0.2\text{m}$, $l=0.05\text{m}$, $t=5.6\text{s}$)

Results of NO.1 pool are the same to NO.2 except the critical rate decreased a bit.

It is noteworthy that the diversion has a significant impact on the shape of oil film. And the increasing of velocity of water may lead to oil blocking failure, while the film becoming more thicker on the increasing of the distance from the boom.

Conclusions

The conclusions based on numerical experiments of new oil booms are follows:

Oil blocking failure caused by downlink of oil should be inhibited by proper diversion.

Critical failure rate getting improved due to the exist of diversion structure for both low and high viscosity oil.

When the depth of water is lower, the depth of the booms stopped the oil effect is not negligible.

Those parameters like the diversion length(L), thickness(d), gap(l), and the boom's height(h) need further research to confirm its effects on oil blocking effect.

References

- [1] CAI Jun, HUANG Rong-fu, WANG Wei. On Prevention and Treatment Measures of Ship's Oil Overflow[J]. Ship & Ocean Engineering, 2010, 39(2):108-110.
- [2] [ZHANG Zheng, CHENG Shiyong, LI Han, An C.F. Preliminary numerical simulation of boom failure with VOF model [J]. ACTA SCIENTIAE CIRCUMSTANTIAE, 1999, (6):604-609.
- [3] YU Gui-feng, WU Wan-qing, FENG Xing. Numerical experiment on applicable conditions of typical oil boom based on the software Fluent[J]. Journal of Dalian Maritime University, 2010, 36(2):117-120.
- [4] Ning Cheng-hao, Numerical Simulation of Boom Failure[D]. Beijing: Beijing University of Chemical Technology, 2002.
- [5] Wei Fang. Oil Booms in Various Sea States Blocked Oil and Shape Optimization of Numerical Simulation[D]. Dalian: Dalian Maritime University, 2007.
- [6] LIU Cheng; SHEN YongMing, LIANG Yan. Relationship between pressure gradient along the boom and the instability of oil-water interface[J]. Scientia Sinica(Physica, Mechanica & Astronomica). 2011, 41:170-177.
- [7] DELVIGINE G A L. Laboratory experiments on oil spill protection of a water intake[J]. Monograph: Oil in Freshwater, 1985:446-458.
- [8] BROWN H M, GOODMAN R H, CHANG F A, et al. Boom failure mechanism: Comparison of channel experiments with computer modeling results[J]. Spill Science & Technology Bulletin, 1996, 3(4):217-220.

Research on Wood Drying Technology based on Mechanics

Zhang Xin

Zhejiang Industry Polytechnic College, North Railway Station Of Shaoxing City, Zhejiang Province, China. 312000

zhangxin@cscsi.info

Keywords: Drying Technology; Wood Manufacture; Energy-Saving

Abstract. There is one of the vital issues to ensure the effectiveness and quality of wood drying, to achieve energy conservation in the process of wood drying, and which it is the development of research and development trend of key content of wood drying technology at present in China. The article firstly reviews the current situation of wood drying technology and development, and expounds the energy-saving technologies in the development of wood drying in China.

Introduce

China's current forest resource is in acute shortage, but it has undertaken a huge pressure on the consumption of timber resource. With China's increasing protection of natural forest, the wood raw materials that we can see on the market are all fast growing timber and small-diameter-grade timber, and the amount of large-diameter-grade is decreasing. In order to meet the market demand for large-diameter-grade timber, timber has become the second largest imported substance in China. Meanwhile, China's current annual consumption of timber resources is more than 300 million m³, of which the total number of logs to be imported accounts for 35% of the total demand for timber resource. Currently, there are many wood-based products on the market, including a variety of wood products, paper and various wood-based panels, these products are widely applied to furniture, building materials, cultural life as well as product packaging. During processing of these woods, an important processing step is to achieve the wood drying. If no good drying effect is achieved in the process of wood drying, or due to improper drying technology and backward drying equipment, it will cause some phenomena such as wood discoloration, insects, decay, deformation and cracking, which are largely responsible for the waste of timber resource.

Therefore, in the development process of wood drying technology, it is one of the crucial issues to ensure the effectiveness and quality of wood drying and achieve energy conservation, while energy consumption caused by wood drying can not be ignored. Based on relevant data, annual consumption of standard coal in wood drying process is 11.55 million tons, this value accounts for 45% of the total energy consumption by timber enterprises in timber production, while the atmosphere environmental pollution caused by emissions produced in drying process can not be ignored, CO₂ emission from drying 10000m³ of wood per hour is 1900 m³, SO₂ is 45 m³, soot volume is 40kg, also including a number of nitric oxide, and these substances can lead to atmosphere environmental pollution. So in the development process of wood drying technology, the above-mentioned two issues have always been studied and have made some progress. This article focuses on research of the progress and related thinking of wood drying technology.

Status and progress of China's wood drying technology

Steam heating drying technology is still dominated China's currently-used more conventional wood drying technology is to use kiln room heated steam heating to dry wood, which has a dominant status. Currently, to achieve reduction in the investment cost and energy consumption, hot water heating method has been added to such steam heating method, and this drying technology, after decades of development and with the increasingly sophistication and maturity, basically can meet wood drying of regular tree species and a variety of sizes, and in order to achieve a better drying result, development of high temperature drying technology is achieved in steam heating

technology, so as to meet the drying requirements of soft hardwood and softwood lumber. The biggest drawback of steam heating drying technology is the larger heat loss caused, according to the relevant information, the heat loss caused by hotter steam in wood drying in Beijing every year is more than 40%, and also it will cause environmental pollution to some extent.

New types of wood drying technology have certain degree of growth In addition to steam heating drying technology; there are a variety of new wood drying technologies now in China. First, in early 1980s, China has successfully applied vacuum drying technology in wood drying, and its main feature is that it has a good drying effect to diffused-porous hardwood. At the same time, in the vacuum drying process, it can guarantee the surface of the wood be always in a wet state, the effect achieved is higher than the vacuum hot-air drying. So, in the future, it will have better application prospect in the drying of hardwood timber; dehumidification drying technology has also started application in 1980s, and compared to conventional drying technology, its performance of energy-saving effect is very obvious. Because of the current development and use of high-temperature heat pump dryer, the efficiency of dehumidification drying has been greatly improved. Especially since Professor Zhang Biguang at Beijing Forestry University developed High Temperature Dehumidify Dryer of Two Heat Sources for Wood Drying, the energy reduction performance in drying process has become more obvious; in addition, China's demand for fast-growing wood, hardly dried wood and hard broadleaf during industrial wood use course is increasing, and microwave heating technology and high-frequency drying technology have demonstrated small stress and deformation, small temperature gradient, uniform drying and other characteristics, so they show great advantages in the drying process of large-section woods, and the development prospect is also very impressive; the last is combined drying technology, its principle is to integrate a variety of drying technologies, absorb their merits, and make up for their shortcomings. Here, we take the example of the combined drying of conventional steam drying technology and dehumidification drying technology. First, we can use steam heating means in the process of wood preheating to avoid shortcomings of high power consumption and slow heat increase existing in the dehumidification drying warm-up process; in medium drying stage, due to large amount of humidity, we can use dehumidification drying technology to recycle residual heat in the drying chamber, so energy saving can be achieved; in the latter stage of drying technology, due to reduction in the amount of humidity, we can then use steam drying way to effectively achieve the shortening of drying cycle, increase drying rate and increase the temperature of drying chamber.

Achieve improved performance of wood in the wood drying process In the current wood processing and application process, it is often not to simply dry the wood, but to transform the performance of the wood in the drying process, where the most prominent is the production technology combining wood drying and heat treatment. Specifically, it is to improve the wood's deformation resistance sign, dimensional stability and corrosion characteristic in the wood drying process. This integrated production process technology has been more widely used in the processing of a lot of wood floorings, and it also includes integration of technology of wood surface performance improvements and hot pressure drying; production technology of wood color change control to produce woods with a variety of colors that people need during the drying process; production technology combining softening of the wood hardness and microwave drying technology, and combining drying technology and softening treatment of fast-growing woods such as Eucalyptus, etc., which has drawn people's attention on the market of floor enterprises and other related industries.

Thinking on the development of wood drying technology

Achieve the theoretical innovation and development of drying technology Drying theory is the related theoretical content of wood drying science, also an important theoretical basis of the applied science of wood drying science in practical application process. Within a very long period of time, people have given enough attention to the promotion and application of new wood drying technology, research on drying technology and equipment, and drying characteristics of different

woods. But they have not paid enough attention to the basic theory of its drying technology. The lack of theoretical innovation, and systematic in-depth research, caused a big gap behind development of wood drying theory in developed countries. However, in early period of development of China's wood drying science, especially because of the constraints in development of China's timber processing enterprises as well as the development level of wood industry, it is relatively correct to emphasize on technology application in research process. Because at that time, we could only rely on more application technologies instead of theoretical technologies so as to better promote the development of China's wood drying industry. At the same time, because China was still very weak in the basis of theoretical study of wood drying, not only the study conditions were not mature, but also we lacked of the necessary experiment funding, laboratory equipment and related experimental method, we could not achieve effective research on this theory on a higher level. But with the current continues development of wood drying science and drying technology in China, the then various restrictions on the theoretical research have been largely improved. And meanwhile wood drying industry has developed to a certain height. They require us to strengthen the theoretical support, and rely on theoretical innovation in drying science to achieve further development in wood drying science and drying technology, and this is also the inevitable guidance requirements for achieving development of drying technology in a long period in the future. So in the development process of drying technology, it is now a period that needs theoretical innovation in the drying science, and needs relevant researchers to pay enough attention to the theoretical study of wood drying science.

Research and innovation of new wood drying technology The author has also mentioned above, probably 80% of China's wood drying uses steam drying means. Because such wood drying technology is relatively mature in the development of China's current processing and application process, there are not much space and meaning in research or innovation of such technology. Thus in the innovative research on new drying technology, the author believes that we need to master the contents in the following aspects:

First, we need to enhance research on intelligent control and digital precision drying technology. And in terms of the current network technology development, it is not a very difficult process to conduct research on intelligent and digital drying technology. But we should be fully aware of the individual differences and wood structure complexity in the wood drying process. We can not simply build the stress model and the internal moisture transfer model in the course of study, but should enlarge the scope of this study, collect and test information on moisture content distribution and structural differences of the wood during the wood pile stacking operation. And take appropriate and targeted drying measures for the situation of each timber, so as to better achieve intelligent and digital accurate drying.

Second, in terms of the current difficult situation in the drying of some woods, we can seek for breakthroughs in the pre-treatment technology and technology integration and innovation. In recent years, China has imported a variety of hardwood timber species, which vary in the ease of drying. But it is clearly impossible for us to find some sort of drying technology which can be applied to all species. Thus it requires us to conduct efficient combined and systematic research on various drying technologies, which is the combined drying technology that the author mentioned above. It will not be further discussed here. In addition, we need to conduct systematic research on various domestic wood drying technologies in input cost, energy consumption, environmental impact, quality effect, drying rate and other aspects. Therefore we can carry out scientific and comprehensive evaluation and establish evaluation system, so as to provide more explicit, scientific and systematic guidance on wood drying production.

Third, we can focus our efforts on the combination of drying and modification technologies against the characteristic of the fast-growing plantation woods. With the depletion of natural forest timber resources, short-period plantation wood (fast-growing wood) will be mainly used for future timber production. Most fast-growing woods are easily dried woods, because of their fast growth, short growing season; they have the problems of large timber growing stress, small density, more pith material, easy cracking, and deformation and so on, affecting the quality of products and the

value of goods. Therefore, it is of great significance to further study the combined drying technology of wood drying and wood properties improvement. China has carried out research in this area, which has also been mentioned above. But the technology maturation is not enough. Product positioning and performance standard are not clear. And no high degree of identity has been got from the market. So we need to conduct in-depth study together with the market development of wood modified products.

Finally, we should expand the field of wood drying technology. Over the years, major object of study of wood drying science has been solid woods, namely sawed dry woods. This is formed based on the then situation of timber resources and wood industry products structure. Today, the use of woods has entered the era of plantation timber and the era of plywood industry, the usable sawed timber resources have significantly dropped, while the drying amount of plywood has increased significantly. In 2009, China's total volume of plywood and block-board has been more than 60 million m³, and will increase later; we should pay attention to exploration of wood drying technology in this area. In fact, due to changes in wood species, the traditional single-board dryer can not fully be applied to existing domestic production mode of plywood and block-board, we need technical innovation.

Promote green drying, and further achieve energy conservation Because China's energy consumption has unreasonable structure and environmental pressure, energy saving and emission reduction will become a very important work in future economic development. Wood drying is the most energy-consuming process in wood processing, so the wood drying industry should assume this major responsibility for the state. We should promote green drying and contribute to energy conservation, which is an important task of timber drying industry in recent period.

For wood drying industry to achieve energy conservation, the most effective method is to vigorously promote biomass utilization technology. In recent years, wood waste furnace gas heating wood drying technology's promotion has met a number of constraints, mainly because the existing combustion system is too small, the operating environment is poor, and there is dust pollution problem, so it fails to adapt to the modernization and large-scale development needs of wood processing enterprises. Biomass energy application in wood drying should be positioned in large-scale, modern development, and we should cooperate with the boiler manufacturers and promote the use of hot water, steam heating with biomass fuels, which may be the future direction of development.

In summary, China's wood drying technology has made encouraging progress over a long period of development, but there are many issues that must be addressed. Energy-efficient wood drying technology and the exhaust heat recovery technology are the focus of future research. China's wood drying technology is shifting from the experience-based to science-based with drying theory as the basis. Future direction is to implement effective and green drying development strategy, turn single extensive drying to intelligent precise drying; implement comprehensive, multi-level energy-saving technological transformation; and establish and improve the overall evaluation criteria and industry standards of drying equipment, so as to promote enterprise progress and development.

$$R_t = K EP = 93.02 (\pm 9.62) - 13.45 \quad (1)$$

They should also be separated from the surrounding text by one space.

References

- [1] Gu Lianbai. Advances and Thinking of China's Practical Wood Drying Technology [J]. Wood Industry, 2006, (02).
- [2] Zhang Biguang. Overview of China's Wood Drying Technology [J]. Machinery, 2010, (08).
- [3] Zhang Biguang, Gao Jianmin, Yi Songlin, Wang Tianlong. Research on Status Quo of China's Wood Drying Energy Saving Technology, [J]. North China Electric Power University (Natural Science), 2009, (03).
- [4] Zhang Qingbo. Thinking on Future Development of China's Wood Drying Technology [J]. Chinese Forestry Industry, 2008, (09).
- [5] Gu Lianbai, Zhuang Shouzeng. The Status Quo and Technology Needs of China's Timber Drying Industry [J]. Wood Industry, 2009, (03).
- [6] Zhuang Shouzeng. Thinking on Innovation and Development of China's Wood Drying Technology [J]. Forest Products Industry, 2008,35 (2).

Influences of Heat Treatment on Spinning Process with Large Thinning Rate and Performance of 30CrMnSiA

Dong Han, He Yang, Mei Zhan, Mingyang Yang, Shaozheng Mou and Tian Li

^{1,2,3}State Key Laboratory of Solidification Processing, Department of Materials Forming and Control Engineering, Department of Materials Science and Engineering, Northwestern Polytechnical University, Xi'an 710072, China

^{4,5}Xi'an Aerospace Power Machine Factory, Xi'an 710025 China

⁶State Key Laboratory of Solidification Processing, Department of Materials Forming and Control Engineering, Department of Materials Science and Engineering, Northwestern Polytechnical University, Xi'an 710072, China

handongxy@126.com, yanghe@nwpu.edu.cn, zhanmei@nwpu.edu.cn, ht7414tuanwei@126.com, moushaozheng@163.com, litiannwpu@163.com

Keywords: Heat Treatment, Flow Spinning, Performance, Microstructure, Large Thinning Rate

Abstract. In order to improve the limits of wall thickness reduction of 30CrMnSiA steel in process of spinning, realize multi-pass continuous spinning process, and furthermore improve the forming efficiency and shape accuracy of thin-walled shell of 30CrMnSiA steel in spinning process, the influence of traditional annealing and austenization plus spheroidal annealing on the structure performance of 30CrMnSiA steel and the spun performance of 30CrMnSiA steel are studied. Process parameters of traditional anneal and austenize plus spheroidal annealing are optimized to obtain higher plastic performance and lower ratio of yield strength to tensile strength. Spinning experiments of the workpieces that have been heat-treated by the optimized traditional annealing process and austenization plus spheroidal process are completed. The result shows that the optimized austenization plus spheroidal annealing is beneficial to achieve a large thinning rate for flow spinning process, and can meet the demands of low cost and high efficiency of batch production.

Introduction

In recent years, spinning technology has attracted more attention in aerospace industry [1]. 30CrMnSiA steel is widely used to make the cylinder shell of small tactical engine that is manufactured by multi-pass spinning forming, but surface defects and poor size accuracy both restrict the spinning efficiency and cost. In order to improve shape and position accuracy of products and product efficiency, it is necessary to improve the limit of wall thinning rate of 30CrMnSiA steel in process of spinning, reduce or avoid annealing between the spinning passes, and realize the multi-pass continuous spinning forming [2-4]. The current researches are mainly on the process control [5, 6], few of them have paid the attention on heat treatment of spinning workpiece during spinning process. However, the improvement of wall thinning limit of raw material in flow spinning deformation requests inevitably more uniform original structure, higher spheroidization levels and lower deformation resistance [7-11]. Although the traditional annealing, which is heated to a temperature above AC1 and held for a certain time, then discharged with air cooling, is easy to operate, it is difficult to meet the above requirements. Due to the low deformation resistance and work hardening, the spheroidized microstructure can meet the requirement of multi-pass continuous cold deformation process [12]. Thus, the optimization on heat treatment process of 30CrMnSiA steel pipe for spinning is urgently needed to improve the microstructure of raw materials, reduce spinning deformation resistance, and achieve high spinning thinning limits for multi-pass continuous spinning. And ultimately improve the spinning efficiency, simplify production technology and provide technical support for high efficiency of mass production and low production cost.

Experiment Methods

The essential condition to achieve spheroidal annealing is that the austenitizing structure contains certain amount of undissolved carbon. 30CrMnSiA is a kind of hypoeutectoid steel. The achievement of carbide spheroidization mainly relies on controlling the austenization because of its relatively narrow spheroidizing annealing interval [13]. Therefore, the influence of annealing time, austenization time and isothermal spheroidal annealing time on the structure property of 30CrMnSiA [14-17] are researched in this paper. The experiment scheme is shown in table 1.1. Then heat treated tubes that using the optimized austenization plus spheroidal annealing and traditional annealing are spun. Finally, the performance indexes of spun product are tested.

Table 1 Experiment scheme of heat treatment

Test scheme	Heat treatment time			
Traditional annealing process	700°C×80min	Air cooling		
	700°C×360min	Air cooling		
	800°C×60min	Furnace	cooling	
	800°C×120min	700°C×120min		
	800°C×180min	Furnace	cooling	
Austenization plus Spheroidal annealing	700°C×80min	Discharged	until	
	700°C×120min	furnace cooled to	600°C	
	800°C×30min	Furnace	cooling	
			700°C×240min	
			Furnace	cooling
		700°C×360min		

Results and Discussion

Influence of Traditional Annealing Process

The influence of traditional annealing process on the mechanical properties of 30CrMnSiA tube is shown in Fig. 1.1. As seen from Fig. 1.1, with the increase of annealing time, tensile strength and yield strength of 30CrMnSiA decrease with the value of 0.07 MPa/min and 0.01 MPa/min, respectively, and the elongation and contraction of area increase slightly. The annealed 30CrMnSiA has a higher yield-strength ratio than that of the original one, which shows work hardening rate of 30CrMnSiA can decrease slightly by annealing. With the increase of annealing time, impact property of 30CrMnSiA increases rapidly and then decreases, and hardness sharply reduces and then slightly decreases. It shows that a shorter annealing time is helpful to improve the impact property and reduce the hardness.

Original microstructure of 30CrMnSiA and the annealed microstructure are shown in Fig. 1.2. As illustrated in Fig. 1.2 (a), the original organizations are typical ferrite and pearlite, but ferrite organization distributes around the grain boundaries, and it is bulky with grain grade of the 2-3. After annealing, the grain of 30CrMnSiA is refined, and the ferrite organization dispersively distributes in the organization, and grain grade reaches to above 5. Grain refinement level after an annealing time of 80 min is more visible than that are annealed for 360 min, as shown in fig. 1.2(b) and 1.2(c). These means that increasing annealing time in a certain time range can optimize the organization of 30CrMnSiA. From the organization enlarged 500 times (Fig. 1.2(d)), lamellar pearlite in original organization of 30CrMnSiA cannot be eliminated regardless of annealing time.

According to the laws of annealing time on tensile, impact and hardness mechanical properties and microstructure, the workpiece after an annealing time of 80 min has the lowest hardness, the finest grain and the largest impact energy. Meanwhile, tensile strength, yield strength, elongation and contraction of area that is annealed for 80 min have little difference with those after an annealing time of longer than 80 min. Therefore, 80 min is a reasonable time for traditional annealing.

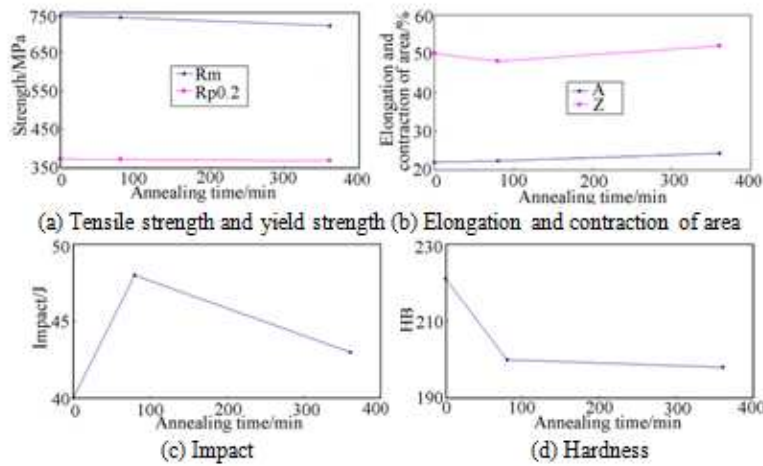


Fig. 1 The influence of annealing process on mechanical properties of 30CrMnSiA

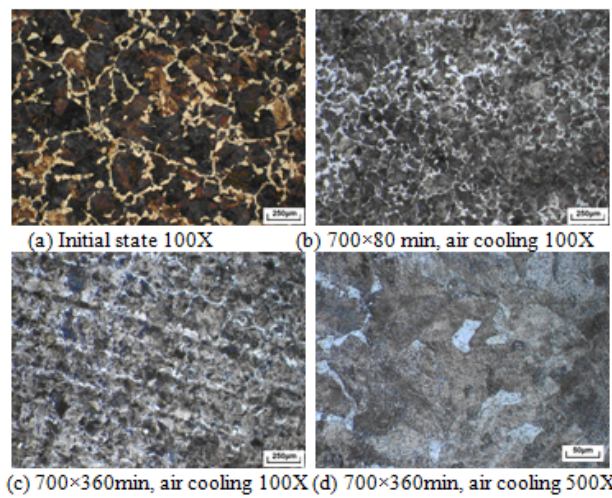


Fig. 2 The influence of annealing treatment on metallographic organization

Influence of Austenitizing Time on Microstructure

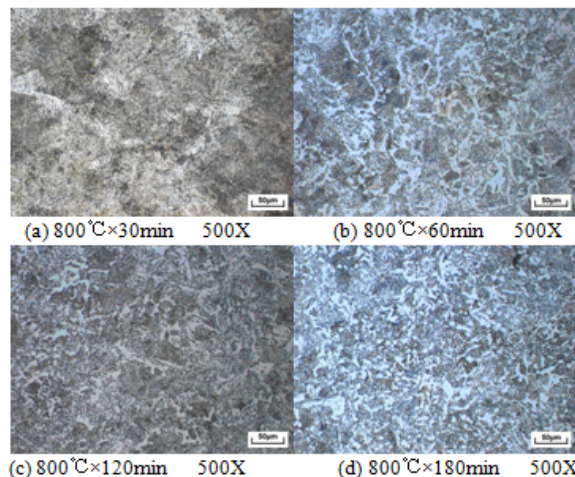


Fig. 3 The influence of Austenitizing time on metallographic organization

The variances of 30CrMnSiA microstructure with austenitizing time are shown in Fig. 1.3. From Fig. 1.3, it can be seen that, austenitization can refine the organization of 30CrMnSiA obviously, and ferrite organization distributes uniformly in the pearlite organization. After an austenitizing time of 30 min, organizations are refined, and original lamellar pearlite organization is eliminated, as shown in Fig. 1.3(a). When the austenitizing time is 60 min, organizations grow up slightly than those are austenitized for 30 min, and the new lamellar pearlite emerges, as shown in Fig. 1.3(b). When the austenitizing time reaches to 120 min, austenitizing still can refine grains, and the grain size reaches

to 6-7 level, just as the organization after a time of 30 min. However, lamellar pearlite still exists, and with increasing of austenitizing time, the length of lamellar pearlite and interlamellar spacing reduce simultaneously, as shown in Fig 1.3(c) and 3(d), which will cause obvious increase in hardness.

Considering that the better the spheroidization effect is, the lower the hardness is[18], prolongating austenitizing time goes against optimizing the spheroidizing organization, and it may even increase the harden rate of material. Although prolongating austenitizing time can also refine grain at some degree, the original lamellar pearlite organization can not be eliminated. Meanwhile, with increasing austenitizing time, the hardness of 30CrMnSiA increases, which is unfavorable to subsequent machining. Thus, 30 min is a reasonable austenitizing time.

Influence of Isothermal Spheroidizing Time on Mechanical Property

The influence of isothermal spheroidizing time on the mechanical properties of 30CrMnSiA is shown in Fig. 1.4. As can be seen in Fig. 1.4(a), with increasing isothermal spheroidizing time, tensile strength and yield strength of 30CrMnSiA first decrease and then increase, but the changes are tiny. So does the yield ratio. Tensile strength and yield strength achieve the minimum value when isothermal spheroidizing time is 240 min. With the increase of isothermal spheroidizing time, elongation and contraction of area of 30CrMnSiA increase first and then decrease. Elongation and contraction of area achieve the maximum value when isothermal spheroidizing time reaches to 240 min, as shown in Fig. 1.4(b).

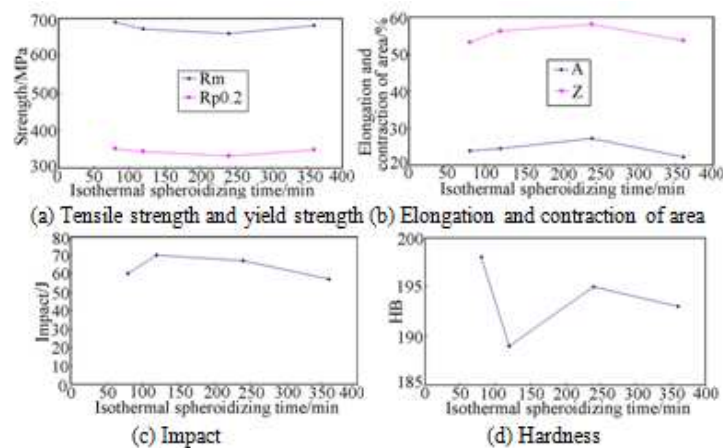


Fig. 4 The influence of heat treatment processes on the spinning performance

With the prolongation of isothermal spheroidizing annealing time, impact first rises to the maximum value in 120 min, then reduces rarely, as shown in Fig. 1.4(c). The changing laws of hardness and isothermal spheroidizing time are relatively complex. With isothermal spheroidizing annealing time prolongating, hardness reduces rapidly at the first time, when time is over 120 min, hardness rises rapidly and then reduces slightly, as shown in Fig. 1.4 (d).

According to the influence laws of isothermal spheroidizing time on tensile, impact and hardness, 120 min isothermal spheroidizing gets the lowest strength, highest ductility and lowest hardness. Therefore, 120 min is a reasonable isothermal spheroidizing time.

Influence of Heat Treatment Processes on the Performance of Spun Workpiece

The 30CrMnSiA cylinder workpiece were heat treated with the optimized traditional annealing process and optimized austenite plus spheroidizing process. And then the workpieces after the two heat treatments were spun at different thinning rate. Mechanical properties of the spun workpieces are shown in Fig. 1.5. As seen from Fig. 1.5, heat treatment process has significant effect on the mechanical properties of spun workpieces. When thinning rate of the spinning reaches to 30%, optimized austenite plus spheroidizing process gets lower plasticity indexes such as material hardening rate, tensile strength, yield strength, while elongation is about 20% more than traditional annealing process. Compared with the hardness of workpiece before spinning process, the hardness of spun workpiece is in favor of subsequent machining due to the lower strain hardening rate and lower deformation resistance. With increasing spinning deformation, intensity index increases,

elongation decreases and hardness increases rapidly, these illustrate that work-hardening obviously happens and resistant force increases gradually in spinning process. Along with the increase of spinning thinning rates, the curve slope of tensile strength against thinning rate and the curve slope of hardness against thinning rate increase. It illustrates that with the increase of spinning passes, spinning force, hardening rate gradually increase. And the higher the thinning rate is, the higher spinning force and hardening rate are.

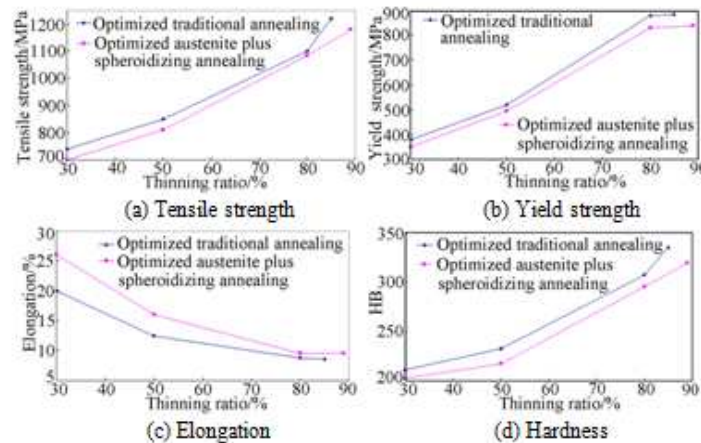


Fig. 5 The influence of heat treatment processes on the spinning performance

Tensile strength, yield strength, yield ratio and hardness of spun workpiece with optimized austenite and spheroidizing are lower than that with optimized traditional annealing in every spinning pass, while elongation with the former annealing is higher than that with the latter annealing. For this reason, optimized austenite and spheroidizing are beneficial to obtain qualified and reliable spun workpiece in the spinning process with a large thinning rate.

Conclusions

The influence of traditional annealing and austenite plus spheroidizing annealing on performance and microstructure of 30CrMnSiA are obtained, and 30 min of austenite time for thick-wall workpiece spinning is considered to be the appropriate time. On this basis, isothermal spheroidizing treatment at different heating preservation time is preceded, and the result indicates that 120 min of austenite time is the reasonable time to achieve excellent comprehensive properties. Then multi-pass spinning experiments for annealed 30CrMnSiA cylinder workpiece with optimized traditional annealing and optimized austenite and spheroidizing annealing are processed. The results show that optimized austenite and spheroidizing annealing can get a reasonable performance index, which is beneficial to spinning process with a large thinning rate.

Acknowledgments

The research is supported by the National High Technology Research and Development Program of China (No. 2008AA04Z122), the National Natural Science Foundation of China (No. 50405039) and 111 Project (B08040), and the authors wish to express their gratitude

References

- [1] M.M.EL-Khabeery, M.Fattouh, M.N.EL-Sheikh and O. A. Hamed. (1991) *Int.J.Mach. Tool. Manu* 2:203-219
- [2] C.C. Wong, T.A. Deann and J. Lin. (2003) *Int. J. Mach. Tool. Manu* 43:1419-1420
- [3] S.C. Chang, C.A. Huang and S.Y. Yu. (1998) *J. Mater. Process. Tech* 80-81:676-677
- [4] Y.T. Yang and L.W. Zhang. (2004) *Aerospace Manu. Tech* 1:49-54

- [5] W.J.He, H.W.Song, H.P.Chang, C.H.Li and S.H.Zhang. (2011) J. Net Shape Forming Engineering 3(2):6-11
- [6] T.C.Wu, M.Zhan, C.G.Gu, H.B.Jiang and H.Yang. (2011) Mater. Sci. Tech 19(1):121-126
- [7] D. Han, L.W. Zhang and Y.T. Yang (2006) China Metal Forming Equipment. Manu. Tech 4:66-68
- [8] H. Yang, M. Zhan and Y.L. Liu. (2002) J. Mater. Process. Tech 122:45-50
- [9] K. Li, N. Hao, Y. Lu and K. Xue. (1998) J. Mater. Process. Tech 79:185-188
- [10] K.Xue, Z. Wang, Y. Lu and K. Li. (1997) J. Material Process. Tech 69:172-175
- [11] H. Stefan, H. Victor, Vazquez and A. Taylan. (2000) J. Mater. Process. Tech. 98:70-80
- [12] HAN, H. YANG, L.W. ZHANG, S.Z. Mu, Y.T. Y and X.X. H. (2010) J. Solid Rocket Tech 2:225-228
- [13] Z.Q. Cui, (2003) in: Physical Metallurgy and Heat Treatment, China Machine Press 1:76-83
- [14] S.C. DUAN, J.D. XING, D.B. YU and D. HAN. (2006) China Metal Forming Equipment. Manu. Tech 4:86-89
- [15] G.S. WANG. (2007) Heat Treatment Tech. Equipment. 28(2):1-10
- [16] D.L. Fan. (2002). in: Key Development Point for Advanced Heat Treatment Practical Technology. Collection of selected Excellent Theses from Modern Heat Treatment Technology and Equipment, China Machine Press 23:29-33
- [17] S.S. WANG. (2006): New Tech. New Process 3:64-67
- [18] Chinese Mechanical Engineering Society and Chinese Heat Treatment Society, (1991) in: volume 1 of Handbook of Heat Treatment, China Machine Press 1:330-337

Experiment System and Test Technology of Oil Fire and Explosion

Xinsheng Jiang^{1,2}, Bo Wang¹, Wenhui Liu¹, Yihong Ou¹, Dong Wang¹
and Haibing Qian¹

State Key Laboratory of Fire Science, University of Science and Technology of China,
230026Hefei, China
Dept. of Petroleum Supply Engineering, LEU, 401311Chongqing, China
e-mail: jxs_dy@163.com

Keywords: Oil Fire and Explosion, Experiment System, Test Technology, Pressure Wave

Abstract: To complete the experiment on occurrence, development, control and suppression of oil fire and explosion in the enclosed space, this paper developed a variety of simulation experiment platform and data test system of key parameters. This paper developed a series of simulation experiment bench, including simulation experiment bench of narrow enclosed space and volumetric enclosed space, see Fig. 1 to Fig. 2. this paper also developed data test system of key parameters, including the ultra-dynamic data acquisition and analysis system and the flame propagation speed test system, see Fig. 3 to Fig. 4. The experimental results show that these simulation experiment benches can provide comprehensive research conditions and support for oil fire and explosion simulation experiment under various conditions. Compared with the traditional fire sensor, the flame propagation speed test system has the characteristics of high sensitivity, zero false positives, and far detecting distance.

Introduction

Most oil fire and explosion accident happens in enclosed space, such as in tank room, tunnel, all kinds of pipe structures, etc. The existing research shows that the confined space helps to speed up the development of explosion, and decides the ultimate form and destructive power of oil fire and explosion. Therefore, establishing scientific and feasible fire and explosion simulation experiment test bench and various data test analysis system is especially important.

Laboratories of the burning and explosion of flammable gas have been set up successively, in former Soviet union, Poland, US, UK, Japan and former west Germany and other major industrial countries; In China University of Science and Technology of China, Nanjing University of Science and Technology, Coal scientific research institute Chongqing branch and other universities and scientific research institutions, various media burning explosion laboratories have been established, test beds with various specifications have been constructed, a large number of experimental simulation and research have been made on all sorts of explosion hazard process and the prevention and control technology, valuable research result has been got [1-2]. But fire process of different types in different environment and system presents strong special phenomenon and law, and therefore must be targeted to establish the test bed and test equipment and means. And because oil fire and explosion laboratory needs big investment, experiment factors are complex, parameter test is difficult, danger is big and other reasons, so far, the research and improvement of experiment facilities and equipment and testing method has been in progress.

To research the development, control and inhibition of oil fire and explosion in confined space, in this paper we developed experiment system of oil fire and explosion including all kinds of simulation experiment test bench and key parameters test.

Development of Oil Fire and Explosion Simulation Experiment Platform

Mixture of oil fire and explosion is difference from other industrial gas and dust in physical and chemical performance. Besides, some existing literature [8-9] about oil fire and explosion can only provide reference for certain field qualitative analysis instead of judgment and standard for quanti-

tative calculation. On the other hand, not many experiment data of gas explosion have been found in complex enclosed space, and most of them are about the gas explosion in enclosed space such as airtight container, pipeline and simple enclosed space. The data are lack of systematic research, and many factors that contribute to gas explosion are not taken into account in the experimental studies; The correlation among the flame propagation law, duration and flame acceleration as well as the relationship with explosive wave especially "pressures buildup" effect and DDT mechanism in enclosed space has not been explored.

The development from ordinary weak explosion to serious explosion in confined space is closely related to the initial model of oil fire and explosion in enclosed space. It's initial model has important influence on the development, superposition, reflection, diffraction of explosive wave and combustion flame and transport effect of the flow field as well as the development law of combustion flame. Different initial model results in difference development law, suppression mechanism and technology of oil and gas explosion. Research on the initial model of oil and gas explosion in enclosed space is the base of understanding blast wave and special phenomenon of combustion flame development and mastering occurrence and development law of oil and gas explosion. Understanding and determining initial model will help draw up technology solutions to prevent and control of explosion hazard, manufacturing and configuration of device and so on. At the same time, it is also of great concern with safety engineering and protection design of oil storage and transportation. Therefore, more deep and systematic study on development mechanism and law of oil fire and explosion in enclosed space and the process of rapid explosion suppression and putting out a fire has very important theoretical significance and practical value. Therefore, this paper developed a series of simulation experiment bench, e.g., the simulation experiment bench of volumetric enclosed space, as shown in fig. 1.

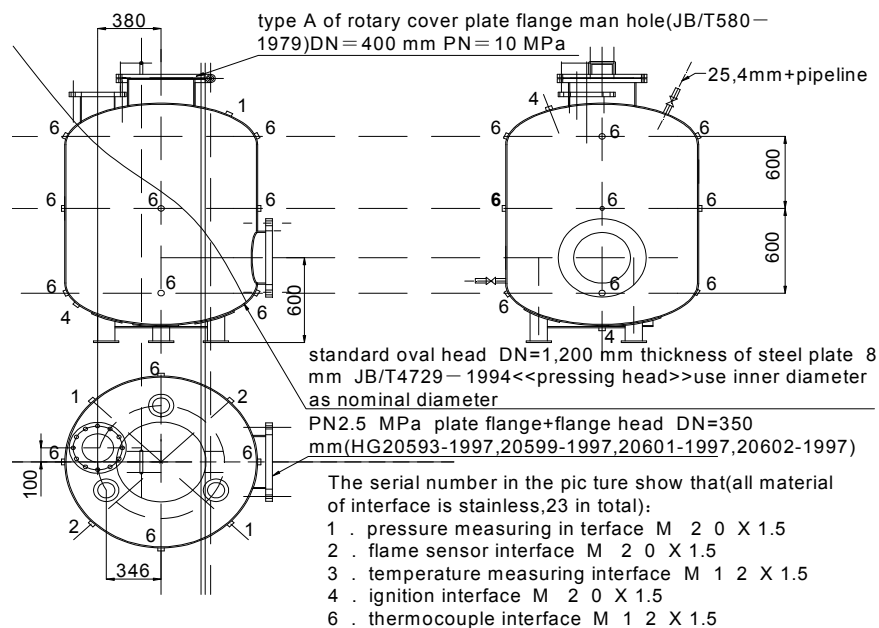


Fig. 1 Simulation experiment bench of volumetric enclosed space (unit:mm)

In order to improve the similarity of simulation experiment bench and "details " and "series" study function of oil fire and explosion, large scale prototype enclosed spaces are designed and produced, such as 5, 20m³ volumetric enclosed space and Φ 700 mm \times 25 000 mm, Φ 2 000 mm \times 10 000 mm narrow enclosed space, structure is shown in fig. 2. At the same time pressure, temperature and molar concentration test system and auxiliary pipeline system is configured to ensure the smooth completion of the experiment.

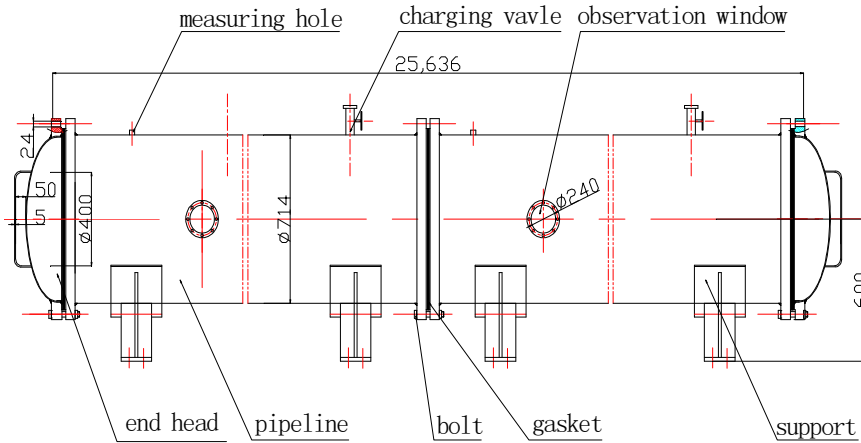


Fig. 2 Structure of simulation experiment bench of the $\Phi 700\text{mm} \times 25\,000\text{mm}$ narrow enclosed space

Development of the Key Parameters Test System

Because the process of oil fire and explosion and fast fire and explosion suppression is a typical transient process, all kinds of signals change frequent and is hard to be accurately captured, it is necessary to use ultra-dynamic measurement system and the flame propagation speed test system, etc. This paper develops the corresponding test system according to actual needs.

The Ultra-dynamic Data Acquisition and Analysis System The paper constructs dynamic data acquisition and analysis system which can be used to complete test of shock wave pressure; transient temperature, flame recognition and DDT process evolution during oil fire and explosion combustion process. this ultra-dynamic data acquisition and analysis system design is: (1) The signal conditioning uses ultra-dynamic strain gauge and charge amplifier, data acquisition system is TST3125 dynamic test-analyzer, collection and analysis software is the DAP3.0. (2) This system integrates industrial computer and transient digital waveform recorder for one, through the high speed data acquisition boards and system software, realizes changing high-speed transient signals into digital signals. At the same time, it uses powerful computer to realize the function of digital signal storage, analysis and processing, printout and other functions. (3) Every channel uses independent A/D and cache, on the one hand, ensure the consistency of acquisition channel phase. On the other hand, equipment index is not influenced by extension of channel number, equipment can work under unified sampling controller and unified sampling clock.

The dynamic data acquisition and analysis system is mainly composed of the following parts: the multi-function ignition controller, the sensors, signal conditioning, data acquisition and processing system as well as transmission cable, interface, calibration, power supply and other accessories part, as shown in fig. 3.

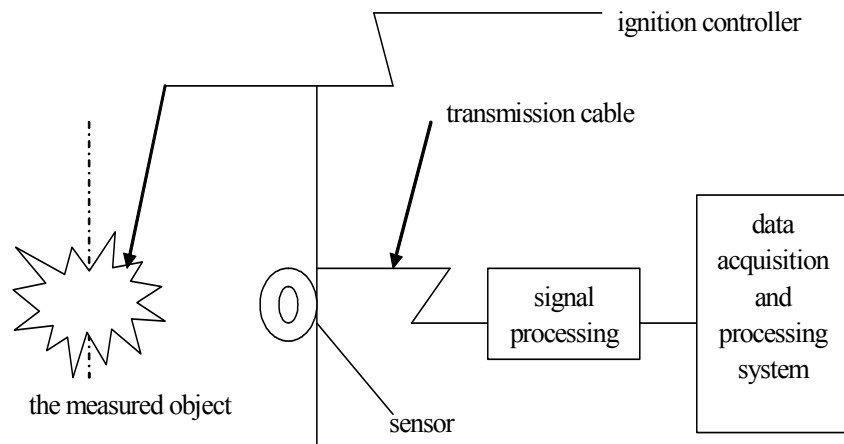


Fig. 3 Structure of ultra-dynamic data acquisition and analysis system

The Flame Propagation Speed Test System Oil fire and explosion is a typical transient process, the flame propagation speed is fast. In order to accurately capture and recognize flame signal generated by exploding, high frequency flame sensor achieves millisecond is needed, but at present the national standard is 30s which is far from meeting the practical needs. Therefore, this paper develops oil and gas explosion flame propagation speed test system based on the uv flame detection, digital signal processing and network intelligent detection technology. The main difficulty of system development is: (1) Flame sensor for oil fire and explosion should have quick response frequency, strong anti-interference ability and can endure high pressure above 3MPa generated by blast wave. (2) Because the blast wave pressure and oil fire and explosion combustion flame are intercoupling, there is so great accelerate motion that the response frequency of the flame sensor must reach 0.1 MHz or even more than 1 MHz. sensor is higher. Therefore this paper adopts ultraviolet flame detection technology.

Ultraviolet light sensor only responds to ultraviolet ray in the narrow range among 185 ~ 260 nm. Because the wavelength of the sunshine to the ground and the light given out by electric light source which uses non transversal ultraviolet material as the glass shell is longer than 300 nm, the ultraviolet ray band among 220 ~ 280 nm of flame detection belongs to the solar spectrum blind area (the sun blind region). Ultraviolet flame detection technology makes the system avoid the complex background created by the most powerful natural light source (the sun), greatly reduce the burden of information processing in the system, so the reliability is high. Flame detector module is mainly composed of the voltage driver module, signal detection module, digital amplifier module, digital filter modules and signal processing module. The flame propagation speed test system is shown in fig. 4.



(a) Highly reflective ultraviolet photodiodes



(b) Flame detection module and detection test photos

Fig. 4 Part of flame propagation speed test system

Key Parameter Testing Experiment

In order to verify the feasibility and effectiveness of the simulative experimental bench and the relevant testing system, this paper take the oil fire and explosion simulative experiment in the narrow confined space which is 9m in length and 367 mm in diameter as an example. To capture the transient signal of the oil fire and explosion, in this paper, the pressure sensors are ranged apart from the ignition of 0.89, 1.76, 2.49, 3.71, 4.38, 5.25, 6.25, 6.85 m. The flame sensors are ranged apart from the ignition of 0.73, 1.00, 2.25, 3.85, 4.85, 5.75, 6.8 m. Pairs of observation windows are set on both sides of the pipe, through which the spread of the fire can be monitored. The dotted line in fig. 5, a typical pressure test curve, shows the flame tracing line tested by the propagating speed testing system. Fig. 6 is a typical experimental result of flame speed test. Curve 1 is to blank experiment, namely the experimental system has no ultra-fine cool aerosol suppressant. In this case the explosive flame is accelerated because the pressure wave and the flame are coupled. Curve 2 shows the case that the oil fire and exploration is not completely restrained by ultra-fine cool aerosol suppress-

sant. The flame which is partly restrained in the exploration-restraining area passes through this area and picks up its speed with the supply of new oil and entrance of new energy. Curve 3 shows the case that ultra-fine cool aerosol suppressant successfully restrains the oil fire and explosion. With the complete restraint, no fire signal was found by the flame sensors behind the exploration-restraining area. It can be a confirmatory proof to prove that instead of breaking through the exploration-restraining area.

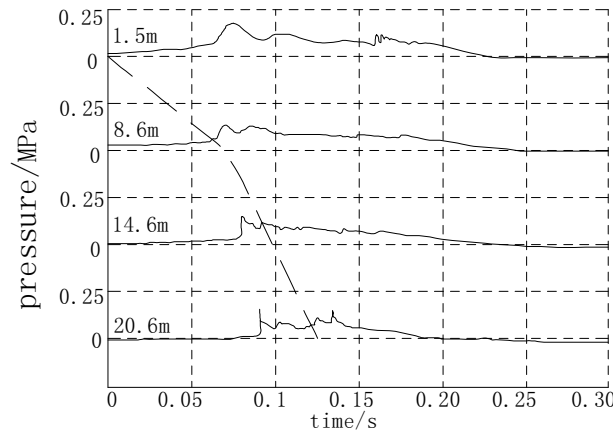


Fig. 5 Pressure testing curve

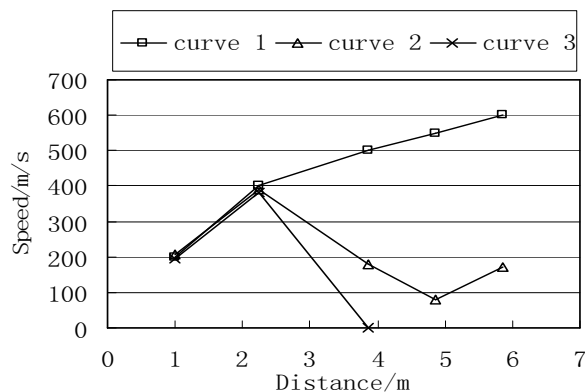


Fig. 6 Flame speed testing curve

Conclusions

In this study, a series of simulative experimental test bench and key parameters test system were developed on our own. The simulative experimental test bench includes different kinds of narrow confined spaces, voluminous confined spaces and assembled confined spaces. The key parameters test system mainly includes the oil fire and explosion ultra-dynamic data acquisition and analysis system and the flame propagation speed test system. As is shown in the oil fire and explosion simulative experiment, the simulative experimental system performs very well both in signal analysis and multiple uses. Thus, it lays an experimental foundation of the in-depth and systematical study on the occurrence and development of oil fire and explosion and how to put out a fire rapidly. In addition, it can be used in a wider area such as other gas explosion and dust explosion.

References

- [1] Fan Weicheng, Li Shufen. (1994) Fire Reserch in China. In: Takashi Kashiwagieds. Fire Safety Science-Proceedings of the Fourth International Symposium. International Association for Safety Science 2:27-45
- [2] XU Sheng-li. (2000) Study on properties of pressure waves generated by steady flames in a duct. Journal of China University of Science and Technology 30(4):387-392
- [3] XIE Bo et al. (2006) Study on active explosion suppression by powder in large-scale duct. Journal of China Coal Society 31(1):54-57
- [4] XIE Bo et al. (2003) Experiment study on active explosion suppression by water Sprays in large-scale duct. Explosion and Shock Waves 23(2):151-156
- [5] XIE Bo et al. (2006) Experiment study on the explosion suppression with passive water Sprays in large-scale duct. Journal of Experimental Mechanics 17(4):511-517
- [6] LIU Xuan-ya, LU Shou-xiang, et al. (2003) The experiment study of the propagation of gas explosion flame influenced by water sprays. Fire Safety Science 12(1):11-18
- [7] FAN Bao-chun. (2001) Experimental research on explosion suppression by inert particles. Experiments and Measurements in Fluid Mechanics 15(4):20-25
- [8] WANG Zhi-rong, JANG Jun-cheng. (2005) The research development on industrial gas explosion in confined space. Industrial Safety and Environmental Protection 31(3):43-47
- [9] LIN Bai-quan. (1999) Influence of barriers on flame transmission and explosion wave in gas explosion. Journal of China University of Mining &Technology 28(2):104-107
- [10] SUN Cheng-wei. (1997) Recent progress of study on detonation propagation. Detonation Waves and Shock Waves 3:1-22
- [11] CHEN Ai-ping. (1999) Experimental studies on the problems of flowing combustible gas explosion in pipeline. Explosion and Shock Waves 19(4):347-352

Analysis on Monitor and Experiment of Blasting Vibration for Sijiaying Iron Mine

Guo Jun¹, Gan Deqing², Tan Jing¹ and Yan Guobin³

¹ Qing gong College, Hebei United University, 063000, China

² Hebei United University, 063000, China

³ University of Science and Technology Beijing, 100083, China

E-mail: 15303156333@189.cn, gdqheut@163.com, hblgdxtj@126.com

Keywords: Blasting Vibration, Detection Experiment, Earthquake Wave

Abstract. The blasting vibration effect is one of the most primary dangerous during blasting excavation process. When ground shake caused by blasting reach to the certain strength, it will have different degree of damage on ground, underground building and project structures etc and affect production stability and security. This article focus on practical project problems during mining and blasting processes of Sijiaying iron mine, the blasting vibration system and scheme are determined through field observation, the blasting vibration regular are experienced study and analysis and they will provide significant guidance for mine safety blasting.

Project General Situation

Sijiaying iron mine is located in the area 10km from south of Luanxian town of Hebei Tanshan, the iron ore comes from simian granulites and belong to Anshan type of sedimentary metamorphic iron deposits. The ore body of mine field from south to north distance is 10km and 2km from east to west, south and north districts are separated by S6 prospecting line. The mineral resources reserves total of 23.48 billion tons, it is one of the three biggest iron ore areas in China.

Iron physical and mechanical properties: the surrounding rock of iron body is mainly grained biotite gneiss. The ore is compacting and hard, the average compressive strength is 1867kg/m² and average pit compressive strength of rock is 1250 kg/cm². Ore weight is 3.2t/m³ and rock weight is 2.7t/m³, surface soil is 2.0t/m³. The safety factor of ore is 12~14 and rock safety factor is 8~12.

Blasting Vibration Test System

The shockproof ness of blasting vibration is the root reason to cause damage of structure and building. The vibration intensity can be expressed by particle vibration displacement, speed, acceleration and physical quantity. According to indication of the majority domestic vibration study and mass blasting vibration actual measurement data, particle vibration speed used as the physical quantity to divide damage standard can approach further to reality, this will get rid of soil characteristics influence. Therefore particle vibration speed is used to test the physical quantity [1]. In view of the vertical velocity value adoption as evaluation standard, so the particle vertical speed is only to be measured.

Blasting Vibration Test System The test system is composed by sensor, vibration measurement instrument and microcomputer etc components, it is shown as Fig.

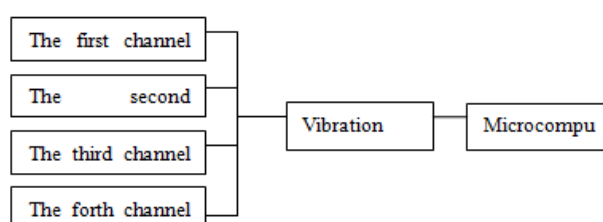


Fig. 1 Blasting vibration test system

The vibration tester with DSVW-4C type is developed by Beijing mining and metallurgy research institute, the high speed microcontroller is used by vibration tester that can process with the voltage output from velocity sensor [2]. The voltage is quantized through high speed 12 A/D converter in vibration sensor and the quantized results are kept in storage. The test data can be inputted into computer discs through communication between vibration tester and computer RS-232 serial interface and experienced process and analysis by assorted software.

Blasting Parameters D-80 type of down –the- hole drill is used during mining perforation, diameter of blast hole is 80mm, hole depth is 10~12m, resistance line is 3.5m, hole distance is 3~4m.

It is 2# rock blasting explosive, detonation method: detonator-detonating tube-explosive, explosive quantity is about 1000kg.

Station Layout The major influence factor of blasting ground shake is explosive quantity and distance from blasting center. The bigger the quantity, the greater the energy that turns to seismic wave, the stronger the ground shake; the farther the distance from blasting center, the greater the vibration damping, the weaker the ground shake.

In addition, the blasting seismic effects are also influenced by geological and terrain conditions greatly. As for seismic wave attenuation regular test process, no less than six stations in one process. The station should be arranged at key site and places required seismic wave error regular test. The three dimensional coordinate of stations and distance from calculation point from blasting center is provided through the practical test.

Table 1 Coordinates of each station in mining area

Coordinate	K1	K2	K3	K4	K5	K6	J1
X	94033.2	94023.9	94011.1	94001.3	93989.0	93967.3	93696.7
Y	3156.28	3160.74	3159.64	3175.14	3185.63	3188.06	3008.34
Z	21.45	20.88	21.28	20.99	22.01	22.11	41.77

Table 2 Coordinates of each station out of mining area

Coordinate	W1	W2	W3	W4	W5	W6	W7
X	93834.2	93806.3	93799.8	93793.8	93781.6	93768.3	93762.6
Y	3295.21	3324.31	3333.73	3346.54	3354.88	3371.80	3391.73
Z	30.55	27.91	27.29	27.03	25.92	25.70	25.21

Totally eight stations are arranged from south to north, the coordinate of each point is shown as Table 1, the second test line is used to observe blasting vibration regular between Sijiaying village and stope, eight stations are chosen outside stope, and the coordinate of each point is shown as Table 2. The nearest station is 56m away from blasting center and the farthest is 440m away from blasting center.

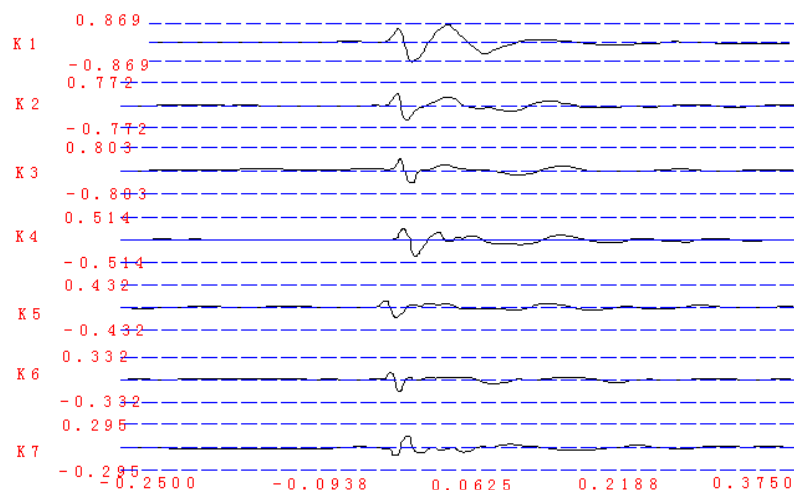


Fig. 2 Particle velocity waveform (The first)

The Result and Data Analysis of Blasting Seismic Wave

Totally five times of blasting vibration tests are conducted, two times belong to blasting seismic wave propagation regular tests and three times belong to blasting seismic wave propagation regular tests between stopes and Sijiaying village.

Blasting Seismic Wave Propagation Regular Test in Mining Area

Totally two times of blasting seismic wave propagation regular tests are conducted, it means the first and fifth tests, the explosive quantity and coordinate are shown as Table 1.3. Totally twelve effective oscillograms are obtained and the practical test data are shown as Table 1.4.

The explosive quantity is 560kg in the first blasting test, the maximum quantity of delay blasting is 201kg, and continuous short-delay blasting is used during this blasting process. It ends with results of seven data and waveform of vibration velocity is shown as Fig. 2.

Table 3 The explosive quantity and coordinate of first and fifth test

test group	explosive quantity(kg)	X coordinate	Y coordinate	Z coordinate
the first time	201	94086.80	3143.11	12.50
the fifth time	160	94116.70	3136.50	11.80

Table 4 Blasting vibration test data table in mining area pit

NO.	Station NO.	maximum explosive quantity (Kg)	distance from test point to blasting center (m)	proportion of explosive quantity $p=Q1/3/R$	peak frequency (Hz)	vibration velocity of particle peak (cm/s)
1	K1	201	55.91	0.105	18	3.374
2	K2	201	65.82	0.089	12	2.246
3	K3	201	78.01	0.075	12	2.048
4	K4	201	91.69	0.064	12	1.712
5	K5	201	107.05	0.055	12	0.982
6	K6	201	127.99	0.046	12	0.750
7	K7	201	147.54	0.040	45	0.692
8	K1	160	86.35	0.063	12	1.197
9	K3	160	108.56	0.050	11	1.059
10	K4	160	122.04	0.044	11	0.717
11	K6	160	158.35	0.034	11	0.568
12	J1	160	440.18	0.012	29	0.100

The explosive quantity is 432kg in the fifth blasting test, the maximum quantity of delay blasting is 160kg, and continuous short-delay blasting is used during this blasting process. It ends with results of five data and waveform of vibration velocity is shown as Fig. 3.

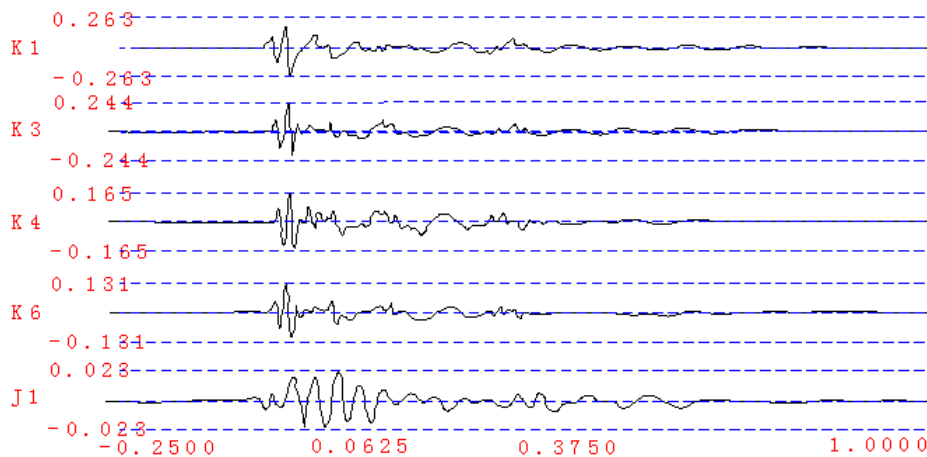


Fig. 3 Particle velocity waveform (The fifth)

Blasting Seismic Wave Propagation Regular Test between Stope and Sijiaying Village

Totally three times of blasting seismic wave propagation regular tests are conducted, it means the second, third and fourth tests, the explosive quantity and coordinate are shown as Table 1.5. Totally seventeen effective oscillograms are obtained and the practical test data are shown as Table 1.6.

Table 5 The explosive quantity and coordinate of test outside stope

test group	explosive quantity(kg)	X coordinate	Y coordinate	Z coordinate
the second time	80	93893.67	3198.96	17.31
the Third time	246	93813.92	3235.20	15.21
the fourth time	210	93845.29	3235.72	20.04

The explosive quantity is 264kg in the second blasting test, the maximum quantity of delay blasting is 80kg, and continuous short-delay blasting is used during this blasting process. It ends with results of seven data and waveform of vibration velocity is shown as Fig. 4.

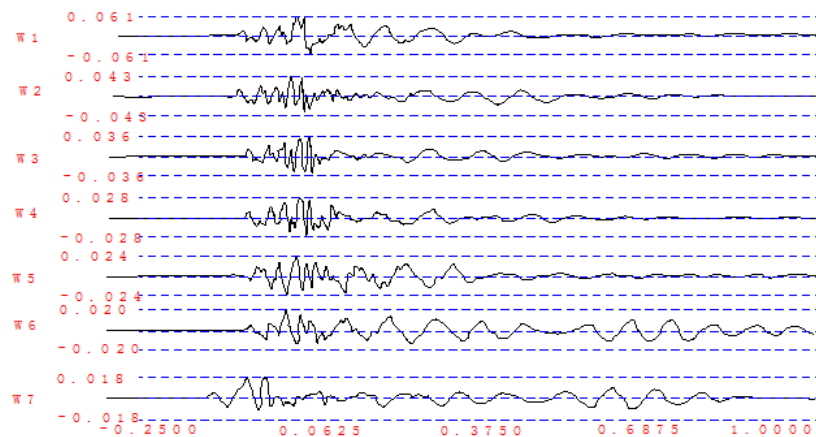


Fig. 4 Particle velocity waveform (The second)

The explosive quantity is 576kg in the third blasting test, the maximum quantity of delay blasting is 246kg, and continuous short-delay blasting is used during this blasting process. It ends with results of seven data and waveform of vibration velocity is shown as Fig. 5.

The explosive quantity is 580kg in the fourth blasting test, the maximum quantity of delay blasting is 210kg, and continuous short-delay blasting is used during this blasting process. It ends with results of three data and waveform of vibration velocity is shown as Fig. 6.

Table 6 Blasting vibration test data of mining outside area

NO	test point No.	max explosive quantity (kg)	distance from test point to blasting center(m)	proportion of explosive quantity $p=Q1/3/R$	peak frequency (Hz)	vibration velocity of particle peak (cm/s)
1	W1	80	113.91	0.0378	13	0.265
2	W2	80	153.15	0.0281	11	0.188
3	W3	80	164.84	0.0261	11	0.155
4	W4	80	178.44	0.0241	12	0.120
5	W5	80	192.23	0.0224	12	0.103
6	W6	80	213.70	0.0202	12	0.086
7	W7	80	233.25	0.0185	12	0.078
8	W1	246	65.18	0.0961	18	1.286
9	W2	246	90.33	0.0694	10	0.714
10	W3	246	100.34	0.0624	10	0.711
11	W4	246	113.75	0.0551	22	0.663
12	W5	246	124.44	0.0504	11	0.577
13	W6	246	144.40	0.0434	11	0.348
14	W7	246	165.04	0.0380	11	0.328
15	W1	210	61.42	0.0968	10	0.982
16	W7	210	176.65	0.0336	14	0.233
17	W8	210	221.01	0.0269	12	0.138

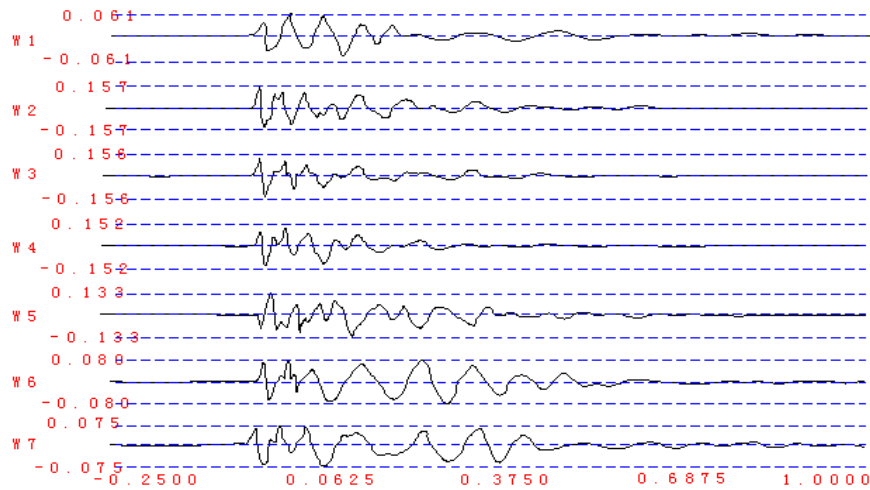


Fig. 5 Particle velocity waveform (The third)

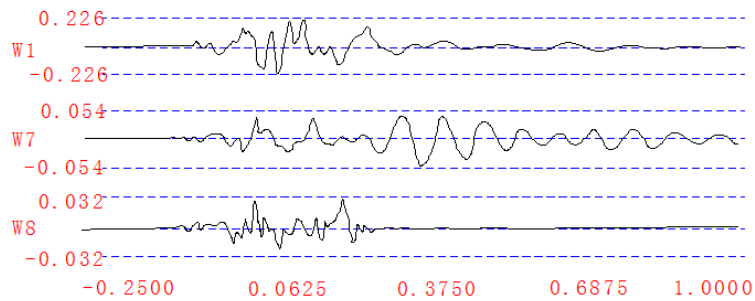


Fig. 6 Particle velocity waveform (The forth)

Conclusions

It is very necessary to monitor key structures around blasting area; the practical monitor shows that during blasting monitor process, the blasting vibration signal can't be monitored beyond 400m, it means under this distance, vertical vibration velocity value of blasting particle is lower than instrument installation trigger value 0.1cm/s. The vibration that from spot surface and underground blasting of Sijiaying iron ore for surrounding private houses are controlled within blasting vibration velocity security standard in China, it means the surrounding private houses are safe. The monitor results can be used to guide forecast of mine blasting seismic effect.

References

- [1] S. S. Shen. (2010) Monitoring and Analysis of Blasting Seismic Effect on One Mine, Nonferrous Metals (Mining Section) 3:56-59
- [2] S. M. Zhang. (2007) Study on the System of Ore Drawing in Sublevel Caving Mining, Journal of Hebei Polytechnic University (M) 3:112-130

Mining Method of Macheng Iron Ore

Guo Jun¹, Gan De-qing², Tan Jing¹, Jia Jing-li¹ and Yan Guo-bin³

¹, Qing gong College, Hebei United University, 063000, China

² Hebei United University, 063000, China

³ University of Science and Technology Beijing, 100083, China

E-mail: 15303156333@189.cn,gdqheut@163.com,hblgdxtj@126.com

Keywords: Phase Drilling, Sublevel Drilling, Afterwards Filling

Abstract: The text analyzed mining method of Macheng Iron Ore. It put forward two projects about afterwards filling mining methods for large and thick inclined ore bodies: phase drilling, ore drawing as well as sublevel drilling and phase ore drawing, according to the thickness of inclined mine. It is greatly propitious to the mine building.

Introduction

Macheng iron mine is located in domestic Luannan country, mine area north far away 15km from the Luan country railway station, south faraway 52km from Jingtang Port [1], and Qing Pingle provincial road passed over west of the mine. The traffic is very convenient. Mine area has village on its surface .Its west is Xingluan River and east is the Luan River levee, the Luan River riverway. The surrounding environment is relatively complex.

The Quaternary rock layer of upper mine is up to about 100 meters thick, containing an abundant supply of water. Its geological conditions and hydro-geological conditions are relatively complicated. The mine can only conducts open-pit mining method at first because of the cost, mining technology and other reasons. But in this way [2], the village will have to move, and the upper part of the Quaternary system may be destroyed and serious environmental impact may have around the mines, so it has not been carried out.

With the rising price of iron ore and the development of mining methods, we are going to use underground mining methods--cemented tailing filled stope to mine, which can effectively prevent the upper Quaternary water and village from being damaged in the mining process .Presently several domestic heavy-water deposits, such as Anhui LiLou and Luo River iron ore, are all using this method .In this way, the problem that too much water will affect mining and mining will affect the Quaternary aquifer as well can be well avoided.

The proposed iron ore production scale of Macheng iron mine is 25 million tons per year [3], limited up to -600m elevation as the boundary, and mining upper as well as lower ore block at the same period.

The Geology and Mining Conditions of Deposit

Geology of Mineral Deposits Macheng iron mine is super large iron ore deposit with 1.04 billion tons reservation, a total of 14 ore bodies .And ore bodies dip at 20° ~ 56° or so, mostly belonging to inclined ore body, which are 8.58m ~ 105.7m thick and divided into three categories according to the thickness: mainly are very thick, thick ore bodies.

The first very thick ore, ore thickness is 87m ~ 108.95m, such as number II, V, VIII ore bodies; second thick ore, ore thickness is 15m ~ 42m, such as number I, IX, X, XII, XIII, XIV ore bodies; the third class is middling thick ore body with a thickness of 7m ~ 15m, such as number III, IV, VI, VII, XI ore bodies.

Mining Technical Conditions Ore roof and floor is the mixed quality of biotite granulite, mixing rock etc, and cracks haven't developed [4]. The rock is complete, vertical and hard. The compressive strength of surrounding rocks are more than 62MPa and up to 145.5MPa maximum.

The compressive strength of ore bodies are more than 71.3MPa of which the maximum is 145.5MPa, and coefficient of rock solid is 8.4. The engineering geological conditions are the second type of exploration - massive rock, is a medium engineering geological bedrock condition.

Mine is located in the top of the Luan River alluvial fan and the hundreds of square kilometers of hydro geological unit, near the southeastern border, within runoff area. Quaternary aquifer is with most abundant groundwater resources. There is no stable impermeable layer between the Quaternary aquifers and the bottom bedrock surface, of which parts exiting "clearstory". And the more than 20 holes which were not sealed in the 1970s' construction, cannot be ignored as well in the direct pit water-filled supply. Therefore, the mine is the middling deposit types of the hydro geological conditions, with the flow of Quaternary pore water supplies and bedrock fissure water directly water-filled.

Major mining projects, including an out channel cut, mounted mine inside channel, pull the trench bottom lane, rock chamber, chamber rock contact channel, ventilation dooryard, slide channel etc.

Mining Method

The Option of Mining Method Mine area has village on its surface. To its west is Xingluan River and east is the Luan River levee, the Luan River channels. The surface cannot collapse. Quaternary aquifer is with most abundant groundwater resources. And there is no stable impermeable layer between the Quaternary aquifers and the bottom bedrock surface, of which parts exiting "clearstory". It will lead to a serious disaster, if a large number of Quaternary water directly flows into the mining area when the impermeable layer was destroyed, meanwhile it will also do harm to the water environment and endanger the safety of the village. Therefore, the mine should adopt the filled stope mining method.

Its advantages:

A: filled stope mining method can be applied to extremely reduce the extent of mining impacts on the environment; the waste mining solid can be filled with mined-out area to achieve reduce waste solid emissions or zero emission sand avoid waste solid polluting the environment. Mine don't build mine tailings and waste rock field, in this way can significantly reduce the occupation of land

B: Considering the resource recovery rate, filled stope can achieve resource recovery rate up to 90% or more, which could fully utilize the resources.

C: From a safety perspective, surface collapse can be avoided while mining, thus the destruction toward the villages and rivers on the mine surface can be prevented. Underground mined-out area can be effectively treated. And with effective support of the mining rock, with no waste rock and tailings yard, mine does not exist gob collapse, tailings collapse and landslides and other geological disasters or accidents.

According to the mining conditions and requirements of production scale, the mine should adopt deep drilling mining, phase mining out, the fan shape sectional drilling hole and filled stope subsequent cementation method after phase mining out methods.

Chamber Parameters A: Deep-hole drilling and phase mining out filled stope

For the very thick ore body, adopt phase drilling, ore drawing and filled stope to mine. Along the strike of ore body, panels are set every 120 meters and the width of columns between panels is 12 meters. Ore blocks are perpendicular to the strike of ore body in every panel and 20 m wide, 44 m long, 100 m high. Two ore blocks which are set in the panel along the strike of ore body are recovered step by step, and the number of ore blocks in vertical strike is determined according to ore body thickness. And tailing-cemented filling is adopted at the first and second steps while tailing backfilling at the third and forth steps. In every panel there are two assigned air shafts which are located in up and down panel areas respectively. Drawn shaft is set between columns with a space of 80 meter, and one ore-recycling drawn shaft is set in down panel area. As shown in Fig.

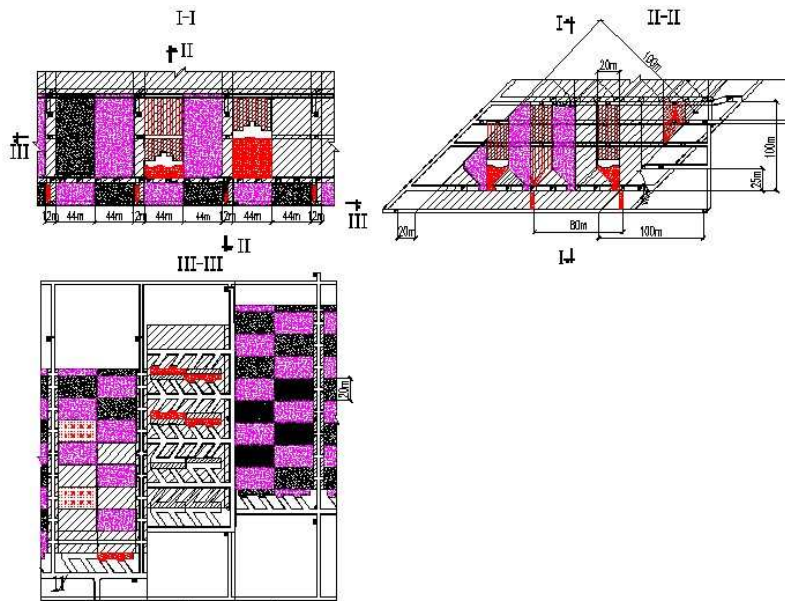


Fig. 1 Deep-hole drilling and phase mining out filled stop

B: Medium-length hole sublevel drilling and phase ore drawing filled stope

For thick ore body, adopt sublevel drilling, phase ore drawing filled stope to mine. Ore blocks are perpendicular to the strike of ore body. Along the strike, a drawn shaft and ventilation raise are set every 120 meters. The sublevel height is 22.5m, and ore blocks are 20m wide, 100m high, of which the length equals its thickness. The tailing-cemented filling is adopted at the first steps while tailing backfilling at the second steps. As shown in Fig. 2.

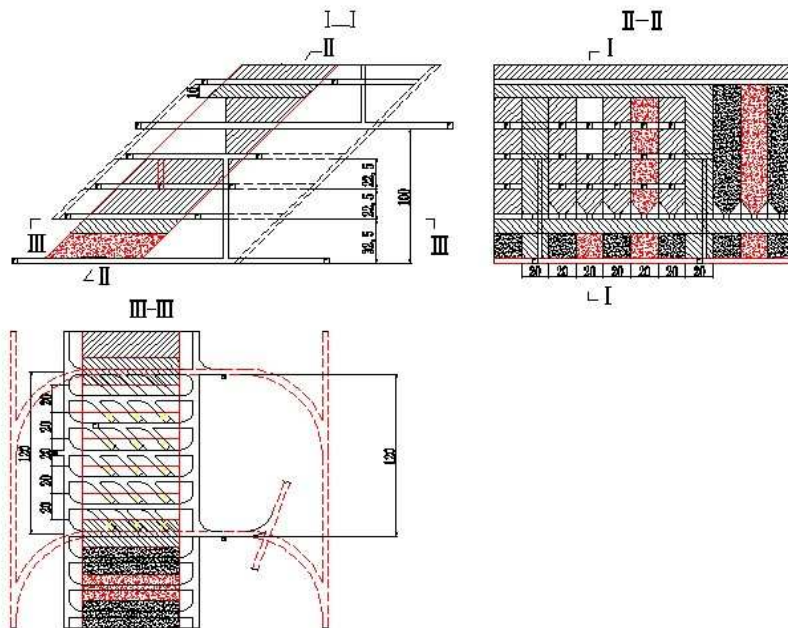


Fig. 2 Medium-length hole sublevel drilling and phase ore drawing filled stope

Mining Preparation and Cutting Operation A: Deep-hole drilling and phase mining out filled stope

Project of mining preparation and cutting operation mainly includes ore removal roadway, ore loading drift, trench drawing roadway, drilling chamber, connecting slots for drilling chamber, air shaft, drawn shaft etc.

B: Medium-length hole sublevel drilling and phase ore drawing filled stope

Project of mining preparation and cutting operation mainly includes ore removal roadway, ore loading drift, trench drawing roadway, sublevel drilling tunnel, connecting slots for sublevel drilling tunnel, air shaft, drawn shaft etc.

Stopping Craft

A: Afterwards filling mining method of deep-hole drilling and phase mining out

Using bottom-up stoping craft, drill Medium-length hole after cutting project in the trench and ore drawing trench are formed after ore blasting out. Drill the large-diameter deep hole in rock chamber, adopting VCR method to form cutting raise, then take the cutting raise as a free surface to conduct side blasting. Shovel out a third of the caved ore and left the remaining ore in the open to support surrounding rock and filling body. When all the ore is caved we conduct ore drawing with high strength and filling after the drawing is completed.

B: Afterwards filling mining method of Medium-length hole sublevel drilling and phase ore drawing

Use the medium-length whole ore breaking. After cutting projects completed, cutting groove is formed on the free surface given by the cutting raise at the end of ore heart. Then we take the cutting groove as the free surface of side blasting. Ore carved is loaded from the bottom of the open into the path then shoveled out by scraper. When it is completed, we conduct the filling program.

Mine Equipment Level

A: Tunneling

Single-boom hydraulic drilling jumbo is adopted in mining and cutting drift tunnel operation by Rocket Bommer281 and a 4 m³ TORO007-diesel-engine scraper with 20t pit truck is applied in tunneling muck hauling. Bolting carriage and shotcreting carriage

The tunneling of raise, drawn shaft and entry adopt air drifter and Z-30mucker for drilling and mucking

B: Stopping and drilling

The Sim262 high pneumatic DTH drill is applied in the large-diameter deep hole drilling, hydraulic drill carriage Simba1354 is used in drilling deep hole, and Vehicle Sim1354 is used in the drilling of trench drawing as well as Vehicle Rocmec in stoping and loading.

C: Stopping and ore removing

At present 6 m³ scrapers are widely adopted in the mining process for newly established large-scale underground mines in our country, such as Dongguashan iron ore (400million t/a), Xing Shan iron ore (300million t/a), Dahongshan iron ore (400million t/a), Lilou iron ore(750million t/a). The south section of Sijiaying iron ore south area is using 10 m³ scrapers(1500million t/a).

Although Macheng Iron Mine has a large scale of production, there are two sections (up and down) putting into operation at the same time. And in addition to very thick orebody (thickness of 80 m to 100 m), there is still a lot of thick orebody (40 m thick). Furthermore, all 10 m³ scrapers are imported, and foreign 10 m³ scrapers manufacturers are relatively less. The maintenance is difficult as well as servicing.

Therefore, 6 m³ scrapers are applied in stoping and ore removing, and 4 m³ TORO 1400E-electromotor and TORO 007diesel-engine scraper is operated in level ore drawing, recycling of down-panel triangle ore and mining on the section with narrow ore body.

Backfilling Craft

The Manufacture and Delivery Craft of Filling Slurry High concentration of tailing-cemented backfilling mining method is adopted in mine. The main filling materials needed are tails and cement, meanwhile, the underground waste rock which isn't taken out of the mine is also using as the materials.

We use vertical sand silo and agitating vessel backfilling craft. Tailings delivery system takes the 50% concentration of tails to the vertical sand silo of the preparation stowing station where the tails get a further consolidation settlement. Tails that reaches a 70% weight concentration after passing through the high-pressure gas and water forming slurry will flow naturally into the agitating vessel cement silo, and the loose cement in cement silo go through the screw conveyor to the agitating vessel to get fully mixed with tailing slurry in a certain proportion. Then the backfilling materials of a 73% weight concentration are formed and flow through the filling pipe to the filling operation. In

hydraulic sand filling, the tails after forming slurry reached a 73% weight concentration through the agitating vessel mixing, then flow to the filling operation through the filling pipe. As shown in Fig. 3.

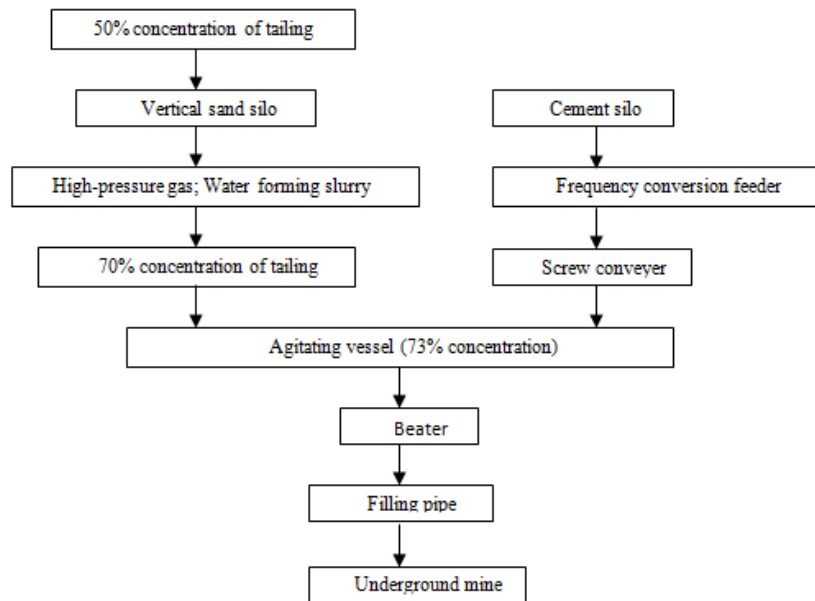


Fig. 3 Filling system flow diagram

Materials Rate The rates of filling materials are shown in Table 1.

Table 1 Fillings rate

Types of backfilling	Ore roof and floor	the first step (the third step)	the second step (the forth step)
cement sand ratios	1:5	1:10	Tailing packing

The Existing Problems and Recommendations

Because using filled stope may cause surface subsidence, mine should adopt low to high type to start mining to minimize the effects of surface.

The mine hasn't conduct filling process test. During the infrastructure building, the experiments of packing technique should be carried out and adjust the technical parameters to achieve technical solutions.

References

[1] M. Zhou. (2007) Mining waste cemented filling, Metallurgy Industry Press 32:56-77
 [2] Y. Z. Xue. (2008) Application of high level long blasthole method in Anqing Copper Mine, China Mine Engineering 37(2):8-10
 [3] R. Q. Liu, R. X. Zheng (2007) Application of backfilling method in Tongshan Copper Mine, Mining Technology 7 (3):6-7
 [4] S. J. Jie. (1986) Underground Mining of Metal mineral deposit, Metallurgy Industry Press, 45: 87-99

Power System with Wind Power Connection Anti-peak Regulation Ability Analysis

Yang Dongfeng and Zhou Suquan

Haerbin institute of technology, 92 West Dazhi Street, Haerbin China
e-mail: ydfnedu@126.com

Keyword: Wind Power Connection, Peak Regulation, Anti-Peak Regulation Ability, Mixed Integer Program

Abstract. In the condition of large scale wind power connection, the uncertain of the wind power output takes great challenge to the peak regulation. In this paper for some wind power connection system, the influence of wind power connection to the peak regulation was studied by analyzing the system load and the historical real data after the wind power connection. The computation model which evaluates the normal units' anti- peak adjusting capability was built and the multiply integer program algorithm was used to solve this model. A real case was used to test the exactness and feasibility of the computation model.

Introduction

Accompany with the energy crisis, allover the world realize the possibility to develop new energy source. Because of the renewable and clean characteristics the wind source is the new energy which develops most quickly in China. China is one of the wind reserve abundance country in the word, and the wind power generation is maturing gradually. Since the 21st century the wind power develops fast in China, the wind power installation grows larger, in [1]. However, with the ratio of wind power installation in the power system increasing the wind power which is random, intermittence and fluctuation takes bad influences to the power system safely and stable operation and dispatching, in [2, 3]. Especially the peak period regulation is influenced most. And the peak period regulation ability is the main constraints that influence the power system's wind power acceptance ability. Therefore to evaluate the grid's peak load regulation ability after the large scale wind power connection is an important task.

Nowadays, many scholars studied the problems to the power system brought by the wind power connection. In [8], influence of wind power connection on the peak load regulation is studied, and the influence of different wind power transmission mode and dispatching modes on peak load regulation is discussed. And the peak regulation shortage probability and expectation index is presented based on non-sequential Monte Carlo stimulation. In [10] and [11], the northwest grid is taken for an example and the hydropower and wind power coordinate operation method is presented. And the algorithm of calculating the hydropower and thermal power peak regulating capability for wind power is also given. We can see from above that how to tack the influent of wind power fluctuation on peak load regulation has absorbed the scholars.

In this paper to solve the peak load regulation problem with large scale wind power connection based on the load and wind power output historical data of some area grid including several wind farms the mechanism of wind power's influence on system peak load regulation is analyzed. And s regular units' anti-peak load regulation ability computation model is built.

Analysis of Wind Power Connection on Power System Peak Load Regulation

Influence of Wind Power Connection on Power System Peak and Valley Difference Mechanism S When studying the influence of wind power connection to the power system most of the papers regard the wind power output as minus load added on the load curve to form a new load curve, namely equivalent load curve. In this paper the same method is used to analyze the influence mechanism of wind power connection on peak load regulation. The peak valley difference changing amount after wind power connection is the equivalent peak valley difference minus the former peak valley difference as following,

$$\Delta PVL(i) = \Delta P_{PVEL}(i) - \Delta P_{PVL}(i) \quad (1)$$

In which, $\Delta PVL(i)$ is the peak valley difference changing amount of the i th day; $\Delta P_{PVEL}(i)$ is the equivalent load peak valley difference of the i th day; $\Delta P_{PVL}(i)$ is the former peak valley difference.

The peak valley difference changing ratio after wind power connection is the peak valley difference changing amount after wind power connection to former peak valley difference as following,

$$\gamma(i) = \frac{\Delta PVL(i)}{\Delta P_{PVL}(i)} \times 100\% \quad (2)$$

In which, $\gamma(i)$ is the peak valley difference changing ratio of the i th day.

1.2.2 Wind Power Anti-peak Regulation Characteristics In [8] two based on the condition of equivalent peak valley difference changing after wind power connection basic definitions are defined as in [8]: 1) Wind power anti-peak regulation characteristic means the wind power output curve tendency is opposite to the system load curve and the equivalent load curve peak load difference becomes larger after the wind power connection, as shown is Fig. 1. 2) Wind power positive peak regulation characteristics means the wind power output curve is similar to the system load curve and the equivalent load curve peak valley difference decreases after wind power connection.

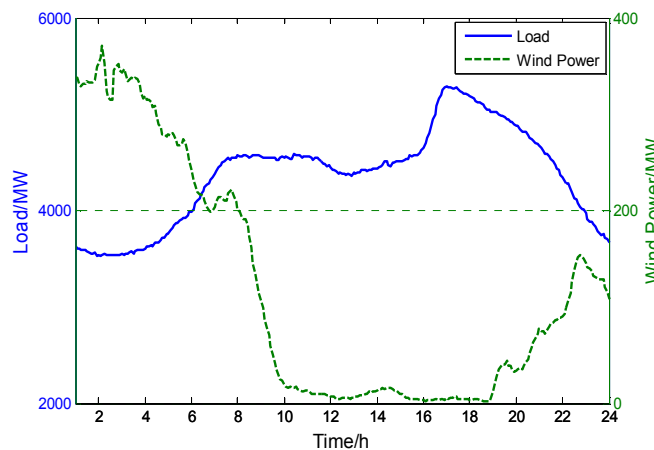


Fig. 1 Wind power anti-peak regulation character

Regular units' anti-peak regulation ability calculation model

Single Period Model In [12] the negative peak capacity limitation model is given. The regular units' negative peak regulation ability is defined. In this paper the defined regular units' anti-peak regulation ability means when the maximum accepted wind power capacity is connected to the power system the maximum regular units' active output ability.

The regular units' peak regulation ability achieved is not accord to the reality because the time relationship among periods is not considered in the single period model during the whole operation cycle. Therefore in this paper the multi-period regular units' reserve peak regulation ability calculation model is presented.

Multi-period Model The same as the load curve the output of the units is also continuous. However for convenient in building model and analyzing the model the periods' division strategy in [13] is suppressed: the load in the continuous periods is separated into T periods. Each period responds to a level line and the data correspond to each line represents the maximum data on the load curve in this period. Although by the periods' division strategy the colligation optimal result for multi-period is not the optimization in each period, but it is the optimization to all and conform to the reality.

It is supposed that there are N regular units in the system. In this paper the minimum operation time and minimum removing time are suppressed based on economic dispatch and the units' time coupling in period. And the multi-period peak regulation capacity optimization model is built. In this paper the load reserve capacity which is about 2 percent to 5 percent of the maximum load is also considered to tact the system reliability level. The object of this model is the total capacity for peak regulation maximizing. The capacity for peak regulation can reflect the system peak regulation ability to tack the large scale wind power connection. The larger the capacity is the greater the ability is. And the system's ability of wind power acceptance is better and the ability of facing the fluctuation of the wind power is better. The minimum peak regulation capacity in a day can reflect the maximum wind power acceptance capacity. The object function is as following,

$$\max F = \sum_{t=1}^T \left(P_{L,t} + S_{lr,t} + P_{loss,t} - \sum_{i=1}^N u_{i,t} P_{Gi}^{\max} \right) \quad (3)$$

In which, t expresses period, $t=1,2,\dots,T$; i is the regular unit, $i=1,2,\dots,N$; $P_{L,t}$ is the load forecasting data in the t th period; $S_{lr,t}$ is the load reserve in the t th period; $P_{loss,t}$ is the network loss in the t th period; P_{Gi}^{\max} is the minimum output of the i th unit; $u_{i,t}$ is the operation mode of the i th unit in the t th period, $u_{i,t} \in \{0,1\}$, 0 means the units is removed, 1 means the unit is in operating; F is the reverse ability of the regular units. The constraints include the following,

$$\sum_{i=1}^N u_{i,t} P_{Gi}^{\min} \leq P_{L,t} + S_{lr,t} + P_{loss,t} \leq \sum_{i=1}^N u_{i,t} P_{Gi}^{\max} \quad (4)$$

$$u_{i,t} (u_{i,t} - u_{i,t-1}) \left(\sum_{j=t}^{t+T_i^{on}} u_{i,j} \right) \geq T_i^{on} u_{i,t} (u_{i,t} - u_{i,t-1}) \quad (5)$$

$$(u_{i,t} - 1)(u_{i,t} - u_{i,t-1}) \left(\sum_{j=t}^{t+T_i^{off}} (1 - u_{i,j}) \right) \geq T_i^{off} (u_{i,t} - 1)(u_{i,t} - u_{i,t-1}) \quad (6)$$

In which, P_{Gi}^{\max} is the maximum output of the i th unit; T_i^{on} is the minimum operating period of the i th unit, $u_{i,t}$ is the operating mode of the i th unit in the t th period, $u_{i,t-1}$ is the operating mode of the i th unit in the $t-1$ th period; T_i^{off} is the minimum removing period of the i th unit.

In the multi-period anti-peak regulation calculation model the up and low output limit of the object function are integer and the load forecasting data may be integer and decimal fraction the mix integer program algorithm can be used to solve this mode.

Case Study

In this paper a system comprising 20 units is used to simulate the model and algorithm in this paper. In this case there are 20 regular peak regulation units in the system the total installation of which is 3924MW, the maximum installation capacity is 472MW, and the minimum installation capacity is 55MW. In the initial states the positive data represents the operating period and the negative data presents the removing period, showed in table .1 the typical day load forecasting data of this system is in Fig. 2.

The unit's anti-peak regulation ability in each period calculated by the model and algorithm is shown in table 1.2 and the curve is in Fig. 3. For single period model, the minimum anti-peak regulation ability appeared in the 3rd period and it was 1632MW. For multi-period model the

minimum anti-peak regulation ability appeared also in the 3rd period and it was 1402MW. From Fig. 2 and Fig. 3 it is seen that the 3rd period is the load valley period and the regular units' anti-peak regulation ability is minimum. This shows that in this period the system's wind power capacity acceptance is the least, and this period is the most difficult period for the system to accept the wind power. In table 1.3 it is seen that the operation states of single period model and multi-period are different in the 3rd period because the unit's minimum removing and operating period are consider in multi-period model.

Table 1 20 units' system parameter

Unit code	1	2	3	4	5	6	7	8	9	10
Low limit(MW)	20	20	100	100	100	100	100	100	20	20
Up limit(MW)	130	130	460	465	160	455	455	470	80	80
Min-off period(h)	24	24	24	24	24	24	24	24	4	4
Min-operation period(h)	24	24	24	24	24	24	24	24	4	4
Initial state	50	50	50	50	45	100	100	50	-5	-5
Unit code	11	12	13	14	15	16	17	18	19	20
Low limit(MW)	25	60	25	25	55	55	55	55	55	55
Up limit(MW)	85	300	162	162	55	55	55	55	55	55
Min-off period(h)	4	7	7	7	2	2	2	2	2	2
Min-operation period(h)	4	7	7	7	2	2	2	2	2	2
Initial state	-20	50	-20	-50	40	40	40	40	40	40

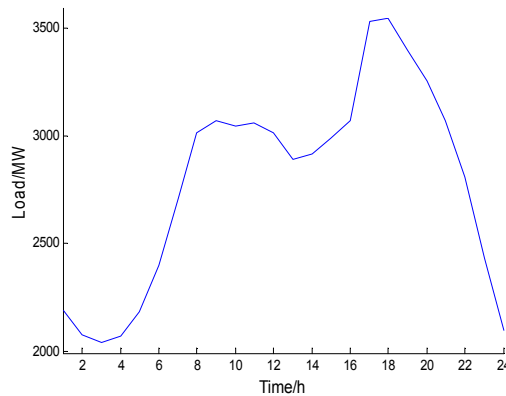


Fig. 2 Typical day load forecasting curve

In the multi-period optimization model the minimum operating period and minimum removing period are introduced so that there is time relationship in the each period optimization objects. That makes the optimization results of the two models are different. The operation states of constrain unit commitment in each period are limited, which avoids the units' on and off frequently. This model accords with the reality.

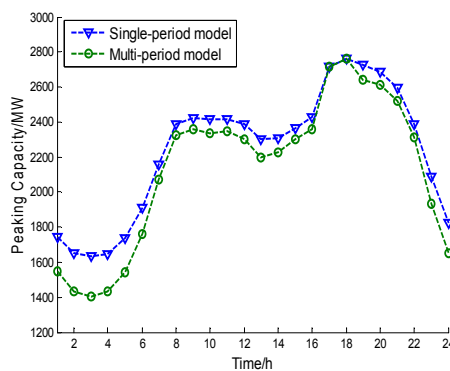


Fig. 3 Comparison of optimized result of the two models

Table 2 Anti-peak regulation ability in typical day

period	Single period model	Multi-period model	period	Single period model	Multi-period model
1	1744	1549	13	2299	2350
2	1649	1434	14	2308	2303
3	1632	1402	15	2364	2199
4	1648	1433	16	2426	2228
5	1739	1544	17	2715	2299
6	1910	1760	18	2764	2361
7	2160	2070	19	2726	2715
8	2389	2324	20	2685	2764
9	2423	2358	21	2595	2641
10	2416	2336	22	2385	2610
11	2415	1549	23	2091	2520
12	2388	1434	24	1824	2310

Table 3 Unit's operating state during load valley period

Unit code	1	2	3	4	5	6	7	8	9	10
Single period	1	1	0	1	0	0	1	1	0	1
Multi- period	1	1	1	1	1	1	1	1	0	0
Unit code	11	12	13	14	15	16	17	18	19	20
Single period	0	0	1	1	0	0	0	0	0	0
Multi- period	0	0	0	0	0	0	0	0	0	0

Table 4 Total regular units' anti-peak regulation ability of some typical day in a wind power connection system

Regular units' anti-peak regulation ability	Single period model	Multi-period model
Minimum anti-peak regulation ability in a day	1632	1420
Total anti-peak regulation ability in a day	53695	51100

From the analysis of the calculation results in Table .4 it is found that the multi-period model is more accurate and reliable in solving the regular units' anti-peak regulation ability to evaluate the maximum wind power acceptance capacity than single period model.

Conclusion

In this paper a regular units' anti-peak regulation calculation model is built and a real case is used to simulate. The simulation shows: (1) the valley load period is the system peak regulation hardness period, the respond system peak regulation capacity is the minimum and the wind power acceptance is the minimum. The peak regulation capacity is the maximum wind power acceptance capacity; (2) the system peak regulation capacity is used to evaluate the wind power acceptance ability can reflect the ability that the system manages the peak regulation to face the large scale wind power connection. The wind peak regulation capacity is larger shows that the system's peak regulation ability is stronger and the wind power acceptance ability is stronger.

Reference

- [1] Chen B S, Hu H L. (2008) General situation and prospect of wind power in China. *Power System Technology*, 32(2):272-275
- [2] Lei Y Z. (2003) Studies on wind farm integration into power system. *Automation of Electric Power Systems* 27(8):84-89
- [3] Ronan D, Mark O. (2004) A new approach to quantify reserve demand in systems with significant installed wind capacity. *IEEE Trans on Power Systems* 20(2):587-595
- [4] Holttinen H. (2004) The impact of large scale wind farm integration in Nordic countries. Espoo, Finland: Helsinki University

- [5] Han X Q, Sun S G, Qi Q R. (2010) Evaluation of wind power penetration limit from peak regulation. *ELECTRIC POWER* 43(6):16-18
- [6] Wang Z M, Sun A L, Lu S. (2010) Analysis on capacity of wind power integrated into liaoning power grid based on power balance. *Automation of Electric Power Systems*, 34(3): 86-89.
- [7] Sun R F, Zhang T, Liang J. (2011) Evaluation and application of wind power integration capacity in power grid. *Automation of Electric Power Systems* 35(4):70-75
- [8] Zhang N, Zhou T R, Duan C G, et al. (2010) Impact of large-scale wind farm connecting with power grid on peak load regulation demand. *Power System Technology* 34(1):152-158
- [9] Zhang H Y, Yin Y H, Shen H, et al. (2011) Peak-load regulating adequacy evaluation associated with large-scale wind power integration. *Proceedings of the CSEE* 31(22):26-31
- [10] Yi L D, Zhu M Y, Wei L, et al. (2010) A computing method for peak load regulation ability of Northwest China power grid connected with large-scale wind farms. *Power System Technology* 34(2):129-132
- [11] Wang C. X, Zhang Y. (2003) *Wind power generation*. Beijing: China Power Publishing Company.
- [12] Yang H, Liu J X, Yuan J S. (2010) Research of peak load regulation of conventional generators in wind power grid. *Proceedings of the CSEE* 30(16):26-31
- [13] Chen J F, Chen H Y, Duan X Z. (2006) Multi-period dynamic optimal power flow in wind power integrated system. *Proceedings of the CSEE* 26(3):31-35

Effect of Different NPK Fertilizers Cooperating Application on Yield and Quality of High Starch Maize

Ma Ruixia¹, Wang Jingshun¹, Li Xiaozhen², Liu Wencheng¹,

Department of Agronomy, Anyang Institute of Technology, Anyang 455000;

Varieties Cultivation Experiment and Demonstration Standing of Agricultural Bureau in Anyang City, Anyang 455000

Keywords: Maize, Fertilization, Yield, Starch

Abstract. Effect of nitrogen, phosphorus and cooperation application on grain yield and qualities of high starch maize Zhengdan 18 was studied. Six different fertilization treatments based on the random-plot experiment. The results indicated that N fertilizer significantly increased yield, as compared with the non-fertilizer treatment, the yield with the combined application of N and P fertilizers was higher than that of maize with single N treatment, the yield with the combined application of N P and K fertilizers was superior to that of maize with the combined application of N and P fertilizers. The yield was increased with the increase of the fertilization amount of the combined application of N, P and K, but there was not the direct proportion between yield and fertilization amount in the growth period, obeying the reward descending rule. The number of grains of ear was important for seed yield. The experiments showed the contents of starch, lipid and protein were increased along with the increase of N fertilization amount. The content of starch was increased in the early stage and reduced in the late stage of postulation, At the same time, The contents of lipid and starch were not increased along with the increase of phosphorus fertilizer, The same is that the contents of lipid with the combined application of N, P and k fertilizers were higher than that of the combined application of N and P fertilizers, the accumulation of lipid was increased, while the accumulation of starch and protein were not increased with the increase of K fertilizers. The contents of protein, starch and lipid were higher in the early stage than that in the late stage of postulation with the low-fertilizer treatment. The accumulation of starch was increased with the increase of the amount of the combined application of N, P and k fertilizers, the content of protein and lipid were increased in its early growth stage, while its content was not increased in the late growth period. Considering for the economic performance and the balanced principle for the supply and demand of applying fertilizer, currently the best applying fertilizer treatment is: N: 225kg/hm², P₂O₅: 112.5kg/hm².

Introduction

High starch maize is used as special maize whose seed starch content exceeding 74%, while the ordinary maize only contains 65% ~ 70%. Under the condition of identical processing equipments, the flour extraction rate of high starch maize seed is over 5% of higher than that of ordinary maize. Therefore, developing high starch maize can obviously increase the income of peasants and the economic benefits of maize processing enterprises, and possesses a highly broader development prospect [1, 2]. The production practices show that the improved variety is the premise for the high yield and quality of maize, but also the cultivation management measures and ecological environment conditions exert very important effect on the high yield and quality of maize. Concerning about the effect of fertilization on maize yield, there are systematic researches at home and abroad, and it is concluded that reasonable application of fertilization has played an important role in the improvement of maize yield. Besides, there are numerous researches on the relation between fertilization and maize quality. Generally, it is thought that seed protein content grows along with the increasing of nitrogenous fertilizer amount [4, 5]. But there is few of researches on the effect of cooperating fertilization on maize seed starch, protein and lipid, and moreover the results are unclear [6, 7]. Therefore, conducting studies on the relation of NPK fertilizers cooperating application with high starch maize seed yield and quality will provide basis for the further improvement of high starch maize production technology system.

Materials and Methods

Basic Situation of Experimental Field The experiments were carried out on the experimental farm of Anyang Institute of Technology in 2005 and 2006. The experimental results in these two years were basically consistent. Here the experimental data in 2005 is adopted for the analysis. The soil belongs to loam whose fundamental nutrients contain 14.3g/kg organic matter (OM), 0.92 g/kg total nitrogen (NA), 83.0 mg/kg Alkali-hydro nitrogen (AN), 23.1 mg/kg quick-acting phosphorous and 130mg/kg quick-acting potassium.

Experimental Materials and Methods Random-plot experiment was adopted to study the effect of NPK fertilizers cooperating application on the grain yield and qualities of high starch maize Zhengdan 18. And six different fertilization treatments were set up, which are Comparison, N225kg/hm², N225kg/hm², P112.5 kg/hm², N225 kg/hm², P112.5 kg/hm² and K112.5 kg/hm², N112.5kg/hm², P56.25 kg/hm² and K56.25 kg/hm², N337.5kg/hm², P168.75 kg/hm² and K168.75 kg/hm². There were three repeats and eighteen sample plots. The planting density was 52500 plants / hm². The length and width of the sample plot were 6m and 4m respectively, and 0.5m walkway was left for the repeated plots. Each sample plot had six rows, in which a paired row planting pattern was employed, and the wide row was 83cm, narrow row was 50cm and the spacing in the rows was 0.28m.

After the wheat was harvested, rotary cultivator was used for stubble cleaning and beds sloughing. The seeds were sowed based on the designed spacing in the rows, and then were watered with overwhelming water. When the earth's surface was very wet, herbicides were used to seal grasses. In the elongation stage, 50% of N fertilizers and total P, K fertilizers were dressed. In the ear formation stage, the additional 50% of N fertilizers were added. The seeds were sowed on June 15 and harvested on September 28. Simultaneously, other management measures were widely produced.

Measuring Items and Methods Quality Measurement In the ear formation stage, 50 plants were selected to be marked from the plants with consistent growth status which were in the two rows of all the treatments, and were bagged in the teaseling stage. Artificial pollination was implemented in the flowering period, after which samples were selected each five days and three ears were taken each time. The 100 complete grains in the middle of each ear were taken into the low-temperature refrigerator and were concentrated for the quality analysis. In the analysis, the samples were picked out and the attachments on the broken grains, impurities and seeds were removed, which were baked to be smashed under the condition of 60 ~ 65 °C temperature, making 95% of samples pass the 60 meshes and mixed into the ground glass stopper bottle for backup.

Measurement on Protein (Crude Protein) Content: Kieldahl Method GB/T 5009.5-2003

Measurement on Lipid (Crude Lipid) Content: Soxhlet Extraction GB/T5009.-2003

Measurement on Starch (crude starch) content: Polarimetry GB/T20194-2006

Measurements on the Grain Yield and Starch Yield Before harvest, the two rows, which had not been sampled in the middle of each plot, were used to conduct field investigation, to inspect the number of harvest plants, the rate of empty stem, the rate of double ears and the number of harvest ears. After harvest, air-dry was necessarily proceeded, and then the grain yield was measured, and then were experimented indoor. The product of each plot grain yield and grain starch content was the starch yield.

Results and Analysis

That's Effect of Different NPK Fertilizers Cooperating Application on the Main Contents of High Starch Maize Grain. It's Effect on Starch Content. Table 1 indicated that all treatment starch contents gradually increased during grouting. The content of treatment 1 was higher than treatment 2, indicating that N fertilizer had promotion effect on the starch accumulation, because N could promote the increasing of the leaf area index and improve photosynthesis, to provide material foundation for the further combination. The content of treatment 3 in the early stage was higher than treatment 2, but was lower in the late stage, indicating that P fertilizer promoted the starch

accumulation in the early stage of grouting, because P had the effect to accelerate grouting and promote early mature. The starch content of treatment 4, treatment 5 and treatment 6 were improved smoothly and steadily, indicating that N, P, K fertilizers cooperating application was beneficial to the stable starch accumulation and represented high yield, and especially treatment 6 had high starch content because the high fertilization could prevent the premature senility of plant, extend photosynthesis and promote the starch accumulation. The content of treatment 5 was higher than that in the early stage of treatment 4, indicating that low fertilization could promote the quick starch accumulation in the early stage.

Table 1 The Dynamic Changes of Starch Content in High-Starch Maize Seeds in The Process of Grouting (%)

Treatment	The Number Of Days After Pollination Treatment (days)						
	20	25	30	35	40	45	50
1	62.98	64.53	67.59	71.96	72.15	72.77	73.36
2	63.51	64.62	67.75	72.94	74.68	74.81	75.89
3	65.44	67.51	69.28	70.93	72.09	73.51	74.79
4	62.60	63.52	65.40	69.57	71.92	72.10	73.05
5	67.08	67.53	68.62	72.33	73.36	73.40	74.12
6	65.40	67.10	68.76	71.16	73.79	74.50	77.24

Effect on the Lipid Content

Table 2 The Dynamic Changes of Lipid Content in High-Starch Maize Seeds In The Process Of Grouting (%)

Treatment	The Number of Days After Pollination Treatment (days)							
	15	20	25	30	35	40	45	50
1	3.57	3.88	4.05	4.10	4.30	4.36	4.52	4.7
2	3.74	4.20	4.23	4.30	4.33	4.46	4.77	5.07
3	3.60	3.80	3.97	4.07	4.23	4.30	4.43	4.53
4	3.60	3.97	4.12	4.36	4.40	4.50	4.81	5.20
5	3.90	4.23	4.56	4.49	4.60	4.85	4.63	4.55
6	3.80	4.10	4.13	4.22	4.30	4.42	4.55	4.60

Table 2 indicated that all treatment starch contents gradually increased during grouting of grain. The content of treatment 2 was higher than treatment 1, indicating that N fertilizer had promotion effect on the lipid accumulation. The content of treatment 3 was lower than treatment 2, indicating that P fertilizer had no promotion effect on the starch accumulation. The content of treatment 4 was higher than treatment 3, indicating that N fertilizer had promotion effect on the lipid accumulation. The content of treatment 5 was higher than treatment 4 in the early stage and lower in the late stage, indicating that low fertilization made lipid accumulated quickly in the early stage but slowly in the

late stage. The content of treatment 6 was higher than treatment 4 in the early stage and lower in the late stage, indicating that high fertilization had promotion effect on the lipid accumulation in the early stage.

Effect on the Protein Content Table 3 indicated that all treatment starch contents gradually reduced during grouting of grain, quickly fell after 15~20 days of pollination, and became the lowest after 40 days, and then gradually increased, indicating that there was a protein accumulation peak in the late stage of grouting. Treatment 1 and treatment 5 reduced again after 50 days of pollination, indicating that both non-fertilization and low fertilization went against the protein accumulation because of the shortage of N in soil in the late stage of grouting. The content of treatment 2 was higher than treatment 1, indicating that N fertilizer had promotion effect on the protein accumulation. The content of treatment 3 was lower than treatment 2, and treatment 4 was lower than treatment 3, indicating that P, K fertilizers had no promotion effect on the protein accumulation. The protein content of treatment 5 was higher than treatment 4 in the early stage and lower in the late stage, indicating that low fertilization promoted the protein accumulation in the early stage, and the shortage of fertilization in the late stage went against the protein accumulation. The content of treatment 6 was higher than treatment 4 in the early stage and lower in the late stage, indicating that high fertilization had promotion effect on the protein accumulation in the early stage

Table 3 The Dynamic Changes of Protein Content in High-Starch Corn Seeds in The Process of Grouting (%)

Treatment	The Number Of Days After Pollination Treatment(days)									
	5	10	15	20	25	30	35	40	45	50
1	16.58	16.45	13.00	10.03	9.67	8.67	8.52	8.35	8.77	8.34
2	18.54	18.00	13.28	11.67	10.81	9.98	9.35	8.65	8.71	9.40
3	16.36	15.75	14.98	11.31	9.63	9.50	9.33	7.54	8.60	9.15
4	15.32	14.95	12.20	9.65	9.16	9.46	9.16	7.32	8.87	8.59
5	17.14	16.48	13.93	9.96	10.45	9.64	9.17	8.01	8.72	8.45
6	18.00	17.20	13.01	9.78	9.07	8.54	8.40	7.67	8.40	8.25

Effect of NPK Fertilizers Cooperating Application on the Grains, Starch Yield and Yield Factors. Table 4 indicated the effect of NPK fertilizers cooperating application on the yield factors of maize production: The ears number of treatment 1 and 5 were fewer, and the ears number of other treatments were identical, indicating that non-fertilization or low-fertilizer made the ears reduced, and the ears number increased with single N, NP cooperating application, NPK cooperating application and high-fertilizer, but they had no obvious difference between each other. The grains/ear of treatment 2 was more than treatment 1, and treatment 3 was more than treatment 2, indicating that K fertilizer had promotion effect on the increasing of grains/ear but was not higher than N, P fertilizers. Treatment 5 was lower than treatment 4, indicating that low-fertilizer made the grains/ear reduced; treatment 6 was higher than treatment 4, indicating that high-fertilizer had promotion effect on the increasing of grains/ear. The 1000 grain weight of treatment 1 was fewer, and other treatments had no big difference. The analysis on the correlation between yield factors and yield indicated: the correlation between ears number and yield did not reach to significant level ($r=0.767$, $r_{0.05}=0.811$); the correlation between grains/ear and yield reached to significant level ($r=0.978$, $r_{0.01}=0.917$); and the correlation between 1000 grain weight did not reach to significant level ($r=0.669$, $r_{0.05}=0.811$). These indicated that the yield difference of different treatments mainly relied on grains/ear.

Treatment 2 was significantly higher than treatment 1, and treatment 3 was significantly higher than treatment 2, indicating N, P fertilizers to obviously promote the increasing of yield. Treatment 4 was significantly higher than treatment 3; indicating K fertilizer had a lower effect on the increase of yield. Treatment 5 was significantly higher than treatment 4, indicating low-fertilizer made yield reduced. The difference between treatment 6 and treatment 4 did not reach to significant level, indicating high-fertilizer unable to increase yield further, which accords with the reward descending rule. The starch content of treatment 2 was significantly higher than treatment 1, indicating K fertilizer able to promote its increase. Treatment 3 was significantly higher than treatment 2, indicating P fertilizer able to promote the increase of starch content. Treatment 4 was significantly lower than treatment 3, but did not reach to significant level, indicating K fertilizer had no promotion effect on the increase of starch content. The starch content of treatment 5 was significantly lower than treatment 4, indicating low-fertilizer made it reduced. The starch content of treatment 6 was significantly higher than treatment 4, indicating high-fertilizer able to increase the starch content.

Table 4 Effect of NPK Fertilizers Cooperating Application on the Grains, Starch Yield and Yield Factors

Treatment	Yield	Starch Yield	Ears Number	Grains Per Ear	1000 Grain Weight
	(kg/hm ²)	(kg/hm ²)	(ears/hm ²)	(grains/ear)	(g/1000 grains)
1	6240 Cd	4577 Dd	44125 b	479.5 Bc	298 b
2	6901 Bc	5237 Cc	45875 a	497.3 Bc	313 a
3	8017 Ab	5996Bb	45875 a	540.4 Ab	310a
4	8158 Aa	5959Bb	45875 a	550.4 Aab	313 a
5	6919Bc	5127 Cc	44125 b	487.7 Bc	312 a
6	8393 Aa	6481 Aa	45875 a	569.3 Aa	313 a

Confirmation on the Optimization fertilization Scheme The price of high starch maize in 2005 was 1.5RMB/kg; N was 3.2 RMB/kg; P₂O₅ was 3.4 RMB/kg; K₂O was 2.8 RMB/kg; and other investment was unchanged. The treatment 2, 3, 4, 5 and 6 increased the incomes of 270 RMB/hm², 1567.5 RMB/hm², 1455 RMB/hm², 315 RMB/hm² and 1095 RMB/hm² respectively compared with treatment 1, indicating that the effect of P fertilizer to increase income was highly obvious, while the effect of N, K fertilizer to increase income was not. Based on the balanced principle for the supply and demand of applying fertilizer, the best fertilizing amount was treatment 3. Meanwhile, it was necessary to pay attention to the amount of quick-acting K in soil, which should be attentively dressed if too low.

Conclusion and Discussion

The yields of six different treatments were compared, discovering that the treatment with non-fertilizer had the lowest yield; the effect of single N fertilizer to increase yield was quite obvious; the effect of N, P cooperating application to increase yield was significant; the yield with the combined application of N, P and K fertilizers was higher than that of N and P cooperating application; the greater the amount of the combined application of N, P and K fertilizers was, the higher the yield would be, but the fertilizing amount and yield increased not by the equal proportion, obeying the reward descending rule. Different treatments had the basically same starch yield and grains yield. The yield difference of different treatments mainly depended on grains/ear.

In the grain grouting process, starch and lipid contents increased gradually, and protein content reduced gradually; and the protein content reached the lowest after 40 days of pollination and latter increased gradually, and would reduced again with non-fertilizer and low-fertilizer after 50 days of pollination.

In the grain grouting process, as compared with non-fertilizer, the contents of starch, lipid and protein all increased with N fertilizer, indicating the application of N fertilizer could increase the main nutrient contents of grain, hence effectively improving the yield and quality. The starch content with the combined application of N, P fertilizers was high in the early stage and low in the late stage, and the lipid and protein contents were low as well, indicating P fertilizer promoted the starch accumulation in the early stage of grouting but not in the late stage, and P fertilizer had no promotion effect on the lipid and protein accumulations. Compared with the combined application of N, P fertilizers, the combined application of N, P and K fertilizers made the lipid content high and both the starch and protein contents low, indicating K fertilizer promoted the lipid accumulation but did not had effect on the starch and protein accumulation. Low-fertilizer made the starch, lipid and protein contents high in the early stage of grouting but low in the late stage, indicating low-fertilizer had the effect to accelerate grain grouting, but representing the premature senility in the late stage. High-fertilizer made the starch content increase, indicating high-fertilizer able to promote the starch accumulation and make the protein and lipid contents increase in the early stage and reduce at the late stage, which showed high-fertilizer promoted the protein and lipid accumulation in the early stage but not in the late stage.

Considering for the economic performance and the balanced principle for the supply and demand of applying fertilizer, currently the best applying fertilizer treatment is: N: 225kg/hm², P₂O₅: 112.5kg/hm².

As compared with single N fertilizer, the combined application of N, P fertilizers were the result from the combination of addressing P fertilizer and N fertilizer with P fertilizer. Similarly, as compared with the combined application of N, P fertilizers, the combined application of N, P and K fertilizers the result from the combination of addressing K fertilizer and K fertilizer with the combined application of N, P fertilizers. Related interaction effects need to be researched further.

Fund Project: national grain high yield science and technology project (2006BAD02A07-3); Henan transformation fund project of agricultural scientific and technological achievements (08221110008)

References

- [1] Li Xinhua, Li Quanmu. Problems in the Current Situation of China's Maize Deep Processing Industry and the Countermeasures [J], Journal of Shenyang Agricultural University, 1999(4).137~139
- [2] Wang ZhenHua, Kang Weimin & Zhang Xin. High Starch Maize and Development and Utilization [J]. Journal of Maize Sciences, 2002,10 (3):90~92
- [3] Peng Zebin, Tian Zhiguo. Analysis on the Industrial Potentials of High Starch Maize [J]. Crops, 2003(6):10~12
- [4] Liu Wencheng, Ma Ruixia. Study on Henan Maize Zero Tillage Cultivation Technology[J]. Journal of Maize Sciences, 2000, 8(2),41~42
- [5] Jin Jiyun, He Ping & Liu Hailong. The Effect of Nitrogenous Fertilizer Amount on the Nitrogen Absorbing Character , Yield and Quality of Ordinary Maize, Plant Nutrition and Fertilizer Science, 2004, 10(6): 568~573
- [6] Ma Ruixia, Liu Wencheng. Study on the Compact Summer Maize Iron Stubby Direct Sowing Cultivation [J]. Crops, 2006(2), 54~55

-
- [7] Guo Zhongyi, Meng Yangfeng & Zhang Ming,etc. The Effect of the Application of NPK Fertilizers on the Yield and Quality of Summer Maize [J]. Soil and Fertilizer, 2004(1):25~26
- [8] Li Caifeng, Analysis on the Effect of Enhanced Ammonium Nutrition on the Quality of Maize[J]. Journal of Maize Sciences, 2003.11(3):82~84
- [9] Liu Kaichang, Hu Changhao & Dong Shuting. Study on the Yield and Quality of High-oil & High-starch Maize and the Group Physiological Characteristics. Journal of Maize Sciences [J]. 2002, 10(1): 61~63
- [10] Nanjing Agricultural University. Field Experiment & Statistical Method [M]. Beijing: Agriculture Press, 1978, 175~181

Power Transmission and Transformation Project Using Analytic Network Process

Huang Yue-hua

Heyuan Power Supply Bureau of Guangdong Power Grid Corporation Heyuan, Guangdong, China,
517000

huangyuehua@hrsk.net

Keywords: Power Transmission Project; Transformation; ANP; Index System

Abstract. Transmission and transformation is an important part of National Electric Power building, Based on the reality of our country, this paper proposed a comprehensive evaluation model, refer to the entire life-cycle environmental friendly, sophisticated products, independent research, cost optimization of management, etc, in order to supply reference for the decision-makers of power transmission and transformation projects.

Introduction

In the past few decades, with the development of electric power industry, in China, power transmission technology has made a considerable progress. Presently, the management for the construction of power transmission and transformation has usually been divided into several relatively independent parts, so the transmission and transformation equipment cannot be the entire life-cycle perspective of their management. This has resulted in a high cost and the decline in utilization of funds. Decision-making and the design are the most important stages, especially for the high-tech power construction projects.

Zheng Huai described the situation of transmission and transformation asset management in China, and a framework of asset life cycle management [1], and Lang Bin bring up a strategy of China transmission facilities construction and integrating technology standard under the lifecycle cost management mode for transmission and distribution project, by analyzing the requirements of reliability of transmission and distribution facilities in the power market [2]. A life-cycle theory was first adopted to analyze the life-cycle conception and life-cycle cost constitution of energy efficiency reconstruction of existing buildings in Liu Yumin's paper [3], and a set of models and indexes were set up for economic benefit evaluation about energy efficiency reconstruction of existing buildings. Hao Yang evaluated the risks of Power transmission and transformation Project by using Analytic Network Process (ANP) [4]. Yves Nguegan proposed an innovative method to monitor the electric power transfer stability on power transmission paths and the voltage profile stability at the power systems nodes in real time modus [5].

Life Cycle of the Transmission and Transformation Project

Characteristics of the Project

During the electricity transmission process, it is need to build-up voltage through the transformer to reduce heat loss, when the current reaches the client, the voltage has to be reduced back to meet the target appliance use requirements. For times of transformer, the current transmission is called transmission and transformation.

Life Cycle of the Project

Equipment Life Cycle includes all stages of its demonstration, development, production, use, security, and retired handle.

Life Cycle of the transmission and transformation Project refers to the transmission life of the project from its inception to the time the end of life, including physical life, functional life, legal life and economic life.

Model Specification and Index System

The Principle of Setting Indices

In this article, combing the characteristics of China's electricity market and power supply chain, we choose index according to the following principles:

Objective principle: Evaluation index system should be established on the basis of the facts and avoid subjective likes and dislikes, to ensure that supply chain solutions to grasp the actual situation.

Systematic principle: The evaluation index system must be a complete whole in order to reflect the actual situation in the electricity supply chain comprehensively and accurately.

Effectiveness principle: The irrelevant or invalid information should be eliminated in the evaluation index system to grasp elements that have an impact on supply chain decisions effectively.

Data availability principle: In the process of selection of indicators, although some indicators are significant, it is hard to get them, we have to use some substitutes or reflect it with multiple sub-indices.

The evaluation index system: Based on the principles described previously, this paper establishes a three-tier indicator system, as shown in Table 1:

Table 1. Definition of the Criteria Index and Notation

Goal	First-level Indexes	Second-level Indexes
Transmission and transformation plan selection (G)	Benefit (P1)	Financial Economic Benefit (C1)
		National Economic Benefit (C2)
	Costs (P2)	Investment-related Costs (C3)
		Utility-related Costs (C4)
		Running-related Costs (C5)
	Technology and Performance (P3)	Equipment Performance (C6)
		Technological Self-innovation (C7)
		Power Transmission Efficiency (C8)
		Network Security (C9)
	Environment (P4)	Power Quality (C10)
		Carbon Emission (C11)
		Resource utilization (C12)
	Risk (P5)	Resource re-utilization (C13)
		Equipment Maintenance Risk (C14)
		Accident Risk (C15)
		Legal Risk (C16)

Essential Theory of Anp

The Analytic Network Process (ANP) is a new theory that extends the Analytic Hierarchy Process (AHP) to cases of dependence and feedback and generalizes on the super matrix approach introduced in Thomas Saaty's 1980 book on The Analytic Hierarchy Process. It allows interactions and feedback within clusters (inner dependence) and between clusters (outer dependence). Feedback can better capture the complex effects of interplay in human society. The ANP provides a thorough framework to include clusters of elements connected in any desired way to investigate the process of deriving ratio scales priorities from the distribution of influence among elements and among clusters, which is based on 1-9 scale. The Fundamental Scale for judgments is shown in Table2:

Table 2. The Fundamental Scale for Making Judgments

1	Equal
2	Between Equal and Moderate
3	Moderate
4	Between Moderate and Strong
5	Strong
6	Between Strong and Very Strong
7	Very Strong
8	Between Very Strong and Extreme
9	Extreme

There are three super matrices associated with each network: the Unweighted Super matrix, the Weighted Super matrix and the Limit Super matrix.

Unweighted Supermatrix

The first phase of ANP is to compare the criteria in whole system to form the supermatrix, which is based on 1-9 scale to represent equal importance to extreme importance.

Assume a network structure has a control hierarchy of $P_1, P_2, \dots, P_i (i = 1, 2, \dots, m)$. For each criterion, assume there exist secondary criteria $C_1, C_2, \dots, C_j (j = 1, 2, \dots, n)$, and the goal is signed as G.

Compare the priority of the element in group C_j and group C_j' both consist of $C_1, C_2, \dots, C_j (j = 1, 2, \dots, n)$ by the influence from 1'; on them, Then, the judgment supermatrix as shown in Table3 for the criteria P_i can be get as follows show in Table2, by using Delphi method [6] to evaluate it.

Table 3. The Judgment Superma Tix

P_i	C_1	C_2	\dots	C_m	Normalized eigenvector
C_1	$N_{i1}^{(1)}$	$N_{i1}^{(2)}$	\dots	$N_{i1}^{(m)}$	$w_{i1}^{(ji)}$
C_2	$N_{i2}^{(1)}$	$N_{i2}^{(2)}$	\dots	$N_{i2}^{(m)}$	$w_{i2}^{(ji)}$
\vdots	\vdots	\vdots	\ddots	\vdots	\vdots
C_m	$N_{im}^{(1)}$	$N_{im}^{(2)}$	\dots	$N_{im}^{(m)}$	$w_{i3}^{(ji)}$

here $N_{il}^{(k)}$ is the priority C_k compared with C_l

By the eigen-value method, we get the weight vectors $w_{i1}^{(ji)}, w_{i2}^{(ji)}, \dots, w_{im}^{(ji)}$.

Repeat the above steps for to $i = 1, 2, \dots, m$ to obtain equation (1).

$$W_{ij} = \begin{pmatrix} w_{i1}^{(j1)} & w_{i1}^{(j2)} & \dots & w_{i1}^{(jm)} \\ w_{i2}^{(j1)} & w_{i2}^{(j2)} & \dots & w_{i2}^{(jm)} \\ \vdots & \vdots & \vdots & \vdots \\ w_{im}^{(j1)} & w_{im}^{(j2)} & \dots & w_{im}^{(jm)} \end{pmatrix} \tag{1}$$

Weighted Supermatrix

The priorities of elements in one hierarchy according to a certain criterion can be denoted with a supermatrix, which means each column of each hierarchy in the supermatrix is column stochastic. But the influence that other hierarchy according to this criterion is not concerned. As a result, each column of the supermatrix is not column stochastic.

It is essential to consider the influence between each two hierarchy. The particular method is: regarding each hierarchy as an element, and pair wise comparing according a certain hierarchy, then computing corresponding priorities. Suppose a_{ij} is the influence weight of the i th hierarchy on the j th hierarchy, let

$$\overline{W}_{ij} = a_{ij} W_{ij} \quad (2)$$

\overline{W} is a weighted supermatrix. In a weighted supermatrix, addition of elements in each column is 1. Matrix has this trait is called column stochastic. This step is much similar to the concept of Markov chain for ensuring the sum of these probabilities of all states equals to 1.

Limited Supermatrix

What we wish to obtain is the priorities along each possible path in a supermatrix, namely the final influence an element on the highest goal. This kind of result can be acquired by solving \overline{W}^{∞}

$$\overline{W}^{\infty} = \lim_{k \rightarrow \infty} \overline{W}^k \quad (3)$$

The weighted supermatrix is raised to limiting powers such as in (2) to get the global priority vector or called weights, so the most important criterion and the best alternative are acquirable.

A Case in Study

ANP has been getting more widely used in decision making and numerous applications in this paper, an ANP model on the transmission and transformation Project Life Cycle management is constructed in Super Decision software and ANP theory is applied to evaluate indices in this system. Steps in the process are shown in Fig. 1

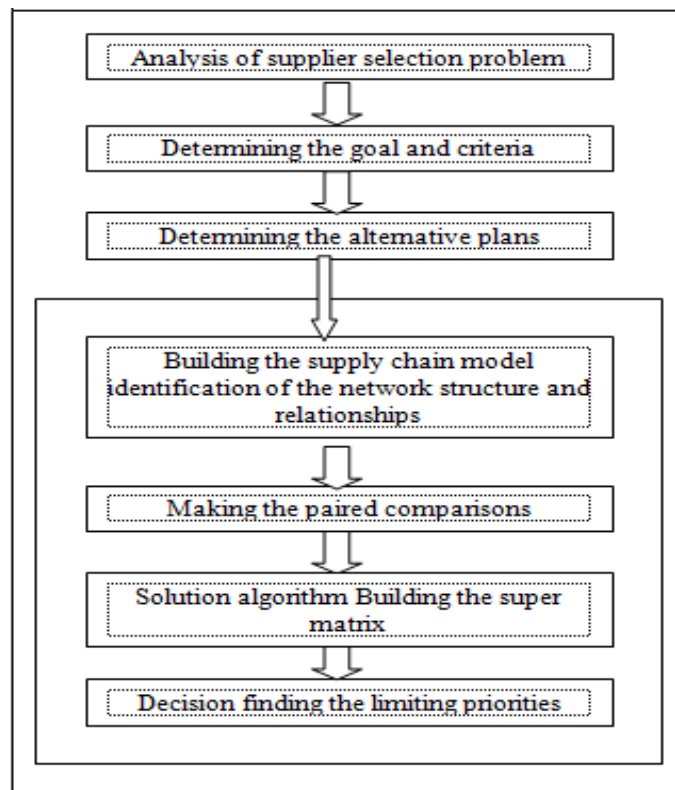


Fig.1. The progress of ANP model

Modeling

Based on the transMISSIon and transformation Project evaluation index system, we establish the ANP model; the control Decision Hierarchy structure of it is shown in Fig2:

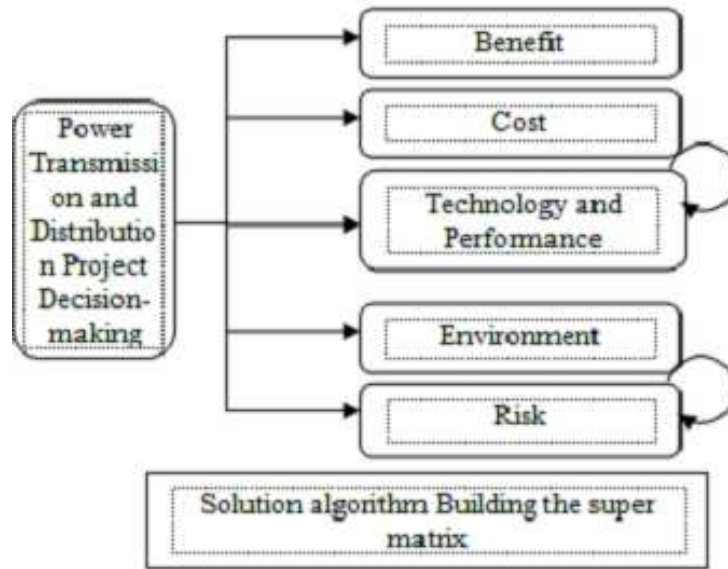


Fig.2. Abstract Representation of the Decision Hierarchy

Comparison decision-making of the plans

In the ANP model we established three plans Plan A, B and C as alternatives, then we try to compare them in the model and make decision finally. The overall synthesized priorities are shown in Fig. 3

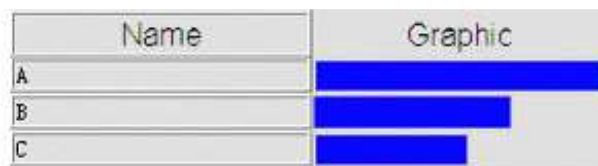


Fig.3. the overall synthesized priorities

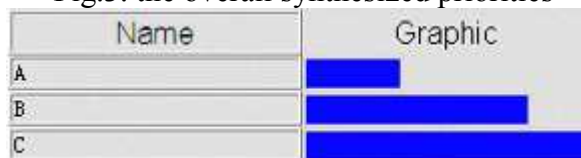


Fig.4. The Synthesized Values - the Results for the Alternatives based on Technology and Performance

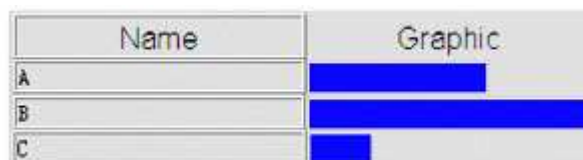


Fig.5. The Synthesized Values - the Results for the Alternatives based on Costs

It can be seen from the program that A scored the highest, followed by B, and C. however, can we concluded that A is the best plan of the three? In fact, there are still more factors have to be consider of to take decision-making. For example, when the decision-makers attached great importance to Technology and Perfonnance of the project, they may place more emphasis on Technology and Perfonnance priority. The priority score synthesized from Technology and Perfonnance of C is much higher than the other two plans as shown in Figure4; thus, decision-makers will be more inclined to choose plan C.

Similarly, according to Figure5, the priority score synthesized from costs of B is much higher than the other two plans; thus, decision-makers will be more inclined to choose plan B.

Conclusions

This paper shows that, ANP is a decision tool by making strategically decisions. Generally, managers might be inclined not to use a sophisticated method, but by using user friendly software like super decision, developed by Saaty, the decision making process by using ANP will be handled more easily.

Evaluating the plan from both objective and subjective criteria will gain flexibility to the decision process. And the proposed model is more reflecting the relation of how the selection criteria affect the selected suppliers and at the same time what is more important for the Plans among the selection criteria.

References

- [1] Zheng Huai; Chen Haibo, "Study of life cycle management for transmission and transformation assets", East China Electric Power, Shanghai China, Vo1.37, No. 5, pp.0739-0741, May 2009.
- [2] Lang Bin, "Study on Cost Optimization of Tansmission and Distributiom Equipment Life Cycle", North China Electric Power University, Beijing China, pp.I-31, March 2008
- [3] Liu Yumin; Liu Changbin, "Economic evaluation of building energy efficiency based on full life-cycle costs", Construction Economy, Beijing China, pp.58-61, March 2009.
- [4] Hao Yang, "Analytic Network Process (ANP) in the Power Transmission Project Risk Assessment", Intelligence, Jilin China, pp.50-51, March 2009.
- [5] Nguegan, Y. ; Claudi, A. ; Strunge, C. , "Online Monitoring of the Electrical Power Transfer Stability and Voltage Profile Stability Margins in Electric Power Transmission Systems Using Phasor Measurement Units Data Sets", Power and Energy Engineering Conference, 2009. APPEEC 2009. Asia-Pacific, Wuhan China, pp.I-9, May 2009.
- [6] Jon Landeta, "Current validity of the Delphi method in social sciences," Technological Forecasting and Social Change, Vol. 73, Issue 5, pp. 467-482, June 2006.

Effect of Co Concentration on Composition and Electromagnetic Shielding Properties of Ni-Co-P

Mingqiu Wang^{1, a}, Jun Yan^{1, b}, Haiping Cui^{2, b}, Shiguo Du^{1, b}, Guo Yi^{1, b},
Li Hongguang^{1, b}

¹The 3rd Department of Mechanical Engineering College, Shijiazhuang 050003, China

²Physics and Chemistry Section of Mechanical Engineering College, Shijiazhuang, 050003, China

^amqwang1514@163.com, ^byan-junjun@263.net

Keywords: Electroless Plating; Ni–Co–P Alloy; Plating Rate; Electromagnetic Shielding

Abstract. Electroless Ni–Co–P alloys on PVC with sodium hypophosphite as a reducing agent in an alkaline bath was investigated. Silane coupling agent (KH560) was used during the pretreatment. The morphology, chemical composition, of the electroless plating film was characterized by scanning electron microscope (SEM) and energy dispersive spectroscopy (EDS). The effect of Co concentration on its composition and electromagnetic shielding properties were examined. The results show that the plating rate decreased totally with increasing Co concentration. The structure of the as-plated Ni–Co–P alloys at all conditions is amorphous. When the concentration of cobalt sulfate concentration is $8\text{g}\cdot\text{L}^{-1}$, electroless Ni–Co–P alloys exhibited better electromagnetic shielding properties, shielding effectiveness of which was 52 dB at 300 MHz. The Ni–Co–P deposits, therefore, are promising for applications in electromagnetic interference for plastics substrate.

Introduction

Electroless plating have been widely used in the fields of plastics because of desirable physical and mechanical properties, simple plating process and of easy practice [1-3]. In addition, plastics after electroless plating have the advantage of both plastics and metal. The Ni–Co–P film possesses the characteristic in magnetism such as low coercivity and high squareness, so it is generally used as a soft magnetic material for the magnetic recording media, electronic industries, aircraft industries, automotive industries [4-7]. It was found that the chemical composition, phase structure, and plating rate of Ni–Co–P films formed by electroless plating were determined by the bath composition and operation parameters [8, 9]. Therefore, many researchers focus their attentions on plating rate control [10] and the effect of cobalt sulfate on the plating rate and deposit composition [11]. There are few papers to report about the effect of cobalt sulfate on their electromagnetic shielding properties. The purpose of the present work is to investigate the effect of cobalt concentration on deposit composition and electromagnetic shielding properties of the deposits on PVC substrate.

Experimental

Preparation of electroless Ni–Co–P films. PVC was chosen as the substrate for electroless Ni–Co–P film deposition. The substrate surface were pretreated as follows: distressing(methyl ethyl acetone and acetone of 1:1, $21\pm 1^\circ\text{C}$) → degreasing($25\%\text{Na}_2\text{CO}_3$ and $25\%\text{NaHCO}_3$) → coarse($5\%\text{KH560}$) → rinsing → sensitization(SnCl_2 solution, 10g/L) → rinsing → activation(PdCl_2 solution, 0.2g/L , 5mins) → rinsing and drying in air. After pretreated, the PVC plate was put into the plating solution with the suitable temperature. The electroless Ni–Co–P electrolyte with a pH 9 was prepared with the composition given in Table 1. The deposition was carried out in a 100 cm^3 of plating bath, maintained at 75°C for 40 mins.

Characterizations of electroless Ni–Co–P films Chemical composition of Ni–Co–P alloy was characterized by EDS. The deposition rate was calculated from the substrate weight gain. A four-point probe system was employed to measure the electrical resistivity of the deposited films. The flanged coaxial test method corresponding to ASTM D 4935-99 was used to test shielding effectiveness (SE) in a frequency range of 5 KHz to 1.5 GHz using apparatus of testing shielding effectiveness (DN1015).

Table 1 Typical composition of the basic electroless nickel-cobalt-phosphorus bath

Ingredient	NiSO ₄ ·6H ₂ O	CoSO ₄ ·6H ₂ O	NaH ₂ PO ₂ ·H ₂ O	Na ₂ C ₆ H ₅ O ₇	(NH ₄) ₂ SO ₄	Stabilizer
Concentration/g·L ⁻¹	30	10	20	64	25	5.5*10 ⁻³

Results and Discussion

Typical Morphology of the Coatings. Fig.1 shows the surface appearance of typical deposit on PVC after electroless plating. From Fig.1, it can be seen that the Ni-Co-P coatings exhibit the typical “cauliflower-like” surface, whereas heave are still observed on the surface of Ni-Co-P coating after coarse treatment with 5% KH560. This may be attributed to the occurrence of defects on the surface of substrate after pretreated with KH560. In the plating process, Ni-Co-P is prone to nucleate, grow, so it formed the superior heave.

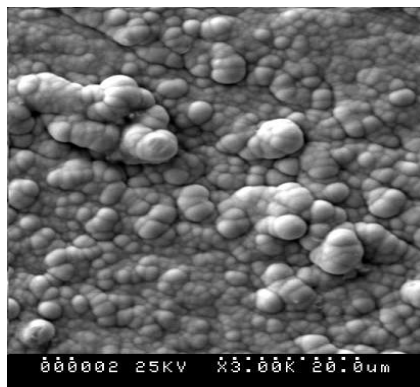


Fig. 1 The surface appearance of typical deposit on PVC

Effect of Co Concentration on Deposition Rate and Deposit Composition. The contents of Ni, Co, and P in various Ni–Co–P films were determined by EDS analysis and shown in Table 2. The effect of cobalt sulfate concentration on the film composition is also shown in Fig.2. It can be seen that the plating rate decreased as a whole with increasing cobalt sulfate concentration. The cobalt content of alloy increased slightly, it increased by about 2%, meanwhile, the phosphorus content increased by 6% and the nickel content decreased about 8%. The reason is that the decrease of the ratio of hypophosphite ions to the metal ions, then the catalytic oxidation of the hypophosphite yield electrons at the catalytic surface reduced. On the other hand, the opposite trends were observed for alloy cobalt (or phosphorus) and nickel contents with increasing cobalt sulfate concentration as shown in Fig.2. This may be attributed to increase of the reduction of the cobalt ions than that of nickel ions with increasing cobalt ion percentage in the plating bath. However, the increase of phosphorus content may be attributed to the diminution from the side reaction of hypophosphite ions. As shown in Table 2, it also can be seen that the minimum of phosphorus content is 10.07%, which indicate that crystalline structure of Ni-Co-P is amorphous.

Table 2 Effect of Co concentration on the chemical composition of the Ni–Co–P alloy deposited on PVC substrate

Co ²⁺ conc./ g·L ⁻¹	Deposit composition/wt.%		
	Ni	Co	P
8(No.-a)	65.77%	24.15%	10.07%
10(No.-b)	59.83%	23.24%	16.94%
12(No.-c)	58.86%	25.21%	15.93%
14(No.-d)	56.99%	26.54%	16.47%

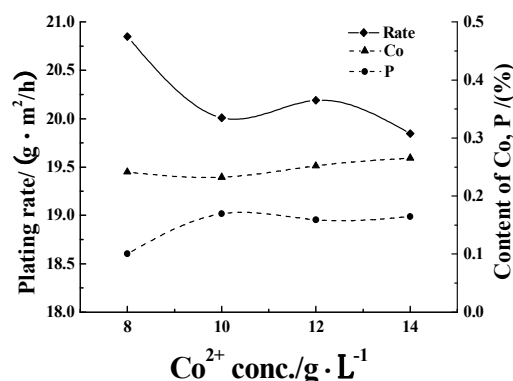


Fig. 2 The relationship of cobalt sulfate concentration and plating rate

Electric Conductive Characteristics The effect of cobalt sulfate on the surface resistivity of Ni-Co-P alloys is shown in Fig.3. It can be seen that Ni-Co-P alloys exhibit a slow rise in resistivity with increasing cobalt sulfate concentration, which have an opposite trend compare to the plating rate. The surface resistivity is found to be close to $5 \times 10^{-2} \Omega \cdot \text{cm}^{-2}$, which indicate that Ni-Co-P alloys make plastics electric conductive. The product of magnetic permeability and conductivity enhanced owing to better magnetism of cobalt, it is helpful to improve a magnetic loss.

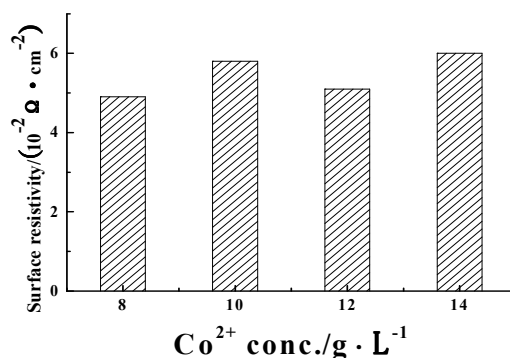


Fig. 3 The dependence of surface resistivity on cobalt sulfate concentration

Electromagnetic Shielding Properties The electromagnetic shielding effectiveness of Ni-Co-P alloys on PVC versus frequency are displayed in Fig.4. Generally, the sample a showed the better electromagnetic shielding than that of the others range from 100MHz to 0.99GHz (the inserted image of Fig.4) and from 1.23GHz to 1.5GHz, there are a following trend: a>c>d>b, while there is no obvious law of electromagnetic shielding effectiveness range from 0.99GHz to 1.23GHz. The difference in electromagnetic shielding properties is resulted from the different composition contents of the plated Co–Ni–P layers. The Bohr magnetons (MB) of Co atom and Ni atom are 1.7 and 0.6, respectively. So, the magnetism of cobalt is better than the nickel. P atom is nonmagnetic. The Co content of the sample d is lower. However, the P content of it is larger. So, the sample b possesses the poorest magnetism. Since the P content of it is lowest in case of sample a, it indicate that few porous was formed because of the amount of H₂ resulting from the following reaction: $\text{H}_2\text{PO}_2 + \text{H}_2\text{O} \rightarrow \text{H}[\text{PO}_2] + \text{H}_2 \uparrow$, more electromagnetic lost through the reflection loss when it contacts the

surface of Ni-Co-P alloy. Therefore, sample a exhibited better electromagnetic shielding properties. the SE value of sample a was 52 dB at 300 MHz and over 43 dB at 1.8 GHz. It clearly demonstrated that coating an electroless Ni-Co-P (a) films on PVC increased the SE of plastics effectively.

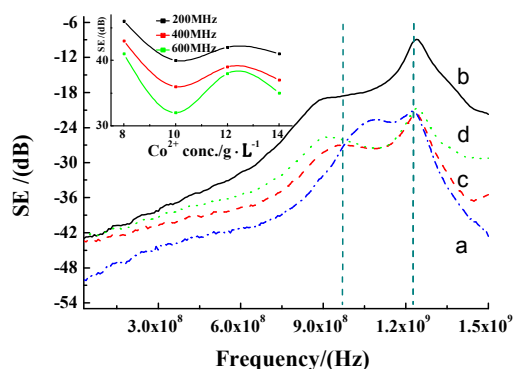


Fig. 4 SE values of various alloy plating on PVC

Conclusions

The Ni-Co-P alloys have been successfully deposited on plastics substrate in an alkaline bath. The following results are obtained in this work:

Owing to the P content of all samples is over 8%, the structure of the as-plated Ni-Co-P alloys plated at all conditions is amorphous.

The plating rate decreased with increasing Co concentration. The cobalt (or phosphorus) content increased with increasing total metal in the plating bath, however, the electric conductive characteristics have no significant difference.

Most of the obtained films exhibited better electromagnetic shielding properties. The best SE of Ni-Co-P in this article was 52 dB at 300 MHz.

Acknowledgements

The financial support provided by the project of Defensive Pre-research Foundation of China for this work was gratefully acknowledged.

References

- [1] H Akiyama, N Zettsu, N Yamamura: *Thin Solid Films* Vol.518 No.13 (2010), p.3 551-3 554
- [2] W B Yang, B J Zhang, Y T Dai: *Fusion Eng. Des.*, Vol.83 No.5/6 (2008), p. 725
- [3] P C Yen: *Polym. Commun.* Vol.36 No.17 (1995), p. 3 399-3 400
- [4] T Osaka, N Kasai, I Koiwa: *J. Electrochem. Soc.* Vol.130 (1983), p. 568
- [5] I Koiwa, T Osaka: *J. Met. Fin. Soc. Jpn.* Vol.38 (1987), p. 434
- [6] D Kim, K Aoki, O Takano: *J. Electrochem. Soc.* Vol.142 (1995), p. 3 763
- [7] S Jhon, K N Srinivasan, M. Selvam: *Proc. SPIE – Int. Soc.Opt. Eng.* Vol. 384 (1994) p. 2 255
- [8] I H M Aly, M M Younan, M T Nageeb: *Met. Finish.* (2003) p. 37-42
- [9] N Kanani. *Electroplating: Basic Principles*, in: *Processes and Practice*, 1st ed., Elsevier, Oxford UK, 2004.
- [10] Z H Xie, G Yu, B N Hu, et al. *Appl. Surf. Sci.* Vol. 257 (2011) p. 5 025-5 031
- [11] M M Younan, I H M Aly, M T Nageeb: *J. Appl. Electrochem.* Vol. 32 (2002) p. 439-446

Numerical Simulation of Eddy Air-curtain Dust Controlled Flow Field in Hard Rock Mechanized Driving Face

Wei Min Cheng^{1, 2}, Wen Nie^{1, 2, a}, Gang Zhou^{1, 2}, Jun Lei Yang^{1, 2},
Wen Zhou Du¹, Xin Hua Zhang¹

¹ College of Resources and Environmental Engineering, Shandong University of Science and Technology, Qingdao, China 266590

² Key Laboratory of Mining Disaster Prevention and Control, Ministry of Education, Shandong University of Science and Technology, Qingdao, China 266590

^asdniewen@163.com

Keywords: Hard Rock Mechanized Driving Face, Mural Cylinder, Eddy Air-Curtain, Dust Control, K-E Model.

Abstract. The author established the mathematical model of single-phase flow of gas based on the k- ϵ two-equation model and numerically simulated the eddy air-curtain dust controlled flow field in hard rock mechanized driving face with the help of FLUENT software. The result showed that, after all the pressure ventilation blown out by the radial clearance of mural cylinder, a full-face eddy air-curtain flow field is formed at the roadway section, forming the air-curtain dust controlled flow field that presses the tunneling place equally in front of the driver of roadheader. After the application of the development of new light polymer materials radial cylinder eddy air-curtain dust controlled system was adopted in hard rock mechanized driving face of north conveyor main roadway, reducing the local dust concentration effectively.

Introduction

Facts show that, it is impossible to control and prevent the dust's drift and diffusion fundamentally in the traditional dedusting way, but to control and capture dust absorption with the eddy air-curtain and the suction flow formed by the dust purification equipment is an effective way to control the spread of dust^[1-4]. Eddy air-curtain dust controlled flow field in hard rock mechanized driving face is a very complex flow process. There are too many influencing factors and they are not easy to obtain through model experiment and field measurement, so numerical simulation is very important to research of this flow field. At the present stage, the most of simulations to eddy air-curtain dust controlled flow field in heading face is two-dimension and the three-dimensional simulation are limited to the simpler form. It can't accurately reflect the diffusion rule of eddy air-curtain dust controlled flow field in working face [5-8].

Numerical Simulation of Eddy Air-Curtain Dust Controlled Flow Field

Physical Model

The tunnel is a semicircle arch area with the length of 35 m, the width of 5.7m and the height of 4.87m; the total length of the roadheader is 11 m. The diameters of the forced cylinder and exhaust cylinder which are arranged in different sides of the roadway are 1m and 0.8m, 0.4m away from the nearest tunnel wall and the axis of cylinder is 3.5m away from the ground. The forced cylinder is 5 m away from the tunneling place. The mural cylinder whose total length is 5m is arranged in the middle of the forced cylinder and 27m away from the tunneling place, opening a radial clearance with the length of 2 m and the width of 0.15m along with mural cylinder per meter and the total number is 2. The exhausting cylinder whose total length is 34m is 1m away from the tunneling place.

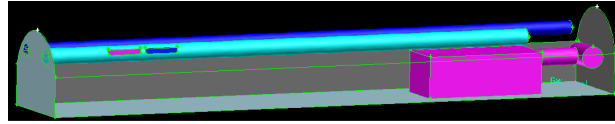


Fig. 1 Physical Model

Mathematical Model

Hypothesis of mathematical model is as follows:

(1) Ventilation flow can be regarded as incompressible fluid flow. Heat dissipation caused by viscous force can be ignored and at the same time we assume that ventilation is adiabatic and isothermal; (2) The turbulent viscosity of fluid is isotropy and the turbulent viscous coefficient ν_t can be handled as a scalar, (3) The flow is the steady turbulence and meets the Boussinesq^[9,10].

Mathematical Model

Based on the above-mentioned assumptions, the fundamental differential time-averaged equations of two-dimensional k-ε of hybrid ventilation in fully rock mechanized excavation roadway can be described by unified model:

$$\frac{\partial}{\partial x_i} (U_i \varphi - \frac{\Gamma_\varphi}{\rho} \frac{\partial \varphi}{\partial x_i}) = S_\varphi \tag{1}$$

Where, φ is general dependent variable to model which can represent speed, turbulent energy and turbulent energy dissipation rate etc; Γ_φ is diffusion coefficient corresponds to φ . S_φ is source term corresponds to φ . Its specific meaning is showed in Table 1.

Table 1 Dependent variable meaning of control equation

equation	φ	Γ	S
continuity equation	1	0	0
momentum equation	U_i	$\nu + \nu_t$	$-\frac{\partial P}{\partial x_i} (\frac{P}{\rho} + \frac{2}{3} \delta_{i,j} k)$
turbulent energy	k	$\nu + \frac{\nu_t}{\sigma_k}$	$\frac{\partial U_i}{\partial x_i} (G - \frac{2}{3} \delta_{i,j} k - \varepsilon)$
turbulent energy dissipation rate	ε	$\nu + \frac{\nu_t}{\sigma_\varepsilon}$	$\frac{\varepsilon}{k} [C_{\varepsilon 1} \frac{\partial U_j}{\partial x_j} (G - \frac{2}{3} \delta_{i,j} k) - C_{\varepsilon 2} \varepsilon]$

where: $\nu_t = C_\mu \rho \frac{k^2}{\varepsilon}$ $G = \nu_t (\frac{\partial U_i}{\partial x_j} + \frac{\partial U_j}{\partial x_i}) \cdot (\frac{\partial U_j}{\partial x_j})$

model empirical constant: $\sigma_k=1.0$ $\sigma_\varepsilon=1.3$ $\sigma_{\varepsilon 1}=1.44$ $\sigma_{\varepsilon 2}=1.92$ $C_\mu=0.09$

In Table 1 $i, j=1, 2, 3$; for example $(x_1, x_2, x_3)=(X, Y, Z)$, U_i is velocity component, m/s, $(U_1, U_2, U_3)=(U, V, W)$; ρ is air density, kg/m³; k is turbulent energy, m²/s²; ε is turbulent energy dissipation rate, m²/s³; P is time averaged pressure, Pa; $\delta_{i,j}$ is Kronecker coefficient ($i \neq j, \delta_{i,j}=0; i=j, \delta_{i,j}=1$); ν is dynamic viscosity coefficient of laminar flow, Pa·s; ν_t is dynamic viscosity coefficient of turbulent flow, Pa·s.

Boundary Condition

The author imports the physical model into FLUENT and sets boundary conditions. The entrance boundary type is VELOCITY_INLET. The forced air volume is 400m³/min. All winds blow through radial clearance of mural cylinder. The exhaust air volume is 550m³/min. The turbulent kinetic energy is 0.8m²/s². The turbulent diffusion ratio is 0.8m²/s³.

The Analysis of Simulated Result

The total simulated result of wind velocity vector is showed in Fig .2. In order to show the wind velocity vector at different cross section clearly, lists the wind velocity vector of different cross section which x equal to 30m, 11m, 5m and 3m are listed, as shown in Fig .3. Units of Fig .2 and figure 3 are all “m/s”.

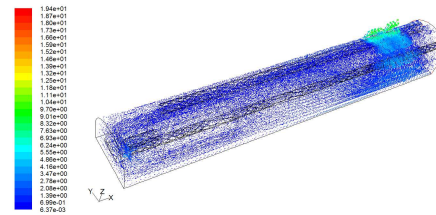


Fig. 2 The total simulated result of wind velocity vector

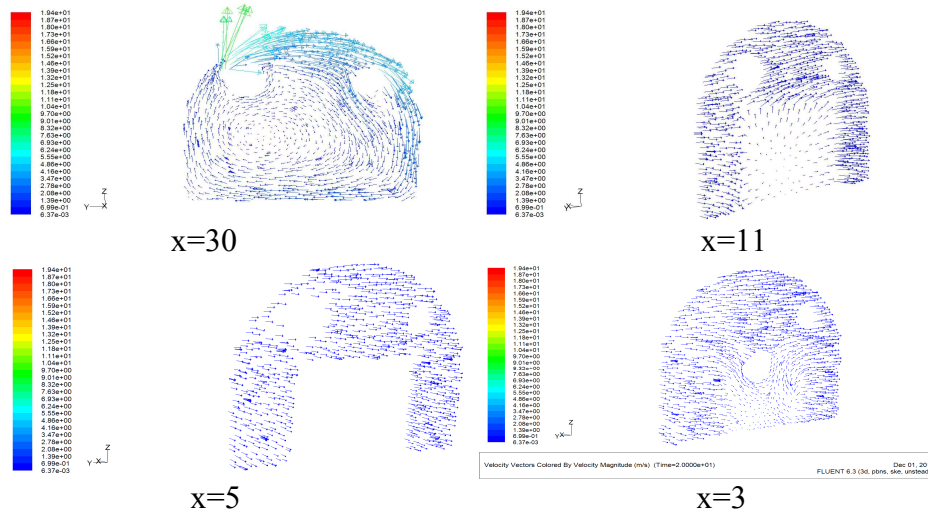


Fig. 3 Definite dust concentration simulated result of cross-section at different locations which X equal to 30m, 11m, 5m and 3m

After the mural cylinder was used in north conveyor main roadway in fully rock mechanized excavation face, in the region of x respect from 27m to 31.3m, all forced air blows through the radial clearance of mural cylinder. The maximum wind speed is 11.8m/s, formed a full-face eddy Air-curtain at the lockable roadway section. For example, a full-face eddy Air-curtain flow field at the lockable roadway section is formed in the cross section which x is equal to 30m. In this flow field, wind speed near the tunnel wall is within the range from 2.08m/s to 11.8m/s. While the wind speed of roadway center is around 0.00637m/s to 0.699m/s.

In the location of $x=3m$, $x=5m$ and $x=11m$, direction of the wind speed arrow heads are pointing to tunneling place and the speed are basically same. The slight difference only exists when there are road-header and other obstructions. This shows that: under the influence of exhaust cylinder, the formation of eddy Air-curtain flow field continue to promote to the tunneling place and make the pressure air flow evenly spread in the roadway section, gradually forming an air-curtain dust controlled flow field that presses to the tunneling place in front of the workers including driver of the roadheader.

Development of Eddy Air-Curtain Dust Controlled System in Hard Rock Mechanized Driving Face

Based on the above simulated results and physical condition of hard rock mechanized driving face, the author developed the eddy air-curtain generator mural cylinder and formed the new eddy air-curtain dust controlled system in hard rock mechanized driving face with the combination of the smoke dust purification equipment.

Mural Cylinder

The mural cylinder can ensure that all forced air flow through the rotating duct, forming a thick and dense air curtain. The new mural cylinder is formed by one cylinder memory whose length is 1.2m, one cylinder with the rotating damper whose length is 1.2m and two cylinders with radial clearance whose length is 2.3m. The total length is 7m. In contrast, the traditional mural cylinder is made of the steel material which is heavy, inconvenient to move underground. In order to improve mine workers' labor efficiency, the developed JQFM light mural cylinder is made of a new high

molecular material whose composition is aliphatic resin while the main component of polyester is resin. The total weight of JQFM light mural cylinder is less than 50Kg, 5 to 10 percent lighter of an ordinary iron or steel cylinder, which greatly reduces the miners' labor strength.

Overall Layout of the Dust Control System

According to the actual situation of north conveyor main roadway in fully rock mechanized excavation face and numerical simulated result of eddy Air-curtain dust controlled flow field, we put the exhaust cylinder whose diameter is 0.8 m in the side of the roadway in opposition to the driver. The distance from the suction exit to the tunneling place is less than 1.25m while the distances between the axis of the cylinder and the ground and the nearest tunnel wall are 3.5m and 0.4m respectively. The exhaust cylinder and dedusting fan are suspended in the monorail crane of tunnel roof, with the dedusting fan adopting the slip mode.

Analysis of Application Effect in Field

This eddy air-curtain dust controlled system in hard rock mechanized driving face was used in mechanized driving face of north conveyor main roadway. Table 2 shows the measurement of the dust concentration of hard rock mechanized driving face in north conveyor main roadway before and after of the eddy Air-curtain dust controlled system was adopted.

Table 2 Dust concentrations before and after eddy Air-curtain dust controlled system was adopted.

measuring position	point	dust characteristics	before [mg/m ³]		after [mg/m ³]		dust suppression rate	
			total dust	espirable dust	total dust	espirable dust	total dust	espirable dust
tunneling place		Hd.sd.	1538.4	768.2	175.4	97.6	88.6	87.3
drivers		Hd.sd.	986.3	497.5	21.7	13.9	97.8	97.2
downwind of loader		Hd.sd.	847.2	413.6	21.2	13.2	97.5	96.8
downwind of telescopic belt		Hd.sd.	811.5	387.9	19.5	11.2	97.6	97.1
100m away from the tunneling place		Hd.sd.	698.7	324.8	18.9	10.7	97.3	96.7
200m away from the tunneling place		Hd.sd.	542.9	259.1	16.8	9.8	96.9	96.2
average dust suppression rate [%]							97.4	96.8

After the eddy Air-curtain dust controlled system was used in hard rock mechanized driving face of north conveyor main roadway, the dust-fall rate of the dust concentration at the working face is significant and the average settlement rate of the of total dust and respirable dust have reached to 97.4% and 96.8% in working face from 2# to 6#. At the location of the driver of roadheader where the dust concentration is the highest, the concentration of total dust and espirable dust is only 21.7mg/m³ and 13.9mg/m³.

Conclusion

After all forced air blow through the radial clearance of mural cylinder, a full-face eddy air-curtain at the lockable roadway section is formed. With the help of the exhaust cylinder, this formed eddy air-curtain flow field continues to move forward to the tunneling place, forming an air-curtain dust controlled flow field that presses to the tunneling place in front of the driver of roadheader.

Based on the simulated results and physical condition of hard rock mechanized driving face, after the developed new light polymer materials radial cylinder eddy air-curtain dust controlled system was adopted in hard rock mechanized driving face of north conveyor main roadway, the average settlement rate of total dust and respirable dust have reached to 91.6% and 90.5%, and the dust concentration was reduced effectively.

Acknowledgments

The authors would like to thank Natural Science Foundation of China (51074100), the Natural Science Foundation of Shandong Province (ZR2010EM016), the Natural Science Foundation of Shandong Province (ZR2011EEQ009), the National Colleges and Universities Specialized Research Fund for the Doctoral Program (20113718110005) and the Science Research Innovative Group of Shandong University of Science and Technology (2010KYTD106) for providing the financial support for conducting this research.

References

- [1] J.S. Zhang, X.K. Yan and K. Wang: Journal of China University of Mining & Technology, Vol. 35 (2006) No.2, p.173. (In Chinese)
- [2] W. Nie, W.M. Cheng and Y.X. Guo: Safety in Coal Mines, Vol. 40 (2009) No.3, p.19. (In Chinese)
- [3] A.C. Liang, X.H. Jin and S.J. Guo: Mining Safety and Environmental Protection, Vol. 36 (2009) No.3, p.4. (In Chinese)
- [4] W.M. Cheng, W. Nie and Y.J. Yao: Journal of China Coal Society, Vol. 36 (2011) No.8, p.1342. (In Chinese)
- [5] X.Z. Wang, Z.A. Jiang and S. Wang: Journal of China Coal Society, Vol. 32 (1994) No.4, p.386. (In Chinese)
- [6] W.M. Cheng, W. Nie and Y.J. Yao: Science & Technology Review, Vol. 29 (2011) No.9, p.48. (In Chinese)
- [7] J. Zhang, X.L. Wang and H.C. Chen: Journal of Hydroelectric Engineering, Vol. 27 (2008) No.1, p.111. (In Chinese)
- [8] D. GIDASPOW: *Theory Descriptions* (Academic Press, New York 1994).
- [9] S. Nakayama, K. Uehino and M. Inoue: Shigen to Sozai, Vol. 112 (1996) No.9, p.639.
- [10] W. Nie: *Application and Research on Closed-End Dust Removal System of Comprehensive Mechanized Heading Face* (MS., Shandong University of Science and Technology, China 2010), p.22. (In Chinese)

Effects of Beipiao Wind Power Development Planning on Local Birds Ecosystem

Wang Lin^{a,b}, Zhu Jinghai^c, Ma Zhongqiang^a

^a. College of Environmental Science, Dalian Maritime University, Dalian 116025, China

^b. Synthetical Research Centre, Dalian University, Dalian 116622, China

^c. Liaoning Provincial Environmental Protection Administration, Shenyang 110031, China

Keywords: Wind Farm, Migratory Bird, Ecology.

Abstract. Liaoning Beipiao is located in "Three north" wind zone which is one of the regions rich in wind energy resources in China. The area is windy throughout the year suitable for wind energy development and utilization. For the next 12 years, Beipiao government plans to construct 16 key wind energy resource development areas. However, the planning wind farms are located in Liaoxi Corridor for birds migrating must pass by. The wind farm may generate adverse effects to migratory bird ecology in Beipiao. The basic characteristic of bird ecological system in Beipiao area is introduced in the paper. The adverse effects of wind farm on birds and answer measures are discussed as well.

Introduction

Along with our country economy development for the continued growth of energy demand, energy supply has been nervous with each passing day and environmental problem has become increasingly prominent. In the consumption of coal resource, coal-fired power plant produce large quantities of soot, SO₂ and other harmful substances every year, bring adverse effect for the atmospheric environment and human health. Therefore, adjust the energy structure timely and make use of renewable energy, have become the urgent task. Scientists began to attach importance to Wind power, solar energy, bioenergy and other renewable energy. Certainly, different region ought to select appropriate energy policy based on their resources advantages.

Wind power is a kind of clean and primary energy source, no consumption of mineral, does not emit any harmful gas. Its production process is mainly the natural wind energy into mechanical energy, and the mechanical energy into electrical energy. The development of wind power in some region rich in wind energy resource can improve the energy supply, optimize power source structure, and reduce harmful gas emission.

Beipiao city is located in "Three North" wind zone suitable for wind energy development and utilization. For the development of wind energy resource, Beipiao municipal government plan to construct 16 developing regions of wind energy, a total of 16 wind power sites, which located in 19 townships of the district, planning a total installed capacity of 2050MW.

Definitely, as clean energy, wind power has incomparable advantages on environmental respect different from conventional energy projects. But the ecological environment impact of the wind power project should not be underestimated. Particularly, Beipiao is located in the Liaoxi Corridor for birds migrating must pass by. Beipiao City, large-scale development of wind power project is likely to produce a series of adverse effects on bird living space and migration. It will be one of important elements to restrict large-scale planning of wind power projects.

Overview of Wind Energy Resources in Liaoning Province

Wind Energy Resource in Liaoning

Liaoning province is wind energy resource-rich area. Wind energy mainly concentrated in three areas, the first areas is 42°N around and its northern region including Changtu, Kangping, Zhangwu, Fuxin, Beipiao, Chaoyang, Jianping. Second is the coastal region of Bohai Sea. The third

is the north coastal zone of Yellow Sea. In these areas, the local terrain and the surrounding environmental conditions are propitious to airflow accelerating. As a result, the region can meet the standard for wind resource abundant district and match the resources condition of large wind power station construction.

Wind energy resources in Liaoning province is the key development area. Because of its geographical conditions, Beipiao is key zones in Liaoning for wind energy resource development.

Wind energy resource division in Liaoning province can be seen in fig.1.

I rich in wind energy resources

II relatively rich in wind energy resources

III commonly rich in wind energy resources

IV poor rich in wind energy resources

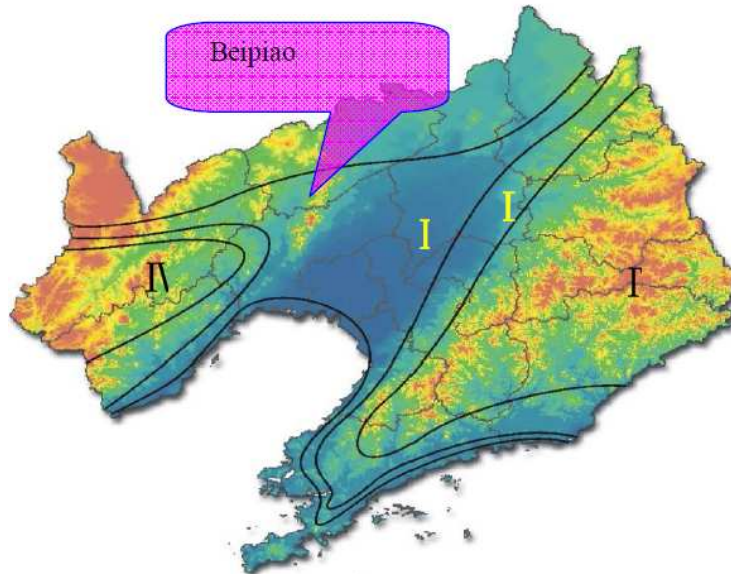


Fig. 1 The wind energy resources regionalization map

Wind Energy Condition in Beipiao

Beipiao wind power development planning areas are in the northwest low hill zones of Liaohe River plain, near Inner Mongolia, are located in our country "Three north" wind zone which is one of the regions rich in wind energy resources in China. The area is windy throughout the year suitable for wind energy resources development and utilization, especially in the spring, wind speed is maximal.

Beipiao municipal government plan to construct 16 developing regions of wind energy with total installed capacity of 2050MW which can be seen in table.1.

Table 1 Overview of 16 wind farm in Beipiao

No.	Name of wind farm	Capacity planning(MW)	Booster stations (kV)
1	Name of wind farm	100	66
2	Beitazi wind farm	300	220
3	Changgao wind farm	50	220
4	Yangshugou wind farm	100	220
5	Gaotaizi wind farm	24	66
6	Xiaotazi wind farm	50	220
7	Heichengzi wind farm	100	220
8	Shangyuan wind farm	100	220
9	Batuying wind farm	50	220
10	Liangshuihe wind farm	200	220

11	Meilingao wind farm	500	220
12	Sanbao wind farm	50	220
13	Taijiying wind farm	100	66
14	Changheyong wind farm	150	220
15	Xiguanying wind farm	76	66
16	Xinglonggou wind farm	50	220

Comprehensive analysis of Beipiao wind resources is given. For the example of Beitazi wind farm, based on the calculating for actual measured data, the annual average wind speed is 6.9m/s at the height of 50m, the annual average wind power density is 361.8w/m², the annual effective wind hours is close to 7000h. The time of wind speed above 8m/s is exceed 3500h, the time above 10m/s is exceed 2000h. The annual average wind speed is 6.4m/s at the height of 30m and the annual average wind power density is 263.4W/m². The wind power density is larger in spring and winter which are correct time of year for wind power generation.

After statistic and analysis, Beipiao belong to the fairly good scale of wind energy. Beipiao is suitable for wind farm construction.

Basic Characteristic of Bird Ecological System in Beipiao Area

Basic Condition of Migratory Bird in Beipiao

Migratory birds in Beipiao are mainly distributed in the wetland of white stone reservoir. Only to the spring of 2010 statistic, the migratory birds already amounted to more than 50000 in the territory of Beipiao. Among it, three kinds are the first level of national protection which are black stork, iconia and red-crowned crane, six kinds are the second level of national protection which are large swan, little swan, white forehead goose, spoonbill, yellow mouth egret, crane, and besides, there are a total of 16 kinds of geese and ducks.

Thickets, forests, farmland and waters in Beipiao with more rivers and gentle mountains provide rest and nutrition condition for birds. Common migratory birds crowd in Beipiao are heron, bean goose, whooper swan, ruddy Shelduck.

Migratory Pathway

Migratory pathway in Liaoning province

Liaoning province is located in the eastern flyway of world's three largest bird migration zones, in the same time, it is the important channel of Northeast Asian birds migrate line. Every year, tens of millions of migratory birds ceased, breeding and wintering pass by the province. According to many years of investigation and study, bird migration channel in Liaoning province is divided into four lanes which as follows in autumn, the spring in contrast.

First lane, including most migratory birds, proceed from Daxinganling area of Heilongjiang, Inner Mongolia and Russia, pass through Liaoxi Corridor, enter Hebei Qilaotu hill and Shandong. Fuxin, Chaoyang, Jinzhou are on route, as well as the city of Huludao.

Second, mainly birds and shorebirds migrating channel, from Jilin, Baicheng, Heilongjiang province and other places, along Liaohe River, Liaohe River estuary and Bohai coast to the mouth of Huanghe River, by way of Tieling, Shenyang, Liaoyang, Anshan, Panjin, Jinzhou, Huludao city.

Third, it is the most concentrated upland fowl migration corridors, especially the birds of prey, from Jilin, Baicheng, Russia by way of Liaodong Peninsula to the LaotieShan in Dalian for break, and then continued going south to Shandong Peninsula temple island archipelago, Fushun, Shenyang, Tieling, Liaoyang, Anshan, Yingkou, Dalian city in the province are on route.

Fourth lane is an important migratory waterfowl channel of Northeast Asia. It is from our country's Jilin and Heilongjiang, Russia, Alaska of United States, through Changbai Mountain or river to Dandong and Dalian coastal for rest, then pass through Dandong, the eastern city of Benxi and Fushun, into Japan, Korea along Yellow Sea coast by Yalu River.

The above four lines are not absolute. Boundaries are not very strict and clear, but relatively apparent concentration.

Migratory pathway in Beipiao

The first lane in above-mentioned four migratory pathways in Liaoning province is crossing over the territory of Beipiao. Beipiao located in western Liaoning mountain which is an overland migration channel, also known as "Liaoxi Corridor".

Beipiao is an important stopover, reproduction on the migratory routes of northeast inferior area. This migratory route is from Hebei Qilaotu hill and Shandong, through land and the west coast of Bohai into the boundary of Beipiao. The birds go there in spring and back in autumn every year, time of up to 4~5 months.

The whole migratory route assume northern and southern curve. Migratory route in Beipiao is in the north elbow line of this lone line.

The Impact Analysis of Beipiao Wind Power Development Planning on Local Birds Ecological System

The next twelve years, Beipiao will construct 16 key wind energy resource development areas and plan a total installed capacity of 2050MW. Large wind farms will constitute a degree of adverse effect on the local ecology of birds. Wind power development planning must be analyzed carefully to avoid or mitigate the adverse effects.

Construction period impact on bird

In the process of wind power development planning, construction period mainly refers to the installation of wind machine, the construction of wind farm roads and other facilities. Typical effects in the period of construction, include noise, dust and waste water from construction machinery and transportation vehicles which will disturb original living environment of the birds which make the birds within the scope have no way for feeding, nesting and breeding. But because the construction period is short and the construction site is small relative to the whole region. Therefore, the adverse impact of construction period is comparatively small and can be acceptable by the bird ecosystem [1].

The impact analysis of operation period

The adverse effect from bombardment

In the Implementation procedures of wind power development planning, the adverse effect is mainly from the fan operation period. In the process of fan movement, the winged birds within the wind electric field may collide to wind turbine impeller and transmission lines. Some larger or heavier birds, waterfowl, predatory bird and some low flying birds in night is more susceptible to crashing[2]. But according to the survey data, these birds are not common on the ground so that the probability of impact event is low and the harmful effect is less.

The familiar birds in place are smaller in size and flexible in flight, further more, fan obstacle is very clear and fairly easy to avoid. Accordingly, on the whole, we can say that the collision probability of birds and wind turbine is minor.

The adverse effect from fan operation noise

Blower noise can be generated in the process of fan operation. Most birds have higher sensitivity to noise. As a result, most birds would choose to avoid the noise and reduce the scope of activities [3].

From 1994 to 1999, the effect of fan noise on the birds had been studied near 30 wind turbines by German. The investigation indicates, as long as keep a distance of 250m, the adverse effect of wind turbine noise on the bird habitat and feeding is very small[4]. According to planning, 16 wind farms on planning in Beipiao city are not in the range of bird habitat and feeding. As a mandatory, the wind turbine layout should be at a distance of greater than 500m from the borderline of secondary protection areas of white stone reservoir drinking water sources which is habitat and feeding location for the birds.

Therefore, it can be concluded that the effect of blower noise on normal activities of birds is negligible.

Effect of wind farm construction on bird flight and migration

The impact of large scale wind turbine on nocturnal migrants is relatively sensible. In the migration of birds, prey migration is generally carried out during the day, and the migration time of a number of small insectivorous birds is in night. The flying height is about 150~600m of bird migration and crossing. Most birds have good eyesight and obstacle avoidance ability, thus in sunny weather conditions, even a very large number of birds, the collision probability is very few and closer to zero. When the weather condition is poor, such as heavy rain, windy weather, birds will usually lower flight altitude. Then wind turbine running will make adverse influence on stopover and direct migration of birds [5].

In the process of planning, 16 wind farms had being outside the range of migratory routes arranged by Beipiao government. It makes sure migratory birds that would not be affected by wind farm construction.

Effect of wind farm construction on bird feeding and shelter

The flying height of migratory birds is lower than 100m in general when habitat and feeding. The fan blades rotate at the altitude of 37~100m range and the running speed is 34~61m/s, so the fan running will affect directly on the birds [6].

When the birds habitat and feeding within the wind farm, the risk of casualties is exist.

Prevention Measures

After realize the possible impact of wind farms for bird, the following measures should be taken.

Migratory birds in Beipiao are mainly distributed in the wetland of white stone reservoir, for reduce the negative effects of fan operation on the birds, some requirements must be carried out. In specific projects, the wind turbine layout and transmission line selection should be at a distance of greater than 500m from the borderline of secondary protection areas of white stone reservoir drinking water sources.

Avoidance is main measure. The high density area of birds (such as area of bird foraging and important activities, migration channel) should not be selected for wind farm. 16 wind farms must be outside the range of migratory routes to prevent casualties of large numbers of birds. Certainly, this has been taken into account by Beipiao government.

Birds' migration situation should be observed within 24 hours in bird migration peak time.

Warning hawkeye should be painted on the blower. The lights ought to be installed on the edge of fan cluster. Matt pigment must be painted on the fan which can prevent birds to chase the wind leaf because of see fan blades rotating light.

Lighting device should be set in wind farm.

Someone is put in charge of inspection in the wind farm during bad weather. The injured birds must be sent to the bird observatory timely. The emergency aid should be implemented by professional functionaries for bird observatory.

Conclusion

As clean energy, wind power development is imperative.

Beipiao wind power development planning area is windy throughout the year suitable for wind energy resources development and utilization. 16 wind farms will be constructing for the next 12 years.

Although wind power is environment friendly project, but adverse ecological environment influence caused should be concerned. Especially in some areas with rich bird resources, more attention should be focused on bird habitat, foraging and migration in the process of wind power development. Bird resources are rich and bird migration channel is relating in Beipiao. Large quantities of wind farm planning and construction will make adverse effect on the birds. As a result, reasonable site selection is important to avoid bird habitat and migration channel. It is to avoid loss of bird resources.

References

- [1] Wang Mingzhe, Liu Zhao, “The Effects of Wind Farm on Birds [J]. Journal of Northwest Normal University (Natural Science).2011, 47 (3): 87~88.
- [2] Cui *huai Feng*, Yang Qian, Zhang Shuxia. Analysis on the Factors of Impacting the Collision between Birds in Aero Generator Sets and Countermeasures [J]. Environmental Science Survey.2008, 27 (4):52~56.
- [3] Bian Xingzhong, Jiang Zhixue. Impact Analysis and Countermeasures of Wind Power Plants on Birds Migration [J].Environmental Science Survey.2010, 29 (4):80~82.
- [4] BRAUN C E, Edeko ven OO, ALDRIDGE C L.Oil and gas development in western North America:effects on sage brush steppe avifauna with particular emphasis on sage grouse[M/C].Transactions of the North American Wildlife and Natural Resources Conference.2002, 67:337~349.
- [5] Desholm M,Fox AD, Beasley P,et al. Remote techniques for counting and estimating the number of bird-wind turbine collisions at sea: A review[J].Ibis,2006,148(Suppl.1):76~89.
- [6] Kikuchi R. Adverse impacts of wind power generation on collision behaviour of birds and antipredator behaviour of squirrels [J]. Journal for Nature Coservation.2008,16:44~45.

A Parameters Optimization of the CO₂ Laser Drilling Process for HDI Microvia Fabrication

YouZuo Hu^{1,a}, Wei He^{1,b}, WeiDong Xue¹, ZhiHuaTao¹, YuXing Huang¹, Huan Xu², and WenQu. Lv²

¹School of Microelectronics and Solid-State Electronics, University of Electronic Science and Technology of China (UESTC), Chengdu 610054, China

²Bomin Electronic Co. Ltd. Meizhou City, 514768, China

^ae-mail:huyouzuo@126.com; ^be-mail: heweiz@uestc.edu.cn

Keywords: CO₂-Laser; Blind Vias; Regression Equation

Abstract. The blind via holes formation by laser drilling is one of the key technologies for demanding high density interconnect printed circuit boards. In this paper, the drilling conditions of drilling the blind via holes and the quality of the drilled holes are examined using a CO₂ laser source against the FR4 board without copper foil. We chose laser energy, pulse shot, pulse width and diameter of beam as the experimental parameter. The results showed that laser energy and beam diameter played a more important role on changing the blind vias' diameter than pulse shot and pulse width. While the pulse shot and pulse width take more important role in changing the depth of vias.

Introduction

High-density interconnect(HDI) is the main developmental direction of printed circuit boards (PCB), which require miniaturization and specialization of blind microvias. Now UV laser and CO₂ laser are two general kinds of laser drilling method being used in PCB production[1,2]. The UV laser could be used to cut high quality blind vias through shorter wavelength and higher energy but the processing time is too long which is not conducive to a large number of production[3,4]. In contrast, the CO₂ laser is much more widely used by PCB production manufactures for its high-speed, high-efficiency and low-cost[5]. Most CO₂ laser can produce infrared radiation at wavelengths around 9.4μm and 10.6 μm [6,7] and the laser energy is much lower than UV[8]. During via drilling process CO₂ laser vaporizes and decomposes the substrate by thermal ablation [9]. Many scholars have done lots of works about the laser drilling technology, but merely mentioned about how the different laser parameters effect on the quality of blind vias [10]. In this paper, Mitsubishi laser drilling machine is used for drilling blind holes of flexible PCB, and the optimal conditions for CO₂ Laser operation is obtained.

Experimental

Selecting Material The experimental materials are 300μm FR-4, 201μm double-sided copper clad board, 600μm 6-layer HDI board. Mitsubishi ML605GTW II CO₂-laser was used in drilling blind vias. ASIDA JX23 metallographic microscope was used to complete the performance test.

Table 1 Adjusting value for parameters

ExperimentNO	Parameter	Adjusting Value					
		4	5	6	7	8	9
1	Pulse Shot	4	5	6	7	8	9
2	Laser Energy[mj]	1.6	1.8	2.0	2.2	2.5	3.5
3	Beam Diameter[mm]	1	3	5	7	9	11
4	Pulse Width[mm]	4.4	4.9	5.6	6.1	6.3	6.5

Results and Discussion

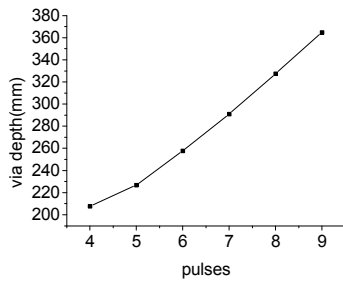
Adjusting Laser Parameters. Numbered the FR4 boards from NO.1 to NO.4 , a set of fixed value will given as 4 pulse shot,1.6mm beam diameter,1mm pulse width,4.4mj laser energy.The laser parameters were changed during drilling processvalue shown in Table1.

Laser Drilling of Blind Vias. According to Lamber-Beer’s Law, when the incident laser arrive at depth of x, the energy density of laser is:

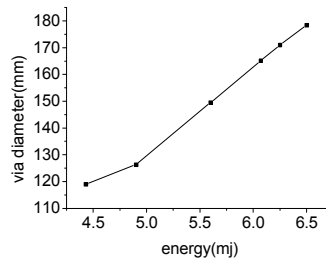
$$\rho = F(th)e^{x\hat{\delta}}$$

Where $\hat{\delta}$ is the absorption coefficient of laser, F (th) is energy threshold. It can be concluded from the equation that the laser energy is attenuating as the depth of laser ablation deepening. As the energy of CO₂ laser is low, it can’t use energy that higher than the bond energy of substrate to break these bonds. Therefore, the CO₂ laser follows laser ablation law to convert the energy absorbed by the substrate into thermal energy, which make the temperature of material surface rise rapidly to vaporize and decompose the material. In the laser ablation process, the spatial distribution of laser energy density is controlled by different parameters, which axial energy density effect the via depth and energy perpendicular to the axis effect via diameter .

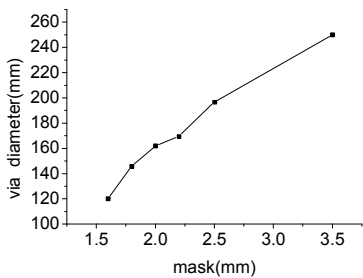
Effect of Laser Parameters on the Vias. Fig.1 showed that the via diameter increased when laser energy and beam diameter get larger , the depth of via changed regularly when pulse width and pulse shot changed.



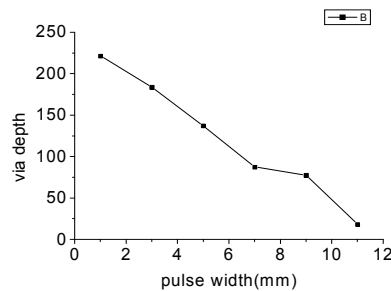
(a)The relationship between pulse and via depth



(b)The relationship between laser energy and via diameter



(c) The relationship between mask and via diameter



(d) the relationship between pulse width and via depth

Fig. 1 The relationship between the laser parameters and vias shape

Fig.1(a)showed that the increase of pulse shot will get deeper via.For series of laser pulse with same width acting on the same via generated longitudinal energy to make the material constantly melt. Fig.1(b) showed that it is a proportional relationship between the laser energy and via depth due to a strong wave with high heat to melting and evaporating the substrate rapidly.The greater energy generated great heat which is strong enough to ablate the copper continuously make the via diameter become larger. Fig.1(c) shows a larger beam diameter can get larger via diameter, because when changing the beam diameter, the laser energy density changed indirectly. Fig.1(d) indicated that a smaller pulse width will get deeper via, for narrower pulse width means greater energy density that can evaporate the substrate quickly.

Fitting Results of Parameters The equation of laser parameters fitted by minitab were obtained as showed in table 2. The equation’s mean square(S) ,regression coefficient square(R-Sq) and adjusted regression coefficient square (R-Sq-adj)are large enough. That means when the laser parameters changed the via depth and diameter which changed along with them were highly significant

Table 2 Fitting equation and the analysis results

Results	S	R-Sq(%)	R-Sq(adj)(%)
Fitting equation			
$y_{(pulses)} = 71.2 + 32.0 x$	6.542	99.1	98.8
$y_{(energy)} = - 14.8 + 29.5 x$	2.463	99.2	98.0
$y_{(mask)} = 25.4 + 65.6 x$	7.286	97.9	97.4
$y_{(pulse\ width)} = 240 - 19.8 x$	10.99	98.3	97.8

Blind Via Drilling Test.With the fitted equation, the value of laser parameters for different depth and diameter vias can be estimated. In order to ignore the effect of copper foil during drilling vias,conformal mask manufacture was used to get rid of copper layer.Double-sided board and 6-layer HDI board were used to testing drill first-order, second-order and third-order blind vias with target diameter are 180µm, 160µm and 200µm respectively ,the test drilling parameters are showed in Table 3.

Table 3 Blind hole test drilling parameters

Parameter value	order	Target diameter (mm)	Target depth (mm)	Pulse shot (shot)	Beam diameter (mm)	Pulse width (µs)	Laser energy (mj)
Test number							
NO.1	First-order	180	205	4	2.2	3	6.6
NO.2	Second-order	160	167	2	2	6	5.9
NO.3	Third-order	200	139	4	2.5	2	7.25

Results of test Drilling.Fig.2shows the diameter deviation between the first-order via and estimated value is 1.3µm,and resin on the bottom of via have been ablated away completely also avoid ablating the copper layer beneath it.Fig.3 shows the diameter deviation between the second-order via and the target value is 0.7µm,the opening copper foil and bottom copper layer warped slightly .The probably reason is that the via is not deep enough to enforce the laser energy completely decay when reached the bottom of the via and been absorbed by copper foil on the bottom ,so the bottom copper layer warped slightly. The rest energy reflected back along the two walls of the via and ablated the resin on the wall, but can’t ablate the copper foil at orifice .Fig.4 shows the diameter deviation between the third-order via and target value is 9.3µm. The bottom and orifice copper foil warped slightly too, but the depth of the third-order via is smaller, that allows the laser back and forth in the via and ablated resin along the via wall, making larger diameter deviation.

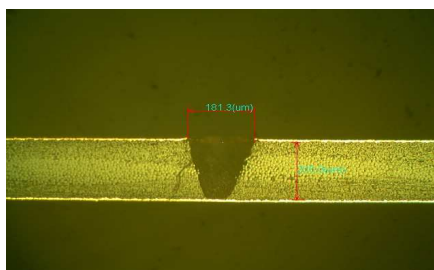


Fig.2 First-order blind via

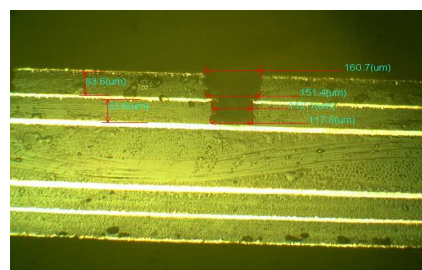


Fig.3 Second-order blind via

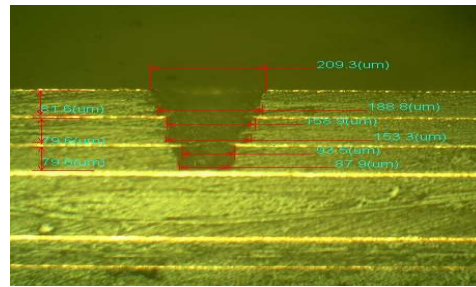


Fig. 4 Third-order blind via

Conclusion

In our test experiment, four pieces of FR4 board without copper foil have been introduced for CO₂ laser parameters test, the results showed that the via depth changed along with the pulse shot and pulse width, while the via diameter change along with the laser energy and beam diameter. The longitudinal energy of CO₂ laser is mainly effected by the pulse shot and pulse width, and the lateral distribution of energy is effected by laser energy and beam diameter. and can be used as the basis of adjustment of laser parameters during the production.

References

- [1] N.B.Dahotre,S.P HarimkarL, Laser Fabrication and Maching of Materials,The University of Tennessee,2008.
- [2] K.H Chen:UV Excimer Laser Drilled High Aspect Ration Submicro Via Hole”,Applied Surface Science ,vol 25,2009,p.183-186.
- [3] L.Weisheng,S.Yunlong and O.Yasu:Multiple Laser Wavelength and Pulse Width Process Drilling,U.S.Patent 8,150,913.(2008)
- [4] Zakariyah,S.S.Conway and P.P.Hutt:Fabrication of Polymer Waveguides by Laser Ablation using a 355nm Wavelength ND:YAG Laser(2011).
- [5] E. K.W .Gan:Laser Drilling of Micro-vias in PCB Substrate,2000 Electronocs Packaging Technology Conference,2000,p.321-326.
- [6] X.Y.Fang and K.C Yung:Copper Direct Drilling with TEA CO₂ Laser in Manufacture of High-density Interconnection Printed Circuit Board,IEEE Transactions on Electronics Packing Manufacturing,vol 29 ,2006,p.145-149.
- [7] Meucci.R and A.Naimee:Polarization Coding in CO₂ laser :Spatial and Temporal Behavior,Complexity in Engineering ,2010,p.106-108.
- [8] L.Romoli,F.Fisher and R.King :A Study on UV Laser Drilling of PEEK Reinforced with Carbon Fibers,Optics and Laser in Engineering Vol.50(2012),p.449-457.
- [9] T.Donnelly,M.Mazoyer and A.Lynch:CO₂ Laser Pulse Shortening by Laser Ablation of Amental Target.Rev.Sci.Instrum Vol.83(2012),p.183-188.
- [10]D.Dieter , J.meier:PCB Laser Technology for Rigid and Flex HDI-via Formation Structring Rounting,Circuitree Campbell,2005,p.471-476..

Nano-Machining Polishing Method on Metal Materials

Ming Yin

JiangSu University of Science and Technology, Zhenjiang, 212004 China

Keywords: Ice Desk Work Piece Plate Nano-Machining Polishing Surface Roughness Metal Materials

Abstract. Ice desk can realize the polishing on the metal material. Ice desk polishing can decrease the surface. Ice desk polishing can get ideal polishing result on LY12 aluminum alloy, which is nonferrous metal and unsuitable for traditional grinding and polishing. Under micro-loading or zero-loading, when the two faces are in sliding friction and the interval of boundary interface decreases to the degree that molecular force can make its function, the main reason removing the metal surface materials is lattice relaxing, structure splitting, surface energy and adherence energy in the interface. Crystal structure, surface crystal orientation, surface bias-gathering effect, adsorbs effect etc. is all have influences on the surface roughness of the metal material.

Introduction

Strict requirements, puts forward the surface roughness of the optical system components. Ha ha. In optical system, the surface roughness of optical element used to reflect or should be close to 12 miles refraction. The surface roughness of the lower is more transparent optical components surface. The development of modern super precision mechanism requires the precision and surface roughness level more and more high components. Some metal parts, such as laser scanning metal rotary mirror, mirror used in metal seal components of nuclear fusion and reflect the surface roughness to meet requirements mill micron grade. The friction pair of space, in many high-tech production such as microelectronics equipment, robot, medical machinery, precision testing instruments are often described and nano-level [1]. Some of the traditional smooth surface treatment methods and ultra smooth surface processing method, developed rapidly in recent years nano-machining the incomparable requirements, and some of them can get nano-level a smooth surface, but high processing cost and complicated equipment limited spread the technology. In this article, metal materials, such as the hard alloy LY12 aluminum alloy YG6, it is widely used in the actual production of polishing experimental research for high precision grinding machine plane self-made polishing abrasives ice tables polishing tools. Conclusion the surface roughness of part, can be further reduced the number of nano and from the original-level smooth surface can get receive better experiment.

Preparation of non-abrasive ice polishing desk and work piece plate

Non-abrasive ice polishing desk (abbreviation below: ice desk) is the self-made polishing tool that used in this experiment. Preparation process is that 100℃ deionized water should be injected into sealed nylon mould(divided into upper mould and under mould) firstly(showed in fig.1), then place the mould in fridge-freezer which temperature is -4℃-6℃.After 24 hours, bring the mould out of fridge-freezer, remove the under mould after 30 minutes slow heat insulation. Then we get the ice desk that the experiment need.

Using 100℃ water is to reduce the alveolar number in polishing desk and shorten time interval that ice desk turn from liquid state into solid state. Meanwhile it can also make ice desk expand uniformly everywhere, as a result, compactness and hardness of ice desk will be enhanced. Surface of ice desk needs pre-dressing before experiment and metal material should be pre-cooled because of its quick heat conduction. While polishing, fix the ice desk on thread spindle of high precise plane grinding machine tool by its inner thread. Work pieces are cohered with work piece plate.

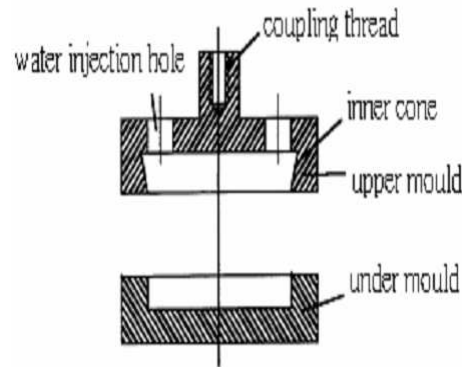


Fig. 1 Structure of mould

The material of work piece is LY12 aluminum alloy, 45steel and YG6 hard alloy: $\phi 10 \times 5$ mm (dia. \times thickness) Work pieces are fixed symmetrically in nylon mould by 502 glue, as showed in fig.2 The number can be 1~4 according to requirement and surface of work pieces should overtop mould surface 0.5mm.

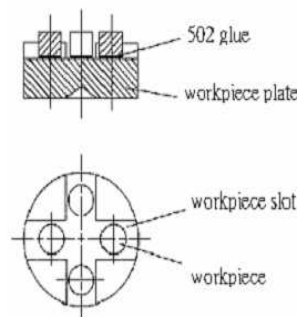


Fig. 2 Diagram of the work piece plate

The Experiment and Analysis

Polishing Experiment

And polishing, ice table's rotation of the machine tool and work piece spindle drive board ice floated on desk, no grip. The rotating disks can also because of friction between the work piece and ice. Pressure head on the top of the piston cylinder pressure on board the ice on the table by the board. It can make the work piece and constraints in the center of the rotating disks only pressure head, not any other sports. The spindle speed can be adjusted. The value of the odd and work piece center the table between ice center also adjustable boards. This experiment by changing the parameters, polishing speed and accumulation is polishing time. Every 50 minutes after polishing and surface roughness of work piece measurement HI-II Ra with scanning probe microscopy. The polishing environment is sealed, cleaning, low temperature, ash less and thermostatic. Fig.3 shows the diagram of machining area. Table1 and table2 shows the test results.

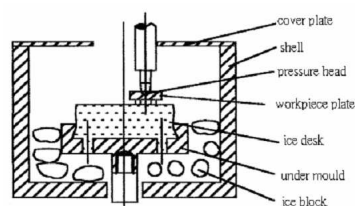


Fig. 3 Diagram of machining area

Table 1 Ra of LY12 aluminum alloy under different ice desk rotary speed Unit: nm

rotational speed (r/min)	0			200			300			400		
	point 1	point 2	point 3	point 1	point 2	point 3	point 1	point 2	point 3	point 1	point 2	point 3
workpiece 1 Ra	10.18	14.76	16.45	9.03	14.12	14.24	9.62	11.94	12.76	8.08	10.74	12.12
workpiece 2 Ra	49.84	47.79	52.74	49.49	44.39	51.47	49.09	47.01	47.66	34.49	40.47	37.49

Table 2 Ra of YG6 hard alloy under different ice desk rotary speed Unit: nm

rotational speed (r/min)	0			200			300			400		
	point 1	point 2	point 3	point 1	point 2	point 3	point 1	point 2	point 3	point 1	point 2	point 3
workpiece Ra	9.16	10.37	10.51	8.67	9.54	11.44	8.23	9.88	9.20	7.82	9.10	9.11

Table 3 Ra of LY12 aluminum alloy under different accumulation polishing time Unit: nm

Polishing times	Original Ra			First time polishing			Second time polishing			Third time polishing		
	point 1	point 2	point 3	point 1	point 2	point 3	point 1	point 2	point 3	point 1	point 2	point 3
workpiece Ra	49.09	47.01	47.66	34.49	40.47	37.49	68.37	80.98	74.55	30.89	36.14	29.06

Table4 Ra of YG6 hard alloy under different accumulation polishing time Unit: nm

Polishing times	Original Ra			First time polishing			Second time polishing			Third time polishing		
	point 1	point 2	point 3	point 1	point 2	point 3	point 1	point 2	point 3	point 1	point 2	point 3
workpiece Ra	10.09	9.88	9.20	9.32	9.67	9.11	8.74	9.10	8.37	8.23	8.89	8.24

Experiment condition: Spindle pressure 0 Mpa

Eccentric distance 7mm

Polishing period 50 min

After experiment, water sample elements analysis is carried on plasma emission mass spectrometer with plasma spectral method and mass-spectrometric method. Some elements such as Al, Cu, Mg, Mn etc. are founded in water sample collected in ice desk after polishing which are not in original deionized water sample.

Experimental Results Analysis

The Influence of Ice Desk Rotary Speed on the Surface Roughness of Work Piece

Ice desk polishing results vary instable. With the ice desk rotary speed rising, Ra of every point on work piece can all fall down and this phenomenon is obvious. The higher the original surface is roughness (e.g. LY12 aluminum alloy workpiece2), the larger the Ra falling down range. Polishing uniformity of every point on work piece surface can be improved too. This tendency can be seen from experimental results in table1 and table2. Once ice desk rotary speed is too high, vibration of machine tool will be intensified and the surface of work piece maybe destroyed. But if ice desk rotary speed is too low, efficiency of polishing will be low too. As a result, polishing period will be prolonged, and this is not what we are expected. So in this experiment, we select ice desk rotary speed about 400r/min.

The Influence of Accumulation Polishing Time on the Surface Roughness of Workpiece

From table3 and table4, we can see that it takes very short time to reach the best polishing effectiveness for LY12 aluminum alloy and YG6 hard alloy. With the increasing of accumulation polishing time, Ra of whole surface will decrease continuously though Ra value of some points fluctuate slightly.

The Influence of Polishing Pressure on the Surface Roughness of Work Piece

Polishing pressure makes the work piece nibble the ice severely, and the ice broken pieces will destroy the soft surface of work piece. After gotten out of mould (or after pre-polishing), the surface of ice desk is always very smooth, stress fissures are in the inner part of the ice desk. Polishing pressure shorten the time period of work pieces getting in touch with the fissures and the scratch will appear very quickly on the surface of work pieces. Internal stress produced in preparation can not make the surface of ice desk departed from the mould absolutely horizontal, and the vibration of piston rod in air cylinder in processing is unavoidable. Polishing pressure will make the piston rod vibrate more severely with the rotation of the ice desk and have a badly effect on the surface of work pieces. So in this experiment, polishing pressure is selected 0Mpa.

Analysis on Mechanism of Metal Removing

In this experiment, wok pieces are placed vertically to the ice desk. The weight of work pieces and work piece plate are only empty gram or so, so we can consider the contact between work pieces and ice desk as micro-contact or zero-contact approximately. In processing, ice surface of ice desk contacted with work pieces will pass through three change states; those are solid ice state, ice-water mixture state and liquid state.

Contact surface state of ice desk and metal work pieces is solid ice state, that is to say, at the beginning stage of polishing, it can be considered as mutual sliding friction between the two solid surfaces, at this time, it is the superlative micro-diverticulum points of the two surfaces that contact each other. In the sliding friction processing, roughness peaks stroke each other with high speed, and high motivating state, crystal lattice slacking and structure splitting will be appeared in very short time, meanwhile accompany series of physical process such as new surfaces formation and lattice disorder[2]. Then the main inducement that changes the metal surface roughness is generated. Some splitted surface peaks may be wholly removed, this can explain the phenomenon that the metal surface roughness decreases very quickly sometimes during the course of experiment. A few higher roughness peaks support the surfaces attribute to elastic compression and the lower roughness peaks do not contact each other in microscope, but because the interface space is too roughness further. 4 small, adhesive forces of the lower roughness peaks are not "submerged", atomic or molecular force in the interface will make the two surfaces adhere by so-called 'boundary bond'. Adherence produced by the surface energy between metal work pieces surface and ice surface which have conquered the interfacial energy make the metal crystal, especially the disorder lattices and relaxed lattices, glide through the boundary of grain or sub-boundary of grain. Dislocation, elastic or plastic deformation is occurred. Adhere removing from basal body of relative relaxed parts of metal roughness peaks decreases the work pieces surface roughness and changes the uniformity of the work pieces surface roughness.

Essential polishing stage comes when the contact place between ice surface and work pieces surfaces goes into ice-water mixture state and liquid state [3]. The expanded area between the surface of ice desk and metal work pieces and the high rotary speed of ice desk relative to work pieces increase the mechanical energy. The increased mechanical energy also raises absolute temperature in the interface and the value of surface free energy of the two surfaces in the interface. As a result, adherence energy is increased; complete plastic deformation of the metal material surface is occurred. Although the phenomenon of crystal lattice relaxing and structure splitting is also happened, in this stage, adherence in the interface is the main cause that changes the surface roughness of the metal work pieces. Some factors relative to surface energy of metal material and adherence energy such as crystal structure, surface crystal orientation, surface bias-gathering effect, adsorb effect etc. will make the most active atoms or molecules, which are in the inner parts of the metal surface crystal, alloy elements and nonmetal materials maybe mixed in the metal material, transfer or be removed by the adherence energy. These can also decrease the surface roughness of the metal work pieces and improve the uniformity of the surface roughness further.

Conclusions

Smooth surface Nano-level used more and more high and new technology of production, and asked them to more and more high. Traditional polishing method keep surface roughness further reduces due to the existence of the abrasive materials. In the Nano-machining polished metal material and ice tables is a kind of innovation polishing method. Polishing desk of ice desk, grinding materials, so nano-level surface roughness can be obtained. The article in the system based on the study of the nano-machining polishing method in metal material and the ice on the desk. Experimental device was put forward, which can make the metal materials ice table polishing, preparation of ice tables, work piece board in detail. This paper also introduces the processing technology of ice on the table polishing and disposal and measuring work-piece processing. Metal materials for polishing experiment with different kinds of water and the pressure head pressure. Water pressure and pressure head is the most suitable for metal materials polishing experiment results. The influence law research of polishing metal material and different ice speed and the plate on the table eccentric. Based on the theory surface interface and metal structure, from the atomic and molecular level, to eliminate the microstructure of the metal surface materials and a variety of surface roughness of work piece nano-machining the desk of metal materials ice polishing are discussed, and analysis of the original.

References

- [1] Yuan Zhejun, Wang Xiankui, Precision and Ultraprecision Machining Technology, Mechanic Industry Press, China, 2010,1, pp.1-8.
- [2] Wen Shizhu, Nano-tribology, Tsinghua University Press, China, 2009, pp.99-115.
- [3] Liu Weina, Ding Yuan, Nano-machining Experiment of 45 Steel Cryogenic Polishing, Mechanic Design, August, 2002 ,pp.136-137.

Quality Control Measures of Concrete Work

Yu Chen, Chengzhu Yan, Chao Ouyang

Department of Southwest Jiaotong University of Emei Leshan, Sichuan Province, China

Keywords: Concrete; Cracks; Prevention

Abstract. Today's social engineering construction cannot be separated from the concrete, Concrete is a non-uniform brittle material, Concrete in the construction process will encounter many real problems. And this article is to discuss common quality problems in concrete construction, and to introduce effective control measures.

Introduction

Concrete is a non-uniform brittle material, from a certain percentage of mixing cement, fine aggregate, coarse aggregate, water and admixtures in accordance with the essential building materials for the project Cracks in the concrete hardening process not only affects the appearance, returned to the quality of the project to stay hidden, so the construction must take reasonable engineering and technical measures to control and reduce the number and width of cracks in the concrete to achieve affordable, safe and reliable, a certain degree of reliability, practical and high performance.

Crack Control

Controlling of Raw Materials

Cementing Varieties

The varieties of cement concrete contraction depends on skillful material cement, cement paste shrinkage of C3A, SO₃ and the content of gypsum and cement fineness, etc. of the C3A content, the fineness of cement has a big change, the gypsum the water content is with a large contraction. also, the content of the SO₃ plays a important role in the cement. The project, according to the engineering characteristics of concrete or the environment conditions, the priority of the cement should be given the choice, so as to avoid cracks.

Aggregating

The aggregate is one of the main factors affecting the concrete shrinkage. The greater the volume content of coarse aggregate, the smaller the shrinkage of concrete. the choice of continuous graded elongated particle content should not be greater than 10% ,less the aggregate of mud, can reduce the shrinkage of concrete to prevent concrete cracks. The fine aggregate should be hard texture and clean, well-graded, and take dehydration, drainage, cover and strengthen the management and other comprehensive measures to ensure the stability of the moisture content, artificial sand saturated surface dry moisture content of more than 6%.

Flying Ash Admixture

Mixed with feed coal ash in concrete can improve the workability of the concrete, reduce the temperature, reduce shrinkage and improve concrete resistance to erosion with good results. cement hydration is an exothermic reaction, 1kg of the cement released the original heat up to 500J, it makes the concrete temperature above 75°C. Because of it sintemally generated heat of hydration caused by the rapid temperature rise, and the concrete surface to form a temperature gradient, so the internal tensile stresses, they can make the concrete cracking. To take technical measures to limit the peak temperature of the concrete temperature to avoid cracking. The cooling measures to reduce the temperature, o that it costs more to replace part of cement with fly ash concrete temperature to reduce it. But low-level fly ash, when the dosage is excessive, the lowearly strength, the temperature difference is large, is not conducive to the concrete crackin. So you should choose high-quality fly ash.

Admixture

Water reducer: general concrete admixtures will increase concrete shrinkage of concrete crack;

Expanders: expansion of the concrete mixture thick, without segregation and bleeding, so the pumping well, adapt pumping construction, no bleeding, and prone to early plastic shrinkage cracks. Concrete full conservation is an important condition to guarantee the expansion agent application, otherwise it will have bad consequences.

With the Ratio Control

Commercial concrete raw materials in certain circumstances, with than on concrete shrinkage cracks have important implications for the mixture ratio control has the following main points:

Commercial concrete response to the concrete mix to optimize

In different seasons, different construction should be a different mix ratio

Different uses of concrete with different mixture ratio

Raw material change should be to redefine the mixture ratio

To enhance the measurement and control of raw materials, in particular, strengthen the control of the rainy season, sand, rock and water content

Commodity concrete water-cement ratio should be 0.4 to 0.6, sand ratio should be 38% to 45%, the minimum cement content should be 300kg/m³.therefore, bad mixture ratio will produce shrinkage of concrete increased, causing cracking.

The Control of the Construction Process

As the commercial concrete is mobility, easy concrete will have the shrinkage cracks in the early, so it is very necessary to strengthen the conservation.

Concrete material is not easy too fast, tapered at columns, walls, deep beams and plates, etc. Should be layered pouring.

Concreting vibrators after 1-2h concrete secondary vibration, or surface compaction trowel, mass concrete should be layered cast on each casting thickness of not greater than 30-50cm.

Concrete should be strengthened the concrete mixing temperature of less than 25°C, to less than 3°C in the casting.

Prevention and Control Measures

Cracks

Configuration of concrete, it is necessary to strictly control the quality of the constituent materials, the appropriate choice of cement and cement grade, use well-graded gravel to reduce the porosity, the choice of a suitable medium coarse sand and qualified admixture; seriously preferred mixture ratio, to ensure that the required strength level, to meet the construction requirements of consistency, with the measurement seriously than the regulations to control the amount of water, stir well, correct grasp of concrete vibrators skills, it is not appropriate vibration, less vibration and leakage vibration.

Cellular

Optimization of concrete mix proportion, regular checks to ensure accurate measurement; to increase the concrete mixing time, watering should be stratified material, layered vibration, to prevent leakage of vibration and vibration phenomena; templates seam to plug tight, watered in, should be checked at any time situation template support, to prevent leakage of the slurry; concrete cutting height of more than 2m should be set to the string tube, under a layer of 2cm should be paved with cement mortar of pouring concrete.

Dew Tendons

Concreting, should ensure that reinforced the position and the correct thickness of the protective layer, and to strengthen inspection, when reinforced intensive, should use the appropriate particle size of the stones, to ensure that the concrete mix and good workability, watering the height of more than 2m.Application string tube or chute feeding, to prevent segregation; template should be fully wet and seriously blocking a good gap, the collision of reinforced concrete vibrators is strictly prohibited, and operation, to avoid stampede reinforced, if the step bend or release such phenomena should timely adjustment of the direct positive; vibrated dense protective layer of concrete, proper understanding of the removal time, prevent premature damage to damage of the edges and corners;

Holes

Reinforced densely and complex parts of fine aggregate concreting, carefully layered vibrator dense set aside the holes, both sides should be at the same time cutting the side an additional watering the door, to prevent the leakage vibration; the holes around the loose concrete and weak serosal chiseled pressure water washing, after moist fine aggregate concrete, high strength grade, carefully watering, tamping; concrete strength fluctuation is too large. Configure the concrete cement ratio and minimum cement content should be consistent with the requirements; strict construction management to ensure accurate measurement of each plate, control within the rang of deviation in the specification allows, and metering equipment to check accurately; determination of the construction aggregate moisture content, when a significant change in moisture content, should be promptly adjust the amount of water and aggregate amount of random sampling to make the specimen. Time sampling produced three specimens in the same plate of concrete, the curing 28 days to detect the compressive strength, as a basis for the assessment of component strength.

Concrete Repair and Protection

Cement-based polymer-modified or polymer-binder-based mortars are used for concrete repair and rehabilitation. The particular characteristics of such mortars are: Good workability also for overhead application, applicable by hand or machine, low shrinkage, good bond to the substrate and high long-term durability. To protect concrete from further deterioration, all-over applied protection systems are used. Such systems can consist of a water-repellent impregnation, an invisible coating or a colored coating. Depending on condition and requirements also elastic systems can be used, able to permanently close movement cracks and thus guarantee durable protection of the structures from further deterioration. Special products for concrete repair and protection: Admixtures for site batch mortars, e.g. emulsions, corrosion protection, ready to use repair mortars, finishing and pore mortars for hand and/or mechanical application as well as anti-corrosion inhibitors and impregnations, paint and coatings for concrete protection. One of the main applications of the Concrete Laboratory has been performed as "Curing Concrete". Curing is the protection of fresh concrete from evaporation and temperature extremes which might adversely affect cement hydration. It has been particularly mentioned that in all but the least critical applications, care needs to be taken to properly cure concrete, and achieve best strength and hardness. This happens after the concrete has been placed. Cement requires a moist, controlled environment to gain strength and harden fully. The cement paste hardens over time, initially setting and becoming rigid though very weak, and gaining in strength in the days and weeks following. Even though the cement reaction with water is completed over period of time (normally about around 240 minutes which is referred to as final setting time), the hardening of concrete and gain of strength is over a period of time 95% to 98% strength is achieved in 28 days. During this period concrete needs to be in ideal conditions, controlled temperature and humid atmosphere, in practice this is achieved by spraying or ponding the concrete surface with water, thereby protecting concrete mass from ill effects of ambient conditions. In the laboratory conditions, the requirements have been provided by placing the samples in ponds after giving them shapes such as rectangle prism and cylinder. After particular time, which may differ from one sample to another, the samples have been removed and placed again at the end of a waiting process.

Concluding Remarks

The above is a comprehensive analysis of the control of commodity concrete cracks, cracks dealing with two questions. You can get the following several conclusions:

Due to various regions of the different raw materials, construction techniques and conservation conditions, have different effects on the shrinkage of concrete and commercial concrete raw materials, control of the construction process should be strengthened to control the cracks;

Optimize the mixing ratio, strengthen the study of the complex admixture to reduce the amount of cement, reduce the contraction of the commercial concrete; improved design methods, reducing the width of concrete cracks, commercial concrete is different from ordinary concrete, and the concrete cracks is not a factor produced, but by complex factors would result from concrete. Although more than several of the effective measures can be better prevention and control cracks. This does not mean that the cracks will not produce. So we should take a different approach to deal with the different circumstances.

References

- [1] M.ning and M.zhang. Hydraulic concrete crack repair [J]. Modern agricultural science and technology,2010(12):233-234
- [2] M.zhao and B.dong Hydraulic concrete cracks causes and control [J]. Shanxi Architecture, 2010(9):162-163
- [3] Engineered Concrete Mix Design and Test Methods, Irving Kett

City Power Grid Planning and Coordination Mechanism

Menglan Huang¹, Yao Xian Li¹

¹ Henan provincial electric power company Xinyang power supply company

Keywords: Urban Grid; Urban Planning; Coordination Mechanisms; Index System; Comprehensive Evaluation

Abstract. As the asset belongs to relations reasons, among China's urban power grid planning and municipal planning, lack of coordination, to some extent, restricted the construction and development of the urban grid, thus constraining the urban social and economic development. According to the characteristics of network planning and urban planning, both the coordinated planning processed. Design a set of network planning and urban planning the coordinated development of comprehensive evaluation index system, the combination of G1 method, entropy method, layer by layer Scatter comprehensive evaluation model, and five typical city grid with the city and coordinated planning empirical analysis and evaluation, to prove the accuracy of the evaluation model The city grid and urban planning, coordination mechanisms and evaluation model for the coordinated planning of China's urban power grids to provide a scientific basis for decision making.

Introduction

The city power grid planning and urban planning and coordination of research has aroused the concern of the stakeholders, to solve the key elements of good load forecasting, grid structure, as well as the land of the station site and the location of line corridor implementation, but also on the coordination mechanism of did not begin [1-3]. More in-depth research on the comprehensive evaluation method and its application, mainly involved in the fuzzy analytic hierarchy process, gray relational degree analysis, improve the integrated weight method [4]. However, no literature on mechanism designing and coordination of evaluation, coordination of network planning and urban planning.

This article first development starting from the city power grid planning and urban planning coordination, explore the city power grid coordinate planning processes and mechanisms; Second, build up power grid planning and urban planning and coordination of the evaluation system of development indicators, the establishment of a comprehensive G1 method and entropy method of subjective and objective integrated Empowerment and Scatter combined with comprehensive evaluation model, and through empirical research to prove its scientific nature; Finally, according to the results of the evaluation of the typical cities, the urban grid coordinate planning policy recommendations.

Network Planning and Urban Planning Coordination Mechanism Design

The geographic distribution of planning up planning for the city controlled. City power grid facilities after the completion of the geographic distribution planning, network planning, general planning stage to deepen the detailed planning stage, through the municipal government for examination and approval, it increased control plan for the city, the geographic information of the grid facilities included in the urban planning geographic information systems by the regulations to protect the city's planning and construction must be set aside land for construction of power grid facilities and corridors as the control condition [3-4]. Rational planning process is a closed-loop feedback process management and continuous adjustment and improvement process, the city power grid planning and coordination of urban planning should be prepared as follows:

Improvement of infrastructure planning report procedure Improve the planning to be built from the project, design, approval, construction to the final stage of records management tracking and management for each project. The design units take into account the purpose of scale construction projects commissioned by the relevant professional departments, co-ordinated by the city planning department to consider the overall layout, determine the location. For the pipeline project, the more unified management, rationalize the layout of the pipeline by the city planning department.

Improving the coordination of the various professional sectors Existing infrastructure regulators are relatively independent, and a certain degree of monopoly. Basis for planning data collection, preparation stage to the final approval stage of the various departments should actively cooperate with and, when necessary, all levels of government to harmonize.

The establishment of planning interactive mechanism Adjustment of urban planning will be a direct impact on the layout plan of the city power grid facilities, the electricity sector and the planning department must establish a timely joint revision of the mechanism, once the adjustment of urban planning, load forecasting is a large deviation, the two sides must exchange information and to take timely revision of measures.

To promote the construction of urban infrastructure investment and financing systems

Network Planning and Coordinated Development of Urban Planning Evaluation

Index System Design

Network planning and urban planning evaluation system designed to coordinate the development of five sub-systems, as shown.

Grid and National Economy: 1.Per capita electricity consumption x_1 ; 2.Per capita residential electricity consumption x_2 ; 3.Electricity consumption elasticity coefficient x_3

The power grid: 1. User supply reliability rate x_4 ; 2.Line loss rate of x_5 ; Voltage qualification rate x_6

Of the grid investment economy: Grid unit supply cost: x_7 ; Grid sales profit margin x_8 ; Grid net assets yield x_9

Covers an area of environmental coordination: Public facilities covering an area ratio of x_{10} ; The Capacity for sustainable development: Proportion of investment of the grid construction x_{12} ; Government's support for efforts to x_{13} ; Urban Land and Environmental Carrying Capacity x_{14}

Indicators of Determining the Weights

G1 Law and Entropy Method subjective and objective integrated enabling. G1 method's advantage is no need to build the judgment matrix, without the need for consistency checking, and doubly reduced compared to the calculation and construction of AHP judgment matrix; Entropy Method according to indicators and quality of the information at the same time the introduction of index weights adjustment.

G1 Method Steps

Determine the sequence relationship of indicators

By the ordering relation of the index position number adjustment index ordering relation to determine for certain evaluation criteria for the $Xx_1 > x_2 > \dots > x_m$

Determine the relative importance between adjacent indicators. The set ρ_{k-1}/ρ_k as:

$$r_k = \rho_{k-1}/\rho_k (k=m, m-1, m-2, \dots, 3, 2) \quad (1)$$

ρ_k the calculation of weight coefficients. If the experts are given the the r_k rational assignment,

$$\text{so } \rho_m \text{ is: } \rho_m = \left(1 + \sum_{k=2}^m \prod_{i=k}^m r_i \right)^{-1} \quad (2)$$

By ρ_m can be drawn from the weight of other indicators:

$$\rho_{k-1} = r_k \rho_k (k=m, m-1, \dots, 3, 2) \quad (3)$$

Entropy Method Empowerment Steps

Entropy method to empower steps [5]:

Calculation of the indices j , the i being evaluated characteristics of the object proportion as follows:

$$p_{ij} = x_{ij} / \sum_{i=1}^n x_{ij} \quad (4)$$

Where: of x_{ij} i th evaluation object j index value, assuming that $x_{ij} \geq 0$.

Calculate the entropy of the index j :

$$e_j = -k \sum_{i=1}^n p_{ij} \ln(p_{ij}) \quad (5)$$

Where: $k > 0$; $e_j > 0$; $k = 1 / \ln n$.

Calculate the differential coefficient of the j index g_j : $g_j = 1 - e_j$ (6)

g_j the greater, the greater the role of the indicators in the Comprehensive Assessment.

To determine the weights β_j :

$$\beta_j = g_j / \sum_{i=1}^m g_i \quad (j=1, \dots, m) \quad (7)$$

G1 Method and Entropy Method Weights

Consider the characteristics of indicators of urban planning and network planning, integration G1 method and entropy method to determine the right weight for comprehensive weight heavy, considering the subjective and objective impact of:

$$w_j = \rho_j \beta_j / \sum_{i=1}^m \rho_i \beta_i \quad (j=1, \dots, m) \quad (8)$$

Based on Layer By Layer to Pull the Grade of Synthetic Evaluation

With n large system, $S_1, S_2 \dots S_n$ as the object being evaluated, each large-scale system has a p -level, all levels n_p sub-systems. $P = 2$, for example, of x_{ij} ($2, t, q$) represents the i th system from two-level subsystem s_q ($2, t$) ($q = 1, 2, \dots, m_t$; $t = 1, 2, \dots, n_1$; $m_1 + m_2 + \dots + m_{n_1} = n_2$) j observations of the evaluation, we might have assumed very large, non-dimensional standard observation [5], b is the feature vector. Comprehensive evaluation of the following steps:

Subsystem S_q ($2, t$), the evaluation function:

The first indicators of the right to treatment

Comprehensive evaluation value of the i -th large system:

$$y = A^{(2,t,q)} b^{(2,t,q)} \quad b \text{ is the feature vector}$$

Subsystem S (1) t - a comprehensive evaluation function:

The first indicators of the right to treatment

Comprehensive evaluation of the value of i -large system on the subsystem: $y = \sum_{q=1}^m b_q x_q$

The comprehensive evaluation of the system's function:
 Of $y(1.t)$, the right treatment
 Comprehensive evaluation of the function of the systems:

$$y = \sum_{i=1}^n b_i x_i$$

Finally, according to the size of y , the evaluation objection classification or sorting.

Empirical Analysis

Use of the proposed comprehensive evaluation model to evaluate five typical city power grid planning and coordination of urban planning, development here with the A, B, C, D, E, data from the Statistical Yearbook [6-10].

First of all consistent and dimensionless indicators, based on (1)-(8) then determine the coefficient of index weights.

Follow by a comprehensive evaluation of the steps to calculate the value of comprehensive evaluation of each city comprehensive evaluation of contrast, the conclusion that the five-city network planning and urban planning the coordinated development of a comprehensive evaluation of comparative results shown in Fig 1.

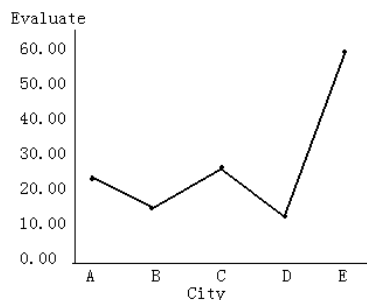


Fig. 1 Five cities comparison chart of comprehensive evaluation on coordination development of power network planning and urban planning

It can be seen, the E grid of the city planning and urban planning degree of coordination, and finally the city D and B cities, consistent with the actual situation of urban planning and network planning. E and C Urban Power Network high degree of coordination with the planning and management methods to be separated from the E region on the development and utilization of land resources very seriously, network planning is an important part of the overall urban planning, network planning is to focus on environmental factors, planning a high starting point, strict control to ensure that the valuable land resources to get the maximum efficient use of its long-term coordination of the concept planning of urban planning and network planning has played a huge role.

Conclusion

Chinese urban power grids and urban planning and coordination should do the following work:

Network planning into the overall urban planning and land use planning, and earnestly safeguards the solemnity of the plan.

Adapt to the urban economic development needs in a timely manner to the revision and convergence of grid planning and municipal planning.

To speed up the approval of the power grid construction projects, reducing the approval procedures, and priority for the relevant examination and approval procedures for power grid construction projects, project review or approval in principle to the way of bundling.

Efforts to alleviate the pressure of the power grid construction funds, multi-channel, multi-channel financing of the power grid construction funds

To strengthen public opinion, and do a good job in the protection of power facilities

Establish a long-term co-ordination of long-term conceptual planning (or system planning) to solve the direction of development, land use, urban planning and network planning.

References

- [1] Zhang qian-an. Characteristics of the power grid planning[J]. China New Technologies and Products,2010(1).
- [2] CHEN Shao-jie. Relation between power network planning and city planning[J]. Rural Electrification, 2006(5): 18-19.
- [3] WAN Guo-cheng, WU Ri-sheng, FAN Ya-liang. Discussion on relation between planning and construction of urban power grid and city planning[J] Guangdong Electric Power, 2006, 19(5): 28-31.
- [4] FAN Ya-liang, WANG Chang-zhao, LIAO Li-ji, et al. Combination of the power network planning and the city planning[J]Guangdong Power Transmission Technology, 2005(4): 5-8.

Multidimensional Grey Evaluation Method for Aeronautic Electronic Components & devices Selection

Xiangfen Wang^{1, a}, Cheng Gao^{1, b} and Guicui Fu^{1, c}

¹ School of Reliability and System Engineering, Beihang University, Beijing 100191, China

^{1,a}wangxf@buaa.edu.cn, ^{1,b}gaocheng@buaa.edu.cn, ^{1,c}fuguicui@buaa.edu.cn

Keywords: Aeronautic Electronic Device, Multidimensional Grey Evaluation, Selection, Evaluation Index

Abstract: Aeronautic electronic components & devices selection is an important means to improve the aeronautic product reliability in its development stage. This paper proposes a multidimensional grey evaluation method to evaluate the electronic components & devices selection process by four indexes after the analysis of aeronautic production contractors and component manufactures. A memory selection example was presented to prove the feasibility of the proposed method. The proposed method can avoid the evaluation error effectively due to subjective factors and help to improve the product use reliability.

Introduction

With the improvement of automation and intelligent of weapons equipment, large numbers and a great variety of electronic components & devices are used in aeronautic products. System failures of aeronautic products caused by electronic components & devices become the main problem. According to statistics recent years, the failures ratio due to improper use of the devices is about 60%. Quality control is necessary. The quality control process mainly includes electronic components & devices selection, procurement, additional screening, DPA, failure analysis, re-inspection. Selection is one of the most important means in the whole process [1]. Currently, there are two major problems in term of development stage of aeronautic product: one is that electronic components & devices selection are more unorganized and uncollected. The selection is not controlled and managed which is causes many problems in the development stage. The other is that the selection information is not dynamic assessment timely.

Multidimensional gray evaluation is based on the grey system theory, which is composed of evaluation target, evaluation index, evaluation categories and objects [2]. According to the system state and through systematic analysis, semi-qualitative and semi-quantitative assessment and description against scheduled target will be made by using multidimensional cross comparison and comprehensive effective measure during some period. This evaluation method has been successfully used in agriculture, industry, management and supplier selection [3,4]. We introduce the method to evaluate key and major electronic components & devices selection based on the analysis of aeronautic production contractors and component manufactures because it can be more objective, fair, rational and scientific than others due to several target traits are considered at the same time. A memory selection example shows that the method can avoid the evaluation error effectively due to subjective factors and obtain full information about selection.

Influencing Factors for Aeronautic Electronic components & devices Selection

Demand Sector Factor. The demand sector cares two matters mostly, one is the selection of the electronic device itself, and the other is the selection of device manufacturer. The demand sector requires the development company of aeronautic product not only to select electronic components & devices of high quality grade which can guarantee the reliability to meet the requirements of aeronautic product, but also to insure the device manufacturers in a stable situation.

Influences for Selection from the Development Company of Aeronautic Product

For selecting an electronic device, the designer of aeronautic product considers its function, quality, scheduling, and lower purchase cost. When a new aeronautic equipment system is designed, it is needed to be smaller, lighter and of complex functions. So the development company of aeronautic product is apt to select large scale integrated circuits, especially programmable logic chip (CPLD and FPGA) to reduce the number of device and making the product small[6]. This brings the problem of a low quality grade and poor batch stability for selection of device of plastic package and small manufacturer without qualification. If the system is designed from previous product, the designers of the aeronautic product use the ideas of old products. They are intended to use electronic components & devices that have been used and tested in old designs. For the old product was designed a few years ago, even ten years ago, some devices lag behind the development of device technology or discontinued, bring hidden troubles for subsequent reliability assurance.

Influences of DSMSM impact

DSMSM, which described as diminishing manufacturing sources and material shortages, means the last supplier of certain goods or raw material no longer exist or will not exist [7]. As the electronic technology innovates, many components have discontinued. The DSMSM impact of electronic components & devices is accelerated, especially of microelectronic components & devices for their high speed of new craftwork greater than others. The life cycle of electronic components & devices becomes shorter and shorter. The selection of backward technology is one of the reasons. Update of Material is another reason. The result of the DSMSM impact of electronic components & devices is the rise of procurement costs.

Influences of the Manufacturer

Many manufacturers of aeronautic electronic components & devices do not have military production qualification. For example, since the standard of filter is immature, many subsystem products choose small manufacturers due to the development cost when purchasing a special circuit for filter.

Index System for Selection of Aeronautic Electronic components & devices

On the basis the performance, quality grade (G), procurement cost (C), DSMSM impact (D) and device manufacturer factor (M) are critical factors for selection of electronic devices. Multidimensional grey evaluation model for selection from the four factors are discussed below.

Multidimensional Grey Evaluation Model for the Selection

Sample Matrix. N-electronic devices assumed to be selected composes evaluation object set, $I=(1,2,\dots,n)$; m-evaluation index constitutes evaluation index set, $J=(1,2,\dots,m)$; the assessment consequence make gray cluster set, $K=(1,2,\dots,p)$; d_{ij} is presumed as the observed value for the i-th electronic devices and the j-th index.

Equal Measure Processing with Samples

Such processing is to calculate the measure among different dimension data, through comparison and make it dimensionless. There are two ways for calculation.

For the index which is the higher the better, such as quality grade, the maximum effect measure is used, i.e.:

$$x_{ij} = \frac{d_{ij}}{\max_i d_{ij}} \quad (1)$$

For the index which is the lower the better, such as purchase cost, the lower effect measure is used, i.e.:

$$x_{ij} = \frac{\min_i d_{ij}}{d_{ij}} \quad (2)$$

The matrix after measure conversion is called phase matrix X, and x_{ij} is the whitening value of gray level.

The Determination of Whitening weight function

The whitening weight function is expressed by segmented function and shows the degree that the whitening value belonging to the gray cluster assessment set. $f_j^k(x_{ij})$ ($i \in I, j \in J, k \in K$) represents the i -th component and the j -th index that belongs to the whitening weight function of the k -th gray cluster assessment set, $x_j^k(1)$ is the lower boundary measure value of the j -th index function, $x_j^k(4)$ is the upper boundary value of the gray type, their meaning are shown in Fig. 1.

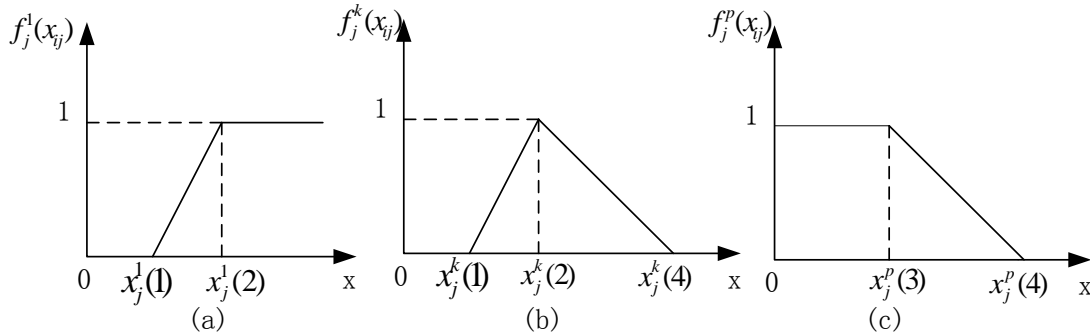


Fig. 1 Typical whitening weight function

The whitening weight function is expressed as:

$$f_j^1(x_{ij}) = \begin{cases} 1 & x_{ij} \in [x_j^1(2), \infty] \\ \frac{x_{ij} - x_j^1(1)}{x_j^1(2) - x_j^1(1)} & x_{ij} \in [x_j^1(1), x_j^1(2)] \\ 0 & x_{ij} \in [0, x_j^1(1)] \end{cases} \quad (3)$$

$$f_j^k(x_{ij}) = \begin{cases} \frac{x_j^k(4) - x_{ij}}{x_j^k(4) - x_j^k(2)} & x_{ij} \in [x_j^k(2), x_j^k(4)] \\ \frac{x_{ij} - x_j^k(1)}{x_j^k(2) - x_j^k(1)} & x_{ij} \in [x_j^k(1), x_j^k(2)] \\ 0 & x_{ij} \notin [x_j^k(1), x_j^k(4)] \end{cases} \quad (k = 2, 3, \dots, p-1) \quad (4)$$

$$f_j^p(x_{ij}) = \begin{cases} 0 & x_{ij} \in [x_j^p(4), \infty] \\ 1 & x_{ij} \in [0, x_j^p(3)] \\ \frac{x_j^p(4) - x_{ij}}{x_j^p(4) - x_j^p(3)} & x_{ij} \in [x_j^p(3), x_j^p(4)] \end{cases} \quad (5)$$

Decision-making authority of the k -th gray assessment set

All evaluation factors of the sample of the j -th indexes can be synthesized to the decision-making authority of the k -th gray assessment set.

$$\delta_{jk} = \frac{\sum_{i=1}^n f_j^k(x_{ij})}{\sum_{k=1}^p (\sum_{i=1}^n f_j^k(x_{ij}))} \quad (6)$$

Synthetical Weight coefficient calculation of every evaluation index

For the whitening weight function in Fig. 1(a) and (b), define $\lambda_j^k = x_j^k$, and that in Fig. 1(c), define $\lambda_j^k = x_j^k$, here λ_j^k is the critical value of k-th gray assessment set for the j-th indexes. Thus:

$$\eta_j^k = \frac{\lambda_j^k}{\sum_{j=1}^m \lambda_j^k} \quad j = 1, 2, \dots, m, k = 1, 2, \dots \tag{7}$$

Synthetical evaluation matrix

The clustering coefficient of the k-th subclass for the j-th index is:

$$\sigma_i^k = \sum_{j=1}^m \eta_j^k f_j^k(x_{ij}) \tag{8}$$

Here σ_i^k presents the weight of the i-th component and the k-th gray set, the evaluation matrix is:

$$R = \begin{bmatrix} \sigma_1^1 & \sigma_1^2 & \dots & \sigma_1^k \\ \sigma_2^1 & \sigma_2^2 & \dots & \sigma_2^k \\ \dots & \dots & \vdots & \dots \\ \sigma_n^1 & \sigma_n^2 & \dots & \sigma_n^k \end{bmatrix} \tag{9}$$

Comprehensive evaluation to the components to be selected

$$\sigma_i^{k*} = \max_{1 \leq i \leq n} \{ \sigma_i^k \} \tag{10}$$

Here σ_i^{k*} is that the i-th evaluation object in matrix R belongs to k class, is the maximum value in $(\sigma_{i1}, \dots, \sigma_{in})$.

Case Analyses

There are six memories which will be selected on a crucial position of some aeronautic product. The evaluation index data of each memory is shown in table 1

Table 1 The selection case of six memories

Indexes / memories	M1	M2	M3	M4	M5	M6
Quality grade(Q)	82	86	84	90	84	84
Procurement cost(C)[yuan]	780	800	1000	1500	900	1200
DSMSM impact(D)[month]	68	60	84	65	66	70
Evaluation of component manufacture(M)	93	96	99	90	85	80

Quality grade is ranking by A1, A2, A3, A4, B1 (domestic devices above), and S, B, B-1(imported devices above), the corresponding point rating is shown in table 2

Table 2: Point rating of quality grade

A1	A2	A3	A4	B1	S	B	B-1	Industry device of Military temperature
10	9.6	9.2	8.8	8.4	9.6	9.0	8.6	8.2

After measure conversion, the phase matrix is:

$$X = \begin{bmatrix} 0.911 & 1.000 & 0.809 & 0.94 \\ 0.956 & 0.975 & 0.714 & 1.00 \\ 0.933 & 0.780 & 1.000 & 0.98 \\ 1.000 & 0.520 & 0.690 & 0.91 \\ 0.922 & 0.867 & 0.786 & 0.86 \\ 0.933 & 0.65 & 0.833 & 0.81 \end{bmatrix}$$

Set gray set is $K=\{\text{priority selection, allowable select, limiting selection, prohibitive selection}\}$, i.e. $p=4$. According to (3)~(10), The model is calculated, the statistical matrix() of memories is:

$$\sigma_1 = \begin{bmatrix} 0.667 & 0.278 & 0.050 & 0.00 \\ 0.237 & 0.385 & 0.277 & 0.12 \\ 0.507 & 0.167 & 0.170 & 0.15 \\ 0.557 & 0.167 & 0.145 & 0.13 \end{bmatrix}$$

According to $\sigma_i^{k^*} = \max_{1 \leq i \leq n} \{c_i\}$, $\{Q, D, M\}$ are good indexes.

The gray clustering evaluation matrix (c_i is also calculated. The selection of memories is comprehensive evaluated. The result is:

$$\sigma_i^{k^*} = \max \{0.721, 0.735, 0.733, 0.837, 0.753, 0.793\}$$

The multidimensional gray evaluation result and sequencing is shown in table 3.

Table 3 The result of multidimensional gray evaluation of the six memories

memories	evaluation	priority rating
M1	not selec	6
M2	limiting selection	4
M3	allowable select	2
M4	priority selection	1
M5	allowable select	3
M6	limiting selection	5

The results suggest that the memory M4 is best through combined evaluation. The quality grade of memory M4 is high, although the procurement cost is the high. Memories M2, M5 are of the second. M1 is the worst evaluation and is suggested not select. The quality grade of this memory is worst. So after a comprehensive evaluation, the aeronautic product company selected the memory M4.

Summary

The main barriers in aeronautic electronic device selection are overlapping management, making the selection scattered and random. By using multidimensional gray evaluation model, the memories are selected. The adoption of multidimensional grey evaluation model for aeronautic selection gives a comprehensive assessment. It has the advantage of taking into account multiple factors at the same time, making the selection more objective and reasonable. The method of multidimensional grey evaluation not only can analyze multiple indicators comprehensively, but also operate by mathematics simply. It is easy to master and not easy to lose information. It has a wider application prospects.

References

- [1] YU Zhen-xing: Use of quality assurance guidelines of military electronic components (Aeronautic Industry Publications, China, 2003)
- [2] LIU Si-feng, DANG Yao-guo, FANG Zhi-geng: grey system theory and its application (Science Publications, Beijing, China, 2004)
- [3] FANG Jin-chen, CHEN Hua, ZHU Bin: Grey decision-making to improve its innovation in technology partner selection. Journal of Harbin University of Commerce (Natural Sciences Edition), Vol.27, No.1 (2011), p. 3-5

- [4] ZHANG Da-wei, GUO Li-wen, DU Tong: Application of Grey System Theory In Predicting Coal and Gas Outburst, Journal of Hebei Polytechnic University(Natural Science Edition), Vol.31,No.2(2009), p.118-121
- [5] SUN Chao-yuan ,PEN GQi-yuan: Multidimensional Grey Evaluation Model for Suppliers Selection and Evaluation, Journal of Southwest Jiaotong University, Vol.39,No.3(2004),p.277-280
- [6] Schüßler, Florian: Reliability aspects of electronic components & devices for advanced requirements, Circuit World, Vol.34,No.3(2008), p.23-30
- [7] Director of USA Defense Standardization Program Office:SD-22 Diminishing Manufacturing Sources and Material Shortages(2010)

Risk Assessment of Error Forgetting and Omitting of Manufacturing Controller

Jianguo Kong, Huang Liu, Xiaoyu Zheng

Civil Aviation Flight University of China, Sichuan Guanghan 618307

Keywords: Air Traffic Controller (ATC); "Error, Forgetting, Omitting" Phenomenon; Unsafe Event; Risk Assessment; Bayesian Network

Abstract. The objectives of Air Traffic Control are to prevent collisions between aircrafts, including collisions between aircrafts and obstructions, maintain and expedite an orderly flow of air traffic. The controller "error, forgetting, omitting" may lead to traffic conflict, or even more severe consequences. This paper is based on the actual situation of air traffic control operation unit. It systematically analyzes the various causes that result in "error, forgetting, omitting". Then establish a risk assessment model combined with Bayesian network to assess the "error, forgetting, omitting" of air traffic control system, in order to reduce and even preclude the phenomenon that happens.

Foreword

Civil aviation is a high-risk industry whose flight accident rate per million hour's average for 0.4 in the 1950s but now descends to 0.06. However, the flight accident rate per million hours is decreasing while the flight accident frequencies are on the rise. In the 1950s, the average accounts for 1.9 accidents and increase to 3.6 in the 1990s, such increase brings up the flight death toll which always make civil aviation employees and the social public feel anxious and uncertain. Along with the development of civil aviation, the controller workload per hour has increased dramatically, together with ATC shortages and other factors, makes the "error, forgetting, omitting" phenomenon more seriously. In recent years, the controller "error, forgetting, omitting" events happened more than two hundred times. In 2009, Civil Aviation Administration of China mentioned in the work report as: since continuous unsafe events happened ranging from last October, it reminds us that because of the shortages and chronic fatigue of mature controllers, the "error, forgetting, omitting" problems have not been totally solved.

Cause Analysis of ATC "Error, Forgetting, Omitting"

Even a minor error made by ATC may endanger the safety of the aircraft. However, controllers are human beings after all, and humans are inevitable to make mistakes, thus the "error, forgetting, omitting" phenomenon is very likely to happen. From five aspects of management, personnel, equipment, operation and environment, we determine the cause of the controller "error, forgetting, omitting" phenomenon.

Management factor: due to the business training not comprehensive, routine supervision inspection not strict, field management disordered, the allocation of group resources unreasonable, operational procedures irrational, responsibilities not clear, controllers lack such management factors that result in all kinds of risks.

Operating personnel factors: mainly refers to the reasons on physiology, mind and skill of controllers during control process.

Support equipment factors, mainly refers to the lack of support equipment (for example, airport with multiple runways and large flow lacks of field monitoring equipment) and equipment with faults operation.

Control command factors, mainly refers to large flight flow, waveguide crowded, pavement invisible, unclear hand off, operation go against procedures and other reasons.

Environmental factors, includes bad weather, military restriction, complex airport environment and so on.

Risk Assessment Model Based on Bayesian Network

Bayesian Network

Bayesian network expresses variable joint distribution and conditional independence with a graphical structure. It is a directed acyclic graph, consists of node (represents variable) and directed arc which connects the nodes. The node is variable and can be the abstract of any question, and the arc represents the relationship among nodes. The following figure is a Bayesian network:

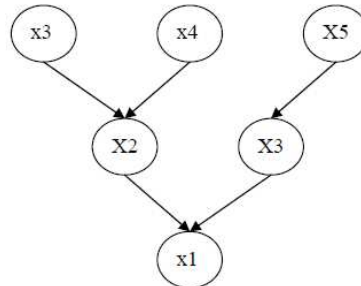


Fig. 1 Bayesian network diagram

As shown in the figure 1: x_3 is the parent node of x_1 , the whole parent node set of x_1 is $\prod_{i=1}=\{x_2, x_3\}$. The directed acyclic graph represents any point set that beyond parent node set $\prod_{i=1}=\{x_2, x_3\}$ of any node x_i conditional independent.

Conditional probability can be represented by $p(X_i | \prod(X_i))$. It reflects the relationship between child node X_1 and parent node $\prod(X_i)$. The joint probability of Bayesian network $p(X_1, X_2, \dots, X_n)$ indicates the product of each node edge probability, that is:

$$p(X_1, \dots, X_n) = \prod_{i=1}^n p_i(X_i | X_1, \dots, X_{i-1}) \tag{1}$$

Causality Chart of Controller “Error, Forgetting, Omitting”

We divide controller "error, forgetting, omitting" factors into two kinds: one is surface factor Z; another is internal factors Y. In Bayesian network, surface factor Z shows no parent node. Build Bayesian network of controller "error, forgetting, omitting" according to the actual condition in control.

Table 1 The classification of internal factors and surface factors

variable name	internal factors Y	variable name	surface factors Z
Y1	human factor	Y0	controller omitting
Y2	environmental factor	Z1	monitoring equipment shortage
Y3	equipment factor	Z2	equipment failure
Y4	control command factor	Z3	bad weather
Y5	controller factor	Z4	large flight flow
Y6	system imperfection	Z5	military restriction
Y7	channel crowded	Z6	improper handling in emergency
Y8	fatigued control	Z7	improper allocation of energy
Y9	control experience	Z8	illegal command
Y10	control skill	Z9	business training
Y11	field control	Z10	staff shortage
		Z11	Emergency and communication

According to the actual situation and statistical data, the matrix of surface and internal factor can be showed as:

$$A_{ij} = \begin{pmatrix} A_2 \\ A_3 \\ A_4 \\ A_5 \\ A_6 \\ A_7 \\ A_8 \\ A_9 \\ A_{10} \\ A_{11} \end{pmatrix} = \begin{pmatrix} & & 0.7 & & 0.4 & & & & & & \\ & 0.6 & 0.5 & & & & & & & & \\ & & & & & & & & & & \\ & & & & & & & & & 0.5 & \\ & & & & 0.7 & 0.3 & & & & 0.4 & \\ & & & & & & & & & 0.3 & 0.8 \\ & & & & & & & & & & \\ & & & & 0.8 & & & & & & \\ & & & & & & & & & 0.6 & & 0.5 \\ & & & & & & & & & & & \\ & & & & & & & & & & & 0.3 & 0.8 \\ & & & & & & & & & & & & \\ & & & & & & & & & & & & 0.7 \end{pmatrix} \quad (2)$$

Among this $i=(2,3 \dots 11), j=(1,2 \dots 11), a_{ij} \neq 0$ indicates Z_j is the parent node of Y_i ; a_{ij} is the degeneration factor which is related to the correlation coefficient of surface factor a_{ij} and internal factor Y_i and mean square deviation.

The matrix of each internal factor, internal factor and Y_0 can be showed as:

$$B_{ij} = \begin{pmatrix} B_0 \\ B_1 \\ B_2 \\ B_3 \\ B_4 \\ B_5 \\ B_6 \\ B_7 \\ B_8 \\ B_9 \\ B_{10} \\ B_{11} \end{pmatrix} = \begin{pmatrix} 1.0 & 0.7 & 0.7 & & & & & & & & & & \\ & & & & 0.7 & 0.5 & & & & & & & \\ & & & & & & & & & 0.4 & & & 0.6 \\ & & & & & & & & & & & & \\ & & & & & & & & & & & & \\ & & & & & & & & & 1.0 & & & 0.6 & 0.7 \\ & & & & & & & & & & & & 0.4 & 0.7 & 0.7 \\ & & & & & & & & & & & & & & 0.4 \end{pmatrix} \quad (3)$$

Among this $i,j=(0,1 \dots 11) b_{ij} \neq 0$ indicates Y_j is the parent node of Y_i ; b_{ij} is the degeneration factor which is related to the correlation coefficient of Y_j and Y_i and means square deviations.

Gauss Bayesian Network Evaluation Model

A variable set $X = \{x_1, x_2, \dots, x_n\}$ is normal distribution. The joint probability distribution is

$$f(x_1, x_2, \dots, x_n) = (2\pi)^{-n/2} |\Sigma|^{-1/2} \exp\left\{-1/2 (X - \mu)^T \Sigma^{-1} (X - \mu)\right\} \quad (4)$$

Variables set μ is n dimension Mean vector of X, Σ is $n \times n$ dimension Covariance matrix. We determine the Inverse matrix W of Σ first. According to $f(x_1, x_2, \dots, x_n)$ can express the product of edge probability distribution of each node, then

$$f(x_1, x_2, \dots, x_n) = \prod_{i=1}^n f_i(x_i | x_1, \dots, x_{i-1})$$

Meanwhile $f_i(x_i | x_1, \dots, x_{i-1}) \sim N\left(m_i + \sum_{j=1}^{i-1} \beta_{ij}(x_j - m_j), v_i\right)$ (5)

m_i is the mean value of X_i , v_i is the conditional variance of X_i when X_1, \dots, X_{i-1} is known. β_{ij} is the degeneration factor when $X_i = x_i$, It is not difficult to get that $\beta_{ij} = \frac{\sigma_i}{\sigma_j} \rho_{ij}$, σ_i is covariance of X_i , ρ_{ij} is correlation coefficient between X_i and X_j . Exceptionally, when $\sigma_i = \sigma_j$ then $\rho_{ij} = \beta_{ij}$. If and only if the variable of x_i and x_j is mutual independence $\beta_{ij} = 0$, Shachter provides for joint distribution method from the above parameters. The recursion formula for inverse matrix W of the covariance matrix

$$W(i+1) = \begin{bmatrix} W(i) + \beta_{i+1} \beta_{i+1}^T / v_{i+1} & -\beta_{i+1} / v_{i+1} \\ -\beta_{i+1}^T / v_{i+1} & 1 / v_{i+1} \end{bmatrix} \tag{6}$$

Type of $W(1) = 1 / v_1$

To the n dimension variables $X = \{x_1, x_2, \dots, x_n\}$ for normal distribution, we divided the distribution $X \sim N(\mu, \Sigma)$ into Y and X two parts. In addition $Y \sim N(\mu_y, \Sigma_y)$ and $Z \sim N(\mu_z, \Sigma_z)$.

Then $E[Y | Z = z] = \mu_y + \Sigma_{yz} \Sigma_z^{-1} (z - \mu_z)$

$$V[Y | Z = z] = \Sigma_y - \Sigma_{yz} \Sigma_z^{-1} \Sigma_{yz}^T \tag{7}$$

The above formulas indicates while Z subset acquiring data $Z = z$, the mean and variance of Y subset will be finally determined. Then evaluate the acquired Y mean. The final evaluation of the goal is $S = \{\text{large risk, biggish risk, medium risk, smaller risk and little risk}\}$. If $s > 4$, that means large risk; If $2 < s \leq 3$, biggish risk; If $1 < s \leq 2$, medium risk; If $0 < s \leq 1$, smaller risk; If $s \leq 0$, little risk.

Risk Assessment of Controller “Error, Forgetting, Omitting”

Initial Value Determine

The initial value of Z subset is $\vec{0}$, Z_i is a real number. Taking value based on the actual situation of each control unit, the greater number shows the greater influence of the factor, and the smaller number shows the reduced influence. Conditional variance takes value based on the following principle:

$$v_i = \begin{cases} 10^{-4} & \text{for internal factor} \\ 1 & \text{for surface factor} \end{cases} \quad (8)$$

While the surface variable related to internal factor is determined, the internal factor becomes the confirmed factor, and conditional variance is small.

Example Analysis

Choose Chengdu Shuangliu airport as an example, determine the Z initial value according to the statistical data and the actual operation situation of Shuangliu airport:

$$Z = [0.4 \ 0.5 \ 1.2 \ 1.5 \ 0.8 \ 0.6 \ 0.9 \ 0.7 \ 0.8 \ 1.3 \ 0.6]$$

Take into calculation, run matlab procedure, then:

$$\text{The mean of } (Y_1, Y_2, \dots, Y_6) = (1.400 \ -0.667 \ 0.001 \ -0.5098 \ -0.6198 \ 0.2000)$$

$$\text{The variance of } (Y_1, Y_2, \dots, Y_6) = (0.3231 \ 0.1000 \ 0.1490 \ 0.2230 \ 0.2010 \ 0.1000)$$

Along with the assignment of surface factor one by one, the internal factor means square deviational is decreasing. It means at present, the uncertainty of controller "error, forgetting, omitting" phenomenon is also decreasing. And along with the assignment of surface factor one by one, the mean value reflects the possibility of controller "error, forgetting, omitting" phenomenon occurring under current condition.

The mean value of human factors causing controller "error, forgetting, omitting" is 1.400, environmental factors is -0.667, as well as equipment factor is 0.001, while system imperfection is 0.2000. From the controller "error, forgetting, omitting" causality chart, we can conclude that the eventual factors that lead to controller "error, forgetting, omitting" are human factors, environmental factors and equipment factor. According to the evaluation standard, human factors belong to medium risk. The rest risk factors are smaller or little risk. We can regard the whole risk level of Shuangliu airport occur controller "error, forgetting, omitting" is medium, which still needs to strengthen the system construction and improve the risk management.

Conclusion

Through the cause analysis of controller "error, forgetting, omitting", this paper analyzes its impact on control operation and flight safety, and establishes a suitable model to evaluate the risk. The evaluation helps to find out the factors that lead to controller "error, forgetting, omitting", then improves the situation according to these specific reasons. Thus reduces the probability of unsafe events caused by controller "error, forgetting, omitting", and benefits the whole ATC system security and healthy development of civil aviation industry.

References:

- [1] Zhou Qiwu, Control work "wrong forget leakage" the reasons and countermeasures, << civil aviation political work >>. 2009. The first period
- [2] Li Fuxing, Fuzzy mathematics method and application [M], tianjin: tianjin science and technology press, 1993
- [3] Hang Li/Mei He/Lu Yumei, AHP-the fuzzy comprehensive evaluation method of analysis and study [J], China security Science report, 2004.14(7):86-89
- [4] 2007 flight accident, aviation ground accident and flight sickness accident statistics, the civil aviation administration of aviation security office, 2008.5.8
- [5] Yu Xiangxun/Xiong Sunchu, System engineering course, Beijing: tsinghua university press, 2006:220-237

- [6] European Air Traffic Control Harmonisation and Integration Programme. Guidelines for Developing and Implementing Team Resource Management. 1996.3.15
- [7] Flight Safety Foundation ICAO circular Flight Safety Digest August-november 2000
- [8] Brenlove M S. The air traffic system: a commonsense guide. Iowa State Press, 2003
- [9] A Plan for the Future 10-Year Strategy for the Air Traffic Control Workforce 2009-2018, FAA Air Traffic Organization
- [10] The Aviation Safety Information Analysis and Sharing (ASIAS) System

Green Agricultural Products Supply Chain Management Mode under Low Carbon Economy

Luo Fenglan

Jiangxi Science and Technology Normal University

Nanchang, Jiangxi, China

E-mail: luofenglan@hrsk.net

Keywords: Green Agricultural Products, Supply Chain Management, Low Carbon Economy

Abstract. The key is to make integration of the supply chain system, lower the cost of agricultural products in the international market, improve the competitiveness of agriculture products and increase the income of the farmers from the supply chain. This paper the concept of agricultural products of agriculture products. The characteristics and supply chain are discussed in the paper. Then, this paper analyzes the agricultural supply chain model based on supply chain management. Finally, this paper puts forward the establishment of China's agricultural supply chain solutions. The purpose of this paper is to help develop agricultural supply chain.

Introduction

China is a large agricultural nation, the problem of agriculture, countryside and farmers, is a strategic opening policy and economic development. This is a long-term problem in the process of modernization. Reform and opening up, China has undergone tremendous changes in rural areas. Agricultural output has greatly increased and agricultural output by shortages, already the rest of the stage. However, agricultural output has increased rapidly, the farmers' income, has not been raised either. This phenomenon is hard to sell their products can always be seen, circulation field has become the bottleneck, increase the income of peasants. At present, the agricultural supplier of agricultural supply chain logistics level in China is still very low, so it means that many developing agricultural supply chain improve agricultural supply chain management and develop the rural economy and increasing the farmers' income [1].

The Supply Chain and Agricultural Supply Chain

Today, the concept of supply chain has been paid more attention in the chain of relationships, net core enterprise supply chain in the core business, through the control information, logistics, capital flow, from the raw materials and intermediate products and agricultural products, in order to sell the final product to consumers hand sales network [2]. This is a network chain structure model from suppliers, manufacturers, distributors and retailers and consumers. Through analyzing the meaning, characteristics and development of agricultural products, and puts forward the concept of agricultural supply chain. This is a network chain structure made of agricultural suppliers and farmers and agricultural production and agricultural product processing enterprise, wholesalers, retailers and consumers, through the farm the control of flow, logistics and cash flow from purchasing raw materials, intermediate, the quality of products and finished products to the produce of the sale into the hands of consumers sales network [2, 3]. Building supply chain, always have a dominant force connection all aspects of the supply chain. The leading force in the supply chain is the company's core business. It can become manufacturers, suppliers, vendors or distribution center. Supply chain is network and upstream and downstream enterprises in the core business.

Agricultural Supply Chain Characteristics

Agricultural production in the process of production obviously depends on the forces of nature, natural conditions and crop individual life. Fresh produce is often; it is very prominent regional, season and dispersion characteristics; meanwhile, fresh produce is the requisite of the life, and its

demand elasticity is small, consumer characteristics of universality and dispersion [5, 6]. Because, on the basis of characteristics described in the context of agricultural supply chain is different from industry, and the agricultural supply chain has following features.

The high asset specificity of agricultural supply chain Because it is fresh, perishable, and agricultural and sideline products circulation field has taken some control measures to ensure that it meets the quality requirements will enter the consumption. And then it has special characteristics in the field of infrastructure, storage conditions, transport and the technical method. In storage, transportation, must adopt a series of measures, such as low temperature, dry, moisture proof and material, in order to ensure the value of agricultural products. To do this, it needs to support hardware measures, such as special warehouse and transportation equipment, wharf, special mode of transportation and processing equipment.

The large uncertainty information of agricultural supply chain Because the location of agricultural production and consumption is very fragmented market information, which led to high dispersion and it is difficult to fully grasp the market demand. In addition, agricultural production is seasonal, fresh and easy to decay. Then it causes the market price fluctuations. Facing the volatility of the market, farmers tend to receive an error message for blind production.

The weakness of farmers market China is a large agricultural nation based on family small farmers; it can with low per capita resource. Most agriculture de-centralized production. Other scattered peasants as the main body of the market are weak. In the small farmers as the main body of the country, no cooperation agricultural co - get photographs, community based organization, bargaining ability is very low, scattered peasants and their interests are not protected.

Connecting randomness and structure instability Agricultural supply chain structure characteristics are: randomness, change the composition of joining the node, then changing the level and width of the chain. Including change peasant behavior and the market price, natural disasters and other factors of agricultural supply chain frequent often leads to restructuring. Agricultural supply chain structure is very fragile, easily the risk of fracture.

Chinese Low-Carbon Economy Policy Status Quo

The low-carbon economic policies focus on the task from the overall sides to co-ordinate the development. The Chinese government has realized that the development of pollution-based on low-power and low-carbon economy will be not only the overall trend in the world but also is an achievement strategic to adjust to the national efforts .So they drew up a lot of policy.

Goal of Chinese low-carbon economy policy Chinese low-carbon economy in the overall policy objective is the development direction of strategic objectives programmatic guidance, and gradually down to all fields. Such as specific to the <Law of the People's Republic of renewable>policy objectives: "By 2020 renewable energy in Chinese energy structure, the proportion reached 16%, guidance from the industry, price, total goals, tax subsidies, All details of special funds for renewable energy development to support and detailed. "[1] Refinement of the policy objectives of such a method allows a low-carbon economy in China is not only the general direction of rules to follow, the specific objectives detailed in the policy process forward also played a significant role, accelerate low-carbon economy in China Development.

Chinese Low-Carbon problem policy experiment - low carbon cities and some construction of pilot in low-carbon areas In recent years, many cities have put forward the goal of building a low carbon city; also have low carbon in the implementation of pilot projects across the country. Experimental low-carbon and low-carbon city has become a common pursuit of cities, urban construction, the promotion of harmony between man and nature.

Problems in Chinese Low-Carbon Economy Policy

Although Chinese low-carbon economy has achieved progress, but not that low-carbon economic policy formulation and implementation process is perfect, impeccable. After all, everything is still in its infancy, Chinese low-carbon economy policy, there are still many problems.

Policies to adapt to conditions of low-carbon economy to be sophisticated level Low carbon economy is the consensus of most countries, but different stages of development in different countries, on the understanding and realization of low-carbon economy are not the same path. As a developing country, development is still the top priority; the development of low-carbon economy must be closely combined with the own stage of development and special conditions. Many energy-intensive industries in China, the short term can not immediately reverse the situation, by the replacement of advanced energy-saving equipment such as changes in industrial structure can only be recommended gradually, so Chinese low-carbon economic policy, for most of the "high energy" and enterprises will be a devastating blow.

Overwhelm input method of low-carbon economy policy In China, a lower degree of differentiation of social structure, expression and synthesis of social interest is not borne by a variety of social structures, but by the power elite within the political system through analysis, research and investigation, identified by their input to the public interests of society policies. "Input" concept originally from the book of Easton's <systematic analysis of political life>. The Chinese scholars, Hu Wei borrow "input" the notion that "input" which means the society does not benefit a wide range of conditions in the <government process>, carrying out by the government elite interests of the people instead of the synthesis and expression, the characteristic performance as a political compromise between the power elite, rather than multiple decision-making of Government interaction. [6]

In the low-carbon economy, policy issues, the low level of public participation, government policy rarely makes public participation in policy-making process at best is finished, a small amount of public comments for "fine tuning" such a low The introduction of carbon policy, not a good guarantee can express the majority view, cannot consider the extent of its scientific and reasonable.

Low-carbon policy is not stable and most of the carbon in the pilot stage not be promoted Chinese low-carbon policy making has not reached the long-term stability, a few years the same level. This may be adjusted at any time of low-carbon policies, making those in the reform of the reform or about to carry out low-carbon businesses fear after the policy change, loss of interest, but has been reluctant to reform a low carbon economy.

Chinese Development Strategy on Low-Carbon Policy Making and Feasibility of the Path

Low-carbon system decisions more scientific and democratic and legal reform in Chinese political system is an important content of policy science research topics. With the deepening of economic globalization, low-carbon, of science and technology, comprehensive national strength in increasingly competitive, countries are increasing emphasis on low-carbon policy formulation and development of science, so that they can better seize opportunities, meet challenges, and develop Growth. Chinese policies on low-carbon economy are in its infancy; scientific and reasonable mechanism for the formation of public policy will be for low-carbon economy in Chinese development and lay a firm foundation.

Low-carbon economic policy strategy the basic task of policy-making strategies is to use analysis or research tools to find actionable solutions to solve the problem. Innovative mechanisms for the establishment of policy, the Government take the lead in guiding and play an active participation of the masses of low-carbon economy is to be more scientific policy-making, help to improve the efficiency of policy implementation in future.

Promote the policy innovation and establish creative mechanism in policy systems. Establishment of mechanisms for policy innovation is a prerequisite for policy innovation. Macro unifying and comprehensive understanding of the situation is the basis for policy innovation. Therefore, local governments should be grass-roots level, good at listening to the voice of the people, the right to guide promotion. For example: "the use of biogas in rural areas and promotion of the government at the grassroots level need to be widely publicized among the public and strengthen promotion efforts." [7] At the same time, to bring together the practical, creative work, the policy of the central carbon integrates with local characteristics.

The Government takes the position of lead guide, building the low-carbon the government first. Mainly carbon dioxide greenhouse gas emissions caused global warming and the consequent variety of ecological problems, economic problems and social issues, often inter-regional issues. This problem and integrated the public needs to have a certain authority and certain macro-control in order to effectively address and resolve. In addition, low-carbon business, as the project capacity, long cycle, investment, government-led management is therefore the most appropriate form.

To increase public participation and overcoming the excessive of the "input" policy model

The establishment survey system is necessary. Through opinion polls, promote the Government's policy for people's understanding and support to ensure that policies in line with public opinion. Development issues in low-carbon economy, increase public participation, information disclosure and media involvement are conducive to the development of low-carbon economic policies more scientific and democratic.

The feasibility of implementing a low carbon path to economic policy Onto the government agenda from the low-carbon policies, to establish the program planning, to legitimize the policy issues are involved in the feasibility of the path. The original intention of a good policy to carry out the smooth implementation of the feasibility of a path with the scientific and rational development is inseparable. Therefore, the establishment of pilot projects for carbon it is very necessary. This will not only be able to narrow the scope of the study, but also to the success or failure of a timely summary of the experience, to facilitate promotion.

To tracks the work of the pilot survey of low-carbon city, conclude and promote success examples

"At present, China established in Shanghai in 2009, two low-carbon city of Baoding ongoing experimental works." With the development of low carbon, low carbon urban policy should be gradually extended, in the typical areas of each country pilot work, and regular research group to collect relevant information and data, using scientific methods to analyze policy, summed up the success and shortcomings. Follow-up survey for low-carbon cities, the model for its progressive development and analyzed the future trend of its development budget.

To establish the cycle of low-carbon economic policy-making mechanisms to exert all levels of superiority

Strengthen and improve the implementation of relevant policies low-carbon economy, involving Government, Market and Social several levels, the complex variety of factors, systems engineering, in addition to political oversight of public power and control mechanism, the concept of awareness of government and society, the government law enforcement capacity, technical level, market development situation and their own governance structure and other basic conditions, but also to strengthen policy formulation - implementation - assessment - feedback - policy change - and then implement - re-evaluation - and then the feedback - and then change the policy cycle mechanism, and constantly improve relevant policies, which also include supporting the development of norms.

To develop the low-carbon economic policies with the use of scientific and rational principles in quantitative and qualitative analysis

Before the introduction of a policy to be defined on the body, and then confirmed after the implementation of low carbon policy wants to achieve, design-related programs. Their implementation of the study area to conduct field research, the use of relevant data, the establishment of relevant models, an expert team seminar programs, low-carbon policy making on major issues but also held a hearing to solicit the views of the people to finalize the program. In the meantime, qualitative analysis of the use of policy methods (such as experts predict that method, Delphi method of law and other related logistics game) will increase the policy of the professional and scientific level. To establish the national low-carbon publicly available information system, and strengthen policy advocacy

The promulgation of these measures involves a wide range; specific and detailed, information can be imagined. Moreover, low-carbon policy options cannot be spontaneously accepted, but cannot automatically be executed. Policy-holders are that people's practice, low-carbon economy policy should have been implemented successfully, and the target group must first have an understanding of low-carbon economic policies.

Countermeasures

In engineering point of view to understand agricultural logistics: agricultural logistics is an important part of rural logistics, while rural logistics is part of the modern logistics; rural logistics should be closely connected with practice, rather the urban logistics, they must not be separated.

Further enhance the understanding of agricultural logistics: improve agricultural logistics is a important content, as well as constructing harmonious society and socialist new countryside, and its premise is that the government should give the policy support, etc, funds, personnel, infrastructure construction, building rural circulation system, construction of information network.

Only applications supply chain management theory can give people hope to China's agricultural logistics. The domestic existing application management less systematic and some overseas practice is not suitable for China's national conditions. Therefore, we have to take energy learn how to use the supply chain management system to solve some practical problem.

Develop core enterprise in our agricultural logistics supply chain. According to actual condition, the formation of logistics operation mode, such as "production enterprise + peasant" and "wholesale enterprise + farm households", "retail enterprise + peasant" and "distribution center and peasants", etc. Utilize JIT, VMI SMI and other supply chain logistics management technology innovation of small and medium-sized enterprises, and by using the collaboration of the coordinated logistics, joint distribution, sharing logistics network solving problems, like scattered peasants and distract the logistics. Supply chain core enterprise form can be considered from the following aspects: the existing agro - or management enterprise; allow other township enterprise; Farmer cooperative organizations; the state-owned sector, in the rural areas have considerable basis postal sector and other units.

At present, some units, such as China postal logistics company by use of the conditions of the rural postal department logistics business activity in some existing agricultural products. Countries should give great support, and it deserves further study the application of supply chain management to expand the business and reduce the cost and improve the economic benefits.

Experience abroad, actively promotes "farmer cooperative organizations", to improve the efficiency of agricultural logistics.

It can improve agricultural logistics support of national industry, for example, car makers, design, manufacturing cars should be suitable for rural both in price and performance.

References

- [1]. Sunil Chopra, Peter Meindl. *Supply Chain Management: Strategy, Planning, and Operation*. New York: PrenticeHall, Inc, 2008.
- [2]. Harrison, A. *Logistics Management and Strategy*. Pearson Education Limited, 2009
- [3]. Fangtao Jiang, "Research on the Creative Model of the Rural Supply Chain of and Strategies," *On Economic Problems*, no.12, 2009, pp: 81-84
- [4]. Min Zhang, "Based on the Core Business of Agricultural Product Supply Chain Analysis," *Logistics Technology*, no.5, 2004, pp: 91-94
- [5]. Juan Li, Shaochuan Fu, "Establishment and Game Analysis on Chinese Agricultural Supply Chain Model," *Logistics Technology*, vol.28, no.8, 2009, pp: 108-111
- [6]. Xiaosheng Li, Limin Yang, Liangyi Bai, "Supermarket-led Supply Chain of Fresh Agricultural Products," *Lanzhou Academic Journal*, no.9, 2009, pp:76-78
- [7]. Zhaoyun Liu, Shimin Sun, Jiyong Wang, "The Trend of Agricultural Supply Chain Management in China," *Commercial Research*, no.3, 2009, pp: 161-164.

Research on Active Aided Knowledge System Push-Pull Technology Oriented the CAPP

Xiai Zhang^{1, a}, Ran Li^{1, b}

¹School of Mechanical Engineering, Hebei University of Science and Technology, Shijiazhuang, China

^azkzxa@163.com, ^bliran_li0@163.com

Keywords: CAPP; the Active Aided Knowledge System; Pull Technology; Push Technology; the Aided Knowledge

Abstract. According to the quick updating of contemporary knowledge and the long learning process for the machinery technologists, this paper sets up an active aided knowledge system oriented the CAPP. On the basis of the knowledge base, the system provides relevant knowledge for the machinery technologists. The technologists can pull the information and this soft not only pushes information customized, but also determines knowledge demanded in order to send the lack of knowledge for the machinery technologists. The active aided knowledge system oriented the CAPP will reduce the machinery technologists' burdens, improve the utilization of knowledge and focus technologists' energy on the creative thinking.

Introduction

With the development and the application of computer technology, information technology, automation technology and Internet technology, the market environment of modern manufacturing is undergoing significant changes^[1,2]. The update cycle of the knowledge of machining technology is becoming shorter and shorter, and product requirements for knowledge are getting higher and higher [3]. However, the data of machinery product and technical information often can't meet the requirements of the effective use of knowledge resources in the design process of machining technology. Therefore the paper proposes to build the active aided knowledge system oriented CAPP, which combines push technology and pull technology together. The system creates the platform of the learning, using, sharing, and innovation of knowledge, and promotes the precipitation, transformation, transmission, and inheritance of the knowledge, and reduces the mental labor cost.

The Overview of the Active Aided Knowledge System Oriented CAPP

The CAPP (Computer Aided Process Planning) uses computer to formulate the parts processing process and process the blanks into the parts required on the engineering drawings [4]. But, in the process of computer aided process design, the required knowledge is scattering, empirical, complex, which make a lot of difficulties for the machinery technologists. Because of the loss of knowledge and the lack of the computer aided system based on efficient professional theory and rich basic data, the machinery technologists still need all kinds of thick process manuals [5]. Based on the above reasons, the paper proposes an active aided knowledge system oriented the CAPP. The system provides targeted active aided knowledge for the machinery technologists and solves problems which may be caused by the lack of experience in the process of computer aided process design.

The active aided knowledge system bases on pull technology, push technology, and "pull-push" technology, in order to provide the required knowledge of completing the task or decision-making for machinery technologists. In a practical task or decision-making process, the system can guide the machinery technologists whose knowledge has defects or irrational structure and maximally reduce the learning burdens. The active aided knowledge system alleviates mental intensity, and realizes the inheritance of the knowledge of experts' experience. The system uses Dreamweaver8.0 to set up the JSP page, which realizes the interface design; the database uses Microsoft SQL Server 2005 to establish the knowledge base; Myeclipse8.5 tests and perfects the functions of the system (Fig. 1 the Structure of the System).

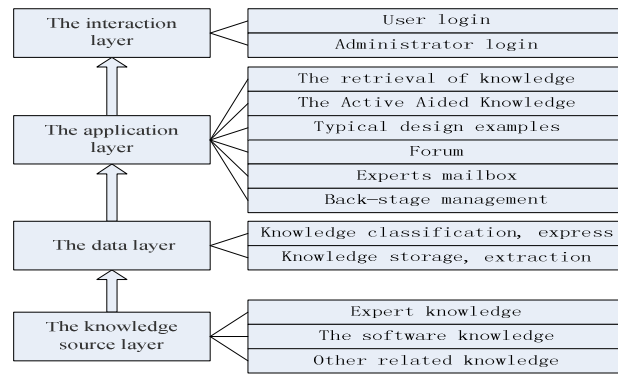


Fig. 1 The Structure of the System

The Push and Pull Technology Research of the Active Aided Knowledge System

The Knowledge Base of the System

The database is the foundation of the active aided knowledge system oriented the CAPP. The database divides the levels basing on the tree structure. Fig. 2 is the picture of the knowledge classification of machining technology domain and the structure of the database. The knowledge classification of machining technology domain is one-to-one corresponding to the classification of the content of the knowledge base.

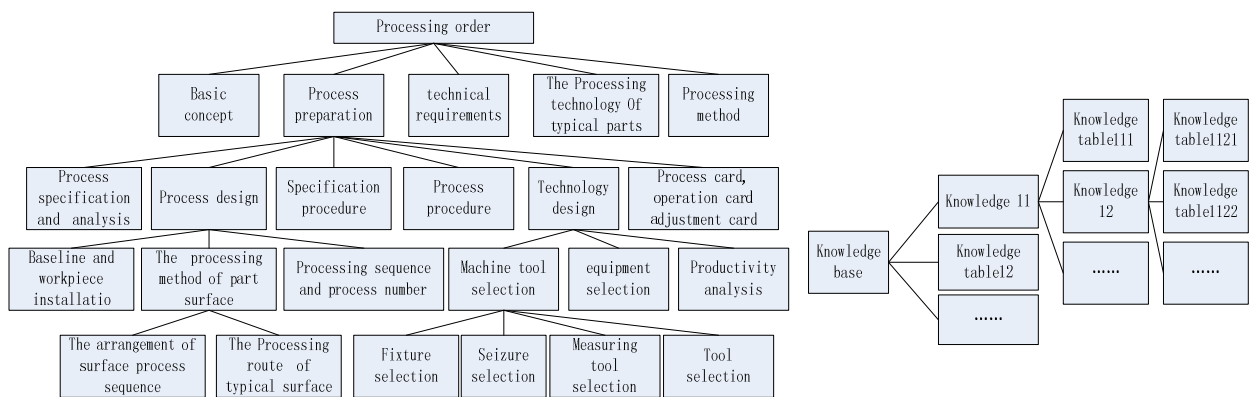


Fig. 2 The Knowledge Classification of Machining Technology Domain and the Structure of the Database

Research on Push Technology and Pull Technology under Active Assisted System

Knowledge providing is a main content of the knowledge management services, aiming to make users get necessary knowledge resources fast and convenient quickly and conveniently. It is divided into technical knowledge supply based on the pull technology and technical knowledge supply based on the push technology [6].

Pull technology requires users to extract information from "database" actively (Fig. 3). Main advantage: users check and search for required information according to their own needs, the task of the information source is light [7]. But the information system can only passively accept the inquires, and provide the user's requirements information; when the source of information is newly changed, it is difficult for the users to pull new dynamic information in time; high demand for users, and it requires the user having corresponding professional knowledge of source system and grasping inquiring technology. In the active knowledge auxiliary system oriented CAPP, the machinery technologists can choose the whole field or field of classification to query in pull type. To avoid knowledge points missing owing to improper use of keyword, the system adopts the fuzzy inquiring way, displaying the search results according to the update time of knowledge content.

Information is actively sent to "user" from "database" in push technology (Fig. 3). Main advantage: it promptly provides dynamic information to the user; low demand for users, it is widely used in the general public, and does not require the user to have special technology, can meet the user's personality requirements. Weakness is that the network load is heavy and pertinence is poor.

Push technology, as a quick and highly effective information acquisition method, is the effective way of solving the problem of obtaining information [8,9]. In the active knowledge auxiliary system oriented CAPP, the machinery technologists can choose push-type auxiliary in child classification. When a the machinery technologist logs the system, the system immediately push the set knowledge units for the machinery technologists, and the machinery technologists can modify the scope of knowledge provided by push-type auxiliary.



Fig. 3 Pull Technology and Push Technology

Research on Pull-Push Technology under Active Knowledge Auxiliary System

Information pushing technology combines with pull technology. These two technologies can complement each other, timely and actively push the latest information to the machinery technologists. "Pull-Push" type knowledge auxiliary contains two parts: knowledge detection and knowledge auxiliary. Knowledge test realizes the information recommendation according to choosing examination scope; knowledge auxiliary realizes information recommendation according to the test results; knowledge inspection affects knowledge auxiliary effect (Fig. 4 Knowledge Test and Knowledge Auxiliary)

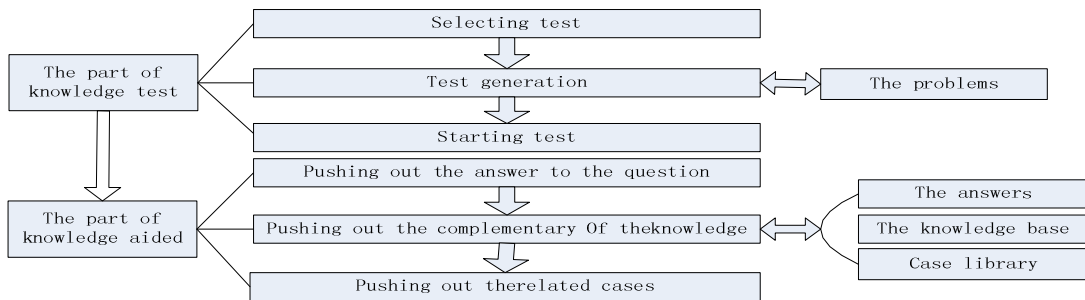


Fig. 4 Knowledge Test and Knowledge Auxiliary

Group Volume Scheme

Group volume scheme includes two ways. The first, the system randomly extracts questions in any number from knowledge base, which can thoroughly investigate the machinery technologists' knowledge structure. The second, the machinery technologist can also set content and number of the subclass of test knowledge. According to these conditions, the system can provide the required questions, if not, the system gives conflict or unreasonable suggest in search range (Fig. 5 Table for Paper-Problems Relations). The first method, the system sets the fixed number of the extraction problem and the total number of abstraction problem; the second method, the machinery technologists can choose knowledge subclass number of abstraction question and the total number of abstraction question. If you don't choose the number, it extracts according to the first method set. In the group volume scheme, different knowledge subclasses can't cross, so that it can guarantee complex group volume scheme, and it does not appear repeated theme according to the record of the group volume scheme.

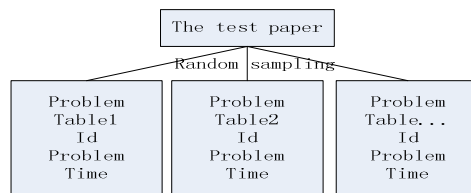


Fig. 5 Table for Paper-Problems Relations

The Testing Process

The machinery technologist selects the basic information of the test paper and submits the selections to the system. When the system groups the test paper, it initially checks whether the programs of the test paper are less than three or not. If the programs of the test paper are less than

three, the system will prompt the machinery technologist to set up basic information of the test paper again, otherwise, the test papers will be prepared. The test paper is randomly selected m records from n records ($m \leq n$) and generated the test paper automatically.

The Auxiliary Process

If the machinery technologist submits the answers to the module of the detection, according to the machinery technologist's answers, the system will actively provide the knowledge assist, pushing the answer to the question and the highly associated knowledge unit to machinery technologist. Due to human factors and random factors, the system uses gray theory to determine whether the test points needs active auxiliary or not, improving the reliability and validity of the detection parts [10].

The Implementation Process

The implementation of the knowledge assist is based on the design of the database. The database establishes knowledge unit tables, the question tables, the answer tables. The different categories of the knowledge of machining technology are corresponded to different knowledge unit tables. The label "id" in knowledge unit table has two implications: First, the label of the content; second, the category of contents. Knowledge base achieves the correspondence of questions and answers by setting out key between the id of the problem table and the id of the answer table and completes the one-to-many association of the highly related knowledge unit by setting foreign key between the id of the problem table and the leibie field of the knowledge unit table. It interrelates between tables owing to the function of the foreign key; it makes the content of the knowledge unit more concrete owing to the classification of knowledge (Fig.6 the Diagram of the Knowledge-Question-Answer Relationship).



Fig. 6 The Diagram of the Knowledge-Question-Answer Relationship

Summary

The system is the active aided knowledge system oriented the CAPP with four layers: the interaction layer, the application layer, the data layer and the knowledge source layer. The active aided knowledge system perfects the combination of pull technology and push technology. The machinery technologist can search the contents needed or gain the knowledge which is required and judged by the system. The active aided knowledge system oriented the CAPP helps the machinery technologists to complete the inference learning, realizing the high-end technology application at low starting point, and form a companion software for the computer-aided process design software gradually.

References

- [1] Gu xinjian, Zhang dong, Ji yangjian, Chen jixi, Tang renzhong, Qi guoning. Integration for Manufacturing Servitization and the Manufacturing Informationization. 2010 Modern Manufacturing Integration Technology Conference Proceedings 822-831 (2010)
- [2] Wang siyuan. Construction of manufacturing information technology building blocks: the Uniform Code. China Management Informationization 14(16).98-99 (2011)
- [3] Ge peng-fei, Jiang cui-qing, Ding yong. Study on integration of knowledge and business for collaborative mechanical product design. Machinery Design & Manufacture (12).261-263 (2011)

- [4] REN yu-zhu. Application of CAD / CAPP / CAM in design & manufacture process of mould, MACHINERY DESIGN & MANUFACTURE (5):233-235 (2011)
- [5] Zhang pei. The Design and Implementation of Common Digital Manual Development Platform. Xi'an: Xi'an University of Technology, a master's degree thesis in 2009
- [6] Woitsch R, Karagiannis D. Process-Oriented Knowledge Management Systems Based on KM-Services: The PROMOTES Approach. Karagiannis, Reimer U. (Eds.), Berlin Heidelberg: Springer-verlag 398-412 (2002)
- [7] Wei ying. The Analysis on HEI Library Service Modes based on Push Pull Technique [J]. ENTERPRISE SCIENCE AND TECHNOLOGY & DEVELOPMENT (6):37-39 (2010)
- [8] Adam Anthony. The Relational Push—Pull Model: A Generative Model for Relational Data Clustering. Proceedings of the Twenty-Third AAAI Conference on Artificial Intelligence 1841-1842 (2008)
- [9] Rashid H. Language of Change: Dynamics of Push-Pull Communication. Unpublished, Case Western Reserve University, Weatherhead School of Management Executive Doctor of Management Program 71-72 (2007)
- [10] Xue guo-qiang, Wang yi-chun, Miao chang-chun. Construction Supervision and Control of Prestressed Continuous Beam Bridge Based on Grey System Theory. Journal of Water Resources Architectural Engineering 9(4):72-75,84 (2011)

Tech-Application for Excess Energy Supplement to Cut Cost In Pump Station

Zhangyasheng, Lixinming, Chenyao, Zhanglisha and Jiayubao

HuaBei Petroleum Corporation, RenQiu, HeBei, 062500

Keywords: Energy Superposition, Excess Pressure Utilization, Centrifugal Pump, Saving-Power

Abstract. The successful practice of benefit reducing supplying water cost, Thus the water plant has stressed to issue on saving power, water conservation, cut water cost, increase economic return, promoting pump efficiency from applying additional energy technique to centrifugal pump in Renqiu number 7 supplying water stations.

Introduction

In the wake of developments in oilfield going into mid-later period production, there are a great change in water demand supply with adjustment of exploiting technology, the manage model for water supply has been changed due to early production water transfer to living water mainly. Thus the water plant has stressed to issue on saving power, water conservation, cut water cost, increase economic return. No.7 water station is key position around water supply system in oilfield, which produce 532.3million cubic meter of water compare with water plant 1298.5 million cubic meter of gross water supply annual, account for 40.9 percent of gross water offered by water plant, this station has greater saving energy potential due to higher energy consumption of 68.95 million cubic meter annual.

The method of operation at No.7 water station: lifting water from water source well

(First class pumping station)->holding tank of water,centrifugal pump pressurized in (second class station) -> system water network-> third class pressurized station-> consumer.

Basic principle of power-saving technology improvement to surplus energy

The Technology for excess power refer comprehensive subject of hydraulics and hydrodynamics, which contain new mind of power-saving and economic running. That the technology boost suction pressure of water pump by means of excess energy given from upper pump device through technique progress and on the base of pump positive pressure, improving intake amount of energy of blade wheel to depress pump net head lift accordingly.

According to computing theory of water pump input power.

$$N_e = \gamma QH / 102 \quad (1)$$

γ —water proportion 1000kg/ m³

Q —flow rate of water pump m³/h

$$H = H_j + SQ^2 \quad (2)$$

H_j —net head lift of water pump

SQ^2 —resistance feature of pipeline

$$N_s = N_e / \eta_p \quad (3)$$

$$N_p = (N_s / \eta_t \eta_m) \times K$$

By Computing Formulary: Ne dropped, NT decreased yet.

It is known that water pump running feature compare according to front and back additional power: the water pump occur obvious variety compare running feature with before and after power addition.

Based on power calculation of water pump:

$$Ne_1 = \rho g Q H_1 / 1000 \eta_1 \eta$$

$$= 1000 * 9.8 * 0.28 * 41 / 1000 * 0.99 * 0.76 = 149.52 kW$$

$$Ne_2 = \rho g Q H_2 / 1000 \eta_1 \eta = 1000 * 9.8 * 0.28 * 26 / 1000 * 0.99 * 0.76 = 94.82 KW$$

Come to a conclusion according to different running condition, computing result of active power:

Effective head lift dropped 15 meter as water pump running.

Net head lift of water pump decrease along with intake up pressure P_2 , and that keep stable pressure in pipe network system, due to saving power theory of frequency converter, reducing output power of electric motor and decrease power exhaust in water supply.

Implement technical improvement for excess power supplement project

There are total 14 water source well used for delivery of water to inside Renqi No.7 water station till now, equip with sum to 6000 cubic meter of holding water tank, two piece pipe extend out from pump station which supply to user and water network respectively. Operation mode is to feed water storage tank by submerged pump drawing underwater, the surplus pressure of submerged pump is around 0.1Mpa, and then the pressured water is transmitted to user by centrifugal pump suction from storage tank, pressure of water network kept is 0.15 to 0.2Mpa.

Through contrast analysis, the amount of energy waster cases was discovered during.

supplying water in water station: about 5 percent of energy loss discharged inside storage pool (tank) while submerged pump lift water from well, surplus energy discharged to tank, next starting from zero Mpa, the centrifugal pump pressurize water into system network, 70 percent of water amount are carried to third class pump water tank (pool), the rest energy was used up again inside tank on which 20 to 30 percent energy loss was wasted.

Fully make use of excess pressure given by submerged pump and centrifugal pump.

Applying part of energy to next pump intake for reducing head lift of centrifugal pump, meanwhile decrease size of storage tank volume in order to receive purpose of saving energy. In terms of theoretic calculation and practice test, surplus head lift indicated is about 10 meter, obviously so many of head lift capacity was worthless exhausted within water tank rather than to be utilized fully.

Through analysis of previous running data for Ren No.7 water station, be aware of water level in the tank show 6 meter height, by means of potential energy the centrifugal pump suction with positive pressure, if water pipe will be connected between input pipe and output pipe in storage tank, when centrifugal pump water supply less than amount of water offered by water source well, feed water to storage tank and centrifugal pump by means of water source well, when centrifugal pump output water exceed input water from water source well, provide water with centrifugal pump depend on common water supply of water source well and storage tank.

In this way fully utilize excess pressure given by water source well and submerged pump, apply surplus energy to pump intake for reducing head lift and to improving inlet pressure of the water pump, keep 10 meter of inlet head lift to intake of pump. As a result of raise intake pressure of centrifugal, as long as supply water pressure is not change, that pumps net head lift decrease, electric motor output power drop, reach goal of saving power.

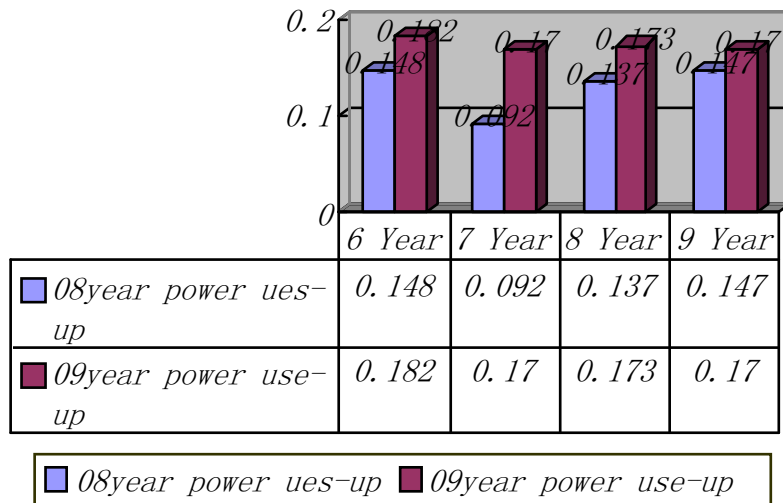
On March of 2008, with improvement subject was implemented, adjustable control valve was installed between main pipe from Number 3 water tank connected with intake of centrifugal pump and main inlet pipe of centrifugal pump during implement of improving project, that make end excess pressure of first class pump extend to centrifugal intake in order to raise import energy and decrease input power of centrifugal

Economic and efficiency analysis:

There is remarkable achievement of saving power via 4 month of practical operation, effective power consumption get to drop contrast to that of corresponding period, specific data see figure below:

Power consumption contrast table in 2008, 2009 year

Time (Year-Month)	Water supply (m ³)	Walt for pressurized (kW·h)	Supply-water Power use up (kW·h/m ³)	Remarks
08-6	380507	69386	0.182	Date tested
08-7	383079	65451	0.170	Date tested
08-8	318066	55142	0.173	Date tested
08-9	334214	56762	0.170	Date tested
09-6	348737	51748	0.148	Date tested
09-7	328954	38631	0.092	Date tested
09-8	314752	43164	0.137	Date tested
09-9	383789	56566	0.147	Date tested



From above figure showed: power consumption pressurized has different degree decrease contrast to that of corresponding period of 6,7,8,9 Month, even range of decrease up to $(0.17 - 0.092) \div 0.17 = 45.9\%$, saving power accumulated till to 07 Year 09 Month is:

$$11857 + 25658 + 11331 + 8827.2 = 57673.2 \text{ kW}\cdot\text{h}$$

It calculated in accordance with tariff 0.588 Yuan/degree: $57673.2 * 0.588 = 33911.8$ Yuan.

Average monthly amount of saving energy is around $14418.3 \text{ kW}\cdot\text{h}$.

Predict yearly saving cost is 101700yuan/Y.

Conclusion

Summarized above statement, since the technology for excess energy supplement has been applied to water station, effective saving power is exact great, this subject is a creative technology for saving energy in water supply system, and it has broad developing.

Future, this technology will be gradually promoted application in other water station, which is helpful for rising operation ability and reducing water supply electric energy.

Reference

- [1] “Water pumps and pump station“, wrote by liuzhuxi. Published by hydraulic and electrical press, hydraulic,saving energy document etc.

Optimizing and Simulating Production Line Balance Based on Human Factors

Puhong Li^{1,2, a}, Zhijun Fan^{1, b}, Jun Zhou^{1, c}, Jianxin Deng^{1, d}

¹School of Mechanical Engineering, Shandong University, Jinan 250061, CHINA

²School of Art Design, Shandong Polytechnic University, Jinan, 250353, CHINA

^aLipuhong@126.com, ^bfanzhijun@sdu.edu.cn, ^czhoujun@sdu.edu.cn,

Keywords: Optimizing; Simulating; Production Line balance; Human factors; Manufacture system

Abstract. In this paper, combining quantitative human factors load with production line balance (PLB), a set of systematic methodology is developed. Firstly, after analyzed the importance of human factors, the evaluation of those is briefly introduced. Then, a model of PLB considering human factors is developed, whose objectives are to minimize the workers number and smooth the human factors load in one cell/worker. Finally, a piston production line as an example is to optimize and simulate by Quest. The optimizing and simulating results indicate that considering human factor load of each process/task can make workers' workload more balance and more practical significance than only time.

Introduction

Bad human factors in workplace especially in manual material handling(MMH) cause a lot of damage on health and quality of life of workers, deteriorate economic results of employers and of the economy as a whole. The human factors in manufacture system is becoming even more important following recent developments in legislation and most renowned companies incorporate methods for human factors estimation of working places in their production routine (Toyota, GM, Volkswagen) [1]. If human factors are detected, re-balancing of the production line is recommended as an effective method in the short-run [2].

Though human factors are becoming increasingly important in practice, they have been hardly quantized in production line balancing literature. Most literatures focus on evaluation of human factors exposure and qualitative analysis. Few articles are those of Costa and Miralles [3], who introduce and analyze a problem of assigning workloads to stations and to workers with different (dis-) abilities. In Ruifeng Yu' doctor paper [4], a set of systematic methodology for analyzing, Facility Layout Problem based on designing and evaluating both human factors and material flow is developed. However, few attempts has been made yet to incorporate quantizing human factors used in practice into PLB models, though they are considered important by manufacturers.

Methods for Estimating Human Factors

In general, there are two methods to evaluate human factor at the workplace: one to determine the workloads, also called quantitative analysis method, another to investigate the subjectively perceived strain, also called qualitative analysis.

The methods are used to determine the workloads, such as Physiological model, OWAS, REBA, NIOSH et al. Degrees of subjectively perceived strain based on the procedure are assessed though asking workers with standardization checklist, in where, some questions, such as load, posture, job satisfaction are described by 0-6 scale.

In the articles[4] [5], the Multicriteria quantizing model of human factors at workplace are built, evaluated and quantized by Entropy Method and AHP.

Production Line Balance Considering Human Factors (PLB-Human)

According to SALBP-1[6], PLB-Human is described as follows:

In a production line, where a set of processes $V = \{1, \dots, n\}$ with operation times t_j (for $j \in V$), worker operating auxiliary time t'_j and human factors coefficient e_j (for $j \in V$) are distributed among a set of cells $C_k = \{1, \dots, K\}$ arranged in a sequential order. The workpieces are launched down the line at a fixed rate such that each cell has access to every workpiece for a constant time span. The objectives are to minimize the number of cells C , and make the worker load in every cell is as much as possible equal to, under the restrictions conditions.

General Assumptions for Modeling

Each device m can only operate a process j , i.e. $j = m$;

The human factors coefficient e_j of each process is known, so, the worker load of each cell is expressed as: $E_j = e_j \cdot t_j$

Each worker's skills is equal to, and they can operate all the devices.

The time $T(C_k)$ of all the processes and worker operating auxiliary time $T'(C_k)$ contained in one cell is defined as:

$$T(C_k) = \sum_{j=1}^k (t_j + t'_j), T'(C_k) = \sum_{j=1}^k t'_j$$

Thus, the worker load of the cell is described as:

$$E(C_k) = \sum_{j=1}^k e_j (t_j + t'_j)$$

Model of PLB-Human

The model of PLB-Human is as follows:

$$\min SI = \sqrt{\sum_{k=1}^c (\max(E(C_k)) - E(C_k))^2} \quad (1)$$

$$\Omega = (c \cdot \max E(C_k) - \sum_{k=1}^c E(C_k)) / (c \cdot \max E(C_k)) \quad (2)$$

Subject to:

$$C_i C_j = \emptyset (i \neq j; i, j = 1, 2, \dots, m) \quad (3)$$

$$C = \bigcup_{K=1}^m C_k \quad (4)$$

$$t_j \leq CT \quad (5)$$

$$T'(C_k) \leq CT \quad (6)$$

$$M_{ij} = 1, i \in W_x, j \in W_y, x \leq y \quad (7)$$

$$c \leq m \quad (8)$$

Where: M is precedence relations matrix. c is the number of cells C (i.e. the number of workers)

Eq.3 ensures the same process can only be assigned to an operator;Eq.4 ensures that all processes must be assigned to all the cells;Eq.5 ensures the processes time t_j at the cell must not exceed the cycle time CT . Eq.6 ensures worker operating auxiliary time in one cell must not exceed the cycle time CT ;Eq.7 ensures that the process assigned to cells must satisfy the precedence relations;

Improved Genetic Algorithm for PLB-Human The PLB is NP-hard optimization problem, and diverse techniques have been used to solved over the years, such as , simulated annealing [7], tabu search [8], and so on. With the rise of artificial intelligent (AI) computational techniques in early 1990s, genetic algorithms [9] are the most well-adopted technique for line balancing control optimisation. Improved Genetic Algorithm (iGA) is used to solve the production line balancing problem considering human factors.

Case Study

The optimizing parameters of PPL. According to Lean Production, the detailed parameters of each process are shown in table 1. The human factors coefficient is calculated by by Entropy Method and AHP[5].

Table 1 The parameters of each process

Serial number	process	Machine time T_j (s)	auxiliary time t'_j	human factors coefficient e_j
1	Rough pin boring	53	8	2
2	Rough and Finish turning iron grooves	52.1	15	2
3	Rough and Finish turning aluminum grooves	45.4	10	2
4	Turning blocking and external ,inner chamfer	51.2	12	1
5	Drilling oil hole	6.4	2	1
6	Finish turning combustion chamber	41.3	6	1
7	Finish turning crown and rough turning head cylinder	47.8	12	1
8	Milling valve pit and open	47.1	8	1
9	Finish pin boring	56.1	15	3
10	Rolling pin bore	8.1	2	1
11	Finish turning skirt cylinder	90.3	13	2
12	Finish turning skirt cylinder	90.3	13	2

The precedence relations matrix of PPL is as follows:

$$M_{12 \times 12} = \begin{bmatrix} 0 & 1 & 1 & 1 & 0 & 1 & 1 & 1 & 1 & 1 & 1 & 1 \\ 0 & 0 & 1 & 1 & 0 & 0 & 1 & 0 & 1 & 1 & 1 & 1 \\ 0 & 0 & 0 & 1 & 0 & 0 & 1 & 0 & 1 & 1 & 1 & 1 \\ 0 & 0 & 0 & 0 & 0 & 0 & 0 & 0 & 1 & 1 & 1 & 1 \\ 0 & 0 & 0 & 0 & 0 & 0 & 0 & 0 & 0 & 0 & 0 & 0 \\ 0 & 0 & 0 & 0 & 0 & 0 & 0 & 0 & 1 & 1 & 1 & 1 \\ 0 & 0 & 0 & 0 & 0 & 0 & 0 & 0 & 1 & 1 & 1 & 1 \\ 0 & 0 & 0 & 0 & 0 & 0 & 0 & 0 & 0 & 0 & 0 & 0 \\ 0 & 0 & 0 & 0 & 0 & 0 & 0 & 0 & 0 & 1 & 1 & 1 \\ 0 & 0 & 0 & 0 & 0 & 0 & 0 & 0 & 0 & 0 & 1 & 1 \\ 0 & 0 & 0 & 0 & 0 & 0 & 0 & 0 & 0 & 0 & 0 & 0 \\ 0 & 0 & 0 & 0 & 0 & 0 & 0 & 0 & 0 & 0 & 0 & 0 \end{bmatrix}$$

After optimized by iGA, the least numb cell is 4, and processes are assigned as shown in table 2.

Table 2 The parameters of PPL after optimized

Serial number	process	Machine time $T_j(s)$	Cells and labor assigned	auxiliary time t'_j	human factors coefficient e_j
1	Rough pin boring	53		8	2
2	Rough and Finish turning iron grooves	52.1	Labor 1	15	2
5	Drilling oil hole	6.4		2	1
3	Rough and Finish turning aluminum grooves	45.4		10	2
4	Turning blocking and external ,inner chamfer	51.2	Labor 2	12	1
6	Finish turning combustion chamber	41.3		6	1
7	Finish turning crown and rough turning head cylinder	47.8		12	1
8	Milling valve pit and open	47.1	Labor 3	8	1
9	Finish pin boring	56.1		15	3
10	Rolling pin bore	8.1		2	1
11	Finish turning skirt cylinder	90.3	Labor 4	13	3
12	Finish turning skirt cylinder	90.3		13	3

Simulation results and analysis From the above result, one virtual piston production line is built in QUEST, as shown in Fig.1. The simulation results are shown in Fig.2-3 respectively.

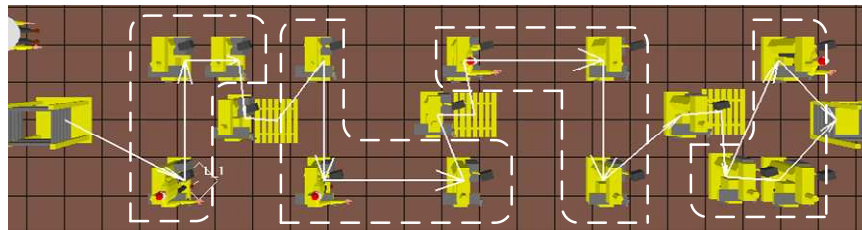


Fig. 1 The optimized simulation of piston production line

The simulation results listed in Fig.2 show that the utilization gap among of labor 1,2,3 is smaller, while, the gap of three and labor 4 is bigger, which indicates the idle time of labor 4 exceeds that of labor 1,2,3. If only from utilization, this virtual PPL isn't balance. But, from the result in fig.3 and, we can see that the utilization considering human factors is more balance, which indicates that all processes operated by labor 3,4 are strong human factors risk, and those by labor 2 are light human factors risk, so then, the curve of human factors risk is difference the curve of utilization. Therefore, in the actual production line design, the task allocation and PLB don't only consider time, considering the human factor load of each process/task can make labors workload more balance and more practical significance.

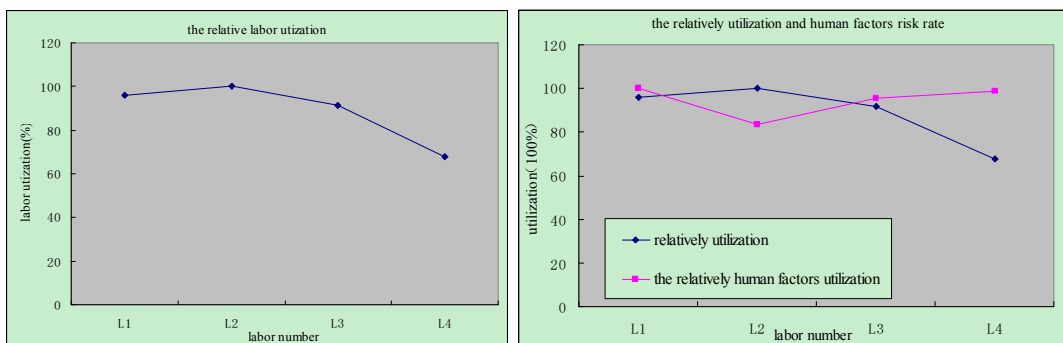


Fig. 2 The relative labor utilization Fig. 3 The relatively rate of human factors risk

Conclusion

In this article, combining quantitative human factors load with production line balance (PLB), a set of systematic methodology is developed. Firstly, after analyzed the importance of human factors, the evaluation of those is briefly introduced. Then, a model of PLB considering human factors is developed, whose objectives are to minimize the workers number and smooth the human factors load in one cell, and an improved Genetic Algorithm is adapt to solving the problem. Finally, a piston production line as an example is to optimize and simulate by Quest. The optimizing results show that the task allocation and PLB don't only consider time, considering the human factor load of each process/task can make labors workload more balance and more practical significance.

References

- [1] Alena Otto, Armin Scholl: Incorporating ergonomic risks into assembly line balancing[J], *European Journal of Operational Research*, vol. 212(2011),no. 2, pp.277-286.
- [2] Hilla, W., Produktivität und Ergonomie gemeinsam entwickeln. Erfahrungen aus der betriebsärztlichen Tätigkeit bei Audi AG. Presentation at MTM Bundestagung, Stuttgart.2006
- [3] Costa, A.M., Miralles, C., Job rotation in assembly lines employing disabled workers[J], *International Journal of Production Economics*, vol. 120(2009), pp. 625–632.
- [4] Ruifeng Yu: Optimization Research on Workplace Facility Layout Problem Based on Human Factors[D], Tsinghua University, 2004.
- [5] Puhong li, Jun Zhou, Jianxin Deng, The Evaluating and Quantizing of Human Factors at Workplace[J], *Advanced Materials Research*, vol. 328-330(2011) , pp 1045-1048.
- [6] Scholl, A., Becker, C., State-of-the-art exact and heuristic solution procedures for simple assembly line balancing[J], *European Journal of Operational Research*, vol. 168(2006),pp 666–693.
- [7] Burcin Cakira, Fulya Altiparmakb, Berna Dengiza, Multi-objective optimization of a stochastic assembly line balancing: A hybrid simulated annealing algorithm[J], *Computers & Industrial Engineering*, vol. 60(2011), no. 3, pp. 376–384.
- [8] Gholam Reza Esmailian¹, et.al., A tabu search approach for mixed-model parallel assembly line balancing problem (type II) [J],*International Journal of Industrial and Systems Engineering*, vol. 8(2011), no.4,pp.407-431.
- [9] Tanzina Zamana, Sanjoy Kumar Paula, Abdullahil Azeema, Sustainable operator assignment in an assembly line using genetic algorithm[J], *International Journal of Production Research*, Available online: 21 Dec 2011.

Facility Layout Model of Production Line Based on Operation Comfort

Puhong Li^{1,2, a}, Zhijun Fan^{1, b}, Jun Zhou^{1, c}, Jianxin Deng^{1, d}

¹ School of Mechanical Engineering, Shandong University, Jinan 250061, CHINA

² School of Art Design, Shandong Polytechnic University, Jinan, 250353, CHINA

^aLipuhong@126.com, ^bfanzhijun@sdu.edu.cn, ^czhoujun@sdu.edu.cn

Keywords: Optimization Model; Facility Layout; Production Line; Operation Comfort; Manufacturing System

Abstract. Combined operation comfort and logistics optimization into the facility layout model of the production line, used Value Engineering theory, facility layout model of a production line based on operation comfort is put forward. After then, the model's characteristics are analyzed. Compared with the traditional logistics-based model, this model optimizes simultaneously the workers' operation comfort and logistics, not only to reduce the cost of production line, but also to increase the operating quality, finally to enhance the production efficiency.

Introduction

As an important part of the manufacturing system, facility layout is closely relationship with the equipment utilization, busy time and waiting time, and production line efficiency. In facility layout design, the costs of material handling are considered firstly, but if just pursuing the lowest logistics costs while ignoring the security and comfort of workers to operate, it is bound to cause bodily injury, and a large number of occupational health compensation would pay. Therefore, in facility layout design of the production line, simultaneously optimizing operation comfort and logistics is the better choice.

Facility layout problems Overview

The placement of the facilities in the plant area, often referred to as “facility layout problem”, is known to have a significant impact upon manufacturing costs, work in the process, lead times and productivity. A facility layout is an arrangement of everything needed for production of goods or delivery of services [1]. A good placement of facilities contributes to the overall efficiency of operations and can reduce until 50% of the total operating expenses [2].

The layout form and optimization objectives The traditional form of layout is divided into fixed product layout, process layout, product layout and cellular layout [3]. With the development of advanced manufacturing technologies, such as agile manufacturing, lean production, layout mode changes, some new layout forms appear: group layout, distributed layout, reconfigurable layout, which can respond quickly to the changing market needs. In the actual layout planning, not a single layout is used, often a variety layout forms are used, which can play advantages of a single layout and avoid its shortcomings.

Layout problems are known to be complex and are generally NP-Hard optimization, whose objectives include two aspects of quantitative and qualitative: the quantized targets are the shortest path of logistics, the minimum cost of material handling; the qualitative aspects are the safety, comfort and aesthetics. Qualitative optimization objectives are secondary, generally to consider after meeting the main optimization goal, and due to done from personal experience, lack of criteria. The layout of the logistics-based optimization target because of neglecting the human factor, could reduce productivity, increase operator fatigue, is easy lead to misoperation, eventually lead to products with inferior quality.

Operation comfort degree. In order to further improve the performance of the production line layout design, many scholars study the human factor of production systems, the research aimed at the human factors in the production system, other factors is the assessment of the ergonomics relevant factors. On the basis of these studies, the concept of comfort is proposed.

Comfort is the subjective feeling, so it is commonly referred to as comfort. Due to the factors and conditions that affect the comfort is complex, the concept is variable and it is difficult to quantify, specifically referring to the satisfactory state of the majority of people at the aspects of physical and psychological to the objective environment. In production systems, production line operations staff operation comfort concept, is a kind of state of the physiological and psychological aspects of the individual operating the equipment and the operation of the work, is the assessment of their work or operation a positive emotional state.

Operation comfort not only by the workload, work posture, the environmental load and impact, but also because of the influence of mental operations and perceived behavior. The main factors are shown in Table 1.

Table 1 The factors affecting operation comfort

Influencing factors	related content
Physical load	Load weight, Handling load frequency, Physical operating time and moving distance
Environmental load	temperature, lighting, noise, vibration and chemical substances
work posture and movement load	Physical exercise as well as standing, squatting, bending, twist, etc.
Mental load	mainly caused by the mental operations and perceived behavioral

How to correctly evaluate factors of operation comfort is the key to improving work comfort level, prevent occupational musculoskeletal disorders. At present, the evaluation method of human factors that exist in the workplace, in accordance with risk factors for exposure is divided into self-assessment, observation and direct method[4]. Human factor coefficient e_{ij} is evaluated and quantized by Entropy Method and AHP [5].

In the layout optimization of production line, if operation comfort considered, it would be able to shorten the logistics path, reduce the material handling cost, improve the utilization rate of area, improve efficiency, and also reduce the workers' load, so as to decrease bad work gesture or cumulative time, improve operation comfort, then reduce the occupational musculoskeletal damage risk .

Layout Model of Operation Comfort-based of Production Line (LOC)

Since R. Muther put forward the systematic layout planning, many modeling optimization methods were formulated, such as QAP, MIP, graph theory, neural network, Tabu search, simulated annealing, genetic and ant colony algorithms, human-computer interaction. However, due to these methods lack of the consideration the operation comfort, a layout model of production line based on operation comfort is proposed.

Description of the problem Assume that there are n equipments in the production line, which is expressed as $M = (m_1, m_2, \dots, m_n)$.Fig. 1 shows the floor plan of M_i and M_j .

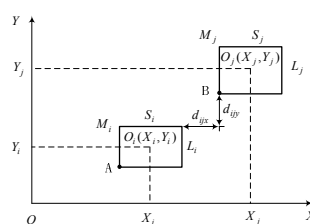


Fig. 1 The floor plan of equipment M_i and M_j .

Value Engineering Value Engineering is a systematic method to improve the "Value" of goods and services by using an examination of function. Value, as defined, is the ratio of Function to Cost, i.e. $V = F / C$. Value can therefore be increased by either improving the Function or reducing the cost. It is a primary tenet of Value Engineering that quality not is reduced as a consequence of pursuing Value improvements [6].

The layout design of production line, under the premise function, the smaller its cost is, the greater value of this production line is.

The logistics value (V_m) of production line layout. The logistics value is the ratio of completing the job requirements to the material handling costs between the various devices in the current equipment placement.

The indicators of the logistics value of the facility layout include the amount of logistics (p_{ij}) of each handling, material handling frequency (r_{ij}), the unit material handling costs (f_{ij}) per unit distance, as well as distance (d_{ij}) between two facilities. The optimizing goal is to make transportation costs (C_m) minimize. Thus, the logistics value is maximum the model is expressed as:

$$V_m = F/C_m = F / \sum_{i=1}^n \sum_{j=1}^n (p_{ij} \cdot r_{ij} \cdot f_{ij} \cdot d_{ij}) = F / \sum_{i=1}^n \sum_{j=1}^n (p_{ij} \cdot r_{ij} \cdot f_{ij} \cdot \sqrt{(X_i - X_j)^2 + (Y_i - Y_j)^2}) \quad (1)$$

The operation comfort (V_e) of production line layout. The operation comfort of production line layout means that operator's subjective satisfaction with the comfort of their work, completing the operational requirements, in the current physical facilities arrangements of production line.

The indicators of the operation comfort include human factor coefficient (e_{ij}) and the operation time (t_{ij}), and the goal is to make the operation comfort maximum, in order to decrease the operator's cumulative occupational injury. Thus, its comfort function is:

$$V_e = F / \sum_{i=1}^n \sum_{j=1}^n (p_{ij} \cdot r_{ij} \cdot e_{ij} \cdot t_{ij}) \quad (2)$$

Layout Model of operation comfort-based of production line LOC) LOC can described by the total value V of production line layout, which refers to the function which the facility layout design synthetically considers the material handling costs and the operation comfort to achieve. With the same conditions, the bigger the function is, the greater the total value of the layout of production line, then the higher the chance of being selected is. The function is as follows:

$$V = V_m + V_e = F / \sum_{i=1}^n \sum_{j=1}^n (p_{ij} \cdot r_{ij} \cdot f_{ij} \cdot \sqrt{(X_i - X_j)^2 + (Y_i - Y_j)^2}) + F / \sum_{i=1}^n \sum_{j=1}^n (p_{ij} \cdot r_{ij} \cdot e_{ij} \cdot t_{ij}) \quad (3)$$

Subject to.

$$|X_i - X_j| \geq \frac{S_i + S_j}{2} + d_{ijx} \quad (4)$$

$$|Y_i - Y_j| \geq \frac{L_i + L_j}{2} + d_{ijy} \quad (5)$$

$$\sum_{i=1}^{n-1} (|X_i - X_{i+1}| + \frac{S_i + S_{i+1}}{2}) \leq L_X \quad (6)$$

$$\sum_{i=1}^{n-1} (|Y_i - Y_{i+1}| + \frac{L_i + L_{i+1}}{2}) \leq LY \tag{7}$$

LX , LY respectively express the workshop width along the direction of X , Y .
Eq. 4, 5 are the interval constraints; Eq.6, 7 are the boundary constraints.

The Comparison between Layout Model of Operation Comfort-based (LOC) and Layout Model of Material Handling-based (LMM)

Different solution ways LOC takes simultaneously logistics optimization and operation comfort into account. While, the traditional LMM is logistics optimization, on the basis of logistics optimization, considers the operator comfort and safety. Due to these two different methods, it could lead to different optimization results, so as to obtain the different layout form.

Different optimization results The optimization result of LOC is the overall optimum value, while that of LMM is local optimum value.

Let: f_1 is the logistics value; f_2 is the operation comfort value. Assume there are three models: Model 1 is based on the logistics optimization; Model 2 considers the operation comfort based on the logistics optimization, and Model 3 is the LOC. Then:

Model 1: $\max V_1 = f_1$; Model 2: $\max V_2 = f_2$; Model 3: $\max V_3 = f_3 = f_1 + f_2$

Let :

f_1^* is the optimum value of f_1 obtained via solving model 1,; f_2^* is the optimum value of f_2 obtained via solving model 2,; f_3^* is the optimum value of f_3 obtained via solving model 3; f_{13}^* is the optimum value of f_1 obtained via solving model 3. According to the Theorem[7]:

Then : $f_3^* \geq f_1^* + f_2^*$

The sensitive coefficient of Logistics value and operation comfort. In order to analyze the impact of logistics value and operation comfort to the total value of the layout, the adjustment coefficients are introduced, called sensitive coefficient. So,the layout model is defined as:

$$V = \theta_1 V_m + \theta_2 V_e$$

$$= \theta_1 \cdot F \left/ \sum_{i=1}^n \sum_{j=1}^n (p_{ij} \cdot r_{ij} \cdot f_{ij} \cdot \sqrt{(X_i - X_j)^2 + (Y_i - Y_j)^2}) \right. + \theta_2 \cdot F \left/ \sum_{i=1}^n \sum_{j=1}^n (p_{ij} \cdot r_{ij} \cdot e_{ij} \cdot t_{ij}) \right.$$

θ_1, θ_2 is the sensitive coefficient, under the function of production line, to maintain total value of layout not variable, the ratio relationship of logistics value and operation comfort can be adjust. This ratio should be determined by the relevant experts and managers who are familiar with the industry or job experience.

Conclusion

In this paper, a new model LOC is developed to deal with simultaneous logistics optimization and operation comfort and combined into the facilities layout of production line. Firstly, the facilities layout problem is described and assumed. Then, because the logistics indicators and operation comfort indicators don't belong to the same dimensionless, the contribution of which to the overall objective cannot be unified to quantify, the theory of value engineering is applied to measure the contribution to the total value of the layout, establish a mathematical optimization model. Finally, after analyzing the characteristics of the model, LOC is compared with the traditional model based on logistics value (LMM), and the sensitive coefficient is introduced to be suitable for different industries, so as to provide decision makers with a reasonable reference.

References

- [1] Amine Drira, Henri Pierreval, Sonia Hajri-Gabouj: Facility layout problems: A survey. *Annual Reviews in Control* Vol.31(2007), p. 255–267
- [2] Tompkins, J.A., White, J.A., Bozer, Y.A., Frazelle, E.H., Tanchoco, J.M., & Trevino, J.: *Facilities planning* (Wiley, New York 1996.)
- [3] Dilworth, J.B.: *Operation management*. McGraw Hill, (1996).
- [4] Lin Sihao: Development a Tool for Comprehensive Evaluation of Ergonomic Exposure at the Workplace and its Application Study. SiChuan University Doctoral Degree Dissertation, 2006.
- [5] Puhong li, Jun Zhou, Jianxin Deng, The Evaluating and Quantizing of Human Factors at Workplace[J], *Advanced Materials Research*, vol. 328-330(2011), p. 1045-1048
- [6] http://en.wikipedia.org/wiki/Value_engineering
- [7] M.B.Aryanezhad, V.Deljoo, S.M.J.Mirzapour Al-e-hashem: Dynamic Cell Formation and the Worker Assignment Problem: a New Model. *Int J Adv Manuf Technol*, Vol.41(2009), p. 329–342

Research on the Green Building Revolution - Solar Energy Research and Development in Taiwan

Yan-Chyuan Shiau^{1, a}, I-Ta Lu^{2, b}, Chen-I Tsai^{3, c} and Chih-Ying Lee^{4, d}

¹Associate Prof., Dept. of Const. Management, Chung Hua University, Hsin-Chu, Taiwan

²Associate Prof., Dept. of Civil Engineering, Kao Yuan University, Kaohsiuan, Taiwan

³Graduate Student, Chung Hua University, Hsin-Chu, Taiwan

⁴ Graduate Student, Dept. Construction Management, Chung Hua University, Hsin-Chu, Taiwan

^aycshiau@ms22.hinet.net, ^bt40089@cc.kyu.edu.tw, ^ca52322002@yahoo.com.tw,
^da210085@yahoo.com.tw

Keywords: Green Energy, Photovoltaic, Building Integrated Photo Voltaic, Power Conversion Efficiency

Abstract. Taiwan is located in the West Pacific Earthquake Zone. Fulda Nuclear power plant disaster caused by March 11, 2011 earthquake not only impact Japan, all countries around this area have been forced to face the radiation threaten. This event strengthens advanced organizations to search the green energy. Solar energy and wind power that utilizes the nature to generate electricity energy are widely accepted around the world. In April, 2011, Germany has passed the waste nuclear provision. The BIPV (the Building Integrated Photo Voltaic) has not only the economic benefits of energy generation also reduce the carbon emissions and building initial cost. The Renewable Energy Sources Regulations has been established in June 12, 2010 in Taiwan that proclaimed the green energy generation has been started. The development of Photovoltaic was discussed in this study. The Government's efforts to construct the wind power energy were analyzed to explore the research potential of green energy development in Taiwan. The development goals and vision were explored for Taiwan's energy resource in this article. The power conversion efficiency of commonly used solar cells was investigated. Through the investment in key bottleneck and innovative technologies, the government provides incentives to increase domestic demand and consumption. Focusing on the international market to enhance the scale can construct a perfect green value chain in Taiwan.

Introduction

Research Motive The Japanese March 11 earthquake in 2011 cause the Japanese Fulda Nuclear power plant disaster, the radiation release event shocks the world; also recall the former Soviet Union nuclear power plant disaster. Germany takes the lead to pass the waste nuclear provision in April, 2011. American wealth star magazine analyst Gunner T. Miller once predicted that the nature green industry soon become the 21st century's star of tomorrow [1].

Similarly, Taiwan finally established the renewable energy sources regulations in June 12, 2010. The comprehensive survey domestic and foreign green energy history of the development, started this research, discusses green energy construction present situation and the development in the Taiwan.

Research Goals Through expert re-design the solar and wind turbine module to replace conventional building materials, as the surface decoration of the building. Not only save the building materials fee but also achieve the power generation function, which is the so-called BIPV. The operation of BIPV case study aimed to the environmental effects of the architectural design on landscape, which estimated the usability between human behavior and renewable energy on the design management [2]. The energy generation efficiency of BIPV system relies much on the panel's surface solar radiation received [3]. The BIPV has not only the economic benefits of energy generation also reduce the carbon emissions. The BIPV will be the mainstream in photovoltaic applications [4].

A wind-solar hybrid experiment system has been constructed by X. Yuan which was consisted of wind energy subsystem, solar energy subsystem and energy storage subsystem [5]. Taiwan, the fourth photoelectric production country in the world, has only few successful cases of wind and solar power design in building construction. Obviously the Taiwan Government promote weakly in this regard. This study will explore the research and development of solar photovoltaic, and for the Government's efforts to construct the current status of power energy in Taiwan.

BIPV and wind power generation system already flourish developed in the world, in Germany and Japan, the active cooperation of the government policies have been brilliant achievements. Contrast, Taiwan the photoelectric products accounted for fourth in the world, the successful cases of wind and solar power design in building construction are few, obviously that the Taiwan Government promote weakly in this regard. Because of this, the development of building integrated photovoltaic and wind power generation system construction has the more growth space. In urgent need of the active involvement of citizens and government can no longer rest on its laurels. This study will explore the new object - the research and development of solar photovoltaic (BIPV), and for the Government's efforts to construct the current status of wind power energy analysis to explore the Green reduced the development potential of carbon in Taiwan.

Range Of Study In this study, only with the application portion of the building components for solar to study, wind, geothermal and tidal power generation part is not in this study scope.

The Current Situation and Development of The Green Industry In Taiwan

Solar Electro-Optic Industry in recent years, the Taiwan government has set plan to help the solar photovoltaic industrial development, the output of real value quickly jumped from NT\$12.3 billion in 2003 to NT\$105.7 billion in 2009, the rapid growth of about 85 times in just six short years [6]. The solar trough concentration photovoltaic/thermal system has been constructed and the experiment performance and analysis of solar cell arrays have been carried out by S.X. Wei to improve electric efficiency of solar cell arrays and obtain available heat energy [7].

W.S Our conducted a study focused on the regional characteristics of global solar radiation of Taiwan. The research utilized the raw meteorological data to establish reliable solar radiation data of weather stations by means of statistic analysis [8]. In order to maintain promoting the development of photovoltaic industry, Ministry of Economic Affairs Industrial Development Bureau has proposed the Taiwan's energy resources development objectives with its vision and strategy shown in Table 1. Expectations can effectively solve the following problems addressed by present industry as followed:

The key materials and process equipment of the upstream of the Photovoltaic Industry controlled by the foreign industry, this aspect tremendous impact the competitiveness of the solar energy industry. The profit often subject to foreign quoted price.

Table 1. Energy development vision and strategy in Taiwan [9]

2010	2015	2020
1. Promote 4 energy resource integration demonstration industrial parks. 2. Reach 40 million tons of links. 3. Emission greenhouse gas by 10 million tons. <ul style="list-style-type: none"> ● Water recycling rate reach 60% for whole country ● Promote an wastewater recycling demonstration plant 	1. Construct real resource link network and environment. 2. Reach 110 million tons of links. 3. Emission greenhouse gas by 30 million tons. <ul style="list-style-type: none"> ● Water recycling rate reach 60% for whole country ● Provide 180 tons industrial reclaimed water each year 	1. Construct real resource link network and environment. 2. Reach 160 million tons of links. 3. Emission greenhouse gas by 40 million tons. <ul style="list-style-type: none"> ● Water recycling rate reach 65% for whole country ● Provide 440 tons industrial reclaimed water each year

Low percentage (70%) of solar modules and solar cells on the chip output value makes the value of science and technology output value rate is not high.

Because of the domestic manufacturers stands in great numbers can not be effectively integrated, resulting in self-price competition and lower profit.

The Taiwan Photovoltaic Industry was introduced domestically through the Turnkey technology, although this technology can immediately achieve the purpose of cut production, but the product is no difference, no standardization neither innovation. These make the industrial not be able to upgrade and enhance real profit.

The present cost of photovoltaic power generation is still higher than the price of the Taiwan Power Company. Under the long cost recovery period and the lack of government subsidies, the development of solar photovoltaic industry is affected, also reduces the industry's willingness to invest, especially the construction industry.

Photovoltaic building applications Example - the implementation of the "Solar Roofs Plan" The benefits of the plan states as following:

The advancement of promotion the PV building applications can open the domestic market.

The Highlights the key areas of solar PV systems in green energy and carbon reduction applications, also to ensure the effect of model projects.

The implementation finance support policy gives the fund subsidy to the PV building applications.

The Encourages the Local authority to draw up the related financial support policy, so the policy development and the impetus can be popularization.

Financial priority to support technological innovation enhances industrial competitiveness and efficient policy.

Popularization of The Implementation of The Policy Execution The Popularization of the implementation of the policy execution can be done through:

Taiwan government already announced the photovoltaic power generation system establishment subsidy regulations, and its flowchart for the grant process is shown in Fig. 1.

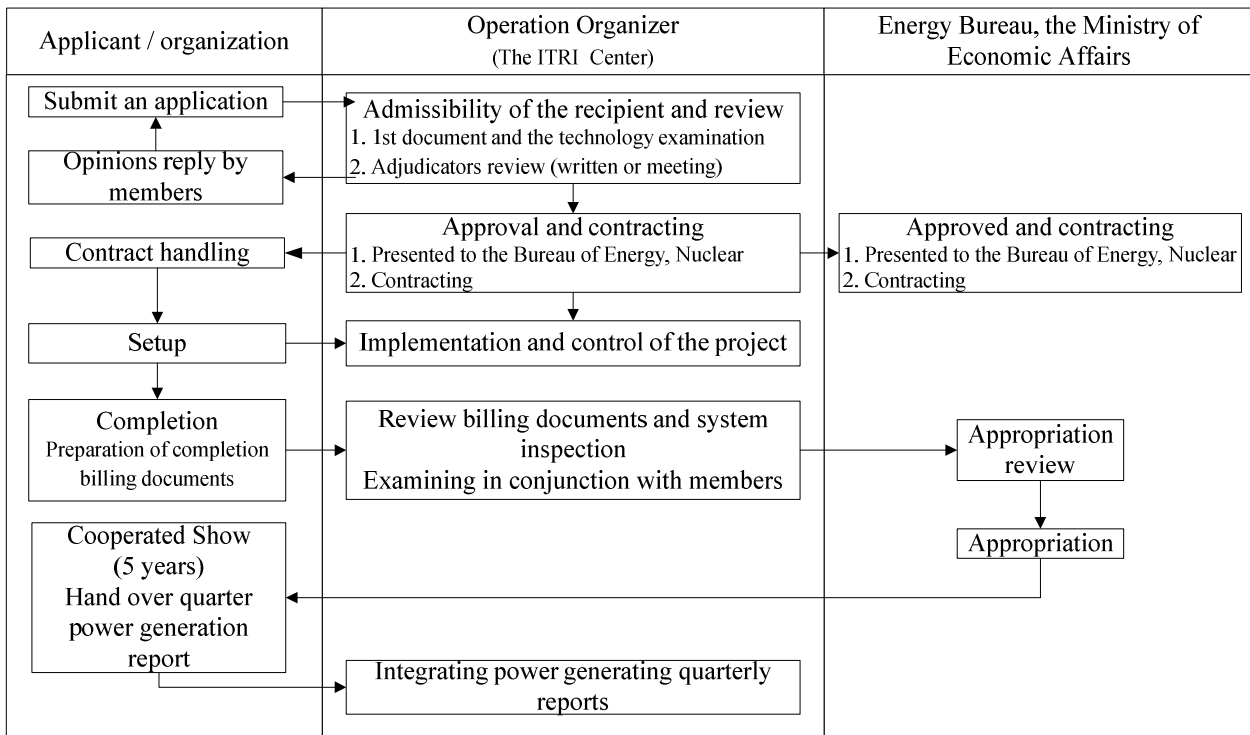


Figure 1 Flowchart of the application of the photovoltaic power generation system [10]

The Legislative department passed the renewable energy sources law in June 12, 2010. The Law explicitly stipulates that the Government must repurchase the solar power electricity generated by the civilization. As a result, will be the resort entrepreneur's gospel, during Monday to Friday the company may sell the unnecessary electric power using the solar electrical energy generation, earning hotel expense on Saturday and Sunday.

Photovoltaic Technology Application in real terms

Solar photovoltaic is a technology which transforms sun light into electrical energy, at present is mainly through the solar cell to achieve. Solar cell's classified way may depend on raw material. The classification of solar cells is shown in Table 2.

Generally speaking, the polycrystalline silicon module is more efficiency then the amorphous silicon type. However the price is also higher and needed more sunlight in order to start the system than the amorphous silicon type. Therefore, build a solar photovoltaic power generation system should not only consider the module efficiency, but also take the time factor and environmental conditions together into consideration, in order to design a suitable solar power system for each case.

Table 2. Types of solar cell

Solar cell type		Semiconductor materials	Market module power conversion efficiency
Silicon: The most widely used in PV systems	Crystalline	Single Crystalline	12~20%
		Poly Crystalline	10~18%
	Amorphous	Si,SiC,SuGe,SiH,SiO	6~9%
Compound: Applied to the polar and concentrating PV systems	Single Crystalline	GaAs,InP	18~30%
	Polycrystalline	Cbs,CdTe,CuInse	10~12%
Nanoscale organic: Used in organic solar cells (under development)	TiO ₂		Less than 1%

Expected Results and Conclusions

Green Energy Development Blueprint The green energy industry is an important link contributed to the growth of green industry and reached the industrial green. such as:

Professor Yang Jinhui and his research team of the National Taiwan University of Science and Technology has innovated the world's first piece, "Three in one solar glass" which successful combine the functions of heat insulation, electricity generation, and self-cleaning, its principle is using of the thin-film photovoltaic technology to place the solar panels inside the glass.

Glass "self-cleaning" function through the photo catalyst technology save the building clean-up costs, saving water resources.

Currently the "Three in one solar glass" being developed for vehicle, Enable the car to generate electricity and at the same time the inside temperature will not rise, kills several birds with one stone.

Expect Taiwan to become the leader of the Green Revolution.

Thomas Friedman addressed that "No country better standing than Taiwan position as the leader of the green energy revolution". In fact, Taiwan has a very important position in the field of the solar photovoltaic industry.

Taiwan solar energy industry development is extremely vigorous in recent years, especially in the case of the serious shortage of material in the upstream, various manufacturers all working actively involved in new plant expansion in pursuit of production capacity.

Due to the global economical recession, Taiwan Photovoltaic Industry also facing the challenges of crisis. However, in the past the photovoltaic power generation system price excessively high, has being corrected during the recent years and promote to popularization.

Taiwan Government is actively handling the expansion of domestic demand through investment in public construction of photovoltaic power generation, will not only promote the development of the industry, but also to reduce the future energy supply pressure. Hoping that one day Taiwan really becomes the leader of the green revolution.

References

- [1] T. Friedman: *The Hot, Flat and Crowded world*, Vision Publishing Co., Ltd., Taipei, (2008)
- [2] H.J. Chen, C.M. Chiang and C.C. Chan: A BIPV case study of the environmental effects with the PV energy performance, *Applied Mechanics and Materials*, v 71-78, p 3020-3024 (2011)
- [3] K.T. Huang and W.S. Ou: Using modified sandia method in developing typical solar radiation year for photovoltaic electricity generation projection, *Applied Mechanics and Materials*, v 71-78, p 4374-4381 (2011)
- [4] G.H. Yang: *Discussion on Trinity Solar Glass*, National Taiwan University of Science & Technology, Research Report, (2007)
- [5] X. Yuan and J. Bin, Jiao: Research of a kind of wind-solar hybrid power experiment system, *Applied Mechanics and Materials*, v 121-126, p 3667-3671, 2012
- [6] A.P. Liu: *The Application of Photovoltaic Cells in the Architecture* (Scientific and Technology Book Co., Ltd., 2003).
- [7] S.X. Wei; C. Tao and H.M. Yang: Effect of temperature on output characteristic of solar cell arrays, *Applied Mechanics and Materials*, v 71-78, p 2675-2678, 2011
- [8] W.S. Ou, K.T. Huang and C.C. Liao: Global radiation for solar architecture design of Taiwan, *Applied Mechanics and Materials*, v 44-47, p 1853-1861, 2011
- [9] Website of Bureau of Energy, <http://www.moeaboe.gov.tw>
- [10] Website Photovoltaic Center, ITRI, <http://solarpv.itri.org.tw/memb/main.aspx>

AP1000 Nuclear Reactor and Primary Loop Modeling Based On Relap5-3D and 3Keymaster Simulation Platform

Huiming Wei^{1, a}, Xuan Zhang^{1, b} and Taili Liu^{1, c}

¹China nuclear power simulation Technology Company limited, Shenzhen 518034, China

^aweihuiming@cgnpc.com.cn, ^bzhangxuan@cgnpc.com.cn, ^cliutaili@cgnpc.com.cn

Keywords: AP1000 Nuclear Reactor; Relap5-3D; 3Keymaster Simulation Platform; Primary Loop; Modeling.

Abstract. In this paper, the advanced 3Keymaster simulation platform and RELAP5 simulation code are introduced. At the same time, the AP1000 nuclear reactor and primary loop modeling method is discussed in detail based on Relap 5 and 3Keymaster simulation platform. The typical Relap5 nasalization cells of AP1000 nuclear reactor and primary loop system are showed in Fig.1. The Fig.2 shows the AP1000 reactor coolant system model. Fig.3 shows the AP1000 reactor core and pressure vessel model. Fig.4 shows the AP1000 nuclear reactor steam generator model.

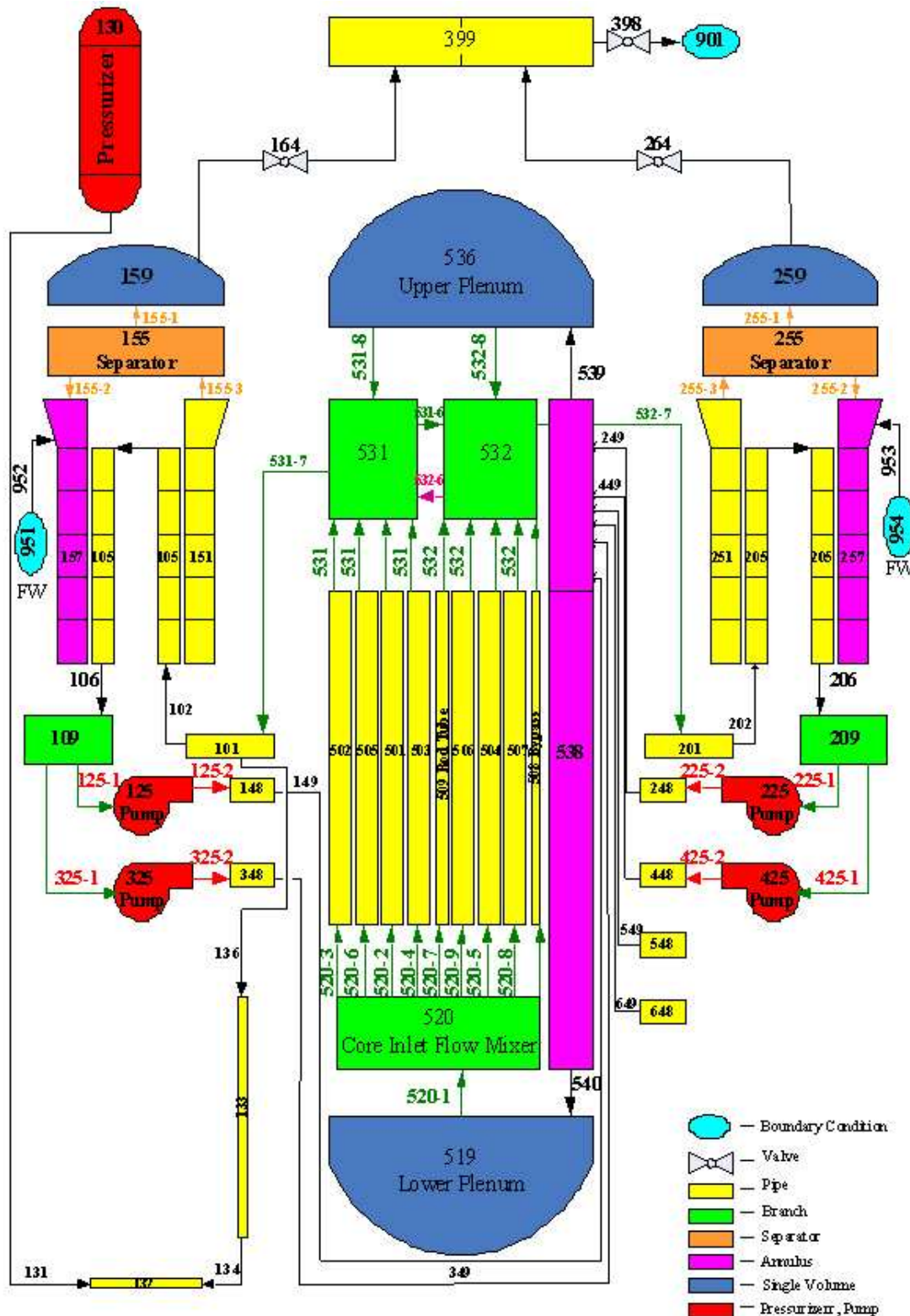
Introduction

RELAP5 is an advanced, best-estimate, reactor thermal-hydraulic simulation code, developed at Idaho National Engineering and Environmental Laboratory (INEEL) [1]. It is recognized today as the worlds most mature and advanced computer program for simulating transient fluid dynamics, neurotics and heat transfer in nuclear power plants. Development of the numerical models and assessment of the RELAP series of codes spans over 25 years. The code has undergone extensive V&V during this time period and has benefited greatly from large experimental programs such as LOFT, PBF, Semi scale and others. Extensive documentation exists for the code's methods, models, correlations, computer architecture and other features. RELAP5 is now routinely used by Reactor Engineering Departments at most nuclear utilities for safety-grade analysis. Therefore, RELAP5 is widely held as the world's premiere code for NPP transient simulation.

Beginning in 1980, the US Department of Energy (DOE), began sponsoring the development of RELAP5 as well, for reactor safety assessment needs for its own test and production reactors. RELAP5/MOD3.2 was the last release of one-dimensional thermal hydraulics code under DOE sponsorship.

After the Chernobyl accident, the DOE undertook a rigorous safety assessment of its facilities, which included reactors of various designs and the application of RELAP5 for this purpose. It was apparent that modeling enhancements to RELAP5 would be needed to handle the various phenomena in the variety of reactor designs. This included: 3-D flow modeling, incorporation of heavy water properties, new critical heat flux correlations, and the incorporation of the 3-D NESTLE neutron kinetics model.

As a result of this, the development of the RELAP5-3D [1] was undertaken, and to preserve the extensive V&V already completed, RELAP5/MOD3.2 was chosen as the base-code for the development of RELAP5-3D. This development was undertaken and completed by INEEL under continued sponsorship by the DOE. All the validation history of RELAP5/MOD3.2 is preserved in RELAP5-3D.



3Keymaster [2] is the first simulation environment developed ground-up for the Microsoft Windows operating system. Its open architecture, fully object-oriented approach, supports for flexible human interface design, and leveraging of the Windows environment, offers distinct advantages in speed and usability.

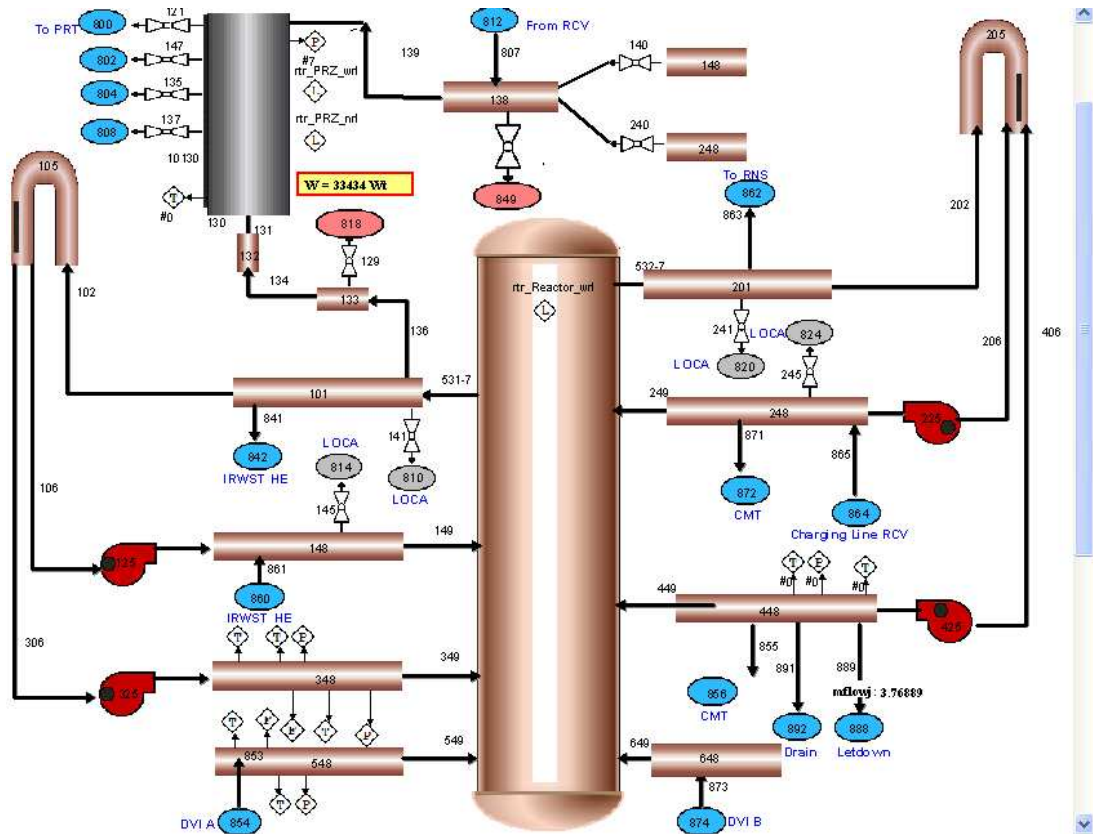


Fig.2 AP1000 reactor coolant system

3Keymaster models will utilize graphical model builders. This allows the users to visually view the model's configuration and to modify and update models by simply changing the graphical representation.

The aim of this study is to introduce the Relap5-3D and 3Keymaster modeling methods. They are employed to establish the AP1000 nuclear reactor and primary loop modeling.

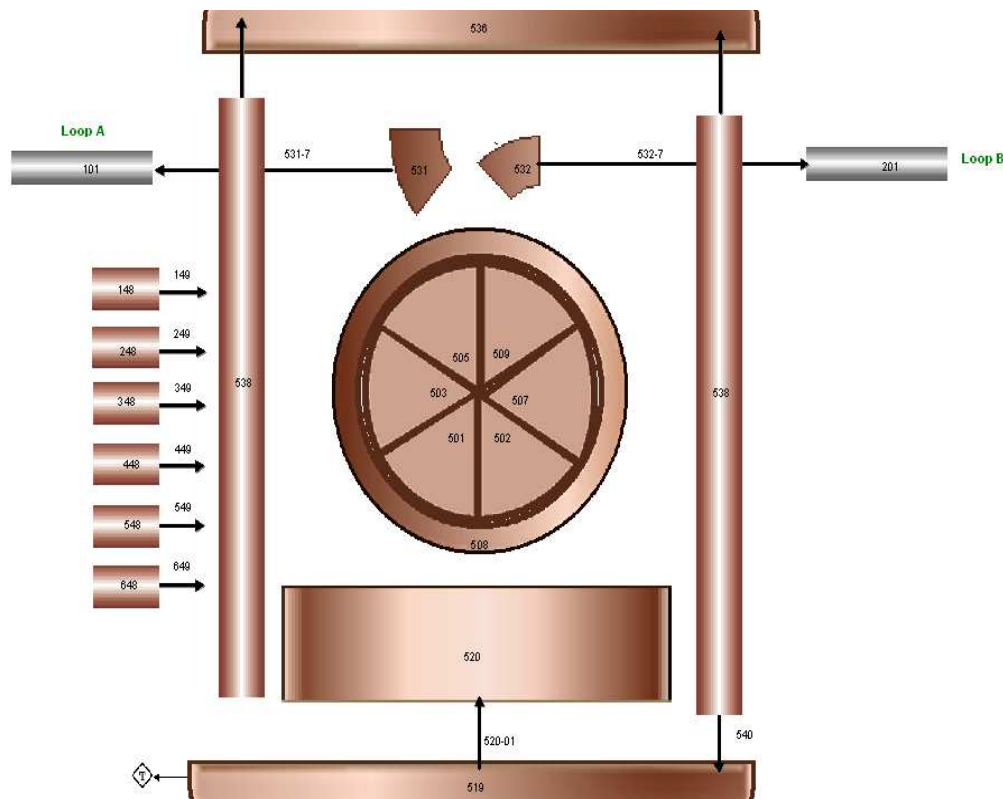


Fig. 3 The AP1000 reactor core and pressure vessel model

AP1000 nuclear reactor and primary loop modeling

In this section, the RELAP5-3D code [3] will be utilized to model the reactor core and vessel, the loop piping and Reactor Coolant Pumps, the tube and shell side of the Steam Generators, the steam lines up to the turbine stop valves, the steam dump valves, the pressurize. In the following, we will discuss how to establish the AP1000 nuclear reactor and primary loop modeling.

Firstly, in order to adapt to real time simulation, the nodes of system and the predigest ion was made according to the characteristic of reactor coolant system which will be simulated. The typical Relap5 nasalization cells of AP1000 nuclear reactor and primary loop system are showed in Fig.1.

Secondly, every component was linked with the corresponding interface and input parameters, and Relap5 data deck was created after checking errors.

Thirdly, the AP1000 nuclear reactor and primary loop system modeling may be established based on the relap5 input data deck and 3Keymaster simulation platform [4].

The Fig.2 shows the AP1000 reactor coolant system model. It includes four cold legs (148, 248, 348 and 448 components), two hot legs (101 and 201 components), four pumps (125, 225, 325 and 455 components), pressurize (130 component), two direct injection pipes (548 and 648 components), auxiliary spray (138 component), EST. The reactor core and steam generator models will be presented individually. Fig.3 shows the AP1000 reactor core and pressure vessel model. The active core nasalization will consist of 18 axial planes in the active core and 2 additional planes for the upper and lower reflector regions. The radial nasalization will consist of 157 nodes representing the fuel assemblies (one node per fuel assembly in radial nasalization). The radial plane will be subdivided into at least 8 Thermal-Hydraulics zones. And from 501 to 508 are said to the 8 Thermal-Hydraulics zones, respectively. Fig. 4 shows the AP1000 nuclear reactor steam generator model. It includes downward part of the feed water tube (157 and 257 components), steam generator heat transfer pipes (151and 251 components), separators (155 and 255 components), steam headers (159 and 259 components), est.

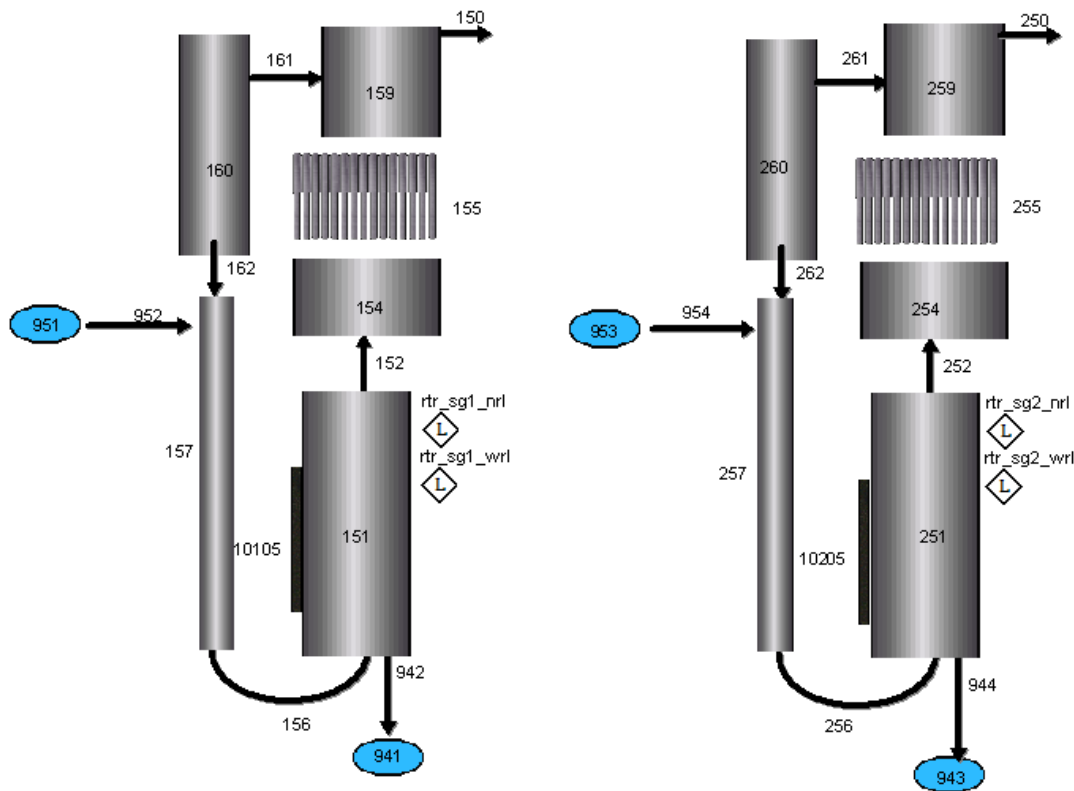


Fig. 4 The AP1000 nuclear reactor steam generator model

Summary

In this paper, the advanced 3Keymaster simulation platform is introduced. Based on the Relap5-3D and 3Keymaster modeling methods, the advanced PWR AP1000 nuclear reactor and primary loop modeling are established by 3KEYRELAP5 GRAPHIC TOOL [4]. They are showed in Figs. 2-4, respectively.

References

- [1] NingDe Nuclear Power Plant Supply Contract Full Scope Simulator_Appendix 5 Technical Description.
- [2] Information on <https://www.ws-corp.com/wsc08/default.asp?PageID=8>.
- [3] RELAP5-3D code manual Volume III: Appendix A RELAP5-3D Input Data Requirements.
- [4] I. Arshavsky, V. Galkin, V. Orlov, R. Felker, L. Severnyak: 3KEYRELAP5 GRAPHIC TOOL User Guide, v. 1.0-1.

Experimental Study on Influence Function of Particle Size at Low-Temperature Oxidation of the Coal

Zuo Qiuling, Wang Gongzhong, Gao Xinchun

Safety Engineering Department, Henan Engineering Institute, Henan, Zhengzhou, China

543755297@qq.com

Keywords: Coal, Particle Size, Oxygen Consumption Rate, Dimensionless Parameter

Abstract. Six coal samples are oxidized by the sequence heating-up experiment. The oxygen consumption rates of six coal samples are calculated and analyzed at different temperature. And the general trend of the same particle size is discussed at different temperature. Then the oxygen consumption rates and particle size are handled by the dimensionless variable. The best-fitting curve of the relationship with dimensionless particle size and oxygen consumption rate is gained. Finally, the particle size influence function of experimental coal samples is determined at low-temperature oxidation.

Introduction

The spontaneous combustion of coal seam has a serious impact on the coal industrial development. It brings great safety hazard to mine production. The essential of coal spontaneous combustion is the physical and chemical adsorption of various active structure and oxygen in the coal surface molecules at low temperature [1, 2]. And the heat is released. If the supply of oxygen is full, the coal temperature rises with the heat accumulation. Then the spontaneous combustion is caused.

In fact, loose coal body is mixed with different coal particle sizes. The oxygen consumption rates of different coal particle sizes must be different at different temperature [3, 4]. Therefore, six coal samples are oxidized by the sequence heating-up experiment. The oxygen consumption rates of six coal samples are calculated and analyzed at different temperature. Then the oxygen consumption rates and particle size are handled by the dimensionless variable. Finally, the particle size influence function of experimental coal samples is determined at low-temperature oxidation.

Experimental Systems

The apparatus included two parts. One is the test tube which is filled with the experimental coal sample. It is controlled by the temperature programmed controller. The other is gas chromatography apparatus. It is used to detect the gas contents which are created during the coal temperature programmed oxidation. The experimental apparatus is shown in Figure 1. Samples are placed in the sample chambers. Air enters into the gas supply system through flow meter at the stated flow. The temperature control systems control its heating rate. The sample gases produced enter into the chromatograph instrument after oxidation.

Experimental Parameters

The coal samples are chosen from 3# coal seam in Yanzhou coal mining area. First, the coal samples are broken in the air during the experiment. Then six coal samples of different particle sizes are sieved. Finally, the sequence heating-up experiment is carried out. The experimental parameters of coal samples are shown in Table 1.

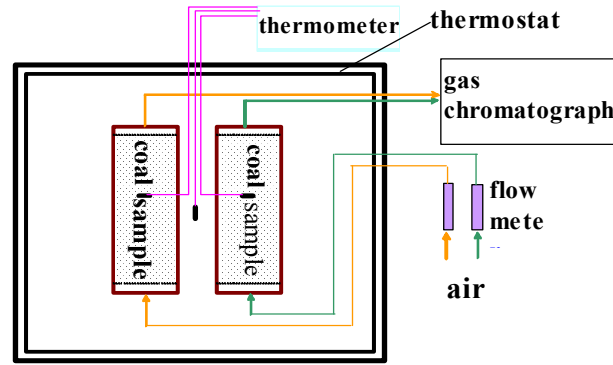


Fig. 1 Relation experimental sketch of coal sample with spontaneous combustion character

Table 1. Experimental parameters of coal temperature programmed oxidation

	particle size(cm)	average particle size d_{50} (cm)	coal high (cm)	coal scale (g)	coal vomule (cm^3)	unit weight (g/cm^3)	n	air flow (ml/min)
11#	0.7~1.0	0.85	21.5	1050.0	1523.9	0.69	0.507	170
22#	0.5~0.7	0.60	22.0	1050.0	1559.4	0.67	0.521	175~180
33#	0.3~0.5	0.40	21.4	1050.0	1516.8	0.69	0.507	160
44#	0.09~0.3	0.20	19.6	1040.0	1417.6	0.73	0.461	160~170
55#	0.025~0.09	0.06	20.7	1099.0	1453.1	0.76	0.443	160~180
66#	mixture coal	0.42	22.0	1250.0	1559.4	0.80	0.429	150~180

Experimental Results and Analysis

Measurement of different oxygen consumption rate of different coal particle sizes

The temperature of coal is uniformity similarly inside the test tube. The entrance air is fresh air. The air is regarded as the ideal gas. The average oxygen consumption rate of unit volume of coal can be calculated by the formula in the fresh air flow [5]:

$$V_0(T) = -\frac{Q \cdot \varphi_0}{nV_m} \cdot \ln \frac{\varphi}{\varphi_0} \quad (1)$$

In the formula (1):

$V_0(T)$ —oxygen consumption rate of coal samples at the standard oxygen concentration, $\text{mol}/(\text{s} \cdot \text{cm}^3)$; Q —supply air volume, ml/min; n — porosity; V_m —the volume of coal samples, cm^3 ;

φ_0 —oxygen concentration in fresh air flow, 21%; φ —the measured oxygen concentration, %

According to the oxygen concentration of different particle sizes at different temperatures, the oxygen consumption rate of different particle size can be obtained at different temperatures (shown as Table 2).

Analysis of Oxygen Consumption Rate of Different Particle Sizes of Coal Samples

According to measured data in Table 2, the oxygen consumption rates of coal sample can be obtained when temperature is 35°C, 40°C, 45 °C, 50°C, 55°C, 60°C, 65°C, 70°C, 75°C, 80°C, 85°C, 90°C, 95°C, 100°C, 105°C, 110°C, 115°C by the linear interpolation algorithm, shown in figure 2.

The followings can be seen from the Fig. 2. The oxygen consumption rates of coal samples increase with the increasing temperature. The smaller of particle size is, the greater of the oxygen consumption rate at the same temperature.

When the temperature is low, the oxygen consumption rates change slowly for the same coal sample. The rise highly when the temperature exceeds 70°C. The curves of oxygen consumption rates show a trend similar to the exponential curve generally.

Deduce of the Influence Function Of Different Coal Samples at Low-Temperature Oxidation

According to Fig. 2, the oxygen consumption rates of the coal are selected at the temperature of 50°C, 80°C, 90°C and 110°C, then the oxygen consumption rate and particle size are handled by the dimensionless variable.

Table 2. Oxygen consumption rates on coal with different particle sizes

coal sample	parameters	1	2	3	4	5	6	7	8	9
1#	T(°C)	30.8	40.3	51.8	59.0	80.5	88.7	98.7	109.0	117.4
	O ₂ (%)	20.89	20.84	20.78	20.73	20.63	20.51	20.38	20.23	20.01
	V ₀ (T)×10 ¹¹	9.15	13.33	18.36	22.55	30.98	41.15	52.23	65.11	84.17
2#	T(°C)	29.8	57.4	86.2	112.6	125.1	137.7	155.4	165.1	176.4
	O ₂ (%)	20.87	20.71	20.39	19.50	18.35	17.07	14.80	13.48	9.38
	V ₀ (T)×10 ¹¹	10.64	23.83	50.51	126.97	231.12	355.00	599.49	759.55	928.64
3#	T(°C)	41.2	79.5	109.5	133.1	145.3	152.4	166.7	180.3	189.7
	O ₂ (%)	20.78	20.25	19.11	16.05	14.32	13.21	11.78	10.23	9.75
	V ₀ (T)×10 ¹¹	17.36	59.94	155.43	443.02	558.3	748.6	952.8	1132.5	1264.5
4#	T(°C)	25.4	45.2	74.5	108.3	121.6	136.3	156.8	174.8	192.6
	O ₂ (%)	20.88	20.68	20.31	19.07	17.56	15.72	13.12	11.23	7.18
	V ₀ (T)×10 ¹¹	10.74	22.76	70.17	180.63	335.19	542.59	881.33	1172.8	2010.5
5#	T(°C)	31.2	67.3	96.8	106.6	123.6	141.0	156.1	178.7	195.4
	O ₂ (%)	20.79	20.26	19.38	18.43	16.36	14.06	11.04	7.96	4.76
	V ₀ (T)×10 ¹¹	17.29	69.43	155.37	211.06	419.86	733.32	1106.2	1668.9	2553.5
6#	T(°C)	26.8	36.6	48.4	51.8	78.3	85.1	94.6	107.3	124.9
	O ₂ (%)	20.61	20.24	19.13	18.87	17.32	16.51	15.35	13.94	11.27
	V ₀ (T)×10 ¹¹	28.68	33.69	52.96	56.93	115.99	143.54	186.01	234.93	458.86

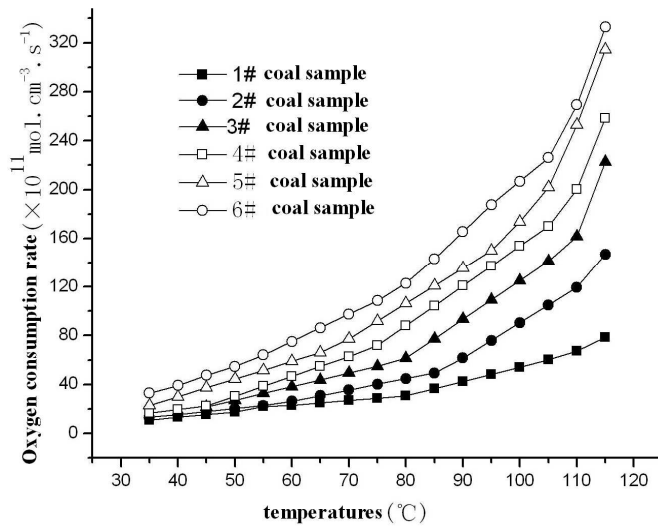


Fig. 2 Curve of oxygen consumption rate with different coal samples

The $V_0(T)/V_0(T)_{ref}$ of coal samples and reference coal sample (mixed coal) and the d_{50}/d_{50ref} of dimensionless particle size are shown as table 3. The parameters of reference coal samples are as follows:

$$d_{50ref}=4.22\text{mm}, V_0(50)_{ref}=54.82 \times 10^{-11}, V_0(80)_{ref}=122.88 \times 10^{-11}, V_0(90)_{ref}=165.45 \times 10^{-11}, V_0(110)_{ref}=269.28 \times 10^{-11}.$$

According to table 3, the relationship between the oxygen consumption rate and dimensionless particle size can be drawn, shown in Fig. 3.

It can be seen from Fig.3 that the relationship between dimensionless size and oxygen consumption rate is nonlinear in the experimental particle size range. The trends of dimensionless coal particle size and oxygen consumption rate are the same. The relationship is consistent with the variation of logarithmic relationship [5]. Fitted by logarithmic relationship, the line in Fig.4 is the fitting curve. When the temperature is 90°C, the fitting equation is:

Table 3. Dimensionless value of oxygen consumption rate and particle size

average particle size $d_{50}(\text{mm})$	0.60	2.00	4.00	6.00	8.50
dimensionless diameter $d_{50}/d_{50\text{ref}}$	0.142	0.474	0.948	1.422	2.014
$V_0(50) \times 10^{11}$	44.44	30.53	27.14	20.29	17.57
$V_0(50)/V_0(50)_{\text{ref}}$	0.811	0.557	0.495	0.370	0.321
$V_0(80) \times 10^{11}$	106.43	88.14	61.53	44.77	30.78
$V_0(80)/V_0(80)_{\text{ref}}$	0.866	0.717	0.501	0.364	0.251
$V_0(90) \times 10^{11}$	135.56	120.82	93.36	61.52	42.59
$V_0(90)/V_0(90)_{\text{ref}}$	0.819	0.730	0.564	0.372	0.257
$V_0(110) \times 10^{11}$	252.82	200.39	161.52	119.44	67.38
$V_0(110)/V_0(110)_{\text{ref}}$	0.939	0.744	0.600	0.444	0.250

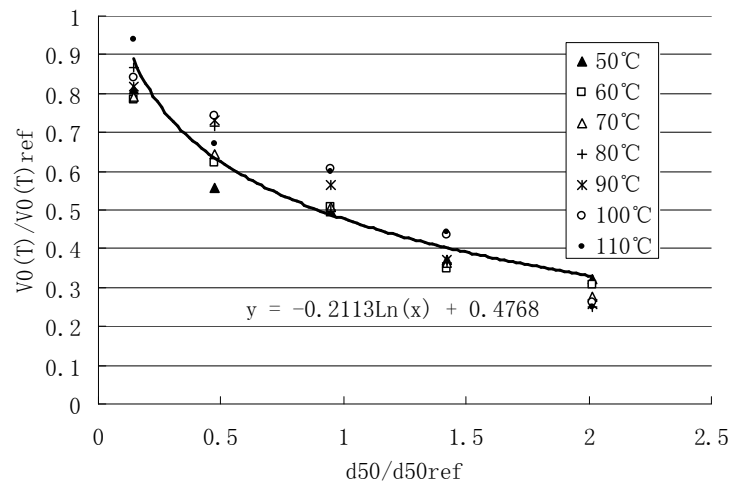


Fig. 3 Relation dimensionless particle size with oxygen consumption rate

$$y = 0.4768 - 0.2113 \ln(x)$$

(2)

Conclusions

The following conclusions can be attained through the above experiments and analysis:

For the same coal sample, when the temperature is low, the oxygen consumption rate changes slowly. If the temperature exceeds 70°C, the curve of oxygen consumption rate changes largely. The curves of oxygen consumption rates show a trend similar to the exponential curve generally.

The trend of dimensionless coal particle size and oxygen consumption rate is consistent with the variation of logarithmic relationship

In the experimental particle size range, the relationship of coal particle size and oxygen consumption rate can be fitted according to the logarithmic function. When the temperature is 90°C, the fitting equation is: $y = 0.4768 - 0.2113 \ln(x)$

References

- [1] Zuo Qiuling, Zhang Jianguo, Wang Guoji. Experimental study on the characteristic of oxygen consumption of coal at low-temperature oxidation[J].<Proceedings of the 2010 International Symposium on Safety Science and Technology>Part B: 1456-1459.
- [2] Wang Haihui. China mine fire safety and coal spontaneous combustion research[J].Promote the Development of Science and Technology ,2009, (12):22—23.
- [3] Zhao Jizhan, Deng Jun.Study on the characteristic of oxygen consumption with different sizes at different temperatures in Qi Xing Mining coal [J].Coal Mine Modernization ,2005,2:61-62.
- [4] Lu Wei,Hu Qianting. Relation between the change rules of coal structures when being oxidized and spontaneous combustion process of coal[J]. Journal of China Coal Society,2007,32(9):939-944.
- [5] Deng Jun, XU Jingcai, Li Li ect. The experimental study on the relationship of Oxygen consumption rate and coal particle size [J]. Xi'an Jiaotong University, 1999,33 (of 12) :106-107.

Improved Phosphate Ore Leaching with Physical Mutagenized *Acidithiobacillus ferrooxidans* Based on Modified Logistic Model

WANG En-wen^{1, 2, a}, LEI Shao-min¹, GONG Wen-qi¹

¹School of Resources and Environmental Engineering, Wuhan University of Technology, Wuhan 430070, PR. China

² School of Resources Management and Environmental Science, Anshun University, Anshun 561000, PR. China

wang_ew@163.com

Keywords: Logistic Model; *Acidithiobacillus Ferrooxidans*; Ultraviolet Mutagenesis; Ultrasonic Vibration; Low Temperature Treatment

Abstract. Strains of *Acidithiobacillus ferrooxidans* (*At.f*) were separated and purified from water sample collected from a hot spring and bioleaching a low grade phosphate ore. The results indicated that bioleaching phosphorus rate increasing sharply was starting at the ending of pH value decreasing, and ascend velocity had slowed down after linear regression of pH was at its second peak. In the environment of ultraviolet mutagenesis, the initial growth of *At.f* (r) was decreased by illumination time increased, but the maximum rate of bioleaching phosphate ore (η_m) was increased. In the condition of ultrasonic vibration, r was increased by vibration time added, and η_m was almost increased, except 20 min, owing to the modificatory coefficient was large enough. In circumstances of low temperature treatment, r was decreased by treatment time raised; η_m was more increase than the sample of un-treatment (CK).

Introduction

Our country's resource of phosphorus is quite rich, but the rich phosphate ore is largely used out and we have to use middle or low grade phosphate ore [1], because it is uneven distribution and has been unreasonably exploited [2]. The traditional processing methods are expensive and polluting for middle or low grade phosphate ore, so people are seeking for other superior methods [3, 4].

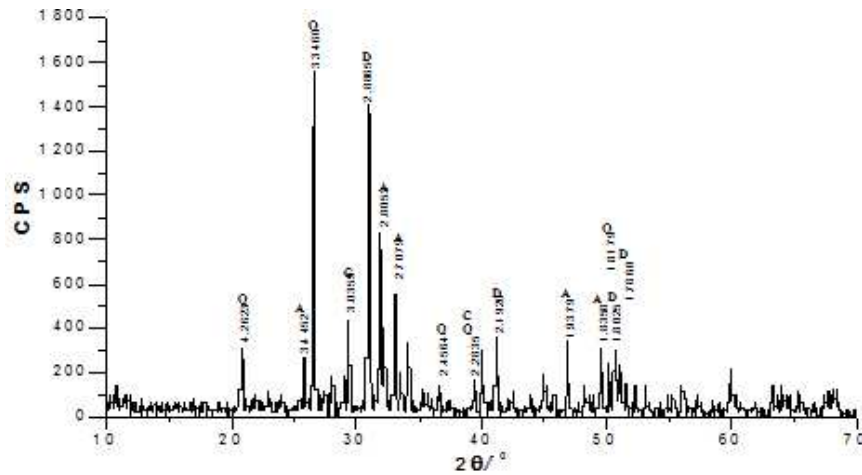
Bacterial leaching ore is cheap and non-pollution, so more and more people pay attention to it. *Acidithiobacillus ferrooxidans* (*At.f*) is the main bacterium for leaching, because it can use oxygen from air to oxidize the reductive state of iron and sulfur [5, 6], from which it gains energy and produces sulfuric acid to leach phosphorus from middle or low grade phosphate ore [7, 8]. Early bacterial leaching research is mainly about metal ores [9] but not non-metallic ores, particularly, with very little work done for phosphate ore [10, 11].

The bioleaching of application area is limited, because the oxidation effect of un-cultivation *At.f* for iron, sulfur and metallic disulfide seems slowly, and its growth conditions need so demanding [12, 13]. And the adaptability and the *At.f* leaching is able to improve highly after cultured by 9K nutrient medium, because of its typical features of simple-system, short-life, fast-multiply, it has more selective adaptation under external environment, and the bacillus will change its genetic material to adapt to the new environment and its offspring will obtain the adaption[14, 15]. But the cycle of cultivation of bacillus adaption seems longer and a little microbe changed. So, most of time, bacillus mutagenizing methods are composed of physical mutagenizing, chemical mutagenizing. And the methods are used to change the bacteria's genetic material to adapt to the new bioleaching environment within a short period of the time [16, 17], and the mutagenic bacteria will become the dominant [18].

So modeling the process of action between physical mutagenesis *At.f* and phosphate ore is very necessary. And it can improve bioleaching of phosphate ore in theory.

Materials and Methods

Materials



A—Apatite, C—Calcite, D—Dolomite, Q—Quartz
 Fig. 1 XRD diffraction pattern of low-grade phosphate ore

The isolation and purification of *At.f* isolated from a hot spring water sample from Guangxi province was used. Low-grade phosphate ore (Table 1 & Fig.1) was used.

Table 1. The chemical composition of low-grade phosphate ore

Chemical composition	P ₂ O ₅	CaO	MgO	Fe ₂ O ₃	Al ₂ O ₃	SiO ₂	Sour insoluble	Loss on ignition
Content [%]	16.19	32.32	6.06	0.95	1.17	29.18	30.00	14.72

Method of Treatment

A sample needs 10 mL *At.f* cell, which has no ferric iron interference, and puts it in Petri dishes (∅ 90cm), and it is illuminated by ultraviolet (power: 15W; illumination high: 15cm) with 0min, 5min, 10min and 15min, or ultrasonic wave (frequency: 59 kHz) with 0min, 5min, 10min, 15min and 20min, or low temperature (4°C) with 0 h, 0.5h, 1.0h, 1.5h. Then every one of the samples was obtained 5mL to 50mL 9K modified nutrient medium (has 1gram but no phosphorus) in a conical flask (100mL) in a gas rocker (120 r/min, 30 °C, no light) which stirred for bioleaching phosphate ore.

Logistic Model Application

Chen and co-workers reported that the *At.f* population correlated positively with the bioleaching phosphate ore rate [19]. Therefore, the Logistic model will be modified to quantify the procedure of improved leaching low-grade phosphate ore with physical mutagenized *At.f*. And the modified Logistic model is below as: $\eta(t) = \frac{24.1}{1 + 475.28e^{-0.3469t}}$ [20].

Results and Discussion

Effect of Ph Value on Bioleaching Phosphate Ore

In order to investigate the effect of pH value on *At.f* leaching phosphate ore, a great number of experiments conducted. The figures of polynomial linear regression and the fit of experimental data are displayed in Fig. 2 and Fig. 3.

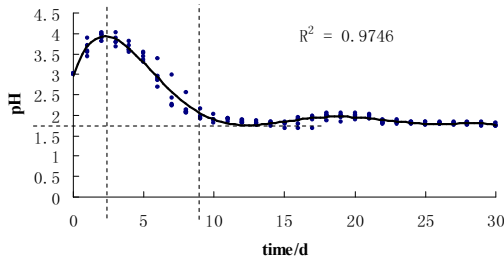


Fig. 2 Linear between pH and bioleaching time

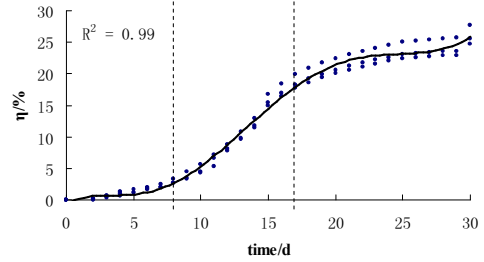


Fig. 3 Linear between bioleaching phosphorus rate and time

In the system, it prompted that: 1) pH value was increasing sharply before the 3th day, decreasing gradually after it to the 9th day, declining gently from the ninth day to the 11th day, and the minimum value of pH (ca. 1.80) might be discovered. But the result of pH value after the 11th day was seemed different from Yang [13] that pH value of sample was to increase gently but not decrease in microbe decline phase; 2) the rate of *At.f* leaching phosphorus (η) kept ascending in the test, and it ascended sharply from the 8th day to the 20th day and then ascended gently.

Quantitative Analysis with Modified Logistic Model

Ultraviolet Illumination

In order to determine the activity of the samples under ultraviolet illumination at 253.7 nm wavelength was chosen. And the figures of polynomial linear regression and fit of the experimental data were displayed in Fig.4 and Fig.5.

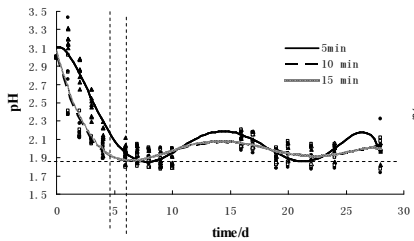


Fig. 4 Linear regression pH-bioleaching time

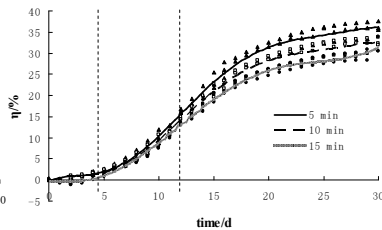


Fig. 5 Linear regression η-bioleaching time

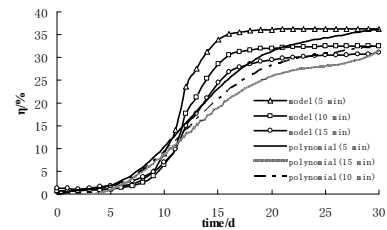


Fig. 6 Modified Logistic model linear regression

The corresponding data was showed in Fig.6 with polynomial linear fitting, which could be found that the initial growth of *At.f* (r) was decreased by illumination time of ultraviolet, but the maximum rate of bioleaching phosphate ore (η_m) was increased.

Table 2. Values of r , t_0 , C and η_m after irradiated by different time of ultraviolet

Illumination time [min]	r	t_0	C	η_m [%]
0(CK)	0.3469	2	1.1023	24.1
5	0.2823	2	4.2566	36.4
10	0.2803	2	3.2003	32.7
15	0.2265	4	1.6384	31.6

If only considered the influence of ultraviolet illumination, the η_m decreases with decreasing of the initial growth. This piece of work does not seem to come up to the above-mentioned rule, owing to the modificatory coefficient (C) was seemed to large.

Ultrasonic Vibration

In order to determine the activity of the samples under ultrasonic vibration at 59 kHz is chosen. And the figures of polynomial linear regression and fit of the experimental data are displayed in Fig.7 and Fig.8.

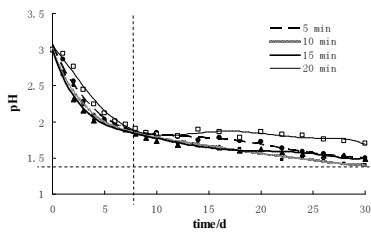


Fig. 7 Linear regression pH-bioleaching time

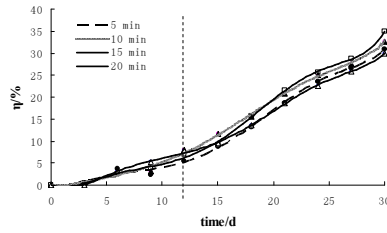


Fig. 8 Linear regression η-bioleaching times

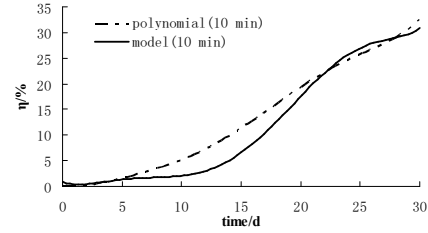


Fig. 9 Modified Logistic model linear regression

The corresponding data was showed in Fig.9 with polynomial linear fitting, which could be found that the r was increased by vibration time of ultrasonic, and the η_m was almost increased, except 20 min ultrasonic vibration, owing to the modificatory coefficient was large enough.

Table 3. Values of r , t_0 , C and η_m after vibrated by different mutagenesis time of ultrasonic

Vibration time [min]	r	t_0	C	η_m [%]
0(CK)	0.3469	2	1.1023	24.1
5	0.2605	3	0.4045	30.8
10	0.2014	3	1.5026	32.6
15	0.1989	3	1.1745	35.0
20	0.1841	3	3.8426	30.0

From Fig.9, the result could be discovered that this piece of experiment seemed to come up to the above-mentioned application model rule, but the model curve seemed to partly fit to the actual curve. Low temperature treatment

In order to determine the activity of the samples under low temperature treatment at 4°C was chosen. And the figures of polynomial linear regression and fit of the experimental data are displayed in Fig.10 and Fig. 11.

Table 4. Values of r , t_0 , C and η_m after refrigerated by different treatment time of low temperature

Treatment time [h]	r	t_0	C	η_m [%]
0(CK)	0.3469	2	1.1023	24.1
0.5	0.2428	4	0.3574	29.5
1	0.2437	6	0.3479	32.6
1.5	0.2674	6	0.7001	27.8

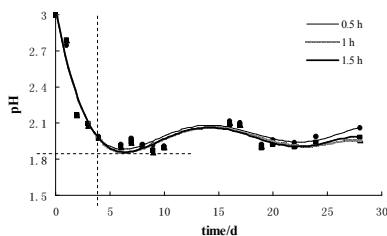


Fig. 10 Linear regression pH-bioleaching time

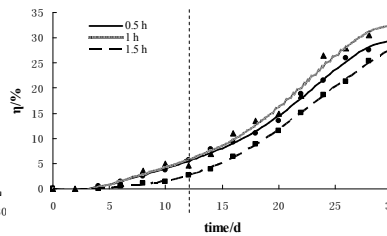


Fig. 11 Linear regression η-bioleaching time

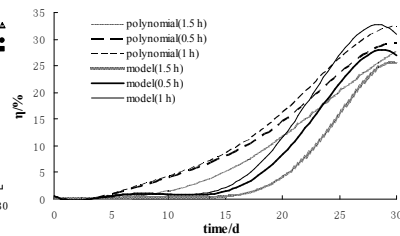


Fig. 12 Modified Logistic model linear regression

The corresponding data is showed in Fig.12 with polynomial linear fitting, which could be found that r was decreased by low temperature treatment (4°C), and η_m was more increased than the sample of un-treatment.

Likely to the above two results of physical mutagenesis experiment, this parameters of modified Logistic model after low temperature treatment would be modified by considerable stack of evidence in the next experiment period.

Conclusion

ynthetic analysis of the above results, it was shown that, to a certain degree, the modified Logistic model with modificatory coefficient from the experiment could guide the bacillus bioleaching phosphate ore experiment.

Compare Fig.4, Fig.7, Fig.10 with Fig.2, it was shown that all of the three physical mutagenesis shorten the adaptation phase of bacteria bioleaching phosphate ore. So it could be concluded that ultraviolet illumination, ultrasonic vibration and low temperature treatment were of advantage in which selecting and breeding the excellent bacteria of bioleaching phosphate ore. And what was certain was that ultrasonic vibration seemed to show the greatest influence to improve in *At.f* acid production the three physical mutagenesis, and the sample ultrasonic mutagenesis 15 min showed the best activation of bioleaching phosphate ore in all of the experiments, and it still has the potential to be faster.

And compare Fig.5, Fig.8, Fig.11 with Fig.3, it was shown that the curves in Fig.5 and Fig.11 were closed to Fig.3. But the beginning of logarithmic growth phase was advanced in the ultraviolet illumination and postponed in the low temperature treatment, and the data of two physical mutagenesis could be linear fitted in "S" curve. However, comparing Fig.8 with Fig.3, it was discovered that the beginning of logarithmic growth phase was latter in ultrasonic vibration than CK, but the upward trend shows no signs of getting smooth down during 30 days, so its linear fitted is showed inapparent "S" curve. The reason is that bacteria will be renovating if gets it out ultraviolet illumination or low temperature treatment for a certain time, so under the two conditions the curves are closed to the initial; but the curve changes greatly under the condition of ultrasonic vibration, it seems to be proved that it is the best physical mutagenesis, and the best stable mutagenized *At.f* may be obtained under the condition.

Acknowledgment

Funded by Natural Science Foundation from the Guizhou Education Department (No.20090076) & Science and Technology Foundation from the Guizhou Science and Technology Department (No.20092105)

References

- [1] Q. Liu, W.C. Xu, C.L. Nie, et al: Progress of the Studies on Leaching Microbe in China. Journal of Central-south Institute of Technology, Vol. 17, No. 1 (2003), p. 21-24
- [2] Z. Liu: The Status Quo and Plan on Exploitation and Utilization of Phosphate Ore Resources in China. China Non- Metallic Mining Industry Herald, Vol. 18, No. 1 (2006), p. 21-23
- [3] G.W. Li: The Geographical Distribution of Phosphorus Resource in China. Cartography, No. 1 (2000), p.41
- [4] R.A. Chi, C.Q. Xiao, H. Gao, et al: Biodecomposition of Low-grade Rock Phosphate with Some Bacteria and Fungi. The Chinese Journal of Process Engineering, Vol. 5, No. 6 (2005), p. 636-639.

CHAPTER 5:

Control, Monitoring and Computer Technologies

Research on Optimization Control Strategy for Limiting Short-Circuit Current Based on Fuzzy Quantitative Control

Guanglei Li^{1, a}, Shumin Sun¹, Yan Cheng¹, Hongbo Li^{2, b}, Shuai Yuan¹

¹Shandong Electric Power Research Institute, Jinan, China

² State Grid of China Technology College, Jinan, China

^aemail: lovexjtulgl@126.com, ^bemail: 250597040@qq.com

Keywords: Impedance Sensitivity, Fuzzy Quantitative Control, Optimization Algorithm, Current-Limiting Measures.

Abstract. To decrease short-circuit current, adjusting the power network operation by breaking transmission lines is the most economic and convenient measure. For large power grid, breaking transmission lines has thousands of combinations, so it's very difficult to find the best combination in a short time. Firstly, this paper formulated the sensitivity relationship between transmission line outage and impedance change. Then preliminary combinations schemes of transmission line outage were selected according to the sensitivity. Index values of factors were given using the fuzzy control evaluation. Finally, this paper determined optimal scheme from maximum priority and accomplished the accessorial intelligent optimize system of limiting short-circuit current. The rapidity and rapidity of the proposed control strategy was verified by calculating the actual power grid.

Introduction

With the gradual expansion of the grid size, short-circuit Current Exceeding has become an important issue for power system planning, dispatching operation department and other departments [1]. While in the initial stage, this will bring the local power supply shortage, reduced reliability and other adverse effects [2]. The paper [3] holds that bus splitting would weaken the electrical connection, reduce safety margin and loose flexibility. Literature [4] and [5] never consider the static security and stability, transient voltage security and other factors. Without additional equipment or changing equipment, breaking transmission lines is more convenient means of inhibiting short-circuit current, which can increase the equivalent impedance of the grid [3].

Sensitivity Analysis of Short-Circuit Current

Short-circuit current of the original network system will decrease in different extent and effect is especially obvious for the excessive short-circuit current [4].

It is supposed that Impedance Matrix of power network is Z_N , line impedance matrix between bus i and bus j is Z_{ij} . Assuming that line impedance matrix between bus 1 and bus i , line impedance matrix between bus 1 and bus j , line impedance matrix between bus m and bus j are separately Z_{1i} , Z_{1j} and Z_{mj} . When breaking transmission line between bus i and bus j , new impedance matrix Z_N' is calculated as follow formula (1) using branch additional method [5, 6].

$$Z_N' = Z_N - \frac{Z_L Z_L^T}{Z_{LL}} \quad (1)$$

$$Z_{LL} = Z_{ii} + Z_{jj} - 2Z_{ij} - z_{ij} \quad (2)$$

Assuming that short-circuit current before breaking n transmission lines, short-circuit current after breaking n transmission lines, impedance matrix of substation before breaking n transmission lines, impedance matrix of substation after breaking n transmission lines are separately $I_k^{(n-1)}$, $I_k^{(n)}$, $Z_{kk}^{(n-1)}$ and $Z_{kk}^{(n)}$. So sensitivity analysis $\eta_k^{(n)}$ caused by breaking n transmission lines can be calculated by the following formula (3):

$$\eta_k^{(n)} = \frac{I_k^{(n-1)} - I_k^{(n)}}{I_k^{(n-1)}} = \frac{Z_{kk}^{(n)} - Z_{kk}^{(n-1)}}{Z_{kk}^{(n)}} = -\frac{Z_{Lk}Z_{Lk}}{Z_{LL}Z_{kk}} \quad (3)$$

The actual operation of the grid is adjusted all the time and the level of each short-circuit current exceeding is also different. So it should have given priority to the optimal combination of breaking transmission lines. In this paper, weighting factors are given to evaluate the overall effect of each scheme. η_{sum}^l Was overall effect after considering weighting factors, while α_k was weighting factor of substation with short-circuit current exceeding.

$$\eta_{sum}^l = \sum_{k=1}^n \alpha_k \eta_k \quad (4)$$

Fuzzy Evaluation Optimal Strategies

Evaluation indexes were described below.

The effect of reducing short-circuit current

Assuming that the effect of reducing short-circuit current, the set of circuit breakers, the decreased amplitude of short-circuit current after breaking transmission lines, the decreased amplitude of short-circuit current after breaking transmission lines are separately λ_{sc} , β , ΔI_{sc} and I_0 . So the effects of reducing short-circuit current is calculated by the following formula (5).

$$\lambda_{sc} = \sum_{\beta} (\Delta I_{sc} / I_0)^2 \quad (5)$$

The constraints

Security check can be effectively realized by over current of transmission line, transformer overload, the degree of bus voltage exceeding. Evaluation index are λ_{N-1} and λ_{N-2} respectively.

Static security

Security check can be effectively realized by transmission lines N-1, main transformer substation N-1, transmission lines erected on same tower N-2. Evaluation index are λ_{N-1} and λ_{N-2} respectively.

Transient safety

This evaluation index adopts the biggest generator power angle, shown as λ_{δ} .

Power supply reliability under maintenance conditions

This index mainly considered power supply reliability under maintenance conditions. The case is that one bus of substation is being repaired and another bus is on the Behavior of failure. The evaluation index adopts $\lambda_{reliability}$.

Verification Algorithm

Weifang power system includes three power stations, three 500kV substations and other 220kV substations. The possibility of three-phase short-circuit is the smallest [8], but it causes the most serious impact on system operation. While during the design of power network, three-phase

short-circuit is usually used as a basis for selecting electrical equipment, setting relay protection parameters [6, 7]. Firstly, this paper analyzes the transmission lines which have higher impact on short-circuit current, then calculate short-circuit current and impedance sensitivity under different circumstances of breaking transmission lines, as shown in Table 1.

Because schemes 6, 9, 10, 11 have bigger resistance sensitivity, fuzzy comprehensive evaluation is finally used to achieve best scheme. According to the above analysis, weighting factors of factors set are calculated as follows. W represents weighting factors of factors set, $W = [0.384, 0.203, 0.172, 0.149, 0.092]$. The behavioral indicators of index membership functions are formulated according to the previous description, shown in Table 2. According to the previous discussion, four options are evaluated using fuzzy quantitative evaluation strategy and the results are shown in Table 3.

Table 1 Schemes of breaking transmission lines

Schemes		Short-Circuit Current		Sensitivity Analysis
Number	Breaking transmission lines	500kV Weifang substation (kA)	220kV Weifang power Plant(kA)	
1	Weimi Line	49.31	50.41	0.231
2	Dayue Line	49.52	51.85	0.214
3	Weiwu Line 1	50.03	52.99	0.153
4	Weiwu Line 2	50.99	51.51	0.138
5	Wangquan Line	50.95	52.25	0.105
6	Dayue Line, Weimi Line	47.73	49.21	0.348
7	Dayue Line, Weiwu Line 1	48.44	49.63	0.294
8	Dayue Line, Wangquan Line	49.37	51.09	0.228
9	Xingjia Line, Wangjia Line Wangquan Line	43.9	46.09	0.425
10	Xinggui Line 1,2, Baowang Line	45.35	47.37	0.402
11	Dayue Line, Weimi Line Wangquan Line	47.58	48.49	0.361
12	Dayue Line, Weiwu Line 1, Weimi Line	48.23	49.74	0.288

Table 2 Index membership functions

Indexes	λ_1	λ_2	λ_3	λ_4	λ_5
λ_{sc}	5	10	15	20	25
λ_{line}	25	35	45	55	65
λ_u	30	45	60	75	90
λ_r	20	30	40	50	60
λ_{N-1}	30	40	50	60	70
λ_{N-2}	35	50	65	80	95
$\lambda_{reliability}$	15	25	35	45	55
λ_δ	85	95	105	115	130

Both scheme 9 and scheme 10 have good effect of reducing short-circuit current, but this cause lower static security and inferior power supply reliability under maintenance conditions. Compared with scheme 6, scheme 9 not only open electromagnetic loop network, but better reduce short-circuit current of two 220kV buses. Therefore, having the largest priority, scheme 11 is the best combination of breaking transmission lines to meet the requirements of electrical production.

Table 3 The results of for options using fuzzy quantitative evaluation strategy

Indexes	Scheme 6	Scheme 9	Scheme 10	Scheme 11
λ_{sc}	12.07	18.76	16.24	13.89
λ_{line}	45.05	46.23	43.39	43.71
λ_u	61.92	65.48	63.18	62.48
λ_T	41.73	42.81	45.61	44.36
λ_{N-1}	51.38	46.14	41.26	54.62
λ_{N-2}	61.24	37.56	33.87	65.02
$\lambda_{reliability}$	35.78	20.21	17.24	38.57
λ_g	107.64	109.09	110.51	108.97
priority	5.72	4.19	3.62	6.01

Conclusion

Using the fuzzy comprehensive evaluation, the optimal scheme of limiting short-circuit current can be determined from maximum priority. The proposed method is verified by the simulation of short-circuit current exceeding limit of 220 kV buses of Weifang Power Grid. This strategy provide a theoretical basis for opening electromagnetic loop network and also provide reference for optimizing the operation of power grids.

References

- [1] Liu Yan, Du Zhi, Wang Jiang-hong. Analysis of Short-circuit Current of Hubei Power Grid in 2011~2012 [J] Hubei Electric Power,2010, 34(5):57-59.
- [2] Sarmiento HG, Castellanos R, Pampin G, et al. An example incontrolling short circuit levels in a large metropolitan area[C]. Proceedings of 2003 Power Engineering Society General Meeting. Toronto, Canada: IEEE Power & Energy Society,2003:589-594.
- [3] Han Ge, Han Liu 2, Wu Lin 1. Application and development of methods on limiting power grid's short-circuit current [J].Automation of Electric Power Systems,2010,38(1):141-144.
- [4] Yang Xiongping, Li li, Li Yangxu, et al. Operation schemes for limiting short-circuit current of 500 kV network in Guangdong power grid. Automation of Electric Power Systems,2009, 33(7): 104-107.
- [5] Yang Dong, Liu Yutian, Niu Xinsheng. Integrated decision method of operation schemes for limiting short-circuit currents in district grids[J]. Automation of Electric Power Systems, 2010, 34(12):34-38.
- [6] He Yangzan, Wen Zengyin. Power System Analysis[M]. Wuhan: Huazhong University of Science and Technology Press, 2001.
- [7] Chen Y, Bose A. Security analysis for voltage problems using a reduced model. IEEE Trans on Power Systems, 1990, 5(3): 933-940.
- [8] Zhou Xue-song, Zhou Xuan-zheng, Ma You-jie, Gu Hai-qing, Liu Xin, Zhu Yi-ran. Selection and Analysis of Maximum Short-circuit Current Point[J].East China Electric Power, 2010, 38(9):1332-1334.

Study Based on TMS320F2812 Synchronous Generator Field Regulator

Zhitian Zhang^{1,a}, Xiaoping Shi², Xiaoling Shi³

¹Hunan Industry Polytechnic, Hunan, 410200, China

²Hunan College of Information, Hunan, 410200, China

³Changsha Environmental Protection Colleges, Hunan, 410004, China

^aZhangzhitian66@163.com

Key words: Excitation Regulator; DSP; Synchronous Generator ; Dual CPU

Abstract. This paper introduces the research on the Excitation Regulator of the Synchronous Generator with dual CPUs, based on Digital Signal Processor (TMS320LF2812). With the multiple functions of monitoring, analysis, controlling and protection, it overcomes the shortage of the domestic excitation device in terms of self-monitoring and self-protection, which effectively improves device reliability. By analyzing the allocation of reactive load of the interconnected Synchronous Motor group, the modeling and simulation of the digital excitation regulator in the power system are illustrated in the paper. The results of the simulation show that the proposed regulation model are feasible, satisfying various running demands of the Synchronous Motor and Power System.

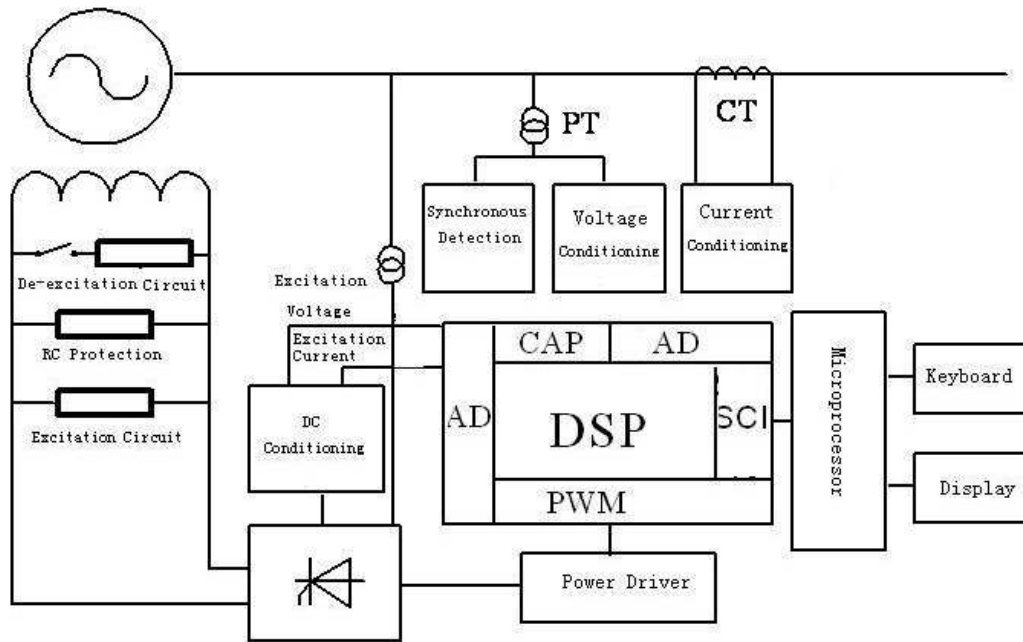
Introduction

In synchronous generators system, excitation system is the core of stable operation of generators and power supply. ^[1] With the development of power electronics and LSI, digital excitation regulator gradually replaced the traditional semiconductor excitation regulator for its strong logical computing capacity and flexibility in software design which not only improved power supply quality significantly, but also put forward higher requirements on the excitation device performance and reliability [2]. Regulator must be able to stabilize the system with fast and strong excitation while providing normal operation of the synchronous generator from no- load to overload, a sudden drop in grid voltage; and must be quickly de-excited in the generator internal short-circuit fault to make failure limited to the minimum, simultaneously must be able to adjustable differential reactive load control when the Synchronous Motor group is interconnected.

This article has studied one kind dual CPU excitation device based on the TMS320F2812 according to the above requests, which can satisfy system targets of the synchronous generator to get up urges, overload step, short circuit trouble shooting with its merits of quick operating speed, high integration rate, strong network interconnection ability, higher performance-to-price ratio compared with the present widely used monolithic type excitation controller.

System Hardware Structure

In order to use the DSP high speed operational capability fully, to enhance the dynamic response characteristic of the field regulator, the control system made by TMS320LF2812 as main CPU, primarily cognizes data acquisition processing and various logical signal judgment, phase-shift pulses and so on, outside expands the MCS-51 monolithic integrated circuit (W77E516) as assistant CPU for low speed pressed key processing, the correspondence and LCD display, the sampling serial port SCI correspondence between dual CPU, as shown in Figure 1:



Work principle: The excitation system first uses the synchronous generator residual magnetism to start, if the start is unsuccessful input excitation power, the terminal voltage reaches the 65% rating, machine the terminal voltage achieved when 65% rated value, separates urges the return route, the system after PT, CT takes the generator machine end three-phase voltage, the electric current, after the process signal recuperation and the band pass filter, the transformation is 0~3.3V power frequency signal input TMS320LF2812A the internal A/D converter, after the digital filter.

The DSP basis exchange synchronization sampling result, the system working, the controlled variable as well as each kind of limit from the protection condition, carry on the PID operation to derive the triggering angle, inputs EVB to produce the high accuracy PWM phase shifting pulse signal, the displayed information through assists CPU to carry on LCD to demonstrate, simultaneously outputs the correlation Warns the information, the start demagnetization function or begins using the spare channel and so on. PWM phase-shift pulse signal forms a closed-loop excitation regulation system by driving triggered thruster bridge rectifier and controls magnetize current size and stables output voltage after isolation [3].

System Software Design

In the process of system software design , functions of the frequency measurement, the exchange sampling, the phase shifting pulse' s form and control adjustment which the excitation controller needed has been completed by unifying the instruction of TMS320F2812 and the hardware structure characteristic in line with the modular design concept.

Synchronous frequency measurement

The measurement of synchronous frequency is the basis of realizing tracking the sampling, pulse forming and restrictions protection, synchronization voltage signal after shaping circuit entirely formed square-wave signals with same frequency which is sent to the capture unit CAP 1, CAP3 pin of TMS320F2812. After the capture unit is used, the jump specified on the input pin will save the general timer counting value on the corresponding FIFO queue [4]. At the same time set the corresponding interrupt flag, and wait for the appropriate interrupt service program executed by the CPU.

AC sampling algorithm

In this paper, using A/D of TMS320F2812 to achieve power measurements, in the sampling process, CAP1 of EVA unit got captured voltage frequency f , and then general-purpose timer T1 to timed start A/D conversion. The specific process is as follows: the ADC module and the general-purpose timer T1 were started and the value of T1 compare register was updated and modified for the sampling interval of the next cycle when each the rising edge of start was captured.

The ADC was started when the timer T1 had compare interruption to achieve a uniform sampling n-point in each cycle, 32 points sampled in this article. Each ADC conversion completed will complete interruption. In the interrupt service routine, the data sampled on the AD can read and processed. FFT computation of AC sampling results, and the compensation algorithm elaborated in the literature 5 [5]overcame the sampling errors brought by the frequency signal changes and the sampling point non-uniform distribution, and calculated the terminal voltage and electric current of the machine and reactive current, active power, reactive power, power factor.

Design of excitation regulator

Equilibrium point farther in the power system or generator group suffered interference leaving the actual running state deviates from the design selected, the conventional PID control effect will be greatly affected, and even lead to system instability.

This article uses control algorithm of incremental PID realizing a positional PID has overcome error accumulated of the conventional positional PID to adapt to the changing control requirements of the power system and generator set. The control unit is the core of the regulator, including the another assignment part and the PID control section, which are used to overcome the effects of the alternator system load fluctuations and to adjust the impact excitation current to a point voltage of the machine-side or in the system at a given level[6].

Conclusions

The advantages of the synchronous generator excitation regulator based on TMS320F2812: It was controlled by dual CPU and takes the advantages of the DSP which can provide efficient data processing, high speed real-time control capabilities and a wealth of on-chip peripheral resources.

AC sampling, frequency measurement, the phase-shift trigger and excitation control algorithms and other functions of the synchronous generator excitation regulator has been achieved by the use of the monolithic system architecture supplemented by the MCS-51 which share real-time less demanding keys and the display section; The combination of the two to effectively alleviates the burden on the DSP, greatly improves the device reliability and practicality and the acceptability of prices and costs.

Author synopsis

Zhitian Zhang, male, (1973) Yangzhou, Hunan province, Senior Engineer of Dept of Electrical Engineering Hunan Industry Polytechnic. The research direction is Power Electronics Application Technology and Electrical Control.

References

- [1] Zhijun Li, Yanping Liu & Qiang Zhang.etc.2003.Self Monitoring and Self Protection of Excitation Device [J]. Small and Medium-sized Motor, 30(3): 53-55
- [2] Guoyun Luo,Dongchao Yan. 2003. Synchronous Generator Excitation System Based on MATLAB[J]. Electrical Transmission, (5):62-64
- [3] Heping Liu,Xiaoling Yang & Jin Cui. 2006. Synchronous Generator Excitation Regulator Based on TMS320LF2812 [J]. Instrument Technology and Sensor, (5): 42-44
- [4] GuanCHeng Yang. 1995. Principle of Automatic Device of Power System [M]. Beijing : China Electric Power Press,125-128
- [5] Jicheng Li.2002.Design and Application of Modern Synchronous Generator Excitation System[M]. Beijing : China Electric Power Press, 28-31
- [6] Shenmao Liu,Guangyi Zhang. 2004. Excitation Regulator SIMULINK Emulation[J]. journal of Sichuan Industrial Institute, 22 (3) :22-24

Intelligent Monitoring Design and Research of Modern Instrumentation Failure Alarm

Yu Shufang^{1, a}, Shi Xiaoping², Huang Xiuliang³

¹Hunan College of Information, 410200, Central South University 410083, China

²Hunan College of Information, 410200, China

³Hunan College of Information, 410200, China

^aYushufang666@126.com

Keywords: Failure Alarm; Intelligent Monitoring; Automatic Diagnosis; State Test

Abstract. The instrumentation is a complexity of the whole system composed by many circuit modules. In order to achieve the detection to the entire system, when the overall system design, the designer must design circuits with judge and test methods suitable for a variety of levels in the case of considering to enables various modules carry on the wrong judgment and state test. This will provide the capabilities of intelligent monitoring and detection for the normal operation of the whole system. This paper has briefly introduced the development trends of modern instrumentation, analyzed the classification level of the failure alarm, given the general intelligent failure alarm circuit and self-test circuit, and provided a theoretical basis and practical reference for the studying of intelligent design of the failure alarm in a variety of instrumentation.

Introduction

As an important part of modern industry, instrumentation has functions such as multiple parameters, wide-band and high-precision and so on [1] and it is gradually developing toward intelligent direction. In order to meet the needs of modern electronic products testing and maintenance, instrumentation itself must have a stable, reliable ability to run. But modern intellectualization design requests the instrumentation must have automatic failure judgment, alarm function [2], to meet the needs of human-computer interaction and follow-up testing, debugging and repair. This provides the intellectualized safeguard method for the long-term stability work of instrument in measuring appliance. This article will discuss the intelligent design and study of the failure warning system in instrumentation.

Classification of the Failure Alarm

Failure alarm system can be simply divided into two levels:

The real-time failure alarm [3]. The exclusive display area is designed and divided in the man-machine conversation interface of modern instrumentation for failure alarm prompt. The prompted alarm display is usually an eye-catching red. Alarm information displayed in these areas is the failure of affecting the machine functions, and the information need to be diagnosed early and real-time alerts. This level of failure alarm is the highest level in the whole system; it belongs to the fatal failure of affecting the normal machine functions.

Failure alarm of the whole system status information obtained through the self-checking. The modern instrumentation has been designed with a self-test feature and even a post of the function [4]. This kind of failures and the error message through self-checking is a non-fatal failure. And they may lead to the offset of the whole machine index. This kind of failure alarm only warns the user to concern the working status associated with this module and the corresponding indicators. Thus the user can further obtain the health status of the machine according to the warning and can understand fault type, fault level and seriousness, so as to finally decide the need for testing, debugging and maintenance, or repair.

Design of Intelligent Failure Alarm

This kind of idea alarm design is to distinguish good or bad of single function on the whole state. During system design, the designers should design, place the monitoring and detection circuit in some Important and key circuit modules affecting the normal function of the system in the instrumentation. When the monitoring status indicator in some module overruns, the self-diagnostic circuit generates failure indication signal [5], and indicates the level signal (usually one-zero) of current state. Then the self-diagnostic circuit carries on real-time receives and processes by working with master machine CPU processor[6],[7] in the way of direct communicating. In order to guarantee a timely processing of that information, the monitoring and judgment circuit carry on real-time processing and to provide alarms, display by the way of using interrupt inquiry of CPU. This provides the judgment basis for the complete machine most basic function quality, and informs the user or debugging, and maintenance personnel in time. Figure 1 is a block diagram of real-time failure alarm circuit design in the instrumentation:

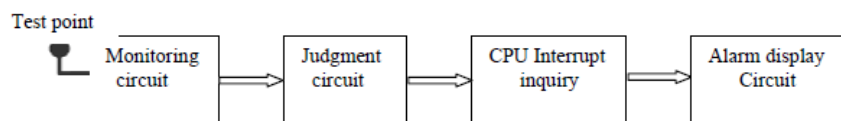


Fig. 1 Design of real-time failure alarms

The monitoring circuit in the figure has functions with a data acquisition and signal conversion. It wills real-time collect the test point information and converts them into the information judged by judgment circuit, and the circuit reflects if the current state of the instrument is normal. When monitoring information voltage exceeds the judgment gate limitation, judgment circuit will send judgment logic (0 or 1). When the output logic level is low, according to the communication protocol with CPU[8],[9], the state will be processed by CPU and displayed in software interface to alert the user that the current state is in the instrument fault conditions. The parameter designed to test the self-diagnostic alarm status must be the significant judgment state in the machine, that is, once the parameters needed to be judged exceed, the working status of the instrument will be in failure. So the priority of such judgments in the CPU interrupt query processing is very high, it is convenient for debug gees and users to obtain information and deal with it for the first time.

Design of Self-Test Failure Alarm

In order to realize that the instruments can intelligently access the status information of the relevant circuit, in the design of machine and systems, many state test points are designed in each module and circuit in the instrumentation to test the working status of the current circuit[10]. The status of the test is no longer a simple logic judgment, while this monitoring status information will be converted to the data which can be processed and stored in CPU. These data are sent into CPU to be judged, processed and stored, as well as displayed in the human-computer dialogue windows to inform the working state of the current instrument to the debug gees and users. These parameters can alter the debug gees and users the current instrument state is in which one: the normal state, the critical state or the overrun state. When some test values are in overrun state, the machine will be prompted in EER by the CPU triggered panel, or after the completion of the whole self-test programs and self-test procedure, alarm dialog box will be pop out to prompt the machine in overrun status, further view, maintain and troubleshoot will be carried out. Figure 2 shows the block diagram of the design of self-test failure alarm.

The data of voltage or current collected from test points of the instruments are analogous. Collections of analogous value depend on multiple-selection switch. Then analogous value is transformed into digital value, after being processed in CPU, transformed digital value will be sent to memory and display block. In this transformation process which uses CPU as a port, a Comparison between collected data and set up-and-down limit of soft parameters is taken. Then a conclusion on whether collected data meet the request or not is got, which can be used to judge the status of instruments. Collected and transformed data will be displayed in a interactive window. Users can watch the status of instruments through the software. When collected data is over the

threshold, the software will be informed that there is something wrong with instruments. Each abnormal status has the corresponding collected data, errors arising from overflow of collected data will be judged and displayed in the self-diagnosis test.

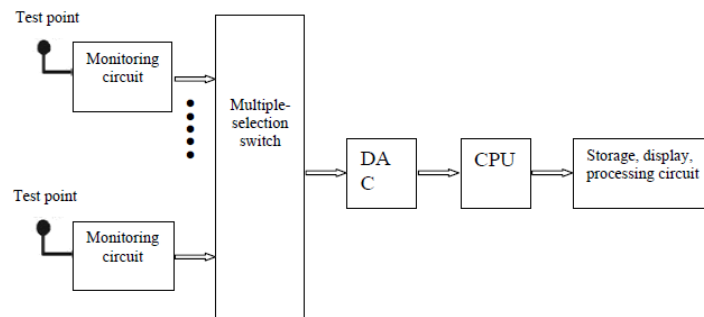


Fig. 2 Design of self-test failure alarm

Conclusion

Intelligent alarm, automatic test design is the inevitable trend of function development of modern instrumentation. Design idea in the text has a certain foundation and a high practical value in the actual project development. With the further development of degree of modernization of the instrumentation, fully automated design including failure alarm, diagnostics, testing, commissioning of instrumentation will be realized eventually, which can improve the intelligence of instrument.

Author Synopsis

Yu Shufang, female, (1977-), Changling, Jilin people, Associate Professor of Information Engineering Department of Hunan College of Information, Engineering Master of School of Physics and Electronic of Central South University. The research direction is theoretical study and system design of electronic and communication technologies.

Communication address: Information Engineering Department of Hunan College of That Information Wang Wang Road, Wang Cheng District, Changsha, Hunan.

References

- [1] Mei Shaochun, Wangyong. Modern telecommunication appliance principle and application [M]. Beijing: The People's Posts and Telecommunications Press, 1998(3): 213-230.
- [2] Tao Dongxiang, Huo Liping, Liu Yajuan. Design of the automatic test diagnostic system of Electro-optical interference equipment based on the VXI bus [J]. Foreign electronic measurement technology, 2008,10(12): 20-23.
- [3] Wu Junxing, Hu Minqiang, Wu Zaijun, et al. Testing of IEC 61850 based intelligent electronic device and substation automation system[J]. Power System Technology, 2007, 31(2): 70-74(in Chinese).
- [4] Liu Dawei, Lu Changhua. The status of digital-analog hybrid circuit failure diagnosis method[J]. Foreign electronic measurement technology, 2007(11): 18-20.
- [5] Huang Sufen, Zhang Jiangxin. Design and Realization of the EMS failure alarm function of GPON systems [J]. Optical communication technology, 2009(10): 32-35.
- [6] Li Guicheng, Yang Yusen, Wei Xiaoli. Measurement errors and the data processing principles [M]. Changchun: Jilin University Press, 1990(6): 166-178.
- [7] Dai Meie, Shi Jiaquan. Micro-computer technology and applications [M]. Beijing: Tsinghua University Press, 1996,5 (2): 228-250.

-
- [8] [Wang Keyou, Zhang Peichao, Yu Weiyong, et al. Research on a new failur information processing system using IEC 61850 communication protocol[J]. Power System Technology, 2004, 28(10): 55-58(in Chinese).
- [9] Gao Zhanfeng, Du Yanliang. Data acquisition system of the bridge remote status based on the virtual instrument [J]. Journal of instrumentation, 2006, 27(10): 1361- 1364.
- [10]Zhang Yunfeng. Paging type intelligence microwave equipment alarm system design [J]. TV technology, 2002(5): 31-35.

Research of Data Server Application Software for NBI Mechanical Control on EAST

ZHANG Xiaodan^a, LIU Zhimin^b, SHENG Peng^c, HU Chundong^d,
ZHAO Yuanzhe^e

Institute of Plasma Physics, Chinese Academy of Sciences, Hefei 230031, China

^azhangxd@ipp.ac.cn, ^bliu@ipp.ac.cn, ^cshengpeng@ipp.ac.cn,

^dcdhu@ipp.ac.cn, ^ezyz@ipp.ac.cn

Keywords: NBI, C/S, Socket, Multi-Threading, TCP

Abstract. For the sake of achieving to manage and query the experimental data scientifically, as well as relevant experiment information for Neutral Beam Injection (NBI) system, NBI Data Server software is developed for data exchanging between the remote server control layer and the field measurement and control layer, data storage and querying. Experimental results show that managing data scientifically can ensure data security and making best use of data will bring data value into full play. NBI Data Server software is programmed by C language, developed with Client/Server program model and multi-threading technology, runs on linux operating system. Experiments show that NBI data server software can work steadily and reliably.

Introduction

Neutral Beam Injection (NBI) heating is one of an important method of EAST (Experimental Advanced Superconducting Tokamak) plasma auxiliary heating^[1]. It makes use of neutral beam with very high energy to heat plasma generated by hydrogen or deuterium, meanwhile drive current of plasma in Tokamak.

While NBI control system (NBICS) is one of key sub-system for NBI heating system, it controls the all operational process of one beam. NBICS achieves the functions of controls of experimental mode, magnitude and time sequence adjustability of power supply, real-time monitoring of experimental states, alarming and protecting, data acquisition and processing, as well as the communications between terminals in different networks^[3].

NBI data server is in charge of managing experimental data and other relevant information for NBI. The records and querying of relevant information during the NBI beam operation, including experimental configuration, states, data and user action and so on, which play an important role in analyzing experimental results and improving the efficiency of experiment.

Due to NBI heating system works under strong electromagnetic environment and the neutral beam is generated with a certain radiation, NBI data server software is required to running on remote server control layer for recording and querying of relevant experimental information; data analyzing and processing, as well as the management services function of beam discharge (shot) number consistency between multiple data acquisition device (DAD) in field measurement and control layer of NBI.

The design and implementation of data server application software used for EAST-NBI will be introduced in this paper.

Requirement and Analysis of NBI Data Server Software for EAST-NBI

Because each subsystem of the NBI heating system in physical position is dispersive, distributed computer network structure is adopted to realize distributed control. NBICS computer network is comprised of following four control network^[3]: the remote server control network (located in Remote Server Control logic Layer, RSCL), remote monitoring network (located in Remote Monitoring logic Layer, RML), field measurement and control network (located in Measurement

and Control logic Layer, MCL), as well as video surveillance network (located in Video Monitoring logic Layer, referred to as VML). Fig.1 shows the network logic structure and software structure of NBICS.

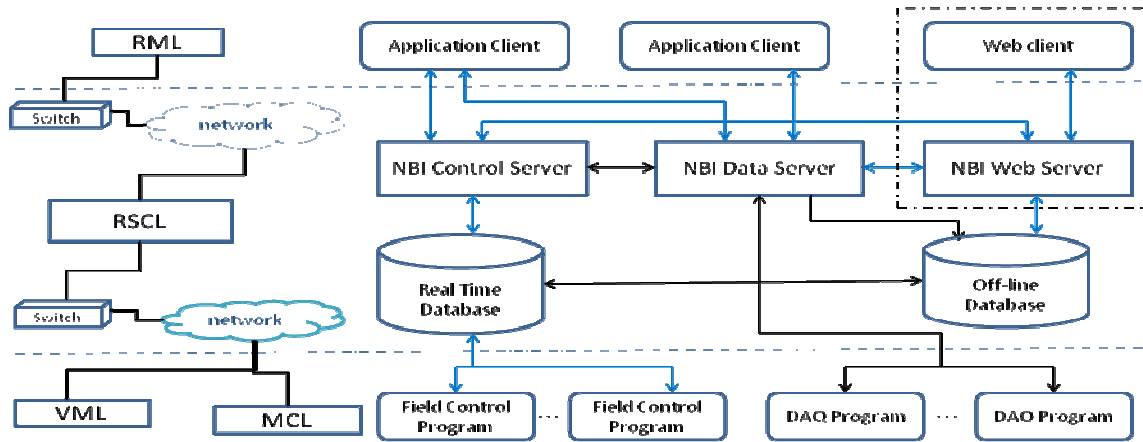


Fig 1 The network logic structure and software structure of NBICS

To achieve independent control between data flow and control flow, NBI data server software is required to be running on the data sub-network in NBI RSCL, mainly to obtain the following functions:

Functions of storage and querying for relevant experimental information

NBI data server software need to communicate with NBI main control server (MCS) to accomplish experimental configuration information receiving and storage functions of the current operating beam line and the function of releasing current shot number. In the mean time NBI data server software need to communicate with query terminal in NBICS, which need to query historical experiment configuration information or other experimental records.

Management service function of shot number consistency

NBI data server software is the only owner who has the authority of modifying and releasing shot number. Experimental shot number is the only identifier of the current running beam line. All of relevant information in current experiment will be restored to file in the specific directory path, which created by the current shot number. So the uniqueness of shot number between multiple data acquisition devices must be guaranteed, or it will result in serious consequences, such as data loss or being covered.

Functions of data exchanging

NBI data server software need to communicate with multiple data acquisition devices in NBI MCL to realize network transmission and receiving functions of experimental data, as well as releasing the current shot number. Fig.2 shows the supply and demand relationship between NBI data server, MCS, DAD and query terminal.

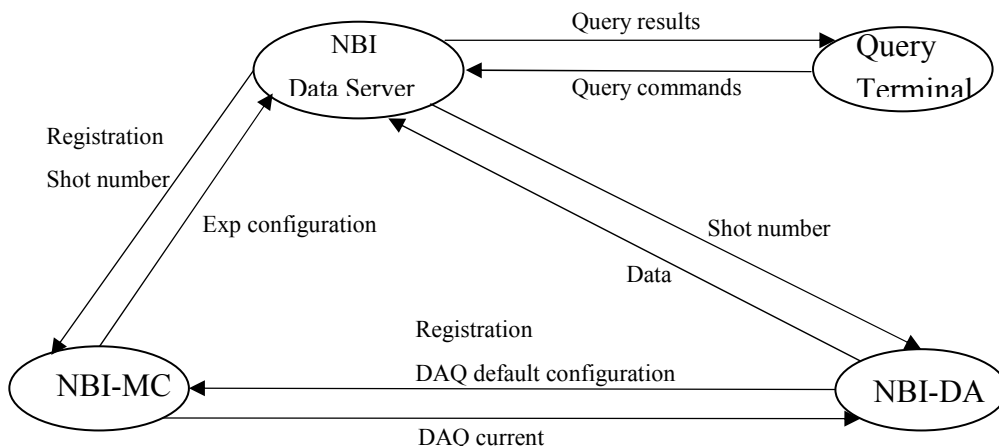


Fig 2 The supply and demand relationship between NBI data server, MCS, DAD and Query Terminal diagram

Implementation of NBI Data Server Software

TCP protocols The work model of NBI data server is based on Client/Server model. In order to realize the security of networks communications, NBICS takes steps of registering to MCS as one of its client when the terminal starts expect for MCS and applying for logout when it exits. Hence, NBI data server will register to MCS when it starts running as one of MCS's client; meanwhile NBI data server software will support services to DAD and query terminals which need to search information from NBI data server.

There are TCP and UDP protocols in network transmission layer. The differences between these two protocols mentioned above are that UDP provides connectionless and unreliable data transmission service, which doesn't guarantee data packet transportation with error-free. While TCP provides a connection-oriented and reliable data transmission service, this will ensure reliable transmission of data packet. Therefore, TCP is adopted when design NBI data server software.

Considering that NBI data server needs to communicate with MCS, DAD and query terminal, those are distributed on different network layer in NBICS, the unified data structure must be harmonized. And in view of that each subsystem in NBICS network need authentication and apply for or provide services as their interaction, the definition of NBI TCP header structure is as follows. Fig.3 shows the structure of NBI TCP header.

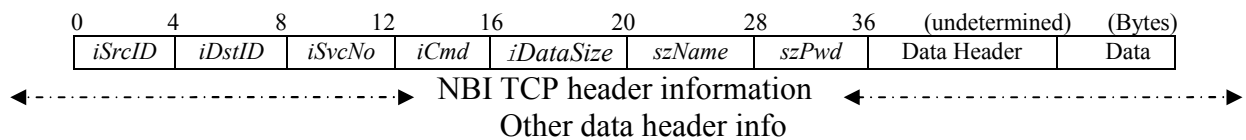


Fig 3 The structure of NBI TCP header

The source device ID and destination device ID, identifying the source and target address of data package, provide reliable data packets transporting protection. The service and command number identify the services and its corresponding commands in this network connection. The data size identifies the size of data packet in this network transmission. And the user name and password provide reliability and security for receiving data.

The structure mentioned above will be added to the top of transmission data segments of all network nodes as a header file. If another data header is needed to identify data information, it will be added to transmission data segments of network nodes following with NBI TCP header as a data header file.

Multi-threading technology based on Socket network communication Socket is a network programming interface; it exists in the communication area, which allows developers to access TCP/IP easily, accordingly to develop a variety of network applications expediently.

Based on multi-threading procedures, there are two threads at least in the process address space, but only one is the main thread^[4]. Each one can accomplish a task independently. The adoption of multi-threading can greatly improve the response speed and the efficiency of procedure.

For the sake of improving the execution efficiency of NBI data server, multi-threading technology will be adopted in the design process. Fig.4 shows the main loop flow chart of NBI data server software.

When NBI data server software starts running, the first thing is initialization. Then a service thread is created by the main thread, after that the main thread enters a sleep sloop state till the exit of NBI data server software, while the service thread takes charge of listening connection request from terminal.

When the service thread in listening state receives a connection request from network, it will create a new service thread which has the same function with itself. New service thread will continue to take the responsibility of listening, while the old one itself goes to deal with request, when done, it will release system resources and exit. That's to say, with this operational mechanism, there is always a service thread which is in waiting for connection request status. As long as a new connection request is established, a specific thread is guaranteed to deal with corresponding request. It realizes the multi-threading parallel operation and greatly improves the processing capability and execution efficiency when there are larges of connection requests.

With multi-threading technology, the entire program will turn into an infinite loop: waiting for a connection request, establishing a connection, creating a new service thread, dealing with request, releasing system resources and exit.

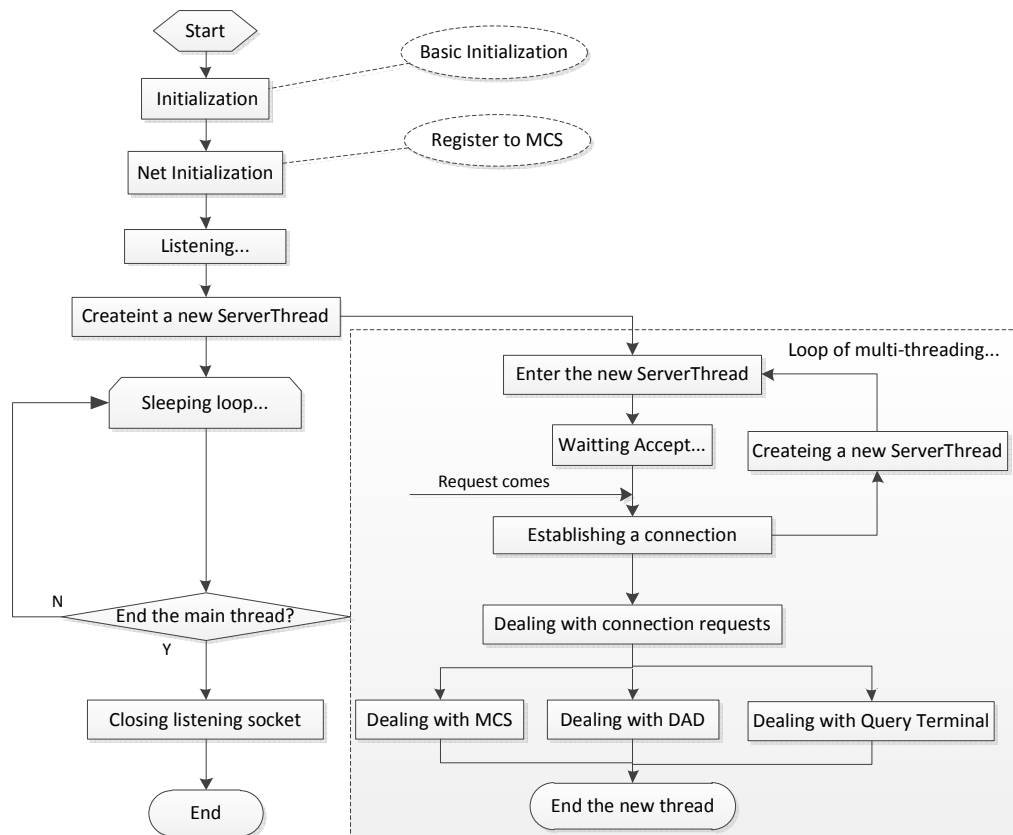


Fig. 4 The main loop flow chart of NBI data server software

Application

The application environment of NBI data server software NBI data server software is applied for EAST-NBI in NBI data server, here is the NBI data server configuration: 8GB of memory, 12TB of hard disk capacity, 4-core Intel Xeon E5506 processors, 1000Mbps network interface card and fiber-optical as the medium of transmission. To improve the ability and efficiency of NBI data server, Ret Hat Enterprise Linux 5.4 operating system is adopted.

Application NBI data server software is putting into operation now. Experiments show that it can work steadily and reliably. Now the query information function of NBI data server software will be taken for example. The procedure of query terminal is programmed by C++ language with MFC based on Microsoft Visual C++ 6.0, which gets the functions of querying the setup values of supply amplitudes, experimental mode and logical time sequence and so on. Fig.5 shows the querying results of filament voltage setup configuration for NBI from shot number 8032 to 8043 from NBI data server.

Summary

Experiments show that as a key software works on NBI data server in NBICS, NBI data server software can perform well under the managing and querying of experimental relevant information, as well as the management service of shot number consistency. However, the later maintenance and the further improvement of other functions in NBI data server, data analysis and calculating for instance, are underway.

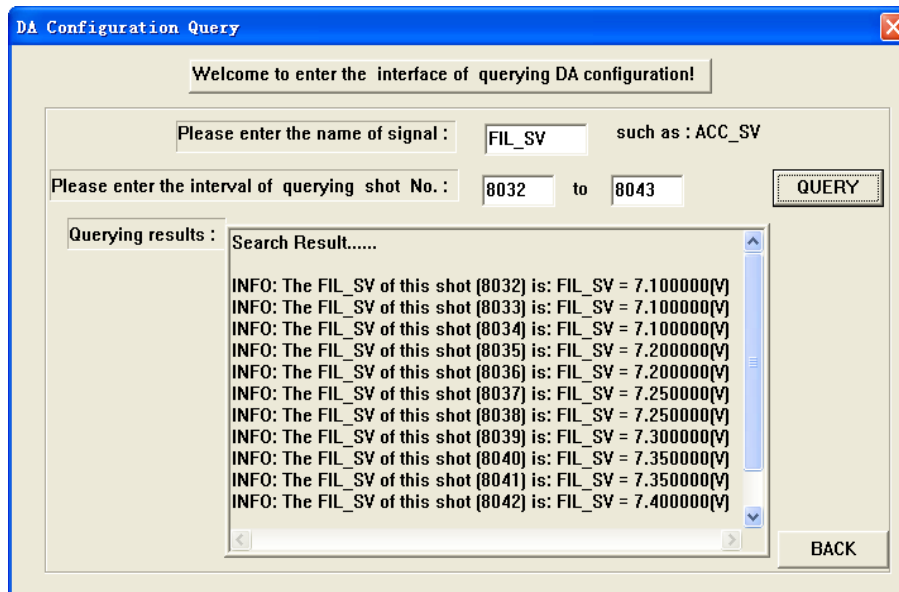


Fig. 5 The querying results of filament voltage setup configurations for NBI from shot number 8032 to 8043

Acknowledgment

supported by National Natural Science Foundation of China (No. 11075188), the Chinese Academy of Sciences Knowledge Innovation. Project: the study of neutral beam steady-state operation of the key technical and physical problems

References

- [1] WANG Yongjun, HU Chundong, LIU Zhimin, et al.2005, Plasma Science and Technology. NBI work team. The physics scheme of NBI. 2009.7, ASIPP NBI lab.
- [2] HU Liqun, ZHANG Xiaodong, YAO Ruohe. EAST-NBI scheme, 2006, Nuclear Techniques, 149:152.
- [3] SHENG Peng, HU Chundong, NBI work team. The scheme of NBICS, 2010.12, ASIPP NBI lab.
- [4] SUN Xin, YU Anping. Detailed in-depth of VC++, 2008.11, Beijing, publishing company of electronics industry.
- [5] YANG Zongde, DENG Yuchun. Linux high level programming (The second publish version), 2010.8, Beijing, the People's Posts and Telecommunications Press.

Mechanics Performance of Elevator Monitoring System Based on GPRS and ZIGBEE Network

Xiangqun Zhang

The college of computer science and technology, Xuchang University, Xuchang ,China

dzzxq18@163.com

Keywords: GPRS Network, Wireless Monitor, Data Acquisition

Abstract. In view of the number of the elevator increasing sharply, difficulty maintenance, repair not timely, this paper proposes the elevator monitoring system based on the GPRS and ZIGBEE network, and introduces the implementation method of the hardware, software design idea and application. The monitor system collects the data of the elevator running state , transmit data to the data center by the GPRS and ZIGBEE network, data center analysis and determine the elevator operation, fault condition, timely notification to relevant personnel, and puts forward the solutions to some of the potential fault, reducing the occurrence of failure. The running results show that: the monitoring system has complete functions, and stable performance.

Introduction

The number of elevator is growing with economic developing.It is very convenient when people access to high-rise buildings.But the casualties and economic losses caused by the elevator failure is also growing. Therefore, how to monitor effectively on the safe operation of the elevator, and remove any hidden faults in time, has become an urgent issue.

The Overall Design of the System

Aim at maintaining the performance and functionality of the equipment and ensuring their safety, remove hidden failure, so the system monitor and detect the elevator in 24 hours every day, strongly reduce downtime because of maintenance; even if the failure occur, the elevator can be repaired quickly.The monitoring staff can monitor the elevator in monitoring center, at a glance from the running where the floor to the door switch, when the elevator install hardware system.

First, the datas was collected by distributed data transmission unit ,which is located in the elevator machine room.second transmitted to zigbee collection[1] ,through zigbee wireless concentrator, send to the data center by the GPRS network, Finally were received and inputted database .If data center received fault code, the program will set a good trigger immediately to conduct a series of operations automatically,and sent failure alarm message to the relevant personnel.in other cases, The operating parameters ,which was extracted from the data center, and was converted to the animation, curves, histograms and other forms, and was shown in the large-screen. The basic composition of the wireless monitoring system was shown in the Fig. 1.The system component are as follows:

The data acquisition module based on the elevator control board: The systems monitor the information of the elevator by collected data and observe subtle changes, diagnosis and measure the machine in 24 hours every day.

The wireless transmission unit transmits the collected information to the monitoring center device by GPRS wireless network.

The Data Acquisition: summary the elevator running state from each DTU wireless transmission device to database system.

The data processing: data process the database of information, and send the elevator fault timely to the portable telephone which the elevator maintenance personnel owned. Quality report of statistical analysis was provided to the design, production and technical personnel [2].

The terminal device: Elevator maintenance personnel must carry mobile phones when they received the fault information; they rushed to the scene timely and removed troubles.

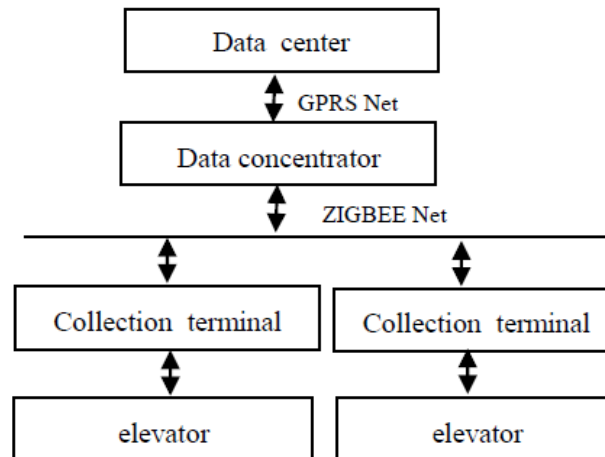


Fig. 1 Basic composition of the wireless monitoring system

According to the functions, the hardware of the system is divided into five parts: power part, control part, data acquisition, data transmission part, shell part.

the power part :Considering the possible use of the power in the industrial scene, the power part adopt the LM2576-ADJ chip as switching power supply, this chip supports 9-36V wide input voltage, its maximum output current is 3A above, meet the system power requirements[3].

control part:Part of data acquisition and data transmission part need the serial port of MCU in the hardware products,which determines the MCU at least have two or more serial ports. considering the price and the subsequent product extension, the system use the ARM as the control core of the product, the product uses the Cortex-M3 core, with more than two serial ports, and with multi-channel A / D, upgrades. When the system upgrade,we just replace the same series of large capacity ,and can be no need to change software and hardware.

Data acquisition part of hardware products adopt separate collection ,and has been collected by the elevator motherboard, so it needn't to specially designed collection device and communicate to the elevator motherboard in accordance with the agreed communication protocol.

The data transmission part: the data transmission part can be multi-point acquisition, and concentrated to upload, or a single point as the data collection and reporting points. Multi-point acquisition, and focus on the upload, we can use the wireless networking technology data collection point data networking acquisition and centralized upload. Remote data return need to use the existing mobile communication network .The existing remote data channel is divided into two kinds of GPRS and CDMA. the simcom of sim900 department of class is adopted in the GPRS ,it is a mature solution on the market. Another advantage of the chip has the integration GPS function inside the chip , we can locate the equipment without the use of GPS.

Communication Protocol Design

The system can ensure not only the completion of elevator data collection but also the reliability of elevator. So the reliability and validity of communication process is the important quality index in the whole system, which is closely related to whether the system can operate reliably. In order to ensure establishing the reliable links in the monitoring system, the serial communication program is designed by calling, answering and then communicating after repeated experiments, and its communication reliability has improved to a large extent.Communication rate:9600b/s; communication method: asynchronous serial method, 1 start bit, 8 data bits, 1 stop bit and 1 parity bit[4].

Establishment of Communication Links

In order to prevent the error code of frame address by interference, redundancy code has been adopted, that is, data concentrator sends 3 sets of call commands in every communication. The call command is made up of 1-word address code and 1-word completion code, specific steps are as follows: if the response code from elevator data acquisition part can be received at 60ms interval, the call command is sent continually, and this communication link can be proved to be established after receiving more than 2 responses; if the response from data concentrator is not received, which means that communication is not successful. And the next data acquisition part's address must be called continually in order to prevent deadlock.

The communication reliability is the important quality index in the whole monitoring system, which is closely related to whether the system can operate reliably. This verification method, which takes 2 from 3 call commands, can effectively improve the reliability of communication, but it can also reduce the communication efficiency to a certain extent. This system has respectively designed the communication protocols between data acquisition part and data concentrator in order to make up for the loss.

Communication Frame Format of Centralized controller

Data concentrator adopts the majority vote method to the received address after receiving the response command from data acquisition part to confirm the right acquisition part's address, and sends the corresponding operation command and data. The operation command consists of 2 same operation code bytes, operation data, check code and stop code[5]. Communication frame format is shown as follows.

Address code: address number of data acquisition part

Operation code: command word, which is sent to data concentrator by administration center computer, Check code: C0H, Stop code: E0E0H

Frame Format of Upload Data of data Acquisition part

After receiving the command from upper computer, data acquisition part will respond to the command and send the corresponding data to data concentrator, and the data format is as follows. Data concentrator uses address code for judging the source of the data in order to conveniently store the corresponding database[6]. The data frame format, which is sent to centralized controller r by data acquisition part, is as follows:

Address code: address number of data acquisition part; Command code: command of elevator data reading, command of elevator's state and command of the elevator's failure; Check code: C0H, Stop code: E0E0H

The communication reliability is the important quality index in the whole monitoring system, which is closely related to whether the system can operate reliably. This verification method, which takes 2 from 3 call commands, can effectively improve the reliability of communication, but it can also reduce the communication efficiency to a certain extent. This system has respectively designed the communication protocols between data acquisition part and data concentrator in order to make up for the loss. And the data in short frame format has improved the communication efficiency effectively.

Software Design of the System

The system uses the C language as development tools, adopts the IAR Integrated Development Environment for software development, including the IAR Embedded Workbench and C-SPY debugger. data acquisition part analyses and processed the received command, then sends its own address, the received command word, the corresponding data, check code and stop code to centralized meter reader. Centralized zigbee module analyses the received address code, command code, check code and stop code, if they are correct, the acquired data will be stored; if they are wrong, the former process will be repeated. And the flow diagram of software design of data acquisition part is shown in the following Fig.2.

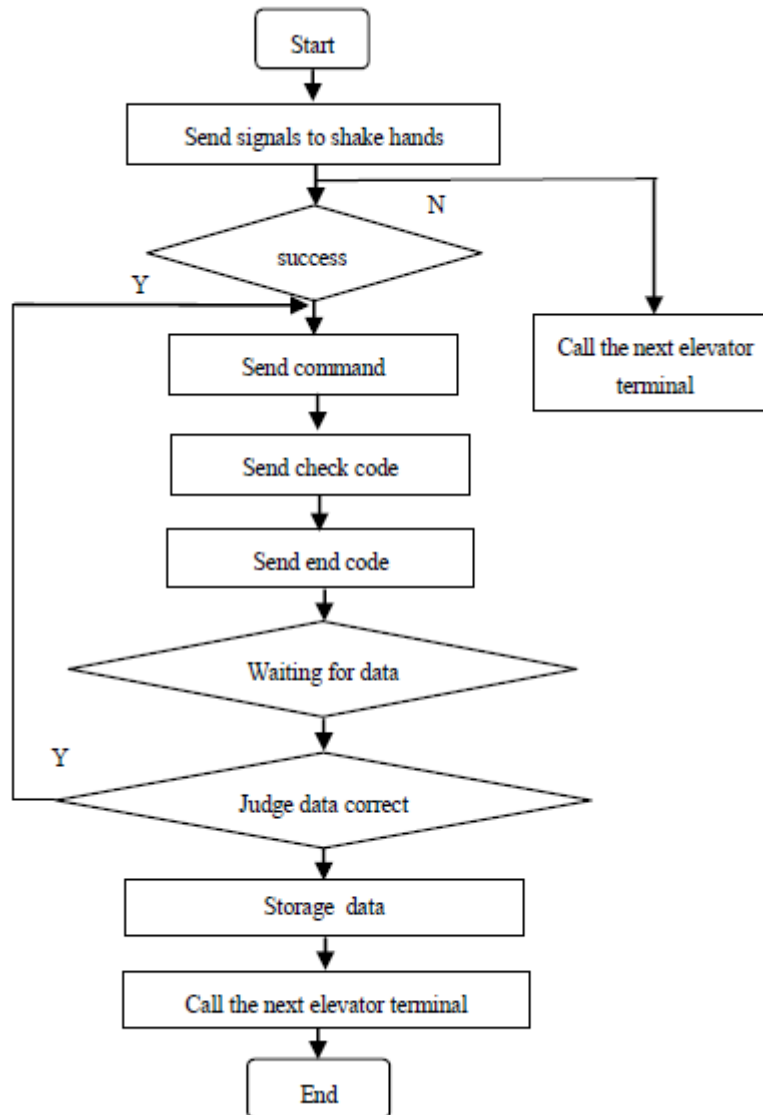


Fig. 2 Programming flow diagram of the system

The Simulation and Test of the System

At present, the system has been run in a district of Xuchang City for six months. for monitoring the stability of the system (in the Fig.3), monitoring center send query information periodically to obtain the operational status of the elevator, datas and pictures will be shown in the big screen demonstration system. the monitoring center find the door of the elevator unclosed tightly on the 9th of the century, the Garden District in November 2011.so the center inform the maintenance person timely and send the message, which contained the detailed arrangement of the type number of the elevator, belt maintenance tools ,was send to the phone.Failure was removed in time.

Conclude

The wireless monitoring system integrates monitoring and collection for data, and transfer data by GPRS and ZIGBEE network, build a dynamic database, analysis and process data, remotely monitor, share resource, to provide basic data for the maintenance and operation of the elevator.The application results indicate that this monitoring system meets the requirements, it has a good stability, low power consumption, easy to operate.



Fig. 3 The big screen demonstration system

References

- [1] Zhu Yongli, Chen Tao, Guo Shaojie. Applications of ZigBee technology in wireless meter reading. *Telecommunications for Electric Power System*, 2008, 29(8): 37-43.
- [2] Li Haiyan. Construction of Wireless Meter Reading System, *Science and Technology Innovation Herald*, 2010, 24: 78-82.
- [3] Xiangqun Zhang, Zhongbiao Zhao. Centralized controller and communication protocol design of remote meter reading system, *ICEIM 2011, Lecture Notes in Electrical Engineering*, v 138 LNEE, p 2153-2161, 2012.
- [4] Bai Tao, Zhang Changli. Based on the ARM and the ZigBee technology, wireless meter reading system research. *Chinese High-Tech Enterprise*, 2009(19): 35-26.
- [5] Sui Huibin, Wang Honghong, Wang Hongwei, et al. Remote meter reading system based on GPRS used in substations. *Telecommunications for Electric Power System*, 2007, 28(1): 57-61.
- [6] Zhang Hongbo, Zhang Yang, Zhao Huiguang, Du Xiaoyong. Design of Wireless Meter Reading Terminal Based on GSM Module, *Journal of North China Institute of Water Conservancy and Hydroelectric Power*, 2010, 31(4): 89-92.

A Information Management Methods Design of Mechanical CAD Drawings

Xiaoxiao Liang^{1, a}, ChongGang Wei^{2, b}

¹ School of Computer Science, Sichuan University of Science and Engineering,
Zigong, 643000, China

² School of Automation and Electronic Information, Sichuan University of Science and Engineering,
Zigong, 643000, China

^a Littlestmx@126.com, ^b 9170162@qq.com

Keywords: AutoCAD; Electronic drawings; Information management; Methods; Design

Abstract. According to the CAD drawings management present situation of small and medium-sized design and manufacture enterprise, the paper proposed mechanical CAD electronically management drawings system based on B/S model. The system use the AutoCAD VBA for secondary development to extraction CAD drawings electronically title bar and list of attributes, then output to database SQL Server file form CAD drawings electronically data, and the implement use and management of a small and medium-sized machinery design manufacturing enterprise CAD drawings electronically management methods.

Introduction

Because the AutoCAD widely used in engineering design manufacturing, so it produce and accumulated a lot of CAD drawings electronically. CAD drawings of these electronic information management, some large enterprise it as rely on product data management (PDM) system of a module for the management, and some large enterprises to adopt the network drawings management system [1,2]. These management way to one-time investment and process management cost and demand is higher, it cannot bear to small and medium enterprises.

To solve the small and medium-sized product design, development and manufacturing process of efficient use CAD drawings electronically, to use a kind of information management methods for the management of the electronic CAD drawings. Therefore, designs and realizes an based on B/S (Browser/Server) of small and medium-sized design manufacturing enterprise CAD drawings electronically management system.

The introduced of related technology

Browser/Server (B/S) architecture. The B/S structure is a collection of user interface layer, application logic layer, data access layer and data layer of multi-layer service system structure, its main advantage is that stratified architecture design make the system in the development, maintenance and upgrade it very convenient; It can adapt to a variety of operating systems, and friendly interface; Break the limitation on district, the user can be in any can connect to the Internet and realize the login place operation; The room needs to zero, the room without any plug-in installation, need to install a browser can achieve management, maintenance and update; The application in the server running, greatly reducing the client and the server is the dependence of, and achieve safety code, effectively improve the system and database security..

C# programming language. C# is a kind of asp.net application development environment, object-oriented program design mainstream language. It has a simple, mechanism design perfect grammar and the characteristics of the Web application closely. In the applications, with c # object-oriented program design including the packaging, inheritance and polymorphism all mechanism, convenient to provide Web services. Its development and application of the basic process for:

In the Visual Studio to create Visual C# projects, including C# source files, reference and resources.

Application C# compiler to compile Visual C# program, get Microsoft intermediate language (MSIL).

Visual c # program running in the.net platform, which the public language runtime provide support and, at the same time, using the.net provides class library, it will Microsoft intermediate language converting local computer code, and eventually operation in the operating system.

SQL Server database technology. We generally chooses SQL Server database to reach large application system. SQL Server database is a kind of typical relational open database management system, can run on a variety of operating systems, and can be and other system of friendly interactive operation. At present, SQL Server 2008 have been issued, but its performance remains to be the test of practice, therefore, this system USES has been widely successful application of the SQL Server 2000 version, it has to provide the data definition language (DDL), application program compiles, interactive inquiry, data organization and access, operation management, the database transaction maintenance powerful functions.

VBA AutoCAD ActiveX Automation object model. VBA is through the AutoCAD ActiveX Automation interface to establish a link between the object and AutoCAD. ActiveX is based on COM object model on a standard communication protocol, it allows objects through certain interface between mutual communication. The AutoCAD ActiveX give user to from AutoCAD internal or external to programmatically to operate AutoCAD. It is through the will to indicate to AutoCAD object "external world" to do it. These objects are shown, many different programming languages and environmental and other applications can access them.

The system framework

The system adopts B/S architecture design, it use asp.net technology for the C# programming language development environment, combined with the SQL Server2005 as backend database, using ODBC technology, AutoCAD secondary development technique, the system frame structure as shown in figure 1 below.

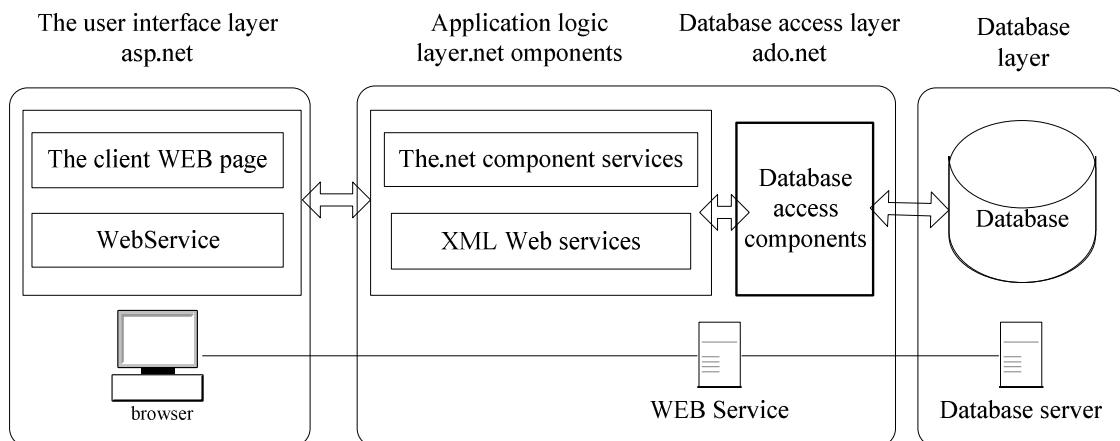


Fig. 1 System framework

The system function. In mechanical CAD drawings electronically management system, for access to different users to build an account, account including usernames, passwords, authority and personal information, etc. Through the account login system, the management of electronic drawings CAD drawing files management, audit management, and personal information management, etc.

Users can create parts information, and modification and deletion of part information has been.

Users can create part drawings of the corresponding file information, and modification and deletion of archives information has been drawing.

Users can create drawings files of the audit information, and modification and deletion drawing information.

The user can change your own user information.

The system administrators can create new account information, and modification and deletion of existing account information, as well as limits of the account set up.

The system administrators can backup, restore database and drawings files.

The system structure. The B/S architecture is a network structure model after the rise of a WEB, the WEB browser is the client the main application software. This model united the client, will realize the core part of the system function on the server, and simplified the system development, maintain and use. A client as long as install a Web browser and Server installation SQL Server database, the browser through the Web Server database for the data interaction.

Technical route. The system through AutoCAD software system to draw electronic drawings as the research object, by the AutoCAD VBA customized secondary design, the CAD drawings electronically title bar, detail column designed to attribute piece, in AutoCAD automatically generate graphics, extract the attribute value the output to independent SQL Server 2005 database file, drawing design technicians in the design is completed, through the client interface store it for local CAD drawings electronically files, and electronic drawings information CAD upload to Web Server.

AutoCAD secondary development. The system mainly with AutoCAD rendering of the CAD drawings electronically as the research object, using AutoCAD VBA customized second development, will title bar and schedules designed to attribute piece, in AutoCAD generate graphics drawing at the same time, graphic attributes and the output to extract the independent ACCESS database file, [2 and 4] designer in the client after the completion of the parts design, through its specific Web browsing interface will be stored in the local electronic drawing files and relevant information from a database file upload to Web database. This module and system data interaction as shown in figure 2 shows.

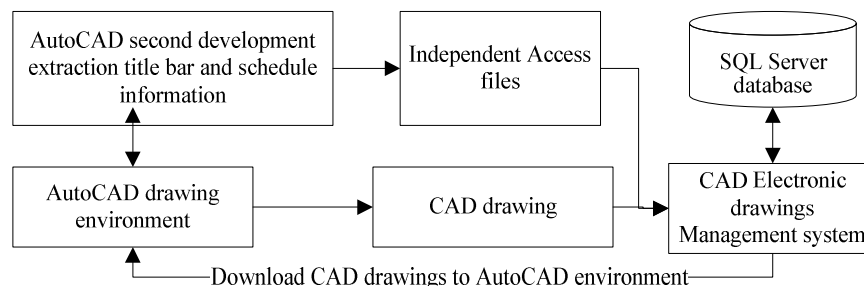


Fig. 2 CAD drawings electronically information interaction diagram

The system accomplish

The management of user. The user manager provides all the legitimate users centralized management, user management can see all user list and each user permissions. The system to provide the drawings inventory, drawings, drawing editors, code query management, user management, and data backup all 7 kinds of privileges. Administrators have all the power, the administrator can according to each user work for them to set up different permissions. In user management user must have "user management authority", but according to need to modify user password, user permission, and can remove users.

The inquires of drawings. The system to provide the level 3 compound conditions inquiries, and realize the drawings of fuzzy query code. Inquires form and form the points two ways to display. Level 3 compound conditions can be "or", "and" and "no" hybrid, after the inquires, press the "return" to realize to query, thus realizing the CAD drawings electronically inquires conditions. Such as parts borrowing and nested relationship of inquires, drawing drawings inquiry, query parts drawings inquires structure drawing inquires, product and so on [5]. At the same time, to all kinds of product structure tree, borrow relations, drawing title bar and detail the fuzzy condition inquires, etc.

The drawings deposited database. When the CAD drawing after auditors review, according to certain encoding rules will be drawing lists and CAD electronic drawings delivery system [6, 7]. The system to provide the three drawings warehousing way:

The intelligent input database of CAD electronic drawings information. CAD drawings of electronic realize to the title bar and detail of intelligent extraction column, and according to the component structure CAD drawings electronically, the borrowing of judgment and nested relationship. Identify the lower parts of borrowing and the nested relationship, along with all the electronic CAD drawings information extraction, and judge effectively title bar and detail column of the human error, give change tip, ensure the correctness of the drawings information.

The automatic warehousing of the electronic CAD drawings parts. CAD drawings electronically entry in parts is wrong or incomplete, drawing in the single can realize the automatic extraction information storage.

The manual warehousing old of the old drawings. There are old drawings as enterprise in the process of development, these drawings because do not adapt to the system of warehousing conditions, can only rely on artificial entry way realization storage. Therefore, the system design the manual entry window, used to solve system need manually input drawings information.

Electronic drawings editor

The system to provide the gallery of CAD drawings of electronic information function checks, when the check is inconsistent, it will hint user modify drawings information or modify CAD drawings electronically, change after completing CAD drawings electronically and system drawings describe the information than inspection, in order to realize the drawings information and CAD electronically drawings consensus.

System maintenance

The system administrator must often maintain system to realize the system database management, system of basic information management, enterprise product classification, installation and management of the products and parts drawings catalogue, parts of the Numbers standards, products type and specification, etc. And in order to prevent accidental loss of data we should backup and restore database regularly.

Summary

The mechanical electronic drawings management system of CAD B/S structure realized the small and medium mechanical design, manufacturing enterprise CAD drawings electronically management of real-time, network, in the CAD drawings electronically to the input, edit, inquires output and directory is realized for information management. Systems use simple and quick, convenient different inquires, it can be play a key role in small and medium-sized machinery design manufacturing enterprise's scientific management.

References

- [1] li qi, LiuXu, Zhen-jie Yan, Yan-xiYang. The system research and implementation based on mixture of architecture engineering drawings files management [J]. Heavy machinery, 2004 (01) : 50-52
- [2] Wei Shen, Chen Kai, Chang-an Zhu. The data management system research based on the.net technology with AutoCAD product [J]. Manufacturing technology and machine tool, 2008 (7) : 126-130

- [3] Yuan-yuanWang. The manufacturing engineering drawings management system design based on VB[J]. Changsha university press, 2011 (02) : 13 to 14
- [4] Zhang fan, Li-kai Zheng, Zhe-lin Lu, Cheng-huang Wang. AutoCAD VBA second development course [M]. Beijing: tsinghua university press, 2006.1
- [5] Shen Lei, Huo-ping Chen, Xiao-qin Li. such as drawing system design and realization based on network [J]. Computer system application. 2010 (6) : 128-130
- [6] Xiao-wen Jia,Jian-ping Liu, ryder, Ke-shu board. The document drawings management system research based on Web [J]. Journal of zhejiang university of technology. 2009 (5) : 738-742
- [7] Quan-ling Mu, The drawing management system automatically converts design and implementation in CAD drawing file [J]. Journal of changchun university, 2010 (10) :-22

Remodeling and Texture Mapping for Rule Polyhedron Based-on Open Scene Graph

Kuifu Wang^{1, a}, Juming Cheng^{1, b}

¹The dept of computer science and technology, Xuchang University, Xuchang ,China

^awkfcnc@sina.com, ^bJuming1201@126.com

Keywords: Open Scene Graph; Rule Polyhedron; Remodeling; Texture Mapping

Abstract. Setting relationship of the texture coordinates with the object's surface vertex points was the main method of texture mapping, but if depart from the modeling software; it would not get the vertex coordinates of the object. This paper describes the technique based-on OSG to remodeling the rule polyhedron and realizes the texture mapping for each side of the object, and get the desired results.

Introduction

The OSG [1] (Open Scene Graph) is an effective and real-time graphics toolkit for the development of high performance graphics applications such as flight simulators, games, virtual reality and scientific visualization. OSG has now become the hot-point of research and application. We use it as the bottom of the development of 3D applications and can get the outstanding performance In the process of the development of 3D applications; we need to solute many issues, two-dimensional texture mapping for 3D object is the key aspect of show the scene's authenticities.

Since the two-dimensional texture mapping for 3D objects should be based on a detailed understanding of the information of 3D objects and its vertex position, the two-dimensional texture mapping is usually done in the modeling stage. For the smooth surface we usually use parameter equation, for the irregular objects we can use two-step texture mapping methods^[2], and there are some other methods[3]. However, these methods should be premised on our grasp of the vertex information on the surface of the objects. Outside of the modeling software, we can hardly know the 3D object's vertex information, so it is difficult to directly realize the texture mapping for 3D objects. In order to realize texture mapping in 3D application platform, this paper studies the method of remodeling rule polyhedron by using OSG, and on the basis of the reconstruction we realize the two-dimensional surface texture mapping, and get the desired result.

Traditional Two-Dimensional Texture Mapping Methods

In order to map the two-dimensional texture onto the surface of the 3D objects, it is necessary to establish the relationship between the object's spatial coordinates (x,y,z) and the two-dimensional texture coordinates (u,v). It can be divided into two cases:

When the mapping targets are the parametric surfaces, we can simply use the method by solving the parametric. That is we must firstly get the two-dimensional parameters (u,v) of any point's on the 3D object's surface, and so can get the point's texture coordinates, and finally can produce the texture patterns on the 3D object's surface.

When the mapping targets are not smooth parametric surfaces, but formed the number of polygons, we may use the two-step texture mapping method. The core idea of the method is to introduce a 3D surface which surrounding the object as a mapping intermediary. The basic process can be completed by two steps as follows:

Map two-dimensional texture coordinates to a simple 3D object's surface, such as sphere, cylinder and so on, and That is establish the mapping relationship such as $T(u, v) \rightarrow T'(x', y', z')$, This mapping relationship is called S-mapping.

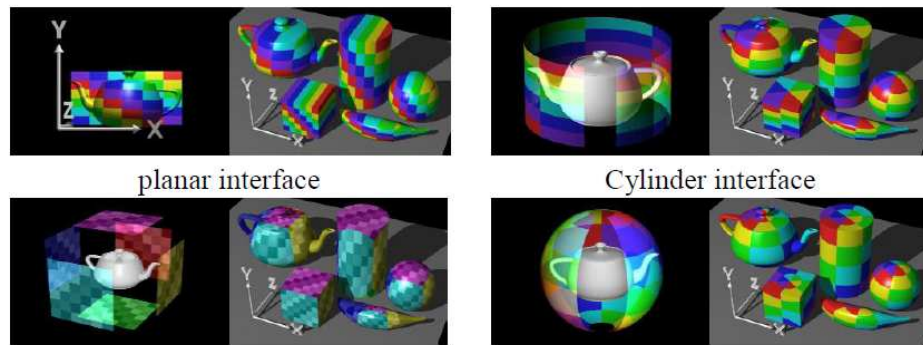


Fig. 1 Result pictures from four middle face

Then map the intermediary surface's texture coordinates to the ultimate object's surface. This can be expressed as $T'(x', y', z') \rightarrow O(x, y, z)$, and is called O-mapping. Fig. 1 is the result of the mapping from four types of intermediary face.

However, these methods which above all only can be realized in based on having detailed knowledge about the vertex information of the 3D object's surface. Outside of the modeling software, we can not get the information of the vertex of the object. So if we want to map texture on the object in the 3D application platform, we have to reconstruct the regular polyhedron.

Reconstruct the Surface of Regular 3D Object and Map the Corresponding Texture

Principle

The goal of texture mapping is to establish the relationship between the textures coordinates and the vertex's physical coordinates of the object. In modeling software, this process can be realized easily. But outside of the modeling software, we can not get the vertex coordinates of the object accurately, and it is difficult to realize texture mapping with anyone of the two ways mentioned above. We studied how to reconstruct and realize the texture mapping by each face of the object.

The surface of 3D models is constructed by much mesh, and they have many vertices. According to the model's different fineness, the number of triangles is not fixed. In order to map texture, we need to know the number of vertices of one face and the way they are arranged, and we need to know how to establish a correspondence between the textures coordinate with each vertex.

Texture is usually regarded as a two-dimensional square texture map, with the extent of coordinate values of $[0.0, 1.0]$. In the mapping process, we need to use texture to cover the object's surface according to the vertex coordinates, and the texture coordinates should be corresponded with the vertex coordinates of the object, that is we should distribute the corresponding texture coordinate for each vertex coordinate.

In the process of constructing virtual engine, for the rule geometric which is not mapped during modeling, we can reconstruct the surface of the object, and then use the method of 2-D texture mapping to set up relationship between texture coordinates with each vertex, we realize the texture mapping for rule 3-D object according each face.

2. Determine the information of the object's shape

Before we reconstruct the surface of the object, it is necessary to determine whether the object is a simple geometry. So we should read out the information of its shape from the node where the object located. In OSG, we can get object's Drawable information by get Drawable() method provided by Geode class, and can use get Shape() method provided by Drawable class to determine whether the object is a simple geometry. In OSG, the simple geometries can be directly set texture, but they can not be set on each side. The code as flows:

```
osg::Drawable* pDrawable= pGeode->getDrawable(0);
pShape=pDrawable->getShape();
```

If the object is not a simple geometry, users can select the specific shape of the object according to the option items. Usually, rule objects are cube, cylinder or sphere. We have realized the reconstructing and texture mapping on each side for cube and cylinder.

3 Reconstruct the surface and texture mapping for rule geometry

Reconstruct the Surface and Texture Mapping for Cube

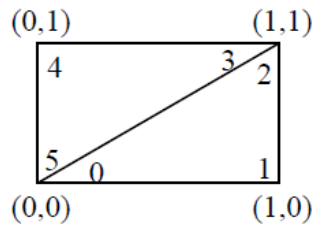


Fig.2 The sequence of six vertexes and their texture coordinate assignment

Through the experimental study we found that each side of the cube are posed by two triangles, which include six vertices, as shown in Fig. 2, so the entire cube has 36 vertices.

Because 4 texture coordinates are needed to distribute for 6 vertices, it should be generated new surface, and the distribution of the texture coordinates should be in order according to the sequence of the surface's vertices. Otherwise, there will be some problems. We can use `getVertexArray()` method provided by Geometry class read the vertices array from the cube, and get the data in array in sequence as the vertex coordinates of each side. By using `setVertexArray()` method, the new Geometry will be generated, according to the sequence of the vertices.

We use a reconstruct one side as an example, the code as flows:

```
osg::Vec3Array* pVertrxArray= (osg::Vec3Array*) pGeometry->getVertexArray();
osg::Vec3Array* GeomVertices1=new osg::Vec3Array (6);
for(int m=0;m<6;m++)
{(*GeomVertices1)[m]=(*pVertrxArray)[m];}
pGeom1=new osg::Geometry ();          pGeom1->setVertexArray(GeomVertices1);
```

Then correspond each vertex texture coordinates with each vertex:

```
texcoords = new osg::Vec2Array(6);
(*texcoords)[0].set(0.0f,0.0f);
(*texcoords)[1].set(1.0f,0.0f);
(*texcoords)[2].set(1.0f,1.0f);
(*texcoords)[3].set(1.0f,1.0f);
(*texcoords)[4].set(0.0f,1.0f);
(*texcoords)[5].set(0.0f,0.0f);
```

So we can allocate the texture coordinates for the six vertices one by one, according to the sequence of the vertex array.

Reconstruct the Cylinder and Texture Mapping in Each Side

For cylinder it is complicated .Different surface fineness we set in modeling can result in different vertex number in surface. Fig.3 shows the surface mesh of a simple cylinder model, The mesh density may be different, but they are still posed by the Triangle.

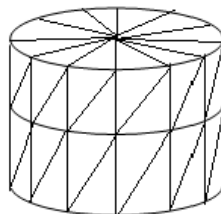


Fig. 3 Surface mesh of a simple cylinder

As an unspecified number of triangular, so in the process of mapping, we need judge the number of vertices of each side of the cylinder according to the normal array of the cylinder's surface. That is we need distinguish the different number of points for side and for the top/bottom of the cylinder, and by this means we can correct reconstruct the cylinder surface. The process is complicated, its simple procedure of computing and generating as follows:

```
osg::Vec3Array*pVertrxArray=(osg::Vec3Array*)pGeometry->getVertexArray();
```

```
int p=pVertrxArray->getNumElements();
//compute the total number of the cylinder surface
osg::Vec3Array* pNormalArray=(osg::Vec3Array*) pGeometry->getNormalArray();
According to the normal array, we can calculate the number of the top/bottom's points and put it
in variables q.
```

```
for(int i=0;i<p;i++)
{If((*pNormalArray)[i].x()==1)
    pnx=pnx+1;
.....
}
if((*pNormalArray)[0].x()==1)
    int q=pnx;
.....
```

Thus, we can calculate the number of cylinder side's points. After we get the number of vertex of every side, we can get the corresponding elements from pVertrxArray to reconstruct the surface. Take top side code as an example, say the point number of top side as q, the simple code are as flows:

```
For (int m=0;m<q;m++)
{(*GeomVerticesTop)[m]=(*pVertrxArray)[m];}
CyliGeom1->setVertexArray (GeomVerticesTop);
osg::DrawElementsUInt* GeomBase1=new osg::
DrawElementsUInt (osg::Primitive Set::TRIANGLES, 0);
PCylitop->addPrimitiveSet (GeomBase1);
```

The reconstruction of side and bottom are the same as above. In order to map texture, we need allocate the texture coordinates for each vertex in the surface after we reconstruct. Take the top side code as an example again, say variable top as the number of vertex on top side, then:

```
Float pai2=osg::PI*2;
int w=top/3;
Float dTheta=pai2/(float)w;
Float ndTheta=-dTheta;//triangle of top side rank in clockwise, the vertices of every triangle
rank in counterclockwise
```

The range of texture coordinate is [0, 1], according to the order of these vertices we allocate the texture coordinate as flows:

```
texcoordstop = new osg::Vec2Array(top);
For (int n=0;n<w;n++)
{(*texcoordstop)[n*3].set(0.5f,0.5f);
(*texcoordstop)[3*n+1].set(0.5f*cosf((n+1)*ndTheta)+0.5f,0.5f*sinf((n+1)*ndTheta)+0.5f);
(*texcoordstop)[3*n+2].set(0.5f*cosf(n*ndTheta)+0.5f,0.5f*sinf(n*ndTheta)+0.5f);
```

Triangles of the bottom rank in counterclockwise and the vertices of each triangle rank in counterclockwise. Others are the same as that of the top side.

According to the number of vertex in top/bottom and the total number of vertex in surface, we can get the number of vertex in side. We can allocate the texture coordinates for it. Then

Say the number of top vertex as topver, the number of side vertex as sidever, then:

```
int rseg=sidever/(topver*2);
int vseg=topver/3;
texcoord = new osg::Vec2Array(sidever);
For (int n=rseg;n>0;n--)
{For (int m=vseg;m>0;m--)
{(*texcoord)[6*(vseg-m)+6*(rseg-n)*vseg+0].set(1.0*(n+0.0)/rseg, 1.0 *(m+0.0)/vseg);
(*texcoord)[6*(vseg-m)+6*(rseg-n)*vseg+1].set(1.0 *(n-1+0.0)/rseg, 1.0 *(m-1+0.0)/vseg);
(*texcoord)[6*(vseg-m)+6*(rseg-n)*vseg+2].set(1.0 *(n-1+0.0)/rseg, 1.0 *(m+0.0)/vseg);
(*texcoord)[6*(vseg-m)+6*(rseg-n)*vseg+3].set(1.0 *(n+0.0)/rseg, 1.0 *(m+0.0)/vseg);
```

```
(*texcoord)[6*(vseg-m)+6*(rseg-n)*vseg+4].set(1.0 *(n+0.0f)/rseg, 1.0 *(m-1+0.0)/vseg);  
(*texcoord)[6*(vseg-m)+6*(rseg-n)*vseg+5].set(1.0 *(n-1+0.0)/rseg, 1.0 *(m-1+0.0)/vseg);  
    }
```

In mapping process, we can choose the side to allocate texture according to the requirement.

The Experimental Results and Summary

The arbitrary one, two or three side of the operation results are shown in the figure. Texture mapping is a very important aspect in virtual reality application, but it is difficult to realize out of the modeling software. Based on engineering practice, with the OSG, the surface reconstruction for rule geometry and the mapping by side in virtual engine outside of the modeling software are realized. We have broken the limitation of only mapping in the modeling software in producing virtual reality engine project application, and increased its flexibility. However, It is of great importance and difficulty to realize the texture mapping for unruly object outside the modeling software, and that can be the focus of future research.

Reference

- [1] www.openscenegraph.org
- [2] Alan Watt.3D Computer Graphics (Third Edition)[M]. Machinery Industry Press,2005,7
- [3] WU Ya-dong, HAN Yong-guo, CHEN bo. Based on the model of two-dimensional triangular surfaces texture mapping methods [J]. Computer Application and Software.2010, Vol.21.No.1:112-114

Mine Detection Technology in Mine Safe Production

Guo Jun¹, Gan De-Qing², Tan Jing¹ and Ren Chao³

¹ Qing gong College, Hebei United University, 063000, China

² Hebei United University, 063000, China

³ University of Science and Technology Beijing, 100083, China

E-mail: 15303156333@189.cn,gdqheut@163.com,hblgdxjtj@126.com

Keywords: Detection Technology, Videos Monitor, Safe Production

Abstract: Shirengou iron mine of Hebei iron and steel group Co., LTD owns annual production capacity of two million tons, which is one of the domestic major metal mines. The study of underground safety detection and monitoring system aims at realizing of mining safety and efficiency. This system prevents mine safety accidents effectively and improves mining production efficiently. The establishment of detection and monitoring system plays the significant reference meaning for promoting monitor of domestic mine pressure disaster and safe management level.

General Instruction

Shirengou iron mine of Hebei iron and steel group Co., LTD owns annual production capacity of two million tons, which is one of the domestic major metal mines that is turned from surface to underground. With the increasing of mining depth, a series of problems appear on safe production management: Frequent pressure activity, great change of work environment, long transportation line, increased difficulty of ventilation system, increased ground temperature etc, which will be affected safe production management. In order to ensure mining safe production, the study of detection and monitor technology will be benefit to safe management work strength reduction, management level promotion, safe management system establishment and perfect and harmonious mining construction.

1.2 Pulverizing Influence Factors

The detection and monitoring system of Shirengou iron mine consist of CO concentration monitor, wind speed monitor, ground subsidence detection, underground pressure detection and mine safety monitoring system etc.

Monitoring System of CO Concentration The normal mine production has 24 driving face and 33 recovery operation plane. Totally 68 CO sensors are installed in every underground driving face, stope entrance and driving raise to achieve monitor for CO concentration of every working plane, the sensor takes numerical display function by itself, it should give a warning signal when the CO concentration is more than 0.0024%. Among them, the pressure ventilation alone head excavation roadway and driving raise, the mix current place 5-10m from driving face and return current place 10-15m from roadway exit are installed a CO sensor respectively; as for the draw out ventilation alone head excavation roadway, a CO sensor should be installed in the mix current place between ventilation duct exit and driving face and every stope entrance should be installed a CO sensor. What's more, according to requirement of production post management, the shift leader, every team and safety supervisor etc crew need to be equipped with a certain number of portable CO alarms, so that they can find problems earlier, and technical personnel can stay away from dangerous area as quickly as possible and take corresponding measures. The models of CO sensor and portable CO alarm are shown as Fig. 1.

Wind Speed Monitor The wind speed sensor is installed in every excavation working face and the wind speed and pressure sensors are installed in all level machine station of ventilation system which can achieve the movement monitor for total air quantity of whole mine.



Fig. 1 CO sensor and portable CO alarm

68 sensors are installed in excavation working face and they will issue warning signal when wind speed is lower or higher than the specified value; 11 wind speed sensor and 11 wind pressure sensor are respectively installed in fan outlet of mine main ventilation room, the sensors upload the data to surface monitor center, so that the movement detection and monitor for total air quantity and air pressure of whole mine will be realized accordingly.

Ground Subsidence Detection and Monitoring System The surface movement of predicted mining area is designed as 1897600 m², the ground subsidence and settlement are detected continuously by detection and monitor equipment. Accordingly to the requirement of observation precision, an observation pile is installed as per 100m-200m at the edge of gob area; an observation pile is installed as per 300m-400m at the center of gob area. A scale plate, reflecting prism, rainproof and sun proof facilities are equipped on the observation pile, two observation points are equipped on safety zone outside rock mobile boundary. The high accuracy total station is utilized to observe and record data that will be input into monitor host to proceed with analysis, meanwhile the ground subsidence can be forecasted and alarmed. The high accuracy total station appearance is shown as Fig. 2, Observation pile distribution is shown as Fig. 3; the position of observation station can be fixed according to actual situation.



Fig. 2 High accuracy total station

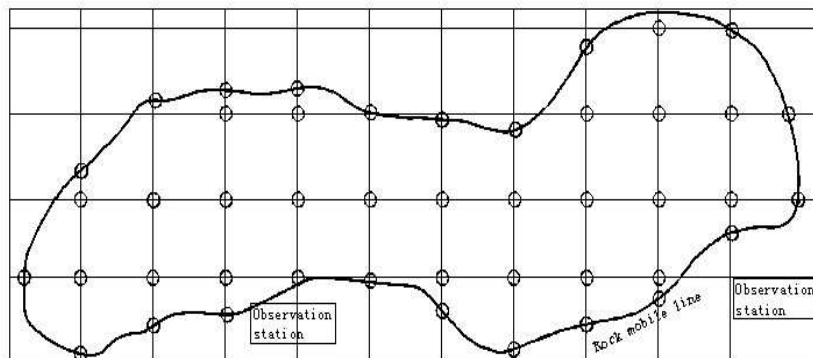


Fig. 3 Observation pile distribution of gob surface subsidence observation system

Underground Pressure Detection and Monitoring System The lowest mining elevation of Shirengou iron mine of Hebei iron and steel group Co., LTD is -300m, mining depth is about 500m, and mine is equipped with underground pressure detection and monitoring system. The mine is adopted by the slice filled stope, open stope and shrinkage stope, the ore exposed area of each mining methods are shown as Table 1

The underground pressure monitor is realized through slight shock monitor and detection system, which can timely catch slight shock movement information that caused by ground pressure activities and realize the position of slight shock source. The position result can be reflected on the constructed three dimensional geological models directly, so that the event location can be observed clearly. Accordingly to the model, the rock destructiveness can be deduced and forecasted.

Table 1 Ore exposed area

Item	Roof exposed area (m2)	Hanging area (m2)
slice filled stope	<990 slicing method	100~150
open stope	<1000	<2060
shrinkage stope	<252	1200

The underground pressure detection and monitoring system is consist of GS, one-way vibration absorber, three-way vibration, communication unit, data control center, GPS and industrial control machine, in addition, this system is also assembled by the corresponding software package, including timing software, data process software, visual of slight shock, explanation software and real-time display software of slight shock event etc.

6 one-way vibration absorbers and 2 three-way vibration absorbers are set in -180m halfway and -300m halfway of roadway respectively, these vibration absorbers are distributed as every 150m at the areas that ground pressure of is obvious in roadway. The absorbers distribution can also be adjusted on the basis of rock hardness and geology distribution status to realize the monitor and alarm for whole mine ground pressure. The system structure chart is shown as Fig. 4, the configuration of vibration absorber and GS are shown as Fig. 5.

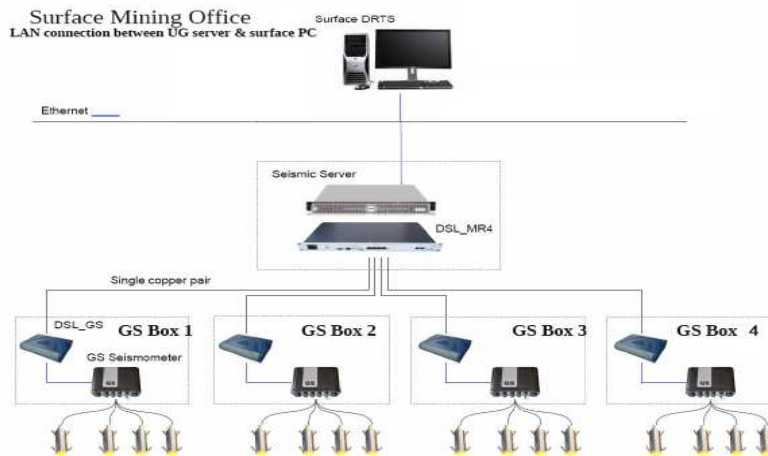


Fig. 4 Structure chart of ground pressure slight shock monitoring system



Fig. 5 Configurations of vibration absorber and GS

Mine Safety Monitoring System The parameters and information that collected by underground monitor instrument are delivered to earth surface monitor center by computer technology, the data experience analyzed, processed, filed and alarmed by monitor software and achieve mine safe and economic operation.

System composition: monitor mainframe, monitor software, communication transmission equipment, controller, network port and filed sensor etc. The safety monitoring system structure is shown as Fig. 6. The realizable functions of monitoring system are mainly display function, user rights management function and checking function etc.

Display function: the multi-screen display can provide dynamic graph, real-time data, historical data, parametric curve, statement show and simulation column display;

User rights management function: the system can provide a unified standard login screen and application picture template, different permissions are opened to different users to improve people do their own work, which will promote the standardization and safety of monitor management.

Checking function: the system can carry the automatic diagnosis on controller, electronic power source, sensor and transmission cable, and it can also provide abnormality alarm.

Moreover, the monitoring system is also installed UPS, it can still keep working more than two hours under power outage condition.

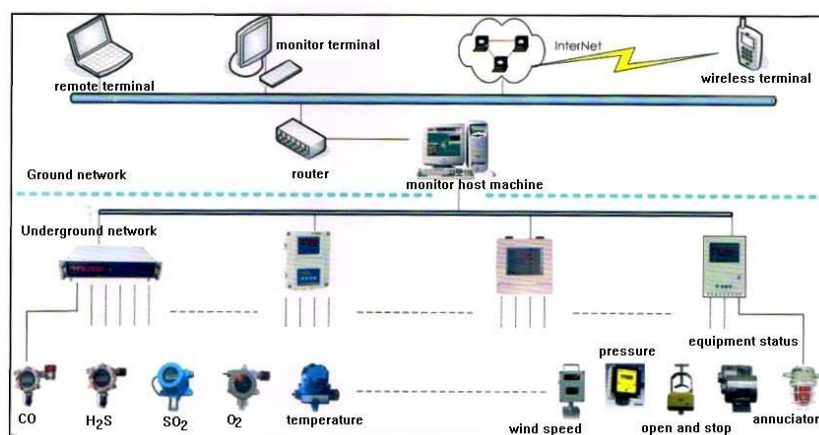


Fig. 6 Structure chart of mine safe monitoring system

Summaries

With the continuous development of information technology and detection monitoring equipment index increase, the mine management experiences from the original traditional form to digital management pattern changes. The establishment of detection and monitoring system possess stronger flexibility and practicality, which has been applied gradually in the iron mine construction projects of Shirengou iron mine of Hebei iron and steel group Co., LTD. The application of detection and monitoring system has reduced the difficulty of mine management, produced the huge economic benefits and improved mine automatic production level.

References

- [1] LI Wen-feng, ZHAO Min. (2010) Bus-based Coal Mine Safety Monitoring System Networking Technology. *Coal Technology* 3 (1):108-109
- [2] GAO Yun, HU Ping. (2010) Application of Streaming Media Technology in Mine Remote Video Monitoring System. *METAL MINE* 9:107-110
- [3] HUANG Wei-xin, JIA Ming-tao. (2008) Study on the Application of Micro-seismic Monitoring Technique to Mine Safety Management. *China Safety Science Journal* 6(1):165-170
- [4] GAO Jian-min, ZHANG Xin-guang. (2010) Application of Information Technology in the Sandaozhuang Open Pit Mine. *Nonferrous Metals (Mine Section)* 5(3):55-58

Study of Mechanics Control Server Application Software on EAST-NBI

Yuanzhe Zhao^a, Chundong Hu^b, Peng Sheng^c and Xiaodan Zhang^d

Institute of Plasma Physics, Chinese Academy of Sciences, Hefei 230031, China

^azyz@ipp.ac.cn, ^bcdhu@ipp.ac.cn, ^cshengpeng@ipp.ac.cn, ^dzhangxd@ipp.ac.cn

Keywords: EAST; NBI; Control Server; Shared Memory; Multithreading; Real Time

Abstract. The Neutral Beam Injector (NBI) is one of the main plasma heating methods for Experimental Advanced Superconducting Tokomaks (EAST). In order to provide unify time-order control, control the power supply and ensure the NBI system stable and reliable effectively, the control system is designed. As the center of the control system, control server plays a crucial role which can control the input/output services of the whole NBI system, verify whether the experimental parameters of EAST-NBI are reasonable, monitor the states of the experimental equipment in real time, storage the real-time data and make it easy to perform self-protection and alarm automatically. This design is related to many kinds of technologies, such as shared memory, multithreading, TCP protocol and so on.

Introduction

In order to fully exploit capabilities of EAST and to study the physical issues involved in steady-state advanced Tokomaks devices [1]. A neutral beam (NB) injection system is being constructed with two injectors at the energy of 80 keV and every injector will supply 4 MW neutral beam power at the dimension of 12cm*48cm [2]

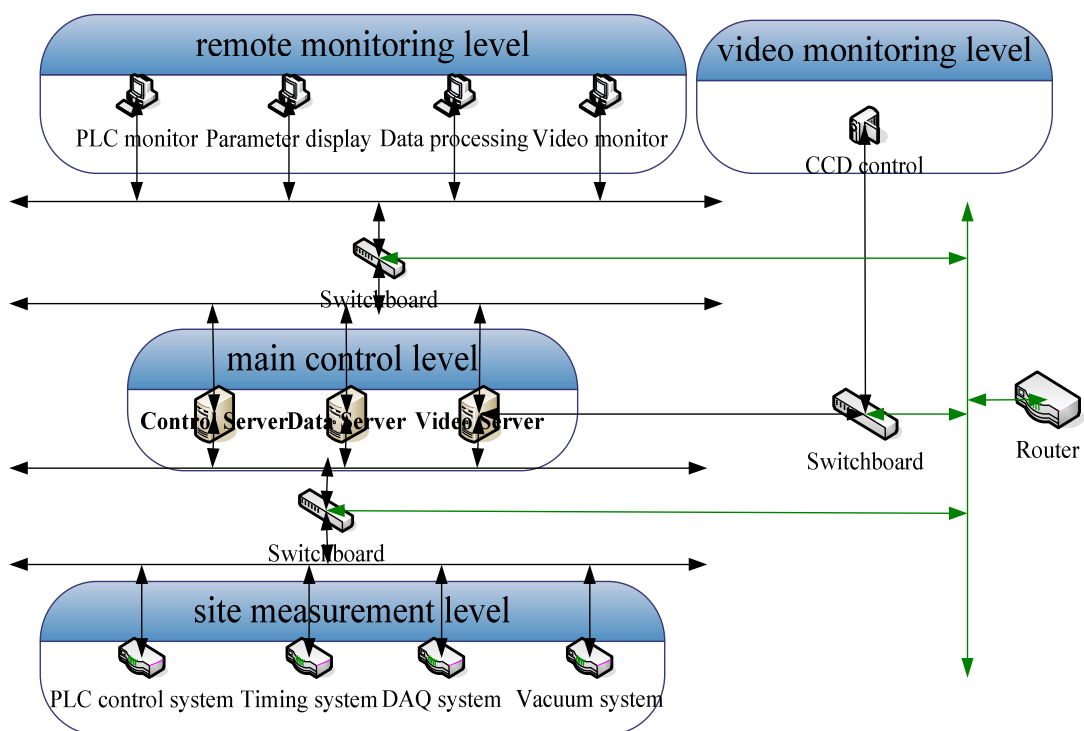


Fig. 1 Ruptures of NBI control system

Every neutral beam injection consists of a neutral beam ion source, arc power supply, filament power supply, high voltage supply, vacuum system, water system, and control system. The NBI control system provides the remote timing, the remote monitoring and command reference control for all power supplies. It has four levels that are shown in Fig.1: remote monitoring level, main control level, site measurement level and video monitoring level [3]. As mentioned, the design of control server application software is indispensable for the realization of the functions of control system. The control server's major function is to coordinate the communication and management between remote monitoring level and site measurement level. It is the center of NBI control system, and it is also the fundamental of remote monitoring.

Terminals of Control Server

As the bridge between remote monitoring level and site measurement level, control server communicates with its terminals through TCP protocol. It is necessary to clear the functions of every terminal that the control server communicates with.

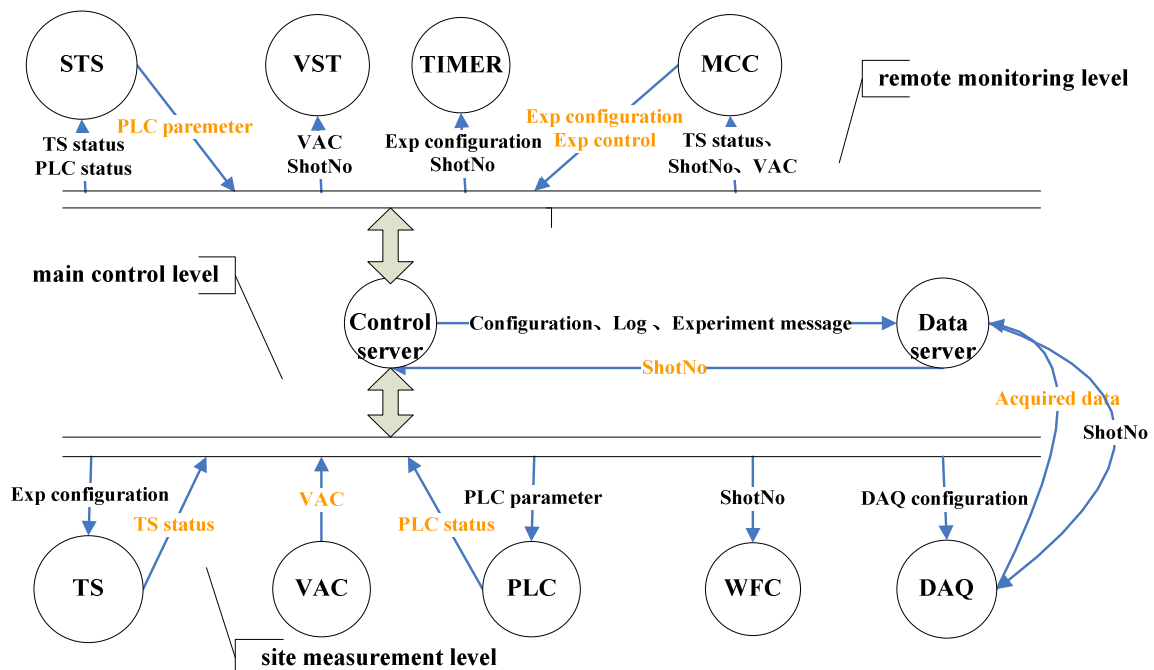


Fig. 2 The data flow diagram of all terminals mentioned above

Fig.2 shows some terminals that the control server communicates with. PLC control system is employed to control the on/off state and operation of the magnet power supply, gas valve, arc power supply, etc. It transmits the states of power system, water system and vacuum system to control server. Timing system outputs precision clock signals to subsystem and realize the synchronous trigger of all subsystem. It gets configuration information from the control server. DAQ system sends experimental data to data server. It gets different configuration from control server, according to the different experiment model. Vacuum system provides a ideal vacuum environment. It transfers the vacuum values to control server to get the real-time display in the vacuum monitoring terminal. Data server receives and saves the data from DAQ system and control system. Another important function is to ensure all subsystems have the same shot-no.

This figure also shows the data transfer between control server and terminals. The words in black indicate the messages that the control server sends to the terminals and the words in blue says the messages that terminals transmit to control server.

Design of Control Server Application Software

Control server application software develops under Linux operating system, using C language. The communication between control server and terminals bases on TCP protocol uses the client/server model. As the server-side, control server application software is always in listening state. It realizes that using different thread deal with different client requests by exploiting multithreading technology.

The Flow of Control Server once the control server application runs there are four threads will be created: thread a, thread B, thread C and thread D.

As shown in Fig.3, user information will be created, updated, and deleted by thread A and B. Thread A monitors the client requests. As soon as one connection is built, thread A will create new thread A' to listen to the client requests and thread A is used to process the request of the current terminal. If the terminal's registration has existed in the User Info able, thread A will update the registration of this terminal; else thread A saves the new registration information to the User Info abl. Thread B checks whether the terminal that has connected with the control server has any action every second. If the terminal has no action during half an hour, it will be forced off line, else user information will be updated and Timer equals to 1800.

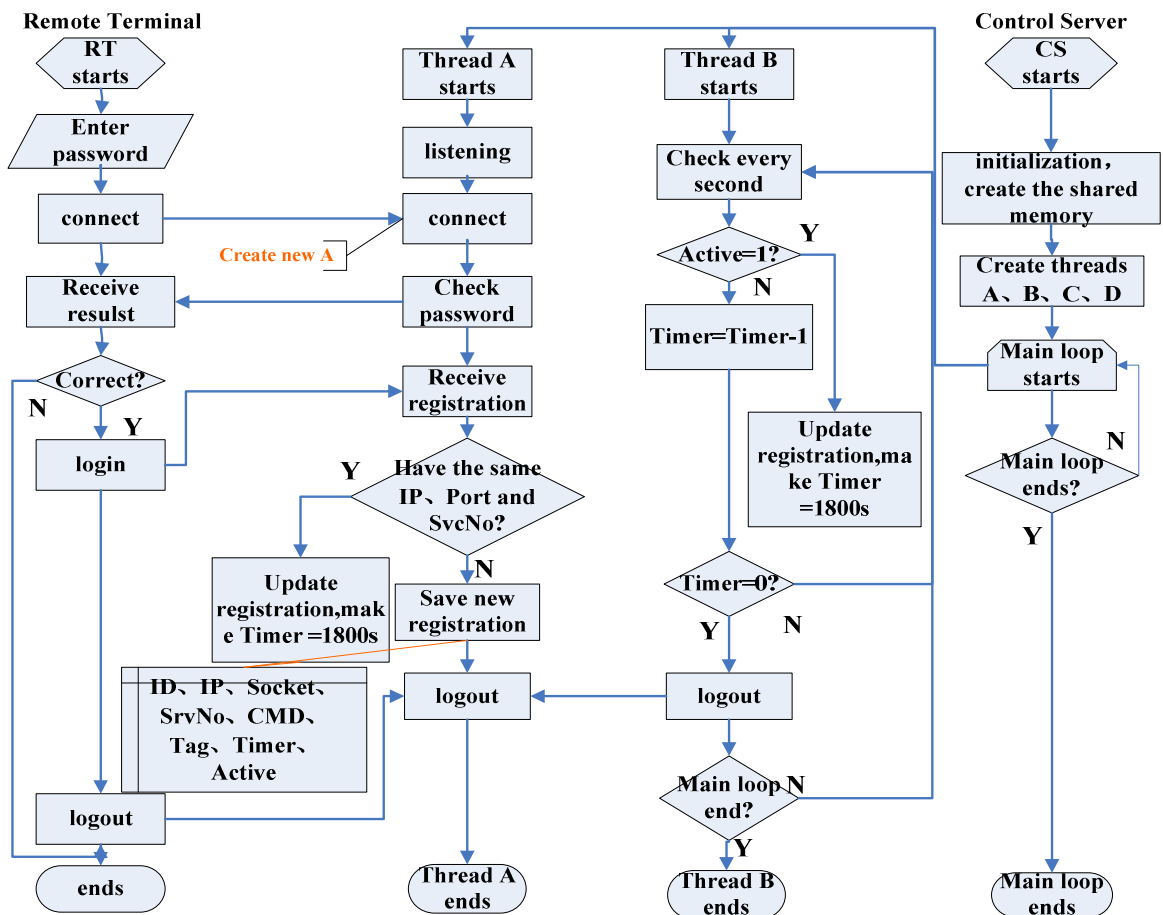


Fig. 3 Low chart of thread A and thread B

Fig.4 shows the flow of thread C and D. Thread C is used to get the socket information of one terminal and assign it to a variable. Thread D inspects the Tag List regularly. If it discovers a certain tag changed, it will send this tag messages to the terminals that take care of this tag according to the socket saved in the variable.

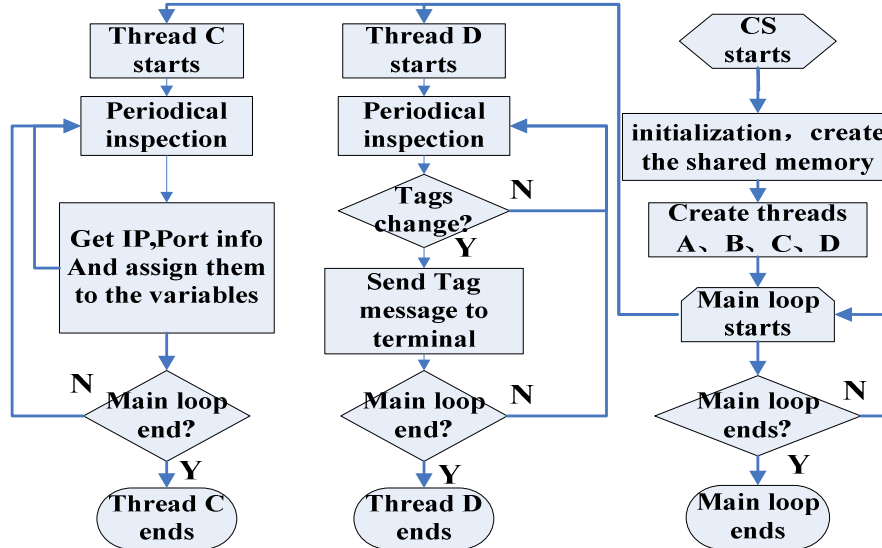


Fig. 4 Low chart of thread C and thread D

Shared Memory As above-mentioned, the design of control server involves multi thread technology, shared memory, TCP protocol, etc. Previous paragraph had made a brief description of the multithreading. This part will explain the shared memory simply.

Under Linux operating system, using the following functions to access to shared memory:

Int shmget (key_t key, size_t size, int shmflg), create a shared memory of size, if creation is successful; return the shared memory identifier [4].

Void *shmat (int shmid, void *shmaddr, int shmflag), map the shared memory whose ID equal to shamed to the address space of the calling process [4].

Int shmctl (int shmid, int cmd, struct shmid_ds *buf), the control function of shared memory, execute different command according to different cud, if cud equal to IPC_RMID, delete shared memory [4].

Once the control server application runs, a shared memory will be applied and it will be divided into several tables which are used to storage different data in real time. Then control server sends different information to different terminals through network communication according to the relationships stored in the tables.

User Info able is used to storage user information including user's IP, device ID, service number, tags that user takes care of and the latest action of users. Control server processes terminal's request differently according to different service number and command Tag able is used to storage the terminal's device ID who takes care of this tag. Constraint able is used to storage valid range of tags. RT evince running able is used to storage the real-time status of the equipment. Once a terminal sends configuration to the control server, if the value is in the valid range that offered by Constraint able and it is different with the value existed in the RT evince running able, control server will send this message to the terminal whose device ID is in the appropriate position of the Tag able.

Table 1 A few examples of the shared memory tables

User Info able:					
IP	DevID	Socket	SrvNo	Cmd	Tag
192.168.200.188	MCC	6	1	2	SHOT_NO
192.168.200.100	TS	9	3	-1	TS_STATUS

Tag_Table:					
Tag	DevID	DevID	DevID	DevID	DevID
SHOT_NO	MCC	WFC	TIMER	PXI	
TS_STATUS	TS	STS	MDS		

Constraint Table:					
ConfigID	Type	Unit	Max alue	MinValue	flag
ArcVoltage	float	v	200	0	1
ShotNo	int	shot	9999999999	0000000000	0

RT evince running able:					
SHOT_NO	TS_STATUS	PLC_STATUS	VAC	TS_CONFIG	DAQ_CONFIG

Table 1 shows some tables in the shared memory which compose a real-time database.

Discussion and Conclusions

The control server application software has been successfully applied to the experiment of EAST-NBI. The results have proved that the multithreading technology reduces the time of program operation, TCP protocol ensures reliable packet delivery through a network and shared memory technology improves the system operational efficiency in processing the rapidly changing data and sharing the data of EAST-NBI. At the same time, the control server designed in present has realized the supply of power systems, the display of vacuum, the output of unify timing, the verification of the experimental parameters, the monitoring of the experimental states and automatic self-protection and alarm. As shown in Fig.5, with the help of control server, the experimental results of EAST-NBI gets energy of 80 key, 3 MW ion beam power and 500ms pulse length.

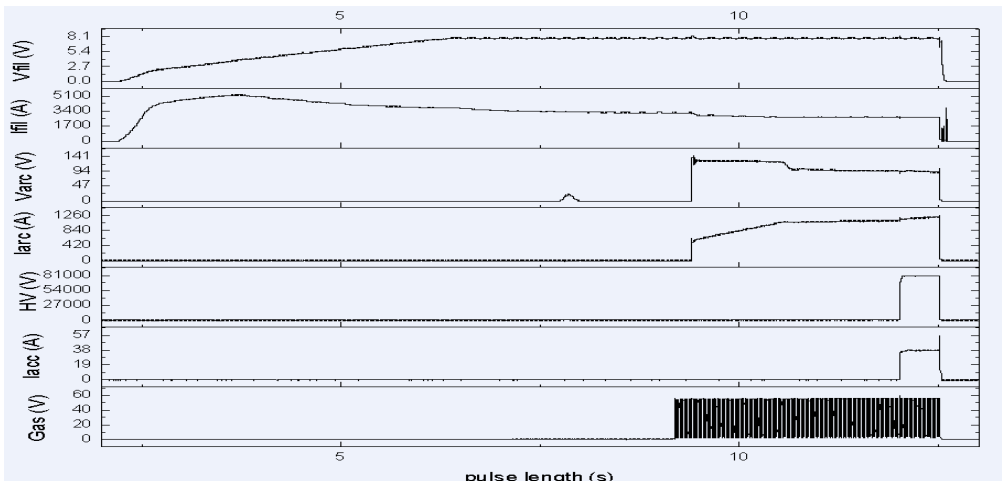


Fig. 5 Experimental results of EAST-NBI

References

- [1] C.D.Hu, NBI Team: Conceptual Design of Neutral Beam Injection System for EAST, Plasma Science and Technology(2012).
- [2] C.D.Hu, Y.L.Xie, Y.H.Xie:velopment of Long Pulse Neutral Beam Injector System for the EAST Tokamak,Chinese Nuclear Society Fall Meeting, Beijing (2009).
- [3] P.Sheng, C.D.Hu, S.H.Song, Z.M.Liu, S.Liu, L.Yu, C.C.Jiang, G.S.Wang, M.H. Zeng, Q.L.Shi, J.S.Wang, L.J.Xiao:ontrol Plan of EAST-NBI Ion Source Test Bench,Asia Pacific Conference on Plasma Science and Technology (2010).
- [4] Information on <http://www.cnblogs.com/skyme/archive/2011/01/04/1925404.html>.

Optimized RBF for CBR-Recommendation System

Jiayang Li, Xiaoping Liu, Rui Li

School of Computer and Information, Hefei University of Technology, Hefei 230009, China

E-mail: lijiaoyang@sina.com

Keywords: CBR-Recommender Modeling; Automatic Acquisition; Optimized RBF Networks; System Construction; Similarity Measurement

Abstract. Recommendation systems are widely used in E-commerce to help their customers find products to purchase, with which an important problem is to efficiently search the contents with their demands, and have been attracting attention from quite a few researchers and practitioners from different fields. This paper proposes the CBR-recommender (Case-Based Reasoning) which is a comprehensive expression of human sense, logics and creativity, and can automatically acquire the user's preferences from the process of adaptation or revision to satisfy the personalized needs; and we deploy radial basis function network (RBF) to control the system scale caused by the large amounts of data with high dimensions, whose performance is also superior with respect to the total time for satisfying a query. Our experiments indicate that our mechanism is efficient since it is bounded by the number of neighbors and scalable because no global knowledge is required to be maintained.

Introduction

Recommendation systems work in different ways under much complex conditions, and must deal with so many problems [1], therefore intelligent web tools are emerging to obtain the behavior in websites automatically, collect user's data for analysis, helps users search, locate and manage various web information, through which personalized knowledge can be acquired for reaching real demands [2]. For example, the system uses data mining and other artificial intelligence technology to generate user model learning, and can use the model of reasoning to generate interests.

The basic idea of recommendation systems can trace down to the acquirement of the personalized knowledge [3]. Differing from the traditional reasoning Rule-Based Reasoning (RBR), CBR originates from human experience learning, and obtains the similar former cases and appropriately adapts to a new situation for the new problem-solving, which is the key for any recommender to achieve successful recommendation. The paper [4] has described that case-intelligence recommendation system can be used for acquiring effective personalized knowledge.

Similarity measurement is the key process in recommendation systems for this basic principle: the relevance of user behavior and choice. For the E-commerce is in complex environment, each data is regarded as the foundation for knowledge representation, but may be represented in semi-structured or unstructured model, or even in natural language texts[5]. How to effectively calculate their similarity is a difficult problem, which infers the quality of recommendation and the performance of e-commerce. Artificial Neural network (ANN) has many advantages, such as good at dealing with noisy data, high adaptability [6], and the parallel processing, and can be easily used in recommendation system as intelligent components. Radial basis function network (RBF) is a good similarity detector, the subsequent research indicates that RBF network has so many advantages like fast learning and global convergence, and then we suggest a model for similar case retrieval based on RBF network.

The Acquisition of Personalized Knowledge

The acquisition of user's data is the key to meet the individual needs and infer the learning ability of the system, which can be collected from three sources: Server, Client, and Proxy, the server is the main data sources. Web DM researchers are covering a number of research areas[7,8], including

database technology, information technology, statistics, artificial neural networks and machine learning, using a variety of data mining technology to exploit potential information or patterns useful.

Information Extraction

Information Retrieval (IR) and Information Extraction (IE) are very important steps in web DM. The purpose of IR is to find relevant Web document, which regards the data from document as collection of unsorted phrases, and IE aims to find the data needed from the document, which cares about the structure of the document and the meaning of the expression, of which the important task is to organize data with appropriate index. The main processes may be described as follows:

Resource seeking: its task is acquiring data from the target document. Sometimes, Information resource is not limited to online web document; it also includes e-mail, electronic documents, news group, or web site log data or through Web formed transaction data in the database. Information selection: its task is that removing useless information from the obtained web resources and consolidating the information in proper style. For example, deleting the advertisement link from the web document, removing excess formatting marks, automatically identifying paragraph or the field or data and organizing into regular logical form even relation table. Pattern discovery: processing pattern discovery automatically. This can be in the same site or among a plurality of sites. Pattern analysis: checking and validating the former pattern generated in the last step. This can be automatically completed, or can be analyzed with personal interact.

Data Preprocessing

We need design the user model through the analysis of his records, including the basic user information, his habits, and personal preferences, to provide personalized services in the e-commerce environment. User session identification is an important step in Web log mining, which is restricted by many parameters such as the content of web page, download time, read speed, etc., and where threshold is used to remove noise.

User identification: can be deal with the two type data, (a) Usage data: describing web usage pattern, such as IP address, URL, webpage citation, access time and date, which indicates each user's behavior model, and a typical use of data originates from server log; (b) User Profile: relative statistics data from web user, including user registration and personal information, for example, user name, education background, career, position, age, income, personal hobby, etc.

User session identification: the session specifies the same user for the requested page, and a different user to access the page belongs to a different session. User access records should be split into individual sessions for a long period session for the user may be access the website many times. Current three heuristic methods are described as follows.

Setting an upper bound for the webpage to the user residence time, it can be regarded as a start of a new session if the time between two queries beyond this threshold. The threshold value should be inferred by the class of web pages, download time, or net speed, which is set to 10 minutes in ordinary state. Setting an upper bound for the website to the user residence time, it can also be regarded as a start of a new session if the time between two queries beyond this threshold. A statistic threshold is 2255 seconds, thus, 30 minutes is set to the default threshold. Setting an upper bound for the two continues web pages to the user residence time.

Personal Interest Degree

$$TM = \begin{bmatrix} w_{11} & w_{12} & \dots & w_{1m} \\ w_{21} & w_{22} & \dots & w_{2m} \\ \dots & \dots & \dots & \dots \\ w_{n1} & w_{n2} & \dots & w_{nm} \end{bmatrix} \quad (1)$$

In order to achieve personalization services, we must trace down user's behavior to study his interest. Though an investment table feed back by user may be acquired, user behavior extraction is compulsory to estimating the user interest degree.

A great number of studies have shown that the user interest degree to the page is closely related to the user's browsing behavior in the page, such as page-concerned time, number of page rolling and page size determine the characteristics of user's behavior, which directly indicates the level of the user's interest on the page. Current researches show there are many existing methods to express personal interest degree, of which we can use topic-keywords in this paper, the expression TM is the topic-keywords matrix of user's weight, where n represents the number of user interested topics, and w is the weight.

$$idf_k = \log(N / df_k); \quad w_{ik}^d = \frac{tf_k * idf_k}{\sqrt{\sum_{s=1}^m [tf_s * idf_s]^2}} \quad (2)$$

Web document representation is important foundation of Web page feature selection. At present, the commonly used method is word-based vector space model, and each weight assumed for a word represents its utility to the document, tf*idf method is used in the paper, where a m-dimensional vector can be represented for a document $(w_{t1}^d, w_{t1}^d, \dots, w_{tm}^d)$. The index item tfk is the frequent number which equals the count number tk discovering in the document d; dfk equals the count number where the index item tk covers the amount of total documents.

System model and construction

Artificial neural network (ANN) is massively parallel distributed neurons and has the natural relationship with CBR, and several successful theories have been put forward to integrate ANN components into the CBR system. Compared with those former algorithms, radial basis function network is a good similarity detector, which recognizes and classifies samples dependence on their non-linear distance through projecting them to a multi dimensional space.

RBF Retrieval Modeling

Radial basis function network is a multi-layer feed forward neural network which has only one hidden layer. Assume X is the n-dimensional vector along with $C \in R^n$, $X - C$ composes an ellipse which canters around C with radius $\|X - C\|$, $\Phi(\|X - C\|)$ as the function for an ellipse that is Radial basis function.

Suppose the networks have N_r hidden layered nodes, the transform function $f(x) = x$, with the input n output m, so our case retrieval model based on RBF can realize that

$$\hat{O}_p = f\left(\sum_{i=0}^{N_r} w_{ip} \Phi_i(\|X - C_i\|)\right) = \sum_{i=0}^{N_r} w_{ip} \Phi_i(\|X - C_i\|)$$

reaches the optimal networks in the minimum error

$$E = \sum_{p=1}^m (O_p - \hat{O}_p)^2 = \sum_{p=1}^m \left(O_p - \sum_{i=0}^{N_r} w_{ip} \Phi_i(\|X - C_i\|)\right)^2$$

of output

The networks can be trained by using LMS method (least-mean-square algorithm) $w_{ji}^{k+1} = w_{ji}^k + \eta(O_j - \hat{O}_j)x_{ji}$, where η is learning rate, and ranges from 0.01 to 1. If the output layer is treated as the similarity measurement, it can output the target set for the similar cases. As the most important process in CBR cycle, case retrieval is the key part which is strongly interrelated with the system efficiency, and can be described as the following steps:

Input the basic characteristics of the problem to be solved; under the control of the main case-retrieval-unit, perform the similar cases recall within the sub-case base.

If retrieve successfully (there are most similar cases in output sets), go to 6);

Else select the K nodes for having the maximum output value, judge which class they belong to, and choose these cases to the candidate cases for which has not partitioned to the inner-class retrieval unit;

Repeat 3) until all these cases have partitioned the inner-class retrieval unit; then go to 6);

Inner case retrieval Under the control of inner-class retrieval unit, perform similar cases retrieval in the field of inner unit, and add the most similar cases L to the candidate set of cases.

Recall the most similar cases. According to the retrieval of similar cases from the case library, find more information for further screening; select the more likely cases to meet the requirements

Case adjustment accordance with the relevant criteria or domain knowledge, combined with the problem to be solved and its differences with the candidate of similar cases, adjust these cases; otherwise, further analysis of the problem to be solved, together with the case information and knowledge with the current set of candidate, gain the new description for the problem to be solved, and go to 1)

After a certain number of iterations to solve the problem in step 7), If cannot get satisfactory results, then prompt the user that the problem may not be solved at present, so the user chooses quit or continue the retrieval.

System Modeling

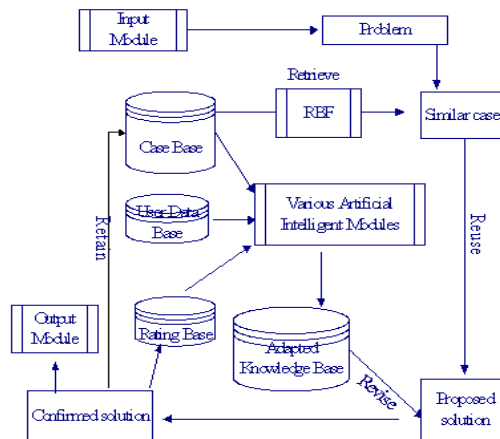


Fig. 1 RBF-CBR recommendation system model

The output of the network meets the actual requirements: the cases in the same class have much more opportunity to the candidate, for they have the larger similarity. The experimental results also indicate that RBF network recognizes and classifies samples dependence on their non-linear distance through projecting them to a multi dimensional space, is a good similarity detector, and has so many advantages like fast learning and global convergence, so it can be selected for case retrieval in our recommendation system as shown in Fig 1.

The details of the components in our personalized recommendation system can be seen in paper [4]. Although the retrieved solution can be reused directly, they are commonly regarded as an initial solution that should be refined to reflect the differences between the new and retrieved problems. The acquisition of adaptation knowledge to achieve this refinement can be demanding, including the knowledge source of stored cases captures a substantial part of the problem-solving expertise.

We care mainly about the new retrieval component prepared for case matching-the similar user group, so the implementation process of personalized recommendation for the same with common recommendation system is also not mentioned, and the experimental results merely records the direct data in this paper, despite the better results from case revision.

Experiments and Review

As the most successful recommendation system in E-commerce, the Collaborative Filtering Recommender works under the same criteria with retrieving cases in the CBR cycle of our model, and the recommender uses the traditional kNN to search similar users.

Firstly, we simply evaluate the both recommendation system’s capability by means of “Recall”. The threshold of similarity is fixed at 0.6 in our experiment as shown in table 1.

Table 1 Average recall in Movie Lens

Item	1	2	3	4	5	6	7	average
KNN	42.5	52.4	29.1	55.3	56.4	60.4	60.7	51.0
Our RBF	54.2	69.7	43.6	64.3	65.1	72.1	72.5	63.1

Secondly, the real complex web text is used to realize the whole system's ability. Our experimental data is downloaded from DELL technical support center, the total is 1,800 Emails from the service forum as shown in Table 2.

Table 2 Experimental results in websites

Item	Average F-score (%)	Average retrieval time(s)
KNN	62.3	42.4
OURS	68.9	24.2

Each Email is pretreated for stop-word processing and low-frequency-word processing, removing stop-words and low-frequency-words including in title and content, 3,420 words are extracted as the characteristic attributes through statistics to the training sets. (2) Each Email is expressed to text-feature vector, and becomes original user-case.

From the both experiments above, our system using RBF techniques performs better than the traditional recommender from any of the recall, average F-score or average time. Our RBF system can classify samples dependence on their non-linear distance, and can recognize cases in non-linear time, thus the system performance time is lower while the amount of samples increasing.

From the view of the E-commerce, knowledge is incomplete, difficult to define, rich cases poor or inconsistent definition which leads to the complex environment, our works not only care about the algorithm, but also take care of extraction of personalized knowledge. From the start of information extraction, the data preprocess, to the definition of personal interest degree, they are all centered on acquiring personalized knowledge, and so many steps are promising the higher successful ratio in our recommender than the ordinary system.

Conclusion

How to obtain personalized demands, expression knowledge to support user from information retrieving and adapting, is the most important task to intelligent recommendation system. Our RBF recommendation system based on case intelligence emphasizes on the former experience and wisdom, can explore all kinds of knowledge from the rich case library, especially to improve recognizing the same user's behavior form his (or her) former rating which can acquire the personalized knowledge implicit in cases automatically, and be analyzed for predicting a certain user's action. The system can adopt different learning strategies varying in demands, is reliable to develop and integrate software system. How to identify unknown words, and suggest a valid recommend within a reasonable time are our future works.

Acknowledgment

We gratefully acknowledge the support of the China Postdoctoral Fund of HFUT, and the Natural Science Project of Anhui Province under grants KJ2011B054.

References

- [1] Henrik Stormer. AAI Workshop (2007), p92-99
- [2] Kim H, Chan P K: Implicit Indicator for Interesting Web Pages, (2005), p. 270-277
- [3] Khalid Al-Kofahi, Peter Jackson etc. AAI Workshop (2007), p. 9-18
- [4] Jianyang Li, Rui Li, Jinbin Zheng, Zhihong Zeng, in: ICEIT 2010, (2010), p. 162-166
- [5] NI Zhiwei, CAI Qingsheng, JIA Ruiyu: Computer Engineering, Vol. 28(7). (2002), p. 12-15
- [6] Lee Y, al: Berlin, Springer, (2004), p. 425-430
- [7] Peng Zhao in: The University of Science and Technology, (2006).
- [8] Choi J, Lee G, Um Y: Berlin, Springer, (2007)

Stability Property of Uncertain Networked Control System with Random and Bounded Delay

Yao Jie^{1, a}

¹The department of mechanical and electronic engineering, Jingdezhen Ceramic Institute, Jingdezhen, Jiangxi province, China, 333403

^ae-mail: njyaojie@yahoo.com.cn

Keywords: Networked Control System; Finite State Markov Chains; Bounded Delay

Abstract. this paper is presenting an important question which is the stabilization of uncertain networked control system (NCS) with random but bounded delay. Normally, this kind of problem can be modeled as discrete time jump linear system controlled by finite-state Markov chains by using augmented state-space method. However, in this paper, a new model is proposed to combat problem of reliable control while actuators become age or partially disabled. Furthermore, the reliable controller is invented to make systems asymptotically mean square stable under several random disturbance by using improved V-K iteration algorithm.

Introduction

As we all know, the NCS has various advantages and is applied different kinds of areas. However, it also introduce some problems such as limited communication bandwidth, network-introduced delay, packets disorder and packets loss which often happen inevitably during information transmission. Consequently, the basic problem of NCS is how to deal with time-varying delay. In this paper, we focus on problems of reliability when actuators inactivate at a certain probability. Concretely, First, a switch mode of NCS is constructed. Second, a sufficient condition of tolerable controllers satisfied mean square stability and its design method are given by using LMI method when NCS have uncertain controlled plant.

Model of Networked Control Systems

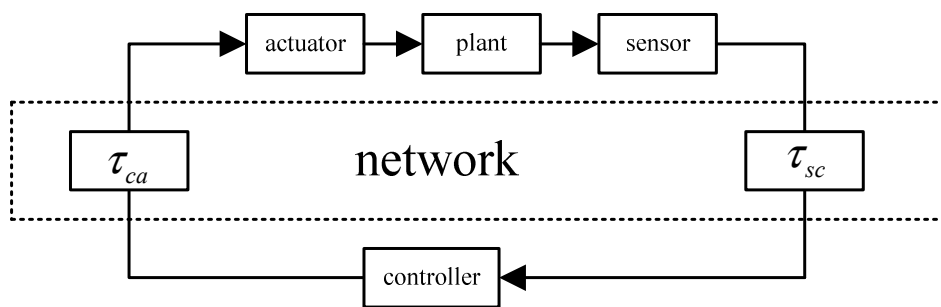


Fig. 1 Networked control system with random delay

A typical NCS as depicted in Fig. 1 consists of three components: A general plant including actuator, plant and sensor to be controlled, a network and a controller. In this paper, it is assumed that the plant is discrete linear systems with uncertainty described by the following differential equation.

$$x(k+1) = (A + \Delta A(t))x(k) + (B + \Delta B(t))u(k) \quad (1)$$

Where $x(k) \in \mathfrak{R}^n$ is the state vector, and $u(k) \in \mathfrak{R}^m$ is the control input vector. Suppose the uncertain structures of the system (1) are given by: $\Delta A(t) = DF(t)E, \Delta B(t) = D_1F_1(t)E_1$

D, D_1, E, E_1 are constant matrices with appropriate dimensions and $F(t), F_1(t)$ are Lebesgue measurable satisfied $F^T(t)F(t) \leq I, F_1^T(t)F_1(t) \leq I$

The mode-dependent state feedback control law in remote part considered in this paper is

$$u(k) = K_{r_s(k)}x(k - r_s(k)) \quad (2)$$

Where $\{r_s(k)\}$ is a bounded random integer sequence with $0 \leq r_s(k) \leq d_s < \infty$ which express time-varying delays of network, and d_s is the finite delay bound. If we augment the state variable $\tilde{x}(k) = [x^T(k)x^T(k-1)\cdots x^T(k-d_s)]$

Where $\tilde{x}(k) \in \mathfrak{R}^{(d_s+1) \times n}$, then the closed-loop system is:

$$\tilde{x}(k+1) = (\tilde{A} + \hat{D}\hat{F}\hat{E}_{r_s(k)} + \tilde{B}_{r_s(k)}K_{r_s(k)}\tilde{C}_{r_s(k)})\tilde{x}(k) \quad (3)$$

And $\tilde{C}_{r_s(k)}$ has all elements being zero except for the $r_s(k)$ block being an identity matrix

For simplicity, Eq. (3) can be rewritten as the following form:

$$\begin{cases} \hat{x}(k) = \hat{A}_{r_s(k)}x(k) \\ x(0) = x_0 \in \mathfrak{R}^n \end{cases} \quad (4)$$

The state of \hat{A} is decided by $r_s(k)$, the jumping rules of random integer sequence $r_s(k)$ can be modeled as a finite state Markov chains, that is

$$\Pr ob\{r_s(k+1) = j | r_s(k) = i\} = P_{ij} \quad (5)$$

Where $0 \leq i, j \leq d_s$, this means that, the dynamic characters of bounded random time-delay can be expressed by a step transition probability matrix P. Here, we assume that P is given.

Stability Analysis

In this section, the problem of stability of linear jump system is discussed. Some relative definitions and lemmas are as follows:

Definition 1. For system (4), let zero point be equilibrium point

asymptotically mean square stable, if for any $x_0 \in \mathfrak{R}^n$ and any initial probability distribution

$$(p_1, \dots, p_s) \in r_s(k), \lim_{k \rightarrow \infty} E\{\|x_k(x_0, \omega)\|^2\} = 0$$

stochastic stable, if for any $x_0 \in \mathfrak{R}^n$ and any initial probability distribution $(p_1, \dots, p_s) \in r_s(k)$

$$E\left(\sum_{k=0}^{\infty} \{ \|x_k(x_0, \omega)\|^2 \}\right) < \infty$$

Lemma 1. Let A, D, E and F be real matrices of appropriate dimensions with $\|F\| < 1$. Then we have the following:

For any scalar $\varepsilon > 0$, $DFE + E^T F^T D^T \leq \varepsilon^{-1} D^T D + \varepsilon E^T E$

For any matrix $P > 0$ and scalar $\varepsilon > 0$ satisfying $\varepsilon I - EPE^T > 0$,

$$A(t)PA^T(t) \leq APA^T + APE^T(\varepsilon I - EPE^T)^{-1}EPA^T + \varepsilon DD^T$$

For any matrix $P > 0$ and scalar $\varepsilon > 0$ satisfying $\varepsilon I - D^T PD^T > 0$,

$$A^T(t)PA(t) \leq APA^T + A^T PD(\varepsilon I - D^T PD^T)^{-1}D^T PA + \varepsilon E^T E$$

Theorem 1. The closed system (3) is stochastic stability .if there are symmetric positive definite matrixes $Q(i) > 0, i \in (0, \dots, d_s)$, satisfying

$$L(i) = \hat{A}_i^T \bar{Q}(i) \hat{A}_i - Q(i) < 0 \tag{6}$$

Where $\bar{Q}(i) = \sum_{j=0}^{d_s} p_{ij} Q_j$ and $p_{ij} \in P$ (7)

Theorem 2 The closed system (4) is asymptotic mean square stability, if there exist positive-definite symmetric matrices $Q(i) > 0$ and constants $n_i > 0, i \in (0, \dots, d_s)$ satisfying the following matrix inequality:

$$\begin{bmatrix} Q_i & \Sigma & \Theta & \Lambda \\ * & \Omega & 0 & 0 \\ * & * & \Xi & 0 \\ * & * & * & \Pi \end{bmatrix} > 0$$

Where

$$\Sigma = [(\tilde{A} + \tilde{B}_0 \tilde{K}_0)^T Q_0, \dots, (\tilde{A} + \tilde{B}_{d_s} \tilde{K}_{d_s})^T Q_{d_s}], \Theta = [(\tilde{A} + \tilde{B}_0 \tilde{K}_0)^T Q_0 \hat{D}, \dots, (\tilde{A} + \tilde{B}_{d_s} \tilde{K}_{d_s})^T Q_{d_s} \hat{D}]$$

$$\Lambda = [n_0 \hat{E}_0^T, \dots, n_{d_s} \hat{E}_{d_s}^T], \Omega = \text{diag}\{p_{j_0}^{-1} Q_0 \dots p_{j_{d_s}}^{-1} Q_{d_s}\}, \Pi = \text{diag}\{p_{j_{d_s}}^{-1} n_0 \dots p_{j_{d_s}}^{-1} n_{d_s}\}, j \in \{0, 1, \dots, d_s\}$$

$$\Xi = \text{diag}\{p_{j_0}^{-1} (n_0 I - \hat{D}^T Q_0 \hat{D}) \dots, p_{j_{d_s}}^{-1} (n_{d_s} I - \hat{D}^T Q_{d_s} \hat{D})\}, \text{ and } n_i I - \hat{D}^T Q_i \hat{D} > 0, i \in (0, 1, \dots, d_s)$$

Stability Analysis Of Switched Networked Control System With Uncertainty

$$\begin{cases} x(k+1) = (A + \Delta A(t))x(k) + (B + \Delta B(t))u_{(i_k, r_s(k))}(k) \\ u_{(i_k, r_s(k))}(k) = K_{(i_k, r_s(k))} x(k - r_s(k)) \end{cases} \tag{8}$$

Where $i \in \{1, 2, \dots\}, r_s(k) \in \{0, 1, \dots, d_s\}$

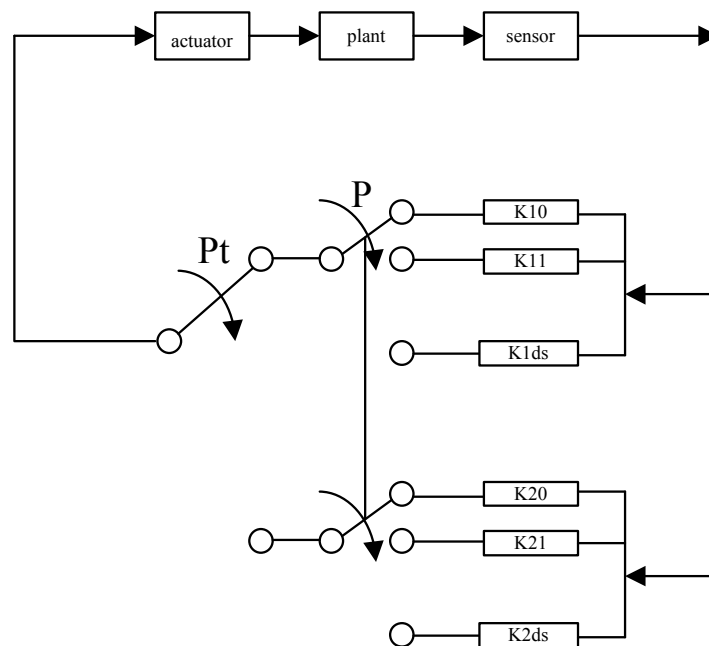


Fig. 2 Stochastic networked control systems under switched control

From Eq (8), this system has two group controllers, i_k indicate the number of controller groups acting in time k , because the maximal delay is d_s , every group of time-dependent controllers has $d_s + 1$ controllers. the general structure of switched control system is shown in Fig.2, where $P \in \mathfrak{R}^{(d_s+1) \times (d_s+1)}$ denotes one step probability matrix of stochastic delay of present network, $K_{10} \sim K_{1d_s}$ are mode-dependent controllers satisfied to transition probability matrix P (if controller $K_{10} = K_{11} = \dots = K_{1d_s}$, they are mode-independent controllers and if $K_{10} \neq K_{11} \neq \dots \neq K_{1d_s}$ they are mode-dependent controllers). $K_{20} \sim K_{2d_s}$ are testing controllers which are used to checkout the reliable ability of designed controllers. regarding every group of control loop, this system can be seen as an independent jump linear system governed by Markov chains and these two Markov processes are irrelative to each other. After inserting a switch, these two Markov processes become relative. Through regulating different switch probabilities of switch and setting suitable gain values of testing controllers, stabilization span and stable performances of system are obtained when actuators of system suffer different fault probabilities. First, the mean square stability of system theorem is given as follows:

Theorem 3. Assume Eq. (8) has switched rules matrix P , the jump rules of jump linear control system governed by a step transition probability matrix P , then the mean square stability of system is equivalent to the existence of symmetric positive definite matrices $Q_0, Q_1, \dots, Q_{(d_s+1) \times 2}$ and constants

$$n_i > 0, n_i I - \hat{D}^T Q_i \hat{D} > 0, i \in \{0, 1, \dots, (2d_s + 2)\} \text{ satisfying}$$

$$\begin{bmatrix} Q_j & \Sigma & \Sigma_1 & \Theta & \Theta_1 & \Lambda & \Lambda_1 \\ * & \Omega & 0 & 0 & 0 & 0 & 0 \\ * & * & 0 & 0 & 0 & 0 & 0 \\ * & * & * & \Xi & 0 & 0 & 0 \\ * & * & * & * & \Xi_1 & 0 & 0 \\ * & * & * & * & * & \Pi & 0 \\ * & * & * & * & * & * & \Pi_1 \end{bmatrix} > 0 \tag{9}$$

Where

$$\begin{aligned} \Sigma &= [(\tilde{A} + \tilde{B}_0 \tilde{K}_{10})^T Q_0, \dots, (\tilde{A} + \tilde{B}_{d_s} \tilde{K}_{d_s})^T Q_{d_s}], \\ \Sigma_1 &= [(\tilde{A} + \tilde{B}_0 \tilde{K}_{20})^T Q_{d_s+1}, \dots, (\tilde{A} + \tilde{B}_{d_s} \tilde{K}_{2d_s})^T Q_{2d_s+2}] \\ \Theta &= [(\tilde{A} + \tilde{B}_0 \tilde{K}_{10})^T Q_0 \hat{D}, \dots, (\tilde{A} + \tilde{B}_{d_s} \tilde{K}_{d_s})^T Q_{d_s} \hat{D}], \\ \Theta_1 &= [(\tilde{A} + \tilde{B}_0 \tilde{K}_{20})^T Q_{d_s+1} \hat{D}, \dots, \Theta_1(2d_s + 2)(\tilde{A} + \tilde{B}_{d_s} \tilde{K}_{2d_s})^T Q_{2d_s+2} \hat{D}] \\ \Lambda &= [n_0 \hat{E}_0^T, \dots, n_{d_s} \hat{E}_{d_s}^T], \Omega = \text{diag} \{ p_{j0}^{-1} Q_0 \dots p_{jd_s}^{-1} Q_{d_s} \}, \\ \Lambda_1 &= [n_{d_s+1} \hat{E}_0^T, \dots, n_{2d_s+2} \hat{E}_{d_s}^T], \Omega_1 = \text{diag} \{ p_{j(d_s+1)}^{-1} Q_{d_s+1} \dots p_{j(2d_s+2)}^{-1} Q_{2d_s+2} \} \\ \Pi &= \text{diag} \{ p_{j0}^{-1} n_0 \dots p_{jd_s}^{-1} n_{d_s} \}, \Pi_1 = \text{diag} \{ p_{j(d_s+1)}^{-1} n_{(d_s+1)} \dots p_{j(2d_s+2)}^{-1} n_{2d_s+2} \}, j \in \{0, 1, \dots, d_s\} \\ \Xi &= \text{diag} \{ p_{j0}^{-1} (n_0 I - \hat{D}^T Q_0 \hat{D}) \dots, p_{jd_s}^{-1} (n_{d_s} I - \hat{D}^T Q_{d_s} \hat{D}) \}, \\ \Xi_1 &= \text{diag} \{ p_{j(d_s+1)}^{-1} (n_{(d_s+1)} I - \hat{D}^T Q_{(d_s+1)} \hat{D}) \dots, p_{j(2d_s+2)}^{-1} (n_{2d_s+2} I - \hat{D}^T Q_{2d_s+2} \hat{D}) \} \\ j &\in \{0, 1, \dots, 2d_s + 2\} \end{aligned}$$

Reliable Analysis of NCS and Design of Fault Tolerant Controllers

Reliable Analysis of NCS

Applying of the model building in Section 4, we obtain steps of reliable analysis of NCS as follows:

Assuming transition probability matrix P is given, request delay-dependent and delay-independent controllers which make system asymptotic mean square stability using Theorem 2.

Construction of the first group of controllers using delay-independent controllers solved in step (1) and setting gains K of the second testing controllers equal to zero. We can simulate actuator damage with varying damage degrees through selecting different switch probabilities

P_t and then using Theorem 3, the maximum redundancy of controllers requested in step (1) which make system asymptotic mean square stability to be obtained.

Construction of the first group controllers using delay-dependent controllers solved in step (1), redundancy degree of these controllers under the condition of part actuators of NCS are stochastic inactivation obtained through setting all gains K of testing controllers equal to zero.

Design of Fault Tolerant Controllers

We obtain the method of designing fault tolerant controller as the following steps:

Let all gains of second group controllers be equal to zero, that is setting gains of testing controllers $K_{20} \sim K_{2d_s} = 0$ and delay-dependent or delay-independent controllers obtained in (1) of Section 5.1 as first group controllers. Set initial switched probability value as pt_{11} (for simplicity, we substitute pt_{11} with pt). In general, let $pt=0.9$.

Applying Theorem 3 and improved V-K iteration algorithm, request controllers $K_{10} = K_{11} = \dots = K_{1d_s}$, satisfying asymptotic mean square stability of systems when fault probability of actuators is $(1-pt)\%$.

Analysis of redundant degree of controllers solved in step (2), using reliable analysis method mentioned in Section 4.

Let controllers solved in step (2) as first group controllers, and adjust switched probability pt , that is $pt = pt - \Delta pt$. Generally, let $\Delta p=0.1$; let all gains of testing controllers equal to zero, and then back to step (2), repeat the cycle from step (2) to step(4), until the redundant degree of system does not increase any more. Through this method, a group of controllers with the highest redundant degree is obtained.

Remark 2 If we choose time-dependent controllers as controllers of jump linear system, then we can design a group of tolerable fault controllers which can make system mean square stability when partial controllers of a group of controllers be damaged entirely through set partial testing controllers' gains and the corresponding controllers' gains in first group controllers to zero.

Conclusions

This paper presents a problem of stabilization about uncertain networked control systems (NCS) with random but bounded delays. A new switched model switching according to probability is proposed to research problems of reliable control. Using improved V-K iteration algorithm, a class of reliable controller is designed to make system asymptotically mean square stable under several stochastic disturbances such as random time delay and stochastic actuator failure and the maximal redundancy degree is given. An example is included to demonstrate the effectiveness of the approach.

References

- [1] L.G. Bushnell, Networks and control, *IEEE Control Systems Magazine* 21 (2001) 22–23.
- [2] S. Hu, Q. Zhu, Stochastic optimal control and analysis of stability of networked control systems with long delay, *Automatica* 39 (2003) 1877–1884.
- [3] G.C. Walsh, O. Beldiman, L.G. Bushnell, Asymptotic behavior of nonlinear networked control systems, *IEEE Transactions on Automatic Control* 46 (2001) 1093–1097.
- [4] G.C. Walsh, H. Ye, L.G. Bushnell, Stability analysis of networked control systems, *IEEE Transactions on Control Systems Technology* 10 (2002) 438–446.
- [5] J. Nilsson, B. Bernhard son, B. Watermark, Stochastic analysis and control of real-time systems with random time delays, *Automatica* 34 (1998) 57–64.
- [6] W. Zhang, M.S. Branicky, S.M. Phillips, Stability of networked control system, *IEEE Control Systems Magazine* 21 (2001) 84–99.
- [7] L. Xiao, A. Hassibi, J.P. How, Control with random communication delays via a discrete-time jump linear system approach, in: *Proceedings of the 2000 American Control Conference, Chicago, 2000*, pp. 2199–2204.
- [8] K. Suyama, Systematization of reliable control, in: *Proceedings of the American Control Conference, Anchorage, 2002*, pp. 5110–5118.
- [9] L. Wang, Y. Liu, J. Bai, Reliable control for uncertain switched systems with time delay, in: *Proceedings of the 6th World Congress on Intelligent Control and Automation, Dalian, China, 2006*, pp. 1285–1289.
- [10] G. Yang, S. Zhang, J. Lam, J. Wang, Reliable control using redundant controllers, *IEEE Transaction on Automatic Control* 43 (1998) 1588–1593.
- [11] O.L.V. Costa, M.D. Fragoso, Stochastic reliable control of a class of uncertain time-delay systems with unknown nonlinearities, *IEEE Transaction on Circuits and System-I* 48 (2001) 646–650.
- [12] J. Kim, Delay and its time-derivative dependent robust stability of time-delayed linear systems with uncertainty, *IEEE Transaction on Automatic Control* 46 (2001) 789–792.
- [13] Y. Cao, Y. Sun, C. Cheng, Delay-dependent robust stabilization of uncertain systems with multiple state delays, *IEEE Transaction on Automatic Control* 43 (1998) 1608–1612.

Transfusion Monitoring and Controlling System Based On Wireless Communication

Ma Jiang^{1,a}, Wen Yuqiao, Du Lingyan, Liang Xiaoxiao, Wei Chonggang

¹: Sichuan University of Science & Engineering Dept. of Electronic Engineering, Zigong Sichuan
643000, PR. China

^a1443672@qq.com

Keywords: Speed; Monitoring; Controlling; Nrf905; RS-485

Abstract. Transfusion monitoring and controlling system of wireless communication is designed for avoidance of medical accident due to inconsiderate care. This system is based on RS-485 bus protocol to build the communication network, consisting of master computer and slave computer. STM32F103R8T6 MCU is the core of the master computer, and MSP430F2132 MCU for slave computer. The wireless transmission of data between master computer and slave computer can be done by nRF905 wireless transceiver module. One new calculation of drop speed is used for better real-time displaying thereof. Provided that abnormal occurrence is during the transfusion, the transfusion tube will be closed by controlling order from system, in order to protect the patient.

Introduction

Venous transfusion is the main method to cure various illnesses for patients in hospital. Transfusion speed will be determined by patient age, condition, illness, medicine nature etc. [1]. Pneumonodema, heart failure will be led by fast speed and expected effects will not reached by low speed. Therefore, the nursing staff should intensify the control consciousness and monitoring of transfusion speed [2]. At present, the automatic monitoring management of transfusion is not realized in majority of hospitals and medical institutions, therefore, the drop speed and balance of observation and monitoring should be done by patient, accompany or medical personnel[3]. All the transfusion will be monitored simultaneously by building communication network in this design. Provided that abnormal occurrence is in the period of the transfusion, the transfusion tube will be closed by controlling order from system so that a safe and effective environment will be provided to patients.

Overall System Structure

System consists of master computer and slave computer. Master computer is in charge of monitoring drop speed, whose signal, by wireless transmission, will be sent to master computer of nurse working station. Core of device for slave computer is Microprocessor MSP430F2132. The power source of the mechanical protection device of closing transfusion tube by the leverage is electromagnet. Infrared sensor is in charge of detection of drop, whose information will be done by MSP430F2132. Core of device for master computer is Microprocessor STM32F103R8T6 in charge of controlling RS-485 serial communication and thus the information is transmitted to computer display. The realization of wireless communication between master computer and slave computer is done by RF transceiver NRF905.

Hardware Design

The Choice of Microprocessor

To reduce the power consumption, the slave computer is in the Sleep-Listener work mode, and only transfer the data when received order from the master computer. Meanwhile, since the lower part of the machine needs to be hanged on the Murphy's dropper of the transfusion, it needs to be as small and light as possible. MSP430F2132 has the characteristic of small in size, ultra-low power consumption (current needed is only 250 μ A when work under 2.2V, 1MHZ, standby current is 0.7 μ A, and the sleeping current is 0.1 μ A), which could just meet the design requirement of the slave computer.

While for the master computer, the receiver needs to process a large amount of data. STM32F103R8T6, the microcontroller produced by ST Company, is based on using ARM Cortex-M3, kernel of which is 32-bit processing and with a clock frequency of up to 71MHz. It could meet the design requirements of master computer [4].

Drop Detection Module

The infrared detection is used for drop detection in this design. The arrangement of infrared emitting diode and photodiode is shown as Fig. 1. If the light change of any infrared receiving tube occurs, it is considered as the drop falling. The said way, with even light, small difficulties, is good for elimination of blind area and no missing of detection.

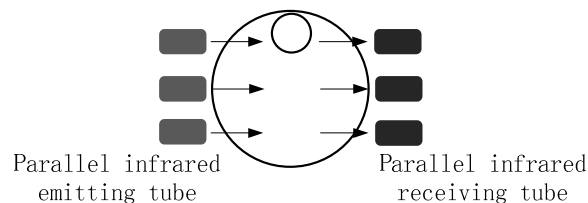


Fig. 1 The arrangement of infrared emitting diode and photodiode

Shown as Fig. 2, D6, D7, D8 are parallel infrared emitting tube, and D9, D10, D11 are parallel infrared receiving tube. Capacitance C22, C23, C24 has the function of "blocking DC and conducting AC", which result in any single change in electrical signal could be passed to MCU at the first time, therefore can make the system more stable. When there is droplet, the infrared received changed, while for the voltage of the capacitor cannot change instantly, then the voltage of CAIN will be changed due to the influence of the capacity. Meanwhile, CAIN connected to the SCM internal comparator and positive input terminal, then the comparator immediately outputs a low to trigger the microcontroller and generates an interrupt.

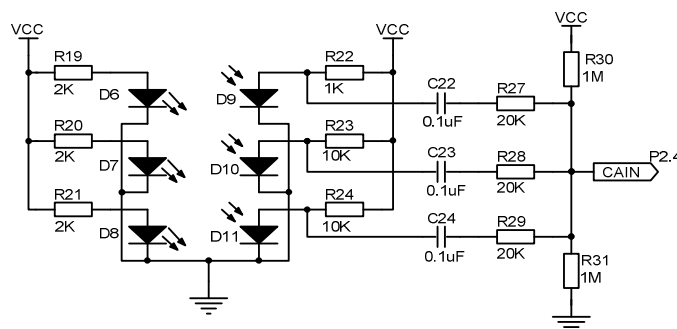


Fig. 2 Drop detection circuit

Mechanical Controlling Module

Prior to transfusion, a safety interval of transfusion should be preset. If unattended and drop speed over preset interval, the mechanical controlling module, by getting controlling order from MCU of slave computer, will close transfusion tube. The electromagnet, as power source of mechanical controlling module in this design, connects power by photoelectric relay AQW214 with the function of electric isolation. Armature of electromagnet connects one end of long arm of lever and transfusion tube is fixed between short arm of lever and base. Shown as Fig. 3, when abnormal drop speed occurs, the transfusion tube is closed by diminishing gap between short arm of lever and base.

NRF905 Wireless Transceiver Module

The single-chip RF transceiver chip NRF905, released by Norwegian Nordic, is used for wireless communication in this system, showed as Fig. 4. VLSI ShockBurst technology is adopted for NRF905 so as to achieve high-speed data transmission. By allowing the digital part of the application to run at low speed, while maximizing the data rate on the RF link, the nRF905 ShockBurst mode reduces the average current consumption in application. NRF905 is inclusive of two operating modes and two energy-saving modes, in transmit only 11mA at an output power of 0.1mW, and in receive mode 12.5mA. The current of idling mode or shutdown mode is 2.5μA. It is easy to realize design of low power [5].

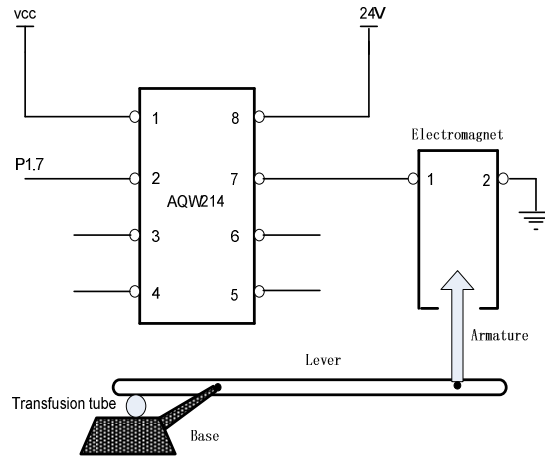


Fig. 3 Mechanical controlling module

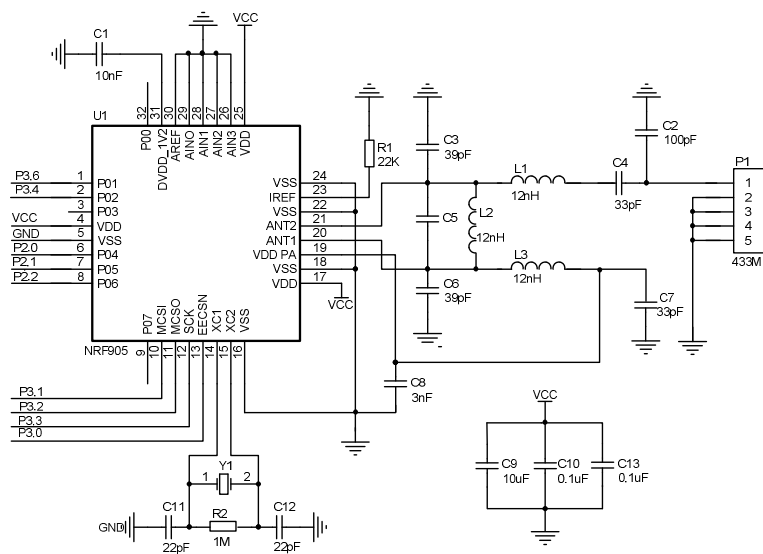


Fig. 4 NRF905 module circuit

RS-485 Communication Module

RS-485 serial bus standard is widely used in the requirements of long distance and anti interference. RS-485 is used for multiple point connection and so many signal lines can be saved, shown as Fig. 5 for RS-485, in which MAX3485 is produced by Maxim, with the working voltage of 3.3V and receiving common-mode input voltage of -7~+12, and also with the function of current limitation and thermal shutdown protection circuit. What's more, R7, the terminal matching resistor, with the value of 120 Ω, is only used for two ends of communication cable.

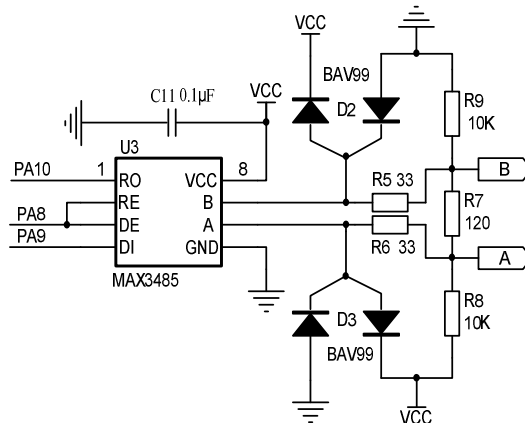


Fig. 5 RS-485 communication circuits

Software Design

This system program design is inclusive of MCU and windows. The function of windows program is mainly for achieving drop speed and showing abnormal condition, which is designed by Visual C++ as development tool. Because of easy program of MCU of master computer, no details will be showed. MSP430F2132 is the core chip of slave computer. The counting of drops, calculation of drop speed, comparison of actual and preset drop speed, controlling of mechanical protection module will be realized by C language programming.

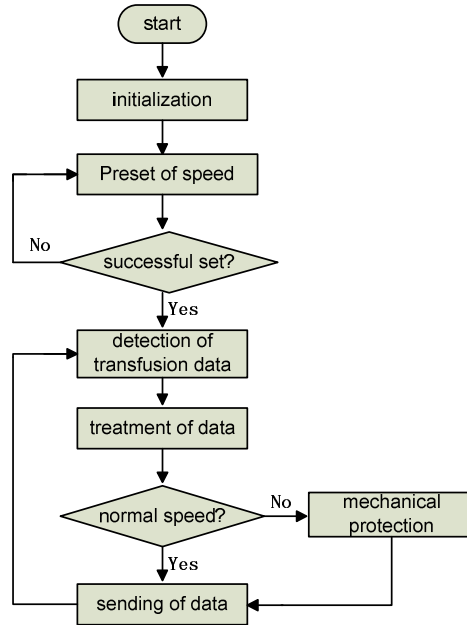


Fig. 6 Flow chart of program design of STM32F103R8T6 MCU

The theory of a different approach used for calculation of drop speed is showed as Fig. 7.

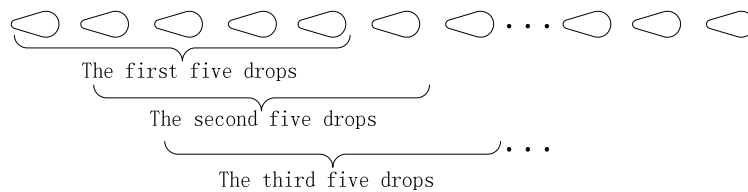


Fig. 7 Calculation of drop speed

When drop speed calculated, 5 drops as basis of calculation, the time used is marked as T. when a new drop detected, the time interval of new drop and previous drop will be added to T and the time interval of first drop and second drop of previous 5 drops will be deducted. 5 drops as basis calculation is unchanged. Therefore, it has the advantages of shortening of calculation cycle, involving of new data, and better real-time display of drop speed than that of previous reference. One new calculation of drop speed expresses as:

$$v = \frac{5 \times 60}{T} (d / \text{min}) n \tag{1}$$

Conclusion

It is likely to lead to medical accident due to inconsiderable care in transfusion, therefore, an effective monitoring method is provided for patient in this design. One real-time and new calculation of drop speed for nurses real-time knowing of transfusion in nurse working station is adopted in this system to reduce the intensity of work. If abnormal condition occurs in the period of transfusion, the system can control and close transfusion tube to avoid the hurt to patient.

Acknowledge

Key scientific and technological projects of ZiGong city key scientific and technological projects of ZiGong city (Project No.:10J02)

References

- [1] Zhou hui. Hospitalized patients with venous transfusion speed Compliance Investigation and analysis [J]. Journal of nursing administration,2008,8(2):19-20
- [2] He Man-hong,Wu Xiao-ju. Dropping speed adjusting in venous transfusion in clinical experience. Application of Chinese Journal of nursing,2009,7(2):87-88
- [3] Zu Long-fe,Li Sai-fei. Infusion alarm stop liquid system research. Medical equipment,2009(1):33-34
- [4] ing Shen-feng, Yao Bo, Tang Jian-jun. STM32F103R8T6 based design and application of digital measuring relays. Low voltage electrical appliances,2010(21):46-50
- [5] Li Qing-yu,Zhang Hua,Liu Ji-zhong.DS1820 based design of wireless temperature acquisition system [J] .Micro computer information,2009,25(9):187~189

Metadata Caching Subsystem for Cloud Storage

Niu Dejiao, Cai Tao, Zhan Yongzhao, Ju Shiguang

School of Computer Science, JiangSu University, ZhenJiang 212013, China

djniu@ujs.edu.cn, Caitao@ujs.edu.cn

Keywords: Cloud Storage, Metadata Management Algorithm, Metadata Caching

Abstract. Cloud storage is a hot topic in current research. Different from previous work, we emphasize the importance of metadata cache in the study of cloud storage. Because the efficiency of distributed file system has much effect on cloud storage. The metadata operation accounts for more than 50% of the total file operation. So the strategy of efficient metadata management is important. There are three parts in this paper. We start with a brief introduction of cloud storage. Then a metadata caching algorithm for cloud storage is proposed. An additional discussion of its performance is also provided. The prototype which incorporates the proposed metadata caching algorithm is realized on Luster to evaluate its performance. Comparing experimental results from this study conclude that the metadata caching subsystem can improve the performance of cloud storage.

Introduction

Cloud computing and cloud storage have been gained much popularity in recent research and development because they have greatly changed the methods of computation and storage people ever used. Using cloud storage people can obtain mass storage resources with higher stability, avoid or reduce the high expenditure to purchase and manage storage devices. Distributed file system is the key supporting technique for cloud computing and cloud storage which directly affects their performances. The amount of metadata is much smaller than the data stored in distributed file system, the metadata operation accounts for more than 50 percent of the total operations since all accesses to the data must recur to metadata [1]. So how to organize and manage metadata efficiently is important to improve the performances of cloud storage and distributed file system.

The Hash-based algorithm, directory sub-tree partition algorithm and LH algorithm are employed for metadata management in distributed file system. Hash-based algorithm can reduce time and space expenditure but it is difficult to choose a suitable Hash function. Higher Hash collision may leads to a dramatically increased time and space spending. In addition, single Hash function cannot adapt to different situations with the metadata variation which is a main cause for unstable query performance [2]. When using the method of directory sub-tree partition, the directory tree is divided into several sub-trees according to its level and relationship which makes it easy to manage the metadata. But time and space spending is rising because all directories along the absolute path where metadata located need to be accessed [3, 4]. LH algorithm is a mixture of the former two methods in which the choosing of Hash function is still a big problem [5]. Mejia Li et al. [6] use dynamic Hash table to maintain the balance of metadata servers. Zhu Yifeng et al. [7] employ Bloom Filter arrays with different levels of accuracies to map filenames to the metadata servers and implement Hierarchical Bloom Filter Arrays (HBA) where a two-level filter is used to index the metadata. But Bloom Filter Arrays have low accuracy for they only calculate the possible partitions where metadata are located. Andrew W. Leung et al. [8] develop Spyglass, a file metadata search system that is specially designed for large-scale storage systems. Spyglass achieves fast, scalable performance through the use of several novel metadata search techniques that exploit metadata search properties. However, the query accuracy is still dissatisfied. Mu Fei et al. [9] present a metadata management mechanism based on route directory to achieve a balanced workload but the directory storage and location expend much space.

The current metadata management algorithms mainly focus on metadata organization and inquiry strategy, local factors result from metadata operation are not exploited sufficiently which lead to a lack of optimization mechanism for local metadata access. In distributed file system metadata access has the same characteristic as ordinary data access that objects just been visited will have greater chance to be visited again especially metadata with storage addresses. Compared with common file systems, distributed file system has a very large amount of metadata which will cost a lot of time and space to make a query. In order to improve the performance of distributed file system, metadata caching should be introduced. In addition, the employment of metadata caching can combine multiple write operations, reduce the number of disk read or write and thus improve the efficiency of distributed file system. We modify the metadata query flow and implement metadata caching by collecting and storing metadata just been visited on an open source distributed file system-Luster.

Metadata Caching Algorithm for Cloud Storage

The current cloud storage is composed of client nodes, storage control nodes and data storage nodes. Client nodes receive access requests from cloud storage users and convert them into corresponding operations for cloud storage. Storage control nodes supervise the metadata information of cloud storage, carry out the user's operations which involve the metadata, at the same time, manage and control the access between client nodes and data storage nodes. Data storage nodes preserve and manage a fraction of data in cloud storage, receive and deal with data requests of client nodes, finally, feedback corresponding information. Generally, there are one storage control node, multiple data storage nodes and many client nodes in cloud storage. Client nodes depend the distributed file system to access the data and the metadata which is centralized kept in storage control node and distributed kept in data storage nodes respectively. The overall metadata concentrated process in the storage control nodes may cause performance bottleneck. So we introduce metadata caching to improve the I/O performance of cloud storage. First, we describe the structure of metadata caching subsystem and the write-back algorithm is subsequently presented.

Structure of Metadata Caching Subsystem: The metadata caching subsystem is added into the storage control node of our cloud storage. Fig.1 shows its structure:

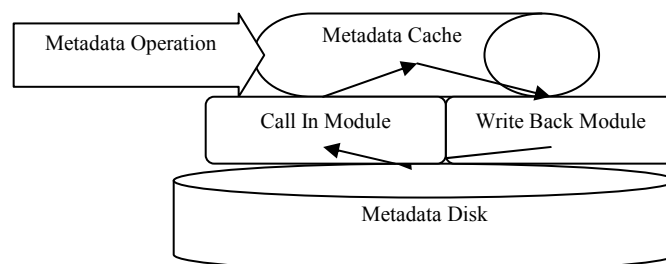


Fig 1 The structure of metadata caching subsystem

When storage control node receives the request of metadata operation, it will search the metadata caching first. If cache misses, the metadata disk will be searched and the metadata entry will be transferred into the metadata cache by the call-in module. The call-out module writes the metadata entries back to the disk when the cache is full or choosing certain entries regularly.

Metadata Active Write-back Algorithm: Main memory is a commonly used channel for metadata caching construction in current cloud storage which inevitably suffers from problems such as metadata loss when power off. Frequent write-back of metadata from cache to the disk is bound to cause serious decline in performance. So it is a thorny issue on how to maintain integrity and performance as well as writing the metadata back to the disk reasonably. To solve the issue, we present an active write-back algorithm which guarantees the metadata write-back not only in case of cache completeness but also when the periodically specified parts will not be modified any more. The problem of metadata loss caused by power off can be reduced accordingly.

For convenient illustration, some symbols and their meanings are defined as follows:

$\Delta T \in N$ denotes the time cycle of metadata caching schedule.

$N_s \in N$ Denotes the probability of re-access for metadata entry

N_{sr} Counts the number of access that the metadata entry is read-only

N_{sm} Counts the number of modification for the metadata caching entry

t Counts the number of time cycles ΔT when metadata is loaded into the cache.

The value of N_{sr} and N_{sm} are updated when every time cycle ΔT is ended using Eq.1 and Eq.2 respectively,

$$N_{sr} = N_{sr} / t \quad (1)$$

$$N_{sm} = N_{sm} / t \quad (2)$$

$N_s \in N$ Defines the probability of re-access for metadata caching entry and the value of which can be calculated by Eq.3:

$$N_s = N_{sr} + N_{sm} \quad (3)$$

$T_d \in N$ And $T_d \geq 1$ is the threshold of periodical write-back for metadata caching entry.

$C \in N$ Denotes the change rate of metadata caching entry and can calculate by Eq.4:

$$C = N_{sr} / N_s \quad (4)$$

$C_d \in N$ Is the threshold of change rate for metadata?

In the algorithm we design three rules for disk write-back of metadata caching entry which correspond to three different situations, such as the metadata caching is full, the entry stays in the cache for too long or the access frequency decreases after metadata modification.

Rule 1: when the cache is full and new entries need to be loaded in, sort the entries from small to large according to the value of N_s . The entry with the smallest N_s and $N_{sm} = 0$ is the one which should be written back. If there is no entry whose N_{sm} equals zero, choose the one with the smallest N_{sm} to write back and delete the corresponding entry in the cache.

Rule 2: at the end of every time cycle ΔT , sort all the entries according to the probability of re-access t . The entries whose value of t is smaller than the threshold T_d and the corresponding N_{sm} do not equal zero are actively written back to the disk. But noted, the entries in the cache do not delete.

Rule 3: at the end of every time cycle ΔT , sort the entries according to the change rate C . The entries whose value of C is greater than the threshold C_d are actively written back to the disk. The corresponding entries in the cache do not delete.

Following above three regulations, metadata entries will be written back to the disk when they are normally eliminated for the completeness of the cache. The entries which have been modified for a long period of time and those have a low change rate will also be written back to the disk actively which reduce the risk of data loss. At the same time, through metadata caching, multiple write operations can be combined together and further improve the system performance.

Define abbreviations and acronyms the first time they are used in the text, even if they have been defined in the abstract. Do not use abbreviations in the title unless they are unavoidable.

Implementation of Metadata Caching Subsystem

The distributed file system is commonly used for accessing and managing in cloud storage. We implement metadata caching subsystem through revising the original codes of distributed file system. Luster is a popular distributed file system which has been widely applied to various kinds' mainframe computers as well as clusters and cloud computers. Fig. 2 gives its structure. Luster consists of three

modules which are Client, Metadata Server (MDS) and Object-based Storage Server (OSS), respectively. MDS includes the codes of metadata management. Client contains the codes for client file system implementation and OSS is the codes for data storage.

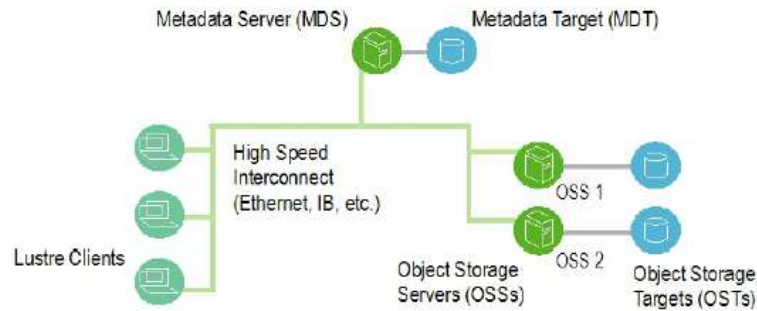


Fig 2 The structure of Luster

The structure named `mds_body` is used to store i-nodes information in MDS which has a 64-bit Hash value named `handle` for metadata query. The structure named `mds_file_data` contains the metadata that used to query a file. The variable named `midlist` is pointed to a list of all file metadata. The details are shown as follow:

```
Struct mds_file_data {
  Struct portals_handle mfd_handle;
  atomic_t mfd_refcount;
  Struct list_head mfd_list; /
  __u64 mfd_xid;
  int mfd_mode;
  struct dentry *mfd_dentry; };
```

In Client module, `libsysio` is used to implement Client file system. *Libsysio* is an open source user mode file system developed by Sandia Laboratory. It constructs a virtual file system to transform between Luster and the underlying file system. The structure named `filesys` is used to keep the information of Luster in `libsysio`. Its structure is shown as follow:

```
struct filesys {
  dev_t fs_dev;
  unsigned fs_ref; /
  unsigned fs_flags;
  struct filesys_ops fs_ops;
  void *fs_private;
  struct itable_entry fs_itbl[FS_ITBSIZ];
  unsigned long fs_id;
  size_t fs_bsize; };
```

The `filesys_ops fs_ops` type variable `fs_ops` is the pointer of file operations and metadata operation functions. The value of variable `fs_itbl` shows that the metadata is organized by Hash table in Luster. The function `_sysio_fs_new` in `Libsysio` is used for initialization when Luster is loaded and a macro `FS_INIT` is provided to initialize parameters of Luster. The function `_sysio_fs_gone` is used to release the memory occupied by Luster. The function `_sysio_i_find` is used to search metadata. The structure `file_identifier` maintains file identifier.

In module of MDS, the function `OBD_ALLOC()` is responsible for creating variables of `mds_file_data` type. The action of creating and deleting the same kind of `mds_file_data` type variables will be repeated whenever metadata is visited and will expend a lot of time and space.

In metadata caching subsystem, we first create a stack `mds_stack` to serve as metadata caching and preserve variables of `mds_file_data` type in `mds_open.c`. The function `mds_mfd_put` releases the variables of `mds_file_data` type. Before the release, we keep them into the stack of `mds_stack`. The function `mds_mfd_new` creates a new variable of `mds_file_data` type. When creating, the stack

mds_stack is searched to see whether there is a variable needed. If the variable is already existed, then directly remove it from the stack mds_stack, otherwise create a new one. The function mfd_cache_put is designed to manage the stack mds_stack.

Test and Analysis of the Prototype

The distributed file system is commonly used for accessing and managing in cloud storage. We implement metadata caching subsystem through revising the original codes of distributed file system. Lustre is a popular distributed file system which has been widely applied to various kinds mainframe computers as

We establish the test environment of Luster on a PC and its configurations of software and hardware are shown in table 1.

Table 1. Configurations of software and hardware

CPU	Intel Pentium 4 2.93 GHz
Memory	1024M
Version of Lustre	1.4.8
OS	Redhat Enterprise 4.0 (kernel:2.6.9-42.14)
Hard disk	Seagate SATA 160G

The testing is conducted before and after the metadata caching subsystem is added respectively by Ionone which is a universal testing tool. First, write performance is tested with cache incorporated. The size of file is 8192K and the size of data block to write is set to 4K, 8K, 16K, 32K, 64K, 128K, 256K, 512K, 1024K, 2048K, 4096K and 8192K, respectively. The comparison of the write performance is shown in Fig.3.

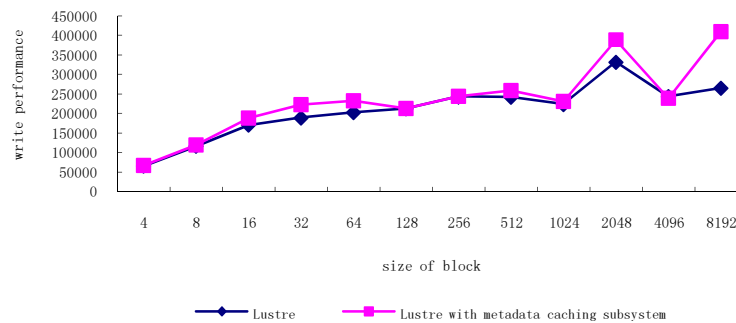


Fig 3 Test results of write performance

From Fig.3, we can find that the write performance of Luster with metadata caching subsystem is always higher than that without metadata caching, especially with the increase of block size, the write performance rises dramatically. This indicates that metadata caching subsystem can improve the write performance of Luster.

Then the read performance is tested when metadata caching sub-system is added too. The size of file is 512K and the size of data block to read is set to 4K, 8K, 16K, 32K, 64K, 128K, 256K and 512K, respectively. The comparison of read performance is shown in Fig.4.

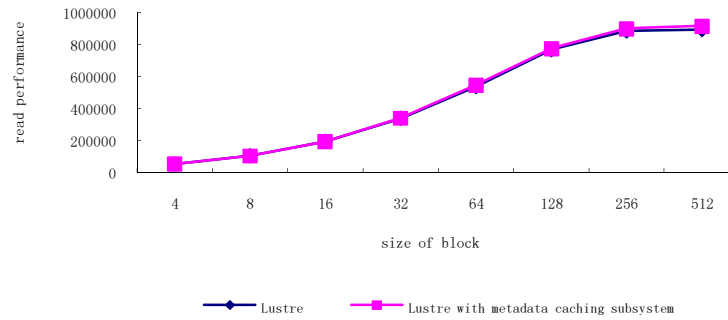


Fig 4 Test results of read performance

From Fig.4, we find that the read performance is very similar when the size of data block is small. The increase of read performance is not obvious because the file system of Client-side has the function of data caching. But with the increase of block size, the read performance rises dramatically. This indicates that the read performance of Lustre can be improved by adding metadata caching subsystem.

Conclusions

In order to improve the I/O performance of distributed file system, we propose metadata caching subsystem to an open source distributed file system-Luster and implement a prototype. The tests results verify that metadata caching subsystem can increase both read and write performance of distributed file system efficiently.

In the future, we will develop new methods of sort management according to the characteristic of metadata and optimize metadata caching to further improve the performance of distributed file system.

Acknowledgments

This work is supported by the Natural science fund of GuangDong province No.S2011010006118, the Natural science fund of Jiangsu Education under Grant No.09KJB520001, Graduate research and innovation fund of Jiangsu province under Grant No. CXZZ11-0576, senior fund of Jiangsu university under Grant No.09JDG038.

References

- [1] D.Roselli, J.Lorch, and T.Anderson. A Comparison of File System Workloads. Proceedings of the 2000 USENIX Annual Technical Conference, page 41-54, June 2000.
- [2] M. Satyanarayanan, J.J. Kistler, P. Kumar, M.E. Okasaki, E.H. Siegel, and D.C. Steere. Coda: A Highly Available File System for Distributed Workstation Environments. IEEE Transaction on Computers, vol. 39, no. 4, Apr. 1990.
- [3] E. Riedel, M. Kallahalla, and R. Swaminathan. A Framework for Evaluating Storage System Security. Proc. First Usenix Conference on File and Storage Technology, pp. 15-30, Mar. 2002.
- [4] S.A. Weil, K.T. Pollack, S.A. Brandt, E.L. Miller. Dynamic Metadata Management for Petabyte-Scale File Systems. ACM/IEEE Conference on Supercomputing, DC, USA, 2004:4
- [5] Brandt S A, Lan Xue, Miller. Efficient metadata management in large distributed file systems: Proceedings of the 20th IEEE/11th NASA Goddard Conference on Mass Storage System and Technologies. San Diego, 2003:290-297.

- [6] Weijia Li, Wei Xue, Jiwu Shu, Weimin Zheng. Dynamic Hashing: Adaptive Metadata Management for Petabyte-scale File Systems. The IEEE Conference On Mass Storage Systems and Technologies, Maryland, USA, May, 2006.
- [7] Yifeng Zhu, Hong Jiang, Jun Wang, et al. HBA: Distributed Metadata Management for Large Cluster-Based Storage Systems. IEEE Transaction on Parallel and Distributed Systems , 2008, 19(6):750-763.
- [8] Andrew Leung, Minglong Shao, Timothy Bisson, Shankar Pasupathy, Ethan L. Miller, Spyglass: Fast, Scalable Metadata Search for Large-Scale Storage Systems, Proceedings of the 7th USENIX Conference on File and Storage Technologies, February 2009:153-166.
- [9] Mu Fei, Xue Wei, Shu Jiwu, Zhen Weimin. Metadata management mechanism based on route directory. Journal of Tsinghua University, 2009, Vol 49, No.8:1229-1232
- [10] Peter J. Braam. The Lustre Storage Architecture. Cluster File Systems, Inc. 2003.10

Research on Two-Speed CAN BUS Technique in Automobile Manufacturing System

Gong Ting^{1, a}, Yan Hui^{2, b}

¹Department of Information Engineering Jilin Business and Technology College Changchun
130062, China

²School of Biological and Agricultural Engineering, Jilin University, Changchun 130022, China
Department of Information Engineering Jilin Business and Technology College Changchun
130062, China

^atingzi0505@sina.com, ^byanhuilonglong@126.com

Keywords: Two-Speed CAN BUS; Automobile Control System; CAN Network.

Abstract. In order to enhance the automation and safety of vehicle, the application of computer technology to the automobile control system has increasingly become a trend. In this paper, the TMS320LF2407 produced by TI Corporation is employed as the microprocessor controller and gateway, which constitute a two-speed CAN communication and control network designed for the automobile control system. Then a specific design plan of application of Two-Speed BUS in automobile control system is elaborated. Through this two-speed CAN bus technique in the vehicle control system, the overall system data sharing is achieved and the performance and security of vehicle control system are improved.

Introduction

With the rapid development of computer technology, new breakthroughs have been made in the application of the computer control technology in automobile industry. With the improvement of the vehicle control system and user-friendly design, a safer performance and a more comfortable space are provided. There are more and more computer control units in the modern automobile and the parameters of the control units need to be shared in real time, while the response time requirements of each control unit is not the same throughout the whole system, for example, for the ABS control and safety assurance system, the response time must be short, while for the air-conditioning systems and lighting systems, the corresponding requirements are lower. In this case, the local area network CAN of the control system is adopted in conducting the automobile control system. In contrast to the heavier load for each control unite under the condition of single network CAN BUS, the applied high-speed and low-speed CAN network are able to serve the control unites of corresponding response requirement separately, with DSP used as micro-control device and gateway. That design greatly simplifies the arrangement of transmission wiring harness, and improves the reliability of the whole system.

Technical Characteristic of CAN BUS

CAN, which is short for Controller Area Network, was first developed by BOSCH, a German company famous for the development and production of electronic products tailored for automobiles, and finally become an international standard (ISO11898). Now it is one of the most widely-used on-site BUS in the world. It has the properties of sound network safety, communications reliability and instantaneity, practical applicability and simplicity, low network cost, which all together make it a particular choice for the automobile computer control system and industries featuring high electronic radiation, severe environments, and strong vibration. Now, CAN BUS is widely used in such fields as industrial automation, Shipbuilding, medical equipment, and industrial equipment etc. Falling into the same filed of on-site BUS, as a major trend of the technological development in the automation industry, CAN now is reputed as a computer local area network in automation.

Since the advent of CAN BUS, there emerged various concentrated high level protocols in order to meet the application requirement of CAN BUS, represented by DeviceNet and CANopen. DeviceNet, CANopen, and CAN constitute a complete protocol system. Considering the distinguished design, excellent performance and high reliability of CAN BUS, people have applied them well in such fields as automobile, medicine, and robot. Thanks to the compatibility and interoperability enjoyed by the high-level forms of CAN—DeviceNet and CANopen—CAN BUS can be designed to have more functions and adapt to more complex applications, which boost the presence of CAN BUS in various industrial areas.

The Automobile Control System Based on TMS320LF2407

TMS320LF2407. TMS320LF2407, launched by TI Company, is a new digital signal processor (DSP) chip with multiple functions and high cost performance. With high-speed parallel BUS structure, it boasts high addressability, speedy operation, rich resources, and strong numerical calculation capacity, hence the great attractiveness in the area of data processing and process control. It is composed of six sets of 16 internal BUS, in-chip DARAM (544 bytes), in-chip SARAM (2k), flash program memory (32 bytes), 16-channel 10 A/D converter, two events manager EV, and a serial interface. By attaching the high-performing DSP core and multiple peripheral equipment of micro controller to the single chip, and operating the instruction with level four-level pine lines, the technician can use the digital control system to do real-time calculations, while reducing the restriction of the hardware to control algorithm. Besides, C language programming can be conducted, with higher interfaceability.

System Implementation. At present, the automobile computer control is concerned with the following aspects of automobile running: dynamic property, economy efficiency, safety, environmental friendliness, comfort. To Be Specific, the system contains such devices as engine control, gear box control, brake control, lighting control, safety control, and air conditioning control. Each unit of the electronic control unit (ECU) is closely links to each other and is in need of real-time communication, so as to realize the resource sharing of the automobile public data.

A real-time control system network based on CAN BUS can realize the collaborative operation of all the control units, hence the effective running of the automobile computer control system. When a control unit gives off a signal, it must be guaranteed that its subsystem responses in-time, otherwise serious accident may occur. Therefore, the CAN communication network of an automobile must be designed to have relatively high baud rate and reliability. The topology structure chart of the communication network in the automobile control system is provided as follows (Fig. 1).

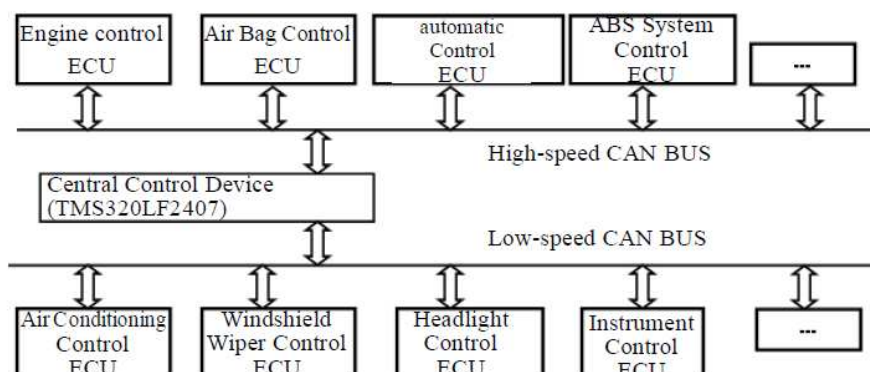


Fig. 1 Topology Structure Chart of the Communication Network in the Automobile Control System

As illustrated in Fig. 1, the control units such as engine control; air bag control and gear box control are of key importance to the operation of modern automobiles, with rigorous requirement for the timing. Therefore, the CAN communication network with a speed of 500Kbps is applied. For units with lower requirement for real time response, such as air conditioning control,

windshield control, and lighting control, it is recommended to use the CAN communication network with a speed less than 125Kbps. The main controller, connected to double-line BUS, is able to exchange data between nodal points, so as to connect the various networks.

The following Fig. 2 shows the wiring diagram of the electronic control unite in the automobile computer system and the CAN BUS. The main controller TMS320LF2407 of the electronic control unite is directly connected to the CAN BUS controller (SJA1000 for instance) through data and address BUS. In order to enhance the anti-jamming capability of CAN BUS nodes, the main controller in the electronic control unite TMS320LF2407 is insulated by high-speed photo isolator through data BUS. CAN_L and CAN_H are two receiving and sending wires of the CAN BUS. When occupying the CAN BUS, the node should receive CAN_H by its sending interface, and receiving interface for CAN_L.

The hardware circuit diagram for the node communication interface of CAN is shown in Fig. 3, composed of CAN control chip, driving chip and photoelectric isolating circuit; the corresponding address line, data and control line is arranged through address assignment and the CAN controller. 82C250 is the interface between the CAN controller and physical BUS, featuring anti-jamming capability, protection for the BUS, and compatibility with ISO standards.

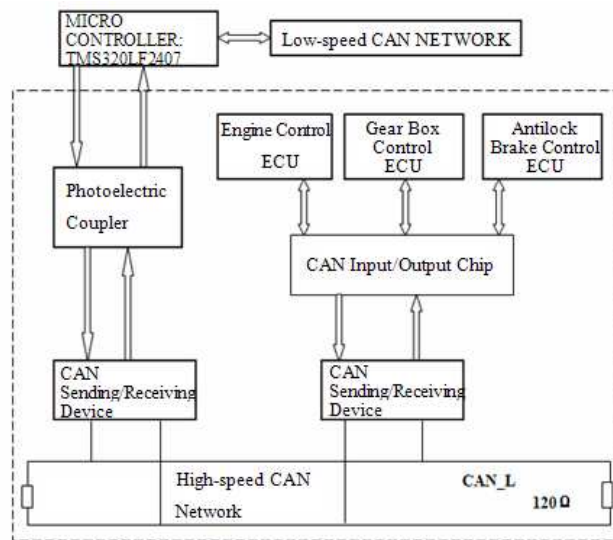


Fig. 2 Cording Diagram on Electronic Control Unite in the Automobile Control System and the CAN BUS

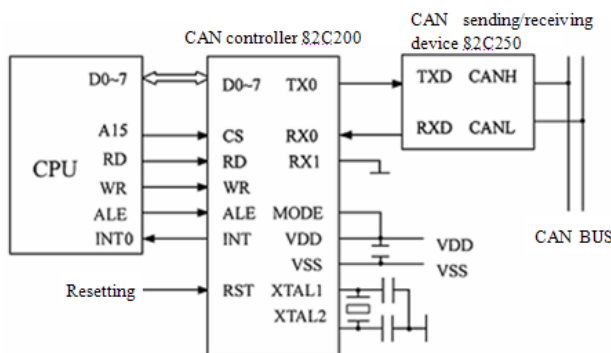


Fig. 3 Circuit Diagram on CAN BUS Communication Interface

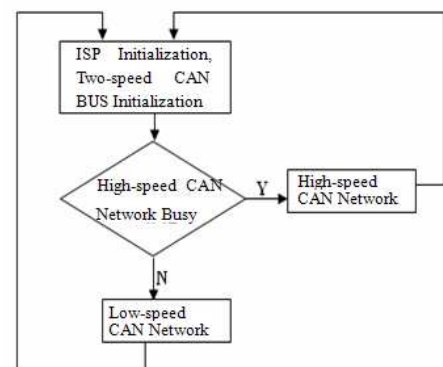


Fig. 4 Flow Chart of the Overall Software System

System Software Design.The system is composed of the overall system software and two-speed CAN BUS network unite software. The overall software flow chart has been shown in Fig. 4. Due to the high requirement for high speed real-time response of the CAN network, the nodes of the high-speed CAN network must enjoy transmission priority, as illustrated in Fig. 4. The data of the low-speed CAN network can be transmitted in the spare time of the high-speed CAN. When the actuating signals of unites, including sending control, safety control or antilock control go through

the microprocessor, they will be dealt with the highest speed, before being transmitted to the ECU of the control unit. In CAN network system, the major functions of ECU is collecting data, sending messages to the BUS, receiving messages from it and sending control instructions to the connected electronic device.

In the CAN network system, various types of ECU need to send the corresponding messages about the automobile control instructions at regular time. Therefore, the software design includes CAN initialization procedures, CAN message receiving program, CAN message sending program, electronic device control program and data collection.

Can Initialization Program

The initialization of the CAN controller is basically about an initiative setting of the register and the buffer zone for message reception. The program in machine code of the CAN initialization is listed as follows:

```
CANINIT; ...
DI                ; disable interrupt
MOV BRPRS, #09H
MOV SYNCO, #0A7H
...
RECEIVE BUFFER INIT; receiving initialization
MOV SYNC1, #04H
MOV MASKC, #02H
CLR CANC.O
EI                ; open interrupt
```

Message Processing

CAN protocol is only concerned about the content rather than the destination to which the message is sent. Therefore, after collecting the information, the low node will send the message to the BUS by broadcasting, for example, by activating the sleep alarm function for the automobile control system. In that case, the CAN devices can be set into sleep mode without any interior operation, resembling the situation of being disconnected to the BUS driver. The sleep mode can be terminated by any BUS activation or the awakening up of the internal conditions of the system. Before BUS driver returns to the on-line state, when the awakening activity has not been started, the transport layer will wait the oscillator of the system to return to stability, and to synchronize with BUS activity (by checking 11 successive recessive bits). For other nodes within the awakening system that are still in the sleep mode, the special awakening message with the least possible identifiers can be used: rrr rrrd rrrr, in which r means recessive bits while d means dominant bits.

Conclusion

As a reliable computer network BUS, CAN BUS is well applied in the automobile industry. In particular, thanks to the resource and information sharing within the automobile control system based on the two-speed BUS, the coordination and compatibility of various control systems have been improved, which contributes to the safety and comfort of the driving experience. In this paper, TMS320LF2407 is taken as the main controller. Relative to a general MCU, it possesses such advantages as fast calculation and high system integration. At present, the domestic research and application in this area started late, but the market prospects are very hopeful. CAN bus in the domestic automotive fields will surely extend its potential usage in the future.

Acknowledgment

The authors gratefully acknowledge the funding of this study by The Ministry of Education humanities social sciences studies "Research on Engineering Technology Talent Cultivation" special task "The Application of Information Technology in Talent of Engineering Technology Cultivation"(10JDGC021) and the Jilin Province Department of Education research project (2012366).

References

- [1] Liu Lifeng, Liao Liqing and Ling Yuhua: Research and Application of High-Low-Speed CAN BUS in the Automobile Control System, Shanghai Automobile, No. 9, (2005).
- [2] Liu Heping: The Development and Application of TMS320LF240x DSP Language. Beijing, BUAA Press, (2002).
- [3] Feng Zhong: Two-Speed CAN BUS Design in the Automobile Control System, Electronic Technology Application, No. 3, (2008).
- [4] Wang Lian and Liu Jian: The Application of the Local Area Network of Controller to VW Automobile, Automobile Electronic Technology, (2000).
- [5] Deng Zunyi and Ning Yi: Research on the Application of CANBUS in the Automobile Control System, Development and Innovation of Mechanical and Electrical Products, (2010).

Research of ISIC-CDIO Question Answer System for Materials Teaching Based on Android

Yan Hui^{1, a}, Hu Hai-Yan^{2, b}

¹ Department of Information Engineering Jilin Business and Technology College Changchun, China

² Department of Information Engineering Jilin Business and Technology College Changchun, China

^ayanhuilonglong@126.com, ^bhhy1979_711@sina.com

Keywords: Android, CDIO, ISIC-CDIO, Similarity

Abstract. This essay innovatively proposes the education mode of ISIC-CDIO and introduces the Android mobile platform to teaching procedures by utilizing the existing mobile wireless network and artificial intelligence technology. It also realizes the question-answering system for teaching under the cultivation mode of ISIC-CDIO, focusing on two similarity algorithm- stereotyped matching and no pattern matching studying. The improvement of algorithm has increased the efficiency of successful matching of problems, which will promote the individual learning of students and thus will cultivate the comprehensive talents with ISIC-CDIO quality.

Introduction

As the reform of CDIO education mode has been developing constantly in the globe, the reform of China's education mode is still at the initial stage. This essay innovatively proposes the ISIC-CDIO education mode, which will better adapt to the reality of China's education and better realize the education reform. A series of sub-systems are concluded in the ISIC-CDIO education system, including the curricula cultivation system, the intelligent teaching system, the intelligent experiment system, the intelligent question-answering system and the expert system. This essay will focus on introducing the realization of the ISIC-CDIO question-answering system.

In the whole learning process, the most important procedure is to offer timely answers and help when students encounter problems. Students will have the right understanding and recognition when encountering problems, which is extremely important from the perspective of education science. The combination of the question- answering system and the Android mobile technology will eliminate the time and space limit of the traditional question-answering system, which helps the users learn more efficiently. The mobile question- answering system will offer convenience for learners in any minute.

This essay combines the Internet technology with ISIC-CDIO education mode by utilizing the Android mobile technology, which has changed the traditional monotonous question-answering teaching mode and has realized the deep integration of the related technologies from interdisciplinary subjects. The information communication and service approaches at any time, anywhere and with anybody will be applied to the teaching platform. It is suitable for students to learn in an open way characterized with mobility, efficiency, width and individuality, which will offer a teaching and learning platform for cultivating the comprehensive talents with the ISIC-CDIO quality.

A Brief Introduction to ISIC-CDIO Cultivating Model

CDIO represents Conceive, Design, Implement and Operate. Its carrier is the life cycle from the research and development of products to the operation of products, and it allows students to learn engineering by closely connecting the initiative, practice and curricula. The CDIO training program divide the ability of a graduate into four parts which are basic knowledge, personal competency, interpersonal competency, process ability. The training program requires that students should achieve the certain target by a comprehensive way of education.

Compared with the foreign universities, China’s colleges and universities still have disadvantages in cultivating engineering talents in terms of information communication, skills, innovation and coordination. Based on the standard of CDIO and the current situation in China, to better realize the reform objectives of the engineering education, this essay innovatively proposes the ISIC-CDIO education mode, that is, Information, Skill, Innovative and Collaborate, closely combined with the approach of Conceive-Design-Implement-Operate, which together makes up a new engineering education mode. The concept and framework is as follows (see the Figure 1).

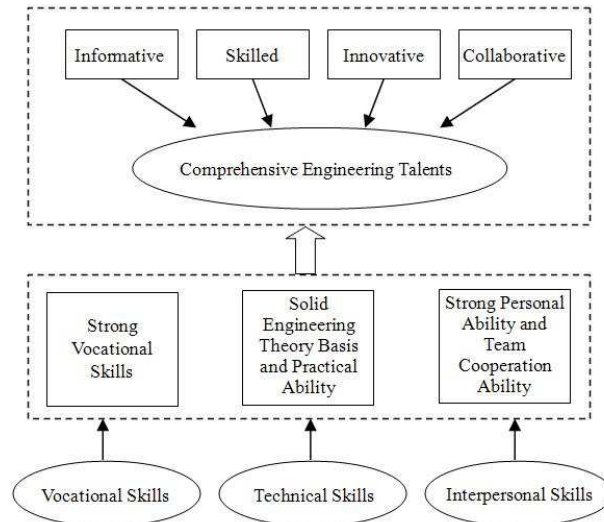


Fig. 1 Concept Framework of ISIC-CDIO

The four-factor integrated mode of ISIC-CDIO aims at letting students get the needed professional skills, technical skills and sociable skills in engineering work by cultivating their capabilities of information communication, skills, innovation and coordination.

Structure of ISIC-CDIO Question Answer System for Teaching Based on Android

Building the Structure of Question Answer System

The four-level structure is adopted in the system, including the user level, the Internet level, the application level and the data access level. The clear structure can bear the load efficiently to reach a better balance. The System structure relation is as follows (see the Figure 2).

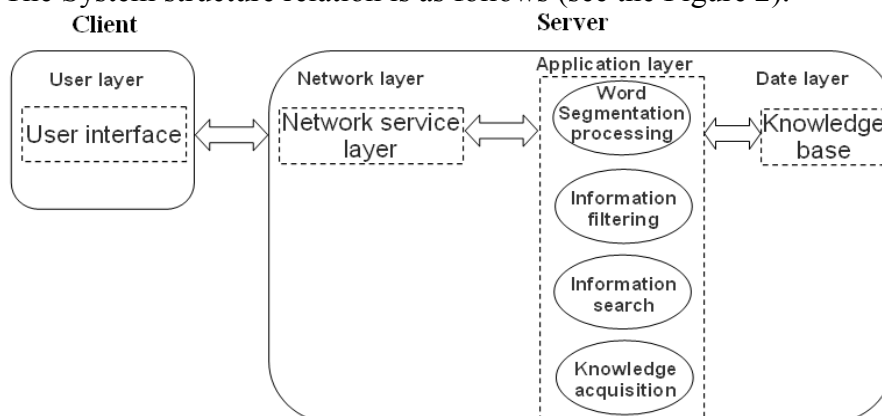


Fig. 2 System structure relation graph

The Specific Plan for the Question Answer System for Teaching

In this essay, the original algorithm of the Chinese word segmentation algorithm and the similarity algorithm is improved to meet the need of intelligent and quick searching. In terms of the mobile and embedded technology, the mode of Internet question-answering system is imitated and the high-performance of the intelligent terminal equipment is fully utilized to improve the intelligence of the system.

The major framework of the question-answering system is as follows:

Asking of the user: all the questions to be solved will be input into the knowledge base,

The analysis of the questions: the input statements of questions will be processed by word segmentation,

The filter of questions: all the questions will be classified by the interrogative words,

The algorithm of statement similarity: the similarity algorithm will be made based on the statement similarity,

The obtainment of the answer: the best answer will be selected by the matching process.

The Key Technologies for ISIC-CDIO Question Answer System for Teaching

Improving the Word Segmentation Algorithm Based on the Matching of Character Strings

The maximum word length in the knowledge base is usually longer than the word length segmented out. To increase the efficiency of segmentation and avoid the ambiguity of word segmentation, this essay improves the forward maximum match algorithm.

The question statement will be searched in the knowledge base. If it is not in the base, word segmentation will be done once more and the search will be done again, if the question statement is in the base, whether the segmented word is a word or not will be judged and then the maximum length of the Chinese character will be obtained from the lower level node of the segmented word mentioned above, when the maximum length mentioned above is zero, the search will be over. If the maximum length is not zero, character strings will be selected in increasing progression from the third character in the sentence, and whether there is any match (complete match is not required) of this character string in the third level will be decided, if there is a match, when the word segmentation is finished, it will return to the latest match of the character string and will make up a new word with the previous rejected character string.

Improving the Similarity Algorithm

In terms of the statement similarity (mainly referring to the Chinese), this essay will decide the final similarity by combining the three approaches of statement similarity algorithm (the morphological similarity, the statement length similarity and the word order similarity). Among the three approaches, the morphological similarity is considered as the major factor, and the statement length similarity and the word order similarity are secondary factors.

a) The Morphological Similarity

L represents a Chinese statement, which can be a sentence or a word. Len (L) represents the number of the individual Chinese character in L, and SameWord(A,B) represents the number of the same Chinese characters in statement A and statement B. Then the morphological similarity of statement A and statement B can be represented as WordSim (A, B):

$$WordSim(A, B) = \frac{SameWord(A, B)}{Max(Len(A), Len(B))}. \quad (1)$$

It is easy to conclude: $WordSim(A, B) \in [0, 1]$, the more the same Chinese characters are in statement A and statement B, the more similar A and B are.

b) The Statement Length Similarity

Len (A), Len (B) represents the number of the individual Chinese character in statement A and statement B. The statement length similarity of A and B can be represented as LengthSame (A, B):

$$LengthSame(A, B) = 1 - \frac{Abs(Len(A) - Len(B))}{Len(A) + Len(B)} \quad (2)$$

It is easy to conclude: $LengthSame(A, B) \in [0, 1]$, the more the same statement length are in statement A and statement B, the more similar A and B are.

c) The Word Order Similarity

Only (A, B) represents the set of the individual Chinese character which appears only once in statement A and statement B. Order1(A,B) represents a vector set, storing the sequence number of Only(A,B)'s individual Chinese character's position in statement A. Order2 (A, B) also represents a vector set, where the sequence number of Order1(A,B) will be stored according to the corresponding Chinese characters' sequence in B. Reorder2(A,B) represents the reverse sequence arrangement of all the value in Order2(A,B). The word order similarity of statement A and B can be represented as OrderSame (A, B):

$$OrderSame(A, B) = \begin{cases} 1 - \frac{ReOrder2(A, B)}{|Only(A, B)| - 1} & |Only(A, B)| > 0 \\ 1 & |Only(A, B)| = 1 \\ 0 & |Only(A, B)| = 0 \end{cases} \quad (3)$$

It is easy to conclude: $OrderSame(A, B) \in [0, 1]$

With combination of the above three parts, the final similarity of statement A and statement B can be concluded as:

$$Same(A, B) = \alpha \times WordSame(A, B) + \beta \times LengthSame(A, B) + \gamma \times OrderSame(S, B). \quad (4)$$

Therein $\alpha + \beta + \gamma = 1$, the value of α , β and γ should be given complying with the principle that the morphological similarity plays the major role while the statement length similarity and the word order similarity plays the supporting role. When the value of α , β and γ is confirmed, substitute the formula with their value and then the value of Same(A,B) will be calculated as a reference value, if the similarity of two statements is higher than this value, the two statements are decided as similarity statements.

Experimental Evidence

Experiment Environment

- 1) OS: WINDOWS 2000 Server operating system.
- 2) Web Server: WINDOWS 2000 Server IIS server.
- 3) Database Server: SOL Server2000 database server.
- 4) Client: Android intelligent mobile phone platform.

Experimental Result

The testing approach is to set a certain number of questions. The search will be done several times, the number of questions will be different in each search and the results will be obtained in each search accordingly. During the testing, the decision with successful matching of the question and the final return to the answer is right, while the decision with failing matching of the question is wrong.

The experimental results are shown in Table 1.

Table 1. The analysis of the experiment result

Question number	The number of correct answers	Degree of accuracy
20	13	0.65
40	29	0.73
60	40	0.67
80	62	0.78
100	68	0.68
(Average)60	(Average)42	(Average)0.70

The analysis of the experiment result: the average passing rate of the question is 0.70, which is within the expected range. If the system can perfect the resource base through constant practicing process, the error probability of the matching result will be reduced greatly.

Conclusion

Based on the CDIO education mode, this essay proposes the ISIC-CDIO education mode which is suitable for the talent cultivation in China's colleges and universities. The focus of this study is realizing the question-answering system for teaching under the ISIC-CDIO education mode and improving the matching algorithm, thus improving the search efficiency and the success rate. Finally, the question-answering experiment based on the Android system was done to test and verify that this approach has obvious advantages in proactively promoting the coordination of production, learning, research and teaching in colleges and universities, which will also improve colleges' capabilities of combining the scientific research and practice, and promote their cultivation of comprehensive talents with ISIC-CDIO quality.

Acknowledgment

The authors gratefully acknowledge the funding of this study by The Ministry of Education humanities social sciences studies "Research on Engineering Technology Talent Cultivation" special task "The Application of Information Technology in Talent of Engineering Technology Cultivation"(10JDGC021) and the Jilin Province Department of Education research project (2012366).

References

- [1] WANG Zhongguo, WU Min, Similarity Checking Algorithm in Item Bank Based Oil Vector Space Model, *Computer Systems & Applications*, (2010), (03):3-7.
- [2] Han Min, Tang Changjie, Duan Lei, et al. TF-IDF similarity based method for tag clustering, *Journal of Frontiers of Computer Science and Technology*, (2010), 4(3):240-246.
- [3] Cattuto C, Loreto V, Pietronero L, Semiotic dynamics and collaborative tagging[J], *Proceedings of the National Academy of Sciences*, (2007), 104(5):1461-1464.
- [4] Qian Ming-Yu, Research of Question Answering System Based on Mobile Technology[D], Northeast Normal University, 2010, (4):17-19.
- [5] XIA Bang-Gui, A Mobile Learning System Based on Android *Journal of Xihua University • Natural Science*, 2011, Vol 30, No.5: 81-84.

Research of Decision Support Technologies in Multi-Dimensional Data Environment

Qiu Ze-guo

Haerbin University of Commerce, Dongbei University of Finance and Economics

Superteacher73@126.com

Keywords: Multidimensional Data; Decision Support, Optimization

Abstract. In this paper, further research has been done on the relevant decision support technology in the multi-dimensional data environment, including decision support system, the environment of multi-dimensional data model, multi-dimensional data combination problems based on data warehouse optimization problems and overall structure, etc.

Introduction

In this paper numerical calculation and experimental verification using a combination of methods, freezing time of was studied. In the current era, the two remarkable characteristics is the integration of the world economy and the rapid development of informational technology which takes the computer as a representative. With the continuous innovation in the informational technology and the managerial conception, enterprises' managerial ways, methods and tools have brought tremendous changes, making the enterprise management efficiency and utility greatly improved. At the end of the 1960S and the early 70S, the Management Information System (MIS) makes the enterprise Information obtain systematic development and utilization ,and helps raise the enterprise management to a new level. But MIS can only helps the enterprise managers with simple organization and administration for the information, rather than deplore the implicit knowledge within information, nor meet the half structured and unstructured [1] decision problems in some of enterprises. Simon, the famous American management expert, pointed out that "management is the decision" [2].

Therefore, people are seeking for the new method which can solve the problem effectively.

In the mid 1970 s, Keen and Scott Morton first proposed the "Decision Support System (DSS)" conception [3], marking the research and application of decision-making supported by computer and information has entered a new stage, and formed a new subject--- Decision Support System. From then on, the DSS obtained a rapid development and utilization.

Basic system Structure of the DSS

DSS's "three parts" structure was proposed by Sprague in 1980 [5].The system architecture of this DSS consists of three parts, namely, the data subsystem, model subsystem and human-computer interaction systems. Among them, the data subsystem is responsible for storage and management of DSS use a variety of data to support the DSS data manipulation, and to achieve the mutual conversion between different data sources; model subsystem to store the pre-decision-making model, support the model of management and analysis operations; human-computer interaction subsystem DSS and the user interface interface is responsible for receiving user requests, and provide users with decision support results. Show in Fig. 1.

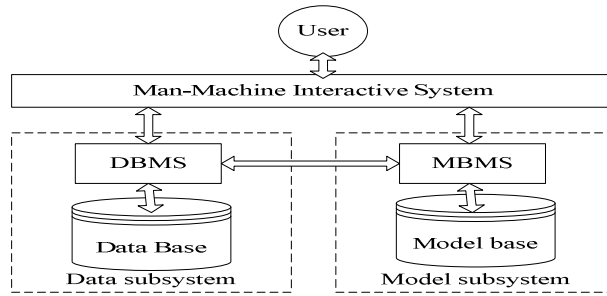


Fig. 1 DSS three parts structure

Bonczek raised in 1981, the DSS system "structure [6]. Shown in Fig. 1, this structure consists of language subsystems (Language subsystem, LS), the processing subsystem (Problem Processing subsystem, PPS), and knowledge subsystem (Knowledge subsystem, KS) three subsystems. The system structure will be unified as all data, models, methods, and knowledge so that knowledge. In contrast, the "knowledge" refers to a broad knowledge. The structure contains a "knowledge system", so that the artificial intelligence technology to be used in DSS. This makes a lot of DSS researchers use this decision support system structure.

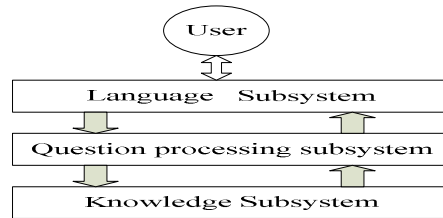


Fig. 2 DSS three system structure

With the help of the computer's powerful computing capability and people's flexibility to analyze and judge the ability of interactive collaboration, DDS provides a strong support for people with semi-structured and unstructured decision-making problems. But the key of DSS is applied to model the quantitative decision making, cannot undertake qualitative analysis and decision. Expert system (Expert System, ES) in the field of artificial intelligence has obtained the rapid development. Expert system is the use of experts' knowledge to deduce in computer , reaching the ability that experts have to solve the problem. Expert system aided decision-making mode belongs to qualitative analysis, DSS aided decision of the quantitative analysis, put the two together, the effect will be improved greatly on aided decision. This ES and DSS are combined to form a system called intelligent decision support system (IDSS). Show in Fig. 2.

The Model Constitution of the Multi-Dimensional Database

The DW based strategic supporting system came into being with the emergency of the database and OLAP. On account of the data dig and OLAP, the DDS's strategic analysis ability is highly developed which offer a new way of strategic supporting. The database collects enormous of historic data that was stored in multi-dimensional process.[7] It is specified used for strategic analysis. In the traditional DDS system, the source of data required by the model usually comes from database. As the DW was integrated into the DDS, it provides new sources for the model operation. However, some relevant series of problems arise, such as the input and output of the model, the description of multi-dimensional data port and the model constitution under the circumstance of multi-dimensional data, etc.

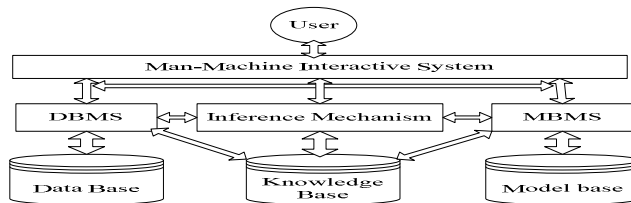


Fig. 3 Intelligent Decision Support Structure

As for the given multi-dimensional data inquiry, the model constitution which through the search of field knowledge and the data sources matching to the inquiry firstly searching whether there is matching data or whether it can meet the inquiry through multiple multi-dimensional data computational operation. Otherwise, [8] it will search for the output multi-dimensional data port which is matching with the model and continues to searching the output data which is satisfied with the model until the multi-dimensional data inquiry is fulfilled. Once obtained the input data, the model will be put into operation to get the output data. Model portfolio and operation procedures of this algorithm are shown in the diagram 2-1.

The OLAP can make a multi-dimensional analysis and handle the data in the database. The data model structures the OLAP application is called Multi-dimensional Database (MDDDB). It is also known as Data Cube. [9] That means the OLAP system is not make analysis in the DW's fact and dimension chart directly. Instead, making it the data sources as the structure of Data Cube and finishing OLAP analysis in the Data Cube. Common measures as follows:

Establish the quick executive statement. The pre-computing techniques are the most effective way to improve the inquiry efficiency. This technique chooses the optimal set of materialized views under the limitation of time and space to improve the inquiry response efficiency.

Reduce the differences between the SQL and Data Cube port can improve the data calculating efficiency. We can handle it by making the detailed data in the Data Cube and relational tables more similar.

Increase the data redundancy. It is opposite to the design principles of OLAP system which increase the data redundancy to avoid overusing the connections among data collection. In turn, the operation efficiency is improved.

The optimization of area and sector inquiries. They are the most common and important inquiries which can be considered as pre-computing techniques in the OLAP. The inquiry response time is shortening by changing data in the database.

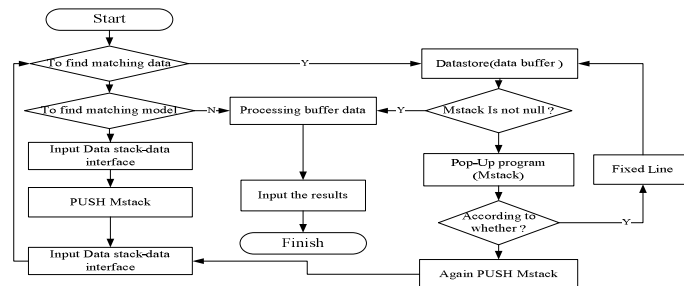


Fig. 4 Model portfolio and operation procedures of this algorithm

Summary

In this paper, I make a deep study in the relevant decision support technology under the circumstance of multi-dimensional. The main work includes the study to the cube environment model portfolio, optimization of part of the multi-dimensional data cube query technology. Model constitution has been a problem in the field of decision supporting systems. [10] In the new environment of multi-dimensional data, this thesis presents a run of the model combination. It proves to have strong practical and application value for meeting the needs of the practical problems.

Acknowledgment

The Project of HeiLongJiang Province's Education Department (The Reach for High School Results Query System Based on WAP) roject code: 11551106

References

- [1] Wenwei Chen. decision support system (the second edition) Tsinghua University, BeiJing: 2000
- [2] Herbert Simon etc. The New Science Of Management Decision. China Social Sciences Press. BeiJing: 1982
- [3] Keen. P. G, Scott Morton. Decision Support Systems: An Organizational Perspective. Addison-Wesley. 1978
- [4] R.H Sprague. A Framework for the Development of Decision Support Systems. MIS Quarterly. 1981. pp1-26
- [5] R. H. Bonczek, C. W. Holsapple and A. B. Winston. Foundation of Decision Support Systems. Academic. 1981
- [6] Belew. R. Representation for Decision Support Systems Evolutionary Decision Support Systems, New York: North-holland, 1985
- [7] Qingda Yao. A new generation of decision support systems. Computer Science, 1988 (2)
- [8] Lin Jing. Meng Bo, "The study on management and coordination agent in gds" Computer Application and Software, Beijing, vol. 12, pp. 11-13, DEC 2004
- [9] Sage A P. An overview of Group and organizational Decision Support Systems. IEEE Control Systems Magazine, vol. 5, PP. 9-33, 1991
- [10] Guo Chaozhen, "Research and Implementation of Communication Component for Group Decision Support System" Journal of software . vol. 3, pp. Nov 2000.

Research of Mine Wireless Video Monitoring Sub-Station Based on WIFI

Wenli Lei, Xincheng Ren, Yanhu Fan

College of Physic and Electronic Information, Yan'an University, Yan'an 716000, China

lei.wenli@163.com

Keywords: WIFI, Mine, Wireless Video Monitoring, Cloud Computing

Abstract. With the development of country's attention to safe production of mine, electronic technology and network technology begin to get widespread application in the mine exploration and monitoring. It has been brought forward a new method of mine wireless video monitoring sub-station based on WIFI wireless network technology, it send the collected video data to the ground monitoring equipment through wireless video capture terminals and wireless access point AP which has been installing in the mine tunnel, with a router connected to the cloud computing platform that enables remote monitoring terminal access, and it can intelligently analyze, search, data mining and other complex calculations by using of super-computing ability of cloud computing , in order to achieve the monitoring of mine production site.

Introduction

Coal is an important strategic resource. Over the years, it become important issues that the development of coal enterprises is restricted by mine safety production , which due to special resources and occurrence conditions, poor working conditions and other factors in the coal mine industry. Improving the level of mine safety production on digital, network, information, ensuring the staff and mine production safety, is an inherent requirement of the health and sustainable development of China's coal industry, also is a major issue for the development of China's digital coal mines [1].

The same time, it becomes possible to achieve mine safety video monitoring for the development of electronic technology and network technology. It has been brought forward a new method of mine wireless video monitoring sub-station based on WIFI wireless network technology, it send the collected video data to the ground monitoring equipment through wireless video capture terminals and wireless access point AP which has been installing in the mine tunnel, with a router connected to the cloud computing platform that enables remote monitoring terminal access, and it can intelligently analyze, search, data mining and other complex calculations by using of super-computing ability of cloud computing , in order to achieve the monitoring of mine production site. This method avoids the problem of laying cable in coal mine complex terrain, and terminal is installed simply, meanwhile, the monitoring staff can remotely view live real-time image data through cloud computing platform.

Model of Coal Mine Wireless Video Monitoring System

Coal mine wireless video monitoring system is consisted of the ground monitoring part and underground video monitoring sub-station. Ground monitoring part include router, cloud computing platform, switch, ground monitoring terminal, remote monitoring terminal and other components. Switch and ground monitoring terminal composed of local monitoring section, which connected to the cloud computing platform through a router, and can access through the remote monitoring terminal. Underground video monitoring sub-stations include wireless access point AP and underground wireless monitoring terminal with a camera. The entire system is shown in Fig.1.

Hardware Design of Underground Wireless Video Monitoring Sub-Station

The design of mine wireless video monitoring sub-station is mainly the design of underground wireless video monitoring terminal. The main function of wireless video monitoring terminal is image data acquisition and wireless data transmission, and it has high requirement of image processing

capability, powerful data processing capability and rich interfaces for processor. At the same time, intrinsically safe design requirements is considered in the design for wireless video monitoring terminal work in the coal mine, systems should has low power consumption. By comparing different processor, the final choice is the Samsung S3C2410 processor which has a good support for embedded operating systems, the operating frequency up to 203MHz, has the MMU (memory management unit), ARM9-based system architecture. The S3C2410 processor can run embedded Linux, WINCE, VXWORKS operating system, etc, while more complex operations and processing.

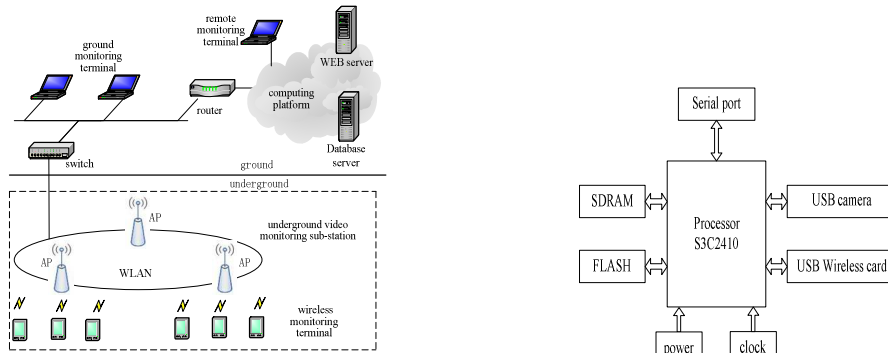


Fig. 1 The model of coal mine wireless video monitoring system Fig. 2 The diagram of Wireless video monitoring terminal hardware composition

This terminal is required for wireless networking capabilities, so the wireless card need support the IEEE 802.11 protocol, and supports the Linux operating system. After comparison, the TP-LINK's TL-WN321G+ 54M Wireless USB Adapter which work in the ISM band 2.4GHz, transmission distance about 100 meters, is final selected. TL-WN321G+ which built-in omni-directional smart antenna can adapt to different working environments, allowing users to easily access the wireless network, supporting wireless roaming; easily connecting with other 11b, 11g wireless devices; supporting 64/128 WEP data encryption and WPA/WPA-PSK, WPA2/WPA2-PSK of security mechanisms; providing centralized control type (Infrastructure) and peer-to-peer (Ad-Hoc) two operating modes; providing easy configuration, monitoring procedures. The camera used for video image capture is the mesh V2000 which master chip is ov511; serial design using the RS232 standard, mainly used for debugging and downloading. Fig.2 shows the entire wireless video monitoring terminal hardware.

Software Design of Underground Wireless Video Monitoring Sub-Station

The software design of underground wireless video monitoring sub-station based on WIFI technology including the transplantation of the operating system, driver development of WIFI wireless network card, the transplantation of the SIP protocol stack, application development four parts.

The Transplantation of the Operating System

The embedded Linux is selected as the operating system of underground wireless video monitoring sub-station based on WIFI technology. According to embedded hardware configuration of the terminal, embedded Linux cuts and modifies the corresponding part of Linux operating system, and after cross-compiling, can be run in the embedded terminal system on a micro Linux operating system. Embedded Linux is characterized by: open-source resources; royalties for free; technical support by free software developers from around the world; has a good support for network characteristics, performance; related software are easy to transplant, to reduce the development cycle, the stability of good, safe; many applications support. The transplantation of an embedded Linux operating system includes the establishment of the startup code, the transplantation of the Linux kernel and the establishment of file system three parts.

The more mature U-boot is selected as the boot loader (Bootloader) for Underground wireless video monitoring sub-station. It is easy and convenient, providing a comprehensive set of commands, supporting for ARM processors.

The Selection version of embedded Linux kernel is 2.4.18 kernel, add migration package of S3C2410 processor to the system source, and select the configuration for supporting the serial port and USB port under the cross-compiler environment, then compile, the process of the specific configuration is as follows.

```
$> make menuconfig //configure the kernel
$> make dep // Establish dependencies
$> make zImage //compile
```

After Cross compiling, the resulting binary kernel file zImage is created. Then compiled kernel file zImage is written in FLASH through the U-boot console.

The file system cramfs and yaffs are used by the underground wireless video monitoring sub-station in the design, the cramfs is used as the operating system's file system, and the cramfs file system is used as the user data file system. File systems is consisted of modules, libraries and applications, built on top of the embedded Linux kernel. In the kernel compile time, increase supporting for the file system Cramfs and YAFFS is needed.

The Transplantation of the SIP Protocol Stack

The SIP protocol is a client/server protocol, used to initiate and manage the session between users. SIP protocol as application layer signaling protocol has a good performance to meet the goal of establishing a manageable, efficient, expanding business platform in the next-generation networks. Osip and eXosip are used to achieve the SIP protocol in the underground wireless video monitoring sub-station based on WIFI technology. Compared with H.323, SIP protocol is independent of transport layer and the media, simple, extensibility, and close to application. Osip is a free open-source SIP stack, in accordance with standards of RFC3261(SIP) and RFC 2327(SDP), prepared by the use of standard C, the structure of Osip is simple and compact, providing API to resolve the SIP / SDP message and state machine to resolve transaction processing, does not providing high-level SIP session control API [2]. Osip protocol stack is consisted of the state machine module, the parser module and tool module.

eXosip is an extended protocol set of Osip2 [3], package a part of Osip2 protocol stack which make it easier to use. eXosip receive and send the underlying SIP protocol through UDP socket, call Osip2 transaction processing functions by using a timed round robin, increase the timeout handling of various types of affairs to avoid an endless loop, use jevent message pipeline to record program event of the underlying layer. Program can view logged events by reading information of jevent message pipeline, handle related events. Application drives the transaction state machine through the message pipeline, and the external SIP signaling and feedback of caller program is passed to the application.

Application Development

Application development of underground wireless video monitoring sub-station based on WIFI technology is achieved by programming under the Linux operating system. Under the Linux operating system, all Linux peripherals are considered as a device file. By calling the interface between the kernel and applications, video capture device is operated. the device file /dev/video is mainly used for video capture programming in application program of underground wireless video monitoring sub-station, video capture process as shown in fig.3. The main functions include [4]:

Camera_open (): statement a video_device type of device file and open the video device files by calling open () function.

Camera_get_capability (): store the device file information that Ioctl() function has obtained to video_capability structure.

Camera_get_picture (): store the video related information that Ioctl() function has obtained to video_picture structure.

Camera_close (): Used to close the device file

Camera_grab_image (): capture image data by the way of mmap, and map the device file /dev/video0 into memory.

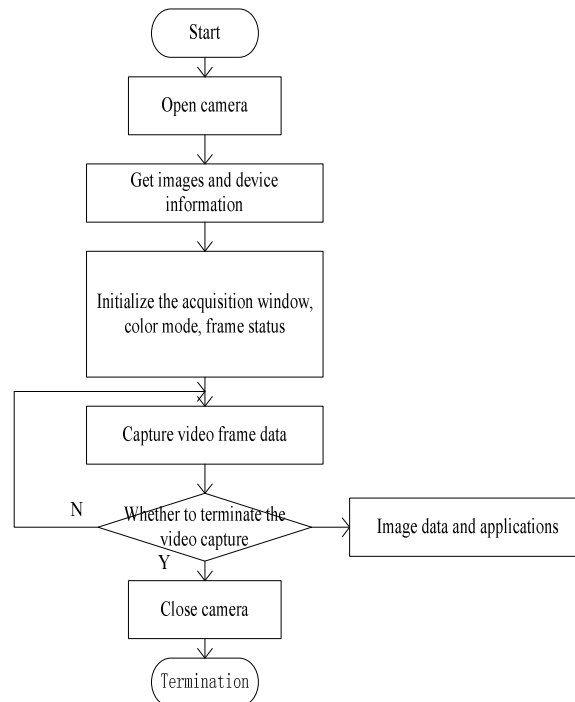


Fig. 3 Diagram of video capture process under the Linux operating system

The Application of the Cloud Computing Platform

For a large number of front-end video capture device are used in underground wireless video monitoring sub-station system, which will generate vast amounts of video data after the device are running, but also intelligent analysis, search, data mining and other complex calculations to vast amounts of data, so it is need for powerful computing and information storage capability. Since the resource requirements of a variety of computing services is dynamic, so calculation mode of "cloud computing" is suitable for the ground monitoring, in this mode it is convenient to use configurable and shared computing resources(network, servers, storage, applications and services etc.), accessing on-demand. The main idea of cloud computing is unified scheduling and management to resource pool formed by virtualing basic resources, to provide users three levels of service from bottom to top, including Infrastructure as a Service (IaaS), Platform as a Service (PaaS) and software as a Service (SaaS). Each layer can provide service to the higher level, and also can provide users with information services. Video surveillance as a service (VSaaS) or cloud computing-based video surveillance technology is by means of cloud computing ideas and methods^[5], take advantage of cloud computing architecture to provide users with a extensible, flexible, central integration of video storage, video access, video management and services. It can be predicted that will has broad application prospects.

Conclusion

It has been brought forward a new method of mine wireless video monitoring sub-station based on WIFI wireless network technology, it send the collected video data to the ground monitoring equipment through wireless video capture terminals and wireless access point AP which has been installing in the mine tunnel, with a router connected to the cloud computing platform that enables remote monitoring terminal access, and it can intelligently analyze, search, data mining and other complex calculations by using of super-computing ability of cloud computing , in order to achieve the monitoring of mine production site. The paper discusses in detail the realization of underground wireless video terminal. the realization of embedded Linux operating system migration on ARM9 platform, SIP protocol transplant, as well as image acquisition are explained in detail, the design is complete the actual application requirements.

Acknowledgements

The authors acknowledge with thanks the financial support by Scientific Research Program Funded by Shaanxi Provincial Education Department (Program No. 2010JK908).

References

- [1] Zhao Anxin (2006) The Research and Application of Digital Mine and Key Technologies. Xi'an University of Science and Technology Page 1
- [2] Wang Shuqi, Sun Yi. (2007) Design Of WiFi Terminal Based on S3C2410 in Mine Tunnel. Microcomputer Information 4-2 :186-188
- [3] MOZARD A (2006) oSIP User Manual[EB / OL]. <http://osip.atosc.org>.
- [4] Lei Wenli, Yang Yanning, Zhang Shuli, Sun Qiling (2010) Design and Realization of oil well wireless monitoring system based on ARM. Electrotechnical Application 2:72 -74
- [5] Wang Junxiou (2011) Application research of video monitoring system based on cloud computing architecture. China Security 8:93 -96

Preconditioned Symmetric Linear BCG Method for Solving FEM Electromagnetism Problems

Li Yuehui^{1, a}

¹ School of Mathematics and Computer Engineering, Xihua University,
Chengdu 610039, People's Republic of China

^aliyuehui899@163.com

Keywords: Preconditioning Technique, Shifted-Laplace, Sparse Approximate Inverse, Electromagnetism

Abstract. A new preconditioning technique for solving large linear systems arising from edge-based finite element method (FEM) analysis of three-dimensional (3-D) electromagnetic problems is presented. This method is achieved by applying a shifted-Laplace operator scheme and sparse approximate inverse to symmetric linear BCG (LBCG). The main purpose is to generate a more robust and efficient preconditioner. Numerical results on several electromagnetic problems show that, by comparing with other conventional preconditioning techniques, this technique is more efficient and robust, and can greatly reduce the simulation time.

Introduction

The edge-based finite-element method (FEM) has been widely used to analyze 3-D electromagnetic problems, which often yields a large sparse complex symmetric and highly indefinite linear system of equations. Krylov subspace iterative methods are popularly applied for solving this kind of systems, in this letter, we employ the symmetric LBCG method [1], which is specially designed for complex symmetric and indefinite system, hence can avoid unnecessary computational costs and memory needs. As is well known, the FEM coefficient matrix usually has bad spectrum property, it's necessary to use preconditioning techniques to improve spectral properties of the coefficient matrix and accelerate convergence of iterative solvers.

As one of the factorized sparse approximate inverses (SAI) preconditioning technique, AINV [2] is useful. Although AINV preconditioner is quite flexible and powerful, special care must be taken in order to avoid pivots breakdowns during the factorization process. In this letter, we propose a more effective preconditioning method, by adding robustness, i.e., by combining shifted-Laplace operator scheme [3] and AINV with pivots compensation strategy, to construct a more stable and efficient preconditioner. Numerical experiments demonstrate that the proposed preconditioner is powerful for solving the 3-D electromagnetic problems.

Theory

We consider solving edge FEM discretization the Helmholtz boundary value problem:

$$\nabla \times (\mu_r^{-1} \nabla \times \bar{E}(r)) - k_0^2 \varepsilon_r \bar{E}(r) = -jk_0 Z_0 \bar{J}(r) \quad (1)$$

With boundary condition given by $\hat{n} \times \bar{E} = 0$. Where \bar{E} is electric field, $\bar{J}(r)$ is electric current source, k_0 and Z_0 are wave number and wave impedance in the free space, ε_r and μ_r are the relative permittivity and permeability respectively. Which result in a large symmetric (non-Hermitian) and ill-conditioned linear system:

$$\mathbf{Kx} = \mathbf{b}, \quad \text{with } \mathbf{K} \in \mathbb{C}^{n \times n}, \quad \mathbf{b}, \mathbf{x} \in \mathbb{C}^n \quad (2)$$

In order to attain efficiency, an appropriate preconditioning matrix \mathbf{M} should be incorporated, which transforms the original system into another equivalent one

$$\mathbf{MKx} = \mathbf{Mb}, \quad \text{with } \mathbf{M} \in \mathbb{C}^{n \times n} \tag{3}$$

That has better spectrum property. In this letter, we construct an effective RAINV preconditioner \mathbf{M} in two steps: first constructing $\hat{\mathbf{K}} \approx \mathbf{K}$ with shifted-Laplace operator scheme and then, computing $\mathbf{M} \approx \hat{\mathbf{K}}^{-1}$ by modified AINV algorithm with pivots compensation strategy. The details are described as follows.

From the FEM discretization process we can see that the coefficient matrix \mathbf{K} is the concise form for

$$\mathbf{K} = \mathbf{R} - \mathbf{Q}, \quad (\mathbf{R}, \mathbf{Q} \in \mathbb{C}^{n \times n}) \tag{4}$$

Where \mathbf{R} relates to the item $\nabla \times (\mu_r^{-1} \nabla \times \bar{E}(r))$ and \mathbf{Q} , the $k_0^2 \epsilon_r \bar{E}(r)$. Most of the conventional preconditioners are constructed based on \mathbf{K} , however it's highly indefinite since \mathbf{R} is positive semidefinite and \mathbf{Q} , positive definite. Inspired by the idea of preconditioning based on purely real and imaginary shifted-Laplace operator [4], a more stable preconditioner can be constructed based on the advanced complex remedy case:

$$\hat{\mathbf{K}} = \mathbf{R} - \xi \mathbf{Q}, \quad \text{where } \xi = \xi_1 - j\xi_2, \quad \xi_1, \xi_2 \in \mathbb{R}. \tag{5}$$

By tuning parameter ξ , spectrum property of $\hat{\mathbf{K}}$ can be better than that of \mathbf{K} , thus the inverse computation based on $\hat{\mathbf{K}}$ is expected to be more robust. In this letter, we employ the following modified AINV algorithm, derived from the basic one, to compute preconditioner \mathbf{M} ($\approx \hat{\mathbf{K}}^{-1}$).

The following basic AINV algorithm builds the preconditioner \mathbf{M} of the form $M = \mathbf{ZD}^{-1}\mathbf{Z}^T \approx \hat{\mathbf{K}}^{-1}$. Where \mathbf{Z} is a unit upper triangular matrix and \mathbf{D} is diagonal:

Algorithm 1.

- 1: Let $\mathbf{z}_i^{(0)} = \mathbf{e}_i \quad (1 \leq i \leq n)$
 - 2: for $i = 1, 2, \dots, n-1$ do
 - 3: for $j = i, i+1, \dots, n$ do
 - 4: $p_j^{(i-1)} := \hat{\mathbf{k}}_i^T \mathbf{z}_j^{(i-1)}$
 - 5: end do
 - 6: for $j = i+1, \dots, n$ do
 - 7: $\mathbf{z}_j^{(i)} := \mathbf{z}_j^{(i-1)} - (p_j^{(i-1)} / p_i^{(i-1)}) \mathbf{z}_i^{(i-1)}$
 - 8: $z_j(t) = 0 \quad (1 \leq t \leq n) \quad \text{for } |z_j(t)| < \tau \|\mathbf{z}_j^{(i)}\|_2$
 - 9: end do
 - 10: end do
 - 11: $p_n^{(i-1)} := \hat{\mathbf{k}}_n^T \mathbf{z}_n^{(i-1)}$
 - 12: let $\mathbf{z}_i := \mathbf{z}_i^{(i-1)}$ and $p_i := p_i^{(i-1)}$, for $1 \leq i \leq n$. return
- $\mathbf{Z} = [\mathbf{z}_1, \mathbf{z}_2, \dots, \mathbf{z}_n]$ and $\mathbf{D} = \text{diag}(p_1, p_2, \dots, p_n)$.

Where $\hat{\mathbf{k}}_i^T$ denote the i th row of $\hat{\mathbf{k}}$ and \mathbf{e}_i , the i th unit basis vector. Step 8 executes the dropping strategy to keep low memory needs, where τ is a positive scaling factor. The pivots p_i 's are computed at step 4 (when $I=j$). In the exact A-orthogonalization process, $p_i = \hat{\mathbf{k}}_i^T \mathbf{z}_i = \mathbf{z}_i^T \hat{\mathbf{K}} \mathbf{z}_i$ (for brevity, we omit the $(i-1)$ superscripts). However, because of dropping and the resulting loss in the \mathbf{z} -vectors, it becomes into $p_i = \hat{\mathbf{k}}_i^T \mathbf{z}_i \ll \mathbf{z}_i^T \hat{\mathbf{K}} \mathbf{z}_i$. Breakdown can occur when there is a zero (usually exceedingly small) pivot p_i since step 7 cannot be carried out. In [2], a stabilized AINV algorithm for SPD matrix

was developed. However, matrix $\hat{\mathbf{K}}$ is indefinite even with shifted-Laplace operator strategy. To get an useful preconditioner, we present a revised AINV technique based on the basic AINV by applying dynamic pivots compensation strategy to exceedingly small pivots. That is, after step 4, if the following criterion is satisfied:

$$|\text{Re}(p_i^{(i-1)})| < \alpha \|\text{Re}(\mathbf{k}_i^T)\|, \quad \alpha \geq 0, \tag{6}$$

it is then recomputed by compensation formula: Where α is a factor used to adjust the compensation threshold. Considering that the spectrum property of the edge FEM coefficient matrix, we set the compensation criterion (4) based on the entries' real part values. Therefore, the exceedingly small pivots can be remedied dynamically; hence most of the breakdowns can be avoided successfully.

Consequently, a high quality robust preconditioner, we call it the new AINV (N-AINV) preconditioner, is generated. And the following numerical results show that it is robust and can dramatically accelerate the symmetric LBCG iteration convergence rate.

Numeric Experiments

To illustrate the performance of the proposed preconditioning symmetric LBCG method, in this section, two typical electromagnetic problems will be analyzed.

Firstly, we will analyze the seven-stage waveguide bandpass filter [5] by using edge FEM, and one block of perfectly matched layer (PML) is placed at the waveguide output to simulate the matched output load. As a result, a large scaled linear matrix equations is to be solved.

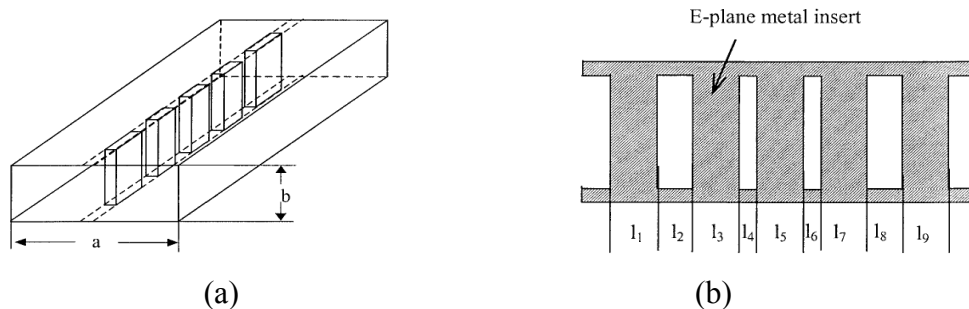


Fig. 1 Geometry of the waveguide bandpass filters (b). Geometry of metal inserts inside of the waveguide bandpass filter.

Several conventional preconditioning methods are also employed for comparison. The iteration process is terminated when the residual error is reduced by -60dB.

Fig. 2 shows the influence of both α and ξ on the iteration number of preconditioning symmetric LBCG methods, when $\tau=0.01$. It can be observed that the influence of ξ_1 on the performance of N-AINV preconditioners is larger than that of ξ_2 ; and the preconditioner based on complex shifted-Laplace operator outperform those based on purely real (when $\xi=(-1,0)$) and imaginary (when $\xi=(0,1)$) cases. It can also be found that the optimal α is in the range of 0.04 ~ 0.1. In this letter we take $\alpha=0.06$ and $\xi=(1, 0.5)$ as the default case.

Table 1 shows the CPU time (in seconds) for symmetric LBCG methods with N-AINV, ILU, SSOR preconditioners, and without preconditioner.

Table 1 CPU time of symmetric LBCG methods with or without preconditioning				
preconditioner	N-AINV	ILU	SSOR	none
CUP time (s)	85	578	182	861

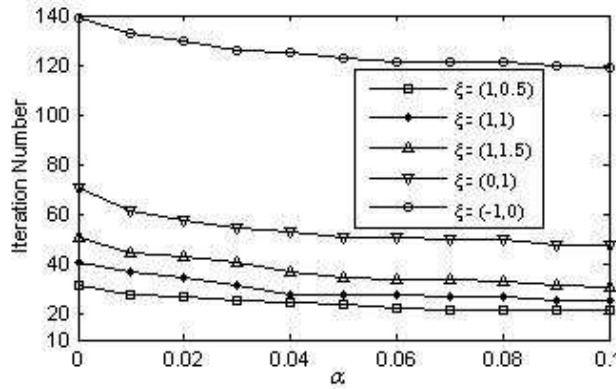


Fig. 2 Iteration number of preconditioned symmetric LBCG method with respect to different α and ξ .

It can be observed that a great improvement in the computational cost is achieved over standard symmetric LBCG and other conventional preconditioning methods.

The simulation results are given in Fig. 3 and are compared with those obtained from mode matching method, and a good agreement can be found between them, thus the accuracy of the FEM simulation methods is verified.

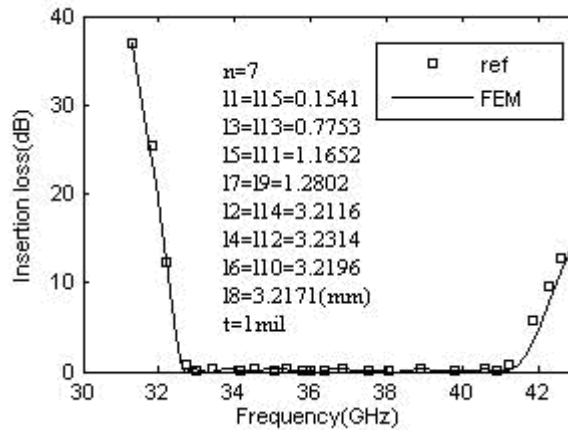


Fig. 3 Insertion loss of Ka-band band-pass filters with wide bandwidth.

Secondly, another example of RCS computation of a perfectly conducting cube [6] is investigated to analyze both the robustness and efficiency of the proposed method. The solution time for N-AINV, AINV, IC, SSOR preconditioned symmetric LBCG methods, symmetric LBCG without preconditioning are displayed in Table. 2.

Table 2 CPU time of symmetric LBCG methods with or without preconditioning

preconditioner	N-AINV	AINV	ILU	SSOR	none
CUP time (s)	246	—	—	373	1683

In this case, the conventional ILU and standard AINV process are failed due to pivots breakdowns (denoted with “—”). This result demonstrates the robustness and effectiveness of the proposed N-AINV preconditioner.

Conclusions

A novel preconditioning technique, which is a combination of shifted-Laplace operator and revised AINV schemes, is applied to symmetric LBCG method for efficiently solving large linear systems in FEM discretization of the electromagnetic problems. The proposed preconditioner, based on complex shifted-Laplace operator, is more advanced than those based on purely real or imaginary case; and the

modified AINV process with pivots compensation strategy is more stable than the basic AINV one, thus can yield robust and high quality preconditioners. Numerical results on two typical electromagnetic problems show that, the proposed N-AINV preconditioner is more robust for difficult problems where other conventional ones may break down; besides, it is very effective for solving large scaled electromagnetic problems and can reduce both the iteration number and the simulation time significantly.

This research is supported by Department of Science and Technology of Sichuan province (09ZC016, 10226020).

References

- [1] Y.H. Li, Z.P. Nie, and X.Y. Sun: *J. of Electromagn. Waves and Appl.*, Vol. 23 (2009), p. 2237
- [2] M. Benzi, M. Tuma, and J.K.Cullum: *SIAM J. Sci. Comput.* Vol. 22 (2000), p. 1318
- [3] Y.A. Erlangga, C.W. Oosterlee, C. Vuik : *SIAM J. Sci. Comput.*, Vol. 27 (2006), p. 1471
- [4] J. Zhu, X.W. Ping, R.S. Chen, Z.H. Fan, D.Z. Ding: *Microw. Opt. Technol. Lett.*, Vol 52 (2010), p. 1036
- [5] Y.C. Shih: *IEEE Trans. Microwave Theory Tech.*, Vol 32 (1984), p. 695
- [6] A. Chatterjee, J.M. Jin, J.L. Volakis: *IEEE Trans. Antennas Propag.*, Vol 41 (1993), p. 221

Spatial Analysis Model for Agricultural Land Grading Based on GIS

Weili Kou^{1, 2, a}, Shu Gan^{1, b}, Xiping Yuan¹

¹ Faculty of Land Resource Engineering, Kunming University of Science and Technology, Kunming, China

² School of Computer and Information, Southwest Forestry University Kunming, China

^akwl_eric@163.com; ^bn1480@qq.com

Keywords: Agricultural Land Grading, Spatial Analyses, Spatial Data; Arcgis Engine.

Abstract. To improve the efficiency of spatial analysis a novel model is proposed. Based on analyzing on workflows and techniques, the research mainly put emphasis on optimizing data organizations, enhancing data accessing efficiency, improving spatial researches, simplifying complex operations, and realizing automation. The model employed ArcGIS Engine, ArcSDE and ADO.net to design and implement its functions through programming under the Dot NET Framework. It has been applied to the grading work of agricultural lands in Lanping County, Yunnan Province, which shows that it can simplify operations, improve accuracy, and has features of good practicality and generality and should be applicable in other settings and over larger extents.

Introduction

Spatial analysis is used extensively in many areas, such as point pollution, spread pollution, and molecular spread analysis. To improve the efficiency of spatial analysis seems to be of greater importance. Qualities of agricultural lands are assessed and graded according to their natural and economic attributes, which is called agricultural land grading. Grading work of agricultural lands is very important and necessary in managements of agricultural lands. To do it successfully, the factor, revising, and sampling methods are used generally by researchers and administrators [1], and the first one is selected to build the model in the study. Factor method refers that people evaluates an agricultural land basing on a set of factors and its weights.

Traditionally, the professional software (MapGIS, or ArcGIS etc.) is employed for spatial analysis [2, 3], which is more efficient than manual operations [4, 5]. According to current literatures, professional software can be mainly used to realize functions such as spatial analysis, spatial data processing, plots, buffer analysis, spatial overlay operations, visualizations, automation and intelligence, etc. To improve the methods [6, 7], some scholars have used components of GIS (Super Map, Map Object, and Arc Engine) to establish special information systems for spatial analysis [8] which can simplify operations, save resources, and reduce finances.

However there are some deficiencies in current methods. Firstly, the efficiency of spatial searches and filtering techniques, that include distance calculations, bounding-box filters, sorting, and query parsing need to be further improved. Secondly, data formats vary in format, such as in shape, TIF, JPG. In traditional methods, the data are stored separately and loosely in relationships, which leads to chaos in data organizations and managements. Thirdly, data accessing efficiency and calculation accuracy should be improved. Fourthly, general software is too complex to operate for operators even if they are trained specially. In addition, spatial analysis models were not specially studied according to the literatures [6-8] that mainly focus on the integrated structures of geographic information systems. So a spatial model needs to be presented

Basic Techniques and Their Applications in the Model

The ArcGIS Engine Component The ArcGIS Engine is a collection of GIS components and developer resources that can be embedded, allowing developers to add dynamic mapping and GIS capabilities to existing applications or build new custom mapping applications. Developers use

ArcGIS Engine to deploy GIS data, maps, and GeoProcessing scripts in desktop or mobile applications using application programming interfaces (APIs) for COM, .NET, Java, and C++.

The ArcSDE Component ArcSDE is the technology that provides framework to support long transactions, which facilitates the versioned editing environment in multi-user GeoDatabase. The GeoDatabase is the primary data storage model for ArcGIS; It provides a single central location to access and manage spatial data.

Application Requirements of ArcGIS Engine and ArcSDE in the Model Interfaces of ArcGIS Engine are employed to enhance the efficiency of spatial searches, simplify operations, and improve accuracy, create buffers; calculate distances; find intersections, unions, or inverse intersections of shapes; Components of ArcSDE are used to manage spatial data store in a relational database management system (RDBMS). Applications can access spatial or attribute data through ArcSDE that can help to optimize data organizations, and is an access to a GeoDatabase.

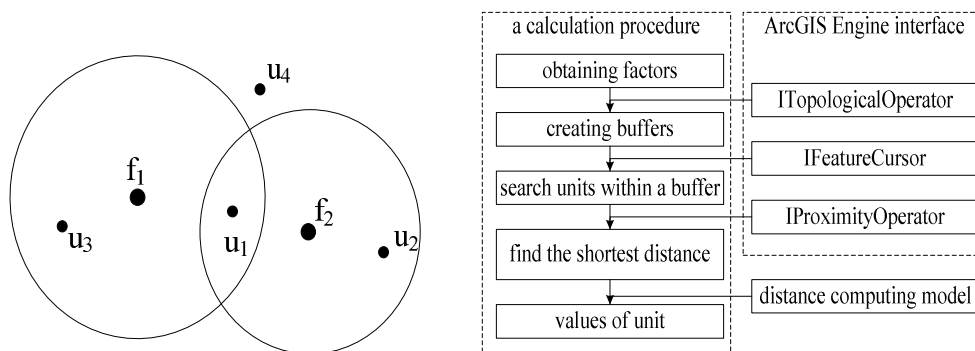
The Spatial Analysis Model

Calculations of Influence Scores Points, lines, and polygons are three basic types of spatial spread factors in spatial analysis. In grading work, points include residential points, central towns, road intersections etc; lines consist of rivers, and roads etc; polygons include reservoirs etc. Evaluation units within the influence scope of factors will get a score computed by distance decay model. According to the model, a shortest distance among all distances that calculates from an evaluation unit to the same level factors must be found out to get a score from the model. The shortest distance can be computed by the ITopologicalOperator interface provided by ArcGIS Engine in the new algorithm.

If an evaluation unit is influenced by factors of a same level, three cases are discussed. (1) An evaluation unit is beyond influence scopes of any factors, it gets a zero score (u_4 in Fig. 1). (2) An evaluation unit is with only one influence scope of factors, it gets only one influence score, and the score is its final score (u_2 and u_3 in Fig. 1). (3) An evaluation unit is within many influence scopes of factors, it gets several influence scores, and the highest score of all scores is its final score (u_1 in Fig. 1).

If an evaluation unit is influenced by factors of different levels, each level factor gives an influence score to an evaluation unit. The final score of the evaluation unit is a comprehensive score. The comprehensive process takes two steps: (1) the factor score of each level times its weight, (2) and then plus them together.

A Flow Diagram of the Model. According to the analysis above, a calculation flow is designed based on ArcGIS Engine (Fig. 2).



(u_1, u_2, u_3 and u_4 are four evaluation units; f_1 and f_2 are two factors)

Fig. 1 Factors influencing evaluation units Fig. 2 A flow diagram based on ArcGIS Engine

In the flow diagram, two models of distance decay calculation are ready to be used depend on different needs of an actual application. The one is linear distance decay model Eq. 1; another is exponential distance decay model Eq. 2.

$$F_i = M_i(1 - d_i / d) \tag{1}$$

$$F_i = M_i^{(1 - d_i / d)}, \quad (2)$$

where F_i is an influencing score of i -grade factors, M_i is a scale exponent of i -grade factors, d_i is a shortest distance between the factors of i -grade and the village committees, and d is an influence radius of a factor.

If an evaluation unit is influenced by factors of different levels, the comprehensive score is computed according to Eq. 3. Before using the equation, weight tables of factors must be established.

$$P = \sum_{i=1}^n W_i \cdot F_i, \quad (3)$$

where P is a final score of an evaluation unit, W_i is a weight of i -grade factors, and F_i is an influencing score of an evaluation unit influenced by i -grade factors.

Data Organizations. A GeoDatabase is established based on Microsoft SQL Server 2005 to store and manage spatial data that is organized with SHP format of ESRI and attribute data that is organized with tables in DBMS (Database Management System). ArcSDE of ESRI and ADO.NET of Microsoft are separately used to access spatial and attribute data to improve the processing efficiency of the model. If the data have same features, they are converted to one shapefile layer by ArcGIS 9.2, such as road layers, river layers, central town layers. Fig. 3 shows the data and their organization manners in the model.

Buffer Analyses. Buffer analyses are used to identifying areas surrounding geographic features. The process involves creating a buffer around existing geographic features and then identifying or selecting features according to whether they fall inside or outside the boundary of the buffer. For example, GIS is used to identify the locations of hazardous chemical storage sites in relation to health care facilities.

Buffer analysis is an important technique of spatial analysis. A buffer is created to search evaluation units within a certain scope of the factor. To improve the efficiency of the model a factor is as a buffer center and an influence radius is as a buffer radius, but in traditional method evaluation unit is as a buffer center. The buffer method of ITopologicalOperator interfaces of ArcGIS Engine can be employed to create buffer.

Filter Techniques of Spatial Searches. In traditional models, an evaluation unit is as the search center, then all factors are searched and each influence score is computed, even if an evaluation unit beyond effective influence scopes of any factors. When the amount of factors is very few and spatial distribution is dispersive, traditional spatial methods will waste tremendous computing resources.

To improve the search efficiency, the search center is changed from evaluation units to factors. If an evaluation unit is in the influence scopes of any factors, the processing module just is called otherwise a zero score is directly given. The model can sharply reduce the search times and workloads of grading work in practical applications.

Normalizing Processing To compare conveniently, the model normalizes the result data to [0,100] interval range according to the formula (4). To make the results better match with the realities, a const C is added to the equation to regulate results to a reasonable interval range.

$$y = 100(y_i - y_{\min}) / (y_{\max} - y_{\min}) + C, \quad (4)$$

where, y is a normalized final score, y_i is an i -th score, y_{\min} is the minimum score, y_{\max} is the maximum score, and C is a constant.

Key Algorithmes and Codes The algorithm is implemented in programming language C#, and interfaces of ArcGIS Engine are used in codes. The key algorithms and codes are as follows.

```
//Getting the features of the factor layer
IFeatureCursor pFeatureCursorFactor=getFeatureCursor(FactorLayerName)
//Reading the first factor feature
IFeature pFeatureFactor=pFeatureCursorFactor.NextFeature();
while (pFeatureFactor!=null)
```

```

{
//Creating buffer, dbTolerance as the buffer radius
IGeometry pGeometry=GetBuffer(oShape,dbTolerance);
//Reading evaluation units within buffer
IFeatureCursor pFeatureCursorUnit = getFeatureCursor(pGeometry);
//read the first evaluation unit
IFeature pFeatureUnit=pFeatureCursorUnit.NextFeature();
while (pFeatureUnit != null)
{
//Getting the shortest distance between unit and factor
dis_min=getMinDistance(pFeatureFactor,pFeatureUnit);
//Computing the influence score
mark=getMark(dis_min);
dao.exeSQL(sql_statement); //store the influencing score into database
//Reading next evaluation unit
pFeatureUnit=pFeatureCursorUnit.NextFeature();
}
//Reading next factor feature
pFeatureFactor=pFeatureCursorFactor.NextFeature();
}

```

Practical Applications and Results Analysis

Application Environments The model was used under the windows platform and an integrated development environment of Microsoft Visual Studio .NET with components provided by ArcGIS Engine. It was used to do grading work of agricultural lands of Lanping County, Yunnan Province. Some factors, which include roads, farm product markets, central towns, reservoirs, rivers, road intersections and etc., are selected for the practical application Layers of spatial spread factors were created using the software ArcGIS 9.2. The influence radiuses of spatial spread factors were established, and stored into related layers.

Research Data The results of the 2nd land inventory work in Yunnan Province is the main source of research data of the practical application, including maps of agricultural land units, land utilization index, distributions of rivers, roads and central towns, etc. Some data come from field investigation and indoor processing.

The parameters of scale and influence radiuses must be prepared to the model. For example, table 1 shows the scale and influence radiuses of central towns, which are established according to field investigation.

Table 1 The Scales and Influence Radius of central Towns

Level	Influence radiuses [km]	Scales
1	70	60
2	35	30
3	20	10

Result Analyses. To analyze the results of the practical application based on the final data, distribution maps were created; Fig. 4 shows a distribution map of central towns. As shown in the map (Fig.4), influence scores decay distribution around the central towns. The more close to the central town it is, the higher the influence score is; the farther from central town it is, the lower influence score is. The practical application results indicate that the distribution is consistent with the actual survey results.

Conclusions and Discussions

In the model, Four main improvements have been made: (1) Spatial data and attribute data were organized and accessed separately by different components, the former was ArcSDE, and the latter was ADO.NET. (2) Spatial filter technology was used to optimize efficiency of spatial research. (3) Programming based on ArcGIS Engine was employed to simplify operations and realize automations. (4) Search centers were changed from evaluation unit to factors to reducing search times of spatial analysis. The result of the practical application shows that the model can meet the requirements of grading work of agricultural lands and obtain good results. It can simplify operations, improve efficiency, and strengthen automations.

Although the model is much better than other traditional ones, it still needs to be further studied. The future studies will focus on taking into account the barriers in calculations, and automatically adjusting the relative parameters of factors (such as search radiuses, factor weights).

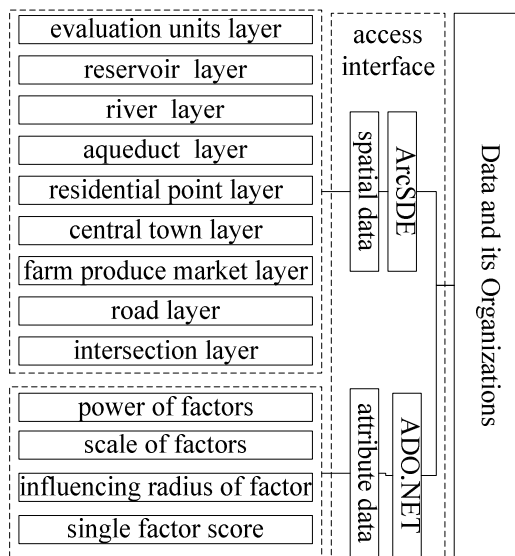


Fig. 3 Data and their organization

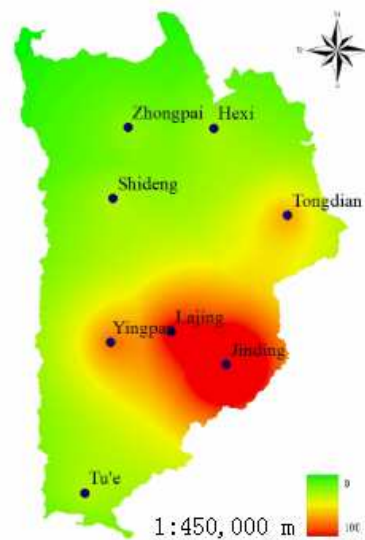


Fig. 4 The spatial distribution map of central towns

Acknowledgment

This study has been supported by the China National Natural Science Foundation of China, (No.71163023), the Natural Science Foundation of Yunnan Province (No.2010ZC047), and the Yunnan Province Education Department Foundation of China (No. 09Y0295).

References

- [1] TD/T1005-2003, "Agricultural Land Grading Specification," Land Resources Industry Standard of The People's Republic of China, 2003.
- [2] Min Xia, Youzhao Liu, and Yan Tang. "Development and application of farmland grading and appraisal system at county level," *Journal Of Nanjing Agricultural University*. Vol. 27, no. 2, p. 125-129, 2004.
- [3] Lin Zhang, "Study on agricultural land grading of FUFENG county based on GIS," Chang'an University, Xi'an China, 2005.
- [4] Jianchao Peng, Qun Wu, and Guancheng Guo. "The application of ArcInfo 8 to farmland grading: a case study of JIANGDU city," *Remote Sensing For Land & Resources*. No. 4, p. 46-50, December 2005.
- [5] Shu-mei Wang, Yong-fu Zhang, and Zhao-ju Fan. "Research on data processing of the agricultural land grading based on GIS," *Geomatics & Spatial Information Technology*, vol. 27, no.2, p. 26-29, 2004.

Research and Implementation of Multi-Bus Converter Based on Intelligent Sensor

Gongping Lu^{1,a}, Zhaoyan Ge^{2,b}, Wei Zhong^{3,c}, Chaogeng Hou^{4,d}

^{1,2,3,4}College of Electrical and Information Engineering, Hunan University, Changsha, China

^a615213015@qq.com, ^bgezy@jonhot.com.cn, ^c357374245@qq.com, ^d736449122@qq.com

Keywords: Multi-bus converter; Intelligent sensor; Reliability

Abstract. To study the communication problem between the intelligent sensor and the host computer or the remote terminal and design a converter. The converter is based on the microprocessor ATMEGA644. Data received from the input interface circuit and repackaged according to message frame format of the output bus and sent to the destination. Verified the reliability of the converter by means of the experiment of digital temperature sensor DS1621 which output is I2C. The converter is able to meet most applications.

Introduction

As the perception of intelligent sensors, acquisition, and the window of detection information as well as the research object monitoring and control system interface, intelligent sensor is widely used in various disciplines and engineering fields along with the development of micro-computer technology and communications technology. Intelligent sensor bus technology is gradually standardization and regulation. At present, the intelligent sensor output signal mode can be divided into the analog signal output mode and the digital signal output mode, the analog signal output mode include analog voltage and analog current, the digital signal output mode include I2C bus, SPI bus, CAN bus and LIN bus and so on. The intelligent sensor requires the use of bus converter to communicate with the host computer or remote terminal. However, on the occasion that needs to use multiple types of outputs of intelligent sensor, even when using multiple types of bus converter may not be able to meet the system requirements. Intelligent sensor integrated multiple output interfaces, which will inevitably contrary to the small size of the design principles of intelligent sensor.

This paper designed a multi-bus converter based on the communication between intelligent sensors and the host computer or remote terminal. Its function characters as follows.

It integrated many kinds of input and output interface, with a adjustable power supply which can provide different voltage to the system or the chip used in the converter.

The work instructs module in the converter can decide the conversion by means of the software programmed before according to the demand of input or output.

System's communication rate is also can be set, high speed is usually use in the short distance and the low speed in the long distance.

The converter can be setted to master mode or slave mode. Master mode is under the occasion of communicating with the intelligent sensor, while the slave mode is transfer data to the host computer or the remote terminal.

Overall Block Diagram Design for Multi-Bus Converter

In order to achieve the function of the bus converter, multi-bus converter needs to have input and output interfaces. Multi-bus converter connects the intelligent sensor through the input interface. Instructed by the work modules, microprocessors repackaged the received data and sent through the output interface to the host computer or remote terminal. Multi-bus converter consists of six modules, microprocessor, input bus interface circuit, output bus interface circuit, the module of work instruct circuit, power circuit and RS232 interface monitor circuit. Taking into account the factors of the transmission distance of the input and output bus, the interface leads as well as network topology, select the analog voltage, I2C bus and SPI bus as the input mode, the CAN bus, LIN bus and the RS485 bus for the output. Figure 1 shows the multi-bus converter hardware circuit block diagram.

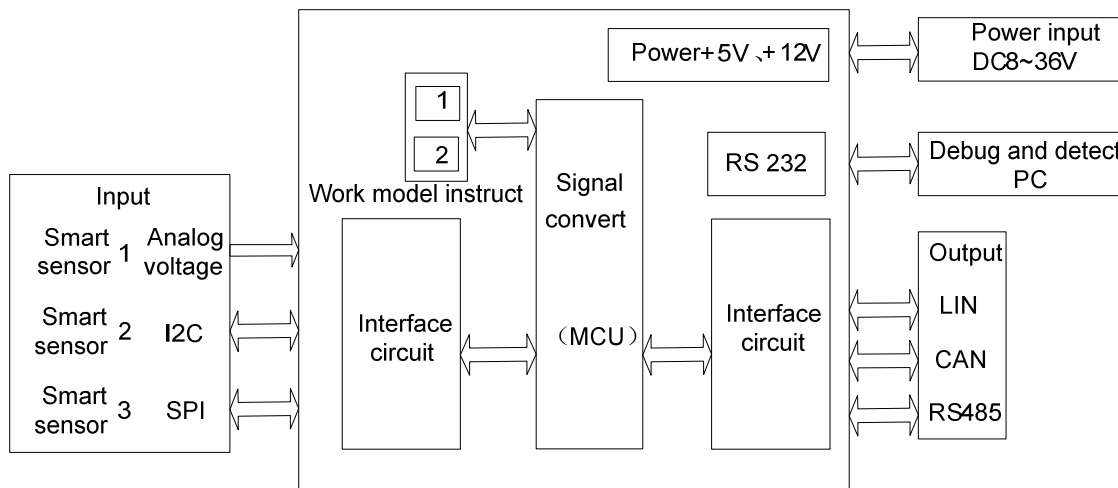


Fig. 1 System overall block diagram

Hardware Circuit Design for Multi - Bus Converter

Select ATMEGA644 produced by ATMEL Corporation as a multi- bus converter microprocessor with two UARTs , I2C , 1 SPI ,2.7-5 .5 V operating voltage , 8-channel 10 -bit ADC , 64K bytes flash , 44 - foot TQFP package , completely symbolic communication interface and pin - demand and cost savings in a large extent.

The part of power supply interface.Input voltage of 24V DC, after the LM2596 voltage dropped to about 12V power supply to the LIN interface chip, the LM7805 and filter circuit generate 5V power supply for the whole converter.

Use the CAN chip controller SJA1000 to connect microcontroller and the CAN transceiver TJA1050 to connect an external CAN physical bus.The isolated part is ADUM1201 produced by ADI Corporation with iCoupler isolation technology of the magnetic coupling of dual-channel digital isolators.Its power consumption is much lower than optocoupler isolation devices , and dual-channel technology allows the hardware circuit is greatly simplified , more reliable performance.In order to improve the reliability of the communication.Set the current limiting resistor,capacitance of filter the high - frequency interference and electromagnetic radiation the end of the circuit .

The main chip of RS485 interface circuit is ADM1483 which contains isolation of the magnetic and produced by ADI Corporation. It integrates 485 transceiver and isolation circuit , with the optocoupler incomparable advantage.Use ZY0505BS - 1W as the ADUM1201 and ADM2483 power isolation chip.

LIN transceiver chip is the TJA1020.The power circuit through a step-down 12V supply to TJA1020. SPI and I2C bus through the power strip directly connected with the processor.

The operating mode indicator circuit selection DIP switch.Called the DIP switch when Knew the input bus,then the microprocessor implemented the corresponding handler to complete the appropriate protocol conversion by testing with the DIP switch pin connected to potential changes.

RS232 circuit displayed the received data on the PC to detect the information is correct or not, and it also can detect the data forwarded out.

Multi- Bus Converter Software Architecture

The key lies in the design of the software as to achieve communication between intelligent sensors and the host computer.Software design, including system initialization procedure, the program of data reception, data transmission procedures and data seized the wrong program.

The main task of the initialization process of system-on-chip include the flows : set the microprocessor into a reset mode , enable the interface chip , configurate each chip transmit and receive pins and the appropriate interrupts and timers and so on.The corresponding flowchart shown in Figure 2.

The data reception program in the system is after the completion of initialization. Enable the appropriate interface according to the input bus, and by the microprocessor configuration for the host to request intelligent sensors to send data. When both sides receive a handshake signal, multi-bus converter receive the data from intelligent sensor through the interface. The reception program flowchar shown in fig. 3.

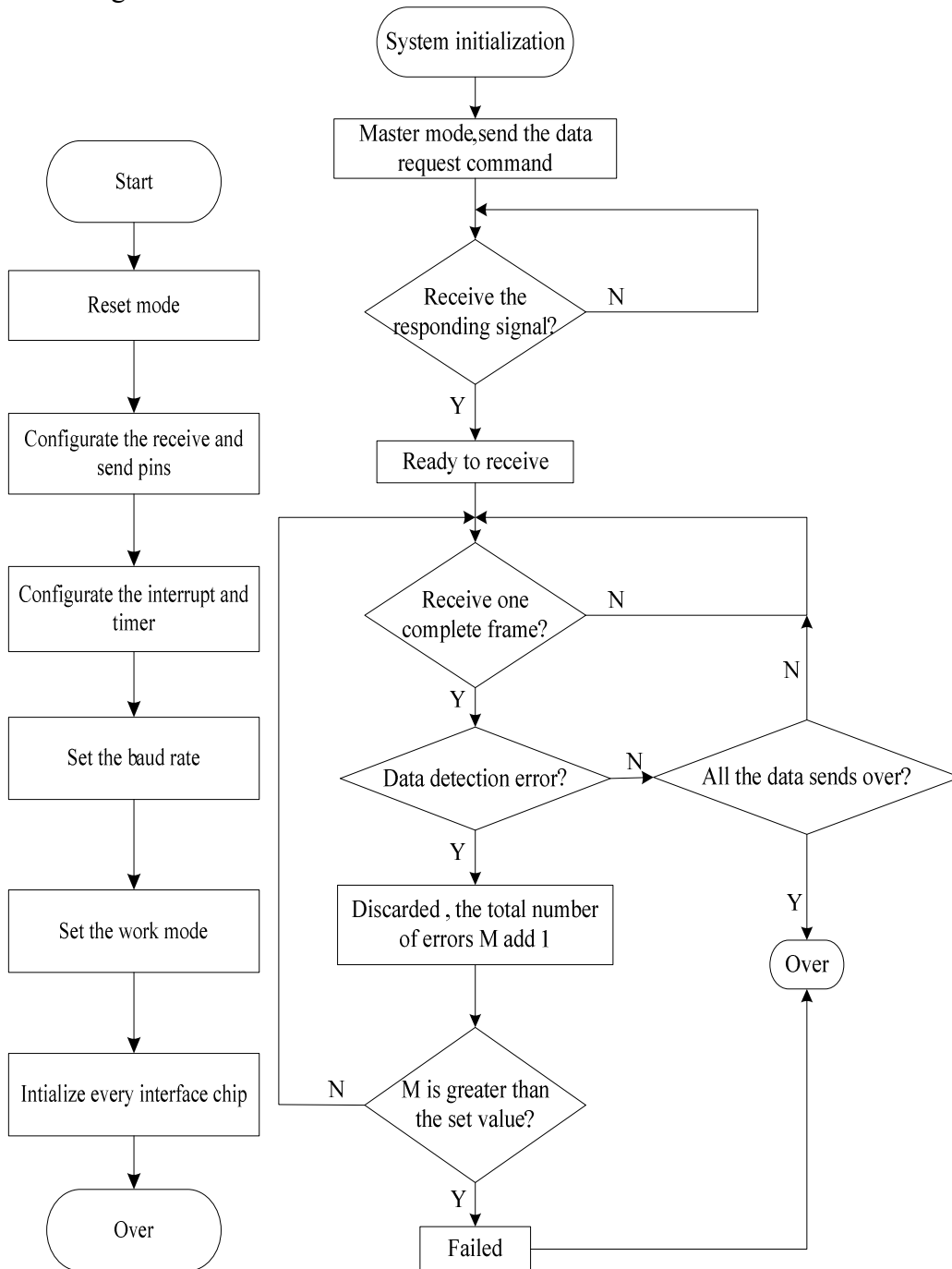


Fig. 2 System initialization

Fig. 3 Reception flowchar

The data sending program related to the success of completion of data conversion functions of the multi-bus converter. Data sending program must be able to enable the appropriate output interface chip and its function pins and configure as a slave, unpack and re-packaged the received data, packaged as required of the output bus data or message format according to the connect position of DIP switch. The sending program such as Figure 4 show.

Data error detection program is included in the data to send and receive procedures inside. So that it can improve the reliability of the receive and transmit and can achieve effective conversion function of the multi-bus converter.

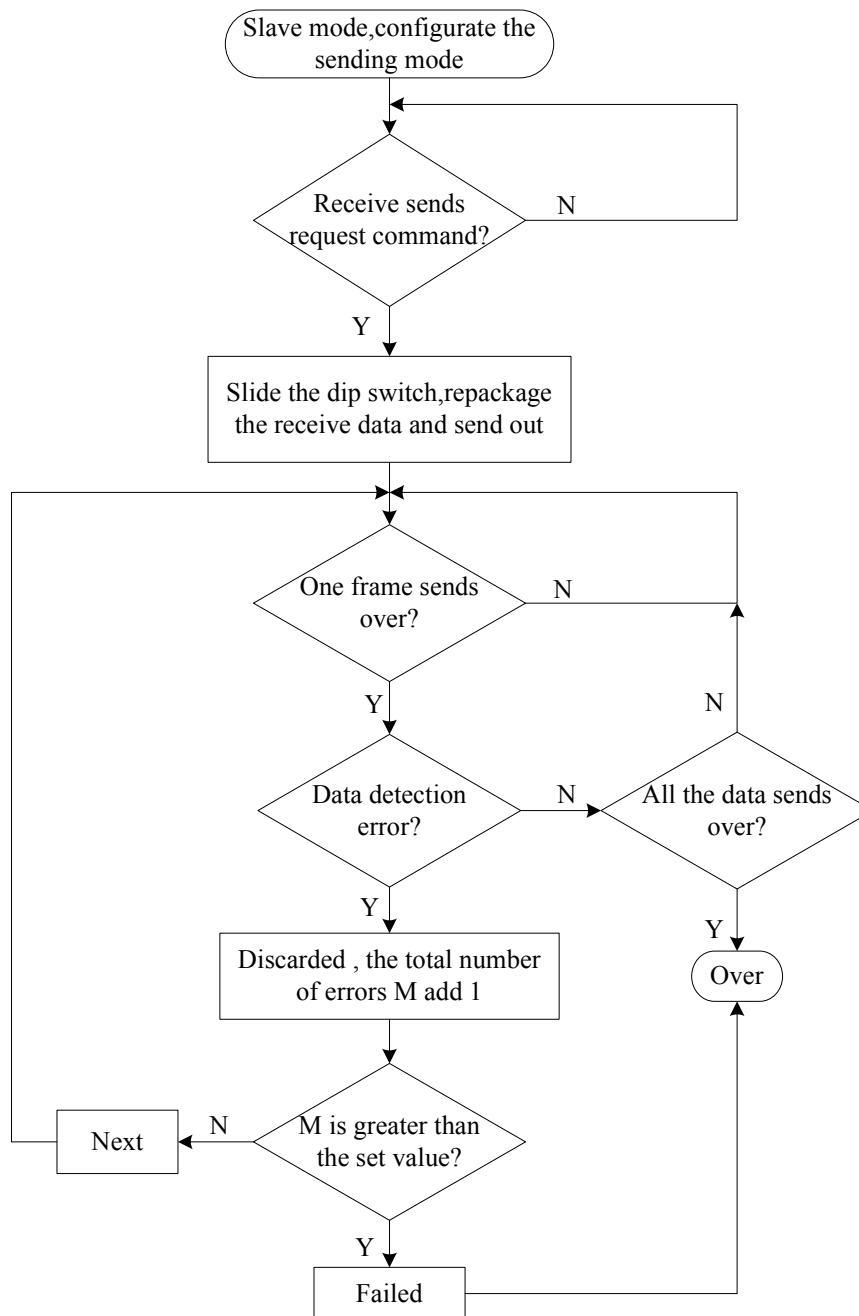


Fig. 4 Sending flowchar

The Test Results

Selected intelligent sensor with different output mode to communicate with the multi - bus converter and it proved the reliability and practicality of the multi-bus converter. Surface gives the results of the DS1621 digital temperature sensor with I2C interface . Convert the I2C bus input mode for the CAN bus , LIN bus way and RS485 bus mode. By setting each other's communication rate in a certain period of time to complete the conversion . Under the surveillance of the RS232 interface, and obtained the results shown in Table 1.

Different bus communication speed is not the same as if the mutual conversion between the bus communication speed that much difference , communication timely and effective forwards them , this will cause the accumulation of data , the data buffer neck bottles , and even cause data lost , resulting in communication failure . Therefore required to set an appropriate value based on the maximum communication speed of the input and output bus.

Obtained the total number of transferred bytes within one second communication time by the format of bus frame and a certain amount of delay after setting the communication speed. And calculated the bit error rate under the monitor of RS232 interface.

Table 1 I2C interface test result

Conversion	Rate(bit/s)	Communication time	Transfer bytes	Error rate
I2C to LIN	15K	1s	1821	0.32%
I2C to CAN	9600K	1s	184615	0.79%
I2C to RS485	2M	1s	41466	0.46%

We can know that the error rate is relatively low within one second and it can meet the requirements from the table.

Conclusion

Designed a multi - bus converter based on the communication problems between intelligent sensors and the host computer or remote terminal. The multi- bus converter can achieve the mutual conversion between multiple bus. It has a small size, cheap, high reliability, strong anti-interference ability, long transmission distance adjustable range of operating voltage and other characteristics. And tested based on the I2C output interface of the DS1621 digital temperature sensor to get good results . Able to meet the actual requirements of great promotional value in use.

References

- [1] CAN Specification V2.0, BOSCH.
- [2] LIN Specification Package, Revision 2.0. Motorola Co, Sep.23,2003.
- [3] Ping Ran, Baoqiang Wang, Wei Wang. The design of communication convertor based on CAN bus[C]. 2008 IEEE International Conference on Industrial Technology, 2008:1 – 5.
- [4] Yurish, S.Y. Universal Intelligent Sensors Interface and Signal Conditioner [J]. Sensors, 2007: 24 – 27.
- [5] Jingcheng Wang, Xiaoming Wang, Xianglin Zhai, et al. CAN/LIN hybrid network for automobile[C]. 2005 IEEE International Conference on Vehicular Electronics and Safety Proceedings, 2005:348-352.
- [6] Ling, Bin; Peng, Fengchao; Li, Ailan. The Car Body Control Bus Design Based on CAN/LIN Bus[C]. 2011 International Conference on Computational and Information Sciences, 2011:885-888.
- [7] TJA1020 Data Sheet 2002.
- [8] Philips Microcontrollers in LIN Applications 2002.

Design of Wireless Power-Meter Reading Data Collector Based on CC2430

Zhiyong Chen, Jianxi Gu, Wenxiang Bu

Xiayi Power Supply Bureau, Xia yi, Henan, China

Keyword: CC2430, RS485 Bus, Power-Meter, STC89C54

Abstract. While large-scale smart electricity meters are going to be applied, it is difficult to solve the problem of acquisition data of smart electricity meters and in order to design a convenient installation and maintenance, low power consumption and reliable data collection terminal, a design of wireless data acquisition system base on wireless network is proposed according to the development of wireless technology. The system used CC2430 as the core controller to process power data and performs intelligent control. Using the technology of Zigbee short-range wireless communication for data transmission, the wiring complexity of the project has been reduced, the reliability of data communication has been improved, and power consumption has been reduced. The results show that the terminal is normal and reliable.

Introduction

The meter is an important tool of modern power system measurement. Traditional power management manually Collecting and settlement consistency is poor, and difficult to manage the problem. Meter distribution point, a wide range of complex environment, automatic meter reading system has been difficult for practical use the major reason is the lack of practical, reliable, inexpensive means of data transfer and meter-reading terminal [1].

For the above reasons, the design an installation and easy maintenance, long-term stable and reliable, not only can copy reading table with data and can monitor table with the operational status of remote meter reading data terminals, has become the industry's problems to be solved. This paper, an automatic meter reading based on Zigbee technology, remote automatic meter reading data terminal, the communication quality, reliable, economical and practical, the user can accurately and timely energy meter data copied from the upload is an ideal solution programs.

Overall Framework for the Design of a Remote Electricity Meter Reading System

The system is running, first of all by the power meter's RS-485 bus data interface transfer to the collector. Collector inspection tables of RS-485 data processing or count, and store the result. Collection and centralized communication using Zigbee wireless communication module, the collector is usually in the receiving state, when received concentrator operating instructions, in accordance with the operation of the instruction content, this acquisition the data through a wireless communication module sent to the concentrator. The concentrator can be timed or real-time acquisition under the jurisdiction of the Data Collecting and storage [2]. Superior equipment - the computer when the call data is stored data package sent. The handheld computer can read each meter data and stored in the SD card, the staff from the SD card back to the power companies, power companies through the computer read the data on the SD card and calculates the electricity bill. Framework of the overall system designs show in Fig.1.

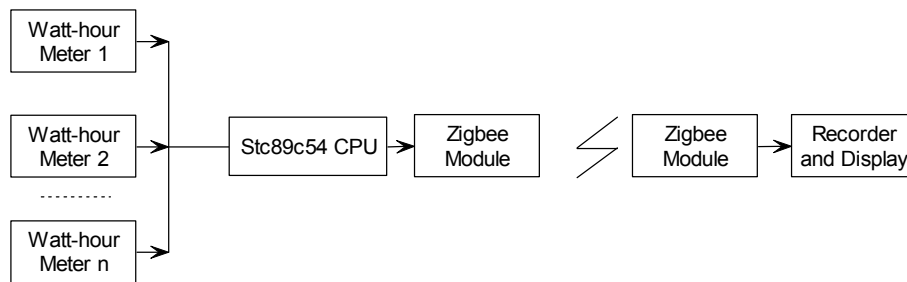


Fig. 1 System block diagram

The Hardware Design of Data Collection Node

The Data Acquisition Hardware Block Diagram

Shown in Fig 2, data acquisition module use STC89C54 microcontroller for data processing unit compatible with the Zigbee / the IEEE 802.15.4 radio frequency (RF) transceiver chip CC2430 design data transmission unit and data acquisition unit patrol all electricity RS_485 bus technology table, and connect LCD128 * 64 and DS1302 each energy meter energy consumption values and the acquisition time [3]. The program design of data collection terminal downstream channel the RS_485 bus Taipower table connection for meter data acquisition and through power control, uplink communication using Zigbee wireless sensor network technology, network and data concentrator for data exchange Remote meter data

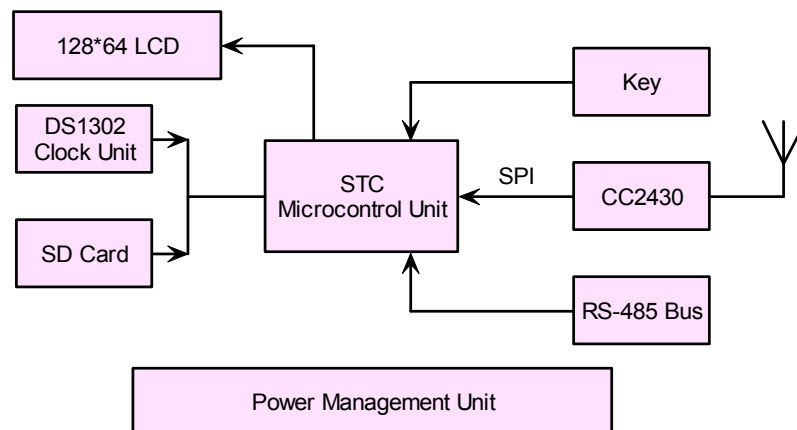


Fig. 2 Data acquisition hardware block diagram

Microcontroller and Radio Frequency (RF) Transceiver Chip Circuit Design

The wireless RF transceiver chip is selected based on the design of low power ZigBee / IEEE 802.15.4 2.4GHz radio transceiver chip CC2430. Shown in Fig 3, the CPU 4 SPI bus interface, as well as the other four control lines and the CC2430 to communicate with the CC2430 on the capacitor C10 and R3 for the reset circuit, C5 and C6 for the power supply decoupling capacitors, crystals constitute a crystal oscillator circuit XTAL load capacitor C7 and C8 can to ensure the stability of the chip operates at low voltage crystal oscillator XTAL load capacitor Cr1 and Cr2 and crystal oscillator circuit [4], the clock frequency. Microcontroller programming control registers through the SPI interface, while the complete data exchange with the C2430.

Acquisition Unit of the MAX485 Interface Circuit Design

In order to achieve the isolation of the bus and microcontroller, optically isolated, asynchronous communication port of the microcontroller and MAX485, shown in Fig 4, P30 of STC89C54, P31, P32, opt-isolator receiving input from the control signal isolation [5]. In the output circuit design, the R8, and the transmission line matching resistor to reduce the reflection of the transmitted signal on the line at the end of the 485 signal output of the MAX485 series of two 20Ω resistors R9, R10, in order to prevent the influence due to the failure of the machine other extensions in the bus communication MAX485 circuit A and B output side plus a pull-down resistors R7, R11, and the A-side potential is higher than the B-side potential, so that RXD level the MAX485 bus is not sent

during the period (bus suspension) showed only high, so you can avoid all transmitters are prohibited on the bus, it is often mistakenly believe that the initial cause of the communication frame is not working properly. Can be achieved through the above design of microcontrollers the MAX485 bus under the jurisdiction of each electricity metering unit, data acquisition, processing, storage, and control purposes.

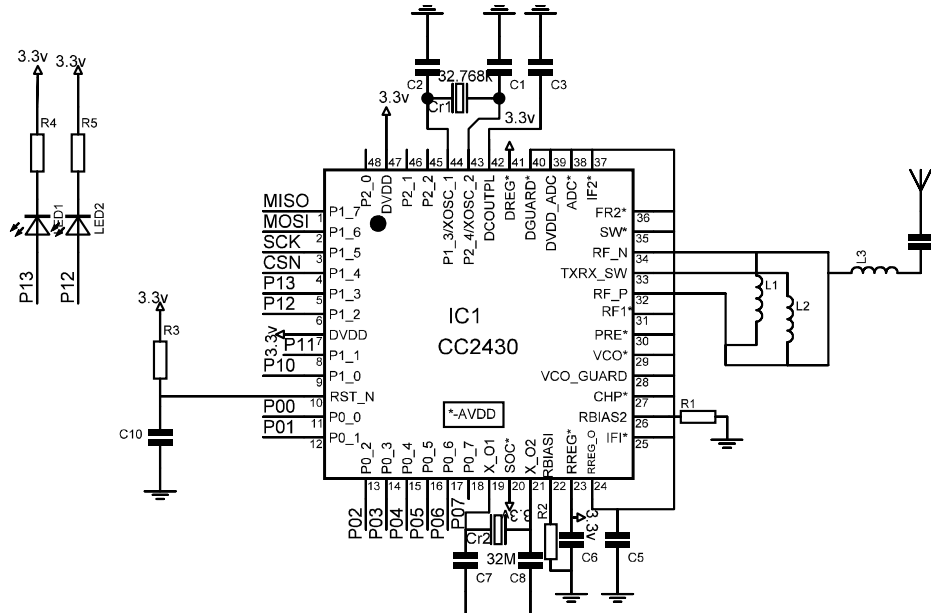


Fig. 3 A CC2430 circuit diagram

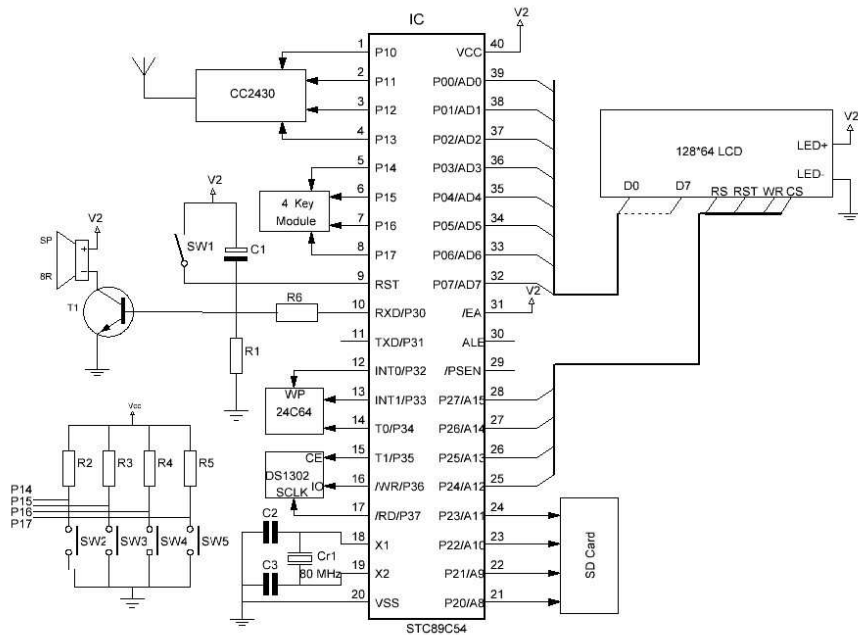


Fig. 3 B: CPU circuit diagram

Data Acquisition Software Implementation of the Terminal Node

Transport Protocol for Data Acquisition Unit

The design the MAX485 network data acquisition part of a multi-function watt-hour meter communication protocol (DL/T645-1997) as remote control of the energy meter communication protocol to communicate across the network link and the lifting of the information will be collected terminal issued frames to control the communication byte format shown in Table 1 shows the transmission direction from low to high, a start bit, one stop bit, a parity bit, eight data bits 11.

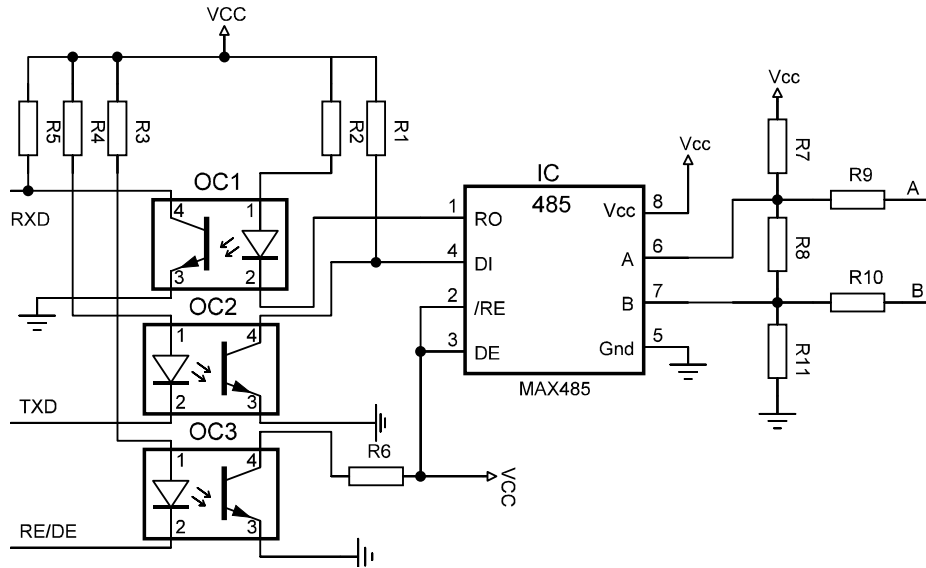


Fig. 4 RS485 interface

Table 1 Communication byte format

0	D0	D1	D2	D3	D4	D5	D6	D7	P	1
---	----	----	----	----	----	----	----	----	---	---

Communication frame format shown in Table 2.

Table 2 Communication frame format

start character	Address field	character start	Command code	length of data field	Data field	Check code	Terminator
68H	(A0-A5)	68H	C	L	D	CS	16H

Among them, the frame starts character 68H: marked the beginning of one. Domain address A0 ~ A5: address length up to 12 decimal number, when received from the controller to a data address field should respond to command, to obtain control of the bus, the bus when the response should be to return control to the main controller. Command code C: and perform the appropriate action. The data field length of L: L is the number of bytes of data fields, the read data is not greater than 200, write data is not greater than 50. L = 0 indicates that no data field. The data field DATA: send data encryption 33H, receive data reduction 33H. The checksum CS: that each byte of binary arithmetic, and not more than 256 of the overflow value. Terminator 16H: identifies the end of information. Its value is 16H.

Data collection terminal nodes and the number of watt-hour meter to form a 485 network, as the MAX485 network host, according to (of DL/T645-1997) communication protocol, its operation the basic send and receive flow chart shown in Fig7, Fig 8, according to the process shown to write programs, you can achieve the normal communication the MAX485 network master and slave, and completion of data collection terminals on the power meter data acquisition functions.

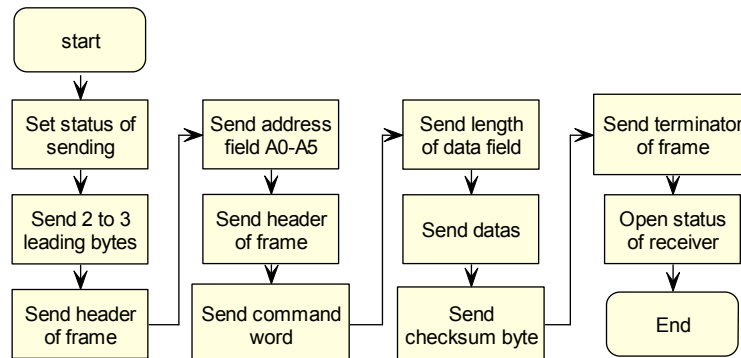


Fig. 7 Sent flowchart

Concluding

This paper, the design of the remote power data acquisition terminal program on the hardware detailed analysis of the various parts of its hardware design and interface circuit, to achieve the purpose of a low-power analysis of specific implementations and key technologies of the layers of communication software, to improve the reliability of data communication, this innovation is the combination of the MAX485 bus technology, Zigbee wireless communication technologies applied to the remote electricity meter reading system, some practical value.

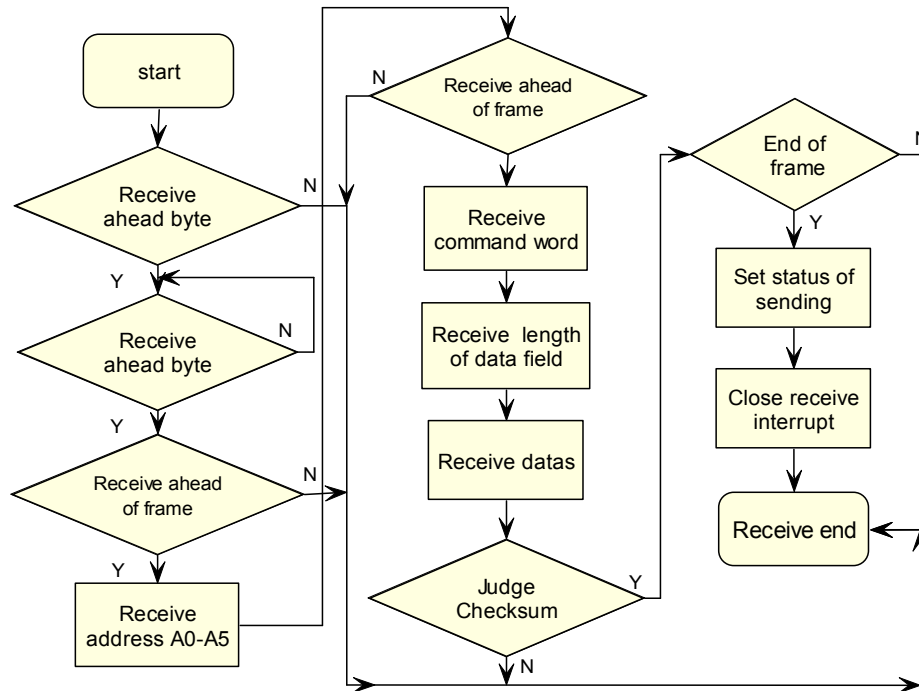


Fig. 8 To receive the flow chart

References

- [1] Xiong Banghong, Li Yang, Zhu Honglei, Liu J unfeng. Application Design of Wireless Sensor Networks in Environmental Pollution Monitoring [J]. Computer Measurement & Control2009, 17(2):258-260.
- [2] Chen Juan, Zhang Hong-li. Survey on wireless sensor network security [J]. Journal of harbin institute of technology.2011.7(43)-90-93
- [3] Xu jianlong, Gong jianrong.Rea l iz ing Remote Automa ticM eter-reading with Ch ipM icrocomputer [J]. Computer application, 2001, 5(27): 17-21.
- [4] STC User's manual.STC Company.2008.
- [5] LU Nan, GUO Yong. Wireless Measurement and Control System for Greenhouse's Temperature and Humidity Based on ZigBee Technology[J].Modern electronic technology,2008,31 (15):98-100.

Application of Three Order Cumulants in Fault Diagnosis

Wu Wenbing^{1, 2, a}, Yang Shuqun^{3, b}, Huang Yijian^{4, c}

¹ Fuzhou College of Foreign Studies and Trade, China

²School of information science and technology, Xiamen University, China

³Faculty of software, Fujian normal university, China

⁴ College of mechanical engineering and automation, Huaqiao University, China

^awwbysq@fjnu.edu.cn, ^bshqyang@fjnu.edu.cn, ^cyjhuang@hqu.edu.cn

Keywords: Bispectrum, 2-D Wavelet, Fault Diagnosis

Abstract. Compared with bispectrum, three-order cumulants have a lower computing complexity, in the experiment, features of fault signals and normal signals are fetched by 2-D wavelet in different directions, then these features are used to diagnose fault. The experiment shows, that the method can achieve satisfactory result through different selections in fault diagnosis. the results prove that the method in the experiment is necessary.

Introduction

High order cumulants can automatically suppress the Gaussian background noise (colored or white), can establish the non-Gaussian signal model under Gaussian noise, and extract the non-Gaussian signal (including harmonic signal) in the Gaussian noise. Because of these, the statistics of high order cumulant has gained growing attention, and has become a very useful tool in signal processing [1-4]. Compared with bispectrum, three-order cumulants have a lower computing complexity; this paper uses three-order cumulants to diagnose faults directly. The decomposition of two-dimensional wavelet is to decompose the low frequency component of the J scale into four parts, which are low frequency component of the J+1 scale, and the high frequency parts of three directions (horizontal, vertical, diagonal) [5-6].

On the basis of the above, in this paper, features are extracted by using two-dimensional wavelet, and then research on fault diagnosis was made by using these features.

High Order Cumulants

Let $\{x(n)\}$ be a real, discrete, zero-mean stationary process with k order cumulants $c_{kx}(\tau_1, \tau_2, \dots, \tau_{k-1})$ is defined as k order joint cumulant :

$$c_{kx}(\tau_1, \tau_2, \dots, \tau_{k-1}) = \text{cum}\{x(n), x(n + \tau_1), x(n + \tau_2), \dots, x(n + \tau_{k-1})\} \quad (1)$$

Then the third order cumulant is given by the expression:

$$c_{3x}(\tau_1, \tau_2) = E\{x(n)x(n + \tau_1)x(n + \tau_2)\} \quad (2)$$

2-D Wavelet Multi-Scale Decomposition

Two dimensional wavelet functions are obtained by one dimensional wavelet function after its tensor transformation. The decomposition of the two dimensional wavelet functions is to decompose the low frequency of the scale j into four parts: low frequency component of the scale j+1 and the high frequency component of three directions (horizontal, vertical, diagonal).

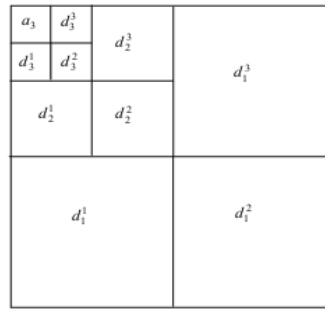


Fig. 1 Decomposition of 2-D wavelet

Let original two-dimensional array has $(N \times N)$ elements, scale parameter $j=0$. The recursive decomposition begins from the original two-dimensional array. In the j decomposition, wavelet coefficient matrix a_j d_j^1 d_j^2 d_j^3 has $(2^{-j}N)^2$ elements respectively (resolution reduces 2^{-j}), due to the factor j denotes the decomposition progression, and has the relation with the resolution of two dimensional array, therefore j often is referred to resolution or decomposition.

Scale a two-dimensional array of three-level wavelet decomposition is set as an example. The distribution of wavelet coefficients is shown in Fig. 1.

Data Collecting

When the oil inlet and outlet of pressure reducing valve has a foreign body, too high or too low pressure will affect the normal operation of pressure reducing valve. In order to obtain the vibration signals of pressure reducing valve in the fault state, in this paper, artificial fault was set in the experiment:

Add 3mm iron core in the oil inlet of the pressure reducing valve.

The fault state of the pressure reducing valve can be simulated through the experiment. Labview software, PCI-6014 data acquisition card and acceleration sensor were used, and the vibration signals of the pressure reducing valve in normal and fault state were collected. During each measurement, the oil pressure is 1MPa~5MPa, divided into 5 pressure levels. The sampling frequency is 250Hz and the reading frequency is 125Hz, the sampling time is about 2min. 18 sets of datum, in this experiment, were respectively collected in normal state and fault state, and 36 sets of datum were obtained in total. 1536 datum are used in this experiment.

Figures of Three Order Cumulants

In this experiment 36 groups of datum in the normal state and fault state were used, and then according to the 3 definitions above, calculated the three order cumulant of each group of datum. In this paper, complex three order cumulants in normal state and fault state were selected to show in Figs.2-5. Set $-127 \leq \tau_1, \tau_2 \leq 127$, when the oil pressure is 1MPa, 3MPa, 5MPa respectively, 1 group datum's three order cumulant in two states is selected, shown in figure 2 and figure 4. Figure 2 and figure 4 show, compared with that in the normal state, the peaks distribution of three order cumulant in the fault state are more sparse than that in the normal state.

Features Extracting

In this paper, on the recognition of the fault, if directly using the data of three order cumulant obtained to input into a neural network, first, a computational complexity is too large; and second, diagnosis result obtained from the experiment is not ideal. Because a variety of frequencies information contained in the original signals must reflected in the third order cumulant, and wavelet decomposition can effectively extract the frequencies information, so, in this paper, as to the third order cumulants of each group of datum measured, two-dimensional wavelet decomposition is used for features extraction. db1 wavelet is used here. Through the experimental comparative analysis, after

the two-dimensional wavelet decomposition of third order cumulants, when scale is 6 the compression coefficients extracted were input to the LSSVM, and best recognition effects were achieved, and compressed coefficients is 4*4 arrays. In this paper features extraction was made from the low frequency part and high frequency part in three directions (horizontal, vertical, diagonal).

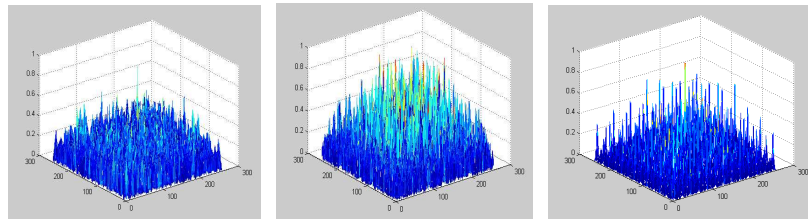


Fig. 2 Three order cumulants of signals in normal state

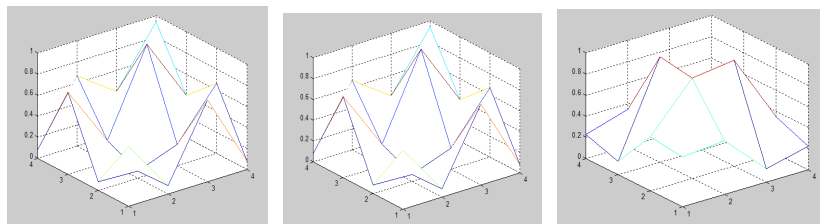


Fig. 3 Compression coefficients when scale is 6 in normal state

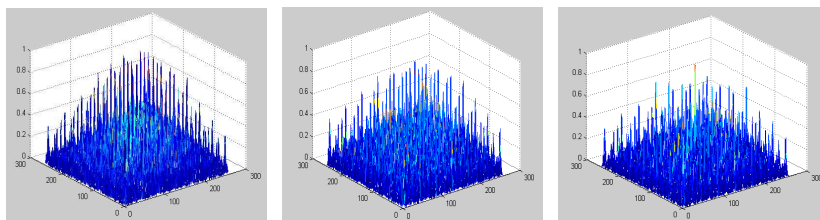


Fig. 4 Three order cumulants of signals in fault state

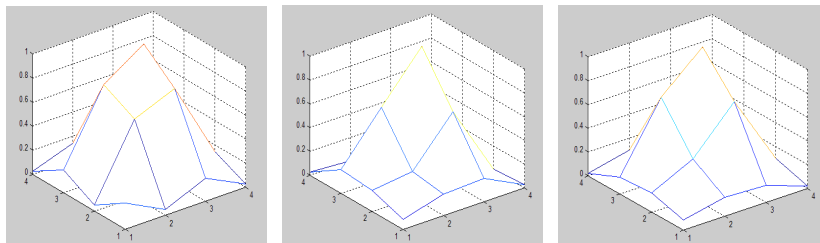


Fig. 5 Compression coefficients when scale is 6 in fault state

Table 1 Features of bispectrum of definition 3 in diagonal direction

Normal state	0.7097	0.0031	0.1928	0.0076	0.0031	0.6755	0.89008
	0.5194	0.3033	0.0104	0.0257	0.7100	0.6532	0.7175
	0.6180	0.6050	0.5037	0.7140	0.4675	0.0001	0.0032
.....								
Fault state	0.0202	0.5574	0.6104	0.9474	0.0074	0.7808	0.0154
	0.0050	0.8754	0.7024	0.0075	0.6832	0.9636	0.5110
	0.5864	0.0047	0.0039	0.5874	0.0047	0.8521	0.0034
.....								

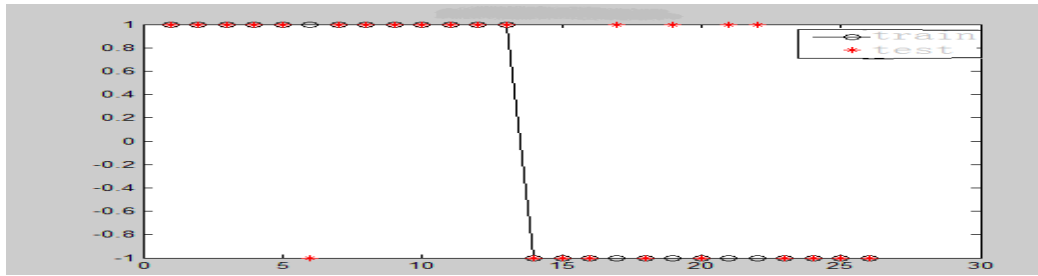


Fig. 6 Simulated result using features fetched in diagonal direction

Fig. 3 and figure 5 show the absolute values fetched in diagonal direction of high frequency. Table 1 shows the features vectors gained in diagonal direction of high frequency part, including both normal and fault state.

Experimental Results

According to the literature (7), the same LSSVM was established, when training LSSVM, the normal and fault state are respectively encoded as 1 and -1, due to the normal datum and fault datum were respectively obtained from 5 different oil pressure, then in normal state and fault state, corresponding to 5 different oil pressure, 5 sets of datum were selected out, and 10 groups in total, to train the LSSVM established. After the LSSVM was trained, it was used for fault identification of the remaining 26 sets of datum. As shown in figure 8, the figure shows the state of the 26 set of datum after simulation, where the hollow circle denotes the predetermined state of the training data. For example, the fore 13 sets of data were measured in normal state, and they should be stayed on the upper line which indicates the 1 state in the diagram; the behind 13 sets in fault state should be stayed on the lower line which indicates the -1 state, and the red solid circles denote the classification results after the simulation of LSSVM. If hollow circle of one set of data is coincident with the red solid circle, the simulation result of this set of data is correct, otherwise error. Figure 6 shows that the feature vectors obtained from the high-frequency part in the diagonal direction were used to identify, and the result shows that in normal state only 1 group and in fault state only 4 groups are error identification, the correct rate is more than 80%, then the same experiments were done in low frequency, in horizontal direction and vertical direction of high frequency, and the error numbers are 6, 8, 7 respectively. Thus, the above experiments show, when features extracted in diagonal direction, the correct rate of diagnosis is highest.

Conclusion

Although the reasons of different mechanical faults produced are not the same, each fault has the most essential difference with that in normal state. For example, the fault in this paper is caused by adding an iron core to the pressure relief valve in the normal state, and this kind of essential difference possibly makes the distinction biggest, and the distinction is referred to one kind of signals' expression form between fault state and normal state. In this paper, features of three-order cumulants extracted by two-dimensional wavelet in different directions were used to find the best diagnostic result, and success was achieved in a certain degree.

Acknowledgement

The paper was supported by National Nature Science Foundation of China under grant no: 50975098

References

- [1] Cai Qizhi, Huang Yijian Study on autoregressive trispectrum slices. Chinese Journal of Scientific Instrument 2009, 30(02).
- [2] Baydar N. Ball A. A comparative study of acoustic and vibration signals in detection of gear failures using Wigner-Ville distributions. Mechanical Systems and Signal Processing. (2001) 15(6). 1091-1107.
- [3] Cheng Junsheng. Yang Yu. Yu Dejie. The envelope order spectrum based on generalized demodulation time-frequency analysis and its application to gear fault diagnosis. Mechanical Systems and Signal Processing, 2010, 24(2), 508-521.
- [4] M.R.Raughveer. IEEE Trans. Time-domain approaches to quadratic phase coupling estimation Automatic Control . 1990. AC 35: 48-56
- [5] DAUBECHIES. I The wavelet transform, time-frequency localization and signal analysis[J]. IEEE Transactions on Information Theory, 1990, 36(5): 961-1005.
- [6] MALLAT S A wavelet tour of signal processing[M], 3rd ed. The Sparse Way: Academic Press, 2008.
- [7] Wu Wenbing, Huang Yijian. Fault Diagnosis of Reducing Valve Based on Bispectra Slices. Computer Measurement & Control, (in chinese)2011(10).

Review on Application Research of Multi-agent Theory in Industrial Process Control

Jianchang Liu^{1, 2, a}, Yulian Jiang^{1, b} and Shubin Tan^{1, 2, c}, Pingsong Ming^{1, d}

¹ State Key Laboratory of Synthetical Automation for Process Industries, Northeastern University, Shenyang, Liaoning 110819, China

² College of Information Science and Engineering, Northeastern University, Shenyang, Liaoning, 110819, China

^aliujianchang@ise.neu.edu.cn, ^bjiang_harmony@163.com, ^ctanshubin@ise.neu.edu.cn, ^dpingsong.ming@gmail.com

Keywords: Industrial Process Control; Multi-Agent Theory; Algorithm; Negotiation; Holonic Agents

Abstract. The paper provides a review of application research of multi-agent theories in industrial process control. Firstly, we introduce characteristics of industrial process control. Then, a comprehensive description of some research achievements for multi-agent theory problems, such as the architecture, algorithm, coordination, cooperation, negotiation, and communication, applied in industrial process control, is introduced to identify main research lines. Further multi-agent theories and applications in industrial process control are discussed in detail, and their significance is revealed, which applies directions for the further research and improvement.

Introduction

In recent years, the development of modern industrial process control systems is showing some characteristics such as large-scale and complication. For traditional hierarchical control systems, the connection is close, structure fixed and extension difficult, as well as the malfunction cannot be predicted and life cycle is short. However, the control requirement of systems is improved gradually, e.g. system deviation is smaller, energy loss less and control speed quicker, etc. Traditional control policies and sole control methods are difficult to satisfy the control quality for complex process control. While autonomous control systems' connection is loose, flexibility good, extension easy, as well as they can forecast breakdown and the life cycle is long. In industrial process control, multi-agent theories play an influential role in autonomous control systems [1-3].

MAS (Multi-Agent System) are a comparatively new concept in the field of Distributed Artificial Intelligence (DAI). It is a system that multi-agents interact mutually for their special goals, and form information sharing, coordination control and computation. Herein, each agent represents an abstract entity that is able to solve a particular or partial problem. Multi-agent theories and applications have been developed for many years, and produced a wealth of research achievements [4-7]. After control problems of complex industrial process appear, in order to decrease solution difficulty, we can apply divide-and-conquer strategy and multi-agent method. These agents' working is highly discrete, while their coordination and cooperation enable to carry out overall goals for the whole system [2].

On the basis of references on domestic and foreign related literatures, this paper provides a review of application research of multi-agent theory in industrial process control for the latest ten years and applies directions for further research and improvement

Characteristics of Industrial Process Control

Industrial process control means in industrial production, to use technical tools, e.g. monitoring instruments, computers and communication network, gain valid information of procedure variables automatically, and then, operate and regulate variables affecting the process condition in order to meet goals, e.g. control requirements, etc.

Modern industrial control systems' characteristics, e.g. difficult modeling, nonlinearity, time variability, coupling, and the uncertainty in parameters and structures, are even more obvious. The traditional control theory based on quantitative model singly has not controlled complex industrial process effectively. Thereby, it is necessary and important to adopt organic integration of holonic systems. For industrial processes and control structures, the inherent identity in local control and distributed decision-making, provides a wide application space for multi-agent theories [8].

The intelligent control based on multi-agent theories does not pursue a single, large-scale and complex system, but according to requirements of control goals, divide the system into multi-agents in accordance with functions or physical entities. Herein, agents collaborate and achieve control tasks together, which possesses resource sharing, easy extension, strong reliability, great flexibility and good real-time nature, and mutual coordination and cooperation of multi-agents, which are beneficial to solve control issues of the large-scale and complex industrial process, and make robustness, reliability, intelligence and self-organization of systems greater [9, 10].

Multi-agent Theories and Applications Research in Industrial Process Control

Multi-agent theories mainly consist of 6 aspects: the system architecture, algorithm, coordination, cooperation, negotiation, and communication. Therefore, we provide an overview of the research in multi-agent theories applied in industrial process control.

Architecture

The implement of complex industrial process control based on multi-agent, needs organic integration of several models with different functions and identities, and define them as multi-agents or a part of an agent. That requires interactions and coordination control among agents, which desires to design architecture of MAS, and show relations of information and control. According to the control way, MAS architecture consists of the centralized, distributed and hybrid architecture [11].

Considering the distribution, many researchers integrate hierarchy and distribution to apply in industrial process control Han et al. [12] use an agent method to handle design knowledge as an object in continuous chemical processes, map a domain model to an agent model, and build an architecture with combination of hierarchies and interdependencies among agents from the task decomposition, which greatly improves the modularity and reusability of that knowledge. While researching holonic manufacturing systems, Deen [13] presents that a holonic manufacturing system is a kind of agent-based manufacturing system, and herein, each holon can be regarded as a special kind of large-grain reactive agent. These holons can be organized into hierarchical or heterarchical structures. Holonic agents acting as autonomous, cooperative units can solve problems of decentralized, highly distributed control where real-time constraints on decision-making are a key challenge [14, 15]. During the research in continuous rolling process, authors of this paper improve hieratical design further [16], use hybrid and heterogeneous architecture combining centralized and distributed structure, and create continuous rolling process control, as shown in Fig.1. The agents can complete the global goals through efficient coordination and collaboration, and do not lose the ability of central monitoring control and optimal analysis. Meanwhile, model encapsulation and measurement of the agent can solve reconfiguration problems in the control system. All that favors to achieve the high automation and intelligence in rolling production.

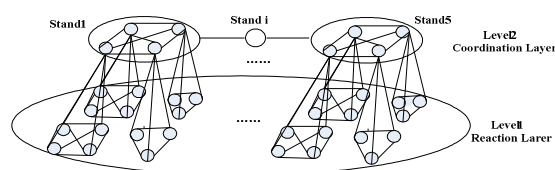


Fig. 1 System architecture model of the continuous rolling process control based on the multi-agent

Algorithm

To problems that in complex industrial process control, it is hard to create accurate system model, we can utilize learning, adaptation, self-organization and optimization characteristics of intelligent control, to design the control system based on rules from experiences, reasoning and intuition instead of on rigor analysis too much [17]. Algorithms in control theories based on multi-agent include reinforcement learning, evolution algorithm, neural network, fuzzy algorithm and simulated annealing algorithm [18-22]. Machado et al. [20] use ANN to enable agents to learn about fault patterns and adapt the algorithm which can be used in fault situations in the presented multi-agent architecture applied to industry automation. Anderson et al. [23] utilize reinforcement learning to make controllers learn by themselves, and obtain optimal control actions finally. However, what it is necessary to point is that in MAS, how to develop a suitable learning approach which is applied to a particular engineering control issue is an essential question to researchers. Ren et al. [24] have addressed that, although it is difficult to develop a general learning approach for different application scenarios, several general principles adopted in this study will be helpful for working out an appropriate learning approach.

Cooperation, Coordination and Negotiation

Applying multi-agent theories in modern industrial process control, we divide the object system into several autonomous agents, and utilize coordination, cooperation and negotiation among agents, to achieve systematic function in the higher hierarchy. That is a new direction in complex system research and modeling in latest years [25-28]. Howard et al. [29] develop a generic framework for the control of a system consisting of a collection of agents, in which they model each agent as a coordinated hybrid agent composed of an intelligent coordination layer and a hybrid control layer, which can settle common tasks in dynamic environments more flexibly and potentially. Authors of this paper build a coordination and cooperation mechanism with self-learning ability, which is suitable to the continuous rolling process control, and also avoids the slow speed of BDI model and the difficulty for negotiation and cooperation model content of the requirement in the real-time and global control system, the model with self-coordination mechanism based on reinforcement learning, is planned to be designed in this project, as shown in Fig.2, and meanwhile, both local utility and overall utility are intended to be used to execute the negotiation strategy as in literature [30].

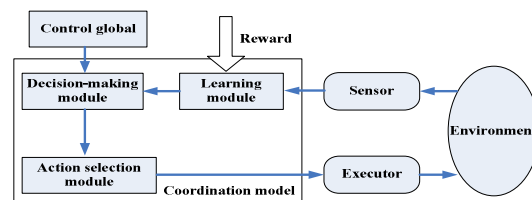


Fig. 2 Coordination and collaboration of the multi-agent control system of the continuous rolling process

Communication

Communication is a significant characteristic for agents. Applying multi-agent theories in industrial process control requires the suitable communication platform, mode, and sorts of messages to interact among agents [31]. Cowling et al. [32] utilize multi-agent method in integrated dynamic scheduling of the hot strip mill and the continuous caster, develop two categories of messages to support communication among agents, i.e. assertions and cooperation messages, which carry out distinct functions, and use XML to form each message. That completes communication between agents easily and effectively.

Future Research

To date there are many research achievements for multi-agent theories applied in industrial process control, while in the process of theoretical research on the architecture, algorithm, coordination, cooperation, negotiation and communication of multi-agent theories, and in practical industrial process control, there are a great many difficult problems that have not been resolved yet.

The multi-agent theoretical research, which needs to be improved mainly includes:

Architecture: hybrid architecture of MAS counterpoises advantages and shortcomings of centralized and distributed MAS and adapts a complex, open and dynamic environment better. Developing the hybrid structure of MAS is the further research direction.

Algorithm: the algorithm with simple structure, easy implementation, good robustness, high efficiency in problem solving and strong currency, is a main aspect to be studied.

Coordination and cooperation mechanism, integrate and counterpoise with negotiation, develop the general autonomous negotiation strategy and framework, excavate the potential possibility of automatic, humanoid coordination, cooperation and negotiation.

Communication: constituting the secure, credible, integrated and general communication protocol, building real-time, rational communication model and realizing high efficient communication are main points for further study.

Combining characteristics of industrial process control, the application of multi-agent theories in it needs to be improved mainly includes:

When multi-agent theories are applied in practical industrial process control, there are multi-targets to evaluate the application value of MAS, such as user interface, system stability, security, accuracy of learning mechanism, reliability and real-time learning and robustness, which are further research and amelioration, to achieve comprehensive optimization of examination targets.

For industrial process control's real-time and dynamic nature, how to utilize model encapsulation and measurement of MAS, to settle dynamic and intelligent reconfiguration issues much more safely and efficiently, is the further research.

How to emulate human's prominent capability in controlling and possess human's flexibility, validity and intelligence in control strategy, based on the summarization of skillful operators' knowledge and experiences, is a significant study.

Concluding Remarks

For industrial processes and control structures, the inherent identity in local control and distributed decision-making, provides a wide range of application for multi-agent theories, which are the key theoretical foundation for industrial process control in next generation, to accomplish decreasing the production cost, distributed control, self-adaptation and dealing with the complex process. How to perfect theory methods further, resolve theoretical problems, and build the rational and general MAS framework, to apply to the practical industrial process control, has an important significance in theoretical research and practical applications. Further study and development of multi-agent theories used in industrial process control is a significant research direction for a long time, and assuredly, there will be new achievements.

References

- [1] V. Mark: IEEE Intell. Syst., vol.20 (2005), p. 27-35
- [2] W. Wang and T.Y. Chai: Control Engineering of China, vol.13 (2006), p. 1-5
- [3] P.Vrba, P.Tichý, V.Mařík, and et al.: IEEE Trans. Syst. Man, Cybern.,C, vol.41 (2011), p. 14-30
- [4] H.W.Zhao, Y.M.Qi, J.Y.Zhan and Y.H.Yuan: 5th Int. Conf. Frontier of Comput. Sci. Technol. (FCST) (2010), p. 576-581
- [5] W.Lepuschitz, A.Zoitl, M.Vallée and M.Merdan: IEEE Trans. Syst. Man, Cybern., C, vol.41 (2011), p. 52-69
- [6] W.C. Regli, I. Mayk, C.J. Dugan, J.B. Kopena and et al.: IEEE Trans. Syst. Man, Cybern., C, vol.39 (2009), p. 572-596
- [7] M. Wooldridge: Appl. Artif. Intell., vol.14 (2000), p. 623-644

-
- [8] J. Dong: *Study on Coordination and Evolution Mechanism in Agent-based Artificial Life Intelligent System* (University of Science and Technology Beijing 2007).
- [9] J.S. Heo and K.Y. Lee: IEEE Power Engineering Society General Meeting, vol.2 (2005), p. 1050-1055
- [10] A.W. Colombo, R. Schoop and R. Neubert: IEEE Trans. Ind. Electron., vol.53 (2006), p. 322-337
- [11] T. He and Z.X. Bai: Modern Electronic Technology, vol.14 (2006), p. 31-34
- [12] C.H. Han, J.M. Douglas and G. Stephanopoulos: Comput. Chem. Eng., vol.19 (1995), p. S63-S69
- [13] S.M. Deen: *Agent Based Manufacturing: Advances in the Holonic Approach* (Heidelberg: Springer 2003).
- [14] G. Adriana and V. Botti: J. Intell. Manuf., vol.15 (2004), p. 645-659
- [15] V. Mařík and J. Lažanský: Control Eng. Pract., vol.15 (2007), p. 1364-1380
- [16] S.B. Tan, Y.L. Jiang, H. Zhang and J.C. Liu: P. World Congr. Intell. Contr. Autom. (WCICA), (2011), p. 75-78
- [17] B.C. Feng: Control Theory and Applications, vol.21 (2004), p. 855-857
- [18] B.N. Wang, Y. Gao, Z.Q. Chen, J.Y. Xie and S.F. Chen: J. Netw. Comput. Appl., vol. 30 (2006), p. 1366-1376
- [19] B. Zhao, C.X. Guo and Y.J. Cao: IEEE Trans. Power Syst., vol. 20 (2005), p. 1070-1078
- [20] V. Machado, A. Neto and J.D. de Melo: IEEE Trans. Ind. Electron., vol. 57 (2010), p. 1823-1834
- [21] C.S. Lee and C.Y. Pan: Fuzzy Set. Syst., vol. 142 (2004), p. 467-488
- [22] W.C. Lee, S.K. Chen and C.C. Wu: Expert Syst. Appl., vol.37 (2010), p. 6594-6601
- [23] C.W. Anderson, D.C. Hittle, A.D. Katz and R.M. Kretchmar: Artif. Intell. Eng., vol. 11 (1997), p. 421-429
- [24] Z. Ren and C.J. Anumba: Adv. Eng. Inform., vol.16 (2002), p. 265-275
- [25] N.R. Jennings and S. Bussmann: IEEE Contr. Syst. Mag., vol.23 (2003), p. 61-73
- [26] Y.S. Ng and R. Srinivasan: Eng. Appl. Artif. Intell., vol.23 (2010), p. 934-949
- [27] J.S. Heo and K.Y. Lee: IEEE Power Engineering Society General Meeting, (2006), p. 18-22
- [28] W.M. Shen, Q. Hao, H.J. Yoon and D.H. Norrie: Adv. Eng. Inform., vol.20 (2006), p. 415-431
- [29] H. Li, F. Karray, O. Basir and I. Song: IEEE Trans. Syst. Man, Cybern., A, vol.38 (2008), p. 534-548
- [30] L. Hodge and M. Kamel: IEEE Trans. Syst. Man, Cybern., A, vol. 33 (2003), p. 648-662
- [31] S.Y. Ding, X.Q. Feng, J. Yang and R.B. Ma: 8th Int. Conf. Electron. Meas. Instr. (ICEMI), (2007), p. 755-759
- [32] P.I. Cowling, D. Ouelhadj and S. Petrovic: J. Intell. Manuf., vol.14 (2003), p. 457-470

A Simulation Research of Artificial Intelligence Control

Xiong Xin¹ and Lu Chaodong^{2,1}

¹Henan Institute of Engineering, Zhengzhou, Henan, 451191

²Wuhan University of Technology, Wuhan, Hubei, 430070

xiongxin@hrsk.net

Keywords: Intelligent Control, Artificial Intelligence, PID Control

Abstract. The traditional control system can not meet the more complex control tasks of the problem, using artificial intelligence control method of imitation, artificial intelligence control system on the overall structure of the design, and given the specific control algorithms. System relies on accurately identify the various features of the error and make the appropriate decisions to multiplexing, open, closed loop control mode of combining control and solve the complex control of the process of identification, decision-making and control problems and achieve A unified identification control.

Introductions

60s of last century, automatic control theory and technology is a powerful, artificial intelligence research have begun to rise, first proposed in 1966, JM Mendel of artificial intelligence for spacecraft control system design [1]; 1971, the famous scholar KS Fu from the perspective of the development of learning control was first proposed intelligent control this emerging discipline [2]; 1977, Saridis from the control theory point of view, put forward a hierarchical intelligent control structure [3]; KJ Astrom proposed " expert control system "[4]. In the ensuing decades, neural networks, fuzzy control, intelligent control of optimization theory has been widespread concern.

Intelligent control is artificial intelligence, operations research and automatic control of the intersection of three disciplines. It is the traditional control of the advanced stage of development, primarily those who use traditional methods to solve difficult to resolve complex system control. These include intelligent robotic systems, complex industrial process control systems.

It's for some of the production process or control objects, difficult to use the general laws of physics or chemistry to create a mathematical model. The object of many factors, some of the factors and the cross coupling between, making the model is very complex and not easy to build, and sometimes not even find the real meaning. For the sort of production process or the controlled object, such as the use of classical control theory and modern control theory methods to design control systems, it is obvious very difficult to have good control effect. But in fact difficult for this type of automatic control of the production process or the controlled object, an experienced operator can manually control but often to achieve a satisfactory control effect. Therefore, the proposed imitation artificial intelligence control, control structure and control behavior from both mimic some of the features and functions, including the identification of people's online properties, characteristics such as memory and logic inference intuition. The intelligent control algorithm can not predict the information needs of online identification controlled object is not an accurate model, we can achieve fast and high precision control, and has strong robustness.

Control the overall design of artificial intelligence imitation

Control Model Comparison and Selection. PID control to a certain extent, imitating the process of manual control, but can not completely imitate the manual control of the whole process [5]. Manual control of the process can also be viewed as a special kind of PID control process, but manual control, compared with the ordinary PID control has obvious difference. Specific performance:

Observation of the human eye has the intelligence and nonlinear characteristics, and the measurement instrument is linear, and no intelligence;

To the error by looking at the size and direction of the control object also proportional control, but the analysis and control of human decision-making and real-time nonlinear time-varying, and has ability to learn, and the role of an ordinary PID controller, only the performance of the ratio of for the simple linear proportional relationship;

It the person's memory effect through the brain accumulation of errors arising from the role of integral control. People are strong and selective memory, people in the adjustment process in the memory of those who have chosen to useful information while ignoring unwanted parts. Ordinary PID controller integral action is not indiscriminately memory all the information, which will contain useless or even harmful information, thereby controlling the level of people can not be achieved the role;

The error by looking at changes to the size and direction of the control object also differential control, and error variation of observation and control decision-making with "predictable" and "selective" to distinguish between changes in the causes of errors take the appropriate control strategy, not only obvious effect of large changes, the error for the slow changes can also be effectively controlled.

The role of ordinary differential PID controller is the error produced by a variety of reasons are treated the same, the trend of large sensitive and difficult to change in response to a slow trend.

For example of the temperature and humidity control: The sensor detects the temperature, humidity, through the corresponding transmitter is converted to DC signals, placed in front of the machine (from the machine) into the controller (host). According to the testing parameters of the host data processing, and control signals are sent to the corresponding actuator solenoid valve to regulate the gas flow, to achieve temperature, humidity and other environmental parameters of the intelligent control. Temperature, humidity, electromagnetic valve by adjusting the appropriate enforcement agency to change the temperature and humidity values, for this process, the object of the mathematical model can be simplified to first order approximation of the inertia plus dead time model, with the transfer function can be expressed as:

$$G(S) = \frac{K}{TS + 1} e^{-\tau s}$$

Where T is the time constant, τ is the time delay

Meanwhile, the temperature of the transfer function $G(S)$ can be simplified to the second inertia model: $G(S) = \frac{K}{(TS + 1)(tS + a)}$

Although this is a very simple mathematical model, but difficult to establish precise temperature, humidity mathematical model, using the classical control theory and modern control theory to design the temperature and humidity control system, it has been difficult to obtain satisfactory control effects, so in a more complex environment parameter control process, using traditional control methods can not adapt to complex environmental parameters.

As can be seen by comparing the above, we use simulation intelligent control method, the error will be very help identify the various features, which make the corresponding control mode to control. It can effectively control the speed of protection, stability and accuracy.

System Structure .Imitation artificial intelligence control system will be divided into the following four components, the system structure shown in Figure 1:

Imitation of artificial intelligence controller: control by computer simulation of artificial intelligence algorithms digital controller.

The input and output interface devices: imitation artificial intelligence control device through the input interface to get the signal from the controlled object, the output interface device through the artificial intelligence controller to imitate the output control signals to the implementing agency, the purpose to control the controlled object.

Generalized objects: including the implementing agencies and charged objects. Controlled object which can be linear or nonlinear, steady or time-varying, single-variable or variables, there is a strong pure time delay and the interference of the object.

Sensor: its role is to be charged object or the production process of electricity or electricity signal is converted to a standard computer can accept voltage or standard current signal. That the conversion accuracy of the level of the control system performance greatly.

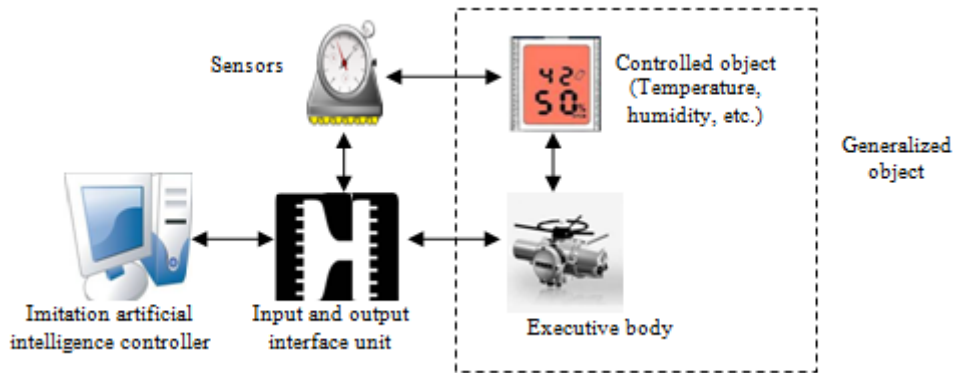


Fig. 1 Control system structure of artificial intelligence imitation

Imitation artificial intelligence control algorithm

Select the appropriate control mode control is the core of algorithm design, simulation of artificial intelligence control algorithm is mainly based on the size of the controller input signal, the direction of its trend to make the appropriate decision-making, relying on accurate identification of the various errors features and make the appropriate decisions and to multiplexer, open, closed loop control mode of combining control. This flexible and clever to rely on the identification, decision-making and control, so for those who control quality of checks and balances (fast, smooth and precision) under the control algorithm is easy to unity. Imitation artificial intelligence control algorithm can be described as follows:

If $|e_n| > M_1$, then output $P_0 = FFH$ or $P_0 = 00H$, Using the switch mode control;

When $e_n \bullet \Delta e_n > 0$ or $\Delta e_n = 0, e_n \neq 0$, and $|e_n| \geq M_2$, then output $P_{0(n-1)} + K_1 K_{pe_n}$, When $e_n \bullet \Delta e_n > 0$ or $\Delta e_n = 0, e_n \neq 0$, and $|e_n| < M_2$, then output $P_{0(n-1)} + K_{pe_n}$, Using proportional control mode; When $e_n \bullet \Delta e_n < 0, \Delta e_n \bullet \Delta e_{n-1} > 0$ or $e_n = 0$, then output $P_{0(n)} = P_{0(n-1)}$, Used to maintain control mode 1; When $e_n \bullet \Delta e_n < 0$ or $\Delta e_n \bullet \Delta e_{n-1} < 0$, and $|e_n| \geq M_2$, then output $P_{0(n-1)} + K_1 K_2 K_{pe_{m_n}}$, Used to maintain control mode 2; When $e_n \bullet \Delta e_n < 0$ or $\Delta e_n \bullet \Delta e_{n-1} < 0$, and $|e_n| < M_2$, then output $P_{0(n-1)} + K_2 K_{pe_{m_n}}$, Used to maintain control mode 2;

After discrimination with the current value of e_n e said, Expressed by e_{n-1} e_{n-2} e cycles before the value of 1 and 2, $\Delta e = e_n - e_{n-1}$ $\Delta e_{n-1} = e_{n-1} - e_{n-2}$ represents the current and previous cycle of time difference e .

Where $e_{m \bullet n}$ is the first n -pole plant of e ; K_p is the proportional gain; K_1 is the gain amplification factor, and $K_1 > 1$; K_2 is the inhibition coefficient, and $0 < K_2 < 1$; M_1, M_2 is the set error limits, and $M_1 > M_2$; n is a natural number, indicating the serial number of the control cycle; $P_{0(n)}$ is the output P for the first time the need to maintain the value of n ; $P_{0(n-1)}$ is the n one cycle before the output to maintain the value of P ; Analysis of the above algorithm as follows:

When the error increases the absolute value of e , which is characterized $e_n \bullet \Delta e_n > 0$: When the error decreases when the absolute value of e , which is characterized $e_n \bullet \Delta e_n < 0$; at the pole t_1 and t_3 , with features $\Delta e_n \bullet \Delta e_{n-1} < 0$; on the contrary, if the $\Delta e_n \bullet \Delta e_{n-1} > 0$, said the system polarity.

When the error is $|e_n| > M_1$, is used to control switch mode; only when the $|e_n| \leq M_1$, the characteristics can be the basis of its corresponding control mode. When the error of the trend toward increased, the amount can be increased in order to adjust the bias control, this time with the ratio model, K_p will get a large proportional gain. When the $|e_n| \geq M_2$, can be multiplied by the gain amplification factor K_p & K_1 , makes the control volume becomes larger. When the error reaches extreme t_1 & t_3 time, you can maintain the value of the original on the basis of a modest increase in the value of (hold mode 2), e to maintain that output up to date against No. (Hold mode 1).

In practical applications, the error curve may be more complex, although there t_1 & t_2 extreme point, but before and after these two points, the error e trends are different, Expressed as: Points in t_1 : $\Delta e_n \bullet \Delta e_{n-1} < 0, e_n \bullet \Delta e_n < 0$; Points in t_2 : $\Delta e_n \bullet \Delta e_{n-1} < 0, e_n \bullet \Delta e_n > 0$. t_1 Point in the use of protective mode 2, the proportion of the t_2 point mode is available; otherwise it will extend the transition process.

Control applications in the system, the conventional proportional control, if a larger proportion of the gain, it will cause system instability. However, in imitation of the proportion of artificial intelligence control algorithm the control period, but will not cause a large K_p system instability, because as long as the error is more than extreme point, the controller will switch to hold mode, not only reduces the control time volume, is more important is to keep the system open-loop model is equivalent to running, the controller output has nothing to do with the current conditions, it is the characteristic quantity by the memory control.

In imitation of artificial intelligence control, when the error when $e = 0$, indicating that the system is in balance, in this case, so long as to maintain this energy balance can be, without having to modify the controller's output, this time can be based on changes, then make new decisions and decision-making. It can be shown that a class of integral functions hold mode, meaning that it can eliminate the residual and thus rely on precise control.

Conclusions

In traditional control systems, control task or request output is constant (control system), or ask to follow the desired output trajectory (tracking system), thus the control requirements of the task relatively simple. The intelligent control system, its requirements are often more complex tasks. For a problem of input, the system needs to have some intelligent behavior; the solution can generate suitable responses. This imitation of artificial intelligence research in the control method, relying on accurately identify the various features of the error and make the appropriate decisions and to multiplexer, open, closed loop control mode is a combination of control, flexible and smart identification, Juice and control, easy to identify a unified control to intelligent control.

References

- [1] Applications of artificial intelligence techniques to a spacecraft control problem. Self-organizing Control systems. Douglas Aircraft Company, 1966.
- [2] Fu K S. Learning Control Systems and Intelligent Control Systems: A Intersection of Artificial Intelligence and Automatic Control. IEEE Trans, 1971, AC-16(1): 70-72.
- [3] Saridis G N. Self-Organizing Control of stochastic systems, Marcel Dekker, New York, 1977: 1-20.
- [4] Astrom K J. Anton J J. Arzen K E. Expert control. Auto-matica, 1986,22(3):277-286.
- [5] Spyros Tzafestas, Nikolaos P Pahanikolopoulos, Incremental fuzzy expert PID control. IEEE Transactions on Industrial Electronics, 1996,37(5): 365~371.

Flowers Temperature and Humidity Control System based on Applied Mechanics

Shao WenMian¹, Li HaiTao² and Jin LiHong¹

¹ Heilongjiang Institute of Science and Technology, Harbin, 150000, China;

² Harbin Institute of Technology, Harbin, 150000, China

Keywords: Flower Greenhouse Temperature; Temperature; Humidity; Automatic Control; PLC

Abstract. Aim to the current shortcomings manual control system of greenhouse flowers and plants, designed of the temperature and humidity control system, introduced the system, working principle and structure in detail to the composition of the various parts of hardware and software components of the processes, PLC as the core of the system, chosen DS18B20 single-wire digital temperature sensor, IH3605 humidity sensors, digital to analog converter, digital display, auxiliary equipment, implemented the automatic control of the flower greenhouse temperature and humidity, had characteristic such as simple structure, high reliability, cost-effective, good temperature, to promote the value of a wide range and so on.

Introduction

As society develops and people's living standards improve, people had become increasingly demanding spiritual life, the demand for flowers and nursery stock would become more and more, while the shortcomings of manual control of greenhouse flowers, for effective control greenhouse temperature and humidity, introduced advanced control methods to the flowers and nursery stock production, the modern greenhouse control system has entered a new stage.

How to use the automatic control system to effectively control greenhouse temperature and humidity, managed efficiently of flower cultivation, was an important topic of greenhouse studies. That's PLC as the core of the design to achieve automatic adjustment of temperature and humidity, with high reliability and stable.

Structural design:

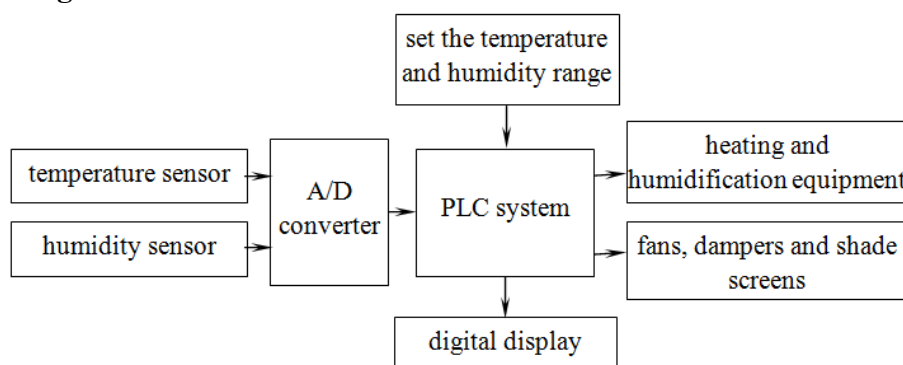


Fig. 1 System Block Diagram

That's PLC as the core of the system by the temperature sensor, humidity sensor, analog to digital converters, digital display and ancillary equipment form, as shown in Fig. 1. System work, PLC system was activated, with keyboard setting the scope of temperature and humidity control, PLC system through the temperature sensor and humidity sensor measurements of temperature and humidity inside the greenhouse and in setting the scope of comparison, if the temperature and humidity inside the greenhouse exceeded the setting range, PLC system connected to the output commands to control fans, dampers, shade screens start to set the range of temperature and humidity dropped, if the greenhouse temperature and humidity was less than the limits set, PLC system to output instructions control of heating, humidification equipment to start, was promoted to set the temperature and humidity range^[2].

Hardware design

Sensor design Sensors. Was able to feel in accordance with the provisions of certain laws to be measured and converted into a class of the output signal device or devices [1]. Usually sensitive components and conversion components as the application of semiconductor devices and integrated technology in sensors, sensor signal conditioning and conversion circuits can be installed inside the shell of the sensor or sensor with integrated in the same chip. Human society had entered the information age, people relied mainly on social activities, the development of information resources and access, transmission and processing. Sensors in the study and test system interface position, namely: the first detection and control system. Therefore, the sensor as perception, information acquisition and monitoring of the window, all scientific research, automatic control systems and automated production process to get the information to be obtained through the sensors and through it easily converted to electrical signal transmission and processing.

Temperature sensor DALLAS Semiconductor Corporation by the United States DS18B20 single-wire digital temperature sensor, DALLAS-wire digital temperature sensor, the latest "first-line device" smaller, for a voltage wider, more economical, was the first one to support "first-line bus" interface temperature sensor. Bus line was unique and economical features, allowing users to easily set up the sensor network, introduced a new concept of the construction of measurement system. DS18B20 to be completed in the temperature sensor measuring the temperature to 12-bit conversion example: sign extension with 16-bit binary form of complement readings to $0.0625\text{ }^{\circ}\text{C}$ / LSB forms of expression, where S is the sign bit. This was obtained 12-bit conversion to 12-bit data, stored in a 18B20 in the two 8-bit RAM, 5-bit binary in front was sign bit, if the measured temperature was greater than 0, it was 0, as long as measured values would be multiplied by 0.0625 to get the actual temperature; If the temperature is less than 0, it was 1, the measured value was inverted plus 1 multiplied by the actual temperature can be obtained at 0.0625. DS18B20 also supported "bus line" interface, measuring temperature range is $-55\text{ }^{\circ}\text{C} \sim +125\text{ }^{\circ}\text{C}$, at $-10 \sim +85\text{ }^{\circ}\text{C}$ range, accuracy $\pm 0.5\text{ }^{\circ}\text{C}$. Temperature directly to the scene "bus line" meant the number of transmission, greatly improved the system's interference. DS18B20 to the voltage, characteristics, and packaging had more choices so that we can build the economy for their own temperature system.

DS18B20's internal structure: Mainly consisted of four parts: a 64-bit lithography ROM, temperature sensor, non-volatile temperature alarm triggers TH and TL, configuration registers.

DS18B20 precautions in use DS18B20 temperature measurement system, while having a simple, high precision temperature measurement, convenient connection port takes advantages of fewer lines, but in practical applications should note the following issues:

The smaller hardware overhead required to compensate for a relatively complex software, as DS18B20 and serial data transfer between the microprocessor, so read and write in the DS18B20 program must be rigorous to ensure that read and write timing, otherwise can not read the temperature results. Using PL / M, C and other high-level language for system programming, the operation of some of the best adopted DS18B20 assembly language.

In the DS1820 no reference to the relevant information linked number to a single DS1820 on the bus, could mistakenly believe that you can hang any number of DS18B20, was not the case in practical applications. When hung on a single bus DS18B20 more than 8, they needed to solve the problem of the microprocessor bus driver, which is conducting multi-point temperature measurement system design should be noted.

Connection DS18B20 the length of the bus cable was limited. Testing, when using common signal cable longer than 50m transfer, the measurement data read errors would occur. When the bus cable to twisted-pair shielded cable, the normal communication distance up to 150m, the number of strands per meter when using the more twisted-pair shielded cable, the normal communication range further extended. This was mainly distributed by the bus capacitance of the signal distortion caused by the waveform generator. Therefore, with the DS1820 temperature measurement system designed for long distance to give full consideration to the distribution bus capacitance and impedance matching problems.

DS18B20 temperature programming design, temperature conversion order issued to the DS18B20, the program always had to wait for the return signal DS1820, once a DS18B20 a bad contact or broken, when the program read the DS1820, it would not return the signal, the program entered an endless loop. This DS18B20 hardware connection and software during the design should give some attention.

Humidity Sensor Produced by HONEYWELL integrated humidity sensor IH3605, using SIP package, can be done internally in the integrated circuit to adjust the signal, and with high precision, good linearity, interchangeability, and many other advantages, so widely used.

The main parameters

Power supply voltage: 4 ~ 5.8V

Supply Current: 200 μ A (DC5V)

Humidity range: 0 ~ 100% RH

Accuracy: $\pm 2\%$ RH (0 ~ 100YoRH, 25 °C, V = DC5V)

Interchangeability: $\pm 5\%$ RH (0 ~ 60% RH); $\pm 8\%$ RH (900RH) $\pm \pm$

Linearity: $\pm 0.5\%$ RH (typical)

Repeatability: $\pm 0.5\%$ RH

Stability: $\pm 1\%$ ARH (50% RH, 5 years)

Response time: 15S (25 °C, and the slow flow of air environment)

Operating temperature: -40 ~ 85 °C

Working principle Since both the internal heat of IH3605 polymer layer formed between the capacitance of the capacitor plates the size of the different classes change with humidity, Completed on the humidity signal acquisition. Heat of the polymer layer had both defensive dirt, dust, oil and other harmful substances function. IH3605 output voltage was the supply voltage, humidity and temperature functions. Power supply voltage increasing, the proportion of the output voltage would become higher. In practice, the first calculation of the temperature under the conditions of 25 °C relative humidity RHO, $V_{out} = V_{Dc} (0.062Rho + 0.16)$. V_{out} was the power supply voltage for the IH3605, RHO 25 °C relative humidity, and temperature compensation calculated the actual current temperature relative humidity values RH. $RH = RH / (1.0546 - 0.00216t)$, RH was the actual value of the relative humidity, t is the current temperature As IH3605 and linear output voltage higher than Okay, the circuit without the need for signal amplification and signal conditioning. IH3605 output signals can be received directly A/D converter, completed analog to digital conversion.

Temperature and humidity sensors If the greenhouse temperature and humidity control requirements of the not particularly precise, requiring a very small error was not the case, it can be integrated with the temperature and humidity sensor, Vaisala temperature and humidity sensor company, the model was HMW40Y. This sensor had high accuracy, short response time, and low demand on the environment, easy to install and so on. The main performance indicators are as follows:

Humidity: 10% ~ 90% RH

Temperature: -5 ~ 55 °C

Accuracy: $\pm 3\%$ RH, ± 0.3 °C

Output signal: 4 ~ 20mA

A/D converter design The design of A/D converter chip's serial Ti chip TLC2543 [3], A/D converter TLC2543 and PLC as the interface circuit, it was a use of 12-bit successive approximation analog switched-capacitor ADC, on-chip 14-bit channels, the output pins can be directly parallel with the PLCI/O port connections. With 12-bit resolution A/D conversion port range in the calibration conversion time was 10 microseconds, the output data length of the programmable chip come with sample and hold circuit.

PLC system design Siemens CTS7-200 [5], CTS7-200 PLC series of small programmable controllers can be used in PLC automatic control system for a variety of small, highly integrated design, low cost so that people were not only the ideal small control solution.

Advantages: high reliability; a rich instruction set; The speed of fast floating-point operations; extensive expansion modules; strong internal integration

Schema: CTS7-200 CPU to a microprocessor, an integrated power supply and digital I / O points in a single compact package, thus forming a powerful small programmable logic controller. CTS7-200 offered two specifications of the CPU to apply to different applications.

Expansion module: To meet the needs of the user a variety of applications, CTS7-200 Series offered a variety of specifications expansion I/O modules to use with these modules and the CPU to complete a variety of complex control.

4 Design of the keyboard and digital display

P3 keyboard port for the high-5^[4], including setting key 1, UP key, DELAY button, DOWN button and set the key 2 keys, etc. 5. Setting key 1, key 2, UP, DOWN with the use, it can completed upper and lower limits of detection range of temperature and humidity settings, and system communication address setting, and five keys can be done with the system calibration.LED digital display digital display can be used.

Auxiliary equipment design

Auxiliary equipment were heating equipment, humidification equipment, fans, dampers, shade screens and other components, and the relay connected auxiliary equipment to systems, which program control by the system startup and shutdown. When the temperature and humidity higher or lower the set value, PLC needed to relay to control the work of the corresponding auxiliary equipment, it can use model G2R1A-12DC, and use of high voltage, high current, internal silicon seven NPN Darlington driver chip composed of ULN2003A to drive^[5].

Humidification equipment with sprinkler system, sprinkler system was the use of machinery and power equipment, water through the nozzle (or nozzles) was shot to the air, landing to the state droplet spray method. Sprinkler equipment composed by inlet, pumps, pipes, distribution and nozzles (or nozzle) and other components, which can be fixed or mobile.

Software part of the design

Software designs program with Siemens Step7-Micro/WIN to achieve various functions. The software achieved the temperature and humidity display, A/D conversion, automatic control temperature, humidity regulation and other functions, with the main program called each subroutine to achieve the corresponding functions. System reset, it would call the initialization procedure initialized the port of PLC, needed to use the memory cell clearly, written the temperature and humidity to upper and lower limits initial value to memory unit and displayed on the digital display. When initialized, called A/D conversion routine, the temperature and humidity sensor circuit from the analog signals into digital signals, to facilitate the PLC to read and convert. Then called and displayed subroutine to convert the data through a dynamic to digital. Each time would read the data, the lower judge, to decide whether to call the thermostat, humidity subroutine. If the temperature and humidity higher than the upper limit, start cooling, humidity device, also if the lower limit, start device to warming. That`s main program flow chart shown in Fig. 2.

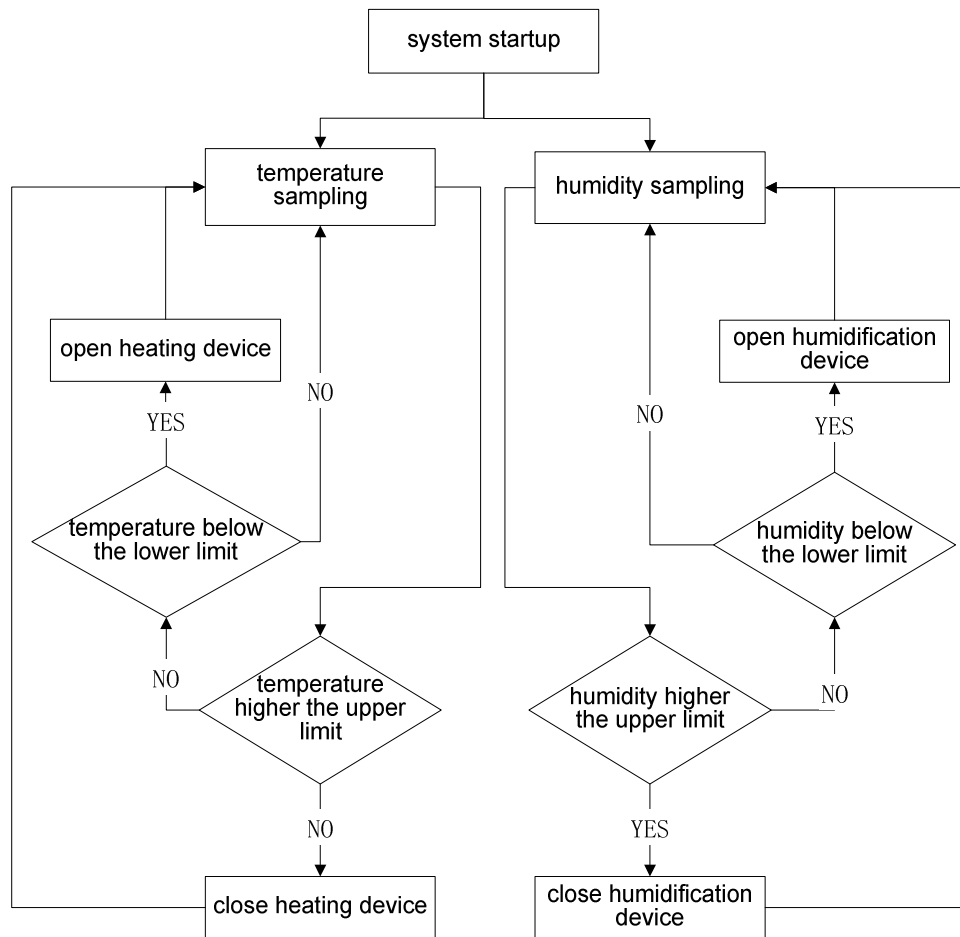


Fig. 2 Main program flow

Conclusion

Flower greenhouse temperature and humidity control system used fuzzy combined with the traditional control method, effectively solved the traditional control deficiencies; also designed module interface and can achieve large-scale greenhouse production and unified management control. The system was a good man-machine interface, easy operation, high automation, stable and reliable. After the actual planting and experimental verification, it was good effect, effectively reducing the workload of farmers, ensuring the quality of greenhouse flower production, with good prospects and promotional value.

References

- [1] Liu Yingchun, Ye Xiangbin, Sensor Design and Application of the Principle [M]. National Defense University Press, July 2002, the fourth edition of the first printing :1-2
- [2] Xue ling, Sun Man, Zhang Council, etc. AT89C51 Microcontroller based Temperature and Humidity Controller [J]. Process Automation Instrumentation, 2010,37 (7) :66-69
- [3] Liu Qiang Army. Microcontroller-based Temperature and Humidity Measurement and Control [J]. Technology Review ,2009,25:94-96
- [4] Ping Xu, Tian Yu, Zhang Zhenren. Universal Temperature and Humidity Testing Instrument [J]. China Instrument,2004,1:35-37
- [5] CTS7-200 PLC Systems User Manual

Digital I/O Training Kit Development for Arduino Platforms

Hong-Hsin Huang^{1,a}, Chien-Yuan Liu^{2,b}, Ming-Chih Huang^{3,c}, I-Chun Ko^{2,d}
and Jia-Ming Lee^{2,e}

¹Department of Electrical Engineering, Cheng Shiu University, Kaohsiung City, TAIWAN

²Department of Computer Science and Information Engineering, Cheng Shiu University, Kaohsiung City, TAIWAN

³Department of Electrical Engineering, Yu Ta Institute of Technology & Commerce, Ping-Tong County, TAIWAN

^afunns@csu.edu.tw, ^bcyliu@csu.edu.tw, ^cm0919172456@yahoo.com.tw,
^dkm0018103@gcloud.csu.edu.tw, ^ekm9903119@gcloud.csu.edu.tw

Keywords: Digital I/O, Training Kit, Open Source, Arduino.

Abstract. In this paper, a *DIO* training kit developed for fundamental embedded system learning was presented. The jobs of the research comprised the developments of a microcontroller board, four *DIO* functional modules with multiplexing circuit, and some control software. At present, the *DIO* training kit was implemented on an experimental breadboard. The integration and verification of hardware and software were conducted successfully. The results showed that the *DIO* training kit for Arduino platform are extremely suitable to support the Arduino based embedded systems training.

Introduction

Embedded systems are deeply involved in modern life, e.g. smart homes, robotics, safety systems, set-top boxes, healthcare systems, automotive vehicles, and popular consumer electronics [1]. Hence, to learn practical development skills is an important training task in technological colleges.

Generally speaking, a microcontroller is the key element of embedded systems; however peripheral devices and input/output (*I/O*) components in connection with a microcontroller to achieve dedicated automation functions are also indispensable. Furthermore, control programs running within a microcontroller for designated specifications are essential too [2].

To release the overhead during teaching and learning, a digital *I/O* (*DIO*) training kit based on open-source Arduino platform [3] is developed in this research to enhance the performance of teaching and to improve the efficiency of learning by integrating a microcontroller, several *DIO* components, and a bunch of written control programs.

The rest of this paper is organized as follows. Section 2 presents the requirement and functional analysis for the *DIO* training kit. Section 3 describes the design and implementation of the kit in details, containing functional modules, modules multiplexing scheme, hardware software design and implementation. Finally, section 4 gives a brief summary of this research and some future works.

Requirement and Functional Analysis

To develop a training kit for conducting fundamental *DIO* experiments, several previous developed boards and books for microcontrollers were referred [4]. The conclusions of the investigation were as follows. The main control processor of the training kit has better to leverage an open-source platform, including a general microprocessor and a friendly integrated development environment (*IDE*) [5] with a free compiler. Therefore, the Arduino platform was chosen for this purpose. It is introduced in the next sub-section. In additions, several typical *DIO* components were utilized for various basic experiments. They are illustrated in the succeeding sub-section. Finally, the executable functions of the experiments are classified in Table 1.

Table 1 Experiments of *DIO* Training Kit

Basic <i>DIO</i> Experiments	Advanced <i>DIO</i> Experiments
LED Blinking	LED Traffic Signals
LED Fading	LED Rolling One Dice
7-Segments Digits	7-Segments Rolling Four Dices
7-Segments Counting	Timer Setting and Running
LED Array Patterns	Scrolling Marquee
4×4 Keyboard Reading	4×4 K.B Map onto LED Array

Arduino Board. Arduino is a popular open-source single-board microcontroller, designed to make the process of using electronics in multidisciplinary projects more accessible [6]. Arduino developing boards utilize *Atmel AVR* processors and many on-board *I/O* support. For instance, one of them named Duemilanove board as shown in Fig. 1A, adopts *ATMEGA 328P* microcontroller which is an 8-bits microprocessor manufactured by *Atmel*. Fig. 2B showed a compatible one fabricated by ourselves. *ATMEGA 328P* is a standard *TTL* device in *DC 5V*. The chip has 20 pins for diverse *I/O* operations, including 6 analog input (*AI*) pins and 14 *DIO* pins. Six of the 14 *DIO* pins could be programmed to be pulse width modulation (*PWM*) outputs. Others *DIO* could be programmed for general *DI* or *DO* actions. Arduino hardware is programmed by using a C++ like language with slight simplifications and modifications. Via the *IDE*, programmer could upload a sketch (Arduino program) through USB link to *ATMEGA 328P* for control processing. The *IDE* is developed for cross platforms, e.g. Windows, Linux, and MAC OS. Windows *IDE* is utilized in this development. The advantages of Arduino platform contain extended hardware boards, abundant application references, and many available software libraries for application expansions, e.g. communications (UART, I2C, SPI, X10, Bluetooth, ZigBee, and Ethernet, etc.) and peripherals (LCD, LED, EEPROM, SD, Servo, and Motors, etc.). Finally, plenty open resources are increasingly joined the Arduino community to support endless creativeness.

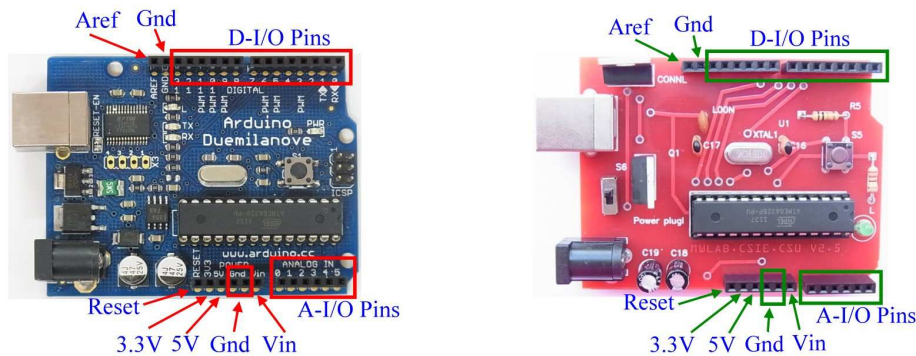


Fig. 1 A Official Duemilanove Board B Compatible Duemilanove Board

Digital I/O Components The components of the training kit contains LED, 8×8 common-cathode LED array, 4×4 keyboard, common positive electrode 7-segments display, 74LS138 decoder, and 74LS373 latch register. There are 9 LED arranged in an 3×3 matrix with red, yellow, and green colors in columns 1, 2, and 3. The matrix would be utilized in related experiments, containing basic LED ON/OFF, traffic signals, and dice rolling. In Fig. 2, the 8×8 LED array has 16 control pins consisted of 8 pins for 8 rows and 8 pins for 8 columns. To turn the top-left corner LED ON, for example, the microcontroller should set HIGH (5V) to row 1 (R1) and set LOW (0V) to column 1 (C1) for the common-cathode LED array. The 4×4 keyboard as shown in Fig. 3 has 8 control pins consisted of 4 pins for 4 rows and 4 pins for 4 columns. To judge the pressed key, a microcontroller should setup 4 *DO* pins from column 1 (C1) to column 4 (C4) separately, and scan the voltage states at 4 *DI* for every columns from row 1 (R1) to row 4 (R4) consecutively. Fig. 4 showed a common positive electrode 7-segments display, it has 12 control pins, including 0, 1, 2, 3, A, B, C, D, E, F, G, and DP (decimal

point). Where, 0~3 need to be connected to 4 DO pins of a microcontroller which would enable each of 4 digits by set HIGH at the corresponding pin. Furthermore, A, B, C, D, E, F, G, and DP must be connected to another 8 DO pins of the microcontroller which would sink current from each of segments by set LOW at the corresponding pin.

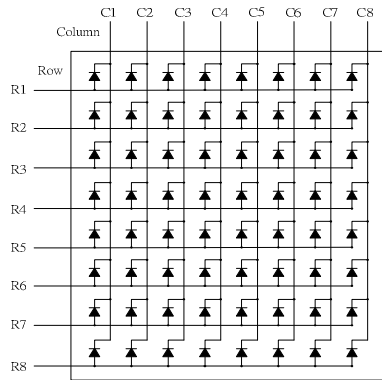


Fig. 2 8x8 LED Array

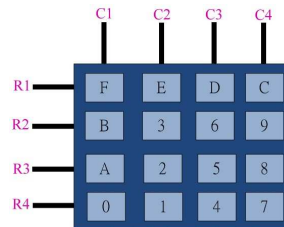


Fig. 3 4x4 Keyboard

The 74LS138o-8 decoder which could setup one of 8 output lines by the combination of 3 selection inputs. Input combination "000" would determine output line 1, for instance, and output line 8 are selected by the input combination "111". The 74LS373 is an 8-bits latch register which has 8 tri-state latches. An input state would be latched on corresponding output line by setup the enabling pin, whereas reset the enabling pin would keep the 8-latches states unchanged until next setup time.

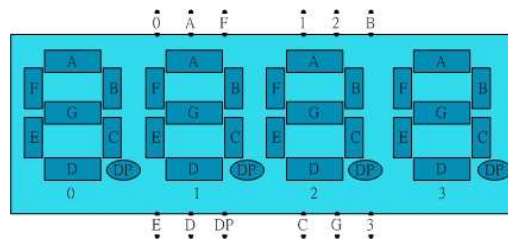


Fig. 4 4-Digits 7-Segments Display

Training Kit Design and Implementation

Functional Modules. The training kit was partitioned into 5 modules, e.g. Microcontroller module, LED module, 7-segments display module, LED array module, and keyboard module. As shown in Fig. 5, the integration of all 5 modules would release both burden of teachers and students. For a teacher, the time for components preparation, components distribution, and components collection is saved. Therefore, the teacher has more time to analyze the function of an experiment, to clarify the operation of the circuit, and to explain the control software flowchart. For students, they won't worry any more about forgetting to bring personal tools for circuit connection and could have more time to understand the circuit function and principle. In addition, the students could focus on control software coding to improve their program writing capabilities. In conclusion, the teaching and learning performance will be enhanced by using the training kit in DIO design and embedded system courses.

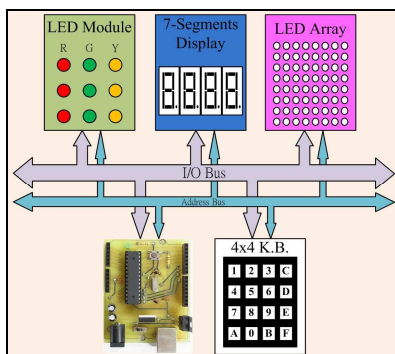


Fig. 5 Functional Modules

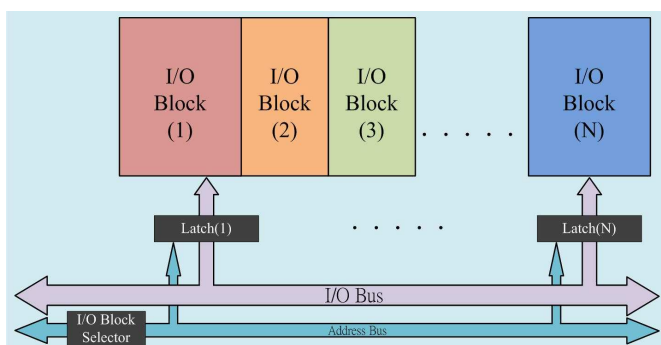


Fig. 6 Multiplexing Scheme

Modules Multiplexing Scheme. *ATMEGA 328P* microcontroller has 20 *I/O* pins. They are not enough for all *DIO* function modules. To virtually extend the *I/O* pins to support all *I/O* modules, a multiplexing scheme is required as shown in Fig. 6. The multiplexer is consisted of one 74LS138 decoder and multiple 74LS373 latch registers. One output line of the 74LS138 decoder is determined by 3 input lines controlled by the microcontroller module. The output line is connected to the enabling pin on the 74LS373 of one of *I/O* blocks. Each *I/O* block is corresponding to a *DIO* functional module. During basic LED blinking experiment, for instance, the multiplexer would enable LED module or block. Accordingly, all necessary control states from *ATMEGA 328P I/O* pins are led to and latched onto the *I/O* lines of the LED module. When rolling dices on a 7-segments display, the multiplexer would enable the 7-segments display module to be connected to all necessary *I/O* pins of microcontroller via the corresponding latches of that *I/O* block. In this manner, all functional modules could be virtually connected to the *I/O* pins of the microcontroller via the intermediate multiplexer. Therefore, the *I/O* pins of *ATMEGA 328P* could be extended for multiple *DIO* experiments.

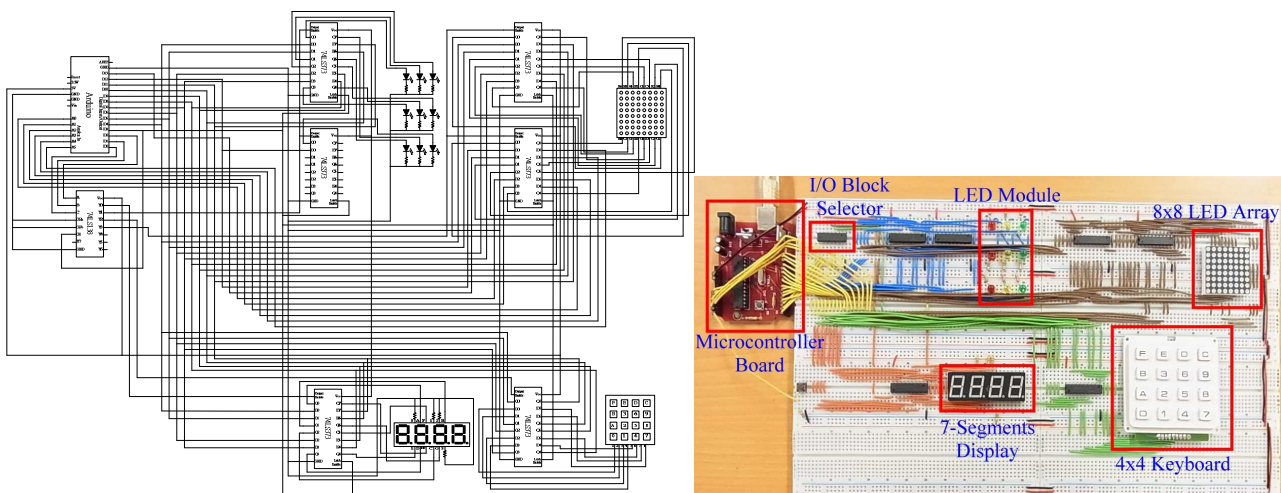


Fig. 7 Circuit Diagram of *DIO* Training Kit Fig. 8 Implementation of *DIO* Training Kit

Hardware Design. The detailed circuit of the *DIO* training kit was shown in Fig. 7. In this Fig., the top left chip is the *ATMEGA 328P* microcontroller. All 20 *I/O* pins are connected to the 74LS138 decoder and 74LS373 latches. $D_0 \sim D_2$ pins are the blocks selection lines of 74LS138. Others *I/O* pins are indirectly connected to separate *DIO* functional modules via the 74LS373. For the LED module, two 74LS373 are utilized to provide 9 output lines for 9 LED. The LED array module needs 16 output lines, thus two 74LS373 are required for the module, too. The 7-segments display utilized 12 output lines, so it also needs two 74LS373. Finally, the 4x4 keyboard module has only 8 lines. Therefore, it merely utilizes one 74LS373. Currently the training kit is temporarily implemented on a breadboard for hardware validation and software verification. Final goal is to build a printed circuit board (*PCB*) of the *DIO* training kit after all necessary expansions and modifications are completed in the near future. Fig. 8 showed the designed hardware board of the *DIO* training kit. The layout of Fig. 8 is similar to that of Fig. 7.

Software Design The control programs for basic *DIO* and advanced *DIO* experiments were developed as the answers for the references by the training students. The program style could be abstracted as the flowchart shown in Fig. 9. In Fig. 9, firstly some related libraries should be included into a experimental program. Then, global variables should be initialized. Next, the process runs into the *setup()* function. This is the first function called by the program. All setup procedures should be done in this function. Such as the mode of each *DIO* pins should be assigned at this stage. Then, the multiplexer should be directed to the corresponding *DIO* functional module utilized by the experiment. Next, the program executes into the endless *loop()* function. This is the key control function of the experiment. All control logic and processing algorithms should be written herein. Since the programming style is pretty clear and logical, it usually isn't difficult for the students to accomplish an experiment per one week, including circuit analysis, module addressing, and program coding.

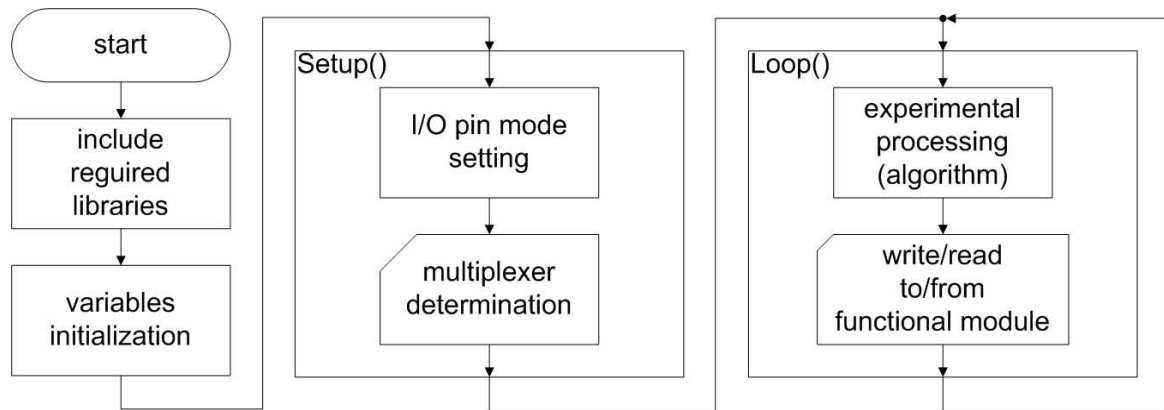


Fig. 9 Typical Flowchart of Experimental Programs

Summary

This paper presents a development research for a *DIO* training kit. The kit is based on the open-source Arduino platform. A compatible Duemilanove board was fabricated for using as the microcontroller module. A breadboard consisted of LED module, LED array module, 7-segments display module, and keyboard module was prototyped. The integration of all above modules and experimental programs are verified regarding the functional requirement specified at the analysis stage. The development is successfully completed at present. Meanwhile, two extra functions will be included recently in the revised kit to enhance the experiments, e.g. LCD display and buzzer.

Acknowledgement

We acknowledge the support of No. 1010046558V from the Department of Technological and Vocational Education, Ministry of Education, TAIWAN.

References

- [1] E. Brunvand and P. Stout, Kinetic art and embedded systems: a natural collaboration. Proceedings of the 42nd ACM technical symposium on Computer science education, Dallas, Texas, USA, March 9-12, 2011.
- [2] Stollenwerk, A modular, robust and open source microcontroller platform for broad educational usage, Proceedings of the 2010 Workshop on Embedded Systems Education, Scottsdale, Arizona, USA, 2010..
- [3] <http://en.wikipedia.org/wiki/Arduino>.
- [4] S. Piperidis, L. Doitsides, C. Anastasopoulos, and N.C. Tsourveloudis, A Low Cost Modular Robot Vehicle Design for Research and Education, Proceedings of Mediterranean Conference on Control and Automation (2007), Athens, Greece, p.T30-026.
- [5] David J. Russell, Introduction to Embedded Systems: Using ANSI C and the Arduino Development Environment. Synthesis Lectures on Digital Circuits and Systems, Vol. 5, No. 1, Pages 1-275, 2010.
- [6] A. Knörig, R. Wettach, J. Cohen, Fritzing - A Tool for Advancing Electronic Prototyping for Designers, Proceedings of the 3rd International Conference on Tangible and Embedded Interaction (TEI'09), Feb 16-18 2009, Cambridge, UK, p.351-358.

Application of Modular Design in the Intelligent Building Product Designing

CHEN Liang, JIAO Rong, LIAO Jinqun

Chongqing College of Electronic Engineering, Chongqing 401331

chenliang@hrsk.net

Keywords: Modular; Design; Intelligent Building; Application

Abstract. Modular design is a standardized approach to organically combine standardization and diversification and to effectively integrate multi-type and small volume-production with efficiency, which is a new technology that has been applied universally. Its basic methods contain the four aspects of identifying the destination domain of modular product, etc. In China, there are about hundreds of intelligent building intercom system manufacturers and products. However, how to make the product internal structure design standardized and modularized and realize the compatibility of different manufacturers' products is a problem necessary to be resolved in this industry. This paper conducts modular design concerning about intelligent building intercom system products, and combines the green design thought with modular design method, which can simultaneously fulfill the product's functional and environmental properties, exerting highly significant roles in the R & D, increasing the production efficiency, reducing cost and improving enterprise management. From a long term, system modular design is the development trend of intelligent buildings.

Introduction

Modular design partitions and designs a series of functional modules, and also constitutes the products customized by different customers by selecting and combining modules, based on the functional analysis on the products with different functions or identical functions of different performances and specifications, to satisfy the different needs at market. Simply speaking, it combines some elements of product together to constitute a sub-system with specific functions, and then takes the sub-system as general module for multi-combination with other product's elements, generating series of products with different functions or identical functions of different performances. Actually, this is the application of similarity theory in the product function and structure, and also is a standardized approach to achieve the organic combination of standardization and diversification, and to effectively integrate multi-type and small volume-production with efficiency. Besides, it is a new developing design thought based on the traditional design, and has become a new technology that has been applied universally. Particularly, along with the continuous innovation and evolution of electronic products in the information era, modular design products are emerging constantly.

Modular Design Approach

In the whole style design of industrial products, concerning about the module designing methods of all objectives of product's whole life cycle, the modular design approach can be applied in the implementations of new-product module design, non-modular product module design and the existing-modular product module improvement design. The basic methods are as shown in Fig. 1

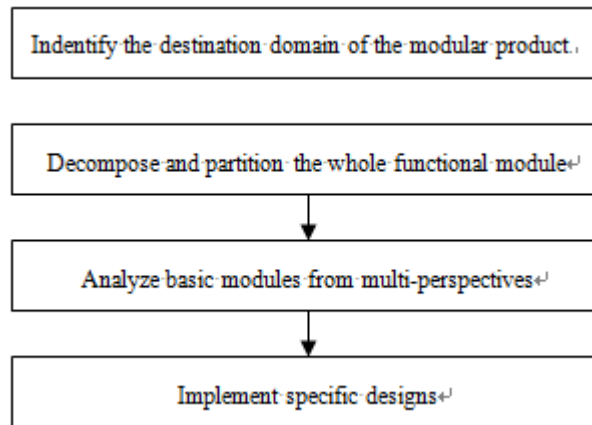


Fig. 1: Basic Methods of Modular Design

In the identification of the destination domains of the modular product, it mainly includes the objective to be achieved, function as well as the objective importance degree, playing a part in the general objective and general function, and giving description and definition on all factors related to modular design, design types (brand new design, adaptability design and deformation design), and life cycle, design scale, etc.

In the decomposition and partition of the whole functional module, the first should decompose a secondary functional module based on the product technological range. If it belongs to an open design, the functional structure framework can be constructed; if an adaptability design, the interface form among all modules should be structured from existing products. Then, the objectives for all modules are identified.

Next, in view of the objectives to be accomplished, it is necessary to multi-dimensionally analyze the basic modules from the aspects of the installation forms, space geometric relations and implemented functional types, and then define the quantitative factors impacting on objectives and the importance degree value between them.

In the specific implementation stage, appropriate constraints can be added to create modules to form a modular product with a small number of modules, and the constraint objectives can also be adjusted to make constraint plans for optimization and comparison based on the whole functional objective. In the actual application of the product style design, it requires the engineering designers to possess high-level technical skills and expression abilities, capable to accurately seize the features of each professional system, effectively manage the complex designs of the modular and series product's organization and stick to the implementation of the general design intention and plan in the development environment of product. Through the loop optimization, the whole design of product can be completed and meanwhile the modular and series resource pool is timely enriched and perfected.

The Modular Design of Intelligent Building Product

In recent years, the development of electronic technology and network communication technology promotes human society to be highly informationalized, and combine information technology and ancient architectural technology with modern high-technology in building interior, hence generating "building intelligence". Building intelligence, integrating the most advanced technologies such as computer and information communication, makes the equipments within building work harmoniously together such as electricity, air conditioner, lighting, disaster alarm, burglarproof security and transportation equipment, making building automation, communication automation, office automation, security automation system and fire-protection automation come true. Building, integrating these five functions plus structural comprehensive wiring system, structural comprehensive networking system and intelligent building comprehensive information management automation system, is intelligent building.

Building intercom system is one of the most basic constituent parts of intelligent building, and is indispensable equipment for fairly well-off houses. This paper takes the modular design of intercom system for example for further discussion.

Currently, there are hundreds of building intercom system manufacturers and products in China. How to make the product internal structure design standardized and modularized and realize the compatibility of different manufacturers' products is a problem necessary to be resolved in this industry. If there is no modular productive technology, it is no doubt that all links will be an indescribable tragedy, such as research and development, purchasing and production. However, besides the most basic function, most of the building intercom systems have the modules of entrance guard, security alarm and information publication, etc. Only by reasonable configuration, can building intercom system satisfy most of the needs of different customers.

Modular product is an effective approach to achieve one-piece production objective with large volume-produce benefit. Moreover, product modularization is also an effective method to support users to design products by themselves. Product modules are standardized input/output components with independent functions. The module design of intelligent building intercom system is as shown in Fig. 2

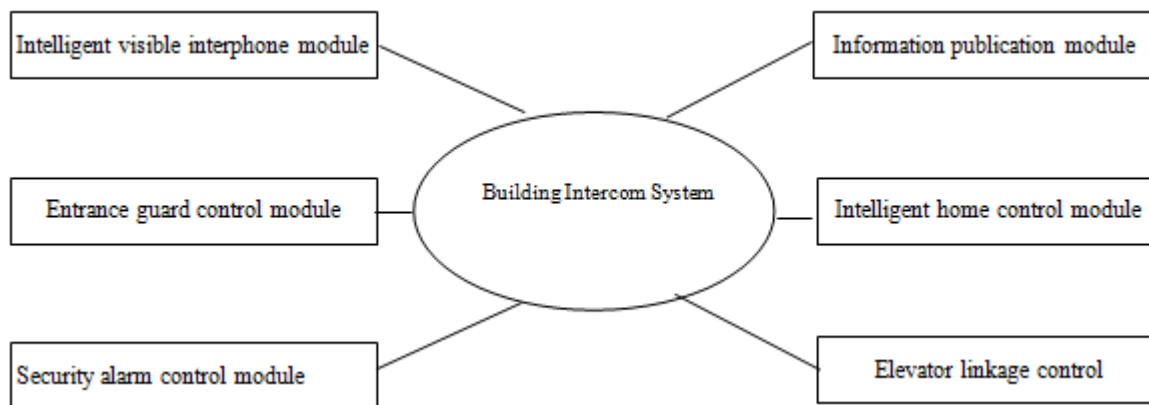


Fig. 2: The module design of intelligent building intercom system

Intelligent Visible Interphone Module Install doorbell intercom system on the iron gates at community gateway and each building entrance. The security personnel take charge of calling for the visited home owner when there are visitors to come to community gateway, confirming there is someone at home to identify the visitors, and then can the visitors enter into the community. After going into community, visitors dial the house number of the visited home owner at the building entrance and gain a permit from the owner through intercom device, and then the owner opens the bottom electronic burglar-proof door by remote control and let visitors enter. Furthermore, this intercom device can be networked to community monitoring center, keeping contact with it anytime. The modules adopt high capacity design and integrate multi-channel technology, allowing multiple fence machines to simultaneously talk back with the households in four different buildings.

Entrance Guard Control Module The control module, taking individual as unit for user authentication, is able to provide secure and convenient service. This module can carry on IC card authentication for hall entrance, elevator entrance, park entrance and commonly-used channels, satisfying different needs of customers.

Security Alarm Control Module The extension is equipped with security alarm control module in which eight secure zones can be configured to the maximum. When the owner presses the emergency button to seek help or triggers the probe in the security configuration, the home intelligent terminal will report alerting and helping signals to property management center in time.

Information Publication Module Through this module, property management companies can establish a bidirectional communication service platform for property management personnel and owners by community intelligence management system.

Intelligent Home Control Module The control of owner on home appliances is not limited by distance, and can achieve cooperative work in security network.

Elevator Linkage Control Through this module, intelligence can call for and control elevator, combining elevator with security and realizing linkage control. For the modular design of enterprise to product, the first is to form several series of products in the appearance design of product.

Analysis on the Advantages of Modular Design

To Help Improve Research and Development Levels. Module is the carrier of knowledge product. It can reduce risks and improve the reliability and design quality of product by greatly using the modules authenticated by production and markets. That module realizes the product functional distribution and separation makes it easy to discover problems and improve design. That module realizes the functional abstraction and actual separation help designers easy to control the whole product and also they can close the details having no connection with their own reach, hence paying attention to the design logic at higher level. The independence and interface consistency of module function allow the module researches to be more professional and deep, and will not impact the other modules of product by unceasingly upgrading its own performance to intensify the whole product performance and reliability. Besides, the independence and interface consistency of module function can promote all modules to be designed and developed relatively independently, and also can conduct concurred design and development as well as concurred experiments and authentication. A different combination of modules are capable to fulfill the diversified needs of users, makes it easy for product configuration and deformation design, and in the meantime ensures the deformation of such a configuration to meet the needs of enterprises on volume production.

To Help Enhance Production Efficiency The repeat application of design and components can greatly shorten the design cycle and so can the concurred product development and test. The application of the existing mature modules can greatly shorten the purchase cycles and thereby speeds up product to market. Similarly, it can shorten the service cycle and resources consumption cycle if the specific needs of enterprise post-sale service are taken into account in the partition of modules.

To Help Enterprise Strength Cost Control. The repeat application of module and knowledge can greatly cut design cost. The application of mature modules authenticated by production can raise purchase batches, lower purchase and logistics cost, and greatly reduce the frequency to adjust production system due to the investment on new products with the purpose to have new product produced easier. Moreover, a great number of interactive modules between product platforms can lessen the post-sale service cost.

Help Improve the Enterprise Management System. The application of modular design in building intercom system is helpful for the labor division of R & D team and normalizing the messages and excuses of different teams to carry on in-depth professional researches and the concurrent development of different modular systems. The establishment of abstract platform and modules can achieve the interaction between enterprise organizational structure and product modular structure, making concurrent engineering have the implantation foundations. And the technology, finance, purchase and post-sale service can get involved in product R & D project in the early stage of product R & D. However, the normalized interface of module is favorable for the formation of standards for of product's suppliers.

The modularization of building intercom system product is the feasible scheme to settle down the current contradiction among the standardization, generalization and individuation of the products in security industry. At present, some intelligent buildings has began to adopt trapezoidal development mode to large communities and form different internetworking plans, and provide the solutions most according with the needs for customers in view of multiple building types such as standard type, mainstream intelligent type and high-end intelligent type by setting up successive lines of defense and various internetworking methods, deeming the pursuit of system modularization as the ultimate objective.

Conclusion

System modular design is the development trend of intelligent building product. Product modularization currently are transforming from enterprise's superior technology to enterprise's necessary technology, and is a development trend of security industry, certainly bringing profound influence on the industrial segmentation at the future market. Modular design in industries is actually the industrial standards. They, who can attain the capability to formulate the industrial standards, will be in an impregnable position in competition.

The modular design of building intercom system reflects the transformation of development thought, design thought and management thought in the application of product style design. Industrial designers apply the modular design thought to develop the product style design, reduce all aspects of research risks to the maximum, save the development expenses, shorten research and production cycle and improve the product quality and reliability through a carefully meticulous overall plan, the full using of the professional system establishment as well as the researches of experts on professional system. Simultaneously, by integrating, planning and modifying the mature product style, it can easily achieve the integration of internal functions and the expansion of external functions, not only maintaining the inherent advantages of the mature product, but also greatly expanding the new space to develop products, allowing the original product to gain new vitality.

Acknowledgment

Chongqing Key Scientific and Technological Project: Study on the Key Technology of Rural Digital Comprehensive Service System Platform and the Demonstration Project

References

- [1]. Li Aijun. Comparison on the Technological Characteristics of Four Types of Field-bus [J]. Urban Mass Transit, 2009, (4).
- [2]. Liu ZengHui. The application Technology of Modular Production Processing System [M]. Beijing: Publishing House of Electronics Industry, 2005.
- [3]. Guo Weijun. The Latest Development of China's Intelligent Building [J]. Sensor World, 2004, (7): 6-13.
- [4]. Qin ZhaoHai, Zhou XinHua. Intelligent Building Technology Design and Construction [M]. Tsinghua University Press, 2003.
- [5]. Zhang Jiugen, etc. Building Equipment Automation System Design [M]. Beijing: Post & Telecom Press, 2003.
- [6]. East China Architectural Design & Research Institute. Intelligent Building Design Technology (Edit. 2). Shanghai: Tongji University Press, 2002.
- [7]. Wang Rongli, Lei Bin. The Current Situation & Development of Industrial Ethernet Technology [J]. Automation Panorama, 2004.

Research on Wireless Alarming System of Transformer Substation

WeihengLi^{1, a}, LinshengWang^{1, b}, FengyanWang¹

¹ Department of Computer Engineering, Henan Polytechnic Institute, Nanyang, China

^a75782558@qq.com; ^bwanglinsheng_317@163.com

Keywords: Substation Fault, Transmission Line, Wireless Alarm, Serial Port Adapter

Abstract: How to find the faults and cope with the trouble in power system in the shortest time, becomes an intractable problem in electric power industry. With SCM technology, the authors put forward the two-level distributed structure composed of substations and transmission wires. Transmission line is provided with a plurality of alarm alarm extensions, information is transmitted to the alarm host through the wireless way. Substation can utilized management system to get alarm information by serial adapter of alarm host, at the same time the alarm information can be displayed on the computer screen. The system has been tested for many times in suburb of Nanyang city. The experiments showed that the systems operation is stable, achieve the expected design goal, which can also played a positive role in power management, power security at the same time.

Introduction

In order to real-time monitoring of power transmission in the process of running state, the power sector electric transmission in the process with monitoring equipment, for the failure in the shortest possible time, timely discharge fault, build an efficient, safe, reliable power monitoring system. Nanyang City Branch constant electrical limited company to undertake the Nanyang city electric power substation construction project of wireless alarm system, the author has favour to participate in the project, combining with the project features and needs analysis, expounds the feasibility of the project.

The Current Situation of Nanyang Grid and Demand Analysis

The current situation of Nanyang Grid With the rapid development of economy, Nanyang city power grid has achieved little energy consumption, rational layout, good expansibility. But the network monitoring tools are not well integrated into the transmission system, is often a point of failure, resulting in a slip even more branches to appear with the same or different fault phenomenon, managers cannot be timely and effectively find the fault point, to the production industry and the service industry caused a great loss.

The project demand Electric Power Bureau as the control center for monitoring room, substation, and transmission line separated by a certain distance set monitoring point. Transmission line running state signals transmitted to the various control points, monitoring point through wireless technology transmits signals to substation, transformer substation staff through management software, check the fault phenomena, determine the fault point according to the fault condition, and decide to fault treatment failure or report the higher processing. Treatment of complete failure, write fault analysis and processing by software to upload to the superior.

Demand analysis there are the following five factors we should consider:

That's system design using substation to the control room, installation of alarm host, in the existing power grid on the basis of the installation of small energy alarm extension programme. Transmission line running state signals transmitted to the corresponding position alarm extension, an alarm extension through wireless technology to transmit the signal to a substation, thereby realizing substation on the territory of monitoring.

The alarm host machine and computer with serial adapter connection, serial port adapter to receive all alarm host alarm signal stored, need to check the alarm information when open management software, no need to shut the computer, realize energy saving.

Alarm host and the monitoring center via the Internet connection, management staff to appear the fault and processing by software upload to substation of the superior.

It's the serial port adapter on the alarm of the large amount of information in the storage capacity estimation.

That the monitoring and management software, user management authority management, alarm information management, information management, police automatic draws management and other basic functions.

Technical Scheme Design

Design principles Economy and the use of the principle: according to the site environment, function design of suitable site conditions, to meet the requirements of the system configuration, achieve the best price performance ratio; ensure the realization of the functions of the system demand, economic use.

The reliability and safety of the principle: the system should have high reliability; fault in the system caused by interruption, to ensure data accuracy, integrity and consistency, and with rapid recovery of function, also has a complete set of system management, to ensure the safe operation of system.

Expansibility principle: considering the future technology development and use, with updating, expansion and upgrades may, according to the project actual requirements may realize the equipment and function of the smooth expansion.

Overall design scheme

Wireless alarm system in substation general topology design diagram as shown in Fig. 1.

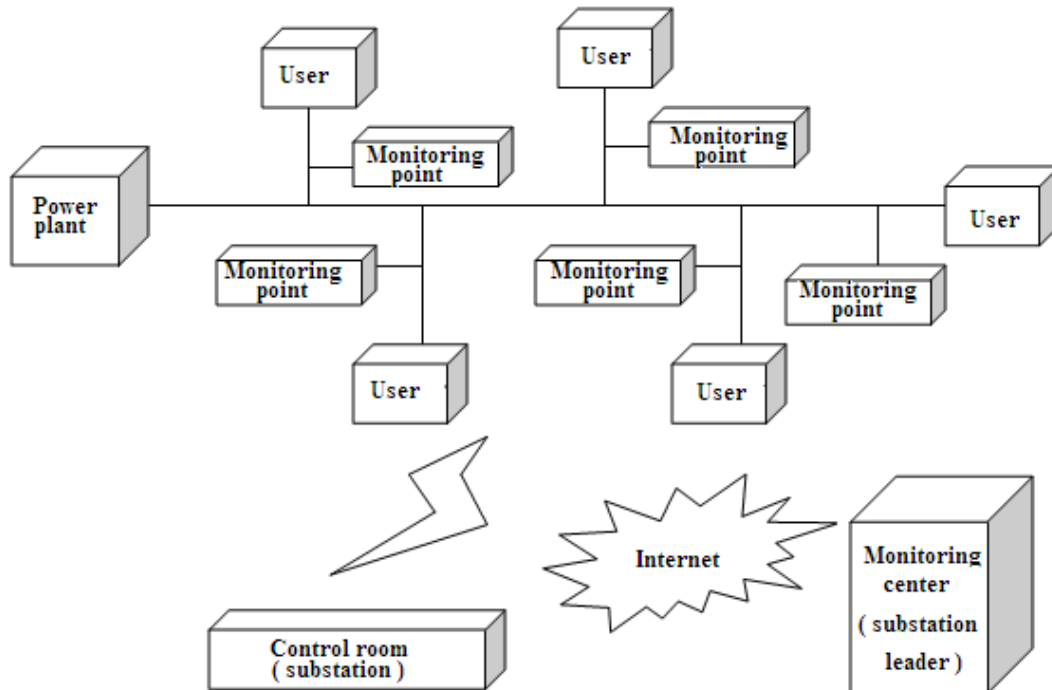


Fig. 1 Overall topology design of substation wireless alarm system

As shown in Fig. 1, substation wireless alarm system includes transmission lead monitoring point, substation monitoring room and substation superior monitoring center.

The monitoring center (substation leader): monitoring center server through the C/S model management software management each substation reporting alarm situation, for a variety of alarm conditions make the guidance and command. In view of the system, because the server is responsible for data storage, data processing can choose the lower grades of the server.

The control room (substation): control room alarm host through wireless technology to receive alarm information, transmitted to the serial port adapter, substation system administrator according to the actual situation through management software to view the alarm information, identify the fault phenomenon and the fault point, according to the fault condition to decide their own fault or report to the superior decision processing scheme. That's Treatment of complete failure to write fault analysis and processing of the situation by software to upload to the superior. The specific process such as shown in Fig. 2

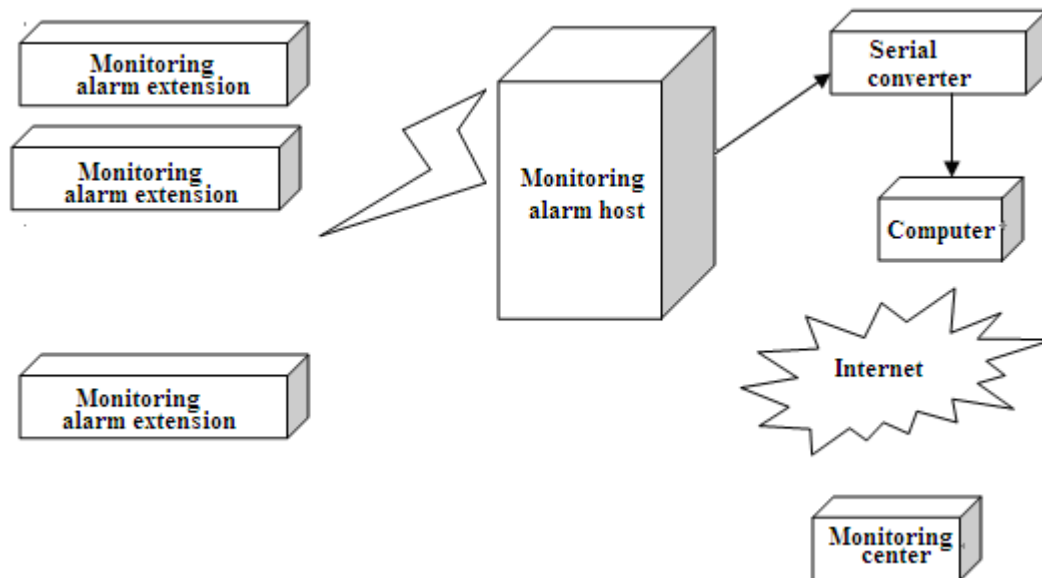


Fig. 2 The transmission process of alarm information

Administrator: in the system have the supreme authority, in addition to the daily management, also need to have certain logic judgment ability, according to the alarm host to report the situation, timely treatment scheme.

The monitoring point: monitoring using existing grid on the basis of the installation of small energy alarm extension, the alarm extension has power-fail protection, can be used in addition to the electricity grid, also carries its own battery power down, line with its battery, has when the electricity automatic charging circuit. That Once the line failure when passing through the wireless technology to send out the signal, in order to ensure that the transmitted signal can be received, the handshake protocol.

Hardware Equipment Selection

According to the project needs analysis and design principle, request an alarm extension of power transmission line fault phase, power wireless alarm monitoring, effectively prevent the 10KV high voltage power transmission line is stolen and destroyed. At the same time the waterproof performance is good, suitable for complex outdoor environment installation. Power off can be sustained for longer time to work at least 20 days; and the alarm host can be correctly received by the wireless transmission of alarm information, sound alarm, and the alarm information correctly transmitted to the serial port adapter; and the serial port adapter can send alarm information correct storage, query time correctly transmitted to the monitoring software. Through the project analysis and field survey, an alarm extension and alarm host using a new starting point for Quanzhou Company developed the DL-110E type wireless power equipment alarm extension and DM-2000B wireless alarm center. That the serial port adapter through independent research and development solutions.

DL-110E wireless power equipment alarm extensions look as shown in Fig. 3.



Fig 3 DL-110E wireless power equipment alarm extension

The appearance of DM-2000B as shown in Fig. 4



Fig 4 DM-2000B wireless alarm center

The serial port adapter: having one end 9V adapter socket and connecting alarm host port, the other end is connected with the computer's serial port. The adapter can be stored in 252 memory alarm host sends the alarm information, if the receiving information over 252, will turn from the first information coverage. Computer and adapter to communication baud rate to 9600,8 data bits, stop bit 1 bit, no parity mode of communication. A computer to send the FEH adapter, adapter will send back the stored alarm information number (one byte 00H~FCH, i.e. 0 to 252), if the return FFH, shows that the system is busy, please try again later. The computer to send the FDH adapter, adapter returns FDH, and information number zero; if the return FFH, shows that the system is busy, please try again later. The appearance of such as shown in Fig. 5

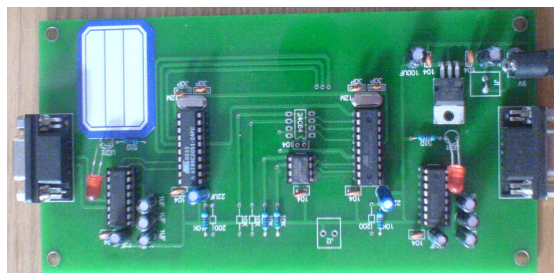


Fig 5 Serial adapter

Software Selection

Monitoring software selection principle is: perfect function, stable performance, friendly interface, easy maintenance. The concrete selection according to market research and project requirements take independent research and development, which can be shown as Fig. 6.

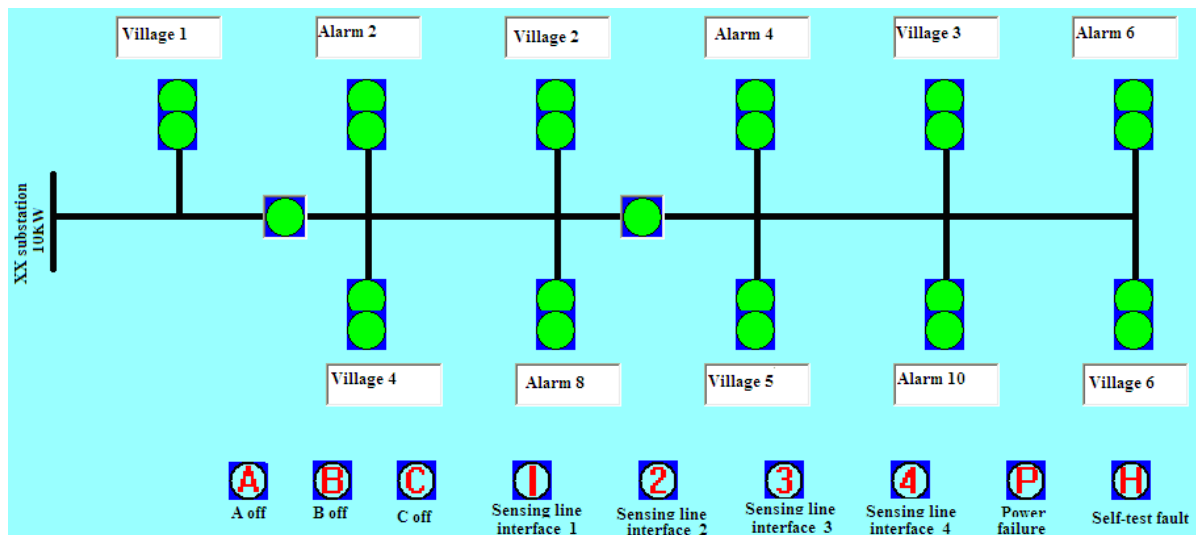


Fig 6 Monitoring software interface

References

- [1] JiaYaxin. Flow meter adopts GPRS/GSM wireless data acquisition system analysis [J]. China new technology and new products,2011(19):22-24.
- [2] Du Xiaoting, Li Meilian. Remote control system based on GPRS[J]. Modern electronic technology, 2011(17):105-108.
- [3] Po Yechao, Yang Bo, Zhang Xinggan. The intelligent gated security system design based on GSM module TC35[J]. Electronic Measurement Technology,2008(01):59-62.
- [4] Xu Jinzeng.The infrared alarm system design based on single chip microcomputer and SMS[J]. Electronic production,2007(07):31-33.
- [5] Liu Jing, Zhao Wangda ZigBee based fire alarm system design [J] microcontroller and embedded system application,2007(1):56-58.
- [6] Li Changlin. Visual Basic serial communication technology and the typical examples [M]. Tsinghua University press,2006:375-377.
- [7] Wang Xiaohua, Zhong Jun. Visual Basic network communication protocol analysis and application examples[M].People's Press of Post &Telecommunications,2008:433-436.

Study of Physics Experiment Teaching System based on Virtual Reality Technology

Shengjian Chen¹

¹School of Physics and Electric Engineering, Qujing Normal University, Qujing, Yunnan 655011, China

Keywords: Virtual Physics Experiment Teaching System, Distributed Remote Teaching And Management, Virtual Reality

Abstract. With the rapid development of the Internet, a remote education assistant system (REAS) is developed to aid the VPETS to be used over the Internet. It is designed in Client/Server mode and is based on virtual reality. It is composed of three parts: the server, the teacher client and the student client. It extends the VPETS to an Internet version and realizes the management of the experiment reports over the Internet. Thus, it can be used for distributed remote teaching and management, freeing teachers and students from the restriction of space and time and stimulating their go-aheadism. It has several advantages: stability, security, and expandability.

Introduction

Based on the physical is a science experiment. Through the experiment teaching physical education is very important. But the fact is, because the experiment resources use, content, steps, and most of the physical experimental conditions are fixed. Students want to do whatever, their teacher will they do in the limited time. And then they were passive and thoughtless. They will not have a deep understanding of the experiment. Don't implement the teaching goal.

However, many systems in many recent articles describe, for example. [1], [2], [3], assist teaching and instructions or demonstrations. Some other countries, such as [6], [7], [8], and even LabVIEW, enabling users to design and research, But offers only a rough interface. Each of them is a computer courseware, the real physical experiment simulating a practical tool, but of them in operation, the whole process of the experiment. A student can be virtual instrument, achieve the expected data is like to be a real experiment. VPETS stressed the practice, let students practice experiment itself.

About The Virtual Physics Experiment Teaching System and Its Remote Education Assistant System

The virtual physics experiment teaching system (VPETS) is experimental physics teaching software for college students. It consists of more than 40 virtual physics experiments (VPEs). Their topics cover mechanics, thermodynamics, electromagnetism, optics, and modern physics. Each of VPEs is a computer courseware, which realistically simulates a real physics experiment: the instruments, their operations, and the whole process of the experiment. A student can operate the virtual instruments and get the expected data just like doing a real experiment. The VPETS emphasizes practice; letting students practice physics experiments on the computer themselves. Because of its high realistic in appearance and interactions, design ability and arbitrariness of operation, it makes students do experiments with a sense of reality. It is easy for students to get acquainted with the knowledge, the operations of the instruments, the whole process of the experiments and experimenting methods. Its application to college teaching shows that students are more interested in using it, more active and more impressed with the experiments.

Thus, it improves the physics experiment education very much. The VPEs was developed on the platform of Microsoft Windows, fully using the graphics abilities of the OS. When we enter into a VPE, we see a virtual laboratory with a table and some instruments in it. As an example, a window of the virtual laboratory of a physics experiment "Designing experiments on optics" is shown in

Figure 1. Clicking the right mouse button in it will pop up a system menu. Selecting the items in the menu, e.g. “purpose”, will open the corresponding online teaching material. The online teaching materials are shown by multimedia technologies, such as texts, pictures, diagrams, animation and sound. After reading them carefully, we will know about the experiment and how to do the experiment. With their guide, we can drag the instruments onto the table and adjust them with the mouse. Double clicking on the instruments on the table can magnify them into a window to fine-adjust them, to observe and measure the results. Finally, we can deal with the data.

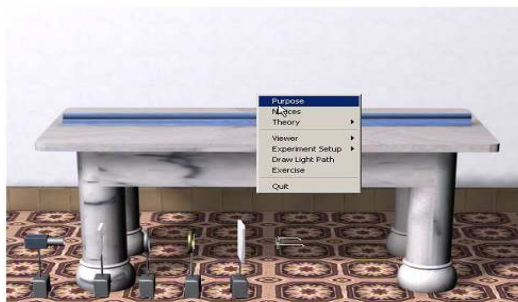


Fig. 1 The virtual laboratory of “Designing experiments on optics”

Due to the realistic simulation, do the computer is just a real test VPETS like doing the experiment. However, VPETS can only be used to focus on teaching, because it can only be used on a single computer or in a local area network. As a very important part of the teaching system, the report system has small coke expansibility: it can't use the Internet; the report is unable to users. They check and feedback is difficult.

With the rapid development of the Internet, distance education assistant system is used to help VPETS used on the Internet. The REAS is composed of three parts: the server, the teacher and the students' client clients. In the server, a database is used to store information of the teachers and students, the key data of experiments, and the report template and students' report; Database management system is designed to answer the needs of the customer's management database. The teacher is for the use of the client connects to the server management user information and handling report template and student's report. Students' party is an expansion of the VPETS. It is the students do the physics experiment of computer network and in your report to the server.

The extension of the Internet version VPETS REAS, achieve management lab reports on the Internet. Therefore, it can be used in distributed distance teaching and management, so that the students and teachers' teaching concentration.

Details of the Reas

The remote education system is developed in Client/Server mode. The server and clients communicate with each other with specified protocols based on TCP/IP. The windows socket is used as programming interface.

The server consists of a network interface, a database management system (DBMS) and a database. It listens to the clients' requests from the Internet, handles them and returns the results to the clients in block mode and in multi-threads way. The framework of the server is shown in Fig 2.

The network interface takes charge of the tasks of listening to and interpreting the messages from the clients, forming the results into feedback messages and sending them back to the clients. Several kinds of data, including the key data of the experiments, the information of the teachers and students, the data of report templates and students' reports, are stored in the database. The DBMS manages all the data, working for the authentication to the users, the access and inquiry to the database.

The teacher client is a teaching management system. It is designed for authenticated teachers to manage the users' information and reports. It receives operations from the teachers, translates them into messages and sends the messages to the server, gets the results from the server and shows them. The architecture of the teacher client is shown in Fig 3 on the next page.

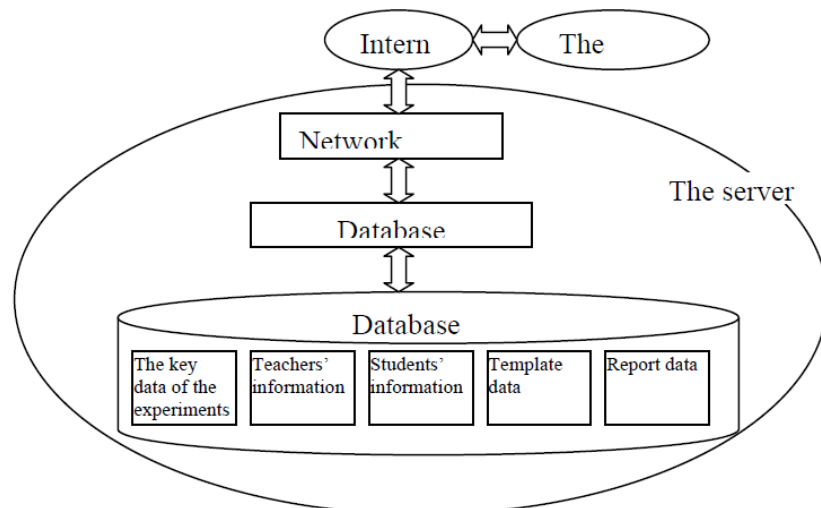


Fig. 2 The framework of the server of the REAS

The user management module is used to deal with all the identity information of teachers and students. Teachers' accounts are treated as special accounts, which have some privileges and belong to the Admin group. They are responsible for managing the identity information of the students. Except for the Admin group all the other groups are student groups. Each student is arranged into a group. Both the student group and account have a series of attributes.

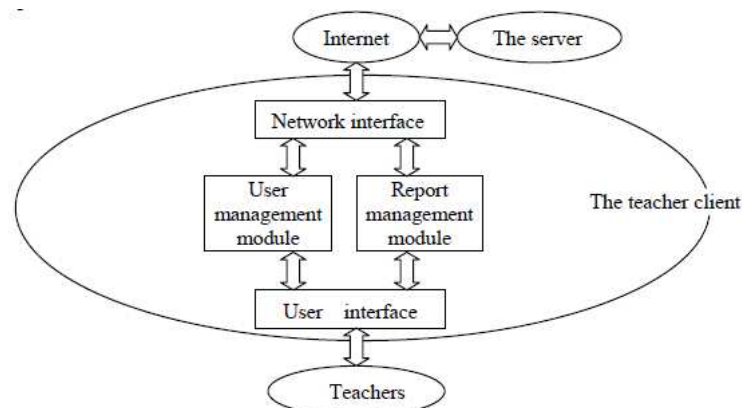


Fig. 3 The architecture of the teacher client of the REAS

A student group has following four attributes:

Status it can be set to either Enabled or Disabled. When it is set to Disabled all the students who belong to the group are forbidden to do experiments.

Experiment it specifies the mandatory experiments which should be carried out by the students in the group in a semester.

Bulletin it is used to publish the announcement and instruction about the experiments. It's edited by the teacher and can show up automatically when students start the virtual experiments.

Comment it is used to record some useful information related to the group.

A student account consists of three private attributes:

Status it can also be set to either Enabled or Disabled. Only when both the group Status and the private Status are Enabled can the student do experiments.

Password it's used for students to login the server.

Comment it's used to record some additional information of the student.

A teacher can do the following operations to manage the student accounts:

Add, delete, or rename student groups.

Add, delete, or rename student accounts.

Specify the group of student accounts.

Set or modify the attributes of the groups and accounts

The report management module is used to handle the experiment report templates and the students' reports. The teacher can make a report template document, post it to the server and specify it to an experiment to ensure the uniform style of the student reports. He can also modify the template at any time. However, teachers who share the same system may differ in their favorite format from each other. To cope with the problem they can change the template in the server by posting a new template. The teacher can query, acquire an experiment report handed in by a student, check and post it to the server.

The Student Client

The student client is the extension of the VPETS. It mainly comprises two parts: the experiment module and the new experiment report module. The architecture of the student client is shown in Figure 4.

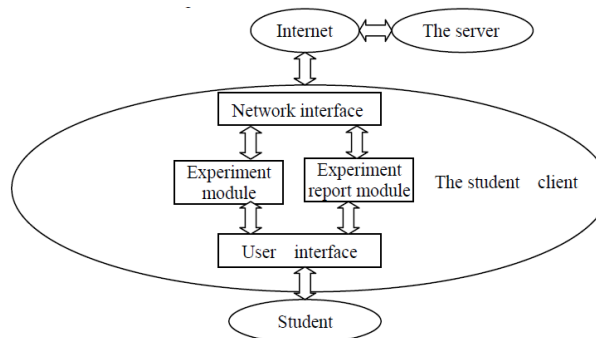


Fig. 4 The architecture of the student client of the REAS

Students need to log in to use the system. Log on to a success, he can get his new password; get the key material operation experiment of experiment and the teacher's instructions. And then he can do virtual experiment and experimental modules. Processing experiment report and the experiment report module, students first get a report template from the server, the input of his personal information and experimental data, the server. His report was examined by the teacher; he can get them again to see score.

Because the distance teaching system developed a client/server mode, standardize the communication protocol, between the client and the server is very important. The main function of the network interfaces and interprets the information transmitted between the client and the server according to the agreement.

The protocols are specified based on TCP/IP, under the principles of simplex, efficiency, and minimum of the transmission data.

A communication process is composed of two parts: a request and its feedback. A client sends a request message to the server; the server handles it and returns the feedback message. A message is composed of the message head, version number, message type, request code or feedback code, comment, space and parameters in sequence.

The primary transmission data are the users' information, the key data of the experiments, and the report data.

The key data of the experiments and the users' information are transmitted as the parameters in the messages. The network interface encrypts them before putting them in the messages for the purpose of security, and decrypts them after taking them out from the messages.

Because the amount of the report data is usually great, it is transmitted as the character stream after being compressed. The transmission steps of the report data are:

A client requests the report data

The server confirms the request information at first then binds a local port randomly and returns it in the feedback information to the client.

The client connects to the port after it gets the feedback information,

The report data is compressed and transmitted from the server to the client after the connection is built up.

The client disconnects from the server and then decompresses the transmission data.

Because the Microsoft word document is very easy to be edited and managed, and is widely used, It is adopted as the format of the report templates and the students' reports. With the form of OLE, the word document can be easily handled in the REAS. Thus, both the reports and templates can be managed at one's pleasure.

By using the clients, the report templates or students' reports can be queried or acquired from the server, edited or checked, posted to the server, or deleted.

In addition to being interacted with the server, the report templates or students' reports can be new, opened, edited, or saved on the local computer temporarily.

Conclusions and Future Work

Distance education of VPETS auxiliary system distributed distance teaching and management of physical experiment on the Internet. Successful experience and REAS as a remote teaching course, and the positive feedback from the teacher and students to use the system encourages us to spread the use of the system. We are planning a new distribution structure design and optimization of the server and client server system more stable, more applicable to different needs and complex network.

Acknowledgement

The paper is supported by Qujing Normal University Teaching Reform Project(No. ZDKC2011004).

References

- [1] G. A. Korn, "Real statistical experiments can use simulation-package software," *Simulation Modelling Practice and Theory*, vol. 13, issue 1, pp. 39-54, Jan. 2010.
- [2] S. Wilson, J. E. Goodall, G. Ambrosini, et al., "Development of an interactive learning tool for teaching rheumatology—a simulated clinical case studies program," *Rheumatology (Oxford)*, vol. 45, issue 9, pp. 1158–1161, Sep. 2009.
- [3] S. Hong et al., "Conducting Laboratory Experiments over the Internet," *IEEE Trans. Educ.*, vol. 42, pp. 180-185, Aug. 1999.
- [4] J. C. Waller, and N. Foster, "Training via the web: a virtual instrument," *Computers & Education*, vol. 35, pp. 161-167, Sep. 2010.
- [5] V. G. Agelidis, "Incorporating Instructional Feedback in Electrical Engineering Laboratory Experiments—An Example," *IEEE Trans. Educ.*, vol. 40, pp. 111-114, Feb. 1997.
- [6] Baker, E. O. Navarro, and A. van der Hoek, "An experimental card game for teaching software engineering processes," *Journal of Systems and Software*, vol. 75, issues 1-2, pp 3-16, 15 Feb. 2009.
- [7] K.T. Chau. "A Software Tool for Learning the Dynamic Behavior of Power Electronics Circuits," *IEEE Trans. Educ.*, vol. 39, pp. 50-55, Feb. 1996.
- [8] J. P. Van't Hof, J. A. Bain, R. M. White and J. G. Zhu, "An Undergraduate Laboratory in Magnetic Recording Fundamentals," *IEEE Trans. Educ.*, vol. 44, pp. 224–231, Aug. 2010.

Correction Algorithm of USB Touch Screen Driver in VxWorks

MingLi^{1, a}, HuipingGuo^{1, b}

¹ Henan Institute of Engineering, Zhengzhou, China

^alm371@qq.com; ^bgghuiping@126.com

Keywords: Touch screen, vxWorks, USB; Driver, Correction algorithm

Abstract. This paper solved driver problem while using a USB touch screen in vxWorks system. After analyzing USB underlying drivers and drivers in the windML, the authors gave detailed introduction on the process of writing driver programme, and put forwards to the relatively simple two-point correction algorithm combined with practical usage. The innovation of this paper is that adding the driver of USB touch screen as an optional component of the vxWorks, and having elaborated USB underlying driver and windML driver.

Introduction

To multi-application user, touch screen devices interaction adopts embedded systems, whose main function is to interrupt trigger report the coordinates of the user's touch and touch gestures. While the USB, with its interface specification, the agreement is flexible, and also increasingly being used in computer peripheral interface. This paper, a detailed analysis of embedded systems vxWorks USB system, as well as how to develop a USB touch screen driver, and a specific implementation, provide a good technical reference for later vxWorks system to develop drivers for other USB devices.

The vxWorks Wind River embedded real-time operating system, The system consists of a number of relatively independent modules, users can select the appropriate components to cutting and configure the system, ensure efficient operation. This paper, USB touch screen driver module is configured as an optional component to the user-friendly.

The structural analysis of vxWorks USB drive

In the vxWorks, the touch screen as a pointer type of equipmen. Using the touch screen in the vxWorks USB, need to write a two-part driver, part of USB touch screen class driver, another part of the touch screen input driver in WINDML. From the underlying hardware to the upper hierarchy shown in Figure 1

From Figure 1, you can see the bottom of the main protocol stack controller driver (HCD) to manage the USB hardware devices in the host system. On three Universal Host Controller: UHCI, EHCI and OHCI. VxWorks5.5 in use of the regulation of UHCI and EHCI interfaces. USB host driver (USBD) is the USB drive has nothing to do with the hardware module, client registration, dynamic connection registration, device configuration, set up a data channel and other operations. This module is by calling the USB class driver manages different types of USB devices connected to the USB host system to communicate with each USB device through the USBD. This is the focus part of the touch screen driver.

USB class driver needs the operation of the following steps:

The drive initialization SIO driver to initialize the USB touch screen. SIO driver maintains a counter, this counter can be multiple calls to the driver. When the system detects the first time initialization is to connect the SIO structure, resource allocation, and class driver to connect to the USB host driver (USBD).

Create a communication pipe

To create a pipeline, in order to meet the needs of communication between the device with a USB client, create the function responsible for allocating the USBD used NodeID, equipment endPoint bandwidth requirements, latency requirements, the direction of data transmission, data transmission. USB data transmission control, synchronization, bulk, interrupt four. Interrupt transmission is mainly used for the timer to query the device interrupt data transmission, and more for the keyboard and pointing device.

The equipment load / unload management functions. Call this function when the system load equipment, the allocation of resources, the callback function to mount and connect the communication pipe, and other preparatory work. Uninstall the management and vice versa.

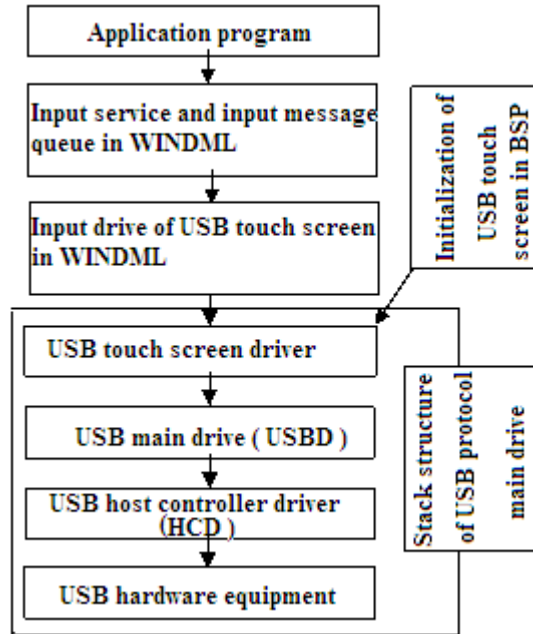


Fig .1 The upper hierarchy diagram

Initialization of USB touch screen in BSP

Initialization is to create equipment, loading equipment and other operations. Create a device to complete to create mutual exclusion semaphores, install the driver layer, I / O management functions, allocation of memory resources, and join the list of devices and a series of work.

USB touch screen driver of WindML application layer

WindML in touch screen drivers touch screen data from the communication pipe to extract coordinate data analysis, send windML the input service routine, the supply layer.

AR1100 controller (ar1100)

The mTouch AR1100 resistive touch screen controller, Microchip Technology Inc. launched a high-performance, low cost, support USB Plug and Play Universal Touch Screen Controller. AR1100 user guidance book, you can get the format of the read data, calculated according to the data format and the current coordinate position. USB interface mode, data format, shown in Table 1.

Table 1 USB interface mode, data format

		Bytes ^o				
		1 ^o	2 ^o	3 ^o	4 ^o	5 ^o
Data bits	0 ^o	B1 ^o	X0 ^o	X8 ^o	Y0 ^o	Y8 ^o
	1 ^o	B2 ^o	X1 ^o	X9 ^o	Y1 ^o	Y9 ^o
	2 ^o	B3 ^o	X2 ^o	X10 ^o	Y2 ^o	Y10 ^o
	3 ^o	0 ^o	X3 ^o	X11 ^o	Y3 ^o	Y11 ^o
	4 ^o	0 ^o	X4 ^o	0 ^o	Y4 ^o	0 ^o
	5 ^o	0 ^o	X5 ^o	0 ^o	Y5 ^o	0 ^o
	6 ^o	0 ^o	X6 ^o	0 ^o	Y6 ^o	0 ^o
	7 ^o	0 ^o	X7 ^o	0 ^o	Y7 ^o	0 ^o

The data format is explained as follows:

B1: Action status. It should be noted that, in the touch screen, 1 for DOWN state; UP state.

B2 and B3 in the USB interface mode have been 0.

X: X-coordinate of the LCD screen position for the 12 data bits.

Y: Y coordinates of the LCD screen position for the 12 data bits.

Accordingly, the touch screen controller to return the coordinates is calculated as follows:

$$X = (byte3 \ll 8) | byte2; Y = (byte5 \ll 8) | byte4. \quad (1)$$

The Preparation Touch Screen Driver

In this paper, the main research subject is a USB touch screen configuration for vxWorks alternative components, therefore, the preparation of the driver is in this premise. Configuration for vxWorks components, enables users in the development process efficient and fast build vxWorks system. To achieve after the component selection screen shown in Figure 2

In Figure 2, added in the left half of the Touch devices Touch the Init component, the windML right side to add a USB touch, components. Added as a component there is another one of the advantages: select the touch, the configuration tool will automatically add the related components, to avoid the omission in the selection of individual components

Therefore, the need to add a USB touch screen driver and a number of configuration files in the vxWorks installation directory. Can be seen from Figure 1, the need to implement the three parts of the driver files

The USB Class Driver

The driver module in the target \ src \ drv \ usb \ folder for the class driver provides vxWorks SIO driver model interface, and hot-swappable USB device. The main functions are as follows: `usbTouchDevInit ()`; class initialization function. Initialize data structures, the class driver to connect to the USBD concrete realization of the call `USBD` in `usbdClientRegister ()` function to a registered client, and call `usbdDynamicAttachRegister ()` function for dynamic loading of the client. `usbdDynamicAttachRegister ()` function is structured as follows:

```
STATUS usbdDynamicAttachRegister
(
  USBD_CLIENT_HANDLE clientHandle,
  UINT16 deviceClass, /*class code*/
  UINT16 deviceSubClass, /*sub-class code*/
  UINT16 deviceProtocol, /*device protocol code*/
  USBD_ATTACH_CALLBACK attachCallback
)
```

The middle of the three parameters can be compatible with the Windows System Device Manager -> Properties -> Details -> ID to obtain, obtain `Class_ID`, `SubClass_ID`, and `Port` to the parameters of the function shown in Figure 3.

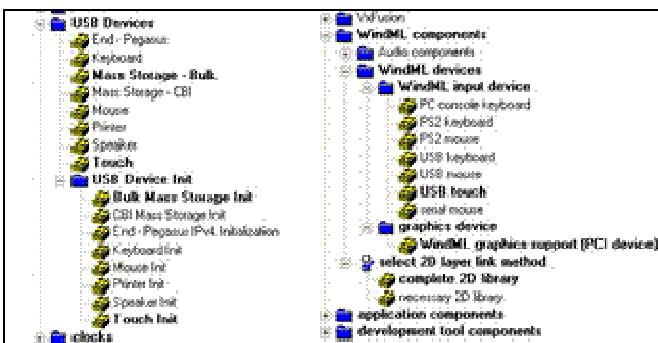


Fig. 2 Components selection interface

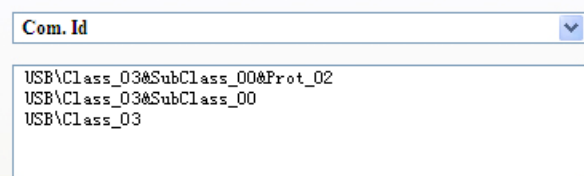


Fig. 3 Parameter selection

The last parameter of the function points to the callback function in the callback function to create a communication pipe (pipe), and is responsible for loading equipment to USBD or uninstall.

`USB TouchAttachCallback ()` initialization function is installed, the function for USBD calls to handle the equipment `USBD_DYNA_ATTACH` and `USBD_DYNA_REMOVE`. These two messages

Function `usbTouchDynamicAttachRegister ()` and function `usbTouchDynamicAttachUnregister ()` calls for the upper. When calling these two functions, add or cancel the corresponding callback function.

`CreateSioChan ()`; after when received `USBD_DYNA_ATTACH` message, call the function, create a new `USB_TOU_SIO_CHAN` structure, and to `sioList`.

`DestroySioChan ()`; for the release of all the resources allocated in the SIO driver, including to delete `sioList` in the structure of nodes and `USB_MSE_SIO_CHAN` message structure

The initialization of the BSP. The module is located in the `config \ the comps \ src \`. The function is the completion of the `USBD` initialization, and the USB class driver has been good foundation, to initialize the USB touch screen. The main functions are as follows:

`usrUsbTouInit()`; USB class driver initialization and after initialization the install callback function

`UsbTouDrvAttachCallback ()`, callback by `usbTouDevCreate ()` function to deal with receive `USB_TOU_ATTACH` message; by call `usbTouDevDelete ()` function to process the received `USB_TOU_REMOVE` message.

`usbTouDevCreate ()`; install a USB touch screen devices, and it drivers function to drive the table, allowing the `fopen`, `close`, `read`, the `write` and other functions to access the touch screen devices.

`IosDrvInstall ((FUNCPTR) NULL, (FUNCPTR) usbTouDevDelete, (FUNCPTR) usbTouOpen, (FUNCPTR) usbTouClose, (FUNCPTR) usbTouRead, (FUNCPTR) usbTouWrite, (FUNCPTR) usbTouIoctl)`;

The function of these drivers installed, its operation is not a standard I / O functions in the handle, but the pipeline of the serial port driver in the USB class driver specific to the function is `pUsbTouDev-> pSioChan`. Each driver's specific, this paper is not in the repeat.

In addition, the need to note is: touch screen coordinates and other data to send out a class driver, the driver module, but also class driven `SIO_CALLBACK_PUT_TOUCH_REPORT` message to install a callback function used to obtain data and save. When the application layer to the `read ()` operation, the actual through `usbTouOpen ()` function to obtain the data transfer out to complete the reading of the data

`usbTouDevDelete ()`; responsible from the `vxWorks` system to remove the USB touch screen devices, and release the occupied resources.

windML touch screen driver

The module is located in `Tornado2.2 \ target \ src \ ugl \ driver \ touch \ usb \ in`. When the Pointer Options the windML graphical configuration interface and a USB TOUCH (shown in Figure 4), compiled windML through macros defined `SYS_POINTER_DRIVER` to load the function of the touch screen driver.



Fig. 4 The Pointer Options in windML graphical configuration interface

The Touch Screen Calibration

Calibration of the touch screen, there are two point calibration, three-point correction, four-point correction or even a five-point calibration method. In general, the more calibration points, the higher the final calibration accuracy. In the the AR1100 given linux program, the calibration procedure used is open source `tslib` in the development process, and not `tslib` ported to `vxWorks`, instead of using a relatively simple two-point calibration method. Now this two correction method analysis as follows:

Click on the upper left corner of the touch screen, access to the upper left corner coordinates for (`leftTx`, `leftTy`);

Click the lower right corner of the touch screen, access to the lower right corner coordinates (`rightBx`, `rightBy`);

To calculate the touch screen in the X direction and Y direction correction factor:

Correction factor in the X direction::;Correction factor on the Y direction::;

The calculation of the touch screen coordinate (x, y) as follows:

$$x = coefficientX(X - leftTx) ; y = coefficientY(Y - leftTy) \quad (2)$$

Where X, Y coordinate data return for the touch screen controller.

In this formula about the touch screen calibration, correction is completed, the correction coefficient coefficientX coefficientY as well as the upper-left corner coordinates of the touch screen leftTx, leftTy saved to your hard drive so that the next boot or reset read.

Configuration Compiler

After the completion of the main driver module, you need to modify a few configuration files can be selected as a component of vxWorks. First, you need to modify the Makefile for the corresponding driver module. Secondly, by the modify 10usb.cdf file shown in Figure 2, the drive module is configured to vxWorks alternative components. Finally, you need to modify the 03windmldev.cdf files and windML_INPUT_DB.cfg files, USB touch screen to add information to the windML graphical configuration interface and choice for users.

Conclusions and Discussions

Mainly through realizing USB touch screen driver in vxWorks, this paper introduced the following aspects, such as USB, driver structure in vxWorks, the realization method from the driver to the application layer driver, and the calibration method of touch screen. Moreover, the driver module is configured to selective components. The complete development process provided the very good reference for other driver development based on USB device in vxWorks.

The USB touch screen driver is developed based on vxWorks5.5 version and windML3.0 version, which have been applied to practical projects. In modifications, it has been successfully transplanted into vxWorks6.x and windML5.x version and the operation works smoothly.

References

- [1] USB Developer's Kit Release Notes 1.1.2 [M] USA: from WindRiver Company, 2002
- [2] USB Developer's Kit Programmer's Guide 1.1.2 [M] USA: from WindRiver Company, 2002
- [3] Kong Xiangying, Gui Zhibo. Embedded real-time operating system VxWorks and its development environment, the Tornado [M]. Beijing: China Electric Power Press, 2011-11
- [4] mTouch™ AR1100 Analog Resistive USB and RS-232 Touch Screen Controller Board User's Guide [M]. USA: Microchip Technology In 2011

Plate Production Line Automation Control System based on Automatic Gauge Control

Wenwei Yu¹, Xuetao Wang¹

Changzhou Institute of Mechatronic Technology, Changzhou, China

Keywords: Plate Mill, Automation Control System, Basic Automation System, Process Automation System

Abstract. The automation control system to plate production line is developed independently. It has been applied for several plants in China and has a good effect. The whole automaton control system is designed as several levels: basic automation system, process automation system and HMI system. The control functions are realized with these levels. With AGC function in plate mill area basic automation system, the plate thickness accuracy can be guaranteed.

Introduction

Board is important product steel industry products, and plays an important role in the development of national economy. Because of it has all kinds of products and complicated process, development and application of automation control system board production line is very difficult. In the past a long time, only a few international well-known automation companies, such as Siemens, VAI, Mitsubishi, Hitachi etc, can undertake this task [1]. But as the standardization and generalization of automation equipment, and strive for the development of the automatic control system, more and more companies and research institutions in China's development and exchange to do the job. Compare these system and development, international companies, control precision of the system is the same as the board make almost, only some differences in the integrated design, stability and standardization. But the high cost of the foreign system, the requirements of the situation is very serious; the system is close to upgrade. In this paper, a typical automation control system design, this paper introduces the plank production line.

Plate Production Line and Automation Control System Overview

Plate Production Line Introduction

A typical illustration of plate production line is shown in figure 1. Refining caster can be transferred to directly on the application of heating furnace, or stored in the courtyard of the slab. After eating, board through the lift furnace, high pressure of the main descaler, removes scale. Normally, there are two stands, is introducing a roughing export, the other is a complete factory. The mill is equipped with automatic generation control (AGC) system to control the thickness of the steel plate handled precision. In the traditional and through the hot rolling mechanical stress (but scroll mode can be used. After rolling, board through the cooling machine (ACC), some local high strength pipeline and other products will be to improve the cooling performance of the board. Adopt double side clip cut, cut the board, the ultimate width, cutting, eventually shear the length of the board. After examination and marking, plate products transferred to warehouse.

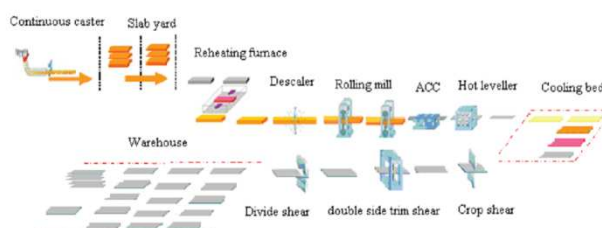


Fig. 1 Schematic of plate production line

Automation Control System Overview

Usually, automation control system of the design of the several levels of plate production line. Level 1 is the basic automation system. This level sequence control technology control functions of special production units. Make sure that all the way of working, in a proper, coordination unit. Control are closely related, the driver and drive. Level 2 process automation systems. Its process, special supervisory units like rolling mill area, and the task of this level to calculate the optimal set level control. It also implements communication, tracking and data management functions. Level 3 is manufacturing execution systems (MES). It is the production control level and cover plate production line by some production unit usually. Some typical manufacturing execution systems (MES) function is the production plan management, quality management and performance analysis.

A practical automation control system designed for a plate production line is shown in Fig. 2. The basic automation system consists of SIMATIC microprocessor based systems for the different sections. SIMATIC S7-400 PLC is used for the logical and sequence control of equipments. SIMATIC TDC PLC is used for the AGC and other technological control functions of mill. PROFIBUS-DP connection is used for communication with sensing, actuating equipments and intelligent remote I/O. Also Industrial Ethernet is applied for communication between basic automation system and other system. PC servers are used as the hardware for the Process automation system and human-machine-interface (HMI) system. The software of process automation system is developed by the VS.net, and also the SQL Server 2005 is applied. SIMATIC WinCC software is used for the HMI system development. It is designed as the server/client form and there are clients in all operating rooms.

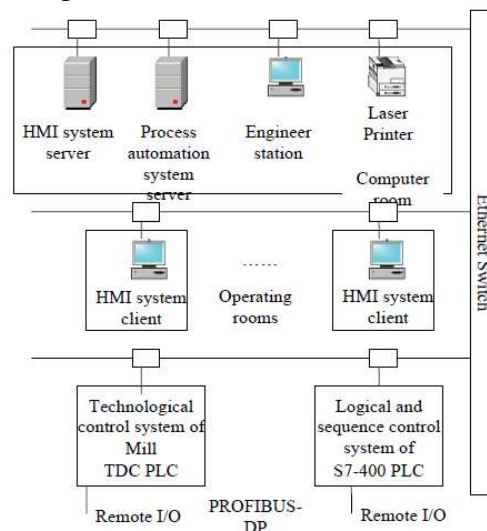


Fig. 2 Schematic of automation control system to plate production line

Basic Automation Systems

Basic automation system logic control, sequence control and the important process control functions, and monitor equipment operation. It ensures high automation of operation and control process and influence the quality and output full directly. The following emphasize basic automation function area board factory, the production of key areas.

Plate Mill Area Basic Automation Functions

The major tasks of the plate mill area basic automation system are: roller table control, master control, roll change control, material tracking, actual data handling, interface to other systems, electromechanical gap control, hydraulic gap control, mill stand zeroing, AGC function and so on. The functions for the vertical gap control are related with the technological quality and need high CPU speed, so these functions are realized by the SIMATIC TDC PLC. Other functions are realized by SIMATIC S7-400 PLC.

AGC Function

In all functions, AGC function is the most important technological control function for the plate thickness accuracy. For the plate thickness calculation, the basic equation is (1).

$$h = S + \frac{P}{M} \tag{1}$$

Where, h is the plate thickness, S is the roll gap, P is the rolling force and M is the mill modulus. During rolling, S and P can be measured, M can be calculated by the mill modulus test data, and then h can be got. The basic principle of AGC function is that according to the comparing between actual thickness and target thickness, change the roll gap, in order to keep the thickness constant. AGC control model is like (2) and (3). If rolling force is changed from P_0 to P, and roll gap is changed from S_0 to S, then thickness deviation Δh can be calculated by (2), and if want to keep the thickness, the gap should be changed as ΔS_{AGC} in (3).

$$\Delta h = (S - S_0) + \frac{P - P_0}{M} \tag{2}$$

$$\Delta S_{AGC} = K_p \left(\frac{Q + M}{M} \right) \cdot \Delta h \tag{3}$$

Where, Q is the plate plastic coefficient, and K_p is the proportional controller amplification factor. There are two modes of AGC, one is the absolute mode. For this mode, the target rolling force and target thickness are calculated by the process automation. The other one is the relative mode. The target rolling force and target thickness is decided at the beginning of the rolling of one plate. Fig.3 is the block diagram of AGC mode.

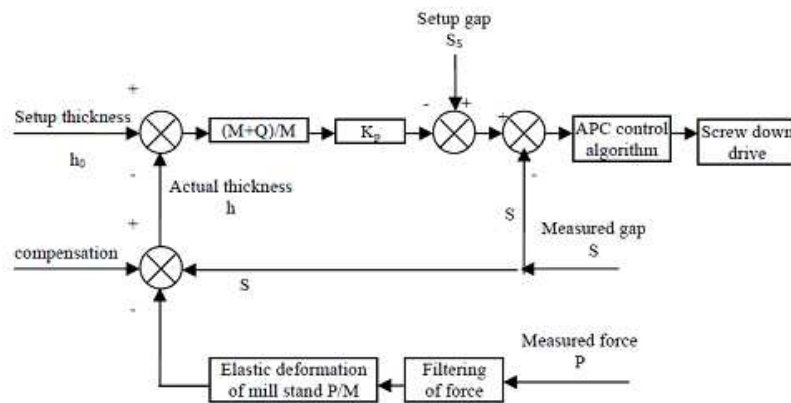


Fig. 3 AGC function block diagram

Process Automation System

Process automation system is an important part of the automation system; it is the key technical control. The main task of the process automation system installation calculation, it supports set information as the foundation of the automation system control. And other auxiliary module, data communication, data management, process tracking is need. The typical building process automation system shows board factory view.

Data Communication Module

Data communication module of the data communication between uses the corresponding process automation systems and other systems. Process system to receive data from basic automation real-time automata; the monitors trigger data change HMI is changing information and send data HMI based automation system installation.

Data communication between process automation system and HMI server is based on the OLE for Process Control (OPC) protocol, and process automation system is defined as the OPC client of the HMI server. The communication data defined as tags in HMI server, and process automaton system can detect changing of these tags, also can change these tags directly.

Data communication between process automation system and basic automation system is according to the TCP/IP protocol. Before communication connection is built, data length and data type need defined at first. With system communication functions, data can be sent and received fast.

Model Calculation Module

Model calculation module is the core module of the process automation. It uses physical models to calculate pass schedules and setup date for the mill, and it also can use the actual measurement data to adapt the models. This ensures that model calculation can deliver high-quality pass schedule and setup information for mill control.

Pass schedule calculation. It uses the initial pass schedule value, based on the physical models of rolling process, according to the optimize iteration and constraints, to calculate the reduction of every pass.

Mill setup calculation. Based on the pass schedule calculation results, it calculates the setup data such as roll gap, roll speed, bending force and so on, for the basic automation control.

Model learning calculation. There are deviations between setup data and actual data, due to the difference between models and actual conditions. Using actual measurement data, model learning calculation can be executed to modify model parameters and improve accuracy of model calculation. Mathematic models are the foundation of model setup module. There are many models for the plate rolling process, and the rolling force model is the key model of them. The rolling force model equation is (4).

$$F = W \cdot \sqrt{R' \cdot \Delta h} \cdot Q_p \cdot \sigma \quad (4)$$

Where, W is the plate width, R' work roll flatten radius, Δh reduction of one pass, Q_p the deformation affect function, σ deformation resistance. Q_p is difficult to be calculated by theoretical analytic model, normally calculated by simplified regressive function. Deformation resistance is the factor according to the steel grade, and the equation is (5).

$$\sigma = \sigma_0 \cdot \exp(a + b \cdot T) \cdot \dot{\epsilon}^c \cdot \epsilon^d \quad (5)$$

Where, T is the temperature, calculated with $T = (t + 273) / 1000$, ϵ strain, $\dot{\epsilon}$ strain rate, and σ_0 , a , b , c , d

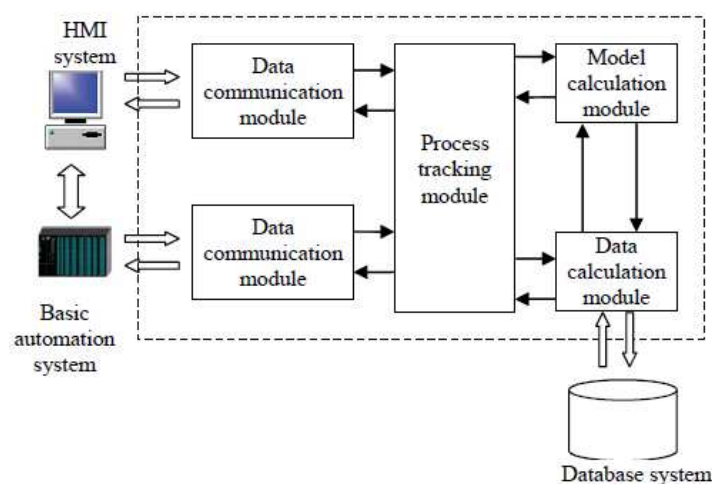


Fig. 4 Architecture of process automation system for the plate mill

Conclusion

Process automation system is a panel factory area and data communication module, data management module, process tracking module and model calculation module. And the model calculation module, installation information for basic automation control supply.

References

- [1] Korans I, and Pichler R, “Modernization and restart of the 3.5m plate mill at VITKOVICE,” *Iron and Steel*, Beijing, China, vol. 35, pp. 32–37, February 2010.
- [2] [Samways Norman L, “Modernization at Lukens Steel: past, present and future,” *Iron and Steel Engineer*, Pittsburgh, vol. 64, pp. 23–29, August 1987.
- [3] Murphy Thomas M, “On-line plate mill process control computer replacement,” *Iron and Steel Engineer*, Pittsburgh, vol. 68, pp. 23–24, June 2009.
- [4] Fazan Bernard, “Optimum computer control of a plate mill,” *Iron and Steel Engineer*, Pittsburgh, vol. 57, pp. 58–64, November 2010.
- [5] Evans Richard D, “Plate mill automation at U.S. steel, Gary works,” *Iron and Steel Engineer*, Pittsburgh, vol. 68, pp. 44–47, March 2008.
- [6] Iida Nagahisa, “Advanced automation on the new plate mill at Mizushima works,” *Iron and Steel Engineer*, Pittsburgh, vol. 55, pp. 34–40, December 2009.

Constant Low Speed PLC Control System of GKD3B Locomotive

Xiuping Zhang

Guangzhou Institute of Railway Technology, Guangzhou 510430 China

Keywords: Locomotive; Constant Low Speed Control; Plc; Gkd3b Model; Coal Transportation

Abstract. The functions, principles as well as the research and system configuration of the PLC control system for Type GKD3B locomotive which runs at a constant low speed are introduced. And the application of the locomotive, which employs this system, in coaling station of Shenhua Western Railway Co. Ltd. is also presented.

Introduction

The constant low speed control system of the GKD3B locomotive is designed by Shenhua Western Railway Co. Limited in accordance with the special requirements of users. The locomotive is required by users to be capable of running at a given constant low speed (0.8~3km/h). Based on this, a constant low speed control function is added into GKD3B locomotive.

Constant Low Speed PLC Control System of GKD3B Locomotive

The system is a multi-functional real-time control system, which is researched and developed based on the CFWJ-1 PLC control system of diesel locomotive and cored at SIMATIC S7-200/CPU226 PLC. The hardware and software of the system are with modular designs, and feature powerful functions, excellent performances, and high reliable operation. Based on the original control functions including locomotive logic control, constant power control, transition control, engine protection, fault self-diagnosis and asynchronous serial communication, a constant low speed control function is added.

Hardware of PLC Control System

The hardware of the PLC control system comprises of case and color LCD display.

Case comprises of PLC host, digital quantity module, analog quantity module, and fault clearing switch. PLC host is used for the receiving and processing of driver's operation instructions, constant power excitation control, locomotive operation logic control, diesel engine control, auxiliary system control, fault detection, diagnosis and protection as well as related data record, relevant parameter organization, displaying, and parameter modification, etc. Digital quantity module is used for the acquisition of device control, key-lifting switch, auxiliary contacts and other switch signals, and its output is implemented through isolating, amplifying and controlling electric pneumatic valve, contactor, relay, etc. Analog quantity module is used for the acquisition and traction of motor current, main generating voltage, diesel engine water temperature and oil pressure, and other analogue signals. Fault clearing switch is used for getting rid of the fault of diesel engine's high water temperature, the fault of differential pressure, the fault of diesel engine's low oil pressure, and the fault of train pipe's insufficient wind pressure, etc.

Color LCD display is equipped with a touch screen of 10.4" and used for displaying the operation state parameters of locomotive, fault warning information, and prompt information.

The Functions of the PLC Control System

Receiving and processing of driver's operation instructions

Constant power excitation control

Constant low speed control

Locomotive operation logic control

Auxiliary system control

Fault detection, diagnosis and protection as well as related data record

Relevant parameter organization, displaying, and parameter modification

PLC System Operating Principle

Constant Power Excitation Control

Constant power excitation control mainly refers to the control on the excitation in exciter of main generator. Specifically, in the locomotive traction condition, constant power control of diesel engine is realized at a different rotating speed of diesel engine. PLC excitation is applied in locomotive excitation control. Through chopping control of control power supply (110V), PLC directly controls the excitation in exciter of main generator, making the system able to give a faster response. At the same time, to ensure the reliability of the system, there are two sets of excitation chopping components, which are backups for each other.

In PLC control device, the rotating speed of diesel engine is used as a benchmark for the giving of electric power. PLC, according to the diesel engine rotating speed actually tested and the diesel engine power-speed curve saved ahead of time, acquires the given power under the current diesel engine rotating speed. Then, the value of the actual power can be calculated according to acquired major-loop voltage and traction motors (6), and PID control operation is conducted according to the difference between the two sides and the minimums of the differences between voltage value and limited voltage value and between current value and limited current value, and also the excitation current of the main generator is controlled through chopper, so as to control the output power of the main generator towards given power value and realize the constant power control of the main generator. The structure of the power control system is shown in fig 1.

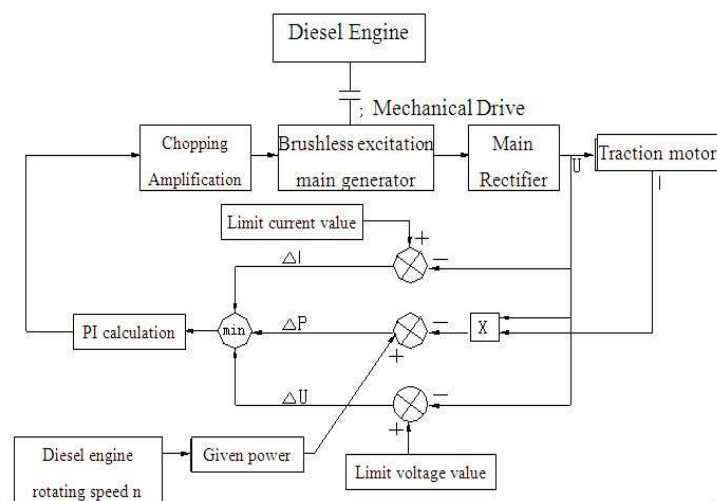


Fig.1: The Structure of the Power Control System

In the process of control, traction motor voltage and current are monitored by PLC, making the fault clearing function of constant power, limited voltage, limited current and single motor realized.

Auxiliary System Control

Auxiliary system control comprises of diesel engine control, air compressor control, and sand and air source purification devices control. Effective control of all components of auxiliary system is realized by PLC according to the working logics of all components.

Magnetic Field Weakening Control

Polar magnetic field weakening is automatically controlled by PLC according to the change of motorcycle speed. To reduce the current surge in transition, there is a function in PLC to reduce power first and then transition.

Anti-slip Control

In the traction of locomotive, PCL gains the maximum current differential and current distribution coefficient through the output current of detected 6 main generators. When current distribution coefficient is higher than specified value and also the current of the smallest motor is higher than specified value, this condition is regarded as slipping, and then PLC will eliminate the slipping by sanding and continuously reducing the output voltage of main generator. After slipping disappears, the output voltage of main generator can return to normal, and sanding will stop after a delay of three seconds. If slipping can't be eliminated, locomotive is uninstalled (this is allowed to happen twice in the same loading process).

Protection When Fault Occurs

PLC compares the detected main generator voltage, all traction motors currents, diesel engine rotating speed, oil pressure, cooling water and other parameters with specified limit parameters. If a parameter exceeds standard, PLC will take protective measures such as warning, unloading or halting, thus realizing the protection on diesel engine and electric system of locomotive.

Diesel Engine Stepless Speed Control

PLC realizes the same functions with WJT. PLC controls the running of stepping motor through detected the position (rising, keeping and falling) driver's main control lever.

Locomotive Constant Low Speed Control

Desired speed can be chosen by driver through the constant low speed universal switch on bench board; PLC controls a fixed rotating speed of diesel engine to ensure the ventilation of traction motor. In PLC control device, locomotive speed is used as a standard for the giving of power; PLC conducts PID control operation according to the difference between actually-detected locomotive speed and preset locomotive speed and the minimum of the difference between current value and limit current value, and also makes locomotive speed controlled towards the given speed by using chopper to control excitation current in exciter of the main generator, thus realizing low constant speed control of locomotive. In the programming of software, many protection functions such as current limit and speed limit protection are added, so as to guarantee secured running of locomotive. The structure of the constant low speed control system is shown in fig 2.

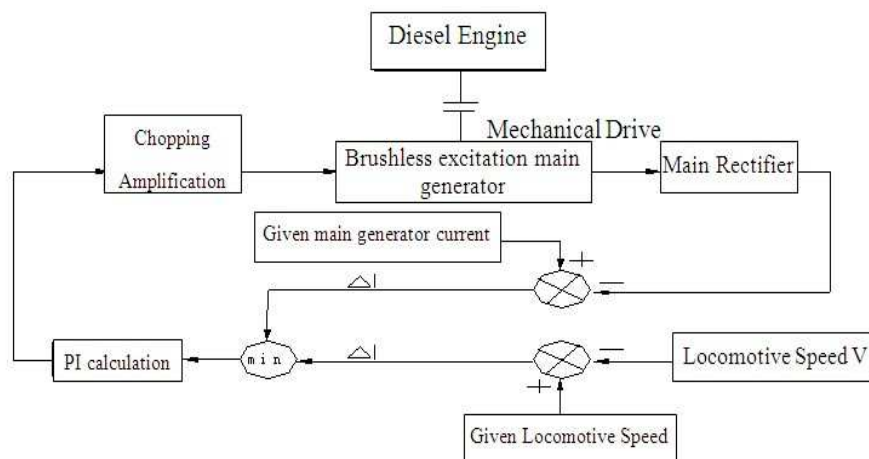


Fig. 2 The structure of the constant low speed control system

Software of the System

Siemens special language is applied in the programming of the software of the control system. Modular structure is applied in programming of software, making program structure clear, logical and rigorous and improving reliability, readability and maintainability of software. The system control flow is shown in fig 3.

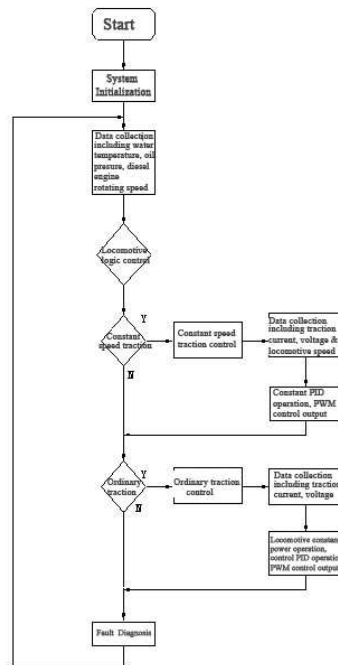


Fig. 3 The system control flow

Constant Low Speed PLC Control Performance Characteristics of GKD3B Locomotive

Locomotive was tested in high load traction after arriving in application site. The test shows two points.

Under the condition of high load and given locomotive speed (0.8~3km/h), the current of the main generator of locomotive stably rises to 5000A, and this can ensure the starting performance of locomotive.

Locomotive can run under the condition of a given speed (0.8~3km/h) and a load (5000t). In starting, locomotive speed overshoot is lower than 20% and becomes stable until the time for the given speed is less than 3s.

Conclusion

The PLC control system of the locomotive is an important component of locomotive, and its performance directly influences the engine performance of the locomotive. Constant low speed PLC control system of GKD3B locomotive worked reliably and featured easy maintenance in the coal loading test of Shenhua Western Railway Co. Limited. Also, the locomotive played a good effect in the coaling station of Shenhua Western Railway Co. Limited. In addition to the untimely coal supply and the necessity for halting in midway, the locomotive always ran at a constant low speed in the loading of coals under the condition of sufficient coal supply, and a wagon box can be fully filled in 45S. Practice shows that constant low-speed locomotive features high efficiency and security. In addition, constant low-speed locomotive owns a good application prospect in the automatic loading operations of mines, ports and oil fields, etc.

References

- [1] Haisheng Yu. Microcomputer Control Technology [M]. Beijing: Tsinghua University Press, 1999.
- [2] SIMATIC Corporation.S7-200 Reference Book [M].
- [3] Shuming Han. Remote Control and Constant Low Speed Control Microcomputer System for DF5B Locomotive [J]. Diesel Locomotives, 2003, (8).

A Family Remote Control System Research Based on GSM Module

Yizhi He^{1, 2}

¹ Northwest University

² Shaanxi Vocational and Technical College

Xi'an City, Shaanxi Province, China

Keywords: TC35I, STC89C516RD+; Smart Home Network; Remote Control; Embedded Gateway;

Abstract. For solving the control problem of smart home equipments in remote, introduce a design method of smart home network which can realize the remote control of home electrical equipments by STC89C516RD+ and mobile telephone module of TC35I, give the home network's mode, describe the software and hardware design of embedded gateway and its control method to the home electrical equipments in detail. The test result indicates that the capability of this system is stable and dependable, the result s was effect, it could meet the design challenge and validates this scheme. The proposed program has the characteristics of high applicability and practical significance.

Introduction

From the beginning in the late nineteen ninties, intelligent community, intelligent home these two concepts gradually into people's lives. With some intelligent home furnishing products come out, people enjoy the intelligent home life is no longer a dream. Our intelligent home furnishing technology than the United States and Europe would probably be a lag of 2to 3 years; foreign intelligent home furnishing products occupy the domestic market for high-end products [1]. For example, HAI (the United States of America Hai Yi) intelligent home furnishing system in the security protection, temperature control and lighting control to provide a simple, reliable, safe operation, but did not provide the function of remote control. At present, domestic low-end products in the function realization is relatively simple, generally only the realization of family security and control function, and has remote control and management function of the intelligent home furnishing products must be in the high-end market in. For example, in 2006, Haier company launched SMS treasure, can pass through the mobile phone text messages to remote control home appliances. Although Haier SMS PO price moderate, for the mass consumer groups, but it is only applicable to a network interface based on e protocol and good home new home appliances, in applications also exist some limitations. While the other has a remote control function of the intelligent home furnishing products, because of their high cost, but also allows ordinary people and step back. Therefore, increasing in intelligent home furnishing system remote control function at the same time, seek a kind of cost-effective technology solutions has become a large number of developers working on a direction.

This paper introduced one kind based on the MCU and GSM wireless intelligent home network design. STC89C54 system used as a gateway, GSM net is connected into the intelligent home network, can realize the mobile phone short message to the home appliances remote control and management.

Connection of Household Electrical Appliance

Intelligent home network refers to the domestic electric appliances and intelligent home gateway connected and the composition of the network, the home gateway through GSM to control networked electrical equipment. Home network connection points for wired and wireless two ways among them, a wired connection means contains connected in star, bus and power line carrier connection in three ways; wireless connection includes a Bluetooth connection, infrared connection (IR) and radio (RF) connection in three ways. From the stability point of view, a wired connection way than the wireless connection of high reliability and stability, in the traditional security system is

used in the stability of the star type connection way best. However, wired connections also existing some disadvantages, such as wiring, affect the indoor beauty; long time is not easy to change, to meet the fire safety requirements. Wireless connection while in stability as a wired connection mode, but can make up for the cable connection in other deficiencies, for some in the stability requirements is not very high electrical appliances, such as air conditioning, rice cookers and other controls can use wireless connections. Considering the current Bluetooth price is relatively high and the infrared connection and is mainly used for remote control, so the paper presents the intelligent home gateway and home appliance of CAN communication scheme.

System Design

The home gateway is the core equipment of home network and the centralized control center, on the home network appliance centralized management and control. The home gateway is the home of internal network and external connection to the GSM interface, the main achievement of GSM network access, remote control and remote connections within the family network function. Visible, the home gateway design is the core of intelligent home system design.

Hardware System Design of Family Gateway

The traditional family gateway based on PC machine has many disadvantages, such as high price and large volume, difficult to move, always in the running state, cannot run on the other interference communication software. Embedded system has the advantages of low cost, low power consumption, high reliability, small, highly automated software code, such as the characteristics of fast response. Therefore, in order to adapt to the ordinary users. Use the embedded system as the intelligent home gateway. In this paper the home gateway hardware system design is based on a STC89C516RD + as the core, the external expansion storage (Flash / SDRAM), CAN module, GSM module, LCD module and keyboard control module to build hardware platform. The home gateway hardware platform such as shown in fig 1

STC89C516RD+ Microprocessor: Hong Jing technology of microprocessor. The chip processing speed, low consumption, and other chip, has a rich film inner peripheral interface, RAM63K, working at frequencies up to 80MHz.

Extra memory: 24C02.

CAN Module (As is shown in fig 2): The MCP2510 is a stand-alone CAN controller developed to simplify applications that require interfacing with a CAN bus. The device consists of three main blocks: 1. The CAN protocol engine, 2. The control logic and SRAM registers that are used to configure the device and its operation and the SPI protocol block. The CAN protocol engine handles all functions for receiving and transmitting messages on the bus. Messages are transmitted by first loading the appropriate message buffer and control registers. Transmission is initiated by using control register bits, via the SPI interface, or by using the transmit enable pins. Status and errors can be checked by reading the appropriate registers. Any message detected on the CAN bus is checked for errors and then matched against the user defined filters to see if it should be moved into one of the two receive buffers. The MCU interfaces to the device via the SPI interface. Writing to and reading from all registers is done using standard SPI read and write commands.

GSM module for mobile phone short message control home appliance this function, in need of home gateway connected GSM module, as the home gateway and the GSM network. The module uses the Siemens Company launched a new generation of wireless communication module of GSM TC35. The TC35AT command set interface, support for text and PDU mode of short message. The GSM module can be connected to the CPU provided by the asynchronous serial port.

The clock module DS1302: for the whole system time.

The LCD display module: module using 12864 LCD liquid crystal.

Control of the keyboard module: 4* 4 key modules.

Temperature and humidity module (DHT11): DHT11 digital temperature and humidity sensor is a familiar with calibrated signal output by the temperature and humidity sensor complex, it application specific digital module technology and temperature and humidity sensor technology, to ensure that the product has high reliability and excellent long-term stability. The sensor comprises a resistive type humidity sensitive element and a NTC element, and a high performance 8bit single

chip microcomputer is connected. Therefore the product has excellent quality, fast response, strong anti-interference capability, cost-effective advantages. Each DHT11 sensor are imminent for precise humidity calibration chamber calibration. The calibration coefficients to form a OTP memory, internal sensor in testing models of processing to call these calibration coefficients. Single-wire serial interface, so that the system integration becomes simple and fast.

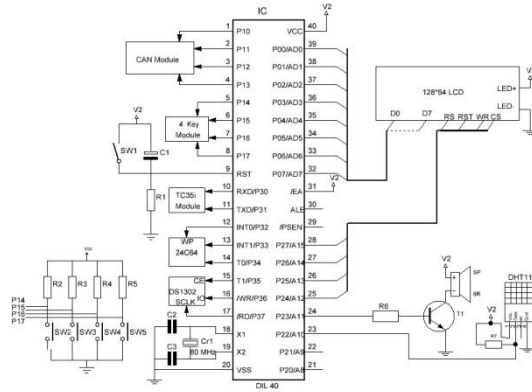


Fig. 1 Hardware schematic circuit for gateway

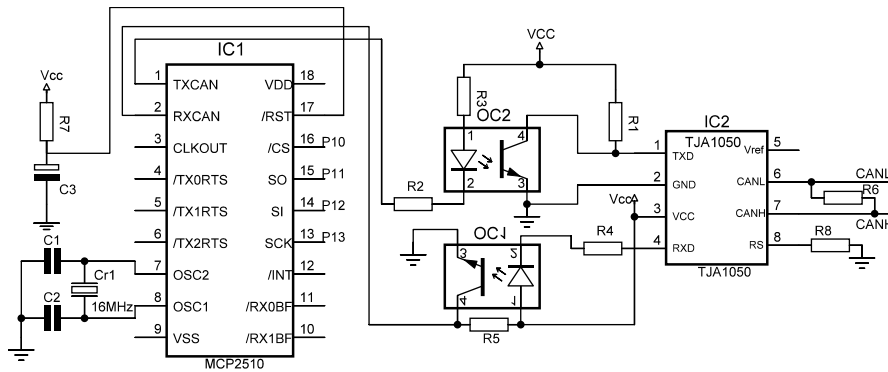


Fig. 2 CAN schematic circuit

Family Gateway Software System Design

The home gateway software system design is one of the focus of system design. In order to realize remote control, home gateway receives from the external network to send control information, therefore, the design procedure is based on the mobile phone AT command, waiting to receive mobile phone short message sent by the control instruction. The home gateway receives a control instruction, the instruction analysis, determine the user wants to perform operations, and in accordance with the communication protocol specification to generate corresponding control frame, via the wireless serial transceiver module is sent to the controlled end. Application of program flow diagram as shown in fig 3

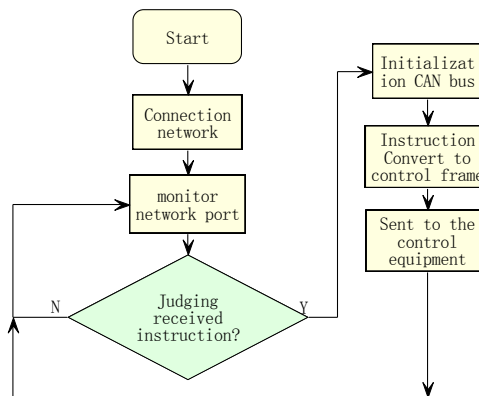


Fig. 3 Flow chart of gateway

Main Functions of the System (Slave Machine Design)

The home gateway and home appliance control communication using master-slave technology, namely the main equipment from the equipment to send out a request command from the device, after executing action and returned to the host device in response to a command. In the end of the controlled electric appliance, the wireless serial transceiver module and a controlled single chip combination, SCM through the relay and home appliances. Chip using C51 language appliance control function, through the serial port interrupt function to send and receive data.

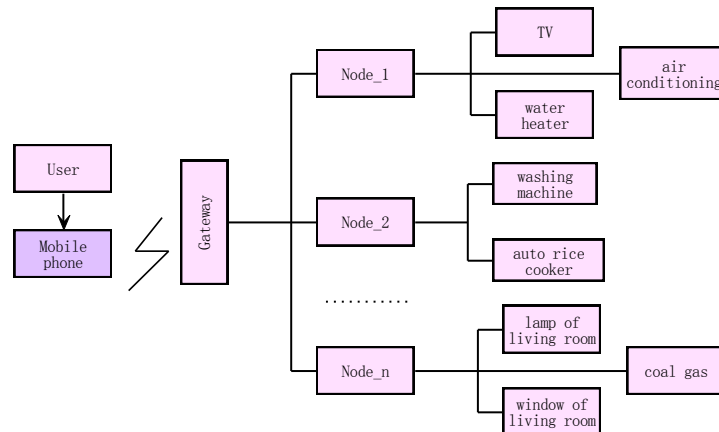


Fig. 4 System structure diagram

The home gateway is equivalent to the Lord from the technology of main equipment, and SCM as a slave device. Singlechip P1mouth as a common I / O port, can be connected with a8electrical appliances. Therefore, in the family electrical equipment can be divided into several groups, each group of up to 8home appliances, with a single-chip microcomputer to control the chip, each have their own number, namely from the device address. Single chip microcomputer in receiving home gateway to the control frame, the first frame in the judgment from the device address field and its device address consistent, if not, then no longer receives the frame; if consistent, then continue to receive the frame data to the other, until the end of a complete frame. Then, according to the control frame of SCM data segment data to determine the address of a few electrical operations, and perform the corresponding action, thus realizes to the household electrical appliance control. SCM operation is completed, returned to the home gateway a response frame, the gateway to the response frame is analyzed, and according to the analysis results by Internet or GSM network to send to the client a return message, informing the customer of operation is successfully executed, if the operation is not successful, but also specifically pointed out that the cause of the error. Fig 4 shows the intelligent home system structure diagram. Among them, nodes represent single chip, i.e. from the equipment in home network.

Gas Detection

The system uses MQ 2sensor. The sensor can detect the liquefied gas, propane, butane gas. M Q 2has 6needle tube feet, 4 of which is used to signal extraction, 2 for providing heating current. Combustible gas sensor is connected with the fig 6fir E / rain, of which 1,2feet to provide heating current, and gas sensor two signal lines received 3,4feet, by adjusting the variable resistor, can adjust the smoke sensor sensitivity, through the STC12C2052AD singlechip AD sampling, processing.

If it detects a combustible gas, immediately through wireless module sending a command to the main control board, main control board recognition through wireless module sending a command to the intelligent window to open the window, control GSM module sends the information to a user specified mobile terminal.

Control Output Circuit

Fig 6 .from the design principle, in which MOTOR O and MOTOR O interface are respectively connected to control windows motor, control windows; other interface can receive gas sensor, which can also be connected with the rainwater detection sensor, SCM can be the interface for A / D sampling.

Temperature and Humidity Detection

DHT11digital temperature and humidity sensor is a familiar with calibrated signal output by the temperature and humidity sensor complex, it application specific digital module technology and temperature and humidity sensor technology, to ensure that the product has high reliability and excellent long-term stability. The sensor comprises a resistive type humidity sensitive element and a NTC element, and a high performance 8bit single chip microcomputer is connected. Therefore the product has excellent quality, fast response, strong anti-interference capability, cost-effective advantages. Each DHT11 sensor is imminent for precise humidity calibration chamber calibration. The calibration coefficients to form a OTP memory, internal sensor in testing models of processing to call these calibration coefficients. Single-wire serial interface, so that the system integration becomes simple and fast. Ultra small volume, low power consumption, the signal transmission distance can reach 20 meters, making it to the application of even the most demanding applications where the best choice. Products for the 4needle single row pin package, convenient connection.

Intelligent Window Design

Intelligent window design of the system is an innovation of. It can automatically close the window in the rain, in the MCU receives the instructions of indoor flammable gas content is too high will automatically open the window, prevent users as the suction to the interior of the flammable gas and toxic and can prevent the happening of fire, in addition to smart windows also installed infrared intrusion detection module.

The windows with STC12C2052AD MCU as controller, through the rainwater detection, wireless data detection, infrared intrusion detection real time acquisition environment so as to determine whether to perform an action of scm. The rainwater detection module is to imitate the remote controller key principle, directly in the PCB board to form; the sensor only received the fire / rain interface, through the MCU A / D sampling to obtain water information. In the aspect of software design, considering the feasibility as well as in the real sense, we detected signal into no grade. As a result of gas leakage is most hazardous, so, we put manual fenestration of the level to the highest, gas leakage signal priority is the second, and rain signal priority ranks lowest.

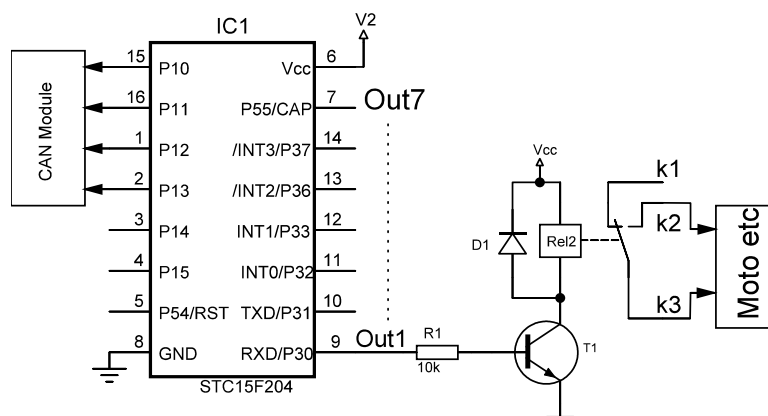


Fig. 5 The control output circuit diagram

5infrared Intrusion Detection

The system of intrusion detection using pyroelectric passive infrared sensor, the sensor will be a two opposite polarity, characteristics consistent with the detecting element is connected in series together, using a two opposite polarity, magnitude equal to the interference signal in the internal offset each other to get the compensation principle of sensors, sensors for environmental background radiation disturbance sensitive to. In its radiation surface covered with only through a

specific wavelength infrared filter, the filter can be obtained by light wavelength in the range of 7~10m, is suitable for human body to detect infrared radiation, and the other wavelength infrared IR filter to absorb, thus forming a kind of specially used to detect the infrared radiation of human body sensor, so that environmental disturbances are obvious control effect. The sensor is added on the outside of the Philippine mud, can enhance sensitivity.

Because of this module was not detectable in human existence when the output is low, detected in human existence when output is high, therefore, we just need to use single-chip I / O port for detecting the output level can know whether the human existence, Fig 6 for infrared intrusion modules. To detect if the low level, there is the existence of human, then through the wireless module sending a command to the host, the host after receiving the instruction, determine whether the security system boot time, if it is through the GSM module to send text messages to a user specified invasion of the mobile terminal; if not in the security system boot time, the signal shielding.



Fig. 6 Infrared invade detection module

The Results of Experiment

Based on the domestic and international intelligent home product function analysis, proposed the intelligent home appliances remote control program, the system makes full use of the mobile phone and GSM two cyber source, the user can easily achieved through mobile phone short message to home appliances remote control and management, to solve the domestic intelligent home products in the remote control function deficiencies, realization of the user through the mobile terminal device can whenever and wherever possible to link into the system of home appliances (air conditioning, lamp, electric water heater) for remote control, can be widely used in home furnishing. At present, the system has been tested in the laboratory, and will be put into use. This system has the following advantages: flexible networking, easy installation and maintenance; system has the advantages of low cost, stable and reliable performance; hardware and software implementation is simple, easy maintenance, system software scalability.

References

- [1] Tatsuya.Yamazaki.Beyond the Smart Home[J/OL].Hybrid Information Technology,2006. ICHIT'06. Volume 2. International Conference on, 2006:350- 355.
- [2] WANG Ying ZHANG Da-bo. Remote Control of Embedded Wireles s Smart Home Network. Microcomputer Information. (2008)08- 2:1008- 057000.48- 51.
- [3] TI. A true system-on-chip solution for 2.4 GHz IEEE 802.15.4 /ZigBee[EB/OL].[2010-01-20].<http://focus.ti.com/lit/ds/symlink/cc2430.pdf>.
- [4] TI.Z-stack developer' s guide.[EB/OL].[2010-01-20]. <http://olmicrowaves.com /menucontents/ designsupport/zigbee/ZStack% 20Developer's% 20Guide% 20-F8W-2006-0022-pdf>.
- [5] Berry P. T he Sunris er - A Design Study in S ol ar Pow ered Flight[A] . In Proc. of th e World Aviat ion Conf erence [C] . San Di ego,USA, Oct 10-12 2000.
- [6] Pathf inder Solar- Pow ered Aircraft f ligh t perf ormance [Z] . AIAA-98-4446.

STBC Study on Reservoir Dispatching and Hydrology Satellite Monitor System

Xinli Cao^{1, 2 a}, Xianjia Wang^{3, b}, Ye Zhu⁴

¹School of Water Resources and Hydropower Engineering, Wu Han University, 430072, Wuhan, China

²School of Electrical and Information Engineering, Wuhan Institute of Technology, 430073, Wuhan, China

³School of Water Resources and Hydropower Engineering, Wu Han University, 430072, Wuhan, China

⁴State Grid Electric Power Research Institute, Nanjing, China, 210061

^acaoxinli@263.net

Keywords: MIMO; QOSTBC; BER; Hydrology Monitoring

Abstract: When MIMO is added in design of satellite signal transmission, it can increase channel capacity and reduce BER multiply. This paper introduced MIMO into satellite monitoring system, studied three kinds of QOSTBC on the mathematical model. Paper also analysed process of transmission for hydrology information and illustrated figures of BER for three QOSTBC. The results show that design of satellite monitoring system using MIMO has a lower BER than using SISO and the BER of rotated QOSTBC is less than other QOSTBC. The original in this paper is that it combines hydrology satellite monitoring with MIMO. It gives theoretical method for hydrology monitoring and transmission.

Introduction

When equipments for information monitoring are installed in hydropower station or various unattended monitoring point, reservoir safety operation can be achieved. Therefore, it is very important to acquire and transmits relative information safely and accurately in real time.

Design of satellite communication net takes into account all demands for low-speed data acquisition not only in speed but also in protocol processing, it can build emergent satellite communication site quickly when necessary. So it can report data of job site to command center, so that command center can give specific orders. In the design, maritime satellite Inmarsat C is selected.

A fundamental reservoir dispatching monitoring is composed of several regime remote telemetry stations and a central site. Telemetry flow station is made up of data transmission apparatus, flow sensor, water level sensor, current and voltage transducer, storage batteries, solar panels, Inmarsat C satellite terminal and satellite antennas. Satellite antennas can be designed as MIMO, which can provide both diversity gain and coding gain.

MIMO technology fully utilizes space resources and can increase channel capacity multiply and reduce BER without requiring increasing spectrum resources and transmit power. STBC method of MIMO has continuous improvements. To increase the transfer rate at which transmit antenna is greater than 2, Jafarkhani and Tarokh put forward QOSTBC, which increases the transfer rate at the expense of reducing diversity gain and increasing decoding complexity [1, 2]. Document [3, 4] pose constellation rotated programme which can achieve full diversity and improve system performance.

This paper is organized as follows: In Section 2 we discuss the channel and signal models and discuss several coding methods of QOSTBC. Section 3 presents some numerical performances. We give some concluding results on water regime satellite monitoring MIMO coding.

System Model

Signal Model. We consider a MIMO-Inmarsat C wireless communication system with N_t transmit and N_r receive antennas. The channel is flat fading rician channels which are represented by matrix H of size $N_r \times N_t$. Input data such as rainfall, water level, hydrology etc. are acquired according to a fixed cycle. After they are quantified and source-coded, they are sent to QOSTBC channel encoder. So the resulted QOSTBC code is the transmit signal block over t symbols by matrix C of $N_t \times t$, where t is time dimension. After being channel encoded, data is transmitted through MIMO channel. Then the receiver signal block Y is:

$$Y = H * C + N \quad (1)$$

Where Y is receiver signal block by matrix Y of $N_r \times t$. $N \in (0, I\sigma^2)$ is the additive complex white Gaussian noise with σ^2 being the noise power.

Channel Model

We assume satellite channel is rician fading channel, i.e. non-zero mean complex Gaussian random variables by matrix H of size $N_r \times N_t$. The receiver is assumed to know the the perfect channel State information, whereas the transmitter only knows the channel mean H_m and R_t . R_t is transmit correlation matrix of size $N_t \times N_t$. R_r is receive correlation matrix of size $N_r \times N_r$. The channel matrix can be written in the form:

$$H = H_m + H_{Ray} = D H_{LOS} + R_r^{1/2} H_0 R_t^{1/2} \quad (2)$$

Where H_{LOS} is channel matrix of direct path, H_{Ray} is channel matrix of scattering path. D^2 , $2\sigma^2$ is power of direct component H_m and scattering component H_0 , the ratio of D^2 and $2\sigma^2$ is rician factor K . R_t and R_r are full rank and invertible. When rician factor is 0, 1, 10, 100, simulation results shows when rician factor has smaller value, it has a smaller effect on channel. On the contrary, when rician factor has larger value, such as $K=100$, it has a large influence on channel, and with the increasing of signal-noise ratio, influence gradually increase. So, direct component damages the channel capacity of MIMO.

QOSTBC

System uses Jafarkhani QOSTBC of full rate and full diversity, which is core technology of MIMO. When input data is $S=[s_1, s_2, s_3, s_4]$, $t=4$, $N_t=4$, $t=4$, $N_t=4$, after QOSTBC, S is transferred to C :

$$C = \begin{bmatrix} s_1 & s_2 & s_3 & s_4 \\ -s_2^* & s_1^* & -s_4^* & s_3^* \\ -s_3^* & -s_4^* & s_1^* & s_2^* \\ s_4 & -s_3 & -s_2 & s_1 \end{bmatrix} \quad (3)$$

TBH Coding

Tirkkonen, Boariu, and Hottinen put forward a new STBC design for 4×1 MIMO, so it is called TBH coding. $N_t=4$, $N_r=1$. Its coding matrix is:

$$C_{TBH} = \zeta(s_1, s_2, s_3, s_4) = \begin{bmatrix} \zeta(s_1, s_2) & \zeta(s_3, s_4) \\ \zeta(s_3, s_4) & \zeta(s_1, s_2) \end{bmatrix} = \begin{bmatrix} s_1 & s_2 & s_3 & s_4 \\ -s_2^* & s_1^* & -s_4^* & s_3^* \\ s_3 & s_4 & s_1 & s_2 \\ -s_4^* & s_3^* & -s_2^* & s_1^* \end{bmatrix} \quad (4)$$

Through simple calculation, we can get:

$$C_{TBH} C_{TBH}^H = \sum_{i=1}^4 |x_i|^2 I_4 + Q_{TBH} \quad (5)$$

Where

$$Q_{TBH} = 2 \operatorname{Re}(s_1 s_3^* + s_2 s_4^*) \begin{bmatrix} 0 & 0 & 1 & 0 \\ 0 & 0 & 0 & 1 \\ 1 & 0 & 0 & 0 \\ 0 & 1 & 0 & 0 \end{bmatrix} \quad (6)$$

We can see that the coding matrix isn't orthogonal, so it is called quasi-orthogonal. The minimum rank of C_{TBH} is 2, the diversity gain of system is $2N_r$ [6].

Jafarkhani Coding

Jafarkhani coding and TBH coding have in common that their coding modules are both Alamouti. Its coding matrix is:

$$C_J = \zeta(s_1, s_2, s_3, s_4) = \begin{bmatrix} \zeta(s_1, s_2) & \zeta(s_3, s_4) \\ -\zeta^*(s_3, s_4) & \zeta^*(s_1, s_2) \end{bmatrix} = \begin{bmatrix} s_1 & s_2 & s_3 & s_4 \\ -s_2^* & s_1^* & -s_4^* & s_3^* \\ -s_3^* & -s_4^* & s_1^* & s_2^* \\ s_4 & -s_3 & -s_2 & s_1 \end{bmatrix} \quad (7)$$

Where matrix ζ^* is Complex conjugate of ζ . Through simple calculation, we can get:

$$C_J C_J^H = \sum_{i=1}^4 |x_i|^2 I_4 + Q_J \quad (8)$$

where

$$Q_J = 2 \operatorname{Re}(s_1 s_4^* - s_2 s_3^*) \begin{bmatrix} 0 & 0 & 0 & 1 \\ 0 & 0 & -1 & 0 \\ 0 & -1 & 0 & 0 \\ 1 & 0 & 0 & 0 \end{bmatrix} \quad (9)$$

We can see this coding matrix isn't orthogonal, so it is quasi-orthogonal. The minimum rank of C_{TBH} is 2, the diversity gain of system is $2N_r$.

Jafarkhani has other forms:

$$C_J = \begin{bmatrix} \zeta(s_1, s_2) & \zeta(s_3, s_4) \\ -\zeta^*(s_3, s_4) & \zeta(s_1, s_2) \end{bmatrix}$$

$$C_J = \begin{bmatrix} \zeta(s_1, s_2) & \zeta(s_3, s_4) \\ \zeta(s_3, s_4) & -\zeta(s_1, s_2) \end{bmatrix}$$

$$C_J = \begin{bmatrix} \zeta(s_1, s_2) & \zeta(s_3, s_4) \\ \zeta^*(s_3, s_4) & -\zeta^*(s_1, s_2) \end{bmatrix} \quad (10)$$

The minimum rank of C_j is 2, the diversity gain of system is $2Nr$.

Rotated Jafarkhani QOSTBC

In ordinary constellation like PSK and QAM, for QOSTBC in (3), the minimum rank of difference matrix $D(C^i, C^j)$ is 2. So when system has Nr receive antennas and code rate is 1, the maximum diversity order is $2Nr$. If all symbols are same constellation, then complex orthogonal codes whose rate is 1 is impossible to achieve a diversity order of $4Nr$. To achieve full diversity, we select different constellations for different emission symbols. For example, before we transmit, we can rotate x_3 and x_4 , or rotate x_1 and x_2 . Theorem proves that when replace (x_3, x_4) with $(\tilde{x}_3, \tilde{x}_4)$, QOSTBC may achieve full diversity [7].

Theorem 1 Assume that we select symbols x_1 and x_2 from L-PSK constellation where L is even, and select \tilde{x}_3 and \tilde{x}_4 from rotated constellation. Then corresponding QOSTBC provides full diversity.

Theorem 2 Assume that we select symbols x_1 and x_2 from L-PSK constellation where L is odd, and select \tilde{x}_3 and \tilde{x}_4 from rotated constellation. Then the corresponding QOSTBC can't provide full diversity when $\phi = \pi / L$. For other rotations, corresponding QOSTBC can provide full diversity.

Research shows that for QPSK, $\phi = \pi / 4$ can achieve optimal rotation and full diversity. So the rotated transmit matrix is:

$$C = \begin{bmatrix} x_1 & x_2 & e^{j\phi}x_3 & e^{j\phi}x_4 \\ -x_2^* & x_1^* & -e^{-j\phi}x_4^* & e^{-j\phi}x_3^* \\ -e^{-j\phi}x_3^* & -e^{-j\phi}x_4^* & x_1^* & x_2^* \\ e^{j\phi}x_4 & -e^{j\phi}x_3 & -x_2 & x_1 \end{bmatrix} \tag{7}$$

Simulation and Performance Analysis

According to flood season or dry season, water level, reservoir capacity are measured in days, in hours, in minutes and even in seconds. Various stations measure reservoir flow to regulate flood. Through digital formatting, data of water level, reservoir capacity becomes binary symbols. After being source encoded, they are sent to STBC (channel encoding), and transmit to satellite.

For example, the water level at 16:45 on April 1st, 2012 is 0.64. After formatting, data becomes digital bit flow. 01H(station number), 7DCH(year), 04H(month), 01H(day), 10H(hour), 2DH(minute), 0.1010001111(water level). The packet is shown as Fig.1.

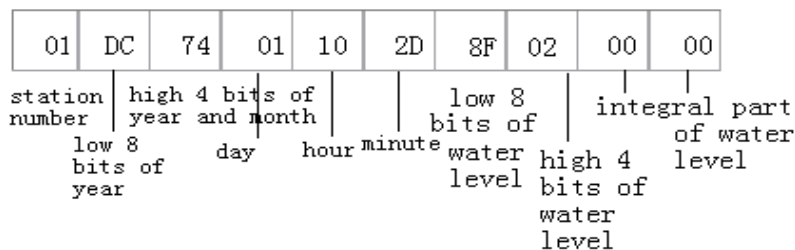


Fig.1 Data packet of hydrology

Inmarsat C satellite usually uses single antenna to perform data transfer. Through comparison, after using MIMO, QPSK modulation, maximum likelihood(ML) decoding, 1000 iterations, the BER of system is shown as Fig.2.

In QOSTBC coding, we use 4×1 MIMO, QPSK modulation, maximum likelihood(ML) decoding, 1000 iterations. We compare TBH QOSTBC, Jafarkhani QOSTBC and rotated QOSTBC ($\phi = \pi / 4$). The BER of system is shown as Fig.3.

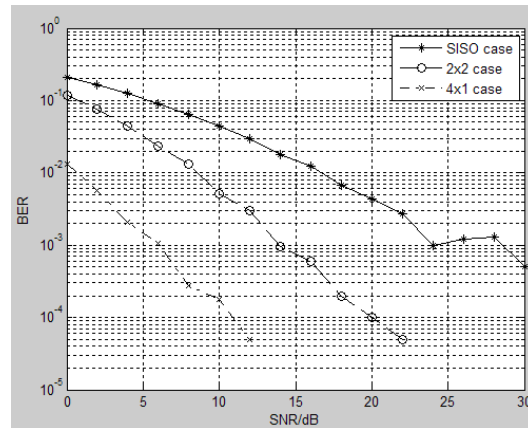


Fig.2 Comparison of BER between SISO and MIMO

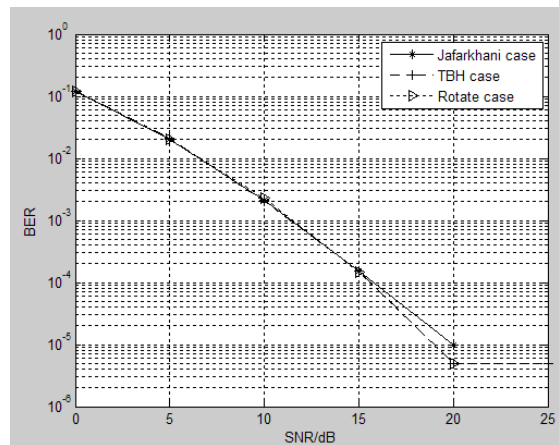


Fig.3 Comparison of BER between several OSTBC

Through repeated simulation, when using MIMO to transfer data of hydrology, the BER decreases much compared with SISO. Under the same conditions, The BER of rotated QOSTBC is less than other QOSTBC.

So, the MIMO and rotated QOSTBC design of MIMO-Inmarsat C for reservoir dispatching and hydrology satellite monitoring system works in theory.

References

- [1] Jafarkhani H. A Quasi-Orthogonal Space Time Block Codes[J]. IEEE Trans on Commun, 2001(49) : 1-4.
- [2] Tarokh V, Jafarkhani H, Calderbank R. Space-time block codes from orthogonal design[J]. IEEE Trans. Info. Theory, 1999, 45(5):1456-1467.
- [3] Sharma N and Papadias C B. Full-rate full-diversity linear quasi-orthogonal space-time codes for any number of transmit antennas[J]. EURASIP Journal on Applied Signal Processing, 2004, 2004(9): 1246-1256.
- [4] Su Weifeng and Xia XiangGen. Signal constellations for quasi-orthogonal space-time block codes with full diversity[J].IEEE Trans Inform on Theory, 2004, 50(10): 2331-2347.
- [5] Dalton LoriA and Georghiades CostasN. A full-rate, full-diversity four-antenna quasi-orthogonal space-time block code[J].IEEE Trans on Wireless Commun, 2005, 4(2):363-366.
- [6] Huang Tao, Yuan WeiChao, Yang Rui Zhe.“MIMO-related technique and application”.Beijing: Jixie Gongye press, 2006:52-55.
- [7] Hamid Jafarkhani. Space-Time Coding:Theory and Practice.Xi'an Jiaotong University Press. 2007: 99-106.

Board Microcomputer Control System to Export Diesel Locomotive

Xiuping Zhang

Guangzhou Institute of Railway Technology, Guangzhou 510430 China

Keywords: New Type; Board Microcomputer; SDD1 Type; Diesel Locomotive

Abstract. This Article based on the new board microcomputer control system structure and function, described in detail the new board microcomputer control system Exported Sudan SDD1 type diesel locomotive. After microcomputer control system is applied in locomotive, not only the performance of locomotive can be improved, and also the reliability of locomotive can be increased.

Introduction

Thus, the operation cost of locomotive is reduced. The new board microcomputer control system has been applied in the narrow-gauged diesel-electric locomotive SDD₁ exported to the Sudan, binging the performances of diesel engine and electric drive system into full play, and ensuring the safe and reliable running, and easy operation and maintenance of locomotive.

The New Board Microcomputer Control System Structure and Function

The new board microcomputer control system comprises of microcomputer control cabinet, display screen, signal conversion device, and microcomputer power filtering device, and has the functions of constant-power control, speed control, auxiliary power voltage adjustment, all kinds of protection, operation parameters displaying, and fault information storage, and man-machine dialogue installation, etc. In the design of the system, full consideration is given to the electromagnetic compatibility measures and the desert climate with high temperature and sandstorms in the Sudan, and also double-backup redundant structure is applied for ensuring the reliability of the system. The composition of the new board microcomputer control system is as shown in fig 1.

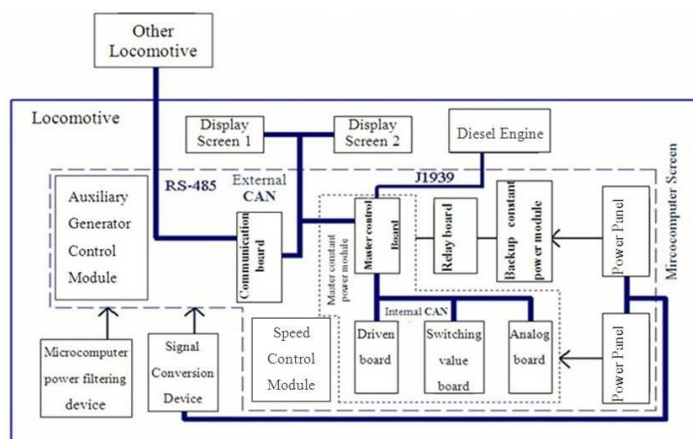


Fig. 1 Composition of the New Board Microcomputer Control System

Hardware Composition of the New Board Microcomputer Control System

Hardware of the new board microcomputer control system mainly comprises of four components, which are microcomputer control cabinet, signal conversion device, microcomputer power filtering device, and microcomputer screen.

Microcomputer Control Cabinet

Microcomputer control cabinet is the core component of the system, and mainly responsible for completing all kinds of control functions. It comprises of auxiliary power control module, auxiliary generator control module, speed control module, and constant power module. All sorts of analog quantities needed by microcomputer control cabinet source from signal conversion device and sensor, and various switches needed by it are directly from the locomotive operation instructions and the feed-back signals of all kinds of executive components.

Signal Conversion Devices (ESM1A and ESM2A)

The new board microcomputer control system includes two signal conversion devices (ESM1A and ESM2A), which respectively convert the analog signals of main power generation voltage, main current, traction motor current, overload feedback current and rotate speed of diesel engine, speed of locomotive, braking exciting current in braking, and front and back checking cylinder pressures into digital signals and then send them to microcomputer control cabinet for being processed by computers.

Microcomputer Power Filtering Device

Microcomputer power filtering device is used mainly for improving the quality of power source (110V) of the new board microcomputer control system. It sends the power source (110V) of locomotive to the microcomputer system through the filtering of three capacitors (250V/2200 μ), for the purpose of preventing the ripple voltage of power source (110V) from giving rise to damages to the new board microcomputer control system.

Microcomputer Display Screen

Microcomputer display screen is a new colorful LCD display device that is installed in the driver room of locomotive. It is connected to the new board microcomputer control system relying on communication lines, and also is display terminal and man-machine interface of the new board microcomputer control system.

Main Control Functions of the New Board Microcomputer Control System

Auxiliary Power Generation Exciting Control

In power generation conditions, the exciting current of starter generator is controlled by the voltage regulator of microcomputer; the output voltage of generator is stabilized in $10V \pm 2V$ if the rotate speed of diesel engine changes in the range of 600-1800 r/min. There are no overpressure protections; when auxiliary power generation pressure is higher than 125V, automatic power generation is transferred to fixed power generation.

Main Power Generation Exciting Control

When locomotive is in traction, resistance braking, and self-load conditions or in water rheostat test, the microcomputer system completes the exciting control of the main traction generator at all speeds of diesel engine.

Locomotive Constant-power Tractive Characteristic Control

When locomotive is in traction condition, microcomputer control can test the main operation parameters and working conditions, making main generator work in an ideal external characteristic and also own voltage and current limiting characteristics.

Locomotive Resistance Braking Characteristic Control

In the range of constant braking current, resistance braking force is higher than 90% of tractive effort, so as to meet the need of the braking characteristics of locomotive.

Diesel Engine Speed Control

Speed control of diesel engine is controlled by electronic thrower; the signal of speed control is current signal (4-20mA): the speed of 600r/min is corresponding to 4mA, and the speed of 1800r/min is corresponding to 20mA. Gear signal of driver's speed controlling hand-wheel is sent to microcomputer, and then converted by the microcomputer to current signal (4-20mA) and sent to electronic thrower of diesel engine for the rotate speed adjustment of diesel engine.

Air Compressor Drive Control

Two air compressors are set in locomotive. The work of the two air compressors is controlled by board microcomputer according to the air compressor wind signals input by locomotive. When air compressor work signal is received by microcomputer, one of air compressors (assumed to air compressor 1) should immediately work; after 30s, if air compressor work signal still exists, air compressor 2 also work until air compressor work signal disappears, and then two air compressors stop working. If two air compressors work together, air compressor 1 should stop working after working continuously for 5 min, and then works again after a delay of 3 min; after air compressor 2, after working continuously for 5 min, continues to work until air compressor 1 starts to work if locomotive still needs wind, and then air compressor 2 stops working. The locomotive output power reaches 22kW if 1 air compressor works, but reduces by 40kW if 2 air compressors work together.

Fault Diagnosis and Protection Functions

Over-voltage and over-current protection of main generator: When the voltage of main generator is equal to and higher than 950V or the current is equal to and higher than 6000A, locomotive is unloaded, and fault is displayed and recorded by microcomputer screen.

Over-current protection of traction motor: When the current of traction motor in a position is equal to and higher than 1000A, locomotive is unloaded, and fault is displayed and recorded by microcomputer screen.

The braking current of traction motor is detected in resistance braking condition: When braking current is equal to and higher than 500A, locomotive is unloaded, and fault is displayed and recorded by microcomputer screen.

Resistance braking and self-load wind loss protection: The braking current (self-load) of traction motor is detected by microcomputer. When the current reaches 100A and microcomputer does not receive the feedback signal of contact action of air pressure relay, resistance braking (self-load) is cut and self-locked, and then fault is displayed and recorded by microcomputer screen. The unlocking lamp is off when hand-wheel returns to 0.

Over-speed protection of locomotive: When locomotive speed is equal to and higher than 105km/h, locomotive is unloaded, and fault is displayed and recorded by microcomputer screen.

Anti-slip/sliding control: board microcomputer judges whether locomotive slips through the comparing the currents of traction motor. If locomotive slips, board microcomputer will take measures according to slip/sliding degrees for preventing and removing slip/sliding, and thus more fully utilizes and improves adhesive performance of locomotive. Then, fault is displayed and recorded by microcomputer screen.

Protection of train pipe pressure: When locomotive starts, board microcomputer will prohibit it to load if train pipe pressure is lower than 400 ± 10 kPa; when locomotive runs, board microcomputer will not receive input signal of air pressure relay, locomotive is unloaded, and fault is displayed and recorded by microcomputer screen.

Reconnection control functions

When locomotive is reconnected, it will communicate with the board microcomputer system of other locomotive for completing data exchange, fault information recording and alarm display.

Communication Circuit of the New Board Microcomputer Control System

In the new board microcomputer control system, the parallel bus of the traditional board microcomputer control system is canceled, but advanced network technology is applied: the communication among all functional modules of microcomputer control cabinet with display screens is implemented by CAN (Control Area Network) bus; the communication between diesel

engine and microcomputer control cabinet is implemented with J1939 protocol, and parameters such as temperature and pressure related to diesel engine are acquired; the reconnection communication between current locomotive and other locomotive is implemented by RS-485 bus, which is with extremely high reliability. It is easy to implement the functional extension of the system with bus data communication.

Display System of the New Board Microcomputer Control System

In the new board microcomputer control system, new colorful LCD display device is set. The functions such as locomotive operating parameters display, real-time fault display, fault information query and dump, parameters settings and self-test can be implemented with it.

CPU Module (referred to as main board)

Over 386DX industrial computer main boards and 4M more memory are selected for this module, and thus it is stable and reliable.

SSD (Solid-state Disc)

SSD is inserted into the DIP socket with 32 pins, and gets rid of batteries with Flash technology.

Big-screen color LCD screen

TFT color LCD screen (10.4 inches, high resolution, and wide visual) is applied, and is with high definition from a different angle of view.

CAN Communication Card

The card is mainly responsible for communication processing, and exchanging data with external CAN bus, and also optical isolation is applied in all communication lines. PC/104 bus sockets, CAN receiving and sending indicator lights and bouncing pins selecting dial switch and interrupt number at port address are installed on board.

Power Module

The module with a wide range of temperature and high reliability is used as power module, providing display diagnosis device with power supplies (110 V/5 V, 12 V).

Inversion Module

Inversion module provides LED display screen with a high-voltage AC backlighting circuit (1000V). Baseboard mainly plays a fixing role, integrating all components or parts together with printed wiring, and thus reducing external connection lines.

Real-time Clock

This function is part of the main board, and can work continuously for ten years relying on DALAS uninterrupted clock. The internal clock can run as usual if no power supply is supplied by the main board.

PC Film keyboard

This is used for the manual operational microcomputer display screen, Manual switching screen interface and relevant parameters settings.

Display Screen Software

Display screen software, based on communication protocol, establishes and controls the serial communication between microcomputer display screen and main board control computer.

Conclusion

The new board microcomputer control system SDD1 is a new generation board microcomputer control system, which is developed based on the conclusion on the experience of many board microcomputer control systems. New software and hardware structure is applied in the system, which features comprehensive functions, easy operation, good control effect, easy functional extension, etc. In the application of the locomotive SDD1 with the new board microcomputer control system in Sudan, locomotive is stable in control performance, and runs in good condition.

References

- [1] Jiawu Li, Yusong Wang. Types, Features and Applications of Flat Panel Displays [J]. Diesel locomotive, 1993 (12).
- [2] Tao Tang. Basic Structure of a Fail—Safe On-board Microprocessor and Its Application in Automatic Train Over-speed Protection System [J]. Journal of Beijing Jiaotong University, 1993 (S1).
- [3] Qiyi Guo, Derong Shao, Weida Xie. Study on the Anti-interference of Board Microcomputers [J]. Electronics technology, 1993 (02).
- [4] Qiyi Guo. Review of Several Problems in Microcomputer System on Board SS4 0038 Electric Locomotive [J]. Electric Drive for Locomotives, 1994 (05).

Research of Automatic Welding Machine Controlling System based Single-chip

Song Jinhu

Shandong Transport Vocational College, Weifang, Shandong, China, 261206

songjinhu@hrsk.net

Keywords: All-position Automatic Welding Machine, C8051F020, Controlling System

Abstract. In this paper, a scheme for the structure and controlling design of an all-position automatic welding machine is studied, and also the automatic welding system is explored in depth. In this system, the C8051F020 single chip is used as the controller and the DC servo-motor as the executive component. Through the interface circuit and software program of the single chip, the system can control and harmonize the wire-feed speed as well as the tread and swing of the welding tractor, and can meet the needs of the all-position welding technology, hence realizing the automation of welding, and increasing the welding production efficiency.

Introduction

In the modern industrial production, the space-position welding is often used for some welding machines with large components. Generally, the manual welding method is adopted in the traditional space-position welding. The traditional manual welding method is with slow speed, low quality, poor efficiency and the restriction from the operators, while the space-position of such a component as the large-size oil storage tank, air storage tank and major-diameter steel penstock has its own laws, so it is completely feasible for the automatic welding to be adopted. Therefore, the all-position automatic welding machine controlling system with good performances is researched and developed in this paper.

Composition of the Automatic Welding Machine

The all-position automatic welding machine locates the position through the specially made tracks, is controlled through the manual macro-control, and completes the welding based on the configured automatic operations. In accordance with the characteristics of the space-position on-site welding, the all-position automatic welding machine is mainly composed of three parts which are the welding power source, mechanical system, and automatic controlling system, which is as shown in Fig 1 below. The NB-630IGBT inverter semi-auto gas shielded MIG welder manufactured by Beijing Time Group Inc is applied to the welding power source, and the self-contained wire-feed machine is selected. The executive system of the all-position automatic welding machine is used as the mechanical system which mainly includes the welding tractor and exclusively-used welding tracks. The main components of the welding tractor include the carriage, the gesture swinger of welding torch, the regulating mechanism of welding torch, and the cable bearer. Through the mechatronics design, the articulated separate structure can be used to finish the automatic treads, and provide supports for the welding swinging and the swinging regulating mechanism. The automatic controlling system is the microcomputer controlling system to implement the gang control of the welding tractor and swinger; and the settings of the welding parameters, displaying, program controlling and other functions are completed through the self-contained welding power source.

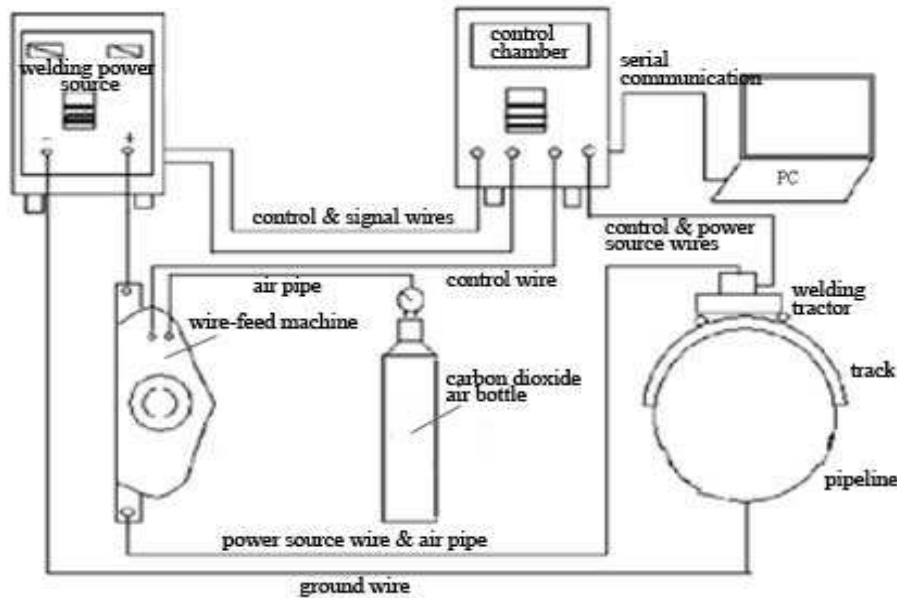


Fig 1: The Composition Structure of the Welding Machine

Hardware of the Controlling System

The Whole Welding System Structure The technologies of carbon dioxide arc welding, all-position and multi-layer welding are adopted in the all-position automatic welding machine. Also, the pipeline is divided into twenty-four space positions; and different welding program is set for each position, including the welding current, voltage, tractor tread speed, torch swinging model and so on.

The all-position automatic welding controlling system is the microcomputer controlling system and implements the integration control on the treading tractor and swinger; and the self-contained welding power source completes the welding parameters setting, displaying, program controlling and other functions. The controlling system is mainly composed of PC and the main controller, and is able to implement the controls on the welding model, programs and parameters. Meanwhile, the automatic treads of the welding tractor is controlled by a DC servo-motor; and the swinging of the welding torch is implemented by another DC servo-motor.

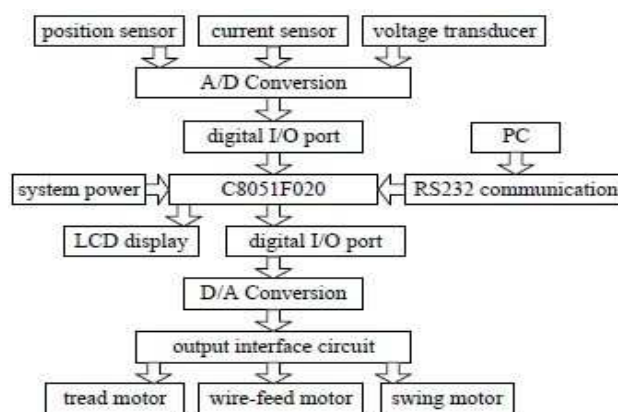


Fig 2: The Framework of the Controlling System Principle

The controlling system principle framework is as shown in Fig 2. The C8051F020 is used for the controller chip; the SD1T-C4V6 sensor is selected as the current sensor; the SA1T-V25V6 sensor is for the voltage sensor; and the AME-B002 angular transducer is for the position sensor. The welding parameters are input through the PC. In the welding process, the sensors (the position, voltage and current sensors) transfer the collected data signals by processing into digital signals, and then feed back to the single chip. Next, the single chip displays the data feedbacks in PC to allow the operators to know the welding real-time state, and simultaneously processes the data feedbacks, and then adjusts the welding parameters (current and voltage), and then implements the controls on the

power supply and electric motor through the output interface circuit. At the mean time, the power supplies of all parts in the controlling system are mutually independent and completely separated, and hence the interference is avoided and the controlling accuracy and reliability are significantly improved.

Welding Power Supply Controlling Interface The welding power supply controlling interface includes the controlling start part, current detection circuit, A /D interface circuit, and D/A interface circuit.

The controlling starts of the single chip and welding power supply use the 74HC573 as the output signal interface, and are doubly isolated through the optoelectronic isolator and the relay in the middle. In the starting, the MCU receives the start command, and then sends out the gating signal CS06 to inform the effectiveness of 74HC573 input single, and then the welding power supply is started.

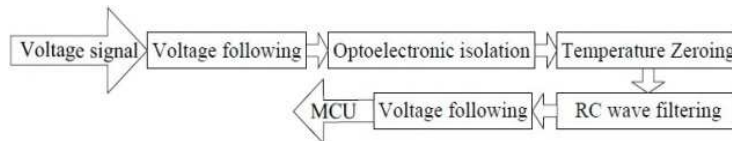


Fig 3: The Principle Framework of the External Parts of A /D conversion

After the current detection circuit sends out the start signal in the single chip and the power major loop begins to generate the current, CPU receives the signal sent by the current sensor, and then executes the next command.

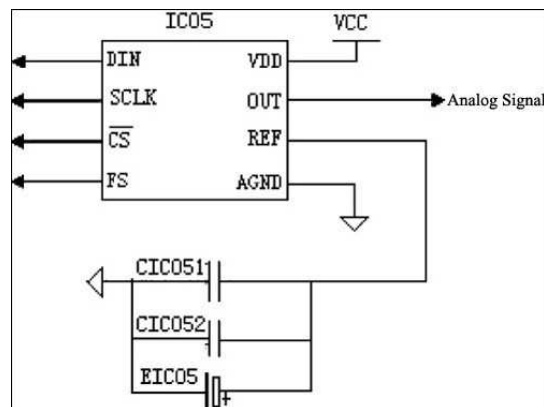


Fig 4: D/A Digital-to-Analogue Conversion Circuit

A/D conversion circuit includes the on-chip A/D circuit and the external interface circuit. The role of A/D conversion circuit is transferring the output analog value into the proportionable digital value. The A/rD CR command register (AD-COMMAND) controls the A/D conversion process; the operators start the A/D conversion by selecting the writing-in methods through the pre-setting A/rD AD-COMMAND or by waiting for the trigger signal from EPA, and then the conversion results are stored into the result register (AD-RESULT). To reduce the impacts of the external interference on the single chip, the simulation optoelectronic isolator OPT1 is used for the external interface circuit to obstruct the direct coupled channel of the external interference to the single chip, and simultaneously the temperature drift zeroing circuit is adopted to reduce the sampling errors. The Fig 3 shows the principle framework of the external parts of the A /D conversion.

D/A interface circuit is divided into the D/A digital-to-analogue conversion (DAC) and the output interface. MCU supplies the digital signal quantity, so it is necessary to use the D/A conversion chip used exclusively by TLV5636 for conversion. The D/A digital-to-analogue conversion circuit is shown in Fig 4; and the D/A output interface principle framework is as shown in Fig 5.

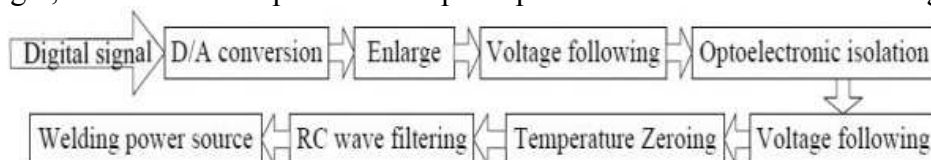


Fig 5: D/A Output Interface Principle Framework

Software of the Controlling System Software

The working procedure of the all-position automatic welding can be divided into three steps (backing, covering and filling) based on its technology. Each step is programmed per its welding technological features; it is unnecessary to be programmed on site in the using regardless of the welding pipes with whatever diameter; and only relevant buttons are selected, a cycle can automatically proceed to complete the welding.

The working process of the controlling system is as shown below: after the current is on, the power source will be switched on as well, and the system will automatically complete the initialization. When checking the motor running state in place, operators need to respectively press the isolated operation buttons of the motor until the motor is loosened. After the equipments are detected to comply with the normal requirements, the welding can be carried out then. Select the swinging motor speed, open the protection air and connect the welding power source, but the next selection of welding can only be conducted when the protection air is opened and the welding power supply is on. In the welding course, the controlling system will detect if the welding torch has undergone a cycle, and the welding will be stopped if yes but continues if no. In the whole operation and working course, relevant contents are always displayed in PC, and the running state of the displaying machine will remind the operators of the next operation. The whole system workflow framework is as shown in Fig 6.

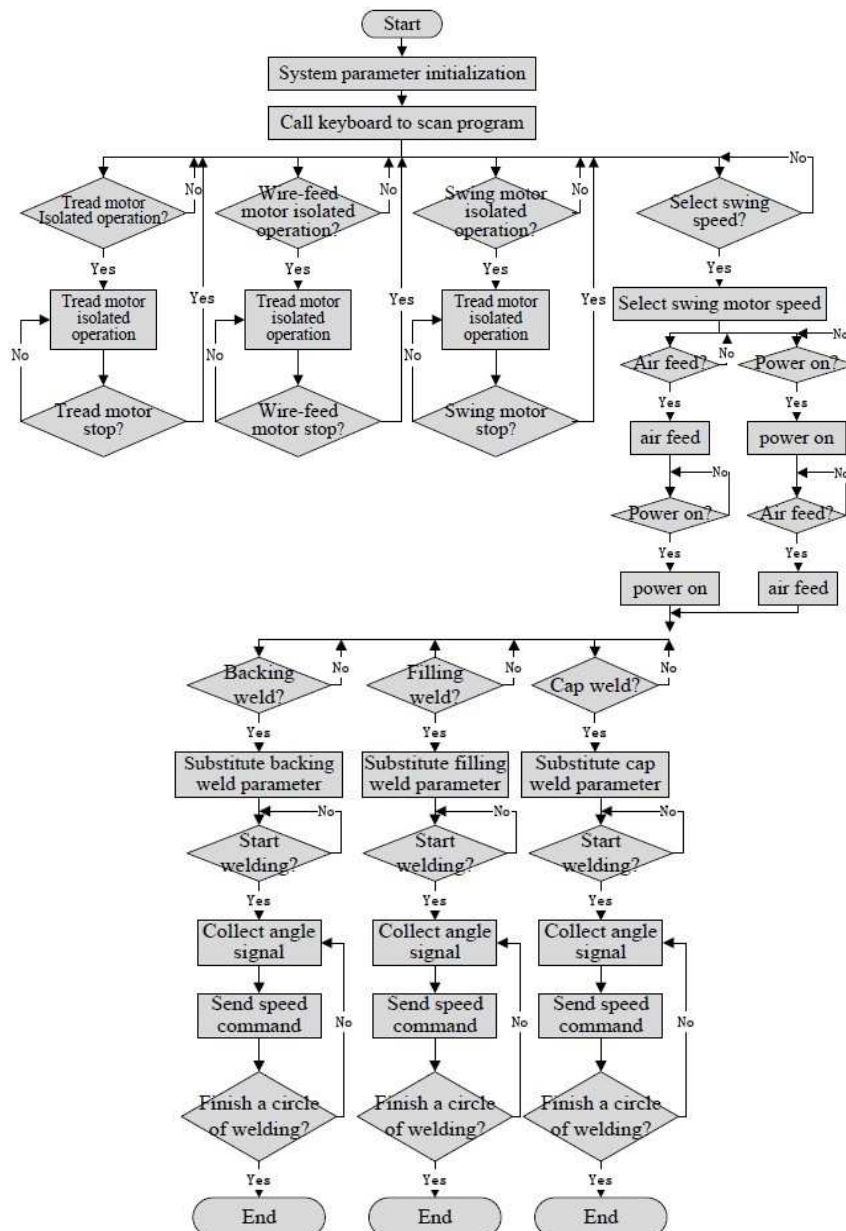


Fig 6: The Controlling System Workflow Framework

Conclusion

The all-position automatic welding machine controlling system designed in this paper is easy to use, and has a low requirement on the operating level of welding personnel. Also, it can change the welding parameters in the real time, hence promoting the welding process to be easier to use. In the real-time welding displaying process, its voltage, current and conversion speed can allow the welding personnel to know the real-time welding state. Also, it can fulfill the requirements of the all-position welding technology, implementing the welding automation and increasing the welding production efficiency. Furthermore, the system as a whole is small and requires the low cost, and thus it possesses a boarder application prospect.

References

- [1] Wu Lei, Sun Yongxing, Hu Rong. Research and Development of the Automatic Controlling System of All-position Automatic Welding Machine [J]. China Petroleum Machinery, 2006 (11).
- [2] Hu Shengsun. Welding Automatic Technology and Application [M]. Beijing: China Machine Press, 2007.
- [3] Zhang Aihua, Yao Haiyan. All-Position Automatic Welding Systems Based on C8051F020 [J]. Microcomputer Applications, 2009 (9).
- [4] Zhang Youde, Zhao Zhiying. Principles, Application and Experiment of Single Chip Microcomputer [M]. Shanghai: Fudan University Press, 2000.
- [5] Chen Guangdong. Principles and Interface Technology of Single Chip Microcomputer [M]. Wuhan: Huazhong University of Science and Technology Press, 1999.
- [6] Wang Wei, Xue Long, Li Mingli. Control System of All Position Pipe Welding Machine [J]. Welding & Joining, 2004 (4).
- [7] Jia Baoli, Wang Bin, Zhang Wenming. R & D of Automatic Welding Mechanism of Girth Welds [J]. Modern Welding Technology, 2008 (10).
- [8] Li Xiao, Li Liangyu, Wang Tianqi, Yang Xu. An Inverter Welding Machine based on DSP for Pipeline [J]. Welding Technology, 2009 (3).
- [9] Zhang Tao, Gui Weihua, Wang Suiping. Research on Separating Digital Inverter Welding System [J]. 2007 (3).

Machine-printed Invoice Number based on Fuzzy Recognition

Xiaoping Xian¹

¹ Gansu Normal University for Nationalities, Hezuo, Gansu 747000 China

Keywords: Fuzzy Recognition; Invoice Code; BP Neural Network;

Abstract. A new fuzzy recognition method of machine-printed invoice number based on neural network is presented. This method includes ten links: invoice number detection and separation of right on top of invoice, binarization, denoising, incline correction, extraction of invoice code numerals, window scaling, location standardization, thinning, extraction of numeral feature and fuzzy recognition based on BP neural network. Through testing, the recognition rate of this method can be over 99%.The recognition time of characters for character is less than 1 second, which means that the method is of more effective recognition ability and can better satisfy the real system requirements.

Introduction

Automatic sorting of invoice is based on the automatic identification of the invoice code location under the gray invoice area numbers 0 to 9 and letters. I propose a neural network-based fuzzy identification method, which includes: frame edge detection and separation, image binarization, numeral recognition feature extraction and fuzzy pattern recognition based on BP neural network 10 links. In order to improve the recognition rate, the use of digital stroke density features as recognition features, the identification of more than 90%.

Edge Detection and Separation of Invoice

Edge Detection of Invoice

The application of edge detection method to extract the invoice box image The edge of the invoice code box of the envelope of gray image edge gray value transition, using the gradient operator to identify the invoice number Code box [1].For continuous image $f(x,y)$, use G_x and G_y to indicate $f(x,y)$ along x and y direction of the gradient:

$$G_x = \frac{\partial f(x,y)}{\partial x} \quad G_y = \frac{\partial f(x,y)}{\partial y} \quad (1)$$

$\theta_g = \tan^{-1}(G_y / G_x)$ is the gradient direction. θ_g (Gradient magnitude) is: $g(x,y) = \sqrt{G_x^2 + G_y^2}$, threshold is λ , if $g(x,y) > \lambda$, then (x,y) is a Edge point.

Approximately calculation of the gradient calculation convenient is commonly used in small area template. Sobel gradient operator sub 2 template is as follows:

$$S_x = \begin{bmatrix} -1 & 0 & 1 \\ -2 & 0 & 2 \\ -1 & 0 & 1 \end{bmatrix} \quad S_y = \begin{bmatrix} -1 & -2 & -1 \\ 0 & 0 & 0 \\ 1 & 2 & 1 \end{bmatrix} \quad (2)$$

For any point (x,y) and including eight of $3 * 3$ matrixes composed of adjacent gray value: $F_{xy} = (f(x,y))_{3 \times 3}$, compute $f(x,y)$ along x and y direction of the gradient $G_x = F_{xy} \times S_x$ and $G_y = F_{xy} \times S_y$, and for $g(x,y) = \sqrt{G_x^2 + G_y^2}$ to get point (x,y) of the gradient magnitude.

Sobel operator edge detection on the grayscale image of the invoice number area as shown in Figure 1, derived from the gradient shown in Fig 2.



Fig. 1 Grayscale image area of invoice code

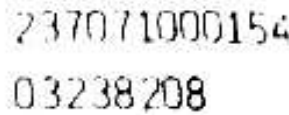


Fig. 2 Edge detection of the region of invoice code

Separate of Invoice Code

Boundary tracking method 6 invoice boxes separated. The border tracking is starting from an edge point in the gradient map, search for and connect to the adjacent edge points so as to gradually detect its regional boundary method [2]. Follow these steps to extract a tag in the box in the gradient map:

from top to bottom, from left to right order on the gradient map scan (scan only the upper left part of the 1/4), the outer edge of the New Invoice box of points X (deposit abscissa), Y (deposit and the vertical axis).

$I = 0$, scan to a black pixel, the edge of the point group in the invoice number box is cleared.

The coordinates of points stored in the group of points of the outer edge of the Zip Code box.

$i = i + 1$, in (x_{i-1}, y_{i-1}) neighborhood pixel, Look for a black pixel (x_i, y_i) , if (x_i, y_i) does not appear in the X, Y, go to (3); if (x_{i-1}, y_{i-1}) Black pixels in the neighborhood of pixels all the X, Y, and it is (x_0, y_0) , go to (6); else go to (5).

Edge point of the round of border tracking to determine the starting point (x_0, y_0) is not a invoice outside the box to continue to scan in the gradient map, go to(2).

(x_{i-1}, y_{i-1}) is end point, stop search, Assume $i = n$ at the time. Outer edge of the point group according to the invoice box, you can draw a box of invoice s to be separated in the original image where the rectangular area: vertex:

(x_{\min}, y_{\min}) , length is $(x_{\max} - x_{\min})$, width is $y_{\max} - y_{\min}$. Among $x_{\min} = \min(x[i])$, $x_{\max} = \max(x[i])$, $y_{\min} = \min(y[i])$, $y_{\max} = \max(y[i])$ $i = 0, 1, \dots, n-1$

The original image to extract the region corresponding grayscale and fill the area with the background color (to prevent interference), this diagram is proposed an invoice block diagram. Similarly, by the above steps to extract the remaining 5 Zip code block diagram.

Image preprocessing for invoice edge

Gray image binarization extracted 6 invoice block diagram of binarization for invoice code

The specified threshold λ , is:

$$f(x, y) = \begin{cases} 0 & f(x, y) < \lambda \\ 255 & f(x, y) \geq \lambda \end{cases} \quad (3)$$

(As in the below expression with value "1") Figure 3 for a binary zip code box.



Fig. 3 Binarization of character

Denoising

Invoice number denoising method based on pixel density "filter method, on a invoice in a black pixel (x, y) in the number of black pixels (x, y) as the center of the neighborhood statistics, if black pixels more than half of the black point of the center in this point is considered to be non-noise points; otherwise removed as noise points. Denoising of the experiment, the invoice number $n = 5$ is more appropriate.

Tilt Correction

When scanning the envelope, the envelope may have a certain degree of tilt (requires no more than), the resulting image will be tilted, this will affect the accuracy of recognition, so the need for the six frame tilt correction.

Invoice number 4 borders is a straight line, so long as calculated on the border or left border of the slope can be dip and then image the geometric center is the origin, Rotate the image θ can be corrected.

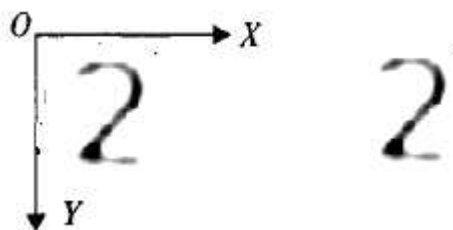
Take a Zip Code box image, the upper-left corner of the image point as the origin $(0, 0)$, horizontal to the right of the x-axis, straight down the y-axis.

Set the column number $i = 0$, along the x-axis from top to bottom scan of the image to find a value of "1" (is black), point A $(0, y_0)$.

$i = 1$, along the image x-axis from left to right scan, to find a value of "1" (ie black), point B $(x_0, 0)$.

Set up the straight line equation is $y = kx + b$, use A, B Two points the coordinates of the calculated slope $k = y_0 / x_0$, and acquire $\theta = \arg \tan k \quad \theta \in (0, \pi/2)$. if $\theta \geq \pi/4$, The straight line is the left border, then counter-clockwise rotating images; if $\theta < \pi/4$, The straight line for the border, then clockwise to rotate the image.

The center of the image is set to the origin (x_0, y_0) , any point (x, y) rotated coordinates is (x', y') , and $x' = x_0 \cos \theta + y_0 \sin \theta$, $y' = -x_0 \sin \theta + y_0 \cos \theta$, as is shown in Fig4 (a), as shown in Figure 4 (b) after tilt correction.



a) Before tilt correction (b) After tilt correction

Fig. 4 Tilt correction

Extract the Digital Character from the Invoice Number

Steps are as follows:

As a unit, from the upper left to the first scan down to the upper part of the image, to find a white pixel, and $f(x_0, y_0-1)$, point (x_0, y_0-1) for the black pixels points.

start from the bottom right corner as a unit to the right to the left lower half of the scanned image points, find a white pixel (x_1, y_1) and $f(x_1, y_1 + 1)$, namely the point $(x_1, y_1 + 1)$ for the black pixels.

Isolated from the Zip Code box Zip Digital pane, the pane of vertex pane height $(y_1 - y_0)$ (x_0, y_0) , and pane width $(x_1 - x_0)$.

Pane Zoom

Pane is scaled to a standard size. Pane zoom ratio along the x-axis direction K_x along the y-axis direction scaling ratio K_y , the original pane of the point (x, y) transform to a point in the standard pane (x', y') , and $x' = K_x \cdot x$, $y' = K_y \cdot y$.

Position Normalized

Digital position normalized Zip figures in the standard pane central location. The experiment, using the location of the centroid normalized than the geometric position of the normalized help to improve the recognition rate of handwritten Zip figures [3].

Gray value is $f(x, y)$ in Standard pane $l \times w$ of point (x, y) , coordinates of tag numbers (x_G, y_G) , and

$$x_G = \frac{\sum_{x=0}^w \sum_{y=0}^l x \cdot f(x, y)}{\sum_{x=0}^w \sum_{y=0}^l f(x, y)} \quad y_G = \frac{\sum_{x=0}^w \sum_{y=0}^l y \cdot f(x, y)}{\sum_{x=0}^w \sum_{y=0}^l f(x, y)} \quad (4)$$

The position of the center of mass to the pane $(l/2, w/2)$, Each black pixel of the character figures (x, y) move to (x', y') , and

$$x' = x + w/2 - x_G, y' = y + l/2 - y_G \quad (5)$$

Digital Refinement

Digital stroke density features as a handwritten numeral recognition feature, you must first refine the standard pane, the connectivity of the refined figures should remain unchanged. Thinning algorithm is as follows [4]:

Standard pane black point (x, y) as the center of the 3×3 neighborhood of eight points, calculated as follows:

And point (x, y) adjacent to eight the number of black spots in the point, denoted by $p(x, y)$

Eight points clockwise (or counterclockwise) direction along the bypass week, eight-point gray value of $f(x, y)$ from 0 to 1 the number of Denoted by $q(x, y)$. If the following four conditions are met, then delete the point (x, y) , that the gray value of point (x, y) $f(x, y)$ from 1 to 0.

$$2 \leq p(x, y) \leq 6$$

$$q(x, y) = 1 ;$$

$$f(x, y-1) \cdot f(x-1, y) \cdot f(x+1, y) = 0 \text{ Or } q(x, y) \neq 1 ;$$

$$f(x, y-1) \cdot f(x-1, y) \cdot f(x, y+1) = 0 \text{ Or } q(x, y) \neq 1. \quad (6)$$

Fuzzy Identifier Designs

Extract the Identification Characteristic of Alphanumeric

Stroke density features shaped distortion and displacement of the better anti-interference ability and due to the invoice number at different times, different alphanumeric glyph, stroke density characteristics as the identifying characteristics of the character figures to get higher recognition rate.

For $l \times w$ standard window, from the horizontal, vertical, 45,145 scanning figure of the four directions in each direction, with n features, the formation of $4n$ components of feature vectors:

$$G = (G_{11}G_{12} \cdots, G_{1n}, G_{21}G_{22} \cdots G_{2n}, G_{31} \cdots G_{3n}, G_{41} \cdots G_{4n}) \quad (7)$$

In order to reduce the number of components in the feature vector in order to reduce the number of nodes of the BP neural network input layer can be several rows of pixels merge into a scan line. This dimensionality reduction processing can effectively reduce the size of the BP network, improve real-time identification. The experiment, in each direction to take the 16 scan lines, the formation of of $16 \times 4 = 64$ component feature vector. Binary image only for the number of black pixels on scan line scan to digital cumulative calculation can be obtained for the coordinates of the four directions pane are quantified as a 16, the function g is used to calculate the number of black pixels in a pixel line. Let p be the total number of pixels along a certain direction, the number of rows of pixels in a scan $pn = p / 16$; set any one scan line of the starting line of the pixel rows pst , a scan line black pixels of the $pn = p / 16$; line number of the starting pixel line set an arbitrary scan line for the pst ,

A scan line of black pixels is $g_{st} = \sum_{k=1}^{pn} g(p_{st} + k - 1)$, among $s=1, 2, 3, 4, t=1, 2, \dots, 16$.

Figure 5 is the stroke density features extracted schematic (horizontal direction).



Fig. 5 The horizontal scan digital stroke density

Based on the Design of the BP Neural Network Fuzzy Recognition

BP neural network for fuzzy recognition of handwritten digits is divided into three layers, input layer has 64 nodes, and 10 nodes in the output layer, hidden layer take 10 nodes. The output value of the output node 10 is to be an identification number is 0 to 9 of the degree of membership. The input layer to hidden layer connection weight matrix $w1 = [w_{ij}]_{64 \times 10}$, Hidden layer to output layer connection weight matrix $w2 = [w_{jk}]_{10 \times 10}$. Transfer function to select the Log-Sigmoid function, the expression is $f(x) = 1/(1 + e^{-x})$. Sample training BP network convergence after get stable weights matrix fuzzy recognition of a handwritten numbers $w1$ and $w2$. In the training of BP neural network, using a variable learning rate method to improve the speed of convergence.

Experimental Results and Summary

Random collection of 20 gray-scale image of the envelope as the sample set, after the pretreatment, get the training sample of $20 \times 6 = 120$ alphanumeric. $64 \times 10 \times 10$ BP neural network training of the identifying characteristics of each character figures after normalization and refined to extract samples. Random collection of 60 of the 10 zip codes handwritten numeral recognition, the fuzzy recognition system correctly identified more than 90%.

The system remains to be improvements from the following two aspects: First, to further improve the recognition rate is to improve the real-time. This requires all aspects of the algorithm used for further analysis, comparison and optimization.

References:

- [1] Rafael C G, Richard E W. Digital Image Processing(2th)[M].New Jersey: Prentice Hall ,2002.
- [2] WEI Wu, ZHANG Qi-sen, HUANG Xin-han. Research of Number-Plate Recognition Using Distributed Processing[j].JOURNAL OF CHANGSHA COMMUNICATIONS UNIVERSITY, 2000(02):77- 81.
- [3] WANG Ming-chang, XING Lixin1b, YANG Yiheng, LIU Zhihui. Directional Weighted Two Dimensional Multistep Median Filtering in Image Processing [J]. Journal of Jilin University, 2006(01):18-22
- [4] WANG Jian Ping, QIN Feng. On the adaptive binarization filtering algorithm for gray character images and its application [j]. JOU RNAL O F HEFE IUN IV ERS ITY O F TECHNOLO GY, 2004(05):509-513
- [5] Zhao Xuechun,Qi Feihu, Automatic Recognition of Vehicle License Based on Color Segmentation [j]. JOURNAL OF SHANGHAI JIAOTONG U NIVERSITY, 1998(10):4:8

Expert System for Fault Intelligence Diagnosis of Gasoline Engine

Jinping Wang

Zibo vocational institute, Zibo, China

Key words: Neural Network; Automotive Engine; Expert System; Fault Diagnosis; MCU

Abstract. This paper describes the composing of Fault Diagnosis Expert System of auto engine. A model for fault diagnosis expert system, based on artificial neural network and expert system, is proposed. Firstly, we build a diagnosis tree, which is based on a fault tree to build an expert system for Diagnosis, then, get training samples from the fault tree and combine the self-study function of ANN to analyze and diagnose faults from different aspects and layers by several different ways to improve the efficiency of system diagnose, overcome the disadvantage of traditional Fault Diagnosis Expert System. This system takes the Single chip microcomputer as a developing tool. It's well operated and visible. Compared with the results obtained by BP- ANN, our method has more fast convergence rate and high computation efficiency. It is an efficient and reliable novel fault diagnosis technology.

Introduction

At present domestic and foreign automobile gasoline engine fault diagnostic technology and equipment can be divided into two categories: the first category is engine comprehensive analysis test instrument, such as a (REPPET63, QFE-3), flute Granville Technology computer engine tester, Pausch Full PC engine analyzer. These devices are widely used at present, but the use of technical requirements high, and can not directly determine fault location, in the diagnostic process of testing personnel needed by experience and relevant manuals, the use is not convenient, and the import of equipment is expensive, so it is difficult to promote the use of. Second is a major fault diagnosis expert system software, which is mainly characterized by inquiry method, qualitative analysis of fault location, in specific work process also need first class equipment testing parameters, the existence of the bottleneck problem of knowledge acquisition, reasoning in knowledge matching problem of conflict, therefore is not practical. This article mainly aims at the above two kinds of technical deficiencies, one in terms of the development of intelligent fault diagnosis expert system, to achieve by the fault repair mode to the fault before the preventive repair mode change; on the other hand, by determining the reasonable parameters for the diagnosis and diagnostic criteria, the real At the time of diagnosis technology and development of the intelligent computer diagnostic software com., through man-machine dialogue in qualitative analysis and quantitative analysis, thus effectively, quickly, accurately for gasoline engine is not the disintegration of accurate diagnosis, distinguish the fault position, given the trouble causes and solutions. This can greatly reduce the repair work blindness, enhance repair quality, shorten the repair time, reduce the cost of repair.

Analysis Method of Automobile Engine Base on Fault Diagnosis Tree

Diagnostic tree (Diagnosis Tree) is guided fault finding due to operation flow chart. It depends on fault tree, the test set, and the best criterion set search strategy research of the integration and innovation of P. For engine exhaust pipe blue smoke, oil leakage fault tree analysis. Diagnosis tree is characterized by fault search along "branches" gradually, in the downlink search encountered at each node are provided "differential" operation, in accordance with its differential results contrast with the corresponding criterion, determine the fault direction finding. Diagnosis tree is mechanics, graph theory, optimization theory, the artificial intelligence technology fusion products, according to the specific type of machine fault tree, the test set, criterion set and optimal search strategy can pose a diagnostic tree. Diagnostic tree out of the "differential" operation, after optimization, avoid

blind search, improving the efficiency of diagnosis. Diagnosis tree is also a fault diagnosis knowledge base of ideal forms of organization, can make the knowledge base of the expert system fault diagnosis. The optimal search strategy theory can be used to guide the real time detection of diagnosis parameters selected, sensor set, to achieve complex "intelligent" accurate diagnosis.

Function Structure of Engine Fault Diagnosis Expert

The traditional expert system (Expert System) in many areas has been widely applied and obtained many achievements, but in the development process also encountered the difficult problem to overcome, such as knowledge acquisition "bottleneck" problem, reasoning and learning ability of. Neural network (Neural Network) is a kind of information processing system, which is composed of many very simple, highly connected between each processing unit comprises a complex network, which is based on numerical calculation of knowledge processing system. Use of neural network expert system can be on the problems encountered in the use of make up for. So both a scientific and comprehensive, deep knowledge of people, give full play to their strengths, this is the essential feature of intelligent systems and inevitable trend.

The system of expert system and neural network and the combination of multimedia technology According to the gasoline engine structure, function principle and repair expert practical experience, using computer simulation based fault diagnosis tree, by diagnostic tree extracted from the training samples, is provided to the neural network learning, learning generated after weight and threshold knowledge.

In the model, according to the gasoline engine of this complex system is main form, divided into the ignition system, fuel system, cooling system, lubricating system and mechanical part of several subsystems, corresponding to the establishment of the artificial neural network model, and ultimately become a has nearly 30subset of complex neural network neural network model. The model of neural network learning algorithm with momentum BP algorithm we use a VB programming language to achieve a diagnosis based on neural network fault diagnosis expert system of gasoline engine. The reasoning process using forward inference mechanism, namely the input fault phenomenon, the cause of the malfunction The diagnostic features of expert system and neural the combination of network technology, from different angles, different levels of diagnostic reasoning, and neural network to complete the self learning function.

Neural network of the engine ignition system fault to explain the formation of neural network build process

The Fault Network Model

According to the ignition system fault classification of relevant knowledge, construct a $5 \times 5 \times 3$ of the 3layer BP network. Network inputs are 5 different fault phenomenon, if the conditions to meet the input value is 1, or 0, if you are not sure, take 0.5, the output layer represents the network classification results, divided into low voltage circuit fault, high voltage circuit fault, high and low voltage circuit fault

The Neural Network Training

The network after the 4300training, error values decreased to below 0.0001%. When in use, the 5 input parameters, the network has 3output value. If a1output equal to or close to 1, is such a failure; if the 3output are 0or much smaller than 1, said ignition system normal work. The resolution reached more than 95%.

Table 3 provides the results of training as the connection weights and threshold value, the data is the knowledge base.

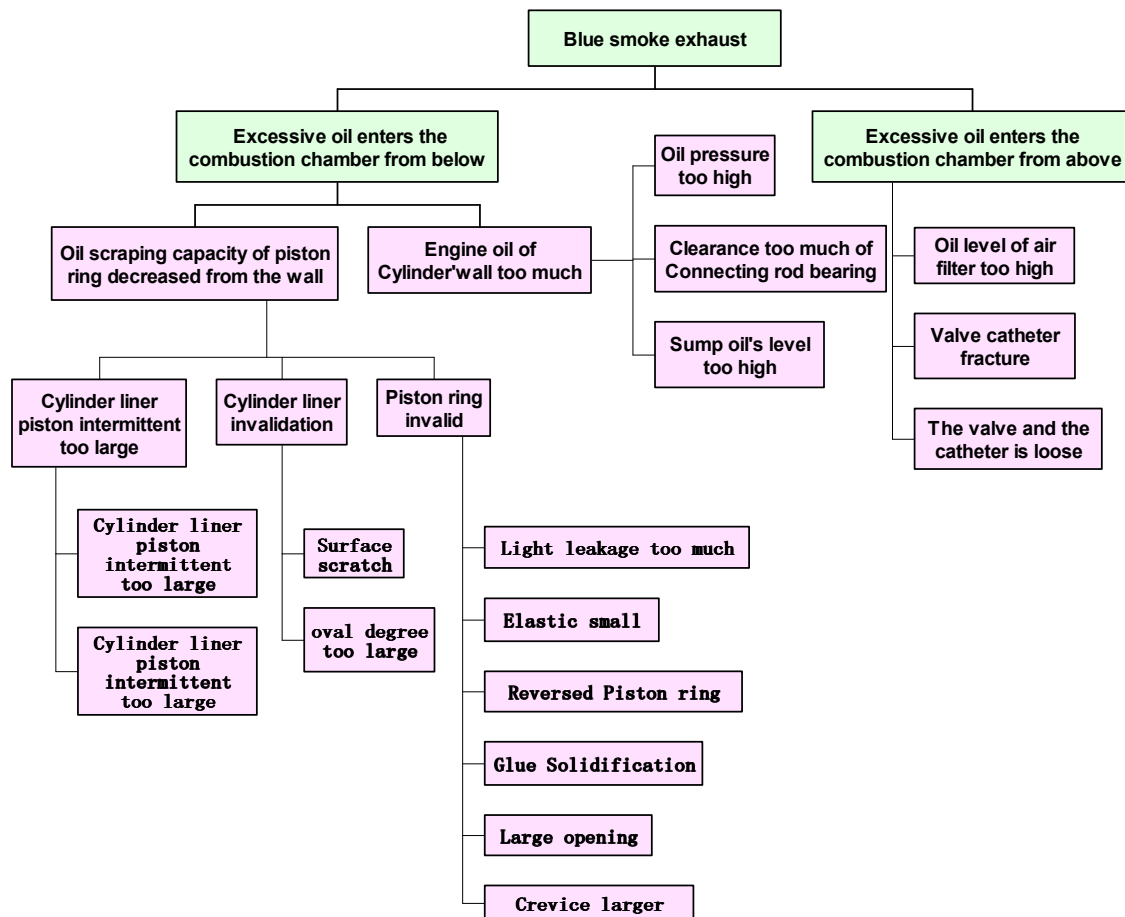


Fig. 1 Blue smoke exhaust from engine pipe and drain engine oil fault tree Ignition failure of sub neural network model (as is shown in table 1)

Table 1 The fault phenomenon

X1: Current situation	0: Normal	1: Abnormal	0.5: Uncertain
X2: Ignition cable electric leakage	0: Normal	1: Abnormal	0.5: Uncertain
X3: Ignition cable spark condition	0: Normal	1: Abnormal	0.5: Uncertain
X4: High voltage wire electric leakage	0: Normal	1: Abnormal	0.5: Uncertain
X5: Start sign	0: Normal	1: Abnormal	0.5: Uncertain

The fault phenomenon

y1:Low voltage circuit fault	0:No	1:Yes
y2:High voltage circuit fault	0:No	1:Yes
y3:both	0:No	1:Yes

Table 2 Fault diagnosis of engine ignition system of training samples

Sample	Input node					Output node		
	X1	X2	X3	X4	X5	Y1	Y2	Y3
1	0	1	0.5	0	0	0	1	0
2	1	1	0.5	0.5	1	1	0	0
3	0	0	1	0.5	1	0	0	1
4	0	0.5	0.5	0	0	0	0	0
5	0	0	0	0.5	0	0	1	0

6	1	0.5	0.5	0.5	0	1	0	0
7	0	0	0.5	0.5	0	0	0	0
8	0	0.5	0.5	1	0	0	1	0
9	1	0.5	0.5	0.5	1	1	0	0

Table 3 The knowledge base structure at the end of network training

Hidden layer		Input layer				Threshold	
	1	2	3	4	5		
1	9.526	-3.45	3.453	-2.466	-4.845	0.395	
2	-3.048	5.777	-11.457	2.401	-3.82	1.625	
3	-3.892	-3.856	4.567	-2.98	0.962	1.782	
4	-0.799	-0.252	-0.887	-0.699	-1.812	6.012	
5	0.812	-0.275	-6.521	0.659	-0.384	-0.28	

Output layer		The hidden layer			Threshold	
	1	2	3	4	5	
1	4.961	-8.449	-8.123	-6.021	3.336	-1.956
2	-13.042	13.478	-6.409	-1.02	-2.094	-2.864
3	-8.022	-7.098	6.412	-2.752	-1.985	-0.512

Figure 2 shows the overall structure of the system, the main fault diagnosis, expert in learning, the phenomenon of fuzzy neural networks in fault diagnosis of gasoline engine, structural parameter diagnosis module.

Knowledge Base Inference Engine and Application of Diagnosis Example

Knowledge Base and Reasoning Machine

Automobile engine fault diagnosis expert system is the core of knowledge base, used for storing the professionals in the field of data, rules, facts and experience knowledge, knowledge level, perfect degree, directly determines the whole system level.

The system of knowledge representation in two / A is the expert experience and formal rules, and stored in the knowledge base. Another is through historical data to train the neural network, thus summed up the new diagnostic rules, continue to expand the knowledge base of the content, so that the knowledge base with self learning function, this is the system and other common diagnostic system of the important difference.

System of intelligent reasoning machine is important reflect, reasoning system mainly includes neural network shallow knowledge reasoning and expert system of deep logical knowledge reasoning neural network system relies on the trained network was calculated using the results of reasoning, forward reasoning mechanism, from the initial state, forward reasoning, to the target state. Neural network inference on the same layer treatment unit is parallel, to overcome the traditional reasoning of " matching conflict" and other difficulties deep reasoning relies on knowledge base and reasoning machine, mainly uses fault tree, system using neural network in combination with expert system, can solve the general expert system can solve the problem.

The Hardware Principle Schematic

Using STC89C58 single chip The use of 4* 4 key, realize the fault input,320240 is led, the realization of the menu display and result output, the circuit through the serial port to transmit data to the computer, thereby enabling real time monitoring and the source code design.As is showed in Fig 3.

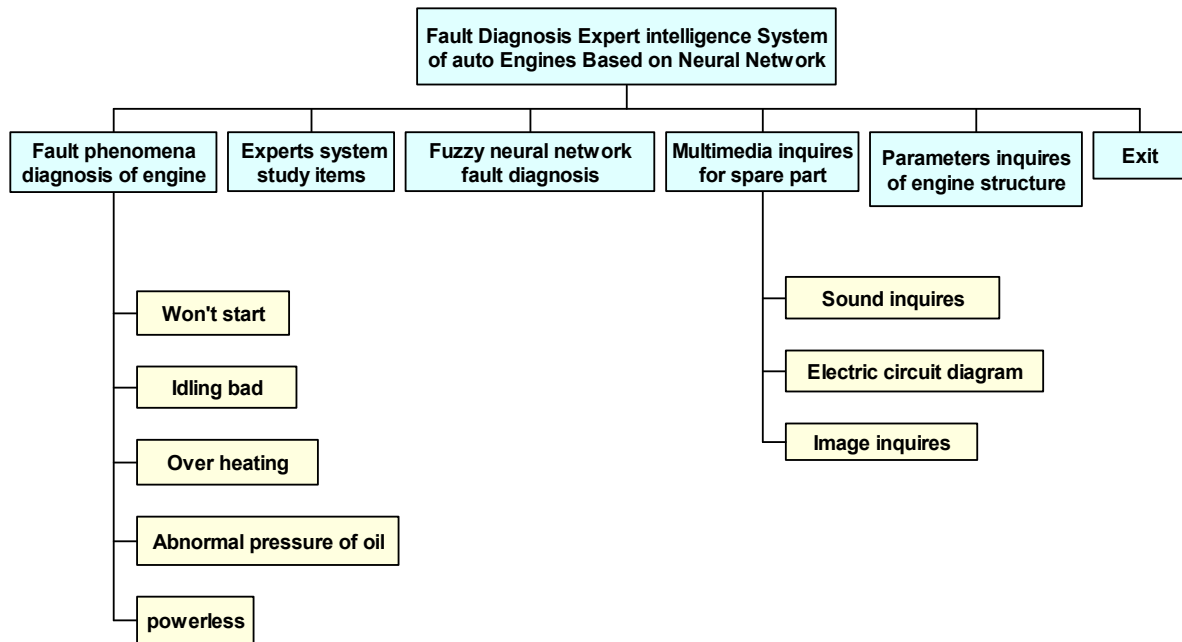


Fig. 2 Schematic block diagram

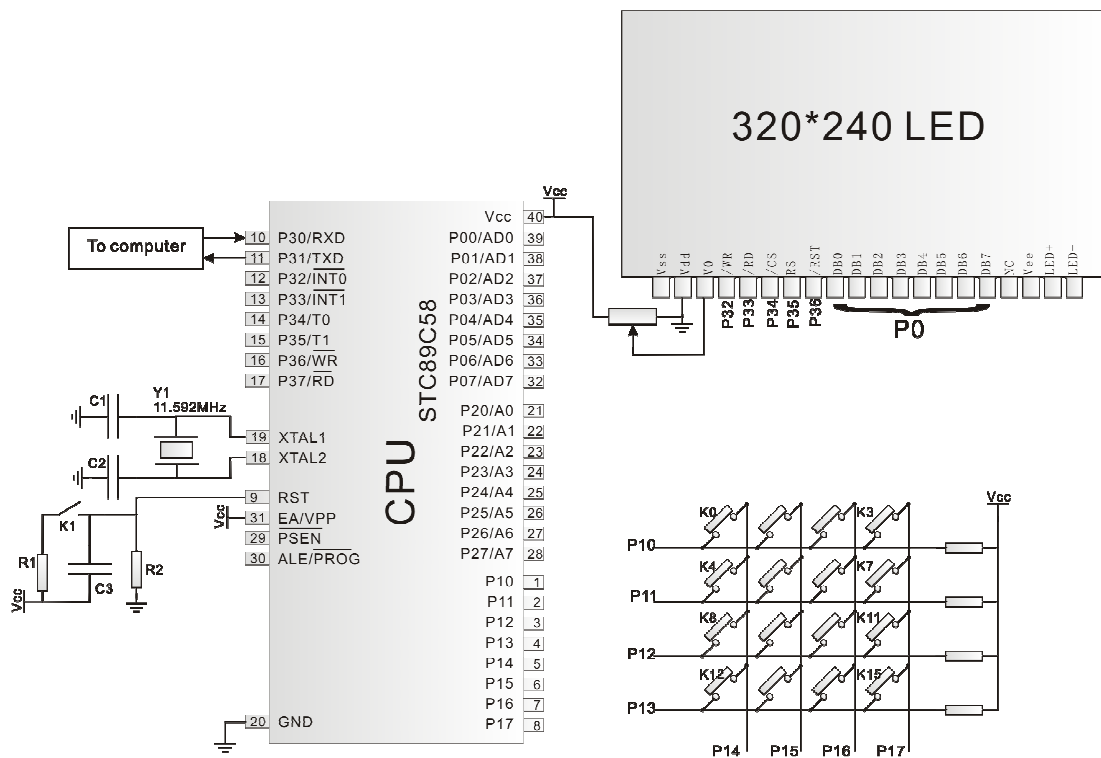


Fig. 3 The hardware principle Schematic

Conclusion

Using neural network and expert system combine two technologies constitute a new intelligent diagnosis system for gasoline engine, is the inevitable trend of fault diagnosis technology. Using VB procedures and neural networks and multimedia technology development of automobile engine fault diagnosis expert system, is one of the systems and components for gasoline engine fault diagnostic system can realize omni-directional, gasoline engine fault fast, accurate and intelligent diagnosis. The system has friendly interface, convenient operation. On the use of personnel is not high, easy in popularization and application of auto repair line.

References

- [1] H R Nielson. Theory of the Back propagation Neural network [J].IEEE UCNN, 1989, 1: 693 - 696.
- [2] Martin T Hagan, Howard B Demuth. Mark Beale [M]. Neural Network Design, 2002
- [3] Y Stephanedes. Implementation of on - line Zone Control Strategies for optimal ramp metering in the Minneapolis Ring Road [C]7th International Conference on Road Traffic Monitoring and Control, 1994. 181 - 184.
- [4] M Papageorgiou, H Hadj - Salem, F Middelham. AL INEA local ramp metering: Summary of field results [J]. Transportation Research Record, 1997, 1603: 90 - 98.
- [5] H M Zhang, S G Ritchie. Freeway ramp metering using artificial neural networks [J]Transportation Research Part C, 1997, 5(5)273 - 286.
- [6] L Jacobsen, K Henry, O Mahyar. Real - time metering algorithm for centralized control [J]. Transportation Research Record, 1989, 1232: 17 - 26.
- [7] T Caylor, D Meldrum, L Jacobson. Fuzzy ramp metering: design overview and simulation results [R]. Transportation Research Record, 1998, 1634: 10 - 18.

Implementation of FIR Filter Based on DSP

Wei Wang

Naval University of engineering, Hubei, Wuhan, 430033

Keywords: DSP; Tms320c5410; Fir Filter

Abstract. DSP chip is especially fit for digital signal processing. Its main application is realizing all kinds of digital signal processing arithmetic such as clove hitch correlation, all kinds of transforms etc. Realizing digital filters with DSP is an important application. The paper discusses the filter's software realization based on TMS320C5410 and finished the hardware systems of noise-restraining. The main works accomplished are as following: realization of FIR filter with window function, and realization on TMS320C5410 chip, the result of experiment to make clear.

Introduction

In digital signal processing systems, are often used for FIR digital filter, this is because the FIR filter can approximate arbitrary amplitude-frequency characteristic of the filter, and obtains good performance, in this paper introduces the FIR low pass filter DSP realize.

FIR Filter Realization Method

In the design of the use of DSP is TMS320VC5410. It belongs to the TI C5000 series C54X series, TMS320VC5410 is a 16 bit fixed-point processor, the compilation of program design, the FIR filter coefficients using Q15 format, i.e. the coefficients must be converted to Q15 format, as long as this will filter the coefficient multiplied by 2.

Using DSP to achieve Z algorithm is very convenient, there are two commonly used methods: linear buffer method and the cycle of the buffer zone method. In this paper uses a circular buffer method, circular buffer method:

For the N order FIR filter, in a data memory to open a also known as sliding window N unit buffer, sliding window for the new N input samples;

Every time into the new samples, to the new sample rewrite of sliding window in the old data, and the sliding window in the other data does not need to move;

Using the on-chip BK (cyclic buffer length of sliding window are) register indirect addressing, circular buffer address both adjacent.

FIR filter core algorithm is the calculation of the input signal and the filter coefficients of the convolution. Let $x(n)$ as input signal, $H(n)$ for the FIR filter impulse response, $n = 0, \dots, N-1$, FIR filter output $y(n)$ is $x(n)$ and $H(n)$ convolution, i.e.:

$$y(n) = \sum_{m=0}^{N-1} x(n-m) * h(m) \quad (1)$$

Since convolution digital signal processing is the most commonly used algorithms, so almost the entire DSP chip is provided with specialized instruction support convolution operation. In TMS3205410 can use MACD instructions complete convolution. The MACD instruction form as follows:

Macd (Smem, pmad, src).

In the Macd commands, Smem is indirect addressing parameters; it is the instruction to the data memory address. Pmad is expressed in program memory address 16 constants. Src said accumulator, can be A or B accumulator accumulator. This instruction in the execution of the instruction, the pmad constants to the program address register in the PAR, then the Smem address data in a PAR address in program memory data read in the multiplication, and the product is accumulated to a

specified by Src accumulator. During instruction execution, Smem address and content was also copied to the T registers and Smem low after the next address unit. If using the repeat command repeat MACD instruction, the execution of instructions at last, PAR automatic register plus 1, such that when the Macd is executed again on the direct use of PAR address is read from the program memory data. Typically, Macd instruction execution requires three cycles. But if you use repeat Macd enters the pipeline instruction execution, as long as a cycle can be performed on a Macd instruction. Thus, the instruction at the same time to complete the multiply-accumulate and data delay (shift) function, which is required by the convolution algorithm.

For an input sequence, it is in the two cycle in the buffer memory as follows, to establish a buffer zone will be the first circular buffer size register value is set to $N / 2$ auxiliary register AR4 refers to the buffer (Buffer1) AR5 refers to the top of the buffer 2(Buffer2) at the bottom, a new sample storage the buffer to the 1 buffer, to be first in 1 top 2 bottom move the data to a buffer, the processor then multiply-add, filtering procedures each operational step after AR4 to move data to the next window, while the AR5 points to the next input data, for the next operation AR4 point to address in 1, AR5 to $N / 2$ address. As shown in figure 1.

Figure 1 Schematic diagram of FIR coefficient storage format

Considering the Macd execution instruction is the low address data replication to high address to complete the delay function, so in MACD instruction computes the convolution, count $x(n-N+1)$ and $H(N-1)$ product, finally the calculation of $X(n)$ and $H(0)$. Therefore, in the process, the coefficients of FIR filter in program memory storage in a reverse order.

FIR Filter in Software Design and Debugging

This design uses the C language and assembly language programming mixed manner, the main program by C language, while the core of the FIR filter is prepared by the assembly language. Using C language to develop DSP procedure not only make DSP development speed is accelerated, and the development of DSP program readability and portability also increased significantly, program modification is also very convenient. Using C compiler optimization function can increase the efficiency of C code, in some cases, the C code efficiency even close to the manual code efficiency. Using C language to develop DSP program, DSP chips in the operational capability is not very tense is very suitable. Although the C compiler optimization function can make the C code efficiency is greatly increased, but in some cases, the C code efficiency or not and manual compilation code efficiency compared, such as the FIR filter program. This is because, even the best C compiler, not in all cases can be optimally using DSP microarrays offer a variety of resources. Using C language interrupt program while the readability is very good, but due to the interruption of the procedure, sometimes regardless of whether to use program, interrupt program will register protection, so as to greatly reduce the interrupt program efficiency. If the interrupt program frequently call, even if an instruction is crucial. In addition, using C language to achieve DSP chip some hardware control is not convenient assembler, some even can't use C language to achieve. Therefore, in many cases, DSP applications often need to use the C language and assembly language mixed programming method to achieve, in order to achieve the best use of the DSP chip hardware and software resources for the purposes of. With the C language and assembly language mixed programming method mainly has the following three kinds:

Independently prepared C procedures and compilation, separately compile and assemble, form the respective object code module, and then use the linker C module and assembly module links up. For example, FIR filtering program in assembler language, on the FIR program in assembler compilation, form the object code module, and the module of C links can be in the C program called FIR procedures.

Directly in the C language program of the corresponding position is embedded assembly language.

On the C compiler Generate corresponding assembler, and then the assembler manual optimization and modification.

The above example is used in the first method, which is a commonly used C language and assembly language interface method, this method is the most important to comply with C compiler defines the function call rules and register usage rules. Following these two rules will ensure the compilation module does not destroy the C language runtime environment. C module and assembly module can access the custom function or variable.

Assembler debugging firstly based on the CCS new fir.mak project, and then the assembly language source file (.asm or.c) file and the interrupt vector file (.asm), a file (.cmd) added to the project. If C language program will have to add "stdio.h", "math's"" rts.lib" compiled by later generation. Out files, can be downloaded directly to the test panel At this time, should pay attention to the hardware condition, special attention should be given to whether the respective hardware lamps in the normal condition, but also should pay attention to hardware emulator is normal. If no hardware problems, procedures can be normal to download, and then open the Memory window, you can see the data memory is divided off_fir, d_data_buffer, in_buffer, out_buffer district. The compiler and the entire FIR project successfully downloaded to the target system board, FIR program can run on the board in the EVM. The procedure sees Appendix C.

In the main program, in flag = 0breakpoint is set; click "Run" to run the program, the program will run to the breakpoint stop; View / Graph / Time / Frequency opened a graphic observation window as shown in fig. 2.

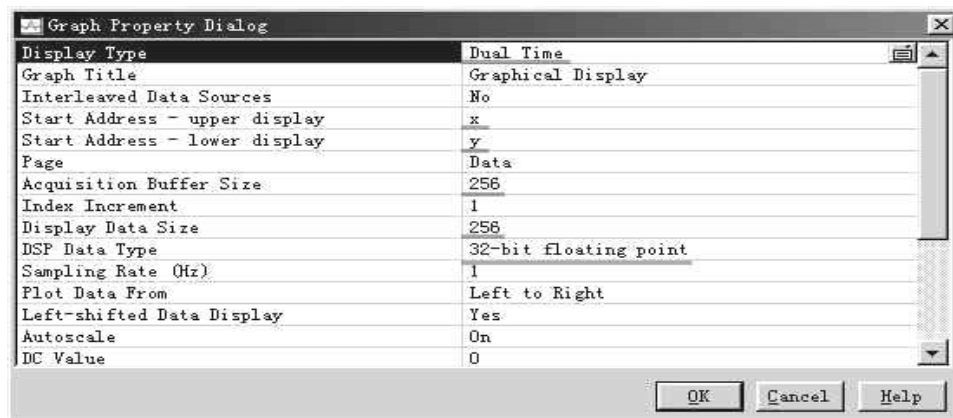


Fig. 2 Graph parameter settings window

An observation window graphics variables and parameters: the dual trace observation start address are x and y, length of 256unit in numerical changes, numerical types for 32 bit floating-point variable, the two arrays are stored by the A/D conversion input aliasing signal (input signal) and the signal FIR filter results; click" Animate" to run the program, adjust the observation window and observed the filtering results, as shown in fig 3.

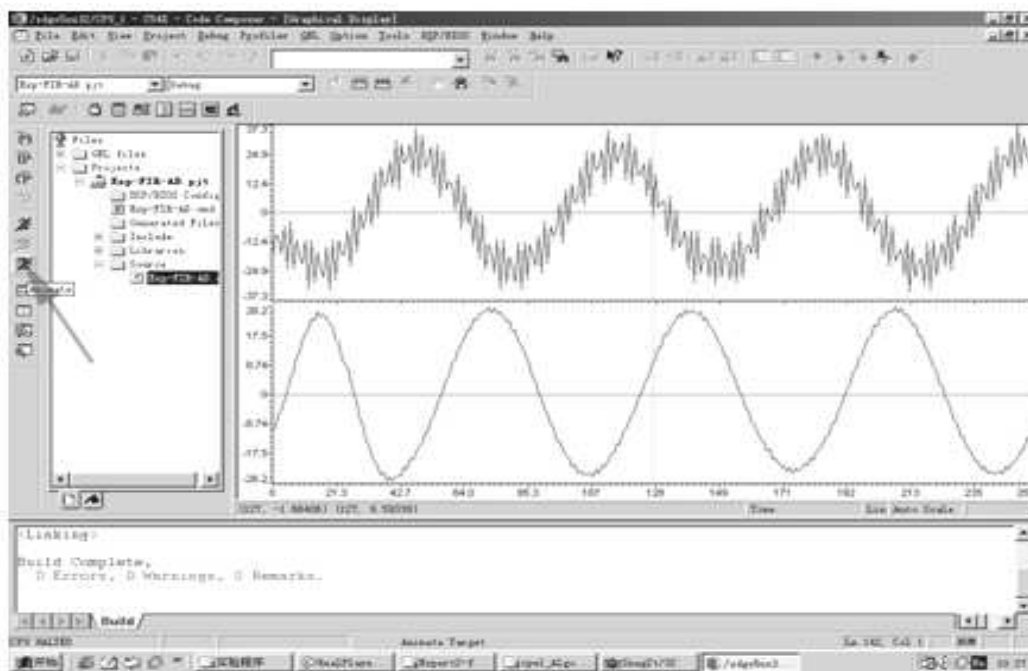


Fig. 3 The test result

Conclusion

Through the test waveforms can be seen, the DSP5410real filter performance achieved algorithm simulation requirements. Considering DSP5410 is fixed point DSP, so the input signal and the filter coefficients are converted into a set of points, in order to prevent the overflow, the input signal amplitude is reduced, its control is in1 to 1 between.

Reference

- [1] TMS320C54X DSP REFERENCE SET VOL.3: Algebraic Texas Instruction Set.Instruments Incorporated. 2001
- [2] Wang Anmin.TMS320C54XX DSP practical technology. Tsinghua University press.2002: 5-15
- [3] Peng Qi DSP and real-time digital signal processing.Chengdu: University of Electronic Science and Technology Press,1995
- [4] Fu Liqin, Gui Zhiguo, Wang Liming.The digital signal processing principle and realization. National defence industry press.2004
- [5] Zhang Xiongwei, Chen Liang, Xu Guanghui DSP integrated development and application examples [M]. Beijing: Publishing House of electronics industry2002.
- [6] TMS320C54x Code Composer Studio Tutorial.Texas Instruments Incorporated. 2000

Research on Program Calling and File Sharing between Windows and Linux

Lan Zhang^{1,a}, Min Yuan^{1,b}, Tao Liu^{2,c}, Li Wang^{1,d}, Peng Gao^{3,e}

¹Center for Genomics and Computational Biology, College of Life Sciences, Hebei United University, Tangshan, Hebei, 063000, China

²College of Science, Hebei United University, Tangshan, Hebei, 063009, China

³Tangshan Branch, Tiandi Science and Technology Co., Ltd., Tangshan, Hebei, 063000, China

^azhanglan0624@gmail.com, ^byuanmin308@163.com, ^cliutaocreate@gmail.com,
^dwlsh219@sohu.com, ^etsgaopeng@gmail.com

Keyword: Plink, PSCP, SSH, Batch Processing, Cross Platform

Abstract. There is often more than one kind of operating systems in enterprises' and organizations' local area network. Therefore, exchanging visits under different operating systems would be very meaningful and important. Especially in the field of bioinformatics, in order to meet the requirements of researchers from various disciplines, such as mathematics, biology and computer science, we develop a new, intuitive and convenient system for exchanging resources between Windows and Linux.

Introduction

Bioinformatics [1] is the study of biological information acquisition, processing, storage, distribution, analysis and interpretation. It uses mathematics, computer science, and biology tool to reveal many biological mysteries conferred by a large number of complex biological data. Since the large amount of biological data and analytical procedure is dependent on Linux operating system which provides higher stability and faster processing speed, it has put forward higher requirements on those mathematical and biological researchers who tend to use Windows operating system. In this paper, under the coordination of the communication protocol, we develop a new, intuitive and convenient system for exchanging resources between Windows and Linux using Plink and PSCP. This system achieves a good and customized human-machine interface through its interaction with software, which can be operated freely by researchers who are not familiar with Linux operating system. It brings much convenience to bioinformatics investigation.

Program Calling and Connection Sharing Structure

In this paper, an intuitive and convenient interactive system for exchanging resources between Windows and Linux is developed. We develop a good human-machine interface on the Windows client using C#.net [2]. On the Windows client, the batch processing program is called for the remote operation by clicking buttons. On the server side, we install a highly customizable operating system called Gentoo [3], which is one of the most popular Linux distributions. In addition, an interpretative language named Perl [4] and its extended module BioPerl [5] are installed for biological data analysis. BioPerl is a set of Perl modules for bioinformatics. It contains objects for Sequences, features on Sequences, and other important bioinformatics attributes. Meanwhile, the interactive processing mode is done by PuTTY in batch processing. The command-line connection tool named Plink coming with PuTTY will initiate a connection to the remote server and trigger the bioinformatics program. PSCP, provided by PuTTY, is responsible for transmitting files between the client computer and the remote server by SSH. Fig. 1 shows the implementation procedure of the system.

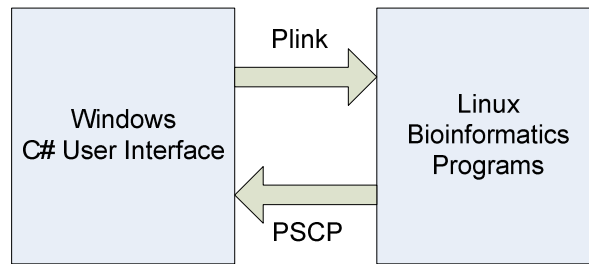


Fig. 1 The implementation procedure

Program Calling and Connection Sharing Technology

Batch Processing [6]

There are three kinds of executable files under DOS system, such as EXE, COM and BAT. Both the EXE file and the COM file are coded by binary form, only the BAT file is coded by text form and could be read directly. So the content of BAT file is much simpler than the other two binary form executable files. BAT file, also named batch processing file, usually consists of a series of DOS commands and calls for other programs. Although the component of batch processing file is not complicated, it is very helpful and widely used in many areas.

PuTTY

PuTTY [7] is a free and cross-platform Telnet/SSH client, which could simulate xterm terminal under both Win32 and UNIX.

Plink [8] is a command-line connection tool coming with PuTTY. It is mainly used for handling automated work, and performing procedures on SSH host fast and simply. PSCP [9] (PuTTY Secure Copy client) of PuTTY is responsible for transmitting files safely between the client and the server by SSH connection. Meanwhile, PSCP is similar to scp command under UNIX/Linux system and it can be used on any SSH server, including SSH v1 and SSH v2 server. SSH [10], short for Secure Shell, is a security protocol built on the basis of the application layer and transport layer. As a more reliable security protocol, SSH is designed to provide security for the remote login session and other network services. The communication process of SSH protocol is shown in Fig. 2. Version negotiation and algorithms negotiation reflect the flexibility and scalability of the SSH protocol. Moreover, its reliability and security can be indicated by the key establishment, server authentication and user authentication. Because SSH is built on TCP protocol, we need to establish a TCP connection at first.

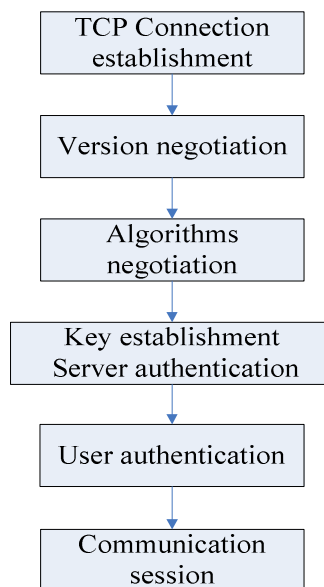


Fig. 2 SSH protocol process

System Implementation Procedures

Batch Processing Application

The application of batch processing is reflected on Button triggering in this paper. When the user clicks the button to run programs, with the help of SSH protocol, plink.exe will enter the command-line interface of Gentoo on the remote server terminal from the default server port 22 according to the preset user name and password. After the order is transmitted from the client terminal to the server end, the server will begin to run bioinformatics analysis program. When the server-side program is done and the progress bar on the bottom of the window shows 100%, the user clicks the program result back button, and then pscp.exe will duplicate the program result to the interface on the Windows client via the default server port 22.

Human-Machine Interaction Interface

In order to meet the needs of genome analysis and modeling, the client interfaces is written by C# language, which is an object-oriented high level language and based on .net framework. The client interface is composed of login interface, main interface of Center for Genomics and Computational Biology and Bioinformatics program interface. All those interfaces perform the massive data collection and collation by triggering buttons, and then discover new rules. Fig. 3 indicates that genome nuclear acids are translated to proteins by calling the module BioPerl on the remote server.

Fig. 3 Genome nuclear acids are translated to proteins by calling the module BioPerl on the remote server.

Summary

We developed a new, intuitive and convenient system for exchanging resources between Windows and Linux. Under the coordination of the communication protocol, the user can log in to the remote Linux operating system. In this system, bioinformatics analytic programs are run under Linux operating system and completed results are returned to the Windows client through batch processing and PuTTY technology. Finally, this system greatly meets the needs of researchers in the interdisciplinary field.

References

- [1] D. Zhang, in: Bioinformatics, chapter 1, Science Press, Beijing (2009)
- [2] K. Prabhakar Rao, G. Ashok Babu: Comput. Geosci. Vol. 35 (2009), p. 1369
- [3] C. Nie, D. Zeng, X. Zheng, F. Wang and H. Zhao: Service Operations and Logistics and Informatics (SOLI), 2010 IEEE International Conference

- [4] J. Julián, M. Guervós, P. A. Castillo and E. Alba: *Soft Comput.* Vol. 14 (2010), p. 1091
- [5] J. Crabtree, S. V. Angiuoli, J. R. Wortman and O. R. White: *Methods Mol. Biol.* Vol. 408 (2007), p.93
- [6] Y. Zhang, G. Li, Y. Chen, W. Chen and H. Yuan: *Exp. Sci. Technol.* Vol. 8 (2010), p. 34-36
- [7] Information on <http://www.chiark.greenend.org.uk/~sgtatham/putty/>
- [8] Information on <http://www.windowstpro.com/article/remote-computing/use-plink-to-reboot-vmware-vm>s
- [9] Information on <http://the.earth.li/~sgtatham/putty/0.60/html/doc/Chapter5.html>
- [10] J. Yang: *Comput. Digit. Eng.* Vol. 39 (2011), p. 112-114

Study of Control and Detection on Firing Circuit

Xiaohu Li^{1, a}, Yujie Wang^{1, b}, Haibo Jia^{2, c} and Jie Liu^{1, d}

¹School of Resource and Environmental Engineering, Wuhan University of Technology, Wuhan 430070, China

²Qianjin Civil Explosives CO., LTD, Luoyang 471600, China

^a lxh19860903@163.com, ^b yjwwhut@163.com, ^c qjjiahaibo@sina.com, ^d 181627661@qq.com

Keywords: firing circuit; signal detection; computer technology; network control

Abstract. To improve the firing circuit security and reliability, methods of control and detection was put forward for firing circuit. The electronic information relevant knowledge is applied to blasting engineering technology, including signal transmission technology, signal emitting and receiving technology and computer technology, etc. Through judging the digital signal to send and receive and using computer technology, network connections and detonating situation can be showed indirectly. So methods can reach. Besides, that can attain other purposes have, such as monitoring network, checking the situation of explosive material initiating and judging blast hole whether to explode or not.

Introduction

Gradually, the non-electric initiation system has been more used and been the main method in our country blasting engineering. But many accidents occurred during working with using them and misfire caused for firing circuit problems. The misfire could be harmful to next work before handled. To make matters worse, that may cause great casualties and huge economic losses. For example, in 1998, misfire appeared in Zhangzhou stone a flat chamber blasting engineering. In 1995, misfires of chamber blasting were detonated by changing initiation holes at the Guiyang Longdong airport camp site slope and lead a major accident. They left in the two years ago because of not check after blasting. In 2008, the open coal mine blasted in Ningxia and caused Heavy casualties accident. The survey found that was due to sympathetic detonation of group of misfires [1]. Yuan Shaoguo analyzed failure explosion in the ShiBao open-air iron ore blasting and found the firing circuit fault was an important reason causing the accident happened [2]. All these accidents occurred by firing circuit problems and misfires that was not checked after blasting. So, it should have to study methods of control and detection on firing circuit, which can improve the safety property of blasting engineering. Besides, it can obtain remarkable economic and social security benefits.

Research Status of Methods on Firing Circuit

Now, only electronic detonator blasting technique can be used to check blasting network on-line. Digital detonators and ignition system have unique technical characteristics, which can set delay time and control detonating network [3]. Chen Huafeng has put forward the development of electronic detonator design software for detonating network and network simulation [4]. But the non-electric initiation techniques have not achieved in advance to control and detect network, as well as other blasting methods.

Some foreign engineers used the method: either a circumscribed plastic blasting tube or fuse was connected in each blasting network node, marked, pulled to the safe distance and placed centrally. After initiation, check them to examine whether detonating network initiation or not indirectly. But there have some shortages.

1) Single function, only can test detonating network node; Amount of ignition material is more, and they are difficult for examination and approval and higher cost;

2) Equipments used in the detection of detonating network are impressionable by outside environment; Easy to give the result of false positives for the initiation material itself quality problem.

In order to improve the disadvantages, a method of control and detection on firing circuit has been put forward. It can monitor network which has been connected correct or not before initiating. After initiation, blasting network was detected whether to initiate accurately and initiation material (detonator) and blast hole whether miss-fire.

Based on this case, the relevant knowledge of electronic information is used. Signal transmission technology, the emitting and receiving technology, computer technology and etc, are applied in blasting engineering technology to study the network control and detection methods.

The features include: signal devices, lord signal device and the computer are used to transfer detonating network by signal to the lord signal device, and digital signal network diagram will be drawn by computer technology [5,6]. That will be the detonating network connection diagram. Purpose is to strengthen the control of detonating network, improve the security of blasting engineering, and reduce the misfire and accidents caused by detonating network connection error. Besides, it also can test initiating situation and strengthen the monitoring use of initiation material.

Principle and Measures

Action principle: first, according to the connecting way of network, a single chip with the wireless signals is fit in every panel point and set signal digital according to the series and position of detonating network panel point[7]. Trigger system should be set during connecting wireless signal device with initiation detonator. So when the detonator initiates, stable information cloud be collected by wireless signal device, and digital signal cloud be transmitted. After the installation of wireless signal, it should be connected with the lord signal device and the computer. So the digital signal form wireless signal device can be shown by the lord signal display device, and drew the signal network diagram with using computer. This signal network diagram is the blasting network connection diagram. According to the detection of line signal, it can judge the connection correct or not, and whether detonating network initiate accurately. The principle is shown in figure 2.

Technical Proposal and Steps Are as Follows:

Preparation for the system device of blasting network: system consists of wireless signal devices and computer; wireless signal device consists of transmitting and receiving device; wireless transmitting device composed by small wireless signal transmitter; wireless signal receiving device composed by lord of signal receiver. The fig. 3 shows the articulation of parallel tubes network [8-9];

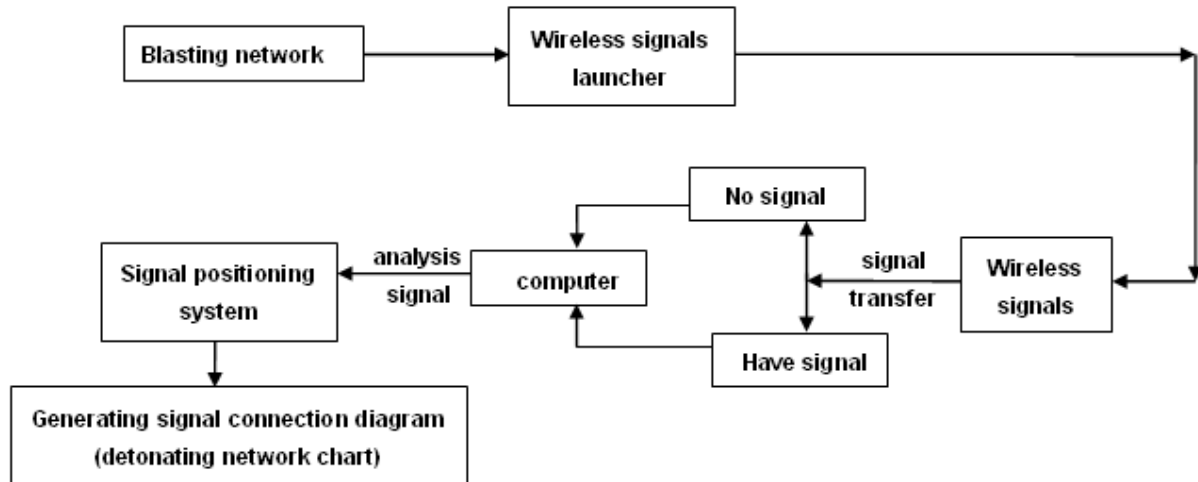


Fig. 2 The signal system of blasting network

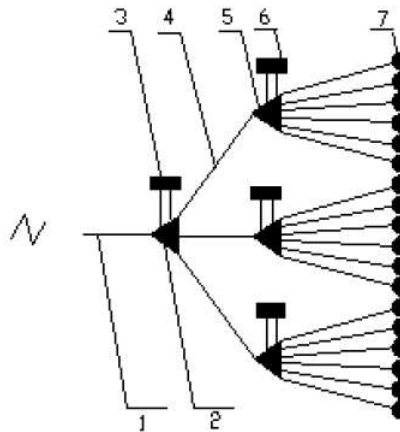


Fig.3 The connection of blasting network with wireless signal device

1-Lord plastic fuse; 2-Lord initiating detonator; 3-wireless signal transmitter connected to lord detonators; 4-second plastic fuse; 5-second detonator; 6-second transmitter; 7-fuse blasting cap in hole

Choose the type of lord receiver according to the detonating network connection nodes series. Lord receiver should simultaneously receive signals which amount must be greater than the number of detonating network connection nodes. The selection of wireless signals is able to have the function of launching digital signal, as shown in figure 4.

After the network connection, wireless sensor is connected with initiating detonator in signal node, and form a trigger signal send system. Then signal transmission must be test with the lord to confirm that the wireless signal cloud be normally triggered, sent, and received by computer. After that, the lord must be connected with computers, and confirmed that the signal could be displayed on the computer.

According to the different reaction of wireless signal device triggered, two manners can adopt. They are as follows:

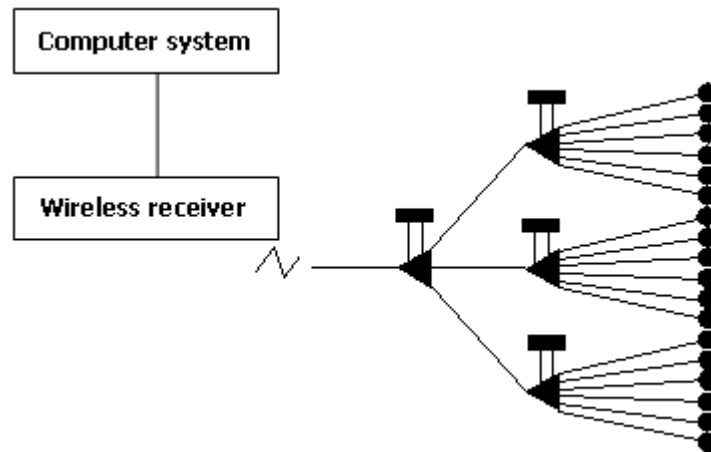


Fig. 4 The system connection of detonating network control and detection

Before the initiation, wireless signal emitter could start to launch the first group digital signals continuously after fit battery, and digital signals are received by the wireless signal receiver. Then they will be transferred to computer and displayed. Computer can automatically draw sequence diagram. After the initiation, if the detonators initiate at the node, the electric wire wined around the detonator will be dynamited at the same time. Then wireless signal emitters are triggered in the electric wire circuit, and a second group of digital signal will be launch to computer and displayed; If not, the computer will also receive and display the first group of digital signals, and sequence diagram will be drawn too. The two diagrams contrast. The result shows that the second group of digital signals displayed indicate the corresponding detonators already have initiated successfully, while the first group miss-fire.

Before the initiation, wireless signal emitter could start to launch the first group digital signals continuously after fit battery, and digital signals are received by the wireless signal receiver. Then they will be transferred to computer and displayed with red color. Computer can automatically draw sequence diagram. After the initiation, if the detonators initiate at the node, the electric wire wined around the detonator will be dynamited at the same time. So the electric wire circuit is broken, and the wireless signal emitter will be not work. The digital signals could be displayed with black color. If not, the computer will also receive and display the first group of digital signals, and they are displayed with red color. The two diagrams contrast. The red is initiated successfully, while the first group miss-fire.

Through the comparison of the two diagrams, not initiation point of the network node can be accurate positioning, and explode rate can be judgment. So the purpose of control and detection on Firing Circuit can be achieved.

Method Effects Analysis

Through research and analysis, the method has many good effects, include exploding monitoring, social security and economic benefits, and so on. There are beneficial effects.

Improve the detonating network monitoring: after the connection of detonating network, signal emitter should be fit in right place. And the computer receives and collects digit signals landed by signal receiver before initiation, then the system analysis digital signal and map digital signals connection diagram. This graph is the blasting network, which should be monitoring.

Add to detect exploding rate of blasting network.

Strengthen the use of regulation of initiation materials. And provide a method of detecting the misfire.

Can be judged on blasting effects: the blasting network diagram, explode rate data and so on, can be assessment for blasting effects

Have lots of advantages such as easy understand, security, and low cost, etc.

Conclusions

This method creatively connects blasting technology with signal system technology, computer technology and so on. By signal collection, transmission and reception, detonating network connection mode and initiating situation can be indirectly shown with computer technology in order to achieve in controlling and detecting on detonating network. At the same time other proposes can be reached, including blasting network monitoring, checking initiating situation and misfire. Besides it can also detect explode rate, strengthen the supervision of initiation materials and many other advantages.

Acknowledgement

It is a project supported by the High-Tech Research and Development Program of China (125Program) (2011BAB05B03) and the Undergraduate Innovation Program of Wuhan University of Technology (116808001).

References

- [1] GU Yi-cheng; SHI Ya-yu; JIN Yu-liang. Engineering Blasting (China Science & Technology University Press, Beijing 2009), in Chinese.
- [2] YUAN Shao-guo; WANG Li; LIU Bing-lei; WEI Xin. Cause Analysis of Electric Detonator Miss-fire Accident in Open Pit Metal Mine [J]. Blasting, 2011, 28(2):112-115.
- [3] TANG Yue; CAO Yue; LUO Ming-rong; WU Yan-li. Application of High-precision Electronic Detonator in Decreasing Blasting Vibration[J]. Blasting, 2011, 28(1):107-110.
- [4] CHEN Feng-hua; TANG Xiao-zai; WANG Zhu-ping. Application and Discussion of Electron Detonator in Explosive Demolition of Dockyard Cofferdam [J]. Blasting, 2011, 28(1):104-106.
- [5] ZHANG Dong; CHENG Guo-shun; WANG Zheng-lin. Proficient in LabVIEW Program Design(Electronics Industry Press, Beijing 2008), in Chinese.
- [6] WANG Yu-de. Digital Signal Processing (Beijing University Press, Beijing 2011), in Chinese.
- [7] CHEN Biao; XU Hai-tao. Radio Digital Signal Communicating System Based on SCM [J].Information Technology, 2011(03):103-106.
- [8] ZHAO Xiang; HUANG Dong-fang; ZHANG Wan-li. Research on Connection Mode of Nonel Priming Circuit [J]. Blasting, 2008, 25(2): 35-37.
- [9] CAO Yue; ZHAO Xiang; ZHAO Ming-sheng. Research on Articulation of Parallel Tubes Network [J]. Blasting, 2006, 23(2): 77-78.

Detector on Dam's Piezometric Tube Level

LinshengWang^{*1}, Donghe Xi¹, Linjing Wang²

¹ Henan Polytechnic Institute, 473009, Nan-Yang, China

² Henan University of Traditional Chinese Medicine, 473000, Zheng-Zhou, China

E-mail: wanglinsheng_317@163.com

Keywords: Dam; Piezometric Tube; Detector

Abstract. The change of reservoir dam's piezometric level can reflect the dam's internal structure, piezometric level number obtained by using detection technology can directly judge the interior defect, therefore, whether piezometric level detection is accurate or not is related to dam's safety. After years' research, the design scheme of integrating mechanics and electrics is put forward by combining with today's popular single chip computer technology and digital measuring technology, which is the scheme that we adopt the digital detection technology to convert the water level into pulse digital signal directly and calculate the piezometric level according to the number of single pulse. It is necessary to develop a Piezometric Tube detector with features of high precision, high degree of automation and high speed of processing and acquiring data and put it into use.

Introduction

The detector of dam's piezometric tube designed in our country is basically based on large or super large reservoir [2], and the surrounding environment is relatively stable. For our country, the small and medium-sized reservoirs are in the majority and the environment is diversified, if these instruments are used in the small and medium-sized reservoirs, on the one hand, the detectors can't make the most of the advantage due to the limit of the environment and requirement, on the other hand, the daily maintenance of instruments brings charges to reservoir, which will increase the burden of the reservoir [3].

According to the actual situation of piezometric level's detection, through analyzing the reasons of the above detector's problems, combining with the SCM technology and digital detection technology, it puts forward adopting the two-level distributed structure, which is provided by the PC and the extension. PC controls the work of the whole system by computer, and the extension is arranged on the area of each piezometric tube's nozzle. The extension can not only work dependently, detect the water level, display and so on through the keyboard interface connecting with the small keyboard, but also it can link with the Communication host through serial interface, and work under the control of the PC, the tested datas are transmitted to the host computer through asynchronous serial interface RS485. And the PC process the datas form each extension.

Design of the Detector on Dam'S Piezometric Tube Level

Design principle of the detector on dam's piezometric tube level Detector's probe is attached to a high-strength metal wire which winds the roller equably, the other end of the metal wire is connected to the monitoring circuit, the roller is turned to positive or reverse rotation under the control of stepper motor to drive the probe up or down. At ordinary times the probe is in the part of the piezometric tube's nozzle, when it need to monitor the water level, the SCM controls stepper motor to positive rotation, and the stepper motor drives roller to positive rotation, and the probe will decline. SCM send a pulse each time, the stepper motor will turn a stepping angle, and the probe falls a pulse equivalent (0.5 mm), when the probe falls to contact the surface, the monitoring circuit's output is from high level to low level, and it controls the stepper motor to stop turning while the SCM monitors the testing circuit's output to be low level [5]. According to the quantity of the sended pulse, SCM calculates the height of the probe's decline, so it could measure the depth of the pipe to the surface of water. Then the SCM controls the stepper motor to reverse rotation, and brings the probe to the nozzle renewedly.

Structure of the detector on dam's piezometric tube level Detector adopts the two-level distributed structure: PC and extension. The PC is made up of computer, RS232 to RS485 serial interface of asynchronous communication and Communication host; The extension is made up of the AT89S51 SCM, RS485 serial interface, the monitoring circuit, the monitoring probe, roller, stepper motor and driving circuit, which is shown as Fig. 1.

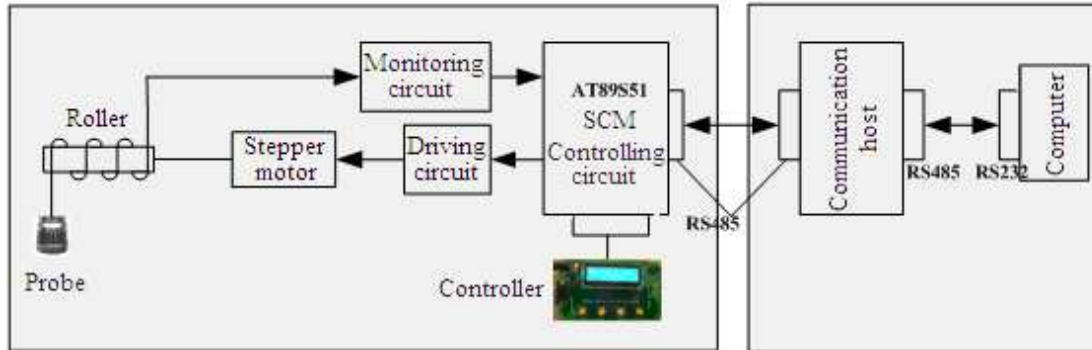


Fig 1 Structure of the detector on dam's piezometric tube level

PC sends command to the Communication host to make the extension measure, the Communication host transmits the measuring command to extension as soon as it receives the command that let extension measure, and the water level detector of the extension starts to measure. After its completion, it returns the water level's data measured automatically to the PC, and the program of PC takes the measured water level's data by the extension into the database.

Functions are completed. The specific function's structure is shown as Fig. 3.

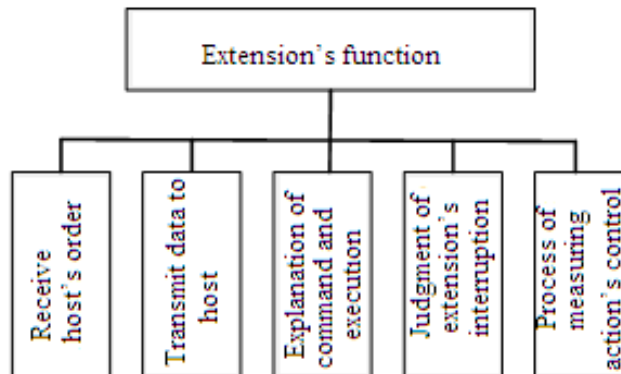


Fig 3 Extension's function

Communication host have two main functions: (1) The exchange of PC's and extension's system information; (2) To control the work of extension's system independently, and the specific function's structure is shown as Fig. 2.

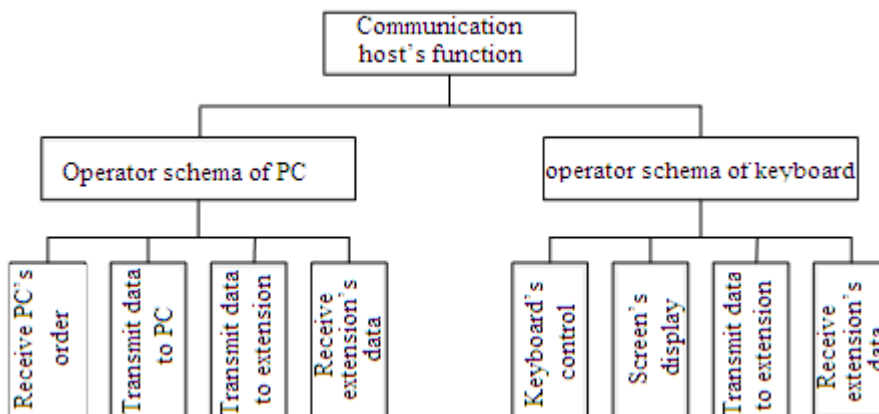


Fig 2 Communication host's function

Extension will carry out the initialization after being electrified, then the probe returns to the original action after its measurement, and it is located in state of waiting order. It will judge whether the operation is to the objective extension when it receives the data from the Communication host. If not, it will continue to wait for the order, and if it is the order of objective extension, it will carry out the corresponding commands, and it doesn't return to the state of waiting for the order until all

Stepper motor selects four-phase stepper motor, which its stepping angle is 1.8 degree. The stepper motor and roller are linked by transmission, which makes the stepper motor turn two laps and the roller turn one lap, so the roller turns 0.9 degree when it sends a pulse every time, the roller turns one lap while SCM needs to send 400 pulses. The roller's perimeter is 200 mm in this system, so pulse's equivalent = $200 \text{ mm} / 400 = 0.5 \text{ mm}$, the system detecting sensitivity is 0.5 mm. The system detecting error is mainly caused by mechanical transmission's error, and it can satisfy the requirement of the water level detection's precision through improving machining precision of the mechanical transmission part.

Communication Design of the Detector on Dam's Piezometric Tube Level

Communication protocol, the system should obey the following communication protocol:

Each extension has its unique number; the extension's number is encoded as 000001B-1111111B, which is up to 62 extensions working at the same time. Extension will reset after conducting the power and the probe will return to origin to wait for orders.

Send 40H+ extension's number (byte mode) to the extension, the extension will measure automatically until the completion of measurement.

Send 80 + extension's number (byte mode) to the extension, the extension will return to the current state's datas in five bytes, and the returned datas from right to left is as follows: (AB + extension's number) (data 3) (data 2) (data 1) (AB + extension's number).

Communication of PC and Communication Host

The computer adopts 8-bit 1200 bps no check RS232 mode to communicate with the host. The PC sends hexadecimal data if it tests the piezometric tube level: Sending 40H+ extension's number (01 H-3 EH) to Communication host, communication host transfers the command to extension through RS232 to RS485 asynchronous communication's circuit, and extension starts measuring. It will send hexadecimal data if the PC tests data: Sending 80H+ extension's number (01H-3EH) to the Communication host, the host transmits command to the extension through RS232 to RS485 asynchronous communication's circuit, and the extension sends the detected data to the host, then the Communication host transmits it to the PC again through RS232 to RS485 asynchronous communication's circuit.

Communication of the Communication Host and the Extension

Serial interface of the extension uses 8-bit 1200bps no check mode and RS485 bus run. RS485 is half-duplex, and adopts a balanced differential signal line, as it transmits differential receiver for the balance, which can reach high-speed and long-distance transmission. It is very convenient to use RS485 serial interface to constitute the distributed system, and the specification is shown as Fig. 4.

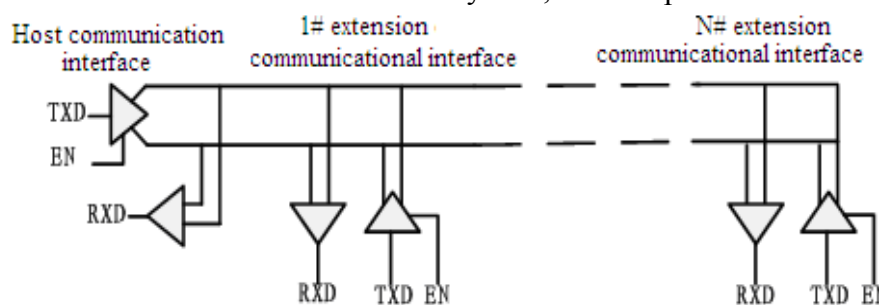


Fig 4 Distributed system of detector

It can send data when one of extensions transmits data to the host and the enabled port (EN) of the extension's transmitter is effective, while other extension's enabled port is invalid, and it can only receive information. Because the extension sends data to the Communication host by using the passive mode, as the Communication host requires the extension to echo data in an ordered manner, then the extension responds to this command. An extension sends data meanwhile other extensions ban from receiving information automatically. The extension will be restored to the state of receiving Communication host's command when the completion of sending data by extension.

Test on the Detector of Dam's Piezometric Tube Level

After the initial research and exploration, using the principle of communicating vessel, test model designed is shown in Fig. 5.

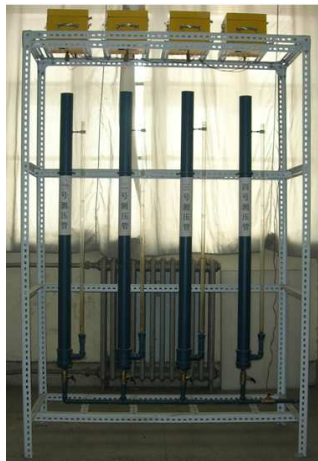


Fig 5 Test model of dam's piezometric tube level

First of test is setting the extension's parameter in the PC, including the setting of each extension's fault bit, the extension's remark, the extension's step, which is shown as Fig. 6.

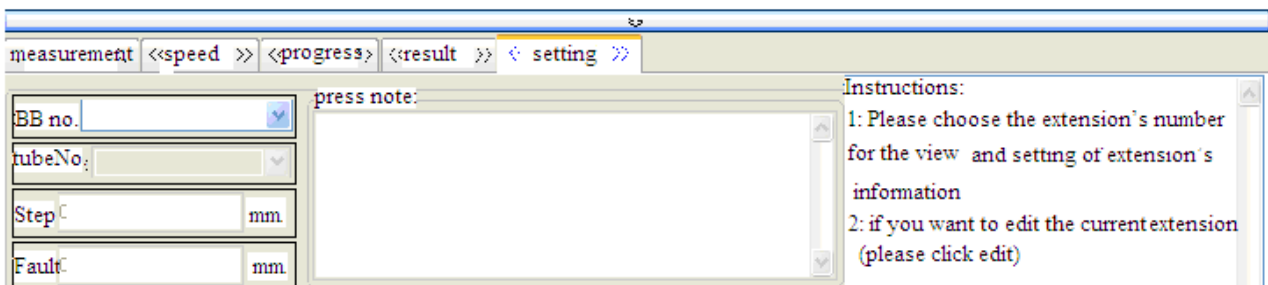


Fig 6 The setting module of tube pressure measurement

Then send instructions of measurement to extension, also it can check the current state of each extension which is measuring, and it is convenient to know the the state of each extension's sending and accepting the data momentarily for customers. It means the system has fault when the extension doesn't return 5 byte data in 5 seconds successfully. It will show different data with each different operation, which is shown as Fig. 7.

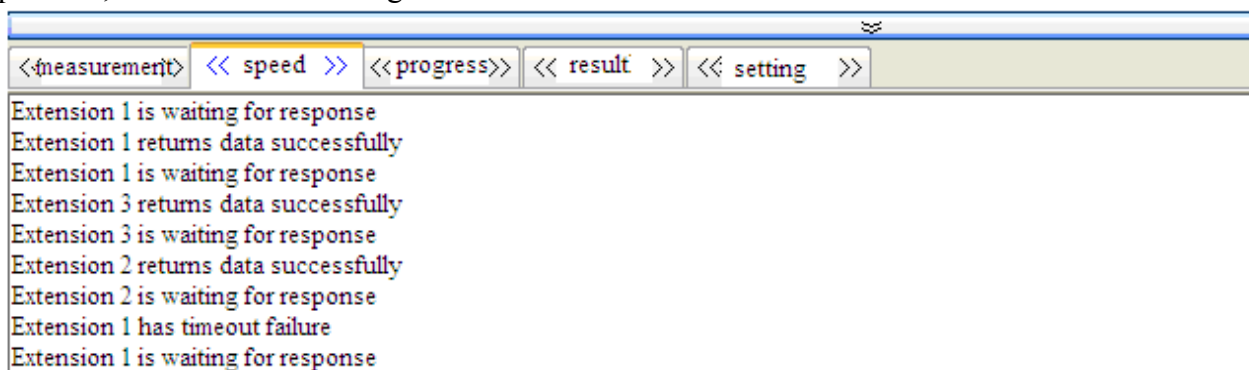


Fig 7 Module of measuring speed

Conclusion

The instrument adopts SCM as the main control component of nozzle extension, so that the degree of system's automation and reliability is greatly improved, at the same time increasing the intelligent function. While the circuit is greatly simplified by using the approach that software instead of hardware, and the cost is lower than other types of detection equipment. The piezometric level is converted to the digital pulse signal directly by the adoption of water level -- digital pulse's converter, which greatly enhances the ability of anti jamming and improve the detecting precision. Based on the instrumentation monitoring software, it can improve the modern management's level of the reservoir and reduces the operating staff of labor intensity.

The installation of instrument is simple, which just put extension in the place above the piezometric nozzle, connect to the serial communication's bus, and connect to the power, then the extension is installed, and the PC can use after installing the control software well. The control circuit and mechanical transmission device of the extension is connected through the plug-in, and the installation and replacement of components is convenient. The operating person can grasp the basic installation and maintenance only need a short time's training.

Acknowledge

The work was supported by the following projects: One is the funded plan project of young backbone teachers in Henan Province with the project number 2011GGJS-249; The other is the plan project of science and technology development in Nanyang city with the project number 2008GG028. Now most of small and medium-sized reservoirs are equipped with piezometric tube in the country to monitor the water level. The detector has a great value of promotion, and its developmental prospect is good. Next step, it gets ready to test the reservoir in Zhonggang temple, WoLong district of Nanyang, and makes more widespread to other small and medium-sized reservoirs with the benefit of the partner Nanyang Science and Technology Bureau.

References

- [1] Li Yanjun, Guo Xiulan, etc. Monitoring technology of the dam's safety [M]. Xi'an Map Press, 2009: 312-317..
- [2] Chen Hao. Construction and analysis on the monitoring information's system of Xiaowan hydropower station dam foundation based on the GIS. [D]. Kunming University of Science and Technology, 2008.
- [3] Wen Zhiping. Open monitoring system of the dam safety [D]. Hehai University, 2010.
- [4] Yang Haiyun. Discussion on the design requirements of dam safety monitoring automation system [J]. Hydropower's automation and dam's monitor, 2010(5): 30-32.
- [5] Luo Hao, Xie Huacheng. A new design of data acquisition system based on ARM [J]. Journal of Xinyang Normal University (NATURAL SCIENCE EDITION), 2011 (4): 203-205.

Research of Stand-Alone Photovoltaic Power Generator Monitoring System

Gin-Shan Chen^{1, a}

¹ Yung-Ta Institute of Technology & Commerce, 316 Chunshan Road, Lin Lo, Ping Tung, 909, Taiwan

^agschen@mail.ytit.edu.tw

Keywords: Monitoring System, Maximum Power Point Tracking, Solar Charger, Human Machine Interface.

Abstract. To design and implement a stand-alone photovoltaic power generator monitoring system with remote control functions. The hardware architecture consists of solar cells, solar charger, DC/AC inverter, energy storage device, energy consumption equipment, electrical load, PLC controller, I/O card, router, and supervisory control computer, while the software is composed of programmable software and graphic supervisory control software. With the self-developed solar charger, the conversion efficiency of this system achieves 93.26%. Besides, with maximum power point tracking function, the solar cells could continuously output maximum power. The user-friendly human-machine interface would transmit the information acquired by PLC controller, through MODBUS TCP communications protocol, to the remote computer; this would supervise and control the voltage, electric current, power, fault detection, network monitoring, and run chart function in the photovoltaic energy generating system; and the supervised and controlled data would be recorded in detail and stored into the database for further study and analyses. The experiment confirms the convenient operation of this system that it could effectively supervise and control the conditions of the system.

Introduction

With the progress of modern technology, the demand of energy is increasing every year. Natural resources for power fuel are gradually exhausted, and the carbon dioxide discharged from traditional electricity generation has seriously resulted in green house effect that it has become a globally concerned focus to find the solution.

Solar energy is not restricted to regions and appears the characteristics of security, noise-free, and pollution-free that it presents the development potential. A lot of advanced countries have invested enormous capitals in the research. The cost of solar energy generation was too high to be commonly utilized. Nonetheless, with the surge of materials and the emergence of environmental consciousness as well as the mature technology of electronics industry and the government policy largely reducing the cost, solar energy generation has been ordinarily acceptable.

The past supervisory control technology was developed in petrochemical industry and food industry. With the large-scale equipment in factories and the promotion of functions, supervisory control systems become more important for the application in factory automation. From the early monitoring distribution frame to modern computer-based digital control, a lot of researchers have devoted to the research related to graphic supervisory control with C++ or Visual Basic language.

With LabVIEW graphic control software to design a user-friendly human-machine interface (HMI) [1]-[4], aiming at renewable energy systems, constructed a complete supervisory control system, which communicated with RS-232 and DSP chips and utilized TCP/IP for transmitting data to the remote computer so as to proceed the supervisory control system for solar energy generating systems and converter fault detection systems.

This study tends to apply the self-developed PIC16C712 MCU (Micro Controller Unit) to the microcomputer-controlled solar charger [5] to establish a Stand-Alone Photovoltaic Power Generator Monitoring System (SPPGMS) for remote network power supervisory control systems. It is expected to design a user-friendly HMI with the graphic control software InduSoft Web Studio to display the

data on the input and output ends of the SPPGMS on the HMI through the communication between Ethernet and PLC controller. It clearly shows the present conditions of the electricity generation system and simultaneously stores the electricity generation values in the database for future study.

Design of Photovoltaic Energy Supervisory Control System

System Hardware Architecture

The architecture for SPPGMS, Fig. 1, contains personal computers, I-8837 PLC controller, I-87017R I/O card, and a Stand-Alone Photovoltaic Energy Generation System (SPEGS). The major work flow is to have the I-87017R I/O card, which is loaded on I-8837 PLC controller, acquire the voltage on the input and output ends in the simple solar charger of the electricity generation system and transmit back to the computer through Ethernet. Furthermore, with the analysis and calculations of the graphic control software InduSoft Web Studio, the voltage, electric current, and power on the input and output ends are displayed on the HMI. The data are regularly recorded in the database for remote control.

The main parts of SPEGS contain solar cells, simple solar charger, lead-acid battery, DC/AC inverter, and DC/AC electrical load, 50W polycrystalline silicon solar cells are produced by Motech; 46B24L 12V/36Ah lead-acid batteries, produced by YUASA, are utilized for charging.

Based on PIC16C712 MCU microcontroller, the structure of the self-developed simple solar charger, applies buck converter for major power conversion, utilizes MOSFET crystal as the converting switch, controls the solar cell to output voltage and electric current close to the maximum power point with programming software, and detects the change of solar illumination with photoconductive cell for charging. From the experimental results, charging with the electric current 3A in strong solar illumination and with the electric current 1A in weak solar illumination, there is still 0.53A electric current in low illumination of $120\text{W}/\text{m}^2$. The charging efficiency therefore is enhanced, and the overall conversion efficiency is increased 93.26%. The charger could be applied to the charging module of electric scooters, solar energy illumination systems, and the charging of solar lamp [5].

System Software Architecture

Graphic supervisory control software and PLC programming software are utilized in this study, as following descriptions [6].

The HMI of Web Studio graphic supervisory control, developed by InduSoft is applied. With powerful and complete functions, the graphic control software contains various functional modules for HMI development, management and control, supervisory control and data acquisition, and embedded control.

The index of the human-machine interface for the user-friendly SPPGMS, Fig. 1, transmits the data acquired by PLC controller back to the computer through MODBUS TCP communications protocol and follows the resolution of I/O card to convert the value in InduSoft Web Studio. The instantaneous voltage, electric current, and power in the photovoltaic energy generation system could then be observed on the HMI, the run chart function is displayed, and the monitored data is regularly recorded and stored into the database for further analyses.

I-8837 PLC controller is the ISaGRAF programmable automatic controller from ISaGRAF SoftLogic. ISaGRAF provides the five PLC programmable logic controllers, which correspond to international standards for electrotechnology IEC 61131-3 and presents the functions of Off-line simulation and On-line supervisory control. ISaGRAF programming software is first utilized for defining the connecting points on I/O card; then, ladder diagram program is applied to the monitoring program of SPEGS. After completing the off-line simulation test, RS232 is applied to transmitting to I-8837PLC controller.

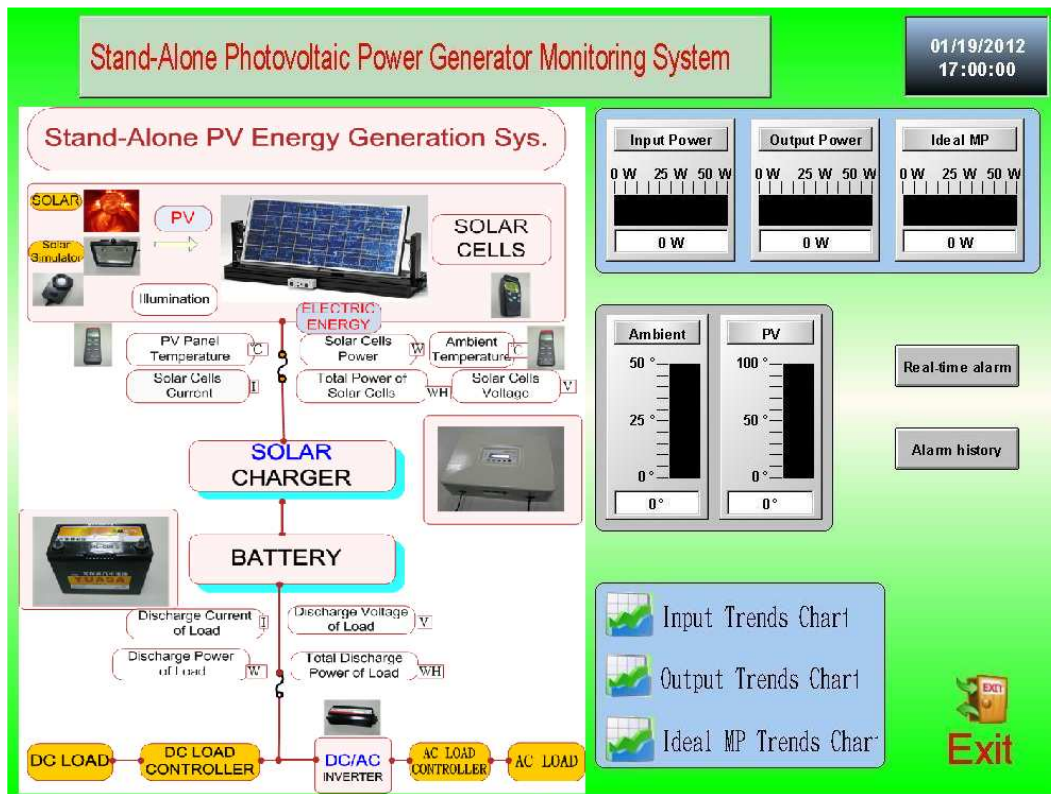


Fig. 1 The architecture for SPPGMS

Experiment and Discussion

Experimental Framework and Planning

The experiment for SPPGMS is planned as I-87017R I/O card precision confirmation, static experiment, and dynamic experiment.

Precision monitoring experiment of I-87017R I/O card: The power supplier was the power source for the experiment. As I/O card presented maximum voltage (10V) limit, and the open voltage of solar cells was 21.2V, three 100 Ω precision resistors were utilized for partial pressure so as to reach the voltage range of I/O card. With I/O card to acquire the voltage, I-8837PLC controller simultaneously transmitted the voltage value back to the computer; then, the graphic control software converted the data on the HMI for the precision test.

Static monitoring experiment: The power supply was the power source for the solar charger, which further charged the lead-acid battery. Besides, the ampere meter was series connected and the voltmeter was paralleled. I-8837PLC controller acquired voltage on the input and output ends and transmitted it back to the computer through Ethernet for displaying on the HMI. Finally, the real data were compared with the data on the HMI.

Dynamic monitoring experiment: It was the real supervisory control test under the sunshine. The solar cell was the input end, which was connected with the simple charger for charging the lead-acid battery. The ampere meter was series connected and the voltmeter was paralleled on the input and output terminals. Moreover, I-87017R I/O card and I-8837PLC controller were utilized for acquiring and transmitting voltage back to the HMI in the computer. The solar power meter was utilized for measuring the solar illumination. The error comparison between the actual data and the HMI was further preceded according to the preset illumination.

Discussion of Experimental Results

The experiment for SPPGMS is planned as I-87017R I/O card precision confirmation, static experiment, and dynamic experiment. In order to ensure the correctness, the lead-acid battery was discharged to 10.6V before the experiment.

Precision monitoring experiment of I-87017R I/O card: It aimed to test the monitoring precision of I-87017R I/O card and I-8837PLC controller. In the experiment, the power supplier supplied distinct voltage, which were acquired by I-87017R I/O card and I-8837PLC controller and further displayed on the HMI. From data analyses, the mean error between the voltage supplied by the power supplier and the voltage shown on the HMI was -0.10% , and the mean error of electric current appeared 1.33% . The electric current on the HMI had to be converted with Ohm's law and interface card resolution that the error was larger, but in the acceptable range. In this case, acquiring data with I-87017R I/O card and I-8837PLC controller for monitoring the HMI was feasible.

Static monitoring experiment (SM): It aimed to test the optimal simulation data. According to the circuit diagram, the power supplier supplied distinct voltage to the charger; then I-87017R I/O card and I-8837PLC controller acquired the voltage on the input and output ends of the charger displaying on the HMI. According to the data analyses, with three-section simulation, the mean power error on the input end of the charger was -2.09% , Fig. 2, and the mean power error on the output end of the charger was -4.08% , Fig. 3.

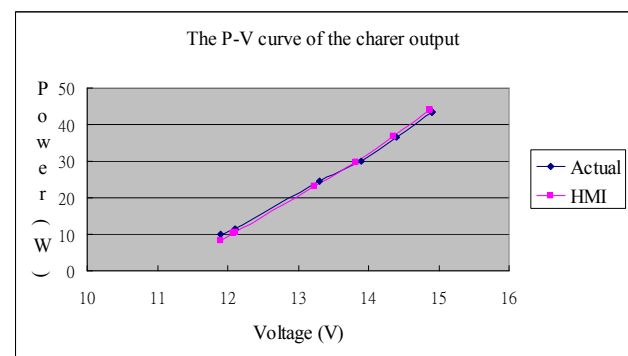
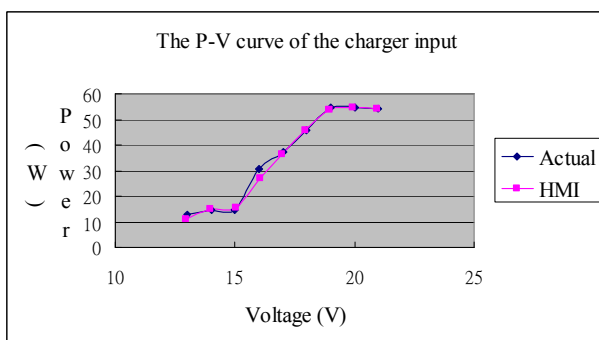


Fig. 2 The P-V curves of the charge input for SM Fig. 3 The P-V curves of the charge output for SM

Dynamic monitoring experiment (DM): It aimed to test if the system supplied with solar cells, under the sunshine, could be properly monitored with the human-machine supervisory control system. The solar cells supplied the charger with distinct power; then, the human-machine supervisory control system acquired the signals on the input and output ends of the charger displaying on the HMI. With the experimental data, the real test and simulated P-V curves for the output end of the charger could be drawn, as Fig. 4, where the mean power error on the output end of the charger was -1.66% . The real test and simulated P/V curves for the input end of the charger was shown as Fig. 5, in which the mean power error on the output end of the charger appeared 2.96% . Fig. 6 shows the run chart of the dynamic monitoring experiments. As a result, it was feasible to have I-87017R I/O card and I-8837 PLC controller acquired data for the HMI. The experimental results (blue curve in Fig. 7) provided the maximum power data for the human-machine supervisory control system as well as for the reference of MPPT.

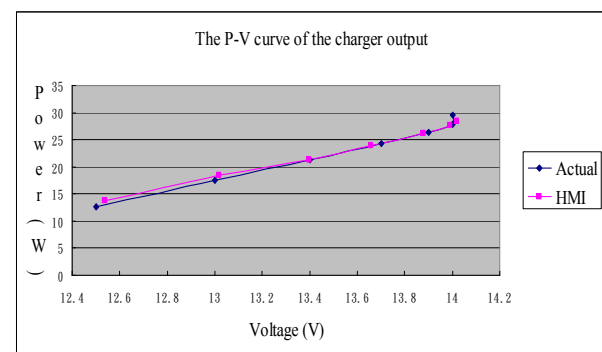
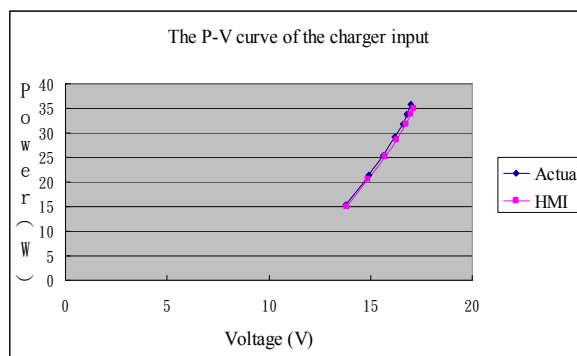


Fig. 4 The P-V curves of the charge input for DM Fig. 5 The P-V curves of the charge output for DM

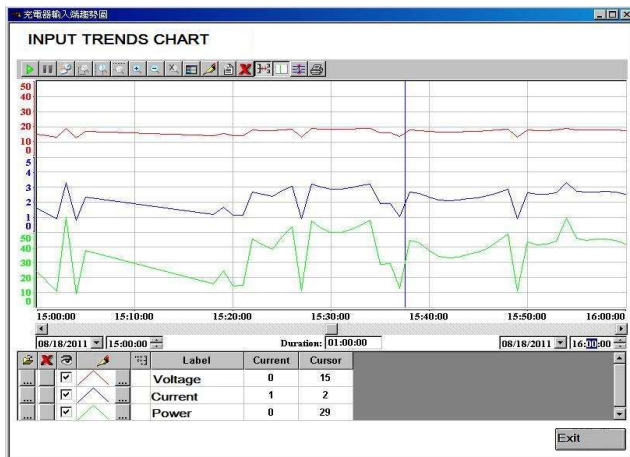


Fig. 6 The run chart of the DM

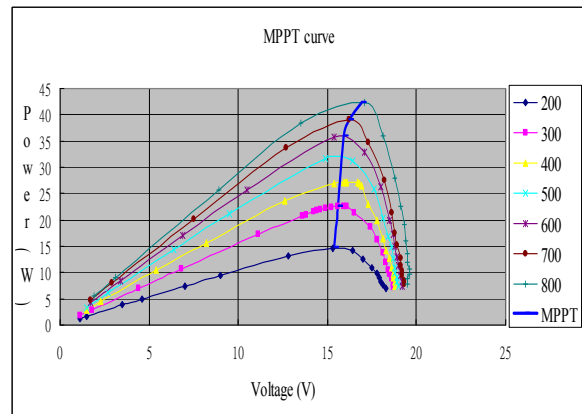


Fig. 7 The maximum power curve of DM

Conclusion and Prospect

With the self-developed solar charger (with average conversion efficiency achieved 93.26% and maximum power point tracking function) to establish the SPPGMS with remote control function, the solar cell could continuously output the maximum power. With the programmable software ISaGRAF and the graphic supervisory control software InduSoft Web Studio to design a user-friendly HMI, MODBUS TCP communications protocol was utilized for transmitting the data acquired by PLC controller to the remote computer. It not only could simultaneously monitor the voltage, electric current, power, fault detection, and run chart function of the photovoltaic energy generation system in the HMI, but could regularly record and store the monitored data in the database for further analyses. The experiment confirmed the convenient operation of SPPGMS that it could effectively monitor the conditions of the system.

The designed supervisory control module has not been strong enough. Presently, it could merely provide a remote computer for supervisory control. In the future, Web browser could be applied to instantaneously monitor the system information through the Internet, or PDA could be utilized for acquiring abnormal message through wireless network so as to achieve the function of network remote control.

References

- [1] K. Eftichios and K. Kalaitzakis: Renewable Energy Vol. 28(1) (2003), p. 139
- [2] N. Forero, J. Hernández and G. Gordillo: Renewable Energy Vol. 47(15-16) (2006), p. 2329
- [3] A. Aristizábal, and G. Gordillo: Renewable Energy Vol. 33(11) (2008), p. 2475
- [4] G. Yang, and M. Chen: WASE International Conference on Information Engineering (2009) Taiyuan, CN.
- [5] G. S. Chen, J. L. Luo, and X. L. Huang: ICIC Express Letters Vol. 5(5)(2011), p. 1571
- [6] Information on <http://www.icpdas.com.tw>

Fault Diagnosis of Power Transformers Based on Membrane Computing Optimizing Neural Network

Yuan Zhijian^{1, a}, Deng Hao^{2, b}, Liu Wenjun^{3, c}

¹Deyang Electric Power Bureau, Sichuan Electric Power Company, Deyang, China

²School of Electrical Engineering and Information, Xihua University, Chengdu, China

³College of Mathematic and Computer Engineering, Xihua University, Chengdu, China

^ayuan-zj@21cn.com, ^b491053363@qq.com, ^c531733372@qq.com

Keywords: Membrane Computing; Power Transformer; Fault Diagnosis; Dissolved Gas-In-Oil Analysis (DGA); Neural Network

Abstract. Presently, dissolved gas content analysis and fault diagnosis are the important segments of power transformer. As to the problem of the back propagation algorithm of neural network commonly used lies in the optimization procedure getting easily stacked into the minimal value locally and strict requirement on the initial value, a fault diagnostic method is presented, based on the membrane computing optimizing back propagation neural network. Throughout the process, compromise is satisfactorily reached among the network complexity, the convergence and the generalization ability. The results of diagnosis test show that the algorithm proposed has high classification accuracy, which proves its robustness and effectiveness.

Introduction

Power transformer is one of the most important electrical equipments within the power system, its operation status has a direct impact on the system safety level [1]. DGA is a key to fault diagnosis within the transformer. The DGA technology is approved as applicable to discover internal latent transformer failure and its development trend [2].

At present, a lot of artificial intelligence method was applied to power transformer insulation diagnosis, and achieved good diagnosis effects [3-7]. Has followed network reasoning theory of development and perfection, using BP network transformer fault diagnosis has been more successful examples [8-9]. But, BP usually adopts gradient descent method to solve it, in handling high-dimension and small sample decision-making problem easily arise "learning", slow convergence speed, easy into the local minimum etc. Membrane computing (MC) has a strong global optimization ability to use it to optimize the BP neural network parameters, and to train BP network, they can be better to overcome the disadvantages, enhancing the robustness of this membrane.

This paper proposes a model of membrane computing optimization BP neural network weights and threshold and successfully applied in large-size transformer in fault diagnosis. The results show that this method can get a higher diagnostic accuracy.

Membrane Computing

November 1998, in many years research based on DNA molecular computing basis, inspired by biological cells, the research report made by European academy of sciences, Romania scientists Gheorghe *Păun* in Finland, TuErKu computer research center, puts forward the concept of membrane operation [10].

Membrane computing is one kind model that has the hierarchical structure of the distributed and parallel computation model. Because many of the membrane operation models are made by Gheorghe *Păun* academician, all sorts of models of standard membrane operations are also called P system [11]. Membrane computing optimization method is different from the standard membrane computing, it isn't a computing model, but a optimizing program and strategy. This paper uses a kind of optimizing method which is called "Cell Membrane Computing" (CMC).

Algorithm structure Algorithm structure is shown in figure 1.

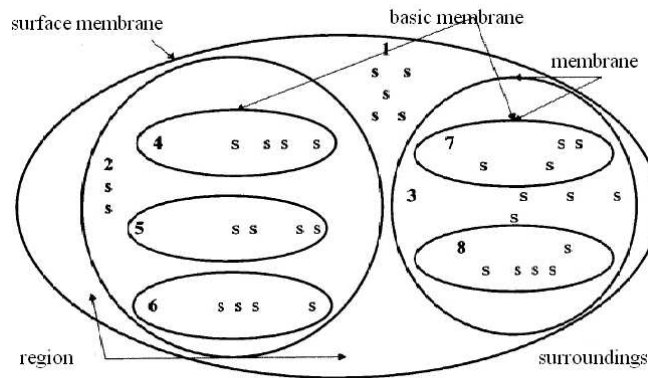


Fig. 1 CMC system structure

Object. According to the need of membrane computing scale, here we also use 200 objects as object sets.

In the initial pattern, every membrane of the third floor, that is to say, in the pattern m_4, m_5, \dots, m_8 has 10 different initial objects that are randomly generated. The second membranes namely m_2, m_3 are filled with 25 different strings. In the surface membrane, there are 100 strings.

Coding Different from genetic algorithm for binary coded, CMC algorithm uses decimal system. The results come from the environment collection. The string for results is composed of the decimal string, namely real number. The string for results is made of the entire target function variable.

Rules

Description of elect, crossover and mutation rules The select rule uses the basics and commonest roulette wheel, which is based on the ratio of fitness value. And crossover operator uses overall crossover; mutation is random.

Communication The communication rule here transports the best object out of the membrane and into the outer membrane which contains it. Aimed to keep the diversity of groups, the specific form and parameters for rule groups R_i of each membrane is different. The diversity can effectively prevent algorithm Deeping easily into the local minimum, increasing the quality of optimal solution.

The third layer of the membrane and the surface send out the best objects only. That's easy to understand intuitively. Bio-cell selects the largest or the smallest one into the membrane, and the largest have higher energy through the membrane easily.

The second layers of the membrane send out more than one object. Here the theory of biochemistry and thermal motion of molecules are introduced. In the field of biochemistry, molecules with higher energy go in reaction easily. As to the lower, they react with a low probability. That's to say, the probability to produce new molecules is considered according to the following probability function.

$$P_r = \exp(-(E_{new} - E) / kt) \tag{1}$$

Which E_{new} represents the energy of new status, E represents the old, k is *Bolzman* constant, t is time.

Use evolution algebra g to replace time t , and at the same time use the fitness value of the function to replace energy function. Considering the molecules with higher energy, (1) can be transfer into the following.

$$P_r = \exp((f_{new} - f_L) / kg) \tag{2}$$

Which f_{new} is the present fitness value, f_L is the performance indicators of better objects in the last evolution for objects in membranes, g is the present generation.

In (2), when $f_{new} \geq f_L$, the string S_{new} will pass through the membrane. If $f_{new} < f_L$, that's to say, the performance of new objects is less than the last better ones. In this condition, produce a random number P_i . If P_i is larger than P_r given, $P_r < P_i \in (0,1)$, the present string will pass through the membrane. Or it won't. The principle is that the membrane doesn't send out the best object with high fitness value, but also the higher ones than the last. If the fitness value is lower than the last, it will go through the out membrane with a small probability $1 - P_r$. This is helpful to keep the diversity of groups, avoiding the algorithm Deeping into the local minimum. And the probability becomes smaller with the increasing of generation.

Implementation of Cmc-Bp Algorithm

Fitness function The CMC in this article assigns the code of the parameters and structure expressed by the set of objects to the BP. The network uses training samples as input and output. And after running, return the reciprocal of the square error as the fitness function set of objects, namely

$$f_i = 1/E_i \quad (3)$$

In formula, $E_i = \sum_{k=1}^n (y_k - t_k)^2$ indicates that the network output values and target output value of the error sum of squares; and t_k stands for the target output of the neural network.

Thus, the CMC-BP model obtaining the maximum can be considered optimal.

Algorithm flow Specific operation achieved by the following steps:

Build the neural network topology structure according to the input and output sample set of neural network; initialize the network weights and threshold; encode all of the connections weights and thresholds between neurons into set of object in the colony, expressed by real numbers; give randomly initialized colony.

Learn and train input samples of neural network according to the input, output samples; calculate E values. Calculate the fitness value and assign to each membrane.

Each membrane evolves in turn according to its own rules, do respectively select, crossover, mutation operation; the order of the use of rule can be arbitrary.

Until each membrane runs the specified generation, according to communication rules, each membrane exchanges some of their objects.

If running to a specified condition generation, then the surface membrane output optimized weights and thresholds. Otherwise, return (4).

Train BP network, and save the neural network weights and thresholds.

Input test samples, and test whether the established network to meet the conditions.

Cmc-Bp Algorithm in Transformer Fault Diagnosis

Determination of input-output model Determine the type of transformer failure by use of five gas volume value in transformer oil H_2 , CH_4 , C_2H_4 , C_2H_6 , C_2H_2 , and the gas content value is the neural network's input vector. For the output vector, this article merges partial discharge into the low- capacity discharge fault, using low-temperature heating, medium-temperature heating, high-temperature overheating, low-capacity discharge, high-capacity discharge five output neurons, respectively, as T1, T2, T3, D1, D2.

The probability of failure, which shows the changes of output value of the network in [0, 1] range, reflect the results of fault pattern recognition with quantizing. To improve the diagnosis recognition rate of transformer single fault, the method of relative probability comparison is put forward, that is, a maximum of the five output values takes 1, and the rest take 0.

Selection of training samples This paper collects 380 typical transformer oil dissolved gas analysis (DGA) test records and the corresponding actual failures which have been identified. The results of these samples are divided into two parts: select 280 groups of DGA data as learning samples; another 100 groups of sample data is used to identify transformer fault of the network later in this article. Sample data of 280 groups for Network training shows in Table 1.

Table 1 Composition of the CMC-BP training data

Fault type	T1	T2	T3	D1	D2
Number of samples	40	60	60	60	60

Network Training parameter's selection Separately use BP algorithm, GA-BP algorithm and CMC-BP algorithm, to train the network. Three algorithms involving the same parameters are set to the same value. Selection of some parameters can be used heuristics based on the actual situation, because the meaning from the operating parameters and optimization of results, they are relatively independent to each other, so it can be assumed that other parameters are fixed, study the optimal selection of a single parameter value and then integrates.

Specific parameters are set as follows: initial colony size for 200, iterations of neural network for 500, learning rate for 0.01, the number of network nodes in the hidden layer for 9, the evolution generation for 1000, the crossover probability for 0.5, the mutation probability range for 0.01, the conditions of film generation for 3.

Analysis with Diagnosis Case Test samples of 100 groups were taken under different typical fault samples for testing, and compare the diagnostic results of CMC-BP to the result of BP, GA-BP algorithm. Diagnosis results are shown in Table 2.

Table 2 Comparison of recognizing results with different algorithms

Fault type	CMC-BP		GA-BP		BP	
	Number of right	Accuracy (%)	Number of right	Accuracy (%)	Number of right	Accuracy (%)
T1	19/20	95	17/20	85	15/20	75
T2	16/20	80	15/20	75	17/20	85
T3	19/20	95	15/20	75	19/20	95
D1	18/20	90	17/20	85	17/20	75
D2	14/20	70	19/20	95	13/20	65
total	86/100	86	83/100	83	79/100	79

Note: The Number of right = right judging number of the transformers / the transformer number of samples for fault diagnosis

From the diagnosis results shown in Table 2:

For the same DGA sample, CMC-BP and GA-BP's recognition rate can be higher than pure BP network recognition rate 79%. This is because the membrane computing and genetic algorithm based on the BP network can optimize its initial values, resulting in a higher recognition. Also it shows that it is feasible for membrane computing optimizing algorithm to be applied to the transformer fault diagnosis.

The horizontal comparison of 5 types of fault shows that, the classification accuracy of CMC-BP algorithm is higher than GA-BP and pure BP network except D1, showing the superiority of the CMC-BP algorithms for the optimal neural network parameters process, and good generalization ability.

The fault identification of CMC-BP algorithm is overall higher than the GA-BP algorithm. This is because the membrane operation contains the select, crossover and mutation operators, while it also has its own communication rule and operation model. Diagnostic results show that the CMC-BP model is more efficient and practical.

Conclusions

This paper proposes a diagnostic model, optimizing BP neural network based on membrane computing (CMC-BP), and apply it to transformer fault diagnosis. The model has the following characteristics:

Compared to pure BP algorithm, the algorithm can get better initial parameters. In network optimization, encoding with real vector, introducing the communication rule, and using the corresponding cell membrane computing structure and parameters to optimize network operations, achieve global optimization;

During the concrete realization of CMC-BP training, use a method of combining select, crossover, mutation and communication rules is helpful to speed up the convergence, improve the algorithm's generalization ability, and get strong robustness.

Examples show that, CMC-BP algorithm can dig fault data information of transformers. It has a high degree of intensification ability in fault pattern recognition, and its practical capacity and generalization are better.

References

- [1] GUO Ze-min: *Transformer Fault Diagnosis Based on Least Squares Support Vector Machine of Immune Optimization*. Mechanical Management and Development (2012).
- [2] DU Li-yan, WEI Guo-hua: *Electric Power Transformer Failure Diagnosis Based on Evolution Neural Network*. Telecom Power Technology (2012).
- [3] Huang Y C: *Condition assessment of power transformers using genetic-based neural networks*. IEE Proc.-Sci. Meas. Technol, 150(2003), p. 19-24.
- [4] Peng Ningyun, Wen Xishan, Wang Yi et al: *A potential fault diagnosis method based on linear classifier for oil-immersed transformer*. Proceedings of the CSEE, 24(2004), p.147-151.
- [5] CHENG Jia-tang, XIONG Wei, XU Shao-kun et al: *Power Transformer Fault Diagnosis Based on Neural Networks with Improved Particle Swarm Optimization*. High Voltage Apparatus, 22(2002), p.121-124.
- [6] Shu Hongchun, Sun Xiangfei, Si Dajun: *A RS approach to founding and maintaining ES knowledge base for fault diagnosis of power transformer*. Proceedings of the CSEE, 22(2002), p. 31-35.
- [7] WU Zhong-li, YANG Jian, ZHU Yong-li et al: *Power transformer fault diagnosis based on rough set theory and support vector machines*. Power System Protection and Control, 38(2010), p. 80-83.
- [8] PAN Chong, CHEN Weigen, YUN Yuxin et al: *Fault diagnosis of power transformers based on genetic algorithm evolving wavelet neural network*. Automation of Electric Power Systems, 31(2007), p.89-92.
- [9] WANG Shaofang, CAI Jinding: *Application of hybrid algorithm based on GA-BP in transformer diagnosis using GAS chromatographic method*. High Voltage Engineering, 29(2003), p.3-6.
- [10] FU Jie: *A study of optimization algorithms inspired by membrane computing*. Zhejiang University (2010).
- [11] HUANG Liang: *Research on membrane computing optimization methods*. Zhejiang University (2007).

Remote Measurement & Control of Ship Mooring System

Yuliang Liu, Lifang Tao, Enling Lin

School of electromechanical engineering, Zhejiang Ocean University, Zhoushan, China, 316004

liu.yuliang@hotmail.com, dianxin2011@126.com, yul_liu@163.com, sxm@126.com

Keywords: Mooring System; Remote Control; Embedded Server

Abstract. Based on thoughts of ship safety, one novel scheme of ship mooring remote measurement & control system is proposed, including information obtaining subsystem and remote control subsystem. The former is to detect mooring system's environmental parameters such as wind speed, water speed, and anchor chain stress, then to submit such parameters to remote control center by wireless channel more than 2.4 GHz. The latter's main body is the aforementioned remote control center and it's based on an embedded WEB server with functions such as calculating probability of mooring movement, emitting alarming signal, etc. Except an ocean water speed detector invented by ourselves, the hardware design in this paper is based on IC (integrated chip).

Introduction

Remote measurement & control of ship mooring equipments is an important path to improve the safety of ship operation. In the process of work, the system first need obtain mooring information, including wind speed, water speed, anchor chain stress, etc., then save them in a hard disk or submit them to remote control center. Before continuing we are aware of important progress made in the last decade. Particularly, Ref. [1] first gave a five-step fuzzy control algorithm to implement mooring state's recognition and control. In Ref. [2], authors analyzed the defect and problem of the original contractor relay control way in mooring system, and then present three speed windlass' control system based on FX2N PLC chip of Japanese Mitsubishi Corporation. Wang Cai-xing [3] ever proposed a novel method to assess mooring system's safety degree according to anchor chain's stress. From the references it's clear that ship safety issue has attracted much attention and some novel achievements have been made, however, the research in point basically stays in theoretical step. Both the related software and hardware's design, particularly its extension application still belongs to an urgent assignment.

Based on status above, we propose a tractable scheme for mooring system's remote detection and control, in which the mooring information can be sampled and saved, and can also be submitted through high frequency wireless channel more than 2.4 GHz with responding time less than one second. After arrival of the mooring information, the control center can forecast mooring system's safety degree or submit mooring alarming signal, if necessary it can also submit order to remote mooring control terminal in ship.

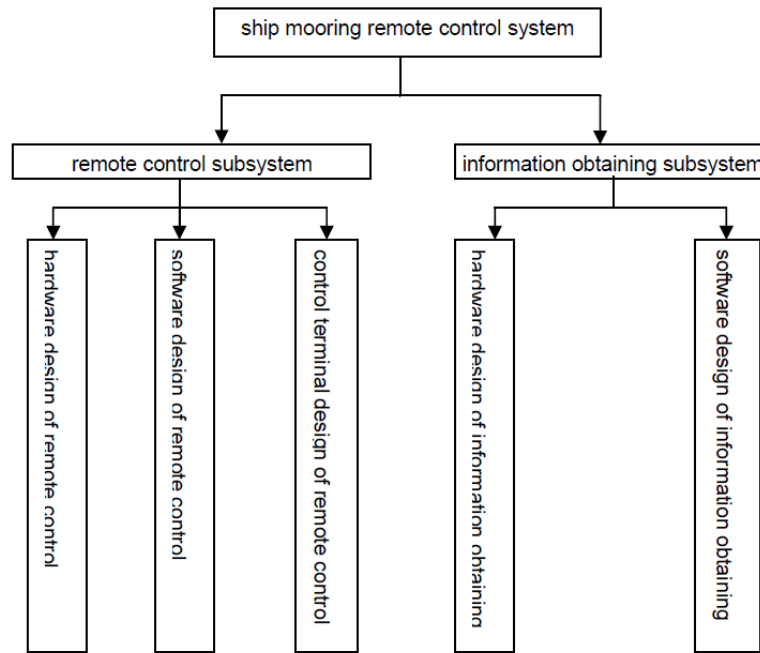


Fig. 1 Components of mooring control system

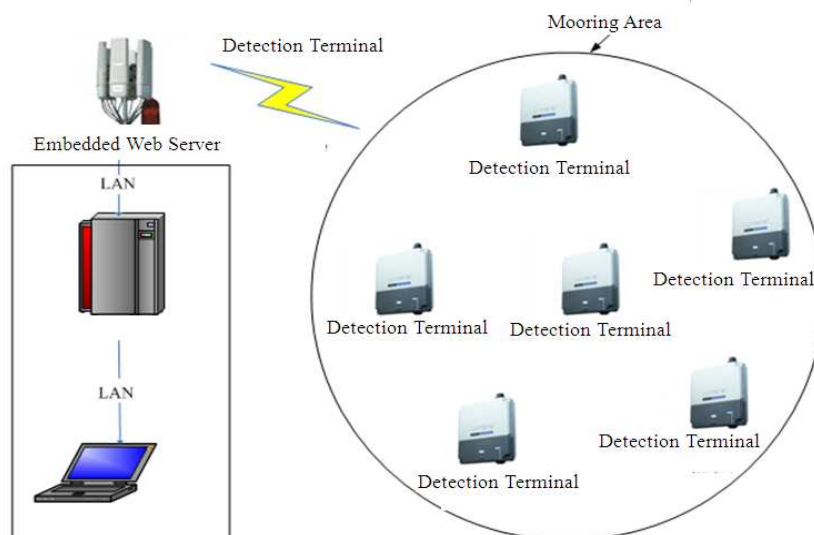
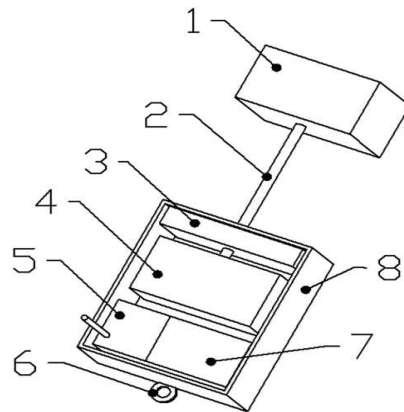


Fig. 2 Design scheme of the mooring control system

Components of Remote Measurement and Control System

As shown in Figs. 1-2, the mooring remote control system presented in this paper includes information obtaining subsystem and remote control subsystem. The information obtaining subsystem is to attain information about mooring system's environmental parameters and anchor chain stress, whose hardware mainly includes a sensor group. The remote control subsystem's main body refers to an embedded processor, so the hardware and software design belongs to an embedded system problem, including safety forecast algorithm's design and coding, remote order's formation and sending, etc. Remote order's execution is based on control terminal installed on a ship. In this paper we use fuzzy control theory [1] to construct mooring system's safety forecast model, then make it embedded in a WEB server to realize mooring equipment's safety alarming and remote control function.



1. suspension 2. connecting rod 3. pressure sensor 4. stressing block 5. wireless transmitter module
6. lifting lug 7. control chip 8. shell

Fig. 3 Stereo map of speed detector of ocean water

Design of Water Speed Detector

Stereo map of the ocean water speed detector invented in this paper is shown in Fig. 3, including eight parts, i.e. suspension, connecting rod, stress sensor, stressing block, wireless transmitter module, lifting lug, control chip and shell. Suspension is connected to one terminal of the connecting rod whose another terminal is connected to a stressing block through shell and pressuring sensor. Pressuring sensor lies between pressure block and shell. The wireless transmitter module and the controller chip are equipped under the shell and they are connected with a mental line. In addition, a lifting lug is installed under the shell. Here the connection rod is made of Titanium alloy material with a surface roughness 0.3. The ocean water speed detector outperforms others in that it can submit information to marine without being launched, i.e. it can save detection price and improve operating safety. In the work process, the detector is fixed underwater and rushed by ocean water, and then its suspension drives stressing block to pressure sensor. Through the control chip's processing, the pressure sensor can make the pressure signal to an electronic signal, then submit the signal to information obtaining subsystem by a wireless submit module.

Software Design

The software functions include initialization, display control, key scan and control drive, receiving or submitting judgment, etc. In the process, program is first initialized, and then circulation subprogram and the display control subprogram operate in turn. Such an arrangement's advantage is that any information modification can be shown in time without refreshing the display model artificially.

Summary

Circuit-level physical map of mooring control system are shown in Fig.4. At Shuanghe wharf of Daishan county of Zhejiang province of China, we have made detections for three times since Oct. 12, 2011. From the experimental results, the mooring remote control system can sample, and save the necessary mooring information such as water speed, wind speed, and anchor chain stress, it can also submit the necessary mooring information on wireless channel more than 2.4 GHz with tolerable error less than 5 percent. The mooring remote control system can display the received

parameters. In addition, it can also calculate the mooring system's movement probability, and then emit the corresponding alarming signal within one second. If the movement probability is bigger than safety threshold, it can emit order to the remote control terminal on ship.

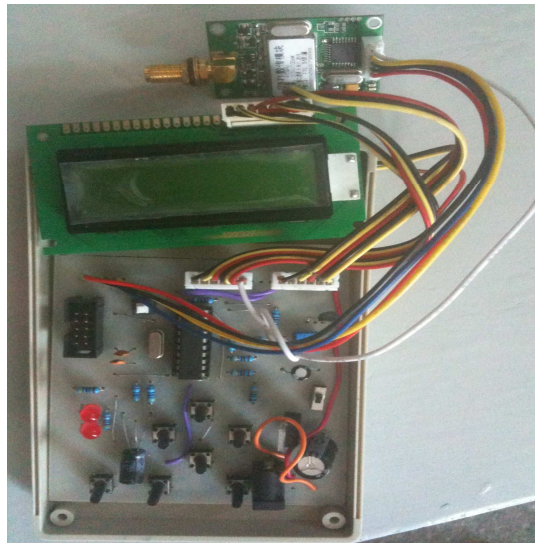


Fig. 4 Circuit-level physical map of the mooring control system

Acknowledgements

This work is supported by non-profit scientific project of science & technology department of Zhejiang province of China (2010C33178), project of science & technology department of Zhoushan city of China (10249) and project of Zhejiang Ocean University of China (200913, 201023, 11182100710).

References

- [1] N. Q. Ma. *Auto control research of anchor machine based on a fuzzy algorithm* [J]. Journal of Wuhan University of Technology (Science and Engineer), 2002, 26(3): 361- 364.
- [2] Q.T. Yang. *PLC application in three speed windlass's control system* [J]. China science information, 2008(24): 112-114.
- [3] C.X. Wang. *Anchorage and pre-test of mooring ship's safety management countermeasure* [J]. Transportation Science and Technology, 2010, 241(4): 108-110.

Algorithm based on Layering Search to Routes Planning of Vehicle Navigation System

Xiong HE¹, Yiyang GAO², Tao CHEN³

¹State Key Laboratory for Information Engineering in Surveying, Mapping and Remote Sensing, Wuhan University, Wuhan 430072, China

²North China University of Water Resources and Electric Power, Zhengzhou, Henan 450052, China

³Xi'an Research Institute of Surveying and Mapping, Xi'an 710054, China

Keywords: Vehicle Navigation System; Global Positioning System; Routes Planning; Algorithms based on Layering Search

Abstract. This paper introduces a method of designing and organizing road network data and clarifies algorithm based on layering search, suitable for computing the routes of vehicle navigation in big districts. The algorithm is calculated in the high grade road network, and then in the local refinement. The method is to get a point in the calculated high grade route and then calculate the optimal route from the start point to the point (the selected point should be a node near to the end), so does the end point. The algorithm was applied to the routes planning and the experimental results show that the use of data structure and algorithm saves storage space and greatly improves the calculation efficiency.

Introduction

Vehicle navigation system, as an important part of intelligent transportation system, has become a hot subject in today's society ^[1]. In this paper, the implementations of road network design and optimal route algorithm of the planning for vehicle navigation dynamic routes in big districts are studied.

At present, the majorities of vehicle navigation systems, which are invested into application, are based on the planning of static routes. However, they can't give reflections to the dynamic information of roads. Therefore, the planning of vehicle navigation dynamic routes changes into a hot research focus of the new-generation intelligent vehicle navigation systems ^[7]. In recent years, the importance of dynamic traffic information monitoring has been highlighted with a gradual step, and also in-depth studies have been made by increasingly more scholars at home and abroad on dynamic traffic information monitoring ^[8-10].

The Road Network Design of Routes Planning

The road network is the foundation and object for the calculation of the optimal route. To realize the dynamic route standards of vehicle navigation, it is necessary to make a design on reasonable network model.

The Road Network Expression

The typical expression way, commonly used in the road network, is weighted directed graph. Usually, point-shaped entities (i.e. nodes), linear entities (i.e. the road between two nodes), attribute information of node and road and topological relations between entities are respectively stored ^[2]. In the road network design, it is necessary to give consideration not only to static attribute information of road, but also to the dynamic information of road. To carry out the selection of the optimal route, it is necessary to use the attribute information as weighted roads and convert them to the same type of description information. In this paper, route computation is implemented by uniformly converting attribute information to be the lengths of roads.

The Determination of Road Network Weight

The standards for the selection of the optimal target are necessary to be taken into account first. Then, the weights of roads are necessary to be determined^[3]. In this paper, the selection of the optimal target is based on the shortest trip distance; on such a basis, other special requirements and road attribute information are taken in account. The advantages of taking the lengths of roads as the way of determining weights are simple and intuitive; the weights of road can be directly obtained^[4]. In this paper, the lengths of roads multiply by a weight coefficient λ (λ is a comprehensive consideration given to real-time traffic information transferred from communication satellite, road attribute information and route calculation way selected by users). Therefore, the weight w_{ij} from node v_i to node v_j can be simply described as follows.

$$w_{ij} = \lambda d_{ij} \quad (1)$$

In equation (1), there is $1 \leq i \leq n, 1 \leq j \leq n, i \neq j, n$ is the number of nodes; λ is weight coefficient. According to the above calculation equation of road weight, because is a comprehensive consideration given to real-time traffic information transferred from communication satellite, road attribute information and route calculation way selected by users, λ can be segmented, and then $\lambda = \lambda_1 + \lambda_2 + \lambda_3 + 1$ is ordered, so as to respectively consider the influences of each factor on route calculation. λ_1 Is used for expressing real-time traffic information (dynamic road information); λ_2 is static road information; λ_3 is weight of different route calculation method, and is decided by the selection of users.

Real-time Traffic Information

Real-time traffic information is acquired through satellite communication technology. Because there is a relationship between the effect of traffic jams on vehicles and the distance of vehicles from traffic jam site, the weight coefficient related to traffic jams can be expressed as follows.

$$\lambda_1 = a \frac{X}{D} \quad (2)$$

In equation (2), a is scale factor; X is traffic congestion; D is distance from traffic jam.

Static Road Attribute Information

Static road information mainly comprises of road grade, direction, width, charge set, traffic restrictions, etc. Here consideration is only necessarily given to road grade and width; the calculation equation of weight coefficient related to road attribute information can be expressed as follows.

$$\lambda_2 = \frac{b}{WG} \quad (3)$$

In equation (3), b is scale factor; W is road width; G is road grade.

Determination on the Weight of Calculation Method of Different Route

Routes in the experiment system of this paper available for users to choose are shown below.

Recommending Route: Recommending route is that the system recommends the optimal route to users by comprehensively considering road grade, distance and other factors, and users only need to consider real-time traffic information and road attribute information. Thus, road weight calculation equation can be expressed as follows.

$$w_{ij} = \lambda d_{ij} = (\lambda_1 + \lambda_2 + 1) d_{ij} \quad (4)$$

Y Given to Distance: If only the length of road is considered, the calculation equation can be expressed as follows.

$$w_{ij} = d_{ij} \tag{5}$$

Priority Given to High Speed: Priority given to high speed means that highway should be selected as far as possible according to the road conditions, and can be implemented through increasing the weight of low grade road. The calculation equation can be expressed as follows.

$$w_{ij} = \begin{cases} (\lambda_1 + \lambda_2 + 1)d_{ij}, & \text{if highway is selected} \\ (\lambda_1 + \lambda_2 + \lambda_3 + 1)d_{ij}, & \text{if highway is not selected} \end{cases} \tag{6}$$

In equation (6), $\lambda_3 > 0$ is established, which can be set according to actual conditions.

General Road

General road means that highway should not be selected as far as possible according to the road conditions, and can be implemented through increasing the weight of highway. The specific realization method is the same as above.

$$w_{ij} = \begin{cases} (\lambda_1 + \lambda_2 + 1)d_{ij}, & \text{if highway is not selected} \\ (\lambda_1 + \lambda_2 + \lambda_3 + 1)d_{ij}, & \text{if highway is selected} \end{cases} \tag{7}$$

In equation (7), $\lambda_3 > 0$ is established, which can be set according to the actual conditions.

Minimum Expense

According the road conditions, the most economic route can be selected, and can be implemented through increasing the weight of toll road. The specific realization method is the same as above.

$$w_{ij} = \begin{cases} (\lambda_1 + \lambda_2 + 1)d_{ij}, & \text{if toll road is not selected} \\ (\lambda_1 + \lambda_2 + \lambda_3 + 1)d_{ij}, & \text{if toll road is selected} \end{cases} \tag{8}$$

In equation (8), $\lambda_3 > 0$ is established, which can be set according to the actual conditions.

The Layering Storage of Road Network Data

In this paper, the classification of all city roads are replaced with the classification of national roads, and their corresponding relationships are shown in table 1.

Layering of Road Data

The way of laying road is shown as follows: (1) the first layer includes highway, the national road and the provincial road; (2) the second layer includes roads below the provincial road.

Table 1. National Road Classification and City Road Classification

No.	National Road Classification	Corresponding City Road Classification
1	Highway	City Highway
2	The National Road	City Fast Road
3	The Provincial Road	Main City Road
4	The County Road	Auxiliary City Road
5	The Village Road	Lane
6	Others	

Layering of Node Data

The way of laying road is shown as follows: (1) the first layer includes the nodes connecting highway, the national road and the provincial road, and the nodes connecting those roads below highway, the national road and the provincial road; (2) the second layer includes other nodes. In the construction of the road network for route search, high grade road can be selected in a wide range, and low grade road can be selected near starting and destination. Thus, the number of roads participating in route calculation is reduced, and simultaneously route search becomes faster.

The Design and Realization of Vehicle Navigation Routes Planning in Large Area

The Heuristic Search Algorithm- Algorithm

At present, the most common and the shortest route algorithms mainly include Dijkstra algorithm, Bellman-Ford-Moore algorithm, and heuristic search algorithm (algorithm) [5]. algorithm is based on Dijkstra algorithm and was proposed by Hart, Nilsson, Raphael, et al. In algorithm, known global information is introduced when next checked node is selected, and then the distance between current node and destination is estimated as the possible measurement of the node in the optimal route. In such a way, the node with the largest probability can be searched, so as to improve the search efficiency [6]. To be specific, estimate function $f^*(j)$ of current node j is introduced in algorithm. Estimate function of current node j can be defined as follows.

$$f^*(j) = g(j) + h^*(j) \quad (9)$$

In equation (9), $g(j)$ is the shortest actual distance from starting point to current node j ; $h^*(j)$ is the estimate of the shortest distance from current node j to destination. If $h^*(j) = 0$ is established, it suggests no global information to be applied, and thus algorithm becomes common Dijkstra algorithm, indicating common Dijkstra algorithm can be regarded as special circumstances of algorithm. Specific form of $h^*(j)$ can be selected by algorithm users based on actual situation. Certainly, $h^*(j)$ has to meet a requirement, namely it can't be higher than the shortest actual distance from node j to destination. To make algorithm implemented smoothly, two linked lists are introduced. T is used for expressing the set of the nodes that are generated but not extended; S is the set of the nodes that have been extended. After algorithm is implemented, S is the set of the nodes of the shortest path route starting from v_s . Algorithm steps are as follows.

Step 1: For starting node v_s , $g_{v_s} = 0$ can be ordered; for other nodes ($\forall v \neq v_s$), $g_v = \infty$ and $S = \Phi, T = \{v_s\}$ are ordered. In this condition, T has the node with the minimum f^* value.

Step 2: If there is $T = \Phi$, algorithm fails. Otherwise, the node v with the minimum f^* value can be selected from T , and $v = \min_{u \in T} \{f^*_u\}$ and $S = S \cup \{v\}, T = T - \{v\}$ are ordered. Whether v is target node is judged; step 3 can proceed if it is, and otherwise subsequent node of v is generated and step 3 is executed.

Step 4: For each subsequent node w , $g_w + w(v, w)$ is calculated. And there are three cases according to the position of w .

If $w \in T$, whether $g_w > g_v + w(v, w)$ exists is judged; $g_w = g_v + w(v, w), p_w = v$ is established if it exists

If $w \in S$, whether $g_w > g_v + w(v, w)$ exists is judged; $g_w = g_v + w(v, w), p_w = v$ is established if it exists

If $w \notin S$, whether $g_w > g_v + w(v, w)$ exists is judged; $g_w = g_v + w(v, w), p_w = v$ and $S = S - \{w\}, T = T \cup \{w\}$ are established if it exists

If there are $w \notin T$ and $w \notin S$, $g_w = g_v + w(v, w)$, $p_w = v$ and $T = T \cup \{w\}$ are ordered and estimate function $f_w^* = g_w + h_w^*$ of node w is calculated, and then step 2 proceeds.

From node w , the optimal route as well as the shortest distance from starting point v_s and destination v is output according to P_v , and then algorithm will end.

Route Planning Analysis of Vehicle Navigation System in Large Area

Vehicle navigation route optimization owns four features: (1) redirection limit at intersections, one-way traffic, traffic accidents, etc; (2) existence of delay at intersections makes nodes have weights; (3) higher requirement on time efficiency of problem-solving; (4) storage space should be taken as less as possible.

The Realization of Algorithm based on Layering Search

Determination of Function $f^*(j)$

In algorithm, estimate is made based on the distance from current node to destination as the possible measurement of the node in the optimal route. In such a way, the node with the largest probability can be searched, so as to improve the search efficiency. Estimate function $f^*(j)$ of current node j is introduced in this algorithm and can be defined as $f^*(j) = g(j) + h^*(j)$. In the experimental system of this paper, the distance $g(j)$ from starting node to current node j is the optimal route; $h^*(j)$ is the spherical distance from current node to destination and meets compatibility condition.

Implementation of Algorithm based on Layering Search

In this paper, the way of layering search is applied, in which the search space of route is essentially divided into the searches of highway's extensive span and common road's narrow span. The Implementation of algorithm is as follows.

According to the positions of starting node P_s and destination P_e , the nodes that are the nearest to starting node and destination are found based on the principle of the nearest distance in the national topological data, and are marked respectively with P_s^1 and P_e^1 ;

The national topological data is extracted and the suspension chains and tree hanging chains containing no P_s^1 and P_e^1 are deleted, and the weight of road is determined according to real-time road traffic information and road attribute information, so as to generate a high grade road network and also store the road network according to forward star structure.

The optimal route from P_s^1 to P_e^1 is calculated with algorithm to gain a route L1 of high grade road network.

A point P_i^1 is selected from L1. The principle of selecting the point is to get far away from P_s^1 under the premise of meeting route calculation speed, and the optimal route L_2 from P_s^1 to P_i^1 can be calculated with route calculation way in a local small span.

A point P_j^1 is selected from L1 with the same method of above (4). The principle of selecting this point is to get far away from P_e^1 under the premise of meeting route calculation speed, and the optimal route L3 from P_j^1 to P_e^1 can be calculated with route calculation way in a local small span.

A route between P_i^1 and P_j^1 of L1 is assumed to be L4. Then, the optimal route from P_s^1 and P_e^1 can be gained by connecting L2, L4 and L3.

In the experimental system of this paper, experiment is made with algorithm based on layering search; the first-layer road network is constructed with high grade road; after the first-layer search is completely implemented with this algorithm, the second-layer road network is constructed with low grade network and then search is continued until the optimal route is ultimately solved.

Conclusion

In this paper, a road network model of dynamic route planning is designed; many practical problems possible in route planning of large areas are analyzed; algorithm based on layering search is proposed. According to the hardware limitations of vehicle navigators and the large amount of information, the road network model and algorithm applied in this paper not only help save storage space, but also greatly improve calculation efficiency.

References

- [1] Liu Jiyu, Li Zhenghang, Wan Yuehu etc. Principle and Application of Global Positioning System [M]. BeiJing: Surveying and Mapping Press, 1993: 126-130.
- [2] Zhao Weihua, Zhang Fujia, Liang Hongbin. Research and Realization of Optimum Path Search in Vehicle Guidance and Location System [J]. Journal of Hangzhou Institute of Electronic Engineering, 2003, 23(1): 56-59.
- [3] Sun Jiaping. Optimization Algorithm for Route Analysis in Embedded Navigation System [J]. Electronic Engineer, 2006, 32(9): 10-12.
- [4] Meng Qinghao, Zhang minglu, Liu dawei, Peng shangxian. AGV Global Path Planning Using Double-Direction Algorithm [J]. Journal of Tianjin University, 1998, 31(6): 747-751.)
- [5] Yue Yang, Gong Jianya. An Efficient Implementation of Shortest Path Algorithm based on Dijkstra Algorithm [J]. Journal of Wuhan Technical University of Surveying and Mapping, 1999, 24 (3): 210-212.
- [6] Zhan F B. Three Fastest Shortest Path Algorithms on Real Road Networks [J]. Journal of Geographic Information and Decision Analysis, 1997, 1(1): 69-82.
- [7] Yan Ge, Jian Wang, Youxin You, et al. Research Progress on Dynamic Route Planning of Vehicle Navigation [J]. Journal of Highway and Transportation Research and Development, 2010, 27(11): 113-117.
- [8] Okutan II, Stephanedes Y J. Dynamic Prediction of Traffic Volume through Kalman Filtering Theory [J].Transportation Research Part B: Methodological, 1984, 18(1): 1-11.
- [9] SM ITH B L, DEMETSKYM J. Traffic Flow Forecasting: Comparison of Modeling Approaches [J]. Journal of Transportation Engineering, 1997, 123 (4): 261-266.
- [10] MARK S D, MARK R C. Short2term Inter2urban Traffic Forecasts Using Neural Networks [J]. International Journal of Forecasting, 1997, 13(1): 21-31.

Research on Remote Meter Reading System Based on PLC Technology

Yijiang Zhang

Yuanpei College, Shaoxing University, Shaoxing, Zhejiang 312000 China

Keywords: Remote Meter Reading; PLC; Communication Protocol

Abstract. With the deepened transformation of China's power system, the stability and reliability of power utilization have been dramatically improved, but meter reading data acquisition does not keep pace with the times. With the continuous maturity of low-voltage power line communication (PLC), this leads us to see hopes of using PLC technology to realize remote meter reading. In this paper, based on current PLC technology and combining domestic and foreign successful cases, a beneficial exploration and research is conducted from the composition and establishment of software and the design of software and protocol.

Introduction

PLC technology, commonly known as "power line communication", refers to a communication way transferring data and simulating signals with power lines. With this technology, remote meter reading system can well solve the problem of traditional door-to-door meter reading way that wastes time and energy, greatly reducing cost and time. Second, the latest PLC technology can reach a transmission speed of 200mbps and also related end-products has been successfully applied in Shenyang, Guangzhou, and Nanjing after years of development, and thus its stability and reliability can be ensured. All these indicate that realizing Remote Meter Reading with this technology owns a good application prospect.

Composition of Hardware

Remote meter reading mainly comprises of meter, collector, concentrator and host server. Meter accesses end-user power line and connects collector upward; collector is used for meter data acquisition in one or multiple meters, connects concentrator upward, and is in charge of data receiving and storing; concentrator can communicate with host server through PSTN, INTERNET, GPRS and others.

At present, low-voltage PLC chips commonly used in China include PL3105/6 chip made by Beijing FUXING XIAOCHENG Company and PLCI36 series chips made by Qingdao East soft Communication Technology Co., Ltd, and their common point is using spread spectrum communication technology and supporting frame relay, making data signals transferred reliably under higher-order attenuation and low-voltage power line environment.

Hardware structure of the whole remote meter reading system is shown below.

System Establishment

From above figure of hardware structure, it can be learnt that meter is at in the bottom of system. Because most meters used in China are mechanical, data communication is unable to realize, giving rise to difficulties to the realization of remote meter reading system. There are methods for solving the difficulties: (1) installing acquisition module for converting users' electric quantity to standard pulse signal through electricity or magnetism and also connecting with connector; (2) directly installing pulsed electric meter. The first is appropriate for some old communities, and the second is applicable for newly-constructed and high-grade communities.

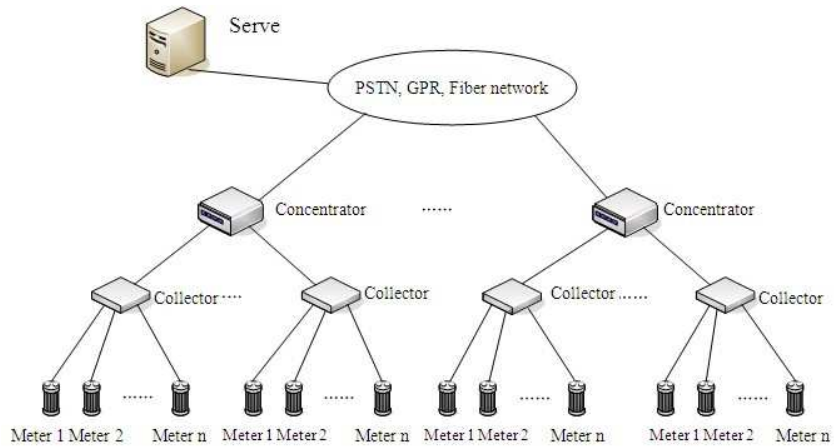


Fig. 1 Hardware Structure of Meter Reading System

Concentrator is usually placed near an 80-v substation of communities, and about 30-50 collectors are configured for one concentrator. Considering the reliability of communication, the furthest distance between concentrator and collector should not be more than 700 meters if the latest PLC technology is applied, and two methods can be used based on actual situation if the distance is too far: (1) add concentrators; (2) install transponder's Relay power line signals. Concentrator can realize the client-server question-answer half-duplex communication online with server through PSTN, INTERNET, GPRS, and OPLC.

Software Design

Overall, the software design of the system requires easy operation, friendly interface, powerful extension and easy maintenance. In the system, C/S and B/S are combined; ORACLE9.0 is database; the client in C/S mode is for setting and managing the meter reading system; B/S interface provides electric quantity, power rate and other information retrievals and queries for users and other relevant personnel, and the main functional modules of the client is shown below.

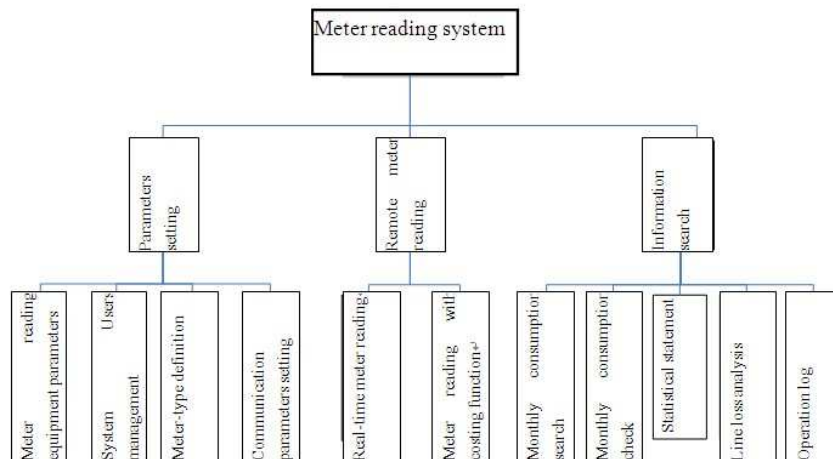


Fig. 2 Main Functions of Meter Reading System Software

Parameter setting:

- Meter reading equipment parameters: set relevant parameters of meter reading system
- System Users management: user account and rights management operated in system
- Communities Information management: managing and maintaining residents information of meter reading communities
- Meter-type definition: setting related parameters such as charge unit and type of gauge table
- Communication parameters: setting communication parameters of remote meter reading

Remote meter reading:

Real-time meter reading: Analyzing unlikely data and on-site calibration meter reading data; capable of reading part or all of mete data, and returning and storing in database in real time

Meter reading with costing function: Regularly reading meter each month, and capable of summarizing and settling power charges

Information search:

Monthly consumption search: searching monthly electricity use per different angles

Monthly consumption check: automatically checking & analyzing unlikely/abnormal data

Statistical statement: providing different summary statistics ways & displaying in report form

Line loss analysis: Making a difference calculation with numerical values of main meter and its sub-meters at one point

Operation log: checking system operation log and playing a function of secured auditing

Protocol Design

Communication protocol standards for collectors and concentrators are implemented based on document Q/GDW 376.2-2009 issued by the state. To improve reliability and security of the communication between meter reading system and concentrator, easily detect and maintain meter reading equipments and make them possess error detection ability, it is necessary to design another concentrator-host server communication protocol applicable for this system, and thus a simple introduction to it is given below.

This communication protocol is based on the three-layer reference model of "enhancing performance system structure" provisioned in GB/T18657.3-2002, including application layer, link layer and physical layer.

Physical layer: a variety of communication ways can be used, including PSTN, INTERNET, GPRS, CDMA, and OPLC network

Link layer: located in the middle of the three-layer reference model

Application layer: sending and receiving various information between host server and concentrator with information transfer function of data link layer

Bytes Format

Each byte contains eight binary codes, but is added with a start bit (0), a parity bit and a stop bit (1) in transferring. Its transferring sequence is shown in fig 3: D0 is the least significant bit of bytes, and D7 is the most significant bit of bytes (the least is transferred first, and the most latter).

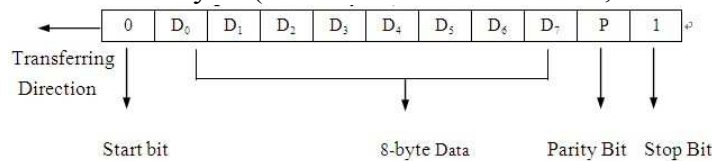


Fig. 3 Transferring Sequence of Bytes

Frame Format

Table 1 Communication Frame Structure

Message establishment filed	AAH
Address information filed	B ₀
	B ₁
	B ₂
	B ₃
	B ₄
	B ₅
Data length filed	L
Data filed	DATA
Verification field	CS
Message end field	BBH

Frame is the basic unit of information transfer. Communication frame format of the protocol is shown in table 1 below.

First, message establishment filed comprises of 1 byte, and is AAH no matter master (server) →slave (concentrator) or master-average is used. Second, address information filed comprises of 6 bytes: the first 4 bytes represent address (0 is filled if bits are less than 8); the second two bytes are reserves for the first 4 bytes, and are 0 uniformly, and the latter 12 bits represent meter number (000H~FFFH), and a concentrator can read 4096 meters. Third, data length filed comprises of 1 byte: L is the number of bytes of date field; $L \leq 255$ and $L = 0$ suggest no data field in reading or writing data. Fourth, the composition and length of data field are decided by specific data message, as shown the table 2below.

Table 2 Data Field Structure

Transferring direction	Composition of data field		
Server → concentrator	Function code	Data code	
Concentrator → server	Function code	Mark code	Data code

Note: Function code: identifying communication frames; mark code: identifying accuracy of response data; data code: specific data string

Examples for differently-requested data fields and response data fields are shown in table3.

Table 3 Examples for Functional Parameters of Data Fields

Type of communication frames	Server → concentrator communication frame		Concentrator → server communication frame		
	Data Field		Data Field		
	Function code	Data code	Function code	Mark code	Data code
Set concentrator address	00H	No	00H	OK	No
				Err	No
Set concentrator clock	01H	8 bytes	01H	OK	No
				Err	No
Set initial value of a meter	02H	3 bytes initial value	02H	OK	No
				Err	No
Read current value of a meter	03H	No	03H	OK	3 bytes (current value)
				Err	No
Read current status of a meter	04H	No	04H	OK	1byte (current status)
				Err	No

Note:

OK is byte 00H; Err is FFH.

Initial value and current value are expressed with three-byte compression BCD code; "concentration meter reading device" value can be accurate to one decimal place. For example, current value is 12345.6 and placed in 4 bytes, namely 12H, 34H & 56H. Concentration meter reading device can record a value of 99999.9 maximally,

2-byte pulse constant is BCD code of "pulse number/degrees" of a meter, and high-order is in the front.

Fifth, verification field is foreign field of message establishment field, address information field, data length field, data field and all byte data. Sixth, message end field is a symbol of communication frame end and is BBH constantly.

Transfer Control

Before frame information is sent, 1-4 bytes of DDH (two usually) are sent first for easy synchronization of receiving party. All data items transfer low bytes first and high bytes latter. Each communication starts from that slave station, selected by master station based on information frame address, sends a request command, and then the requested slave station makes responses based on requirements of control code in command frame; response time delay (T_d) after command frame is received is $20\text{ms} \leq T_d \leq 500\text{ms}$; pause time (T_b) between bytes is $\leq 20\text{ms}$; bytes verification is parity check, and frame verification is the sum of longitudinal information verification, and thus receiver will abandon the information frame and give no responses no matter parity check error or longitudinal information verification error are detected; transfer rate is fixed as 4800bps.

Conclusion

In this paper, based on current PLC technology and combining domestic and foreign successful cases, a beneficial exploration and research is conducted from the composition and establishment of software and the design of software and protocol. Although PLC technology still has shortcomings, greater economic benefit will certainly be produced if electric meter, water meter, and gas meter can be integrated into remote meter reading system with the unceasing development of new technology.

References

- [1] Wei Li, Weiming Lin. Current Situation and Prospect of Power Line Carrier [J]. Instrument Standardization & Metrology, 2004, (05): 24-26.
- [2] Ziliang Cai, et al. Study on Communication Protocol of a New Remote Reading Meter System [J]. Relay, 2007, (07): 46-48.
- [3] Yun Hu. Analysis and Comparison among Several Remote Electrical Energy Meter Reading System [J]. Low Voltage Apparatus, 2009, (08): 27-30.
- [4] Jun Liu. Broadband Centralized Meter Reading of Power Line and Online Integration System [J]. Electric Power Information Technology, 2009, (10): 35-39.

Simulation Environment for Dangerous Chemicals Transportation

Haiyan Hu^{1, a}, Weida Li¹, Pengfei Wang² and Lining Sun^{1, 2}

¹School of Mechanical and Electric Engineering, Soochow University, Suzhou, China

²State Key Laboratory of Robotic and System, Harbin Institute of Technology, Harbin, China

^ahuhyhit@gmail.com

Keywords: Simulation environment, Dangerous chemicals, parallel platform, control system, embedded controller.

Abstract. Aimed at the disadvantages of real test method for micro system, a simulation environment for dangerous chemicals transportation is developed. This simulation environment is based on the motion simulation platform, which is a kind of Hexaglide operation platform and has a total of 8 dof. With the motion simulation platform and the simulation environment, the motion parameters such as attitude, angular rate, velocity and acceleration and the environment parameters such as temperature, humidity, concentration of combustible gas, the inner pressure and liquid level of tank are measured by micro system and standard sensors simultaneously. With the comparison of test data, the micro system can be validated. In this paper, the structure of motion simulation platform is presented; the hardware structure and integration are described respectively; the software of simulation environment is introduced and some experiment results are shown.

Introduction

With the development of social economy and industrialization, the production and transportation of energy and chemical materials increases rapidly. Therefore, the security situation of dangerous chemicals transportation becomes very severe [1, 2]. The dangerous chemicals are inflammable, explosive, corrosive and poison, their transportation has significant risk of fire, explosion, leakage and poisoning. In recent years, several accidents of dangerous chemicals transportation on highway occurred in China, resulting in huge economic loss and abominable society influence [3, 4]. In order to reduce the accidents of dangerous chemicals transportation, protect the environment and people's life, the micro system for monitoring and tracking of the dangerous chemicals' transportation, storage and using is researched [5,6]. The micro system can be integrated in the tanker or ships to realize the monitoring and tracking of the transportation and storage for dangerous chemicals [7]. Usually, the test of micro system is realized by installing the test system in the tanker or ship and then testing it on real land transportation or sea transportation. This method has the advantage of good authenticity, but has many disadvantages also: long test cycle, high test cost, high test risk and bad reproducibility.

Aimed at the disadvantages of real test method, based on the support of High Technology Research Development Program of China (863 Program), a simulation platform for dangerous chemicals transportation is constructed. This simulation environment is used to provide good simulation environment and experimental platform for the simulation tests of the micro system, which can realize the monitoring and tracking of the transportation for dangerous chemicals. In this paper, the structure of motion simulation platform is presented; the hardware and software of the simulation environment are introduced respectively, and some experiment results are shown.

Motion Simulation Platform

The structure of motion simulator generally adopts the 6-dof (degrees of freedom) parallel Stewart platform [8, 9]. This kind of parallel platform can simulate vehicles' yaw, pitch and roll and other action in the process of traveling. As the limitation of its working space, it is hard to maintain a long time in the simulation of acceleration and deceleration. Aimed at this shortcoming, another parallel

structure is adopted in the simulation of the dangerous chemicals transportation. As shown in Fig. 1, the parallel platform uses Hexaglide operation structure[10]. The mechanical structure of this simulation platform mainly includes 6-dof upper platform, hook joint of upper platform, linkage, hook joint of lower platform and the moving pairs with screw, nut and guide. The 6-dof upper platform linked to 6 moving pairs by hook joint of upper platform, 6 linkages and hook joint of lower platform. The lengths of 6 linkages are equal. Each screw of the moving pairs is connected to an AC servo motor. The 6-dof motion of simulation platform can be realized through the linear motion of 6 moving pairs driven by AC servo motors. The 6 guides of this platform are parallel to each other and in the same plane. Therefore, this simulation platform has the advantage that it not only can realize the 6-dof motion, but also can provide pure linear motion in the X direction. And the movement distance is only restricted by the length of guides. Thus the workspace of simulation platform can easily to extend in this direction. When the moving direction of tanker is consistent with the X direction, the acceleration and deceleration simulation of tanker will have longer distance and providing a better simulation platform for dangerous chemicals transportation.

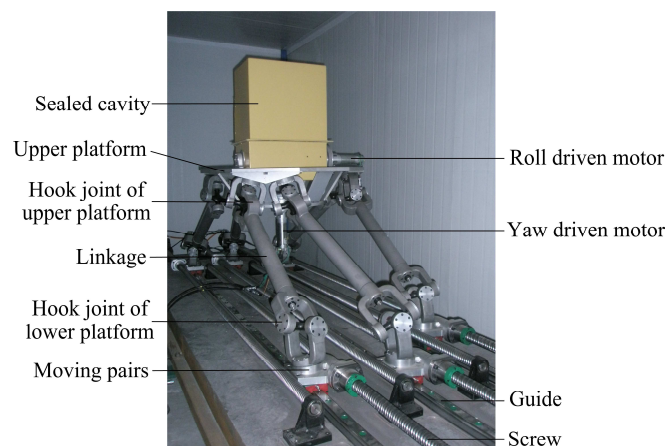


Fig. 1 Structure of motion simulation platform

The sealed cavity, which is used to realize the simulation environment of the dangerous chemicals transportation, is fixed in the upper platform of 6-dof motion simulation platform. Generally, the angular displacement of yaw and roll of 6-dof parallel platform is comparatively small. Two DC servo motors, which are the yaw driven motor and the roll driven motor, are added to increase the motion displacement of the sealed cavity. The micro system for dangerous chemicals transportation is integrated in the sealed cavity. The test of micro system for dangerous chemicals transportation can be realized by this simulation system with the 6-dof motion platform for motion simulation and the sealed cavity for environment simulation.

Hardware of Simulation Environment

System Structure of Simulation Environment The simulation environment is developed to providing a test environment for the micro system, which is used to monitor and track the transportation of dangerous chemicals. As shown in Fig. 2, the system structure of simulation environment is a kind of distributed system. The upper level computer is the industrial control computer and the lower level computer is the embedded controller based on C8051 micro processor. The upper level computer includes information display module and data storage module. The main function of information display module is receiving measured data from each standard sensor and micro system in the sealed cavity, and synchronously displaying the measured data through the forms of value and visualization curve respectively. At the same time, all the measured data are stored in the hard disk of industrial control computer by the data storage module.

The sealed cavity is used to construct the simulation environment for dangerous chemicals transportation. In the sealed cavity, there are embedded controller, sealed tank, environment adjusters, micro system and standard sensors. The embedded controller is the core processor of the sensor data

sampling and environment parameter adjusting. The sealed tank which is loaded with water and fixed in the sealed cavity is used to simulate the tanker filled with liquefied combustible gas. As the temperature and humidity is always changed in the transportation of dangerous chemicals, the temperature and humidity of the simulation environment can be regulated by the embedded controller and environment adjuster. The concentration of combustible gas in the sealed cavity can be adjusted to simulate the leakage of combustible gas loaded in tanker. And, the pressure and liquid level of the liquefied combustible gas in the sealed tank can be regulated. The motion parameters, such as the angle of yaw, pitch and roll, the angular rate, the velocity and acceleration of X, Y and Z direction, and the environment parameters, such as temperature, humidity, concentration of combustible gas, pressure and liquid level, are sampled by standard sensor and micro system respectively. The data of micro system and sensors are transmitted to upper level computer through CAN bus and serial interface, and the validity of micro system can be verified by the comparison with standard sensors.

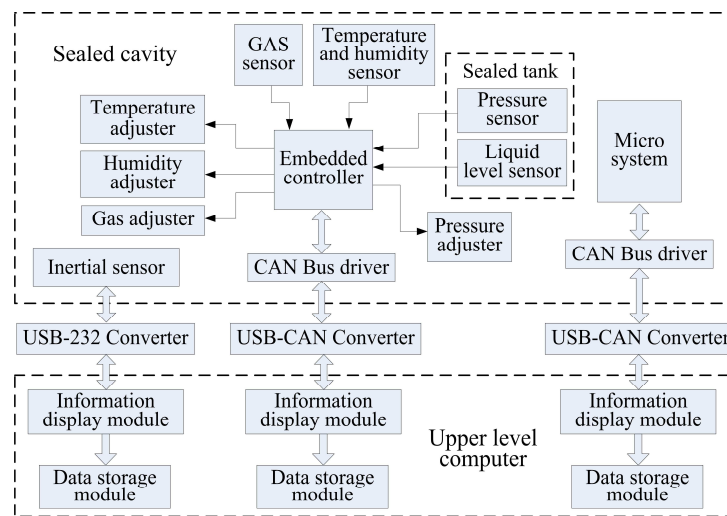


Fig. 2 System structure of simulation environment

Integration of Simulation Environment After the integration of standard sensors and simulation environment construction module, the structure of sealed cavity is shown in Fig. 3. The sealed tank is used to simulate the tanker for dangerous chemicals transportation and its diameter and height are 300mm and 500mm respectively. The dangerous chemicals mainly include liquefied petroleum gas (LPG) and liquefied natural gas (LNG). In addition to the standard pressure sensor and liquid level sensor, the pressure and liquid level of liquefied gas in tanker are measured by the micro system. And the value of pressure and liquid level is changed by injecting water or high pressure gas into the sealed tank through valves. The environment temperature in the sealed cavity is regulated by controlling the heating membrane. The inertial sensor, which is fixed on the bottom of sealed cavity, is NAV420CA and produced by Crossbow Company. The NAV420CA is a combined navigation and attitude and heading reference system that can measure stabilized pitch, roll and yaw angles and angular rate in a dynamic environment along with GPS-based position, velocity and acceleration. The measured data of NAV420CA inertial sensor is transferred to the industrial control computer through the serial interface. After the coordinate transformation, the motion of the sealed cavity can be computed by the attitude, velocity value and acceleration value of the inertial sensor. Combustible gas sensor is used to measure the concentration of combustible gas in the sealed cavity. The sensor is TGS6812 and produced by Figaro Company. This sensor is a kind of catalytic type gas sensor. It features high accuracy, good durability and stability, quick response, and linear output. Gas concentration can be measured by the embedded controller based on TGS6812 and Wheatstone bridge. If the concentration exceeds the set value, it means that leakage is occurring in the transportation of dangerous chemicals.

In order to measure the temperature and humidity in sealed cavity, the standard temperature and humidity sensor are installed in the top of sealed cavity. The humidity value in sealed cavity is regulated by the control of humidifier. In order to install and integrate the sensors and micro system in the sealed cavity conveniently, the sealed cavity is designed to be a composite structure which

consists of base and cover. The base is made of steel and stiff enough to sustain the sealed tank, sensors and other parts. The material of cover is glass fiber reinforced plastic. This kind of material not only ensures the stiffness of the cover but also reduces the weight of the sealed cavity.

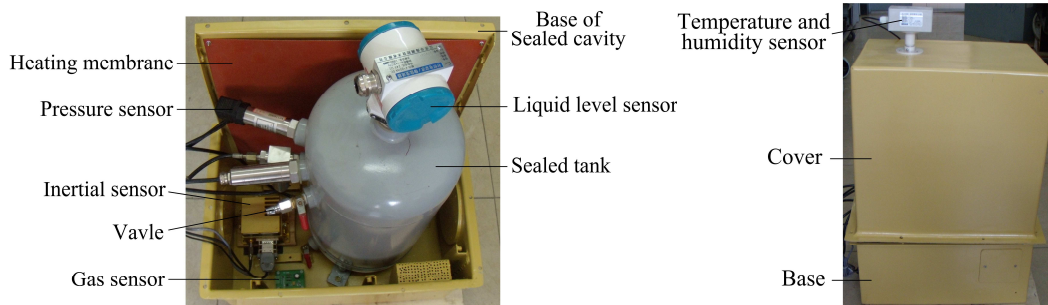


Fig. 3 Integration of simulation environment

Software of Simulation Environment

Software of Lower Level Computer The lower level computer of the control system of simulation environment is the embedded controller. It is developed based on the C8051F040 microcontroller using C language. The software structure of the controller is shown in Fig. 4. It is composed of main loop, CAN bus communication module, AD conversion module, the I²C bus communication module and the I/O control module. The accuracy of AD converter module is 12 bits and it is used to complete the acquisition of two-wire analog input of the temperature and humidity sensor, pressure sensor and liquid level sensor. The I/O control module are used to control the on and off of the relays, achieving the adjustment of temperature, humidity, pressure and gas concentrations in the sealed cavity. The AD acquisition accuracy of the combustible gas detection module is 16 bits. And the transmission of gas concentration data from the TGS6812 sensor to controller is based on the I²C bus communication modules. CAN bus communication module is used to communicate with the host computer, and its data transfer rate is up to 1Mbit/s.

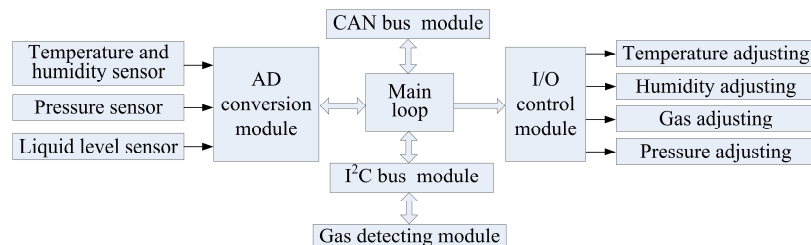


Fig. 4 Software structure of lower level computer

Software of Upper Level Computer The software development of upper level computer is based on the Windows platform using VC++ 6.0. The software can display the real-time value of sensors in each simulation environment. The data of standard sensors and micro system are transferred to upper level computer based on CAN bus and serial interface. In order to improve the reliability, the software is developed using modular design method. The entire software system is divided into the CAN bus communication module, temperature display module, humidity display module, pressure display module, the gas concentration display module, liquid level display module and data storage module. The data of the sensors collected by the embedded controller is sent to the host computer through the USB-CAN converter card. After the data processing, the data of sensors and micro system are stored in hard disk of host computer in the form of TXT text by the data storage module. At the same time, the sensor data will be displayed in the two forms of value and visualization curve respectively by the data display module. As shown in Fig. 5, the Human-Machine Interface of upper level software and experiment data of standard sensors is listed.

Summary

Aimed at the disadvantages of real test method, a simulation environment for dangerous chemicals transport is developed. It is based on the motion simulation platform with Hexaglide structure. The simulation environment is constructed in a sealed cavity, in which a sealed tank is used to simulate the tanker for dangerous chemicals transportation. Within the simulation environment, the temperature, humidity, concentration of combustible gas, the inner pressure and liquid level of tank can be regulated by embedded controller. Besides those environment parameters, the motion parameters such as attitude, angular rate, velocity and acceleration are measured by the standard sensors and micro system simultaneously. With the motion simulation platform and the simulation environment, the micro system can be validated by the data comparison of the standard sensors and micro system.

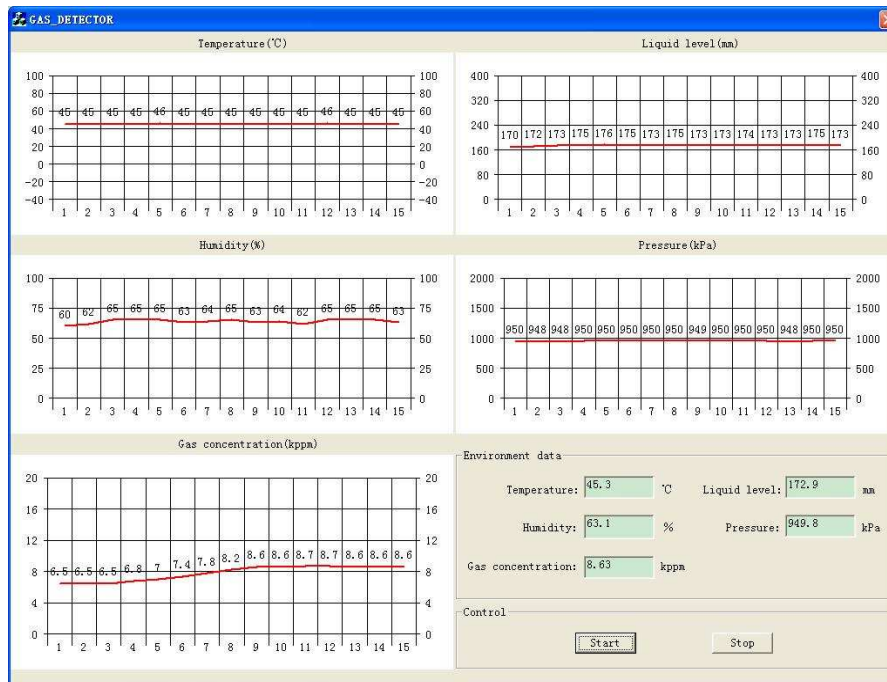


Fig. 5 Human-Machine Interface of upper level software

Acknowledgements

This work was financially supported by the High Technology Research Development Program of China (2006AA040103) and Jiangsu Natural Science Foundation (BK2011378).

References

- [1] T. Xia and Z.B. He: *Electronic Measurement Technology*, Vol. 34, No. 5 (2011), p. 85-89
- [2] W. Sun and Y.H. Dong: *China Safety Science Journal*, Vol. 21, No. 2 (2011), p. 147-151
- [3] Z.F. Zou and B.Q. Zhang: *China Safety Science Journal*, Vol. 21, No. 6 (2011), p. 129-134
- [4] Q.S. Fang, Q.F. Wang and W.W. Xiao: *Logistics Sci-Tech*, No. 3(2012), p. 29-31
- [5] Y.S. Zhang, Z.G. Duan, S.Q. Zhou and G.Z. Cao: *Computer and Communications*, Vol. 25, No. 6 (2007), p. 106-108
- [6] G.F. Wei, Z.A. Tang, J. Yu and S.Q. Zhou: *China Safety Science Journal*, Vol. 20, No. 6 (2010), p. 33-39
- [7] Y.F. Yang, J.H. Lin and G. Li: *China Measurement & Test*, Vol. 37, No. 1 (2011), p. 60-62
- [8] E.F. Fieter: *International Journal of Robotics Research*, Vol. 5, No. 2 (1986), p. 157-182
- [9] Y. Yang, S.T. Zheng and J.W. Han: *Key Engineering Materials*, Vol. 460-461(2011), p 642-647
- [10] M.X. Kong, Y. Zhang, L.N. Sun and Z.J. Du: *International Conference on Mechatronics*, (2007), p.1-6

Fuzzy Self-tuning PID Controller in SEHS

Sun Lan

Suzhou Institute of industrial Technology, Jiangsu Suzhou 215104, China

Keywords: Fuzzy Self-Tuning PID Controller; Servo Electro-Hydraulic System; Motor Speed Control

Abstract. Because of the existing hybrid fuzzy PID controller does not perform, using electric hydraulic servo system application (SEHS). Therefore, when the system parameters change will require a new adjustment of PID controller variable. Therefore, a hybrid fuzzy and fuzzy self-tuning PID control was put forward. With this control scheme was divided into two parts, and the fuzzy controller and fuzzy self-tuning PID controller. Fuzzy controller is used to control the output of the system of the values of the system away from target value. We proved that the performance of the control scheme through the experiment of the motor speed control SEHS. The experimental results show that the proposed a hybrid fuzzy PID controller and fuzzy self-tuning effect is better than that of a hybrid fuzzy and PID controller.

Introduction

Application of hydraulic pressure drive reflects the heavy equipment in the ability of the hydraulic loop pass more power, easy to control. It has many outstanding qualities, such as response from lubrication and heat transfer performance precision, relatively large torque fluid, large torque-to-inertia high yield ratio, circulation, relatively high stiffness and positioning error is smaller. Although the high cost of hydraulic components and power plant, power loss due to the leakage, rigid, nonlinear response, and easy to make a mistake of low power operation tend to limit the use of hydraulic pressure drive, but to constitute a subset of the whole industry drive and widely used in transportation and manufacturing [1], [2].

SEHS, other, maybe it is the most important system, because it requires the advantages of both the output power of traditional hydraulic system and rapid response of the power system. However, there are also many challenges SEHS design. For example, they are highly nonlinear phenomena, such as fluid of compressibility, flow/pressure relationship and dead-band due to internal leakage and hysteresis, there are many uncertain factors, due to the hydraulic system of linear. So, it seems to be quite difficult for high accuracy servo control by using the linear control method [3], [5].

Controller Designs

There are various types of control system used in classical control, modern control and intelligent control system, each of which has been research and implementation in many industrial fields. Control system method has its advantages and disadvantages. Therefore, the trend is to realize hybrid system by more than one type of control technology.

PID Controller The PID control method has been widely used in industry during last several decades because of its simplicity. The implementation of PID control, as shown in (1), requires finding suitable values for the gain parameters K_P , K_I , and K_D . To tune these parameters, the model is linear zed around different equilibrium points,

$$u(k) = K_p e(k) + K_I \sum_{i=0}^k e(i) + K_D [e(k) - e(k-1)] \quad (1)$$

where $e(k)$ is the error signal.

Fuzzy Controller Fuzzy logic control (FLC) has the advantage that it does not require an accurate mathematical model of the process.

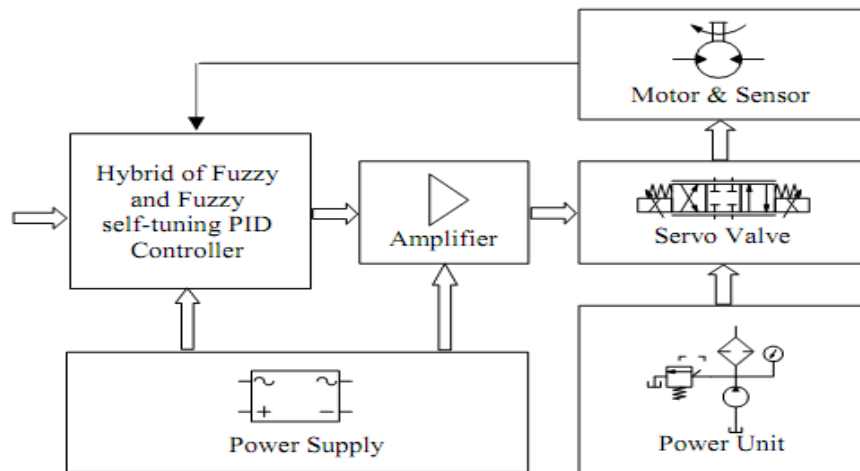


Fig 1. Block diagram of using a hybrid fuzzy and fuzzy self-tuning PID controls the SEHS

Fig. 4 shows a schematic diagram of a fuzzy control system. Input variables go through the fuzzification interface and are converted to linguistic variables. Then, a database and rule base holding the decision-making logic are used to infer the fuzzy output. Finally, a defuzzification method converts the fuzzy output into a signal to be sent out.

First, the two input variables must be defined in terms of linguistics. The error (e) in velocity is expressed by a number in the interval from -10 to 10. There are five linguistic terms of the error in velocity: negative big (NB), negative (N), zero (Z), positive (P), and positive big (PB). Similarly, the fuzzy set of the error change of the velocity or acceleration (Δe) is presented as {NB, N, Z, P, PB} over the interval from -10 to 10V. Finally, the fuzzy set of the output signal is presented as {Z, PS, PM, P, PB} over the interval from -5 to 5V.

The knowledge base for a fuzzy controller consists of a rule base and membership functions. It is reasonable to present these linguistic terms by triangular-shape membership functions, as shown in Fig. 3. A fuzzy control knowledge base must be developed that uses the linguistic description of the input variable. In this paper, an expert's experience and knowledge method is used to build a rule base [6]. The rule base consists of a set of linguistic IF-THEN rules containing two antecedences and one consequence, as expressed in the following form:

$$R_{i,j,k} : \text{IF } e = A_i \text{ and } \Delta e = B_j \text{ THEN } u = C_k \quad (2)$$

where $1 \leq i \leq 5$, $1 \leq j \leq 5$, and $1 \leq k \leq 5$. The total number of IF-THEN rules is 25 and is represented in matrix form, called a fuzzy rule matrix.

The decision-making output can be obtained using a max-min fuzzy inference where the crisp output is calculated by the center of gravity (COG) method.

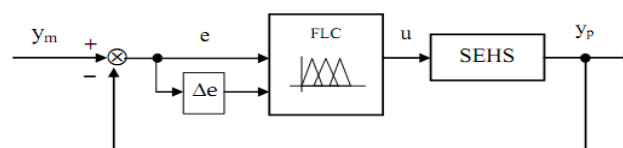


Fig 2. Block diagram of a FLC

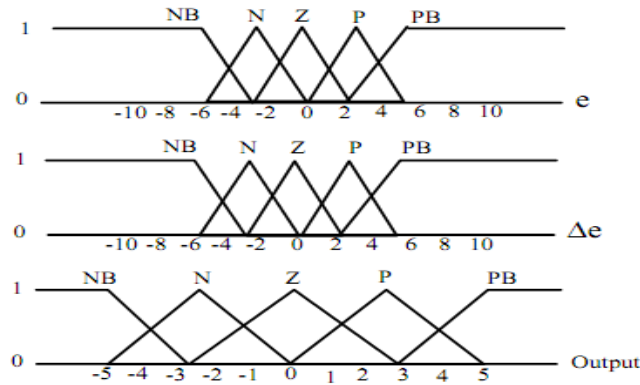


Fig 3. Fuzzy sets of a FLC

Hybrid of Fuzzy and PID Controller While the traditional PID controller is sensitive to changes, and the fuzzy controller control system parameters don't need precise information system variables to be effective, However, PID controller can better control and reduce the steady-state error of the system. Therefore, a hybrid system is as shown in Fig 4, the development of the advantage of the two, using PID control and fuzzy controller [4], [5].

Fig 4 shows a switch between fuzzy controller and PID controller, in the position of switch will depend on the actual value and the error between the set point values. If the error in the speed of higher than the threshold value of mixed system e_0 , fuzzy controller, it has a rapidly rising time and a small amount of overshoot, the system to correct speed is set point. When speed below the threshold e_0 or close to the set point change, the hybrid system PID control, and has good accuracy rate set near [4], [5].

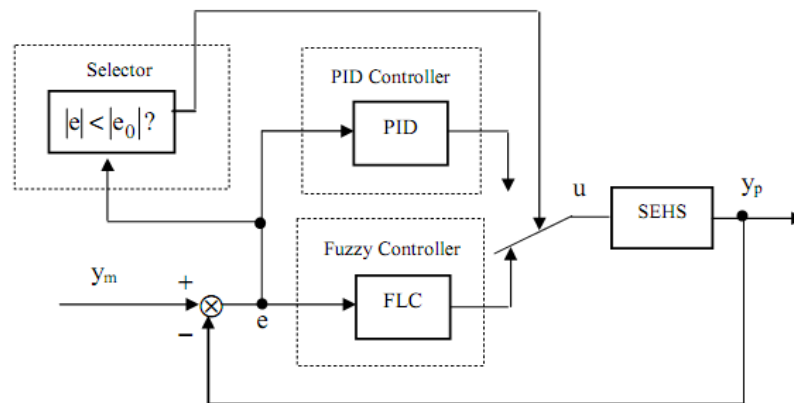


Fig. 4 Block diagram of a hybrid fuzzy PID

Fuzzy self-tuning PID Controller Fuzzy self-tuning PID controller means that the three parameters K_p , K_i , and K_d of PID controller are tuned by using fuzzy tuner [6]. The coefficients of the conventional PID controller are not often properly tuned for the nonlinear plant with unpredictable parameter variations. Hence, it is necessary to automatically tune the PID parameters. The structure of the fuzzy self-tuning PID controller is shown in Fig. 5. Where e is the error between desired velocity set point and the output, $e\Delta$ is the derivation of error. The PID parameters are tuned by using fuzzy tuner, which provides a nonlinear mapping from e and $e\Delta$ of error to PID parameters.

Regarding to the fuzzy structure, there are two inputs to fuzzy inference: e and $e\Delta$, and there are outputs for each PID controller parameter K'_p , K'_i , and K'_d respectively. Mamdani model is applied as structure of fuzzy inference with some modification to obtain the optimum value for K_p , K_i , and K_d . Suppose the variable ranges of the parameters of PID controller are $[K_{pmin}, K_{pmax}]$, $[K_{imin},$

$K_{I_{max}}$], and $[K_{D_{min}}, K_{D_{max}}]$ respectively. The range of each parameters was determined based on the experimental on PID controls the SEHS. The range of each parameters are, $K_P \in [0.5, 1.5]$, $K_I \in [0.1, 1]$, and $K_D \in [0.001, 0.01]$. Therefore, they can be calibrated over the interval $[0, 1]$ as follows:

$$K'_P = \frac{K_P - K_{P_{min}}}{K_{P_{max}} - K_{P_{min}}} = \frac{K_P - 0.5}{1.5 - 0.5}, K_P = K'_P + 0.5$$

$$K'_I = \frac{K_I - K_{I_{min}}}{K_{I_{max}} - K_{I_{min}}} = \frac{K_I - 0.1}{1.0 - 0.1}, K_I = 0.9K'_I + 0.1$$

$$K'_D = \frac{K_D - K_{D_{min}}}{K_{D_{max}} - K_{D_{min}}} = \frac{K_D - 0.001}{0.01 - 0.001}, K_D = 0.009K'_D + 0.001$$

The membership functions of these inputs fuzzy sets are shown in Fig. 6. The linguistic variable levels are assigned as: negative big (NB), negative (N), zero (Z), positive (P), and positive big (PB). Similarly, the fuzzy set of the error change of the velocity or acceleration (Δe) is presented as {NB, N, Z, P, PB}.

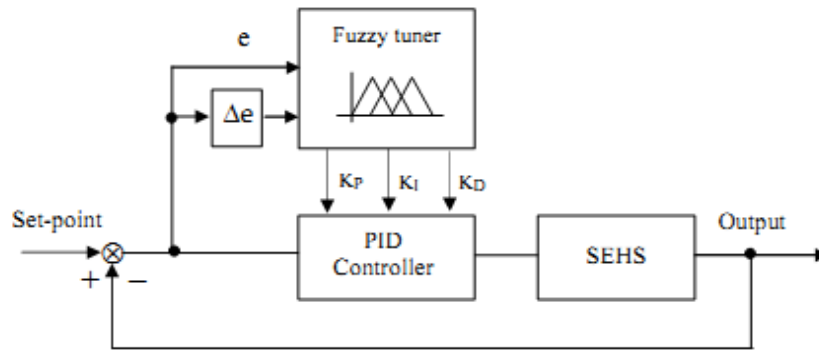


Fig 5. Block diagram of a fuzzy self-tuning PID controller

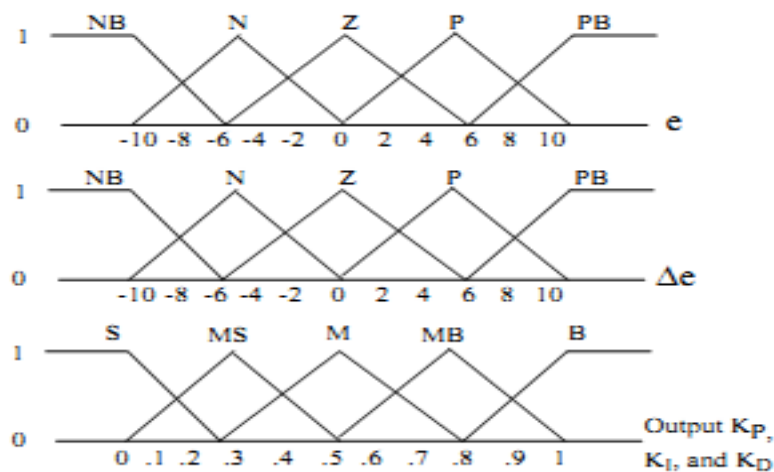


Fig. 6 Fuzzy sets of fuzzy tuner

Experimental Results

The effectiveness of the proposed hybrid of fuzzy and fuzzy-tune PID controller is evaluated experimentally with the SEHS and is compared with that of the hybrid fuzzy PID controller which uses the nominal values of the gains obtained by experiment. The control algorithms described in section IV of topic A, B, C, D, and E were hybridized and applied to the SEHS using by LabVIEW program as the development platform and shown in Fig. 8.

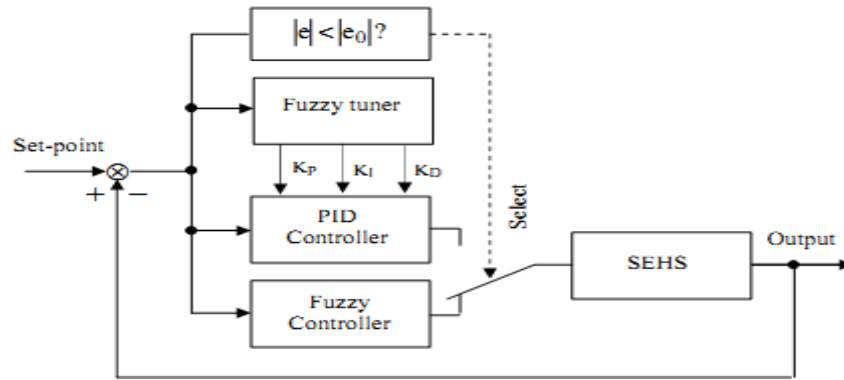


Fig. 7 Block diagram of a hybrid of fuzzy and fuzzy self-tuning PID

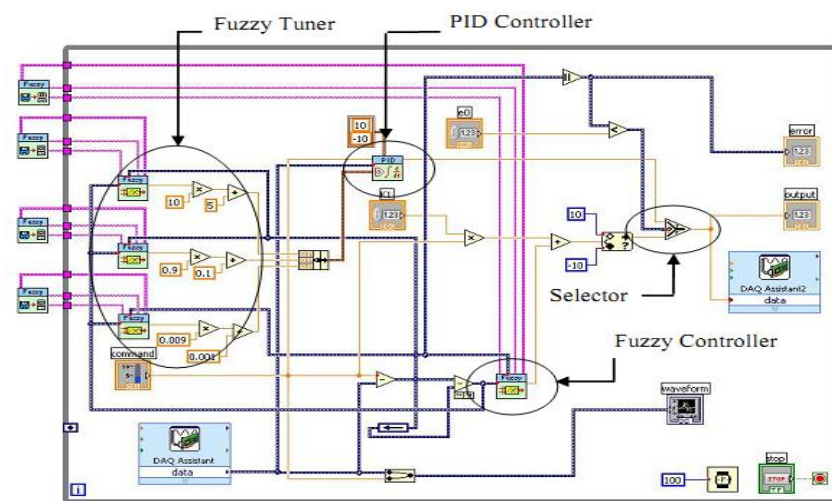


Fig. 8 The control algorithms are developed by LabVIEW program

The proposed of a hybrid of fuzzy and fuzzy self-tuning PID controller is evaluated experimentally with the motor speed control of SEHS and is compared with that of the conventional of a hybrid of fuzzy and PID controller. For the first experiment to observe the response of the SEHS control output of the both controller, which shown in Figs. 9 and 10, respectively.

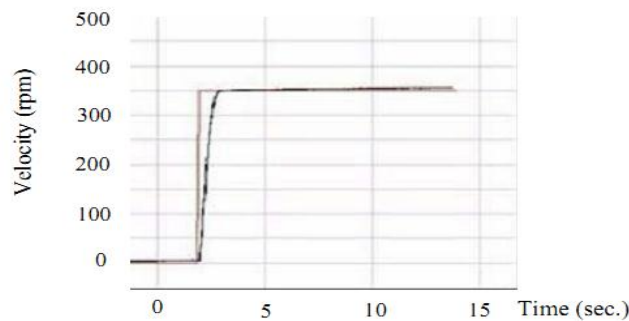


Fig. 9 Output responses of a conventional controller

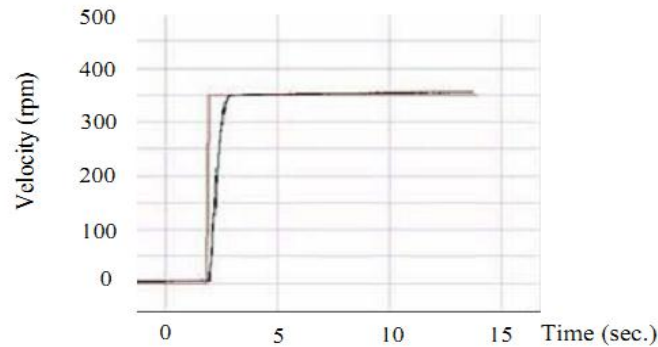


Fig. 10 Output responses of a proposed controller

Conclusion

The purpose of this study, we put forward the hybrid fuzzy and fuzzy self-tuning PID controller SEHS motor speed control. With this control scheme was divided into two parts, and the fuzzy controller and fuzzy self-tuning PID controller. Fuzzy controller is used to control the output of the system of the values of the system away from target value.

References

- [1] Merrit, H.E., "Hydraulic Control System". John Wiley, New York, 1976.
- [2] Rong-Fong Fung, Yun-Chen Wang, Rong-Tai Yang, and Hsing-Hsin Huang., "A variable structure control with proportional and integral compensations for electrohydraulic position servo control system," *Mechatronics* vol.7, no. 1, 2009, pp. 67-81.
- [3] M. Aliyari, Shoorehdeli, M. Teshnehlab, and Aliyari Shoorehdeli., "Velocity control of an electro hydraulic servosystem," *IEEE*, 2007, pp. 1536-1539.
- [4] Parnichkun, M. and C. Ngaecharoenkul., "Hybrid of fuzzy and PID in kinematics of a pneumatic system," *Proceeding of the 26th Annual Conference of the IEEE Industrial Electronics Society, Japan*, 2009, pp: 1485-1490.
- [5] Pornjit Pratumswan, Siripun Thongchai, and Surapan Tansriwong., "A Hybrid of Fuzzy and Proportional-Integral-Derivative Controller for Electro-Hydraulic Position Servo System" *Energy Research Journal*, vol. 1, issue 2, 2010, pp. 62-67.
- [6] Jianming Zhang, Ning Wang, and Shuqing Wang., "Developed method of tuning PID controllers with fuzzy rules for integrating processes," *Proceeding of the 2004 American control Conference, Massachusetts*, 2004, pp. 1109-1114.

Research of Universities Teaching Materials and Resources Based on Semantic Grid Portal Construction

Hu Changlong^a, Liu Wei^a, Zhang Jidong^a (Corresponding author)

^a School Of Management, Hubei University of Technology, Wuhan, 430068, Hubei, China

HuChanglong@163.com

Keywords: Semantic Description, Grid Portal, Teaching Resources

Abstract. This paper discusses the college teaching resources based on semantic grid portal construction, which starts from the system architecture and explained how to construct a grid portal application that can support learning service in the area of semantic retrieving of teaching resources on the basis of description of the teaching resources based on semantic, and use the grid technology in SOA to improve the structure of teaching grid portal system.

Introduction

The use of grid technology in web-based instruction has become a research hotspot, some scientific research departments, institutions of higher learning, commercial corporations and even higher education institutes have invested a lot of manpower and material resources for research and development. For example, European proposes a "European teaching grid framework (ELeGI)", and China has put forward building "China education scientific research grid (ChinaGrid)" and "the national basic teaching grid". After building a basic teaching grid framework, the high-level application of teaching grid becomes cutting-edge research, this research will combine the research result of traditional network teaching, and it will improve the network teaching research to a new stage.

The university teaching resources grid portal model expounded in this paper is based on the above idea to research. On the one hand this paper has realized the generalization of university teaching resources object described by standard ontology language RDF and OWL, On the other hand it has improved on the basis of the former, and proposed the ontology molecular concept which is suitable for the description of college teaching resources and the inherent knowledge in the body of resources and relative knowledge, and realized fusion of the changeable college teaching resources and grid portal on the basis of semantic, makes a beneficial exploration in the university teaching resource for user's better transferring and interacting.

Universities Teaching Resources Portal on the Basic of Semantic

System architecture Nowadays the research of teaching grid is in the beginning stage. The key point of research is on the study of teaching grid architecture. For example: the literature gives the teaching grid architecture and proposes imagine of special middleware for teaching grid; the literature is developing LMS on the foundation of grid and composing teaching grid structural framing. The literature proposes imagine of teaching grid portal.

We settle teaching grid structural framing and Portal of teaching grid on the founding of these researches. Course evaluations, education resources will be constructed through the semantic ontology, then integrate the resources through the semantic grid portal and offer it to users. It aims to break the restrictions of time and space, support resources sharing and learning collaboration and provide personalized and adaptive learning environment. The current network technology can only support the lower levels of learning resources sharing and learning activities' simple collaboration, and it still has many unsolved problems, including how to realize sharing resources and cooperation study in a distributed, autonomous, heterogeneous network environment; how to make semantics tap its potential in system, how to construct the essential components portal of a grid environment, how to regulate and simplify the environment of development. Therefore, this paper proposes a platform system structure on the basic of grid semantic.

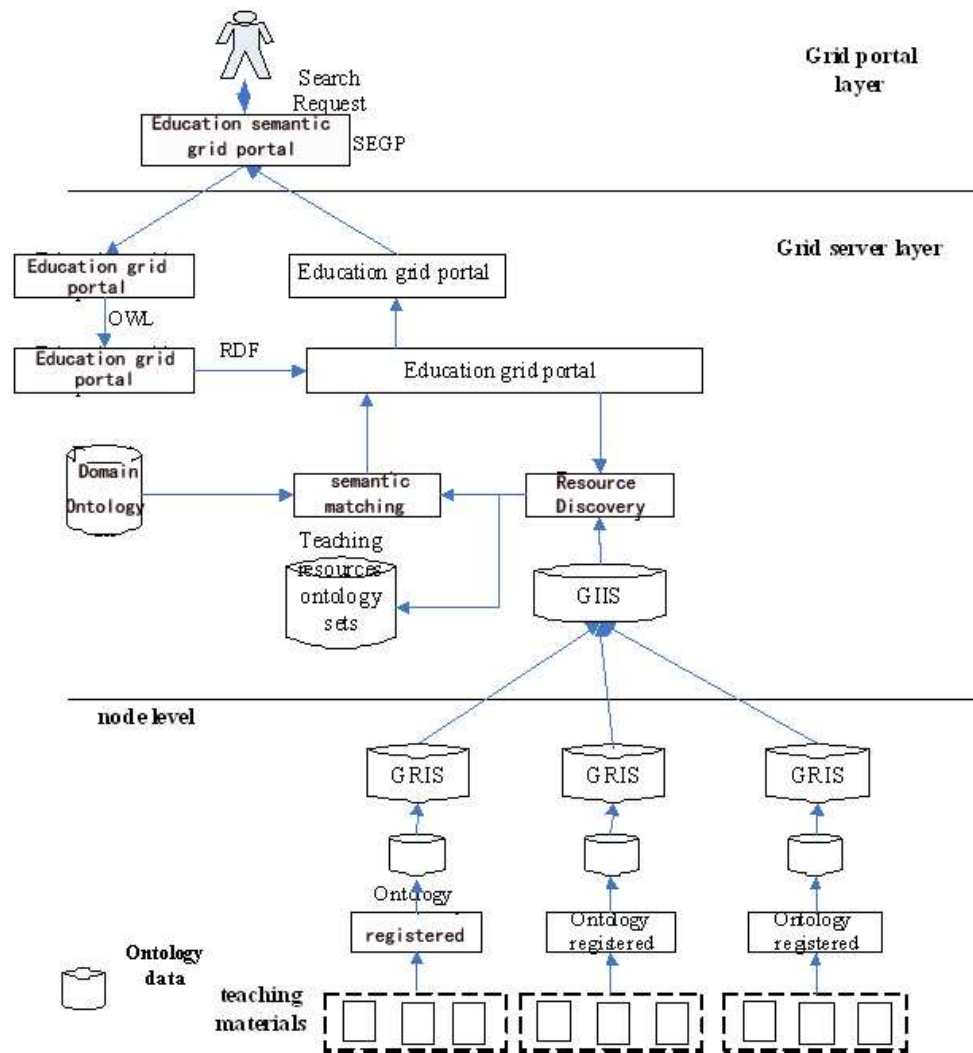


Fig. 1 The grid portal based on SOA

The grid portal based on SOA By analyzing the teaching grid system, on the basis of the characteristics of the network teaching and the structure of the network teaching system, makes as much use of the service-oriented architecture in using the grid technology and gives a more reasonable teaching grid portal system structure. Service oriented architecture (SOA) makes the loose coupling between learning partners possible and provides higher abstract in the form of open interface. Semantic grid technology can promote learning resources sharing and interconnected interoperability of all kinds of learning support system in higher level, to make it easy to use the existing resources and services, construct a new service dynamically and transparent, that is gather and coordinate resources a flexible way. Dynamic grid computing environment is autonomous entity, heterogeneous and distribution, this is a kind of environment that can't be agreed beforehand; consequently, cooperation relations must be able to be selected, negotiated, established and monitored dynamically. In order to gather grid components and resources effectively, not only need service-oriented architecture model, but also require the relative functional, available information and the information of different components interface information to have consistent interpretation which can be understood and dealt by the machine.

Through the identity authentication and other security technology to prevent illegal users through Internet use or get any resources of the grid, guarantee the security of data. Meanwhile, by using the technology of access control and data hiding users can only get the allowable information and knowledge and can't steal unauthorized information. The grid security needs to realize security functions as follows the user authentication, access control, billing, confidentiality, integrity, certainty and non-repudiation. The grid security also needs to realize the network flow control, load balance and congestion control, monitoring the grid resources, tasks, and the state of application, providing performance evaluation and fault-tolerant processing.

Teaching resources description on the basic of semantic Based on the semantic teaching resources description and Instructional Resources Management to classify and improve the existing teaching resources, thus for better formal description, build semantic description model of teaching resources. Based on the grid Monitoring and Discovery System (trMDS) establish a model for teaching resources register in the teaching grid, using this model and specially designed teaching resources information server and complete the registration, sharing and reuse of teaching resources in the grid.

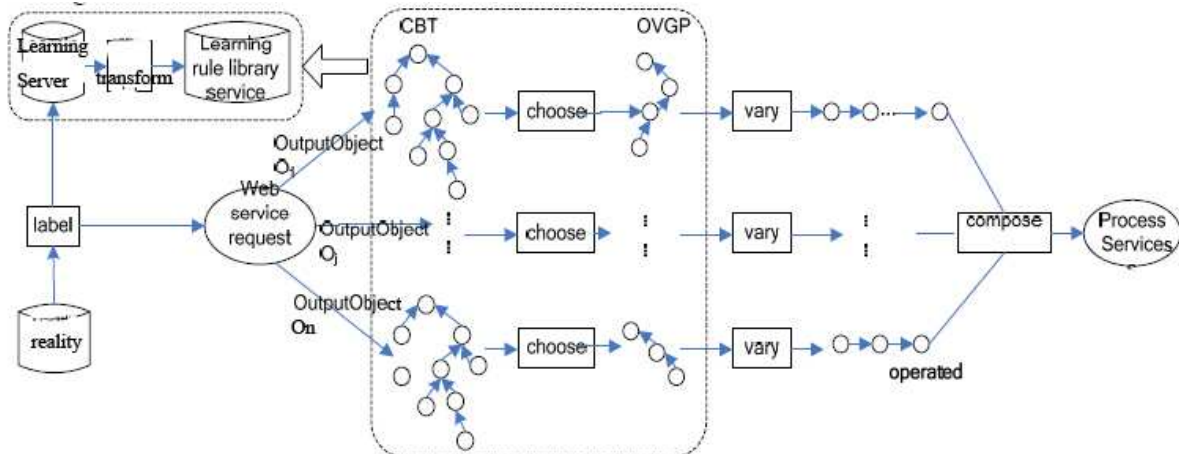


Fig. 2 Teaching resources description on the basis of semantic

The application involves large amounts of data and computing resources and usually needs to cross the organizational boundaries to share security resources. In order to reduce the complexity of application development, general grid services layer can shield the heterogeneity of the network resources (physical resources and logic resources) and support the unity of management of the network resources, distribution scheduling and safety control, provide a platform that is convenient to use, similar to a unified operation system for the upper applied to.

Distribution resources coupled service. The goal of the grid is organizing all the resources and working together, by using the distribution resources coupled service can submit the resource to the top of the grid applications in the form of service.

The student model based on ontology The research of student model based on ontology use ontology framework to integrate student model and establish the domain ontology and mapping that covering the ontology, and study mapping algorithm, build cognitive ontology, to integrate the cognitive characteristics, cognitive style and cognitive abilities into the other common cognitive student model. And then based on these models propose active teaching resources recommended mechanism.

Semantic retrieval of teaching resources Semantic retrieval of teaching resources makes the traditional semantic retrieval expand to the teaching grid, to realize the distributed, heterogeneous semantic retrieval of teaching resources, and realize the description, registration, discovery, searching, distribution, migration, reservation and recovery work of resource. Grid resource has the following characteristics: the geographical distribution of resources is very wide, resources and resources, resources and customer, customers and customers always connect each other by WAN; the quantity and type of resource are huge, and required a certain degree of collaborative work resources is dynamic changed, including resource attribute changes and copy and transfer in the grid, etc; Resources work in heterogeneous platforms and is controlled by different management strategy. In such an environment, need a kind of resource discovery mechanism which do not depend on the centralized control, distributed, and can be expanded, can adapt to the dynamic change of resources and has good positioning performance. Unlike the traditional distributed system which is using URI to positioning resources such as the Web, grid resource discovery mechanism should not only consider the position information of resources, but also should consider the attributes of resources and the other semantic information.

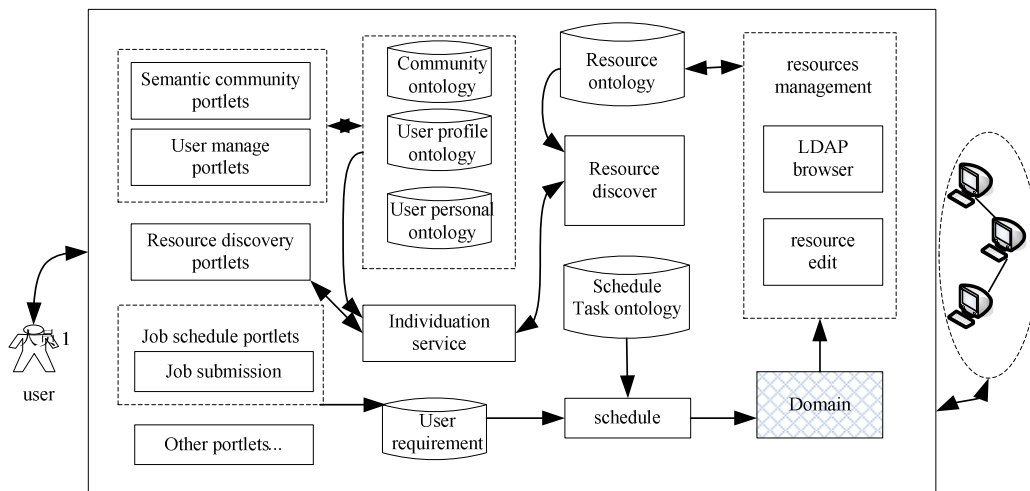


Fig. 3 Semantic retrieval of teaching resources

Summary

This paper expounds the basis and requirements of university teaching resources grid portal construction based on semantic, pay attention to the analysis of users' demand and experience and will make attempt in college teaching resources' semantic expression, When induction of the semantic ontology knowledge, make creatively try and research on the teaching resources description based on semantic and its application to teaching resources management.

Meanwhile, this paper describes the complete process of a universities teaching resources grid portal system based on semantic, from requirements analysis, design to the system modeling and finally realize, In practical projects, try and record the process and considerations of the grid portal system modeling, provide a reference of using the semantic in university teaching resources management field, and finally forming a unified and standard modeling approach provides reference.

Ontology knowledge in the process of teaching is a new promising field of research. It still has not appeared complete ontology model and the framework. How to analyze dominant and recessive knowledge in teaching process better, How to select right ontological form of the different types of knowledge, The research with a combination of universities teaching resources which is based on the semantic and grid portal still has a lot of the unknown waiting for people to explore. With the development of research, believing that the expression of semantic study will become more and more mature, and grid portal that based on the semantic will also be better serviced in the spread of human knowledge, sharing and creating.

References

- [1] zhongzhi Shi. Agent based Semantic Grid China Agent systems School. Chongqing: Southwest China NormalUniversity, 2004.16222.
- [2] Research Projects Focus:EleGILearning GRID (a Newsletter from the Kaleidoscope Learning GRID SIG). Learning Grid, 2004, 7(1):427.
- [3] Panhkratius V, G Vossen. Towards E-learning Grids:Using Grid Computing in Electronic Learning.Proc.of IEEE Workshop on Knowledge Grid and Grid Intelligence, Halifax, Canada, 2003.4215.
- [4] Research Projects Focus:Diogene Learning GRID(a Newsletter from the Kaleidoscope Learning GRID SIG).Learning Grid, 2004, 7(1):7210.

Research of Optimal Control Model with Multiple Inputs and Multiple Outputs Based On Logic Algebra

LING Yichun

Guangxi Vocational & Technical Institute of Industry, Nanning, Guangxi, 530001 China
lingyichun@guigu.org

Keyword: Mathematical describe, Optimal-control laws, Control-law analysis, Truth-table

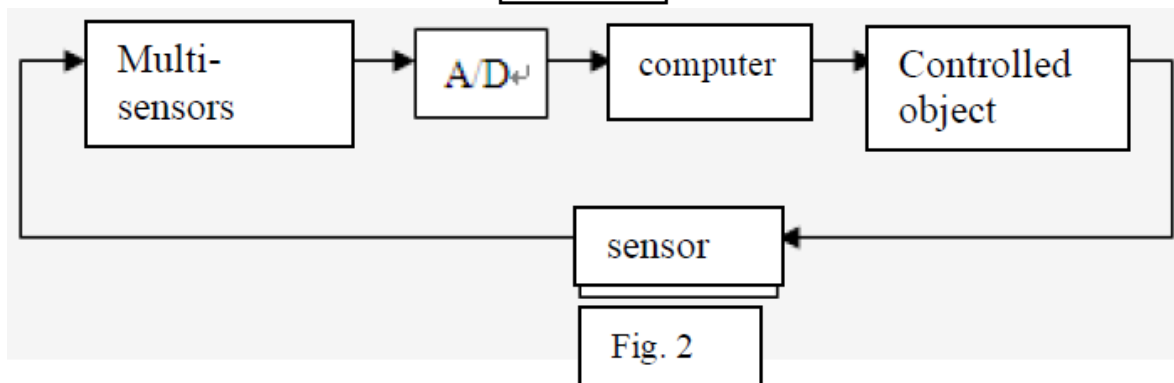
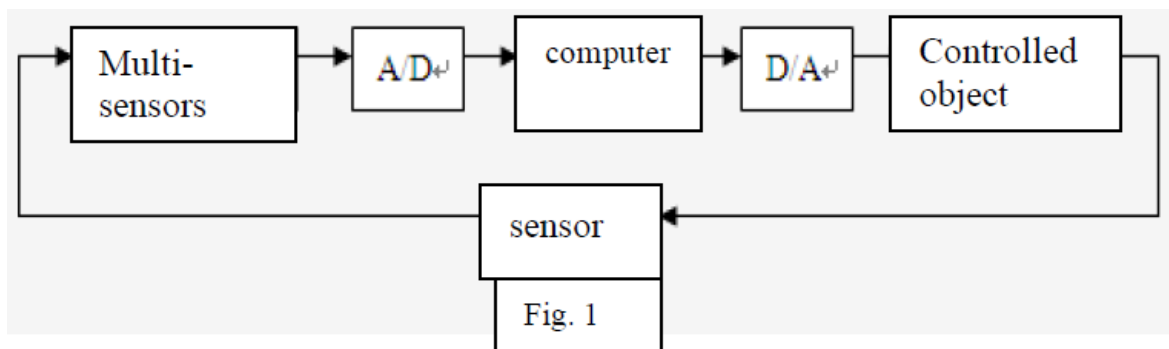
Abstract. Through the study of computer control system, article puts forward a mathematical model in the computer control system which controlled object is digital, and describes the mathematical model through logic algebra to form a set of method solving optimal index control laws which has the characters of easy to understand and easy to operate.

Introduction

Computer control system is a hybrid system that analog components and digital components exist together. The signal transmission and transformation process is relatively complicated. Signal conversion devices A/D and D/A are inevitable for the hybrid system that analog components and digital components exist together. If the controlled subject of the system is analog signal, the corresponding computer control system can be described with the structure Fig. 1. The theory of mathematic description is mainly discrete mathematic.

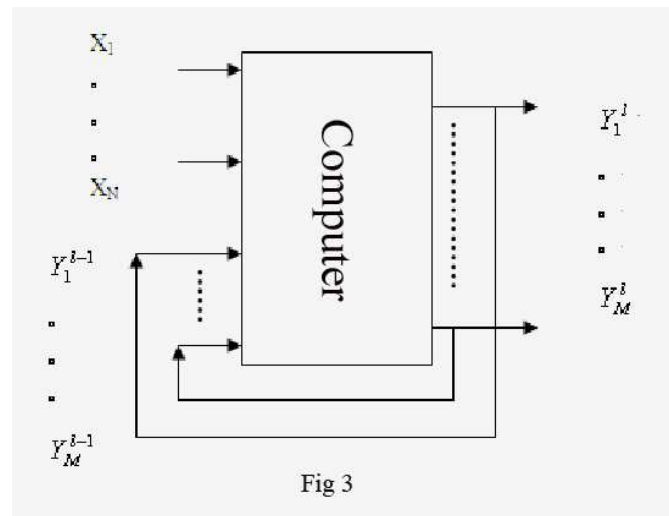
If the controlled object of the system is digital quantity (switch signal), the corresponding computer control system can be described by the structure Fig. 2.

The author uses logic algebra tool to study the optimum control rule methods that can be applied into many types of industry control.



Mathematic Description

Fig. 2 the key to the computer control system is the computer control rule. The mathematic description is shown as Fig. 3.



X represents input, Y represents output. There are N inputs and M outputs. $Y_1^{l-1} \dots Y_M^{l-1}$ Represent the previous condition of each output. $Y_1^l \dots Y_M^l$, it represents the current condition of each output. The current condition of each output $Y_1^l \dots Y_M^l$ is determined by the input $X_1 \dots X_N$ and the previous condition of each output $Y_1^{l-1} \dots Y_M^{l-1}$.

The relationship between the input and output is represented as:

$$\begin{aligned} Y_1^l &= F_1(Y_1^{l-1}, \dots, Y_M^{l-1}, X_1, \dots, X_N) \\ &\dots \\ Y_M^l &= F_M(Y_1^{l-1}, \dots, Y_M^{l-1}, X_1, \dots, X_N) \end{aligned} \quad (1)$$

Above is the computer control rule. The adding of the optimum index should be added according to the requirements of specific application.

Control rule analysis

How to carry out the optimum control rule solution? As X and Y are the digital quantities, the value selections can only be 0 and 1. The optimum control rules for the computer can be divided into three steps so as to find out the solution.

$$\left\{ \begin{aligned} Y_1^l &= F1(Y_1^{l-1}, Y_2^{l-1}, Y_3^{l-1}, X1, X2) \\ Y_2^l &= F2(Y_1^{l-1}, Y_2^{l-1}, Y_3^{l-1}, X1, X2) \\ Y_3^l &= F3(Y_1^{l-1}, Y_2^{l-1}, Y_3^{l-1}, X1, X2) \end{aligned} \right\} \quad (2)$$

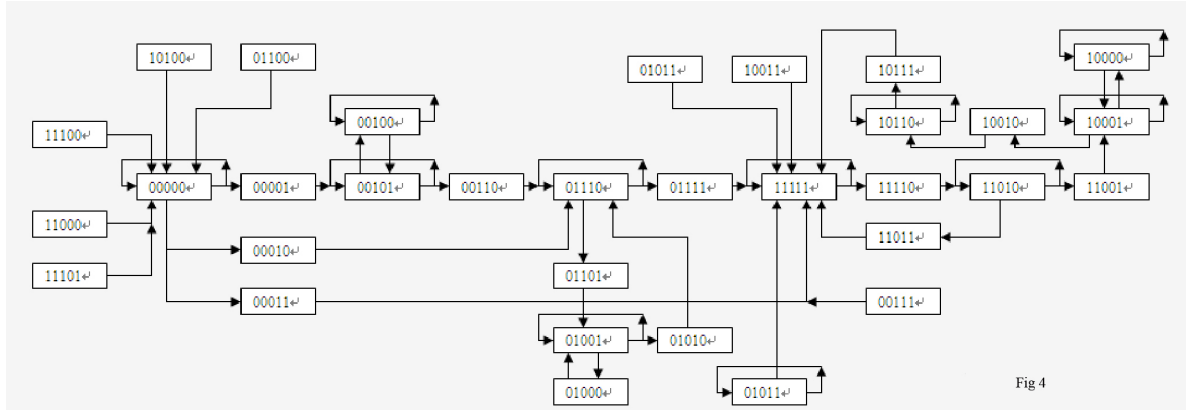
Determine computer output Y according to production equipment control requirements

As for the computer output Y in Fig. 3, the most representative application is the switch quantity that is equal to the digital signal. The combinations are very limited. Therefore, the output Y requirements are determined by the production equipment requirements.

The output combinations determined by the output requirements and optimum index and the truth value table is formed

In formula (1) the output condition $Y_1^l \cdots Y_M^l$ is determined by the value combinations of the input $X_1 \cdots X_N$ and the previous condition of output $Y_1^{l-1} \cdots Y_M^{l-1}$.

Use the switch matrix system controlled by the programmable logic controller as an example; it makes it clear how to form the truth table of input X and output Y with the determination of output Y and the lowest equipment loss rate. The mathematic model is shown in Fig. 3.



The determination of output Y

The object of switch matrix system controlled by the programmable logic controller is the electric valve. The controlling precision can be determined according to the quantities of connecting switches.

The description of optimum index

In the system design, with the description of output Y, the optimum index according to the actual situations.

The formation of the work state transition table of input X and output Y is shown as the Picture 4.

The work state transition table is of great necessity in the digital control system analysis. It is an efficient tool to find out the conflicts in the optimum control rule.

The following formula is written showing the optimum control rule, connecting the requirements of the output Y requirements and the optimum index: The work state transition table of input X and output Y is shown as the Fig. 4.

The work state transition table has found the contractions between the control and the optimum index. When $X_1X_2=00$, the output terminal has output.

The solution for this is that through adding restrictions items, and permitting $X_1X_2=00$, let L act as the restriction condition, the relationship between X_1 and X_2 is:

$$L = G (X_1, X_2) = X_1 + X_2 \tag{3}$$

When $X_1X_2=00$, $L=0$; when $X_1X_2=01$, $L=1$; when $X_1X_2=10$, $L=1$; when $X_1X_2=11$, $L=1$. The control rule can be revised as:

$$\left\{ \begin{array}{l} Y_1^l = L \cdot F_1(Y_1^{l-1}, Y_2^{l-1}, Y_3^{l-1}, X_1, X_2) \\ Y_2^l = L \cdot F_2(Y_1^{l-1}, Y_2^{l-1}, Y_3^{l-1}, X_1, X_2) \\ Y_3^l = L \cdot F_3(Y_1^{l-1}, Y_2^{l-1}, Y_3^{l-1}, X_1, X_2) \\ L = X_1 + X_2 \end{array} \right. \tag{4}$$

According to Fig. 4, the truth table of input X and output Y is shown as Table 1:

Table 1

Y_3^{l-1}	Y_2^{l-1}	Y_1^{l-1}	X2	X1	Y_3^l	Y_2^l	Y_1^l
0	0	0	0	0	0	0	0
0	0	0	0	1	0	0	1
0	0	0	1	0	0	1	1
0	0	0	1	1	1	1	1
0	0	1	0	0	0	0	1
0	0	1	0	1	0	0	1
0	0	1	1	0	0	1	1
0	0	1	1	1	1	1	1
0	1	0	0	0	0	1	0
0	1	0	0	1	0	1	0
0	1	0	1	0	0	1	1
0	1	0	1	1	1	1	1
0	1	1	0	0	0	0	0
0	1	1	0	1	0	1	0
0	1	1	1	0	0	1	1
0	1	1	1	1	1	1	1
1	0	0	0	0	1	0	0
1	0	0	0	1	1	0	0
1	0	0	1	0	1	0	1
1	0	0	1	1	1	1	1
1	0	1	0	0	0	0	0
1	0	1	0	1	0	0	1
1	0	1	1	0	0	1	1
1	0	1	1	1	1	1	1

Determine optimum control rule according to truth table

$$\begin{aligned}
 & Y_3^{l-1} Y_2^{l-1} Y_1^{l-1} X_2 X_1 + Y_3^{l-1} Y_2^{l-1} Y_3^{l-1} X_2 \overline{X_1} + Y_3^{l-1} Y_2^{l-1} \overline{Y_1^{l-1}} X_2 X_1 + Y_3^{l-1} Y_2^{l-1} \overline{Y_1^{l-1}} X_2 \overline{X_1} + Y_3^{l-1} \\
 & \overline{Y_2^{l-1}} Y_1^{l-1} X_2 X_1 + Y_3^{l-1} \overline{Y_2^{l-1}} \overline{Y_1^{l-1}} X_2 X_1 + Y_3^{l-1} Y_2^{l-1} Y_1^{l-1} X_2 X_1 + Y_3^{l-1} Y_2^{l-1} Y_1^{l-1} X_2 \overline{X_1} + Y_3^{l-1} Y_2^{l-1} \\
 & Y_1^{l-1} \overline{X_2} X_1 + Y_3^{l-1} Y_2^{l-1} \overline{Y_1^{l-1}} X_2 X_1 + Y_3^{l-1} Y_2^{l-1} \overline{Y_1^{l-1}} X_2 \overline{X_1} + Y_3^{l-1} Y_2^{l-1} \overline{Y_1^{l-1}} \overline{X_2} X_1 + Y_3^{l-1} Y_2^{l-1} \overline{Y_1^{l-1}} Y_1^{l-1} \\
 & X_2 X_1 + Y_3^{l-1} \overline{Y_2^{l-1}} \overline{Y_1^{l-1}} X_2 \overline{X_1} + Y_3^{l-1} \overline{Y_2^{l-1}} \overline{Y_1^{l-1}} X_2 X_1 + Y_3^{l-1} \overline{Y_2^{l-1}} \overline{Y_1^{l-1}} X_2 \overline{X_1} + Y_3^{l-1} \overline{Y_2^{l-1}} \overline{Y_1^{l-1}} X_2 X_1 \\
 & Y_3^{l-1}, Y_2^{l-1}, Y_3^{l-1}, x_1, x_2) = (x_1 + x_2) \cdot F_3(Y_1^{l-1}, Y_2^{l-1}, Y_3^{l-1}, x_1, x_2) = \\
 & (x_1 + x_2) \cdot (Y_3^{l-1} Y_2^{l-1} Y_1^{l-1} X_2 X_1 + Y_3^{l-1} Y_2^{l-1} Y_3^{l-1} X_2 \overline{X_1} + Y_3^{l-1} Y_2^{l-1} \overline{Y_1^{l-1}} X_2 X_1 + Y_3^{l-1} Y_2^{l-1} \overline{Y_1^{l-1}} X_2 \overline{X_1} + Y_3^{l-1} \\
 & X_2 \overline{X_1} + Y_3^{l-1} Y_2^{l-1} \overline{Y_1^{l-1}} \overline{X_2} X_1 + Y_3^{l-1} \overline{Y_2^{l-1}} \overline{Y_1^{l-1}} X_2 X_1 + Y_3^{l-1} \overline{Y_2^{l-1}} \overline{Y_1^{l-1}} X_2 \overline{X_1} + Y_3^{l-1} \overline{Y_2^{l-1}} \overline{Y_1^{l-1}} X_2 X_1 + \\
 & X_1 + Y_3^{l-1} \overline{Y_2^{l-1}} \overline{Y_1^{l-1}} X_2 \overline{X_1} + Y_3^{l-1} \overline{Y_2^{l-1}} \overline{Y_1^{l-1}} \overline{X_2} X_1 + Y_3^{l-1} \overline{Y_2^{l-1}} \overline{Y_1^{l-1}} \overline{X_2} \overline{X_1} + Y_3^{l-1} \overline{Y_2^{l-1}} \overline{Y_1^{l-1}} \overline{X_2} X_1 + \\
 & \overline{Y_3^{l-1}} Y_2^{l-1} \overline{Y_1^{l-1}} X_2 X_1 + \overline{Y_3^{l-1}} \overline{Y_2^{l-1}} \overline{Y_1^{l-1}} X_2 X_1 + \overline{Y_3^{l-1}} \overline{Y_2^{l-1}} \overline{Y_1^{l-1}} X_2 \overline{X_1} + \overline{Y_3^{l-1}} \overline{Y_2^{l-1}} \overline{Y_1^{l-1}} X_2 X_1) \\
 & = Y_3^{l-1} Y_2^{l-1} Y_1^{l-1} X_2 X_1 + Y_3^{l-1} Y_2^{l-1} Y_3^{l-1} X_2 \overline{X_1} + Y_3^{l-1} Y_2^{l-1} \overline{Y_1^{l-1}} X_2 X_1 + Y_3^{l-1} Y_2^{l-1} \overline{Y_1^{l-1}} X_2 \overline{X_1} + Y_3^{l-1} \\
 & Y_2^{l-1} \overline{Y_1^{l-1}} \overline{X_2} X_1 + Y_3^{l-1} \overline{Y_2^{l-1}} \overline{Y_1^{l-1}} X_2 X_1 + Y_3^{l-1} \overline{Y_2^{l-1}} \overline{Y_1^{l-1}} X_2 \overline{X_1} + Y_3^{l-1} \overline{Y_2^{l-1}} \overline{Y_1^{l-1}} X_2 X_1 + Y_3^{l-1} \overline{Y_2^{l-1}} \\
 & \overline{Y_1^{l-1}} X_2 \overline{X_1} + Y_3^{l-1} \overline{Y_2^{l-1}} \overline{Y_1^{l-1}} \overline{X_2} X_1 + Y_3^{l-1} \overline{Y_2^{l-1}} \overline{Y_1^{l-1}} X_2 X_1 + Y_3^{l-1} \overline{Y_2^{l-1}} \overline{Y_1^{l-1}} X_2 \overline{X_1} + Y_3^{l-1} \overline{Y_2^{l-1}} \overline{Y_1^{l-1}} \\
 & X_2 X_1 + \overline{Y_3^{l-1}} \overline{Y_2^{l-1}} \overline{Y_1^{l-1}} X_2 X_1
 \end{aligned}$$

Conclusions

This kind of practical solution digital system can be formed into rule and then be applied into more input and output analysis. From the analysis of the above control rule, there is a great amount of work load to solve the digital system.

Complimentary Close

The limitation of the application software has stopped the construction of control rules. Since the programming method is found out, the author has solved the application design problems.

References

- [1] GAO Jin-yuan and so on, Computer control system-theory, design and realization, Beihang Universtiy Press, 2001.2
- [2] (America)Thomas Floyd. Digital fundamentals. Beijing: Science Publishing House, 2000
- [3] Tim Williams. The Circuit Designer`s Companion. Great Britain,2005
- [4] LI Ren, Factory electronic control equipment, China Machine Press, 1979.8
- [5] XU Miu, Factory electronic control equipment, China Machine Press, 1990.9
- [6] LING Yi-chun, electronic basic knowledge and skills, China Electronic Press, 2006.2
- [7] Liao Chan-chu, PLC Programming and its applications, China Machine Press, 2005.7
- [8] LI Da-you, Digital circuit logistic design, Tsinghua University Press, 2002.7

Eyelid Noise Detection Based on Gray-scale Morphology and Judgment of Noise Occlusion

Li Su, Qian Li and Yuqian Wang

College of Automation, Harbin Engineering University, Harbin, China
e-mail: sul406@hrbeu.edu.cn

Keywords: Iris Recognition, Eyelid Occlusions, Noise Occlusions Relation, Gray-scale Morphology

Abstract: In iris recognition, eyelid occlusions will reduce the accuracy of iris recognition, an algorithm of eyelid occlusions detection based on Gray-scale Morphology and the judgement of the noise occlusion is proposed in this paper. By judging the projection relation between eyelid and eyelashes, the algorithm in this paper could determine which part need to be detected, instead of detecting all of the eyelid and eyelashes occlusion blindly. So the efficiency of the algorithm is largely improved and in addition, the noise detection method based on gray-scale morphology could perfect fit out the eyelid edge.

Introduction

Iris is the annular region with rich texture information between the pupil and sclera, as shown in Fig. 1. As an important feature of identification, iris has the advantages as uniqueness, stability and non-invasive etc. Comparing with other biometric recognition, such as fingerprint recognition, face recognition etc, iris recognition has higher accuracy and is getting the attention of academia and business community.

The iris texture is the main study object of iris recognition. However, in highly non-invasive iris recognition system, as the images are collected from the normal opening eyes, there are so many eyelash occlusions, as shown in Fig.1, if they can not be detected and suppressed, they will be considered as part of iris texture. In the following processing the eyelashes will be coded and matched, finally reduce the rate of iris recognition. So it is necessary to find an effective method that can determine the eyelash occlusions region and get a pure iris region (the effective iris region), which doesn't contain the noise of eyelashes, eyelid, etc.

In this paper, an algorithm of eyelid occlusions is studied. In the previous literatures, there are two main eyelash occlusions detection methods: (1) Daugman's method is that the parabolic template of fuzzy edges used to determine the upper and lower eyelid boundaries, and then the eyelid is fitted out by the statistical fitting parameters [1,2]. As it relates to the iterative search, the detection time is longer and the effect of parabola fitting also not very well; (2) Wilders used the method of combining edge detection and the Hough transform to detect eyelid [3]. When detection begins, the eyelid shape is assumed parabolic, but in practice the eyelid shape is not parabolic, and therefore bound to produce errors.

In response to these issues, an algorithm of eyelid noise detection based on gray-scale morphology and the judgment of the noise occlusion is proposed. No longer like the old methods, which detect the upper eyelid and lower eyelid at the same time, the method in this paper according to judge the relations between the projection of the eyelids and eyelashes noise occlusions in the iris area, and then determine the need for testing the eyelid. In this way, the efficiency of the eyelid noise detection algorithm is improved. On this basis, using the effective the eyelids noise occlusions detection method based on gray-scale morphology, the edge of the eyelid is accurately fitted.

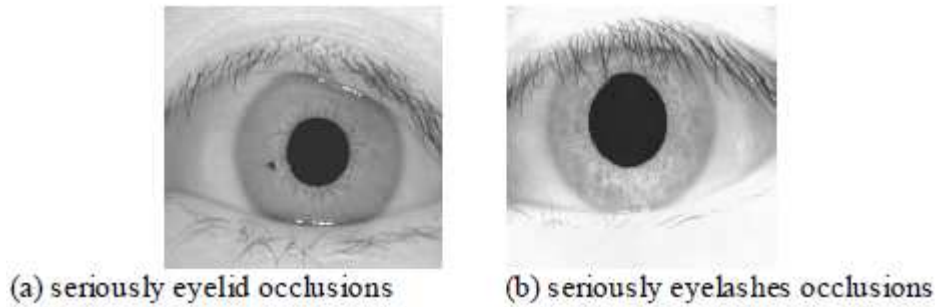


Fig. 1 Iris image

Eyelid Occlusions Detection Based on Gray-Scale Morphology and the Judgement of the Noise Occlusion

These years, people are interested in directly detecting the eyelid noise occlusions. But we have ignored the question: is it necessary to detect eyelid noise at any time? Why ask this question, first let us see a group of pictures, as shown in Fig.1, maybe it would be a revelation for everyone in these pictures.

By analyzing the two pictures in Fig. 1, some results can be found:

In the first image, the eyelashes do not cause the iris region block and the main noise of the iris region is the upper and lower eyelids noise. If you want to get the pure iris region (the effective iris region), only need to remove the area covered by the eyelid in the iris region. So the eyelid noise must be detected.

In the second picture, obviously, eyelash noise region covering a large part of the iris area. If you want to get the effective iris area, you only need to extract out the eyelash coverage area and the area covered by the lower eyelid. So the detection of the upper eyelid noise is likely not important.

From the above two points, the need of the eyelid noise detection is directly impacted on the projection relations between the eyelid occlusions and eyelashes occlusions. On this point, an algorithm of eyelid occlusions detection based on and the judgement of the noise occlusion is proposed in this paper.

The Judgement of the Noise Occlusion

Before detecting the eyelid occlusions by the method of Gray-scale Morphology, the range of judging the relations between the eyelid occlusions and eyelashes occlusions should be determined. The steps are as follow:

Image Segmentation

In the normal iris image, as shown in Fig. 2, block range of the upper eyelid does not exceed the pupil area, generally located in the upper part of the pupil area. Therefore, in order to narrow the scope of testing, the iris image segmentation is necessary.

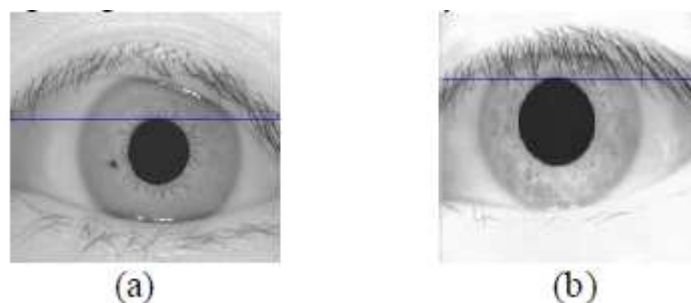


Fig. 2 Iris image segment

As during the process of iris inner and outer edge location before noise detection, the upper vertex of the pupil region has been obtained as (x_u, y_u) . So it is easily divided the iris image into two parts by the horizontal line pass through the point (x_u, y_u) . And, on the upper part of the horizontal line including upper eyelid noise and eyelashes noise, the lower part, including the under eyelids noise, as shown in Fig. 2.

Judgement

From the two pictures in Fig. 2, it is found that in the Fig. 2 (a) the region above the horizontal line, there is no eyelashes occlusions but eyelid occlusions. But in the Fig. 2 (b), contrary, the region above the horizontal line is not only occluded by eyelid occlusions but eyelashes occlusions, and the eyelashes noise account for the most iris region block the eyelid noise.

According to this characteristic, a method is designed in this paper to determine under which circumstances eyelid noise should be detected:

Firstly, during the process of iris inner and outer edge location before noise detection, the radius of the iris inner and outer edge has been determined. Here we set them as r_p and r_i . Compared to the eyelids and the iris gray level threshold, eyelashes gray threshold is smaller, which is set as T_y . Also we set the horizontal line in Fig. 2 as P_d . So the upper search starts from the line in the $(r_p - r_i)/2$ part of the iris region, and then the threshold results which are searched smaller than T_y will be putted in the matrix S_{yy} . After the search, the number of values in the matrix if is little or zero, then it means there is no eyelashes occlusions, and when detect the noise only need to detect the eyelid occlusions. Contrary, the number of values in the matrix is large which means that the eyelashes are the main occlusions and when detect the noise, just need do the eyelashes occlusions detection [4].

In addition, the iris region also may be occluded by the lower eyelid noise, the eyelashes of the lower eyelid part are seldom or eyelashes scroll down, which couldn't block the iris region. Therefore, the noise of the lower eyelid could be directly detected no need to discuss it and eyelashes noise projection relationship to determine the need for the detection of the lower lid noise.

Eyelid Occlusions Detection Based on Gray-Scale Morphology By judgement results, it is necessary to detect the eyelid occlusions, an algorithm based on Gray-scale Morphology could be used to detect the eyelid occlusions [5].

This method is divided into three parts:

Grayscale Morphological Processing. The gray-scale morphology is an extension of mathematical morphology, including erosion, dilation, opening and closing operation etc. Erosion and dilation describe as follow:

Erosion image f with the structural element b is $f \ominus b$, which defined as:

$$(f \ominus b)(s, t) = \min \{ f(s+x, t+y) - b(x, y) \mid (s+x, t+y) \in D_f, (x, y) \in D_b \} \quad (1)$$

Where D_f and D_b were f and b 's definition domains.

Erosion image f with the structural element b is $f \oplus b$, which defined as:

$$(f \oplus b)(s, t) = \min \{ f(s-x, t-y) + b(x, y) \mid (s-x, t-y) \in D_f, (x, y) \in D_b \} \quad (2)$$

In this paper, there are the elements of other non-eyelid as eyelashes and noises etc in the segment image after gray-scale morphology processing. Therefore it is necessary to use opening processing to eliminate these interference region.

Open computing described as follows:

$$f \circ b = (f \ominus b) \oplus b \quad (3)$$

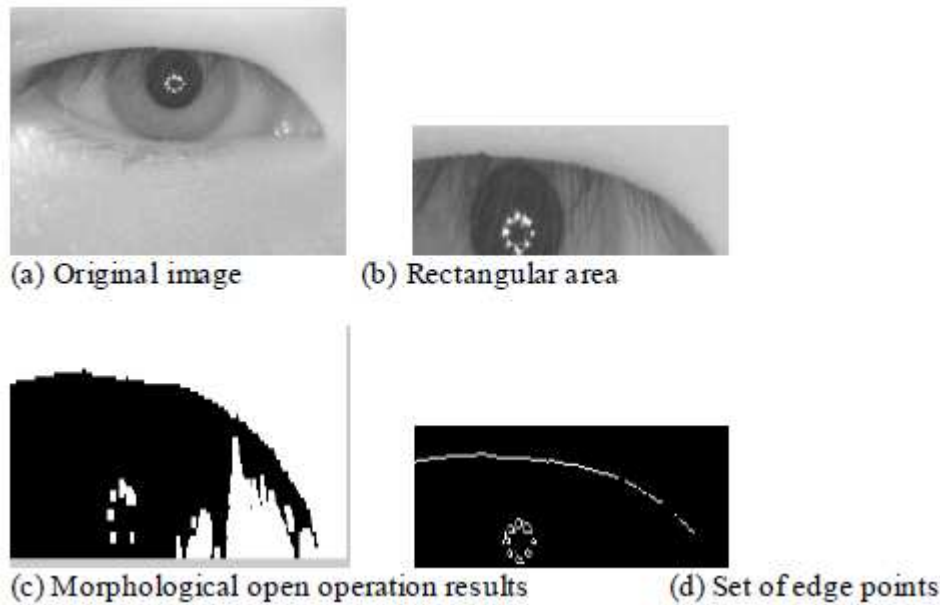


Fig. 3 Grayscale morphological processing

The aim of using gray-scale morphology is getting the points including the eyelid edge points. First, a rectangular region is extracted by eyelid segment from the iris image. The region should try to include eyelid noise. After the gray-scale open operation, the interference of eyelashes, etc is eliminated in this rectangular region. Then the edge set of points are obtained through edge detection on the rectangular area by Sobel edge detection operator. Process of the algorithm is shown in Fig. 3.

Getting the Edge Point of the Upper Eyelid

This step is used to get a more accurate set of edge points from the binary image which has been removed noise. After gray-scale morphological processing, the concentrate of edge points contains the point of the edge of the upper eyelid, eyelashes and pupil section, etc. And the eyelashes and pupil points are noise points, which must be removed. We can use the positional parameters to remove the pupil point, while use morphological opening operation to eliminate eyelash noise. And now a binary image F is obtained, which contains only the edge points of the upper eyelid and a small amount of noise points.

The key of fitting the eyelid edge points is accurately getting the upper eyelid edge points. By observing the eyelid structure, it is found that if a point $B_{i,n(t)} = \frac{n!}{i!(n-i)!} t^i (1-t)^{n-i} = C_n^i t^i (1-t)^{n-i}$ of $i = 0, 1, \dots, n$

iris image is the point on the edge of the eyelid, the gray level variations in the horizontal direction among the neighborhood of this point are small but bigger in the vertical direction. Accordingly this, the edge of the eyelid points could be determined out, and the results shown in Fig. 4. The mathematical expression of the method is as the following formula:

$$\begin{cases} |f(i, j) - f(i \pm 2, j)| < T_1 \\ |f(i, j) - f(i, j \pm 2)| < T_2 \\ T_3 < f(i, j) < T_4 \end{cases} \quad (4)$$

Where $|f(i, j) - f(i \pm 2, j)|$ express the gray-scale changes of horizontal direction and $|f(i, j) - f(i, j \pm 2)|$ express the gray-scale changes of the vertical direction. T_1 and T_2 is the experience value, T_3 and T_4 is determined by the mean of the statistical edge of the eyelid gray.



Fig. 4 Set of eyelid edge points

Upper Eyelid Edge Fitting

When get the eyelid edge point set, the edge of the eyelid can be fitted out by the Bezier curve. Taking into account that in practice, not all of the eyelid shapes are parabolic, so the Bezier curve is the fantasy tools to fit the eyelid edge. The main significance of the Bezier curve is that whatever straight line or curve can be described mathematically. The Bezier curve fitting is described as follow:

$$C(t) = \sum_{i=0}^n p_i B_{i,n}(t) \quad 0 \leq t \leq 1 \quad (5)$$

Where p_i the characteristic polygon of the curve, $B_{i,n}(t)$ is the Bernstein base function, which is the harmonic function of the position vector of the curve. The Bernstein base function is described as follow:

$$B_{i,n}(t) = \frac{n!}{i!(n-i)!} t^i (1-t)^{n-i} = C_n^i t^i (1-t)^{n-i} \quad i = 0, 1, \dots, n \quad (6)$$

The upper eyelid detection results are shown in Fig. 5. Similarly, it can detect the noise of the lower eyelid.

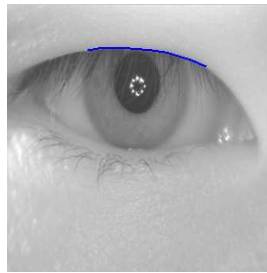
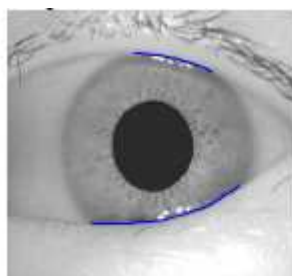


Fig. 5 Upper eyelid detection

Experimental Results and Discussion

The experiments are based on the iris databases of Harbin Engineering University and the Institute of Automation, Chinese Academy of Sciences (CASIA). The whole algorithm is tested and simulation based on MATLAB 2010R.

Some detection results are shown in Fig.6. In the Fig. 6(a), as there is most eyelid noise in the iris region but no eyelashes occlusions, so base on the judgement method of this paper, the upper and lower eyelid noise should be both detected. In the Fig. 6(b), as there is more eyelashes occlusions and the range of eyelashes noise is far more than the eyelid occlusions, so when use the algorithm to detect the noise occlusions just need detect the eyelashes and lower eyelid noise occlusions.



(a) Upper and lower eyelid detection results (b) Lower eyelid detection results

Fig. 6 Eyelid detection results

Conclusion

The advantages of the algorithm in this paper for detecting the eyelid noise occlusions is that by judging the projection relation between eyelid occlusions and eyelashes occlusions to determine which part need to be detected, not blindly detect all of eyelid and eyelashes occlusion. So the detection results accuracy is better. In addition, the noise detection method based on gray-scale morphology could perfect fit out the eyelid edge.

Acknowledgment

Supported by the Fundamental Research Funds for the Central Universities (HEUCF041214) and Youth Foundation of Heilongjiang Province (QC07C14)

References

- [1] Daugman J G.High. (1993) Confidence Visual Recognition of Persons by a Test of Statistical Independence [J]. IEEE Transactions on Pattern Analysis and Machine Intelligence 15(11):1148-1161
- [2] J.G Daugman. (1994) Biometric personal identification System based on Iris Analysis. U.S. Patents 29:529-540
- [3] R.P Wilders, AmSouth J C, Green G L, et al (1994) A system for automated iris recognition. In Proceedings of the Second IEEE Workshop on Applications of Computer Vision. Sarasota, Florida, 1(4):121-128
- [4] Su Li, Li Qian, Yuan Xin (2011) Study on algorithm of eyelash occlusion detection based on endpoints identification. 2011 IEEE 3rd Work Shop on Intelligent Systems and Application. ISA-2011, Wuhan, China 2(12):144-147
- [5] Lai Yi, Lu Chenhong, Lu Zhaoyang (2007) Eyelid and Eyelash Occlusions Detection for Iris Recognition. Journal of Computer-aided Design & Computer Graphics. Mar 19(3):346-350

Application of Multivariable Non-linear Decoupling Control Based on Neural Network

Zhang Jianbo, Fan Donghai and Hu Renzhi

State Grid Electric Power Research Institute, Nan Rui Lu.8, 210003 Nan Jing, China

E-mail: zhangjianbo@sgepri.sgcc.com.cn, fandon-
ghai@sgepri.sgcc.com.cn, hurenzhi@sgepri.sgcc.com.cn:

Keywords: Neural Network, Nonlinear System, Distributed Control System, BP Network, Steady State

Abstract Aimed at Neural Network can approach any nonlinear system with arbitrary accuracy, the frame of distributed NN decoupling system are proposed to decouple the MIMO nonlinear system. In this paper, we designed and finished the Distributed Control System based on ABB's Freelance 800F, and collected experimental data to model the thermostatic heater, then we have carried out the mathematical model by means of MATLAB dynamic simulation. In sequence, we trained the neural network controller in MATLAB. When the decoupling is completed, we used controller to control the MIMO nonlinear system in DCS. Experiment result shows that it is conscientiously feasible and deserves to be widely applied in the process of controlling industry.

Introduction

All kinds of natural and social systems are more or less non-linear. For the nonlinear systems, the traditional design method is to linearize the process model, and then use linear control methods. However, it always cannot get satisfactory results when using linearization for nonlinear object. Especially in some kind of control problems, such as attitude control, robot control, brushless DC motor and chemical processes, etc., it will not be possible to replace non-linearity relationship by linearity relationship, especially in MIMO [1] system.

In order to study the application of neural network in a nonlinear multivariable control system, we study the actual control object model in this paper, and expect to achieve a practical result in engineering.

Object Model

The controlled object is a thermostatic heater based on PTC [2] ceramic heating elements. Its internal is fitted with two Silicon Controlled Rectifiers, which makes it possible to control the strong electricity by weak electricity. Using software platform to control the current across the PTC element, the heating power of the element can be adjusted. Between the output and the electric current relations are nonlinear. The nonlinear function is:

$$W = f(i) \tag{1}$$

Then the heat is blown out of the glass tube by a fan, and the temperature θ of the tube at the mouth varies with the heating power of the elements PTC, as shown in Fig.

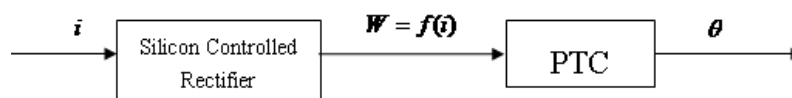


Fig. 1 Object model

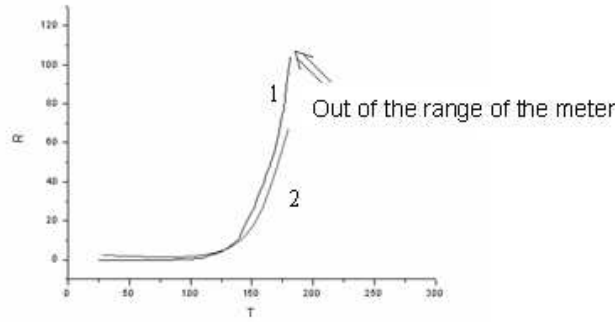


Fig. 2 R-T curve of the PTC

PTC ceramic, the positive temperature coefficient ceramic [3], is a kind of material with nonlinear R-T characteristics. Fig. 2 shows the resistance-temperature characteristics of a typical PTC heater, where the curve 1 is the characteristic of temperature increasing, while the curve 2 is the characteristic of temperature decreasing. The temperature is in degrees centigrade, and the resistance in ohms. The system includes two PTC heating elements. Each of them controls the temperature of an exit respectively. Meanwhile, the components can also affect the other loop, which constitute the following multivariable coupling control system. For the non-linearity of the control object, the output gain varies with the input voltage. Assuming that the relationship between the output variable y and input variable u is:

$$y = f(u) \tag{2}$$

The system model is shown in Fig. 3. u_1 And u_2 is the input voltage signal, y_1 is the temperature of the first tube at the mouth, y_2 is the temperature of the second tube at the mouth. The gain function of the first forward channel is $f_{11}(u)$, the first forward channel function in the second forward channel's gain is $f_{12}(u)$. Likewise, we may define the gain function $f_{22}(u)$ and $f_{21}(u)$.

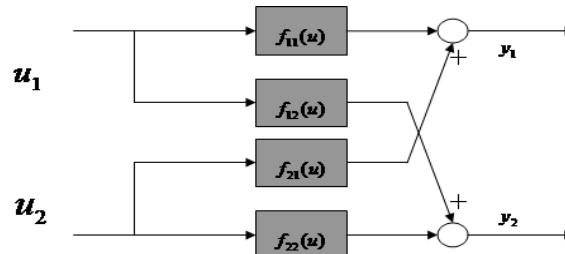


Fig. 3 System model

In order to determine the gain function, we set $u_2 = 0V$, and add step input signal of $0.1V$ to u_1 in sequence, then measure the static temperature of y_1 . Table 1 shows part of the data.

Now, gain function $f_{11}(u)$ is obtained.

$$f_{11}(u) = -16u^3 + 60u^2 - 17u + 0.65 \tag{3}$$

Similarly

$$f_{12}(u) = -0.35u^3 + 0.45u^2 + 5.6u + 0.36 \tag{4}$$

$$f_{21}(u) = -3u^3 + 10u^2 - 4.2u + 0.25 \tag{5}$$

$$f_{22}(u) = -13u^3 + 33u^2 + 27u + 5.6 \tag{6}$$

Table 1 The input and output data

Variable	Data				
u_1	1.0	1.1	1.2	1.3	1.4
y_1	30.85	30.85	30.85	33.18	33.2
u_1	1.5	1.6	1.7	1.8	1.9
y_1	33.95	37.82	41.97	47.41	52.6
u_1	2.0	2.1	2.2	2.3	2.4
y_1	59.11	64.58	69.8	74.5	80
u_1	2.5	2.6	2.7	2.8	2.9
y_1	85.79	89.71	93.39	96.55	101.8

Simulation Model and Decoupling

In order to solve the problem of coupling between two loops, it is designed to decouple the system using BP neural networks [4], as shown in Fig. 4 [5].

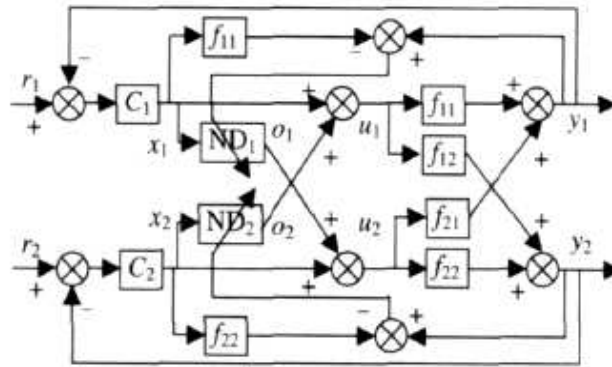


Fig. 4 Decoupling control model

In Fig. 4, $f_{11}, f_{12}, f_{22}, f_{21}$ are the object properties, the distributed decouple control system [6] is composed of two controllers (C_1 and C_2), and two NN decouplers (ND_1 and ND_2). For f_{11} and output y_1 of the first main channel, input u_2 of the second channel can be considered as an interference, and it can be eliminated by introducing compensation part ND_1 , while taken

$$ND_1 = f_{12} \cdot f_{11}^{-1} \quad (7)$$

Similarly, so does the second main channel.

$$ND_2 = f_{21} \cdot f_{22}^{-1} \quad (8)$$

Neural network modifies weighting factor using gradient algorithm, and the learning process can be carried out in Matlab. In the environment of Simulink, controlled object can be built based on the mathematical model. First, set $u_2 = 0V$, and input step signal to u_1 . Next, make $u_1 = 0V$, input step signal to u_2 . And then the simulation output value of θ_1 and θ_2 is obtained. Compare it with the experimental data, as shown in Fig. 5:

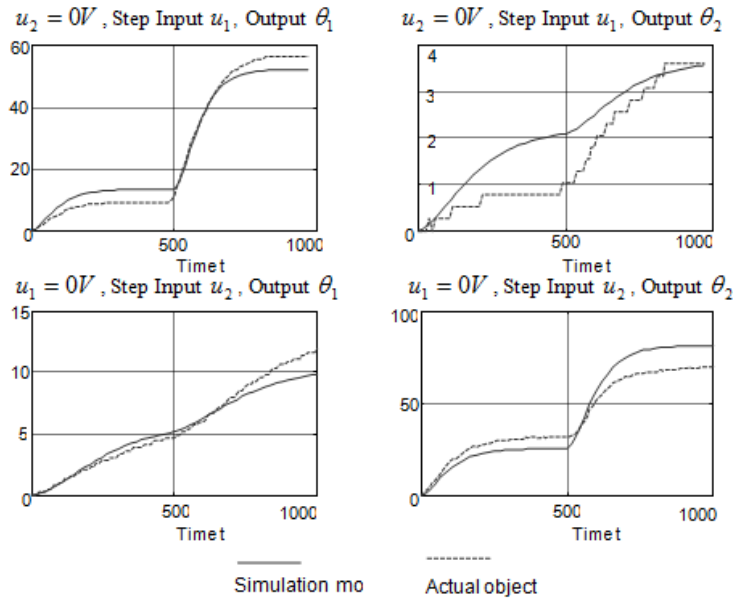


Fig. 5 Simulation model and actual model

It can be seen that the output errors of the object model and actual object are less than 5 °C, essentially accorded with requirement.

Set $u_2 = 0V$, and apply step input signal to u_1 , then set $u_1 = 0V$ step input signal to u_2 . The weighting factor of neural network decoupling controller can be determined through the continuous learning process. Decoupled output of the system is shown as Fig. 6.

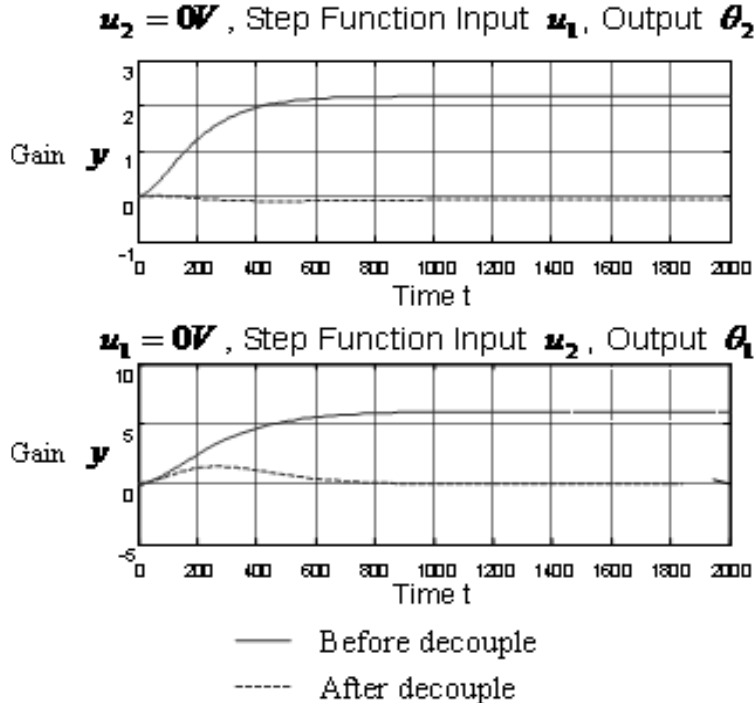


Fig. 6 Coupled and decoupled outputs of the system simulation

It can be seen that the steady-state gain of two coupled channels is zero. The decoupled result of channel $u_1 - \theta_2$ is satisfactory. The dynamic performance of the channel $u_2 - \theta_1$ has a little fluctuation.

Application of Control Strategy in DCS

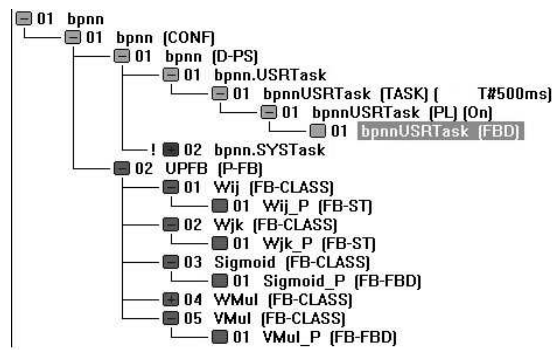


Fig. 7 Configuration files

The Software environment is FreeLance 800F V8.1 configuration software. The control system based on this platform can implement simple engineering ideas to open, technologically advanced systems, and currently has more than 14,000 applications in all walks of life.

In the article, the learnt BP neural network controller is implemented on the platform. System configuration files are shown in Fig. 7:

Start system, and set $\theta_1=40^\circ\text{C}$, $\theta_2=45^\circ\text{C}$. The result of system operation is shown as Fig. 8.

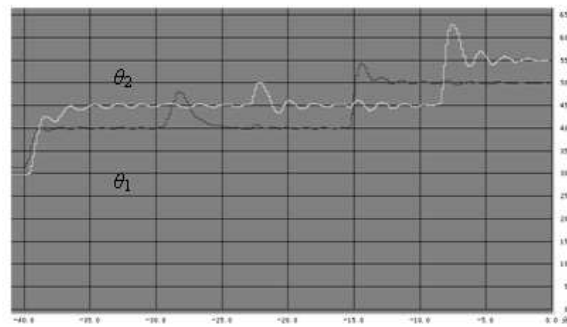


Fig. 8 DCS control curves

The system gradually achieves the steady state. In order to observe the ability of the system to overcome the disturbances and the effects of decoupling, we continue the experiment in the steady state. Give θ_1 a disturbance signal, and then. As shown in Fig. 8, the system is self-regulated to overcome the disturbance, and has anti-interference ability. Setting $\theta_1 = 50^\circ\text{C}$, observing θ_2 , it is founded that θ_2 becomes stable after a slight volatility. Make $\theta_2 = 55^\circ\text{C}$, and observe θ_1 . θ_1 , Is found basically the same. Overall, the decoupling result of the system is satisfactory.

In order to compare the situation before and after decoupling, we remove the decoupling links and then do experiment again; the control curves before decoupling are shown as Fig. 9.

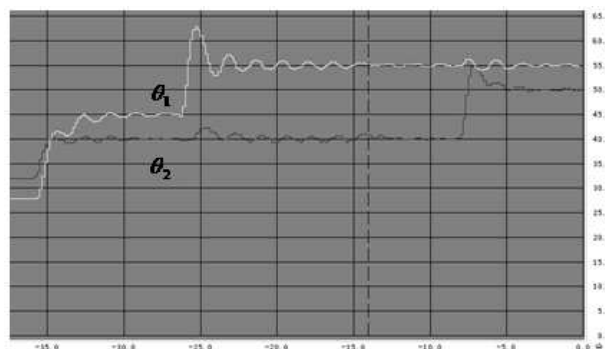


Fig. 9 Control curves without decoupling

In the chart, first we set value $\theta_1=40\text{ }^\circ\text{C}$ and $\theta_2=45\text{ }^\circ\text{C}$, when the system is stable, then we set value $\theta_2=55\text{ }^\circ\text{C}$ and $\theta_1=50\text{ }^\circ\text{C}$. Looking at Fig. 9, the impact of the first forward channel function in the second forward channel is obvious, and it is same to the second forward channel function in the first one. Compare of the Fig. 8 and Fig. 9, the curves of latter are fluctuating largely, the impact on main loop is greater. In other words, it means the main loop need a long time to regulation.

In summary, the experiment successfully accomplished decoupling control for nonlinear PTC ceramic heater system. At the same time, anti-interference ability of the system is relatively good, basically meeting the purpose of this design.

Conclusion

In this paper, BP neural network is implemented in DCS, means it is possible that the configuration software can use complex algorithms without the shackles of Matlab environment. It greatly improves the operation speed, saves system resources, and reduces requirement for operating environment.

References

- [1] D. He, X. ZH. Dai. (2000) Novel Method for Decoupling MIMO Nonlinear System with Linearization (II)-Discrete-time System. *Control and Design* 14(6):631-635
- [2] YOUN H.TING (1972) Self-Regulating PTC Heating Systems: A New Approach for Electric Heating Appliances. *INDUSTRY APPLICATIONS* 8(3):338-344
- [3] HOWARD BECKER, HELMUT OHNMACHT. (1985) PTC Heating Elements-Background Analysis and Design Attributes. *Industry Applications* 21(4):896-898
- [4] YANG Peng, LIU Pin-jie, ZHANG Yan, LI Yong-fu. (2009) Improved Multivariable Predictive Control Based on RBF Networks. *Control Engineering of China*. 16(1):39-41,55
- [5] HUANG Jun-an, WANG Yue, LI Xiu-zhen. (2009) Neural network decoupling available to a multivariable control system. *Industrial Instrumentation & Automation* 11:11-14

MHD: A New Method towards Privacy Protecting Datasets Published

Fei Liu, Yan Jia and Weihong Han

School of Computer Science, National University of Defense Technology,
Changsha 410073, China
e-mail: 1986figo@163.com

Keywords: K-anonymity, Privacy Protection, Clustering, Hierarchical Diversity

Abstract: In this paper, we proposed a multi-hierarchical diversity algorithm MHD to prevent privacy disclosing in dataset. We proposed some definitions of multi-hierarchical diversity firstly. Sensitive values are partitioned into several classes. We ensured no proportion of class exceeding the threshold. We generalized some values of sensitive attribute to reduce information loss. Clustering method was used to lower data distort. Greed algorithm was used to lower time cost. We compared MHD with classic algorithms, ϵ -cloning and m-Invariance about Time Cost, Data Distort, Usability and Imbalance. Empirical results showed that our algorithm could protect privacy and publish datasets with high security and lower information loss.

Introduction

In modern society, large amounts of datasets are often published for statistical analysis and study, such as census, health, income surveys, employment, education and many other areas, while these data often contain a large number of privacy and sensitive information. In order to support legitimate research, data publishers need to release as much detail as the original datasets while preventing loss of privacy. With the development of network, personal data are often stored in distributed systems and published by different organizations independently. Publishers must prevent attackers to get sensitive information by associating different datasets. The risk of privacy disclosure motivated us to study an effective method.

Related Work Privacy preservation has received considerable attention from the database community in past years and k-anonymity [1] has been an effective method toward privacy protection of data publication. The method uses quasi-identify (QI) attributes to identify a person and these attributes are generalized or suppressed to shield sensitive information. Every tuple in dataset published are requested to be confused among at least k tuples. These k tuples own same values of QI attributes and form an equivalence class. Based on k-anonymity researchers have done a lot of improvement. L-diversity [2] requires that there are at least L different values of sensitive attribute in an equivalence class and no proportion of value exceeds limitation. t-closeness [3] requires that distribution of sensitive attribute values in each equivalence class is as close as that in the entire dataset. [4] did out-of-art research in publishing dynamic dataset with privacy protection. They proposed the concept of m-Invariance and the algorithm. It requested that signatures of different equivalence class containing the same tuple have to be coincident. [5] divided sensitive values into permanent value and transient value and gave a method to protect permanent value in serial of datasets. [6] focused on datasets published independently by different publishers. They found that there may be some overlapping tuples in these datasets which can be used by attackers. They proposed ϵ -clone algorithm and requested that there should be as much values of sensitive attribute as possible so that overlapping tuples can be associated with many sensitive values. Attackers would not get the specific sensitive value of the object. But the algorithm brings much data distortion and information loss.

Contributions We proposed the concept of Multi-Hierarchical Diversity and a new method named MHD to publish datasets while preventing privacy disclosure. Similar with ϵ -clone, all sensitive values contained by some dataset must appear in each equivalence class.

Table 1 Original dataset.

ID	Age	Gender	Birthplace	Disease
1	26	Male	Wisconsin	gastric cancer
2	44	Female	Minnesota	cancer of liver
3	32	Male	California	lung cancer
4	48	Male	Sweden	cancer of colon
5	39	Male	Arkansas	glycuresis
6	37	Female	Wisconsin	flu
7	33	Male	Arizona	skin cancer
8	77	Male	Virginia	flu

Table 2 Dataset published using 4-diversity.

ID	Age	Gender	Birthplace	Disease
1	1-50	unknown	U.S.A	gastric cancer
2	1-50	unknown	U.S.A	cancer of liver
3	1-50	unknown	U.S.A	lung cancer
4	1-50	unknown	U.S.A	flu
5	1-100	Male	unknown	glycuresis
6	1-100	Male	unknown	cancer of colon
7	1-100	Male	unknown	skin cancer
8	1-100	Male	unknown	flu

Table 3 Dataset published using MHD.

ID	Age	Gender	Birthplace	Disease
1	1-100	Male	U.S.A	unknown
2	1-100	Male	U.S.A	unknown
3	1-100	Male	U.S.A	cancer
4	1-100	Male	U.S.A	flu
5	1-50	unknown	unknown	unknown
6	1-50	unknown	unknown	unknown
7	1-50	unknown	unknown	cancer
8	1-50	unknown	unknown	flu

We found that diversity of sensitive values in an equivalence class was insufficient to protect privacy. If a kind of sensitive values occupied a large proportion in a equivalence class, attackers could exclude other values of sensitive values easily. To take Table 1 for an example, there are eight tuples with several sensitive values. Age, Gender and Birthplace are QI attributes and Disease is sensitive attribute. When published datasets are produced as shown in Table 2, no proportion of disease is larger than 1/4. Although the proportion of every sensitive value is consistent with 4-diversity, attackers can estimate in proportion 3/4 that the person in equivalence class 1 suffered cancer, a serious disease. That is because gastric cancer, cancer of the liver, and lung cancer are all cancers. In MHD (Table 3), sensitive values were assigned to several classes and no class could occupy too large or small proportion in equivalence classes and the problem described above could be solved successful.

Our Work

Basic Definitions We adopt definitions of k-anonymity and QI attributes introduced by L. Sweeney [1].

DEFINITION 1 (Class of sensitive values): AS is the sensitive attribute in dataset. All values of AS construct a hierarchical taxonomy tree. Each value is associated with a node in the tree. The more nodes are close in the tree; the similar values are with each other. Every sub-tree in the hierarchical taxonomy tree constructs a class of sensitive values. Root node of the hierarchical taxonomy tree belongs to no class. For example, as shown in Fig. 1, angina pectoris and coronary disease are two kinds of heart disease, so nodes associating with these diseases construct a sub-tree. They also construct the class of heart disease.

DEFINITION 2 (Hierarchic rank of class): The hierarchic rank of specific sensitive value is 1. The hierarchic rank of a class containing no other class is 2. For arbitrary class A, if the highest hierarchic rank of classes contained in A is i , the hierarchic rank of A is $i+1$. The rank of a node is the rank of class associating with the sub-tree whose root is the node. Root of the entire tree own the highest rank.

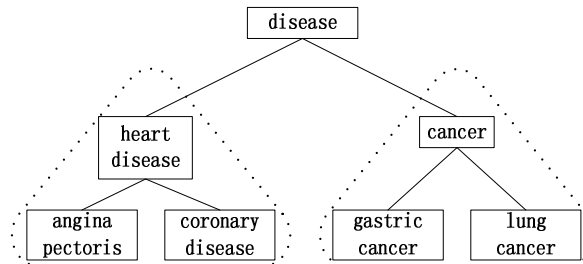


Fig. 1 Hierarchical taxonomy tree

DEFINITION 3 (H-hierarchical rank diversity): A dataset is H-hierarchical rank diversity when it meets following conditions: Supposing H is root's hierarchic rank and $i(1 < i < H)$ is the rank of class $Class_{ij}$ where j is the number of classes with rank i . Proportion of tuples whose sensitive values are contained in $Class_{ij}$ is no more than the upper bound $1/S_i$ and no less than the lower bound $1/L_i$ in the entire dataset. Proportion of tuples associated with every sensitive value is no more than the $1/S_1$ and no less than $1/L_1$ in the entire dataset.

DEFINITION 4 (2-hierarchical rank diversity): if $Class_{ij}$ is H-hierarchical rank diversity and $H=2$, $Class_{ij}$ is 2-hierarchical rank diversity.

DEFINITION 5 (Group of tuples): Tuples with same sensitive value construct a group.

DEFINITION 6 (Distance between values): Distance between to nodes in a hierarchical taxonomy tree is the sum of distances between each node to their nearest common ancestor. In an arbitrary hierarchical taxonomy tree about attribute A_i , distance between node p and its ancestor q is similar with its WHD (Weighted Hierarchical Distance) [4], which is described formally as:

$$WHD_{p,q} = \sum_{j=p}^{q-1} w_{i,j} / \sum_{j=p}^{h-1} w_{i,j} \quad (1)$$

Where h is the the root node and $p, p+1, \dots, q, q+1, \dots, h$ are nodes on the path from p to q in the tree. w_{ij} is the weight between node i and j , where node i is the father of node j in the tree. In order to displaying the importance of different nodes. We proposed an new WHD, whose w_{ij} is described as follows:

$$w_{i,j} = Son_i \quad (2)$$

Son_i is the amount of i 's sons. When node i has more sons, node j is more useful to distinguish tuples and generalization from j to i would cause more information loss. For example, as shown in Fig. 1, weight between "heart disease" and "disease" is 2 and weight between "angina pectoris" and "heart disease" is 2 too. So that WHD from "heart disease" to "heart disease" is $2/(2+2)=1/2$.

DEFINITION 7 (Distance between tuples): Distance between two tuples is the sum of distances in every attributes.

DEFINITION 8 (Information Loss/Data Distortion): The information loss or data distortion of a tuple t in generalization is the distance between t and t' , the tuple after generalization.

The information loss or data distortion of a dataset is the sum of all tuple's information loss or data distortion.

DEFINITION 9 (Data Usability): Data usability of a dataset is the precision of query operation, that is the range of tuples' amount with some specific sensitive values. For example, when we query the amount of people caught a cold, the result may be the range of $[\min, \max](\max \geq \min)$. Because of counterfeit tuples (m-Invariance and ϵ -clone) or sensitive values' generalization, we can't get a certain value but the range. \min/\max is the precision of query operation, that is the data usability.

DEFINITION 10 (Imbalance): Imbalance is the extent of tuples' proportion beyond the bounds. For specific sensitive value v , its Imbalance is as follows:

$$\text{Imbalance}_{v_i} = R'_{v_i} / (1/S_i - 1/L_i) \quad (3)$$

Supposing R_{v_i} is the proportion of tuple with value v_i , $R'_{v_i} = R_{v_i} - 1/S_i$ if $R_{v_i} > 1/S_i$, otherwise $R'_{v_i} = 1/L_i - R_{v_i}$ if $R_{v_i} < 1/L_i$.

For class Class_{ij} , its Imbalance is as follows:

$$\text{Imbalance}_{\text{Class}_{ij}} = R'_{\text{Class}_{ij}} / (1/S_i - 1/L_i) \quad (4)$$

Imbalance of the entire dataset is the sum of all specific values and classes' Imbalance.

Publication of Dataset Keeping Privacy In MHD algorithm, hierarchical taxonomy tree of every attribute need to be constructed first. For categorical attributes every node in the tree is corresponding to a specific value. Node of numerical attribute is corresponding to a specific or range of value.

Based on the hierarchical taxonomy tree, we researched 2-hierarchical rank diversity of dataset publication. Every equivalence class contains all sensitive values and the proportion of every value in a equivalence class is equal to that in the entire dataset. Attackers would difficultly estimate sensitive value of the object associating a series of independent datasets.

So we smooth the proportion of values in datasets. If the proportion is lower than the low bound, we generalize the value and combine it with other values. If the proportion is upper than the up bound, we detach some tuples and generalize the value to a new value or combine it with other one. In order to lower information loss, the value would be attempted to be generalized to its nearest ancestor in the tree first.

As smoothing specific sensitive values, we also smooth the class of sensitive value to make the proportion of every class in the range predefined. If there are too many tuples with same sensitive value in a class, some values near should be generalized to the value of root.

Every tuple in a dataset should be assigned to a unique equivalence class. Amount of equivalence classes is equal to the smallest size of the tuples' groups corresponding to different sensitive values. Every tuple is assigned to a group uniformly. In order to make tuples similar with each other in QI attributes be assigned to the same equivalence class and lower information loss, we use cluster algorithm in MHD.

Details of MHD Algorithm Step 1, construct groups of tuples. Tuples with same sensitive value compose a group G_i , where i is the number of group. Each group is corresponding to a sensitive value and associating with a node in the hierarchical taxonomy tree. These concepts are often equivalent in this paper. The size of G_i is $\text{size}(G_i)$. Their sizes are arranged in ascending order.

Step 2, smooth sensitive value of groups whose size is smaller than the low bound. We check the size of every group whether it is in the range of $[1/L_1, 1/S_1]$, where $S_1 < L_1$. Size of the entire dataset is M . Groups smaller than M/L_1 should be generalized and merged with other group. Suppose the smallest group is a , $\text{size}(a) < M/L_1$, b is the nearest group in the tree.

If b is the ancestor of a , sensitive value of a is generalized to b 's sensitive value and tuples of a is merged into b ; If b is not the ancestor of a and $\text{size}(b) + \text{size}(a) \geq 2M/L_1$, several tuples are token randomly to compose b' , a temporal group. c is the nearest common ancestor of a and b . b' and a are generalized and compose group c' . If c is existing, c' is merged with c , else c' is renamed as c ; If b is not the ancestor of a and $\text{size}(b) + \text{size}(a) < 2M/L_1$, a and b are generalized and compose group c' . If c is existing, c' is merged with c , else c' is renamed as c . This is reasonable as following reasons: $\text{Size}(b)$ is lower than M/L_1 , if $\text{size}(b) + \text{size}(a) < M/L_1$, and b should be generalized; If $\text{size}(b) + \text{size}(a) \geq M/L_1$ and $\text{size}(b) - \text{size}(b') < M/L_1$, $b - b'$ should also be generalized. If b doesn't exist, a is generalized to General, the sensitive value associating with root of the tree. All a 's neighbor checked must be in the same sub-tree with a and neighbors whose common ancestor's rank is small should be checked in priority.

New groups composed are inserted into the queue of groups in ascending order and groups without tuple are removed from the queue. This step is executed iteratively until no group is smaller than M/L_1 .

Step 3, smooth sensitive value of groups whose size is larger than the up bound. Supposing size of the smallest group is M_{\min} after step1, up bound of groups' size is set as: $M_{\max} = y * M_{\min}$, where $y * M_{\min} \leq M/S_1$ and $(y+1) * M_{\min} > M/S_1$. y is a positive integer. For arbitrary group d , where $(x-1) * M_{\min} \leq \text{size}(d) < x * M_{\min}$ and $x > 1$, group e_1 is corresponding to d 's father node in the tree. Additional tuples of d are generalized and merged into e_1 .

Additional tuples of d can be described as follows:

On condition that $\text{size}(d) > M_{\max}$, size of additional tuples is $\text{size}(d) - M_{\max}$;

On condition that $M_{\min} \leq \text{size}(d) < M_{\max}$ and $x_1 * M_{\min} < \text{size}(d) < (x_1+1) * M_{\min}$, where x_1 is integer. Scale of additional tuples is $\text{size}(d) - x_1 * M_{\min}$;

Z is the sum of e_1 's sons' amount. When $z < M_{\min}$, e_1 is generalized to its father. All groups are processed from bottom to top in the tree. After process in this step, size of every group is a whole-number multiple of that of the smallest one. That's convenient for steps later.

Step 4, diversity of classes. Classes of sensitive value should be diversified. Proportion of every class can't be beyond $[M/L_2, M/S_2]$, M/L_2 is the low bound and M/S_2 is the up bound. For arbitrary class of sensitive value $Class_i$:

$$\text{size}(Class_i) = \sum_{j=1}^{n_i} \text{size}(Group_j) \quad (5)$$

$Group_j$ is the group whose sensitive value are contained by $Class_i$. n_i is the amount of groups and j is the index.

If $\text{size}(Class_i) < M/L_2$, tuples' sensitive value in all groups associating with $Class_i$ are generalized to General.

If $\text{size}(Class_i) > M/S_2$, sensitive value of tuples in group a is generalized to General. a is the group corresponding to the root of sub-tree in $Class_i$ (Definition 1). If $\text{size}(a) = 0$, all groups corresponding to its sons are generalized one by one until $\text{size}(Class_i) \leq M/S_2$. The order in which these groups are generalized is as follows:

If there exist several groups $b_j (1 < j < N_a, N_a$ is no more than the amount of a 's sons), where $\text{size}(b_j) \geq M/S_2 - \text{size}(Class_i)$, $\text{size}(Class_i) - \text{size}(b_j) \geq M/L_2$ and $\text{size}(b_k) = \min \{ \text{size}(b_j) (1 < j < N_a) \}$, b_k is generalized; if there exist no group meeting condition above, all groups in the sub-tree are generalized.

As shown in Fig. 1, if scale of class Cancer is larger than M/S_2 , tuples in node "cancer" have to be generalized. If there is no tuple in node "cancer", nodes "gastric cancer" and "lung cancer" are checked with the rules above.

Step 5, decide the amount of equivalence class. Supposing g_1 is the smallest group, $\text{size}(g_1)$ is the amount of equivalence class. For arbitrary group g_i , $\text{size}(g_i)/\text{size}(g_1)$ tuples are assigned to every equivalence class. Size of every equivalence class is $M/\text{size}(g_1)$. If $\text{size}(g_1) < k$ (according to k -anonymity), two equivalence class would be merged

Step 6, clustering. Tuples in a group are partitioned into N_c clusters using k -means algorithm. Distance between tuples is based on Definition 7.

Step 7, assignment. N_c is the amount of clusters in a group produced in step 6. A cluster is represented by its center. Supposing N_g is the amount of groups. An equivalence class is composed by N_g sets of data coming from different groups. Target of this step is to assure that equivalence classes are produced with lowest information loss. MHD provides two methods. Method 1: checking all combinations of clusters from different groups and compute total information loss; Method 2: Clusters are assigned to equivalence classes based on greed algorithm. For arbitrary cluster C_i , it's attempted to be assigned to every equivalence class to calculate information loss one by one and chosen the assignment with lowest loss. Equivalence class has own tuples in the group would not be checked. Supposing S_c is the amount of tuples a equivalence class need. If size of a cluster is S_i , where $S_i > S_c$, S_c tuples would be token randomly to be assigned to a equivalence class. If $S_i < S_c$, $S_c - S_i$ tuples would be token from other clusters later.

Step 8, recoding. QI attributes are generalized in every equivalence class.

Experiments

We perform experiments on real dataset OCC9. Each data set contains 600K tuples from American census data. OCC data set has a sensitive attribute Occupation, in addition to four QI attributes, Age, Gender, Education and Birthplace. All attribute values are discrete. We used part of the dataset in our experiments. 2-hierarchical rank diversity is used to restrict the dataset published. Values of Occupation are partitioned into 26 classes. We designed three experiments to test MHD's performance.

In experiments 1 and 2, we did our experiments on a Core(TM)2 duo computer with two 2.66 GHz processors and 1.98 GB RAM running Windows XP. We test the infection of parameters in MHD. In experiment 3, we did our experiments in one node of TH-1A supercomputer with 12 2.93 GHz Intel(R) Xeon(R) processors and 12 4096MB RAM running Kylin OS. We compared MHD with ϵ -cloning and m-Invariance. Time cost, information loss, data usability and imbalance are evaluated. Some parameters are changed to get sets of experiments results.

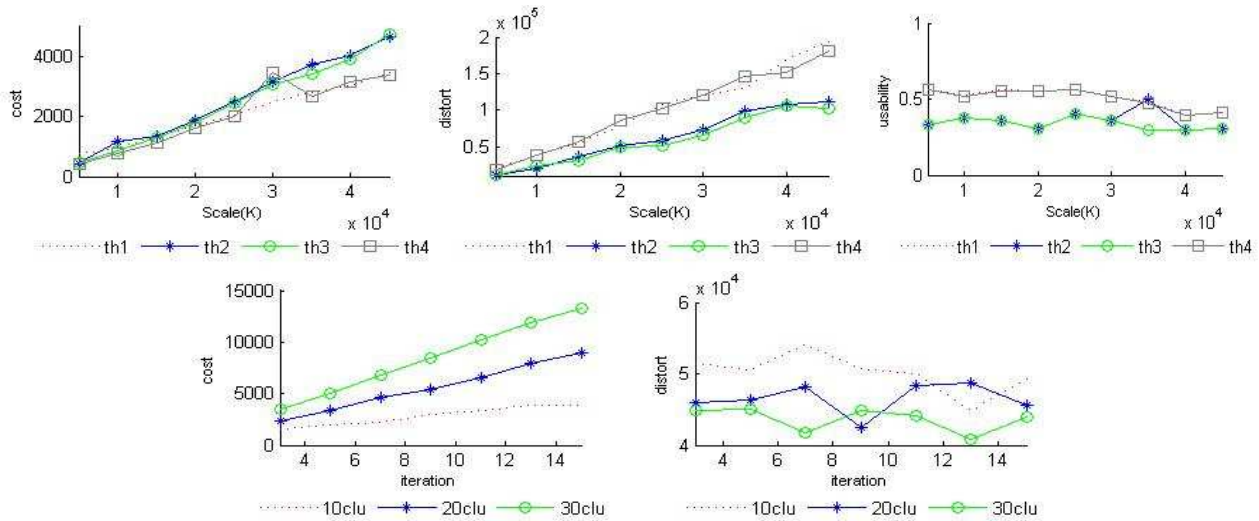
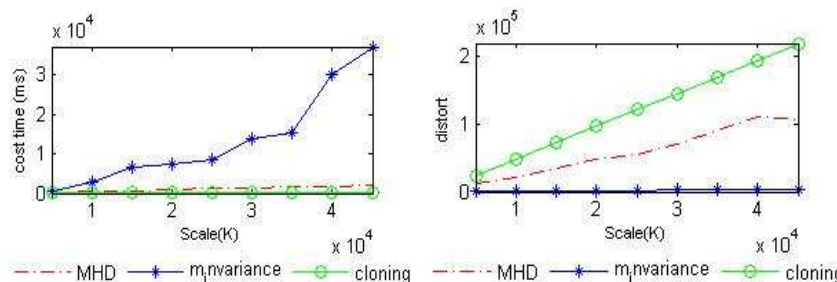


Fig. 2 Cost (1st Fig.), distort (2nd Fig.) and usability (3rd Fig.) of MHD with different dataset scales; cost(4th Fig.) and distort(5th Fig.) of MHD with different times of iterations.

Experiment 1. Thresholds $\{1/L_1, 1/S_1, 1/L_2, 1/S_2\}$ were changed to test the performance of MHD. Greet algorithm is used in clustering stage. The amount of clusters N_c was set to be 10 and iteration times in k-means N_i was set to be 5. Four sets of thresholds: $\{0.01, 0.2, 0.2, 0.7\}$, $\{0.1, 0.3, 0.2, 0.7\}$, $\{0.1, 0.3, 0.3, 0.8\}$, $\{0.01, 0.2, 0.3, 0.8\}$ were compared in time cost, data distort and usability. Size of datasets improved from 5000 to 45000. Result of experiments was described in Fig. 2 (1st, 2nd, 3rd Fig.). We can find that less clusters means less time cost but the effect is weak. Distort and usability of dataset was affected by threshold of specific sensitive value. As shown in Fig. 2(1st, 2nd Fig.), thresholds 1 and 4 brought less distort.

Experiment 2. N_c were changed to test the performance of MHD. $\{1/L_1, 1/S_1, 1/L_2, 1/S_2\}$ was set to be $\{0.1, 0.3, 0.2, 0.7\}$ and N_i changed from 3 to 15 with interval 2. Result of experiments was described in Fig. 2(4th, 5th Fig.). MHDs using 10, 20 and 30 clusters were compared. Fewer clusters caused less time cost

and curves of cost were stable. In Fig. 2 (5th Fig.), MHD with less clusters caused more data distort or information loss, but curves were fluctuant. That is affected by the distribution of dataset.



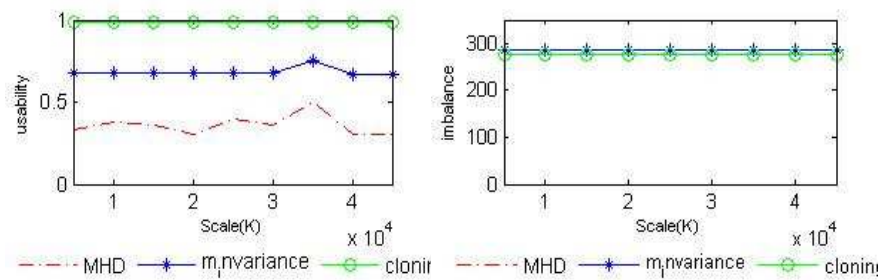


Fig. 3 Cost(1st Fig.), distort(2nd Fig.), usability (3rd Fig.) and imbalance(4th Fig.) of different algorithms

Experiment 3. Thresholds were set to be $\{0.3, 0.1, 0.7, 0.2\}$. Different size of samples are used to compare the performance of MHD, ϵ -cloning and m-Invariance. Dataset produced by MHD was the source of m-Invariance and new tuples are inserted. Parameter m is set to be 4 in m-Invariance. As shown in Fig. 3(1st Fig.), both MHD and ϵ -cloning cost much less time than 4-Invariance. With the growth of datasets' size, cost of 4-Invariance increased sharply, but increment of cost in MHD and ϵ -cloning were steadily. In data distort, shown in Fig. 3(2nd Fig.), ϵ -cloning was the worst one, m-Invariance was the best one and MHD was in the middle. In MHD algorithm, some sensitive values were generalized and more equivalence classes were constructed and small equivalence classes mean little distort. In usability comparing, ϵ -cloning was almost full marks and m-Invariance performed better than MHD. Curves in Fig. 3(3rd Fig.) showed that usability of algorithms are irrelative with sizes of datasets. In Fig. 3(4th Fig.), we can find that the imbalance of m-Invariance and ϵ -cloning are stable and hard to distinguish, but the imbalance of MHD is 0.

Acknowledgment

This work was supported by 863, The National High Technology Research and Development Program of China, 2011AA010702.

References

- [1] Sweeney, 2002, L. k-anonymity: a model for protecting privacy. *Int. J. Uncertain. Fuzziness and Knowledge-based Systems*. 10(5), (2002) 557-570.
- [2] Machanavajjhala, A., Kifer, D., Gehrke, J., Venkatasubramanian, M. 2006, L-diversity: Privacy beyond k-anonymity. *ICDE (2006)* 24-24.
- [3] Li, N, Li, T, Venkatasubramanian, S. 2007, t-closeness: Privacy beyond k-anonymity and L-diversity. *ICDE, (2007)* 106-115.
- [4] Xiaokui Xiao, Yufei Tao. 2007, m-Invariance: Towards Privacy Preserving Re-publication of Dynamic Datasets. *SIGMOD(2007)* 689-700.
- [5] Yingyi Bu, Ada Wai-Chee Fu, Raymond Chi-Wing Wong, Lei Chen, Jiuyong Li. 2008, Privacy Preserving Serial Data Publishing By Role Composition. *VLDB (2008)* 1:845-856.
- [6] Muzammil M. Baig, Jiuyong Li, Jixue Liu, Hua Wang. 2011, Cloning for Privacy Protection in Multiple Independent Data Publications. *CIKM(2011)* 885-894.
- [7] <http://ipums.org>. 2010, Steven Ruggles, J. Trent Alexander, Katie Genadek, Ronald Goeken, Matthew B. Schroeder, and Matthew Sobek integrated public use microdata series: Version 5.0. Minneapolis: University of Minnesota, 2010.

Simulation of Large Amount of Data Liquid-solid Coupling based on the SPH

Fang Hao^{1,2}, Zhang Lei², Liu Yan², Sun Shibo²

¹. National Engineering Research Center for Multimedia Software Computer School, Wuhan University, Wuhan, 430072, China

². School of Art and Communication China University of Geosciences, Wuhan, 430074, China

Keywords: SPH; Large Amount of Data; Liquid-Solid Coupling; Visual Simulation

Abstract. The visual simulation of large volumes of liquid-solid coupling According to the analysis of the form and movement, design an improved and simplified algorithm method based on the previous SPH aims to rapidly simulate out the interactive visual effect between the large volumes of solid and incompressible fluid.

Introduction

Fluid Simulation in computer has experienced from modeling method based on the parameter to the change of physical method [1], simulation realism has greatly improved in the form of fluid and the movement.

In 1987, Barzel began to put in the fluid simulation method based on the physical model, this method has received wide attention from then on . Method based on physical also developed very rapidly, many new methods turned up, such as monte carlo method, a molecular dynamic method simulating the fluid at molecular level,as well as the lead before moving to, reverse flow algorithm and BFECC method derived by Navier-Stokes equation .The basic idea is the fluid movement constrained by physical laws, therefore the physical reality degrees has greatly increased in fluid forms and movement, this method is particularly popular in the application in visual simulation.

Liquid-Solid Coupling

Liquid-Solid Coupling Definition

Liquid-solid coupling problem mainly study the interaction between the fluid solid: the mutual coupling and influence between solid and fluid. A lot of research simplified the process: one kind is the movement of known solid, and the movement is not affected by fluid impact, using the solid movement to change fluid motion state; Another case is the influences of fluid to the movement of solid, that is, in the function of fluid ,solid motion state change but fluid movement is away from solid influence. But, considering that only one-way function can not represent the performance of real liquid-solid coupling movement, so that we need to study both the various kinds of behavior in the fluid of solid and also need to consider the influence of solid exercise on fluid.

The two phase media interaction is an important feature of liquid-solid coupling: solid in fluid load will generate distortion or sports, and deformation or sports and in turn affect flow field and change the distribution of flow load, it is this interaction will be in different conditions of different color produced form liquid-solid coupling phenomenon.

Liquid-Solid Coupling Simulation Method

Liquid-solid coupling has diverse performances; the researchers use a variety of method to simulate the problem. According to degree of simplification, there are two-way coupling and one-way coupling [3]. According to the numerical discrete method [5] classification, there are three: the first kind of method is boundary with law, the fluid of fluid-solid coupling area can use the finite volume, the finite difference method, and solid area is using the finite element method for the discrete. The second method is with boundary method, this method does not require fluid and solid grid with the grid, and therefore do not need any update on fluid grid work, is suitable for

simulation of fluid-solid coupling with large deformation or distortion on interface. The third type of method is meshless method, do not need to use unit or grid to a variable interpolation, also do not need to describe the relationship between nodes, such spares in fluid and solid areas are areas of different types of grid and boundary of want to cooperate with the fluid and solid boundary grid of trouble, but large amount of calculation.

Analysis of Large Amount of Data Liquid-Solid Coupling

Large amount of data liquid-solid coupling is mainly similar to the debris flow. For the simulation of visual signs, the significant part is to simulate the movements of numerous rigid bodies in fluid. The two-way function between rigid body and fluid is needed to be considered. That is, the rigid body and the fluid can affect each other through the power of the colliding. In addition, the mutual colliding of rigid body is another point worthy of being considered.

In the simulation of liquid-solid coupling, when fluid is faced by external power, its internal motion will happen, which is different from the rigid body that can keep rigidity between each other. Fluid, under its own internal movement, can also produce a torque for rigid body so that the rigid body rolls inside the fluid, and rigid body's own movement makes the reaction of fluid again, which can interfere the original direction of fluid's movements. As for large volumes of fluid-solid coupling, what's need to do is to seek for an appropriate method in order to deal with the interaction between rigid body and fluid, a method needs to quickly determine the position of the fluid and rigid body.

The Large Volume of Data Flow Solid Coupling Simplified Algorithm

SPH Method

The most accurate method to describe the fluid motion is Navier-Stokes equation, the Navier-Stokes equations derived the fluid calculation of Euler method and Lagrange method. SPH method is developed based on Lagrange method, called the smooth particles fluid dynamics method [6], this method [7] is through a called "nuclear function" integral nuclear for "nuclear function valuations" approximation, convert the basic equations of fluid mechanics to numerical calculation equation of SPH. The whole flow field discrete into a series of "particle", all mechanical loaded by these particles, the particle can arbitrarily flow according to fluid mechanics.

In SPH method, arbitrary macro parameters (density, pressure, velocity, internal energy, etc.) $A(r)$ all can achieve through the calculation in the domain integral interpolation. Integral interpolation use similar δ delta function kernel function of inner product to realize.

$$A(r) = \int_D A(r') W(r-r', h) dr' \quad (1)$$

Type: D-the whole solving area; R-a particle position vector radius; H-is the particle smooth length; W-interpolation nuclear, it is an interpolation kernel function has the nature of a delta function.

The numerical integral can put on the written form of the following:

$$A(r) = \sum_{j=1}^N \frac{A_j}{\rho_j} W(r-r_j, h) \quad (2)$$

$$\nabla A(r) = \sum_{j=1}^N \frac{A_j}{\rho_j} \nabla W(r-r_j, h)$$

The Large Volume of Data Simplification Process Analysis

For the visual simulation of fluid-solid coupling, it's more important to determine the position of rigid than to determine its self-movement, because in the fluid-solid coupling, the position of rigid body changes more noticeable than their own rotation, and human's visions are more sensitive to it.

In fluid-solid coupling, when numerous rigid body and fluid interact, the most difficult thing is to quickly determine the position of rigid body. As for the interaction between few rigid bodies and fluid, using the above method can get better results, but when the rigid number rises to a larger number of levels, it's essential to find out a quick way to determine the position of plenty of rigid bodies.

The SPH method provides such a possibility. SPH method is completely based on Meshfree particle method. Consider the fluid as a particle composition, and as for a large number of rigid bodies, we consider them as a particle macroscopically. From the characteristics of large amount of data, particle is simplified into rigid particle and fluid particle with same size, which can quickly calculate the change of position of rigid body. Figure 1 shows the distribution of particles in space grid diagram, dark particles represent rigid, light particles represent fluid.

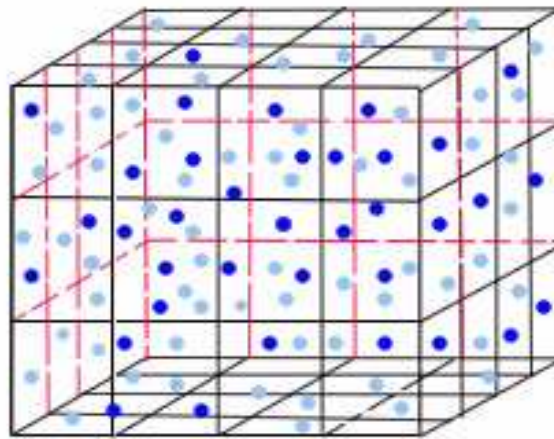


Fig. 1 The distribution of particles in space grid diagram

Algorithm Design and Results

According to the above analysis, in SPH method, define the rigid body particles for R, fluid particles for F, the position of these particles are given an initial value, rigid body particle R and fluid particles F use the same kernel function, unified smooth nuclear radius h , every particle has a mass m , density ρ , pressure p , position ρx , speed u attribute.

The update of the particle state (speed, position, etc) is the key to describe liquid-solid coupling. In SPH method, rigid body particle R and fluid particles F follow Lagrange fluid control equation:

$$\rho \frac{D}{D_t} u = -\nabla p + \mu \nabla^2 u + \rho g \quad (3)$$

Among them, u represent the speed of the particle, ρ for the density, p represents pressure on particles, g means unit quality force of particles in the direction of gravity, μ means viscosity coefficient. If we take the expression on the right side as the resultant force of the particles i , the expression above degenerate the Newton's second law of motion.

$$a_i = \frac{D u_i}{D_t} = \frac{f_i}{\rho_i} \quad (4)$$

Among them, the f_i, a_i, p_i, ρ_i respectively represent particles' total force, acceleration, pressure and density. The resultant force of particles include the pressure I, gravity, and viscous force, according to the kernel function interpolation and SPH discrete particle formula I by the force of particles, such as the following formula.

$$\begin{aligned}
 f_i &= f_i^{pressure} + f_i^{viscosity} + f_i^{gravit} \\
 f_i^{pressure} &= -\nabla p_i = \sum_{j=1}^N m_j \frac{(p_i + p_j)}{2\rho_j} \nabla W(x_i - x_j, h) \\
 f_i^{viscosity} &= \mu \nabla^2 u_i = -\mu \sum_{j=1}^N m_j \frac{(u_j - u_i)}{\rho_j} \nabla^2 W(x_i - x_j, h) \\
 f_i^{gravit} &= \rho_i g = g \sum_{j=1}^N m_j W(x_i - x_j, h)
 \end{aligned} \tag{5}$$

The formula above, the force gR per unit mass of rigid particles R on the direction of gravity is different from fluid particles F , rigid body particle R viscosity coefficient μR and fluid particles F viscosity coefficient μF is not the same also, rigid body particles with fluid particles F R in force under the action of f_i happening position and speed change, thus gain large volumes of liquid-solid coupling fast calculation results, the experiment results are shown below:

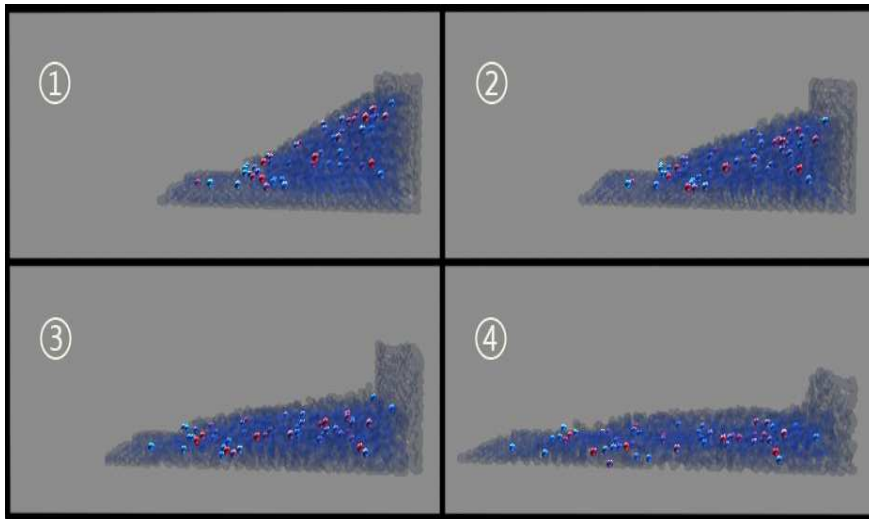


Fig. 2 The result of this experiment

Summary and Outlook

This article makes the analysis of the simulation of large volumes of liquid-solid coupling, and studies how to use the SPH method to design data quantity liquid-solid coupling simplified algorithm. The experimental results show that the algorithm can be based on the interaction between rigid body and fluid to rapidly determine the position of massive fluid and rigid body. The next step can be more accurate depth of debris flow simulation in the interaction of rigid body and fluid movement, especially consider importing the stress analysis of rigid body rotation in order to have a better simulation towards the visual effect of liquid-solid coupling.

Acknowledgments

This research is supported by the project of “Graduate’s Fund of training mode and educational reform of CUG (No. CUGYCX0811)”, and the project of “Excellent Young Teachers’ Characteristic Discipline Group of Central Government University Basic Scientific Research-related Subsidy Special Fund (No. CUG090115)”.

References

- [1] Peachey Darwyn R1 Modeling waves and surf [J]1 ComputerGraphics,1986 , 20 (4) ,pp.65~74
- [2] Lihua Cao,Xiaodan, Liu, XiaoPeng Sun, Based on Newton-the euler equations solid-liquid coupling simulation Computer Engineering and Applications 2008,44(31) ,pp. 208-209.
- [3] Metropolis, N.et al. ,J. Chem. Phys.,21(1953),1087.
- [4] Alder, B.J. and Wainwright,T.E, J.Chem Phys., 27(1957),1208.
- [5] Matthias H. An efficient solver for the fully coupled solution of large-displacement,fluid-structure.interaction.Problems[J].Computer.methods.in.applied.mechanics.and.Engineering,2004,193(1),pp,1-23.
- [6] Jose S,Antonio H. Jean D.Arbitray Lagrangian-Eulerian formulation for fluid-rigid body interaction [J].Computer Methods in Applied Mechanic and Engineering,2001,190,pp,(24-25).
- [7] Suochun Zhang , Smoothed Particle Hydrodynamics(SPH) [J] Computational Physics 1996, 13 (4) ,pp, 385-397

A Study on Component Composition Technology Based on XCM

Yuan-Yong LIU

Normal College of Technology, Chongqing University of Arts and Sciences, Chongqing 402160
China

yuanyongliu@cscssi.info

Keywords: Software Reuse, Component Description, Component Composition

Abstract. Component description and component composition are one of key technology of CBSD and software reuse. At present the different components depend on different component description model, which determines how to construct a single component and specific interaction and component assembly standards, and to generate interactive problems limiting component composition. The paper presents a model of component composition based on XCM, which to define components from the component selection and instantiate and to describe the connections from the component interface and to provide a mechanism of component composition from the components of the event and based on the deployment of the container. The XCM component composition model not only provides a unified description mechanism, also effectively solves the interaction problems.

Introduction

With the development of software reuse and component technology, the Component Composition Structure based on XCM (CBSD) has become one of the main methods for software development (1). The component composition software, as the core and key, has been a major research point (2). Under the network computing environment, the component composition technology should consider components that are trans-regional, long-time and heterogeneous. Different components rely on different component mode. From the perspective of assembling, the interactivity problem made by different component modes has restricted the component composition (3) (4). This paper assumes that XML is popularly accepted as the component description system. It brings out a Component ontology Model based on XCM (5) (6). XCM component model offers standards for the complex component composition from different component models according to the attribute of components, description of event and methods and reflection on components in preparation stage as well as self-examination system needed by their composition. In this way, it can effectively lower the incompatibility problem caused by component composition of different component models.

Component composition

Component model and feasibility of XML description Component model is the core content for component technology and the abstract description of component essence characteristic. Component description can be extended as a description tree, while XML has tree structure feature and good standardization, making it the best choice of component model (13)

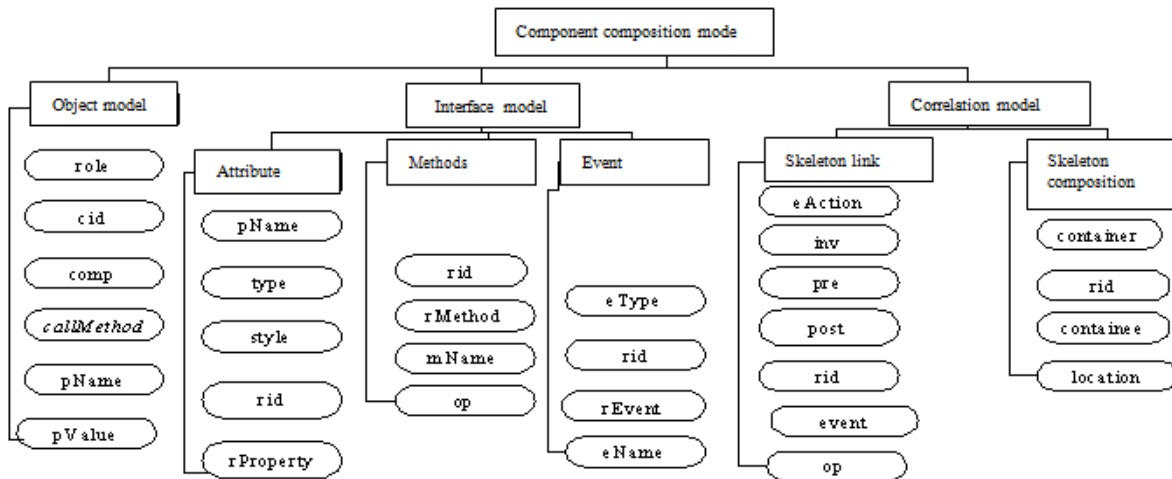


Fig.1 The Component Composition Structure based on XCM

Therefore, apply XML to describe the component model based on XCM. This can make easier different individuals and different software have agreement on the information structure exchanged on the Internet. At the same time, compared to the other component descriptions, its description to component bases on component and can make reflections on component codes through automatic tools (7) (8). On the other hand, it gets rid of the differences for different component models.

Component model based on XCM Component model based on XCM relies on the formal specifications of 3C component description model. It specifies the formal description of component into ternary codes (9). That is:

ComponentDefinition := {<ComInfo>, <Features>, <Design >}

Among it, ComInfo description is the basic information part of component; Features describe the attribute values interface, methods interface, event interface; Design represents whether the component is complex component and its composition manner. As atomic module, the value of Design is null.

Component assembling description tree

According to the component model based on XCM and the key points in assembling stage, this paper establishes an assembling model from the perspectives of attribute, methods, and event and design mode (10).

Object model: Object model specifies basic information of component through role, comp, cid, configuration, pName, pIndex, pValue, etc.

Interface model: Interface model is the standard of interfaces in complex component or application program. From the current component model, interfaces are represented through a group of attributes, event and methods.

Properties: Properties often care for name, writing types and styles. The attribute types in interface model (readWrite or readOnly) and the style (simple or indexed or bound) can support any language.

Events: Monitoring and service cares for the name and types of event. eName is the name and offers package. The area of Type is multiCast or uniCast. The current event types are mainly multiCast and uniCast.

Methods: mBinding appoints binding one or more components through the mbCompInstance method by mName. For two or more assembling, it is assembled through op. This is defined through sMethod.

Correlation model:

Assembling faced linkage

Constraint linked between event and monitor is divided into inv and contracts.

Assembling based on composition

Correlation model based on composition offers popular container to manage construction of components.

Component Assembly Practice Based on XCM

Design of component assembly system Component assembly model is a united component model. When the researchers and developers make component assembly, they determine the production of specific case (12).

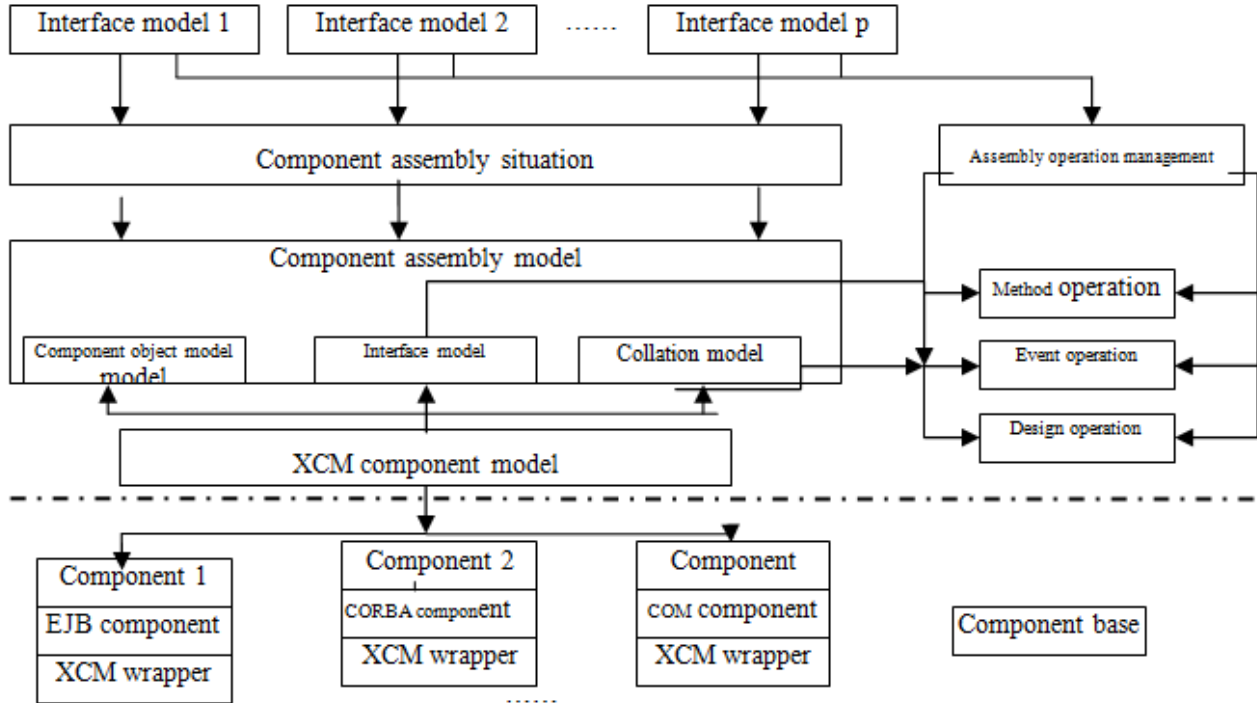


Fig.2 The Component Composition Frame

Practice of component assembly technology This is the real case for part of the sub-system in assembly technology based on XCM, which is applied in the electronic government affairs system by the city.

Design of component interface

Reasonable design for the interfaces can get rid of problems existed in frame and component stage (14).

Assembly of components

In the component assembling process, the system defines a component assembling description text based on XCM model. Part of the description text is shown as Fig.3.

In it:

Node ego web: root node;

Node components-mapping: record the corresponding relationship between component and service methods;

Node component: Allocate registered components; the attribute is as the followings:

Cid: component identification;

Type: class type reflected by the component;

Description: function description;

```

<Ego web>
  <Components-mapping>
    <component cid="" type="" description="">
      <property pid="" description="" sjlx="" czlx="" isalert="" type="" />
      .....
      <method mid="" description="" xtgn="" czlx="" isalert="" type="" >
        <returnType sjlx="" description="" />
        <paraNums num="" paraType="" />
      </method>
      .....
    </ Component >
    .....
  </ components-mapping>
<errornumlist>
<error number=""></error>
</errornumlist>
</egovweb>

```

Fig.3 Component Configuration Corresponding to Application-config.xml

Node property allocates the attribute interface offered externally by component

```

.....
<component cid="Fwnwgl" type="com.egov.gwgl.fwdj.FwdjBP" description="management">
  <method mid="addFwdj" description="success" xtgn="writing" czlx="newly add" isalert="YES"
type="addFwdj" >
  <returnType sjlx="void" />
  <paraNums num="10" paraType="string,string,string,string,string,string... " />
  </method>
  <method mid="addGztz" description="register success" xtgn="notice to register" czlx="newly add"
isalert="YES" type="addFwdj" >
  <returnType sjlx="void" />
  <paraNums num="3" paraType="string,string,string" />
  .....
</component >
<component cid="DadjBP" type="com.egov.gwgl.fwdj.DadjBP" description="document files">
  <method mid="add" description="register success" xtgn="document registration" czlx="新增" isalert="YES"
type="addDaxx" />

```

Fig.4 Component Configuration Section about dispatch management

Conclusion

The application of component composition technology can be seen everywhere in practical projects. Of course this kind of application is still basically the application with the handwork way. This paper sets forth in the component automatic assembling tool (15). It elaborates the basic function that a basic component assembling tool should be equipped with. In addition, it gives a framework about the component assembling tool. Proceeding to the next step, it elaborates the component assembling methods that is used by the electronic government affairs system for certain government. Moreover, it makes elaboration on the component assembling technology and its application in practical project development.

References

- [1] Yang Fu-qing, Mei Hong, Li Ke-qin. Software Reuse and Software Component Technology. ACTA ELECTRONICA SINICA. Vol.27 No.2 Feb.1999:68-75.
- [2] Yang Fu-qing, etc. Software Reuse. Journal of Software. Vol.6 No. 9 Sep.1995:525-533.
- [3] WU Qiong. Component composition software study: academic dissertation. Beijing: Peking University Doctoral dissertation, 1998.
- [4] Mili H.,Mili F.&Mili A.,Recusing. Software: Issues and Research Directions, IEEE Transaction on Software Engineering, 1995,Vol.21,No.6:528-562.

- [5] Franz Achermann. Forms, Agents and Channels - Defining Composition Abstraction with Style. PhD thesis, University of Bern, Institute of Computer Science and Applied Mathematics, January 2002.
- [6] Dietrich Birngruber. CoML: Yet Another, But Simple Component Composition Language. In Workshop on Composition Language, 2001.
- [7] Franz Achermann, Markus Lumpe, Jean-Guy Schneider, and Oscar Nierstrasz. Piccola – a Small Composition Language. In Howard Bowman and John Derrick, editors, Formal Methods for Distributed Processing – A Survey of Object-Oriented Approaches, p403-426. Cambridge University Press, 2001.
- [8] Dietrich Birngruber. CoML:Yet Another,But Simple Component Composition Language[C]. In:2001 WorkShop on Composition Languages (WCL 2001) ,2001:11-24
- [9] Brown A, Wallnau K. 1996.Engineering of Component-Bases systems in Component Based Software Engineering. Software Engineering Institute, IEEE Computer Society:37-47.
- [10]M. R. Wgder and I. Dean. An architectural approach to building systems from COTS software components. In
- [11]Sanjiva Weerawarana, Francisco Curbera, Matthew J. Duftler, David A. Epstein, Joseph Kesselman. Bean Markup Language: A Composition Language for JavaBeans Components. In Proceedings of the 6th USENIX Conference on Object-Oriented Technology System (COOTS
- [12]U. Zdun. A pattern language for the design of aspect languages and aspect composition frameworks. Draft; accepted for publication in IEE Proceedings Software, special issue on Unanticipated Software Evolution, 2004.
- [13]Gan Guohua, Sun Changsong, Deng Liyan. A Component Composition Description Language Based on XML. Proceedings of the International Workshop on Modern Science and Technology Kitami, Japan, September 2004.
- [14]ZHANG Shi-kun, ZHANG Wen-juan, CHANG Xin, WANG Li-fu, YANG Fu-qing. Building and .Assembling Reusable Components Based on Software Architecture. Journal of Software.2001, 12(9): 1351-1359.
- [15]MEI Hong, CHEN Feng, FENG Yao-dong. ABC: An architecture based, component oriented approach to software development[J]. Journal of Software, 2003 ,14(4) :721-732.

Based on OLAP Realize Real-time Integrated Analysis of the Underground Metal Mines Cost Information

Guo Jun¹, Gan De-qing², Tan Jing¹ and Yao Xu-long³

¹ Qing gong College, Hebei United University, 063000, China

² Hebei United University, 063000, China

³ University of Science and Technology Beijing, 100083, China

E-mail: 15303156333@189.cn,gdqheut@163.com,hblgdxtj@126.com

Keywords: Metal Mines, Cost Information, OLAP, Multidimensional Data

Abstract: Through OLAP technology study and solve the data issues during the real-time integrated of cost information process. Using OLAP technology does classified and sequenced analyses on mines production cost multi-dimensionally and multi-angle computationally. It is carried the deep study that the application of OLAP theory and technology in underground metal mines cost analysis field, and meanwhile the relative OLAP modeling is put forward.

Introduction

With the construction of domestic digital mines, some metal mining enterprises have formed a series of information management system, data collection system and the corresponding industrial control system. Such as energy measurement information management system, equipment information management system, production information management system, financial management system, human resource management system, underground various automatic control and information collection system, underground human orientation, personnel attendance system. Meanwhile the information integration of MES control platform is achieved. The data include both relational database and industrial database with diverse forms and complicated sources. These data show the multidimensional space distribution, the prominent contradiction is exist between universality of data collection and polymerizability of data presentation [1].

Study and solve the data issues during the real-time integrated of cost information process through OLAP.

Basic Concept of OLAP

The access and analysis from OLAP are aimed at a particular problem of online data. The basic concept contains mainly dimension, dimension hierarchy, dimension value, multidimensional data cube, etc.

Dimension: it is the abstract that factors related with some events in relation model, it is the particular angle of data observing. Such as work time, place, etc factors in metal mining operation event [2]. These factors should be problem concerned, the factors that not the problem consideration should be neglected in abstract.

Hierarchy: a specific angle of data observation (i.e. a dimension), the different detailed degree of multiple description is exist, which can be regard as dimension hierarchy. For example, the time dimensions description that can be described from different hierarchies: date, month, quarter, year, etc. Therefore date, month, quarter, year are the hierarchies of time dimensions.

Member: a value of dimension, it is the description of data position in dimension.

Data cube: the combination express of dimension and variable.

Architecture Model of OLAP Calculation

The production cost control system basic on MES, and the calculation and analysis section of OLAP during this system can be divided into four parts:

OLTP grassroots database, it is the source of data analysis.

Store data warehouse that used for data analysis, the source data adopt DTS or script obtains from OLTP data warehouse [3].

OLTP server, which is data processing engine that support and manage multi dimension data structure. The multi dimension data sets created by Microsoft OLAP Services can also be called Cube, which owns good performance and manage original data flexible and quickly, it is has the faster response speed.

The production cost control system basic on MES is taken as front-end browsing tool; it can inquire multi dimension data sets and provide them to customers through table or graphic.

The specific calculation architecture design as shown in Fig. 1.

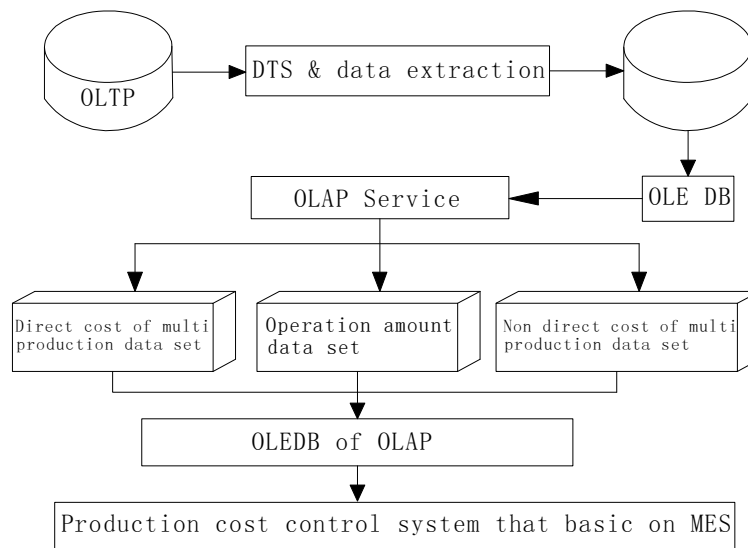


Fig. 1 Architecture of OLAP cost information

Accordingly with physical models of business data and analyze data, the realization of data acquisition, collection and uploading from OLTP system to OLAP system through data transaction service of database management tools. The consistency check should be taken necessarily before uploading. Every business data record is stamped with time. Data acquisition is not for conversion and summary of business data; therefore it keeps the minimum size of business information. Data acquisition is not only taken as the base of business statistical index, and it is also data base of data mining for data store. Data acquisition of each data mart can be operated separately, it is can be automatically acquired the statistical data from business database through system control every day or every month.

The Establishment of OLAP Multi Dimension Data of Cost Information

The dimensionality should be confirmed firstly before establishment of OLAP multi dimension data of cost information, it is to observe based angle of an object, it is the basis of problem consideration, and it is also the basis of multi dimensional operation for data cube. The dimensionality contains grade, hierarchy and member. The data in dimensionality always exist the condition that one grade contains anther grade, and this grade construction is regarded as dimensionality grade; the relations among each grade of specific dimension data is called dimension hierarchy; dimension member is the specific numerical data of dimensionality.

The dimensionalities as following are involved in undressed ore cost model of the underground metal mines:

Time dimensionality

The time dimensionality is a special dimension table among multi dimensionality model, it is also one of the most important special dimension tables. Almost all multi dimensionality models need to use time dimension tables, which have same requires. Therefore it is always to establish a public time dimension table to use for each multi data model. Time dimension table have five properties: time number, year, quarter, month and date, which are completed by separated filling program.

Table 1 OLAP multi-dimension data set of raw ore cost analysis

Multi data set	Measurement	Dimensionality members	Calculation members
Direct cost of production Data set	Material consumption Power consumption Duty working hour	time number material number power number personnel number working unit	material consumption cost power consumption cost labor cost raw ore cost work center/direct unit cost
work quantity data set	task plan quantity practical task quantity	time number Work cost center/unit	accumulative consumption Accumulative work quantity
Non-directed cost data set	Constant expense allocation Variable expense allocation	time number Work cost center/unit	accumulative cost Work center/unit allocation expense
Total raw ore cost Data set	Plan, accounting, cost analysis(cost amount, unit work cost, unit raw ore cost)	time Work cost center	Practical daily work cost Monthly accounting cost Year, historical cost Cost variance analysis

Cost/homework unit dimensionality

The homework unit dimensionality embody operation place and excavation engineering, Place dimensionality is a peculiar dimension table in multi dimensional model system, this system refines undressed ore production cost to operation place, therefore place dimensionality is also one of the most important dimension tables. It is the necessary dimension table for all cost multi dimensionality models during this system. The place dimensionality is used by many multi data models, and it contains the following properties place number, mining site, breast and work stope, etc.

Father-son dimensionality

Father-son dimensionality is a special dimensionality that owns only a dimension table, there are two lines exist the parent-child relationship in table. According to code appointment, any grade of dimensionality can be obtained through the recursive parent-child relationship. Father-son dimensionality is designed for solving dimensionality whose grade relations are not asymmetrical.

Subsidiary dimensionality

Subsidiary dimensionality: it is the detailed sub item list of a large item; this dimensionality is applicable to the dimensionality that contains a large number of sub items.

Common dimensionality

Common dimensionality: it is the medium sized dimension data that between time dimensionality and subsidiary dimensionality.

The multi dimension data is needed to be established after building completion of dimensionality. The OLAP cost multi data set of gold mining contain mainly cost multi data set that related with production directly and cost multi data set that related indirectly. And it is also contain the amount of data set that related with cost calculation. The specific design is shown as Table 1.1.

The OLAP Calculation Realization during Cost Information Real-Time Integration of Metal Mine

In this paper, the underground gold mine work cost data from January to march in 2008 is taken as the example, part of OLAP calculation model as above is used to calculate and analysis the cost from different dimensions of the gold mine. Some results as shown in bar Fig. 2 to bar Fig. 5.

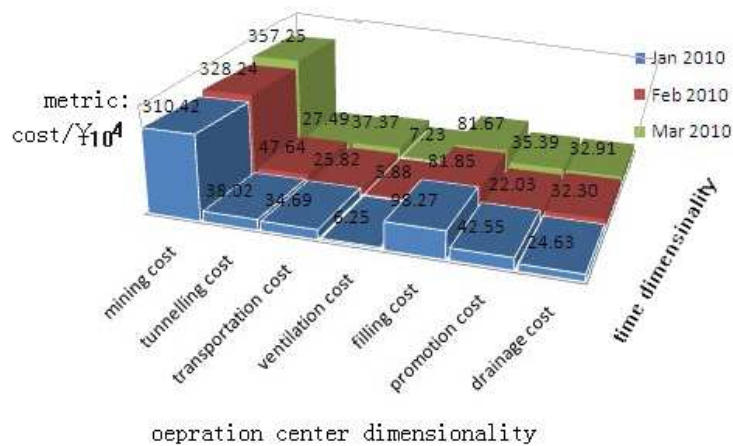


Fig. 2 Assay plan of OLAP raw ore cost –time dimension month, operation center dimensionality

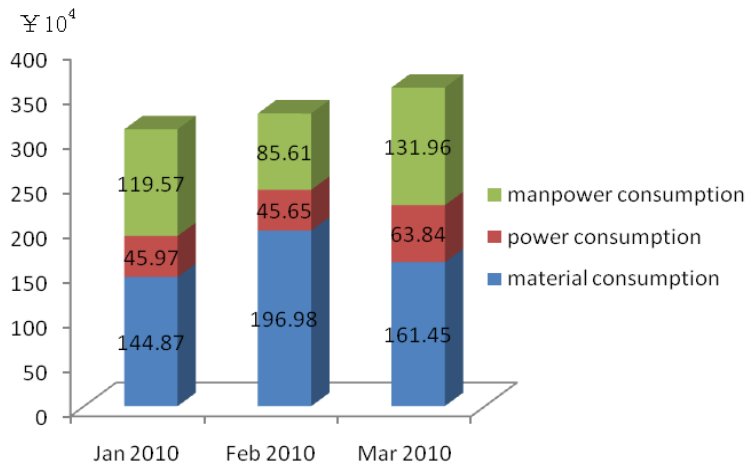


Fig. 3 Assay plan of OLAP raw ore cost- time dimension month, slice of mining operation center, month direct cost measurement

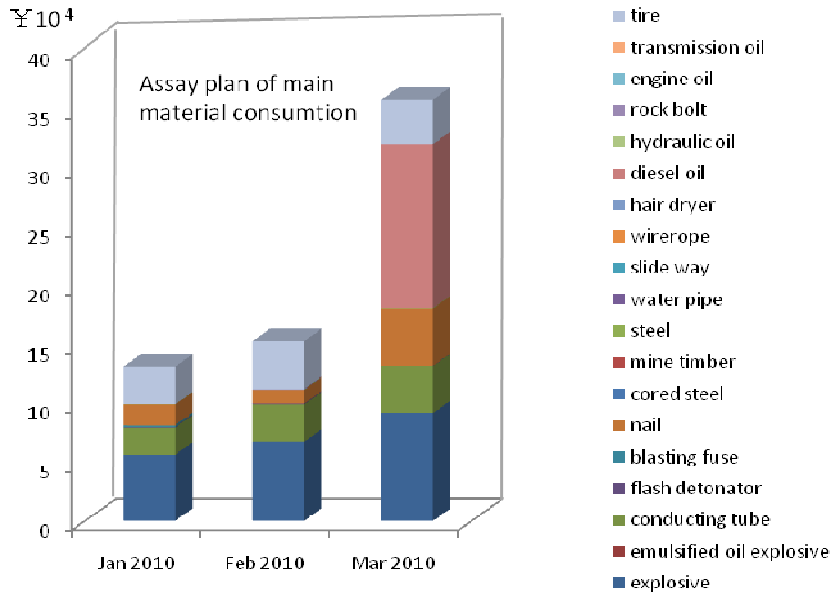


Fig. 4 Assay plan of OLAP raw ore cost- time dimension month, slice of mining operation center, main material consumption drilling

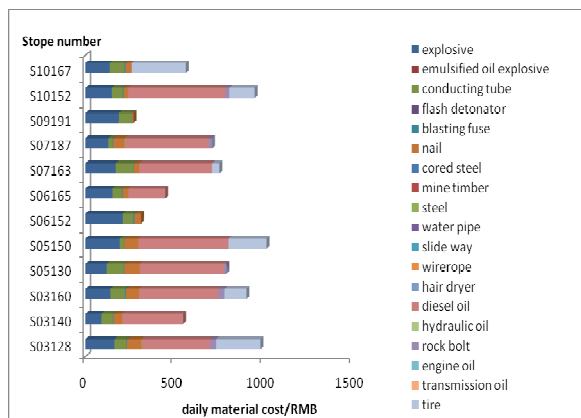


Fig. 5 Assay plan of OLAP raw ore cost- daily slice, mining operation unit stripping, main material consumption drilling

Conclusions

This article study and solve the data issues during cost information integration process through OLAP. Mines production cost is analyzed through OLAP technology multi-dimensionally and multi-angle computationally. So that the mine production cost management can be refined to production link, the specified operation item. The application of OLAP theory and technology in underground metal mines cost analysis filed is carried on deep study, and the related OLAP modeling is put forwarded simultaneously. The study achievements have some guiding and realistic significant on development and application of related data resources.

References

[1] L. Chen, H. Q. Wu, M. H. Zhang. (2009) Application of OLAP Based on Enterprise Manager System. Journal of Nantong Vocational College 35(12):78-81

[2] L. Zhang, G. Z. Lv. (2010) The Application and Prospect of Filling Material in Metal Mine Filling Mining Methods. Modern Mining 20(1): 20-22

[3] L. J. Chen. (2008) Strategic Study on Chinese Metal Mining Development under Background of Rising Costs. Metal Mine 46(3):1-6

CHAPTER 6:
Mechatronics and Applications

Precise Mechanics Control and Simulation of Automotive ABS

Yakun Wang^{1, a}, Peng Tan^{2, b}

^{1, 2} Institute of Electrical and Mechanical Engineering, Hainan University, Haikou, 570228, China

^{a, b}yakun_wang@163.com

Keywords: FPGA; Image data; Acquisition system; Design and development

Abstract. The rapid development of computer technology has brought a huge boost to the automotive industry. This paper uses computer technology to carry out simulation studies of automotive anti-lock braking system (ABS), through braking characteristics of the dynamic equations, we establish the simulation model, and get ABS braking distance and time in different roads, and through optimizing the system design simulation, we provide parameters in accordance with the precise control of the anti-lock braking system.

Introduction

The three themes of the modern automobile technology development in the field are safety, energy conservation, and environmental protection. Safety and comfort can get even more attention of people to the car first. A very important indicator of characterizing the vehicle safe driving is braking performance, and excellent vehicle brake is an important means to protect the safety of traffic. With the social and economic development, road infrastructure to improve and improve the vehicle speed is improving, thus braking system is particularly important to the safety of a car's braking performance and to protect human life and safety.

The ABS (Anti-the lock Brake System), also known as anti-lock braking system, is the vehicle braking system configuration, such as vehicle standards in Europe and other countries as foreign in the country. This safety brake system in the new car design standards has also been increased to 80%. In China, we also issued relevant regulations and standards, mandatory provisions vehicles with standard ABS system. To do this research the car's ABS system is important. The anti-lock braking system block diagram is shown in Fig. 1.

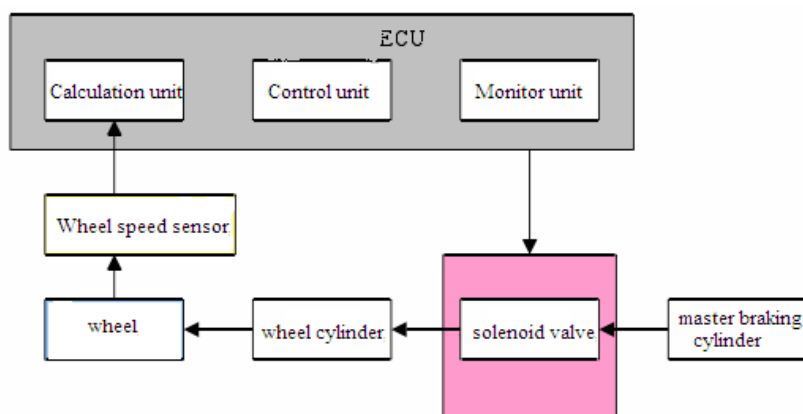


Fig. 1 Anti-lock braking system block diagram

Auto ABS Definitions and Principles

The ABS system is the electronic control technology applied in the conventional braking system, when the automobile brake to prevent the car wheel locking is a new mechatronics technology system. Its block diagram is shown in Fig. 2.

In the normal braking process, not with their feet all the brake equipment trampled to death, but step by step execution brake

Repeatedly we can gently depress the brake to stop the car. But in case of emergency, because people instinctive reaction is often immediately stomped the brake to stop immediately, which led to the wheels from locking, the occurrence of rollover and other dangerous situations. And the ABS system is designed to help prevent this from happening when there is the emergency brake. This system has greatly improved vehicle braking stability and security, and sensors are mounted on the wheel or drive shaft continuous feedback to the wheel speed car microcomputers to calculation of the car sliding to change the brake command in order to let the car to maintain a very safe state of emergency stop. Therefore, there must be anti-lock system device so that the wheel has been maintained in the case of rotation optimize braking to prevent wheel locking, and achieve the purpose of the safety brake. The control principle is shown in Figure 2.

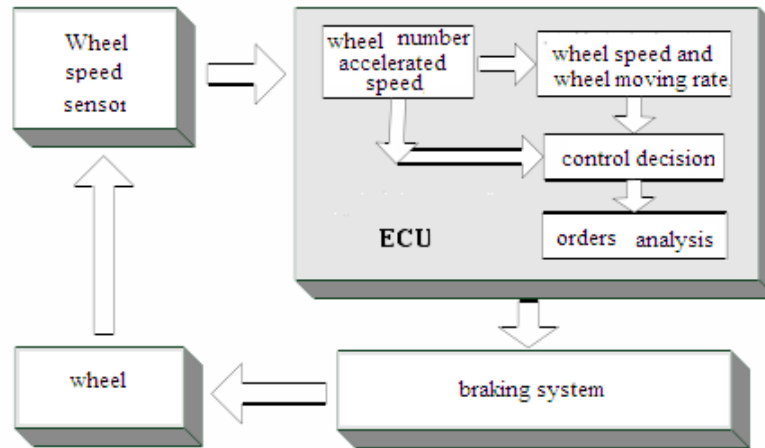


Fig. 2 Anti-lock system (ABS) control schematic

Anti-Lock Braking System (ABS) Has Three Significant Advantages:

Emergency brake in the car improves the manageability of the steering wheel. Its purpose is to make the wheels are locked at the moment, with a sudden change in the braking force of the wheels, reducing the brake pressure to prevent their locking to ensure the directionality of the car ahead.

Increase the Stability When the Car Brakes

Antilock brakes, once you start running, can ensure that the wheels continue to slip and rolling state alternately, slip a small car to resist lateral force with greater force, in order to ensure the car's lateral stability to prevent rollover accidents.

Reduce the Brake Stopping Distance

Anti-lock system allows the car wheel to take full advantage of the adhesion coefficient, to obtain the maximum vehicle braking performance and reducing brake stopping distance.

The Anti-Lock (ABS) Systems Precise Control Model

Based on automotive systems, we use the car's single-wheel ABS system model, as is shown in Figure 3, to get the vehicle motion dynamics equation:

$$mv \geq -F_s \quad (1)$$

$$I\omega \geq F_s R - M_b \quad (2)$$

$$F_s = N\mu \quad (3)$$

Among them: m is quality; v is speed; I is moment of inertia; R is rolling radius; F_s is in-road friction; ω is angular velocity; M_b is torque; μ is attachment coefficient; N is reaction force.

Motors motion dynamics from the differential equation is as follows:

$$J \frac{d\omega}{dt} = F_h \cdot r - M_h \tag{4}$$

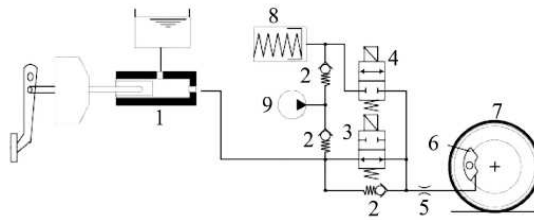


Fig. 3 Car single on the ABS system model

Combined with the vehicle system equations and a variety of surface parameters simplified, we can get:

$$\dot{v} = \frac{\lambda \cdot v + \omega \cdot r}{\omega \cdot r} \cdot v \tag{5}$$

ω Is vehicle angular velocity; λ is slip rate; Δt is time period;
At the beginning of the automotive brake, $\lambda = 0$, then:

$$\dot{v} = \left(\frac{\dot{\omega}_n}{\omega_n} + \frac{\dot{\lambda} \cdot v_n}{\omega_n \cdot r} \right) \cdot v_n \tag{6}$$

This is the vehicle deceleration speed.

By using the speed of slip of the vehicle equations of motion antilock brakes and braking distance calculation to improve accuracy, we have improved the precise control of the anti-lock braking system within the computer program design, and also improved the car ABS systems control precision.

The Anti-Lock (ABS) System Simulation

Anti-lock braking system (ABS) is very complex, and the use of the experimental system is unrealistic, which requires a lot of money and time. In order to be able to carry out the control of the ABS system, through car mechanics, it is deduced kinetic equation for the simulation of the ABS system.

First, the selected models are passenger cars, and its parameters are listed in Table 1, and the simulation platform based on MATLAB and ECU software environment is shown in Figure 4.

Table 1. Car parameters

1/4 Weight (kg)	Moment of inertia (kg·m)	Wheel radius (m)	S_T	K	d(mm)	r(mm)	Pressure (mPa)
800	21	0.312	0.21	0.72	55	130	13

ST - adhesion coefficient at slip rate; d - wheel cylinder diameter; K-braking coefficient of performance; r - brake disc radius; P0 - brake lines maximum pressure.

Based on the nonlinear model formula, we can get:

$$\begin{cases} \mu = \frac{\mu_h \cdot s}{s_h} \\ \mu = \frac{\mu_h - \mu_g s_g}{1 - s_g} - \frac{\mu_h - \mu_g}{1 - s_g} \cdot s \end{cases} \quad (7)$$

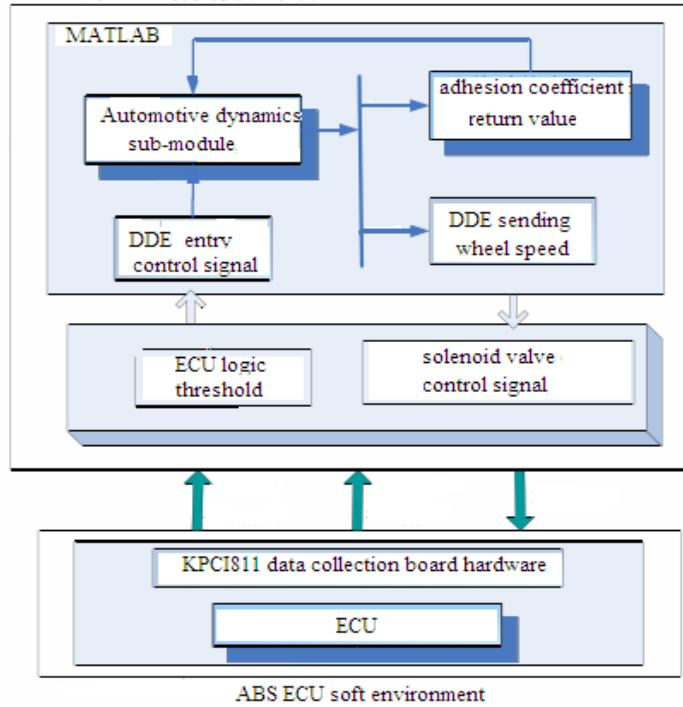


Fig. 4 ABS simulation system block diagram

According to the road reference data, the simulation results obtained are shown in Table 2:

Table 2. Simulation results data

Road surface	Braking distance /m	Braking time /s
Loose snow	35.12	3.55
Dry bitumen	24.12	2.39
Icing	47.35	4.79

Through computer simulation, the dry asphalt pavement simulation results are shown in Figure 5; loose snow on the road simulation results is in Figure 6; icing on the road simulation result is shown in Fig. 7.

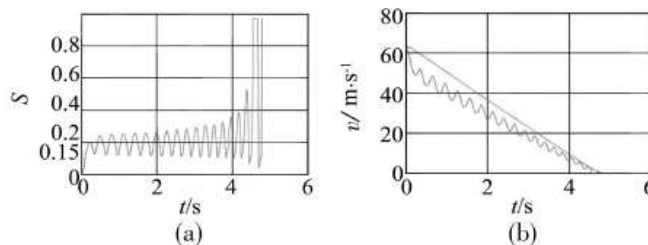


Fig 5. Dry asphalt pavement simulation results

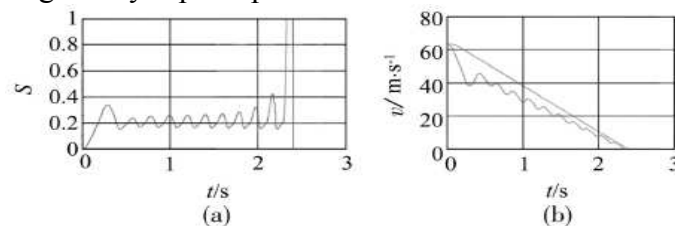


Fig. 6 Loose snow on the road simulation results

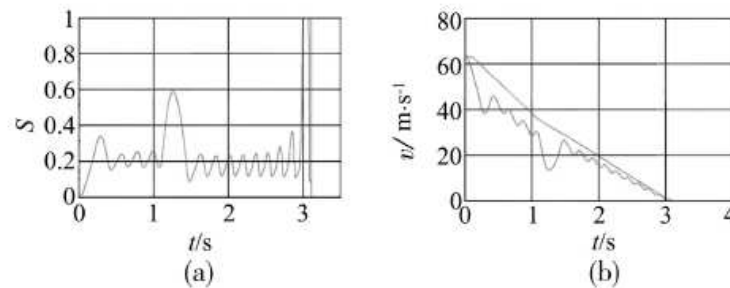


Fig. 7 Icing on the road simulation result

From the simulation of automotive wheel speed and brake slip rate data in the graphic, it can be seen that the ABS system in the course of the velocity waveform is slowly declining. This proves that the anti-lock system to effectively improve automobile emergency brake when the car deceleration of stability and security.

Conclusion

In this study, it can be shown that the state of motion in the car's ABS system can accurately control the car during braking to prevent wheel locking accident. Through automotive anti-lock braking system (ABS) simulation, we can verify and improve the precise control of the car computer ABS system, and achieve effective security to protect the car during braking.

References

- [1] Feng Yuan, Ge Ruhai. Automotive electronic control technology [M] Beijing: Mechanical Industry Press, 2005, 7.
- [2] Dong Changhong, Yu Xiaohai. Matlab interface technology and application [M] Beijing: National Defense Industry Press, 2004, 3.
- [3] Zhang Wei. MATLAB external interface programming [M]. Xi'an: Xidian University Press, 2004. Lou Shuntian, Yao Ruoyu, Ye Jimin. MATLAB7.X system analysis and design - control system [M]. Xi'an: Xidian University Press, 2005(11).
- [4] Fan Ligang. ADAMS-based vehicle ABS system Semi-physical simulation [D]. Xi'an: Xi'an University of Technology, 2011.
- [5] Guo Wei, Pan Zhongming. DSP control system simulation based on MATLAB platform [J]. Beijing: Measurement and Control Technology, 2006(11).
- [6] Zhang Like. MATLAB7.0 from entry to master [M] Beijing: People's Posts and Telecommunications Press, 2006.
- [7] Liu Shujun, Gai Xiaohua, Fan Jing. MATLAB7.0 control system applications and examples [M] Beijing: Mechanical Industry Press, 2006.

Simulation of Automatic and Intelligent Mechanical Arm

Wang Xin

School of Mechanical Engineering and Automation, Xihua University, Chengdu, Sichuan, China,
610039

wangxin@hrsk.net

Keywords: Design, Simulation, Intelligent Mechanical Arm

Abstract. This paper presents a robot image processing combined with the working principle of the technique on the intelligent mobile robot design. Mechanical arm can quickly determine the locations of target and Grip the target through image processing techniques, doesn't need to use the theory of complex image processing or additional sensors to measure depth. Programs can significantly reduce computation time, achieve real time operation. In this study, the company launched Autodesk Inventor software to simulate the mobile mechanical arm. In the simulation experiments, must consider the designed arm degree of freedom, and action fluency.

System Model

In this study, the theory of kinematics constructed the Mechanical arm with six degrees of freedom and a mobile device. Linear motor simulated mobile devices. To install visual servo system, has two CCD on the gripper. Mechanical arm can detect distance by visual servo system between the target and the gripper. Through mechanical arm can grip target or other tasks. Mobile device is in order to increase the working range of mechanical arm. The mobile mechanical arm overall construction contains has the mechanical arm, the mobile installment, the gripper and the visual servo system. "Fig. 1" is schematic framework of the mechanical arm.

Principles of Mobile Mechanical Arm Motion

The following were the design of this research, the mechanical arm and the mobile device works.

The mechanical arm In this study, we use the method of D-H coordinate system [6]. According this rules of D-H coordinate system. We set the length of link (a), twist of link twist (α), offset of link (d) and angle of joint (θ). The defined the connecting rod as shown in "Fig. 2".



Fig.1 Schematic framework of the mechanical arm

d_i Is the distance form X_{i-1} to X_i along Z_i θ_i is the angle form X_{i-1} to X_i along Z_i . a_i is the distance form Z_{i-1} to Z_i along X_i , α_i is the angle form Z_{i-1} to Z_i along X_i .

We can know coordinate system of (i-1) is continuous displacement and rotation to transform to coordinate system of (i). The distance (d_i) along the coordinate system of (i-1) to Z_{i-1} -axis can coincide with O_{i-1} and Z_{i-1} . Transition matrix as follows:

Along the Z_{i-1} -axis, we move angle in coordinate system of (i-1), making D-axis and the H-axis in a straight line. Transition matrix as follows:

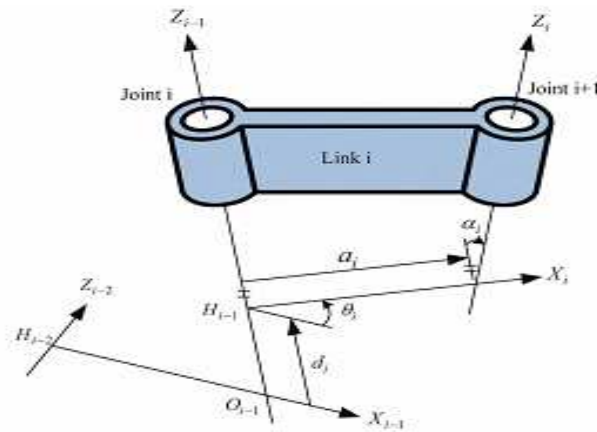


Fig. 2 The defined the connecting rod

$$T(z, d) = \begin{bmatrix} 1 & 0 & 0 & 0 \\ 0 & 1 & 0 & 0 \\ 0 & 0 & 1 & d_i \\ 0 & 0 & 0 & 1 \end{bmatrix}$$



Fig. 3 Schematic diagram of mechanical arm

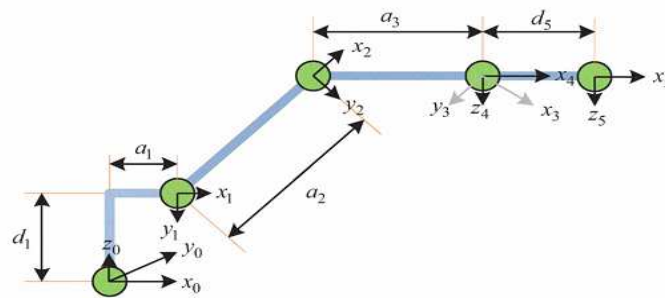


Fig. 4 Coordinate system model

$$T(z, \theta) = \begin{bmatrix} \cos \theta_i & -\sin \theta_i & 0 & 0 \\ \sin \theta_i & \cos \theta_i & 0 & 0 \\ 0 & 0 & 1 & 0 \\ 0 & 0 & 0 & 1 \end{bmatrix}$$

The distance (a_i) along the coordinate system of (i-1) to X_i -axis can coincide with O_{i-1} and O_i . Transition matrix as follows:

$$T(x, a) = \begin{bmatrix} 1 & 0 & 0 & a_i \\ 0 & 1 & 0 & 0 \\ 0 & 0 & 1 & 0 \\ 0 & 0 & 0 & 1 \end{bmatrix}$$

Along X_i -axis rotation angle (α_i), making the two coordinate systems coincide. Transition matrix as follows:

$$T(x, a) = \begin{bmatrix} 1 & 0 & 0 & a_i \\ 0 & \cos \alpha_i & -\sin \alpha_i & 0 \\ 0 & \sin \alpha_i & \cos \alpha_i & 0 \\ 0 & 0 & 0 & 1 \end{bmatrix}$$

Therefore, by the above four transformation matrix can be obtained by converting (${}^{i-1}A_i$):

Table.1 Link parameter of D-H notation

Joint	d_i	θ_i	a_i	α_i
0	0	0	0	0°
1	d_1	θ_1	a_1	-90°
2	0	θ_2	a_2	0°
3	0	θ_3	a_3	0°
4	0	θ_4	0	-90°
5	d_5	θ_5	0	0°

$${}^{i-1}A_i = T(z, d)T(z, \theta)T(x, \alpha)$$

According to (3.1)-(3.4)

$${}^{i-1}A_i = \begin{bmatrix} \cos \theta_i & -\cos \alpha_i \sin \theta_i & \sin \alpha_i \sin \theta_i & a_i \cos \theta_i \\ \sin \theta_i & \cos \alpha_i \cos \theta_i & -\sin \alpha_i \cos \theta_i & a_i \sin \theta_i \\ 0 & \sin \alpha_i & \cos \alpha_i & d_i \\ 0 & 0 & 0 & 1 \end{bmatrix}$$

It is D-H transformation matrix form (i -1) conversion to (i).

We assume that ${}^i p = [p_x \ p_y \ p_z \ 1]^T$ is a position coordinate system. This position is converted by the (i) coordinate system to (i -1) coordinate system.

$${}^{i-1} p = {}^{i-1} A_i {}^i p$$

In accordance with the methods described earlier to identify the parameters of the coordinate systems, such as d_i , θ_i , a_i and α_i . From "Fig. 3" and "Fig. 4" shows six-axis mechanical arm coordinate system of various institutions. Using transformation matrix of D-H to obtain the relevant parameters (d_i , θ_i , a_i and α_i). Table.1 shows D-H parameters. We can get D-H transformation matrix between the bars.

$${}^0 A_1 = \begin{bmatrix} \cos \theta_1 & 0 & -\sin \theta_1 & a_1 \cos \theta_1 \\ \sin \theta_1 & 0 & \cos \theta_1 & a_1 \sin \theta_1 \\ 0 & -1 & \cos \alpha_i & d_1 \\ 0 & 0 & 0 & 1 \end{bmatrix}$$

$${}^1A_2 = \begin{bmatrix} \cos \theta_2 & -\sin \theta_2 & 0 & a_2 \cos \theta_2 \\ \sin \theta_2 & \cos \theta_2 & 0 & a_2 \sin \theta_2 \\ 0 & 0 & 1 & 0 \\ 0 & 0 & 0 & 1 \end{bmatrix}$$

$${}^2A_3 = \begin{bmatrix} \cos \theta_3 & -\sin \theta_3 & 0 & a_3 \cos \theta_3 \\ \sin \theta_3 & \cos \theta_3 & 0 & a_3 \sin \theta_3 \\ 0 & 0 & 1 & 0 \\ 0 & 0 & 0 & 1 \end{bmatrix}$$

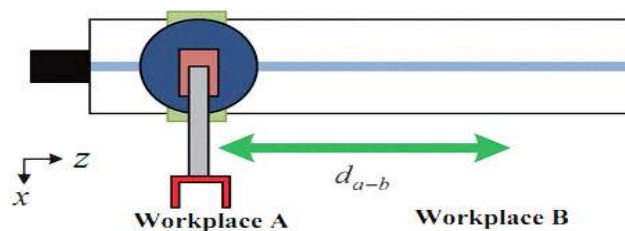


Fig. 5 Movement of 2 mobile devices diagram

$${}^3A_4 = \begin{bmatrix} \cos \theta_4 & 0 & -\sin \theta_4 & 0 \\ \sin \theta_4 & 0 & \cos \theta_4 & 0 \\ 0 & -1 & 0 & 0 \\ 0 & 0 & 0 & 1 \end{bmatrix}$$

$${}^4A_5 = \begin{bmatrix} \cos \theta_5 & -\sin \theta_5 & 0 & 0 \\ \sin \theta_5 & \cos \theta_5 & 0 & 0 \\ 0 & 0 & 1 & d_5 \\ 0 & 0 & 0 & 1 \end{bmatrix}$$

The mobile device The mobile device is a single degree of freedom linear platform. It can carry out its mandate under different working areas, as shown in “Fig. 5”. It’s from A’s workspace to B’s workspace move $d_{a,b}$. Only need to do to change the coordinate system of Z-axis.

Visual Servo System

This study used image processing techniques including capture image and position coordinates of objects. Image processing section does not require too complex and rigorous theory, most just get the object size, shape and color information. The important is the image correction, and depth measurements.

Image pre-processing

This study used image pre-processing techniques including capture image and position coordinates of objects. Image processing section does not require too complex and rigorous theory, most just get the object size, shape and color information. The important is the image correction, and depth measurements. On image processing procedures, including gray, binary, extract features and enhanced edge, doesn't require repeated or complex processing. Pre-processing time can be shortened, and can get real-time operating system. In "Fig. 6", we can see Image pre-operation flow chart.

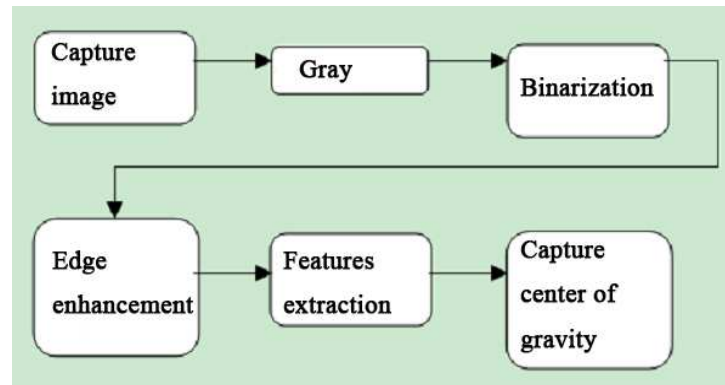


Fig.6 Image pre-operation flow chart

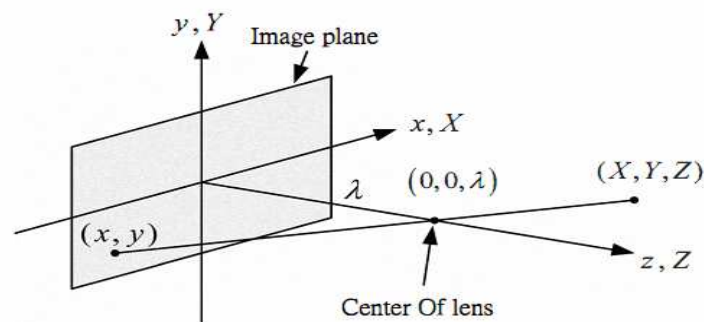


Fig. 7 Schematic diagram of imaging lens

3D imaging theory and image correction

It's imaging perspective transformation. A is the lens focal length. If the coordinate image system coincides with the world. (X, Y, Z) compose of image in the image plane (x, y) , as shown in "Fig. 7".

Using triangle can get follow:

$$\frac{x}{\lambda} = \frac{X}{Z - \lambda} = \frac{X}{\lambda - Z}$$

So

$$x = \frac{\lambda X}{\lambda - Z}$$

$$y = \frac{\lambda Y}{\lambda - Z}$$

Set the world coordinate system point vector as:

$$w = [X \quad Y \quad Z]^T$$

The corresponding homogeneous coordinates as:

$$w_h = [kX \quad kY \quad kZ \quad k]^T$$

In which k is constant.

Define P as the perspective transform coordinates.

$$P = \begin{bmatrix} 1 & 0 & 0 & 0 \\ 0 & 1 & 0 & 0 \\ 0 & 0 & 1 & 0 \\ 0 & 0 & -\frac{1}{\lambda} & 1 \end{bmatrix}$$

C_h is the homogeneous form of image coordinates. Cartesian coordinates as:

$$C_h = [x \quad y \quad z]^T = \left[\frac{\lambda X}{\lambda - Z} \quad \frac{\lambda Y}{\lambda - Z} \quad \frac{\lambda Z}{\lambda - Z} \right]^T$$

PW_h is a perspective coordinates of the world coordinate system transformation, as C_h :

$$C_h = PW_h = \begin{bmatrix} 1 & 0 & 0 & 0 \\ 0 & 1 & 0 & 0 \\ 0 & 0 & 1 & 0 \\ 0 & 0 & -\frac{1}{\lambda} & 1 \end{bmatrix} \begin{bmatrix} kX \\ kY \\ kZ \\ k \end{bmatrix} = \begin{bmatrix} kX \\ kY \\ kZ \\ -\frac{kZ}{\lambda} + k \end{bmatrix}$$

Anti-perspective transformation

Derivation of the anti-perspective in conversion

$$w_h = P^{-1}C_h, P^{-1} = \begin{bmatrix} 1 & 0 & 0 & 0 \\ 0 & 1 & 0 & 0 \\ 0 & 0 & 1 & 0 \\ 0 & 0 & \frac{1}{\lambda} & 1 \end{bmatrix}$$

$$\text{Let } C_h = \begin{bmatrix} kx_0 \\ ky_0 \\ kz \\ k \end{bmatrix}$$

Where x_0 and y_0 is the image plane center.

$$w_h = P^{-1}C_h = \begin{bmatrix} kx_0 \\ ky_0 \\ kz \\ \frac{kz}{\lambda} + k \end{bmatrix}$$

$$w = [X \quad Y \quad Z]^T = \left[\frac{\lambda x_0}{\lambda + z} \quad \frac{\lambda y_0}{\lambda + z} \quad \frac{\lambda z}{\lambda + z} \right]^T$$

In which

$$(X, Y, Z) = \begin{bmatrix} \frac{\lambda x_0}{\lambda + z} & \frac{\lambda y_0}{\lambda + z} & \frac{\lambda z}{\lambda + z} \end{bmatrix}$$

In $Z = \frac{\lambda z}{\lambda + z}$, Z can be obtained by z.

So

$$z = \frac{\lambda Z}{\lambda - Z}$$

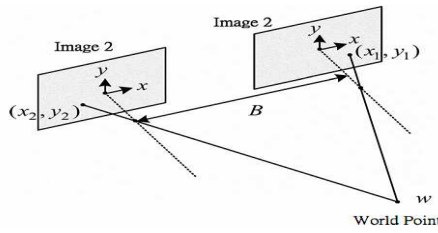


Fig. 8 Schematic diagram of 2-CCD camera imaging

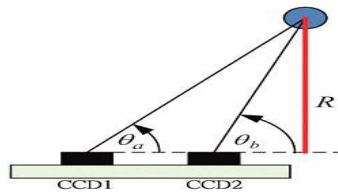


Fig. 9 Diagram triangle theory

Similarly

$$X = \frac{x_0}{Z} (\lambda - Z)$$

$$Y = \frac{y_0}{Z} (\lambda - Z)$$

Spatial coordinates of image depth

Cartesian coordinates derived

In section IV.B, we can get the object information in the space as (X, Y), but needing to calculate the depth information, "Fig. 8" is schematic diagram of 2-CCD camera imaging , mages of the same point were falling at (X₁, Y₁) and (X₂, Y₂) in world coordinate systems, respectively. B is distance between the centers of which 2-CCD. Where A is distance between Lens center and the CCD chip.

$$Z = \lambda - \frac{\lambda B}{x_2 - x_1}$$

Space spherical coordinates

Because they are not using the wide-angle lens, it is necessary with a mobile device. This study proposes a CCD device rotation machine ride on the mechanical arm at the end. It can move within point of image acquisition or racking. θ_a , θ_b and R calculated using triangulation theory, as shown in "Fig. 9".

Experimental Simulation

In this study, the company launched Autodesk Inventor software to simulate the mobile mechanical arm. In the simulation experiments, must consider the designed arm degree of freedom, and action fluency. To avoid poor design agency, so that mechanical arm can't move. Statement of work as "Fig. 10": (a) Using Visual servo system to detect target position servo system, (b) Move to the target position, (c) Grip the target, (d) Pick up the object, (e) Move to another workspace, (f) Reach the workspace, (g) Put down the object, (h) Restore the initial state, (i) Move to initial position, (j) Restore the initial state of system.

Conclusion

Mobile mechanical arm is a general mechanical arm installed on the mobile device, has more working space and flexibility than fixed mechanical arm, which can be more widely applied. But the mobile mechanical arm complex than the fixed mechanical arm, and kinematic analysis and control rules are more difficult. We represent the Principles of mobile mechanical arm motion and visual servo system.

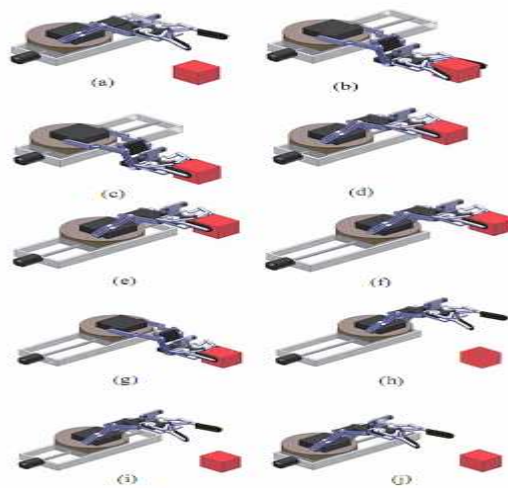


Fig. 10 Statement of work

References

- [1] G. Eason, B. Noble, and I. N. Sneddon, "On certain integrals of Lipschitz-Hankel type involving products of Bessel functions," *Phil. Trans. Roy. Soc. London*, vol. A247, pp. 529-551, April 1955. (references)
- [2] J. Clerk Maxwell, *A Treatise on Electricity and Magnetism*, 3rd ed., vol. 2. Oxford: Clarendon, 1892, pp.68-73.
- [3] I. S. Jacobs and C. P. Bean, "Fine particles, thin films and exchange anisotropy," in *Magnetism*, vol. III, G. T. Rado and H. Suhl, Eds. New York: Academic, 1963, pp. 271-350.
- [4] K. Elissa, "Title of paper if known," unpublished.
- [5] [5] R. Nicole, "Title of paper with only first word capitalized," *J. Name Stand. Abbrev.*, in press.
- [6] Y. Yorozu, M. Hirano, K. Oka, and Y. Tagawa, "Electron spectroscopy studies on magneto-optical media and plastic substrate interface," *IEEE Transl. J. Magn. Japan*, vol. 2, pp. 740-741, August 1987 [Digests 9th Annual Conf. Magnetics Japan, p. 301,1982.
- [7] M. Young, *The Technical Writer's Handbook*. Mill Valley, CA: University Science, 1989.

Explosion-Proof Soft Starter Control System Based On DSP

Xin Niu^{1, a}, Yaqiong Wang^{2, b}

¹Department of Electrical Engineering, Jiyuan Vocational and Technical College, Jiyuan, Henan
459000

²Department of Electrical Engineering, Jiyuan Vocational and Technical College, Jiyuan, Henan
459000

^aniu9911@163.com, ^b13903892889@139.com

Keywords: Digital Signal Processor TMS320LF2406A, Explosion-Proof Soft Starting, Starting Characteristics

Abstract. According to requirements for the use of explosion-proof and intrinsically safe AC motor soft start device in coal mine, the paper designed and realized explosion-proof soft starting control device based on the TMS320LF2406A as soft starter control core. TMS320LF2406A is TI company's new DSP products, superior to the MCU extensive used in general micro-control unit. It has advantages of low cost, low power consumption and high performance processing ability.

Introduction

Motor soft start controller experienced the process of electromechanical transistor type, transistor, integrated circuit, computer type of the development gradually introduced in 1990's. Computer type is a kind of intelligent soft starting device by adopting microcomputer control technology, digital electronic technology, control theory, sensor technology and communication technology. It has been widely used in power system now [1].

However, the microcontroller itself is lack of resources and the ability to process data word length and floating point performance was poor, resulting in its own limitations, such as data processing capability and immunity levels, so the computer protection device usually of multi-CPU, and electrical components and power line protection, monitoring and control functions required by the demand by different units. This will inevitably result in their wiring complexity, the use of maintenance problems and low level of intelligence shortcomings.

Compared with microcomputer chip, the DSP device uses Harvard architecture, high-speed hardware multiplier, enhanced multi-stage pipeline, Instruction cycle can reach up to tens of nanoseconds, with a high-speed data processing capabilities. Another, DSP devices built-in large capacity memory, baud rate generator and FIFO and high-speed bus interface, this DSP-based intelligent explosion-proof soft-start control device, not only can complete motor soft-start process and the protection function in normal working condition, but also can integrated measure, control and monitor online. Its data processing capabilities and reliability have an incomparable superiority of the microcomputer chip.

Hardware Design of Soft Starting Controller

Hardware Structure The hardware of soft starting controller includes the DSP digital control core part, digital input and output part, an analog input part, a variety of fault protection circuit, data storage and communication interface circuit, a current detection circuit, three-phase voltage synchronous signal acquisition and thyristor pulse trigger circuit. Its main core is TMS320L2406ADSP chip of TI. The LCD module uses serial connection mode of OCM4X8C. CAN network is used in real-time monitoring of the starting situation. In the thyristor trigger circuit, EPM7064TC44 chip is adopted to replace the traditional digital logic. Its structure diagram is shown in fig. 1.

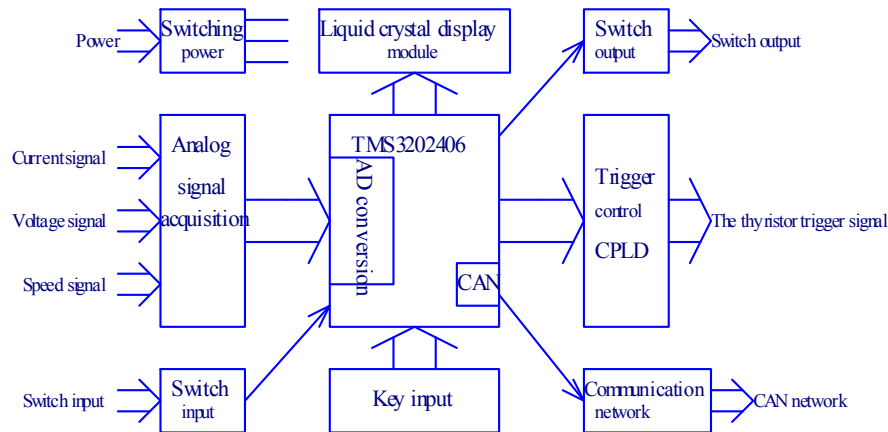


Fig. 1 Comprehensive control device's static structure diagram

The Core DSP Selection TMS320L2406ADSP chip[2][3] with high-speed A/D function is used as the core DSP. It is manufactured in IT company that there is a 16-channel 10-bit A / D converter, program memory capacity of $32K \times 16$ -bit, including 0.5K DRAM and 2K SRAM. It can use the C language and assembly programming; in addition to having Harvard structure with the procedures and data separate, pipeline operation function, complete the multiplication and hardware multiplier in single cycle. It also has the following features:

It uses high-performance static CMOS technology, and the supply voltage reduced to 3.3V, reducing power consumption of the controller.

It has a high 32K x 16-bit flash memory, programmable solutions that provide economic products for a variety of purposes. FLASH-based chip with the 256K boot guides ROM can make online programming more convenient.

The high performance of 10 bit analog-to-digital converter (ADC) conversion time is 500ns, which provides up to 16 analog input with automatic sorting functions, so that the conversion of up to 16 during the same conversion is without increasing the CPU's overhead.

In addition to providing a serial communication interface (SCI), so that it can complete asynchronous communication (RS-485) with other controller within the systems. For additional communication interface system, 2406 provides a 16 bit synchronous serial peripheral interface chip (SPI), which provides a CAN communication module.

Therefore, TMS320LF2406ADSP has the advantages of low cost, low power consumption, high performance characteristics, several resources and peripherals are integrated into the chip, forming a true single chip controller.

Three phase synchronous signal acquisition and thyristor trigger circuit. Thyristor trigger circuit synchronous signal is extracted through transformer three-phase power phase, so that the resulting trigger synchronous signal is stable, accurate and consistent with the grid, to ensure triggered reliable. It uses the EPM7064TC44 chip to replace the traditional digital logic circuit in the thyristor trigger circuit. CPLD flexible application, convenient realization, pin reconfigurable, and when in use to reduce the PCB area of the plate, improves the reliability.

Analog Data Acquisition System. The device data acquisition includes AC analog, analog data acquisition system, DC analog and switch. AC analog includes three-way measure current speed signal all the way, all the way to the voltage signal.

The current signal acquisition: coal mine using the three-phase three-wire connection mode, therefore, only need to test the two-phase current detection current while test the current. The voltage signal acquisition: sampling the voltage channel exchanges, not only to determine the operation voltage range, but also the right to display the grid voltage rms. Speed detection circuit: speed detection circuit external speed signal (frequency signal) after filtering, optical coupler, the signal is sent to the F / V conversion circuit, formed after the F / V conversion AD converter voltage sent TMS320LF2406A. Finally, convert the digital signal sent to the DSP to process. Its diagram is shown in fig. 2.



Fig. 2 Speed detect circuit diagram

Switch Input / Output Circuit. The digital inputs include two categories: one is the output of the circuit breakers, isolating switches and other equipment to help contact or relay contact, to detect the status of this equipment, and the other is intelligent protection device itself contacts.

The trip circuit exports the key is how to prevent malfunction in the optical isolation at the same time, the soft-start device sub-gate signal output by the DSP issued a two-way signal control at the same time, only when the two sub-gate signals for the "high" "low" effective level, the trip circuit to work.

Design of Protection Circuit. In soft start control device, in addition to meet the requirements of soft starting control, but also monitor motor voltage, current and other failures that may occur in the operation process. By theoretical analysis, multiple protections include hardware protection circuit and software protection program are designed. Here only analysis phase unbalance protection hardware circuit.

Phase imbalance protection is divided into two situations: the voltage unbalance and current unbalance. Voltage phase failure protection circuit is shown in Figure 3, ER_UQX output is high under normal circumstances, but change low in the phase failure. Judging whether a voltage is imbalance can be finished by detecting ER_UQX.

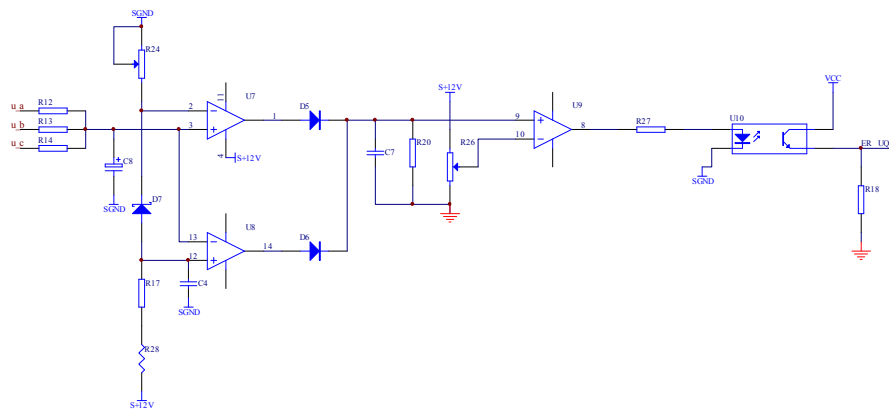


Fig. 3 Voltage phase failure protection circuit

Current phase failure protection circuit is shown in Figure 4, when the current phase failed, the node voltage of C5 changes, the 14-pin output is positive, query the pin level is high or not at any time, it can determine whether the current is not phase.

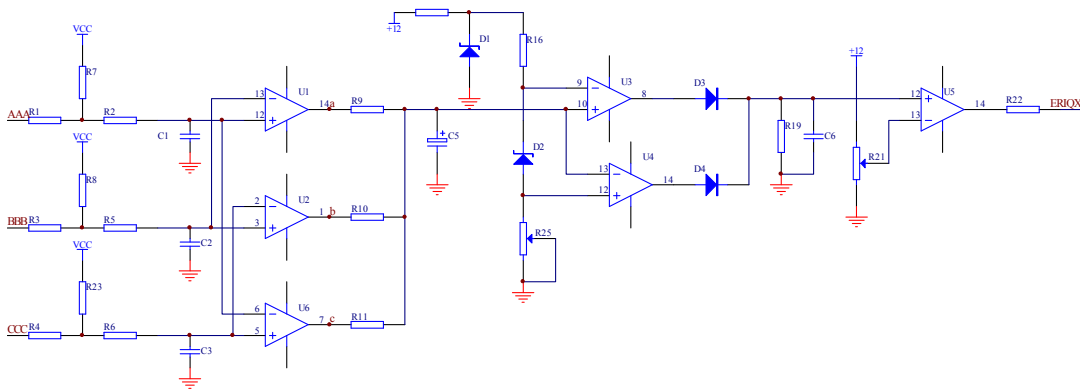


Fig. 4 Current open-phase protection circuit

Software Design of the Soft Start Controller

System core DSP program structure consists of the following nine modules [4, 5], program initialization, MCU processing with registers, memory, peripheral signal initial. The basic input and output control module is using to realize of the external button order, button command, control output, display output control. Parameter control module can modify internal parameters according to the parameters of button, the modified parameters are stored in memory. The module of realization of state and parameter can display parameter values of power supply, initial, operation, fault, set the basic state and Real time state. The voltage detection and synchronization signal detection module complete detection and three-phase voltage synchronous signal detection. Current detection of A / D conversion module, realize reading of the current value. Soft start control module control double closed loop according to the speed and current, or using simple direct slope control to realize the soft start control according to the parameter selection command. Three phase control module can achieve the triggering angle command according to the synchronizing signal is assigned to the 6 phase thyristor. Operation control module, running after starting program the module, judging whether faults occur in the operation [6].

Test Data

The control device with the core of mine flameproof and intrinsically safety type soft starter had a large number of tests in the laboratory, the test data indicates that the test procedure is no abnormal phenomenon, test results are qualified, the protection unit operation parameters can meet the design requirements, the soft starting process is normal.

Soft Start Characteristic Curve. The curve is shown in figure 5.1-5.2.

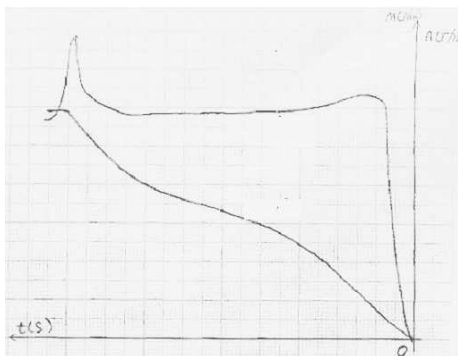


Fig. 5.1 Voltage ramp load curves

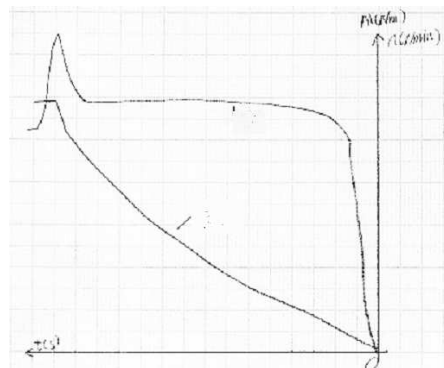


Fig. 5.2 Current limiting mode and full load curves

Data of Protection Characteristics. Protection performance testing projects consist of Leakage atresia, phase failure protection, short circuit protection, overvoltage protection, under-voltage protection and overheat protection, the test table is shown in table 1.

Conclusions

Through of research, testing and operation with low-voltage explosion-proof soft start control system based on TMS320LF2406A, We have the following conclusions:

1. We can make high voltage soft starting device performance more wide, reliability and high accuracy than conventional microcomputer soft starting device adopting DSP device equipped with the appropriate hardware and software. This device can sampling and operation fast and complete the detection and real time control function that Microcomtupter cannot do.

2. We can simplify the circuit, reduce the external extension module, improves the reliability of the system by adopting the high performance DSP-TMS320LF2406A as the central control unit, the mine flameproof and intrinsically safe type AC motor soft starter with the core of control device runs successfully in laboratory. It has advantages of stable performance, reliable action, start smoothly, with Practicability and the reliability that traditional starter can not Compare. The further work is to transform the design plan into products to improve intelligent level better.

Table 1 Protection characteristic test table

Test conditions	Rated current(A)	400		Main circuit voltage	1140	
	Test power supply	Current generator				
Test data	Test item	Rated current		Action value		
		Any phase	two phase	Third phase	Required value	Measured value
	Overload protection	1.05			2h No action	2h No action
		1.2			<20min	6.8min
		1.5			<3min	1.8min
		6.0			>8s	8.9s
	Short circuit protection	8.0			200-400ms	260ms
	Phase failure protection	1.0		0.9	2h No action	2h No action
		1.15		0	<20min	0.1min
	Leakage atresia	Blocking resistance(k Ω)			40+20%	40.6
Unlock resistance(k Ω)			42.4~62.0	45.1		

References

- [1] *Coal mine safety regulation*. (Powered By SiteEngine,2010).
- [2] K.J. Xu. *DSP and its application in electrical engineering and automation*. (BeiHang University Press,2009).
- [3] Y.Z. Qin. *Principle and application of TMS320LF240xDSP*. (Tsinghua University press,2009).
- [4] Y.R. Lin. *TMS320F240x DSP compilation and C language control application*. (BeiHang University Press,2009).
- [5] L. Dong. *DSP principle and application of motor control system*. (BeiHang University Press,2007).
- [6] B.C. Xie. *Motor DSP control technology and Application* (BeiHang University Press, Chain 2005).

Analysis of Attribute Reduction of Rough Set and CNC Machine Fault Diagnosis Based on Particle Swarm

Zhuang Wu

Information College, Capital University of Economics and Business Beijing 100070, China

e-mail: wuz9080@163.com

Keywords: Particle Swarm, Rough Set, Fault Diagnosis

Abstract: After reasoning and calculation, fault diagnosis can automatically identify the causes of malfunction based on the fault symptoms, which is the core task of fault diagnosis. This paper applies the particle swarm algorithm and rough set to the fault diagnosis, and proposes fault diagnosis knowledge acquisition, rules optimization and fault identification based on rough set attribute reduction of particle swarm. Firstly, this paper introduces the rough set attribute reduction. Secondly, the particle swarm algorithm is applied to the rough set attribute reduction algorithm. Finally, the correctness and superiority of this algorithm are proved from the reduction experimental results of related data sets.

Introduction

At present, due to subjective and objective reasons in the practice of mechanical malfunction diagnosis, the judgment conditions of the diagnosis rules are redundant or incomplete with uncertainty of descriptions of the fault symptoms, which is not conducive to practical application. How to optimize the diagnostic rules and eliminate the unfavorable factors have become a new topic in the machinery industry practice and the rough set theory has laid a theoretical foundation to solve such problems. In the field of fault diagnosis of CNC machine tools, the application of rough set method can remove redundant information by extracting or optimizing the diagnostic rules from the diagnostic data or diagnostic cases and detect the key diagnostic conditions through finding the symptoms sensitive to the failure. Due to factors such as a large amount of data and multi-sample properties, the attribute reduction in rough set theory, often fail to find the smallest reduction in the limited time period. However, the swarm intelligence algorithm provides an effective way for the rough set attribute reduction. Particle swarm optimization is an important branch of the swarm intelligence algorithms and it mainly carry out a reduction iterative search by simulating the process of information exchange among biological populations to obtain the smallest reduction or a similar one. Therefore, the particle swarm algorithm applied to the rough set attribute reduction has a certain practical significance and the method of particle swarm and rough set theory is an important development direction of the CNC machine tool failure diagnosis.

Attribute Reduction of Rough Set Based on Particle Swarm

The rough set theory thinks that knowledge is an ability to classify the objects. Presumed that necessary information or knowledge of the elements in the whole domain is obtained initially, and then objects can be classified into different categories according to this knowledge. If two elements share the same information, they are indistinguishable. Indistinguishable relation is the most basic concept of the rough set theory, on which the membership and concepts of Upper and Lower Approximation will be introduced to characterize the imprecision and fuzziness [1].

Attribute Dependence and Attribute Importance

Attribute dependence is a relationship between the properties. If an attribute is regarded as a kind of knowledge reflecting certain objects, this concept will become the capacity of deriving a kind of knowledge from another one. That is to say, the attribute dependence can be seen as a measurement of knowledge dependence.

When all the concepts in Q can be defined by some certain concepts in P , then we say that Q depends on P , denoted by $P \Rightarrow Q$. When knowledge Q depends on knowledge P , we say that knowledge Q is derived from knowledge P .

Attribute dependence: supposing that $K = (U, R)$ is a knowledge base and $P, Q \subseteq R$, when $k = r(P, Q) = r_p(Q) = |POS_P(Q)|/|U|$, we say that knowledge Q depends on P ($0 \leq k \leq 1$) in degree k , which is denoted as $P \Rightarrow_k Q$. The $\|$ here represents the number of elements in the collection and the $POS_P(Q) = \bigcup_{x \in U/Q} P(x)$ is the positive domain P of Q in the domain of U .

Therefore, in the formula $k = r(P, Q) = \sum_{x \in U/Q} \frac{|P(x)|}{|U|}$, if $k = 0$, then Q is completely independent from P ; if $0 < k < 1$, then Q partially depends on P ; if $k = 1$, then Q is completely dependent on P .

Attribute Importance

The concept is to describe the importance of knowledge classification. We measure the attribute importance according to the concept of quality with approximate classification. Strictly speaking, when facing different problems, the properties show different degree of importance. The importance presented by "weight" requires prior assumptions under the conditions of auxiliary information. In the decision-making system, the association between condition attributes and decision attributes reflects the degree of importance of the condition attributes. When the condition attribute a obtains an attribute value of V_a , the number of possible values of decision attribute is capable of reflecting the importance of the condition attribute to the decision attribute. If the value of condition attribute a is V_a but there is only one possible value of decision attribute, then the condition attributes a can be uniquely mapped to this decision attribute. Therefore, the object building rules of condition attribute a with a value of V_a , do not need to consider properties of other conditions[2].

Attribute Reduction of Decision Table The decision table is a special and important class of knowledge representation system and a majority of decision-making problems can be displayed in a decision table. Let $S = (U, A, V, F)$ be an information system, then in $A = C \cup D$, $C \cap D = \varnothing$, C is the condition attributes and D is the decision attribute. An information system contains condition attributes and decision attributes is called a decision table. When the decision attribute in a decision table is unique, it is called a single decision-making; otherwise, it is known as multi-decision-making. In fact, a decision table with multiple decision attributes can transform into a single decision-making table, which is conducive to the simplification of and the solution to a problem.

Particle Swarm Algorithm and Its Application in the Attribute Reduction

Standard Particle Swarm Algorithm Suppose there are n particles in the M -dimensional search domain and they form a group. $X_i = (x_{i1}, x_{i2}, \dots, x_{im})$ is the current position of particle i , and $V_i = (v_{i1}, v_{i2}, \dots, v_{im})$ is the current flight speed of particle i . $P_i = (p_{i1}, p_{i2}, \dots, p_{im})$ is the position of most suitable applied value of particle i in the optimization process and $P_g = (p_{g1}, p_{g2}, \dots, p_{gm})$ is the optimal location of the whole particle swarm. Among them, $i = 1, 2, \dots, n$, and the particles are M -dimensional.

So, when the i th particle in generation t turns to generation $t+1$, its speed and position in j -dimensional can be described with the following iterative equation:

$$v_{ij}(t+1) = \omega \cdot v_{ij}(t) + c_1 \cdot r_1 \cdot (p_{ij}(t) - x_{ij}(t)) + c_2 \cdot r_2 \cdot (p_{gj}(t) - x_{ij}(t)) \quad (1)$$

$$x_{ij}(t+1) = x_{ij}(t) + v_{ij}(t+1) \tag{2}$$

Among them, $i=1,2,\dots,n$ and $j=1,2,\dots,m$; ω is the inertia weight; c_1 and c_2 are the acceleration constant; r_1 and r_2 are two independent and uniformly distributed random functions within $[0,1]$.

The main parameters included in the PSO algorithm are shown as follows: the inertia weight function ω , the weighting factor c_1 and c_2 , the maximum number of iterations $iter_{max}$, the maximum speed V_{max} , the population size N , the length of the particle D , the coordinates of the particles and the termination condition [3].

The inertia weight ω : Usually, the inertia weight takes a constant within $[0.8, 1.2]$, but sometimes a variable ω is needed to achieve better convergence effect of the iterative algorithm. The weighting function ω is determined by the following formula:

$$\omega = \omega_{max} - \frac{\omega_{max} - \omega_{min}}{iter_{max}} \times iter \tag{3}$$

Among the above formula, the maximum and minimum values of ω are respectively represented by ω_{max} and ω_{min} with $\omega_{max} \in [2,3]$ and $\omega_{min} \in [0.8,1.2]$. Besides, the current number of iterations and the maximum number of iterations are indicated respectively by $iter$ and $iter_{max}$ [4].

Performance Tests of the Particle Swarm Optimization Algorithm In this paper, the performance test will be carried out on three test functions that are frequently used in the literature. The first two are multimodal function while the last one is a uni-modal function with all of their optimal values equal or near the origin. x Represents a vector of a type of real number with n as its dimension and x_i is the i th element.

Let the range of the search space be $|x| < 10$, the population number of particles be 30, and the evolution of algebra be 10000.

The test results are as follows:

Griewank Function

$$f(x) = \frac{1}{4000} \sum_{i=1}^n x_i^2 - \prod_{i=1}^n \cos\left(\frac{x_i}{\sqrt{i}}\right) + 1 \tag{4}$$

Griewank Function is a multi-peak function, and its minimum value is zero. When it evolves to the 400th generation, it will gain the global minimum of 0.

Rosenbrock Function

$$f(x) = \sum_{i=1}^{n-1} [100(x_{i+1} - x_i)^2 + (1 - x_i)^2] \tag{5}$$

Rosenbrock Function is also a multi-peak function with a minimum value of 0. When it evolves to the 10,000th generation, it will gain the minimum value of 0.000176.

Rastrigrin Function

$$f(x) = \sum_{i=1}^n (x_i^2 - 10 \cos(2\pi x_i) + 10) \tag{6}$$

Rastrigrin Function is a unimodal function with a minimum value of 0. When it evolves to the 610th generation; it will gain a local minimum value of 195.5158.

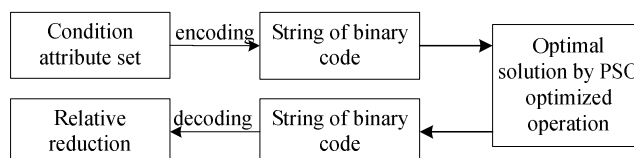


Fig. 1 The reduction conversion diagram

Decoder Design Attribute coding converts the attribute of each object to a corresponding positive integer and then obtain the particles with most suitable value through PSO algorithm, which is a relative reduction of information system S. In contrast, design of attribute decoding turns the positive integer particles into corresponding binary string of code that is a relative reduction of information system S. Relationship between them is shown in Fig. 1:

Description of the Framework of the Algorithm With reference to Fig. 1, the specific steps of the algorithm are as follows:

Input: information systems $S = (U, A, V, f)$; U is the domain; $A = C \cup D$ is a collection of properties; C and D is the condition attribute and decision attribute respectively.

Output: a relative reduction of information systems $S = (U, A, V, f)$.

Step1: randomly generate a population that contains w particles with each particle randomly given initial velocity v_0 and the initial position x_0 (x_0 is a real integer).

Step 2: round the particle position x generated through iteration into real integer, then convert it into a binary string correspondent to the attribute reduction (0 means that this attribute is not included and the vice versa takes 1). The number of bits of binary string is determined by the number of condition attributes of the information system S.

Step 3: search the corresponding fitness value for each particle. If the value exists, then it is directly taken for the particle; otherwise, turn to Step4 to calculate the fitness value;

Step4: use formula (1) to calculate the attribute dependency k_i , and calculate the number ratio of 0 in each particle (m_0^i/m). m_0 Is the number of 0 in a particle and m is the length of the particle while the fitness value of the particle $f_i = k_i + m_0^i/m$;

Step5: compare the new fitness value, current fitness value and the historical best fitness value, then determine the two extreme values of $pBest_i$ and $gBest$.

Step 6: use the formula (2), (3) to update the position of the particles x_i and its velocity v_i as well as check the range of the new position x_{i+1} and the new speed v_{i+1} to prevent the particles getting out of the maximum search range;

Step7: determine the termination condition (namely, the number of iterations). If the conditions are met, terminate the iteration; otherwise return to Step 2 to continue the cycle iterations;

Step8: convert the optimal integer to a binary string to gain the relative reduction of the attributes.

Selection and Diagnosis of Faults Features Based on the Attribute Reduction Algorithm of Rough Set of Particle Swarm

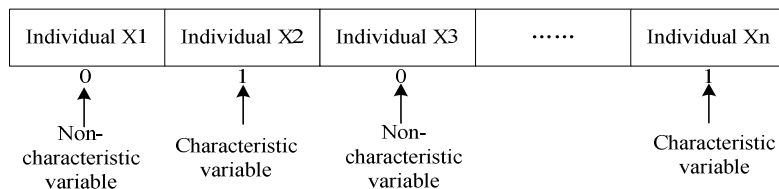


Fig. 2 Coding diagram

As the variables measured within the fault system cannot be recognized as fault-related feature variables, our objective is to find an optimal subset that contains all the related fault characteristic variables. Since the selection of fault characteristics is a combinatorial optimization problem, the particle in the optimization algorithm had better be a series of binary encoding that can express the variable information of the fault feature. Each system variable is indicated by 1 or 0. If 1 is selected, the corresponding variable is chosen as the characteristic variables; if 0 is taken, the corresponding characteristic variable is not selected.

Faults features are selected based on the attribute reduction algorithm of rough set of particle swarm and the diagram of particle encoding is shown in Fig. 2: In terms of the selection of training set and the test set in evaluation of particle adaptability, 200 sets are respectively chosen randomly

from normal data and three kinds of fault data as the training set from the primary simulating original data while 300 sets are respectively chosen randomly as the test set. The obtained data shall be first preprocessed then dimensioned and normalized before corresponding fault feature extraction and selection.

Table 1 Results of Attribute Reduction in Each Data Set

Name of the data set	Number of the attributes	record Number of the records	Number of the reduction attributes	Number of the minimum reduction attributes	The excellent rate	The running time
Vote	17	435	9	8	90	6453.751
Wine	14	178	6	5	80	1082.538
Soybean large	36	307	9	9	100	4031.657
Zoo	17	101	6	5	80	463.136
Lymphography	19	148	6	6	100	737.375
Sponge	45	76	8	8	100	417.636

The following indicators will be used to compare and measure the influence of this algorithm on the reduction performance: (1) the number of reduction attributes, (2) the excellent rate, (3) the running time

From the effect of the reduction, the algorithm can acquire a reduction on the relatively small number of attributes in all data sets, which is attributed to the larger search space of particle based on the optimization capability of the PSO algorithm.

Conclusions

In this paper, the particle swarm optimization algorithm with rough set theory is applied to the fault diagnosis knowledge acquisition, rules optimization and fault identification. Besides, the attribute reduction algorithm of rough set based on the particle swarm is put forward to enrich and improve the intelligent diagnosis technology for machinery and equipment. The experimental results show that the algorithm convergence speed and optimization capabilities have been improved, which means such combination is not only feasible and effective but also can significantly improve the diagnostic accuracy of CNC machine tool failure.

Acknowledgment

This research was supported by the Funding Project for Academic Human Resources Development in Institutions of Higher Learning Under the Jurisdiction of Beijing Municipality (No.PHR201007117), the "11th Five-Year Plan" project of Beijing Philosophy and Social Science (No.10BaJG384), the Beijing Natural Science Foundation (No.9123025), the Beijing Philosophical Social Science Project (11JGB077), the Beijing Natural Science Foundation (No. 9122003), the Special Project of Beijing Municipal Education Commission (00791154430107) and the Teaching Reform Project of Capital University of Economics and Business.

References

- [1] Mi J S, Wu W Z, Zhang W X. Approaches to knowledge reduction based on variable precision rough set model. *Information Sciences*. 2004, 159: 255-272.
- [2] Salvatore G Masahiro I, Roman S. Fuzzy rough sets and multiple-premise gradual decision rules. *International Journal of Approximate Reasoning*. 2006, 41:179-211
- [3] Ali M M, Kaelo P. Improved particle swarm algorithms for global optimization. *Applied Mathematics and Computation*, 2008, 196(2): 578-593.
- [4] Cai X J, Cui Z H, Zeng J C, Tan Y. Dispersed particle swarm optimization. *Information Processing Letters*, 2008, 105(6): 231-235.

Numerical Control Machines Performance Test Platform

Song Juan, LI Ming

Henan Mechanical and Electrical Engineering College, Henan Xinxiang 453002

Keywords: Numerical Control Machine, Performance Test Platform, Test Research

Abstract. Research on the dynamic performance testing test platform of numerical control equipment high-grade guarantee numerical control machine running reliable quality and machining, effectively predict the occurrence of equipment failure and effective, and save a lot of the cost of maintenance, improve the level of management of equipment. It has a very important significance are safe and reliable, and the production of numerical control equipment and modern scientific maintenance and management. The purpose of the research is to provide test equipment work show high-grade numerical control machine dynamic performance, another purpose of study is to provide the critical test technology, and reveals the dynamic performance of faults and development, the deterioration of the accuracy of the factors that lead.

Introduction

The prosperous development of the manufacturing industry, large numerical control machine processing the key equipment manufacturing industry, the rapid development of automation degree not satisfied, but just flexibility and integration is more, and intelligence information and network. Now, the modernization of production processing equipment and the requirements of the increasingly complex traditional numerical control machine tool cannot meet the machining precision and high quality equipment, high speed and high precision CNC machine tool is gradually becoming the leader of the modern manufacturing industry. However, the technology of the current situation of the study testing machine the process of face more challenges, so. The traditional numerical control machine processing state test system cannot meet the requirements of the modern production. Therefore, real-time, intelligence, and information dynamic testing system with high precision and consistency become the focus of research [1].

Construction Technology of Dynamic Performance Test Platform

Processing process is numerical control machine processing complex and changeable and state test and fault diagnosis of a numerical control machine will involve a lot of related technologies. A test of the construction of the platform, state test and fault diagnosis of a numerical control machine processing basically include the following four parts: equipment testing instrument, collection of data and information, the characteristics of the extraction of the base, establish a sample. Refer to the details of the Fig. 1.

To create a dynamic performance test platform to test the numerical control mechanism, must be equipped with testing instrument dynamic performance, reflected the numerical control equipment, such as laser interferometers to measure cells, and vibration, m. The running situation of the signal, including numerical control machine processing precision, vibration and noise, force and displacement, through the testing instrument collection signal and experimental samples provide reliable data for the research and development of unit monitoring technology. Performance numerical control machine tools work out these signal acquisition accuracy directly affect the success of the signal of the monitoring system.

According to the data of the effective access, the key is to build dynamic performance test platform to realize the dynamic testing nc machinery and the basis of performance, analysis and evaluation. A numerical control machine tool has large data collection capacity in the actual processing process, in this case the characteristics and attributes of the relationship between attributes can have a rule when a fault occurs. Rule is the data mining technology rules samples. Application ripper training

sort algorithm, a regular set can be the regular set can be regarded as the extraction (or) of expression; each rule number of several features rule is connected to express entry. The main contents of the sampling the ripper the method is as follows: filter in the development law, stop accelerate the stage and the cause of the process, filtering rules in the clip process, etc.

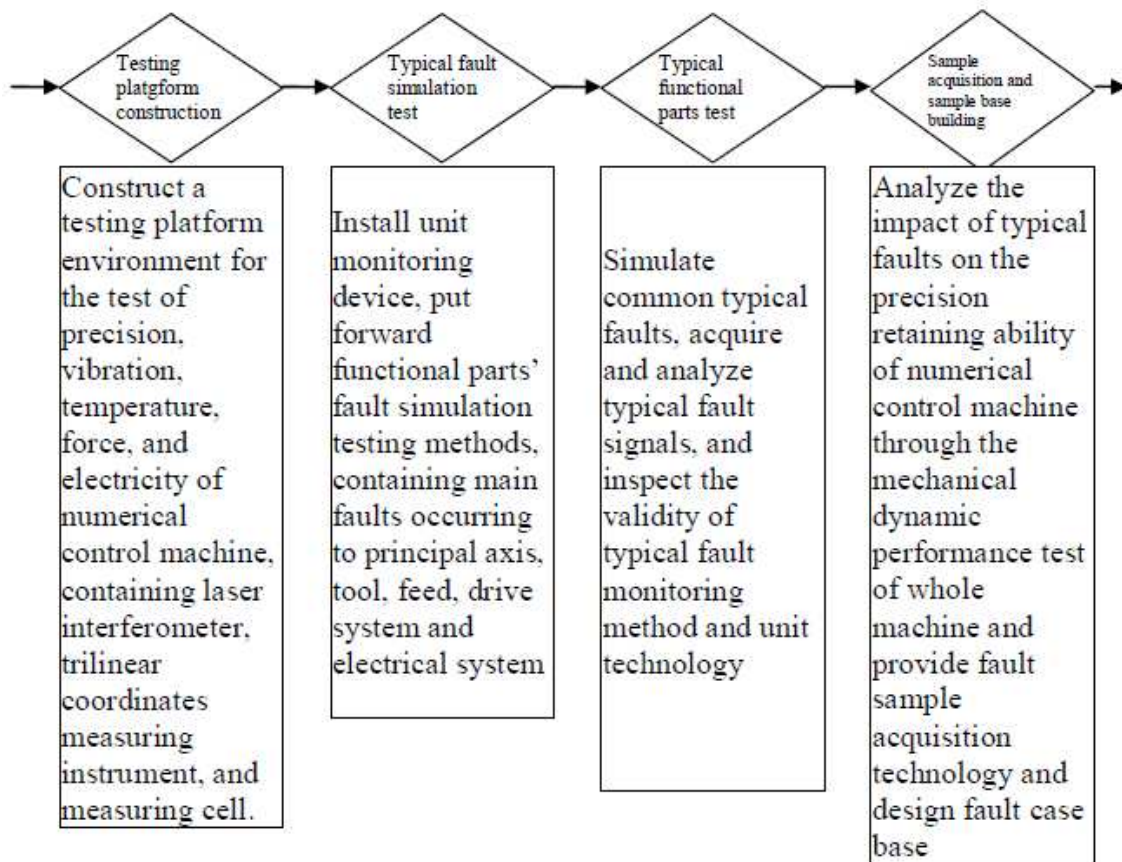


Fig. 1 Schematic Diagram of the Construction of Dynamic Performance Monitoring Platform for Typical Functional Parts of Numerical Control Machine

Purpose dynamic performance test of the numerical control machine processing is to establish a flexible, open, and reconfigurable database and knowledge base fault analysis of influence factors nc machine tools machining precision and confirm fault diagnosis and effective warning methods. Inductive analysis of the sample data acquisition and design fault samples of the sample under test data base, can realize storage and retrieval, management and maintenance of the data and samples, and help realize sample data, using data and information integration, and reconstruction base construction. Using a rough set theory based on the construction of the basic in a sample of fault samples and historic test data attributes group fault diagnosis and state prediction, as fault diagnosis and fault mode decision, and establish stable diagnosis information decision table. Application based on granularity binary matrix calculation principle and property value reduction, evaluation and attribute rules rules scope and confidence, and then establishes knowledge base of rule base and fault diagnosis and prediction. See Fig. 3 capital constructing knowledge foundation.

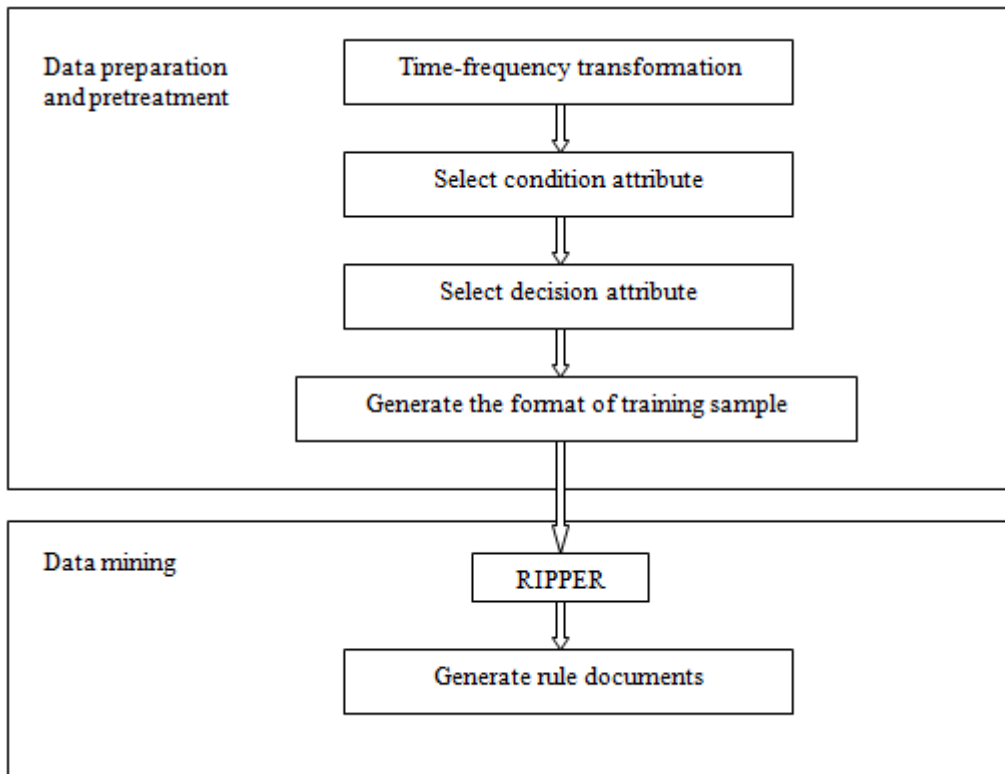


Fig. 2 Block Diagram of Sample Knowledge Acquisition Based on RIPPER

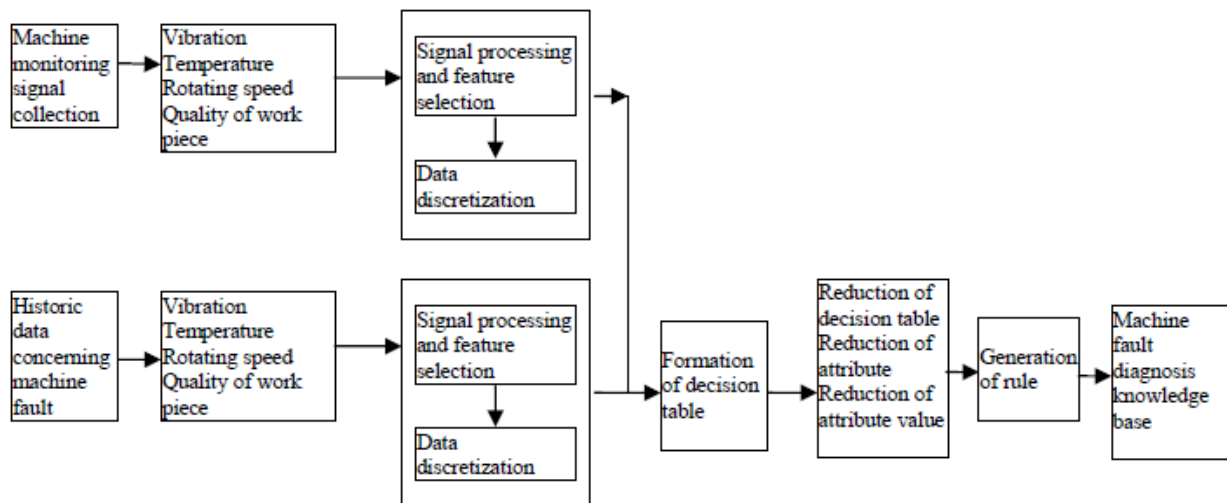


Fig. 3 Establishing Method of Sample Data Knowledge Base

Experimental Study

Taking DMC75V linear high-speed five-axis machining center as the research object, the machine is five-axis blocking high-grade machining center made in Germany, all axes of the machine point at motor drive, the acceleration is up to 2g, the rapid moving speed reaches 90m/min, and the rotating speed of electric main shaft can reach 28000rpm. Mechanical dynamic performance sample data collection system is equipped with PCI-2 acoustic emission testing system (DISP system researched and developed by American Physical Acoustics Company), 9257B piezoelectric type machining force measuring system, HG9200 intelligent signal collection and processing system, vibration noise testing and analysis system, SCM05-SCM-V8 researched by LMS (Belgium), and INV-USB high-speed data collection, analysis and treatment system researched by Beijing Dongfang Vibration Noise Research Institute. Perform dynamic performance sample data acquisition on the characteristic signals of the machine, such as displacement, speed, acceleration, amplitude of vibration, frequency and work piece stress.

Apply Belgian SCM05-SCM-V8 vibration noise testing and analysis system to the measurement and sample acquisition test of vibration condition of main axis in the practical machining process of the machine. The site is as shown in Fig. 4, 5, 6.



Fig.4 Vibration Monitoring of Machining Process



Fig. 5 Vibration Noise Testing and Analysis System



Fig. 6 Vibration Monitoring Picture

Conduct a loading test on work pieces in the machining process of the machine, adopt SwissKis+Le Company's 9257B piezoelectric type machining force measuring system to performing a loading test and sample acquisition test. The site is as shown in Fig. 7, 8.



Fig. 7 Force Sensor



Fig. 8 Data Monitoring System

Conclusion

Construction machinery dynamic performance test platform inspection sample collection and refers to the base construction concentrated in DMC75V linear five axis high-speed machining center, and equipped with of sample collection and testing system such as the machine performance and cutting force, in view of the vibration signal typical functional tool and parts of main shaft system construction, complete sampling testing system, design case base fault; Provide knowledge fault samples of database construction method.

References

- [1] Xu Xiaoli, Zhu Chunmei, Zhang Jianmin. Tend Prediction Method Based on the Largest Lyapunov Exponent for Large Rotating Machine Equipments. Journal of Beijing Institute of Technology, 2009, 18(4): 433-436
- [2] Xu Xiao-li, Chen Tao, Wang Shaohong. Research on Data-Driven Nonlinear Fault Prediction Methods in Multi-Transform Domains for Electromechanical Equipment[C]. Proceeding of the Fourth World Congress on Engineering Asset Management(WCEAM) 2009: 614-619
- [3] Xu Xiaoli, Chen Tao. ISOMAP Algorithm-based Feature Extraction for Electromechanical Equipment Fault Prediction. Proceedings of the 2009 2nd International Congress on Image and Signal Processing[C]. 2009 IEEE, 2009, 9: 4622-4625

Simulation Method for ARM Fragment Killing Ground Targets

Hong Wang¹, Yin Jun ZHAO²

¹Equipment department of Missile Institute Air Force Engineering University San Yuan Shann Xi, 713800, China

²Equipment department of Missile Institute Air Force Engineering University San Yuan Shann Xi, 713800, China

Keywords: Anti-Radiation Missile; Fragments Killing; Killing Probability; Damage Simulation

Abstract. Aiming at the characteristic that the ground complex electronic equipments are apt to be killed by fragments, and for the purpose of solving the problem about the damage data shortage of the complex equipments BDAR study, on the basis of current study production, perfected is the fragments damage probability model of the ground target, and the geometrical model describing method, the explosion rule, the fragment simulation method and the target damage simulation method are put forward. By developing the damage simulation platform, the damage simulation method's validity is affirmed.

Introduction

The ARM is one of the main means of attacking the ground radar equipments in the modern high technology war, which has the characteristic, such as fast speed and acute hitting precision. Currently much research has been carried on the ARM killing [1,2,3], which focus on the ARM killing capability, the Warhead emulation, the Warhead killing simulation method and so on, which result can be used for reference and used to instruct the complex equipments BDAR research. But as for the complicate electronic equipments, such as guidance radar, if the equipments particular structure model is not set up, the effective damage data cannot be achieved by simulation method. And if the damage data can only be gotten by experiments, which would result in the high cost and the high risk, and may be effect the combat mission. In this thesis when the experiment status on some type of guidance radar killed by ARM was considered, and it was assured that the ground targets are killed by the fragments of the ARM chiefly, the Warhead fragments killing simulation method, the equipment model method and the killing targets method are mainly analyzed. Finally the simulation system is developed, which can be taken as the damage simulation platform used to research the complicate electronic equipments BDAR.

The Damage Model of the Targets Killed By Fragments'

The fragments kill targets by mechanical penetrating capability, and the penetrating capability is affected by the initial speed, the scattering angle, the weight, the effective fragments number, the fragments killing probability and the targets characteristic apt to be killed. The study work had been done on the models above, which would not be iterated again. In the reference literature [3] the effective fragments nubmer was calculated by the equivalent area, but in this thesis the number is calculated by equivalent volume. So the damage model of the targets killed by fragementis is followed:

$$P_t = 1 - e^{-P_e n_e} \quad (1)$$

$$n_e = V_K N / V_M \quad (2)$$

Where P_i is the damage probability of the targets killed by fragments, p_i is the killing probability of single effective fragment killing target, n_e is the effective fragments number hitting the target part apt to be killed, V_K is the equivalent volume of the target part apt to be killed, V_M is the equivalent volume of the target, N is the fragments number hitting the target.

Targets Damage Simulation Method

The Equivalent Geometric Describing Model of the Targets

Any ground target almost can be equivalent to the model combination of the cuboid, the sphere, the prism and the taper. So firstly found the ground orthogonal reference frame on the basis of ground targets distribution status, and disassemble the target into some basic geometric models, then the model's geometric description can be given according to the equipments plan approximatively. After the equipments geometric models are founded, considered should be the equipment mechanical, physical and the chemic property, such as the manufacturing material, which can be equivalent to some thickness duralumin. And the mutual enveloping connection should be considered. Take the common movement disciplinarian into account, confirm the enveloping connection of the equipments, and give the enveloping equivalent duralumin thickness.

So the targets description geometric classes can be founded, which are the equipment class, the groupware class and the subassembly class. These classes can be set up by the rule of programming language. Because of the difference of the equipments, the groupware and the subassembly, such as the shape, the manufacturing material and the enveloping connection, the abstract class should be founded firstly, which can be taken as the base class to describe the common characteristics, and define the interface to describe the different geometric models as followed.

Define the interface and the abstract class:

```

Using System
Namespace Equipment
{
    Interface Cuboids
    {
        Void Parameters ()
    }
    Abstract class Target Class
    {
        Protected float equivalent-duralumin-thickness;
        Protected float frontal-duralumin- thickness;
        Public abstract void Cal Damaging (string missile type, in number missile);
    }
    Class Equipment: Target Class, Cuboids,
    {
        Float equivalent Epvolume;
        Public override Cal Damaging (string missile type, in number missile)
    {
        //Calculate the equipments damage
    }
        Public Equipment (Float Epvolume , Float _Keyvolume, int _EpParts, int _KeyParts )
    {
        //Initialize the parameters
    }
        Void Cuboids. Parameters ()
    {
        //set the parameters
    }
    }
}

```

The groupware class is similar to the equipment class, so it is unnecessary to iterate them. As for the simulation method, for the purpose of predigesting equipment structure, the subassembly is equivalent to the sphere.

The Disciplinarian of detonating the Warhead

The gesture of the Warhead and the detonating position can show the the Disciplinarian of detonating the Warhead, and the detonating position can be ascertained when the kind of the Warhead fuze is considered. Currently most of the air to ground missiles has the trigering or the radio fuze, and some of which have the two fuze. In this thesis the fragments killing is the emphasis, so only the radio fuze is taken into account. According to the fuze measure error and the Gauss distribution sample, confirm the detonating height. And on the basis of the circle probability error radius of the missiles point of hitting the targets, take the target position as the origin, and take the point of hitting the target as the circle distribution, then make the detonating surface coordinates sure according to the symmetry distribution sample. As shown in the figure 1, the Warhead gesture is ascertained by the detonating and the target corordinates, that is to say that the Warhead fuze sensitivity orientation run parallel to the line between the detonating and the target coordinates' and is consistent with the movement orientation of the missile.

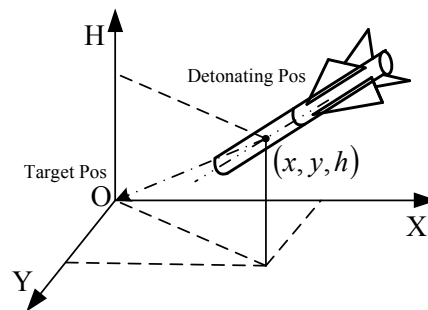


Fig. 1 Gesture of the detonated Warhead

Fragments Simulation of Warhead

The visual simulation of fragments field was studied, and the method of judging fragments killing the targets was given in the reference [4], which provide the way for studying the cooperating of the fuze and the Warhead. But the way cannot be used to deal with the problem of calculating the fragments killing, so the fragments killing is also simulated by the fore radial method here, the difference is that the simulating radial is endowed with killing kinetic energy. After the radial touches the targets, its residual kinetic energy should be confirmed, which can be used to judge its possibility of repeated killing. The mehod is followed:

According to the total fragments number n , produce n radials in the position of detonating the Warhead, and restrict the radial orientations in the fragments scattering angle and in the circle field of the Warhead taper scattering field intersecting the target surface. Then ascertain the corordinates of point of intersection by the symmetry distribution random sample, and confirm its idiographic orientation, as shown in figure 2. Because only the prefab fragments are taken into account here, the kinetic energy of every radial can be figured same, and considered is not the kinetic energy loss caused by the fly range change before the radial intersects the targets.

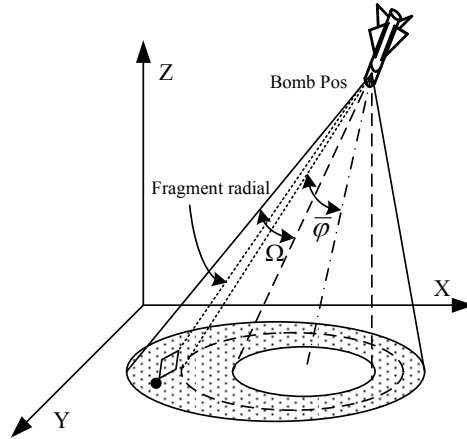


Fig. 2 The Simulation diagram of fragments radial

Targets Damage Simulation

The targets damage is simulated according to the fragments killing models, the damage models of targets killed by fragments, the geometric description models, the disciplinarian of detonating the Warhead and the fragments simulation, which is shown in the following flow chart.

The Damage Simulation Instance of Some Type of Equipment

Firstly set up the targets models of some type of guidance radar, and found the Warhead killing correlative models of some type of air to ground ARM, and then validate the simulation method according to the steps above. The simulation result data is shown in tables 1 to 4.

By analyzing the data gotten in the simulation platform, drawn is the conclusion that the killing effect can be improved by enhancing the hitting precision and the killing kinetic energy, and that the ground group equipments damage can be lessened by distributing the equipments dispersedly. As for the complicate electronic equipments, the damage probability can be reduced by protecting the key place and parts necessarily.

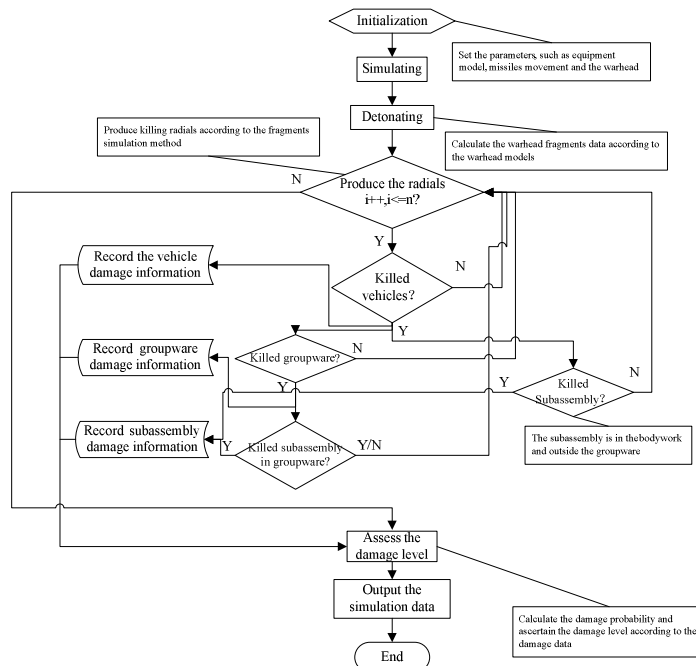


Fig. 3.The damage Simulation flow chart

Table 1 Vehicles damage data

serial number	The time	Vehicle name	Vehicle code	Killing fragnumber	Total fragnumber	remark
1	0:0:25	Power vehicle	DP-××	162	162	Plan1
2	0:0:25	Command vehicle	FA-××	2	2	Plan1
3	0:0:25	Frequency vehicle	BP-××	99	99	Plan1
⋮	⋮	⋮	⋮	⋮	⋮	⋮

Table 2 Groupware damage data

serial number	The time	groupware name	group code	Killing fragnumber
1	0:0:25	Control group	DP6P1	5
2	0:0:25	Fire group	FK1203	1
3	0:0:25	Commun group	TX1201	4
⋮	⋮	⋮	⋮	⋮

Table 3 Subassembly damage data

serial number	Vehicle name	subassembly name	subassembly code	subassembly weight	Damage probability	remark
1	Power vehicle	Frequency outfit	DP015-1	100	0.97	Plan1
2	Command vehicle	Command screen	ZH802-12	100	1	Plan1
3	Frequency vehicle	Knob switch	ZH802-15	5	0.55	Plan1
⋮	⋮	⋮	⋮	⋮	⋮	⋮

Table 4 The assessment result based on function importance limit

serial number	Vehicle name	Vehicle code	Damage level	remark
1	Power vehicle	DP-××	Large scale damage	Effect the combat mission, and need much time to repair them.
2	Command vehicle	ZH-××	Large scale damage	Effect the combat mission, and need much time to repair them.
3	Frequency vehicle	BP-××	discarded as useless	Destroyed completely, it is impossible or unnecessary to repair them.
⋮	⋮	⋮	⋮	⋮

Tag

Though much production about BDAR has been procured, the BDAR about the ground complicate electronic equipments should be researched deeply, which difficulty is that it is high cost and high risk to obtain the damage data which is the basis of the BDAR. So the impactful resolvent is urgent

need to provide the valuable damage data in battle field. The fragments killing simulation, structure model of ground electronic equipments, the killing simulation method, and the simulation platform on the basis of them, would be used to solve the problem that damage data is scarce and that it is high cost to acquire the data. The method also can support the correlative research.

References

- [1] Hua TANG, Chang wen QU. Study of Assessment Model for Anti-radiation Missile's Damage Capacity Against Ground Radar[J].Journal of Projectiles, Rockets, Missiles and Guidance, 2008, Vol.28, 104-106.
- [2] Hui YAO, Zhi feng ZHANG. Damage Calculation of fragments Warhead killing Ground battalion equipments[J].Journal of Weapon and Industry in Szechwan, 2009.9, Vol9.30, 53-56
- [3] Pei WANG, Yan jun LI. Damage Calculation and Simulation of Air to Air Missile to Target[J]. Journal of Firepower and Command and Control, 2009.12, Vol.34,53-56
- [4] Wei dong KONG, Wen jie ZHAO. Visual Simulation of Fragments Killing Field on Basis of Particle System[C]. Thesis Concourse of the Ammunition and Warhead Learning Proseminar, 2005, 334-338.
- [5] Jia Jun WANG, Shi Cai LI. Study Summarization of Explosion Domino Effect about Unitary Blast-fragmentation Warhead. 107-115.
- [6] Yi Chun PAN, Li CHEN. Damage Standard Reseach of Ground-based Equipment by Blast-fragmentation Warhead. Journal of Projectiles, Rockets, Missiles and Guidance, 2010.4,Vol.30,145-148

Nonlinear Adaptive Observer-Based Fault Diagnosis for Satellite Actuator

Zhi Wang

Computer Science and Engineering College, Xi'an Technological University, Xi'an 710032, China
zhi_wang_xa@163.com

Keywords: Satellite Actuator, Structural Failure, Fault Diagnosis, Nonlinear System, Adaptive Observer.

Abstract. This paper studies the multi-structural fault mode of satellite actuators, and use numbers of unknown parameters as fault indicators. The problem of adaptive state observer design for nonlinear systems with unknown parameters is dealt with by applying Lypunov method. The nonlinear object is firstly linearized into Lipschitz system, and then by analyzing the sufficient condition for asymptotic convergence of the observer, the structure of observer and the adaptive laws for parameter estimation are given. Finally, the adaptive observer is employed to estimate the faults of satellite actuator. Numerical simulation results show that this method is effective and able to quickly detect faults.

Introduction

The attitude control system is one of the most complex sub-systems of satellite, and has very high probability of failure. According to a survey in literature [1], the faults that occur in this sub-system account for more than 30% of all satellite faults. Since the existence of rotating parts, the flywheels are the highest incidence of fault of attitude control components. In recent years, some achievements have been made in the field of fault diagnosis for satellite actuator. In literature [2], the method of fault detection and diagnosis for satellite reaction wheels is proposed, which uses state space approximation to study neural network fault recognition with nonlinear parameter. The literature [3] employs a set of detection filters to detect the faults of satellite reaction wheels. In addition, fault diagnoses based on expert systems have also been widely studied.

In the field of fault diagnosis, adaptive technology is widely valued and applied, which the advantage of is that the adaptive observer can provide information about fault estimation that can be further used into fault-tolerant control. In literature [4,6], adaptive observers and the corresponding fault diagnosis strategies are applied to the non-linear systems which the whole state of can be measured. However, the widespread defects in the literatures are that the convergence of parameter estimation is not guaranteed and the thresholds for fault isolation are designed to be too conservative. In literature [7,10], a more general class of Lipschitz nonlinear systems are studied, and the corresponding adaptive observers are designed. The literature [8] proposes a new adaptive observer design method for Lipschitz nonlinear systems with unknown parameters, which the inadequacy of is that the unknown parameter items are limited to a certain special form, and the conclusions about convergence of parameter estimation are also not perfect.

Based on the observer design in literature [9,10] for nonlinear systems with Lipschitz linearization errors, this paper studies the adaptive observer design for nonlinear systems with unknown parameters, and applies it to the fault diagnosis of satellite actuator.

Satellite Model and Fault Mode

When the servo is three-orthogonal-flywheel, the kinematics and dynamic equation of satellite are described as follows

$$\dot{q}(t) = \frac{1}{2}(q'(t) + q_0(t)E)\omega(t) \quad (1)$$

$$\dot{q}_0(t) = -\frac{1}{2}q^T(t)\omega(t) \quad (2)$$

$$I\dot{\omega}(t) + \omega(t) \times (I\omega(t) + J\omega_f(t)) = U(t) \quad (3)$$

Where $q \in R^3$, $q_0 \in R$ denote quaternion vector and $q_0^2 + q^T q = 1$; q' is the skew symmetric matrix of q , E is unit matrix; $I \in R^3 \times R^3$ ($Kg \cdot m^2$) is the total moment of inertia matrix of satellite, $\omega \in R^3$ (rad/s) is its inertial angular velocity vector, $U \in R^3$ ($N \cdot m$) is the control torque acting on satellite, $J \in R^3 \times R^3$ ($Kg \cdot m^2$) is the moment of inertia matrix of flywheel, $\omega_f \in R^3$ (rad/s) is its angular velocity vector. Then, the state equation and observation equation of satellite attitude control system can be denoted as follows

$$\dot{x}(t) = f(x(t)) + BU(t) \quad (4)$$

$$y(t) = Cx(t) \quad (5)$$

As long continuous mechanical movement, the flywheels are the highest incidence of fault of attitude control components. When the actuators of satellite go wrong, the fault mode can be described as follows

$$U_i'(t) = \alpha_i(t)U_i(t) + \beta_i(t) \quad (6)$$

Where $\alpha_i(t)$ is the gain fault indicator of the i th flywheel, $\beta_i(t)$ is the bias-type fault indicator; $\alpha_i(t) \neq 1$ will mean that the gain fault occurs, $\beta_i(t) \neq 0$ will mean that the bias-type fault occurs. Then, the fault system can be expressed as

$$\dot{x}(t) = f(x(t)) + BU''(t)\theta(t) \quad (7)$$

$$y(t) = Cx(t) \quad (8)$$

Where $U''(t) \in R^3 \times R^6$, $\theta(t) = [\alpha_1(t), \beta_1(t), -\alpha_2(t), \beta_2(t), \alpha_3(t), \beta_3(t)]^T$.

The goal of this paper is to design an adaptive observer, and using it to estimate system states and fault parameters, and to ensure the convergence of estimates.

Observer Structure Design

The nonlinear state equation (9) is linearized near the estimate value $(\hat{x}, \hat{\theta})$ as follows

$$f(x) + BU''\theta - (f(\hat{x}) + BU''\hat{\theta}) = A(t)(x - \hat{x}) + BU''(\theta - \hat{\theta}) + \varphi(x, \hat{x}, t) \quad (9)$$

Where $A(t) = \frac{\partial f}{\partial x} \Big|_{\hat{x}}$. As the satellite attitude control system generally works in relatively small attitude angle, so the linearization error satisfies Lipschitz condition, i.e.

$$\|\varphi(x, \hat{x}, t)\|_2 \leq \gamma \|x - \hat{x}\|_2, \quad \gamma > 0 \quad (10)$$

Assumption: The time-varying system $(A(t), C)$ is uniformly observable, and the θ is the unknown constant parameter vector, i.e., $\dot{\theta} = 0$.

The Assumption is the basic condition to construct an adaptive observer. Inspired by literature [9, 11], the following adaptive observer is designed

$$\begin{cases} \dot{\hat{x}} = f(\hat{x}) + BU''\hat{\theta} + L(t)(y - C\hat{x}) + \Upsilon(t)\hat{\theta} \\ \dot{\hat{\theta}} = \Gamma\Upsilon^T C^T (y - C\hat{x}) \\ \dot{\Upsilon} = (A - LC)\Upsilon + BU'' \end{cases} \quad (11)$$

Where $\Gamma \in R^6 \times R^6$ is a symmetric positive definite matrix, $\Upsilon(t) \in R^3 \times R^6$ is a signal matrix; the feedback matrix $L(t)$ makes the system $(A - LC)$ is stable, which will be designed below; as the $BU''(t)$ is persistently exciting, so that exist positive constants χ, σ and T such that, for all t , the following inequalities hold

$$\chi I \leq \int_t^{t+T} \Upsilon^T C^T C \Upsilon dt \leq \sigma I \quad (12)$$

So $\Upsilon(t)$ is uniformly bounded. The equation (12) is typically required for system identification.

From (9) and (11), the estimation error dynamics are then seen to be given by

$$\begin{cases} \dot{e} = (A - LC)e + \varphi(x, \hat{x}, t) \\ \dot{\tilde{\theta}} = -\Gamma\Upsilon^T C^T C (e + \Upsilon\tilde{\theta}) \end{cases} \quad (13)$$

Where $\tilde{x} = x - \hat{x}$, $\tilde{\theta} = \theta - \hat{\theta}$, $e = \tilde{x} - \Upsilon\tilde{\theta}$

Parameter Design and Convergence Proof

The core task of this section is to design the feedback matrix $L(t)$ and the learning rate Γ , and to prove the observer (7) is uniformly asymptotically stable.

For simplicity, the learning rate is taken as $\Gamma = \lambda I$ ($\lambda > 0$), and the feedback matrix $L(t)$ is determined by the following Riccati equations

$$\dot{P}(t) = A(t)P(t) + P(t)A^T(t) - P(t)(\lambda C^T C - \mu^2 I)P(t) + I \quad (14)$$

$$L(t) = \lambda P(t)C^T \quad (15)$$

Lemma1: The feedback matrix $L(t)$ determined by the equations (14), (15) will ensure the system $\dot{z} = (A - LC)z$ is exponentially stable.

Proof: Consider the Lyapunov function candidate $V = z^T P^{-1}z$, use equations (14) and (15), the derivative of V is

$$\begin{aligned} \dot{V} &= \dot{z}^T P^{-1}z + z^T \dot{P}^{-1}z + z^T P^{-1}\dot{z} = \dot{z}^T P^{-1}z - z^T P^{-1}\dot{P}P^{-1}z + z^T P^{-1}\dot{z} \\ &= -z^T (\lambda C^T C + \mu^2 I + P^{-1}\dot{P}P^{-1})z < 0 \end{aligned} \quad (16)$$

The system $\dot{z} = (A - LC)z$ is exponentially stable.

Lemma2: Suppose there is a constant $\varepsilon > 0$ and make $\int_0^\infty \tilde{\theta}^T \Upsilon^T C^T C \Upsilon \tilde{\theta} \geq \varepsilon \int_0^\infty \tilde{\theta}^T \tilde{\theta}$, i.e., $\|C \Upsilon \tilde{\theta}\|_2^2 \geq \varepsilon \|\tilde{\theta}\|_2^2$. If the parameters λ, μ in equation (10) satisfy

$$\mu > \gamma, \lambda \varepsilon \geq \mu^2 \quad (13)$$

Then the adaptive observer (7) is uniformly asymptotically stable.

Proof: Consider the Lyapunov function candidate $V = e^T P^{-1} e + \tilde{\theta}^T \tilde{\theta}$, use equations (7), (9), (10) and (11), the derivative of V is

$$\begin{aligned} \dot{V} &= e^T P^{-1} e + \tilde{\theta}^T \tilde{\theta} = -e^T (\lambda C^T C + \mu^2 I + P^{-1} P^{-1}) e + 2e^T P^{-1} \varphi - 2\lambda \tilde{\theta}^T \Upsilon^T C^T C \Upsilon \tilde{\theta} - 2\lambda \tilde{\theta}^T \Upsilon^T C^T C e \\ &= -\mu^2 e^T e - \lambda \tilde{\theta}^T \Upsilon^T C^T C \Upsilon \tilde{\theta} - \lambda \|C e + C \Upsilon \tilde{\theta}\|_2^2 - \|P^{-1} e - \varphi\|_2^2 + \varphi^T \varphi \\ &\leq -\mu^2 \|e\|_2^2 - \lambda \|C \Upsilon \tilde{\theta}\|_2^2 + \|\varphi\|_2^2 \leq -\mu^2 \|e\|_2^2 - \lambda \varepsilon \|\tilde{\theta}\|_2^2 + \|\varphi\|_2^2 \leq -\mu^2 (\|e\|_2^2 + \|\tilde{\theta}\|_2^2) + \|\varphi\|_2^2 \end{aligned} \quad (14)$$

From the Lipschitz inequality (6), we get

$$\|\varphi\|_2^2 \leq \gamma^2 (\|e\|_2^2 + \|\tilde{\theta}\|_2^2) \quad (15)$$

Substitute (15) into (14) and consider (13), we obtain $\dot{V} < 0$. So the adaptive observer (7) is uniformly asymptotically stable.

Numerical Simulation and Conclusions

The main physical parameters of a satellite are given as follows

$$I = [5247.97, -230.52, 115.30; -230.52, 5110.05, 41.11; 115.30, 41.11, 4142.48]$$

It is assumed that, during the adjustment process of satellite attitudes, several of its flywheels go wrong in uncertain times. The initial and desired values of attitudes are respectively

$$\begin{cases} [\varphi(0), \phi(0), \psi(0)]^T = [2^\circ, 1^\circ, 1^\circ]^T & [\varphi_d, \phi_d, \psi_d]^T = [0^\circ, 0^\circ, 0^\circ]^T \\ \omega(0) = [0.06, -0.02, 0.04]^T (\circ/s) & \omega_d(\infty) = [0, 0, 0]^T (\circ/s) \end{cases}$$

And the fault modes are set as follows

$$\alpha_1 = \begin{cases} 1, & t < 20s \\ 1.1, & 20s \leq t \leq 50 \end{cases}, \beta_2 = \begin{cases} 0N \cdot m, & t < 30s \\ 0.15N \cdot m, & 30s \leq t \leq 50 \end{cases}, \beta_3 = \begin{cases} 0N \cdot m, & t < 20s \\ 0.1N \cdot m, & 20s \leq t \leq 35 \\ 0.1 \cdot (t - 5) / 30 N \cdot m, & 35s \leq t \leq 50 \end{cases}$$

A given task is to estimate directly the fault parameters by a well-designed adaptive observer. At the same time the accuracy and speed of estimates should be ensured. For the simulations, we insert $A(t)$ and C into the Riccati differential equation (14). The feedback matrix $L(t)$ is given by (11), and the differential equation for the observer by (11). The relevant parameters are chosen as follows.

Lipschitz constant $\gamma = 0.25$. The learning rate $\lambda = 3$; $\mu = 0.5$

We solve the state differential equations numerically by the Runge–Kutta method. The simulation results are shown in Figures 1 through 3.

In the simulation, in a certain period of time, several actuator faults occur simultaneously. The simulation results show that the proposed adaptive observer can estimate directly the fault values with higher accuracy and faster speed. Worthy of note is that, in the design of adaptive observer, we declare in advance $\hat{\theta} = 0$; however, it can still be seen from Figure 3 that this diagnosis is applicable not only to jump type faults, and can be used for the detection of slowly developing faults.

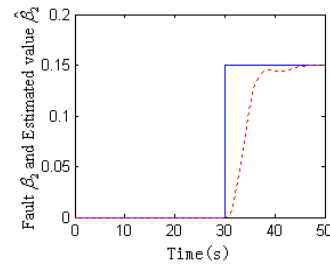
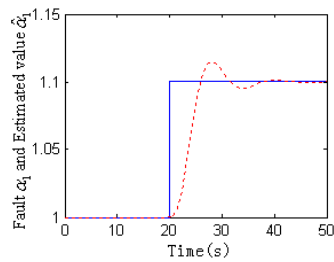


Fig. 1 The fault estimation of first actuator (gain fault) Fig. 2 The fault estimation of second actuator (bias-type fault)

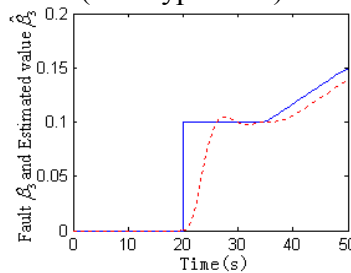


Fig. 3 The fault estimation of third actuator (bias-type fault)

References

- [1] Mak Tafazoli. A study of on-orbit spacecraft failures [J]. *Acta Astronautica*, Vol.64:195~205 (2009)
- [2] HA Talebi, RV Patel, K Khorasani. Fault detection and isolation for uncertain nonlinear systems with application to a satellite reaction wheel actuator[C]. *Systems, Man, and Cybernetics*, P.3140-3145 (2007)
- [3] N Meskin, K Khorasani. Fault detection and isolation in a redundant reaction wheels configuration of a satellite[C]. *Systems, Man, and Cybernetics*, P. 3153-3158(2007)
- [4] Trunov A B, Polycarpou M M. Automated fault diagnosis in nonlinear Multivariable systems using a learning methodology. *IEEE Transactions on neural networks*, Vol.11:91~101(2000)
- [5] Polycarpou M M, Trunov A B. Learning approach to nonlinear fault diagnosis: detectability analysis. *IEEE Transactions on Automatic Control*, Vol.45:806~812(2000)
- [6] Zhang X D, Polycarpou M M, Parisini T. A robust detection and isolation scheme for abrupt and incipient faults in nonlinear systems. *IEEE Transactions on Automatic Control*, Vol.47:576~592(2002)
- [7] Rajamani R. Observers for Lipschitz Nonlinear Systems. *IEEE Transactions on Automatic Control*, Vol. 43:397~401(1998)
- [8] Cho Y M, Rajamani R. A systematic approach to adaptive observer synthesis for nonlinear systems. *IEEE Transactions on Automatic Control*, Vol.42:534~537(1997)
- [9] Reif K, Sonnemann F, Unbehauen R. Nonlinear state observation using H-inf filtering Riccati design. *IEEE Transactions on Automatic Control*, Vol.44:203~208(1999).
- [10] Li Ling-lai. Robust fault diagnosis of nonlinear systems. Ph.D. Dissertation, Tsinghua University (2006).
- [11] Zhang Q H. Adaptive observer for multiple-input-multiple-output (MIMO) linear time-varying systems. *IEEE Transactions on Automatic Control*, Vol. 47:525~529(2002)

An Acoustic Source Localization Method Based on Equal Distances Multi- sensors Array

Xingwang Wang^{1, a}, Bingyi Sun^{1, a}, Bin Li^{1, a}, * Lili HE^{1, 2, a}, Chengquan Hu^{1, 2, a}

¹College of Computer Science and Technology, Jilin University, 130012, China;

²Key Laboratory of Symbolic Computation and Knowledge Engineering of Ministry of Education, Jilin University, 130012, China

^a helili@jlu.edu.cn

Keywords: Acoustic Source Localization, Linear Intersection, Multi-Sensors Array

Abstract. The traditional acoustic source is sensitive to time. A novel sound source location method using linear intersection spacing multi-sensors array is provided in this paper. Each array is composed of three spaced nodes, and least squares method is used to calculate the final position according to ternary array results. Multi-arrays method is more robust than the ternary one, and much wider scope is covered. Location scope extends from 120m to 800m when the relative positioning error is 10%. A multi-array group based on linear intersection sound source localization method is provided in this paper too. Experiment results show that the proposed method has higher precision on angle locating than distance locating.

Introduction

Acoustic source localization technology is widely used in civilian areas [1, 2]. Most of the sound source method is relatively accurate which mainly use three physical measurements, that is, the energy intensity of received sound signal, direction of arrival (DOA) and the time difference of arrival (TDOA) of sound signal, to calculate the location of the sound source. Sheng and Kitakoga proposed an energy attenuation model of sound propagation which uses the maximum likelihood method (MLE) to locate the sound source and meanwhile, reduces the calculation of MLE by importing the EM (Expectation-Maximization) algorithm[3,4]; Asano et al. proposed the near-field two-dimensional MUSIC algorithm based on microphone array, it evaluates the azimuth and distance of the arrived sound to locate the sound source[5]; Ajdler and Knapp et al. calculated the location of sound source by evaluating the time difference of TDOA, when sound signal reaches multiple sensor nodes and combining it with location information of sensor nodes[6,7]. The above method requires the sensor nodes to capture the sound information accurately, and information must assemble at the sink node to commit centralized computing which needs heavy computation, making it difficult to achieve a real-time locating of moving sound source.

For sound source locating under water, G. Clifford analyzed the ternary array locating method which requires simple computation [8]. The method is only suitable for array whose gap between array elements is large, so when the ratio of gap between array elements against the distance between sound source and array is small, it will cause calculation failure due to time deviation generated by sound propagation in inhomogeneous media, imprecise time service, etc. Michael et al. analyzed a linear intersection method to locating sound source [9]. The method is aimed at locating sound source indoor which cannot meet the needs of large-scale locating outdoor. LEE et al propose a k-means clustering algorithm for unknown number of clusters and applied it to sound source localization for multi-source sound localization and achieved satisfying results [10].

In this paper, a linear intersection locating method suitable for the Cartesian coordinate system is proposed; a multi-arrays locating method is designed for the poor robustness problem of ternary array when the ratio of gap between array element against the distance between sound source and array; to solve the problem that the ratio of locating radius of multiple arrays against gap between array elements is small, a multi-array groups of arrays locating method is proposed. The experiment analyses the rationality and effectiveness of linear crossover locating method, multi-arrays locating method and multi-array groups.

Sound Source Locating Of Ternary Array in a Cartesian coordinate system

We assume that the sound source is located at $S(x, y)$, the three array element nodes in the same line is, respectively, $A(x_A, y_A)$, $B(x_B, y_B)$, $C(x_C, y_C)$ the gap between array element nodes is d . We assume that sound speed is c , it takes, respectively, $T_A T_B T_C$ for sound to travel from S to $A B C$. The time difference of arrival between A and B are $\Delta t_{AB} = T_A - T_B$, the time difference of arrival between C and B is $\Delta t_{CB} = T_C - T_B$, angle θ is the azimuth of the sound source.

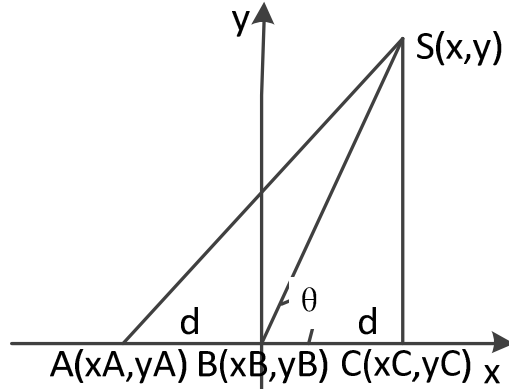


Figure 1: Ternary array locating principle

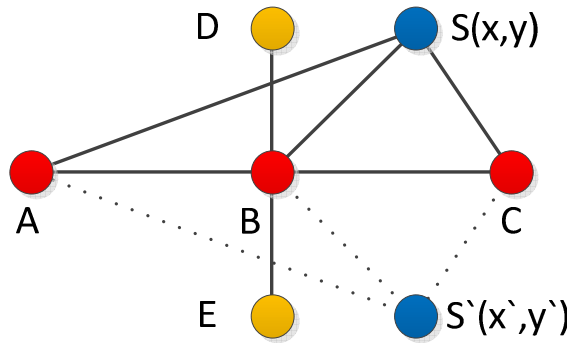


Figure 2: Ternary array locating orientation decision

$$\text{We can get: } x = \frac{(c^2 \Delta t_{AB} \Delta t_{CB} + d^2)(\Delta t_{AB} - \Delta t_{CB})}{2d(\Delta t_{AB} + \Delta t_{CB})} \tag{1}$$

$$y = \sqrt{\left(\frac{2d^2 - c^2(\Delta t_{AB}^2 + \Delta t_{CB}^2)}{2c(\Delta t_{AB} + \Delta t_{CB})}\right)^2 - x^2} \tag{2}$$

We will get two opposite sign values to the same solution. We can determine the sign of y by add two sensor nodes on the basis of the ternary array. D And E are auxiliary sensors helping judge the direction of sound (D is far from E so that the time deviation between D and E impacts less on the direction of the sound source). When the speed of sound is constant, we can see by the geometric relationship: if the sound signal reaches D earlier than E , then sound signal is above ABC (the side of the point D), and vice versa.

Sound source locating of multi-array in a Cartesian coordinate system

As a result of sound propagation in the air is influenced by the wind, and temperature, and the timing is not accurate synchronization, may cause the sound arrival time has a big deviation than the nodes displaying, so the calculation results of contradiction cause the failure. For example: if the measured

sound arriving at the node *A* and the node *B* time has the time difference $\Delta t_{AB} < 0$, the sound arriving at the node *C* and the node *B* has the time difference $\Delta t_{CB} < 0$. By $\Delta t_{AB} < 0$ knowing the sound source is located near the perpendicular bisector of the node *A* and the node *B* close to *C* side; and by $\Delta t_{CB} < 0$ knowing the sound source is located near the perpendicular bisector of the node *B* and the node *C* close to *C* side, so the sound source locates in the both sides of the perpendicular bisector of the node *A* and the node *C*, conflict, so failure.

Calculation of the contradiction is generally made by a few nodes producing bigger time deviation. Multi-array can solve the failure problem which is result by a few nodes' error: in multi-array, arbitrary equidistant three nodes compose a three element array; assuming there are $m+2$ nodes (*M* element array, 2 auxiliary nodes), so there is a total of three element array. Since most nodes time deviation is small, and only a few groups have calculation failure, most grouping calculation results is effective. Every three element array respectively calculates the location of a sound source, recording all the effective results and the coordinates of three element array center node. Assuming that the *I* effective three element array calculates the location of a sound source for $S_i(x_i, y_i)$ the central node coordinate is $B_i(x_{B_i}, y_{B_i}) (n > i > 0)$, so we can obtain the linear $S_i B_i$ equation, simultaneous available equations 3:

By the method of linear least squares, the solution of the equations is the point which has the shortest distance arriving all the linear. Because all of the separate calculation of sound source position has a certain error, using the least squares to get the sound source position is generally relatively accurate sound source position $S'(x', y')$

$$\begin{aligned}
 (y_{B_1} - y_1)x - (x_{B_1} - x_1)y &= (y_{B_1} - y_1)x_1 - (x_{B_1} - x_1)y_1 \\
 (y_{B_2} - y_2)x - (x_{B_2} - x_2)y &= (y_{B_2} - y_2)x_2 - (x_{B_2} - x_2)y_2 \\
 \vdots \\
 (y_{B_n} - y_n)x - (x_{B_n} - x_n)y &= (y_{B_n} - y_n)x_n - (x_{B_n} - x_n)y_n
 \end{aligned}
 \tag{3}$$

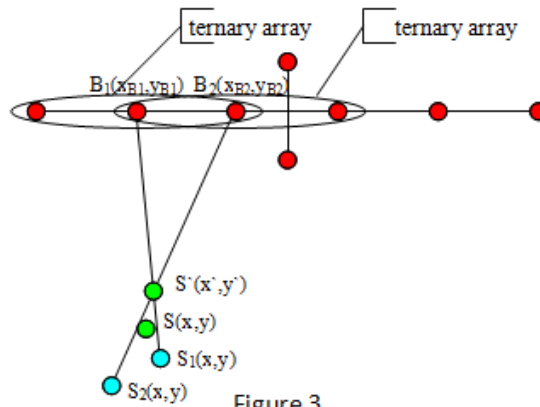


Figure 3
Multiple arrays locate principle diagram

Sound source locating of multi-array group in a Cartesian coordinate system

When the array element spacing small (less than 1m), the range of multi-array can accurate positioning (distance deviation was less than 10%) is small. and when the angle of the connection of sound source and the center of the array and the straight line where the array in is small (less than 30 degrees), the positioning distance deviation is big.

In accordance with the principle of multi-array positioning, through place many multi-arrays separately computing the sound source location, this addition to the minority position to calculate the presence of errors the sound source is at most one, then using the least squares method can calculate a more accurate source position.

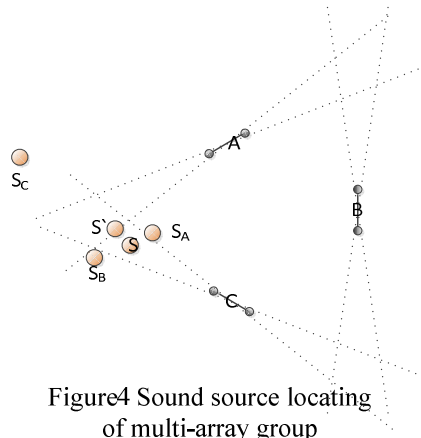


Figure4 Sound source locating of multi-array group

Assume S is the location of the sound source, A, B, and C is the three multi-arrays. In Fig. 4 the angle between each dotted line and the straight line where the multi-array in is 15 degree, the sound source is positioned within the dotted line angle will cause large errors. SA, SB, SC, are the sound source locations calculated by the multi-arrays A, B, and C. Due to the smaller angle of the connection of sound source and the center of the array and the straight line where the array in, the deviation of the location where the sound source is calculated by multi-array C is big, the position S' is the result calculated with the least squares method and the distance deviation is small.

Simulation

Case I: now many devices, such as GPS makes the time synchronization accuracy of $1\mu s$, so accepted by the sensors in the simulation to introduce random $-1 - 1\mu s$ time bias, the simulation results as shown below Fig. 5, picture a shows the ternary array positioning simulation, the gap between array elements is 1m, The picture b shows a multi-array locating simulation, this multi-array has six elements whose gap between the array element is 1m, The picture c shows the positioning simulation of multi-array group which comprised of four multi-arrays, and each multi-array contain six nodes with the 1m gap between the array elements. And isolated 100m four arrays were cross with the x axis and y axis coincides.

One can be seen from case I, when there is a certain time deviation and the space between array elements is small: ternary arrays, precise locating area is small, multi-arrays greatly improved the locating place than the ternary arrays, and the group of multi-array positioning range can cover almost $10000 * 10000$ region of the plane.

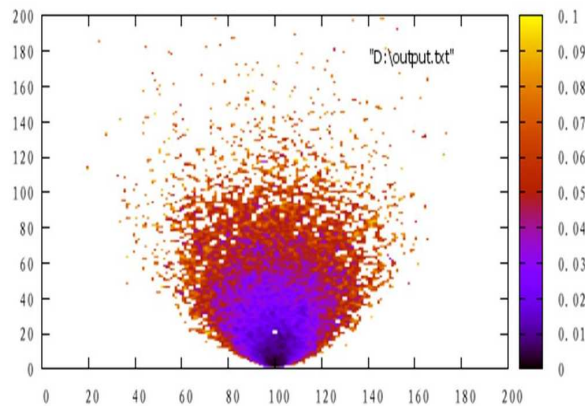


Fig. 5a: Sound source simulation locating of ternary array

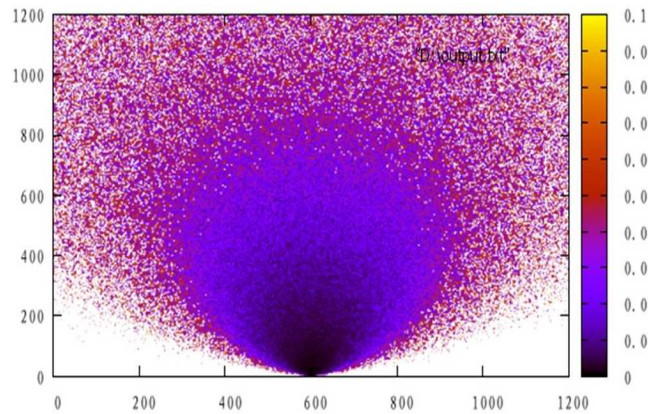


Fig. 5b: Sound source simulation locating of multi-array

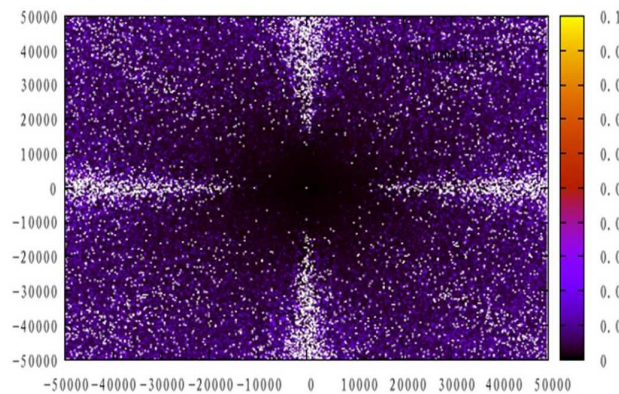


Fig. 5c: Sound source simulation locating of multi-array group

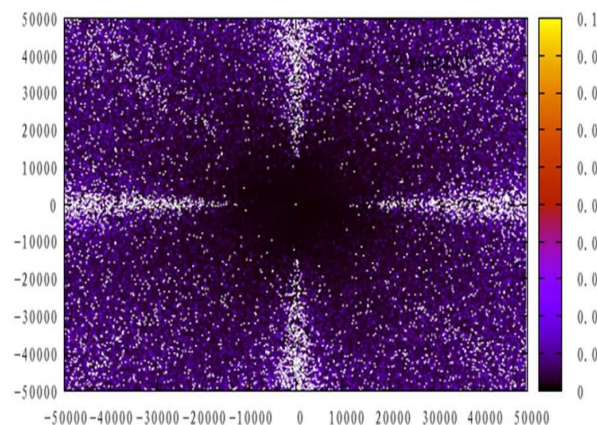


Fig. 6: Sound source simulation locating of multi-array group

Case II: now between the two objects mutually positioning through GPS and other devices to make the distance error within 3m, and by the direction of error in the magnetic compass and other equipment within 1 degree. Therefore, in this simulation, accepted by the sensors in the simulation to introduce random $-1 - 1\mu\text{s}$ time bias, and the distance between the array import about 1m deviation (the left side of the array shifted to the right 0.8m, down 0.6m; the upside array left shift 1.1m, Move 0.3m). The angle of multi-array import about 1 degree deviation (the downside array compared with the original along the clockwise rotation of 0.6 degrees, the right side of the array along the counterclockwise rotation of 0.8 degrees), the statistical relative error of less than 10 % of the number of source station about 97.5% of the total number of enumeration. The results are as follows in Fig. 6.

As can be seen from Case II, when locate the sound source position, there is no significant differences exist between the situation which only exist time error and the situation which has time error and position error.

Conclusion

The proposed method is fit for the needs of real-time positioning of the sound source. Detection scope ranges according to the array number and array element number. Similarly, the proposed method has higher precision on angle locating than distance locating.

Acknowledgements

This work is funded by Special funds for basic research and operating expenses under Grant No201103134, Innovation Experiment Program for Jilin University under Grant No2011B53129.

References

- [1] X.F.LI, H. Liu. A survey of sound source localization for robot audition, CAAI Transactions on Intelligent Systems, vol 7(1) (2012), p1-11.
- [2] SUN Hao, YANG Peng, LIU Zuojun, et al. Microphone array based auditory localization for rescue robot. Chinese Control and Decision Conference. Taiyuan, China (2011).
- [3] X.H.SHENG, Y.H HU. Maximum likelihood multiple-source localization using acoustic energy measurements with wireless sensor networks. IEEE Transactions on Signal Processing, vol 53 (1) (2005), p. 44~53.
- [4] N. KITAKOGA, T.OHTSUKI. Distributed em algorithms for acoustic source localization in sensor networks. IEEE Vehicular Technology Conference (2006).
- [5] F. ASANO, H. ASOH, and T. MATSUI. Sound source localization and separation in near field. IEICE Transactions on Fundamentals of Electronics, E83-A(11)(2000), p. 2286-2294.
- [6] T. AJDLER, I. KOZINTSEV, and R. LIENHART et al. Acoustic source localization in distributed sensor networks. Conference Record -Asilomar Conference on Signals, Systems and Computers, vol 2(2004), p1328-1332.
- [7] C.H. KNAPP, G.C.CARTER. The generalized correlation method for estimation of time delay. IEEE Transactions on Acoustics, Speech and Signal Processing, vol 24(4) (1976), 320-327.
- [8] G.C. CARTER. Time Delay Estimation for passive sonar signal Processing. IEEE Transactions on Acoustics, Speech and Signal Processing, ASSP-29(3)(1981), p. 463-470.
- [9] M.S.BRANDSTEIN, J.E.BRANDSTEIN, and Silverman H.F. A closed-form location estimator for use with room environment microphone arrays. IEEE Transactions on Acoustics, Speech and Audio Processing, vol 5(1)(1997) p.45-50.
- [10] B. LEE , J.S. CHOI. Multi-source sound localization using the competitive K-means clustering. IEEE Conference on Emerging Technologies and Factory Automation. Bilbao, Spain(2010).p.1-7.

Research on Wideband Guiding System Receiving Technology

Yongli Chen^{1, a}, Shuyong Lv^{1, b}

¹Department of Electrical Engineering, Jiyuan Vocational and Technical College,
Henan Jiyuan 459000, China

^ach_yongli@126.com, ^blv_shuyong@126.com

Keywords: Ultra -high speed data acquisition, Band -pass sampling, Time -interleaved parallel sampling, FFT spectrum analysis

Abstract. The ultra-high speed data acquisition system is introduced, which has sampling rate of 3GSPS. The design scheme of hardware circuit is given in condition to analyze the theory and technology of signal sampling. The design of the main part circuit is described. The module of serial -parallel conversion and FFT spectrum analysis are designed in software realization. The system has strong commonality because of application of the ADC + FPGA + DSP framework.

Introductions

With the rapid development of electronic technology, data acquisition systems are widely used, especially in the field of software defined radio applications, and with the innovation of high-speed analog-digital converter, data acquisition systems of signal sampling frequency is getting higher and higher[1]. For broadband and ultra-wideband radar signals, the signal bandwidth is up to several hundred megahertz. At the same time, under the conditions of ensuring signal band-pass sampling, it requires sampling frequency of the data acquisition system at least greater than or equal to two times the signal bandwidth, which means that the sampling rate of the data acquisition system up to GSPS. At present, some foreign companies launched the sampling rates of up to GSPS products, for example, the VMETRO company launched the ultra-high-speed data acquisition system sampling rate can be achieved 1.5GSPS; the sampling rate of LNX company's RX00103-005 is 2GSPS, resolution is 10bit[2].

This paper designs an ultra-high-speed data acquisition and analysis system, the system rates are up to 3 GSPS, high-performance FPGA and DSP is used the system to meet the ultra-high-speed data acquisition system, to achieve the data analysis and signal processing algorithms.

Signal Sampling Theory and Related Technology

For ultra-high-speed data acquisition system, it often needs to satisfy the Nyquist sampling theorem, namely the sampling frequency is at least 2 times of the highest signal frequency. It will be too high for A / D converter, having brought a burden to the subsequent data processing. Therefore, it usually uses the band-pass sampling theorem, namely Nyquist sampling theorem.

Band-pass sampling theory A frequency band-limited signal range is (f_L, f_H) , if $f_H \gg B = f_H - f_L$, at this point, if using Nyquist sampling theorem, it requires a higher sampling rate, which will lead to follow-up no achieve real-time signal processing, but band-pass sampling theorem solves exactly this problem.

Assuming a frequency limit (f_L, f_H) of band-limited signal $x(t)$, if the sampling frequency f_s meets the formula 1

$$f_s = \frac{2(f_L + f_H)}{2m + 1} \quad (1)$$

Where m is taken to ensure conditions $f_s \geq 2(f_H - f_L)$ of the maximum positive integer, obtained sampling discrete sequence $x(nT_s)$ is able to accurately recover the original signal $x(t)$, this process is called band-pass sampling theorem.

If the center frequency of the signal is $f_0 = \frac{f_L + f_H}{2}$ Expression (1), to get

$$f_s = \frac{4f_0}{2m+1} \quad (2)$$

Where m is taken to meet the $f_s \geq 2B$ of the maximum positive integer (B is the frequency bandwidth).

Parallel alternate sampling technique In the ultra-high-speed data acquisition system, due to the impact of the single-chip ADC performance, it is often sampling rate higher ADC, its resolution is low; it can not meet the require acquisition system, parallel alternate sampling technique may solve the problem. Parallel interleaved sampling system structure is shown in Figure 1.

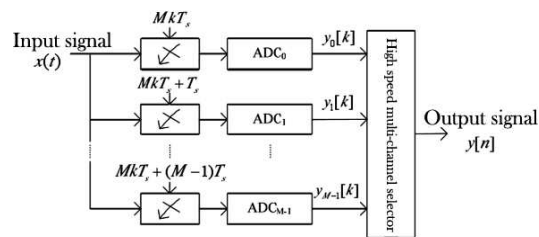


Fig. 1 Parallel interleaved sampling system structure

The system is by M Road parallel of ADC composed, each sampling rate is f_s/M , $ADC_0, ADC_1, \dots, ADC_{M-1}$, in accordance with the order of the input waveform is sampled, the time interval between two adjacent sampling is $1/f_s$, and to maintain a fixed phase. After follow-up data restructuring, the system sampling rate is increased by M times, that is, the sampling rate can be achieved f_s . The parallel sampling technique uses multiple low-speed and high-resolution ADC parallel sampling, in order to achieve a system of high-speed and high resolution, to resolve the contradiction between the monolithic ADC chip rate and resolution[5].

Design of Ultra-High-Speed Acquisition System Hardware

For the application of parallel alternate sampling technique, there is systematic error correction problem, including the time error correction, the gain error correction and offset error correction, which uses more number of channels, and error correction work is larger. Taking into account the above reasons, the design uses a two-channel parallel sampling, and selects an integrated two-channel high-speed ADC devices, this can be as much as possible to reduce the above-mentioned three kinds of error.

Designed ultra high-speed data acquisition and analysis system hardware block diagram shown in Figure 2 that is, using the ADC + FPGA + DSP architecture. The ultra-high-speed data acquisition system chip ADC selects a chip by the U.S. National Semiconductor Corporation, its model is ADC08D1500, and the chip integrates two channels. When the chips work in cross-sampling mode, the sampling rates are up to 3 GSPS. In order to achieve ultra-high-speed data reception, the system has selected a FPGA of ALTERA company; its model is EP2S60, which is Stratix II family of products. The chip has LVDS interface, it can achieve ultra-high-speed data reception. In order to analyze the signal for the ultra-high-speed data acquisition, the design uses the production of TI's high-performance DSP, its model is TMS320C6416, it is mainly used for the analysis of follow-up data collection and processing. The system also will be collected the data and analyzed the processing data into the PC via the USB interface, to completing data storage, processing and display.

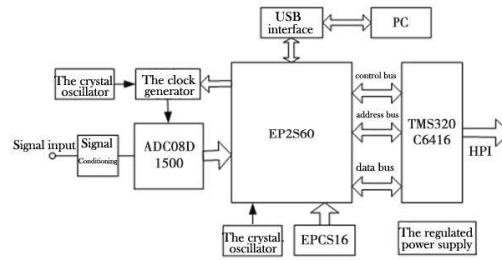


Fig. 2 Ultra-high-speed data acquisition and analysis system

Clock Generation Module When the system sampling rate is 3 GSPS, working in a cross-sampling mode, it needs to provide high-speed ADC clock signal which frequency is 1.5GHz. The system uses an ADI's new PLL frequency synthesizer ADF4360-7 to provide the required clock [4].

The ADF4360-7 chip provides 350 ~ 1800MHz Output frequency range to meet system needs, the clock module is made up internal integration of integer-N synthesizer and voltage controlled oscillator (VCO), the center frequency is determined by the external inductor. The chip internal is mainly composed of R registers, C registers and N registers to achieve the configuration, it uses 3-wire control to complete control and use of internal registers. The ADF4360-7 chips provide an 8/9 or 16/17 two kinds of counting mode, to selecting 8/9 counter for lower output frequency, and to selecting 16/17 counter for higher output frequency. The chip output frequency is calculated as follows 3.

$$f_0 = N \times f_{REFIN} / R = (B \times P + A) \times f_{REFIN} / R = [(B - A)P + A(P + 1)] \times f_{REFIN} / R \quad (3)$$

Where f_{REFIN} is the input reference frequency; A, B, and R is respectively input values of the three registers; P is frequency division module. In the system, reference frequency is selected as $f_{REFIN} = 12\text{MHz}$, the frequency division module is selected as 16/17 counter, that is $P = 16$. According to the above formula, it can be calculated or assigned the values of other parameters in the formula, to meet the output frequency that is 1.5GHz.

Signal conditioning and ADC circuit. The signal conditioning circuit is mainly single-ended input signal to differential conversion, it can meet the needs of the ADC08D1500, and the system uses ADT1-1 as a signal conditioning modules. The system uses ADC08D1500 chip, which works in a cross-sampling mode, the sampling rate can reach 3 GSPS. The ADC08D1500 chips that is National Semiconductor has introduced the dual-channel low-power high-speed 8-bit A / D converter, the full-power bandwidth is 1.7GHz; using single power is 1.9V power supply, power consumption relative to other products is only 1.6W. Chip input signal sampling range is optional 650mV or 870mV (P-P). In the case of the 500MHz standard signal input, it can get the sample median of 7.4.

FPGA circuit The system FPGA has selected Altera's Stratix II series EP2S60 device, the main reason for using the device is receiving the LVDS interface chips to meet the ultra-high-speed data. And as the TERA company's products, its corresponding development environment QUAR-TUSII carry out string and convert for the LVDS receiver data, providing a special string and conversion module, easy to use. In addition, taking into account the development of data acquisition system function, needing the resources of the device is relatively more, the chip has 24,176 adaptive logic module, 8 fast PLLs, 4 enhanced PLL, 60440 logic cells, 36 DSP module, 144 18bit multiply 18bit multipliers and other resources, its basically meet the demand for general data acquisition system. In allocation of the FPGA, the system actives serial configuration with JTAG ways of combining through the MSEL3, MSEL2 the, MSEL1, and MSEL0 of pin mode selection, EPROM select the EPCS16.

DSP circuit and USB circuit. DSP adopts TI's TMS320C6416; the clock frequency is 1GHz. The DSP has two extended memory interface (EMIF), 1 64bi (tEMIFA), 1 16bi (tEMIFA), 32bit/33MHz, 3.3V PCI master / slave interface, and 64 independent DMA channels 1GHz. The chip is mainly used for data analysis and processing after data acquisition, including some of the specific signal processing algorithm, for example, signal spectral analysis, etc.. USB interface

circuit using USB2.0 integrated microcontroller CY7C68013 of Cypress Company, It integrates 1 USB data transceivers, 1 enhanced 8051, 1 smart USB serial interface engine, 16 address lines, 38 I / O port, 8.5KB of RAM and 4K BFIFO, etc., mainly to facilitate the data acquisition system, data storage, processing and display[5].

Voltage regulator module As a result of the ADC + FPGA + DSP architecture to meet the different voltage of electricity needs, the entire system uses different voltage regulator module to meet the needs of the ultra-high-speed data acquisition system. In the design, voltage regulator module uses TI's power module the TPS54310, TPS76918, TPS72625, etc., provides 3.3V, 1.8V, 1.5V, 2.5V, 1.9V, and other different voltage.

System Software Design

Serial-to-parallel conversion module Due to the ADC08D1500 outputs data rate higher, it uses FPGA receives with LVDS. However, the data rate is still high for received FPGA chip data storage or pretreatment, it needs to slow down the data rate through the string and conversion functions. The module uses QUARTUSII environment that comes with SERDES / DESERDES circuit, it can generate a string and conversion module.

The call function modules only need to complete some specific parameter settings can be achieved by string and conversion functions, including the data several times of extracted, the data arrangement, etc. Design of generated string conversion module is shown in Figure 3.

The module is four times extracted for sampling data; The ADC08D1500 sends 16bit data in the FPGA, after four times extracted, it becomes a 64bit output, the data rate is reduced to 1/4.

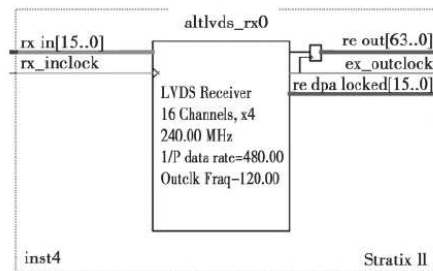


Fig. 3 Serial-to-parallel conversion module

FFT spectrum analysis module based on FPGA Another feature of the ultra-high-speed data acquisition and analysis system is analysis of the data, it can take advantage of the DSP implementation, but also can be used FPGA. Two different points is that FPGA implementation is faster; the disadvantage is resource-intensive. The design of FFT spectrum analysis capabilities use the FPGA to implement, it mainly uses the IP core to design of the FFT module with operational flexibility, short development cycle. The resulting FFT spectrum analysis module is shown in Figure 4.

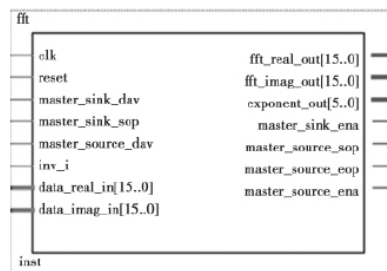


Fig. 4 FFT analysis module

Conclusions

Ultra-high-speed data acquisition and analysis system uses the ADC + FPGA + DSP architecture, system sampling rates up to 3 GSPS. The system not only can be used the narrow-band signals of ultra-high-speed data acquisition system, but also be used for broadband, ultra-wideband radar signal acquisition and processing system, with a high practical value. FPGA designs a flexible and programmable features, making the system has strong versatility.

References

- [1] Y.J. Zhang. High-speed high-precision data acquisition system of the lidar signal[D]. Xi'an: Xi'an Electronic Science and Technology University, 2009
- [2] X.j. Ma, L. Kao, G.L. Zhao. Design of High Speed Data Collecting and Processing System in Time Based on FPGA and DSP[J]. Electron Devices,2007, 30(3):1009-1013
- [3] Z. Huang. High-speed ADC systems based on time-interleaved sampling structure[D]. Chengdu: University of Electronic Science and Technology,2007
- [4] Y.j. Qiu, G.X. Shen. Analysis on Signal Integrity of High Speed Signal Collection and Processing System Based on DSP and FPGA [J]. Measurement & Control Technology, 2007,26(12):8-14
- [5] Z.J. Tang. Designing and Realizing High Speed Multicenter Data Acquisition System on USB[D]. KunMing : Kunming University of Science and Technology, 2007

Ultrasonic Rangefinder Based on P89LPC932

Weidong Cheng^{1, a}, LiSong Zhang^{2, b}

¹Professional Department, BEIJING Information Technology College, BEIJING, 100070, China

²Electronic Engineering Department, University of Science and Technology Liaoning, ANSHAN, 114051, China

^achengwd@bitc.edu.cn, ^bdongfengren@sina.com

Keywords: P89LPC932, Ultrasonic, Distance Measurement

Abstract. In order to overcome the limitation, some traditional distance measurement methods in some special occasions go beyond measure flaw. This design centres on P89LPC932 and realizes non-contact air measurement by use of an ultrasonic sensor, which fully considers the close relationship of velocity and temperature, thus temperature compensation, further get measurement distance about 700cm, optimal precision at 1%. This design has some features, such as the strong anti-jamming capability, simple installation, small size, low power consumption, easy to embed in other system.

Introduction

Some of the traditional distance measurement methods in some special occasions exist insurmountable defects. for example, Liquid level measurement is a kind of distance measurement, The traditional electrode method is using differential distribution of electrode which detects liquid level by the electric or pulse. Electrodes lead to easy corrosion, electrolysis, loss of sensitivity because of long time immersion in water or other liquid. Ultrasonic distance measurement can solve these problems. Ultrasonic distance measuring technology has been widely used [1] in industrial control, surveying, robot localization, security etc. The ultrasonic frequency is higher than that of 20000 Hz referring to the mechanical wave with characteristics of great strength, good direction. Ultrasonic generally uses the piezoelectric and magnetostrictive effect.

In this paper, the design of ultrasonic range finder selects jumper J1(short range, medium range, adjustable pitch) from three ranging mode. The whole scheme for measuring is that ultrasonic is transmitted when the key is pressed, When the ultrasonic wave meeting obstacles generated the echo signal; the system will probe the received echo signal amplifier is fed to the controller; temperature is measured by the temperature measurement circuit [2], the measured distance is obtained by calculation, displays on the digital display, the low 4 bits display the distance, the master 2 bits show temperatures.

The Basic Principle of Ultrasonic Range Finder

The basic principle of Ultrasonic range finder displayed by Fig 1 a simple description: ultrasonic is periodically transmitted, reflection occurred when encounter obstacles, wave emitted by the receiver receives and converted to electrical signals, as long as the measured transmission and transmitting time difference ΔT , then the distance can be obtained from according to formula (1)

$$s = C\Delta t / 2 \quad (1)$$

In the formula, C is the ultrasonic wave propagation velocity in air that is 331m/s for 0°C, 347m/s for 25°C relationship of the temperature T (°C) as type (2):

$$C = 331.4 + 0.61 \times T \quad (2)$$

Thus, there is a close relationship between ultrasonic velocity and temperature. In the application, if the temperature changes little, without special accuracy requirements, substantially considered as constant velocity. Otherwise, must carry out temperature compensation [3]. Temperature compensation method is that calculates the velocity C for each time first according to formula (1-2), then according to the formula (1-1) calculates the distance.

In addition, seen from Fig 1, the ultrasonic calculates the distance by the use of receiving and transmitting wave, thus angle is existed inevitably between the transmission and reflection, the size of angle is 2α . When α is very small, the distance can be calculated directly according to formula (1-1). When α is large, it must be corrected, correction formula (1-3) is showed below.

$$s = \cos\alpha \times C\Delta t / 2 \tag{3}$$

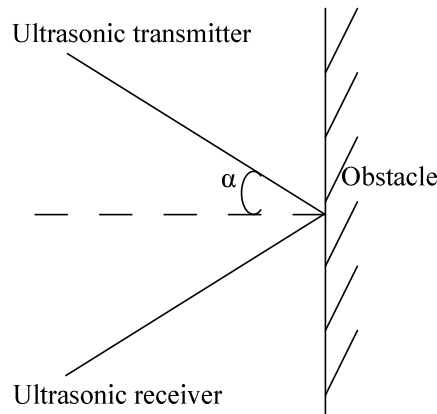


Fig. 1 Ultrasonic rangefinder principle diagram

System Hardware

Ultrasonic distance measurement instrument mainly Includes six parts: a temperature detection circuit, an ultrasonic emission and control circuit, an ultrasonic receiving and signal processing circuit, display circuit, microprocessor and its auxiliary circuit [4], RS-232 communication interface circuit . The structure diagram shows in Fig. 2.

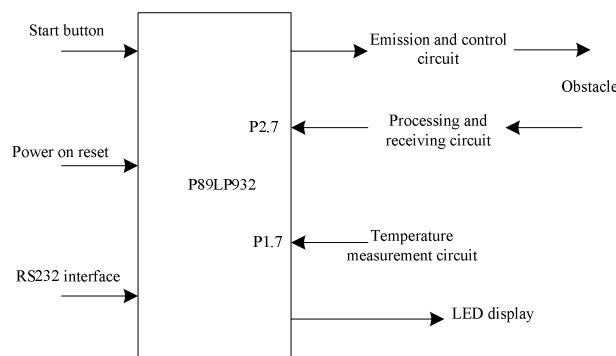


Fig. 2 Ultrasonic range finder structure diagram

Ultrasonic Emission and Control Circuit

Ultrasonic probe model is CSB40T, software generates an ultrasonic 40kHz signal, input to the driver through the output pins, drive the probe to produce ultrasonic. From the Fig 3 shown, 40 kHz ultrasonic signal is generated using a 555 time-base oscillation circuit. Oscillation frequency calculation formula is showed as follows:

$$f \approx 1.43 \div ((R9 + 2 \times R10) \times C5) \tag{4}$$

The adjustable resistor R10 is designed to adjust the signal frequency, the natural frequency is consistent with the transducer. The 555 time-base [5] should be applied by the +12V power In order to ensure enough driving ability. CNT is ultrasonic emission control signal, controlled by a microprocessor.

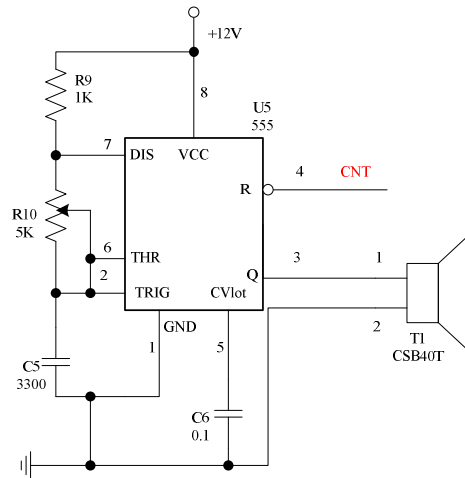


Fig. 3 Ultrasonic emission and control circuit

The Ultrasonic Receiver Design

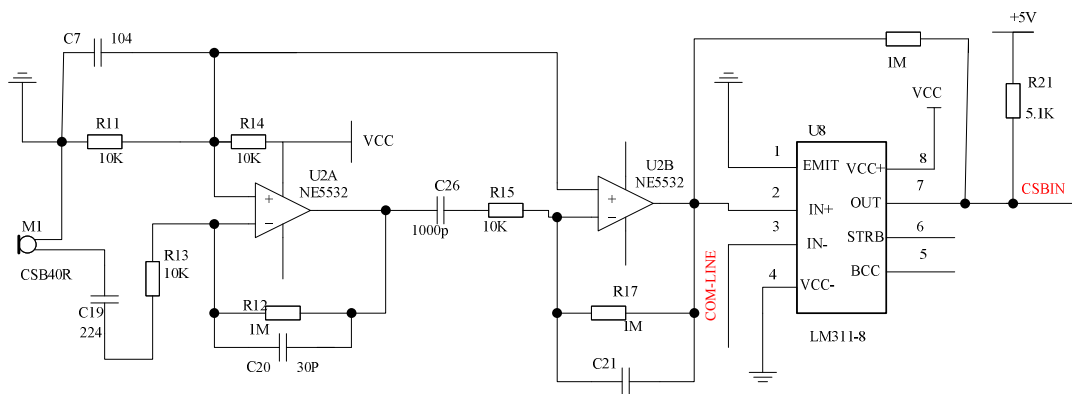


Fig. 4 Echo receiving circuit diagram

The ultrasonic receiver includes three parts: an ultrasonic receiving probe, a signal amplifying circuit and a waveform transform circuit [6]. Ultrasonic probe model must be corresponded with a transmitting probe, that is CSB40R. Since sine wave Electric signal through the probe transform is very weak, so it must be amplified by the amplifying circuit. Sine wave signal can not be received by the microprocessor [7]. it is necessary to carry out the waveform transform [8]. As shown in Fig 4, front class adopts NE5532 to form the 10000 times amplifiers. the received signal is amplified; behind class comparator uses LM311 to adjust received signal. comparative voltage of LM311 is input in pin 3. As shown in Fig 5, jumper J1 corresponding with the different comparison voltage chooses a different distance measurement model.

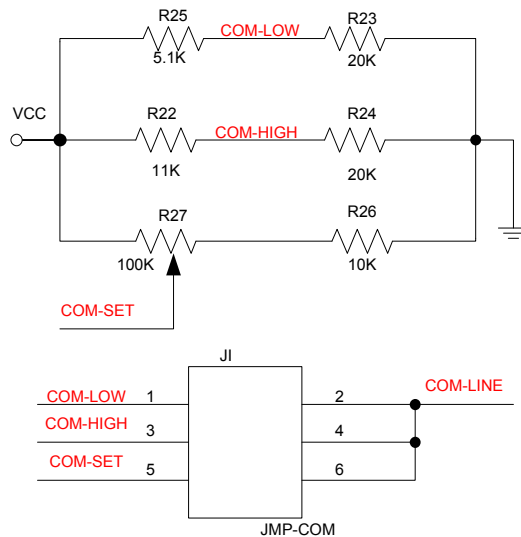


Fig. 5 Select jumper circuit diagram

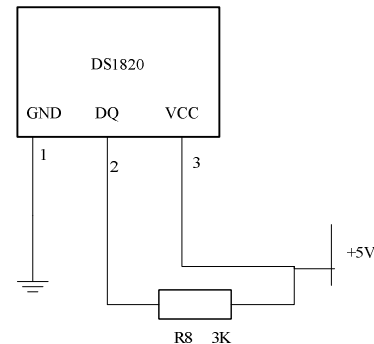


Fig. 6 Temperature measurement circuit

Module provides a ranging mode by jumper J1 selection, such as a short distance measurement mode, middle distance measurement mode, or distance adjustable mode. Select jumper J1 LOW for short-range measurement mode, select HIGH for middle distance measurement mode; select SET for distance adjustable mode.

Temperature Measurement Circuit

When the environment temperature changes, the ultrasonic wave velocity will change. So it must be amended. Thus the system provides a temperature detection circuit. Real-time temperature is collected to amend the velocity. Temperature measurement circuit uses a sensor [9] with DS1820, as shown in Fig 6. With 9,10,11,12 bits conversion accuracy, no programming default precision is 12. Measurement error is about 0.5°C , 0.1°C after software processing.

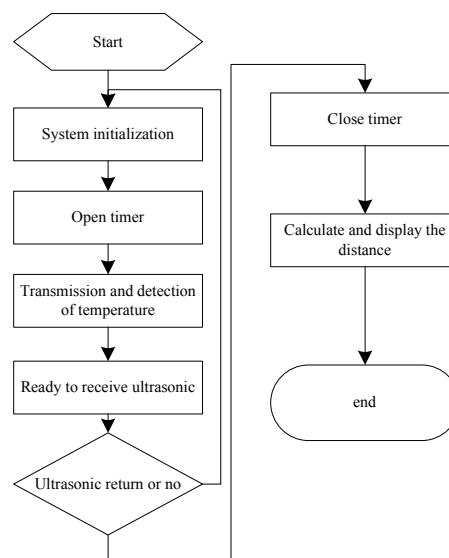


Fig. 7 System program flowchart

Systems Software

System flow diagram is showed in Fig 7. The microprocessor P89LPC932 set P1.6 as 0, start the probe transmitting ultrasonic, start at the same time the internal timer T0 used for timing. Then check the temperature and compensate it. The ultrasonic signal return immediately when meet

obstacles signal. The microprocessors constantly scan the pin P2.7. If received signal in pin P2.7 change from high level to low level, signals have been returned. Microprocessors break off timer. The timer data after the conversion can obtain the distance measurement.

The End

The system can realize the non-contact air distance measurement by use of ultrasonic sensor^[10], and give full consideration to the measurement of environmental temperature on ultrasonic transmission velocity. The temperature compensation method corrects the speed. And the system has three kinds of mode selection, so it has high measurement accuracy, strong anti-interference ability, fast response etc. Experiments show that the measurement accuracy is priority to 1%. the most distant distance is about 700cm.

References

- [1] Peng Zhang, Youzhi Zhang. A new ultrasonic range finder system[J], Journal of Shandong University, 2003.
- [2] ShengGuo Zhou. Mechanical Engineering Testing Technology[M], BeiJing: National Defense Industry Press, 2006.
- [3] JingCai, Yongjun Yang. under the special conditions of temperature measurement [M]. China Measurement press, 2009.
- [4] Hongwei Shen. Intelligent system design and implementation based on MCU [M]. Beijing: Publishing House of electronics industry, 2005.
- [5] Guang Zhao. 555 time-base circuit applied in 280 cases[M]. Beijing: Chemical Industry Press, 2010.03
- [6] Chunfang Lin. Digital electronic technology[M]. Anhui University press, 2006.
- [7] Yingkui Ma. The application of microprocessor[M]. Chemical Industry Press, 2009.
- [8] Limin He. The singlechip microcomputer application corpus[M]. Beijing: Beihang University press, 1991.
- [9] Wilson, Longxin Lin, Bin Deng, Liu Qijun. Handbook of sensor technology[M]. Beijing: People's post and Telecommunications press, 2009.
- [10] Lifan Meng .sensor principle and application[M]. Beijing: electronics industry press, 2007.

Microcontroller System Design for Robotic Vehicles

Chien-Yuan Liu^{1,a}, Cheng-Yi Chen^{2,b} and C.F. Huang^{1,c}

¹Department of Computer Science and Information Engineering, Cheng Shiu University, Kaohsiung City, TAIWAN

²Department of Electrical Engineering, Cheng Shiu University, Kaohsiung City, TAIWAN

^acyliu@csu.edu.tw, ^balbert@csu.edu.tw and ^chcf0937@csu.edu.tw

Keywords: Microcontroller, Robot, Vehicle, Arduino, System Design.

Abstract. In this paper, a microcontroller system designed for economic robotic vehicles was presented. The system is consisted of hardware and software design. In the hardware design, the layout of the main control *PCB* was designed and implemented by the researchers themselves. The software function currently merely specified the obstacles avoiding capability for verifying the design of the integrated system. Performance evaluation was conducted to prove the effectiveness and the response time of this system. The results showed that the vehicle could pass the lane stuffed with obstacles in expected time limit.

Introduction

Mobile robots are interesting research issues. They combine the mechanic, electrical, electronic, and computer knowledge and techniques. The research works include constructing a stable frame, choosing suitable motors, deciding proper sensors, using efficient microcontroller, and soldering them and all required electronic components together to become a functional vehicle.

There are already plenty of mobile robots in the market. However, a programmable controller with enough flexibility for a low cost robotic vehicle is not easy to find. Therefore, this research tried to design a feasible and cheaper microcontroller system for robotic vehicles. During the design work, we tried some vehicle frames, motors, sensors, and created a main control *PCB* for the vehicles. All required components are acquired from commercial shops with cheaper price. Total cost of the vehicles is normally less than half of that of off-the-shelf mobile robots. In addition, the control program is fully flexible to tune for various applications, such as speed racing, obstacle avoidance, track guidance, and even remote control, etc.

The rest of this paper is organized as follows. Section 2 presents the hardware design of the system. Section 3 depicts the software design. In section 4, the performance evaluation of the system and the vehicle is explained. Finally, section 5 describes a brief summary and some further works.

Hardware Design

The goal of the hardware design is to provide flexible capabilities of the vehicle with the lowest cost. Nowadays, there are plenty of preassembled vehicles with abundant functionalities and relatively expensive charge [1]. These vehicles normally equipped with necessary frame structure, wheels and motors, microcontroller, system *PCB*, *USB* or *RS-232* communication interfaces, IO connection slots, sensors, drivers, and basic control program. They are easy for rich beginners to learn the control program. For most usual learners, the amount of the cost may be unaffordable. Therefore, the feature of the design is to find some cheaper commercial parts and to construct them together to form a versatile economic vehicle. The prototype of the hardware design was consisted of the following major portions:

Microcontroller *PCB* A main control *PCB* was designed to hold the microcontroller which is an 8-bits CPU (*ATMEGA 328*) manufactured by *Atmel*. *ATMEGA 328* is a standard *TTL* device in DC 5V. The power of the *PCB* is supplied by DC 8.4V power source cascaded by two DC 4.2V rechargeable

lithium batteries. This power is for two DC motors and the *PCB*. To supply DC 5V and 3.3V for the *PCB* and extending external low-voltage components, a *KA7805* and a *LM1117* voltage regulator IC are placed on the layout of the *PCB*. In addition, a 16 MHz crystal oscillator is added for the digital clock of the microcontroller. The *CPU* chip has 20 pins for diverse IO operations, including 6 *AI* pins and 14 *DIO* pins. Six of 14 *DIO* pins could be programmed as *PWM* outputs. Others could be programmed for general *DI* or *DO* actions. Thus, at least 20 female pin-slots are required for the IO connections.

The layout of the main control *PCB* in Fig. 1 was designed by *Fritzing* [2] which is an open source tool for the design of a *PCB* layout. The output formats of the *Fritzing* include pdf, gerber, and ftz. The pdf format is used to print the circuit layout on a screen tracing paper for the fabrication of handmade *PCB*. The gerber format can be submitted to a *PCB* processing factory for mass production. The ftz format is to keep the original circuit layout for future maintenance or enhancement. The made-up *PCB* and assembled main control *PCB* is shown in Fig. 2.

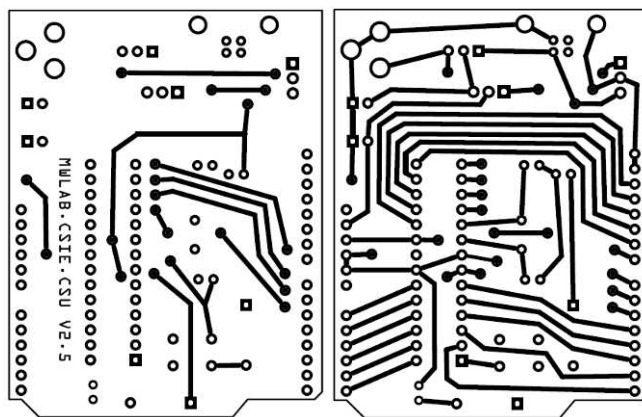


Fig. 1 Main Control *PCB* Layout

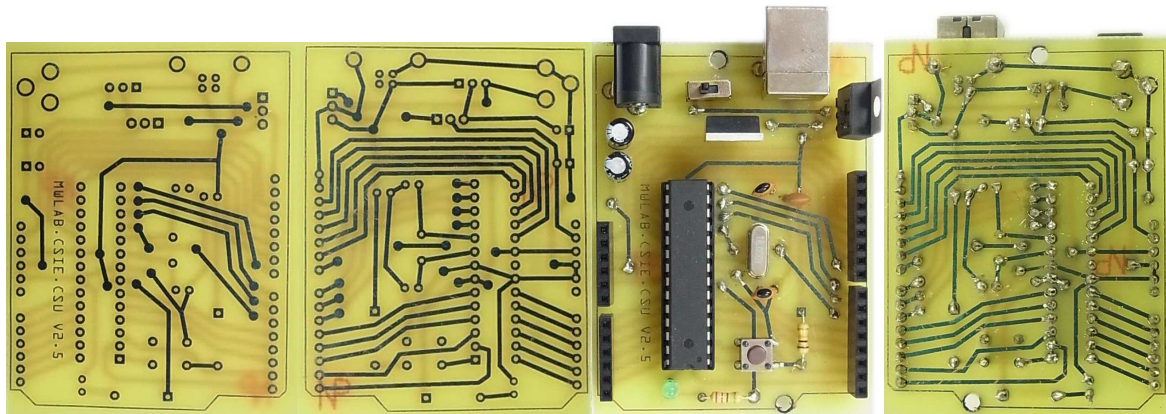


Fig. 2 Made-up *PCB* and Finished *PCB*

Vehicle Frame The frame of the vehicle can be composed of motors, wheels, and multi-purpose *PCB* or can be decomposed from a purchased toy car. The former decision is more flexible for the selection of motors, but the combination of motor axle and a wheel becomes a challenge. The later one is a quick solution to have a ready frame with motors and wheels. Both kinds of frames are feasible for implementation and two samples are shown in Fig. 3. It is possible to drive the robot in different ways, e.g. 4-wheels drive, 2-wheels drive at rear and one pilot wheel at front, or 2-wheels drive at front and one pilot wheel at rear, etc. Different motor-driving styles should have various control algorithms in order to fulfill the required functionalities of vehicles.

Sensor and Driver Sensors are very important to a robotic vehicle to complete the designated capabilities of the robot. For instance, mid-range (4~40cm) Infra-red sensors are suitable for the obstacle-detection and collision-avoidance at the front end of the vehicle. Short-range (0.1~2cm) Infra-red sensors are suitable for the ground-track-detection and self-guidance at the bottom-side of

the vehicle. Ultrasonic sensors are usually installed to detect an object at a longer distance. Light, gas-ingredient, humidity, temperature, accelerometer, gyroscope, pressure sensors etc. are also useful in variant autonomous applications of robots [4]. Regarding the experimental vehicle in this research, two mid-range IR sensors were installed at the front end to detect a front obstacle. The assembled vehicle is shown in Fig. 4.



Fig. 3 Handmade and Toy-Car Frames

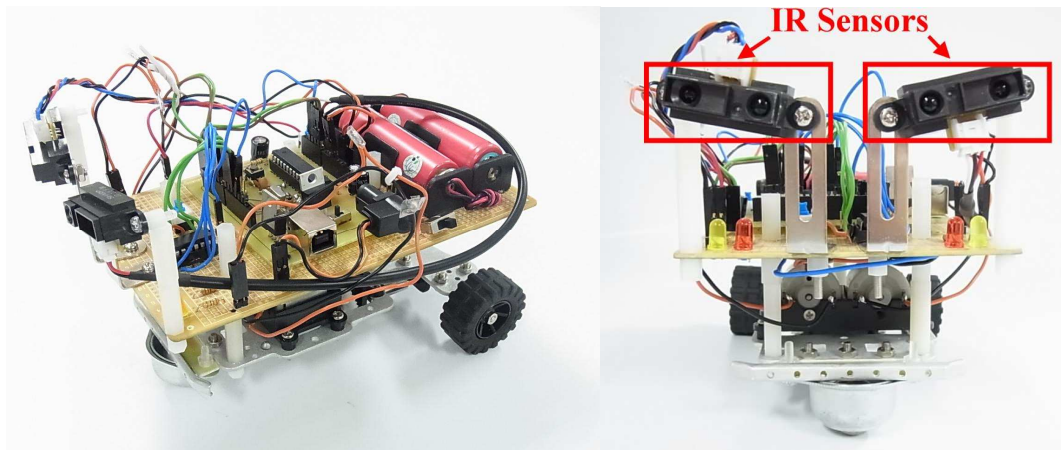


Fig. 4 Assembled Robotic Vehicle

The rated voltage of the motors in Fig. 3 is 4~7V. The rated current of them is 300mA. This current value is too big to drive directly by the microcontroller itself. Thus, a powerful motor driver IC is necessary to amplify the current for motors. *L293D* is H-bridge driver for motors. It can drive two motors in one chip and provide up to 1A for each motor. Since 2-wheels driving vehicle with a front-guiding wheel is adopted for further software design and testing. One *L293D* is enough to support this vehicle. Furthermore, 4 *LED* were installed at the front end to show the status of obstacle distance in front of the vehicle.

Software Design

The behavior of the robotic vehicle is determined by the control firmware downloaded in the microcontroller. Typically, the firmware is designed by a programming language. In this research, the control program is written in C-language. The integration of the programming work is explained as follows.

IDE Platform to reduce the cost of the vehicle, an open integrated development environment, named *Arduino IDE* [3], is chosen as the developing platform. *Arduino IDE* is an open-source and cross-platform environment. The developing environment was installed in *Windows XP*. The developed control program was downloaded into the flash memory of *ATMEGA 328* microcontroller via a USB link. The microcontroller supports 32 KB program size and 2KB data memory. This is quite a large space for the most of control applications.

Control Algorithm. The goal of current stage is to verify the correctness of the integration of the designed system. Thus, the simple obstacle-avoidance function is developed in the control program [5]. The algorithm for obstacle avoidance is depicted in C-like pseudo statements as follows.

```

if (L-IR >= X and R-IR >= M) then Stop, Back-Off, and then Detour-Right
else if (L-IR >= M and R-IR >= X) then Stop, Back-Off, and then Detour-Left
else if (L-IR >= M and R-IR >= S) then Detour-Right
else if (L-IR >= S and R-IR >= M) then Detour-Left
else if (L-IR <= S and R-IR <= S) then Go-Ahead

```

Where, $L-IR$ and $R-IR$ denote the reflected signal strength (RSS) from left Infrared and right Infrared sensors, respectively. X , M , and S separately mean large (long distance), medium, and small (short distance) of RSS . As for the indication of obstacle, two indication LED (yellow and red) at each side are both turned on when $RSS \geq X$. If $X > RSS \geq M$, then red LED is turned on. If $M > RSS \geq S$, then yellow LED is turned on. Both LED are turned off when $RSS < S$. While *Back-Off*, the motors are driven in reverse rotation and kept for a parameterized short time S_1 . Next, the *Detour-Right* or *Detour-Left* implies that the vehicle would turn right or left first, then go-ahead for a parameterized short time S_2 , then turn left or right again for keeping the vehicle in straight direction to the destination. While *Go-Ahead*, two motors are driven in forward rotation. However, the properties of two motors are different. Therefore, even the PWM outputs of two drivers are of same values. The actual rotation speeds would not be the same one. Carefully speed correction should be tuned and compensated to the slower motor to keep the direction in the right way.

Performance Evaluation

After the hardware design and implementation, software design and implementation, the robotic vehicle was integrated and tested iteratively. Once the values of parameters, e.g. X , M , S RSS levels, S_1 and S_2 , are tuned. The control program should be recompiled and downloaded into the microcontroller again. It takes a non-trivial time for the function verification and performance enhancement. Fig. 5 showed the lane for racing test. The circles in Fig. 5 represent the bottle obstacles inside the lane. The robot starts to run from the bottom baseline, should avoid the bottles and reach the target of the top line. The faster robot performs better. During the test, the robot generally can achieve the goal within 20 seconds. Current duty cycle of PWM output was less than 60 percent. This implies the timing performance are possible to increase if the duty cycle is increased, the settings of parameters are tuned exactly, and the detour control algorithm is further refined.

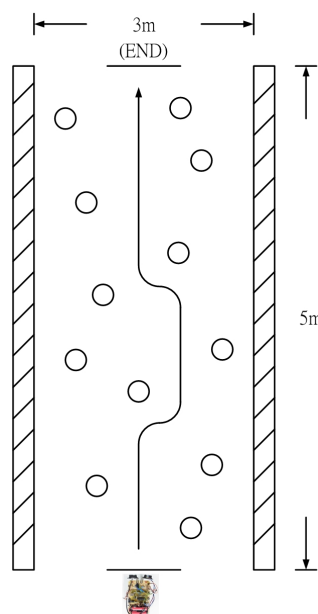


Fig. 5 Racing Lane

Summary

This paper presents an implementation research of the microcontroller system design for robotic vehicles. The system and the vehicle are constructed in modular way [6] by general commercial electrical and electronic components. The integration and verification proved that the goal of the research is accomplished with valid performance. In future, some extended functions would be added for more versatile capabilities, e.g. track guidance, obstacle avoidance with fastest speed, and remote communication and control.

References

- [1] S. Piperidis, L. Doitsides, C. Anastasopoulos, and N.C. Tsourveloudis, A Low Cost Modular Robot Vehicle Design for Research and Education, Proceedings of Mediterranean Conference on Control and Automation (2007), Athens, Greece, p.T30-026.
- [2] A. Knörrig, R. Wettach, J. Cohen, Fritzing - A Tool for Advancing Electronic Prototyping for Designers, Proceedings of the 3rd International Conference on Tangible and Embedded Interaction (TEI'09), Feb 16-18 2009, Cambridge, UK, p.351-358.
- [3] Information on <http://arduino.cc/en/Guide/Introduction>.
- [4] W.R.Fahrner, R. Job, and M. Weener, Sensors and Smart Electronics in Harsh Environment Applications, Microsystem Technologies, 7 (2001), p.137-144, Springer-Verlag.
- [5] J. Minguez, Extending Collision Avoidance Methods to Consider the Vehicle Shape, Kinematics, and Dynamics of a Mobile Robot, IEEE Transaction in Robotics, Vol.25, No.2, April 2009, p.367-381.
- [6] U.D. Hanebec, N. Saldic, and G. SchMidt, A Modular Wheel System for Mobile Robot Applications, Proceeding of the IEEE Robots and Systems (1999), p.17-22.

Data Fusion of Ultrasonic Wave Sensor Static State Based on BP Neural Network

Xuesong Wang¹

¹ Zhongshan Torchs Polytechnic, zhongshan, 528436 China

Keywords: BP Neural Network; Ultrasonic Sensor; Data Fusion; Temperature Affect

Abstract. Because Ultrasonic sensor is affected by temperature in the applications, the output of Ultrasonic sensor not only depends on objection parameter (distance). The method of eliminating affection caused by non-object parameter based on BP neural network data fusion is adopted. The results show the method elimination affection based on neural network data fusion is feasible.

Introduction

Ultrasonic sensor output is limited only by the ultrasonic effect in the practical application of the accuracy of less demanding situations, usually; fact, in the case of constant input ultrasonic p value, the operating temperature t change will cause the sensor output voltage u change, that is, unless affected by the of parameters of p , the ultrasonic sensor by the impact of non-target parameters the amount of t and accurate test ultrasonic signal of the case, simply think of the ultrasonic sensor output only by the ultrasonic of the will to produce large errors, therefore need to eliminate the parameter t of the non-target sensor input and output characteristics. Usually multi-sensor data fusion, so that the ultrasonic sensor output is single-valued function of the input p . Data fusion method is commonly used multidimensional regression analysis and neural network method [1]. The former through the establishment of the analytical expression of function, including non-target parameters to be eliminated, to eliminate the impact of non-target parameters on the sensor. But there are two limitations of this method. This method is the need to establish strict parameters, including non-target function analytic form; The method in solving the equation for the multi-dimensional matrix, the equation may be morbid equation. The rules of neural networks do not have to establish the equation; network training can be directly through the calibration data. In this regard, the article uses the neural network method to eliminate the influence of temperature interference on the input and output characteristics of the ultrasonic sensor.

BP neural network

The artificial neural network is an emerging cross-disciplinary. In the practical application of artificial neural networks, artificial neural network model using BP neural network (Back - Propagation Neural Network) [2]. The BP algorithm consists of two parts: the forward pass and error back-propagation of information. In the process of the forward pass input information calculated from the input layer hidden layer, layer by layer to the output layer, each layer of neurons status affects only the state of the next layer of neurons. If the output layer does not have the desired output, the calculation of the change of error value of the output layer, and then turned to the back-propagation, the error signal through the network along the connection path to anti-pass back to modify the weight of the layers of neurons until they reach the desired goals. Fig 1. BP neural network learning rules: adjust the network weights and thresholds of the square of the network errors and the smallest; it is to adjust the network weights and thresholds in the direction of steepest descent, [3].

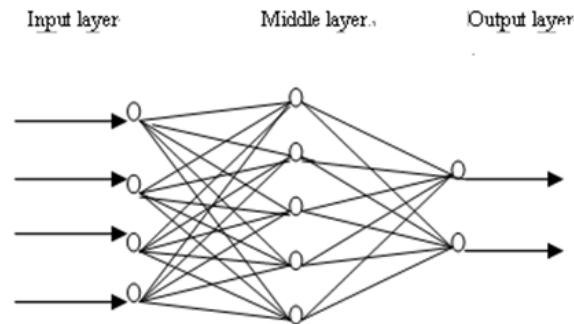


Fig. 1 BP ANN module

BP model consists of multiple nodes of input layer, hidden layer and an output of the output layer, each node of individual neurons, one-way connection between adjacent layers. Transfer function between the nodes for the S-shaped function, which is:

$$f(x) = \frac{1}{1 + e^{-x/Q}} \quad (1)$$

Layers of nodes output calculated:

$$y = f\left(\sum_{i=0}^n w_{ij}x_i - \theta\right) \quad (2)$$

Each node input is connected by the weights ω of the input information and the threshold θ . Where y is the node output, x_i is the node to accept the information the ω_{ij} is related to the connection weights, θ is the threshold, n is the number of nodes.

BP Neural Network Data Fusion

The Ultrasonic Ranging Principle

Ultrasound is a mechanical oscillation of an elastic medium, which is caused by contact with the media oscillation source frequency above 20000Hz. Because it has a strong point, good direction, energy spread, propagation distance and other characteristics commonly used to measure the distance of the object thickness, level and so on. In addition, it is a non-contact detection. Compared with other methods, such as electromagnetic or optical methods, it is not light, the measured object color effects. Analyte in the dark, dust, smoke, electromagnetic interference, toxic, etc. have a certain ability to adapt to harsh environment. Therefore, the robot control, automatic vehicle navigation, object recognition has widely used. It is noteworthy that ultrasound propagation speed in the air with the medium temperature increased, the temperature rise for every 1 ° C increase in acoustic velocity of 016m / s, temperature changes in the factors to be considered in the measurement, temperature compensation correction reduce the measurement error.

Ultrasonic ranging there are several ways, such as phase detection, the acoustic amplitude detection method and the transit time detection method. Although the high accuracy of phase detection, but the detection range is limited; acoustic amplitude detection method is sensitive to the influence of the reflected wave. The system uses ultrasonic transit time detection. Ultrasonic elapsed time from launch to destination transmission measurements taken emit ultrasound, ultrasonic generator start time, to the ultrasonic wave through the air to the target, and then *reflected* back propagated to the ultrasonic receiver, the timing is stopped, the measured transmission time t . The distance L between the acoustic emission with the target can be calculated by the following formula,

$$L = ct/2 \quad (3)$$

Where, c is the propagation velocity of ultrasonic wave in the air. Measurement of transit time (t), using a single-chip pulse-counting method can be accurately measured. Time t convert the pulse count number N , then

$$L = Nc / 2 f \tag{4}$$

Where N is the count number of pulses; f is the count of the pulse frequency. As the acoustic wave speed is affected by temperature, the relationship between propagation velocity and the ambient temperature T is given by description.

$$c = 33114 / 1 + T / 273 \tag{5}$$

Basis having the above formula in the measurement of acoustic velocity correction, in order to reduce measurement error.

The experimental data shown in Table 1, U is the ultrasonic sensor output voltage, U_t for the temperature sensor output voltage.

Table 1 Under different temperature sensor input and output calibration value

Norm	$T = 5^{\circ}C$		$T = 25^{\circ}C$		$T = 45^{\circ}C$	
L/cm	U_L/mV	U_T/mV	U_L/mV	U_T/mV	U_L/mV	U_T/mV
100	17.12	11.20	17.12	45.2	17.12	92.51
200	33.56	11.42	33.56	48.4	33.56	93.52
300	52.14	11.01	52.14	46.5	52.14	96.5
400	68.77	11.02	68.77	47.12	68.77	95.55
500	86.15	11.12	86.15	48.20	86.15	96.24
600	103.55	11.26	103.55	46.25	103.55	97.58

Normalized and training of the neural network training sample data

Hidden layer neuron activation function is S-shaped function of the saturation value of 0, 1, so the data submitted to the neural network processing, press (3) is normalized [2].

$$X' = (x - x_{min}) / (x_{max} - x_{min})$$

$$P' = 0.9 (p - p_{min}) / (p_{max} - p_{min}) + 0.05 \tag{3}$$

X' , p' maximum normalized value; x , p is the calibration value; x_{max} , x_{min} , the ultrasonic sensor output voltage, output voltage of temperature sensor calibration, the minimum value; p_{max} , p_{min} for ultrasonic calibration minimum. The output of the neural network input normalized standard sample database shown in Table 2.

Table 2 Neural network input and output standard sample library

No	$T = 5^{\circ}C$		$T = 25^{\circ}C$		$T = 45^{\circ}C$	
L	U_L	U_T	U_L	U_T	U_L	U_T
0	0.0000	0.2532	0.0030	0.4532	0.0030	0.8532
0.2	0.2310	0.3556	0.2510	0.6576	0.2510	0.8576
0.3	0.3852	0.1550	0.3332	0.2540	0.3332	0.5580
0.4	0.4521	0.1210	0.3821	0.3210	0.4821	0.7910
0.5	0.5652	0.2562	0.5662	0.5672	0.4662	0.8972
0.6	0.6011	0.3562	0.6311	0.6562	0.6311	0.9562

Standard BP algorithm is essentially a simple and most rapid decline in the static optimization algorithm, correction $w(k)$, be amended only in accordance with the time k of the negative gradient direction, without taking into account the previously accumulated experience, that is, before time gradient direction, which often makes the learning process to oscillate, the convergence slow

[3]. In the design, using a library of hidden layer neuron activation function as sigmoid function, the output layer neuron activation function is a linear function of $y = x$, the algorithm uses the MATLAB neural network tool provided by the Levenberg-Marquardt learning algorithm [4].

The ultrasonic sensor output voltage normalized value in the training process, the calibration, the calibration of the temperature sensor output voltage normalized values as input to the neural network, the ultrasonic sensor input calibration of ultrasonic owned by one of value as a network the output. T of 5 ° C, 25 ° C, 45 ° C input and output normalized value as the input. Through training BP neural network training process shown in Fig 2

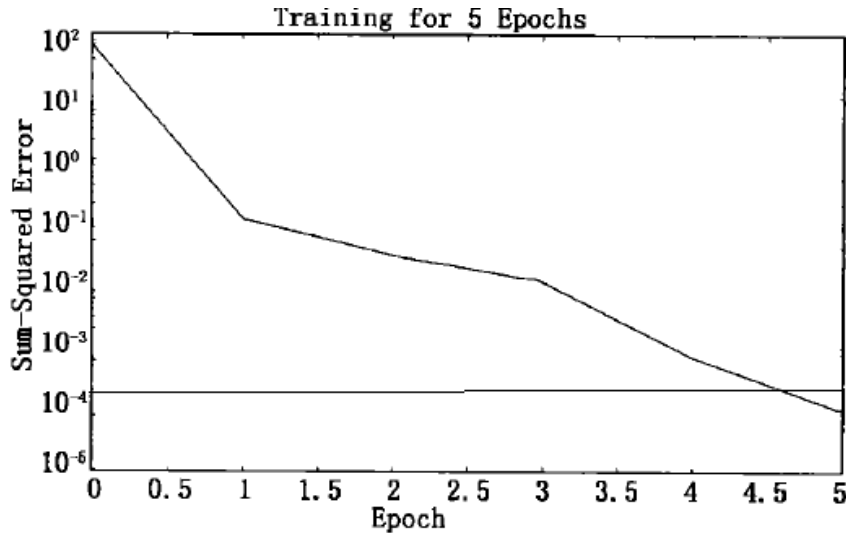


Fig 2 Neural network training error curve

Fusion of the Neural Network Results and Evaluation

The use of neural network computing the integration value of the measured ultrasonic, the calculated results shown in Table 3

Table 3 Data fusion results

Temperature	Norm	Fusion	Norm	Fusion	Norm	Fusion	Norm	Fusion
$T = 5^{\circ}C$	0.3	0.3028	0.4	0.4025	0.5	0.5088	0.6	0.6074
$T = 25^{\circ}C$		0.3014		0.4057		0.5036		0.6024
$T = 45^{\circ}C$		0.3024		0.4047		0.5047		0.6028

Ultrasonic sensor temperature sensitivity coefficient is defined as:

$$\alpha_p = |U_{t2} - U_{t1}| / (t2 - t1)U_{t2} \tag{4}$$

Where: t2, t1, is the operating temperature of the upper and lower limits; Ut2, Ut1 ultrasound under the same input, the operating temperature is t2, t1, when the ultrasonic sensor output value.

From Table 3 can be drawn, fusion than the fusion temperature stability improved. Therefore, the neural network integration technology to eliminate the impact of the sensor in the course of their work by non-target parameters is very effective.

Conclusion

Ultrasonic sensors, for example, the use of neural network integration technology to eliminate the influence of non-target parameters on the sensor output, the neural network data fusion, temperature stability can be increased by two orders of magnitude, so you can ensure that the ambient temperature changes the case of still higher measurement accuracy. The results show that this method can effectively improve the output of the sensor accuracy and the elimination of non-target parameters on the sensor output.

References:

- [1] Kevin M Passion, Stephen Yurkovich. Fuzzy Control [M]., 2001, (11): 374-378.
- [2] Zhang Dan , Yu Chaomin , Li Dong. Data Fusion of Pressure Sensor Static State Based on BP Neural Network[J] Computer Measurement & Control, 2004, 12(6) 598- 600.
- [3] PAN Xiao1, GAO Yu-ling1, KANG Ya-na2. Intellectualized Temperature Control System of AT89C2051Singlechip Based on Fuzzy-PID [J]. Measurement and Control Technique, 2006, 25(6)65- 68.
- [4] LIU Quan-jin1 , SUN Cheng-x un2 , REN Guang-Yong 1. Applicat ion of Back- Propagation Netword Based on Genet ic Algorithm in Predicting Meiyu Precipitation[J]. Journal of Anqing Teachers College, 2004, 2(10): 98- 101.

A Discrete Realization of Higher Resolution Phase Detection

Ping-Sung Liao¹ and Chien-Hua Lee²

^{1,2} Department of Electrical Engineering, Cheng Shiu University, No. 840, ChengChing Road, Neau-song (833), Kaohsiung, TAIWAN

¹bsliao@csu.edu.tw, ²chienhua@csu.edu.tw

Keywords: Phase Division, Phase Splitter, Phase Range Mapping, A/D Converter.

Abstract. To improve the resolution of optical meter in manufacturing machines, novel discrete higher resolution phase detection for optical grids in optical meter is proposed. It is well known that the output of optical grid is a pair of sinusoidal and co-sinusoidal signals. The way enriching the phase information roots upon three primitive elements: (1) the phase angle 2π per cycle can be encoded into eight $\pi/4$ phase regions, (2) the chopping signal of each $\pi/4$ region is either the replica or the mirror of the first phase region, and (3) amplitude-to-phase mapping is used to digitize the pair of sinusoidal and co-sinusoidal signals into a pulse sequence. The empirical result shows that the proposed diagram with an 8 bits A/D converter can digitize the resolution of a complete sinusoidal signal up to 800 pulses per cycle. When coupling to the manufacturing machines, the proposed phase splitter can promote their resolution to 1600 times.

Introduction

Optical encoder has been widely used as the position detector of linear motion and rotary motion in manufacturing automation. It can immediately reflect the position about the working platform. The optical grid is an alternative of optical encoder and is marked in either simple division or Gray coded division. As it is coupled to the shaft of an electrical machine, it can detect the angular position either in increment /decrement or absolute position indicator [1]. In the detection of linear motion, optical meter (linear scale) embedded with optical grid is often used to accurately measure the position of working platform that moves quickly within 3m, 5m and even 7m [2,3]. Shieh invented a digital protractor based on the idea from optical grid [4].

Manufacturing accuracy is fully dependent on the resolution of mechanical divisions in optical grid. However, the light variation between two adjacent optical grids is often ignored and seldom considered further. Actually, the light variation through optical grids is sinusoidal. Based on the periodic property of a sinusoidal signal, Liao proposed differential and synchronous method to promote the resolution of optical encoder four times than before [3]. Lee and Chiu [1] proposed a resolution-scale division method to improve the accuracy of phase resolution up to 32 times. Their main ideas roots upon more electrical pulses being created per mechanical division (optical grid).

Clearly, inserting more phase position information during an optical transition can improve the measuring accuracy of optical meter. This paper proposes a constructive way of phase splitter to convert the phase relationship of a pair of sinusoidal signal and co-sinusoidal signal into a pulse sequence. Thus, each optical transition appears in pulse trains and the phase position of each optical transition can be detected by counting the number of pulses. This proposed phase splitter will vastly promotes the resolution of manufacturing machines.

Criterion of Phase Detection

The output of an optical meter basically looks like the waveforms 1 and 2 in Fig. 1, sinusoidal and co-sinusoidal signals with phase difference 90° [5]. If such an original sinusoidal signal is firstly quantized at fixed sampling rate time interval, it is possible to obtain the phase angle at any sampling time by taking the inverse computation over sine function. However, the mathematical computation about arcsine and/or arccosine could not be performed in real time without any special numerical processor. Hence, the anticipatory method for phase detection would depend on counting the number of pulses that are generated from sinusoidal signals as the researches done in [2, 6].

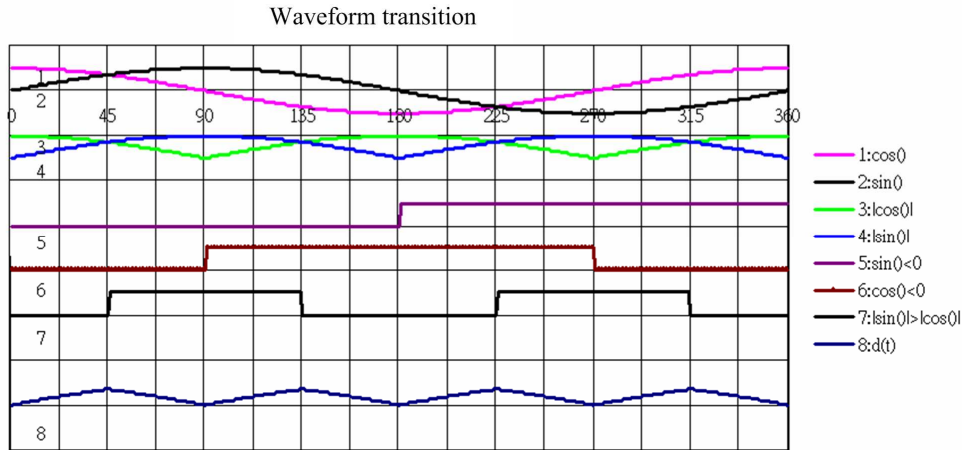


Fig. 1 Sinusoidal signal, co-sinusoidal signal, their absolutes, and other waveforms derived from the amplitude comparison.

It is well known that an optical meter always generates a pair of sinusoidal and co-sinusoidal signals when it is moving. The method described in [2] sufficiently catches up with the characteristics of an optical meter. Its system consists of two building blocks: one is the conversion table between amplitude and phase; the other is the immediate detection of moving direction. Since the former plays an important role to make up a sequence of pulses in phase axis, it will be discussed below.

As for n bits A/D converter, the amplitude from peak to peak for a cosine signal could be divided into 2^n levels. Because the relationship between the amplitude and the phase of a cosine signal is nonlinear, the mapping phase range corresponding to the quantization level at phase 0 and π would be the greatest as shown in Figure 2. Therefore, in [2], the greatest mapping phase range is chosen as

$$\theta_{\max} = \cos^{-1}\left(1 - \frac{1}{2^n}\right) \tag{1}$$

The phase division (splitting phase unit) θ_s in phase axis must be greater than the greatest mapping phase range. Otherwise, it is confused to assign which phase division associated with a mapping phase range due to conflictive assignment. Thus, the minimal phase division $\theta_{s,\min}$ must be greater than the greatest mapping phase range θ_{\max} . To achieve more chops a cycle, the maximal multiplier D_{\max} must satisfy the inequality below,

$$D_{\max} \leq \frac{\pi}{\theta_{\max}} \tag{2}$$

For an A/D converter, the criterion “the minimal phase division $\theta_{s,\min}$ is greater than the greatest mapping phase range θ_{\max} ” must be obeyed. Thus each quantization level has its own mapping phase range that is less than the pre-assigned phase division. However, some mapping phase ranges may span across two phase divisions. What is the solution to this problem? The reasonable match method is that the winning phase division is the one possessing more overlaid area with this mapping phase range than the other. Thus, any mapping phase range always belongs to one unique phase division.

Integrated Phase Detection Diagram

Identifying Phase Region Regarding the output of optical meter denoted as $v_1(t) = \sin(t)$ and $v_2(t) = \cos(t)$, their absolutes can be obtained by rectified circuit and are expressed as $m(t) = |\sin(t)|$ and $n(t) = |\cos(t)|$, respectively. As shown in Figure 1, three different operations, $\sin(t) < 0$, $\cos(t) < 0$ and $|\sin(t)| > |\cos(t)|$, can divide the cycle of 360° of $v_1(t)$ and $v_2(t)$ into eight encoded phase regions. Thus, each phase region can be addressed by three-bits Gray code $G_2G_1G_0$ shown in Table 1.

Table 1 The region encoder

Code Phase Region	Gray code			d(t)	BCD
	G ₂	G ₁	G ₀		B ₂ B ₁ B ₀
Degree	$v_1(t) < 0$	$v_2(t) < 0$	$n(t) < m(t)$		index
0-45	0	0	0	m(t)	0
45-90	0	0	1	n(t)	1
90-135	0	1	1	n(t)	2
135-180	0	1	0	m(t)	3
180-225	1	1	0	m(t)	4
225-270	1	1	1	n(t)	5
270-315	1	0	1	n(t)	6
315-360	1	0	0	m(t)	7

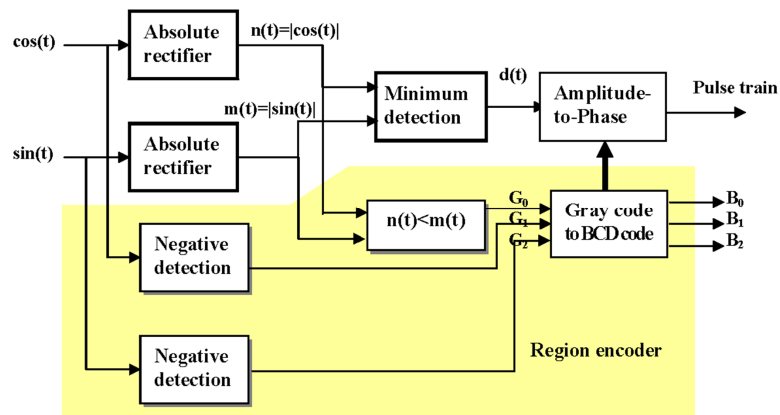


Fig. 2 Integrated phase detection diagram

Phase Splitter. Figure 2 shows the complete phase detection diagram. As shown in Fig. 1, each phase region is apparently either the replica or the mirror of sine signal from 0° to 45°. The yellow region in Fig. 2 can determine the phase index of each region as mentioned in the last paragraph. For improving the accuracy of phase detection, only the replica or the mirror of the first phase region is applied for chopping. Thus minimum detection over both $m(t)$ and $n(t)$, i.e. $d(t) = \min(m(t), n(t))$, is performed, and the signal $d(t)$ will be chopped by amplitude-to-phase mapping realized by an A/D converter and ROM chip in which the pattern in association with pulse train for chop resides.

Empirical Analysis

As for an 8-bit A/D converter, the amplitude of can be quantized into 256 discrete levels and the greatest phase mapping range θ_{max} is near 0.2234° at phase $\pi/4$ (45°). Consequently, the maximal number to split the phase region $\pi/4$ into quasi-equipollent interval is 200, that is, 45.0000/0.2234. The way to chop a sine signal must be done on its phase domain, not on its amplitude. The ideal phase divisions shown in Fig. 3 indicate the ideal chopping can result in equal divisions in phase domain. But A/D quantization on amplitude of a sinusoidal signal only can approximate the ideal phase by the actual phase divisions shown in Fig. 3. The fundamental of amplitude-to-phase mapping is discussed briefly below.

Because the maximal amplitude is $\sqrt{2}/2$ for each phase region, the quantization level on amplitude for an 8-bit A/D converter is

$$f_Q = \left(\frac{1}{256} * \frac{\sqrt{2}}{2} \right) \tag{3}$$

The phase range $\phi(n)$ relative to the n -th quantization level ($f_Q(n)$, $f_Q(n+1)$) will be

$$\phi(n) = \left(\sin^{-1}\left(\frac{n}{256} * \frac{\sqrt{2}}{2}\right), \sin^{-1}\left(\frac{n+1}{256} * \frac{\sqrt{2}}{2}\right) \right), n=0,1, \dots,255 \tag{4}$$

And the index N associated with $\phi(n)$ can be derived by

$$N(\phi(n)) = \text{floor} \left(\left(\sin^{-1}\left(\frac{n}{256} * \frac{\sqrt{2}}{2}\right) + \sin^{-1}\left(\frac{n+1}{256} * \frac{\sqrt{2}}{2}\right) \right) / 2\theta_s \right) \tag{5}$$

Where θ_s is the phase division?

Herein, the center of each ideal phase division is considered to be the delegate of this phase range. Eq. (4) obviously implies that each phase range $\phi(n)$ owns its unique number n . But in Eq. (5) two adjacent phase ranges can belong the same index, that is, index $N(\phi(n))$ index $N(\phi(n+1))$ and the maximal error of each actual phase division is restricted within one phase division.

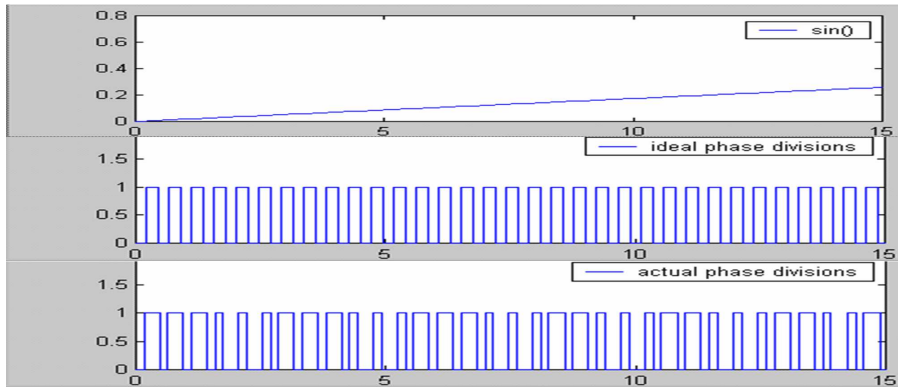


Fig. 3 Sinusoidal signal with phase from 0 to 15 radian (top), ideal phase divisions (middle) and actual phase divisions by 8-bit A/D converter.

As mentioned previously, the ideal phase divisions in Fig. 3 is a sequence of rectangular pulses. Therefore, we can assign those phase divisions an odd index on their high-level part and an even index on their-low part. This concept also can apply to the actual phase divisions. This leads to the result that the 0/1 patterns for the amplitude-to-phase module can be stored n a ROM chip. Consequently, the output from the amplitude-to-phase module will interlace high and low alternatively and phase detection is performed by counting the changes happening at the rising edges and the falling edges of the pulse train.

The Applications of Phase Splitter

Since the output of optical grid is essentially a pair of sinusoidal and co-sinusoidal signals, the application of the proposed phase splitter can be extended to optical meter. It is also applicable to magnetic dependent recorder, sine-cosine potentiometer and two- phase AC motor due to their identical phase signals. If the proposed phase splitter is embedded to these devices, their original resolution of measurement would be improved more accurate. For instance, with a phase splitter with an 8 bits A/D converter, the resolution of manufacturing machine could promoted to 1600 times.

Conclusions

The success of the proposed phase detection diagram is below: (1) Region encoder is designed to reduce the span of phase chopping; (2) The linearity of phase region from 0° to 45° is better than that of phase region from 0° to 180°. The greatest mapping phase range of the proposed method is smaller than that in [2]; (3) Each mapping phase range has a unique index of phase division and the center of

each phase division is considered to be the delegate of this phase range. Thus, the maximal error of phase detection is restricted within one phase division based on error analysis. Both the rising edges and the falling edges of the actual pulses are used to trigger the event of frequency counting so that the multiplier of improving phase resolution is extended to 1600 for an 8 bits A/D converter. Finally it worth saying that the proposed phase detection method can also be applied to detect the angular position sensed from optical meter, magnetic dependent recorder, a pair of sine and cosine potentiometer and two-phase AC motor.

References

- [1] Lucas-Nulle, *Measurement of Geometric Quantities*, IMT-3, SO 5157-2P, Ver. 1, Lucas-Nulle, (1987).
- [2] H.Y. Lee and H.H. Chiu, *Resolution-scale division method of linear scale and its implementation*, J. of Technology, Vol. 13, No. 1, (1998) pp. 95-102.
- [3] H.Y. Lee, *Sensors and Transducer Application*, Kao-Le, ISBN 957584560-9, pp.53-64, 1998.
- [4] Jen-Yu Shieh, *Digital protractor*, <http://140.125.235.7/cases/98/13.pdf>, (2010).
- [5] T. J. Maloney, *Modern Industrial Electronics*, Prentice-Hall, (1996), pp.359-364.
- [6] W.H. Liao, *The analysis and realization for four multiplier circuit with optical encoder* (in Chinese), J. of Technology, Vol. 8, No. 3, (1993), pp. 327-331.

Analysis of Characteristics and Safety of Numerically Controlled Lathe

Yingnan Zhou

Changchun University of Technology, Changchun, Jilin 130012, China

Keywords: Numerically Controlled Lathe; Characteristics; Safety

Abstract. Numerically controlled lathe has the features of high flexibility and high precision machining, efficient and conducive to the production management, and requires the operator to high technology, knowledge of programming concepts. During operation, the following security issues can use the following ways to reduce: numerically controlled lathe's commonly programmed must be right, numerically controlled lathe's processing procedures must be checked to get rid of its being breakdown, coordinate system and tool radius compensation's install must be right, pay attention to teaching and management to reduce the rate of accidents' happen, set up physical structure to separate machine and operator. By knowing the features of numerically controlled lathe can reduce accidents. Numerically controlled lathe has good processing quality, high product efficiency, simple operation advantages, but it may easily get into trouble when processing. So knowing numerically controlled lathe's features and security problems can promote production's rate and guarantee operator's safety.

Numerically Controlled Lathe'S Features

Ordinary lathe's marching range, marching quality and production efficiency seriously hindered by the technical level of *equipment* and personnel's operating level. It can't meet the development of new products, hindering productivity and improving product quality. From the rapid developing areas and enterprises, we found that the numerically controlled lathes are rapidly used in the production and processing. In the analysis of the technology of processing parts and a lot of trials, we understand and appreciate the scope of the numerically controlled lathes can process a very wide range and its product efficiency is very high. Why numerically controlled lathe has such a big advantage is because it has features as following:

Numerically Controlled Lathe'S Features

High Flexibility and High Precision Processing

Most people think that the higher degree of automation numerically controlled lathe's cost is high; it is not suitable for single pieces of small quantities of parts processing. This awareness is with certain one-sidedness. Because we only need to modify the processing procedures and do not have to do with any part of the numerically controlled lathe, it can changes forming surface to be processed into what we need. It makes numerically controlled lathe reflects what ordinary lathes don't have that unparalleled features in a single, small batch processing of the work piece. Meanwhile, numerically controlled lathe is using electronic pulse technology to ensure accuracy. Its pulse equivalent is 1 micron per pulse (High-precision CNC system can get up to 0.1 micron), It can fully ensure that the technical requirements of the work piece can also complete the processing of high-precision parts.

High Efficiency and Conducive to the Production Management

Numerically controlled lathe's high flexibility and high precision machining will make processing easy to get quality assurance, macaronis applications makes it significantly reduces the operator's labor intensity, it has shorten the processing in motor and auxiliary time. Therefore, the processing cost significantly decreased, and the production efficiency is improved. Numerically controlled lathe turn data quantitative and consistent processing time and fixed, making the process of simplification of production management. It also because the computer has been progressively applied to production management, and numerically controlled lathe machining for the production management leveled to provide a scientific and accurate basis, so that turning the processing of production management (such as quota management and so on) to a more scientific standard.

It Requires the Operator to Have High Technology and Knowledge of Programming Concepts

In general lathe shape is particularly complex or high precision parts, often rely on older workers a wealth of experience and technical skill manual control later completed, it's not equal to the old. Numerically controlled lathe is operating out of the shortcomings in this section, and it is only a higher demand on the operator's scheduling process and programming.

To Hardinge Numerically Controlled Lathe to Describe Its Characteristics

Numerically Controlled Lathe'S Features

We are using a full-featured Great Wall Machine Tool Plant production cK3732A type numerically controlled lathe. Its features are as following:

Processing a wide range able to process cylindrical, conical, ladder-shaped, about threads, taper threads and imperial threads, circular surface, and various internal and external Cambers.

Cheng Code convenience Positioning Repeatability in 0.01mm

Tool upper tool knife, 8 knives under the turret can be installed at the same time. A variety of surfaces can be processed in a single setup.

Machine tool automatic tool, tool changed rapidly, less auxiliary time. When "Hardinge Machine" was originally created, it mainly produces series of lathes and numerically controlled lathe, turning centers, after over a hundred year, the product quality of numerically controlled lathe and turning centers in this industry has a significant representative. Hardinge numerically controlled lathe including the QUEST, TALENT, the ELITE Series can be assembled in Shanghai Co.,Ltd. to manufacture. QUEST series, for example, Hardinge numerically controlled lathe machine tools the main structural features include the following aspects:

Bed Designing Structure'S Features

Hardinge CNC's bed material is mainly of pure marble, marble or granite fill and cast iron these three types. Compared to other brands of machine tools, many other brands of CNC lathes cast iron bed exists cavity in the cutting process in when trachoma cutting into the workpiece, rigid inclusion and other parts will produce localized intermittent cutting. When in the heavy cutting of superhard materials, will produce cutting vibration wave cavity parts can not prevent or eliminate vibration. With the continuation of these vibration waves on the bed, it will affect the continuity of the cutting tool, the tiny chatter in the workpiece's surface and the workpiece surface accuracy will be the impacted. Through the use of marble or granite fill can effectively eliminated harmful vibration wave in the cutting processing and to eliminate the surface chatter, thereby it can increasing the surface machining accuracy of about 30%, and then increasing the tool life to about 37%. Filled cast iron bed (mainly for the ELITE series) with a wide rib to strengthen the bed, and further enhance the rigidity and vibration damping. It is because of these characteristics, Hardinge CNC lathe bed with the other brands compared to the same type of machine weight, rigidity and vibration absorption and better.

Spindle Structural Features

Hardinge numerically controlled lathe spindle is divided into two categories of mechanical spindle and motor spindles. Mechanical spindle Hardinge patented product, the design structure is very unique. Hardinge CNC lathe mechanical spindle has five main structures: that is colletting chuck (workpiece all inclusive, clamping length of the shortest), quick-changing chuck (mass production, between the collet chuck, all populated by the rubber pad, so that the impurity can't enter the adapter, then it will applies to a large variety of shaping colletting chuck structure), the step chuck (it is also suitable for the large diameter parts clamping), within the up-type structure (mainly used for thin-walled parts, or within the hole parts of the locating datum), three-jaw self-centering chuck. To the "QUEST" series of numerically controlled lathe, the uses of the built-in collet chuck "TALENT" series of multi-jaw self centering chuck. Hardinge numerically controlled lathe spindle's maximum speed can get higher up to 6000r/min, Hardinge built-in collets chuck with the inner cone structure, as shown in the Fig. 1, with the common general mechanical spindle structures (as shown in Fig. 2) compared with the following significant advantages:

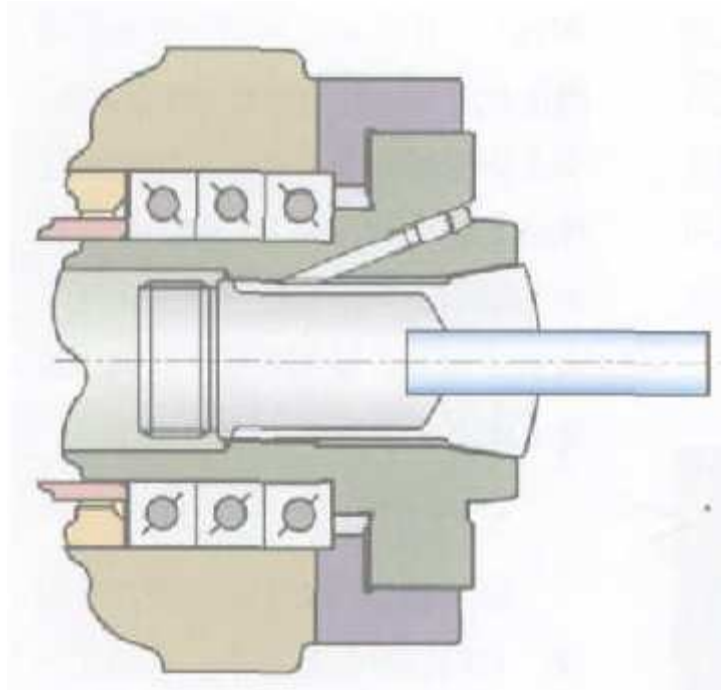


Fig. 1 Numerically controlled lathe spindle structure

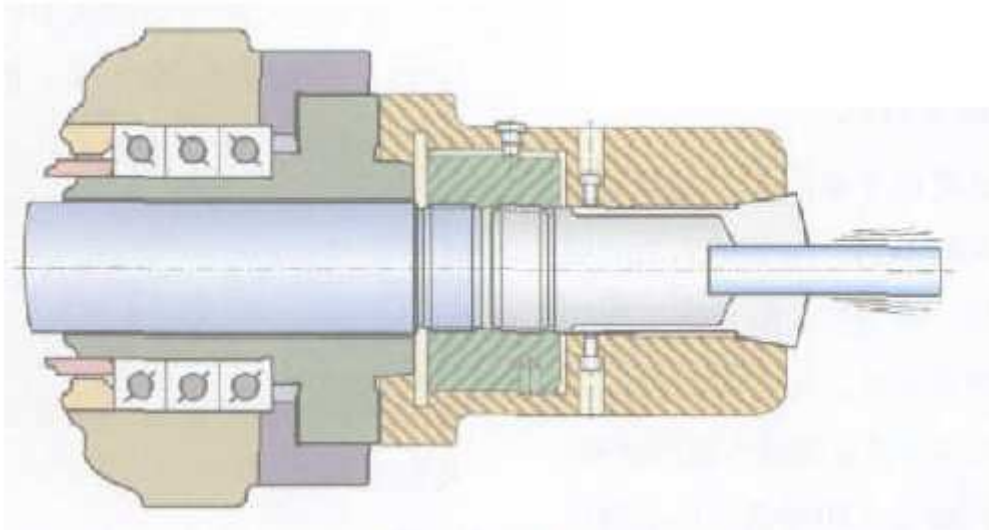


Fig. 2 Numerically controlled lathe spindle structure

Analysis the Safety Issues Of Numerically Controlled Lathe

Numerically Controlled Lathe'S Commonly Used Programming Skills Instruction

Programming is a very important link in CNC machining, improving programming skills can largely avoid unnecessary collision safety incidents.

CNC lathe processing steps to boot - back to the reference point (the establishment of the machine coordinate system) - programming - graphical simulation (check whether the processing path is correct or not) - knife (the establishment of the workpiece coordinate system) - automatic processing. The existence of an unsafe factor between the knife -automatic processing, whether the knife is the right tool or not, from the reference point of the departure we can not find the workpiece coordinate system, the automatic processing is much more likely to hit the knife in the accident. This is why the NC practice the direct many accidents occurred. The previous solution is usually to the machine operator's panel, also to press a single button, the program step-by-step implementation. If an error occurs, the machine will no longer run the next step, but it will continue to imply this section's programmer, the possibility of accidents' happening will still exist. Teachers of our university training center explored new ideas based on experience, the preparation

of the test tool the correctness of the NC programmer. Prior to processing to test the correctness of each knife on the knife, so to find the errors can be promptly corrected, thus avoiding the knife errors caused the accidents, so the quality that also is of the workpiece also have a good guarantee.

CNC Lathe'S Programmer of Safety Checks

Using Computer Simulation System

With the development of the computer technology, CNC machining teaching continues to expanding, CNC machining simulation system's functions are becoming more perfect, it has been able to simulate the CNC lathe programming operation. Preliminary inspection procedures can be used to observe the movement of the tool, then determining whether it will be a collision.

Using the function analog display that comes with the CNC system

Nowadays most advanced numerical control system with graphical can display capabilities When you want to use the input programmed, you can call the display of the graphic simulation, the detailed observation of the trajectory of the tool, in order to check the tool and workpiece whether there will be a collision.

Using CNC Lathe'S Dry Run Function

Empty running CNC lathes can check whether the correctness of the tool path is trajectory. When the programmer goes into the machine tool, it can be installed into the tool or the workpiece and the knife, when the knife is completed, the workpiece will be removed then you can press the dry run button, the spindle does not turn the turret according to the trajectory of the program to run automatically at this time it can be seen that the tool is it possible to collide with the workpiece or fixture. In this case, must ensure that is not installed on the workpiece in the chuck, otherwise they will collide.

Using the lock function of the CNC lathe

Ordinary CNC lathe has a lock function, when the lock switch is ON, the machine do not exercise, but the location coordinates of the display and the machine motion, and M, S, T can perform. When the input programmed locked the X-and Z-axis, automatic operation's processing procedures X-and Z-axis will coordinate values to determine whether there will be a collision.

CNC Machine Tools or Mechanical Failure

Stepper motor appears to a mechanical failure or in the operation of stepper motor wiring will pulled off the stepper motor and ball screw connection pin off, it can move out of sync that between the motor and extension units, or screw a foreign body (such as chips etc.), resulting in the two-axis machine tools, one direction does not move or moves slowly, so that the machine will crash appears. The operation should be done according to its color, sounds and abnormal timely manner, machine tool and screw after using should be clean. What is called that the crash phenomena should be based on prevention? First the operator must be familiar with a variety of operating systems master system function keys then to reach proficiency in operating, so that you can reduce the errors, and then the error probability of operation will bottoming out; especially for beginners to start using the system, should control the operation step, step by step to avoid mistakes happening, operator's programmings also should be based on the characteristics of the work; retraction and back to zero ordering is the first retreat in X or withdraw the Z determined to be the shape of the workpiece and also the machining position; the operator should also pay more attention to the maintenance of the machine; usually after processing, the screw and the guide should be wiped clean to avoid chips and other debris caught in the ball screw and guide rail, causing the processing error in the damage rail, the impact of processing.

Coordinate System and the Tool Compensation Settings Must Be Correct

The Correct Choice of Cutting Parameters Is the Basis

With the development of computer's software technology that the computer's simulation study is becoming a novice. CNC technology of choice for beginners where you can learn some basic operations, but in the computer simulation, the choice of machining parameters and cutting speed of cut requires and practice a great distance. That the computer simulation can quickly take the speed of that knife's cutting can be larger. However, in practical operation, the parameter selection is too

large to this that will also cause the pop knife and the consequences of damage to the workpiece, tool or machine. However in the NC machining, the cutting parameters to select the troubled CNC parts processing. Due to improper selection of cuttings parameters will also lead to cutting, deformation that caused by ultra-poor parts scrapped. Production practice, the greatest impact on the efficiency of the machining feed rate and cutting speed of the cutting depth. Therefore, it is the main consideration in the practical application of these parameters. The choice of cutting parameters, but also taking into account the clamping of the workpiece, workpiece clamping stability, cutting parameters can be selected largely; on the contrary, if the clamping stability is very poor, then the cuttings parameters would choose smaller.

The Correct Choice of the CNC Machining Process Route Is the Core

CNC machining and traditional processing methods are much in common, it has many unique areas in the process design. Irrational processing design and what CNC machining technology, quality problems and inefficiencies are very common? The processing line drawings, process a single request to determine the processing route, it is in order to ensure the accuracy of the size and position of the parts you want to select the appropriate processing sequence and clamping methods. When it is in the determining process, pay attention to follow the first rough after the fine, the first after nearly far, inside and outside the cross, and the general principles of programming, the workpiece should be margin taken into account to avoid the accident.

Focus On Teaching Management, and Reduce the Probability of the Accident

Establish Rules and Regulations of the Equipment, the Development of Safe Operation

To protect the security NC internship teaching there must be strict management. In order to achieve strict management for the premise have a system to follow. The training center of the CNC lathes has built up the rules and regulations of CNC lathes and CNC lathes for safe operation on their own characteristics, and then posted on the training workshop, so that each student can understand. Rules and regulations established by clear expression of the instructor to the students responsible for this critical thinking enhanced the sense of responsibility of the instructor. Students should apply to the instructors before using the equipment and then filling in the equipment records, so that instructors can know exactly who is operating the equipment, would also facilitate the instructor according to the specific circumstances of the student's counseling. In case of an accident can quickly find those responsible, while enhancing the students' own sense of responsibility. The training center has to develop "safe operation of CNC lathes" is very detailed, from the preparation phase before processing to the processing stage that is to have very detailed requirements, and links prone to security risks such as work coordinate system, graphics, simulation, automatic processing also made a special prompt. Strict accordance with "the safe operation of CNC lathes", to do can be a good prevention of accidents

Extensive Safety Education for Students

The training center must be strictly implemented of rules and regulations, while also using a variety of forms to carry out education on the safety of students. Make it clear that the importance of safe production and the dangers of the accident and the severity. CNC lathe's special button and turn twist, some students just started an internship at the curiosity always wanted to try some operations for their psychological training center teachers patiently explain to students in strict accordance with the guidance of teachers to develop teaching plans need to learn, thus enhancing the students a correct understanding of the safe operation of CNC lathes. In addition, the training center is going to carry out the "safety production" as the theme of the discussion. It will allow students to express their views and their own safety in that the production experience. We have also invited the NC technicians of big enterprises to explain to students that the actual working environment in the enterprise, in order that the students will realize that now is necessary to set strict demands on themselves, to lay the foundation for future work. Through this series of safety campaigns to educating the sense of that the safety of the students improved in the internship procession can be done in according to the "safe operation of CNC lathes", and enhance security in the internship process.

Set the Physical Structure of the Isolated Machine Operator

The rectangle metal hoses with all metal constructions, has all adapted to all kinds of metal cutting machine tools and cutting machine to prevent fever iron damage your power supply, water vapor line to protect labor safety.

The armor-type machine guard is a flexible organ protective cover on the basis of the outer surface with a stainless steel sheet, the alternative not a substitute for the location of a small space steel shield protection, has a beautiful appearance, light weight, no noise, and familiar features. Can be divided into fixed and movable armor machine shields

It can be used to protect the screw, light bars, columns, spindles and other round-rotating cylinder. Such shields can be horizontal or vertical using. The level of using is recommended to use plastic or aluminum support to ringing, and to maintain the guard a certain uniform distance between the cavity and the screw, and extend the service life. Stretch the length of a large compromises together with metal rings to improve that all that the stability of the guard. Connection or fixed side usually use a metal flange can also choose to set hoop.

Conclusion

Since the establishment of the training center of the CNC lathe practice teaching security system, security of the practical classes in NC car is greatly enhanced. The quality and quantity for the community to cultivate a large number of CNC lathe the application of technical personnel. Practice has proved that: the characteristics of the CNC machine tools, and links prone to failure prevention, and strengthen arrangements for the education and management can effectively reduce the security issues in the operation, you can promote the practice of other types of work.

References

- [1] Gai liwu, Zhu xuechao. Constructing and training of Practical Education System for numerically controlled lathe [J] Research and exploration in laboratory, 2007,26,8.
- [2] Xie hu. The character of part of edit module for numerically controlled lathe[J] Management & Technolosy of SME.2010,3.
- [3] Zhou junlin. The character and teaching for numerically controlled lathe [J]teaching research, 1995.2.

Three-Degree-of-Freedom Step Motor Control Strategy based on DSP

Yunbo Tang, Jingchang Yang, Ziyu Zhang, Xiaoke Gu, Qiuli Liu

Xihua University, Chengdu 610039 China

Keywords: Three-Degree-Of-Freedom Step Motor; DSP; Vector Control.

Abstract. Based on the basic principles of analysis of vector control, given three-degree-of-freedom step motor vector control of software and hardware design based on TMS320F2812 for the control, from the simulation results show that: start and 0.2s faster when the speed reaches a given value, the torque increases instantly, but then resumed, when the speed is close to a given torque value becomes 0; 0.8s torque generated when the transition, 0.03s, the torque is stable at 200N • M, show that the system has a good rapid response capability and steady state performance. Realize the decoupling flux and torque control, which makes asynchronous motor DC motor with the same access to instant-response performance, and improve the control performance and system performance.

Introduction

Vector control can achieve rapid control of the AC motor torque, and meet the requirements for high speed of motor. TMS320F2812 has a strong signal processing and control capability which can realize complex control algorithm for Asynchronous motors. This article, studies the realization of vector control on three-degree-of-freedom step motors, design a three-degree-of-freedom step motor vector control system and then simulate using Simulink.

The Vector Control Principle of Asynchronous Motor

Induction motor vector control is reference to DC motor torque; get decoupling torque expression by coordinate transformation similar to the DC motor torque, which can easily control its speed. It produces the equivalent of the rotor flux as the premise, the three-phase static coordinate system in the induction motor stator current and rotor flux converted to two-dimensional synchronous rotating coordinate system, in order to achieve the exciting current component and torque component of current decoupling between to connect the same as the control of DC motor to control the induction motor. After decoupling the state equation of induction motor torque:

$$T_e = n_p \frac{L_m}{L_r} i_{M1} \Psi_2 \quad (1)$$

Among them $\Psi_2 = \frac{L_m}{T_r p + 1} i_{M1}$, T_r is the time constant for the rotor excitation; $T_r = L_r / R_r$ is the rotor circuit time constant.

Seen from the equation, Ψ_2 rotor flux generated by only i_{M1} , With nothing to do i_{T1} , Therefore, the i_{M1} is known as the stator current component; When i_{M1} constant, that is, Ψ_2 is constant, i_{T1} decision by the induction motor torque, so i_{T1} is called the torque component of stator current. The magnetic field and torque decoupling control were realized. Figure 1 shows the basic structure of vector control.

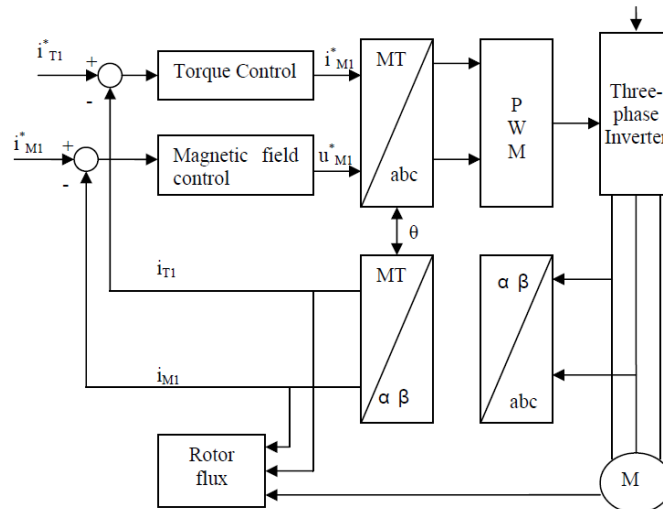


Fig.1 Three-degree-of-freedom step motor vector control system

THE CONTROL SYSTEM of THE PLATFORM

Three-degree-of-freedom step motor vector control system based on DSP, which hardware platform by the control circuit, driver circuit, and other external auxiliary circuits, on this basis, to achieve the vector control software design.

DSP as the core of the Hardware platform control circuit. TMS320F2812 is TI's latest 32-bit fixed-point DSP controller, a modified Harvard architecture with high-speed data processing capabilities. The chip integrates rich motion control specific peripherals: PWM generation circuit, SVPWM state machine, programmable dead zone, compare / capture unit, etc.; and other peripheral functions: A / D conversion unit, SCI, CAN structure controller is very suitable for use in the field of high precision servo control. Drive circuit is a typical three AC - DC - AC voltage source inverter using intelligent power module (IPM) as the main inverter switching devices, the internal integration of the six-way high-speed, low power form of Three Phase IGBT bridge and one is used to brake the IGBT, as well as over voltage, over current and overheating fault detection and protection circuit. Other external auxiliary circuit including communications interface circuits, current and voltage sampling circuit, speed detection circuit. The system block diagram is shown in Fig 2:

The main circuit is a typical AC - DC - AC voltage source inverter circuit, through the three-phase non-controlled rectifier supply power to the inverter and switching. Smart power module (IPM) as the inverter's main switching devices, which has external components, simple structure and high reliability. Equip with comprehensive protection measures to ensure system reliability.

Development platform was the typical three phase AC- DC - AC voltage source circuit inverter circuit, use Mitsubishi Intelligent Power Module (IPM) PM50RL1A120, the voltage 1200V, rated current of 50A, the internal integration of the six-way high-speed, low-power IGBT composed of three-phase full controlled bridge and one for braking IGBT, as well as over voltage, over current and overheating fault detection and protection circuit, and detection signal to the DSP to interrupt handling. All controller's output signals send into the IPM are isolated by opt-coupler circuit, suppress interference effectively.

Detection system in order to better the work of the circuit to achieve closed-loop control system and advanced control strategies, the system bus voltage, phase current and rotor position detection. Detected by the voltage signal into the analogy input circuit, through the conditioning of the signal sent after the DSP, through the A / D conversion in order to achieve closed-loop control system.

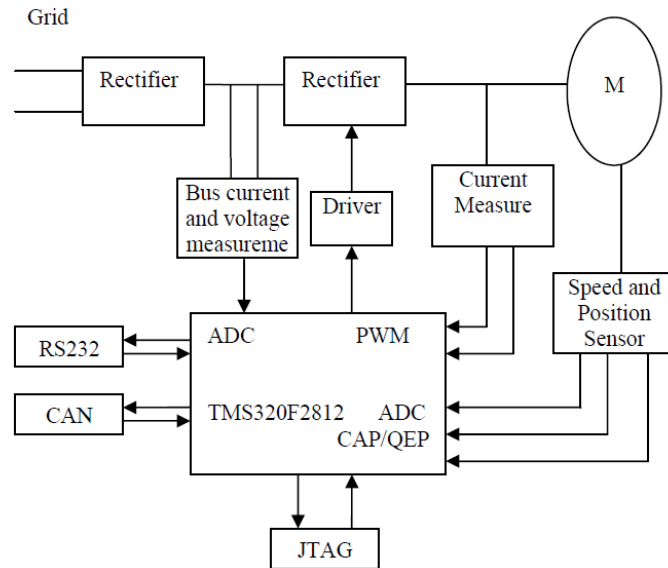


Fig. 2 DSP-based induction motor vector control system block diagram

In the inverter circuit’s DC and the output of the AC side, design the voltage and current detection circuit, through the Hall voltage and current sensors to obtain voltage and current signals, sent over by the isolation amplifier DSP to the ADC module, then A / D conversion, to achieve closed-loop control system. When the system Occurred over current, over voltage, the circuit will be low-level signals and quickly sent it to the DSP PDPINT protect the pin block PWM pulse output, to avoid system failure.

TMS320F2812 is dual power supply; the system would let +3.3 V for all I / O power, and then connect 1.9V core power supply. For this Power requirement, choice TI dual-power supply TPS767D301 provided power to the DSP chip, the chip is dual output, one constant 3.3V output voltage, the other adjustable output voltage, achieve timing requirements for DSP power supply. By TPS3823S chip power to monitor and manual / automatic reset, monitor program to prevent it running out into endless loop. TPS767D301 level output circuit is shown in Fig 3.

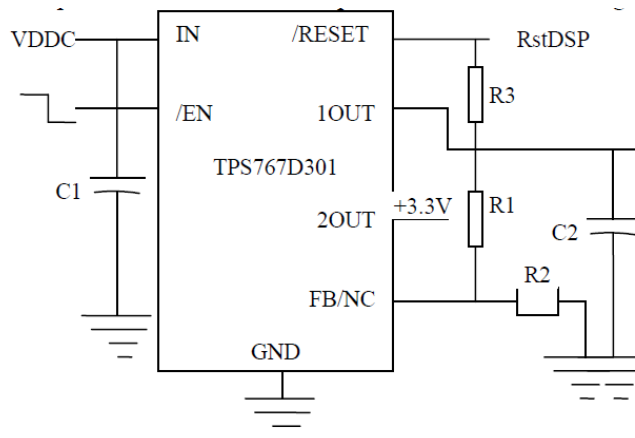


Fig. 3 TPS767D301 level output circuit

$1OUT = (1 + R1/R2)$, $2OUT = 3.3V$. Where $VREF = 1.1834V$ Select the appropriate $R1$, $R2$ resistor values, can get adjustable voltage.

TMS320F2812 internal has $128K \times 16$ bit Flash program memory, usually run the compiled programs into the Flash, however, the use of Flash programming approach simulation, not only a limited number of programming, but also inefficient. In the commissioning phase, usually write a program on the PC, and then generate the corresponding object code, through the JTAG Interface emulator download data to the target board, thereby improving the real-time simulation. Simulation can use the on-chip SARAM as the program memory, but when the program is too large, the

commissioning phase, the simulation will not proceed smoothly. To facilitate debugging, the expansion of the one-chip $64K \times 16$ bit memories, for program / data memory. Memory addresses space occupied by a total of 256K. This will not only avoid the frequent programming chip Flash, but also improve debugging speed.

When complete variety of control strategies and various algorithms of data processing in the system development platform will cause lots of temporary data, if only by the DSP RAM commitment will no doubt add to the burden of DSP, make system control lower precision, limit the system full operation. To meet the data storage needs expand a model SARAM IS61LV6416. IS61LV6416 and DSP Connection diagram is shown in Fig 4.

- Chip extended memory chips used IS61LV6416, $64K \times 16$ bits, the chip features are as follows:
- High-speed, maximum access time is 20ns;
- By COMS technology, to obtain the optimal speed and low power consumption;
- Low-power, maximum 250mW;
- 3.3V voltage supply;
- Fully static operation: no clock or refresh required;
- High and low bytes of independent data control;
- 44-pin SOJ, 44-pin TSOP, 44-pin mini BGA package of three

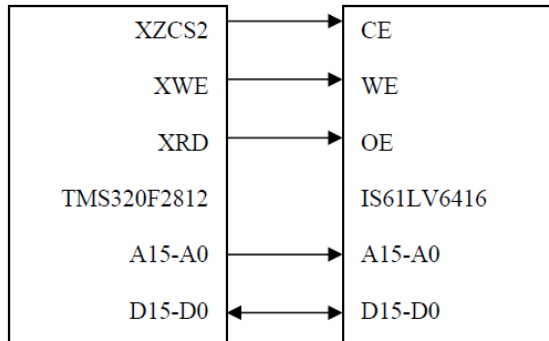


Fig. 4 IS61LV6416 and DSP connection diagram

In order to protect system reliability and design with the LCD liquid crystal display interface circuit, the system man-machine interface, making the system has good man-machine interface. LCD modules can be controlled via the bus; GPIO port can also be controlled. F2812 has many GPIO ports, so the choice in the design of GPIO port to control the LCD module. LCD module who use Sun Electronics Co., Ltd. Changsha SMG12864ZK standard point of formation of Chinese characters and graphics LCD modules, can display 128×64 dot matrix or 8 characters \times 4 lines, DSP and the LCD interface circuit is shown in Fig5.

Induction motor vector control system software using C language, and programmed on CCS3.3 in the DSP software integrated development environment. System software composted with the main program and interrupt service routine. The main program was completed for the system I / O, ADC, event manager module, and system requirements such as variable initialization and interrupt system settings and so on.

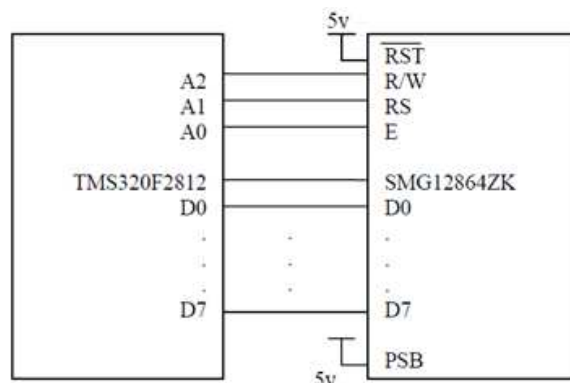


Fig. 5 DSP and the SMG12864ZK interface circuit

Simulation Analyses and Conclusions

For the design of three-degree-of-freedom step motor vector control system Simulink simulation, three-degree-of-freedom step motor parameters are as follows: Rated power 3KW, rated voltage 460V, rated frequency 50HZ, the stator resistance of 0.09Ω , the stator leakage inductance 0.75mH . Rotor resistance 0.23Ω , rotor leakage inductance 0.75mH , stator and rotor mutual inductance 35mH , the pole number is 2, moment of inertia $0.2 \text{ kg}\cdot\text{m}^2$, inverter DC power supply is 510V, output torque limit for the 300N.M.

Given speed 120rad/s , no-load motor speed and torque at start-up simulation waveform were shown in Figure 6. When 0.2s given speed 60rad/s , when 0.8s given speed 120rad/s , and in the 0.8s to load $200\text{N}\cdot\text{m}$, motor speed and torque simulation waveforms were shown in Fig7.

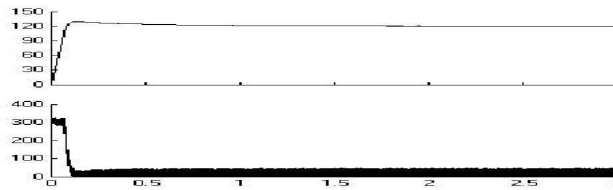


Fig. 6 Load given 120rad/s speed, torque waveform

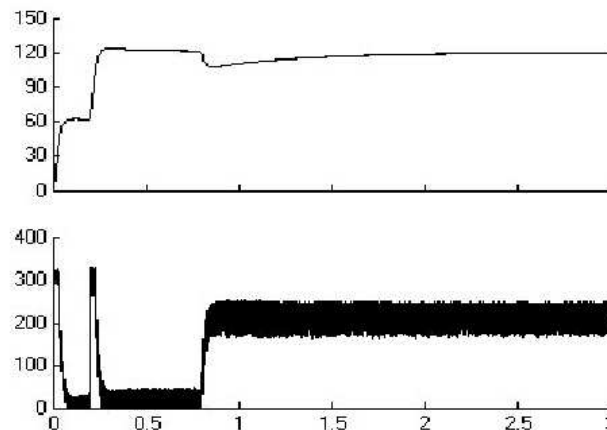


Fig. 7 8s to load $200\text{N}\cdot\text{m}$, 0.2s given 60rad/s , 0.8s Given 120rad/s speed, torque waveform

Acknowledgement

Supported By the Innovation Fund of Postgraduate, Xihua University

References

- [1] Ning Li, Gui Chen. The Motion control system [M]. Beijing: Higher Education Press, 2009.
- [2] Hong Xing Wu, Zong Wu Xie, Qiang Zhang. Motor control technology based on DSP [M]. Beijing: China Electric Power Press, 2010.
- [3] Xiao Sheng Pan, Shi Yong Hao. 50 essence examples of motor use MATLAB simulation [M]. Beijing: Electronic Industry Press, 2007
- [4] Bo Shi Chen. Power Speed Control [M]. Beijing: Mechanical Industry Press, 2005.
- [5] Lu Ping Hu. Simulation of asynchronous machine slip vector control system based on simulink platform [J]. Zhejiang Water Conservancy and Hydropower College .2006, 18 (3):56-58.
- [6] Xiang Liu, Dong Sheng Zuo. Vector control system of Induction motor based on DSP [J]. Techtronic .2010, 3:47-48.

Study of a novel demodulation method for FBG sensor

Lu Wang, Bao-jin Peng, Fei Xu, Dan Wu, and Hao-wei Wu

Zhejiang Normal University, Institute of Information Optics, Jinhua, Zhejiang Province, China
e-mail: jhpbj@zjnu.cn

Keywords: Fiber Bragg Grating (FBG); Matching Grating Demodulation; Demodulation; Cascade; Temperature/Strain Cross-Sensitivity

Abstract: A novel demodulation method for Fiber Bragg Grating (FBG) sensor based on matching grating demodulation is proposed. It is means using several fiber gratings to cascade, and programming to make the computer automatically select different wavelengths. So that it can expand demodulation range based on high sensitivity. The photoelectric detector (PD) makes the reflected light intensity which form FBG change into voltage. And the voltage is amplified to 0~5v by amplifying circuit. Then through the data collection box, voltage sent to computer for data acquiring. Real-time analysis data and display the variable of center wavelength for sensing FBG. Because the same type of sensing FBG and demodulation FBG, they have the same temperature drift, so it can control the influence of environmental temperature. Therefore, this system can successfully solve the temperature/strain cross-sensitivity issue. The experimental results show that it is feasible to demodulate wavelength using the cascaded FBG. And the experimental measuring wavelength error is less than 0.009 nm, the measuring micro-strain error is less than 7.5 $\mu\epsilon$.

Introduction

Fiber Bragg grating (FBG) sensors have for years been studied as optical sensors in a variety of applications due to their important properties. The outstanding property of FBG is that the measuring signals are wavelength-code signals, so how to achieve wavelength demodulated, that is the key technology of distributed sensors[1,2]. Thus, there are many demodulation schemes proposed by domestic and foreign scholars[3,4], including spectrometers, hypotenuse filters, tunable filters, interference scanning methods, matching grating methods, etc. In these methods, the spectrometers have high-cost, the resolution of hypotenuse filters is low, the tunable filters have long scanning cycle, and the interference scanners have bad repeatability. So in recent years, matching grating methods are more and more favored by people.

Matching grating method provides a range of advantages pertaining to low-cost, high-resolution, ease of fabrication, and especially for real-time dynamic monitoring. So it has a broad prospect of application in the optical fiber sensors fields. But it also have some disadvantages: the 3 dB bandwidth of the general FBG is about 0.2 nm, so the demodulation range is small for the single matching grating demodulation system. And in many cases, it can't enough to use; the single matching grating demodulation system also exists double values problem [7, 9].

This paper introduces a demodulation system of FBG sensor with cascaded FBG, which based on matching grating demodulation. According to the practical targets, this system not only avoids the above problems of the matching grating demodulation, it also has many other advantages: large measurement range, high sensitivity, low-cost and wide application, etc [8].

Experimental Principle

Fig. 1 shows the experimental setup for the demodulation system of FBG sensor, which based on matching grating demodulation method. The light, from broadband light source, that through 3dB coupler into sensing FBG. And the reflected light signals are divided into n parts through another coupler. Each part connects to a 3dB coupler respectively. Afterwards, the signals transmit into a demodulation FBG. The reflected light signals from cascaded demodulation FBGs are received by the corresponding PDs, and then the light signals changed into electrical signals by the PD. The

obtained voltage values corresponding to the change of detected physical variables. After voltage values amplified by amplifying circuit, the signals, through the data collection box, are sent to the computer to analyze and show.

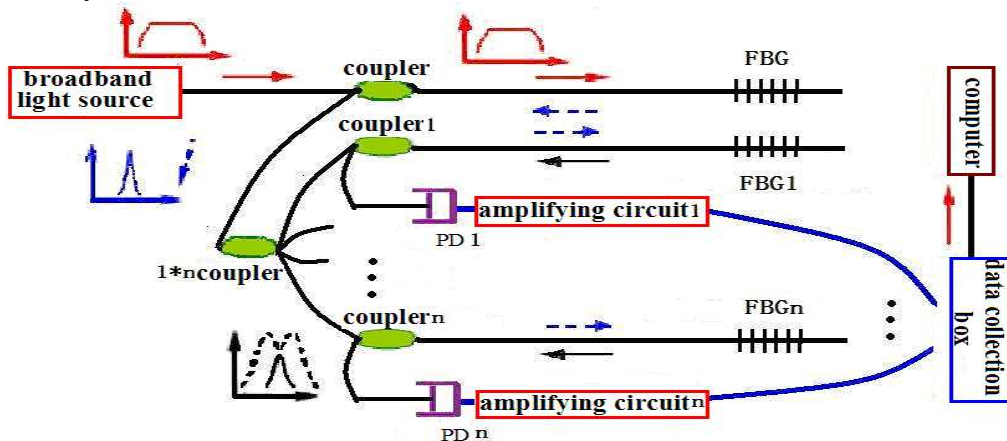


Fig.1. The demodulation system of FBG sensor based on matching grating demodulation method

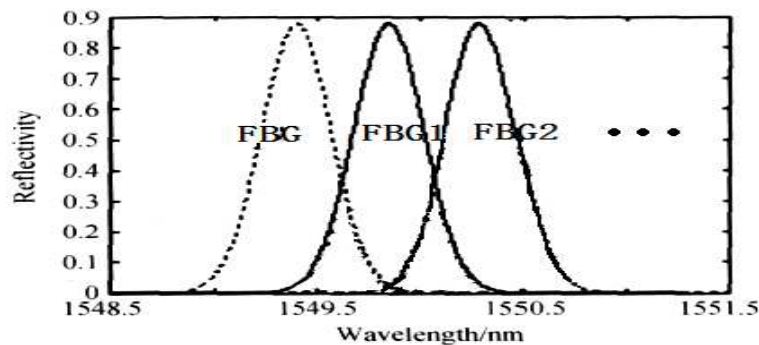


Fig.2. Spectra of the sensing FBG and the matched FBGs

Fig. 2 shows the reflection spectrum diagram of sensing FBG and cascaded demodulation FBGs [9]. When the overlap of reflection spectrum decreases gradually for sensing FBG with the first matching FBG, the overlap is gradually increasing with the second matching FBG. And the power detected by the first PD, which corresponding to the first matching FBG, gradually decreases; while the power detected by the second PD increases gradually. Therefore, using overlap of cascaded matching FBG, it can achieve to increase the range of sensing measurement.

In the demodulation method of single matching grating, for the light intensity received by PD, the wavelength of the corresponding sensing FBG may be equal to the two different symmetrical wavelength values, which match on both sides of the grating center wavelength. So it can't be recognized by demodulation system. That is the double values problem of the single matching grating [10]. Fig. 2 shows that when the sensing FBG has a strain, two PDs are received signals. But the received light power are different, the output voltage is also different. In other words, there are two output signals corresponding to the measured strain. The two output signals from different PDs, as long as selecting the appropriate center wavelength and bandwidth, it can be determined the output value in the later circuit According to the former circuit output and vice versa. So it already inherently possesses the ability to solve the problem of double values for the demodulation method of cascading FBGs.

Because the same type of sensing FBG and demodulation FBG, they have the same temperature drift. So if sensing FBG measures strain, as long as sensing FBG and demodulation FBG are under the same environmental temperature, the temperature changes, the relative position between the reflection spectrums does not change. It can efficiently control the influence of environmental temperature. Therefore, it successfully solves the problem of temperature and strain cross-sensitivity.

Design and Analysis of Demodulation System

This experiment takes two cascaded FBGs for example. The Fig. 3 shows the experimental system, it can be structured according to the schematic, which is shown by Fig. 1. And in the Fig. 3, the number 1,2,3,4,5,6,7,8 respectively represents broadband light source, fiber Bragg grating (sensing), fiber Bragg grating (demodulation), coupler, strain controller, photoelectric detector, data collection box and computer. In this experiment, the center wavelengths of demodulation FBG1, FBG2 are 1549.80nm and 1550.01nm respectively. The center wavelength of sensing FBG is 1549.68nm. The reflectivities of three fiber gratings are similar to equal, but the center wavelengths are different.

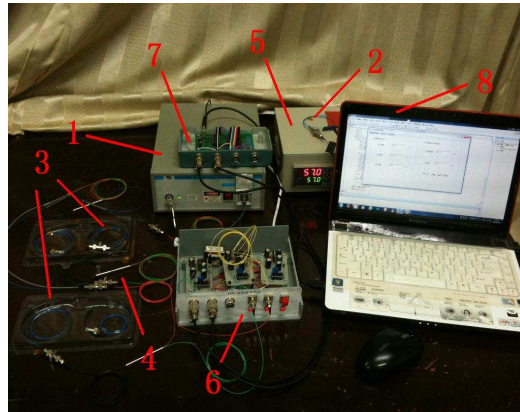


Fig.3. Experimental device

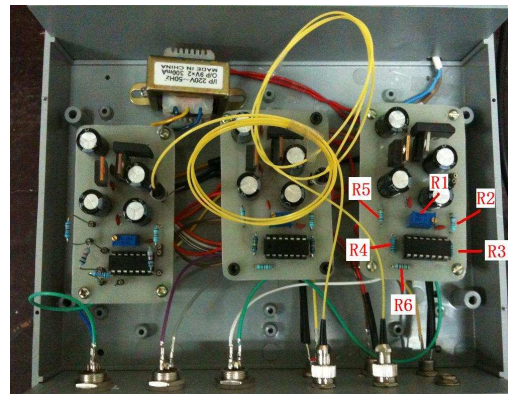


Fig.4. Photoelectric converting and amplifying circuit

System Hardware Design The Fig. 4 shows the system hardware. It can be seen that, in the photoelectric conversion amplifying circuit, the light signals, which reflected by matching demodulation grating, received and switched to voltage signals by the corresponding PDs. Changing the resistance values of R3, R4, R5, R6, so that the voltage can be amplified to 0-5V. And then the data sent to the computer for data acquiring.

System Software Design Collecting data to the computer, and writing relevant VB program, so that it can real-time analyse data and display the physical quantities. It can be seen from Fig. 5 and Fig. 6 that: if the center wavelength position of sensing FBG intersects with the rising edge of demodulation FBG1, the PD1 can detect the corresponding voltage. The interface displays that the current work is in the first channel, and it can calculate wavelength drift according to the first channel. If the center wavelength location of sensing FBG intersects with the rising edge of demodulation FBG2, when the PD2 has voltage output, the interface shows that the current work is in the second channel, and wavelength drift calculated according to the second channel. According to the formula [7]:

$$\Delta\lambda_{BS} = \lambda_B(1-P_e) \Delta\varepsilon. \quad (1)$$

It can obtain the strain capacity corresponding to the wavelength shift.

The Analysis of Experimental Results The selected initial wavelength is 1549.802nm. Running the VB program, the error analysis data can be summarized with the temperature changing; it is shown in table 1. It can be seen that the experimental measuring wavelength error is less than 0.009 nm, and the measuring micro-strain error is less than 7.5μ ϵ .

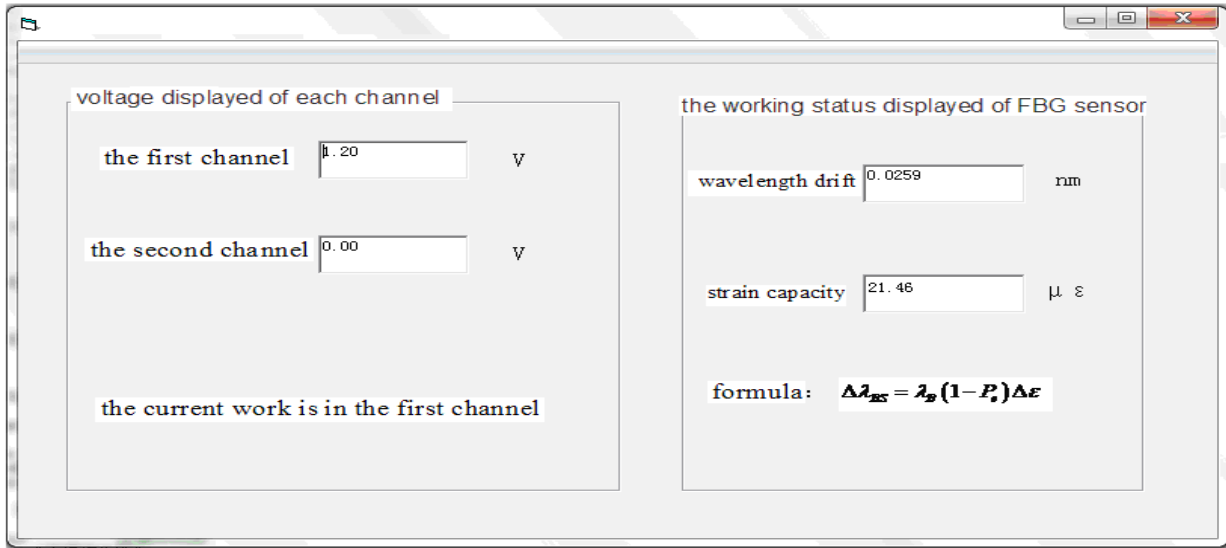


Fig.5. The software interfaces on working in the first channel.

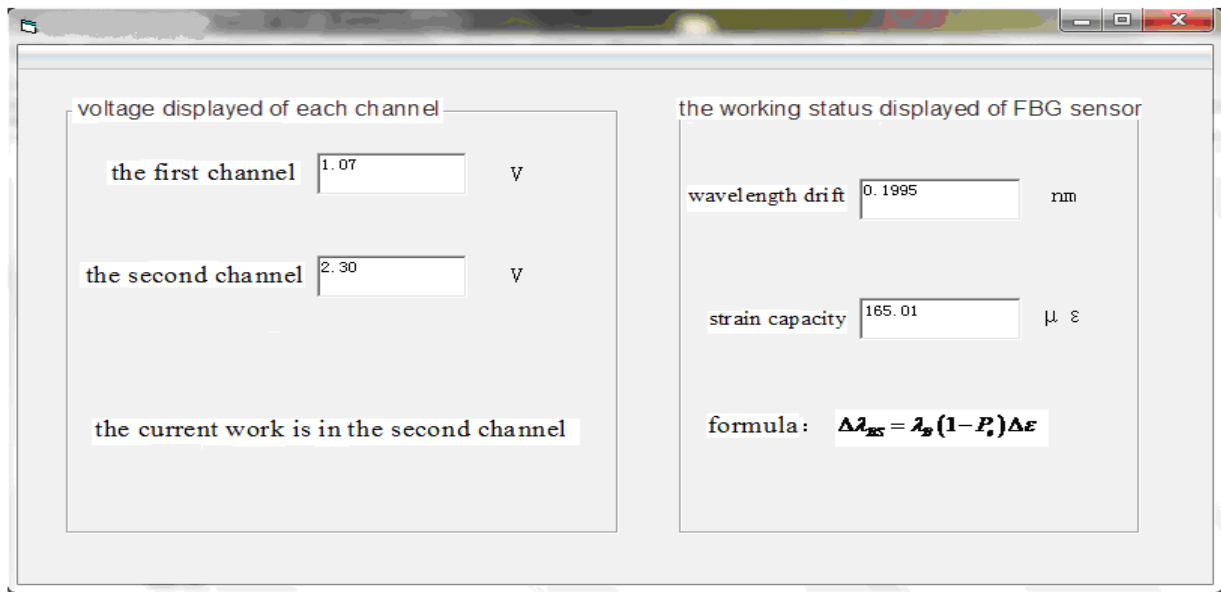


Fig.6. The software interfaces on working in the second channel.

Table 1 The data of error analysis

Initial wavelength: 1549.802nm

Strain (μ ϵ)	Wavelength drift(nm)	Measuring wavelength(nm)	Standard wavelength(nm)	Error(nm)
19.03	0.023	1549.825	1549.816	0.009
27.30	0.033	1549.835	1549.830	0.005
33.09	0.040	1549.842	1549.842	0.000
47.98	0.058	1549.860	1549.869	-0.009
138.13	0.167	1549.969	1549.966	0.003
149.17	0.181	1549.983	1549.980	0.003
161.29	0.195	1549.997	1549.997	0.000
173.70	0.210	1549.012	1550.019	-0.007

Conclusion

The experiment shows that it is feasible to demodulate wavelength using the cascaded FBG. This system inherits the advantages of the matching grating method: simple structure, low-cost, easy implementation, etc. It solves the problems of small measuring rang and double values of the matching grating method. And it also solves the problem of the temperature and strain cross-sensitivity. So this system has practical value.

Acknowledgements

Corresponding author.jhpbj@zjnu.cn; phone +86-579-82298849; the paper supported by the Zhejiang science and technology Project (No.2011C22051) and Zhejiang Provincial Natural Science Foundation of China (No.Y1100041)

References

- [1] K. C. Chuang, C. C. Ma, and C. H. Wang: Appl. Opt. 5243-5255 (2011), p.27.
- [2] Jeong Hyun Huh, Y. M. Chang, Lianshan Yan, and J. H. Lee: Appl. Opt. 348-355 (2012), p.3.
- [3] H. T. He, G. Z. Yao, B. G. Li and Y. Q. Li: Optical Communication Technology. 5-7 (2010), p. 6.
- [4] M. Wang, L. M. Zhao: Electronic components application. 17-19 (2010), p. 3(12).
- [5] Y. L. Huang, S. Dai: Chinese Journal of Sensors and Actuators. 1266-1269 (2009), p. 22(9).
- [6] W. B. Gan, C. Zhang, Y. B. Qi: Journal of Wuhan University of Technology. 118-120(2009), p.31(5).
- [7] Y. F. Zhai, N. Zhou, Y. Liu and A. Wang: Acta Photonica Sinica. 1088-1091 (2007), p. 6(6).
- [8] Y. Cao, Z. Gu: Optical Technique. 49-55 (2011), p. 37.
- [9] X. C. Yang, J. C. Pei, and Y. G. Zhan: Acta Photonica Sinica. 42-45 (2008), p. 37(1).
- [10] Y. G. Zhan, Q. Lu, S. Q. Xiang: Acta Photonica Sinica. 711-715 (2004), p. 33(6).

M Optimized Multi Virtual Gravity

Lipeng YUAN^{1, a}, Liming YUAN^{2, b} and Hongying LU^{3, c}

¹Department of Mechanical and Aerospace Engineering, College of Engineering, Cornell University, 306 Kimball Hall, Cornell University, Ithaca, NY, USA 14853

¹School of Mechatronics Engineering, Harbin Institute of Technology, China 150001

²Capital Aerospace Machinery Company, No. 1, Nan Dahongmen Road, Sub-box 91, P.O. Box 34, Beijing, China 100076

³Department of Mechatronics and Controls, Beijing Research Institute of Precise, No. 1, Nan Dahongmen Road, Sub-box 77, P.O. Box 9200, Beijing, China 100076

^ahitylp@126.com, ^bannieliuxiaolei@163.com, ^chitluhy@126.com

Keywords: Biped robot; Virtual passive; Optimization; Energy.

Abstract. A popular hypothesis regarding legged locomotion is that humans and other large animals walk and run in a manner that minimizes the metabolic energy expenditure for locomotion. Here, we just consider the walking gait patterns. And we presented a hybrid model for a passive 2D walker with knees and point feet. The dynamics of this model were fully derived analytically. We have also proposed optimized virtual passive control laws. This is also a simple and effective gait-generation method based on this kneed walker model, which imitates the energy and torque behaviors in every walking cycle. Following the proposed method, we use computer optimization to find which gaits are indeed energetically optimal for this model. We prove some walking rules maybe true by the results of simulations and experiments on the existing walking robot.

Introduction

Why do people select walking and running from the other possibilities [1]? We address such questions by modeling a person as a machine describable with the equations of newtonian mechanics. We wish to find how a person can get from one place to another with the least muscle work.

Passive dynamic walkers exhibit a stable gait [2] when placed on a downward slope with no actuation. These systems demonstrate how the inherent dynamics of walkers can be exploited to achieve natural and energy-efficient gaits.

Our main goals about biped robot's gait synthesis, motion planning and energy optimization are the following aspects.

To present a mathematical model for a simple two-dimensional planar kneed walker with point feet and knees, making it both a logical extension of the compass gait model and a physically realizable model

Realization of safe virtual passive dynamic control against human being and outside environment

According to the control strategy, energy optimization will be carried out. For simplicity, we seek an explanation of gait choice with no essential dependence on elastic energy storage; we assume no springs (tendons) in series or parallel with the actuators.

Model of a Kneed Biped

This section addresses the walking robot model. We deal with a planer biped model which has knee joints. Fig. 1 shows the model of a kneed biped walking robot and its notations and numerical settings for simulations.

At the start of each step, the stance leg is modeled as a single link of length L , while the swing leg is modeled as two links connected by a frictionless joint. The system is governed by its unlocked knee dynamics until the swing leg straightens out. When the leg is fully extended, the kneestrike occurs. At this point, the velocities change instantly due to the collision, and immediately afterwards, we switch to a two-link system in its locked knee dynamics phase.

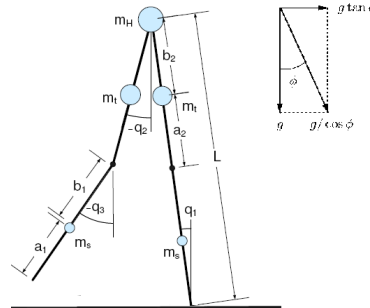


Fig. 1 Four -link kneed biped model.

m_t	Thigh mass	0.5 [Kg]
m_s	Shank mass	0.05 [Kg]
m_H	Hip mass	0.5 [Kg]
a_1	Shank length (below point mass)	0.375 [m]
b_1	Shank length (above point mass)	0.125 [m]
a_2	Thigh length (below point mass)	0.175 [m]
b_2	Thigh length (above point mass)	0.325 [m]

Dynamic Equations. During the unlocked swing phase, the system is a three-link pendulum[3]. The full equations of motion for such a system are derived using Lagrangian formulation[4]. The dynamics are shown in the standard form of planar manipulator dynamics in Eq. (1).

$$H(q)\ddot{q} + B(q, \dot{q})\dot{q} + G(q) = -J^T \lambda + \tau + \tau_e. \quad (1)$$

Where, $J^T \lambda$ is the constraint force at knee-joints, τ is the control input and τ_e is the vector due to the environmental forces of the robot.

Collision Event We model the kneestrike as a discrete collision event in a three-link chain and switch to the compass gait model afterwards. Since the only external force on this system is at the stance foot, angular momentum is preserved for the entire system about the stance foot and for the swing leg about the hip. When looking at the lower link of the swing leg, however, the kneestrike acts as an external impulse. Therefore, angular momentum is not conserved about the knee. But the knee joint angle corresponding to the knee is locked after the collision. Therefore, its post-collision velocity will be that of the second link.

The heelstrike is modeled as an inelastic collision about the colliding foot. This heelstrike event is, again, identical to the heelstrike for the compass gait. Angular momentum is then conserved for the entire system about the colliding foot and for the swing leg after impact about the hip. Right after the event, the model switches both legs and the impact foot becomes the new stance foot. The model also switches back to the unlocked three-link dynamics to start a new step cycle. The third joint angle starts with the same angular position and velocity as the second one.

Optimized Virtual Passive Dynamic Walking

Passive dynamic walkers exhibit a stable, natural and energy-efficient gait. However, the passive walker cannot walk on the level ground without any external energy sources, so we will introduce “optimized virtual gravity” for biped robots to create the walking pattern automatically with the least muscle work and without loss of properties of passive dynamic walk on the floor.

Virtual Passive Dynamic Walking. A virtual gravity toward the horizontal direction is as a driving force to walk forward[5]. We can transform the virtual gravity effect to the actuator’s torque and it can be expressed as follows:

$$\tau = \begin{bmatrix} -\left(m_h L + m_s a_1 + m_t (l_s + a_2) + m_t L + m_s L\right) \cos(q_1) \\ \left(m_t b_2 + m_s l_t\right) \cos(q_2) \\ m_s b_1 \cos(q_3) \end{bmatrix} g \tan \phi \quad (2).$$

Where, ϕ is the virtual slope angle. The transformation of control inputs are:

$$\tau = S \cdot u = \begin{bmatrix} -1 & -1 & 0 \\ 0 & 1 & -1 \\ 0 & 0 & 1 \end{bmatrix} \cdot \begin{bmatrix} u_1 \\ u_2 \\ u_3 \end{bmatrix} \quad (3)$$

we get:

$$\begin{aligned} u_1 &= \left[\left(m_h L + m_s a_1 + m_t (l_s + a_2) + m_s L + m_t L\right) \cos(q_1) \right. \\ &\quad \left. - \left(m_t b_2 + m_s l_t\right) \cos(q_2) - m_s b_1 \cos(q_3) \right] \cdot g \cdot \tan(\phi) \\ u_2 &= \left[\left(m_t b_2 + m_s l_t\right) \cos(q_2) + m_s b_1 \cos(q_3) \right] \cdot g \cdot \tan(\phi) \\ u_3 &= \left[m_s b_1 \cos(q_3) \right] \cdot g \cdot \tan(\phi) \end{aligned} \quad (4)$$

The dynamics of kneed biped robots is more complex than that of compass-gait ones. So the steady gait of a kneed walker with single virtual gravity cannot be obtained easily without suitable parameter choice. At the same time, we also want to optimize the total energy that the biped robot has consumed on the actuators during the walking. Based on the observation, we propose “Multi Virtual Gravity” for the kneed biped robot in order to generate steady walking patterns and optimize the walking energy without loss of virtual passivity (Fig. 2.).

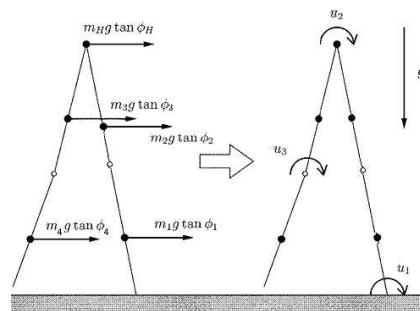


Fig. 2 Optimizing multi virtual gravity fields.

The transformed torque of Multi Virtual Gravity effect is given by:

$$\tau = R_c(q) \cdot \Gamma \cdot \tan \phi \cdot g \cdot \alpha_{nks} \quad (5)$$

Where, α_{nks} is the sensitivity function of control inputs (virtual gravity scale), and:

$$\tan(\phi) = \begin{bmatrix} \tan \phi_H \\ \tan \phi_1 \\ \tan \phi_2 \\ \tan \phi_3 \\ \tan \phi_4 \end{bmatrix} \quad R_c(q) = \begin{bmatrix} \cos(q_1) \\ \cos(q_2) \\ \cos(q_3) \end{bmatrix} \quad \Gamma = \begin{bmatrix} -m_h \cdot L & -m_s \cdot a_1 & -m_t (l_s + a_2) & -m_t \cdot L & -m_s \cdot L \\ & & & m_t b_2 & m_s l_t \\ & & & & m_s b_1 \end{bmatrix}$$

The passivity of virtual passive walker is also able to be shown using “virtual energy”:

$$E_v = \frac{1}{2} \dot{q}^T M(q) \dot{q} + P_v(q, \phi) \quad (6)$$

The virtual potential energy is given by:

$$P_v(q, \phi) = \frac{J_H \cdot g}{\cos(\phi_H)} + \sum_{i=1}^4 \frac{J_i \cdot g}{\cos(\phi_i)} \quad (7)$$

Optimized Multi Virtual Gravity Why do humans and other animals move the way they do? An ancient hypothesis, dating back at least to a contemporary of Galileo and Newton (Borelli [6]), is that animals move in a manner that minimizes effort, perhaps as quantified by metabolic cost per distance travelled[7,8].

In order to optimizing the total actuator’s torque energy and keep steady walking pattern without loss of virtual passivity, we use the ‘SNOPT’ software to calculating the suitable control parameter of the biped robot.

The optimizing target is the total actuator’s torque energy. During the Unlocked Knee Stage the optimizing target is setting as follows:

$$\int_0^t (\tau(1)^2 + \tau(2)^2 + \tau(3)^2) dt \quad (8)$$

A gait is characterized by the position and velocity of the body at the start of a stance phase relative to the stance foot, by the step period, and by τ .

The optimal solutions have cost arbitrarily close to zero unless the optimization is further constrained. Firstly, the cost P can be reduced nearly to zero by taking small steps [9]. So, we optimize for various fixed values of step length d . Secondly, the cost P has a non-anthropomorphic lower bound (corresponding to standing on one leg for an infinite time mid-step), approached as the average speed v goes to zero, so we constrain v .

Because we just want to find the walking gait with the least muscle work W , we choose low speed $v=0.185$, and short step length $d=0.1$. These can guarantee that the robot operates a classic inverted-pendulum walking gait but not an impulsive running gait. We can find a steady fixed point for the table 1 parameters when the virtual slope angle ϕ is 0.0504 rad. We use the fixed point and ϕ as the optimizing initial condition.

By using the ‘SNOPT’ software and according to the optimizing target and constraint condition, we can get the result which makes the total actuator’s torque energy minimal. At the same time, the result has steady walking patterns and can walk without loss of virtual passivity. A limit cycle for the upper link of one leg starting from this fixed point is shown in Fig. 3(a).

The instantaneous velocity changes from the heelstrike and kneestrike events can be observed in this limit cycle as straight lines where the cycle jumps with the instantaneous velocity changes while the positions remain the same. In contrast with the compass gait, however, in addition to the two heel-strikes, there are two more instantaneous velocity changes produced by the kneestrikes.

The actuator’s torques of the multi virtual gravity control dynamic walking is also shown. Fig. 3(b) is the result with energy optimization, and Fig. 3(c) is without energy optimization. From Fig. 3 we can see that the constant-like torque is also succeeded. It means that these walking patterns are natural motion.

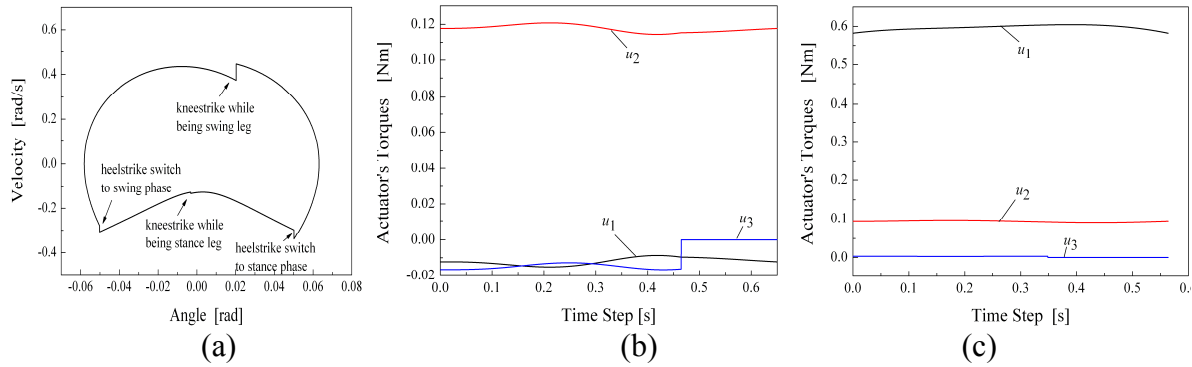


Fig. 3 Virtual passive dynamic walking with energy optimization

Optimization with Piecewise Multi Virtual Gravity

If we use the piecewise function to take the place of $\tan(\phi)$ in equation 7, and set the sensitivity function α_{rbs} equal to 1, we can get a 'Piecewise Multi Virtual Gravity' control method. According to the range of $\tan(\phi)$, the value range of piecewise function could be very large. But because here we use small and slow step, so piecewise function is restricted into $[-0.5; 0.5]$.

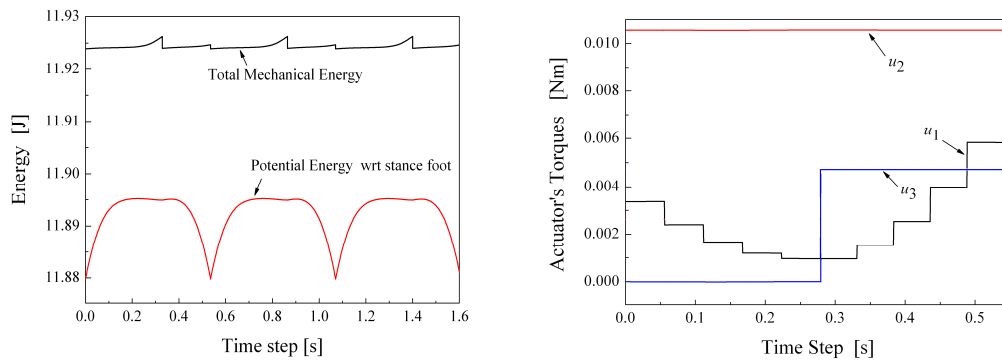


Fig. 4 Simulated energy and torques with the piecewise control

The simulated energy result by using the piecewise function driving all legs' joints is shown on the left hand of Fig. 4. And the actuator's torques with the piecewise controls in one step shown on the right hand of Fig. 4.

In the figure, the ankle's torque u_1 has a push-off impulse. And the hip's torque u_2 and the knee's torque u_3 are both constant, this is very important feature for the stability of biped robot's posture.

On the other hand, if we compare the results between Fig. 3 and Fig. 4, we can realize that these optimized torque curves show similar trends. And we can also know that real human ankle joint should have heel-strike and push-off impulses at the beginning and ending of one step[10]. And hip joint does approximately perform a positive constant-like torque during one step unless after the step, he will stop. And the knee joint torque of the swing leg is also approximately constant before the knee is locked.

Summary

In the figure, the ankle's torque u_1 has a push-off impulse. And the hip's torque u_2 and the knee's torque u_3 are both constant, this is very important feature for the stability of biped robot's posture.

On the other hand, if we compare the results between Fig. 3 and Fig. 4, we can realize that these optimized torque curves show similar trends. And we can also know that real human ankle joint should have heel-strike and push-off impulses at the beginning and ending of one step [9]. And hip joint does approximately perform a positive constant-like torque during one step unless after the step, he will stop. And the knee joint torque of the swing leg is also approximately constant before the knee is locked.

References

- [1] R. McN. Alexander. *Mechanics of bipedal locomotion*. Pergamon Press, New York, Vol. 1 (1996), p. 493-504.
- [2] Vanessa F. Hsu Chen. *Passive Dynamic Walking with Knees: A Point Foot Model*. Massachusetts Institute of Technology Press, Massachusetts (2007).
- [3] Simon Mochon and Thomas A. McMahon. *Ballistic walking: An improved model*, *Mathematical Biosciences*, 52(3-4):241-260 (1980).
- [4] Jean-Jacques E. Slotine and Weiping Li. *Applied Nonlinear Control*. Prentice Hall (1990).
- [5] Fumihiko Asano and Masaki Yamakita. *Virtual Gravity and Coupling Control for Robotic Gait Synthesis*. *Systems and Humans*, 31(6): 737-745 (2001).
- [6] J.A. Borelli. *On the movement of animals (De Motu Animalium, Pars prima)*. P. Maquet (trans.) (1989). Springer-Verlag, Berlin, p. 152.
- [7] M. Srinivasan. *Optimal speeds for walking and running, and walking on a moving walkway*. *Chaos*, 19: 026-112 (2009).
- [8] A. D. Kuo. *A simple model predicts the step length-speed relationship in human walking*. *Journal of Biomechanical Engineering*. 123, 264-269 (2001).
- [9] A Ruina, J.E. Bertram, and M. Srinivasan. *A collisional model of the energetic cost of support work qualitatively explains leg-sequencing in walking and galloping, pseudo-elastic leg behavior in running and the walk-to-run transition*. *J. Theor. Biol.*, 237:170-192 (2005).
- [10] Manoj Srinivasan and Andy Ruina. *Computer optimization of a minimal biped model discovers walking and running*. *Nature*, 439, 72-75 (2006)

Research on Video Processing System Based on Artificial Fish Swarm Algorithm

Xianmei Fang^{1, a}, Xiaobo Gao^{1, a}

¹Department of Computer and Information Science, Hechi University, Yizhou 546300, China
^aaspone@qq.com

Keywords: Artificial Fish School Algorithm; Video Processing; Image Enhancement; Adaptive Transform

Abstract. This paper uses a new intelligent computational method-artificial fish swarm algorithm to have applications of the image in the video processing. Based on the understanding and analysis of artificial fish swarm algorithm, and it will be applied to video image processing to enhance the technical, its algorithm is designed at the same time. Initial conditions and termination conditions can be determined according to the specific video image problem in the design process. And then it can enhance the video image gray contrast in video image process by using the adaptive conversion, this can improve the effectiveness and quality of the image,. The experimental comparison results show that the artificial fish swarm algorithm can be used as a simple, fast and effective way in video processing system.

Introduction

Artificial fish swarm algorithm is with self-organizing, adaptive characteristics as a new method of intelligent computing; it has a very large self to find the optimal parse. Artificial fish swarm algorithms have shown superiority in many areas as well as the difficult problems encountered in NP technology. Video processing of the multimedia field is one of the most important areas.

Principle of Artificial Fish Swarm Algorithm

The theory of artificial fish swarm algorithm can be developed based on the foraging behavior of fish in the water. Behavior of fish in the water mainly consists: foraging, follow and aggregation, Its performance is as follows:(1) foraging: the basis of survival, the fish tend to place where has much food; (2) follow: in the fish, if the fish find food, and other fish will follow and go to the place with food; (3) aggregation: fish in water are generally gathered in order to escape to survive in the face of disaster, they exist in the center of an aggregate, between the fish and the fish there is a certain distance, but near to the center.

The evolution of artificial fish swarm algorithm has the following main characteristics:(1) the algorithm fast convergence for the relatively high demand for time calculation; (2) the calculation accuracy is not the highest, suitable for fast calculation to get feasible solution to the problem; (3) do not need to issue a complete description and the establishment of the mechanism model. Because of these characteristics that make the artificial fish swarm algorithm able to adapt to the vast range.

Termination of the algorithm conditions are:(1) continuous convergence error range several times to obtain the results of mean square error is lower than the algorithms allow; (2) continuous convergence has won the average result value is not greater than the target value; (3) the number of judgment of the area of artificial fish and judge the basis for setting a ratio; (4) reaches the set maximum number of algorithm iterations.

General artificial fish swarm algorithm firstly defines the distance between two titles:

$$d(q, p) = \left\{ [v(p,1) - v(q,1)]^2 + \dots [v(p,n) - v(q,n)]^2 \right\} \times (1/n) \quad (1)$$

Among them: $x_p(v_1, v_2, \dots, v_n)$ is the current position of the two bodies, v is a fish to maintain spacing. Calculation process is as follows:

Feeding: The position of fish is X_i , randomly selects X_j in the visible domain. If $x\{i, j\} = x\{j, k\}$ is unchanged, the value is X_{j+1} , else $X_{j+1}, k = 0, 1$.

Following: n fish are visible in the region, then the value of K is: $K = \{Xi | Dij \leq v\}$, If K is not empty, the value of X is: $X_{\text{center}} = (x_{j1} + x_{jn} + \dots + x_{jn}) / n$, $FC_c / n > FC_i$, and FC_c is the density of the fish center food, FC_i is the density of food density in the X_i region point. When the value of k in the central region is equal to X region, indicating that the fish move to the center, and have feeding.

When the value is within the value of v , the food's density within a given region is X_{max} , the fish move to the food when $FC_{\text{max}} / n > FC_i$.

The Application of Artificial Fish Swarm Algorithm in the Video Image Enhancement Technology

The enhancement of image can improve the video image effect, increase or computer video image further detailed identification, understanding and analysis during video processing. The use of artificial fish swarm algorithm makes it have optimal parse through constant iteration. First, the algorithm of the artificial fish randomly initial sets an artificial fish, during the process of artificial fish every iterative can constantly determine the algorithm to set extreme value with new value, and the global extremism. It is the artificial fish to be able to search the optimal solution of the iterative process; the experience is the best position of itself. Through constant iteration of analysis, updating, and ultimately artificial fish swim to best position in the water space.

The value of artificial fish in a fish can be set of n , as well as its search space for the area is set of the e -dimensional, then can achieve active position of j artificial fish is: $x_j(x_{j1}, x_{j2}, \dots, x_{je})$, the step size is set of: $k_j(k_{j1}, k_{j2}, \dots, k_{je})$. It shows that the algorithm for each iteration time, changes in the artificial fish swarm algorithm are:

$$k_{ij}(t+1) = \omega k_{ij}(t) + c_1 r_{1j}(t)(p_{ij}(t) - x_{ij}(t)) + c_2 r_{2j}(t)(p_{gj}(t) - x_{ij}(t)) \tag{1}$$

$$x_{ij}(t+1) = x_{ij}(t) + k_{ij}(t+1) \tag{2}$$

Among them: t is the generation t of i -dimensional of the j artificial fish, w suggests that the step size coefficient. And r is the two independent iterative random coefficients. Through the iterative updating of w we can get the formula of w as follows: $w = (w_{\text{max}} - w_{\text{min}}) \times \frac{\text{iter}}{\text{iter}_{\text{max}}}$, and iter_{max} represents the algorithm

the total number of iterations. The algorithm is obtained equations transform diagram as shown in Figure 1.

Algorithm Design of Artificial Fish Swarm Algorithm in the Video Processing

Changes in the fish swarm algorithm can be taken to the fitness function variance measure compared transform:

$$f(i) = \frac{1}{n} I^2(x, y) \left| \frac{1}{n} \sum_{x=1}^m \sum_{y=2}^n I(x, y) \right|^2 \tag{3}$$

Where A represents the video on a given image, m and n are height and width of video image. When the video image gray level distribution tends to be uniform, the image contrast of high image of the show is getting higher and higher, and quality of process is getting better and better, then the value of f is big.

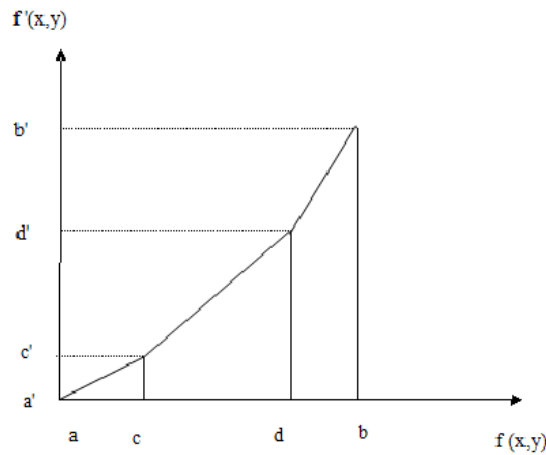


Fig. 1 Algorithm transform schematic

The enhancement algorithms of artificial fish swarm algorithm of video image are to be able to find the beta function to fit the transfer function for adaptive transform image contrast. Therefore, the design of algorithms is:

Algorithm: the use of the beta function for parameter optimization algorithm

Input: linearization function to get new image

Output: beta function parameter is set as: $(a, b) = p$, when $(a, b) = x_i$, the video image after the function transform corresponding to the fitness of gray contrast is:

For an artificial fish $i=1 \dots n$

Randomly initialize the position of the artificial fish;

$P_i = x_i$;

$P_i = x_i$;

Endfor for the initial position of every artificial fish is x_i , calculate gray of image after i converted;

Calculate the adaptive value

If $f_i < f$

$f_g = f_i; P_g = p_i$;

$f_g = f_i; P_g = p_i$;

Because j dimension of the space x_i , the value of step is v_i ;

Artificial fish swarm algorithm is in termination condition.

Comparative experiment after taking the two gray-scale image analysis, artificial fish swarm algorithm gray-scale image enhancement is shown in Figure 2 and Figure 3.

From the chart, it can achieve better visual effects by using artificial fish swarm algorithm during the video image process. The quality of the enhanced image is greatly improved.



Fig. 2 Enhanced former image renderings



Fig. 3 Enhanced image effect diagram

Conclusion

Artificial fish swarm algorithm is introduced to video image processing for video actual problems, according to the actual situation of the artificial fish swarm algorithm to analyze, calculate and optimize, effectively get the method of video image processing. The advantages of algorithm are simple, easy to implement and adaptive. And it can quickly search for optimal function parameters in the application of its image adaptive gray-scale conversion and image enhancement parameter optimization problem, indicating that the artificial fish swarm algorithm can be used as an effective way when video handles images of the system.

Acknowledgements

The author is much appreciated the financial support for this research from the scientific research project of the Education Department of Guangxi Province with the project number 201106LX578, and the project name Research on Fine Management of Digital Campus Information Based on Data Mining

References

- [1] Song Zhiyu, Li Junjie, Wang Hongyu. Chaos Artificial Fish Swarm Algorithm gravity dam material parameter [J]. Rock and Soil Mechanics, 2007,28 (10):79-80.
- [2] Cheng Xiaorong, Zhang Qiuliang, Wang Zhihui. Planning based on artificial fish swarm algorithm with power grid optimization [J]. Relay, 2007,35 (21):25-26.
- [3] Gao Defang, Zhao Yong, Guo Yang. Mixed fish - the ant colony algorithm-based modular product configuration design [J]. Design and Research, 2007,34 (1) :7-10.
- [4] Duan Haibin. The principle of ant colony algorithm and its application [M] Beijing: Science Press,2005:11-12.
- [5] Chang Qing,Wang Li, Xing Chao. Selected image thresholding based on genetic algorithm [J]. Computer Engineering and Applications, 2012(2):35 -37.
- [6] Chen Guo. Image segmentation based on Fisher criterion function method[J].Journal of Scientific Instrument, 2010, 24(6): 57-58.
- [7] Liu Jianping. Two-dimensional maximum between-class variance and genetic algorithm in infrared image segmentation [J]. Zhejiang University of Technology, 2005, 22 (4): 75-76.
- [8] Yang Tian, Li Defang. Grayscale images dimensional Otsu automatic threshold segmentation [J]. Southwest China Normal University (Natural Science), 2010,23 (6): 58-59.
- [9] Bi Weihong, Ren Hongmin, Wu Qingbiao. A new genetic algorithm for optimal preservation strategies [J]. Journal of Zhejiang University (Science Edition), 2006,33 (1): 32-33.

Study of Remote Sensing and Remote Sensing Robot Technology

Fuqin Guo, Yuanqing Wang

Department of Shipping Engineering Yan'an Vocational and Technical College, Yan'an, Shaanxi
716000, China

Keywords: Remote Sensing; Robot Remote Sensing; Detection; Monitoring; Target Orientation

Abstract. Remote sensing robot technology is an emerging research area, which attains a development in recent years. In this paper, the definitions of remote sensing and robot remote sensing will be discussed, and then the remote mines detection technology of RAT-1 eight-wheeled robot, the application of IR-optical sensor in mobile robot for detection and source location of gas leakage, the monitoring of environment intelligent robot on environment and the positioning of mobile robot on targets and other focuses are emphatically introduced, and finally the important problems in each application as well as possible development of remote sensing robot technology are proposed.

Introduction

Remote sensing technology is founded on modern physics, electronics and computer technologies, mathematics methods, Geological rules, etc. In the traditional sense, it is a remote detecting technology, which can acquire desired data without touching any target [1].

The traditional remote sensing technology can be divided into low earth orbit remote sensing, aerial remote sensing, space remote sensing, and outer space remote sensing. Remote sensing platforms, which are commonly used, include vehicle or moving frame, plane or balloon, satellite or space station, aero-boat, and extraterrestrial or trans-lunar targets, which measure the executing tasks mainly with infrared remote sensing, and their wave bands are between 0.76 mm ~ 1000 mm [2].

According to working way, remote sensing can be divided into active remote sensing and passive remote sensing, respectively.

Development and Application of Remote Sensing Technology

Main Characteristics of Remote Sensing Technology [2]

Main characteristics of remote sensing technology can be concluded from four aspects.

First of all, a wide range of data can be acquired.

Second, data can be acquired with fast speed and short cycle.

Third, there are few limited conditions in data acquisition. When it is difficult for human beings to target destination, all kinds of valuable information can be easily and timely acquired if remote sensing technology without restrictions from ground conditions is applied.

Fourth, data can be acquired by a good many means, and also the amount of data is large.

Development Trends of Remote Sensing Technology [3]

At present, pursued developments of remote sensing technology can be concluded from five aspects:

Higher spatial resolution

More refined spectral resolution

Remote sensing satellite platform integrating multiple sensors

Synthetic aperture radar satellite with multiband, multi-polarization and multi-mode

Development of strabismus, stereoscopy, and interferometry technology

New Fields for Application of Remote Sensing Technology

Through years of research and development, remote sensing monitoring technologies in aviation and space have been mature, and also have been applied widely all over the world.

In China, typical remote sensing satellite image has been extensively applied in transportation infrastructure and earthquake disaster detection.

Remote Sensing Robot Technology and Study Situation

Definition of Robot Remote Sensing

Robot remote sensing is defined as "human beings operate robot and acquire desired data or mechanical operation using zero-touch technology".

Remote sensing robot technology can be understand as "a technology, based on operation platform and traditional method, makes robot complete the tasks, which can't or difficult to be done by human beings".

Application of Robot Remote Sensing

In the following, studies on the applications of several robot remote sensing technologies that are commonly used by human beings are introduced.

Remote mine detection [5]

In the traditional sense, removal of mines mainly relies on metal detector or hand breaching.

However, because many mines are made of plastics or contain less than 1g of metal contents, the success rate of a metal detector for removal of mines is very low, and its successful detection rate is less than 1/700 according to statistics.

In Japan, an eight-wheeled robot (RAT-1) was proposed for the detection of mines. Its principle is detecting the temperature difference between ground and underground where mines are buried using infrared camera, and then sending back images after analysis and hence determining the location of mines. Each front wheel of RAT-1 robot needs a metal sensor, and the marching of the robot is controlled by pacing algorithm, as shown in fig 1

Gas Leakage Detection

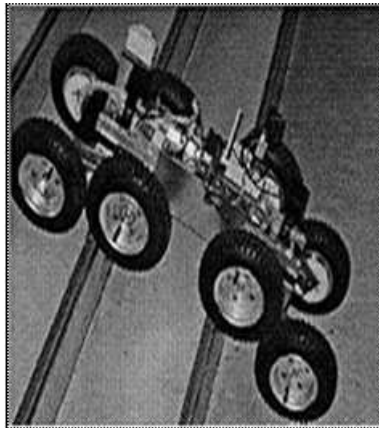
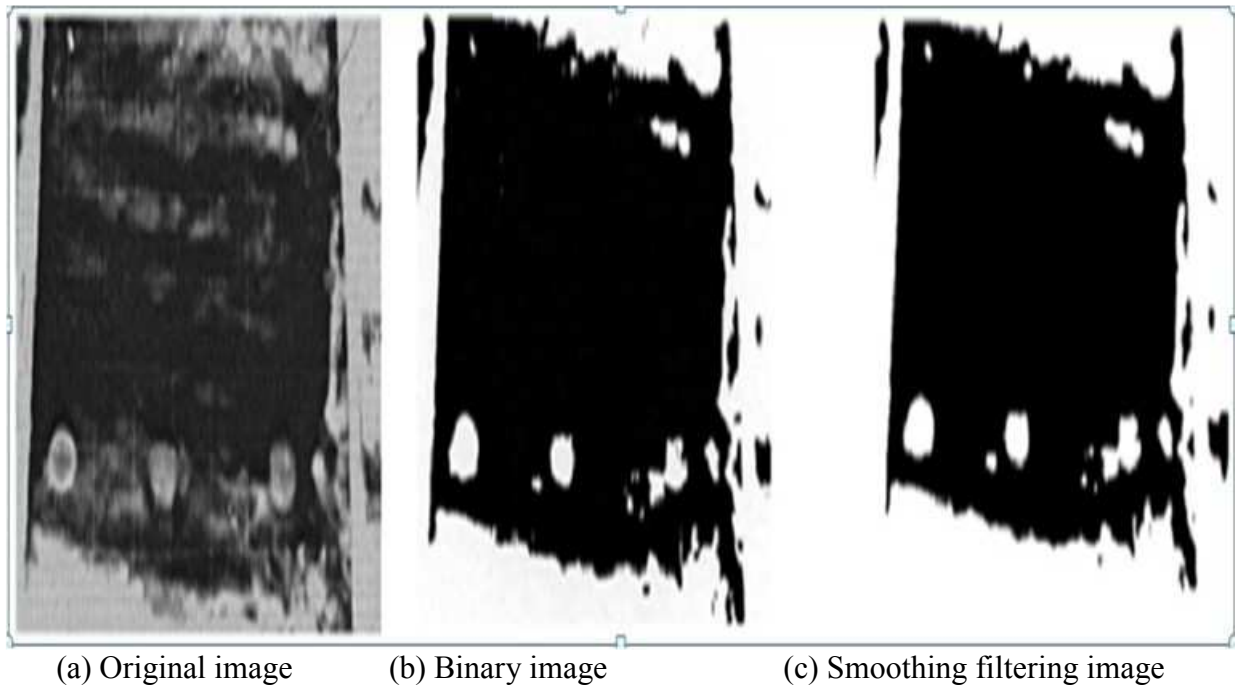


Fig. 1 The marching of the robot

Namely, before the simulation mines about 3 cm deep are detected with infrared radiation camera, cooling agent is sprayed on ground covered by mines, and then acquired infrared radiation photos are analyzed with image processing technique.

Image in processing can be acquired, namely image after Gaussian filtering: six white points after image processing are the positions of simulation mines, as shown in fig 2.



(a) Original image

(b) Binary image

(c) Smoothing filtering image

Fig. 2 The positions of simulation mines

Mobile robot with IR sensor is applied to the positioning of gas leakage detection and resources [6]. To detect leakage points, an in-situ gas sensor is usually used in traditional robot, but it has several shortcomings:

The security is reduced, and also the ability to carry out detection in a large range is limited

A large scanning area is necessary

It is sensitive to interference [7]

Environmental Monitoring with Intelligent Robot [8]

Generally, a sensor, which is highly sensitive to environment and has a powerful ability in anti-interference, is used by scientists for completing the task of monitoring environment.

A unique environment sharing information system is combined by it with land and water sensor together for removing and sensing as well as the regional environments where monitor is located.

Also, new technology and method has been designed by them for making an increase to the cognitive abilities of mobile robot which is constructed in a diversified sensing network.

At the same time, the result of the overall plan is based on real environment.

Target Positioning with Mobile Robot

In George Mason University, new methodology and algorithm were described, namely removal judgment is necessary to be shown through a mobile robot.

The method, which is used for determining the position and heading orientation of robot, has residuated lattice: two modes of kinematics for a mobile robot will be present if a Carmen filter is applied.

Other Applications [9]

A rescue robot was designed by Tokyo Fire Department. It is s mainly used in fire sites, especially for the search and rescue of explosion sites. It can be used as ultrasonic sensor and infrared camera for positioning persons who get into trouble.

At the same time, oxygen tank can be carried by it and the injury can be transferred to a safe place in good condition, as shown in fig 3.



Fig. 3 Safe place in good condition

Scientists, from German, said that this timeline detection equipment (robot "wall") had opened up a new field of vision for the researches of seas and oceans, and could be used for earthquake monitoring by relying on submarine cable system and exploring oil and gas under ocean.

According to reports, Germany navy is making a plan of testing the robot "wall" for the military purposes at present. It is necessary to give consideration to some bad or dangerous environments in detection position.

In the mean time, it is necessary to not only avoid a large expense on electric power and material resources, but also make an improvement to efficiency and accuracy through experiment.

Problems and Prospects of Studies of Remote Sensing Robot Technology

Remote sensing robot technology is a new research area and has not been mature yet.

In fact, at present, it still relies on the infrared detection technology for reference. Simulation mines in experiment are buried on the places with a few centimeters from the earth's surface, and thus the experimental result is still largely different from the realities.

In addition, remote mines detection with robot can also be affected by the limited image processing and cooling material technology. Moreover, even if the specific positions of mines are detected by robot, it is still necessary to make a study on what effective ways to use for the removal of mines.

Also, when gas leakage points are detected remotely with a robot, steady spreading is shown. However, the fact is not so simple, because the speed and direction of gas transmission are changed at every moment.

Therefore, it is possible that the diffusion coefficient of gas is not a constant.

With reference to the relevant literatures, the development trends of robot in the future can be mainly concluded from the following points.

Improvement of Sensor

A direct contact is usually brought by sensors. However, what method more suitable for the current situation will not be considered by them.

For this reason, detection with sensors is the key technology for developing remote sensing robot.

Hardware Design of Robot

It is possible that dramatically deviation occurs in the accuracy under the complex environment conditions because of the hardware limitations.

Design of Algorithm

It is necessary to make an increase to the speed and accuracy of remote sensing robot further.

Conclusion

In short, the rapid development of satellite remote sensing technology takes the mankind into the new age, in which earth observation can be implemented at three-dimension, at multi-level, multi-angle and full-time. A more refined satellite system than "Google maps" is being developed in China, namely high-resolution earth observing system.

Relying on this system, the whole earth can be fed into man's pocket by 2020. In the mean time, relying on automation control, human beings can be replaced by remote sensing robots for making detection and executing tasks in dangerous zones.

All sorts of signs can be observed with the system before the earth gets angry and natural disasters come, thus preventing the occurrence of tragedies.

References

- [1] Jiaorui Zhang, et al. Remote Sensing Technology. Science Press, 2007.
- [2] Wei Chen, et al. Remote Sensing Principle and Application (Second Edition). Wuhan University Press, 2010.
- [3] Shimoi.N, Xurui Xiao, Takita. International Conference on Cyber Technology in Automation, Control, and Intelligent System (Gyeonggi-do, Korea, Research in October, 2010) (Vol.1). p622.
- [4] E Tunstel.G.T. Anderson, E.W.Wilson. International Conference on Cyber Technology in Automation, Control, and Intelligent System (Quebec, Canada, 2007) (Vol.1). p2348.
- [5] W.Baetz,A.Kroll and G..Bonow. International Conference on Automation and Automation (Kobe, Japan, 2009) (Vol.1). p2773.
- [6] D A.Rodic.D.Katie.and.G.Mester. International Conference on Intelligent System and Information (Serbia, 25-26 September, 2010) (Vol.1). p39.
- [7] Fields for Remote Sensing Applications. The Principle and Practice of Remote Sensing. Learning Materials, 2009.
- [8] Yong Zhang. Application of remote sensing technology in seismic resistance and Post-disaster Reconstruction. Transportation experimental study materials, 2010.
- [9] An Overview of Remote Sensing Technology and Its Applications. Learning Materials, 2011.8

Study on Multidisciplinary Design Optimization of 3-RRS Parallel Robot

ZHANG Jing^{1, 2}, LI Bailin¹

¹ Southwest Jiaotong University, Chengdu 610031, China

² Chengdu University of Technology, Chengdu 610059, China

Keywords: 3-RRS Parallel Robot; Collaborative Optimization; Genetic Algorithm

Abstract: The paper aims to apply the idea of multidisciplinary design optimization to the design of robot system. The main idea of collaborative optimization is introduced. The collaborative optimization frame of 3-RRS parallel robot is analyzed. With the method of genetic algorithm and Sequential Quadratic Programming, the investigation is made on the executing collaborative optimization of working stroke, driving performance and hydraulic components. The numerical results indicate that the collaborative optimization can be successfully applied to dealing with the complex robot system, and lay a foundation to solve more complex mechanical system.

Introduction

Much MDO research has been conducted over the last decade, particularly in the aerospace industry [1-4]. The success in the field of aerospace has been paid attention to by the researchers in non-aerospace fields. The yield of multidisciplinary design optimization (MDO) application has been expanded to the field of the mechanical design. However, the investigation depth is inadequate, and it is imperative and important to pay more attention to the MDO application research of the mechanical design.

In this paper, the idea of MDO is applied to the design of robot. An improved collaborative optimization [5], based on genetic algorithm (GA) and sequential quadratic programming (SQP), is proposed to get the optimum 3-RRS robot. Three disciplines are involved in the design optimization of the robot. They are working stroke, driving performance and hydraulic components. The optimized 3-RRS robot not only satisfies constraints but also has synthesized optimum function value.

Collaborative Optimization Architecture of 3-RRS Robot

Collaborative optimization is a design architecture specifically created for large-scale distributed-analysis applications. In this approach, a problem is decomposed into a user-defined number of subspace optimization problems that are driven towards interdisciplinary compatibility and the appropriate solution by a system-level coordination process [6] [7]. As sketched in Fig.1, the collaborative optimization architecture of 3-RRS robot is analyzed. It includes three disciplines, which are running route, driving performance and hydraulic components.

MDO of 3-RRS Robot

Shaking device is a 3-RRS mechanism, which is shown in Fig.2. It is composed of moving platform, fixed platform and three hinged branched chains. Each group branched chain includes two connecting linkages, which are connected by revolute joint. Moving platform is connected to upper linkage by ball friction coupling. Fixed platform is connected to lower linkage by revolute joint. Axis of revolute joint is parallel and perpendicular to linkage. The parallel driving platform, with three degrees of freedom, can move along z axis, and rotate around x axis, y axis, respectively [8] [9].

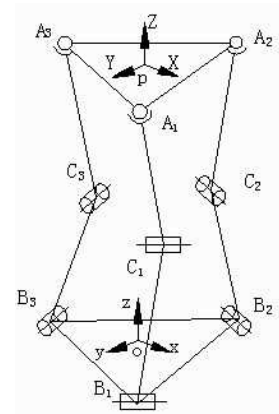
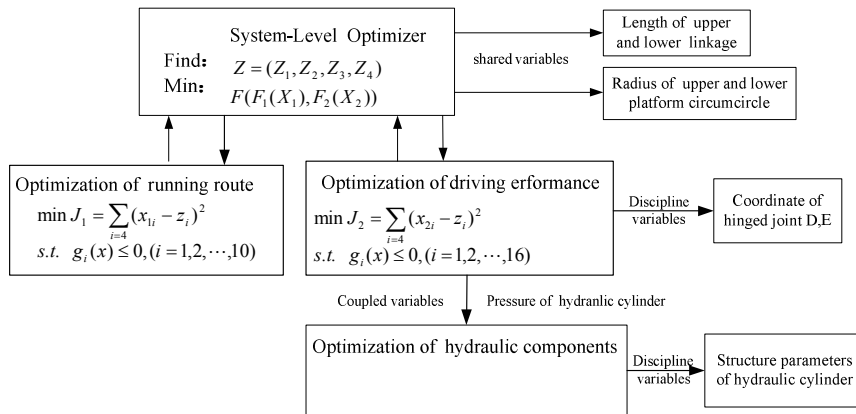


Fig. 1 The collaborative optimization architecture Fig. 2 The structure sketch of 3-RRS robot

Optimization model of subsystem.Comprehensive design of robot is a complex problem. In this study, three disciplines are involved, which are running performance, driving performance and hydraulic performance.

Optimization model of working stroke.The objective function of the working stroke is to minimize the working stroke of upper and lower platform.

$$\text{Find: } Z_1 = \{x_1, x_2, x_3, x_4\} \tag{1}$$

Where, x_1 is the circumcircle radius of upper platform, x_2 is length of upper linkage, x_3 is length of lower linkage, x_4 is the circumcircle radius of lower platform.

$$\text{Min: } f_1(x) = \gamma - \gamma_0 \tag{2}$$

$$\gamma = \arccos\left(\frac{L_{cai}^2 + L_{bci}^2 - |L_{bai}|}{2L_{cai}L_{bci}}\right) \tag{3}$$

Where, γ is the angle of linkage CA and linkage CB when the upper platform is at the highest position, γ_0 is the angle of linkage CA and linkage CB when the upper platform is at the lowest position.

$$\text{Boundary constraints } x_{i \min} \leq x_i \leq x_{i \max} \quad , \quad g_1(x) = (h_{\max} - h_{\min}) / 2 \sin \theta_{x,y} - x_1 \leq 0 \quad ,$$

$$g_2(x) = x_1 - 1000 \leq 0 \quad , \quad g_3(x) = h_{\max} / 2 - x_2 \leq 0 \quad , \quad g_4(x) = x_2 - 880 \leq 0 \quad , \quad g_5(x) = h_{\max} / 2 - x_3 \leq 0 \quad ,$$

$$g_6(x) = x_3 - 880 \leq 0 \quad , \quad g_7(x) = (h_{\max} - h_{\min}) / 2 \sin \theta_{x,y} - x_4 \leq 0 \quad , \quad g_8(x) = x_4 - 1000 \leq 0$$

$$\text{Spatial position constraints: } g_9(x) = x_2 - x_1 < 0; \quad g_{10}(x) = x_3 - x_4 < 0 \tag{4}$$

Optimization model of driving performance (actuating performance) the driving performance includes two objective functions. One is to minimize the hinged joint pressure of the hydraulic cylinder and the mechanism, the other is to minimize the working stroke of piston [9].

$$\text{Find: } Z_2 = \{x_1, x_2, x_3, x_4, x_5, x_6, x_7, x_8\} \tag{5}$$

Where, $D(x_1, x_2)$ is the upper hinged joint coordinate of hydraulic cylinder when the upper platform is at the lowest position, $E(x_3, x_4)$ is the lower hinged joint coordinate of hydraulic cylinder when the upper platform is at the lowest position, x_5 is the hinged joint circumcircle radius of upper platform, x_6 is the length of upper linkage, x_7 is the length of lower linkage, x_8 is the hinged joint circumcircle radius of lower platform.

$$\text{Min: } f_3(x) = w_1 F_1(x) + w_2 F_2(x) \quad (6)$$

Where, $F_1(x)$ is the function of initial driving force coefficient, $F_2(x)$ is the function of hydraulic cylinder working stroke, w_1 is the weight factor of $F_1(x)$, w_2 is the weight factor of $F_2(x)$.

$$\text{Boundary constraints: } x_{i\min} \leq x_i \leq x_{i\max} \quad (7)$$

$$\begin{aligned} g_1(x) = x_1 \geq 0, g_2(x) = L_{BC} \cos(\beta_0 - \alpha_0) - x_1 \geq 0, g_3(x) = x_2 \geq 0, g_4(x) = L_{BC} \sin(\beta_0 - \alpha_0) - x_2 \geq 0, \\ g_5(x) = x_3 \geq 0, g_6(x) = L_{BC} \cos(\beta_0 - \alpha_0) - x_3 > 0, g_7(x) = x_4 - L_{BC} \sin(\beta_0 - \alpha_0) > 0, \\ g_8(x) = L_{AB} \cos \beta_0 - x_4 \leq 0 \end{aligned} \quad (8)$$

$$\text{configuration constraints of driving mechanism: } g_9(x) = x_1 - x_3 < 0, g_{10}(x) = x_2 - x_4 < 0 \quad (9)$$

$$\text{transmission angle constraints: } g_{11}(x) \geq 40/\pi, g_{12}(x) \geq 40/\pi \quad (10)$$

$$\text{dimension constraints: } g_{13}(x) \geq 0, g_{14}(x) \leq 0 \quad (11)$$

$$\text{stability constraints of hydraulic cylinder: } g_{15}(x) \leq 0, g_{16}(x) \leq 0 \quad (12)$$

Optimization model of hydraulic components. The design of hydraulic cylinder involves reliability, cost, weight, service life, ect. In this study, three factors are considered, including cost, service life and reliability [10].

$$\text{Find: } Z_3 = \{x_1, x_2, x_3\} \quad (13)$$

Where, x_1 is inner diameter of hydraulic cylinder d , x_2 is thickness of hydraulic cylinder δ , x_3 is pressure of hydraulic cylinder p .

$$\text{Min: } f_3(x) = w_1 F_1(x) + w_2 F_2(x) + w_3 F_3(x) \quad (14)$$

Where, $F_1(x)$ is the section area of hydraulic cylinder, $F_2(x)$ is the ratio value of stress and allowable stress of material, $F_3(x)$ is the ratio value of inner pressure of hydraulic cylinder and allowable maximum stress.

$$\text{Constraints: } g_1(x) = F - f \leq 0, g_2(x) = p - P \leq 0, g_3(x) = \sigma - [\sigma] \leq 0, g_4(x) = T - \delta \leq 0 \quad (15)$$

Optimization model of system Based on the idea of improved collaborative optimization, the system-level optimization model of 3-RRS is as follows:

$$\text{Find: } Z = [z_1, z_2, z_3, z_4] \quad (16)$$

$$\text{min: } f(Z) \quad (17)$$

$$\text{Constraints: } J_1 = 0, J_2 = 0, J_3 = 0, J_4 = 0$$

Where, $[z_1, z_2, z_3, z_4]$ are shared variables, they are respectively the length of upper and lower linkage, the circumcircle radius of upper and lower platform.

Optimization results. An improved collaborative optimization algorithm is proposed to get the optimum 3-RRS robot. Genetic algorithm (GA) is used to perform the subsystem optimization work on MATLAB platform. Sequential Quadratic Programming (SQL) is applied to perform the system optimization work. The results are shown in Table1, Table2 and Table3.

Table 1 Optimization results of working stroke

Design variables	x_1 (mm)	x_2 (mm)	x_3 (mm)	x_4 (mm)	Fval
values	877.4	875.1	918.4	910.0	1.59

Table 2 Optimization results of driving performance

Design variables	x_1 (mm)	x_2 (mm)	x_3 (mm)	x_4 (mm)
values	171.5	46.5	679.5	674.2
Design variables	Fval	F_1	F_2	$[F](N)$
values	69.0	2.7	135.3	5528.2

Table 3 Optimization results of hydraulic components

Design variables	x_1 (mm)	x_2 (mm)	x_3 (MPa)	$A^* / (10^{-3} m^2)$
values	80.9	11.0	1.98	3.2
Design variables	$\frac{\sigma^*}{[\sigma]}$	$\frac{p^*}{P}$	Fval	
values	0.2	0.4	0.18	

Conclusions

In this investigation, the improved collaborative optimization is applied to perform multidisciplinary design optimization of a 3-RRS robot. Working stroke, driving performance and hydraulic components are involved. Genetic algorithms and Sequential quadratic programming are respectively used to perform the subsystem optimization work and the system optimization work on MATLAB platform. The results indicated that the idea of MDO can be successfully applied to dealing with the complex robot system, and lay a foundation to solve more complex mechanical system.

References

- [1] Sobieski I P, Kroo I. Aircraft design using collaborative optimization[R]. AIAA-96-0715, Nevada: AIAA, 1996.
- [2] Dudley J, Huang X, Macmillan P E, et al. Multidisciplinary optimization of the high-speed civil Transport[R]. AIAA-95-0124, Nevada: AIAA, 1995.
- [3] Consoli R D, Sobieszczanski-Sobieski J. Application of advanced multidisciplinary analysis and optimization to vehicle design synthesis [J]. Journal of Aircraft.1992, 29(5): 811~818.
- [4] Stelmack M A, Batill S M, Beck B C, et al. Application of the concurrent subspace design framework to aircraft brake component design optimization[R]. AIAA98-2033, CA: AIAA, 1998.

-
- [5] Xiong-qing YU, Fei XUE, Xue-feng MU,etal. Improving Robustness of the Collaborative Optimization Using Genetic Algorithms [J]. Journal of China Mechanical Engineering, 2003, 14(21):1808-1811.
- [6] ZHU Zhi-lei. The Dynamic Analysis and Control of the Articulated Drived 3-DOF Swaying Platform[D]. Changchun:Jilin University,2007.
- [7] Braun R D, Kroo I. Use of the Collaborative Optimization Architecture for Launch Vehicle Design [A]. Proceeding of 6th AIAA/NASA/ISSMO Symposium on Multidisciplinary Analysis and Optimization, Bellevue,WS,1996.
- [8] LI Bing. The Research on the Single Degree of Freedom Control System of the Simulated Platform for Carrier Landing Guide D].Harbin: Harbin Engineering University, 2006.
- [9] YUAN He-ling. Kinematic Analysis and Optimization of Joint-Drive Type 3-DOF Parallel Manipulator [D].Changchun:Jilin University,2007.
- [10] SONG Jun,WANG Shu-lian. Optimization of hydraulic components [M].Beijing: China machine press, 1999.

Modeling and Simulation Research of NC Machine Servo System Based on Fuzzy PID Control

Maoyao Ao^{1, a}

¹Department of Machinery, Guangxi Vocational & Technical College 530226, China

^aaomy_ren@yahoo.com.cn

Keywords: NC Machine, Servo System, Fuzzy PID Controller, Modeling

Abstract. Traditional PID control has not been able to meet the control requirements. This paper has designed one type of Fuzzy PID controller to use in NC Machine Servo System. Simulate the response of Fuzzy PID controller and traditional PID controller by Simulink in MATLAB. The simulation results indicated that the Fuzzy PID controller had quick response speed, strong robustness, high precision and non-overshoot etc. It improved the whole control performance of NC Machine Servo System.

Introduction

Servo System is one kind of position servo and location system. It is composed of mechanical drive and electrical drive, which acts on the position, displacement and speed of control actuator [1]. At present, CN Machine Servo System usually uses PID control mode. But, compared with CNC Servo System, the traditional PID control has nonlinear and uncertain, and cannot meet the design requirements. This paper designed Fuzzy PID controller and simulated the system by MATLAB. The simulation results indicated that the Fuzzy PID controller had quick response speed, strong robustness, high precision and non-overshoot etc. It improved the whole control performance of NC Machine Servo System[2].

Mathematical Model of CN Machine Servo System

CN Machine tool is mainly composed of position control, speed control, motor, mechanical drive and position detection components etc. It usually uses half-closed loop control. It can control the speed and position according to the comparative result between feedback signals and command signals. It has high control precision. Half-closed loop position detection usually installs detection element on motor axes, in order to control motor's angle accurately. Then convert angle into worktable's linear displacement through ball screw drive mechanism. Because of the CN Machine Servo System's complexity, it will analyze the mathematical model of every tache, which is composed of the system.

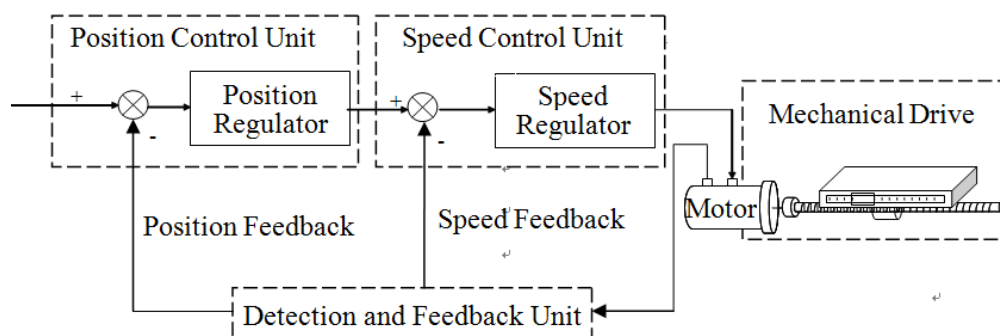


Fig. 1 The Half-Closed Loop Control of CNC Servo System

Mathematical Model of Position Loop

$$U_c(t) = K_i [P_p(t) - P_L(t)] = K_i [P_p(t) - K_p X_L(t)] \quad (1)$$

In Eq.1, $U_c(t)$ figured position loop command voltage; K_i figured position loop gain coefficient; $P_p(t)$ figured position loop command Pulse; $P_L(t)$ figured position loop feedback pulses; K_p figured position loop feedback gain coefficient; $X_L(t)$ figured worktable movement distance.

Mathematical Model of Speed Loop

$$U_M(t) = K_a[U_c(t) - U_g(t)] = K_a[U_c(t) - K_f \frac{d\theta_M(t)}{dt}] \quad (2)$$

In Eq.2, $U_M(t)$ figured armature circuit input voltage; K_a figured speed loop gain coefficient; $U_c(t)$ figured speed loop command voltage; $U_g(t)$ figured speed loop feedback voltage; K_f figured speed loop feedback gain coefficient; $\theta_M(t)$ figured motor angle.

Mathematical Model of servo motor

$$\begin{bmatrix} \dot{i}_q \\ \dot{\omega}_r \end{bmatrix} = \begin{bmatrix} -R/L & -p_n\psi_f/L \\ \frac{3}{2}p_n\psi_f/J & 0 \end{bmatrix} \begin{bmatrix} i_q \\ \omega_r \end{bmatrix} + \begin{bmatrix} u_q/L \\ -T/L \end{bmatrix} \quad (3)$$

Eq.3 is servo motor linear state equations. In Eq.3, i_q figured q axis current; ω_r figured rotor velocity; R figured winding equivalent resistance ; L figured inductance; p_n figured number of pole pairs; ψ_f rotor magnetic field equivalent flux; J figured rotation inertia; T figured torque.

$$T_e = \frac{3}{2} p_n \psi_f i_q = K_c i_q \quad (4)$$

Eq.4 is electromagnetism torque equation, which K_c figured torque coefficient.

Mathematical Model of Mechanical Drive

$$x_L = i_{pt} \theta_L = \frac{P_h}{2\pi} [i\theta_M - \frac{M_s}{K_L}] \quad (5)$$

In Eq.5, x_L figured worktable movement distance; $i_{pt} = P_h / 2\pi$, i_{pt} figured screw transmission ratio, P_h figured screw lead; $i\theta_M$ figured screw input angle; M_s figured torque; K_L figured torque stiffness.

According to all aspects of the mathematical model of servo system in Eq.1~Eq.5, do Laplace transform and finishing, on order to obtain the transfer function G(s) of CNC Servo System:

$$G(s) = \frac{X_L(s)}{P_p(s)} = \frac{K_i K_c K_a K_L i_{pt}}{A_1 S^5 + A_2 S^4 + A_3 S^3 + A_4 S^2 + A_5 S + A_6} \quad (6)$$

In Eq.6:

$$A_1 = J L J_L$$

$$A_2 = J R J_L + L B J_L + f J L$$

$$A_3 = R B J_L + J_L K_c \psi_f + K_c K_a K_f f_L + J R f_L + L B f_L + J L K_L$$

$$A_4 = f_L K_c \psi_f + R B f_L + K_c K_a K_f f_L + J R K_L$$

$$A_5 = R B K_L + K_c \psi_f K_L + K_c K_a K_f K_L$$

$$A_6 = K_i K_c K_a K_L K_p i_{pt}$$

Fuzzy PID Controller Design

The structure of Fuzzy PID controller is shown in Fig.2. The system is composed of given input, current machine position feedback access, fuzzy decision control and PID controller. The key of fuzzy PID control technology is to find out the fuzzy relationship between the three parameters (proportion (P), integral (I) and differential (D)) with error (e) and error rate (ec). Namely, find out the material fuzzy control rule according to the actual experience. The designed fuzzy PID control system collects numerical value of error and error rate from time to time. Then calculate the material control output by fuzzy controller, amend the P, I, D in real-time, and realize the self-adaption accurate control to the object. In Fig.2, r figured set value, y figured machine tool’s moving distance [3].

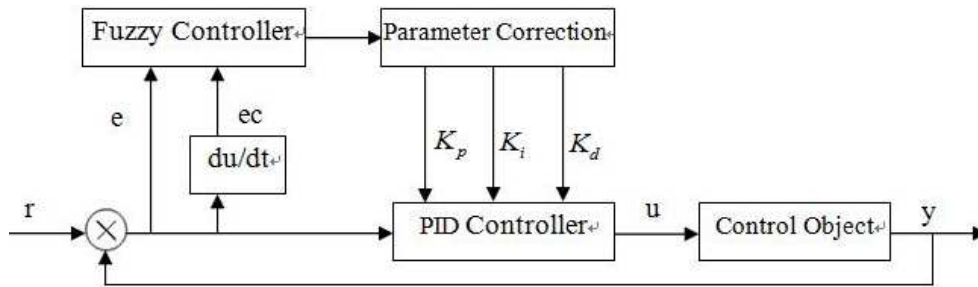


Fig. 2 Fuzzy PID Control Principle Diagram

Design of Fuzzy Controller The system takes CN Machine displacement as control object, takes goal displacement, actual deviation e of displacement and change rate of displacement ec as input, takes Kp, Ki, Kd of PID controller as output, and mapping them to each universe E, EC, Kp, Ki, Kd by blurring. The fuzzy set of E, EC, Kp, Ki, Kd is {NL, NM, NS, 0, PS, PM, PL}. The universe of E and EC is {-6, -4, -2, 0, 2, 4, 6}. The universe of KP, Ki, KD is {-1.5, -1, -0.5, 0, 0.5, 1, 1.5}. Choose fuzzy membership function of normal distribution, when the fuzzy subset is “NL” or “PL”. Otherwise, choose triangle membership function. Each variable membership figures are shown in Fig.3and Fig.4.

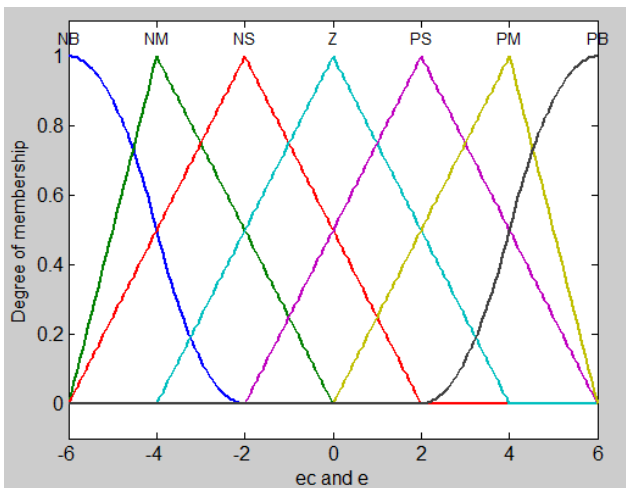


Fig. 3 Membership degree of E and EC

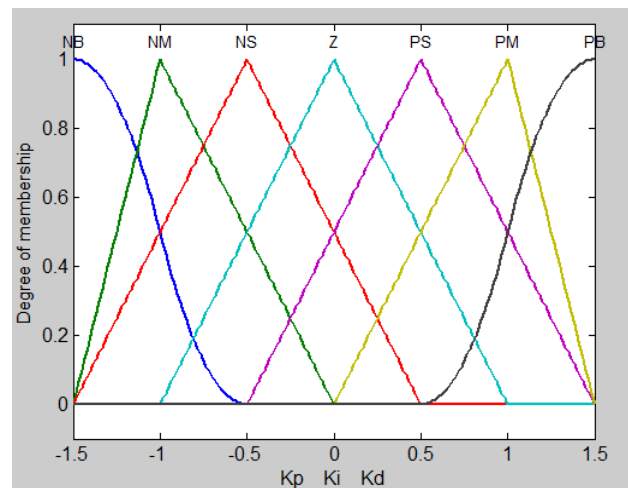


Fig. 4 Membership degree of Kp Ki and Kd

Fuzzy Control Rule Establish fuzzy control rule by empirical induction. The self-tuning fuzzy control rules of Kp, Ki and Kd are shown in Table 1, Table 2, Table 3.

Table 1 Fuzzy rules of KP

E	EC						
	NL	NM	NS	O	PS	PM	PL
NL	PL	PL	PM	PM	PS	O	NS
NM	PL	PL	PM	PS	PS	O	NS
NS	PM	PM	PM	PS	O	NS	NS
O	PM	PM	PS	O	NS	NM	NM
PS	PS	PS	O	NS	NS	NM	NM
PM	PS	O	NS	NM	NM	NM	NL
PL	O	O	NM	NM	NM	NL	NL

Table 2 Fuzzy rules of Ki

E	EC						
	NL	NM	NS	O	PS	PM	PL
NL	NL	NL	NM	NM	NS	O	O
NM	NL	NL	NM	NS	NS	O	O
NS	NL	NM	NS	NS	O	PS	PS
O	NM	NM	NS	O	PS	PM	PM
PS	NM	NS	O	PS	PS	PM	PL
PM	O	O	PS	PS	PM	PL	PL
PL	O	O	PS	PM	PM	PL	PL

Table Fuzzy rules of KD

E	EC						
	NL	NM	NS	O	PS	PM	PL
NL	PL	PL	PL	PM	PM	O	NS
NM	PL	PL	PM	PM	PS	O	NS
NS	PL	PM	PS	PS	O	NS	NM
O	PM	PS	PS	O	NS	NM	NM
PS	PM	PS	O	NS	NM	NM	NL
PM	PS	O	NS	NS	NM	NL	NL
PL	O	O	NM	NM	NM	NL	NL

In general, fuzzy PID controller uses incremental online adjustment to KP, Ki and KD.

$$K_p = K_{p0} + \Delta K_p \tag{7}$$

$$K_i = K_{i0} + \Delta K_i \tag{8}$$

$$K_d = K_{d0} + \Delta K_d \tag{9}$$

K_{p0}, K_{i0}, K_{d0} is controller initial value; $\Delta K_p, \Delta K_i, \Delta K_d$ is the result of fuzzy inference.

Simulink Modeling and Simulation

Simulink Modeling. In this paper, the experiment chose SIMENS 840D CNC Machine Servo System as research object. Take the parameter into Eq.6 and ensure the Transfer Function:

$$G(s) = \frac{11.5467}{4.21S^5 + 3.56S^4 + 14.85S^3 + 1.43S^2 + 6.71S + 23.52} \tag{10}$$

Establish the system control model in Simulink combined with Fuzzy PID control principle, as shown in Fig.5.

Simulink Simulation The experiment selected step signal and the amplitude was 1. The signal began from 0s. The simulation time was set to 1s. The simulation result (as shown in Fig.6) showed fuzzy PID control had less overshoot, faster response speed, less error and better real-time than traditional PID control in step signal response process. Fuzzy PID control improved the reliability and anti- interference ability of the whole system. The system's robustness has been enhanced, and the Servo's capability has been improved [4].

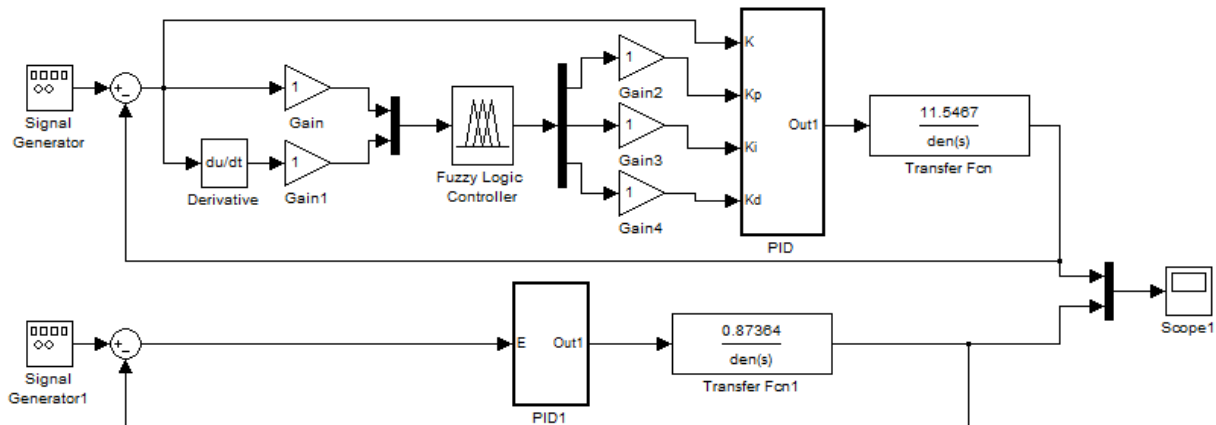


Fig. 5 Simulation Structure Diagram of Fuzzy PID Servo Control System in Simulink

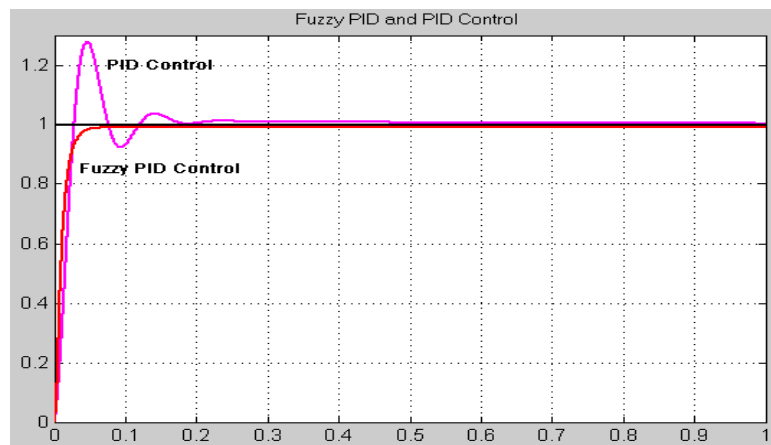


Fig. 6 Effect Comparison Chart between Fuzzy PID Control and Traditional PID Control

Summary

Because there was some problems in traditional PID control servo system, such as slow response speed, low control precision and bad robustness etc., this paper designed one kind of fuzzy PID controller by fuzzy PID control algorithm. Simulate the CNC Machine servo system by Matlab. The results indicated that the designed fuzzy PID controller had fast response speed, strong robustness, high precision and non-overshoot etc. It improved the control performance of the CNC Machine.

References

- [1] Zhang,Rui: *International Conference on Fluid Power and Mechatronics* (Beijing, China, August 17-20, 2011)Vol.1,p.498.
- [2] Cheng,Min: *Equipment Manufacturing Technology and Automation*(Guangzhou, China, September 16-18, 2011)Vol.317,p.1495.
- [3] Yuan,Xiuping: *Manufacturing Science and Technology*(Singapore, September 16-18, 2011)Vol.383,p.2173.
- [4] Wang,Zhongwen: *International Conference on Mechatronics and Automation*(Changchun, China, August 9-12, 2009)Vol.1.p380.

Coupled-Field Finite Element Analysis of MEMS Compound Electrostatic Actuator by Using the ANSYS Software

Yinjun Chen^{1, a}, Qinghua Chen^{1, b, *}, Yanmei Li^{1, c}, and Wengang Wu^{2, d}

¹Institute of Electronic Information and Electrical Engineering, Zhaoqing University, Guangdong 526061, China

²National Key Laboratory of Micro/Nano Fabrication Technology, Institute of Microelectronics, Peking University, Beijing 100871, China

^achenyj@zqu.edu.cn, ^{b, *}chenqh@ime.pku.edu.cn, ^cliym@zqu.edu.cn, ^dwuwgime@pku.edu.cn

Keywords: MEMS, Coupled Field, Finite Element, Electrostatic Actuator, ANSYS

Abstract. MEMS (Microelectromechanical Systems) electrostatic actuators have been successfully applied in a number of areas, including accelerometers, gyroscopes, pressure sensors, and optical devices. In this paper, the actuator optimization of a silicon bulk-micro machined MEMS compound electrostatic actuator of an optical device is discussed. The actuator uses folded-beam structure to enhance the electromechanical performance. The movable block is connected to the compound electrostatic actuator through unequal-height folded-beam springs. The lower-height springs connect the block with parallel plates, and can convert the descending motion of the plates into out-of-plane tilting motion of the block efficiently. Additionally, the block is capable of in-plane motion by applying the driving force of the comb-drive actuator through structural connection. ANSYS FEM simulation is used to extract the device electromechanical performance and resonant frequency of the device. By gradually varying the design parameters in ANSYS simulation, the relationship between the actuator electromechanical performance and various design parameters is derived. The curves of actuator electromechanical performance versus beam length and beam height are derived and they are in good agreement with theoretical prediction. From the analysis it is concluded that the actuator behavior strongly depends upon various actuator parameters. By adjusting design parameters, desired electromechanical performance can be obtained. Based on the simulation results, a set of optimized design parameters for the compound electrostatic actuator is decided. The above-proposed MEMS compound electrostatic actuator may be used for many applications, such as optical device and micro-operating.

Introduction

Comb-type and parallel-plate type micro electrostatic actuators are the most common micro electro mechanical systems (MEMS) due to their rapid speed, high force, and low power consumption. Micro electrostatic actuators have a wide range of significant applications such as precision positioning, optical scanners, probe-based data storage, large vertical displacement, fatigue testing of low-stress thin films, and blood vessel manipulation. Therefore, MEMS electrostatic actuator design optimization is becoming an important research issue [1, 3].

In order to design a MEMS actuator to meet the given specifications, the relationship between the actuator performance and various key actuator parameters must be investigated. Various efforts on MEMS actuator design optimization have been made [4, 6]. Considering the popularization success of the MEMS electrostatic actuators, the design optimization of MEMS compound electrostatic actuator is discussed in this paper. The relationship between the actuator electromechanical performance and the design parameters (such as beam length, beam height) is analyzed. ANSYS FEM simulation is used to derive the actuator electromechanical performance for various design options. Based on the analysis, an optimized design of the MEMS compound electrostatic actuator is suggested.

Actuator design

The schematic drawing of the actuator is shown in Fig. 1. The actuator mainly comprises an isosceles-triangular-shaped movable block, parallel-plate actuators, comb-drive actuators and springs (folded beams and bending beams). The block is supported by the unequal-height beam springs. The lower-height bending beam springs connect the block with parallel plates and can convert the descending motion of the plates into out-of-plane tilting motion of the block efficiently. Also, the block is capable of in-plane motion under the driving of the comb-drive actuator through structural connection. By combination of the block motion types, the actuator can has the in-plane movement ability and the out-of-plane tilting ability, respectively.

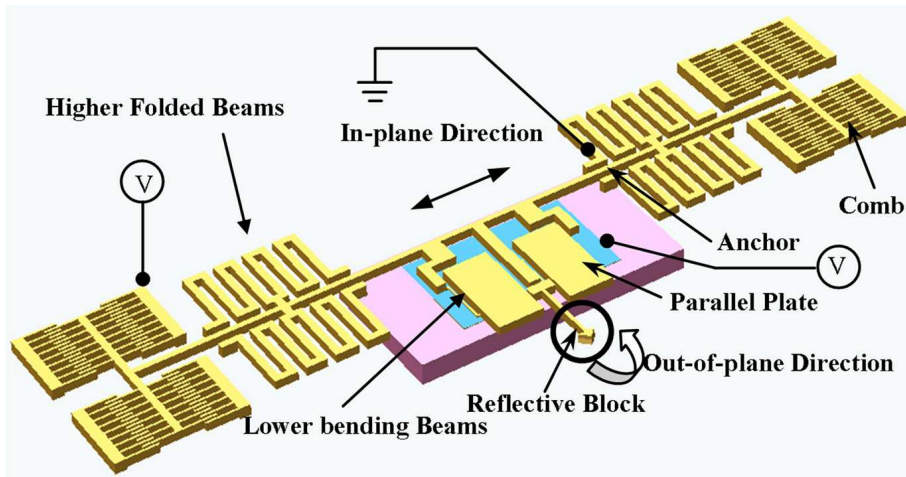


Fig 1 Schematic structure of the compound actuator Parallel-plate actuators and comb-drive actuators connect with a reflective block supported by the unequal-height beam springs.

Figure 2 illustrates the structure of the parallel-plate actuator. As shown in Fig. 2, each of the parallel plates connects with the two lower-height bending-beam springs and the spring is composed of meander beams.

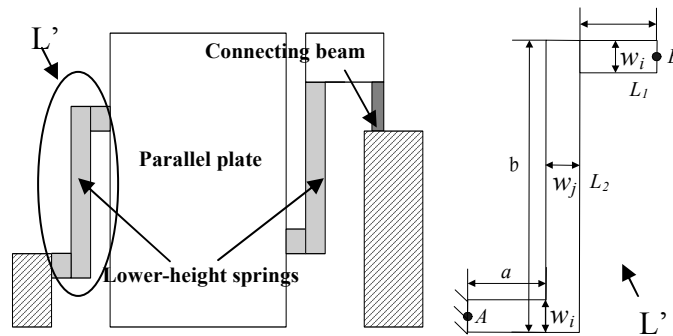


Fig 2 The designed parallel plate structure

The approximate equivalent model of the actuator can be shown in Fig. 3 since the flexibilities of the two lower-height springs are approximately equal to each other. Neglecting the deformation of the movable parallel plate electrode during operation as well as the fringing effect of the electric field around the edges of the electrode, the electrostatic force acting on the upper plate electrode is given by

$$F_{e-p} = \frac{\epsilon_0 V_p^2 S}{2(g-z)^2} \tag{1}$$

On the other hand, the mechanical restoring force of the actuator can be expressed as

$$F_{r-p} = 2k_z z = 24 \frac{E G I_i I_j J_i}{(8 G a^3 I_j J_i + G b^3 I_i J_i + 6 a b^2 E I_i I_j)} z \tag{2}$$

where k_z is the derived spring constant, E is the Young's modulus of the silicon, G is the shear modulus of the silicon, α is the length of L_1 and L_3 , b is the length of L_2 , I_i , I_j , J_i and J_j are all defined in Table 1. In addition, the necessary dimensions and material constants of the springs and plate are also given in

Where ϵ_0 is the permittivity of air, g is the gap between the electrodes; z is the displacement of the parallel plate in z-axis direction, V_p is the applied voltage and S is the area of the parallel plate.

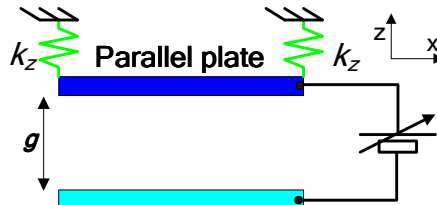


Fig 3 The approximate equivalent model of the electrostatic parallel-plate actuator

Table 1. Physical parameters design of the parallel plate actuator.

Parameter	Value
L_1 and L_3 inertia moment: I_i	$w_i t^3/12$
L_2 inertia moment: I_j	$w_j t^3/12$
L_1 and L_3 polar moment of inertia: J_i	$0.413(w_i t^3 + w_i^3 t)/12$
L_2 polar moment of inertia: J_j	$0.413(w_j t^3 + w_j^3 t)/12$
Young's modulus of the silicon: E	167 GPa
Silicon Poisson ratio: ν	0.066
Shear modulus of the silicon: G	$E/(2(1+\nu))$

Coupled-Field Finite Element Analysis

The above theoretical analysis predicts the relationship between device sensitivity and various design parameters (such as beam height and beam length). However, the theoretical analysis is based on the simplified spring-mass model. In order for a more accurate analysis, ANSYS FEM simulation is required to simulate the device sensitivity for various design options. Based on ANSYS coupled-field simulation, the relationship between device sensitivity and various design parameters are extracted.

This paper uses the direct method to solve the coupled-field problems and evaluate the actuator. The direct approach is the most efficient method for this problem and the results can be very helpful for guiding the device design optimization. In order to extract the relationship between device sensitivity and each individual design parameters, first the beam height of the suggested actuator is varied while keeping other design parameters (beam length, etc.) unchanged. Similarly, the relationship between device sensitivity and beam length is also extracted. ANSYS model (after electrostatic coupled field simulation) for an optimized design of the MEMS actuator is shown in Fig 4.

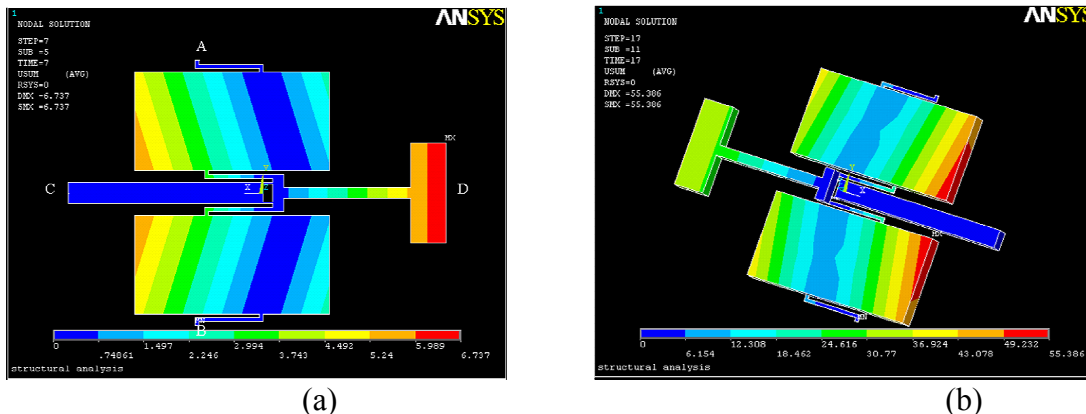


Fig 4 ANSYS/Metaphysics FEM model of the electrostatic parallel-plate actuator for out-of-plane motion: (a) top view (b) pull-in state (the applied voltage of 149 V)

We used ANSYS command line programming to build the device model and perform the ANSYS coupled-field simulation. Here only the movable parts (bending-beams, movable block and movable plates) and the anchor are shown in the figure.

As shown in Fig. 5, we can see that the out-of-plane displacement sensitivity of the block increase rapidly with the decreased bending beam height. This is in good agreement with the previous theoretical analysis that the device sensitivity is inversely proportional to third power of beam height . This proves that the bending beam height is the most effective parameter to adjust the device sensitivity. If we can shrink the beam height to one-fourth of the original height, the sensitivity can be increased by approximately 64 times.

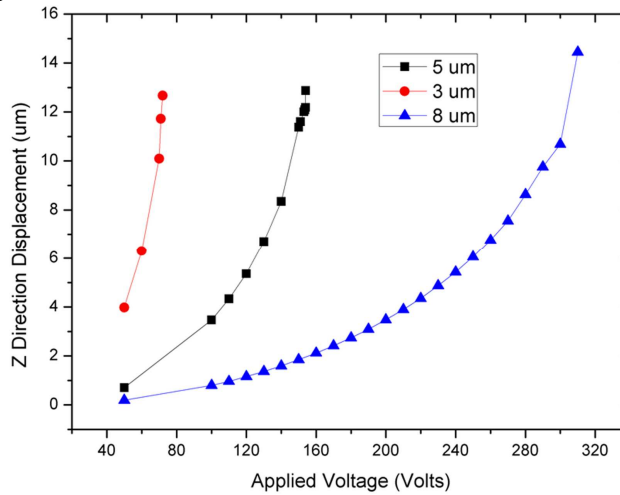


Fig 5 Simulated and theoretical characteristic of displacement versus voltage for electrostatic parallel-plate actuation with pull-in effect

Based on ANSYS simulation results, the relationship between the out-of-plane displacement sensitivity and bending beam length is plotted, as shown in Figure 5. In Figure 5, the sensitivity of the device increases with the beam length. The sensitivity analysis predicts that sensitivity is directly proportional to the third power of beam length. From Figure 5, we can see that the trend of the curve from simulation results matches theoretical expectation well.

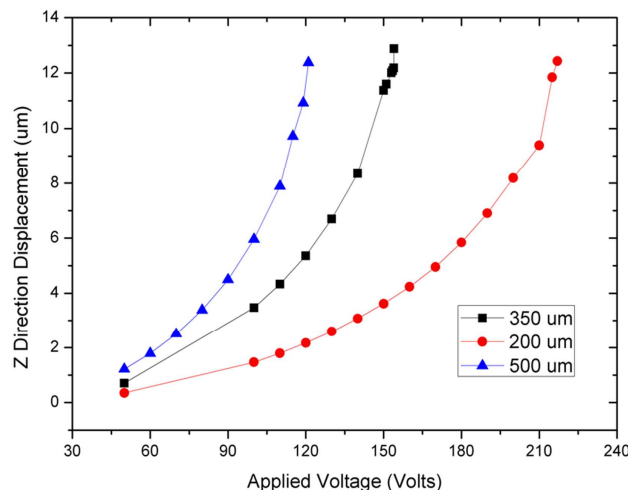


Fig 6 Simulated and theoretical characteristic of displacement versus voltage for electrostatic parallel-plate actuation with pull-in effect

From the above simulation results, we can see that the device sensitivity can be adjusted by design parameters such as beam width, beam length and beam height. Among these parameters, the beam height is the most effective parameter to adjust the actuator sensitivity without increasing the overall device area. However, the minimum beam height is limited by the fabrication techniques we can achieve in the bulk-micromachining process. Therefore we should combine other parameters (such as beam length and beam width) to further improve the actuator sensitivity. Generally we would prefer

larger actuator sensitivity so that it is easy to lower the driving voltage due to the demands change. Therefore we need to have a trade-off between the device sensitivity and fabrication for the design optimization.

Based on the above analysis and simulation, an optimized design of MEMS compound electrostatic actuator for balanced device movement sensitivity and fabrication is achieved. The optimized design parameters are shown in Table

Table 2. Physical parameters design of the parallel plate actuator.

Parameter	Value
L_1 and L_3 beam length: α	20 μm
L_2 beam length: b	350 μm
L_1 and L_3 beam width: w_i	20 μm
L_2 beam width: w_j	6 μm
Spring thickness: t	5 μm
Gap of the parallel plate actuator: g	40 μm
Parallel plate dimension: S	1000 μm \square 500 μm

Summary

In this paper, the design optimization of silicon bulk-micro machined MEMS compound electrostatic actuator with unequal-height folded beam structure is studied. A simplified spring-mass model is used to predict the device electromechanical performance. Based on the theoretical analysis, ANSYS simulation was used to extract the relationship between the device electromechanical performance and various design parameters, such as beam width, beam length and beam height. Simulation results demonstrate that the in-plane electromechanical sensitivity of the device increases rapidly with beam width of folded beams, and the out-of-plane electromechanical sensitivity of the device increases rapidly with beam height of bending beams. Thus the folded beam width and the bending beam height can be very efficient design parameters to adjust the device electromechanical performance. By adjusting design parameters a device having desired electromechanical sensitivity can be achieved. Based upon this analysis, an optimized compound electrostatic actuator is designed. Simulation results show that the device has the in-plane movement ability of 50 μm and the out-of-plane tilting ability of 2 degree. The above-proposed MEMS compound electrostatic actuator may be used for many applications, such as optical device and micro-operating.

Acknowledgements

This work was supported in part by the National Natural Science Foundation of China under Grant No. 60278028 and No.61006075.

References

- [1] Li, J., Liu, Z.S., Lu, C., Zhang, Q.X. and Liu, A.Q., "A Self-Limited Large-Displacement-Ratio Micromechanical Amplifier", The 13th International Conference on Solid-State Sensors, Actuators and Microsystems, 725-728, 2005.
- [2] Miller, D.C., Boyce, B.L. Dugger, M.T., Buchheit, T.E. and Gall, K., "Characteristics of a Commercially Available Silicon-On-Insulator MEMS Material", Sensors and Actuators A 138, 130-144, 2007.
- [3] Pedersen, C.B.W. and Seshia, A.A., "On the Optimization of Compliant Force Amplifier Mechanisms for Surface Micromachined Resonant Accelerometers", Journal of Micromechanics and Microengineering, 14, 1281-1293, 2004.

- [4] G. Henkelman, G. Johannesson and H. Jónsson, in: Theoretical Methods in Condensed Phase Chemistry, edited by S.D. Schwartz, volume 5 of Progress in Theoretical Chemistry and Physics, chapter, 10, Kluwer Academic Publishers (2000).
- [5] Elata, D., “Modeling the electromechanical response of RF MEMS”, Eurosime2006, Como, Italy, 2006.
- [6] Burg, V., den Toonder, M., van Dijken, A., Hoefnagels, J., Geers, M., “Characterization of freestanding thin film material properties for RF-MEMS”, Eurosime2006, Como.

Modeling and Simulation of a Switchable Chaotic System with Fractional Order

Suhai Huang

School of Science, HuaiHai Institute of Technology, Lianyungang 222005, China;

yzhshjsu@126.com

Keywords: Chaotic System, Fractional-Order, Switchable, Modeling and Simulation

Abstract. A new three-dimensional autonomous chaotic system is constructed. Some basic dynamical characteristics of this system with integer order are studied. The switchable chaotic system is constitutive of two subsystems. The dynamic characteristics of the fractional-order switchable system varying with the differential operator orders with fixed parameter are analyzed. Numerical simulations on the dynamics of new system with fractional-order have been carried out.

Introduction

Chaos is a very interesting phenomenon closely related to nonlinear systems, and the study of chaotic systems is an important aspect of dynamical systems that finds applications in different areas. In 1963, Lorenz [1] discovered chaos in a simple system of three autonomous differential equations to describe the implied Rayleigh–Bernard problem. In recent years, a variety of chaotic systems has also been proposed and has been researched extensively [2, 3]

In this paper, a new switchable chaotic system is constructed and some basic dynamical characteristics of this system with fractional order are analyzed.

Dynamical Behaviors of a New Chaotic System

A new three-dimensional chaotic system derived from the Chen system is proposed. The nonlinear differential system is given by:

$$\begin{cases} \frac{d^q x}{dt^q} = a(y - x) + yz \\ \frac{d^q y}{dt^q} = -xz + cy \\ \frac{d^q z}{dt^q} = y^2 - bz \end{cases} \quad (1)$$

Where $\mathbf{x} = (x, y, z)^T \in \mathbf{R}^3$ the state variables of the system (1) are a, b, c are constant coefficients.

The modified chaos system is obtain by $y^2 \rightarrow xy$ in system (1), resulting in

$$\begin{cases} \frac{d^q x}{dt^q} = a(y - x) + yz \\ \frac{d^q y}{dt^q} = -xz + cy \\ \frac{d^q z}{dt^q} = xy - bz \end{cases} \quad (2)$$

In this paper, the switchable chaotic system is constitutive of above systems with switch function

Considering Integer Ordered Dynamical System (1) ($q = 1$)

Let $a = 35, b = 3, c = 28$, a chaotic attractor is observed as shown in Fig. 1.

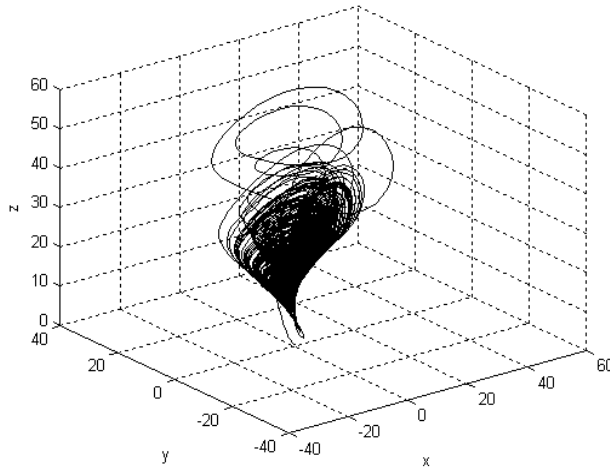


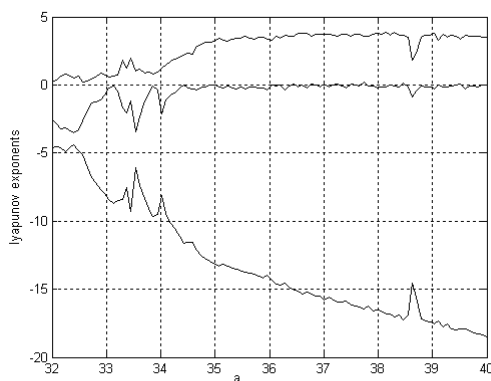
Fig 1 The chaotic attractor of system (1) with parameter values $a = 35, b = 3, c = 28$

Computation shows that system (1) has the following Lyapunov exponents: $\lambda_{L1} = 3.2737, \lambda_{L2} = -0.4296, \lambda_{L3} = -12.3046$. The positive Lyapunov exponent indicates that system (1) is chaotic.

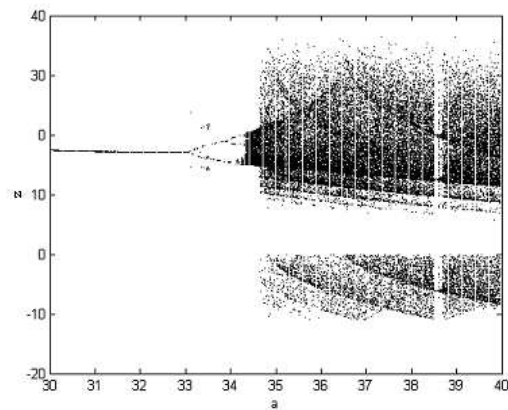
By the Kaplan-Yorker conjecture formula, we can obtain Lyapunov dimension:

$$D_L = k + \frac{1}{|\lambda_{L,k+1}|} \sum_{i=1}^k \lambda_{L,i} = 2 + \frac{\lambda_{L1} + \lambda_{L2}}{|\lambda_{L3}|} = 2 + \frac{3.2737 - 0.4296}{|-12.3046|} = 2.2311 \tag{3}$$

When the parameters $b=3, c=28$, while a is varied on the closed interval $[32, 40]$. Fig. 2 shows the bifurcation diagram of state z and the Lyapunov-exponent spectra.



(a) Lyapunov-exponent spectrum



(b) Bifurcation diagram of z ;

Fig 2 Bifurcation diagram and Lyapunov - exponent spectrum versus parameter a

The Switchable Chaotic System

A new switch function is designed as:

$$f(p) = \begin{cases} y, & p = 1 \\ x, & p = 0 \end{cases}, p = g(z) = \begin{cases} 0, & z \geq 0 \\ 1, & z < 0 \end{cases} \tag{4}$$

The switchable chaotic system (5) derived from system (1) and(2) can be expressed as follows:

$$\begin{cases} \frac{d^q x}{dt^q} = a(y - x) + yz \\ \frac{d^q y}{dt^q} = -xz + cy \\ \frac{d^q z}{dt^q} = yf - bz \end{cases} \quad (5)$$

if $z \geq 0$ subsystem (2) would operate, and $z < 0$ subsystem (1) would operate. While $t \rightarrow \infty$, the switchable chaotic system (5) can transform between the system (1) and system (2) randomly. The switchable chaotic system has more complex dynamics and better randomness, and the broader application in secure communication.

Considering Fractional Ordered Dynamical System (5) ($0 < q < 1$)

According to the predictor–corrector scheme, phase portraits of fractional system(5) will be simulated, while q is varied on the closed interval $[0.85, 0.9]$. From Fig. 3(c-f), it has been found that when $q=0.87 \sim 0.90$, the fractional-order system exhibits chaos. As q continues to decrease, no chaos can be found (seen Fig. 3(a-b)).

The largest Lyapunov exponent spectrum of system (5) with respect to the varying parameter q shown in Table 1

Table 1. Maximum LE of system (5) with different fractional-order

the fractional order q	System order	Maximum LE
0.85	2.55	-0.2501
0.86	2.58	-0.1083
0.87	2.61	0.2860
0.88	2.64	0.8767
0.89	2.67	1.5624
0.90	2.7	0.3834

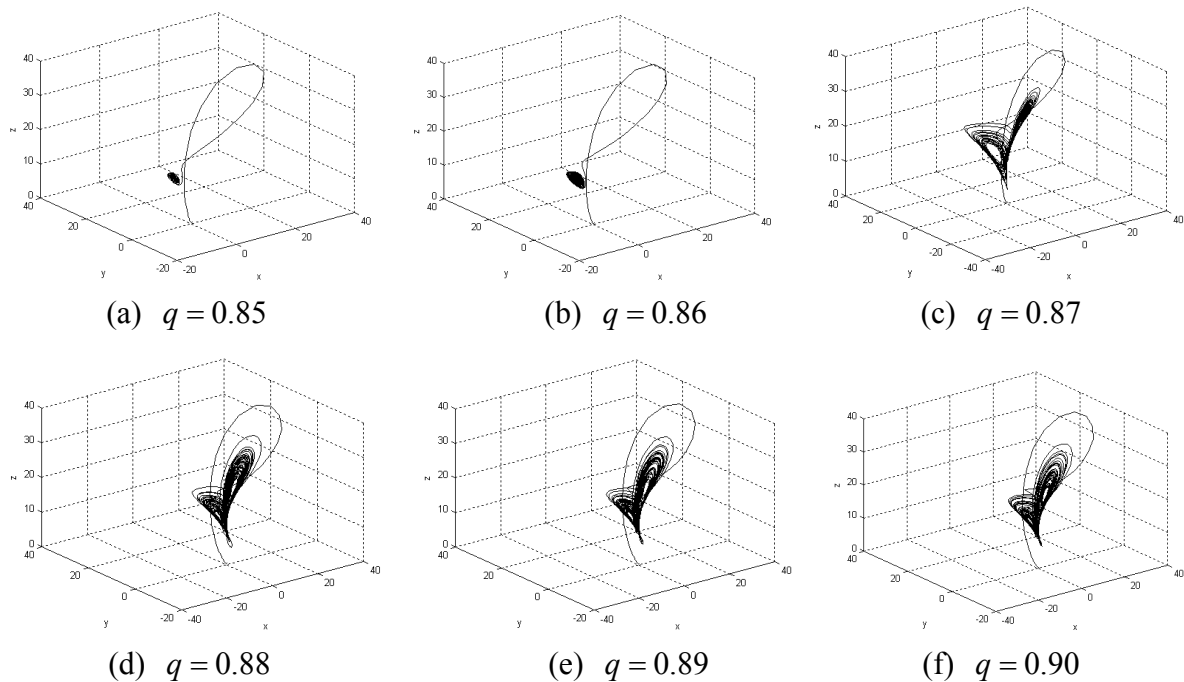


Fig.3 Phase figure of system (5) with different fractional-order on3-D plane

Conclusions

A new 3-D switchable chaotic system is presented. Some basic dynamical characteristics of this new system with fractional-order are studied by numerical simulation and the maximum Lyapunov exponent. Moreover, the routes to chaos in the fractional order system are analyzed.

Acknowledgements

This research is supported by the Nature Science Foundation of HuaiHai Institute of Technology (Z2009042)

References

- [1] E N.Lorenz: JAtmos Sci Vol.20(1963),p.130
- [2] K.M.Tsang: Nonlinear Analysis: Real World Applications Vol.12 (2011), p. 3199
- [3] R.F.Mohammad, D. Hadi: Communications in Nonlinear Science and Numerical Simulation, Vol.17(2012),p.731
- [4] Z. Wang, X. Huang, G.D. Shi: Computers & Mathematics with Applications Vol.62(2011),p.1531
- [5] A. Alireza: Chaos, Solitons & Fractals Vol.45(2012), p. 351

Reform of CNC Machine Tool and Programming Based on CDIO Model

Jingping Liu^{1, a}, Yuzhong Li^{2, b}

^{1,2}Department of mechanical and electrical engineering, Jiaozuo University, Jiaozuo, Henan, China

^aliujingping1023@163.com, ^bnyliyuzhong@126.com

Keywords: CNC machine tools and programming; Curriculum reform; Combination of engineering; CDIO mode

Abstract. CNC machine tools and programming is a professional core curriculum of the vocational colleges in machinery manufacturing and automation, and CNC machining technology. This course involves teaching and professional practice, which requires us to improve teaching methods, improve the quality of teaching to promote students' understanding of CNC machine tools and programming course and mastery, in order to develop students' practical capacity. In this paper, we use the conception, design, implementation, and operation of the CDIO model implementation of teaching reform, providing engineering teaching model with a new teaching ideas, and this also plays an active role in the training to cultivate innovative talents.

Introduction

Due to the development of the machinery manufacturing industry in recent years, the enrollment scale of higher vocational colleges' machinery manufacturing professional also continues to expand. For each of the machinery, CNC machine tools and programming is the core curriculum, and theory class is not a good combination and practice, which caused the students to complete the theoretical study of the course, through the course of the theory test, but can not properly prepared parts of moderate complexity processing procedures, even in the training is completed, most students can not be more skilled to click the image processing technology development, programming and operating the machining of a line with the requirements of the drawings (even very simple) parts.

CDIO teaching mode concepts have achieved good results in many domestic institutions. It's mainly use is to conceive, design, implementation, and operation. It is highly summarized and embodied in a "do" science ", " learning "to do" and the project of education and teaching students through the project from development to run initiative, practice, course between the organic way to study engineering, project organization, design, development and implementation capacity, as well as strong communication skills and coordination. It also reflects the international consensus of today's engineering education, and it is the latest achievements in recent years' the international engineering education reform. The CDIO teaching mode is shown in Fig. 1.

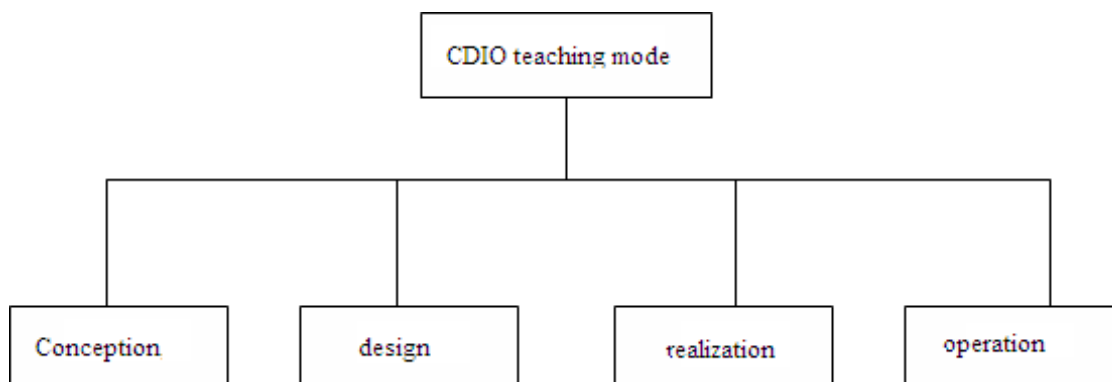


Fig. 1 CDIO teaching mode

The construction of this course fully learns the CDIO engineering education model, built CNC machine tools and programming courses teaching reform project teaching as a carrier of the implementation of the program, through the efforts of the teaching team of CNC technology. It is believed that we will achieve the clear teaching objectives, teaching content optimization, teaching structure science, practice and reasonable three-dimensional construction of teaching materials, stability of the faculty, teaching and curriculum goals with rich research fruits.

The Implementation Program of the Teaching Mode Reform

Based on the CDIO engineering education model on students' knowledge goals, ability goals and quality objectives for training and reform, the cultivation of each target is divided into five projects.

Knowledge goals: the knowledge goal of the training is divided into process analysis capabilities, the basis of numerical control programming, CNC lathe operation, CNC milling machine operation, and machining center operations.

Capacity goals: the ability to target the training is divided into reading the ability of the drawings, the preparation of the program the ability to practice the ability to operate, part detection capabilities, machine tools, the ability to debug.

Quality goals: the cultivation of quality goals, including professional quality, cooperation, quality, innovation, and communication skills.

In the teaching of CNC machine tools and programming in our college, we adopt different teaching methods to teach the students. After the end of the semester, we compare consolidated results of these two classes of students to study the learning outcomes of students in these two different teaching modes.

Objects

We took two classes of 09 mechanical manufacturing and automation students as our objects.

Research process

We use 09 mechanism class 1 and class 2 as our objects, and for 09 mechanism we implement the traditional teaching methods. The CDIO the teaching model is used for 10 class 2. After a semester of their learning and statistics to be compared, the course of the study is shown in Fig. 2.

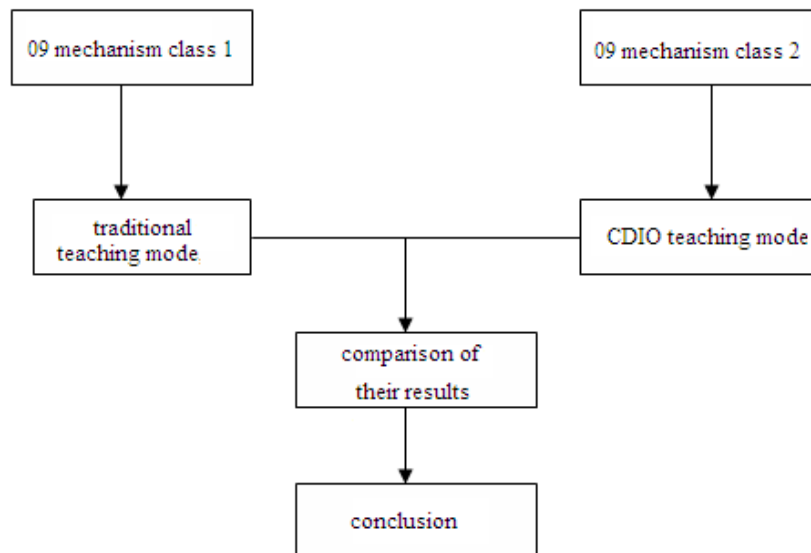


Fig. 2 Teaching reform process

Results

After a half-semester group teaching this course on CNC machine tools and programming for an assessment.

Table 1. Results of 09 mechanism class 1

Scores	0-59	60-69	70-79	80-89	90-100
Amount	1	16	9	5	3
Proportion	3.7%	45.8%	27.4%	14.9%	6.9%

The assessment task includes: the task 1 of CNC machine cognition; task 2 of two-part process analysis; task 3 of simulation processing; task 4 of training processing, and task 5 of detection.

These two classes of students' comprehensive performance assessment statistics, and apply the methods of mathematical statistics significance test.

The results of 09 mechanism class 1 are shown in Table 1.

The histogram of their score proportion is shown in Fig. 3.

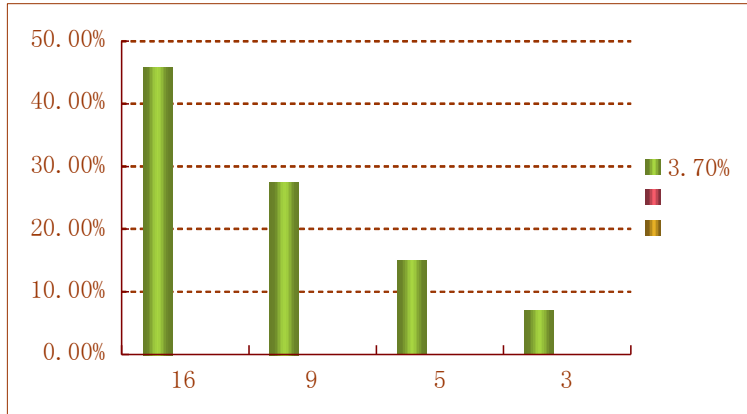


Fig.3 The histogram of the score proportion of 09 mechanism class 1

We applied the CDIO teaching mode for 09 mechanism class 2, and after a semester of teaching, our results are shown in Table 2.

Table 2. Results of 09 mechanism class 2

Scores	0-59	60-69	70-79	80-89	90-100
Amount	0	5	16	11	7
Proportion	0.00%	14.7%	43.2%	28.9%	18.1%

The histogram of their score proportion is shown in Fig. 4.

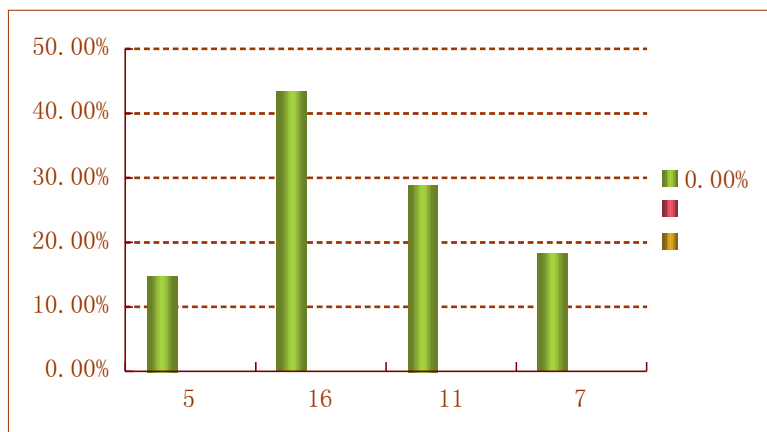


Fig. 4 The histogram of the score proportion of 09 mechanism class 2

Research and analysis

CDIO teaching process is divided into classroom teaching, computer simulation, group discussions, factory practice and projects to reply the link. Classroom instruction emphasizes knowledge sufficient for the degree of theoretical knowledge to serve the project. Through the project, we study and master the theoretical knowledge and practical experience. The computer simulation is not only a test of theoretical knowledge of CNC programming, and also provides a strong guarantee for factory practice, reducing the probability of occurrence of accidents in production. The panel discussion is the exchange of programming experience between the various groups from each other, to expand students' knowledge. Factory practice is a means of testing theory of knowledge, and also a means of assessment of student learning and an effective way to use the knowledge and ability. Project the respondent is not only to assess students on a project-related knowledge levels, but also to test students' practical ability. This assessment method is more scientific and reasonable.

Data Processing

We use the T method to get the results of the two classes of 09 for data processing. By line comparison, and then we verify its significance.

When the overall results showed a normal distribution, the population standard deviation is unknown, but the sample size <30 , then when all possible sample mean and the overall average deviation statistic was distributed. The test is to infer the differences in the probability of occurrence distribution theory, to compare differences in the average significantly.

Single overall test is to test a sample mean with a known overall average of the difference is significant. When the overall distribution is normal distribution, such as the population standard deviation is unknown and sample size <30 , then the sample mean and the overall average deviation statistic was distribution. The test statistic is:

$$t = \frac{\bar{X} - \mu}{\frac{\sigma_x}{\sqrt{n-1}}}$$

If the samples are large sample ($n > 30$), this can also be written as:

$$t = \frac{\bar{X} - \mu}{\frac{\sigma_x}{\sqrt{n}}}$$

Here, the sample t means and the overall average deviation statistics; \bar{X} means the sample average; μ means the overall average; σ_x is the sample σ_x standard deviation; n is the sample size.

The inspection procedures are as follows:

Step 1: the establishment of H_0 as the null hypothesis;

Step 2: calculate t value;

Step 3: Determine the 0.05 significance level, and check the t value table.

After calculation, the effect is very significant.

Conclusion

After we apply different teaching model for students, we can implement CDIO teaching model and it has a good effect. However, the implementation of the CDIO teaching model must go through several steps: First, the idea of the project, an innovative project designed to enable students to be completed within the stipulated time. Second, the design of the project, according to the students, has to grasp the situation to arrange a suitable plan. Third: implementation of the plan. Fourth: the operating display. Fifth: inspection and evaluation. Teaching content and process of teaching the implementation should be combined. The layout of the tasks to students, allow students to study in the discussion, training students in group learning is responsible for their own learning. Make a positive contribution to group results. While allowing students to exchange experiences in cooperative learning, the combination of "doing science". The theory of learning and capacity-building are combined.

In short, CDIO teaching is "project as the main line, teacher-led, and student-centered" teaching method, which has changed the traditional mode of teaching, not only improve the students' theoretical level and practical operation skills, and teachers destination under the guidance of trained student cooperation, problem-solving ability. At the same time, the teachers observe the students and help the students in the process to broaden their horizons and improve professional standards. Significantly enhance students' interest in learning, with learning enthusiasm showing a substantial increase and significant improvement in teaching effectiveness.

References

- [1] Zhang Wenzhuo. Status quo of the demand for CNC talent and post Is]. <http://www.ci0360.net/h/1798/261484-9327.html>2008-09.
- [2] Jiang Qingbin, Hao Chao. Curriculum development in higher vocational project practice and exploration [J]. Education and occupation, 2007 (6) :120-121.
- [3] Zhang Jian. Of vocational education projects and curriculum reform [J]. Communication of Vocational Education, 2006 (3): 41.43.
- [4] Lu Gang. Research and practice of CNC machine programming and operation Course Test Reform. Liaoning Teachers College (Natural Science), 2008 (4).
- [5] Hua Lijuan, Jianwen. Of CNC machining technology teaching reform 2002 (04)
- [6] Chen Zhixiong. CNC machine tools and CNC programming techniques.
- [7] Xia Jianguo, Guo Yang. Development of vocational education curriculum model
- [8] Hanhong Jiang, Wang Shaolan. Understanding of and research on the open of teaching laboratory [J]. University of Petroleum: Social Sciences, 2003,19 (1) :110-112.
- [9] Wu Nengbiao, Tian Hong, Peng Hongjun, et al. Teaching laboratory open exploration [J]. Journal of Southwest Agricultural Admission: Social Science, 2005, 3 (4) :192-194.
- [10]Ma Handa, Wang Gang. Open experimental teaching research and practice [J]. Experimental Technology and Management, 2006,23 (9) :103-104.

Research of Virtual Cutting Based on Haptic Feedback

Yan Zhou^{1, a}, Dengming Hu^{2, b}

¹School of Mechatronic Engineering, Harbin institute of technology, Harbin, 150001, China

²School of Mechatronic Engineering, Harbin institute of technology, Harbin, 150001, China

^azhouyan@hit.edu.cn, ^bhudengming880120@163.com

Keywords: Virtual Cutting, Haptic Feedback, Triangular Grid Unit, Collision Detection, Cutting Force.

Abstract. As product design has entered the stage of green design, virtual design becomes increasingly important, and cutting research is the core of it. This paper established a basic virtual cutting system and the grid models of virtual objects based on PHANTOM Omni haptic feedback device and its system development toolkit and built up oriented bounding box and operated bounding box collision detection. On the base of these, the paper also presented a new method of cutting force condition judgment of cutting tool, and gave the cutting path planning and grid model reconstruction on the basis of virtual cutting methods of triangular grid unit model. At last, the paper researched the virtual cutting of grid model using computer programming language, providing design methods for product design. The relative methods may advance the effect of product design drastically.

Introduction

The rapid development and broad application of virtual reality and haptic feedback technology promotes the innovation and development of all aspects in society. Especially since it entered the stage of green design, virtual design has played an increasingly larger role. It makes design inspiration of designers reproduce in a great degree, breaking the constraints existing in traditional design software. The research of related algorithms and methods of virtual cutting based on haptic feedback provides a theoretical basis for product design.

Establishment of Virtual Cutting System

Establishment of Basic Virtual Cutting System

The basic virtual cutting system mainly consists of hardware system and software system (shown in Fig. 1). They both cooperate with each other, each of which includes a number of different parts playing their important roles respectively.

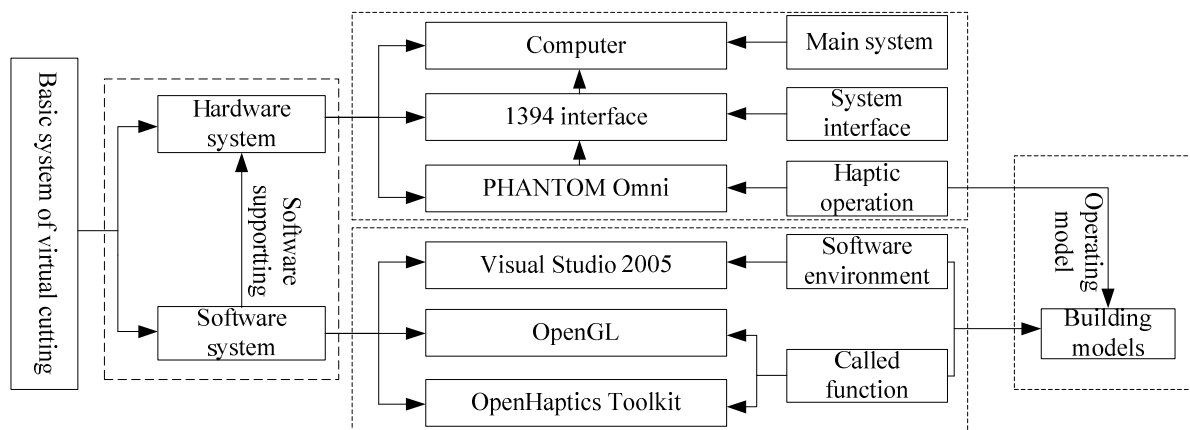


Fig 1 Basic virtual cutting system

Establishment of Virtual Object Model

The establishment method of virtual object model is usually divided into two kinds: building up object model directly, namely, building up the required virtual model with construction algorithm of its related models in virtual reality system; building up object model indirectly, using this method, first we build up the object model in 3D software such as Pro/Engineer, then save it in a workable format, and import it into the virtual reality system through model conversion algorithm.

In this paper, we use the first method to build up a cube grid model. After setting the boundary conditions in the system environment, we draw the triangular units row by row in counterclockwise direction. Each grid surface is drawn respectively in this order: front - back - top - bottom - left - right. Finally the whole cube mesh is completed (shown in Fig. 2).

Collision Detection Based on Oriented Bounding Box

Construction of Oriented Bounding Box

We build up the bounding box of triangle mesh surface for a general shape in triangle mesh units (shown in Fig. 3).

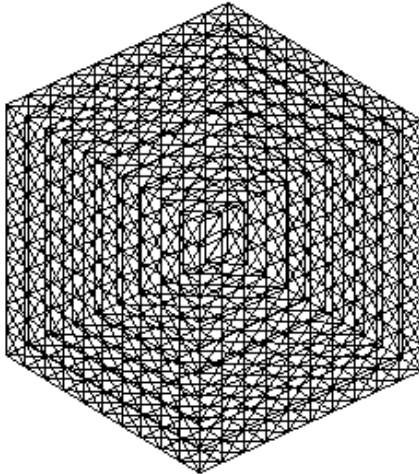


Fig 2 Grid model built up directly

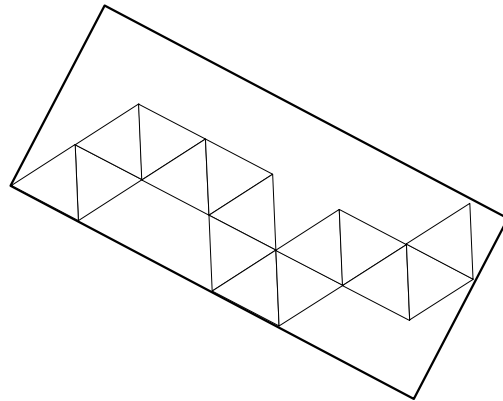


Fig 3 Oriented bounding box

According to the method of oriented bounding box [1, 2] construction, the location of the center point of the bounding box can be found out using the data of all vertices in triangles. The eigenvectors can be solved in the covariance matrix. After their being normalized, vectors of vertices location in all triangles are projected to three axes in the coordinate system. Then we find out the maximum of the absolute value of the projection on each axis, as the three dimension lengths of the bounding box (These lengths are especially considered as half of actual lengths). While in some cases, these triangular units are not the same. A function related to the area of triangles needs to be created to correct the covariance matrix.

Judgment Conditions of Collision Detection

We assume two bounding boxes A and B, and give their judgment conditions of collision detection based on separating axis theory [3, 4]. SAB is a separating axis outside the bounding boxes, TAB is the translation vector connected with the center of the bounding boxes. Ai and Bi are the unit vectors on the three axis of A and B, and ai and bi are the three dimension lengths of A and B. la and lb are the sum length of projection to SAB of each radius vector in A and B.

If the collision does not take place, the judgment condition is

$$|T_{AB} \cdot S_{AB}| > l_a + l_b = \sum_i |a_i A_i \cdot S_{AB}| + \sum_i |b_i B_i \cdot S_{AB}| \quad (i = x, y, z) \tag{1}$$

If there is a collision, the judgment condition is

$$|T_{AB} \cdot S_{AB}| < l_a + l_b = \sum_i |a_i A_i \cdot S_{AB}| + \sum_i |b_i B_i \cdot S_{AB}| \quad (i = x, y, z) \tag{2}$$

If there is just a contact collision taking place, the judgment condition is

$$|\mathbf{T}_{AB} \cdot \mathbf{S}_{AB}| = l_a + l_b = \sum_i |a_i \mathbf{A}_i \cdot \mathbf{S}_{AB}| + \sum_i |b_i \mathbf{B}_i \cdot \mathbf{S}_{AB}| \quad (i = x, y, z) \quad (3)$$

For two bounding boxes, there are fifteen different cases for the location of separation axis \mathbf{S}_{AB} according to the arrangement of three axes in each bounding box. All cases are required to be analyzed when the collision detection of two bounding boxes is operated.

Captures of Mesh Grid Nodes

After the algorithm simplify of collision detection judgment conditions, we need to traverse all nodes in the cube grid, to get the captures of all nodes for collision detection. According to related algorithm, the screen coordinates (coordinate system in workspace) are calculated. At the same time the three-dimension coordinates of the proxy point of PHONTOM Omni haptic feedback device also converted to screen coordinates. Then the two screen coordinates are compared to check out the grid nodes within the capture distance. So the collision detection is done, providing a basis for the following virtual cutting research.

When the cube grid unit model is being built up in the computer program, we use PHONTOM Omni haptic feedback device to detect the collision of grid nodes (shown in Fig. 4). The dot is the capture of a grid node.

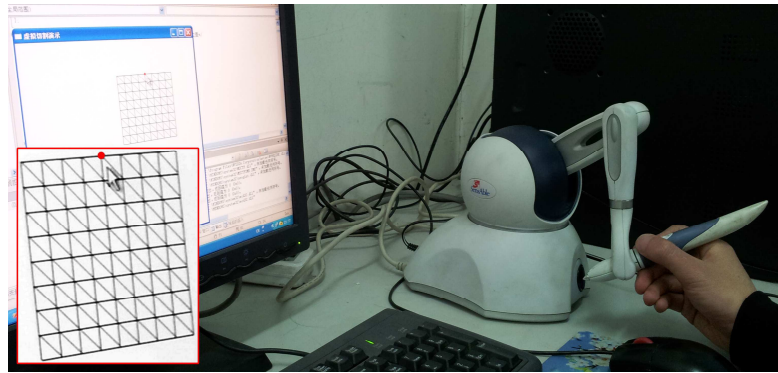


Fig 4 Captures of grid nodes in collision

Virtual Cutting Method

Judgment Conditions of Virtual Cutting

Through the collision detection, we detect the collision of the cutting tool and the virtual object model. When the force imposed by the cutting tool meet the following formula, the cutting condition is considered to be satisfied.

$$F \cdot k_D > F_m \quad (4)$$

F stands for the force imposed by the cutting tool.

k_D stands for the sharpness of the cutting tool. $k_D \in [0,1]$. When $k_D=1$, the tool is sharp, when $k_D=0$, the tool is blunt.

F_m stands for the pre-set threshold of material force, related to material properties.

Path Planning of Virtual Cutting

We use the captures of grid nodes to replace the actual location of collision the cutting tool and the grid model, which will not destroy the grid unit and has a rapid calculation speed. In the path planning of virtual cutting, we only find out the key points: cutting starting point T1 and cutting ending point T2, then we can get the additional grid nodes between the two points through the calculation in the linear equation. The cutting path is divided into eight different types according to different slopes of the connection line of T1 and T2. In the actual planning, if T1 or T2 is not in the maximum row or in the minimum row of the grid, additional cutting path is needed. The specific process of cutting path planning is shown in Fig. 5.

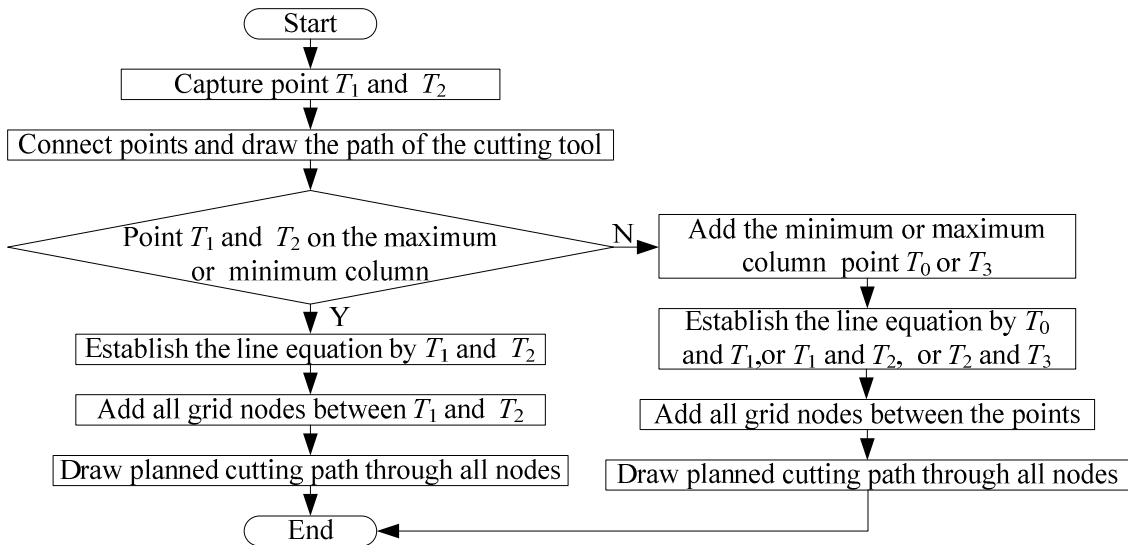


Fig 5 Cutting path planning process

When incomplete cutting occurs, it could be different from the previous planning. Such as cutting one unit, it needs to removal this unit, as shown in Fig. 6. Moreover, when cutting two more units, the planned path could be different because of starting points, as shown in Fig. 7. The left side of Fig. 7 only requires removal of one unit, while the right requires removal of two units, but because of the particularity of the vertex, where it needs to removal the three units. It needs to say that the thick solid line of diagram represents the cutting path planning, while the thick dashed line indicates the path of the cutting tool.

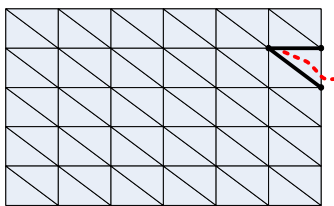


Fig 6 Cutting one unit

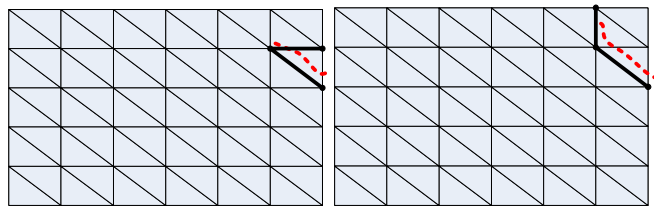


Fig 7 Cutting two units

Mesh grid removal and model reconstruction

After planning the cutting path, it should cut the grid model according to the planned cutting path, remove the needed grid portion by grid nodes of the path, and reconstruct the new grid model in accordance with the order. Virtual cutting is based on the front grid surface, so the planned cutting path of the back grid surface is the same as the front, and the path of the right and left grid surface is the line.

As is shown in Fig. 8, line 1 represents the path of cutting tool; line 2 represents the planned cutting path. Fig. 9 shows the mesh grid surface after being cut. Fig. 10 and Fig. 11 show the grid model after being cut in two different views.

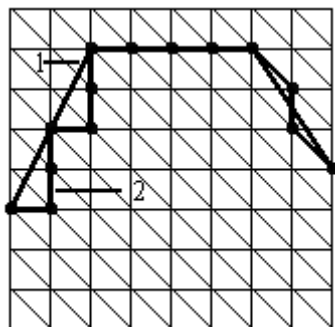


Fig 8 Planning cutting path

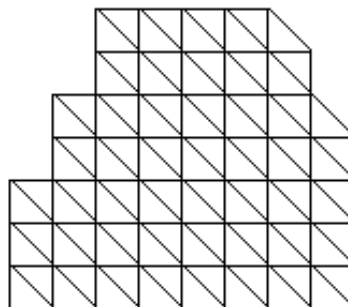


Fig 9 Mesh grid after being cut

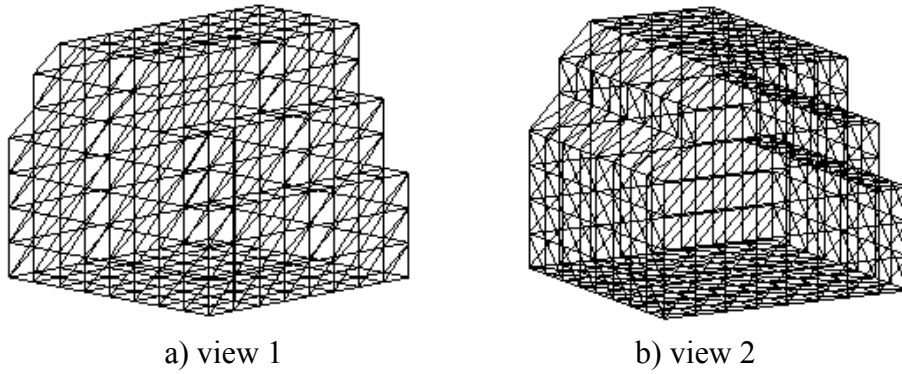


Fig 9 Grid model after reconstruction

Precision study of virtual cutting

As for the precision of virtual cutting of grid model, it could be improved by sparse density of dividing the cube grid model. Fig.11 and Fig.12 respectively show the eight equal portions and sixteen equal portions of the cube grid model cut by the same planned cutting path. It can be seen from the comparison, when the greater dividing density of grid model, the higher precision of virtual cutting.

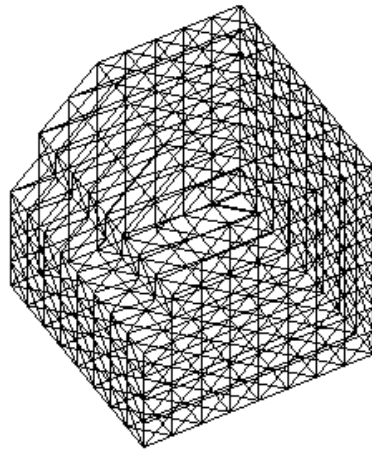


Fig 11 Cube grid model of eight equal portions

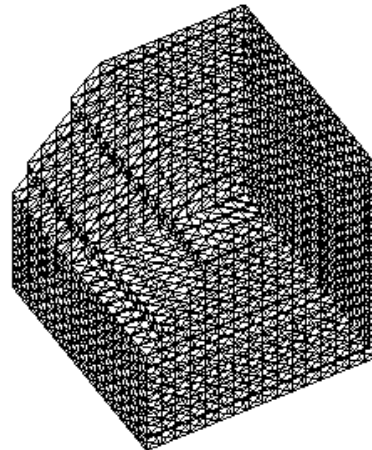


Fig 12 Cube grid model of sixteen equal portions

Summary

This paper researches the relevant aspects of the virtual cutting, operates the cutting path planning of the cube mesh model, completes the virtual cutting of the cube mesh, and draws the conclusion that larger grid sparse density in virtual cutting will get higher cutting accuracy.

References

- [1] S.Gottschalk, M.C. Lin and D. Manocha, OBBTree: A Hierarchy Structure for Rapid Interference Detection, in: Proceeding SIGGRAPH '96 Proceedings of the 23rd annual conference on Computer graphics and interactive techniques, p.171-180 (1996).
- [2] M.Lahanas, T. Kemmerer and N. Milickovic, Optimized bounding boxes for three-dimensional treatment planning in brachytherapy, Medical Physics, Vol. 27 (2000).
- [3] S.Ding, M.A. Mannan and A.N. Poo, Oriented bounding box and octree based global interference detection in 5-axis machining of free-form surfaces, Computer-Aided Design, Vol. 83(2004), p. 1281-1294.
- [4] [A.Gregory, M.C. Ling and R.Taylor, A framework for fast and accurate collision detection for haptic interaction, in: Proceeding SIGGRAPH '05 ACM SIGGRAPH 2005 Courses, 34(2005).

Keywords Index

“Error, Forgetting, Omitting” Phenomenon	475	Artificial Neural Network (ANN)	306
2-D Wavelet	630	Attribute	343
3-D Modeling CAD System	320	AutoCAD	548
3-RRS Parallel Robot	919	Automatic Acquisition	568
3Keymaster Simulation Platform	510	Automatic Control	644
A	114	Automatic Diagnosis	534
A		Automation Control System	674
A/D Converter	882	Automobile Control System	591
Abscission Layer	287	Automotive Engine	711
Accumulation Control Factors	23	B	
Acidithiobacillus Ferrooxidans	520	Band Gap	227
Acoustic Source Localization	856	Band-Pass Sampling	862
Acquisition System	817	Bank Revetment	333
Active Knowledge Aided System	486	Basic Automation System	674
Active Rake Angle	370	Batch Processing	721
Adaptive Observer	851	Bayesian Network	475
Adaptive Transform	909	Beam Characteristics	223
Additional DC Power Supply	254	BER	690
Aeronautic Electronic Device	469	Biped Robot	903
Afterwards Filling	412	Bispectrum	630
Agricultural Land Grading	615	Blasting Vibration	407
Aided Knowledge	486	Blind Vias	451
Air-Gap	76	Block Sand Mechanism	282
Air Traffic Controller (ATC)	475	Board Microcomputer	695
Algorithm	635	Bolt Support	287
Algorithms Based on Layering Search	749	Bounded Delay	573
All-Position Automatic Welding Machine	700	BP Network	786
Amorphous Cellulose	7	BP Neural Network (BPNN)	705, 877
Analog to Digital Converter	232	Bridge	292
Analysis	63	Building Construction	267
Analytical Method	315	Building Integrated Photo Voltaic	505
Android	596	Building Material	27
ANP	430	C	
ANSYS	929	C/S	538
Anti-Peak Regulation Ability	417	C8051F020	700
Anti-Radiation Missile	845	Cable Support	287
AP1000 Nuclear Reactor	510	CAN Network	591
Application	320, 654	CAPP	486
ArcGIS Engine	615	Car Parking	52
Arduino	649, 872	Car Taking	52
Artificial Fish School Algorithm	909	Carbon Fiber	12
Artificial Intelligence	58, 640	Cardiac Motion	108
		Cascade	898

Casing Drilling	63	Controlling	579
Cavitating Flow	102	Controlling System	700
CBR-Recommender Modeling	568	Coordination Mechanisms	464
CC2430	625	Coronary Artery Angiography	108
CDIO	596	Correction Algorithm	669
CDIO Mode	939	Corrosion Behavior	272
Centrifugal Pump	491	Cost Information	809
Centrifugal Style Speed Controller	200	Coupled Field	929
Chaotic System	935	Crack	460
Characteristics	887	Crack Extension Direction	370
Chemical Properties	3	Cross Platform	721
Circulation Type Stereo Garage	52	CTMU	232
Classical Logic	58	Current-Limiting Measures	527
Cloud Computing	605	Curriculum Reform	939
Cloud Storage	584	Curvature	301
Clustering	792	Cutting Force	944
CNC Machine Tools and Programming	939	Cutting Lay	370
CO ₂ -Laser	451	D	
Coal	515	Dam	730
Coal Gangues	375	Damage Simulation	845
Coal Roadway	296	Dangerous Chemicals	760
Coal Transportation	679	Data Acquisition	543
Collaborative Optimization	919	Data Fusion	877
Collision Detection	944	DDS Signal Generator	141
Combination of Engineering	939	Decision Support	601
Combustion	114	Demodulation	92, 898
Combustion Diagnostics	237	Denaturing Gradient Gel Electrophoresis (DGGE)	366
Communication Protocol	755	Design	47, 343, 548, 654, 817, 822
Component Composition	804	Detection	914
Component Description	804	Detection Experiment	407
Composite	12	Detection Technology	558
Composite Slab	311	Detector	730
Compost	366	Development	817
Compound Rock Strata	287	DHT11	177
Comprehensive Evaluation	464	Diesel	3
Computer Technology	725	Diesel Engine Bearings	97
Concrete	460	Diesel Locomotive	695
Condenser	136	Digital I/O	649
Condensing Heat Recovery	136	Digital Multi-Meter	141
Constant Low Speed Control	679	Digital Oscilloscope	141
Construction	63	Digital Signal Processor TMS320LF2406A	830
Construction Technology	35	Dimensionless Parameter	515
Control-Law Analysis	775	Discontinuous Pulse-Width Modulation	71
Control Method	361	Dissolved Gas-in-Oil Analysis (DGA)	740
Control Server	562		
Control Strategy	213		
Control System	760		
Control Technology	381		
Controllable Reactor	259		

Distance Measurement	867	Explosion-Proof Soft Starting	830
Distributed Control System	786	Eyelid Occlusions	780
Distributed Remote Management	664		
Distributed Remote Teaching	664	F	
Diversion Structure	386	Facility Layout	500
Double Wishbone Independent Suspension	161	Failure Alarm	534
Drilling Technology	63	Fatigue Damage	97
Driver	669	Fault Diagnosis	630, 711, 740, 835, 851
Drying Technology	390	Feature	47
DSP	531, 717, 893	Fertilization	423
DTCSS	296	FFT Spectrum Analysis	862
Dual CPU	531	Fiber Bragg Grating (FBG)	92, 898
Dual Stator-Winding Generator	154	Finite Element (FE)	929
Dust Control	440	Finite Element Method (FEM)	87
Dynamic Response	327	Finite State Markov Chains	573
		Fir Filter	717
E		Firing Circuit	725
E.H. Hall Effect	124	Fit	249
Earthquake Wave	407	Flexible Rotation Beam	165
EAST	562	Flow Spinning	395
Ecology	445	Flower Greenhouse Temperature	644
Eddy Air-Curtain	440	Flue Gas Desulphurization	40
Edge-Breakage	370	Gypsum	
Edge Detection	375	Fluent Software	386
Electroless Plating	436	Flywheel	249
Electromagnetic Shielding	436	Fold Region	296
Electromagnetism	610	FPGA	817
Electronic Drawings	548	Fractional-Order	935
Electrostatic Actuator	929	Fracture Prediction	301
Elongation	272	Fractured Gas Reservoir	301
Embedded Controller	760	Fragments Killing	845
Embedded Gateway	684	Fuel Oil	114
Embedded Server	745	Furnaces	237
Energy	903	Fuzzy PID Controller	924
Energy-Saving	390	Fuzzy Quantitative Control	527
Energy-Storing Density	249	Fuzzy Recognition	705
Energy Superposition	491	Fuzzy Self-Tuning PID Controller	765
Engineering Database	320		
Epoxy Resin	12	G	
Ethanol	3	Genetic Algorithm (GA)	919
Evaluation Index	469	Gkd3b Model	679
Excess Air	114	Glass Transition Temperature	7
Excess Pressure Utilization	491	Global Positioning System	749
Excitation Regulator	531	GPRS Network	543
Experiment System	401	Grain Effects	130
Experimental Study	97	Gray-Scale Morphology	780
Expert System	711	Green Agricultural Products	481
Explosion	401	Green Concrete	353

Green Energy	505	Invoice Code	705
Green Industrial Buildings	348	Iris Recognition	780
Green Lighting	348	ISIC-CDIO	596
Grid Portal	771	Isolated Coal Pillar	296
H		J	
Hap Tic Feedback	944	Juice Extractor Stent	173
Hard Rock Mechanized Driving Face	440	K	
Harmonic	154	K-Anonymity	792
Heat Rate	67	K-E Model	440
Heat Storage Performance	82	Kevlar Fiber	12
Heat Treatment	395	Killing Probability	845
Heating System	82	Knowledge Reasoning	58
Hierarchical Diversity	792	L	
High Leakage Reactance	259	Large Amount of Data	799
High-Performance Concrete (HPC)	35	Large-Scale Refrigeration System	136
High Strength Single Angle	315	Large-Span	311
Highway Bridge	35	Large Thinning Rate	395
Holonic Agents	635	Leakage	254
Human Factors	495	Lens	227
Human Machine Interface	735	Light Pollution	338
Humidity	644	Limiting Factor	119
Hybrid Brake	213	Linear Intersection	856
Hydrofoil	102	Liquid-Solid Coupling	799
Hydrology Monitoring	690	Locomotive	679
Hygrothermoscope Monitoring	177	Logistic Model	520
I		Low Carbon Economy	481
Ice Desk	455	Low Carbon Lighting	338
Image Data	817	Low Temperature Treatment	520
Image Enhancement	909	M	
Image Processing	27, 237, 375	Magnetic-Flux	124
Impedance Sensitivity	527	Maize	423
Improvement Measures	97	Manufacture System	495
<i>In Situ</i> Test	333	Manufacturing System	500
Index System	430, 464	Marine Diesel Engine	114
Industrial Process Control	635	Matching Grating Demodulation	898
Influencing Factors	244	Material	47
Information	58	Mathematical Describe	775
Information Management	548	Max485	177
Injection Mould	173	Maximum-Likelihood Sequence Estimation (MLSE)	208
Intelligent Building	654	Maximum Power Point Tracking (MPPT)	735
Intelligent Control	640	MCU	711
Intelligent Mechanical Arm	822	Membrane Computing	740
Intelligent Monitoring	534		
Intelligent Sensor	620		
Inversion	244		

MEMS	929	NC Machine	924
Mercury Processing	381	Negotiation	635
Mesoporous Material Granulation Technology	17	Network Control	725
Metadata Caching	584	Networked Control Systems (NCSs)	573
Metadata Management Algorithm	584	Neural Network (NN)	711, 740, 786
Metal Materials	455	New Type	695
Metal Mines	809	Ni-Co-P Alloy	436
Methods	548	Night Landscape Lighting	338
Methods of Measuring the Magnetic-Field	124	Nine-Switch Converter	71
Micro-Photographic Observation	370	NIOS Soft-Core	141
Microbial Additives	366	NMR	244
Microcontroller	872	Noise Occlusions Relation	780
Microlite	343	Nonlinear System	786, 851
Microstructure	27, 395	Nonlinear Vibration	165
Migratory Bird	445	nRF905	579
MIMO	690	Nuclear Magnetic Resonance	124
Mine	605	Numerical Control Machine	840
Mirrors	223	Numerical Simulation	76, 315, 327
Mixed Fuel	3	Numerically Controlled Lathe	887
Mixed Integer Program	417	O	
Mobile HCI	219	Oil Boom	386
Modeling	510, 924, 935	Oil Fire	401
Modification	31, 136	OLAP	809
Modular	654	Open Scene Graph	553
Moisture Exhaust System	361	Open Source	649
Molecular Dynamics Simulation	7	Operation Comfort	500
Monitoring	579, 914	Optical Fiber Transmission	119
Monitoring System	735	Optical-Grade Polycarbonate	31
Mooring System	745	Optical Microcavities	92
Motion Estimation	108	Optimal-Control Laws	775
Motor Speed Control	765	Optimization	213, 601, 903
Multi-Agent Theory	635	Optimization Algorithm	527
Multi-Body Dynamics	161	Optimization Model	500
Multi-Bus Converter	620	Optimized RBF Networks	568
Multi-Sensors Array	856	Optimizing	495
Multi-Threading	538	Organic Montmorillonite	31
Multi-Tooth Meshing Effect	87	Oxygen Consumption Rate	515
Multidimensional Data	601, 809	P	
Multidimensional Grey Evaluation	469	P89LPC932	867
Multithreading	562	Parallel Platform	760
Mural Cylinder	440	Partial Discharge (PD)	148
MVDR	188	Particle Size	515
N		Particle Swarm	835
Nano-Machining	455	Passive Location	188
Nanocomposite	31	Peak Regulation	417
NBI	538, 562	Peculiar Smell Processing	361

Performance	219, 395	Pull Technology	486
Performance Test	67	Push Technology	486
Performance Test Platform	840	Putaohua Reservoir	23
Phase	40	PVC Production	381
Phase Change Heat Storage	82	PWM	154
Phase Division	882		
Phase Drilling	412	Q	
Phase Range Mapping	882	QOSTBC	690
Phase Splitter	882	Quality Management	276
Photonic Crystal	227	Queuing Theory	52
Photovoltaic	505		
Physical Properties	3	R	
PID Control	640	Radiation Heat Transfer	76
Piezometric Tube	730	Radioactive Property	237
Plastic Optical Fiber	92	Random Waves	183
Plate Mill	674	Rate of Energy Recovery	213
Plating Rate	436	Reactive Force Field	7
PLC	644, 679, 755	Real Time	562
Plink	721	Regression Equation	451
Polishing Surface Roughness	455	Reinforced Concrete Beam	306
Polycrystalline Diamond (PCD)	130	Reinforcement	292
Polymer Bonded Explosive	370	Reinforcing Bar	272
Power Conditioner	71	Relap5-3D	510
Power Consumption	259	Reliability	620
Power Conversion Efficiency	505	Remodeling	553
Power-Meter	625	Remote Control	684, 745
Power Transformer	740	Remote Meter Reading	755
Power Transmission Project	430	Remote Sensing	914
PP/Rice Husk Composites	27	Resolution	232
Practice-Based Design	267	Resonators	194, 223
Precast Track System	276	Resource Evaluation	23
Precise Time Measurement	232	Retaining Wall	333
Precision	200	Rigid-Flexible Coupling	161
Preconditioning Technique	610	Risk Assessment	475
Predicate Logic	58	Robot	872
Pressure Wave	401	Robot Remote Sensing	914
Prestressed Laminated Concrete Slab	311	Robust High-Resolution Algorithm	188
Prevention	460	Rotating Flow	76
Primary Loop	510	Rotor	249
Privacy Protection	792	Rough Set	835
Process Automation System	674	Routes Planning	749
Process Feature	348	RS-485	579
Product Quality	361	RS485 Bus	625
Production Line	500	Rule Polyhedron	553
Production Line Balance	495		
Production Platforms	320	S	
Program Design	320	Safe Production	558
Properties of Cement	40		
PSCP	721		

Safety	887	Structural Form	311
Satellite Actuator	851	Sublevel Drilling	412
Saving-Power	491	Substation Fault	659
Scheduling Optimization	52	Subway Station	327
SDD1 Type	695	Suggestion	353
Section Gear Plate	200	Superquadrics	108
Selection	469	Supersonic Vibration Wave	183
SEM	27	Supply Chain Management	481
Semantic Description	771	Suspension Stiffness	161
Serial Port Adapter	659	Sustainable Development	353
Servo Electro-Hydraulic System	765	Switch Function	154
Servo System	924	Switchable	935
Shape Memory	12	Synchronous Generator	531
Shared Memory	562	System Construction	568
Shear Strength	333	System Design	872
Shifted-Laplace	610		
Side Core-Pulling Mechanism	173	T	
Signal Detection	725	T.L.	194
Similarity	596	T2 Spectrum	244
Similarity Measurement	568	Taiwan High Speed Rail	276
Simulating	495	Target Orientation	914
Simulation	822, 935	TC35I	684
Simulation Environment	760	TCP	538
Slab Track	276	Teaching Reform	267
Smart Home Network	684	Teaching Resources	771
Smart Phone	219	Technical Measures	119
Socket	538	Technique	47
Software Reuse	804	Temperature	644
Solar Charger	735	Temperature Affect	877
Sound Level Limits	183	Temperature/Strain Cross-Sensitivity	898
Sound Radiation	183		
Sound Transmission	194	Tennis	47
Southern Daqing Placanticline	23	Test Research	840
Sparse Approximate Inverse	610	Test Technology	401
Spatial Analyses	615	Texture Mapping	553
Spatial Data	615	Thermal Distortion	223
Speed	579	Thermal Treatment	40
SPH	799	Three-Degree-of-Freedom Step Motor	893
SSH	721		
Starch	423	Three-Ring Gear Reducer	87
Starting Characteristics	830	Threshold	148
State Test	534	Tight Sandstone	301
Static Excitation Regulator	154	Time-Interleaved Parallel Sampling	862
STC89C516RD+	684		
STC89C54	177, 625	Time Reversal Mirror	188
Steady State	786	Tms320c5410	717
Strength	272	Torsion Spring	161
Strong Seismic	327	Torsional Strength	306
Structural Failure	851	Touch Screen	669
		Training Kit	649

Transformation	430	Water Spraying	287
Transformer	148	Wave	227
Transmission Line	659	Waveguide	227
Transverse	165	Wavelet Threshold Denoising	148
Triangular Grid Unit	944	Wavelet Transform (WT)	375
Truth-Table	775	Wear	130
Turbid Water Experiment	282	Whispering Gallery Modes	92
Turbine Generators	67	WIFI	605
Turbo-Generator	76	Wind Farm	445
Turbulence Model	102	Wind Power Connection	417
Two Cavity	173	Wireless Alarm	659
Two-Speed CAN BUS	591	Wireless Monitor	543
		Wireless Video Monitoring	605
U		Wood Manufacture	390
Ultra-High Speed Data Acquisition	862	Work Piece Plate	455
Ultrasonic	867	Y	
Ultrasonic Sensor	877	Yield	423
Ultrasonic Vibration	520	Z	
Ultraviolet Mutagenesis	520	Zero Sequence Current	254
Unsafe Event	475	Zero-Sequence Voltage	254
Upgrade	292		
Urban Grid	464		
Urban Planning	464		
USB	669		
V			
Variator	200		
Vector Control	893		
Vegetation “Flexible Dam”	282		
Vehicle	872		
Vehicle Navigation System	749		
Vertical Type Stereo Garage	52		
Vibration Suppression	165		
Video Processing	909		
Videos Monitor	558		
Virtual Cutting	944		
Virtual Passive	903		
Virtual Physics Experiment Teaching System	664		
Virtual Reality	664		
Visual Aesthetic Feeling	343		
Visual Simulation	799		
Viterbi Algorithm	208		
Volume of Fluid (VOF) Model	386		
vxWorks	669		
W			
Water Purification Material	17		

Authors Index

A

Ao, M.Y. 924

B

Bai, H. 108

Bian, C.R. 301

Bu, W.X. 625

C

Cai, T. 584

Cao, J. 7

Cao, K.N. 259

Cao, X.L. 315, 690

Cao, X.Z. 173

Chang, Y.S. 219

Chen, C.Y. 872

Chen, G.S. 735

Chen, H.A. 244

Chen, H.F. 23

Chen, H.L. 23

Chen, J.X. 333

Chen, L. 654

Chen, L.L. 282

Chen, Q.H. 929

Chen, R. 276

Chen, S.J. 664

Chen, S.L. 165

Chen, T. 749

Chen, X. 136

Chen, Y. 460, 491

Chen, Y.J. 929

Chen, Y.L. 862

Chen, Z.Y. 625

Cheng, J.M. 553

Cheng, W.D. 867

Cheng, W.M. 440

Cheng, Y. 527

Chu, X.J. 320

Cui, H.P. 436

Cui, Y. 227

D

Deng, H. 740

Deng, H.Y. 76

Deng, J.X. 495, 500

Ding, K.W. 311

Ding, M.C. 200

Ding, X. 200

Du, L.Y. 579

Du, S.G. 436

Du, W.Z. 440

F

Fan, D.H. 786

Fan, Y.H. 605

Fan, Z.J. 495, 500

Fang, H. 799

Fang, X.M. 909

Fang, Z. 92

Fu, G.C. 469

G

Gan, D.Q. 407, 412, 558, 809

Gan, S. 615

Gao, C. 469

Gao, L. 102

Gao, P. 721

Gao, W.L. 63

Gao, X.B. 909

Gao, X.C. 515

Gao, Y.Y. 749

Ge, Z.Y. 620

Geng, J.M. 254

Gong, H.W. 227

Gong, T. 591

Gong, W.Q. 520

Gu, J.X. 625

Gu, X.K. 893

Gu, Y.F. 244

Guo, B. 31, 136

Guo, F.Q. 31, 914

Guo, H.P. 669

Guo, J. 407, 412, 558, 809

Guo, Y. 188, 436

Guo, Z.J. 97

H		Jing, X.H.	12
Han, D.	395	Ju, S.G.	584
Han, W.H.	792	K	
Hao, B.	40	Ko, I.C.	649
He, C.X.	27	Kong, J.G.	475
He, L.L.	856	Kou, W.L.	615
He, R.	213	Kou, Z.L.	130
He, W.	451	L	
He, X.	749	Lee, C.H.	882
He, X.H.	102	Lee, C.Y.	505
He, Y.Z.	684	Lee, J.M.	649
Hou, C.G.	620	Lei, S.M.	520
Hou, X.W.	161	Lei, W.L.	605
Hu, C.D.	538, 562	Li, B.	856
Hu, C.L.	771	Li, B.L.	919
Hu, C.Q.	856	Li, C.G.	254
Hu, D.M.	944	Li, G.L.	527
Hu, H.Y.	596, 760	Li, G.S.	348
Hu, N.N.	259	Li, H.	348
Hu, R.Z.	786	Li, H.B.	527
Hu, Y.Z.	451	Li, H.G.	436
Hua, Q.Y.	219	Li, H.R.	52
Huang, C.F.	872	Li, H.T.	366, 644
Huang, C.M.	276	Li, J.Y.	568
Huang, H.C.	306	Li, M.	669, 840
Huang, H.H.	649	Li, N.	67
Huang, M.C.	649	Li, P.	272
Huang, M.L.	464	Li, P.H.	495, 500
Huang, S.H.	935	Li, P.J.	244
Huang, X.L.	534	Li, Q.	3
Huang, Y.H.	430	Li, R.	486, 568
Huang, Y.J.	630	Li, R.Q.	130
Huang, Y.X.	451	Li, S.	52, 780
J		Li, T.	395
Ji, M.F.	52	Li, T.X.	17
Ji, X.Y.	82	Li, T.Y.	375, 381
Jia, H.B.	725	Li, W.D.	760
Jia, J.L.	412	Li, W.H.	659
Jia, M.H.	227	Li, X.H.	725
Jia, Y.	792	Li, X.M.	491
Jia, Y.B.	491	Li, X.Z.	423
Jiang, M.R.	188	Li, Y.	40, 87, 130, 296
Jiang, S.X.	17	Li, Y.H.	610
Jiang, X.S.	401	Li, Y.J.	119
Jiang, Y.L.	635	Li, Y.M.	929
Jiao, R.	654	Li, Y.X.	464
Jin, L.H.	644		

Li, Y.Y.	31	Luan, Z.Y.	244
Li, Y.Z.	939	Luo, F.L.	481
Li, Z.G.	102	Lv, D.H.	267
Liang, H.	31	Lv, S.Y.	862
Liang, X.X.	548, 579	Lv, W.Q.	451
Liao, J.Q.	654		
Liao, P.S.	882	M	
Lin, E.L.	745	Ma, J.	579
Lin, M.H.	276	Ma, J.R.	333
Ling, Q.	188	Ma, L.	282
Ling, Y.C.	775	Ma, R.X.	423
Liu, C.L.	130	Ma, Z.	141
Liu, C.Y.	649, 872	Ma, Z.Q.	445
Liu, D.C.	40	Ming, P.S.	635
Liu, F.	282, 792	Mou, S.Z.	395
Liu, H.	475		
Liu, H.B.	102	N	
Liu, J.	366, 725	Nie, W.	440
Liu, J.C.	635	Ning, B.	386
Liu, J.P.	939	Niu, D.J.	584
Liu, K.	327	Niu, X.	830
Liu, L.	259		
Liu, M.L.	141	O	
Liu, Q.L.	893	Ou, Y.H.	401
Liu, S.Z.	130	Ouyang, C.	460
Liu, T.	370, 721		
Liu, T.L.	82, 510	P	
Liu, W.	370, 771	Peng, B.J.	92, 898
Liu, W.C.	423	Peng, F.	223
Liu, W.D.	136	Peng, Y.F.	223
Liu, W.H.	401		
Liu, W.J.	740	Q	
Liu, X.P.	568	Qian, H.B.	401
Liu, Y.	799	Qian, L.	780
Liu, Y.L.	745	Qiu, Z.G.	601
Liu, Y.X.	12, 232	Qu, L.C.	301
Liu, Y.Y.	12, 141, 804		
Liu, Z.G.	208	R	
Liu, Z.M.	538	Ren, C.	558
Liu, Z.X.	348	Ren, F.S.	165
Lu, C.D.	640	Ren, X.C.	605
Lu, D.R.	27		
Lu, G.P.	620	S	
Lu, H.Y.	903	Shao, W.M.	644
Lu, I.T.	505	Sheng, P.	538, 562
Lu, J.	188	Sheng, X.L.	188
Lu, Y.	208	Shi, L.M.	183, 194
Lu, Y.P.	76		
Lu, Y.X.	58		

Shi, S.Q.	7	Wang, L.J.	730
Shi, X.L.	531	Wang, L.P.	348
Shi, X.P.	531, 534	Wang, L.S.	659, 730
Shi, Y.J.	82	Wang, M.Q.	436
Shiau, Y.C.	276, 505	Wang, P.F.	760
Song, J.	840	Wang, Q.	71
Song, J.H.	700	Wang, R.C.	213
Song, M.	259	Wang, W.	717
Su, X.P.	161	Wang, W.D.	259
Sun, B.Y.	856	Wang, X.	822
Sun, L.	765	Wang, X.F.	469
Sun, L.N.	760	Wang, X.J.	690
Sun, S.B.	799	Wang, X.S.	386, 877
Sun, S.M.	527	Wang, X.T.	674
Sun, Y.	82	Wang, X.W.	856
Sun, Z.	108	Wang, Y.	272
		Wang, Y.J.	725
T		Wang, Y.K.	817
Tan, H.F.	12	Wang, Y.Q.	780, 830, 914
Tan, J.	407, 412, 558, 809	Wang, Z.	851
Tan, P.	817	Wang, Z.M.	76
Tan, S.B.	635	Wang, Z.Y.	35
Tang, L.	76	Wei, C.G.	548, 579
Tang, W.	370	Wei, G.H.	282
Tang, Y.B.	893	Wei, H.J.	114
Tao, L.F.	745	Wei, H.M.	510
Tao, Z.H.	451	Wen, Y.Q.	579
Tsai, C.I.	505	Wu, D.	898
Tschopp, M.A.	7	Wu, G.Z.	92
		Wu, H.W.	898
		Wu, J.H.	40
W		Wu, W.B.	630
Wan, Y.	227	Wu, W.C.	92
Wang, B.	401	Wu, W.G.	929
Wang, D.	154, 401	Wu, X.B.	177
Wang, D.D.	259	Wu, Y.S.	361
Wang, D.H.	333	Wu, Z.	835
Wang, E.W.	520		
Wang, F.Y.	659	X	
Wang, G.Z.	515	Xi, D.H.	730
Wang, H.	845	Xi, Q.	370
Wang, H.N.	161	Xian, X.P.	705
Wang, J.	287	Xiao, D.S.	23
Wang, J.P.	711	Xie, H.B.	114
Wang, J.S.	423	Xiong, X.	640
Wang, J.Y.	292	Xu, F.	82, 92, 898
Wang, K.F.	553	Xu, H.	451
Wang, L.	92, 259, 445, 721, 898	Xu, K.	92
		Xu, Q.Y.	208

Xu, T.F.	287, 296	Zhang, J.	919
Xu, X.F.	47	Zhang, J.B.	786
Xu, X.H.	366	Zhang, J.D.	771
Xue, W.D.	451	Zhang, L.	200, 721, 799
		Zhang, L.S.	491, 867
Y		Zhang, R.	130
Yan, C.Z.	460	Zhang, X.	390, 510
Yan, G.B.	407, 412	Zhang, X.A.	486
Yan, H.	287, 296, 591, 596	Zhang, X.B.	52
Yan, J.	436	Zhang, X.D.	538, 562
Yan, J.X.	223	Zhang, X.H.	249, 440
Yan, X.Z.	130	Zhang, X.L.	249
Yang, A.H.	141	Zhang, X.M.	7
Yang, D.F.	417	Zhang, X.P.	679, 695
Yang, H.	395	Zhang, X.Q.	543
Yang, J.C.	893	Zhang, X.X.	386
Yang, J.L.	440	Zhang, Y.	148, 259, 311
Yang, M.Y.	395	Zhang, Y.J.	755
Yang, S.Q.	630	Zhang, Y.S.	491
Yang, S.Z.	353	Zhang, Z.Q.	58
Yang, X.Q.	338	Zhang, Z.T.	531
Yang, Y.	227	Zhang, Z.Y.	893
Yang, Y.G.	343	Zhao, X.F.	249
Yao, J.	237, 573	Zhao, Y.J.	845
Yao, X.L.	809	Zhao, Y.Z.	538, 562
Yao, Z.G.	165	Zheng, D.Y.	136
Yin, M.	455	Zheng, X.Y.	475
You, F.C.	148	Zhong, W.	620
Yu, J.B.	213	Zhou, G.	440
Yu, M.	27	Zhou, H.L.	333
Yu, S.F.	534	Zhou, J.	495, 500
Yu, W.W.	674	Zhou, S.M.	259
Yuan, L.M.	903	Zhou, S.Q.	417
Yuan, L.P.	903	Zhou, Y.	944
Yuan, M.	721	Zhou, Y.N.	887
Yuan, R.M.	386	Zhu, C.	87
Yuan, S.	527	Zhu, J.C.W.	92
Yuan, X.P.	615	Zhu, J.H.	445
Yuan, Z.J.	740	Zhu, S.K.	124
		Zhu, Y.	690
		Zou, Y.C.	17
Z		Zuo, Q.L.	515
Zeng, X.C.	292	Zuo, X.Q.	232
Zhan, M.	395		
Zhan, Y.Z.	584		
Zhang, B.T.	154		
Zhang, D.G.	370		
Zhang, G.	333		
Zhang, H.	27		